2022 TAPPI Journal Yearbook



TAPPI JOURNAL

Copyright© 2023 by



TAPPI PRESS
15 Technology Parkway South, Suite 115
Peachtree Corners, GA. 30092 U.S.A. www.tappi.org
All rights reserved

The Association assumes no liability or responsibility in connection with the use of this information or data, including, but not limited to, any liability or responsibility under patent, copyright, or trade secret laws. The user is responsible for determining that this document is the most recent edition published.

To obtain copyright permission to photocopy pages from this publication for internal or personal use, contact Copyright Clearance Center, Inc. (CCC) via their website at www.copyright.com. If you have questions about the copyright permission request process, please contact CCC by phone at +1-978-750-8400.

ISBN: 978-1-59510-331-4
TAPPI PRESS Item Code: TJYB22EL
Printed in the United States of America

Please note: The following TAPPI Journal pages are sequenced chronologically according to publication order. Therefore, you can expect breaks in page numbering, as time sensitive, full-page advertisements have been removed for your convenience.



Welcome to the 2022 *TJ* Yearbook

As global recovery continued during 2022, our scientific and academic communities were able to more easily collaborate and share knowledge with each other and the industries they serve. These talented researchers have always known that pulp, paper, tissue, and packaging are "critical industries"—and we are lucky to have them continuing to innovate on our behalf.

To support this important work, we publish *TAPPI Journal* (*TJ*), TAPPI's flagship research publication. In 2022, *TJ* officially adopted its 100 percent Open Access publication model to improve the accessibility of published articles, increase researcher engagement, and boost the visibility of our industry's research community. This format also helps researchers meet their funding and grant application requirements. As always, copyright remains with the author and, unlike other technical journals, *TJ* does not require a publication fee.

This annual *TAPPI Journal* (*TJ*) yearbook helps us bring 11 issues' worth of scientific research, along with other valuable resources, to you and every TAPPI member. We hope you find it useful. In 2022, *TJ* technical papers shared new findings on pulping, tissue, paper physics, the recovery cycle, nanocellulose, coatings, and much more.

To help attract high-quality research, all accepted papers are eligible for the Honghi Tran *TAPPI Journal* Best Research Paper Prize, presented annually at TAPPICon. This US$2,000 cash prize is endowed by Professor Emeritus Honghi Tran, Ph.D., of the University of Toronto, author or co-author of more than 80 *TJ* papers. From the January 2022, issue, editors selected **"Microbial load and proliferation associated with various face mask types and sources during the COVID-19 pandemic"** by Srinivasan Narasimhan, Meenashree Balakrishnan, Olukayode James Ayodeji, and Seshadri S. Ramkumar—the first time ever that a Nonwovens-focused paper received this honor. From the November special issue on Coating, editors selected **"Review of coating cracking and barrier integrity on paperboard substrates"** by Joel C. Panek and Peter W. Hart. *TJ* Editorial Board member Steve Ottone calls it "a great starting point for anyone looking to develop sustainable packaging solutions."

TAPPI has introduced a new TAPPI Journal Research Ambassador Program. TJ Research Ambassadors are companies that show their support of scholarly activity, research and innovation within the industry through advertising and sponsored content in the Journal.

When we combine the expertise of our members, the passion of our volunteer leaders, and the dedication of our TAPPI staff, we can achieve so much. Here is just a small sample of what else TAPPI accomplished this past year:

- **TAPPICon** returned to an annual, fully in-person format in 2022 with a successful event in Charlotte, NC. More than 1,400 mill and other professionals gathered to enjoy a robust technical

session and a sold-out exhibit floor. TAPPICon also included The Women in Industry Division's first in-person Women's Summit, with outstanding results.

- **TAPPI Press** released *Chemical Recovery in the Alkaline Pulping Processes, Fourth Edition*. Written for engineers, technicians, and industry newcomers, this completely updated book covers the entire liquor cycle. Editor Peter W. Hart, TAPPI Fellow and director, research and innovation for WestRock, worked with a team of subject matter experts to bring together this highly useful guide.

- With support from our Corrugated Division members and the Corrugated Packaging Council (CPC), **we expanded *Paper360°* magazine to include a new CorrFocus section.** This section provides informative articles and technology updates to the corrugated industry, augmenting TAPPI's already robust content delivery to this sector.

- **Technical Information Papers** (TIPs) this year. Our enhanced communications and reporting for volunteers helped sustain interest in **Standard Specific Interest Groups** (SSIGs) and the opportunities they offer members.

- TAPPI continues to build and expand on **diversity, equity, and inclusion (DEI) efforts** by launching a DEI Scholarship for underrepresented students interested in a career in the paper, packaging, or converting industry. The PIMA Division also formed its new DEI Committee to promote the engagement of a more diverse workforce for a more sustainable industry.

- With more than 120 facilities using more than 170 courses, **TAPPISAFE** has now served **more than 250,000 students** representing over 10,000 different vendors and contractors. The enhanced TAPPISAFE website continues to support this impactful growth.

- The **TAPPI Standards** team updated **174 Standards** and helped streamline the process for upcoming reviews by completing the rosters for 225 Standard Specific Interest Groups (SSIGs). By the way, there's always room for more in the review process—we'd love your participation.

These highlights merely scratch the surface of all we accomplished together in 2022. One thing is clear: from R&D to DEI, from standards to safety, the work our members do accomplishes so much for our critical industries, with far-reaching benefits around the world.

Now more than ever, TAPPI is ready to keep you connected to our amazing industry. I hope you find much in these pages to help you and your company learn and innovate through 2023 and beyond. I welcome the opportunity to meet more of our members in person and I look forward to learning how TAPPI can support your professional growth—we are Better Together.

Sincerely,



Larry N. Montague
TAPPI President & CEO

TAPPI JOURNAL RESEARCH AMBASSADOR PROGRAM

Amplify Your Company's Commitment to Scientific Research

Become a *TAPPI Journal* Research Ambassador

As a *TAPPI Journal (TJ)* Research Ambassador, your support helps bring immediate, free access to the most current and relevant scientific developments, processes and products in the pulp and paper industry, as well as related fields such as nanocellulose, biorefinery and nonwovens to industry innovators, TAPPI members, universities, industry organizations, and research institutions.

TJ Research Ambassadors support scholarly activity, innovation, and the sustainability of the industry through advertising and sponsored content in the Journal. The program is flexible, allowing companies to share their support and expertise through publishing white papers and case studies on cutting-edge research, as well as ad placement in the Journal. Publishing your content in *TJ* educates *TJ* readers on the benefits of using your product or service, while also designating your company as a supporter of innovation to industry leaders.



BECOME A RESEARCH AMBASSADOR BY CHOOSING THE OPTION THAT BEST FITS YOUR STRATEGY

1. Purchase 3 full-page ads in *TJ*
2. Purchase a Sponsored Content placement, choosing either 1 White Paper or 1 Case Study placement
3. Include a *TJ* ad placement in your overall TAPPI media buy (minimum of $10K total spend)

Then, prominently display the official Research Ambassador digital badge on your company website and marketing collateral to further demonstrate your company's commitment to the future of the industry, whether it's pulp, paper, tissue, packaging, nonwovens or converting.

MORE WAYS YOU'LL BENEFIT:

PROMINENT VISIBILITY

TJ is easily found on TAPPI.org attracting an average of 24K visitors per month. Also indexed by academic and corporate libraries.

REACH

Delivered digitally to TAPPI members and more than 25k industry professionals 11 times per year.

OPEN ACCESS

Your support enables readers to gain free, timely access to impactful research and technical reviews from an internationally recognized source.

SOCIAL MEDIA

In addition to the exposure in the issue, *TJ* Research Ambassadors will also be recognized on TAPPI's social media outlets.

For more information on the Research Ambassador program, contact Shane Holt at sholt@naylor.com, 352-333-3345, or view the media kit at tappi.org/tjmediakit.

BLEACHING

Using bleaching stage models for benchmarking softwood ECF bleach plants

By: Brian N. Brogdon

July, pp. 353 – 362 Steady-state bleaching delignification and brightening models were used to gauge how well elemental chlorine-free (ECF) bleach plants were using chlorine dioxide to bleach 25-kappa softwood brownstocks.

Case 1 examined the $D_0(EOP)D_1$ portion of Mill 1's five-stage sequence that brightens the pulp to 86% ISO. Case 2 studied the $D_0(EO)D_1$ portion of Mill 2's four-stage sequence, which brightens the pulp to 82% ISO, and Case 3 re-examined the same bleach plant several years after it made improvements around the extraction stage. The models highlighted days in the previously mentioned cases where high bleach usage occurred, presumably because of high brownstock and/or extraction washer carryover, and days where bleach usage was normal. In Case 2, the model estimated that 10 kg of the 44 kg chlorine dioxide/metric ton pulp consumed in bleaching was likely reacting with washer carryover sources; approximately two-thirds of this extra consumption was assumed to be reacting with extraction filtrate. Changes that Mill 2 made (Case 3) reduced the unproductive chlorine dioxide usage from 10 to 5 kg/metric ton pulp. When the delignification and brightening models were simultaneously solved, the models predicted somewhat different optimized distributions of chlorine dioxide to D_0 and D_1 vs. actual values used in bleach plants. However, the forecasted chlorine dioxide totals agreed with the actual values when washer carryover sources were considered. This study showed the bleaching models could be used as hypothetical benchmarks for softwood ECF bleach plants.

Application: Multistage models are used to identify how much chlorine dioxide is being used inefficiently, which can infer how much brownstock and/or extraction washer carryover is occurring with $D_0(EO)D_1$ or $D_0(EOP)D_1$ sequences. The models can show if brownstock and/or extraction washing is problematic, or if certain shower water sources at the washers are beneficial or detrimental to overall bleach usage.

Brogdon is president of Future Bridge Consulting Services LLC in Marietta, GA, USA. Email Brogdon at Brian.Brogdon@gmail.com.

CELLULOSE

Ultrastructural behavior of cell wall polysaccharides

By: Dietrich Fengel

April, pp. 219 – 225 Studies on the behavior of wood polysaccharides inside and outside the cell wall were carried out under varying conditions using the electron microscope in combination with physicochemical methods to gain new information on the super-molecular structure of the polysaccharides. Several fractions containing different polyoses were obtained by fractionation of the alkali extract of holocellulose. Isolated polyoses are at least partially able to arrange themselves in fibrillar elements. After delignification, the cellulose is recognizable within the cell wall as microfibrils with an average diameter of about 250 Å. However, these fibrillar units seem to be rather treatment. After partial hydrolysis, isolated cellulose shows more subunits about 30 Å in diameter at higher magnification. Moreover, the more sensitive portions of the fibrils in the longitudinal direction are attacked by partial hydrolysis, and these portions seem to grow with increasing duration of the hydrolysis. Fractionation of cellulose isolated from thermally treated wood shows that the chain fragments are multiples about 300 Å in length. A tentative model of the supermolecular arrangement of the cellulose in relation to the other cell wall components is presented.

The effect of component removal upon the porous structure of the cell wall of wood. II. Swelling in water and the fiber saturation point

By: J.E. Stone and A.M. Scallan

May, pp. 283 – 288 The fiber saturation point is defined as the amount of water contained within the water-saturated cell wall. Previous techniques for the determination of the fiber saturation point of wood and pulp fibers are criticized and it is suggested that the values of about 0.3 g/g frequently quoted in the literature are too low. Two entirely independent methods for finding the true fiber saturation point are presented and the results by both methods are in agreement. The fiber saturation point of air-dried and re-swollen black spruce wood was found to be 0.4 g/g rising to 1.2 g/g as the wood was pulped by the kraft process to progressively lower yields. A method of calculating the relative changes in water-swollen cell wall thickness from changes in the fiber saturation point is given, and the changes brought about by kraft pulping are calculated and discussed in terms of cell wall structure.

The influence of the fine structure of cellulose on the action of cellulases

By: Curtis S. Walseth

June, pp. 335 – 340 In the hydrolysis of cellulose with enzymes of *Aspergillus niger* at 47°C., it was shown that a great decrease in the rate occurred in the late stage of the reaction, usually with considerable cellulose still remaining undissolved. The most important factor contributing to this lowered rate was shown to be a decrease in the reactivity of the residual cellulose during the course of the reaction, but the activity of the enzyme solution itself decreased somewhat during the course of the reaction. Inactivation of the enzyme by heat and inhibition by the presence of glucose were both shown to contribute to the loss in activity, with the former being somewhat more important. As the enzymic hydrolyses progressed the moisture regain values for the undissolved residues decreased. This is evidence that amorphous regions were attacked most rapidly and that this preferential removal of amorphous cellulose was the reason for the decrease in reactivity of cellulose noted during the course of the enzymic hydrolysis. The relative content of amorphous cellulose, as indicated by moisture regain values, was shown to be the main factor which could account for the great differences that were observed in the ease and extent of decomposition of various celluloses by enzymes. A striking difference between the nature of acid and enzyme hydrolysis of cellulose was detected. By means of enzymic treatment, it was found possible to dissolve a considerable portion of a cellulose sample, but still to retain a relatively high degree of polymerization in the residual cellulose, whereas an acid hydrolysis, which results in any appreciable loss in weight, decreases the degree of polymerization of undissolved cellulose to a very low level. The most likely explanation for the difference lies in the relative size of the two hydrolytic agents and their consequent ability to penetrate the cellulose fine structure.

Investigation of the cellulose-water relationship by the pressure plate method

By: A.A. Robertson

July, pp. 387 – 392 The water properties of papermaking fibers have been investigated by a "pressure plate" technique which permits a measurement of equilibrium moisture contents of pulp samples at precisely controlled relative vapor pressures between 0.99 and 1.00. This range encompasses the water contents of interest in papermaking from the table to the middle of the drier section. Water retention isotherms are drawn and are satisfactorily related to desorption isotherms which have been reported in the literature. Isotherms for a variety of pulps are reported. These are related to the papermaking properties of the fibers

and show the effects of wood species, cooking method, pulp yield, bleaching, drying, and beating on the cellulose-water relationship.

COATING

Review of coating cracking and barrier integrity on paperboard substrates

By: Joel C. Panek and Peter W. Hart

November, pp. 589 – 603 Barrier packaging formats are major growth areas for the pulp and paper industry. It is technically challenging to maintain barrier properties during converting and end-use applications. Improved manufacturing capabilities and coating formulation knowledge will help maintain barrier integrity and enable growth of barrier products in challenging applications. These improvements will accelerate product development and commercialization and allow faster response to product performance issues such as cracking.

The literature on coating cracking provides knowledge mostly on the effects of coating formulations and to a lesser extent on substrate effects. Despite a large number of publications dedicated to coating failures, the approach to improve coating cracking remains empirical, and the transferability between studies and to real life applications has not been well established. Model development that successfully predicts commercial performance is in its infancy. However, some of these simplified models do a fairly good job predicting experimental data. The current work reviews the state of understanding as regards coating and barrier cracking and highlights the need for more research on cracking and barrier integrity.

Application: Through this review, readers will learn more about coating cracking and the current state of knowledge on the topic. This can be used to guide product development and fundamental research.

Panek is senior principal R&D scientist and Hart is director, Fiber Technology and Innovation, at WestRock in Richmond, VA, USA. Email Panek at joel.panek@westrock.com.

Modeling the influence of rheology on smooth rod coating systems

By: John A. Roper III, Douglas W. Bousfield and Gregory W. Welsch

November, pp. 605 – 614 Rod coating methods are of interest for the application of barrier coatings, especially at off-line facilities that may run at moderate speeds and narrow web widths. At lower line speeds and lower coating solids, it is difficult to achieve good coat weight control because of poor loading of the rod. While there is extensive literature available about blade and roll coating, there seems to be less reported on the rod loading of smooth rods to obtain various coat weights. Much of the work is around metering rods working on applicator rolls at high speeds that are associated with the metered size press, with a focus on ribbing instabilities. This work employs a simplified model, neglecting some complex features of rubber deformation and film split, to estimate the influence of the process parameters such as speed, rod diameter, viscosity, and rod loading on the coat weight obtained. As found in practice, at low speed and low viscosities, the coat weight-load curve is steep, leading to poor control of the coat weight and coat weight uniformity. If the viscosity is increased, the curve is modified, and control is possible with rod loading in a normal range. For shear thinning fluids described by the Carreau model, the power law index and other parameters need to be in the correct range to obtain the desired effect. Modeling predictions show a steeper dependence of coat weight with rod pressure when compared to pilot coater data. This may be caused by missing details in the mechanical loading of the rod related to tube pressure or from neglecting the impact of filter cake formation of the applied coating in the model.

Application: The model and experimental results should help guide the smooth rod coating of paper grades, especially for barrier coatings applied off line.

Roper is Fellow/consultant at PaperCote LLC in Midland, MI, USA. Bousfield is Calder professor in the Paper Surface Science program, Department of Chemical and Biomedical Engineering, at the University of Maine in Orono, ME, USA. Welsch is Global Innovation Leader for the Latex Binders Business at Trinseo LLC in Midland, MI, USA. Email Roper at jaroperiii@gmail.com.

Coatings for sustainable paper-based flexible packaging: Barrier properties and processability

By: Hanze Ying, Luqing Qi, Dave Malotky, Joseph Harris, Bernhard Kainz, Ray Drumright, William Liechty and Jonathan Mason

November, pp. 617 – 622 In this study, the use of waterborne barrier dispersions from trademarked BLUEWAVE Mechanical Dispersion Technology as thin coatings for paper-based flexible packaging was investigated. Prototypes were designed and examined for their performance in process, rheology, barrier, heat-seal/hot-tack, and coefficient of friction (CoF). Compositional details such as the type and amount of base resins and dispersants were found to significantly impact performances and were key to the development of new prototypes that deliver the performance profiles for implementation in paper-based flexible packaging applications.

Application: This paper describes a waterborne coating solution with good liquid/gas barrier, high heat-seal/hot-tack, and low CoF. It was designed and tailored for paper-based flexible packaging applications.

Ying is associate research scientist in the Department of Coating Materials at Dow Inc. in Midland, MI, USA. Qi is associate research scientist, Malotky is senior research scientist, and Harris is R&D/TS&D technologist in the Department of Core Research and Development at Dow Inc. in Midland, MI, USA. Kainz is principle TS&D scientist in the Department of Coating Materials at Dow Inc. in Rheinmünster, Germany. Drumright is senior R&D/TS&D Fellow in the Department of Coating Materials at Dow Inc. in Midland, MI, USA. Liechty is senior R&D/TS&D leader in the Department of Coating Materials at Dow Inc. in Collegeville, PA, USA. Mason is associate R&D/TS&D director in the Department of Coating Materials at Dow Inc. in Midland, MI, USA. Email Ying at hying@dow.com.

Novel test method for measuring defects in barrier coatings

By: Dustin Burton, Don Ventresca and Gregory W. Welsch

November, pp. 625 – 643 In the last several years, activity to develop water-based barrier coatings (WBBCs) that meet challenging packaging performance requirements has increased dramatically. Cellulose-based packaging solutions can provide a more sustainable packaging option for replacing single-use plastic-based options like extrusion-based and laminated materials. An advantage of WBBCs is the opportunity to reduce the coating thickness applied, as long as the barrier requirements can be met. A challenge that must be overcome is the ability to maintain a defect and pin-hole-free coating layer after coating and drying to retain the barrier performance. Many formulation and coating parameters can affect the barrier coating layer quality; however, methods for detecting more subtle differences in these types of studies are not widely available.

Work was carried out to develop a quantitative technique for detecting and measuring the quantity and size of defects in the barrier coating layer. A test method has been developed using a combination of dyed oil and image analysis to be able to characterize the imperfections in the coating surface. The use of dyed oil serves two purposes. First, it better simulates the types of materials, in this case, oils and grease, for which the barrier

coating is expected to hold out. Second, it also provides contrast between the coating and failure points for testing.

An image analysis technique is employed to characterize the number and size of the imperfections. For the former, it reduces the testing time required if a quality control or laboratory technician counts the dots. For the latter, it assists with judgment on the source of the root cause of the imperfection, such as base sheet defects, coating dispersion issues, or perhaps micro-blisters in the coating, as some examples.

To show the benefit of this technique, several pilot coating studies were designed to see if the new technique could be utilized to detect differences in WBBC performance. Both process and chemical variables were evaluated. With refinement, it is believed this technique can be utilized in development work, as well as for a potential quality control technique for manufacturing of coated paper and paperboard products

Application: With the refutation of many current oil and grease resistance (OGR) test methods, it was time to develop a more accurate and easily administered test. The test technique described here is easier to administer, provides the user with better data, and allows the user to better see and identify defects in coated paper that has been exposed to oil and grease.

Burton is senior research technologist and Welsch is Global Innovation leader for Trinseo LLC in Midland, MI, USA. Ventresca is technical service and development specialist for Trinseo LLC in Petrolia, ON, Canada. Email Burton at DBurton@trinseo.com.

Improvements in oil and grease resistance (OGR) test methodology for waterborne barrier coatings

By: Allyson Marianelli, Brian Einsla, Elizabeth Snow, Samantha Woodfin, Bo Shuang, Kevin Henderson, Mike Linsen, Jonathan Derocher and Shaun Oliver

November, pp. 645 – 651 Paper-based food packaging is becoming more popular due to consumer demands for sustainable packaging options. Waterborne paper coatings that provide performance properties (i.e., resistance to oil and grease) not inherent to paper and board substrates offer improved sustainability profiles over earlier paper treatment options, including fluorocarbon treatment and coating with extruded plastics. The continued development of new paper coating technologies requires re-evaluation of current test methods and development of new methods to ensure lab evaluations can serve as accurate predictors of real-world performance.

This paper provides an overview of commonly used oil and grease resistance (OGR) test methods within the paper coatings industry, and then describes improvements and developments made to two key methods: the 3M Kit test and an internally developed oil breakthrough test. The combined use of these adapted methods provides a more efficient testing workflow and a more complete understanding of the OGR performance of barrier coatings.

Application: The development of new barrier coatings for paper packaging requires robust and quantitative methods for performance evaluation. This paper reviews industry standard oil and grease resistance (OGR) test methods and describes improvements to two key methods: the 3M Kit test (TAPPI Standard Test Method T 559) and an internally developed oil breakthrough test.

Marianelli is associate research scientist, Einsla is senior research scientist, Snow is R&D/TS&D technologist, Woodfin is senior R&D/TS&D technician, Henderson is senior TS&D scientist, Linsen is senior TS&D specialist, DeRocher is senior TS&D scientist, and Oliver was a senior R&D/TS&D technician for Dow Coating Materials in Collegeville, PA, USA. Shuang was a research scientist at Dow Polyurethanes in Freeport, TX, USA. Email Marianelli at amarianelli@dow.com.

CORRUGATED BOXES

Edge crush testing methods and box compression modeling

By: Benjamin Frank and Douglas Cash

August, pp. 418 – 433 While multiple test procedures have been developed to assess the inherent compressive strength of corrugated materials (edge crush test, ECT), limited work has explored the appropriateness of each in the context of box compression modeling. This study incorporates a variety of real-world samples, highlighting the varying challenges different ECT methods face in measuring the intrinsic compressive resistance of combined corrugated board. We examine each of these methods as inputs for different types of models, as well as discuss the propagation of measurement variation through the modeling effort. By highlighting the cases in which a given ECT method no longer proves to be an optimal parameter in box compression strength modeling, we explore how we might better measure this material property.

Application: This work highlights the importance of identifying and developing more optimal test methodologies to measure the inherent compressive strength of corrugated materials (ECT).

Frank is director of Materials Research and Innovation for Packaging Corporation of America in Mundelein, IL, USA. Cash is senior data analyst with Norvax LLC in Chicago, IL, USA. Email Frank at bfrank@packagingcorp.com.

DISSOLVING PULP

Preparing prehydrolyzed kraft dissolving pulp via phosphotungstic acid prehydrolysis from grape branches

By: Li Tao, Ma Ying Hua and Zhang Jun Ke

January, pp. 35 – 48 Dissolving pulp was successfully prepared via phosphotungstic acid (PTA) prehydrolysis kraft (PHK) cooking followed by an elementary chlorine-free (ECF) bleaching process from grape branches. The effects of prehydrolysis temperature, reaction time, and PTA concentration that potentially affect the quality of dissolving pulp product on chemical components of pulp were studied via an orthogonal experiment. The structure of lignin was activated during the PTA prehydrolysis phase, and lignin was easily removed during the following cooking process. Thus, relatively mild conditions (140°C, 100 min) can be used in the cooking process. During the prehydrolysis phase, temperature exhibited the most significant influence on the cellulose purity of the obtained pulp fiber, followed by reaction time and PTA concentration. The optimized prehydrolysis conditions were as follows: prehydrolysis temperature, 145°C; reaction time, 75 min; and PTA concentration, 1 wt%. Whether the excessively high prehydrolysis temperature or prolonging the reaction time did not favor the retention of long chain cellulose, the delignification selectivity for the cooking process could not be further improved by excessive PTA loading. Under these prehydrolysis conditions, 94.1% and 29.0% for α-cellulose content and total yield could be achieved after the given cooking and bleaching conditions, respectively. Moreover, the chemical structure and crystal form of cellulose were scarcely changed after PTA prehydrolysis, which could be confirmed by results from Fourier transform infrared (FTIR) spectroscopy and X-ray diffraction (XRD). PTA prehydrolysis could be considered as an alternative method for preparing PHK dissolving pulp under relatively mild cooking conditions.

Application: Phosphotungstic acid prehydrolysis presents an alternative approach for preparing a PHK dissolving pulp product, as well as solving the acid recovery problem during the PHK process.

Li is associate professor, Ma is lecturer, and Zhang is professor at the Institute of Chemical Engineering, Shaanxi Institute of Technology, Xi'an, Shaanxi, China. Email Li at l1tao@163.com.

ENVIRONMENTAL

Utilization of kraft pulp mill residuals

By: Tortsen Meyer

February, pp. 83 – 92 Kraft pulp mills produce on average about 100 kg of solid residuals per metric ton of pulp produced. The main types of mill waste are sludge from wastewater treatment plants, ash from hog fuel boilers, dregs, grits, and lime mud from causticizing plants and lime dust from lime kilns. Of these, about half is disposed of in landfills, which highlights the need and potential for waste recycling and utilization.

Sludge is either incinerated in hog fuel boilers to generate steam and power or used in various forms of land application, including land spreading, composting, or as an additive for landfill or mine waste covers. The majority of hog fuel boiler ash and causticizing plant residues is landfilled. Alkaline residuals can be conditioned for use in land application, manufacture of construction materials, and production of aggregates for road work.

This technical review summarizes residuals utilization methods that have been applied in pulp and paper mills at demonstration- or full-scale, and therefore may act as a guide for mill managers and operators whose goal is to diminish the costs and the environmental impact of waste management.

Application: This technical review provides information about industrial-scale applications of residuals utilization, and therefore may act as a guide for mills that are seeking to implement waste reduction or utilization programs.

Torsten Meyer is senior research associate at the Pulp & Paper Centre, University of Toronto, Toronto, ON, Canada. Email Meyer at torsten.meyer@utoronto.ca.

LIGNIN

Economic and competitive potential of lignin-based thermoplastics using a multicriteria decision-making method

By: Cédric Diffo Téguia, Nima Ghavidel Mehr, Wolfgang G. Glasser and Paul R. Stuart

September, pp. 479 – 494 As a result of new lignin extraction plants hatching and increasing volumes of technical lignin becoming available, a variety of lignin derivatives, including phenolic resins and polyurethane (PU) foams, are reaching the marketplace or being used as intermediate products in many industrial applications. In the spectrum of possible lignin derivatives, thermoplastics appear particularly attractive due to a symbiosis of market, policy, and technology drivers.

To assess the preferredness for lignin-based thermoplastics, this paper adapted a risk-oriented methodology formerly applied to assess lignin usage in various applications (phenol-formaldehyde [PF] resins, PU foams, and carbon fiber applications) to the case of lignin-based thermoplastics using hydroxypropylated lignin (HPL) and miscible blends of lignin and polyethylene oxide (PEO). The HPL is considered for garbage bags and agricultural films applications, while lignin-PEO blends are used as replacement for acrylonitrile butadiene styrene (ABS) in applications such as automotive parts. In the methodology, two phased-implementation strategies were defined for each thermoplastic derivative, considering perspectives for profit maximization (90 metric tons/day integrated units) and revenue growth (350 metric tons/day overall capacity), which were considered for implementation within a softwood kraft pulping mill. A set of six criteria representative of the main economic and market competitiveness issues were employed, and their respective importance weights were obtained in a multicriteria decision-making (MCDM) panel.

Early-stage techno-economic estimates were done as a basis for the calculation of decision criteria. Compared to product derivatives previously assessed, capital investment for thermoplastic strategies appeared marginally higher due to the required lignin modification steps (on average 30% higher at similar capacity, and 6% for higher-scale revenue diversification strategies). Higher operating costs were also observed due to increased chemical expenses for all thermoplastic strategies, which are ultimately balanced by revenues associated with targeted thermoplastic products, leading to greater annual margins and cash flow generation over the project lifetime for thermoplastic strategies compared to other product applications (58% to 66% higher on average, at similar scale). Benefits of improved economics were reflected in economic criteria, internal rate of return (IRR), and cash flow on capital employed (CFCE), as well as in the price competitiveness criterion, CPC. Overall, the combination of relatively high lignin content in the plastic formulation and the less costly modification method contributed to lignin-PEO strategies, gaining the top two rankings. Based on their overall scores, both strategies defined for HPL would also integrate the group of "preferred" strategies, but are outranked by strategies that consider lignin positioning on PU foam applications.

Application: This paper highlights the market and technical drivers for the use of lignin in bio-based thermoplastic products such as garbage bags, agricultural films, and automotive parts. Additionally, the potential preference for such applications is assessed against phenolic resins and polyurethane foams previously studied, using a multicriteria approach.

Diffo Téguia and Mehr are process engineers at Natural Resources Canada, CanmetENERGY, in Varennes, QC, Canada. Glasser is professor emeritus, Sustainable Biomaterials, at Virginia Polytechnic Institute and State University, Blacksburg, VA, USA. Stuart is professor in the Chemical Engineering Department at Polytechnique Montreal in Montreal, QC, Canada. Email Diffo Téguia at cedric.diffo@gmail.com.

NANOCELLULOSE

Nanocellulose–cationic starch – colloidal silica systems for papermaking: Effects on process and paper properties

By: Larden J. Garland, Brandon D. Leib, Nelson A. Barrios and Martin A. Hubbe

October, pp. 563 – 570 Laboratory tests were conducted to better understand effects on the papermaking process and handsheets when recycled copy paper furnish was treated with combinations of nanofibrillated cellulose (NFC), cationic starch, colloidal silica, and cationic retention aid (cPAM; cationic polyacrylamide). Dosage-response experiments helped to define conditions leading to favorable processing outcomes, including dewatering rates and the efficiency of fine-particle retention during papermaking. Effects were found to depend on the addition amounts of cationic starch and colloidal silica added to the system. It was shown that the presence of a polymer additive such as cationic starch was essential in order to achieve large strength gains with simultaneous usage of NFC.

Application: Papermakers can regard NFC as an option for increasing the bonding strength of the resulting paper beyond what generally can be achieved with conventional wet-end additives. However, as shown in the present work, other additives, such as cationic starch and colloidal silica, may be required at suitable levels of addition to achieve the potential benefits of nanocellulose.

Garland and Leib are undergraduate students, Barrios is a graduate student in the Ph.D. program, and Hubbe is a professor in the Department of Forest Biomaterials at North Carolina State University, Raleigh, NC, USA. Email Hubbe at hubbe@ncsu.edu.

Effects of orders of addition in nanocellulose–cationic starch–colloidal silica systems for papermaking

By: Brandon D. Leib, Larden J. Garland, Nelson A. Barrios and Martin A. Hubbe

October, pp. 572 – 579 Two orders of addition were compared when preparing paper handsheets from recycled copy paper furnish in combination with nanofibrillated cellulose (NFC), cationic starch, colloidal silica, and cationic retention aid (cPAM; cationic polyacrylamide). Faster dewatering and higher fine-particle retention were obtained at equal optimized dosages of additives when the colloidal silica was added last, after addition of the cPAM. The same order of addition also provided a higher gain in the paper's tensile strength. However, higher paper stiffness was achieved when the colloidal silica was instead added to the NFC, after its pretreatment with cationic starch. Results were consistent with the principle that papermaking additives added shortly before sheetforming tend to have the largest effects on drainage and retention. The results also demonstrated a sensitivity to the relative dosages of positively and negatively charged additives.

Application: Changing the order of addition of various chemical additives to the papermaking process often can be achieved with near-zero capital investment. The results in this paper provide an example where the order of addition can be expected to have important consequences.

Garland and Leib are undergraduate students, Barrios is a graduate student, and Martin A. Hubbe is a professor in the Department of Forest Biomaterials at North Carolina State University, Raleigh, NC, USA. Email Hubbe at: hubbe@ncsu.edu,

NONWOOD PULPING

Development of reinforced paper and mitigation of the challenges of raw material availability by utilizing Areca nut leaf

By: Kishan K. Jaishwal, Izhar Alam and Chhaya Sharma

September, pp. 469 – 476 Paper industries are facing a raw material crisis and searching for alternate raw materials that may be able to help mitigate the issue. Many industries use agro-waste as a raw material, irrespective of it having low bleachability and poor mechanical strength.

Areca nut leaf (ANL) is a nonwood-based material that may be acceptable as an alternate source of raw material that contains 61.5% holocellulose and 13.6% lignin, which is comparable to other agro-wastes and hardwood pulps. Kraft anthraquinone pulping with 20% active alkali as sodium oxide (Na_2O), 25% sulfidity, and 0.05% anthraquinone produced 15 kappa pulps with about 38.5% pulping yield. The bleachability of ANL pulp was good, and 83.5% ISO brightness could be achieved using the $D_0(EOP)D_1$ bleaching sequence. The ANL fiber has 33.8% better tensile, 54.5% better tear, and 15.2% better burst index than hardwood fiber. Similarly, 60.4% better tensile, 56.5% better tear, and 21.7% better burst index were observed in ANL than in wheat straw. Thus, the study revealed that Areca nut leaf can be used as an alternative raw material for papermaking, as well as to improve the physical property of paper products by blending it with inferior quality pulp.

Application: Areca nut leaf was used in this study as a potential raw material for papermaking, with good pulping and bleachability. The paper properties were also good as compared to other agricultural residues and hardwood pulp, so Areca nut fiber pulp can be used in place of hardwood to improve the physical properties of paper products, as agro-based paper industries are using hardwood pulp to improve its strength.

Jaishwal is a Master's student, Alam is research scholar, and Sharma is professor in the Department of Paper Technology at the Indian Institute of Technology Roorkee, Saharanpur campus, in Saharanpur, Uttar Pradesh, India. Email Sharma at chhaya.sharma@pt.iitr.ac.in.

Utilization of palm fiber as papermaking materials: Microscopic structure and chemical pulping

By: Zhulin Li, Shuai Gao, Lei Tang, Ding Liu, Qun Li, Guoyo Tian and Zhaojiang Wang

October, pp. 543 – 551 The microscopic structure and pulping properties of palm fiber were explored. Soda cooking and sulfate cooking were conducted and compared in terms of physical strength of the obtained pulps. Sulfate pulp showed better performance than soda pulp, as indicated by the 23% higher tensile index, 49% higher tear index, and 36% higher burst index.

To further elevate physical strength, long fibered pulp (LFP), namely commercial softwood sulfate pulp, was mixed with sulfate pulp of palm fiber at levels from 20% to 50%. At the blend level of 50%, tensile index of 52.13 N•m/g, tear index of 15.63 mN•m^2/g, and burst index of 3.42 kPa•m^2/g were attained. The lignin in spent liquor from pulping was isolated and characterized. Soda lignin of palm fiber was mainly composed of guaiacyl and syringyl units, and showed weight-average molecular weight of 3616 g/mol.

Application: We explored the properties of soda pulp and sulfate pulp of palm fiber. Comparison was made with hardwood and softwood pulp in terms of fiber length and physical strength. The reported results suggested the feasibility of palm fiber for papermaking.

Z. Li and Gao are master's degree candidates, Tian is assistant professor, and Wang is professor at the State Key Laboratory of Biobased Material and Green Papermaking, Qilu University of Technology (Shandong Academy of Sciences), in Jinan, China. Tang is technical director and Liu is manager of the Technical Department at Shengquan Group Co. Ltd., in Jinan, China. Q. Li is professor at Tianjin University of Science and Technology in Tianjin, China. Email Wang at wzj@qlu.edu.cn.

NONWOVENS

Microbial load and proliferation associated with various face mask types and sources during the COVID-19 pandemic

By: Srinivasan Narasimhan, Meenashree Balakrishnan, Olukayode James Ayodeji and Seshadri S. Ramkumar

January, pp. 23 – 31 Due to the shortage of personal protective equipment during the COVID-19 pandemic, homemade face coverings were recommended as alternatives. However, the capability of alternative face coverings to proliferate microbes have not been fully documented.

The current study evaluated bacterial load and proliferation associated with the use of common face masks during the COVID-19 pandemic. Mask type-specific and surface-related bacterial load and pattern were noticeable in the study. Results indicated that roadside masks are among samples that contained relatively higher initial bacterial load. The highest

number of bacterial forming colonies were observed in the inner surface of mask samples. Proliferation of microbes over time was also noticeable among the non-certified face coverings included in the study. Sterilization or washing of non-certified fabric face masks before use is recommended.

Application: Apart from protecting the wearer from getting exposed to the infection, face coverings also stop the spread from infected individuals. The present study examined the population of microbes distributed over the mask surface during use. The microbial load on each type of mask, the health, and potential safety risks were highlighted. This information could guide policy and mitigating measures against severe acute respiratory syndrome (SARS) related infections.

Narasimhan is the chairman of Asthagiri Herbal Research Foundation and Meenashree Balakrishnan is a senior scientist at Asthagiri Herbal Research Foundation in Chennai, India. Ayodeji is a Ph.D. candidate and Ramkumar is professor in the Department of Environmental Toxicology at Texas Tech University in Lubbock, TX, USA. Email Ramkumar at s.ramkumar@ttu.edu.

Effectiveness of masks in the suppression of COVID-19 cases during the ongoing pandemic in India

By: Shreyas Ganesh, Mirza M.O. Khyum, Kenneth N. Kikanme and Seshadri Ramkumar

October, pp. 521 – 529 Perhaps the worst predicament faced by humanity in the twenty-first century is the COVID-19 pandemic, which is caused by the SARS-CoV-2 virus. Most parts of the world, including India, went into lockdowns for some period because of the massive increase in cases throughout 2020. Face masks became an important countermeasure for protecting the populace, health professionals, and medics, particularly during the period prior to the mass availability of vaccines.

This study intends to evaluate the effectiveness of face masks in limiting the spread of the virus. The data for the number of COVID-19 cases was analyzed from January 1, 2022, to May 31, 2022, using Python programming. This timeframe involved face mask mandates and no mask requirement, and hence was considered to be ideal for analyzing the usefulness of face masks. A decline in cases during the mandate was observed, while the opposite occurred without the mandate. The outcome of the research showed that face masks are effective additional measures against the spread of SARS-CoV-2. This study elevates the value of personal protective equipment (PPE), such as face masks, made with nonwovens and other fabrics, as lifesavers in the case of airborne diseases such as COVID-19 and other pulmonary disorders.

Application: This study shows that extra precautions like wearing face masks helped stop the spread of SARS-CoV-2, along with vaccinations.

Ganesh is a Computer Science and Engineering student at PES University, Electronic City Campus, Bengaluru, India. Khyum and Kikanme are graduate research assistants and Ramkumar is professor at Texas Tech University in Lubbock, TX, USA. Email Ramkumar at s.ramkumar@ttu.edu.

PAPERMAKING

Web lateral instability caused by nonuniform paper properties

By: Frédéric Parent, Jean Hamel and David McDonald

January, pp. 09 – 20 Lateral or cross-machine direction (CD) web movement in printing or converting can cause problems such as misregistration, wrinkles, breaks, and folder issues. The role of paper properties in this problem was studied by measuring lateral web positions on commercial printing presses and on a pilot-scale roll testing facility (RTF). The findings clearly showed that CD profiles of machine direction (MD) tension were a key factor in web stability. Uneven tension profiles cause the web to move towards the low-tension side. Although extremely nonuniform tension profiles are visible as bagginess, more often, tension profiles must be detected by precision devices such as the RTF. Once detected, the profiles may be analyzed to determine the cause of web offset and weaving problems.

Causes of tension profiles can originate from nonuniform paper properties. For example, by means of case studies, we show that an uneven moisture profile entering the dryer section can lead to a nonuniform tension profile and lateral web movement. Time-varying changes in basis weight or stiffness may also lead to oscillations in the web's lateral position. These problems were corrected by identifying the root cause and making appropriate changes.

In addition, we developed a mathematical model of lateral stability that explains the underlying mechanisms and can be used to understand and correct causes of lateral web instability.

Application: Lateral web movement can cause misregistration in printing, as well as wrinkles and breaks in converting. These problems can be eliminated by reducing CD and MD variations in basis weight, caliper, and moisture. Precision measurement of the MD tension profile in the CD is critical in locating the source of the problem, and a mathematical model is helpful in guiding corrective measures.

Parent is research engineer and Hamel is vice president, Industry and Member Relations, for FPInnovations in Pointe Claire, QC, Canada. McDonald is president of JDMcD Consulting Inc. in Vaudreuil-Dorion, QC, Canada. Email Parent at Frederic.Parent@fpinnovations.ca..

Furnishing autohydrolyzed poplar weakly alkaline P-RC APMP to make lightweight coated base paper

By: Bo Zhang, Kaili Wu, Qingxi Hou, Tongbao Jiang, Wenwen Zhang, Kaisheng Luo and Wei Liu

February, pp. 71 – 79 This work investigated the effects of autohydrolysis pretreatment severity on poplar (*Populus tomentosa Carr.*) woodchips used to make a type of high-yield pulp (HYP) known as preconditioning followed by refiner chemical treatment, alkaline peroxide mechanical pulp (P-RC APMP). It also investigated the ratios for partially replacing sodium hydroxide (NaOH) with magnesium oxide (MgO) in the high-consistency (HC) retention stage of the P-RC APMP process on the obtained HYP's properties.

The results show that the pretreatment severity of autohydrolysis at combined hydrolysis factor (CHF) = 10.77 and the 50 wt% ratio for partially substituting NaOH with MgO were the optimum conditions for making lightweight coated (LWC) base paper. Compared to the conventional P-RC APMP, the optimized P-RC APMP had similar bulk and higher tensile, burst, and tear indices, as well as opacity, but a slightly lower ISO brightness. When the optimized P-RC APMP and commercial softwood bleached sulfate pulp (SBKP) were blended to make LWC base paper, the most favorable pulp furnish was comprised of 50% optimized P-RC APMP and 50% commercial SBKP. The obtained LWC base paper handsheet had better bulk, and its other properties could also meet the requirements of LWC base paper.

Application: In the manuscript, poplar woodchips were subjected to autohydrolysis pretreatment with different levels of intensity, and then the autohydrolyzed woodchips were used to make P-RC APMP by partially substituting NaOH with MgO in the HC retention stage. Finally, the obtained P-RC APMP was blended with commercial SBKP to make LWC base paper. The present work investigated the optimum conditions for the

autohydrolysis pretreatment, substitution ratio of NaOH by MgO, and adding a proportion of the P-RC APMP in the pulp furnish.

B. Zhang is a Master's student, Wu* is a Ph.D. candidate, Hou is professor, Jiang is a Master's student, Zhang is a Master's student, Luo is a Master's student, and Liu is associate professor at Tianjin Key Laboratory of Pulp and Paper, Tianjin University of Science & Technology, Tianjin, China. Email Hou at qingxihou@tust.edu.cn.*

** B. Zhang and Wu contributed equally to this work.*

Numerical investigation of the effect of ultrasound on paper drying

By: Munevver Elif Asar, Zahra Noori and Jamal Yagoobi

March, pp. 127 – 139 The paper drying process is very energy inefficient. More than two-thirds of the total energy used in a paper machine is for drying paper. Novel drying technologies, such as ultrasound (US) drying, can be assessed numerically for developing next-generation drying technologies for the paper industry.

This work numerically illustrates the impact on drying process energy efficiency of US transducers installed on a two-tiered dryer section of a paper machine. Piezoelectric transducers generate ultrasound waves, and liquid water mist can be ejected from the porous media. The drying rate of handsheet paper in the presence of direct-contact US is measured experimentally, and the resultant correlation is included in the theoretical model.

The drying section of a paper machine is simulated by a theoretical drying model. In the model, three scenarios are considered. In the first scenario, the US modules are positioned in the dryer pockets, while in the second scenario, they are placed upstream of the drying section right after the press section. The third case is the combination of the first and second scenarios. The average moisture content and temperature during drying, enhancement of total mass flux leaving the paper by the US mechanism, total energy consumption, and thermal effect of heated US transducers are analyzed for all cases. Results show that the application of the US can decrease the total number of dryer drums for drying paper. This numerical study is based on the US correlation obtained with the US transducer direct-contact with the paper sample. Thus, future work should include US correlation based on a non-contact US transducer.

Application: In this paper, for the first time, the effect of the application of a US mechanism in a multi-cylinder dryer section is numerically investigated. The results of this study aim to uncover the potential impact of US drying on a paper machine.

Asar is graduate research assistant; Noori is graduate research assistant; and Yagoobi is professor at the Center for Advanced Research in Drying, Multi-Scale Mass and Heat Transfer Laboratory, at Worcester Polytechnic Institute, Worcester, MA, USA. Email Asar at masar@wpi.edu.

Predicting strength characteristics of paper in real time using process parameters

By: Shivamurthy Modgi and Kamala Rajan

March, pp. 143 – 153 Online paper strength testing methods are currently unavailable, and papermakers have to wait for manufacture of a complete reel to assess quality. The current methodology is to test a very small sample of data (less than 0.005%) of the reel to confirm that the paper meets the specifications. This paper attempts to predict paper properties on a running paper machine so that papermakers can see the test values predicted in real time while changing various process parameters.

This study was conducted at a recycled containerboard mill in Chicago using the multivariate analysis method. The program provided by Braincube was used to identify all parameters that affect strength characteristics. Nearly 1600 parameters were analyzed using a regression model to identify the major parameters that can help to predict sheet strength characteristics. The coefficients from the regression model were used with real-time data to predict sheet strength characteristics.

Comparing the prediction with test results showed good correlation (95% in some cases). The process parameters identified related well to the papermaking process, thereby validating the model. If this method is used, it may be possible to predict various elastic moduli (E11, E12, E22, etc.) in the future as the next step, rather than the traditional single number "strength" tests used in the containerboard industry, such as ring crush test (RCT), corrugating medium test (CMT), and short-span compression strength test.

Application: The information presented in this paper is useful for operators to track sheet properties as the paper is being made. It also helps them to understand the effect of each parameter change they make in their day-to-day operation and how it impacts sheet quality.

Modgi is technical quality manager for Domtar's packaging mill in Kingsport, TN, USA. Rajan is president of Alsip MiniMill LLC in Alsip, IL, USA. Email Rajan at krajan@alsipminimill.com.

The Shendye-Fleming OBA Index for paper and paperboard

By: Awadhoot Shendye, Paul D. Fleming III, Alexandra Pekarovicova, Veronika Husovska and Kiran Deshpande

March, pp. 157 – 165 We are proposing a new one-dimensional scale to calculate the effects of optical brightening agents (OBA) on the bluish appearance of paper. This index is separate from brightness and whiteness indices.

In the paper industry, one-dimensional scales are widely used for determining optical properties of paper and paperboard. Whiteness, tint, brightness, yellowness, and opacity are the most common optical properties of paper and paperboard. Most of the papers have a blue cast generated by addition of OBA or blue dyes. This blue cast is given because of the human perception that bluer is whiter, up to a certain limit. To quantify this effect, it is necessary to determine how much blue cast paper and paperboard have.

As the printing industry follows the ISO 3664 Standard for viewing, which has a D50 light source, this also plays a very important role in showing a blue cast. Color perception is based on light source and light reflected from an object. The ultraviolet (UV) component in D50 interacts with OBA to provide a reflection in the blue region of the visible spectrum.

Use of a UV blocking filter results in measurements without the effect of emission in the blue region. This difference is used in determining the OBA effect in the visible range of the paper. This equation is known as the Shendye-Fleming OBA Index.

Application: The new OBA index proposed here provides a new one-dimensional scale for measuring the effect of OBAs.

Shendye is technical development engineer at The Challenge Printing Company in Clifton, NJ, USA. Fleming III is professor and Pekarovicova is professor in the Department of Chemical and Paper Engineering, Western Michigan University, Kalamazoo, MI, USA. Husovska is owner at Pressburg LLC in Kalamazoo, MI, USA. Deshpande is global senior color expert – color management at Siegwerk (UK) Ltd., Swadlincote, UK. Email Shendye at ashendye@gmail.com.

Comparative study of guar gum and its cationic derivatives as pre-flocculating polymers for PCC fillers in papermaking applications

By: Indrasena Ghosh, Chhaya Sharma and Rita Tandon

April, pp. 203 – 216 In this work, gums from guar seeds were evaluated as a potential precipitated calcium carbonate (PCC) filler pre-flocculant to induce functional filler in papermaking applications. In recent years, guar has been considered one of the promising wet-end additives due to its abundance, rich source of hemicellulose content, and bio-degradability. However, application of guar gum in filler pretreatment methods for producing high ash paper has scarcely been reported.

In this paper, the flocculating ability of three types of guar gum was established with charge analysis and turbidity (NTU) of the system at 1% and 5% for each gum: native gum (NG) having a degree of substitution (DS) of 0, and cationic gums having a DS value of 0.07 (CL) and 0.15 (CH). It was interesting to observe that even at a 5% dose of NG, the charge density of PCC did not deviate much from the initial values. The system carried a weak negative charge, resulting in an unstable colloidal suspension that led to PCC-PCC particle bridging. On the other hand, the operative mechanism of CL and CH during adsorption and PCC flocculation was predicted to be charge neutralization and electrostatic-patch formation, accompanied by particle bridging. Note that CL, with a maximum 47.5% reduction in residual turbidity of PCC at a 1% dose, was much more efficient in doing so than the other two gums; NG had a 40% maximum reduction in residual turbidity at a 5% dose and CH had a maximum 30% reduction at a 1% dose. Later on, floc formation and structure were correlated with optical and field emission scanning electron microscopy (FE-SEM) images.

In the next set of trials, paper properties were determined by varying the different gum dosages from 0.2% to 5% at a constant dose of 20% filler. It is also noteworthy to mention that with 1% CL (low DS) dose, PCC retention increased by 39%, which also enhanced the tensile, tear, burst, and opacity properties by 11%, 19%, 5%, and 4.4%, respectively, without significantly affecting the bulk properties. Further, wide-angle X-ray diffraction (XRD) analysis and Fourier transform infrared (FTIR) analysis revealed that pre-flocculating PCC with a 1% gum dose did not induce any change in crystalline transformation. Based on observation, it was found that cationic gums with low DS values are a better choice for maximizing the strength of paper while maintaining bulk and high opacity when pre-flocculation is adopted to increase the filler retention in paper.

Application: This work aims to identify the flocculation mechanism of PCC with guar gum and its derivatives in order to establish pre-flocculated filler slurries prior to stock addition. The most important contribution from the study is selection of the optimum degree of substitution (DS) value, which is crucial when adopting pre-flocculation technologies that later affect strength of paper and filler retention.

Ghosh is research scholar and Sharma is professor in the Department of Paper Technology, IIT Roorkee, Saharanpur Campus, Saharanpur, Uttar Pradesh, India. Tandon is senior scientist, retired, at Central Pulp and Paper Research Institute, Saharanpur, Uttar Pradesh, India. Email Sharma at chhaya.iitr@gmail.com.

The chemistry of aluminum salts in papermaking

By: Thomas R. Arnson

April, pp. 229 – 234 Alum and related aluminum salts and used extensively in a variety of papermaking operations. The versatility of these aluminum additives stems from the ability of the various aluminum species to absorb and interact with the other materials in the papermaking system. Underlying these interactions in the aqueous chemistry of the aluminum ion. A review of the current views on the aqueous chemistry of the aluminum ion and papermaking aluminum chemistry is presented. Application of the aqueous aluminum equilibria to aluminum adsorption and alum-rosin sizing are also discussed.

Development of paper quality parameter measurement in China

By: Lianhua Hu and Jin Ma

May, pp. 247 – 256 Paper quality parameters are important indicators of paper production, such as paper moisture, basis weight, ash content, strength, and so on. This study focuses on the online measurement methods and development of paper basis weight, moisture, and ash measuring.

First, the measurable paper parameters and quality control system products in China are analyzed. Then, the basis weight measurement methods, accuracy, and development are given in the range of 10~1000 g/m^2. Third, the distinction between infrared and microwave methods for moisture measurement is discussed. Finally, the ash measurement is introduced.

Production and consumption of tissue paper in China have continually increased during the past decade. Near-infrared light technology is mature for the measurement of paper parameters in the range of 10~200 g/m^2 basis weight. However, the near-infrared online measurement of tissue paper is not widely used, and few tissue paper lines are equipped with this type of quality control system in China. Therefore, technology for near-infrared measurement of basis weight has a great potential market in the field of tissue paper production. This article analyzes the future development trend of near-infrared light in tissue paper basis weight measurement and summarizes the difficulties in near-infrared light measurement of tissue paper basis weight.

Application: Different measurement methods suitable for measuring basis weight, moisture, and ash of various paper types are summarized in this paper. The near-infrared light measurement method is suitable for the measurement of tissue paper, but influences such as ambient temperature and humidity interference, along with onsite dust, need to be overcome.

Hu is associate professor and Ma is a Master's student in the College of Mechanical and Electrical Engineering, Shaanxi University of Science and Technology, Xi'an, Shaanxi Province, China. Email Ma at majin2@sust.edu.cn.

Web instability in the open draw and the impact on paper machine efficiency

By: Frédéric Parent, Daniel Ricard, J. David McDonald and Richard J. Kerekes

May, pp. 271 – 280 Paper is most likely to break in the first open draw on a paper machine where it is unsupported, wettest, and weakest. Tension is applied to peel the web from the roll surface, as well as minimize web flutter in the open draw. The average tension is well below the breaking point and is often set by adjusting the speed difference between the press and the next machine element by visually observing the behavior of the web. However, machine direction variations caused by instabilities in the paper machine can cause tension swings that exceed the strength of the web.

Measurement of the web's release point from press rolls on pilot and commercial paper machines was used to identify the cause of tension instabilities. Variations in the speed of the paper machine drives and the work of adhesion from the press roll surface were identified as key factors. Fluctuations of paper moisture, which affects the elastic modulus and strength of the web, appear to be less important.

Application: Measurement of the release point of the web from a press roll can be used to identify tension stability problems in the open draw and the source of web breaks. Paper machine drive stability and the web adhesion to the press roll surface are possible problem areas.

Parent is research engineer and Ricard is senior scientist, Pulp and Paper Innovations Group, at FPInnovations in Pointe-Claire, QC, Canada. McDonald is president, JDMcD Consulting in Vaudreuil-Dorion, QC, Canada. Kerekes is professor emeritus at the University of British Columbia, Pulp and Paper Centre, Vancouver, BC, Canada. Email Parent at frederic.par-ent@fpinnovations.ca.

Water chemistry challenges in pulping and papermaking – fundamentals and practical insights: Part 1: Water chemistry fundamentals and pH

By: Przemyslaw Pruszynski, Lebo Xu and Peter W. Hart

June, pp. 313 – 324 Water is an essential component of the papermaking process. Nevertheless, papermakers often overlook its importance compared to fibers and chemical additives. A better understanding of water properties and chemical interactions associated with water at the wet end leads to a sound foundation for high-quality paper production and smooth operation. Not all fresh water and process water is the same. Fresh water varies from mill to mill, primarily due to the location and availability of water sources. Some industrial trends, such as enhancing water conservation and production yield, gradually shift process water quality over time.

The current work serves as a primer on water and water chemistry fundamentals to help the papermaker prepare for the future challenges of increased contamination of process water associated with reduced fresh water usage. This paper focuses on basic water chemistry definitions and discusses the impact of pH on wet-end operation. It is clear that pH is a fundamental factor that directly affects the process and impacts other factors relevant to the papermaking process. It is crucial to understand what pH represents, how it is measured, how to select the proper pH and carefully control it, and how to closely maintain the process at target setpoints. Understanding the sensitivity of operation to pH change will lead to an appropriate focus on these issues. In addition to basic theory, we also review onsite experience and practical mill cases. It is imperative to stress that, although critical, pH is not the only chemical parameter impacting papermaking operations. Other factors, such as ionic concentration measured by conductivity, surface, soluble charge, and hardness, are critical and will be discussed in Part II of this series. As pH is a primary and independent factor that impacts various forms of charge and conductivity, the authors decided to start the current series of papers by discussing pH.

Application: By gaining comprehensive and fundamental understanding on how pH affects wet end chemistry, mills can be better prepared to address water challenges and obtain more efficient operation.

Pruszynski is technical director and owner at Pruszynski Paper Chemistry Consulting LLC, Naperville, IL, USA. Xu is senior research scientist/engineer and Hart is director, Fiber Science and Innovation, at WestRock in Richmond, VA, USA. Email Xu at lebo.xu@westrock.com.

Rewet suppression through press felt engineering

By: Sumner Dudick, Dennis W. Hess and Victor Breedveld

June, pp. 327 – 332 Due to the immense energy and associated financial cost of drying paper, achieving a drier web entering the dryers is a key objective in paper manufacture. One major research thrust has been finding a way to increase press solids by mitigating or eliminating rewet in the press section. For decades, solutions to this problem have remained elusive.

In this work, we develop a novel approach that significantly reduces rewet by rupturing the liquid channels between felt and web. We illustrate the effects that altering the mechanical and surface properties of the press felt matrix have on the stability of these liquid channels. In a laboratory-scale platen press, a 40% reduction in the residual water of 120 g/m^2 southern bleached softwood kraft (SBSK) pulp handsheets after pressing was observed, corresponding to an increase in press solids from 48% to 61%. For reference, pressing under identical conditions with paper blotters, in which minimal rewet is presumed to occur, resulted in 64% solids. Furthermore, we observed enhanced dewatering across a range of basis weights, applied pressures, and felt types. In addition to measuring the solids content of pressed sheets, we capture and analyze video evidence of the mechanisms at play in our improved dewatering technology.

Application: This work describes a novel approach to prevent rewet in the press section. The authors hope that the papermaking community will use these insights to design press fabrics that increase the energy efficiency of the mill.

Dudick is graduate researcher, Hess is professor emeritus, and Breedveld is professor in the school of Chemical & Biomolecular Engineering and Renewable Bioproducts Institute at Georgia Institute of Technology, Atlanta, GA, USA. Email Breedveld at victor.breedveld@chbe.gatech.edu.

Calender barring review with experiences

By: Jake Zwart

July, pp. 377 – 384 Excessive calender vibration affects all styles of calender stacks from single to multi-nip, all hard rolls, or a combination of hard and soft rolls. Calender vibration can be forced vibration or self-excited vibration. Forced vibration occurs at the first few harmonics of the calender roll rotational speeds and is caused by imbalance, misalignment, eccentricity, etc. Self-excited vibration, the focus of this paper, occurs at higher frequencies.

Feedback paths for self-excited vibration must be understood in order to ameliorate the problem. This is presented in the context of the historical development of the theory of self-excited feedback mechanisms, followed by a survey of self-excited feedback mechanisms in various types of calender stacks. Methodology to determine which feedback path is present and techniques to control or eliminate the resulting vibration follow. To obtain a flavor of the types of problems faced and practical remedial actions, a variety of experiences with barring issues are provided.

Application: This paper provides background information on the history of calender barring on a calender stack, along with the factors that contribute to the problem and resolutions to the problem.

Zwart is principal at Spectrum Technologies in Puslinch, ON, Canada. Email Zwart at jake.zwart@spectrum-tec.com.

The creep properties of paper

By: J.P. Brezinski

August, pp. 445 – 457 The creep properties of alpha-pulp handsheets were determined at various constant tensile loads and relative humidities for the purpose of clarifying the prerupture mechanical behavior of paper. Included in this investigation were studies of first-creep properties, creep recovery, mechanical conditioning and primary creep, the dependence of creep behavior on handsheet solid fraction, and the relative permanence of nonrecoverable deformations. It was concluded that the delayed creep deformation of the handsheets was of at least two general types which were separated in time and varied in their recoverability and dependence on relative humidity. The general patterns of first-creep behavior could be described by the formation of master creep curves. The creep behavior

does not appear to be reconcilable with rate-controlling mechanisms of deformation which embrace macroscopic reorientations of the fibers in the sheet or the rupture of fiber-fiber bonds.

The mechanism of bonding

By: W. Boyd Campbell

September, pp. 507 – 509 Three factors are involved in cellulose bonding – available area, contact and hydrogen bonding. Since the use of the electron microscope and the synthesis of cellulose, it has become clear that the primary form of cellulose is elementary fibrils with about 100 molecules cross-section and about 400 sq. m. area per g. Because of internal bonding only a small part of this area is available. Consideration of various possibilities indicates that exterior surface of fibers, which varies from 1.0 to 2.3 sq. m. per g. depending on the degree of beating, is the main source of usable area. Wet pressing, which is much more intense than average pressure applied, is first factor in securing contact and is much assisted by softening due to internal fibrillation by beating. More intimate contact is brought about by liquid internal tension on drying. Final hydrogen bonding differs from crystallizing force in that there is no need for parallel orientation in the fibers to be bonded but does require close contact. Tension during drying will diminish the bonding between surfaces at right angles to the tension.

PULPING

Effects of agitator blade scaling on mixing in dissolving tanks

By: Patrick Gareau, Markus Bussmann and Nikolai Demartini

April, pp. 189 – 199 Hard calcium carbonate scale often forms on the agitators in smelt dissolving tanks. The effects of this scale on mixing are not well understood. While mixing in tanks has often been modeled in the literature, there have been no studies involving agitator scaling.

To better understand the impact of agitator scaling on hydrodynamics and tank concentrations, a steady state, three-dimensional (3D) model has been developed for a smelt dissolving tank at a kraft pulp mill. In this work, four cases are compared: an agitator with no scaling, mild scaling, moderate scaling, and extreme scaling. The extreme scaling case is representative of scale buildup on a dissolving tank agitator that was significant enough that the agitator had to be stopped and cleaned. The reduction in the agitator fluid jet velocity is relatively small for the mild and moderate scaling cases, but it becomes more significant for the extreme scaling case, for which the results indicate that the mixing of the smelt with the weak wash is likely poor and that there would thus be a risk of smelt pooling.

Application: A smelt dissolving tank model has been developed to predict how tank hydrodynamics and smelt concentrations respond to the presence of agitator scaling.

Gareau is an MASc graduate and Bussmann is professor and chair of the Department of Mechanical & Industrial Engineering at the University of Toronto, Toronto, Canada. DeMartini is associate professor in the Department of Chemical Engineering & Applied Chemistry at the University of Toronto, Toronto, Canada. Email Bussmann at markus.bussmann@utoronto.ca.

Improving refining efficiency with deflocculation

By: Dwight Anderson and Len Schuster

May, pp. 259 – 267 The ability to load a refiner requires the formation of a fiber mat between opposing refiner bars. One of the consequences of this is the formation of flocs that persist through the refiner grooves and exit the refiner. These flocs interfere with sheet strength, requiring additional energy to make up the strength deficit. In addition, flocs can initiate string formation, resulting in machine efficiency issues such as cross-machine profile deterioration and the downtime required to correct it.

Novel refiner plate modifications have been shown to improve refining efficiency in otherwise identical refiner plates. Energy savings are typically around 15% of gross refining energy on the basis of the treated stock, although much higher reductions have also been seen. Addressing this previously underappreciated flaw in conventional refining enables greenhouse gas reduction and other benefits related to sheet strength and machine efficiency.

Application: Conventional refining of softwood and old corrugated containers (OCC) is compromised by the creation of flocs. A novel refiner plate modification counteracts this, making refining more energy efficient. The improvement in refining efficiency is typically greater than can be achieved through no-load reduction. Additional research could yield further optimization.

Anderson is manager of Innovative Technology Development at International Paper in Puyallup, WA, USA. Schuster is principal scientist at International Paper in Loveland, OH, USA. Email Anderson at dwight.anderson@jpaper.com.

On the usage of online fiber measurements for predicting bleached eucalyptus kraft pulp tensile index — an industrial case

By: R.B. Demuner, C.A. Faria, A.A.R. de Almeida and P.N. Pignaton

July, pp. 365 – 374 Cellulose pulp's physical-mechanical properties are determined by laboratory tests obtained from prepared handsheets. However, this procedure is time intensive and presents a lead time until the results are available, hindering its utilization for monitoring and decision-making in a pulp mill. In this context, developing real-time solutions for physical-mechanical properties prediction is fundamental.

This work applied a mathematical modeling approach to develop a soft sensor for tensile index monitoring. The mathematical model considers online morphology measurements obtained from the last bleaching stage outlet stream and important process variables for tensile index prediction. The results obtained are satisfactory compared to laboratory results, presenting a mean absolute percentual error of 2.5%, which agrees with the laboratory testing method's reproducibility.

Application: This paper presents the use of online morphology information to predict pulp physical-mechanical properties in real-time measurements.

Demuner is quality manager at Suzano S/A and is based in Mato Grosso do Sul, MS, Brazil. Faria is a graduate student at Universidade Federal de Uberlândia in Uberlândia, MG, Brazil. De Almeida is quality manager at Suzano S/A in Três Lagoas, MS, Brazil. Pignaton is executive quality manager at Suzano S/A and is based in Aracruz, ES, Brazil. Email Demuner at rafael.demuner@suzano.com.br.

Fiber-based characterization of pulp refining

By: Richard J. Kerekes and J. David McDonald

September, pp. 497 – 503 Fiber development in pulp refining can be characterized by three parameters: number of impacts on pulp, *N*; energy per impact, *I*, and bar force on fibers, *F*. These parameters enable comparisons of radically different refining conditions; determination of intensity for hardwoods and softwoods; assessment of effect of bar width on fiber shortening; and predictions of tensile strength increases.

Application: Simple equations for *N*, *I*, and *F*, using readily available data, can be used to understand and guide the operation of refiners.

Kerekes is professor emeritus at the University of British Columbia, Pulp and Paper Centre, in Vancouver, BC, Canada. McDonald is president of JDMcD Consulting Inc. in Vaudreuil-Dorion, QC, Canada. Email McDonald at mcdonald.jdavid@gmail.com.

RECOVERY CYCLE

Experiments and visualization of sprays from beer can and turbo liquor nozzles

By: Ari Kankkunen, Santeri Koivisto, Kari Saari, Mika Järvinen, James Biggs and Andrew Jones

February, pp. 95 – 106 Industrial scale swirl-type black liquor nozzles were studied using water as the test fluid. Simple water spraying experiments were found to be very beneficial for studying and comparing nozzles for black liquor spraying. These kinds of experiments are important for finding better nozzle designs.

Three nozzle designs were investigated to understand the functional differences between these nozzles. The pressure loss of nozzle 1 ("tangential swirl") and nozzle 3 ("turbo") were 97% and 38% higher compared to nozzle 2 ("tangential swirl"). Spray opening angles were 75°, 60°, and 35° for nozzles 1, 2, and 3, respectively. Video imaging showed that the nozzles produced sprays that were inclined a few degrees from the nozzle centerline. Spray patternation showed all the sprays to be asymmetric, while nozzle 2 was the most symmetric. Laser-Doppler measurements showed large differences in spray velocities between nozzles. The spray velocity for nozzle 1 increased from 9 m/s to 15 m/s when the flow rate was increased from 1.5 L/s to 2.5 L/s. The resulting velocity increase for nozzle 2 was from 7 m/s to 11 m/s, and for nozzle 3, it was from 8 m/s to 13 m/s. Tangential flow (swirl) directed the spray 6°–12° away from the vertical plane. Liquid sheet breakup mechanisms and lengths were estimated by analyzing high speed video images. The liquid sheet breakup mechanism for nozzle 1 was estimated to be wave formation, and the sheet length was estimated to be about 10 cm. Sheet breakup mechanisms for nozzle 2 were wave formation and sheet perforation, and the sheet length was about 20 cm. Nozzle 3 was not supposed to form a liquid sheet. Nozzle geometry was found to greatly affect spray characteristics.

Application: Spray properties are experimentally characterized. Knowledge of spray opening angle, velocity, and mass distribution can be used to compare different nozzles for better char bed, fouling, and emissions control. Spray characteristics can be adapted for computational fluid dynamics (CFD) modeling.

Kankkunen is research engineer, Koivisto is research assistant, Saari is laboratory manager, and Järvinen is professor at Aalto University, Espoo, Finland. Biggs is research and development manager at Crenshaw Machine Systems, Bay Minette, AL, USA. Jones is senior engineering Fellow at International Paper in Loveland, OH, USA. Email Kankkunen at ari.kank-kunen@aalto.fi.

A model black liquor formulation for use in development and evaluation of membranes for concentrating weak black liquor

By: Scott A. Sinquefield

February, pp. 109 – 112 As part of a larger program to develop robust membranes for concentrating weak black liquor prior to the evaporation step, several commercially available membranes were tested for suitability in this application. Given the variation in kraft black liquor for various wood species, the mill-to-mill variations, and the challenges of obtaining fresh samples, the need became apparent for a synthetic reference black liquor that would allow any membrane developer to test a new prototype membrane and compare the results with others.

We present a formulation for a model black liquor (MBL) similar to real kraft black liquor in the composition of the major species that can be formulated from readily available reagents. The MBL was tested with two commercial membranes and resulted in similar levels of lignin retention as the real black liquor. It also showed similar viscosity behavior to real black liquor as a function of solids content.

Application: A recipe for a model black liquor is presented for use in developing and testing robust membranes for concentrating black liquor. The use of a common reference liquor allows developers to directly compare prototype membrane performance to that of other commercial or prototype membranes.

Sinquefield is a senior research engineer at the Renewable Bioproducts Institute, Georgia Institute of Technology, Atlanta, GA, USA. Email Sinquefield at scott.sinquefield@rbi.gatech.edu.

Effects of rings on flow and temperature in lime kilns

By: Patrick Gareau, Markus Bussmann, Nikolai Demartini and Honghi Tran

June, pp. 301 – 309 A steady state, two-dimensional (2D) axisymmetric model has been developed to help understand how rings form and grow in a typical lime kiln. Rings of varying length, thickness, and geometry at the front and back faces were modeled to study the effects on flue gas flow and temperature.

The results show that ring growth causes the gas velocity to increase and insulates the adjacent refractory, resulting in a lower kiln shell temperature. The results also reveal the formation of recirculation zones immediately downstream of the rings, as well as temperature deviations upstream and downstream of the rings that might promote recarbonation and further ring growth. The model was applied to a kiln from a kraft mill with front-end and mid-kiln rings and good agreement was obtained between the measured and predicted kiln shell temperatures, providing confidence in the modeling.

Application: A lime kiln model has been developed to predict how gas flow and kiln temperatures respond to the presence of ring deposits and may provide insights into how rings form and grow.

Gareau is an MASc graduate and Bussmann is professor and chair of the Department of Mechanical & Industrial Engineering at the University of Toronto, Toronto, ON, Canada. DeMartini is assistant professor and Tran is professor emeritus in the Department of Chemical Engineering & Applied Chemistry at the University of Toronto. Email Bussmann at markus.bussmann@utoronto.ca.

A feasibility study of using the organic Rankine cycle for power generation from the flue gases of recovery boilers

By: Seyed Javad Amirfakhri

August, pp. 405 – 413 Almost 415 tons/h of flue gases with a temperature of 160°C are released to the atmosphere from the recovery boiler of a pulp mill with capacity of 1000 air dried (a.d.) metric tons of pulp per day. This is a large waste heat stream that can be used to generate power, to decrease the operating costs of a pulp mill, and to save carbon dioxide (CO_2) emissions.

In this work, the feasibility of using an organic Rankine cycle (ORC) with ammonia as the working fluid to generate power from the flue gases of recovery boilers is studied. CHEMCAD and Taguchi methods are used for simulation of the process and for optimization of operating conditions, respectively. The temperature of the ammonia and flue gases at the exit of evaporator, exit pressure of the pump and turbine, and the degree of subcooling of ammonia at the exit of the condenser are five operating

parameters that are manipulated to optimize the process. Three different scenarios are defined: minimizing the net power cost, maximizing the ORC efficiency, and maximizing the net profit.

Different aspects of these scenarios, such as net power generation, cost, efficiency, and CO_2 emission savings are discussed, and optimum operating conditions are reported.

Application: This work presents the application of an organic Rankine cycle as a waste heat recovery system to generate electric power from flue gases of recovery boilers at pulp mills.

Amirfakhri is assistant professor in the Department of Paper Science and Engineering and Chemical Engineering at the University of Wisconsin–Stevens Point in Stevens Point, WI, USA. Email Amirfakhri at samirfak@uwsp.edu.

Causes of poor dregs settling in a green liquor clarifier

By: Torsten Meyer, Heather Munn and Honghi Tran

August, pp. 435 – 442 A study was conducted to examine the most likely parameters responsible for poor dregs settling at a kraft mill over a 2.5-year period, using multivariate data analysis (MVDA) and machine learning (ML) techniques. The dregs settling behavior seems to be seasonally influenced, implying that wood quality variation can be a factor. The results from the MVDA/ML analysis show that poor dregs settling is correlated to incomplete combustion and/or low load conditions in the recovery boiler, low sulfidity in the causticizing plant, and high flow in the green liquor–weak wash cycle. Compositions of dregs and black liquor were also examined to identify correlations with impaired dregs settling. The results show that poor dregs settling strongly correlates with high silicon (Si) content in dregs and moderately correlates with high iron (Fe) and high aluminum (Al) contents, and with low bulk density in dregs. For mills that experience dregs settling or green liquor filtering issues, regular compositional analyses of dregs, green liquor, weak wash, and black liquor are recommended in order to monitor the dynamics of silicon and other constituents in the recovery cycle.

Application: This paper provides evidence to support several reasons for poor dregs settling in a green liquor clarifier. The insights gained and the information provided may help mills that have been experiencing persistent dregs settling issues.

Meyer is senior research associate and Tran is professor emeritus in the Department of Chemical Engineering & Applied Chemistry at the University of Toronto, Toronto, ON, Canada. Munn is process engineer at Irving Pulp and Paper Ltd., Saint John, NB, Canada. Email Meyer at meyer.torsten@yahoo.com.

RECYCLING

Application of ATR-IR measurements to predict the deinking efficiency of UV-cured inks

By: Hirohiko Koizumi, Masato Takayama, Seiki Yoneshige and Shisei Goto

January, pp. 51 – 59 In recent years, ultraviolet (UV)-curable ink has been developed and widely used in various printing applications. However, using UV-printed products (UV prints) in recovered paper recycling causes end-product dirt specks and quality issues.

A new method was developed that can distinguish UV prints from other prints by means of attenuated total reflectance infrared (ATR-IR) spectroscopy. Application of this method could allow more efficient use of UV prints as raw materials for paper recycling.

First, a mill trial was performed using UV prints alone as raw materials in a deinked pulp (DIP) process. Second, test prints were made with four types of UV inks: a conventional UV ink and three different highly-sensitive UV inks. Each print sample had four levels of four-color ink coverage patterns (100%, 75%, 50%, and 25%). Next, deinkability of all prints was evaluated by laboratory experiments. Finally, each print was measured using the ATR-IR method, and the relationship between the IR spectra and deinkability was investigated.

Mill trial results showed that UV prints caused more than 20 times as many dirt specks as those printed with conventional oil-based ink. There were variations in recycling performance among UV prints taken from bales used for the mill trial. Lab tests clearly revealed that not all UV-printed products lead to dirt specks.

In order to clarify the factors that affected deinkability of UV prints, the print samples were investigated by lab experiments. Key findings from lab experiments include:

- The number of dirt specks larger than 250 μm in diameter increased as the ink coverage increased.
- Higher ink coverage area showed stronger intensity of ATR-IR spectral bands associated with inks. These results indicate that deinkability of UV prints could be predicted by analysis of ATR-IR spectra.
- Finally, the method was applied for assessment of recovered paper from commercial printing presses. It was confirmed that this method made it possible to distinguish easily deinkable UV prints from other UV prints.

Based on these findings, we concluded that the ATR-IR method is applicable for inspection of incoming recovered paper.

Application: The developed method can determine the deinkability level of UV-printed products simply by analyzing the surface of those prints. Thus, it can be useful for incoming quality control in mills.

Koizumi is assistant manager, Takayama is research manager, and Yoneshige is senior research manager at the NPi Research Laboratory, Nippon Paper Industries Co. Ltd., in Tokyo, Japan. Goto is general manager, Business Transformation Promotion Office, for Nippon Paper Industries Co. Ltd., Tokyo, Japan. Email Koizumi at hirohiko-koizumi@nipponpapergroup.com.

A new method of studying the fundamental mechanisms involved in pigment liberation from recycle papers

By: Kaiwu Huang, Kris Strickland, Aaron Noble, Roe-Hoan Yoon and Cesar Basilio

October, pp. 533 – 540 Deinking flotation is the most efficient and widely used method of removing ink particles from printed papers to improve the recyclability. A prerequisite for successful deinking flotation is detachment of pigments from paper fibers, a subprocess known as liberation. The degree of liberation is usually determined via hyperwashing tests, which are costly and time consuming. Furthermore, they provide no information on the fundamental mechanisms controlling liberation.

In the present work, we developed a new method in which potentials of the particles in a pulp are measured and analyzed. If pigments are not liberated from paper fibers, a frequency distribution plot gives a single peak, while two peaks appear when they are liberated. One can readily determine the degrees of liberation from the peak positions and peak heights. In addition, the potential data can be used to construct disjoining pressure isotherms using the DLVO theory that are useful to better understand the fundamental mechanisms involved and the roles of different reagents used to improve pigment liberation.

Application: Flotation deinking is widely used to remove ink from paper fibers. A prerequisite to flotation is the liberation of ink particles from fibers. We have developed a new method of determining the degree of liberation. The new method will also be useful for better understanding the mechanisms involved in liberating ink particles from paper fibers.

Huang is research associate, Strickland is graduate research assistant, Noble is associate professor, and Yoon is professor in the Department of Mining and Minerals Engineering at Virginia Tech in Blacksburg, VA, USA. Basilio is group leader at Thiele Kaolin Company in Sandersville, GA, USA. Email Yoon at ryoon@vt.edu.

TISSUE

Research on improving the basis weight measurement accuracy of tissue paper based on PSO-BP neural network

By: Lianhua Hu, Yuxiu Feng and Jin Ma

October, pp. 553 – 561 The near-infrared (NIR) sensor can be used for measuring the basis weight and moisture of tissue paper, but the measurement accuracy is not ideal for this paper grade. The weight range of the tissue is 10~30 g/m^2, indicating that it is a low gram weight paper. The temperature and humidity of the production environment significantly impact an NIR sensor.

This paper focuses on improving the measurement accuracy of tissue paper basis weight. In order to reduce the influences of temperature and humidity, a mathematical model based on a particle swarm optimization back propagation (PSO-BP) neural network is proposed. In comparison with multiple linear regression measurement models, the basis weight measurement error with the PSO-BP model is within ± 0.5 g/m^2. This model can effectively improve the measurement accuracy and has a good effect on overcoming the basis weight nonlinear effect caused by the changes in ambient temperature and humidity.

Application: The PSO-BP neural network model can eliminate the nonlinear effects of temperature and humidity on basis weight, which provides a new idea for online measurement of paper basis weight for mills in the future.

Hu is associate professor, Feng is a Master's student and Ma is a Master's student in the College of Mechanical and Electrical Engineering, Shaanxi University of Science and Technology, Xi'an, Shaanxi, China. Email Hu at hulianhua@sust.edu.cn.

WASTEWATER TREATMENT

Considerations in managing wastewater odor at pulp and paper operations

By: Amanda Johansen Mattingly, Paul Wiegand and Robert Sackellares

March, pp. 167 – 175 Many pulp and paper mills are, at least periodically, faced with the release of odors that can migrate offsite and be considered a nuisance by nearby residents. At chemical pulp mills, perceptible odors associated with reduced sulfur compounds (RSCs) are common, many of which are highly perceptible owing to their low odor thresholds. As releases of RSCs and other odorous substances from production processes are progressively controlled, the proportional contribution from wastewater treatment systems to areal odors can increase.

This review paper summarizes important fundamentals of odor generation, source identification, and control. Common odorous substances are identified, and mechanisms for their generation are summarized. Approaches for measuring odorous substances are detailed to enable more effective management, and various odor control strategies are discussed.

Application: This article reviews the fundamentals of odor generation, sources of odor, potentially offending substances, and the basis for control at pulp and paper mills. Approaches for identifying odorous substances, their origins, and means for their control are provided.

Mattingly is research engineer and Wiegand is vice president at the National Council for Air and Stream Improvement (NCASI), Cary, NC, USA. Sackellares is senior industrial water engineer, GHD, Duluth, GA. Email Mattingly at amattingly@ncasi.org.

TAPPI JOURNAL
WWW.TAPPI.ORG
THE PAPER AND PACKAGING INDUSTRIES' TECHNICAL RESOURCE
JANUARY 2022 | VOL. 21 NO.2



PAPERMAKING 9
Web lateral instability caused by nonuniform paper properties
Frédéric Parent, Jean Hamel, and David McDonald

NONWOVENS 23
Microbial load and proliferation associated with various face mask types and sources during the COVID-19 pandemic
Srinivasan Narasimhan, Meenashree Balakrishnan, Olukayode James Ayodeji, and Seshadri S. Ramkumar

DISSOLVING PULP 35
Preparing prehydrolyzed kraft dissolving pulp via phosphotungstic acid prehydrolysis from grape branches
Li Tao, Ma Ying Hua, and Zhang Jun Ke

RECYCLING 51
Application of ATR-IR measurements to predict the deinking efficiency of UV-cured inks
Hirohiko Koizumi, Masato Takayama, Seiki Yoneshige, and Shisei Goto

January 2022

TABLE OF CONTENTS VOL. 21 NO. 1

5 **EDITORIAL**
Looking forward, looking back
Monica Shaw

9 **PAPERMAKING**
Web lateral instability caused by nonuniform paper properties
Frédéric Parent, Jean Hamel, and David McDonald

23 **NONWOVENS**
Microbial load and proliferation associated with various face mask types and sources during the COVID-19 pandemic
Srinivasan Narasimhan, Meenashree Balakrishnan, Olukayode James Ayodeji, and Seshadri S. Ramkumar

35 **DISSOLVING PULP**
Preparing prehydrolyzed kraft dissolving pulp via phosphotungstic acid prehydrolysis from grape branches
Li Tao, Ma Ying Hua, and Zhang Jun Ke

51 **RECYCLING**
Application of ATR-IR measurements to predict the deinking efficiency of UV-cured inks
Hirohiko Koizumi, Masato Takayama, Seiki Yoneshige, and Shisei Goto

»**COVER CREDIT**: Researchers Narasimhan et al. (p. 23) studied six different face masks from various sources for initial microbial load, proliferation, and horizontal dispersion that could contribute to diseases outside of respiratory viruses.

TAPPI JOURNAL
WWW.TAPPI.ORG

Editor-in-Chief
Douglas W. Coffin coffindw@miamioh.edu
+1 513 529-0771

Associate Editor
Peter W. Hart peter.hart@westrock.com
+1 409 276-3465

Editorial Director
Monica Shaw mshaw@tappi.org
+1 770 367-9534

PRESS Manager
Jana Jensen jjensen@tappi.org
+1 770 209-7242

Webmaster
Trina Heath theath@tappi.org
+1 770 209-7416

***TJ* EDITORIAL BOARD**

Brian N. Brogdon, FutureBridge Consulting & Training LLC
brian.brogdon@gmail.com, +1 678 581-9114

Douglas W. Coffin, Miami University
coffindw@miamioh.edu, +1 513 529-0771

Mahendra Doshi, Doshi and Associates
mahen@aol.com, +1 920 832-9101

Marc Foulger, Valmet
marc.foulger@valmet.com +1 315 767-2920

Peter W. Hart, WestRock
peter.hart@westrock.com, +1 409 276-3465

Carl J. Houtman, USDA Forest Products Laboratory
choutman@fs.fed.us, + 1 608 231-9445

Vamsi Jasti, Ahlstrom-Munksjo Nonwovens LLC
jvamsik1@gmail.com, +1 818 585-3524

Lucian Lucia, North Carolina State University
lucian.lucia@gmail.com, +1 919 889-7059

John A. Neun, John A. Neun LLC
john.neun@gmail.com, +1 518 275-8139

Jim Niemiec, Jim Niemiec Consulting LLC
jim.niemiec@outlook.com, +1 715 213-4766

Steven P. Ottone, Omya
steven.ottone@omya.com, +1 919 641-7854

Gaurav Pranami, Imbed Biosciences
gpranami@imbedbio.com, +1 515 230-7005

Arthur Ragauskas, Oak Ridge National Laboratory
aragausk@utk.edu

Seshadri Ramkumar, Texas Tech University
S.Ramkumar@ttu.edu, +1 806 742-4567

Gregg Reed, Imerys
gregg.reed@imerys.com, +1 478 553-5747

Gerard J.F. Ring, University of Wisconsin—Stevens Point
gerrryring@wi-net.com, +1 715 592-3732

Scott Rosencrance, Kemira Chemicals
scott.rosencrance@kemira.com, +1 770 429-2753

Paul Wiegand, NCASI
pwiegand@ncasi.org, +1 919 941-6417

Junyong Zhu, USDA Forest Products Laboratory
jzhu@fs.fed.us, +1 608 231-9520

Join TAPPI *today!*
TAPPI JOURNAL is a free benefit of TAPPI membership, and is only available to members. To join TAPPI, to renew your TAPPI Membership, or to learn about other valuable benefits, visit www.tappi.org.

TAPPI, 15 Technology Parkway S., Suite 115, Peachtree Corners, GA 30092, publishes *TAPPI JOURNAL* monthly.

ATTENTION PROSPECTIVE AUTHORS: All papers published are subject to *TAPPI JOURNAL's* peer-review process. Not all papers accepted for review will be published. Before submitting, check complete author guidelines at http://www.tappi.org/s_tappi/doc.asp?CID=100&DID=552877.

Statements of fact and opinions expressed are those of individual authors. TAPPI assumes no responsibility for such statements and opinions. TAPPI does not intend such statements and opinions or construe them as a solicitation of or suggestion for any agreed-upon course of conduct or concerted action of any sort.

Copyright 2022 by TAPPI, all rights reserved. For copyright permission to photocopy pages from this publication for internal or personal use, contact Copyright Clearance Center, Inc. (CCC) via their website: www.copyright.com. If you have questions about the copyright permission request process, please contact CCC by phone at +1 978 750-8400. To obtain copyright permission to use excerpts from this publication in another published work, send your specific request in writing to Editor, TAPPI JOURNAL, 15 Technology Parkway S., Suite 115, Peachtree Corners, GA 30092, USA; or by fax to +1 770 446-6947. Send address changes to TAPPI, 15 Technology Parkway S., Suite 115, Peachtree Corners, GA 30092, USA; Telephone +1 770 446-1400, or FAX +1 770 446-6947. www.tappi.org

Editorial



MONICA SHAW | EDITORIAL DIRECTOR
mshaw@tappi.org

Looking forward, looking back

Much like 2020, 2021 was another year of remarkable highs and lows delivered by the COVID-19 pandemic. Vaccines, variants, and infection surges altered the way we behaved personally and professionally last year.

As we move into 2022, we are now grappling with health and business concerns from the omicron variant that has overwhelmed hospitals in some areas and contributed to a global supply chain crisis. The ability to adjust has once again become a key skill in adapting to our shifting "new normal."

Conferences adjust to the times

Keeping an eye on health and safety, TAPPI modified its conference schedule in 2021. There was a virtual TAPPICon in the spring of last year and an in-person TAPPICon in the fall. The TAPPI International Conference on Nanotechnology for Renewable Materials (TAPPI NANO) was virtual, and the 2021 Pulping, Engineering, Environmental, Recycling and Sustainability (PEERS) Conference was rescheduled for 2022.

This year, however, the hope is to meet in person for all conferences. TAPPICon 2022 is scheduled for April 30-May 4 in Charlotte, NC. From June 13-17, TAPPI NANO will be held in Helsinki. TAPPI PEERS, co-located with the International Bioenergy & Bioproducts Conference (IBBC), is set for October 30-November 2 in Providence, RI. Both the PEERS call for papers and IBBC call for papers are still open, with an abstract submission deadline of March 14.

Looking forward to the coming year, we will see research on the lignin-based biorefinery, effects of ultrasound on paper drying, foam forming, and black liquor concentration, to name a few.

TAPPI Journal highlights

As we move into 2022, it's interesting to look at the research topics that were covered the previous year in *TAPPI Journal* (*TJ*), as well as to look forward to topics that will be covered this year. Highlights from last year include special issues created by members of the *TJ* editorial board on Papermaking Additives, along with research

TJ editorial board, reviewers, and authors — Thank you!

TAPPI and the *TJ* staff would like to thank the 2021 Editor-in-Chief Peter Hart, Associate Editor Douglas Coffin, and all of the editorial board for their tremendous help this past year in providing expertise and handling the peer review process so *TJ* can provide readers with cutting-edge research in the forest products and related industries. We'd also like to thank all of the authors and peer reviewers who participated in this important process. Your efforts in advancing research in this field are very much appreciated.

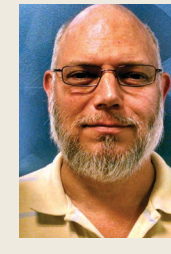

Peter Hart



Douglas Coffin

As of January 2022, Douglas Coffin assumes the role of *TJ* editor-in-chief, and Peter Hart will become associate editor. This year, *TJ* readers can expect to see more special content organized by our editorial board. Stay tuned for another year of interesting new research in *TAPPI Journal*!

submitted for the 2020 PEERS Conference. Both were peer-reviewed for publication in *TJ* through our regular process.



Organized by *TJ* Editorial Board Member Scott Rosencrance and Guest Editors Joe Mahoney and Lebo Xu, the January 2021 Papermaking Additives issue covered a range of topics that would be highlighted at TAPPICon 2021. These topics included a device for applying foamed wet-end additives to handsheets, laboratory methods for studying wet tear strength, spray starch technology, addition level and location optimization, and microfibrillated cellulose.



The March 2021 issue featured peer-reviewed papers from PEERS 2020. Organized by *TJ* Editor-in-Chief Peter Hart and *TJ* Editorial Board Member Brian Brogdon, this issue covered recycling of pizza boxes, a recovery boiler retrofit, bleaching, black liquor evaporator upgrades, and multi-jet nozzles for smelt shattering in a recovery boiler.

Looking forward to the coming year, we will see research on the lignin-based biorefinery, effects of ultrasound on paper drying, foam forming, and black liquor concentration, to name a few. Of note in this issue on p. 23 is a paper from researchers in India and *TJ* Editorial Board Member Seshadri Ramkumar of Texas Tech University on the microbial loads carried by various types of face masks, reflecting the ongoing concerns of the pandemic. Also, we will be naming the winner of the *TAPPI Journal* Best Research Paper and Honghi Tran Prize for 2021 this spring. **TJ**

For information on publishing in TAPPI Journal*, contact mshaw@tappi.org or tjournal@tappi.org. You can submit your papers to our online peer review system at http://www.editorialmanager.com/tappi/.*

Web lateral instability caused by nonuniform paper properties

FRÉDÉRIC PARENT, JEAN HAMEL, AND DAVID MCDONALD

ABSTRACT: Lateral or cross-machine direction (CD) web movement in printing or converting can cause problems such as misregistration, wrinkles, breaks, and folder issues. The role of paper properties in this problem was studied by measuring lateral web positions on commercial printing presses and on a pilot-scale roll testing facility (RTF). The findings clearly showed that CD profiles of machine direction (MD) tension were a key factor in web stability. Uneven tension profiles cause the web to move towards the low-tension side. Although extremely nonuniform tension profiles are visible as bagginess, more often, tension profiles must be detected by precision devices such as the RTF. Once detected, the profiles may be analyzed to determine the cause of web offset and weaving problems.

Causes of tension profiles can originate from nonuniform paper properties. For example, by means of case studies, we show that an uneven moisture profile entering the dryer section can lead to a nonuniform tension profile and lateral web movement. Time-varying changes in basis weight or stiffness may also lead to oscillations in the web's lateral position. These problems were corrected by identifying the root cause and making appropriate changes.

In addition, we developed a mathematical model of lateral stability that explains the underlying mechanisms and can be used to understand and correct causes of lateral web instability.

Application: Lateral web movement can cause misregistration in printing, as well as wrinkles and breaks in converting. These problems can be eliminated by reducing CD and MD variations in basis weight, caliper, and moisture. Precision measurement of the MD tension profile in the CD is critical in locating the source of the problem, and a mathematical model is helpful in guiding corrective measures.

Web lateral stability is critical for printing equipment to ensure good runnability and print quality. Web weaving may lead to performance issues such as wrinkles, misregistration, web breaks, and folder problems [1-4]. Although some printing presses have lateral position control, it cannot compensate for movements that are too quick or severe [1,3].

Troubleshooting web lateral instability is difficult because the problem could originate in the printing equipment [2,4], the roll build [5,6], the paper web [2,4,5], or a combination of all three.

Printing equipment, such as rollers and blankets, is generally aligned to stabilize the web, but nonuniformity caused by rewetting and drying can alter this. The tension control of the press is another potential cause for web weaving, especially if the drives are not well tuned [5].

Nonuniform paper properties in cross-machine direction (CD) and in machine direction (MD) can also generate web lateral instability [5,7-9]. Measurements on commercial printing presses have shown that the web moves laterally in the opposite direction to the tension stiffness orientation (TSO) angle [1,2]. Uneven tension profiles in the CD, which in extreme cases lead to baggy edges [9], can also cause lateral movement to the slack side [1,2]. Not surprisingly, web wandering issues are often associated with edge rolls [1,2,7,10].

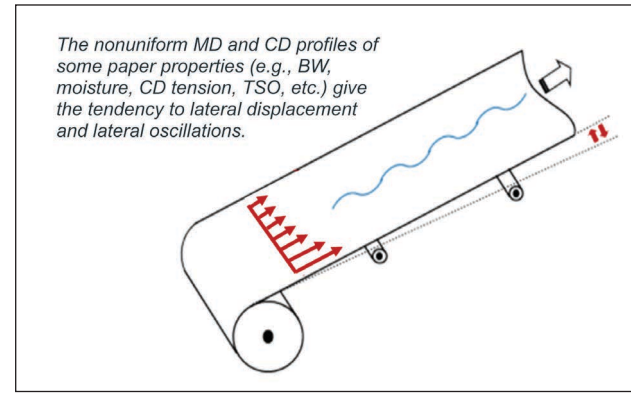

1. Cross-machine direction (CD) and machine direction (MD) nonuniformity leading to web lateral instability on a printing press. The blue line is the average lateral movement, and the red arrows represent the MD tension at specific CD positions. The web tends to move towards the low tension side, which is illustrated with the two red arrows (BW = basis weight; TSO = tensile stiffness orientation).

The MD variations can further amplify lateral instability and lead to web oscillations in the CD (**Fig. 1**). A comprehensive study of misregistration of gravure printed, bleached paperboard found basis weight pulsations were responsible for web wandering in the edge rolls [10].

A common approach to modeling lateral web movement is to start with the fourth order differential equation that

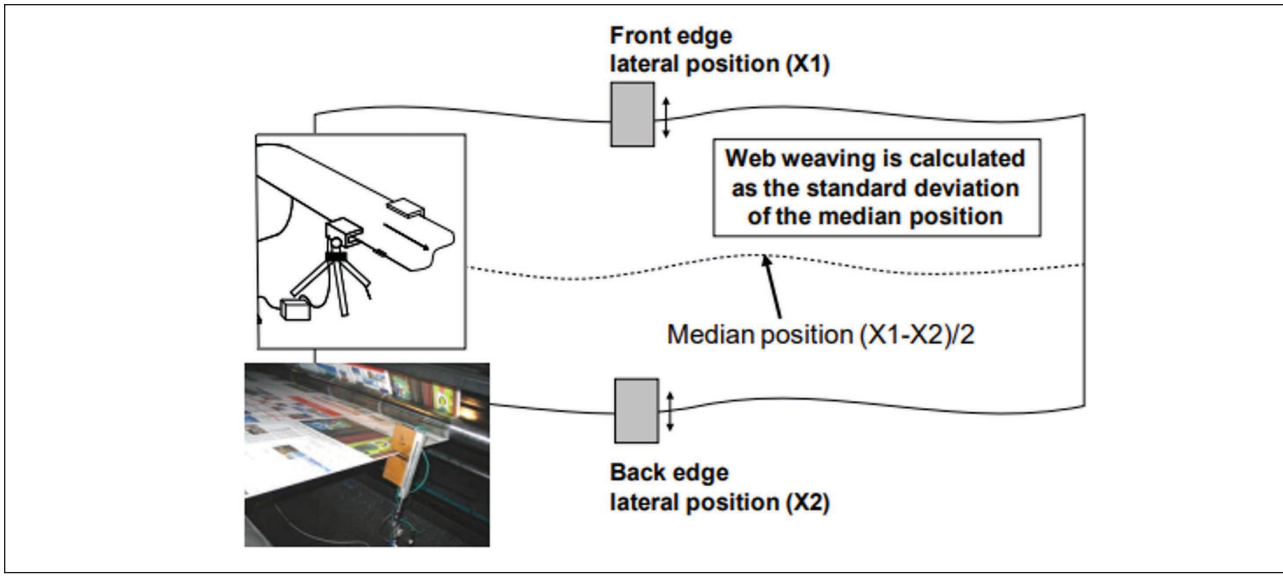

2. Web lateral displacement measurements with laser sensors on a printing press.

describes the bending of a beam (as a thin, two-dimensional plate) in the plane [11-15]. This equation can be explicitly solved, but the selection of suitable boundary conditions has proved elusive for a cambered web [11-15]. Numerical solutions have had limited success in explaining web tracking behavior of webs with nonuniform CD profiles [16-21].

Measurements of lateral movement of cambered webs [21] or belts [13,14] have shown that they tend to track towards the permanently elongated (lower tension) side if there is sufficient friction over a wrapped downstream roll. Obviously, for nipped rolls, there is no slippage.

In this study, we describe tools that can quantify web lateral stability in printing and converting equipment. By correlating these results with laboratory measurements, the main paper properties affecting web lateral stability were identified. A mathematical model was developed to explain the underlying mechanisms and can be used to troubleshoot issues beyond those addressed in this paper.

METHODOLOGY

This study focused on understanding which paper properties are important for lateral stability of a web. Products from four different mills were selected (newsprint, top-coated linerboard, supercalendered, and lightweight coated paper) that experienced lateral web movement, wrinkles, or misregistration issues in printing presses. Measurements were made in pressrooms where the rolls performed poorly. The CD and MD paper properties of a second set of rolls was measured in the laboratory and correlated with the pressroom measurements.

Pressrooms trials: Measuring web lateral movement

Web lateral movement was measured in different newsprint and commercial pressrooms in North America with an in-house device. The device consists of two portable laser beam sensors installed at the edges of the web (**Fig. 2**) to measure web lateral movement before and

Trial	Paper Grade	Type of Press	Problems Observed on the Press	Press Speed, m/min	Roll Width, m	Roll Diameter, m
1	**Newsprint**	Goss newsprint offset, 4 colors	Wrinkles, misregistration, and web breaks	600	1.27	1.27
2	**Supercalendered (SCB)**	ManRolland commercial heatset offset, 8 colors	Web shifting to one side of the press after drying	808	1.14	1.27
3	**Top-coated linerboard**	Goss Commercial heatset offset, 8 colors	Misregistration after print due to web weaving	350	1.27	1.14
4	**Lightweight coated (LWC)**	No tests on commercial press	Excessive web movement on press	N/A	0.86	1.07

I. Specifications of paper rolls and presses.

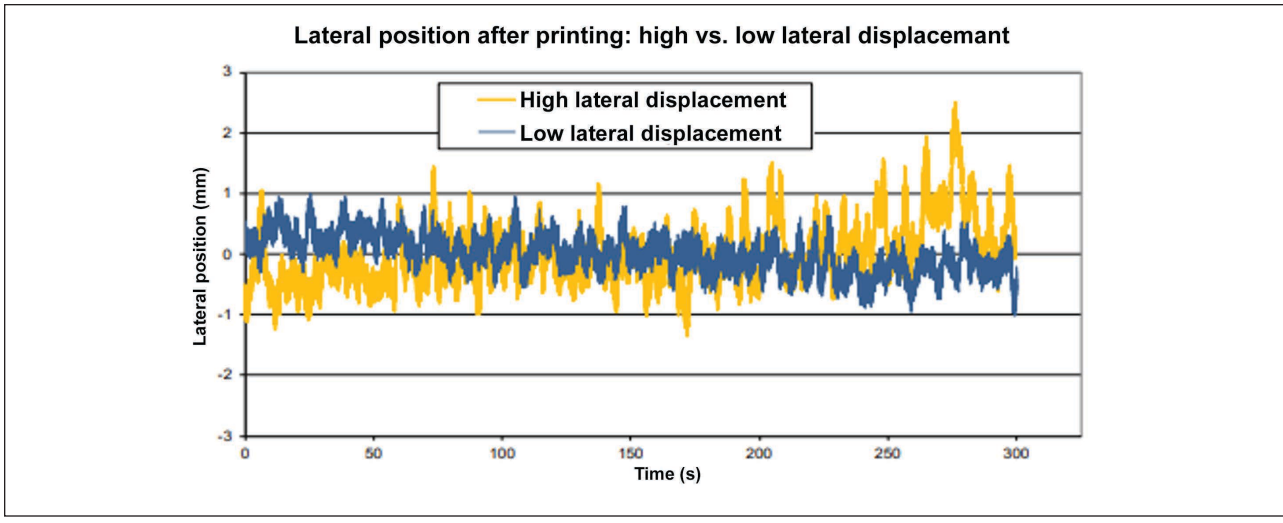

3. Lateral displacement examples (low in blue vs. high in yellow).

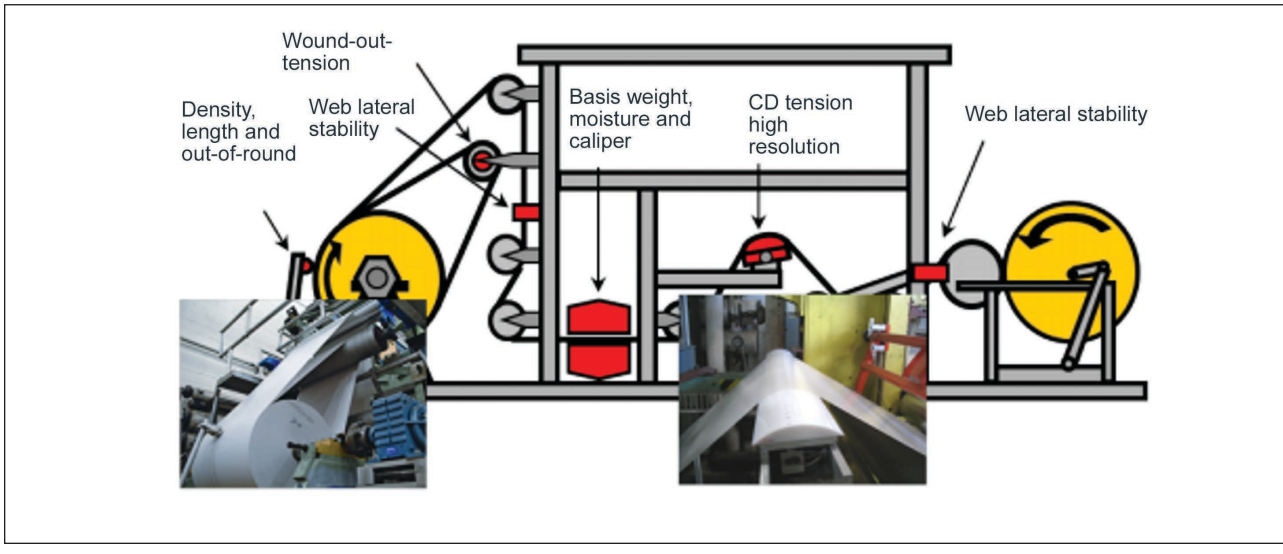

4. Schematic representation of the measurements performed on the roll testing equipment. The unwind is on the left.

after printing. Web weaving is calculated as the lateral movements of the median line, or the difference between the front and the back sensors divided by two. Calculating the average lateral movement eliminates the impact of variations in the web width (web shrinkage, for example). The paper products, press specifications, and problems observed on the press are summarized in **Table I**.

The web weaving was measured before print (just after press infeed) and after printing/drying (just before the slitter/folder). Only the measurements at constant press speeds were analyzed. The pasting and press stops/slowdowns were excluded from the calculation. The web weaving for an entire paper roll was calculated as the standard deviation of the median position of the web. For example, **Fig. 3** compares a low lateral displacement (in blue) to a higher lateral displacement (in yellow).

Laboratory trials: Measuring paper properties and variations

Web weaving and CD tension were measured on the roll testing facility (RTF) shown in **Fig. 4**. The web lateral instability was quantified using two pairs of laser beam sensors (the same as those used on printing presses) at the roll's unwind and rewind. The CD tension profile was measured at high resolution (2.5 cm) and high accuracy with a 1.27-m-wide tension beam equipped with load cells [9]. A Honeywell Measurex (Cupertino, CA, USA) scanner was used to measure basis weight, moisture and thickness.

In order to get a much higher resolution for the basis weight and thickness properties, additional analyses were conducted with the trademarked Tapio Paper Machine Analyzer (Tapio Measurement Technologies; Espoo, Finland), which has a resolution of 0.8 mm in CD and 12.8 mm in MD, enabling detection of variations from long

(0.003 Hz) to very short wavelengths (40000 Hz). Wavelengths and frequencies can then be correlated to machine component dimensions or time loops, thus allowing identification of specific machine elements causing these periodic variations.

Tensile stiffness was measured with a Lorentzen & Wettre (Kista, Sweden) tensile stiffness index-tensile stiffness orientation (TSI-TSO) instrument that has a resolution of 0.5 m in the MD and 0.1 m in the CD.

Based on the literature [1,3,4,5,8,22] and on our experience with paper webs on printing presses, it was believed that these properties would be the leading contributors to web lateral instability.

Lateral displacement

The lateral displacement of the web in the draw between two sets of nipped rolls can be estimated using the beam bending equation (see Appendix). The following equation is for the special case where there is a linear variation of either the MD stress in the CD (σ_x) or thickness (t) across the entire width of the web:

$$\delta \propto \frac{(LW)^2}{E_g I}\Delta\sigma_x t \quad (1)$$

where:

$\Delta\sigma_x$ = MD stress difference in the CD across the width of the web
W = web width
L = web span in the MD
E_g = geometric mean of the moduli in the MD and CD = $\sqrt{E_x E_y}$
I = area moment of inertia
T = thickness of the web

An equation for $\Delta\sigma_x$ was derived in [9]:

$$\Delta\sigma_x = -E_x\left[\left(\frac{\beta}{m_r}(\epsilon-\epsilon_0)+\frac{\partial\epsilon_0}{\partial m_r}\right)\Delta m_r + \frac{\partial\epsilon_0}{\partial m_p}\Delta m_p + (\epsilon-\epsilon_0)\frac{\Delta t}{t}\right] \quad (2)$$

where:

E_x = MD elastic modulus
β = exponent in equation ($E = \alpha m_r^{-\beta}$) [9], that relates modulus E to paper moisture in the roll, m_r
ϵ = strain or draw
ϵ_0 = permanent elongation in the MD
$\frac{\partial\epsilon_0}{\partial m_r}$ = hydro-expansion of dry paper that depends on many factors, including tension during drying
$\frac{\partial\epsilon_0}{\partial m_p}$ = plastic expansion in the press and dryer sections per percent moisture entering the first open draw

Uneven CD profiles for the moisture entering the dryers or basis weight and the caliper after the calender stack can lead to nonuniform MD stress profiles across the machine [9], which will cause lateral web movement.

There are two ways of quantifying the lateral movement of the web. The average lateral movement of the web can be measured with the laser positioning system described in the previous section. The second method is to calculate the standard deviation. Variations over time in the lateral web position could be caused by basis weight pulsations that change the values of the elastic moduli or the thickness of the web. In addition, there is often a measurable variation of the draw (ϵ) over time in any press. The time dependence of the draw is described by a nonlinear equation [23], which means that its behavior is often aperiodic and appears random. These MD variations will amplify the effects of any CD nonuniformities, as expressed in Eqs. 1 and 2.

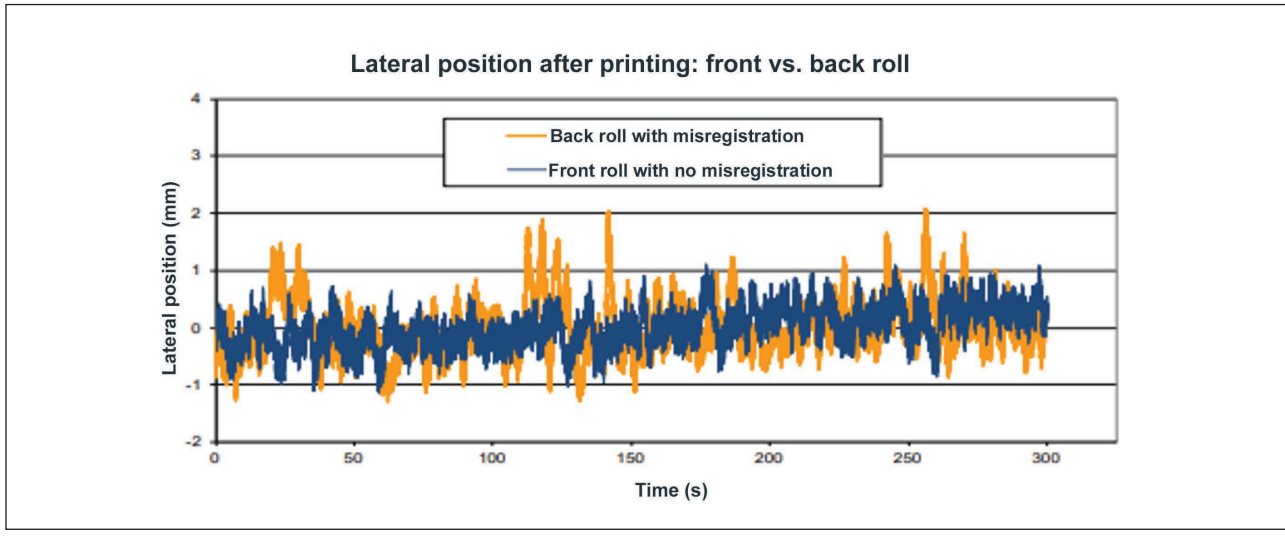

5. The lateral web stability of back side rolls (orange) was poorer than that for front side rolls (blue), which resulted in problems with misregistration.

RESULTS

Three properties were found to be critical for lateral web stability: CD tension profile, elastic modulus, and MD basis weight uniformity. These findings are described in more detail in the following sections.

Nonuniform CD tension profile as a result of nonuniform moisture profile entering the dryers

Case Study A: Newsprint

Rolls from the back side of a newsprint paper were being rejected by many customers because of loss of register. Compared to the front rolls, the back rolls showed higher lateral web instability after printing (**Fig. 5**), leading to misregistration and wrinkles. The lateral instability was mostly random, and the lateral control of the press was unable to react to these sudden movements.

The lack of tension on the back side roll is clearly visible and corresponds to the paper machine's back edge (**Fig. 6**). Both the TSO and TSI profiles and basic properties of the paper (moisture, basis weight, and thickness) measured on the RTF did not explain this drop in tension.

Attempts to correct the tension profile by optimizing the fiber alignment were not successful.

Measurements of CD tension on the RTF found the tension was 0.20 kN/m lower on the back side (**Fig. 7**). An uneven CD tension profile can be caused by nonuniform profiles in basis weight, caliper, moisture, or pressed moisture entering the dryers [9]. After some investigation, it was found that the moisture after the presses was higher on the back side, causing the paper to elongate more in the dryer section [9].

These observations follow from the combination of Eqs. 1 and 2, where $\frac{\partial \epsilon_0}{\partial m_p}$ is the permanent elongation per percent moisture entering the dryers.

To correct the moisture profile, the flow from the steambox was increased on the back edge of the machine to increase the pressed dryness, which leveled the CD tension (Fig. 7). This improved web tracking on printing presses and eliminated the misregistration problems for the back edge rolls.

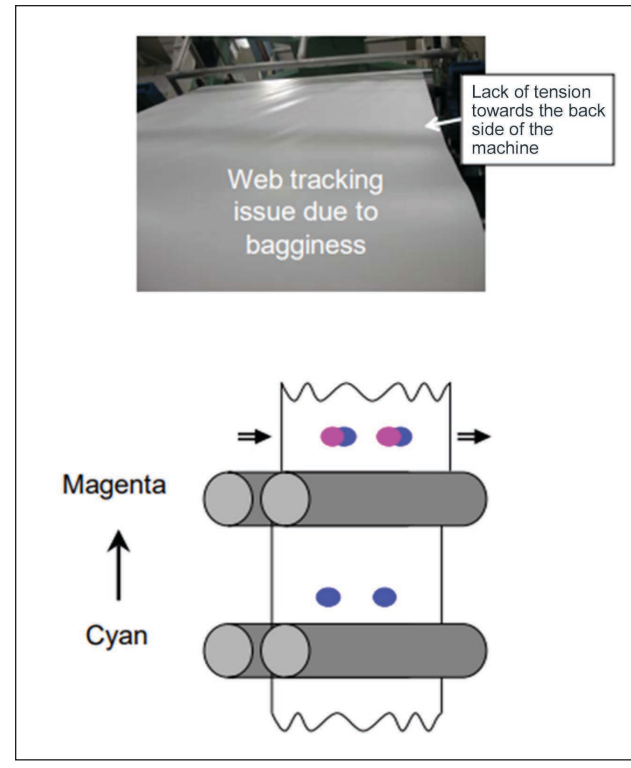

6. Baggy edge at the back of the machine is clearly visible at the unwind station of the roll tester. The web tends to move towards the low tension side between printing units (to the left). Misregistration is illustrated for the first two printing units; the printed dots from the cyan unit will not align with the magenta dots because the web has moved laterally. This problem will continue in subsequent color units, leading to distorted and blurred images.

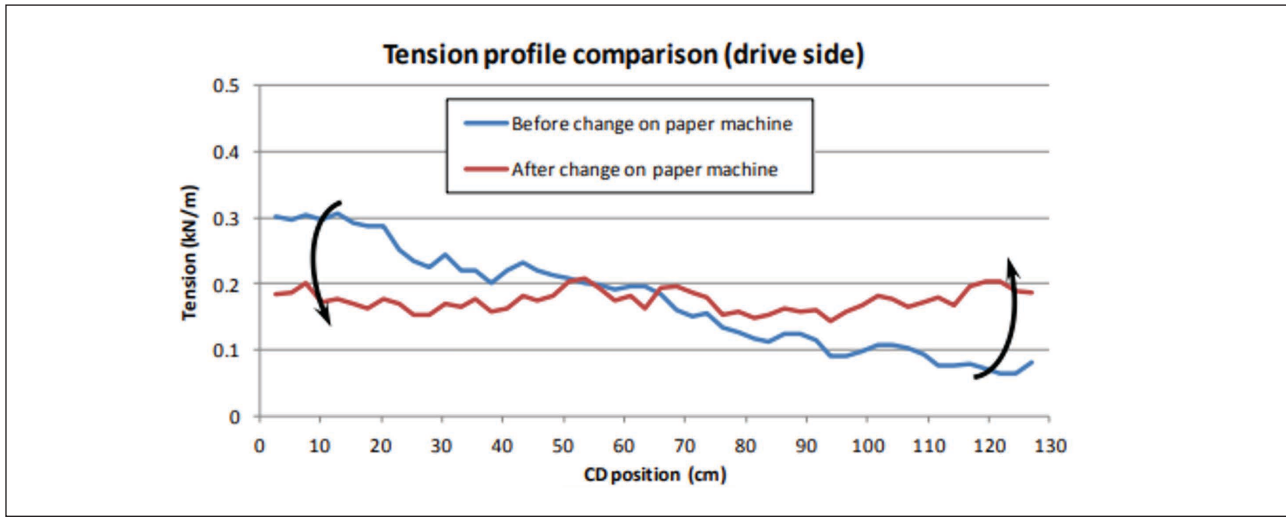

7. Correction of tension profile by leveling moisture profile after the press section.

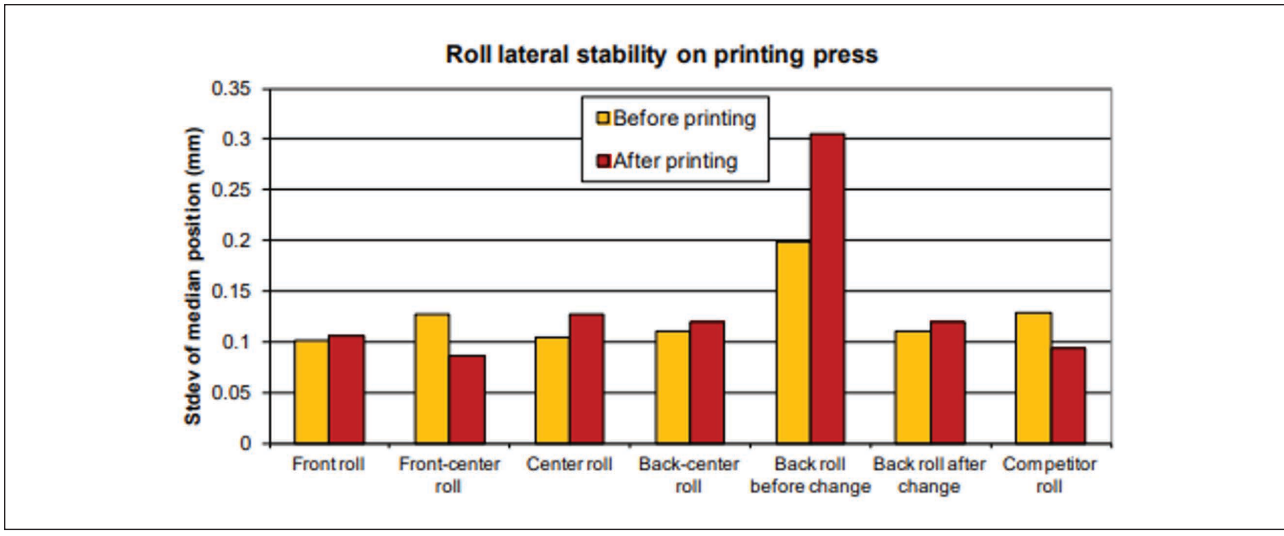

8. Web stability on press: comparison of problematic roll with good running rolls.

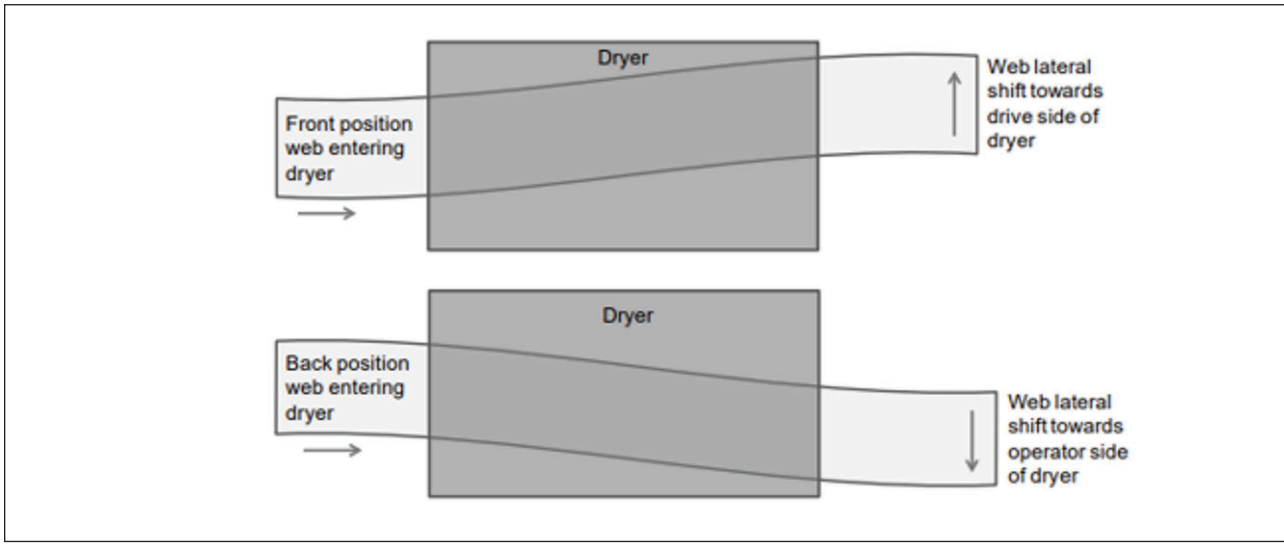

9. Schematic representation of web shifting after the dryer on a commercial highspeed printing press; shift is towards opposite sides, depending on the position of the rolls.

After the changes to the press section, the lateral stability of rolls from the back side of the machine were comparable to problem-free rolls from other machine positions and from a competitor (**Fig. 8**).

Case Study B: Supercalendered paper

Edge rolls from a supercalendered paper machine (SCB grade) had a problem with web shifting after the dryer section on a commercial printing press. The front rolls shifted towards one side of the press, whereas the back rolls shifted towards the other side (**Fig. 9**). The movement was so severe (up to 25 mm) that the lateral control of the press could not compensate, which caused wrinkles at the cutter and folder.

Measurements of MD tension at 2.54 cm intervals in the CD on the RTF showed that the profiles of both the front and back edge rolls were not uniform, with a difference of more than 0.20 kN/m from side to side (**Fig. 10**). The profiles were also opposite in shape, which explained why the front rolls shifted towards one side and the back rolls shifted towards the other side in the dryer of the printing press.

The problem was a nonuniform moisture profile after the press section caused by a worn press roll cover. Replacing the roll made the moisture profiles more uniform after the press section, which leveled the MD tension profiles in the CD (**Fig. 11**) and eliminated the web tracking issues.

Machine direction fluctuations in elastic modulus

Top-coated linerboard

A top-coated linerboard machine had a periodic lateral instability with a wavelength of approximately 16 m, which caused printing misregistration (**Fig. 12**).

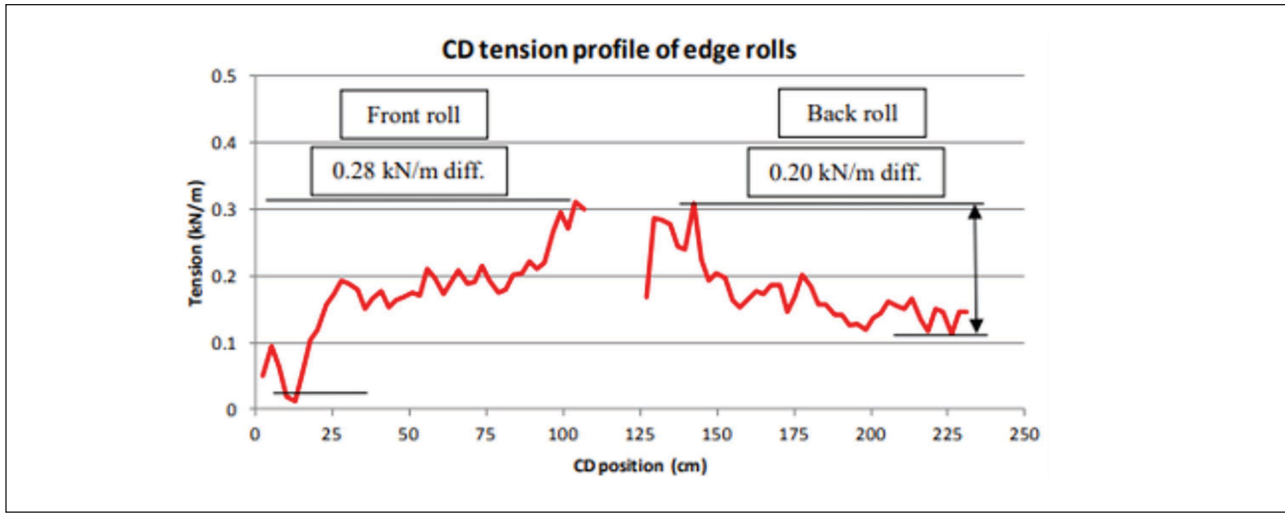

10. Nonuniform MD tension profiles in the CD at the paper machine's edges.

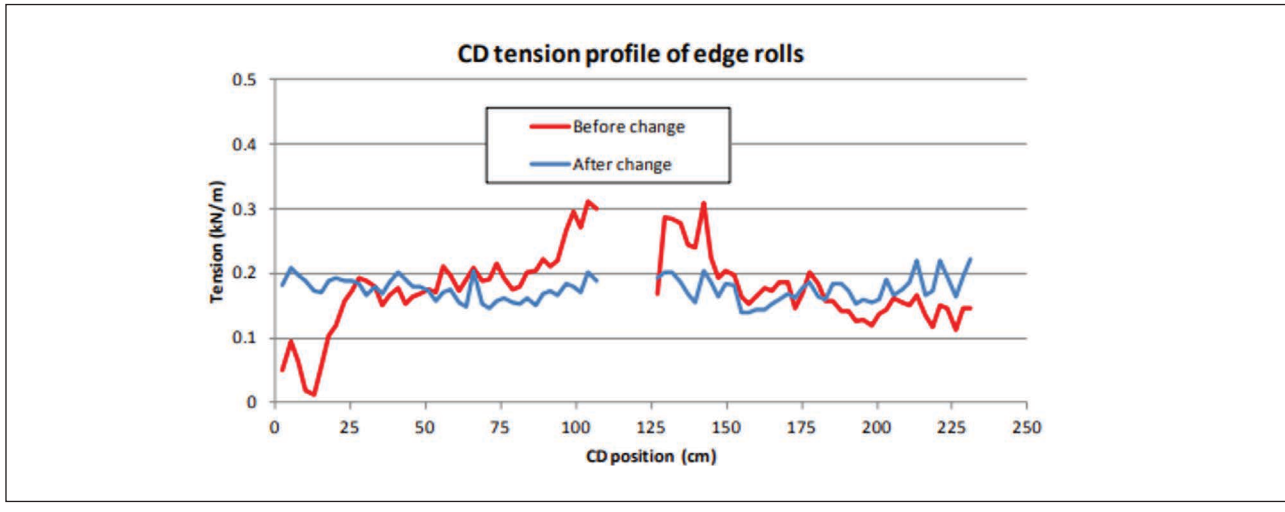

11. Uniform MD tension profiles in the CD at the paper machine's edges after moisture corrections on the paper machine.

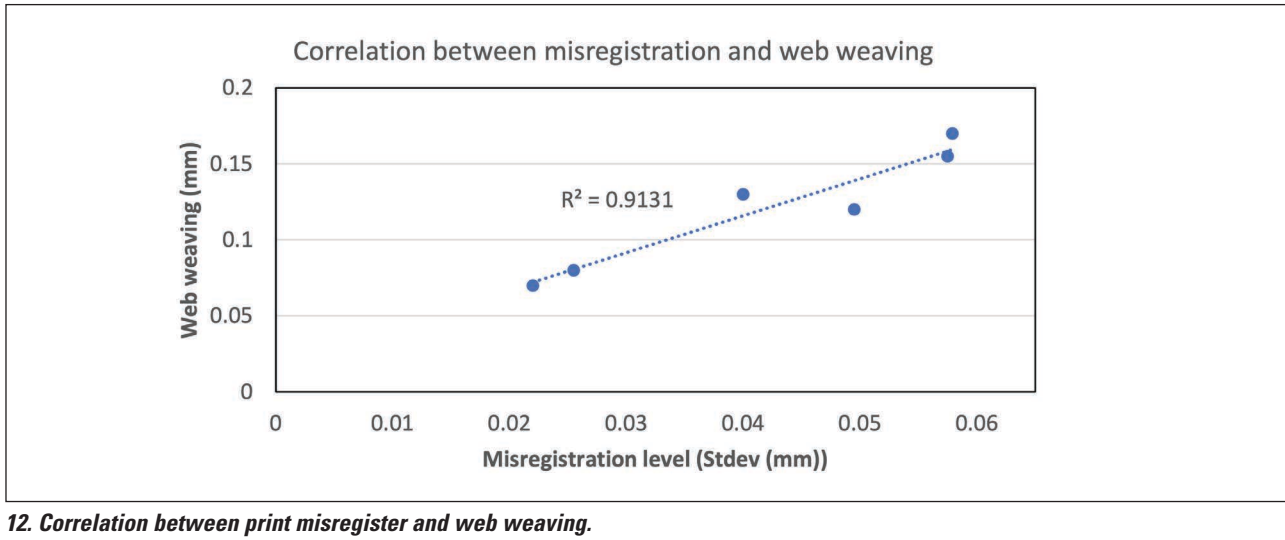

12. Correlation between print misregister and web weaving.

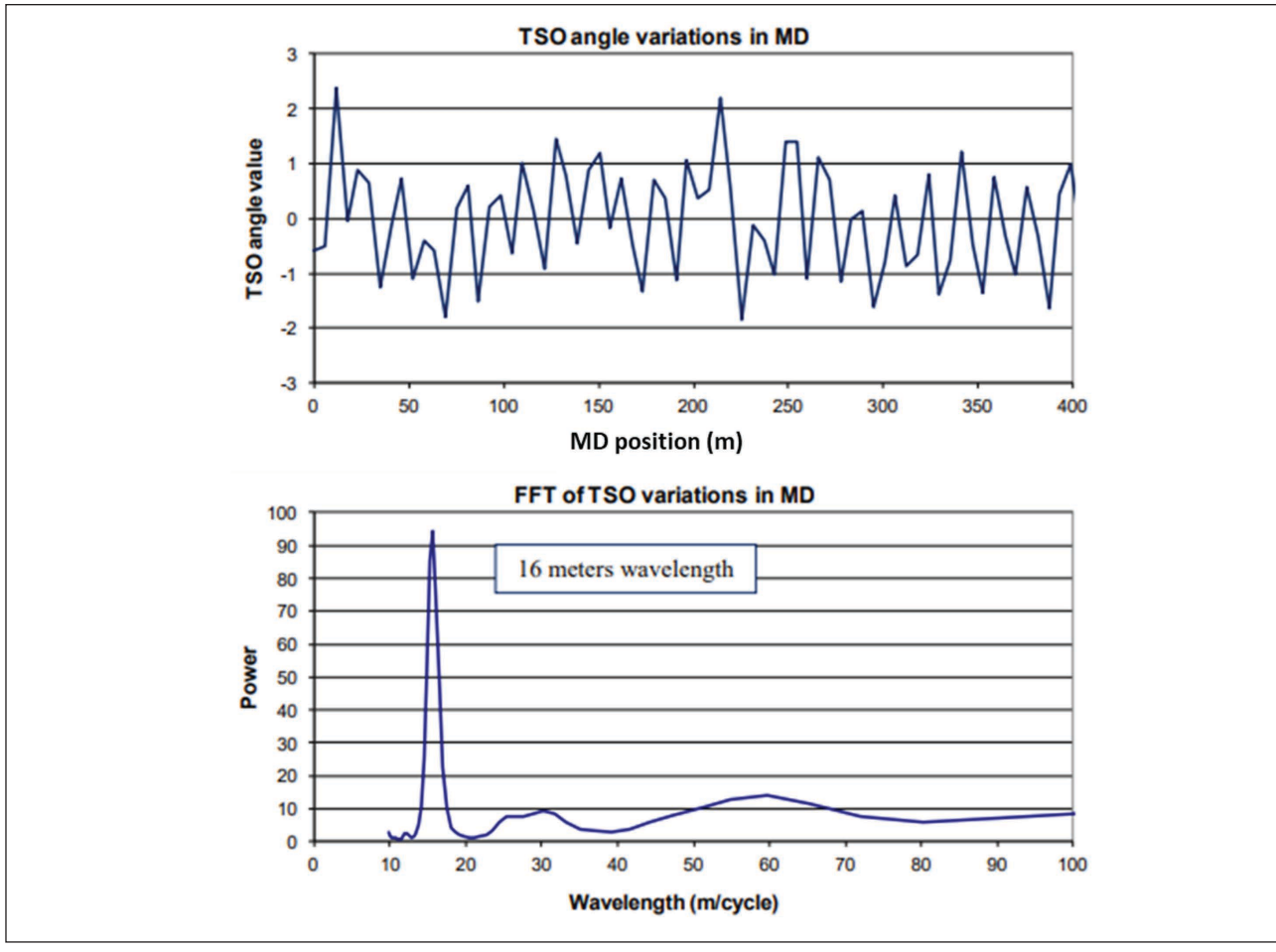

13. Periodic TSO angle variations in the MD led to web weaving on the press (FFT = fast Fourier transform).

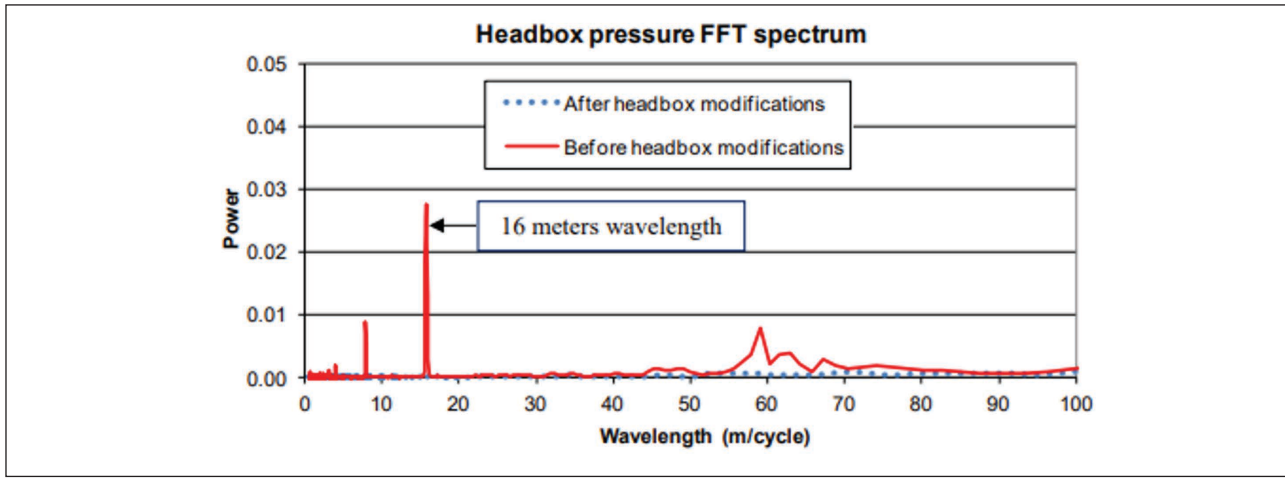

14. Periodic variations found in MD TSO and headbox pressure before and after correction to the fan pump on the paper machine.

The short wavelength made it impossible for the press operators to control or reduce the weaving. The addition of an S-wrap gave a slight improvement for longer wavelengths (above 50 m), but not at 16 m. Measurements of fiber orientation found that it varied with the same wavelength as weaving on the press (**Fig. 13**).

The TSO angle variations in MD were traced to headbox pulsations generated by the fan pump. After the fan pump was replaced, the main frequency (as well as the harmonic at 8 m) in the headbox pulsations disappeared (**Fig. 14**), as well as the TSO variations in MD. This reduced the web weaving on the printing press to an ac-

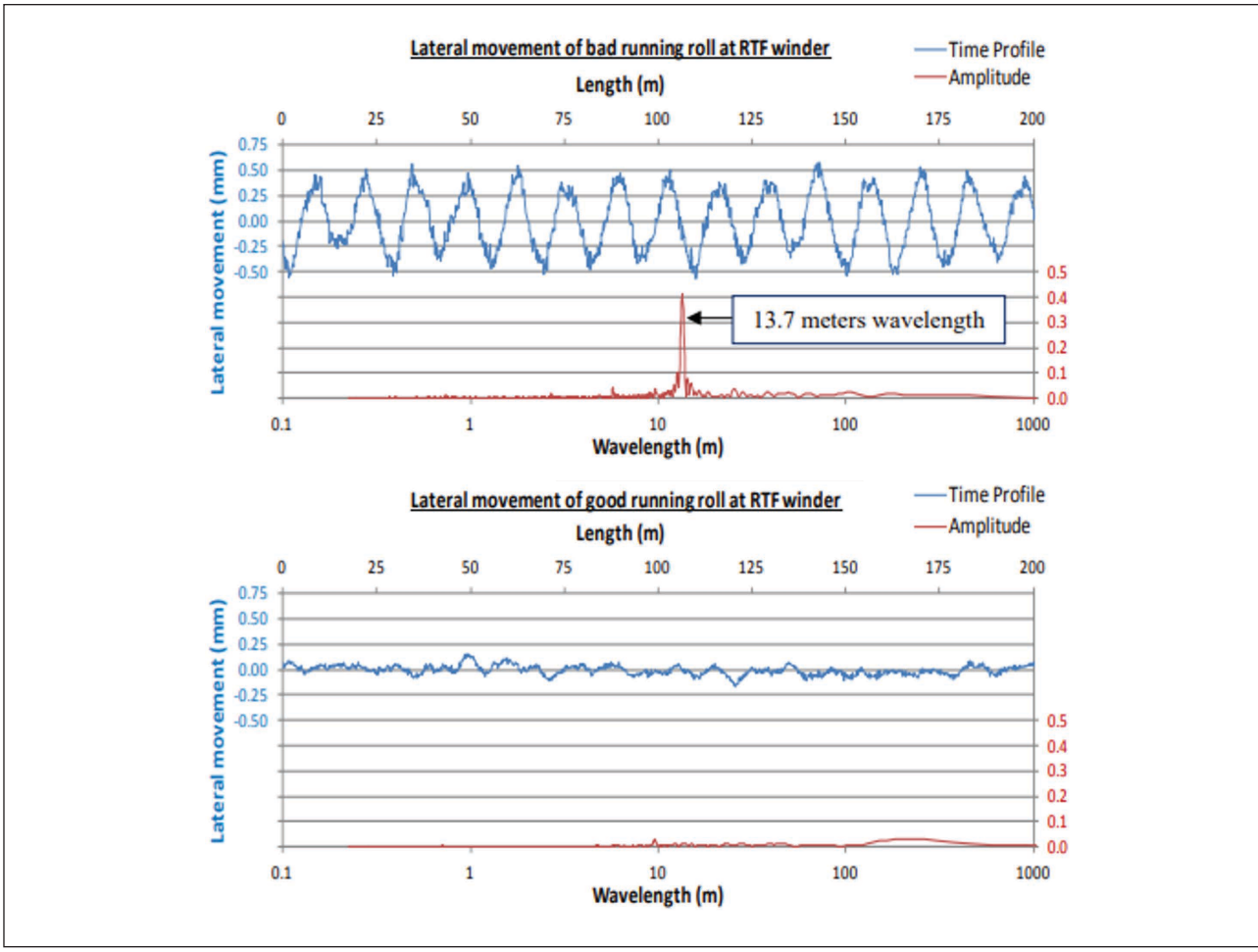

15. Lateral movement measured at the RTF winder (bad vs. good running roll).

ceptable level. These pulsations would lead to periodic changes in the moduli and thickness in Eqs. 1 and 2, which would cause the lateral movement over time.

Machine direction basis weight pulsations

Lightweight coated paper

A lightweight coated (LWC) paper web was weaving up to 10 mm at the press folder. Folder adjustments could not compensate for this high lateral variation. Web lateral movements were also observed at the printing units, causing misregistration. Lateral oscillations, measured on the RTF, were greater for rejected rolls than good rolls from the same machine (**Fig. 15**). The web weaving of the rejected rolls had a periodic variation with a wavelength 13.7 m in the MD, whereas good rolls did not show any web weaving.

The MD basis weight (**Fig. 16**) varied at the same wavelength as the web weaving with about the same amplitudes. This suggested that nonuniform basis weight was the source of the problem. Good rolls did not show any variation in MD basis weight (Fig. 16).

The wavelength found in the basis weight variations corresponded to some process variations on the paper machine. The changing basis weight affected the stiffness of the paper (E_gI) and thickness of the paper, which would amplify any CD nonuniformities.

CONCLUSION

Lateral web movement can be caused by nonuniform CD moisture profiles after the press section or basis weight profiles or caliper profiles after the calender stack. Weaving caused by poor profiles can be amplified by pulsations in the stock delivery system that cause MD variations in basis weight or fiber alignment. A mathematical model was developed to understand the connections between paper machine operation and lateral instability in printing presses. This model can be used as a troubleshooting tool. **TJ**

ACKNOWLEDGEMENT

The authors gratefully acknowledge the advice of Professor Richard Kerekes in the theoretical section of this study.

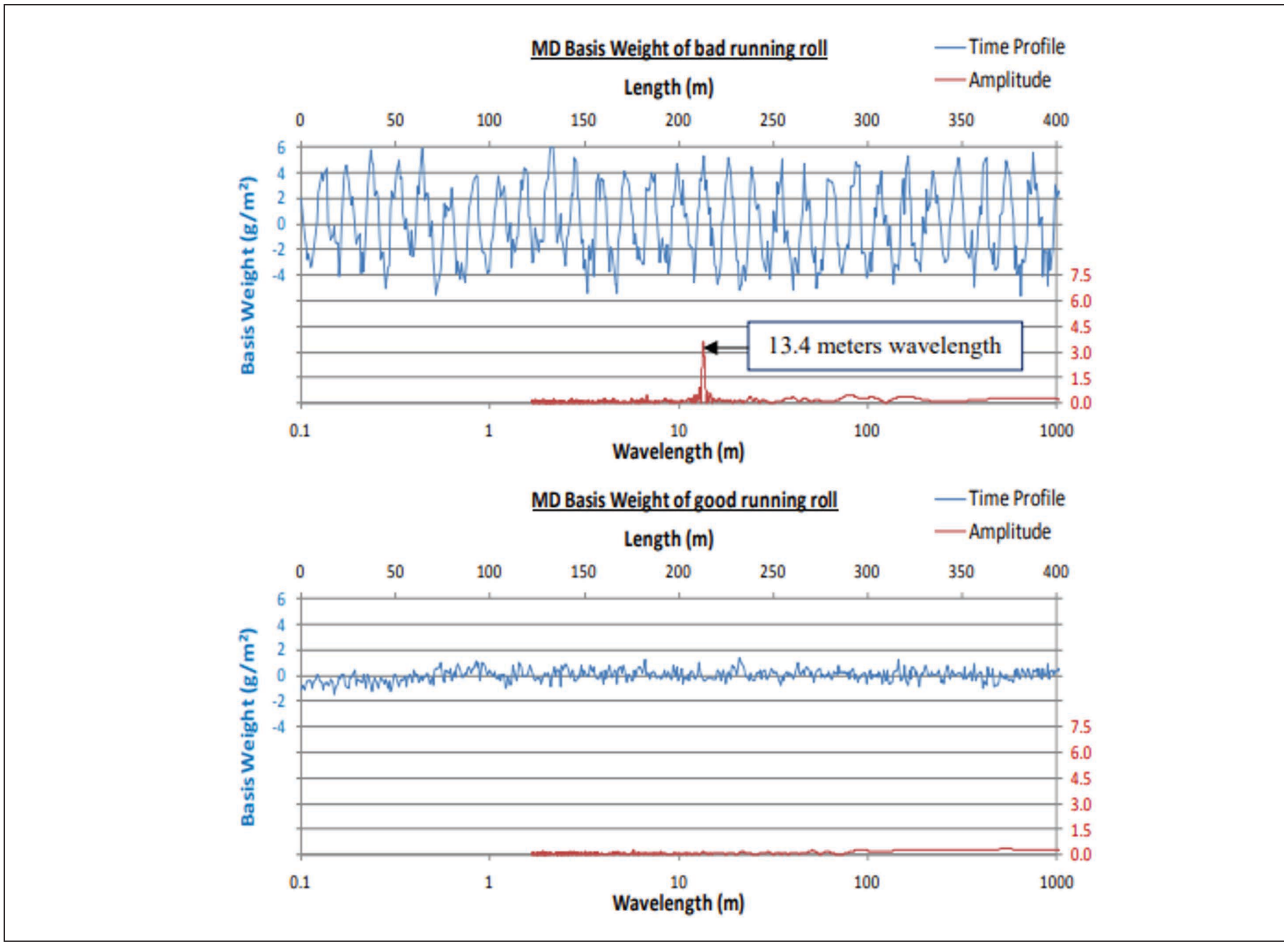

16. Basis weight variations in MD measured for good and bad running rolls.

LITERATURE CITED

1. Paukku, J., Parola, M., and Vuorinen, S., "Web widening and lateral movements of paper web in a printing press," *Int. Printing Graphic Arts Conf.*, PAPTAC, Montreal, QC, Canada, 2004.
2. Parola, M., Kaljunen, T., Beletski, N., et al., "Analyzing the printing press runnability by data mining," *TAGA Proc.: 55th Annu. Conf.*, TAGA, Warrendale, PA, USA, 2003.
3. Parola, M., Sundell, H., Virtanen, J., et al., *Pulp Pap. Can.* 101(2): T35(2000).
4. Roisum, D., *The Mechanics of Web Handling*, TAPPI Press, TAPPI, Atlanta, GA, 1998.
5. Smith, R.D., *Roll & Web Defect Terminology*, 2nd edn., TAPPI Press, TAPPI, Atlanta, 2007.
6. Roisum, D., *The Mechanics of Winding*, TAPPI Press, TAPPI, Atlanta, 1994.
7. Fox, J., "Back from the edge? – Mill experiences on the problems of edge reels," *Newsprint Production and Use – the Future of Newspapers Seminar*, London, UK, 1999.
8. Lindblad, G. and Furst, T., *The Ultrasonic Measuring Technology on Paper and Board: A Handbook*, Lorentzen & Wettre, Kista, Sweden, 2007.
9. Parent, F., Hamel, J., and McDonald, D., *TAPPI J.* 20(6): 365(2021). https://doi.org/10.32964/TJ20.6.365.
10. Enk, T., Urban. P., Dattner, M., et al., *J. Print Media Technol. Res.* 9(2): 103(2020).
11. Shelton, J.J., "Lateral dynamics of a moving web," Ph.D. thesis, Oklahoma State University, Stillwater, OK, USA, 1968.
12. Shelton, J.K., "The effects of web camber on handling," *Int. Conf. Web Handling, 4th*, Oklahoma State University, Stillwater, 1997.
13. Swanson, R.P., "Mechanics of nonuniform webs," *Int. Conf. Web Handling, 5th*, Oklahoma State University, Stillwater, 1999.
14. Swanson, R.P., "Lateral dynamics of nonuniform webs," *Int. Conf. Web Handling, 10th*, Oklahoma State University, Stillwater, 2009.
15. Benson, R.C., *J. Dyn. Syst., Meas., Control* 124(1): 25(2002). https://doi.org/10.1115/1.1435643.
16. Olsen, J.E., "Lateral mechanics of an imperfect web," *Int. Conf. Web Handling, 6th*, Oklahoma State University, Stillwater, 2001.
17. Olsen, J.E., "Shear effect and lateral dynamics of imperfect webs," *Int. Conf. Web Handling, 7th*, Oklahoma State University, Stillwater, 2003.
18. Olsen, J.E., "Lateral mechanics of baggy webs at low tensions," *Int. Conf. Web Handling, 8th*, Oklahoma State University, Stillwater, 2005.
19. Jones, D.P., "Web sag and the effect of camber on steering." *Int. Conf. Web Handling, 9th*, Oklahoma State University, Stillwater, 2007.

20. Olsen, J.E., "An updated model for lateral displacement of non-uniform webs," *Int. Conf. Web Handling, 10th*, Oklahoma State University, Stillwater, 2009.

21. Fu, B. and Good, J.K., "Explicit simulations of cambered web steering," *Int. Conf. Web Handling, 13th*, Oklahoma State University, Stillwater, 2015.

22. Kniivila, J., "On-line tension profile optimization via moisture profile controls on the newsprint papermaking process," *Int. Conf. Web Handling, 6th*, Oklahoma State University, Stillwater, 2001.

23. Niskanen, K., Ed., *Mechanics of Paper Products*, 1st edn., de Gruyter:Hawthorne, New York, 2012, pp. 94-100.

APPENDIX

Lateral movement of a paper web in an open draw

Consider a web in a span between two sets of nipped rollers (**Fig. A-1**). Within the nips, the paper is constrained, which prevents lateral (CD) movement. However, in the open draw, the web is free to move in the CD and thereby enter the downstream nip in a new location.

A CD gradient in MD tension creates a moment in the plane of the web causing it to bend as a beam according to the Bernoulli-Euler equation:

$$\frac{1}{r} = \frac{M}{E_g I} \tag{A1}$$

where:

r = imposed radius of curvature
M = moment
E_g = geometric mean of the moduli in the MD and CD = $\sqrt{E_x E_y}$
I = area moment of inertia

This radius produces a CD direction deflection in the web, causing it to enter the downstream nip in a new location. Equation A1 has sometimes been used as one of the four boundary conditions in the solution of the fourth order equation that describes beam bending [14]. This approach is a simplification that ignores out-of-plane bending and deflections, which are apparent in practice for severe, nonuniform CD web properties or low applied tension (draw). In reality, the web has insufficient stiffness to fully bend as a beam. Instead, the web can buckle in the out-of-plane direction, which under extreme conditions will appear as wrinkles or streaks. The web then follows a straight-line rather than an arc.

It is beyond the scope of this study to examine this complex 3-D instability problem in detail. However, this simple beam bending equation can be used to identify the web properties that can cause web lateral movement.

Consider the special case where there is a linear change in MD stress in the CD direction ($\Delta\sigma_x$) across the entire width of the web (W) or the CD thickness (t) as a result of the gradient shown in **Fig. A-2**. The moment (M) for this case, which is often encountered in practice, is proportional to $\Delta t\sigma_x$:

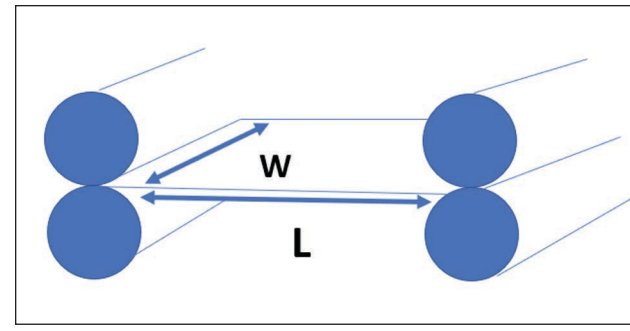

A-1. Web with width (W) and free span (L) between two sets of nipped rollers.

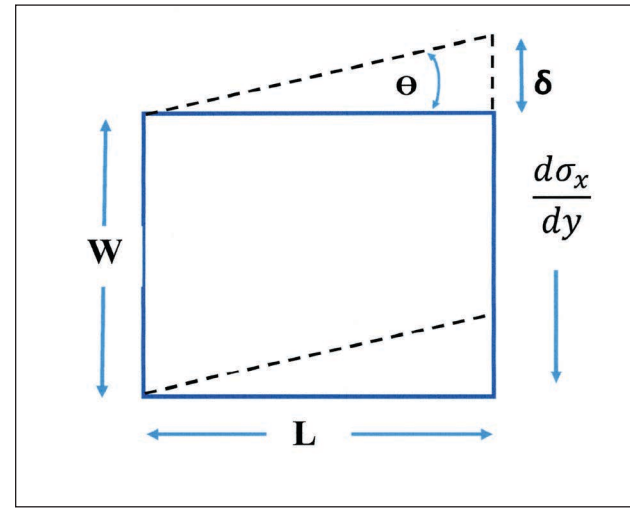

A-2. MD stress difference in the CD ($\Delta\sigma_x$) will cause the web to deviate.

$$M \propto W^2 \Delta(t\sigma_x) \tag{A2}$$

The resulting arc is equal to the span (L) from which the radius of curvature (r) can be calculated:

$$r\theta = L \tag{A3}$$

If θ is small, the lateral deflection, as shown in Fig. A-2, is:

$$\theta = \frac{\delta}{L} \tag{A4}$$

As Fig. A-2 shows, an MD stress difference in the CD ($\Delta\sigma_x$) will cause the web to deviate from the MD by an angle θ and lateral displacement δ.

Combining Eqs. A1 – A4 gives:

$$\delta \propto \frac{(LW)^2}{E_g I} \Delta(t\sigma_x) \tag{A5}$$

Thus, as a result of the imposed moment, the web will be forced towards the low-tension side up to a potential distance of δ before buckling. Increasing the MD stress difference in the CD direction ($\Delta\sigma_x$) or lowering the stiffness of the web will lead to greater lateral deflection. The MD stress ($\Delta\sigma_x$) is itself a dependent variable, produced by strain imposed by the draw and the web response to this strain dictated by the modulus E and web thickness. Thus, imperfect draw control, varying moduli, and web thickness will cause the lateral displacement to change over time.

ABOUT THIS PAPER

Cite this article as:
Parent, F., Hamel, J., and McDonald, D., *TAPPI J.* 21(1): 9(2022). https://doi.org/10.32964/TJ21.9.22

DOI: https://doi.org/10.32964/TJ21.9.22

ISSN: 0734-1415

Publisher: TAPPI Press

Copyright: ©TAPPI Press 2022

About this journal

ABOUT THE AUTHORS

We studied this topic because lateral instability or weaving of the web causes printing problems, including misregistration or runnability issues like wrinkles, breaks, or folder problems. Lateral instability is the result of uneven MD web tension in the CD. Under extreme conditions, this appears as bagginess, which we have previously studied.

The most difficult aspect of this study was the many possible causes of lateral stability (uneven tension). In this paper, these were identified by means of trials on commercial printing presses and paper machines.

We found that a simple mathematical equation can explain the tendency of the web to deviate from a straightline path. A surprising finding was that although web tension profiles have an impact on printing and conversion performance, they are rarely measured on paper machines.

For mills, this paper describes several case studies that identify the origin of lateral stability on paper machines. Simple changes to machine operation were able to eliminate these problems.



Parent



Hamel



McDonald

There are other quality issues that are caused by uneven tension profiles. These problems will be investigated in future work.

Parent is research engineer and Hamel is vice president, Industry and Member Relations, for FPInnovations in Pointe Claire, QC, Canada. McDonald is president of JDMcD Consulting Inc. in Vaudreuil-Dorion, QC, Canada. Email Parent at Frederic.Parent@fpinnovations.ca.

Microbial load and proliferation associated with various face mask types and sources during the COVID-19 pandemic

SRINIVASAN NARASIMHAN, MEENASHREE BALAKRISHNAN, OLUKAYODE JAMES AYODEJI, AND SESHADRI S. RAMKUMAR

ABSTRACT: Due to the shortage of personal protective equipment during the COVID-19 pandemic, homemade face coverings were recommended as alternatives. However, the capability of alternative face coverings to proliferate microbes have not been fully documented.

The current study evaluated bacterial load and proliferation associated with the use of common face masks during the COVID-19 pandemic. Mask type-specific and surface-related bacterial load and pattern were noticeable in the study. Results indicated that roadside masks are among samples that contained relatively higher initial bacterial load. The highest number of bacterial forming colonies were observed in the inner surface of mask samples. Proliferation of microbes over time was also noticeable among the non-certified face coverings included in the study. Sterilization or washing of non-certified fabric face masks before use is recommended.

Application: Apart from protecting the wearer from getting exposed to the infection, face coverings also stop the spread from infected individuals. The present study examined the population of microbes distributed over the mask surface during use. The microbial load on each type of mask, the health, and potential safety risks were highlighted. This information could guide policy and mitigating measures against severe acute respiratory syndrome (SARS) related infections.

Studies have shown that the use of face masks can minimize the spread of COVID-19 [1,2]. Masks provide a physical barrier between the outside environment and the respiratory organs of the user [3]. Filtration efficiency is one of the major factors in the evaluation of the effectiveness of face masks. Face masks that provide the highest bacterial filtration and high resistance to body fluids are categorized as Level 3 by the American Society for Testing and Materials (ASTM) Standard [4]. In response to the shortage of face masks during the COVID-19 pandemic, the use of homemade masks designed from regular fabrics was recommended by the U.S. Centers for Disease Control and Prevention [5]. The shortage is expected to persist, and the World Health Organization has estimated that approximately 89 million medical masks will be needed every month during the COVID-19 pandemic [6].

As most countries lift lockdowns, individuals are required to wear face masks, especially in public [1], resulting in greater demand for masks to meet the increasing needs [7]. The use of homemade cloth face coverings and reuse of disposable face masks have become a common habit due to a critical shortage in supply of masks during the COVID-19 pandemic [8]. The global price of face masks significantly increased during the pandemic [9,10]. Between January and February 2020, the price of face masks increased by 319% in the United States [10]. Because of a large customer base, Asia Pacific became the largest market for face coverings at the onset of the COVID-19 pandemic, accounting for 33.7% of global market share in 2019. India and China are among the top manufacturing countries of face masks in the world [11].

For these reasons, non-certified and homemade masks were designed, manufactured [7], and sold in open markets [12]. In most cases, the purchased masks fall below the required health standards. In developing countries, a low level of income has been cited as another major reason for low-quality manufacturing of face masks, because many people cannot afford protective masks that meet required health standards or certifications [12]. Most users of face masks made from regular fabrics (roadside tailors) use them without washing and are prone to contracting other diseases besides COVID-19 [13].

Bacterial dispersion has been associated with the use of face masks [14,15], and such dispersion may be influenced by the design of the face mask [16]. Aerosol filtration performance of household fabrics and surgical masks and their effectiveness at blocking droplets have been investigated [5,8,17,18,19], but their capability to proliferate microbes during use has not been fully documented. The goal of the current study is to evaluate bacterial load and proliferation associated with the use of face masks during the COVID-19 pandemic. In the study, we (1) quantified initial bacterial loads on face masks of differ-



1. Images of face covering sample types utilized in the current study: (a) N95 mask with filter (FiltAir-FFP2); (b) N95 mask without filter (VENUS: V-4400N95 National Institute for Occupational Safety and Health [NIOSH]); (c) two-layered (two-ply) surgical disposable face mask; (d) three-layered (28 polypropylene [PP] + 20 meltblown [MB] + 20 PP) mask; (e) roadside mask (baniyan cloth); and (f) Velcro face mask (cotton fabric).

ent types and sources, and (2) examined their proliferation on the inner and outer mask surfaces during use. Masks with varying qualities and prices were utilized.

EXPERIMENTAL

Materials and methods

N95 masks (VENUS: V-4400N95 National Institute for Occupational Safety and Health [NIOSH]) with a filter (FiltAir-FFP2) and without a filter were purchased from New Venkateswara Medicals (Chennai, India). Two-layered and three-layered polypropylene masks were purchased from a retailer in Chennai. Velcro face masks were purchased from a retailer in Bengaluru. Roadside masks (baniyan cloth) were purchased from a market in Chennai, India. **Figures 1a-1f** shows images of the masks used in this study.

Soyabean casein digest agar was purchased from HIMEDIA (Mumbai, India) and prepared according to the manufacturer's specifications. Briefly, 40 g of the agar was suspended in 1 L of distilled water in a 2 L volumetric flask followed by thorough mixing to obtain complete dissolution. The suspension was sterilized in an autoclave (Raagaa

Volunteers							
Masks	**Surfaces**	**Control (A)**	**(B)**	**(C)**	**(D)**	**(E)**	**(F)**
N95 (with filter)	Inside	1	65	166	136	NA	123
	Outside	2	244	313	65	NA	140
N95 (no filter)	Inside	3	195	163	153	245	121
	Outside	0	89	257	58	52	9
Two-layered	Inside	1	439	107	91	347	163
	Outside	2	110	158	12	10	19
Three-layered	Inside	29	453	263	840	529	577
	Outside	38	515	200	320	9	35
Roadside	Inside	26	835	457	602	387	635
	Outside	46	200	213	19	44	18
Velcro	Inside	2	430	471	455	145	371
	Outside	10	86	188	40	9	18

NA = N95 masks (with and without filters) missed by volunteer E.

I. Viable microbial load observed within the internal and external surfaces of different face masks. Number of bacterial colonies (colony forming units; CFUs) is presented.

Volunteers							
Masks	**Surfaces**	**Control (A)**	**(B)**	**(C)**	**(D)**	**(E)**	**(F)**
N95 (with filter)	Inside	0	0	0	1	NA	1
	Outside	0	0	3	5	NA	2
N95 (no filter)	Inside	0	0	0	2	2	1
	Outside	0	0	0	6	1	4
Two-layered	Inside	0	0	0	1	1	0
	Outside	0	0	0	4	3	1
Three-layered	Inside	0	0	0	1	2	0
	Outside	0	0	0	1	0	0
Roadside	Inside	0	0	0	0	0	0
	Outside	0	0	0	2	1	2
Velcro	Inside	0	0	0	0	0	0
	Outside	0	0	1	1	1	0
NA = N95 masks (with and without filters) missed by volunteer E.							

II. Fungal colonies observed within the internal and external surfaces of different face masks. Number of bacterial colonies (CFUs) is presented.

Industries; Nanganallur, Chennai) at 120°C for 30 min. The flask was allowed to cool down and the agar media was poured into petri dishes and allowed to solidify. Sabouraud dextrose agar (SDA) was purchased from SRL Chem (Chennai, India) and prepared according to the manufacturer's specifications. Briefly, 65 g of the SDA powder was suspended in 1 L of distilled water, mixed thoroughly for complete dissolution, and sterilized in an autoclave at 120°C for 30 min. The media was allowed to cool, and the content was dispensed into petri dishes and allowed to solidify.

The study was conducted at Asthagiri Herbal Research Foundation, Chennai, India. Five volunteers who work within the premises were selected for the study. The volunteers were comprised of three females and two males with an age range of 23–68. One female and one male were diabetic. To avoid post-purchase contamination, masks remained sealed in a clean Ziploc bag immediately after purchase, and volunteers were discouraged from touching the masks or adjusting the fit during the experiments. Each participant was asked to wear the mask types for a period of 1 h per mask. All participants were non-smokers, and they consumed food and water during the study. All the volunteers remained within the premises until the end of the experiment.

At the end of the experiment, the center part of all masks at an area of 3 mm × 8 mm was collected inside a laminar air flow chamber by making a cut using sterile surgical blades. The cut centers were immediately imprinted on the sterile soyabean casein digest agar medium in separate petri dishes. The inside and outside layer of the mask was imprinted separately. Unused masks were used as a control and were also imprinted on agar media before and after the period of the experiments. After imprints, the plates were incubated at 30°C and observed for the growth of bacterial colonies after 24 h. The incubator used was previously purchased from Elegant Equipment (Thirumullaivoyal, Chennai). The SDA medium was used to observe the fungal colonies after 5 days of incubation at 30°C.

Samples of observed bacterial colonies were diluted in 500 µL of sterile distilled water by suspending an inoculating loop full of the culture. A clean and sterile glass slide was taken and 100 µL of the suspension was placed at the center. It was fixed by gently heating the slide over a burner. A crystal violet was added and kept for about 30 s and then rinsed with water. The smear was covered with Gram's iodine for 1 min and washed with water, followed by 95% ethanol wash for about 10–20 s. Safranin was added and after 1 minute washed with water. The dried slide was observed under a Binocular Microscope (Deep Vision Plus DXL 25T, GA Instruments; Chennai, India) at 40X.

RESULTS

The results of viable microbial load on the inner and outer surfaces of face masks at the beginning (control) and the end of the experiments are given in **Tables I and II** and in **Figs. 2 and 3** as colony forming units (CFUs).

Images of face masks utilized in the study are presented

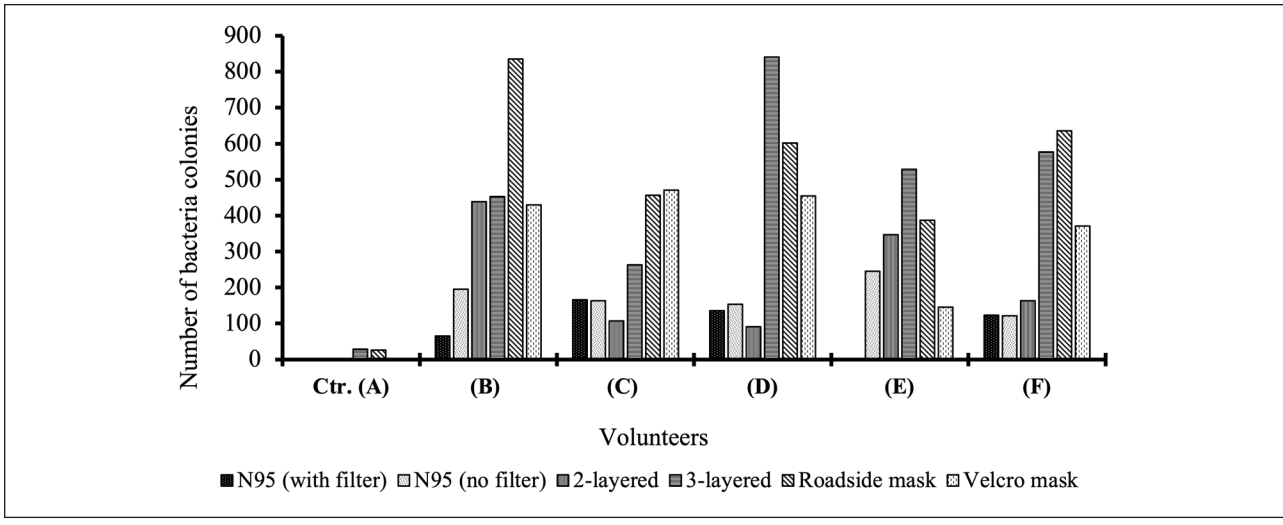

2. Bacterial loads counted as colony forming units (CFUs) obtained from the inside part of various face mask types from different sources.

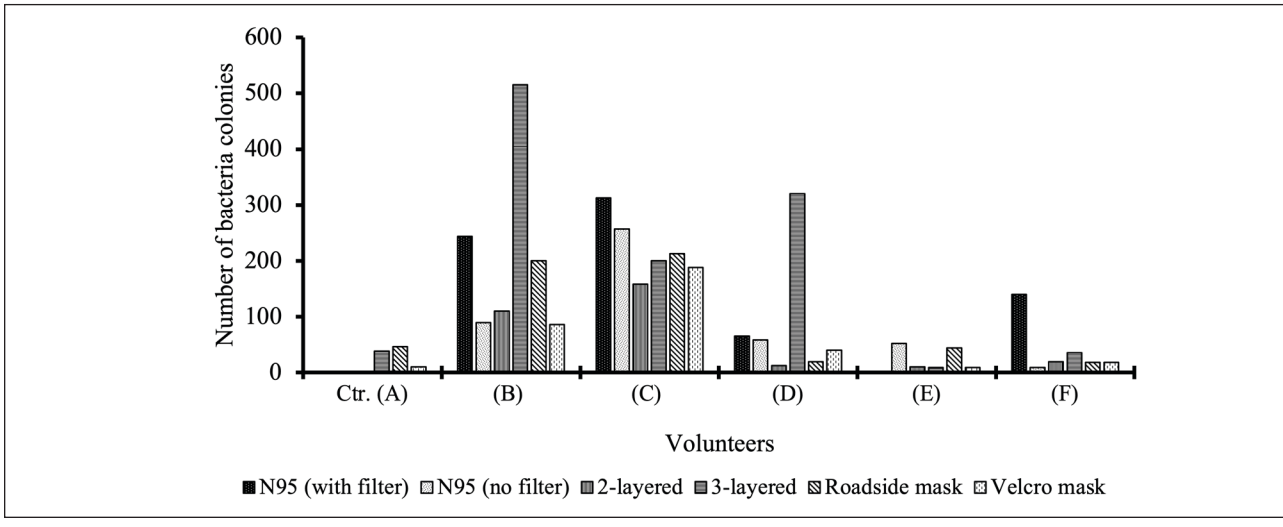

3. Bacterial loads counted as CFUs obtained from the outside part of various face mask types from different sources.

as Figs. 1a–1f. Images of petri dishes showing viable CFUs observed from samples collected from inner and outer surfaces of masks are given in **Figs. 4a–4f**.

Similar bacterial colonies were observed in the mask imprint of all the volunteers. Most of the bacterial species were cocci shaped. The outside of the mask primarily contained five repeatedly occurring colonies, three out of which were gram positive and two that were gram negative (**Figs. 5 and 6**). The inside of the mask had three repeatedly occurring colonies, one out of which was gram positive and two that were gram negative (**Fig. 7**). All the volunteers had similar bacterial load on the masks used. No unique colonies were found aside from *Streptococci sp* and *Bifidobacterium* generally observed on most masks.

DISCUSSION

It has become necessary to wear face masks during and after the COVID-19 pandemic. The universal use of face coverings has attracted interests from different disciplines to understand their effectiveness [2,16]. However, there are no data on bacterial load of various face masks, especially those sourced from uncertified outlets, including roadside markets. Additionally, it is important to understand bacteria proliferation capabilities of different face mask sources and types.

In the current study, we found that the N95 (with and without filters), two-layered face masks, and Velcro masks included in the study contained the lowest initial number of bacterial CFUs. Three-layered and roadside masks contained the highest initial number of bacteria forming units (Table I). The high initial number of bacteria colonies observed in roadside-sourced face masks is consistent with the potential risk associated with the use of uncertified substandard face masks as reported by Mwema and Nyika [12]. In the present study, both surfaces of roadside masks contained a high initial number of bacterial CFUs (Figs. 2 and 3).

a. N95 with filter.

b. N95 without filter.

c. Two-layered mask.

d. Three-layered mask.

e. Roadside mask.

f. Velcro mask.

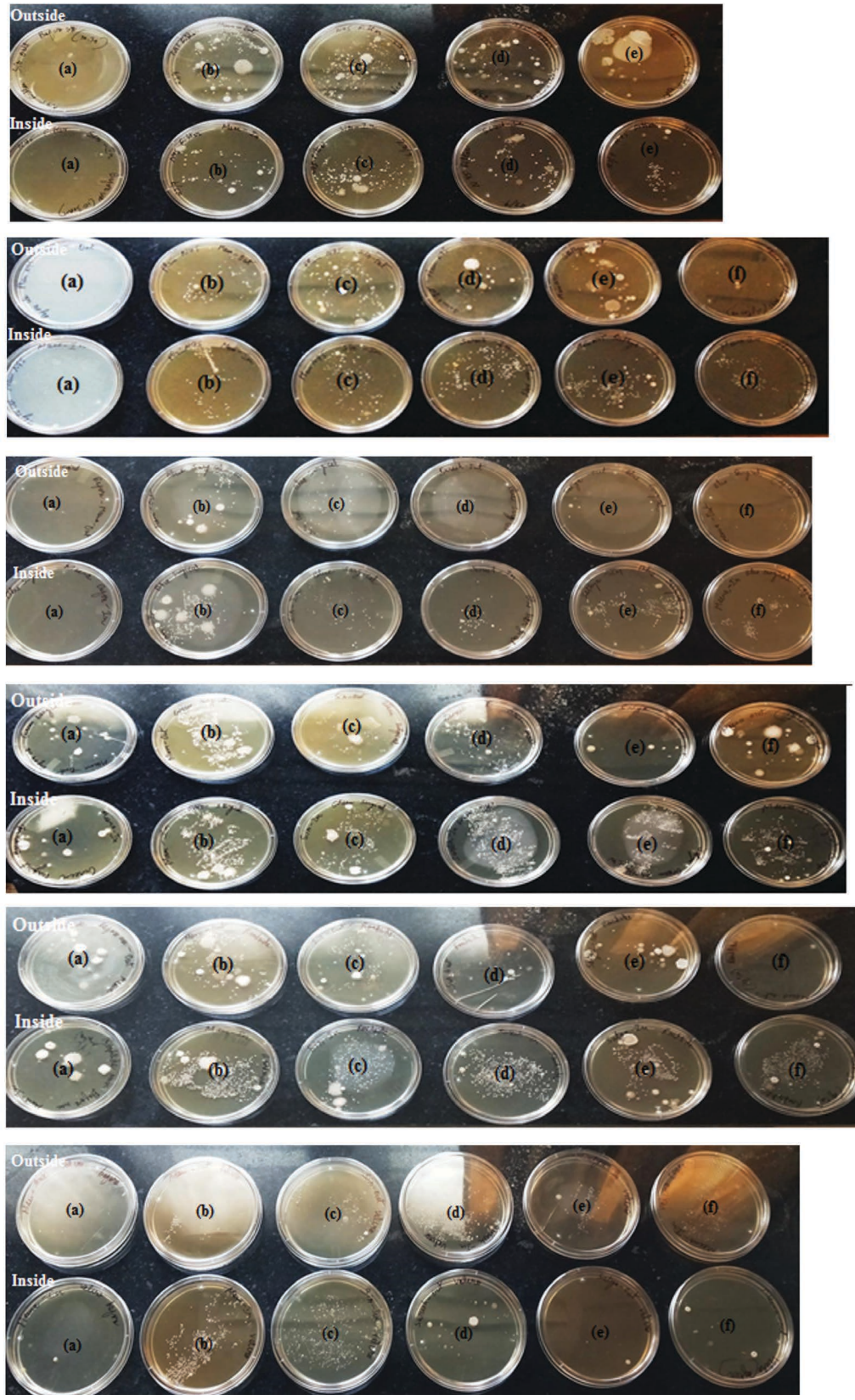

4. Post-experimental microbial colonies observed on both sides (outside and inside) of mask samples after 24 h of incubation: (a) microbial colonies in N95 mask with filter; (b) microbial colonies in N95 mask without filter; (c) microbial colonies in two-layered face mask; (d) microbial colonies in three-layered face mask; (e) microbial colonies in roadside mask; and (f) Velcro mask.

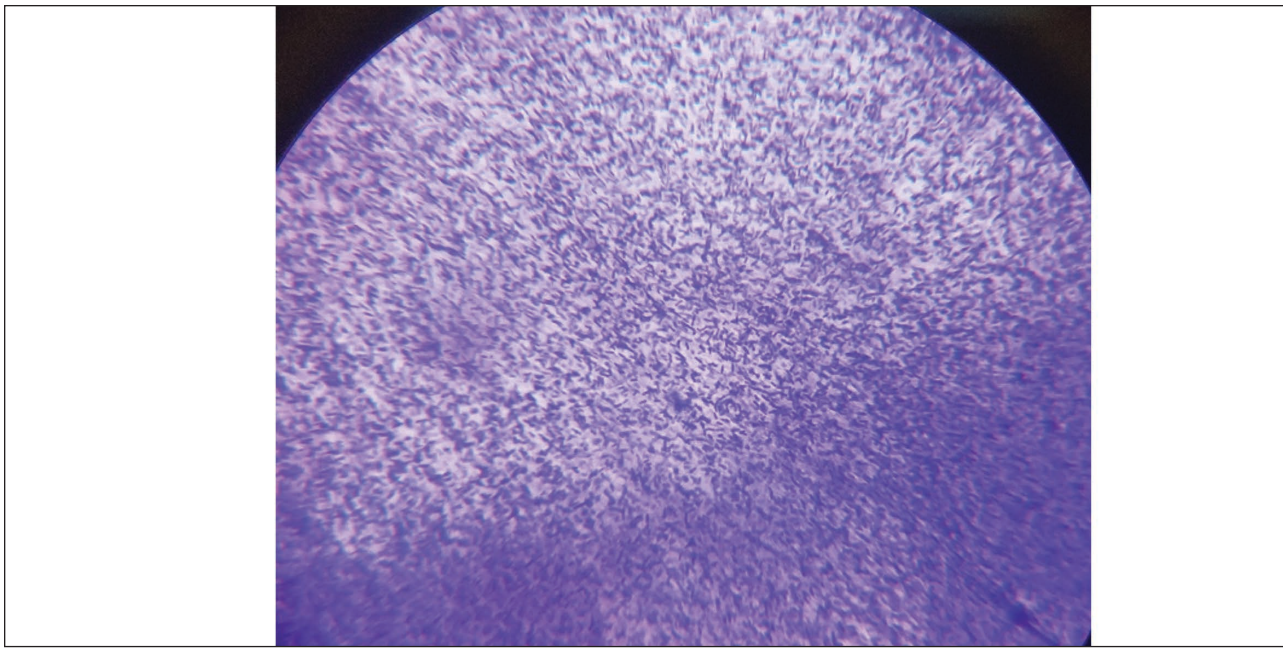

5. Gram positive **Streptococci sp** *observed on the outside of the masks.*

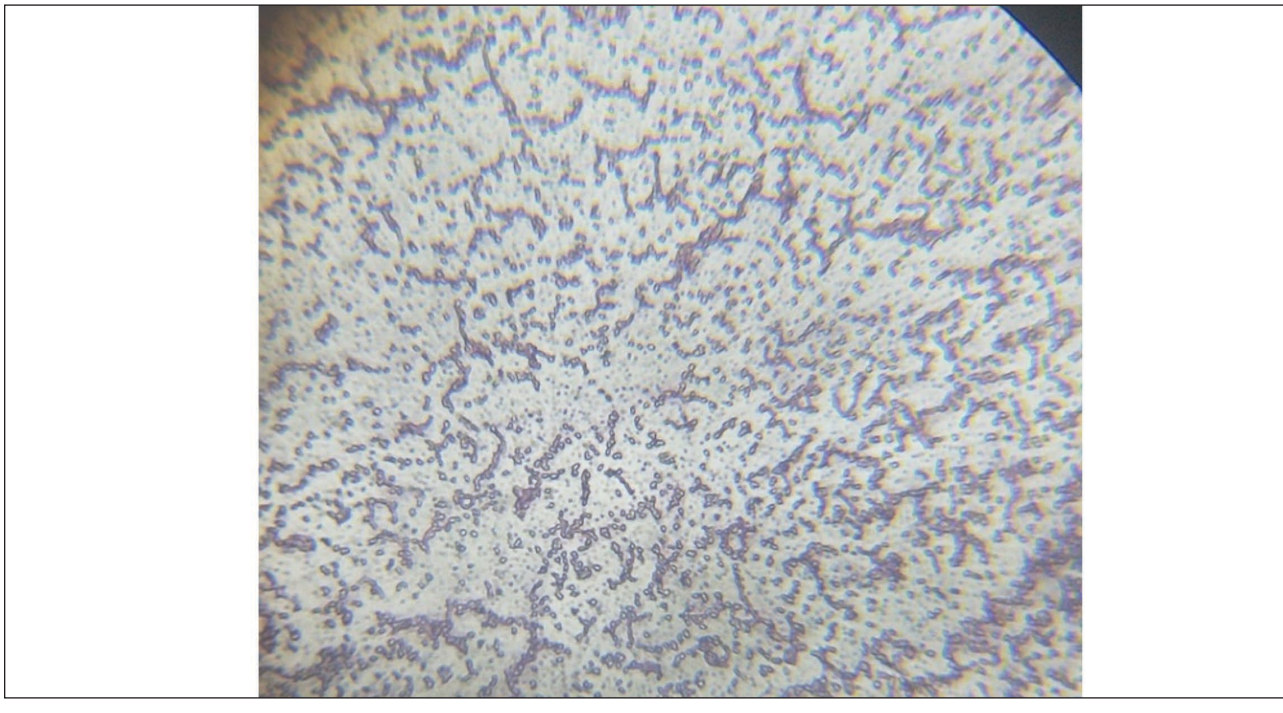

6. Gram negative cocci observed on the outside of the masks.

At the end of the experiments, the highest number of bacterial forming colonies were observed on the inner side of the three-layered face masks (840 CFU), followed by the inner side of the roadside face mask (835 CFU). For the outer side of the masks, the lowest CFUs were observed in N95 (without filter), three-layered, and velcro masks (9 CFU each), followed by two-layered masks (10 CFU). Bacterial proliferation with wearing time and surfaces observed in the current study is consistent with the one reported by Zhiqing et al. [20]. Face masks could proliferate bacteria with increased wearing time. Zhiqing et al. [20] demonstrated that mask users can also contribute to the source of contamination to the inner side of masks, and face masks with higher filtration could significantly reduce horizontal dispersions, resulting in the contamination of the reverse side of the mask. The higher CFUs observed in the three-layered and roadside masks at the end of the experiment may have resulted from proliferation and bidirectional hor-

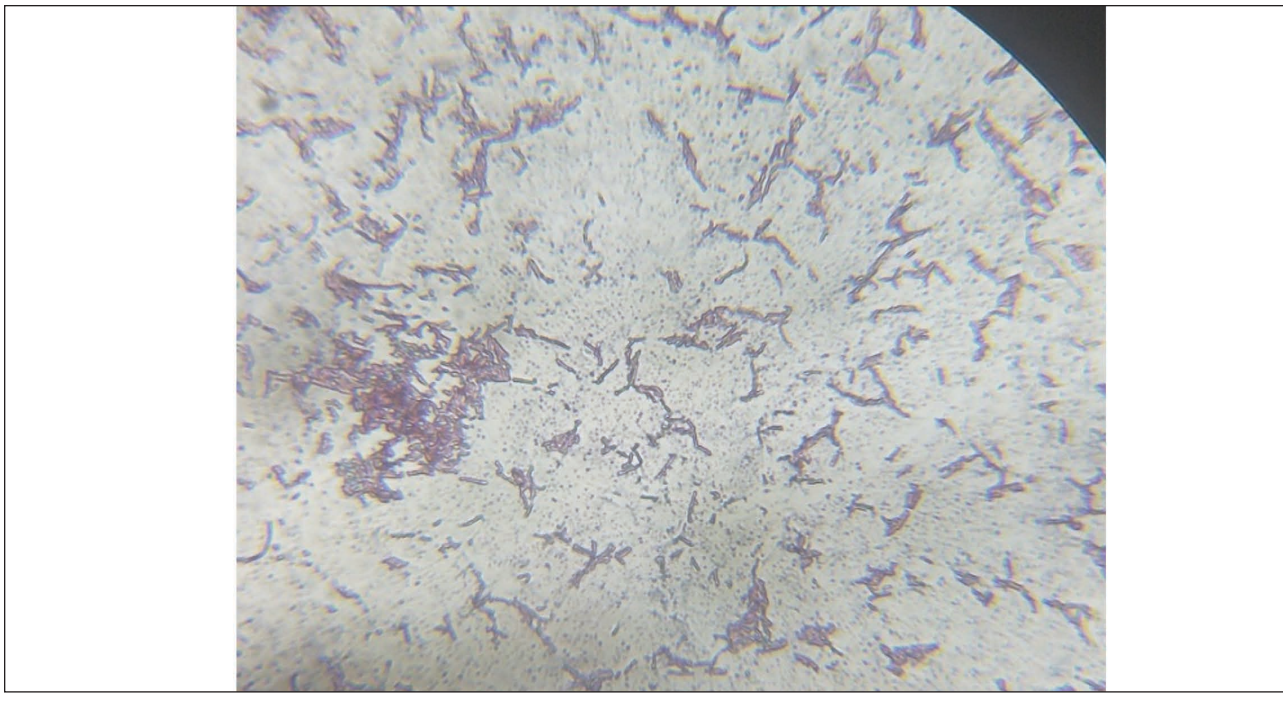

7.* Bifidobacterium *observed on the inside of the mask.

izontal dispersion, which could be prevented or minimized by using face masks with high filtration capacity.

How microbes can survive and propagate on personal protection equipment is a factor to be considered [21]. Different patterns of proliferation and dispersion were observed in the results of the present study (Figs. 2 and 3). Cellulose-containing face mask materials are known to support the propagation of certain fungi and bacteria in ideal conditions because of their ability to digest cellulose [22]. Industrial grade polypropylene materials are recommended for the manufacturing of face masks, because they cannot serve as a nutrient for bacteria [21,23]. Differences in mask materials may have contributed to the variations in proliferation patterns observed in the current study. The material contents of roadside masks cannot be ascertained because of the absence of the manufacturer's label, which is typical for roadside face masks. Fungal load and proliferation were observed in the current study to be generally low.

The microbes associated with different face masks in the present study are ubiquitous. Streptococci species were observed in samples collected from volunteers D and E. Streptococci have been isolated from saliva samples and oral cavities [24,25]. Microorganisms of the genus Streptococci are of clinical importance because of their capability to be pathogenic [24]. They are known to cause common bacterial infections [26]. Bifidobacteria was found in samples collected from all of the volunteers. Bifidobacterium belong to the Actinobacteria phylum and are normally found in the gastrointestinal track [27]. They are considered non-pathogenic and promoted as a probiotic due to their potential beneficial effects on the gastrointestinal track. However, there have been reports implicating Bifidobacteria as pathogenic agent in various conditions such as urinary tract infections [28].

Although their classification was not a focus in the current study, the number of microbes observed on the surfaces of face coverings assessed the level of hygiene of masks available in open markets. The sources of contamination of the inner surface of the masks cannot be ascertained, but the results suggested contamination from volunteers. It should also be noted that the observed microbes proliferated differently on different mask samples. Microbial load observed on the outside surface of the masks and on controls suggests possible pre-purchase contamination.

CONCLUSIONS

Although respiratory viruses are the primary reason for the use of face coverings during the pandemic, the safety and hygiene of purchased masks in causing other diseases deserve closer attention. In this study, different types of masks from various sources, including roadside sourced masks, were examined for initial microbial load, proliferation, and possible horizontal dispersion. The initial number of bacterial CFUs was observed to be very high on both surfaces of the roadside and three-layered face masks. After wearing the masks (1 h), there was a sharp increase in the microbial load when compared to the initial load. The N95 masks with filters showed a higher number of colonies on the outside when compared to the inside, suggesting higher filtration capabilities and resistance to microbial dispersion. The microbial load was observed to be very high in roadside and three-layered face masks.

On roadside masks, the outer CFUs were lower when compared to the inside, suggesting either poor filtering capacity or material contents that support the proliferation of microbes on the inner surface and not on the outer surface. Since the masks carried some microbial population, it is suggested to sterilize or wash purchased masks before using them. Although the current study is a rapid assessment of microbial loads on common face masks sold in open markets, its results provide insights into possible prepurchase contamination of poorly designed and manufactured masks. It also highlighted health and safety risks of masks sold in open markets in causing other diseases. Sterilization or washing of fabric face masks before use is recommended. The present study was limited in the number of replications for statistical comparison. Future studies should include more elaborate and inclusive molecular studies that classify colonies up to species and subspecies levels. **TJ**

LITERATURE CITED

1. Rab, S., Javaid, M., Haleem, A., et al., *Diabetes Metab. Syndr.* 14(6): 1617(2020). https://doi.org/10.1016/j.dsx.2020.08.021.
2. Ayodeji, O.J. and Ramkumar, S., *Int. J. Environ. Res. Public Health* 18(7): 3666(2021). https://doi.org/10.3390/ijerph18073666.
3. WHO, "Coronavirus disease (COVID-19): How is it transmitted?," World Health Organization, Geneva, Switzerland, 2020. Available [Online] https://www.who.int/news-room/q-a-detail/coronavirus-disease-covid-19-how-is-it-transmitted <27Dec2021>.
4. O'Dowd, K., Nair, K.M., Forouzandeh, P., et al., *Materials* 13(15): 3363(2020). https://doi.org/10.3390/ma13153363.
5. Chughtai, A.A., Seale, H., and Macintyre, C., *Emerging Infect. Dis.* 26(10): 1(2020). https://doi.org/10.3201/eid2610.200948.
6. WHO, "Shortage of personal protective equipment endangering health workers worldwide," World Health Organization, Geneva, 2020. Available [Online] https://www.who.int/news-room/detail/03-03-2020-shortage-of-personal-protective-equipment-endangering-health-workers-worldwide <27Dec2021>.
7. Rubio-Romero, J.C., Pardo-Ferreira, M.C., Torrecilla-García, J.A., et al., *Saf. Sci.* 129: 104830(2020). https://doi.org/10.1016/j.ssci.2020.104830.
8. Aydin, O., Emon, B., Cheng, S., et al., *Extreme Mech. Lett.* 40: 100924(2020). https://doi.org/10.1016/j.eml.2020.100924.

ABOUT THIS PAPER

Cite this article as:
Narasimhan, S., Balakrishnan, M., Ayodeji, O., et al., *TAPPI J.* 21(1): 23(2022).
https://doi.org/10.32964/TJ21.1.23

DOI: https://doi.org/10.32964/TJ21.1.23

ISSN: 0734-1415

Publisher: TAPPI Press

Copyright: ©TAPPI Press 2022

About this journal

ABOUT THE AUTHORS

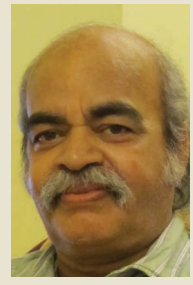
Narasimhan


Balakrishnan


Ayodeji


Ramkumar

We chose to research this topic for two reasons: (1) to explore usefulness of face masks; and (2) to assess the risk involved in continuous wearing of a mask at longer durations, resulting in increased microbial load due to filtration. This triggered our interest in knowing the effect of wearing masks that differed in cost and filtering potential; the more a mask filters, the greater likelihood of enhanced viral load and increased risk to the host.

We discovered that the use of masks carries a potential risk of enhanced viral load, which is detrimental to the host. Therefore, it is necessary to disinfect in situ. Our most interesting finding was that the microbial load is higher on the inside portion of the mask. The research showcases the importance of sterilization in offering enhanced protection.

Mask manufacturers may benefit from this information by understanding the need to develop disinfecting material and coating for cotton fabric masks. Our next step is to evaluate a non-alcoholic, nontoxic disinfecting material that can destroy a microbe on contact.

Narasimhan is the chairman of Asthagiri Herbal Research Foundation and Meenashree Balakrishnan is a senior scientist at Asthagiri Herbal Research Foundation in Chennai, India. Ayodeji is a Ph.D. candidate and Ramkumar is professor in the Department of Environmental Toxicology at Texas Tech University in Lubbock, TX, USA. Email Ramkumar at s.ramkumar@ttu.edu.

9. Cuthbertson, A., "Coronavirus: Face mask price gougers continue to profit from COVID-19 pandemic on Facebook and Instagram," *Independent*, 27 March 2020. Available [Online] https://www.independent.co.uk/life-style/gadgets-and-tech/news/coronavirus-face-mask-buy-facebook-instagram-covid-19-a9429671.html <27Dec2021>.
10. OECD, "The face mask global value chain in the COVID-19 outbreak: Evidence and policy lessons," Organization for Economic Co-operation and Development, Paris, 4 May 2020. Available [Online] https://www.oecd.org/coronavirus/policy-responses/the-face-mask-global-value-chain-in-the-COVID-19-outbreak-evidence-and-policy-lessons-a4df866d/ <27Dec2021>.
11. GVR, "Nonwoven fabrics market size, share & trends analysis report by product, by technology, by application, by region (North America, Europe, Asia Pacific, Middle East & Africa, Central & South America), and segment forecasts, 2015 – 2020," Grand View Research, San Francisco, 2020. Available [Online] https://www.grandviewresearch.com/industry-analysis/nonwoven-fabrics-market <27Dec2021>.
12. Mwema, F.M. and Nyika, J.M., *Sci. Afr.* 10: e00563(2020). https://doi.org/10.1016/j.sciaf.2020.e00563.
13. George, B.,"Reusable cloth masks won't prevent COVID-19, MoH and KEBS warn," *The Standard,* 9 April 2020, Available [Online] https://www.standardmedia.co.ke/article/2001367475/reusable-cloth-masks-won-t-prevent-covid-19-kebs-and-moh-warn <27Dec2021>.
14. Wen, J.C., McCannel, C.A., Mochon, A.B., et al., *Arch. Ophthalmol.* 129(12): 1551(2011). https://doi.org/10.1001/archophthalmol.2011.227 <27Dec2021>.
15. Doshi, R.R., Leng, T., and Fung, A.E., *Retina* 32(3): 473(2012). https://doi.org/10.1097/IAE.0b013e31822c2958.
16. Patel, S.N., Mahmoudzadeh, R., Salabati, M., et al., *Am. J. Opthalmol.* 223: 178(2020). https://doi.org/10.1016/j.ajo.2020.10.017.
17. Li, L., Niu, M., and Zhu, Y., *Aerosol Sci. Technol.* 55(3): 332(2020). https://doi.org/10.1080/02786826.2020.1846679.
18. Maher, B., Chavez, R., Tomaz, G.C.Q., et al., *Int. J. Infect. Dis.* 99: 505(2020). https://doi.org/10.1016/j.ijid.2020.07.066.
19. Verma, S., Dhanak, M., and Frankenfield, J., *Phys. Fluids* 32: 061708(2020). https://doi.org/10.1063/5.0016018.
20. Zhiqing, L., Yongyun, C., Wenxiang, C., et al., *J. Orthop. Transl.* 14: 57(2018). https://doi.org/10.1016/j.jot.2018.06.002.
21. Fisher, E.M. and Shaffer, R.E., *J. Occup. Environ. Hyg.* 11: D115(2014). https://doi.org/10.1080/15459624.2014.902954.
22. Pasanen, A.L., Nikulin, M., Berg, S., et al. *AIHA J.* 55(1): 62(1994). https://doi.org/10.1080/15428119491019285.
23. Clase, C., de Lannoy, C., and Laengert, S., "Polypropylene, the material now recommended for COVID-19 mask filters: What it is, where to get it," *The Conversation*, Melbourne, 19 November 2020. Available [Online] https://theconversation.com/polypropylene-the-material-now-recommended-or-covid-19-mask-filters-what-it-is-where-to-get-it-149613 <27Dec2021>.
24. Amoroso, P., Avila, F.A., and Gagliardi, C.M.O., *Braz. J. Oral Sci.* 2: 164(2003).
25. Naik, T.B., Nadagir, S.D., Biradar, A., *J. Lab. Physicians* 8(1): 45(2016). https://doi.org/10.4103/0974-2727.176235.
26. Mather, R., in *Current Ocular Therapy* (F.H. Roy, F.W. Fraunfelder, and F.T. Fraunfelder, Eds.), Elsevier, Amsterdam, 2008, Chap. 48. https://doi.org/10.1016/B978-1-4160-2447-7.50053-0.
27. Arboleya, S., Watkins, C., Stanton, C., et al., *Front. Microbiol.* 7: 1204(2016). https://doi.org/10.3389/fmicb.2016.01204.
28. Pathak, P., Trilligan, C., and Rapose, A., *BMJ Case Rep.* 2014: bcr2014205122(2014). https://doi.org/10.1136/bcr-2014-205122.

Preparing prehydrolyzed kraft dissolving pulp via phosphotungstic acid prehydrolysis from grape branches

LI TAO, MA YING HUA, AND ZHANG JUN KE

ABSTRACT: Dissolving pulp was successful prepared via phosphotungstic acid (PTA) prehydrolysis kraft (PHK) cooking followed by an elementary chlorine-free (ECF) bleaching process from grape branches. The effects of prehydrolysis temperature, reaction time, and PTA concentration that potentially affect the quality of dissolving pulp product on chemical components of pulp were studied via an orthogonal experiment. The structure of lignin was activated during the PTA prehydrolysis phase, and lignin was easily removed during the following cooking process. Thus, relatively mild conditions (140°C, 100 min) can be used in the cooking process. During the prehydrolysis phase, temperature exhibited the most significant influence on the cellulose purity of the obtained pulp fiber, followed by reaction time and PTA concentration. The optimized prehydrolysis conditions were as follows: prehydrolysis temperature, 145°C; reaction time, 75 min; and PTA concentration, 1 wt%. Whether the excessively high prehydrolysis temperature or prolonging the reaction time did not favor the retention of long chain cellulose, the delignification selectivity for the cooking process could not be further improved by excessive PTA loading. Under these prehydrolysis conditions, 94.1% and 29.0% for α-cellulose content and total yield could be achieved after the given cooking and bleaching conditions, respectively. Moreover, the chemical structure and crystal form of cellulose were scarcely changed after PTA prehydrolysis, which could be confirmed by results from Fourier transform infrared (FTIR) spectroscopy and X-ray diffraction (XRD). PTA prehydrolysis could be considered as an alternative method for preparing PHK dissolving pulp under relatively mild cooking conditions.

Application: Phosphotungstic acid prehydrolysis presents an alternative approach for preparing a PHK dissolving pulp product, as well as solving the acid recovery problem during the PHK process.

Dissolving pulp is a kind of purified chemical pulp with high α-cellulose content. It can be used as the feedstock for many high value-added cellulose products, such as viscose fiber, cellophane, cellulose ester, and/or ether. Dissolving pulp is mainly produced via a prehydrolysis kraft (PHK) process or acid sulfite (AS) process. The amount of dissolving pulp produced by these two methods accounts for 85% to 88% of the total dissolving pulp production all over the world, whereas the pulp obtained via the AS process exhibits a wider distribution of polymerization degree than that from the PHK process and a relatively higher requirement for raw materials. Until now, the PHK process, which has a wide range of feedstock from which to select, is usually adopted for newly-built production lines of dissolving pulp [1,2]. During the PHK process, part of the hemicelluloses and lignin can be degraded and removed from raw materials, and the reactivity of lignin can also be improved by the prehydrolysis process, which favors the removal of lignin during the subsequent cooking process. Many studies on prehydrolysis of wood chips or other raw materials have been reported, for example, dilute acid prehydrolysis [3] and hot water extraction [4]. Dilute acid prehydrolysis (0.5%–10%) was once widely considered due to its good economy and high efficiency, though subsequent equipment corrosion and acid recovery hindered its further development [5].

As a new and emerging type of solid heteropoly acid catalyst, phosphotungstic acid (PTA) exhibits some unique physicochemical properties, including strong Brønsted acidity, proton mobility, low corrosion to equipment, high stability, and reusability [6]. Due to these special characteristics, PTA was used to depolymerize cellulose to platform chemicals [7,8] or to realize viscosity control and accessibility/reactivity improvement for dissolving pulp [9], and even to prepare nanocellulose-based materials [10]. The depolymerization effect of PTA on hemicelluloses was also reported. The enzymolysis efficiency of cellulase for agricultural biomass could be remarkably improved via PTA pretreatment [11,12]. Moreover, solid heteropoly acids are insoluble in nonpolar hydrocarbons, making it possible to recover them from the reaction mixture without the need for neutralization and simply by extraction or precipitation [13]. As reported, lignin can be depolymerized into phenolic monomers under the catalytic effect of solid heteropoly acids [14,15]. Moreover, the catalytic effect of solid heteropoly acids

combined with neutral deep eutectic solvent [16] or MCM-41 zeolite [17] on lignin macromolecules was also reported. Since the structure of a lignin macromolecule can be activated and/or depolymerized by incorporating solid heteropoly acids under varied conditions, it is reasonable to infer that solid heteropoly acid catalysts can be used to replace dilute acid prehydrolysis for a dissolving pulp preparation and can be expected to solve the acid recovery problem during the PHK process.

At present, many studies have been made for expanding the material source of dissolving pulp. Global demand for dissolving pulp has been increasing at a remarkable pace over the last few years [18]. China is the biggest consumer of dissolving pulp in the world. Nonetheless, more than 50% of the consumption of dissolving pulp relies on imports [2]. As a kind of widely planted agricultural product, the cultivated area of grapes has been increasing year by year in China. As reported, the cultivated area exceeded one million hectares in 2020. As a result, increased grape pruning has increased the land accumulation of pruning residual, as well as pollution from burning it. With the goal of expanding the raw material source for preparing dissolving pulp and solving the pollution caused by grape pruning residual, the PHK process using grape branches via PTA prehydrolysis was investigated. The effects of prehydrolysis temperature, reaction time, and PTA concentration that potentially affect the quality of the dissolving pulp product were studied via an orthogonal experiment. Moreover, the morphological and structural characteristics of specimens after PTA prehydrolysis and cooking were also analyzed.

EXPERIMENTAL

Materials

Grape branches, with average length of about 20–30 mm and average diameter of 7–12 mm, were provided by the Agricultural Bureau of Xunyi District, Xi'an, China. The chemical components of the grape branches (w/w) were as follows: holocellulose, 65.45%; Klason lignin, 26.83%; acid-soluble lignin, 0.55%; pentosane, 14.13%; and benzene-alcohol extractive, 5.48%.

Phosphotungstic acid ($H_3O_{40}PW_{12}$) (PTA, AR); ammonium ferrous sulfate [$(NH_4)Fe(SO_4)_2{\cdot}6H_2O$, AR]; potassium dichromate ($K_2Cr_2O_7$, AR); sulfuric acid (H_2SO_4, purity≧98.0%); sodium hydroxide (NaOH, AR); hydrogen peroxide (H_2O_2, 36.5%); sodium metasilicate (Na_2SiO_3, AR); magnesium sulfate ($MgSO_4$, AR); acetic acid (CH_3COOH, AR); sodium chlorite ($NaClO_2$, AR); and potassium bromide (KBr, SP) were purchased from Tianli Chemical Co. Ltd. (Tianjin, China) and were used as received without further purification. Bis(ethylenediamine) copper(II) hydroxide solution (1 M in H_2O) was purchased from Sigma-Aldrich Co. Ltd. (Shanghai, China). The chlorine dioxide (ClO_2) solution was generated in the laboratory prior to performing the bleaching procedure.

Level	Factors		
	Prehydrolysis Temperature, °C	Reaction Time, min	PTA Concentration, %
1	110	25	0
2	125	50	1
3	140	75	2
4	155	100	3

I. Orthogonal experimental design parameters of prehydrolysis (PTA = phosphotungstic acid).

Methods

PTA prehydrolysis

PTA was prepared into aqueous solution with a certain concentration. Subsequently, around 150 g of grape branches (dry weight) and the required amount of PTA aqueous solution were added into a stainless steel reactor of 1000 mL volume, sealed, and put into a digester kier (ZQS1, machinery factory of Shaanxi University of Science and Technology, China). The wood-to-liquid ratio was 1:4. The system was heated to a pre-seated maximum temperature within 40 min, and then kept at the maximum temperature for a required duration. After prehydrolysis, specimens were washed until neutral with deionized water and air dried.

The main factors, including prehydrolysis temperature, reaction time, and PTA concentration, were investigated via an orthogonal experiment. The factors and levels of the orthogonal experiment are shown in **Table I**, and the treatment conditions for specimens are given in **Table II**. In addition, the untreated grape branches were named OS for further analysis.

Kraft cooking

All the selected specimens after PTA prehydrolysis were subjected to the kraft pulping process. The active alkali loading based on specimen was 16 wt%, and sulfidity was 18 wt%. The wood-to-liquid ratio was 1:4. The temperature in the reactor was raised from 25°C to 140°C within 40 min, and it was kept constant for 100 min. Kraft cooking was conducted in an oil-bath reactor (ZQS1, machinery factory of Shaanxi University of Science and Technology, China) that contained four rotating autoclaves of 1000 mL.

Bleaching sequences and conditions

An O-D_0–E_p–D_1 ECF bleaching was used to treat PHK pulp after cooking. Kraft pulp (10 g, as o.d. weight) was oxygen bleached at the pulp consistency of 30 wt%. After washing, the pulp was treated with ClO_2 in a polyethylene bag at the pulp consistency of 10 wt%, washed again, and treated in a polyethylene bag with NaOH and H_2O_2. Finally, the pulp was washed and treated with ClO_2 again.

Specimen	Prehydrolysis Temperature, °C	Reaction Time, min	PTA Concentration, %
1	110	25	0
2	110	50	1
3	110	75	2
4	110	100	3
5	125	25	1
6	125	50	0
7	125	75	3
8	125	100	2
9	140	25	2
10	140	50	3
11	140	75	0
12	140	100	1
13	155	25	3
14	155	50	2
15	155	75	1
16	155	100	0

II. Orthogonal experimental conditions of prehydrolysis (PTA = phosphotungstic acid).

The bleaching conditions were as follows:

- O phase: pulp consistency, 30 wt%; initial oxygen pressure, 0.5 MPa; NaOH loading, 5 wt%; $MgSO_4$ loading, 0.5 wt%; temperature, 95°C; reaction time, 60 min.
- D_0 phase: pulp consistency, 10 wt%; ClO_2 loading, 1.5 wt%; temperature, 75°C; reaction time, 90 min.
- E_p phase: pulp consistency, 10 wt%; NaOH loading, 1.0 wt%; H_2O_2 loading, 1.5 wt%; Na_2SiO_3 loading, 2.0 wt%; initial oxygen pressure, 0.5 MPa; temperature, 90°C; reaction time, 60 min.
- D_1 phase: pulp consistency, 10 wt%; ClO_2 loading, 0.5 wt%; temperature, 70°C; reaction time, 60 min.

Characterizations

The holocellulose and lignin contents of specimens were measured according to TAPPI Standard Test Method T 222 om-15 "Acid-insoluble lignin in wood and pulp." The α-cellulose content and alkali solubility (S_{10} and S_{18}) of delignified specimens were measured according to TAPPI T 203 cm-09 "Alpha-, beta- and gamma-cellulose in pulp" and TAPPI T 235 cm-09 "Alkali solubility of pulp at 25°C," respectively. The obtained results were defined as α-cellulose content and alkali solubility based on holocellulose, respectively. The average degree of polymerization (DP) of specimens was measured using the viscosity method according to TAPPI T 230 om-19 "Viscosity of pulp (capillary viscometer method)."

The α-cellulose content and alkali solubility (S_{10} and S_{18}) based on the specimen were calculated according to the following formula:

$$A = B * C$$

where A is the α-cellulose content/alkaline solubility (S_{18} or S_{10}-S_{18}) based on the specimen; B is the corresponding α-cellulose content/alkaline solubility based on holocellulose; and C is the holocellulose content based on this specimen.

The dried specimens were mixed with KBr and pressed into tablets. Then, analysis was performed using Fourier transform infrared (FTIR) spectroscopy (VERTEX-70; Bruker, Germany) in the range of 4000-400 cm^{-1} with a resolution of 4 cm^{-1}.

The X-ray diffraction (XRD) patterns were collected on a Bruker D8-Advance instrument (Karlsruhe, Germany) equipped with a Cu Kα radiation (k=1.54 A°) as an X-ray resource operating (40 kV, 30 mA) by a scan rate of 0.1° per second in a 2θ range of 10° to 60°.

The morphology of raw material and specimens was observed using a HITACHI S-8100 SEM (Hitachi; Tokyo, Japan) apparatus at 5.0 kV accelerating voltage. Before SEM measurement, the dried specimens were dispersed on double-sided conductive tape and sprayed with gold in a vacuum.

RESULTS AND DISCUSSION

Influences of process variables on chemical components

The influences of prehydrolysis process variables, including prehydrolysis temperature, reaction time, and PTA concentration, on the chemical components of specimens after prehydrolysis and cooking were investigated via an orthogonal experiment with four levels. The corresponding results are shown in **Table III** and **Table IV**, respectively. Moreover, the influences of process variables on the carbohydrate components after prehydrolysis and cooking calculated by range analysis are shown in **Figs. 1–3**. According to the range analysis, the influence order of process variables on the cellulose purity of obtained pulp fiber was as follow: prehydrolysis temperature > reaction time > PTA concentration.

Influences of prehydrolysis temperature

Figure 1 shows the influences of prehydrolysis temperature on carbohydrate contents of specimens after prehydrolysis and cooking. As indicated by Table III and Fig. 1a, both the yield and holocellulose content of specimens exhibited significant decrease with increasing temperature during the prehydrolysis phase, especially at 155°C, indicating the dra-

Specimens	Holocellulose Content, %	α-Cellulose Content, %		$S_{10'}$ %		$S_{18'}$ %		S_{10}-$S_{18'}$ %		Lignin Content, %		α-Cellulose Yield, %	Yield, %
		For Specimens	For Holo-cellulose	For Specimens	For Holo-cellulose	For Specimens	For Holo-cellulose	For Specimens	For Holo-cellulose	Acid Insoluble	Acid Soluble		
OS	65.45±2.53	51.93±0.51	79.34±0.78	14.88±0.58	22.73±0.88	13.55±0.23	20.70±0.35	1.33±0.81	2.33±1.23	26.83±0.42	0.55±0.08	-	-
1	71.29±1.97	52.18±0.99	73.20±1.40	14.27±0.45	20.02±0.63	12.20± 1.07	17.12±1.50	2.07±1.52	2.90±2.13	27.51±0.63	0.52±0.03	94.21±3.85	95.08±1.88
2	71.39±0.93	54.24±0.22	75.98±0.31	10.97±0.83	15.37±1.17	9.64±0.30	13.51±0.42	1.33±1.13	1.86±1.59	27.40±0.60	0.43±0.09	95.42±3.74	94.59±1.77
3	66.58±0.70	48.92±0.32	73.47±0.49	10.93±0.08	16.42±0.12	8.10±0.11	12.17±0.16	2.83±0.19	4.25±0.28	29.12±1.28	0.40±0.05	86.28±1.10	91.59±0.17
4	61.78±0.78	46.14±0.91	74.68±1.51	9.87±0.20	15.98±0.50	6.92±0.27	11.20±0.44	2.95±0.47	4.78±0.94	29.02±0.19	0.39±0.07	81.60±1.07	91.84±0.29
5	66.59±1.70	53.56±0.80	80.43±1.23	11.07±1.04	16.63±1.59	8.34±0.70	12.53±1.08	2.73±1.74	4.10±2.67	27.25±0.94	0.39±0.02	95.08±3.22	92.48±1.52
6	64.23±1.74	51.40±0.79	80.02±1.27	10.74±0.70	16.72±1.12	8.54±0.13	13.29±0.21	2.20±0.83	3.43±1.33	28.99±1.00	0.40±0.04	91.50±2.01	92.45±0.27
7	64.43±0.50	50.92±1.00	79.03±1.60	10.47±0.49	16.25±0.78	7.63±0.25	11.85±0.40	2.83±0.74	4.40±1.18	29.84±1.31	0.37±0.05	87.87±1.97	89.62±1.47
8	62.15±1.01	49.67±0.04	79.91±0.06	12.98±0.32	20.89±0.53	7.35±0.92	11.83±1.54	5.63±1.24	9.06±2.07	29.67±0.93	0.36±0.05	85.27±2.91	89.16±1.90
9	66.39±1.75	52.46±0.45	80.00±0.70	11.53±0.66	17.58±1.04	7.45±1.14	11.36±1.79	4.08±1.70	6.22±2.83	29.75±0.54	0.35±0.02	88.70±3.76	87.80±2.01
10	66.09±1.73	52.53±1.15	80.50±1.83	11.22±0.37	17.20±0.59	7.20±0.33	11.03±0.52	4.03±0.70	6.17±1.11	31.19±1.24	0.32±0.01	84.48±1.84	83.52±0.09
11	64.09±0.91	51.61±0.75	81.56±1.24	11.95±0.95	18.88±1.55	7.44±0.10	11.75±0.16	4.51±1.05	7.13±1.71	27.52±1.01	0.37±0.03	93.16±1.26	93.74±0.35
12	63.45±1.48	50.31±0.77	80.31±1.29	10.80±0.77	17.24±1.28	6.79±1.19	10.84±1.99	4.01±1.96	6.40±3.27	29.40±0.34	0.36±0.07	86.16±2.44	88.93±0.96
13	64.61±0.65	46.80±0.86	72.43±1.42	12.51±0.72	19.36±1.19	7.07±0.29	10.94±0.48	5.44±1.01	8.42±1.67	29.79±1.29	0.23±0.06	78.645±1.92	87.27±1.27
14	64.04±1.07	48.74±0.40	76.11±0.67	8.32±0.45	13.00±0.75	6.56±0.72	10.24±1.20	1.77±1.17	2.76±1.95	30.22±0.18	0.25±0.04	80.85±1.71	86.15±0.64
15	64.46±1.05	51.47±1.11	79.86±1.85	11.63±0.99	18.05±1.65	5.92±0.27	9.18±0.46	5.72±1.26	8.87±2.11	32.24±0.88	0.28±0.02	79.37±2.17	80.07±1.12
16	63.55±0.50	51.47±1.07	81.00±1.83	9.16±0.99	14.41±1.69	3.95±0.50	6.22±0.86	5.20±1.49	8.19±2.55	32.84±0.35	0.33±0.05	77.32±2.32	78.01±1.82

III. Chemical components of specimens after prehydrolysis (OS = untreated grape branch).

Specimens	Holocellulose Content, %	α-Cellulose Content, %		$S_{10'}$ %		$S_{18'}$ %		S_{10}-$S_{18'}$ %		Lignin Content, %		α-Cellulose Yield, %	Yield, %	Dissociated to Fiber, Yes/No
		For Specimens	For Holo-cellulose	For Specimens	For Holo-cellulose	For Specimens	For Holo-cellulose	For Specimens	For Holo-cellulose	Acid Insoluble	Acid Soluble			
1	57.45±1.22	54.27±0.11	94.46±0.19	6.28±0.03	10.93±0.06	2.96±0.09	5.16±0.16	3.31±0.12	5.77±0.22	35.92±1.16	0.18±0.03	48.20±2.54	43.85±1.32	N
2	63.55±1.22	59.55±0.06	93.71±0.10	6.22±0.01	9.78±0.01	3.53±0.03	5.55±0.05	2.69±0.04	4.23±0.06	26.55±2.03	0.18±0.01	52.34±3.28	43.17±2.06	N
3	75.34±1.10	70.75±0.78	93.91±1.04	6.87±0.05	9.12±0.06	4.17±0.03	5.53±0.04	2.70±0.08	3.59±0.10	18.03±0.96	0.17±0.04	62.51±1.68	42.02±0.58	N
4	68.86±0.66	64.90±0.18	94.25±0.26	5.77±0.08	8.38±0.12	3.53±0.03	5.13±0.05	2.24±0.12	3.25±0.17	27.08±1.11	0.17±0.02	57.93±1.90	42.57±1.24	N
5	82.66±0.87	78.17±0.04	94.57±0.05	6.90±0.01	8.35±0.01	4.10±0.13	4.96±0.16	2.80±0.14	3.390.17	13.17±1.02	0.15±0.02	61.75±2.07	37.94±1.20	Y
6	68.52±0.07	65.35±0.69	95.38±1.00	6.30±0.11	9.19±0.16	3.89±0.08	5.68±0.11	2.41±0.29	3.51±0.28	23.08±0.91	0.15±0.03	52.00±0.49	38.20±0.42	N
7	75.11±1.43	70.99±0.14	94.52±0.18	5.92±0.10	7.88±0.13	3.11±0.11	4.14±0.15	2.81±0.21	3.74±0.28	16.53±0.85	0.14±0.05	54.25±1.61	35.56±0.18	Y
8	79.78±1.90	74.94±0.45	93.93±0.56	6.85±0.10	8.59±0.12	1.99±0.14	2.50±0.17	4.86±0.24	6.09±0.29	14.78±1.11	0.13±0.01	53.52±2.06	33.07±0.16	Y
9	87.30±0.43	82.43±1.27	94.42±1.45	6.40±0.04	7.33±0.05	3.58±0.10	4.10±0.12	2.82±0.14	3.23±0.17	10.52±0.83	0.12±0.02	55.86±2.42	30.90±1.99	Y
10	91.44±1.87	85.91±0.38	93.95±0.42	6.75±0.16	7.38±0.17	2.52±0.12	2.76±0.13	4.22±0.28	4.62±0.30	7.63±0.88	0.11±0.02	53.78±2.61	27.15±0.74	Y
11	83.97±1.91	79.78±0.18	95.01±0.21	6.94±0.07	8.26±0.08	2.94±0.16	3.50±0.19	4.00±0.23	4.76±0.27	13.85±1.20	0.11±0.01	50.68±3.58	30.92±1.67	Y
12	90.08±1.61	85.97±0.02	95.43±0.02	6.13±0.15	6.81±0.17	2.82±0.02	3.13±0.02	3.32±0.17	3.68±0.19	6.08±1.02	0.12±0.01	53.73±3.65	28.87±2.04	Y
13	92.75±0.04	86.99±1.16	93.79±1.25	6.85±0.19	7.39±0.20	1.96±0.05	2.11±0.05	4.90±0.24	5.28±0.25	3.59±0.71	0.11±0.05	45.18±0.83	23.54±0.79	Y
14	96.79±1.18	91.71±1.05	94.75±1.08	5.76±0.06	5.95±0.06	1.98±0.12	2.05±0.12	3.77±0.28	3.90±0.18	0.93±0.08	0.1±0.03	50.93±1.49	24.85±0.31	Y
15	96.44±0.94	91.44±1.60	94.82±1.66	5.89±0.14	6.11±0.14	1.46±0.16	1.51±0.17	4.44±0.30	4.60±0.31	1.17±0.93	0.11±0.03	51.10±3.15	23.24±2.21	Y
16	88.59±1.39	84.38±1.13	95.25±1.28	6.99±0.13	7.89±0.15	3.04±0.17	3.43±0.19	3.95±0.30	4.46±0.34	7.09±0.28	0.12±0.05	51.10±1.63	24.53±0.24	Y
16	63.55±0.50	51.47±1.07	81.00±1.83	9.16±0.99	14.41±1.69	3.95±0.50	6.22±0.86	5.20±1.49	8.19±2.55	32.84±0.35	0.33±0.05	77.32±2.32	78.01±1.82	

IV. Chemical components of specimens after cooking.

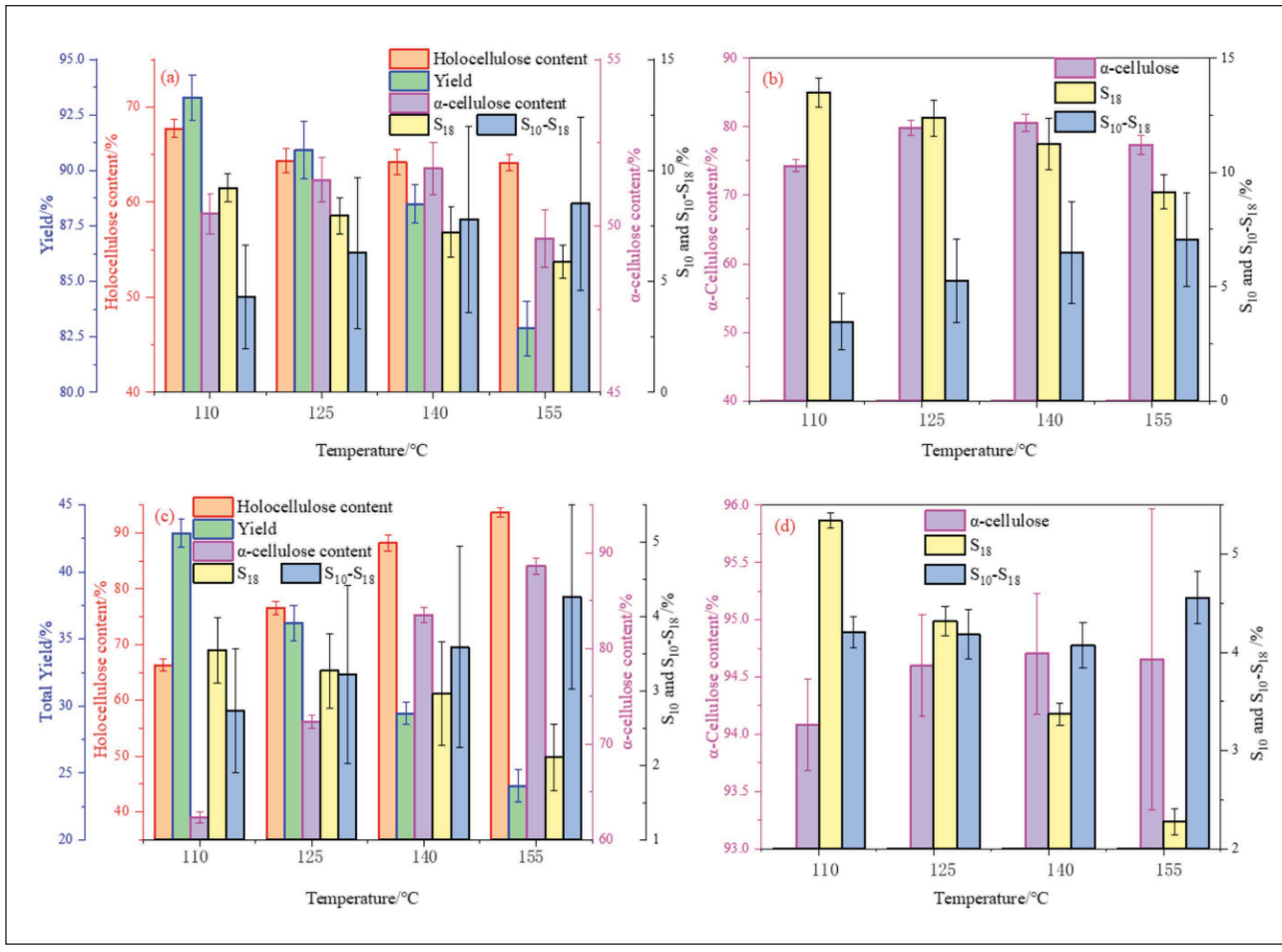

1. Influences of temperature on carbohydrate components of specimens after prehydrolysis and cooking: (a) based on specimen after prehydrolysis; (b) based on holocellulose after prehydrolysis; (c) based on specimen after cooking; and (d) based on holocellulose after cooking.

matic degradation of carbohydrates at high temperatures. On the other hand, the lignin content in specimens increased with increasing temperature, as shown in Table III. This is attributed to the different reactivity between carbohydrates and lignin. During the acidic PTA prehydrolysis process, lignin exhibits lower activity compared with carbohydrates, and it is more difficult to be degraded and dissolved [19]. The α-cellulose content also remained within a relatively stable range when the temperature was below 140°C, and it exhibited a certain decrease when the temperature increased to 155°C. From another perspective, the α-cellulose content based on holocellulose increased with increasing temperature until 140°C and decreased at 155°C, as can be seen from Fig. 1b. This also indicated the weakened selectivity on carbohydrates under high temperature during the prehydrolysis phase.

For alkali solubility, it is generally considered that S_{10} represents hemicelluloses and short-chain cellulose; S_{18} is typical hemicelluloses, also known as α-cellulose; and S_{10}-S_{18} represents α-cellulose, most of which are short-chain cellulose [20]. During the prehydrolysis phase, S_{18} exhibited significant decrease with increasing temperature, indicating the intensive hydrolysis effect on hemicelluloses, whereas S_{10}-S_{18} increased with the increasing temperature. These trends can be observed both in Fig. 1a (based on specimens) and Fig. 1b (based on holocellulose). This may be attributed to the intensive depolymerization effect on long chain cellulose under high temperature. It seems that excessively high temperature does not favor the retention of long chain cellulose during the prehydrolysis phase.

Figures 1c and 1d show the influences of prehydrolysis temperature on carbohydrate components of specimens after cooking. What needs to be explained here is that the specimens could not be reduced to fibrous mass when the cooking temperature was below 130°C, according to the results of preliminary experiments. Thus, the cooking temperature was selected as 140°C. It is notable that the specimens could not be reduced to fibrous mass when the prehydrolysis temperature was 110°C and even at 125°C, without the addition of PTA during the prehydrolysis phase, as indicated in Table IV. However, with the incorporation of PTA, the specimens could be dissociated to fibrous mass after cooking, even with the prehydrolysis temperature maintained at 125°C. This indicates that the

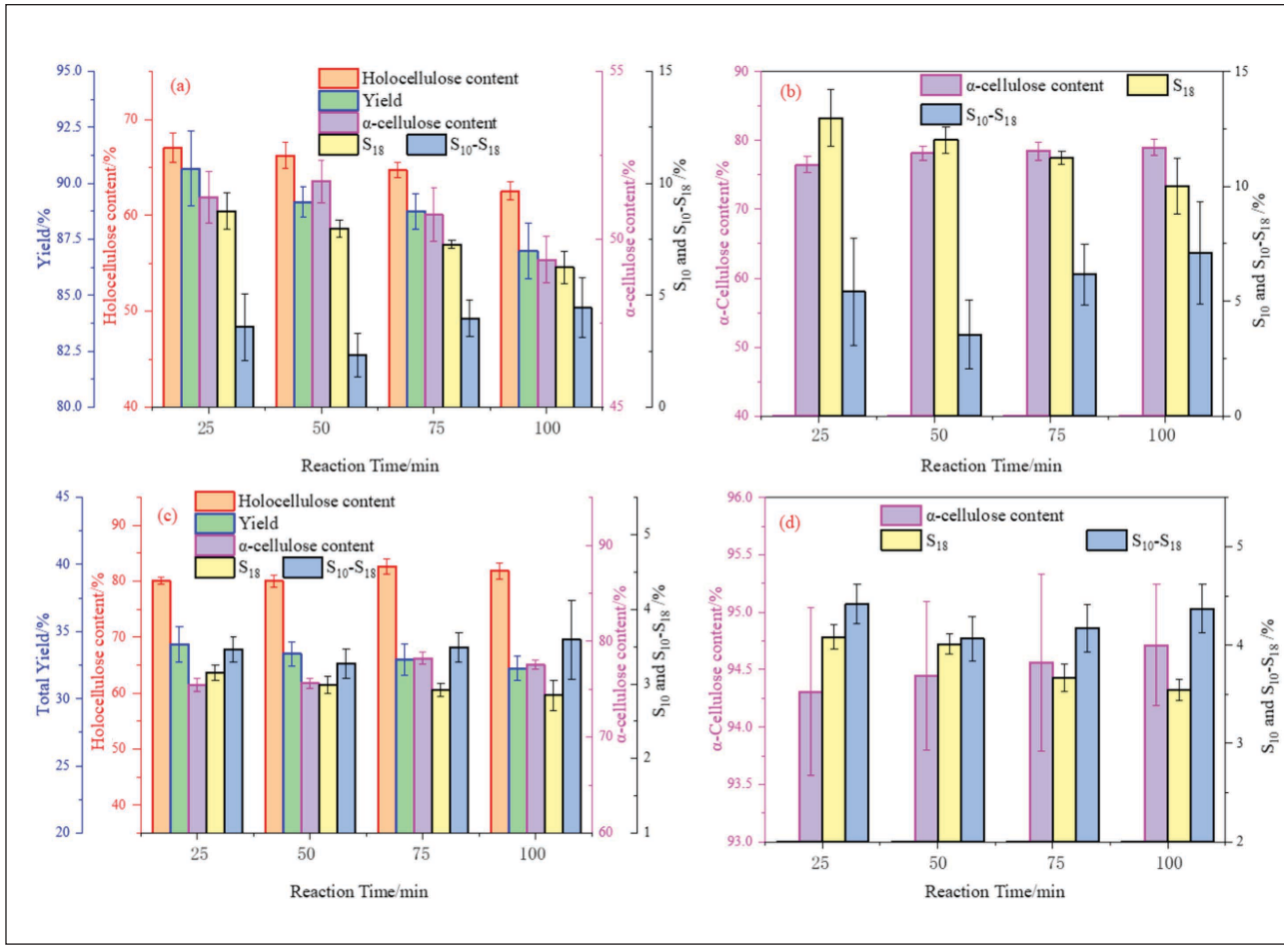

2. Influences of prehydrolysis reaction time on carbohydrate components of specimens after prehydrolysis and cooking processes: (a) based on specimen after prehydrolysis; (b) based on holocellulose after prehydrolysis; (c) based on specimen after cooking; and (d) based on holocellulose after cooking.

structure of lignin in raw materials was activated by the addition of PTA and is easily removed during the subsequent cooking process.

Due to the degradation of carbohydrates during the prehydrolysis phase, more lignin was exposed, and even deposited, on the surface of specimens. This resulted in a relatively high lignin removal ratio during cooking and increased holocellulose and α-cellulose contents based on specimens with increasing temperature, and it was also accompanied by a significant decrease of yield (Fig. 1c). Simultaneously, the α-cellulose content based on holocellulose also increased with increasing temperature and remained at a relatively high level (≥94.5%), as shown in Fig. 1d. This demonstrated that a specimen with relatively high cellulose purity can be obtained during cooking with PTA prehydrolysis treatment — one that achieves the qualitative requirements of dissolving pulp. However, the α-cellulose content based on holocellulose exhibited a slight decrease when the temperature increased from 140°C to 155°C. It can be inferred that long chain cellulose of specimens that were prehydrolyzed at a relatively high temperature suffered a stronger depolymerization effect during cooking. This is also demonstrated by the increased S_{10}-S_{18} component within the same temperature intervals. Furthermore, as indicated by Figs. 1c–1d, when the temperature gradually increased, S_{18} decreased rapidly, demonstrating the purification effect of the cooking process, which favors the qualitative enhancement of dissolving pulp.

Influences of reaction time

Figure 2 shows the influences of prehydrolysis reaction time on carbohydrate components of specimens after prehydrolysis and cooking. As indicated by Fig. 2a, both the yield and holocellulose content decreased with prolonged reaction time. It is notable that the α-cellulose content based on specimens showed a declining trend, while the α-cellulose content based on holocellulose exhibited a slight increase with prolonged reaction time, as indicated by Fig. 2b. Although α-cellulose suffered degradation to a certain extent during the prehydrolysis phase, the resistance of α-cellulose to hydrolysis is higher than that of hemicelluloses.

For alkali solubility, S_{18} decreased gradually with pro-

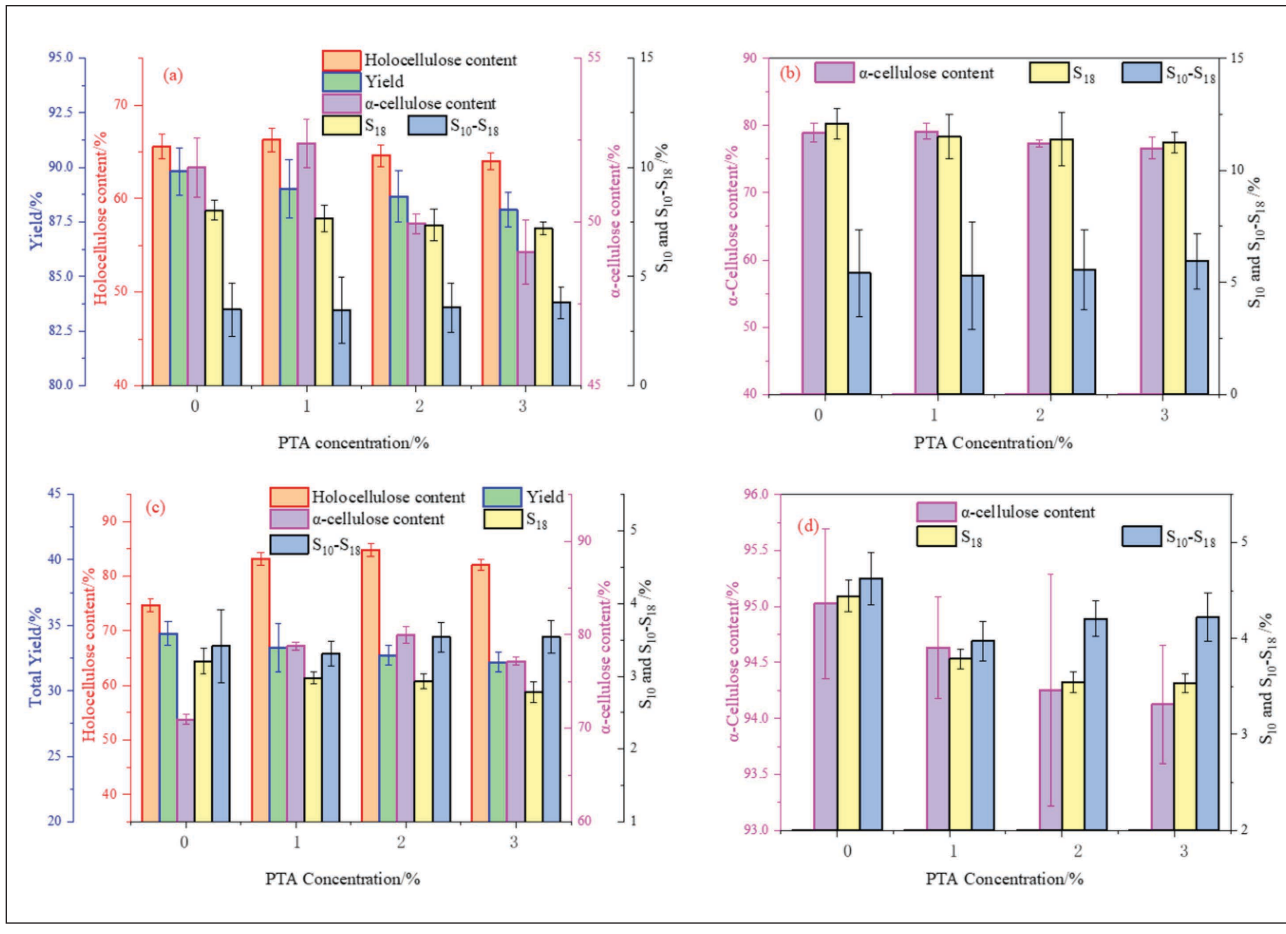

3. The influences of phosphotungstic acid (PTA) concentration on carbohydrate components of specimens after prehydrolysis and cooking: (a) based on specimen after prehydrolysis; (b) based on holocellulose after prehydrolysis; (c) based on specimen after cooking; and (d) based on holocellulose after cooking.

longed reaction time, demonstrating the serious degradation of hemicelluloses. Moreover, S_{10}-S_{18} displayed a tendency to decrease at the initial phase and increased later, with the minimum value appearing when the reaction time was 50 min. This indicated that the depolymerization of long chain cellulose was aggravated with the prolonged reaction time and also demonstrated that the reaction time should be controlled within a suitable range to retain the long chain cellulose.

The influences of reaction time on carbohydrate components of specimens after cooking are shown in Figs. 2c–2d. As can be seen from Fig. 2c, the holocellulose content, as well as the α-cellulose content, of the specimens increased with the initial increasing prehydrolysis reaction time, and the maximum values were achieved when the reaction time was 75 min. This was caused by the dissolution of lignin. With the prolonged reaction time during the prehydrolysis phase, more lignin was exposed on the surface of the specimens due to the degradation of hemicelluloses and was easily removed from specimens, thus resulting in increased holocellulose and α-cellulose contents based on specimens. Moreover, as mentioned previously, prolonged reaction time does not favor the retention of long chain cellulose during the prehydrolysis phase. Thus, with prolonged reaction time, the degradation rate of carbohydrates exceeded that of residual lignin, resulting in lower holocellulose and α-cellulose contents when the reaction time was 100 min.

In addition, as shown in Figs. 2c–2d, S_{18} and S_{10}-S_{18} both exhibited similar trends after cooking to those of prehydrolysis process. The drastic decline of S_{18} was attributed to the serious depolymerization of hemicelluloses, whereas the increased S_{10}-S_{18} when reaction time exceeded 50 min mainly originated from the depolymerization of long chain cellulose, which was further proof of the degradation of cellulose under prolonged prehydrolysis reaction time.

Influences of PTA concentration

Figure 3 shows the influences of PTA concentration on carbohydrate components of specimens after prehydrolysis and cooking. As shown in Fig. 3a, the yield and S_{18} of specimens decreased with increasing PTA concentration. This demonstrated that the carbohydrates, especially hemicelluloses, suffered an intensive hydrolysis effect with the in-

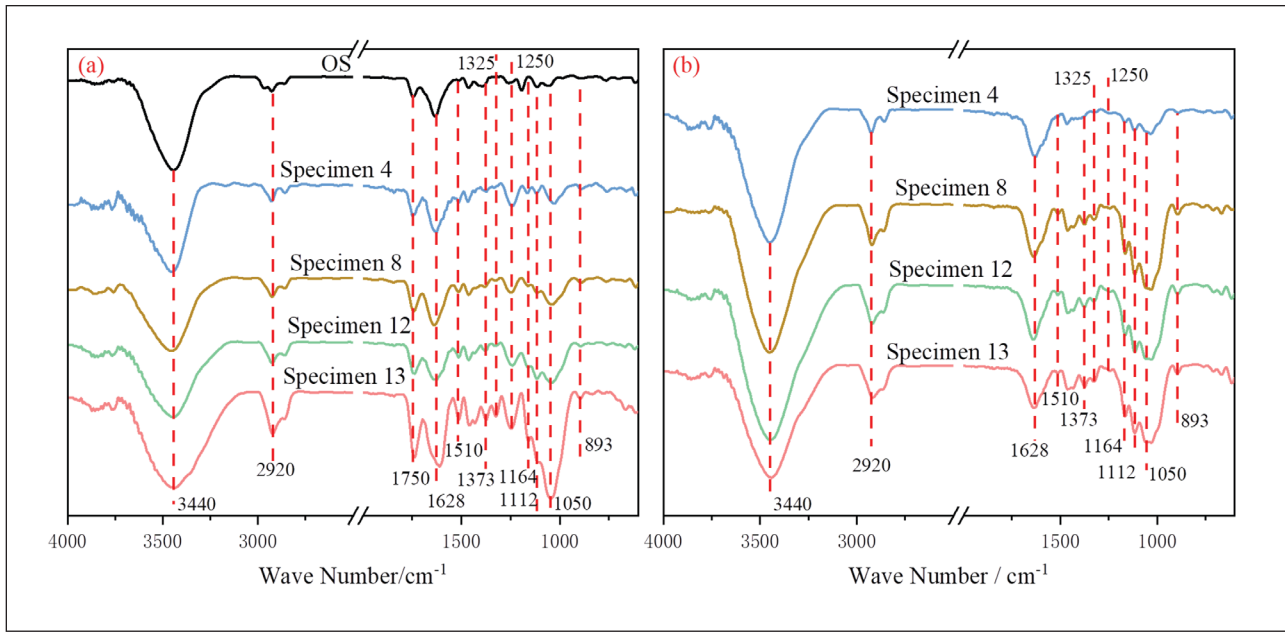

4. Fourier transform infrared (FTIR) spectra of specimens after (a) prehydrolysis and (b) cooking.

creasing system acidity. It is interesting to note that when PTA concentration was 1 wt%, both the holocellulose and α-cellulose contents increased in comparison with those of specimens only treated by hot water. This might be attributed to the partial degradation of lignin. When system acidity initially increased, partial lignin macromolecules, including acid soluble lignin and lignin fraction with low molecular weight, were dissolved. Similar results can be observed during the preparation process of lignin-rich microcrystalline cellulose by high temperature liquid water extraction catalyzed by transition metal ions [21]. Then, the holocellulose and α-cellulose contents decreased with further increased PTA concentration. During the PTA prehydrolysis phase, the residual lignin in specimens was relatively stable under acidic conditions, whereas the carbohydrates were further hydrolyzed by the catalytic effect of PTA, resulting in lower carbohydrate contents. In addition, the S_{10}-S_{18} remained within a relatively stable range but exhibited a slight increase depending on whether it was based on specimen or holocellulose, as indicated by Fig. 3a or Fig. 3b. This demonstrated that the concentration variation of PTA did not exhibit significant influence on the hydrolysis resistance of cellulose.

The influences of PTA concentration on carbohydrate components of specimens after cooking are shown in Figs. 3c–3d. In comparison with the specimens that were pretreated only by hot water, the holocellulose and α-cellulose contents of specimens both exhibited a significant increase with the incorporation of PTA, although the yield decreased. This indicated that the delignification selectivity was improved by the addition of PTA. However, both the holocellulose and α-cellulose contents of specimens decreased when PTA loading exceeded 2 wt%, demonstrating that excessive PTA loading during the prehydrolysis phase could not promote the lignin removal ratio but accelerated the carbohydrate degradation during the cooking process. A possible reason for this is that the crystalline region of cellulose was partially destroyed under relatively high acidity during the prehydrolysis phase [22], and it was easily depolymerized during the following cooking process.

For alkali solubility, S_{10}-S_{18} of specimens that were prehydrolyzed by 1 wt% PTA decreased to a certain degree compared with the specimens without the addition of PTA, whereas they increased with further increasing PTA concentration, as indicated by Fig. 3d. This also proved the previously mentioned inference, i.e., that the delignification selectivity could not be further improved by excessive PTA loading during the prehydrolysis process.

Structural characteristics

Figure 4 plots the FTIR spectra of specimens after prehydrolysis and cooking. As indicated by Fig. 4a, the absorption peaks of 1164 cm^{-1}, 1112 cm^{-1}, and 1050 cm^{-1} are caused by the stretching vibration of C–O–C, which are generally considered as typical absorption peaks of cellulose [23]. The absorption band at 893 cm^{-1} is typical of the β-linkage within glucose polymers between sugar units [24]. These peaks can be clearly observed in the spectra of specimens after prehydrolysis, indicating that more basic structural units of cellulose were exposed after prehydrolysis. The absorption bands at 2920 cm^{-1} and 1373 cm^{-1} are related to the stretching vibration bands of –CH in the $–CH_2$ and $–CH_3$ groups, respectively. These two bands also showed a remarkable increase after prehydrolysis. Furthermore, the absorption peak near 1628 cm^{-1} corresponds to the –CHO stretch vibration. The increased intensity of these absorp-

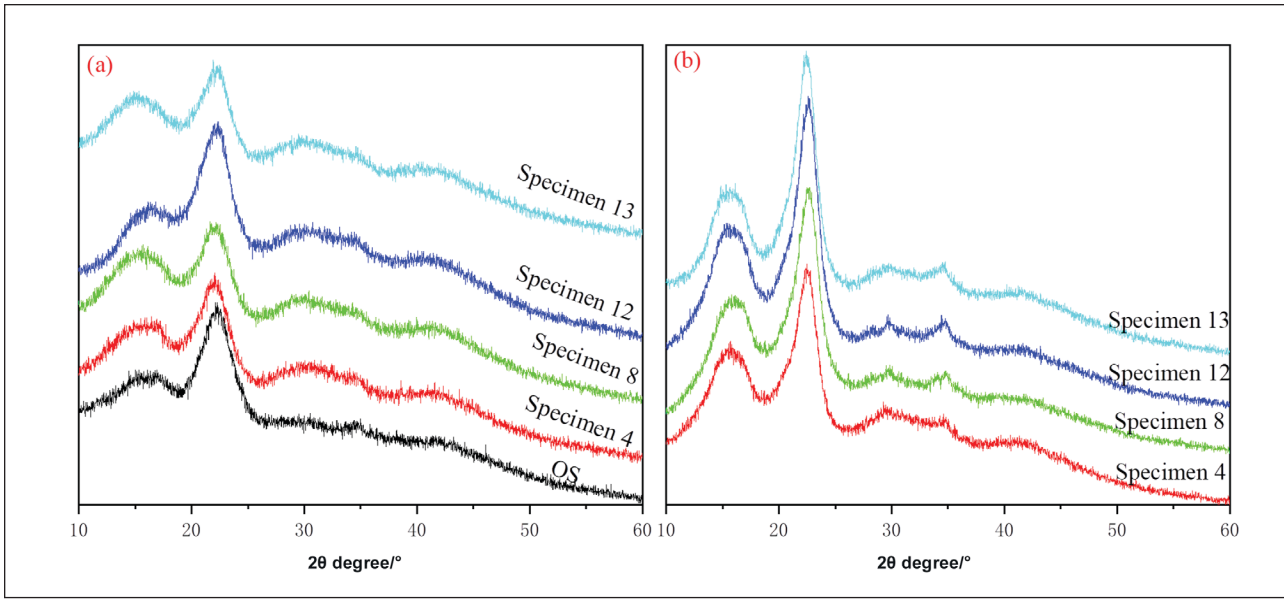

5. X-ray diffraction (XRD) spectra of specimens after (a) prehydrolysis and (b) cooking.

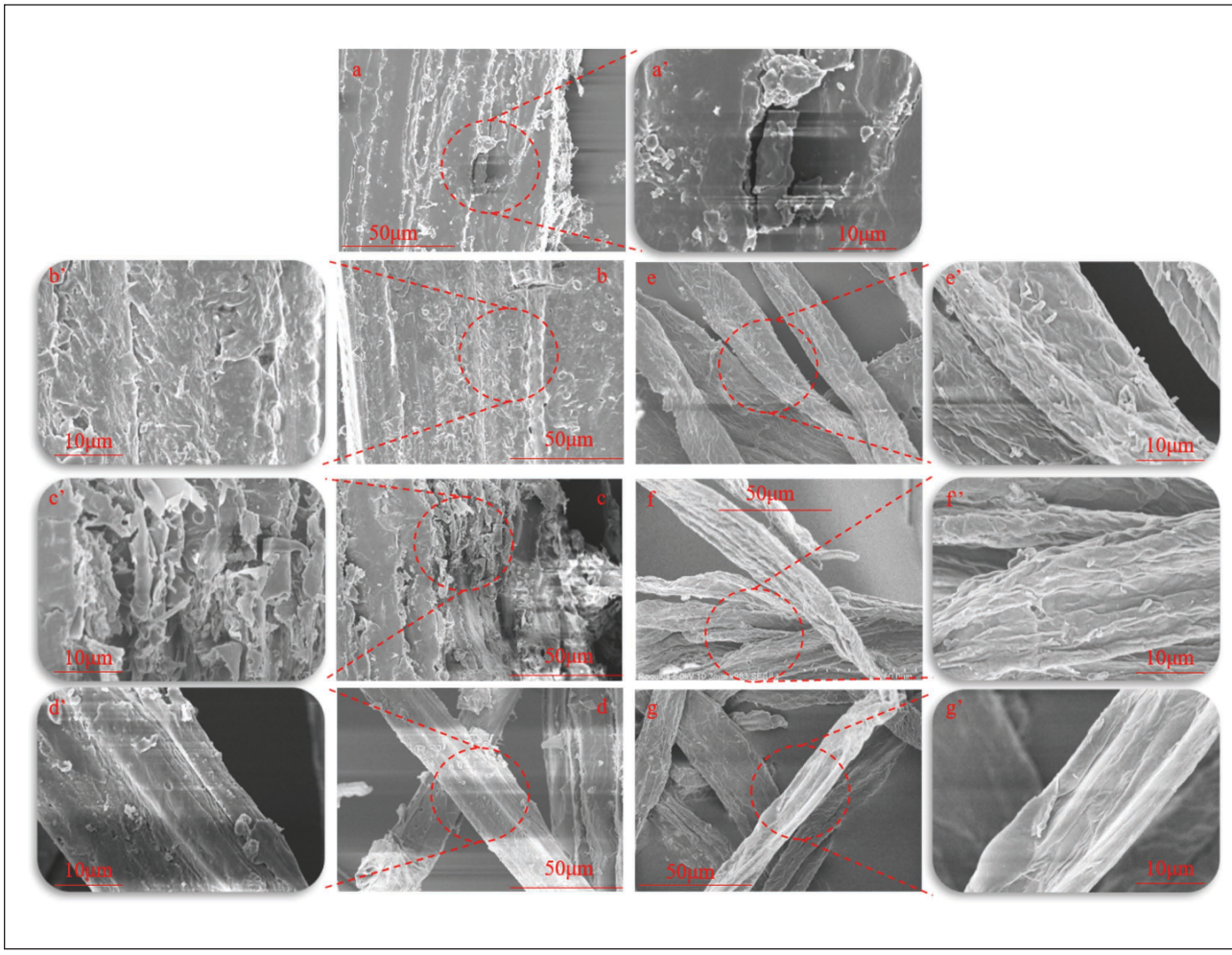

6. SEM images of (a) untreated grape branches (OS); and specimens after (b-d) prehydrolysis and (e-g) cooking under different magnification. Among them, (b) and (e) are specimen 8 after prehydrolysis and cooking, respectively; (c) and (f) are specimen 12 after prehydrolysis and cooking, respectively; (d) and (g) are specimen 13 after prehydrolysis and cooking, respectively.

tion peaks might be attributed to breakage of the cellulose backbone and the increase of –CHO groups during the prehydrolysis process. Although the relative content of lignin in specimens increased, the cellulose structure was loosened, and more reactive groups were exposed under the catalysis effect of PTA, resulting in the enhanced absorption peaks for cellulose after prehydrolysis.

In addition, the absorption peak of 1750 cm^{-1} is related to the –C=O groups unconjugated to aromatic rings. The peak at 1510 cm^{-1} corresponds to the aromatic C=C stretch of the aromatic rings of lignin [25]. Moreover, the absorption peaks at 1250 cm^{-1} and 1325 cm^{-1} represent the stretching vibration of guaiacyl (G) and syringyl (S) units, respectively. These absorption peaks are weakened and even disappeared after cooking, demonstrating that lignin was greatly removed during the cooking process.

Figure 5 shows the XRD patterns of OS and the specimens after prehydrolysis and cooking. It can be clearly seen that they exhibited similar diffraction patterns. There are three main diffraction peaks at 2θ=15.1°, 16.4°, and 22.6° for all specimens, which correspond to (1-10), (110), and (200) crystal planes, respectively [26,27]. Moreover, the diffraction peak at 22.6° in the XRD pattern of specimens after cooking became sharper, as shown in Fig. 5b, which indicates a higher crystallinity after cooking [28]. Also, the diffraction peak at 2θ=34.5° that represents (004) crystal plane appeared in the XRD patterns of specimens after cooking. Obviously, the crystalline structure of specimens after hydrolysis or cooking had not changed and remained cellulose I.

Morphological characterization

Figure 6 shows the SEM images of selected specimens after prehydrolysis and cooking. As can be seem from Fig. 6a, OS exhibited compact morphological structure with a relatively smooth surface, whereas the integral structure of specimens gradually changed to become looser after prehydrolysis. Moreover, the more intensive the prehydrolysis conditions, the more loose the structure that was observed. It is notable that the fiber cells of specimens treated at relatively high temperature (Fig. 6d) were separated after prehydrolysis, although the cells always maintained relatively high lignin content. In addition, as can be seen from Fig. 6d, spherical lignin exudates attached on the fiber surface could be observed in the magnified SEM image. It has been reported that thermochemical pretreatments reaching temperatures above the range for lignin phase transition caused lignin to coalesce into larger molten bodies that migrated within and out of the cell wall and redeposited on the surface of plant cell walls [29,30]. The spherical exudates on the fiber surface might be attributed to the redeposited lignin under high temperature. The hydrophobic lignin, which was melted and repolymerized during pretreatment, tends to form droplets to minimize its exposed surface in contact with aqueous solution.

As can be seen from Figs. 6e–6g, all the selected specimens were dissociated to fibrous mass after cooking. Moreover, with enhanced prehydrolysis conditions, a smoother surface and less deposited lignin particles can be observed in the SEM images of specimens, indicating the satisfactory pulp quality after the cooking process.

Prehydrolysis temperature optimization

Based on the results of the orthogonal experiment, temperature is the most important factor for PTA prehydrolysis. In order to obtain the optimal prehydrolysis temperature, a further optimized experiment focused on the prehydrolysis temperature using constant cooking and bleaching conditions was conducted.

Figure 7 illustrates the influence of prehydrolysis temperature on the carbohydrate components of specimens within the range of 130°C to 150°C during various treatment phases. As shown in Figs. 7a–7b, the maximum value for α-cellulose content of specimens, whether based on specimens or holocellulose, appeared when the prehydrolysis temperature was 145°C. During the cooking process, the α-cellulose content based on specimens also increased with the increasing temperature, whereas the α-cellulose content based on holocellulose achieved the maximum value when the prehydrolysis temperature was 145°C, as shown in Figs. 7c–7d. Moreover, the highest α-cellulose content of specimens after bleaching appeared at 145°C (94.04%), achieving the quality standards for dissolving pulp, and then decreased to a certain degree when the prehydrolysis temperature increased to 150°C (Fig. 7e). These findings are consistent with the results of the orthogonal experiment, indicating that excessive degradation of cellulose might be caused by the intensive prehydrolysis conditions.

During the cooking and bleaching phases, the total yield exhibited a significant decrease, typically decreasing from 29.0% to 26.1% when the prehydrolysis temperature increased from 145°C to 150°C. This is also consistent with the results of the orthogonal experiment and indicates the excessive degradation of cellulose, further resulting in decreased yield during the subsequent process. This can also be demonstrated by the increased S_{10}-S_{18} within the same temperature intervals. Furthermore, the DP of bleached specimens was measured, and the DP of specimens after bleaching was 853 when the prehydrolysis temperature was 145°C and exhibited a further decrease under 150°C. This is consistent with the results of carbohydrate components after prehydrolysis and cooking. It seems that 145°C can be selected as the optimum prehydrolysis temperature.

CONCLUSIONS

Dissolving pulp of a relatively high-quality grade can be prepared by grape branches via a PTA prehydrolysis kraft process. The lignin in grape branches can be efficiently activated by PTA prehydrolysis treatment, and relatively

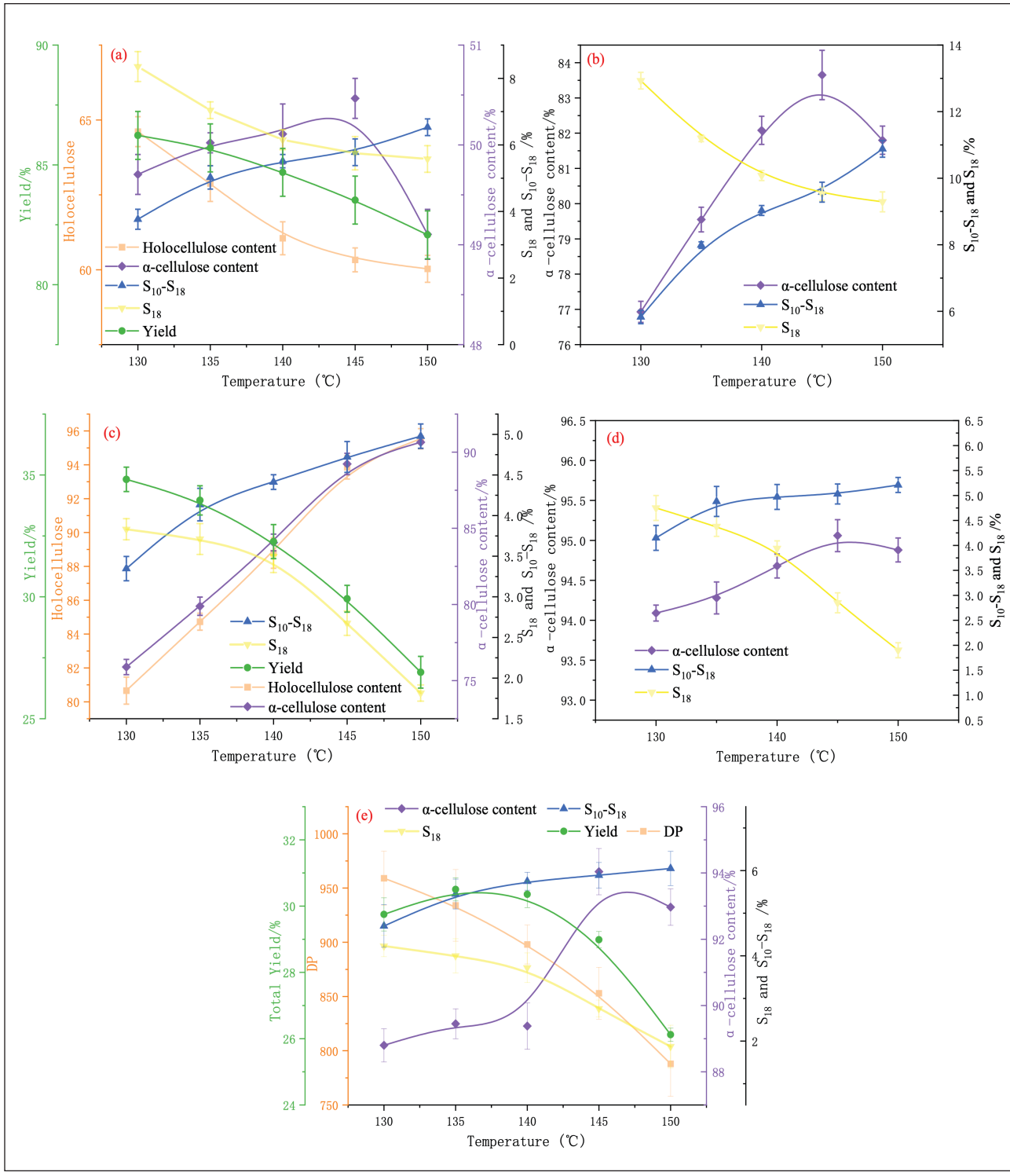

7. The influences of prehydrolysis temperature on carbohydrate components of specimens: (a) based on specimen after prehydrolysis; (b) based on holocellulose after prehydrolysis; (c) based on specimen after cooking; (d) based on holocellulose after cooking; and (e) based on specimen after bleaching.

mild conditions can be used during the subsequent cooking process.

Among the process variables during prehydrolysis, temperature exhibited the most significant influence on the cellulose purity of the obtained pulp fibers after cooking, followed by reaction time and PTA concentration. The elevation of prehydrolysis temperature favored the enhancement of pulp quality after cooking. However, serious degradation of long chain cellulose occurred under excessively high prehydrolysis temperature or prolonged

reaction time. In addition, the incorporation of PTA improved the delignification selectivity during the cooking process, whereas the delignification selectivity could not be further improved by excessive PTA loading.

The optimized prehydrolysis conditions were as follows: prehydrolysis temperature, 145°C; reaction time, 75 min; and PTA concentration, 1 wt%. Under these prehydrolysis conditions, 94.1% and 29.0% for α-cellulose content and total yield can be achieved after the given cooking and bleaching conditions, respectively. **TJ**

ACKNOWLEDGMENTS

The authors are grateful for financial support from the Natural Science Basic Research Program of Shaanxi Province (Grant No. 2020JQ-991).

LITERATURE CITED

1. Zhou, S., Li, Y., Huang, L., et al., *BioResources* 13(2): 2861(2018). https://doi.org/10.15376/biores.13.2.2861-2870.
2. Chen, Z.C., Zhang, H.W., He, Z.B., et al., *BioResources* 14(4): 7627(2019).
3. Nayeem, J., Jahan, M.S., Popy, R.S., et al., *TAPPI J.* 18(5): 287(2019). https://doi.org/10.32964/TJ18.5.287.
4. Borrega, M., Nieminen, K., Sixta, H., *BioResources* 6(2): 1890(2011).
5. Wang, G.S., Lee, J.-W., Zhu, J.Y., et al., *Appl. Biochem. Biotechnol.* 163(5): 658(2011). https://doi.org/10.1007/s12010-010-9071-4.
6. Galadima, A. and Muraza, O., *Int. J. Energy Res.* 39(6): 741(2015). https://doi.org/10.1002/er.3257.
7. Li, X., Lu, X., Nie, S., et al., *Ind. Crops Prod.* 145: 112154(2020). https://doi.org/10.1016/j.indcrop.2020.112154.
8. Qu, H., Liu, B., Li, L., et al., *Fuel Process. Technol.* 199: 106272(2020). https://doi.org/10.1016/j.fuproc.2019.106272.
9. Wang, X., Duan, C., Feng, X., et al., *Sep. Purif. Technol.* 266: 118562(2021). https://doi.org/10.1016/j.seppur.2021.118562.
10. Torlopov, M., Udoratina, E., Martakov, I., et al., *Cellulose* 24(5): 2153(2017). https://doi.org/10.1007/s10570-017-1256-3.
11. Chen, B.-H., Wang, Z.-Q., Jin, Z.-C., et al., *Biomass Convers. Biorefin.* (2021). https://doi.org/10.1007/s13399-021-01849-4.
12. Xiao, Z., Zhang, Q., Wang, X., et al., *Biomass Convers. Biorefin.* 10(4): 1007(2020). https://doi.org/10.1007/s13399-019-00518-x.
13. Zhang, J., Liu, X., Sun, M., et al., *ACS Catal.* 2(8): 1698(2012). https://doi.org/10.1021/cs300342k.
14. Demesa, A.G., Laari, A., Sillanpää, M., et al., *Molecules* 22(10): 1625(2017). https://doi.org/10.3390/molecules22101625.
15. Du, B., Liu, B., Yang, Y., et al., *Catalysts* 9(5): 399(2019). https://doi.org/10.3390/catal9050399.
16. Guo, Z., Li, D., You, T., et al., *ACS Sustainable Chem. Eng.* 8(32): 12110(2020). https://doi.org/10.1021/acssuschemeng.0c03491.
17. Du, B., Chen, C., Sun, Y., et al., *RSC Adv.* 10(52): 31479(2020). https://doi.org/10.1039/D0RA05069E.
18. Mateos-Espejel, E., Radiotis, T., Jemaa, N., *TAPPI J.* 12(3): 29(2013). https://doi.org/10.32964/TJ12.2.29.

ABOUT THIS PAPER

Cite this article as:
Li, T., Ma, Y., and Zhang, J.K., *TAPPI J.* 21(1): 35(2022). https://doi.org/10.32964/TJ21.1.35

DOI: https://doi.org/10.32964/TJ21.1.35

ISSN: 0734-1415

Publisher: TAPPI Press

Copyright: ©TAPPI Press 2021

About this journal

ABOUT THE AUTHORS



Li



Ma



Zhang

Equipment corrosion and acid recovery hinders further development of dilute acid prehydrolysis during the prehydrolysis kraft (PHK) cooking process. Considering its unique physicochemical properties such as high Brønsted acidity, high stability, and reusability, phosphotungstic acid (PTA) was expected to be used as a catalyst in the prehydrolysis phase of the PHK process for dissolving pulp preparation.

We found that lignin can be efficiently activated by PTA prehydrolysis treatment and is easily removed during the cooking process. Under optimized prehydrolysis conditions, relatively mild conditions can be used during the subsequent cooking process. Thus, PTA prehydrolysis represents an alternative approach for preparing a PHK dissolving pulp product. Our next step is to characterize and illustrate the structural variation of lignin during the PTA prehydrolysis process and to provide more information on this pretreatment approach.

Li is associate professor, Ma is lecturer, and Zhang is professor at the Institute of Chemical Engineering, Shaanxi Institute of Technology, Xi'an, Shaanxi, China. Email Li at l1tao@163.com.

19. Yue, X., He, J., Xu, Y., et al., *Carbohydr. Polym.* 208: 115(2019). https://doi.org/10.1016/j.carbpol.2018.12.072.

20. Miao, Q., Chen, L., Huang, L., et al., *Bioresour. Technol.* 154: 109(2014). https://doi.org/10.1016/j.biortech.2013.12.040.

21. Yue, X., He, J., Li, T., et al., *Cellulose* 28(3): 1405(2021). https://doi.org/10.1007/s10570-020-03620-w.

22. Wang, X., Duan, C., Zhao, C., et al., *Bioresour. Technol.* 253: 182(2018). https://doi.org/10.1016/j.biortech.2018.01.022.

23. Elanthikkal, S., Gopalakrishnapanicker, U., and Varghese, S., *Carbohydr. Polym.* 80(3): 852(2010). https://doi.org/10.1016/j.carbpol.2009.12.043.

24. Zhong, C., Wang, C., Wang, F., et al., *Carbohydr. Polym.* 136: 979(2016). https://doi.org/10.1016/j.carbpol.2015.10.001.

25. Agblevor, F.A., Ibrahim, M.M., and El-Zawawy, W.K., *Cellulose* 14(3): 247(2007). https://doi.org/10.1007/s10570-006-9103-y.

26. Ren, H., Shen, J., Pei, J., et al., *Cellulose* 26(15): 8367(2019). https://doi.org/10.1007/s10570-019-02712-6.

27. Trache, D., Khimeche, K., Mezroua, A., et al., *J. Therm. Anal. Calorim.* 124(3): 1485(2016). https://doi.org/10.1007/s10973-016-5293-1.

28. Lu, Q., Tang, L., Lin, F., et al., *Cellulose* 21(5): 3497(2014). https://doi.org/10.1007/s10570-014-0376-2.

29. Donohoe, B.S., Decker, S.R., Tucker, M.P., et al., *Biotechnol. Bioeng.* 101(5): 913(2008). https://doi.org/10.1002/bit.21959.

30. Ko, J.K., Kim, Y., Ximenes, E., et al., *Biotechnol. Bioeng.* 112(2): 252(2014). https://doi.org/10.1002/bit.25349.

Application of ATR-IR measurements to predict the deinking efficiency of UV-cured inks

HIROHIKO KOIZUMI, MASATO TAKAYAMA, SEIKI YONESHIGE, AND SHISEI GOTO

ABSTRACT: In recent years, ultraviolet (UV)-curable ink has been developed and widely used in various printing applications. However, using UV-printed products (UV prints) in recovered paper recycling causes end-product dirt specks and quality issues.

A new method was developed that can distinguish UV prints from other prints by means of attenuated total reflectance infrared (ATR-IR) spectroscopy. Application of this method could allow more efficient use of UV prints as raw materials for paper recycling.

First, a mill trial was performed using UV prints alone as raw materials in a deinked pulp (DIP) process. Second, test prints were made with four types of UV inks: a conventional UV ink and three different highly-sensitive UV inks. Each print sample had four levels of four-color ink coverage patterns (100%, 75%, 50%, and 25%). Next, deinkability of all prints was evaluated by laboratory experiments. Finally, each print was measured using the ATR-IR method, and the relationship between the IR spectra and deinkability was investigated.

Mill trial results showed that UV prints caused more than 20 times as many dirt specks as those printed with conventional oil-based ink. There were variations in recycling performance among UV prints taken from bales used for the mill trial. Lab tests clearly revealed that not all UV-printed products lead to dirt specks.

In order to clarify the factors that affected deinkability of UV prints, the print samples were investigated by lab experiments. Key findings from lab experiments include:

- The number of dirt specks larger than 250 μm in diameter increased as the ink coverage increased.
- Higher ink coverage area showed stronger intensity of ATR-IR spectral bands associated with inks. These results indicate that deinkability of UV prints could be predicted by analysis of ATR-IR spectra.
- Finally, the method was applied for assessment of recovered paper from commercial printing presses. It was confirmed that this method made it possible to distinguish easily deinkable UV prints from other UV prints.

Based on these findings, we concluded that the ATR-IR method is applicable for inspection of incoming recovered paper.

Application: The developed method can determine the deinkability level of UV-printed products simply by analyzing the surface of those prints. Thus, it can be useful for incoming quality control in mills.

Due to the shrinkage of paper markets in Japan and exports of recovered paper to China and/or other countries in Asia, the amount of recovered paper as a raw material for secondary fiber has decreased. In addition, the development of new printing methods has given rise to different kinds of printed products in the market today. One that stands out as a trend is ultraviolet (UV) printing, which uses UV curable ink. Ultraviolet printing offers advantages such as reduction in volatile organic compounds (VOCs) and short job delivery times. However, acrylic resin, the major component of UV ink, forms a rigid coating layer on the paper surface after UV curing. This highly rigid layer is difficult to break down [1-4] and leads to unacceptable speck contamination in deinked pulp (DIP). For this reason, UV printed products (UV prints) have been regarded as raw materials to be avoided in the recycling process.

In our previous papers [5,6], we discussed a method that can distinguish UV prints from other printed products (such as products printed with oil-based ink) by means of attenuated total reflection infrared (ATR-IR) spectroscopy. We named this method the "ATR-IR method" [7-10]. When the method was applied in mills for recycled stock quality control, prints that gave poor-deinkability, such as UV prints, were sorted out more efficiently. Improved sorting reduced the incidence of dirt specks in DIP production.

The development of highly-sensitive UV (HS-UV) prints in recent years has made the pulp from these prints more easily deinkable [11]. The ease of deinking UV prints continues to be the subject of debate; for example, see the proc-

ceding of the INGEDE Symposium [12]. Thus, the development of UV prints is progressing. In order to maintain the productivity and quality of DIP, a deeper understanding of the deinkability of UV prints is required.

First, a mill test was performed as part of this study to establish the deinkability of conventional UV (C-UV) prints and HS-UV prints as raw materials. Second, to investigate the factors affecting the deinkability of UV prints, test prints were made with several types of UV-curable inks at various coverage ratios, and these test prints were evaluated for deinkability.

Finally, the application of the ATR-IR method for distinguishing easily deinked prints from difficult ones was examined. Up to this point, the method had been used only for distinguishing UV prints from those of other printing processes (such as prints made with oil-based inks or polystyrene coated prints). Laboratory deinkability tests revealed that not all UV prints were difficult to deink. In fact, some UV prints were as easy to deink as prints with oil-based ink. For more efficient use of UV prints as raw materials, it is necessary to sort UV prints by their level of deinkability. We explored the possibility of distinguishing easily deinked UV prints (those resulting in fewer dirt specks) from more difficult to deink UV prints (those resulting in more dirt specks) by evaluating the relationship between IR spectra and deinkability of several kinds of UV prints.

EXPERIMENTAL

Mill trial for comparing quality of UV and conventional prints as raw materials

A mill trial was conducted to compare the quality of UV prints and conventional prints (printed with oil-based ink) as raw materials. Three types of bales were collected from commercial printing presses for this mill trial:

- Conventional UV-curable ink (C-UV) prints only
- Highly-sensitive UV-curable ink (HS-UV) prints only
- Oil-based ink (OB) prints only

Table I shows the sources of the bales. Bales of C-UV prints were procured from printer B, those of HS-UV prints from printers A and B, and those with OB from printer C. The recovered paper grade of these prints was a mixture of sorted office waste (SOW) and colored ledger. All were evaluated in a DIP mill at Nippon Paper Industries. The comparison of deinking quality for each print as a raw material was based on the frequency of dirt specks in handsheets made from each deinked pulp according to TAPPI Standard Test Method T 205 sp-02 "Forming handsheets for physical tests of pulp." Specks were measured by image analysis (Easy Scan, Nippon Paper Unitec Co. Ltd.; Shizuoka, Japan), with only those larger than 250 µm in diameter being counted.

Test	Ink Type	Paper	Printer
1	C-UV	SOW/Colored ledger	B
2	HS-UV	SOW/Colored ledger	A and B
Blank	OB	SOW/Colored ledger	C

UV = ultraviolet; C-UV = conventional UV-curable ink; HS-UV = highly-sensitive UV-curable ink; OB = oil-based ink; SOW = sorted office waste.

I. Raw materials and printer sources for bales used in tests at Nippon Industries deinked pulp (DIP) mill.

Procedure for laboratory experiments

The HS-UV printing samples were taken from bales collected from printers A and B that were used for the mill trial. Then, those samples were evaluated by a laboratory experiment to investigate whether there was a difference in deinkability between products from each of the two printing presses.

The measurement procedure is shown in **Fig. 1**. First, print samples from printers A and B, respectively, were cut into 2 cm × 2 cm pieces by a shredder machine. Then, they were mixed with woodfree copy paper at a ratio of 1:9 on a weight basis. Next, the mixtures were disintegrated in a lab mixer at 5% consistency with deinking chemicals at 40°C for 5 min. A deinking agent (DP150, Nicca Chemical Co. Ltd.; Fukui, Japan), sodium hydroxide (NaOH), and sodium metasilicate (Na_2SiO_3) were used as the chemical package. Dosages of these chemicals were 0.2%, 0.7%, and 0.7%, respectively, based on dry weight of the pulp. At the completion of the pulping process, the slurry was hyper-

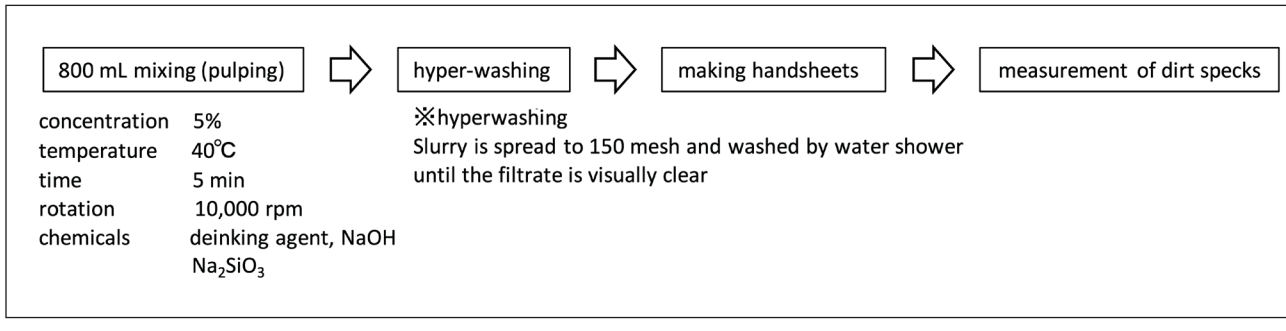

1. Schematic of the measurement procedure used in the deinkability test method (NaOH = sodium hydroxide; Na_2SiO_3 = sodium metasillicate).

Ink Maker	X		Y	Z
Ink Type	C-UV	HS-UV	HS-UV	HS-UV
Ink Coverage Ratio	100%, 75%, 50%, 25%	100%, 75%, 50%, 25%	100%	100%
Paper Grade	WFC			

UV = ultraviolet; C-UV = conventional UV-curable ink; HS-UV = highly-sensitive UV-curable ink; WFC = woodfree coated.

II. Print samples used for laboratory deinkability test and attenuated total reflectance infrared (ATR-IR) spectroscopy analyses.

washed through 150 mesh wire with openings of 100 µm. Washing continued until the filtrate was visibly clear. The number of dirt specks of 250 µm or larger in handsheets made from the pulps was measured by image analysis.

As outlined in **Table II**, test prints were made with four types of UV inks: a C-UV ink and three kinds of HS-UV inks. The C-UV ink was obtained from ink maker "X" in Japan, and HS-UV inks were obtained from ink maker X, as well as ink makers "Y" and "Z." Each test print had four levels of ink coverage patterns (100%, 75%, 50%, and 25%). A picture of the forms used for printing is shown in **Fig. 2**. Woodfree coated (WFC) paper sheets were used as a base paper for all prints. The region of the four-color part of the form was printed to an optical density target in the range of 1.90–1.95 using a Macbeth transmission reflection densitometer (GretagMacbeth RD-19, Videojet X-Rite K.K.; Grand Rapids, MI, USA).

The impacts of UV ink from the three ink makers and the ink coverage pattern on deinkability were investigated on the test prints. As shown in Table II, 10 kinds of print samples were tested: C-UV and HS-UV from ink maker X (ink coverage ratio 100%, 75%, 50%, 25%; 8 total prints); and HS-UV from ink makers Y and Z (ink coverage ratio 100%, 2 total prints). The evaluation of deinkiability was judged from the numbers of dirt specks in handsheets made from hyperwashed samples following the procedure shown in Fig. 1.

Application of the ATR-IR method

To obtain the IR spectrum, the surface of each sample shown in Table II was analyzed using the ATR-IR apparatus (Target ID, S.T. Japan; Tokyo) with ATR resolution of 4 cm^{-1} and zinc selenide (ZnSE) beamsplitter; in total, 16 samples were measured. By correlating IR peak patterns and results from deinkability experiments, IR spectra were classified into three patterns of deinkability: poor, good, and very good. Then, those spectra data were added to the database of the ATR-IR apparatus in order to update the ATR-IR method. Finally, printing samples taken from bales collected from printers A and B and were tested using the ATR-IR method to verify the usefulness of this method.

RESULTS AND DISCUSSION

Mill trial for investigating the quality of C-UV and HS-UV prints as raw materials

Figure 3 shows the number of dirt specks of C-UV, HS-UV,

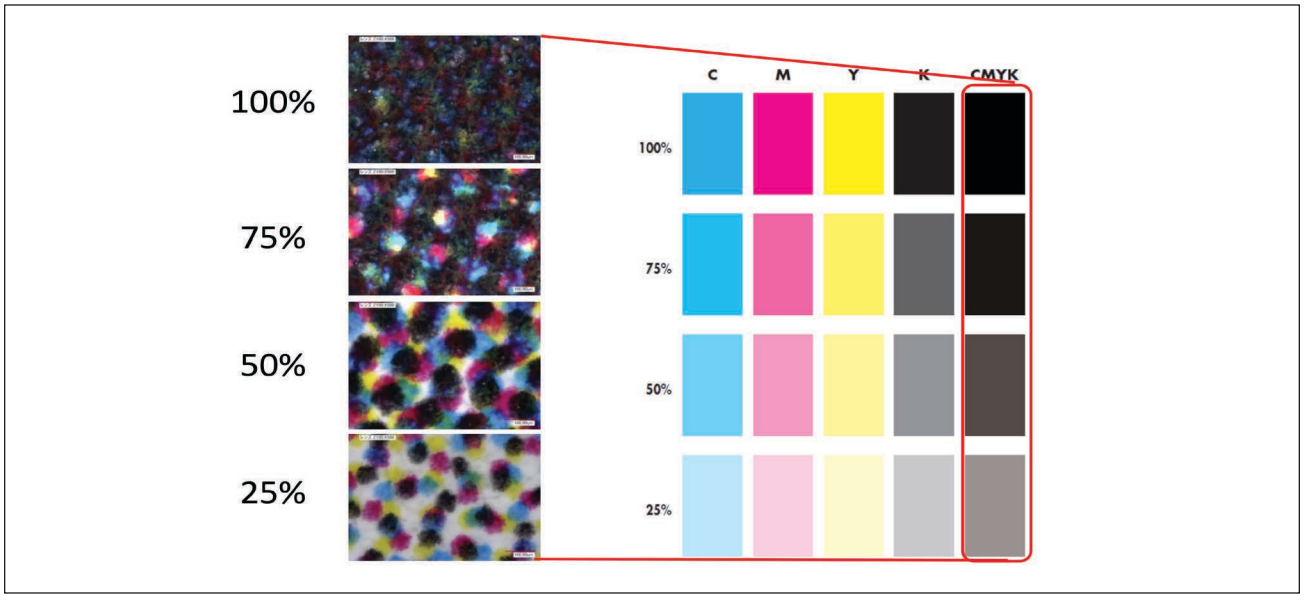

2. Form and ink coverage patterns of test prints (C = cyan; M = magenta; Y = yellow; K = black).

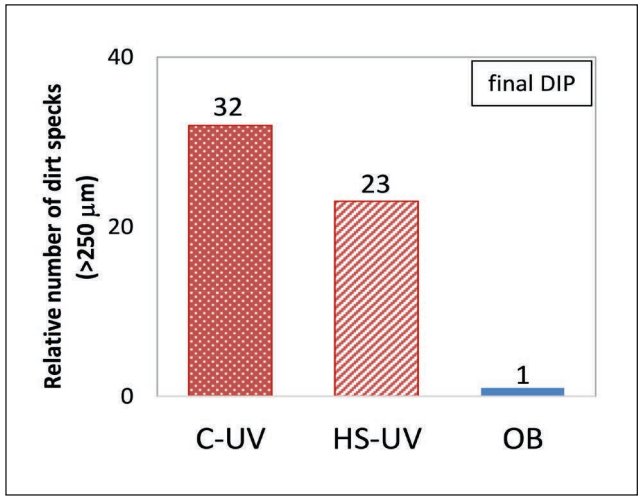

3. Number of dirt specks from conventional ultraviolet-curable (C-UV), highly-sensitive UV-curable (HS-UV), and oil-based (OB) inks in the final deinked pulp (DIP) test. Relative value is used based on the number of OB.

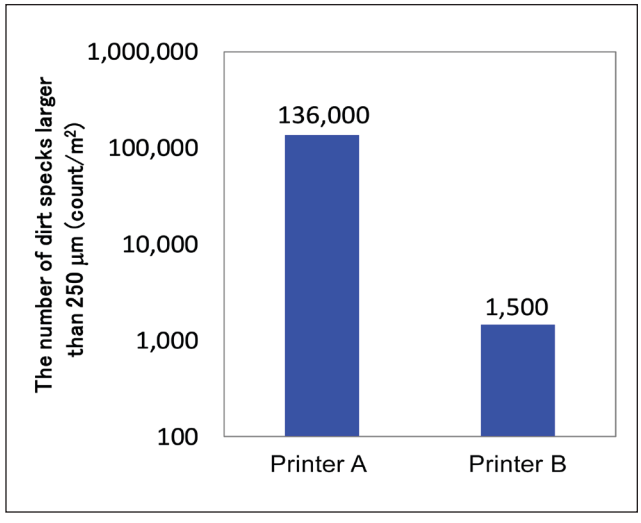

4. Number of dirt specks in samples from printer A and printer B after the laboratory experiment shown in Fig. 1.

and OB in the final DIP test. The relative number of dirt specks was based on the number of dirt specks in the OB. The relative number of dirt specks of C-UV and HS-UV was over 20 times more than that of OB. When comparing C-UV with HS-UV, HS-UV produced fewer dirt specks. However, it should be noted that whether the ink used was C-UV or HS-UV, unacceptibly large numbers of specks would result if these prints were used as the only raw materials.

Comparison of HS-UV print deinkability between printers A and B

Two kinds of HS-UV prints were used in the mill trial. One was from printer A and the other was from printer B. Laboratory work was performed to investigate whether there were differences in deinkability between the two sources. There was a large difference between the deinkability of

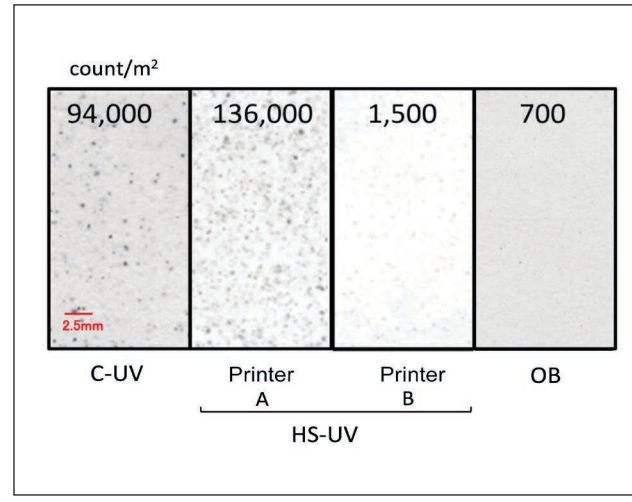

5. Images of handsheets after laboratory experiment shown in Fig. 1.

samples from printing press A and that from printing press B (**Fig. 4**; note log scale Y-axis).

Figure 5 shows images of lab-produced handsheets. The C-UV and OB sample results are also shown as comparative results, though these samples (C-UV and OB) were not taken at the same time as the mill test. It is easy to understand the difference in deinkability by comparing the images. The HS-UV samples from printer A actually showed more dirt specks than the C-UV sample. By comparison, samples from printer B had nearly as few dirt specks as the OB sample.

The results described here suggest that not all the UV prints were hard to deink. Some UV prints might become a cause of unacceptable dirt contamination, while other UV prints might not. Thus, it is important to understand what factors bring about these differences. For this purpose, we made test prints that had fixed ink coverage patterns using several kinds of UV inks; the pattern of these prints is shown in Fig. 2.

Comparison of deinkability of C-UV and HS-UV between different ink makers

To examine differences in deinkability between several kinds of UV inks, laboratory experiments were performed with test prints. An area of 100% ink coverage ratio with the four color components (shown as CMYK in Fig. 2) in each test print was used.

Figures 6 and 7 show the results of the comparison. Figure 6 is a comparison of the relative deinkability of C-UV vs. three different HS-UV printed samples. Note that, to varying degrees, the HS-UV ink caused fewer dirt specks than did C-UV ink. This result suggested that the film from HS-UV ink was easier to break into small pieces than that of C-UV ink.

Figure 7 shows the distribution of the dirt specks by diameter. Note that the peak speck size of the HS-UV ink from ink maker X was shifted to the left side of the figure

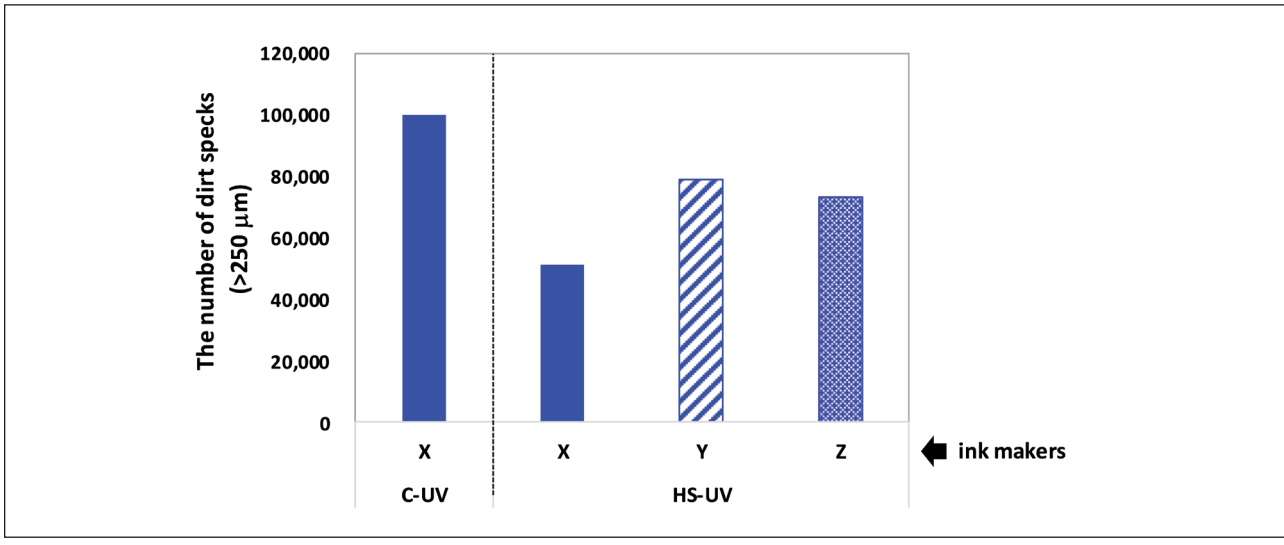

6. Comparison of the number of dirt specks from C-UV and HS-UV inks in test prints.

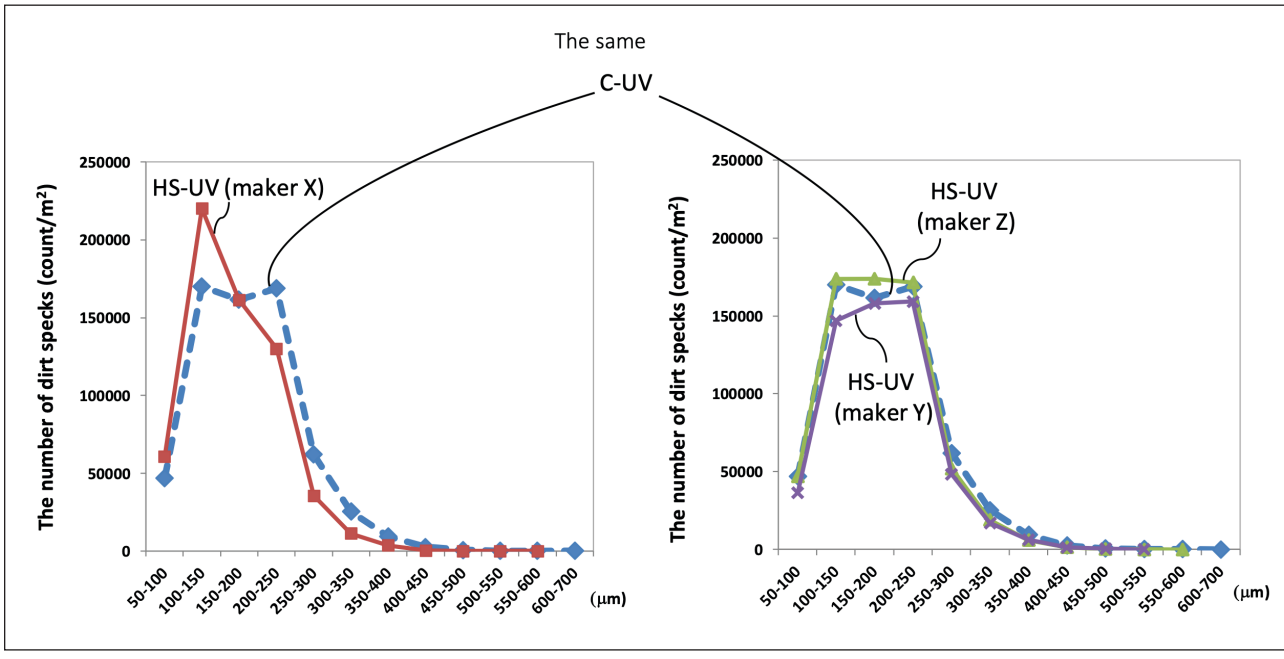

7. Distribution of dirt specks by diameter: HS-UV from ink maker X vs. C-UV (left), and HS-UV from ink makers Y and Z vs. C-UV (right).

(smaller particles) compared with other types of ink. The increase in the number of dirt specks of 100–150 µm in diameter inferred that the HS-UV ink from ink maker X was more easily fractured during deinking than the other HS-UV inks tested in this laboratory experiment. Therefore, it was obvious that there were also differences in the deinkability of the HS-UV inks.

The impact of four color printing on deinkability was tested by using 100% ink coverage ratio of the four color components (CMYK as shown in Fig. 2) and also the single color component (K), respectively (note log scale Y-axis in **Fig. 8**). The number of dirt specks of OB (the same data shown in Fig. 5) is shown as a reference.

Clearly, single color prints caused far fewer dirt specks than four color prints. Furthermore, the number of dirt specks caused by single color prints was nearly the same level as that of the OB sample. Finally, the appearance of contaminants from C-UV ink and from HS-UV ink on single color prints was roughly the same. Therefore, the ink coverage printing pattern can strongly affect the deinkability of UV prints.

Investigation of ink coverage pattern's influence on deinking

Ink coverage patterns of 100%, 75%, 50%, and 25% were used for laboratory tests to investigate how much impact

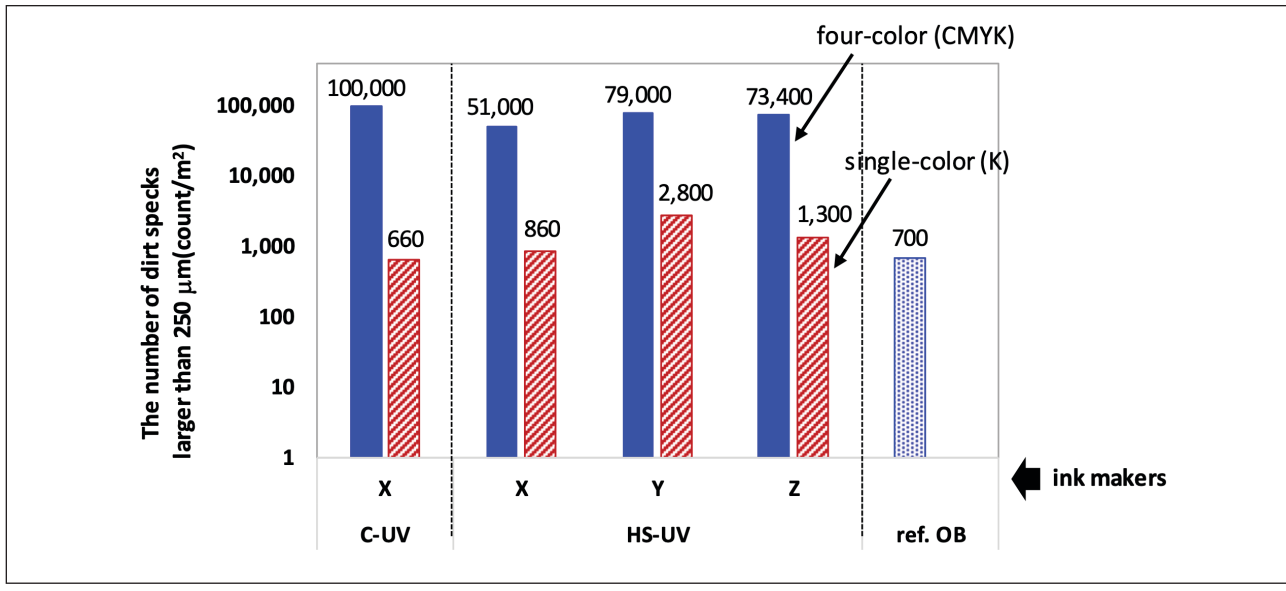

8. Comparison of the number of dirt specks from the four color components (CMYK as shown in Fig. 2) with the single color component (K). Number of dirt specks from OB is shown as reference.

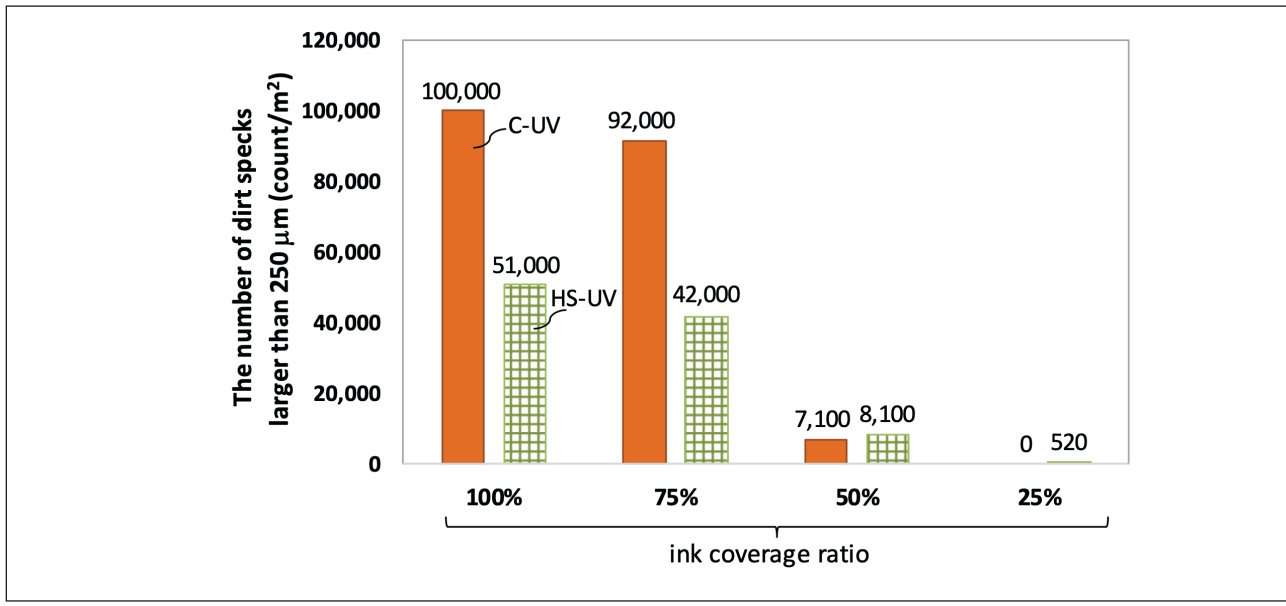

9. Number of dirt specks occurring at different ink coverage ratios (100%, 75%, 50%, and 25%) was examined with the laboratory experiment shown in Fig. 1.

different printing patterns had on deinkability. In this test, C-UV and HS-UV inks from ink maker X were examined. Areas evaluated were the four color printing areas that are circled in red in Fig. 2.

Figure 9 shows that the number of dirt specks decreased as the ink coverage ratio was reduced. This tendency was confirmed for both C-UV and HS-UV ink, particularly below 75% coverage. There was not much difference in dirt speck content between ink coverage ratios of 100% and 75%. Ratios of 50% and 25% gave much smaller counts. These results suggest that ink coverage ratios under 50% may be more easily handled by the DIP process. At 25% ink coverage, there appears to be little detrimental effect on dirt content.

Application of the ATR-IR method

Results so far indicate that the ink coverage ratio has a large impact on deinkability. With the sharp difference in deinkability between ink coverage ratios of "100% and 75%" vs. "50% and 25%," it would be useful if one could use ATR-IR to distinguish printing patterns.

To achieve this goal, the surface of each sample shown in Table II was analyzed using ATR-IR apparatus to obtain IR spectrum. The IR spectra vs. ink coverage

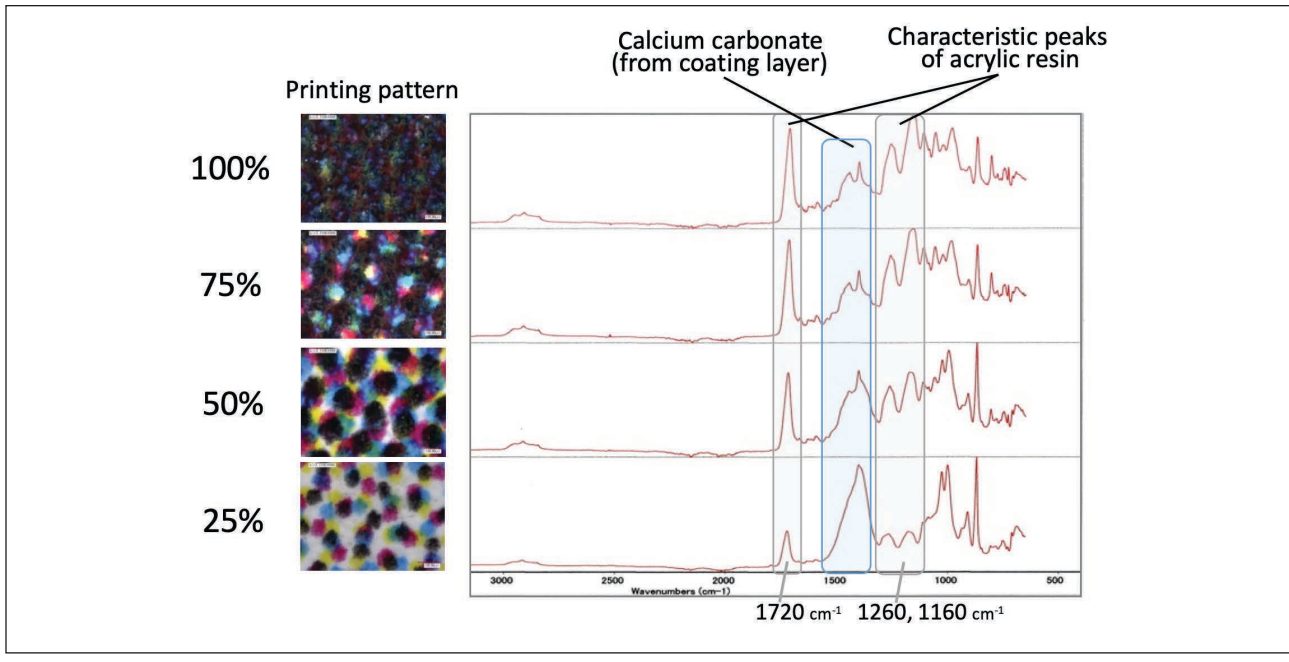

10. The IR spectra of different ink coverage patterns. Characteristic peaks of UV prints are 1160, 1260, and 1720 cm^{-1}.

Ink Coverage Ratio	Surface of Prints	Intensity Compared with 2920 cm^{-1}	IR Spectra	Dirt Specks >250 µm (count/m^2)	Deinkability
100%, 75% Category I		more than 4.8 times		42,000～100,000	poor
50% Category II		3.8～4.6 times		around 8000	good
25% Category III		2.5～3.5 times		around 500	very good

around 2920 cm^{-1} | around 1720 cm^{-1} | around 1260, 1160 cm^{-1}

11. Relationship between IR spectra and deinkability results.

ratio is shown in **Fig. 10**. UV prints had three peaks at 1160, 1260, and 1720 cm^{-1}, which were characterized as acrylate. It was obvious that those characteristic peaks for UV prints were getting lower intensity as the ink coverage ratio decreased. This was accompanied by an increase in peak intensity at 1440 cm^{-1}, which was characteristic of calcium carbonate derived from coating. Judging from these results, ink coverage ratio can be predicted from IR spectra by the differences in peak intensity. Thus, we examined enhancing the ATR-IR method by combining these IR spectra and the results of laboratory experiments.

According to laboratory experiments, it is practical to divide the results into three categories:

- Category I: ink coverage ratio of 100% and 75%; deinkability is poor.
- Category II: ink coverage ratio of 50%; deinkability is good.
- Category III: ink coverage ratio of 25%; deinkability is very good.

To define the categorization by peak intensity, we measured 16 samples by means of the ATR-IR apparatus and examined each IR spectrum. We found that each category could be defined based on the average intensity of the peaks that were characteristic of acrylate (1160, 1260, and 1720 cm^{-1}) compared with that of 2920 cm^{-1} (Category I: more than 4.8 times; Category II:

between 3.8 to 4.6 times; Category III: between 2.5 to 3.5 times).

Finally, the spectra related to UV prints were stored in an ATR-IR database, as shown in **Fig. 11**. Hence, when UV prints were inspected with the ATR-IR method, they were categorized into three groups: poor, good, or very good. With this uploaded data from the ATR-IR method, UV prints from commercial printing presses that were used for the mill trial (Test 2 shown in Table I) were assessed. Eventually, prints from printer A were judged as poor, while those from printer B were very good. Therefore, we confirmed that this method made it possible to distinguish easily deinkable UV prints from other UV prints.

CONCLUSIONS

The following are key findings from this study:

- According to the final DIP image analysis, whether conventional UV or highly-sensitive UV ink was used, high levels of dirt contaminants are likely if these prints are used as the only raw material.
- Laboratory experiments in this study made it clear that not all UV prints are hard to deink.
- There were differences in the deinkability of HS-UV prints between two printers.
- Laboratory experiments using test prints revealed that the ink coverage ratio strongly affected the deinkability of those prints. Examination of several UV prints using the ATR-IR apparatus found that they could be distinguished based on the intrinsic peak intensity that reflected the UV ink coverage ratio.
- Laboratory experimental results and IR spectra were combined, and a database for enhancing the ATR-IR method was created. Deinkability of UV prints could be categorized into three types by means of the ATR-IR method: poor, good, and very good.
- Prior to upgrading the ATR-IR method, the method could only classify prints into UV prints, polystyrene overcoated prints, and prints made with oil-based ink. Now, the method can also determine the deinkability level of UV prints simply by analyzing the surface of those prints.

ABOUT THE AUTHORS


Koizumi


Takayama


Yoneshige


Goto

We chose to study this topic because paper manufacturers have many product quality issues from dirt specks caused by ultraviolet-curable (UV) ink in paper used for recycling, and a way is needed to avoid them. Most UV-printed products (UV prints) have thus far been regarded as hard to deink.

We discovered that not all UV prints are difficult to deink, meaning that some of them may be used as raw materials in the recycling process. In addition, we also found a way to distinguish easily deinked UV prints (those carrying few dirt contaminants) from more difficult to deink UV prints (those carrying many dirt contaminants) using an attenuated total reflectance infrared (ATR-IR) spectroscopy apparatus. This discovery is new in this field.

Determining the deinkability between various UV prints was difficult. To address this, we made many test prints with different inks and analyzed them.

We found that some UV prints had nearly the same deinkability as conventional prints made with oil-based ink. If we can determine those usable UV prints, they can be used as a raw material for recycled paper products.

It was interesting to find that the IR spectra of printed inks differed in accordance with the deinkability of UV prints. We believe that the amount of printed ink directly affected the deinkability of the UV prints.

The deinkability of UV prints can be easily and promptly determined by analyzing the surface of the prints with the ATR-IR apparatus. Therefore, this approach is helpful for entrance quality control in mills.

Our next step is to apply this novel method in mills for entrance quality control. In addition, related industries in this field should work on developing easily deinkable inks and explore mill processes that can remove UV inks more efficiently.

Koizumi is assistant manager, Takayama is research manager, and Yoneshige is senior research manager at the NPi Research Laboratory, Nippon Paper Industries Co. Ltd., in Tokyo, Japan. Goto is general manager, Business Transformation Promotion Office, for Nippon Paper Industries Co. Ltd., Tokyo, Japan. Email Koizumi at hirohiko-koizumi@nipponpapergroup.com.

- Finally, the ATR-IR method was applied for the assessment of recovered paper from commercial printing presses, and the method's effectiveness was confirmed.

Due to diminishing supplies of recovered paper, expanding the usable pool of recycled paper is becoming more important. Sorting out prints that are hard deink by using the ATR-IR method is a first step in solving the problem of dirt contamination driven by UV prints.

Also, in light of the these findings, work on developing easily deinkable inks and exploring mill processes that can remove UV inks more efficiently should be considered among related industries. **TJ**

ABOUT THIS PAPER

Cite this article as:
Koizumi, H., Takayama, M., Yoneshige, S., et al., *TAPPI J.* 21(1): 51(2022). https://doi.org/10.32964/TJ21.1.51

DOI: https://doi.org/10.32964/TJ21.1.51

ISSN: 0734-1415

Publisher: TAPPI Press

Copyright: ©TAPPI Press 2022

About this journal

LITERATURE CITED

1. Blanco, A., Miranda, R., and Monte, M.C., *For. Sys.* 22(3): 471(2013). *https://doi.org/10.5424/fs/2013223-03677*.
2. Carré, B. and Magnin, L., "Digital prints: A survey of the various deinkability behaviours," *Res. Forum Recycl., 7th*, PAPTAC, Brossard, QC, Canada, 2004.
3. Galland, G., Vernac, Y., Julien, S., et al., *Pap. Technol.* 32(12): 30(1991).
4. Forester, W., "Deinking of UV-cured inks," *Tappi J.* 70(5): 127(1987).
5. Koizumi, H., Fukuoka, M., Toyota, K., et al., "The novel method to distinguish poor recyclable prints from recovered papers by using ATR-IR," *Res. Forum Recycl., 11th*, TAPPI, Peachtree Corners, GA, USA, 2016.
6. Koizumi, H., Fuchise-Fukuoka, M., Otsuhata, T., et al., *Jpn. TAPPI J.* 75(5): 469(2021). *https://doi.org/10.2524/jtappij.75.469*.
7. Hirabaru, C., Toyota, K., Otsuhata, T., et al., *Pulp Pap. Res. Conf.,* Japan TAPPI, Tokyo, 2015, p. 37.
8. Fukuoka, M., Hirabaru, C., Toyota, K., et al., *Pulp Pap. Res. Conf.,* Japan TAPPI, Tokyo, 2015, p. 41.
9. Koizumi, H., Fukuoka, M., Toyota, K., et al., *Pulp Pap. Res. Conf.,* Japan TAPPI, Tokyo, 2016, p. 47.
10. Koizumi, H., Takayama, M., Yoneshige, S., et al., *Pulp Pap. Res. Conf.,* Japan TAPPI, Tokyo, 2018, p. 61.
11. JFPI/PRPC, "The research reports on easy-recyclable print materials," Japan Federation of Printing Industries/Paper Recycling Promotion Center, Tokyo, 2011.
12. INGEDE, "Deinkable ink for LE- and LED-UV printing introduced at the INGEDE symposium," I*NGEDE News*, International Association of the Deinking Industry (INGEDE), Munich, February 2019.

TAPPI JOURNAL
WWW.TAPPI.ORG
THE PAPER AND PACKAGING INDUSTRIES' TECHNICAL RESOURCE
FEBRUARY 2022 | VOL. 21 NO.2

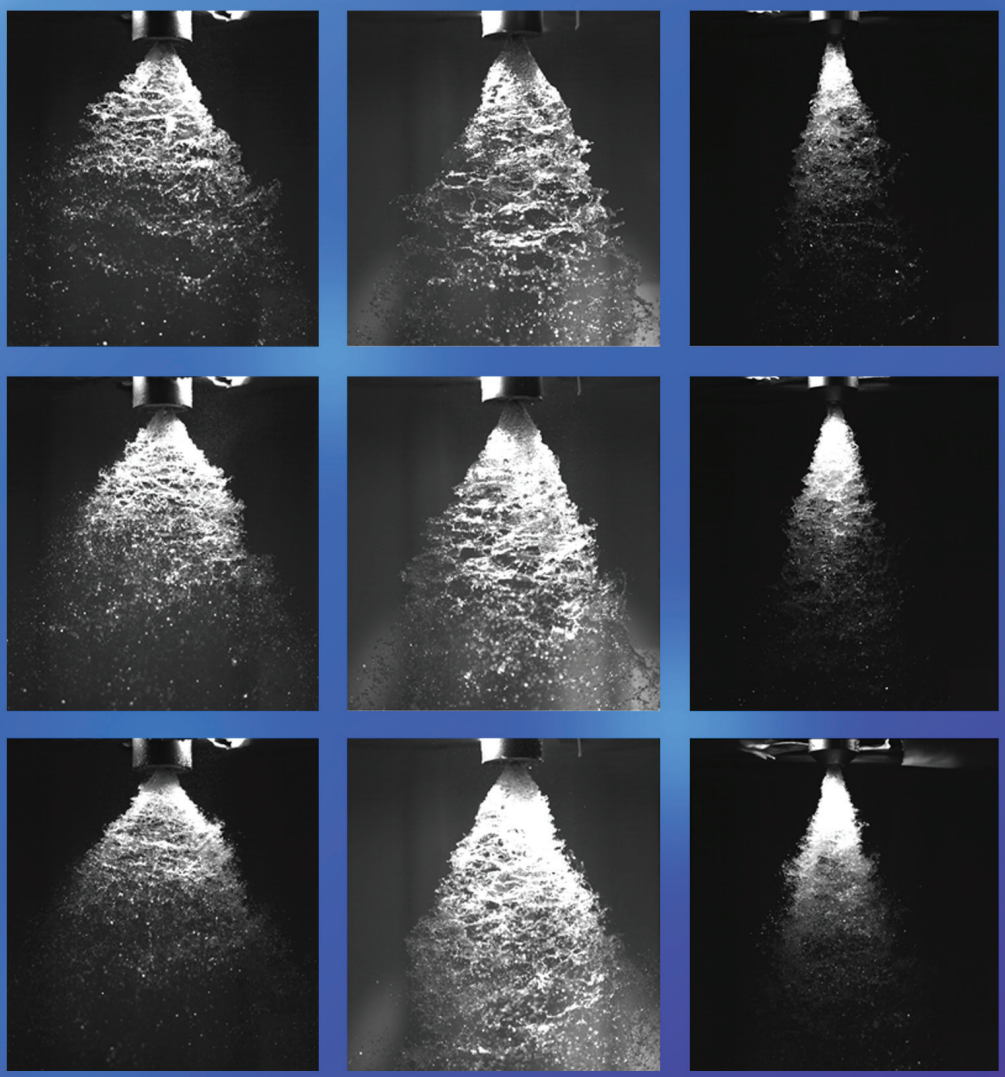

PAPERMAKING 71
Furnishing autohydrolyzed poplar weakly alkaline P-RC APMP to make lightweight coated base paper
Bo Zhang, Kaili Wu, Qingxi Hou, Tongbao Jiang, Wenwen Zhang, Kaisheng Luo, and Wei Liu

ENVIRONMENTAL 83
Utilization of kraft pulp mill residuals
Torsten Meyer

RECOVERY CYCLE 95
Experiments and visualization of sprays from beer can and turbo liquor nozzles
Ari Kankkunen, Santeri Koivisto, Kari Saari, Mika Järvinen, James Biggs, and Andrew Jones

TECHNICAL BRIEF: RECOVERY CYCLE 109
A model black liquor formulation for use in development and evaluation of membranes for concentrating weak black liquor
Scott A. Sinquefield

February 2022

TABLE OF CONTENTS VOL. 21 NO. 2

67 EDITORIAL
Innovation: How useful is it?
Seshadri Ramkumar

71 PAPERMAKING
Furnishing autohydrolyzed poplar weakly alkaline P-RC APMP to make lightweight coated base paper
Bo Zhang, Kaili Wu, Qingxi Hou, Tongbao Jiang, Wenwen Zhang, Kaisheng Luo, and Wei Liu

83 ENVIRONMENTAL
Utilization of kraft pulp mill residuals
Torsten Meyer

95 RECOVERY CYCLE
Experiments and visualization of sprays from beer can and turbo liquor nozzles
Ari Kankkunen, Santeri Koivisto, Kari Saari, Mika Järvinen, James Biggs, and Andrew Jones

109 TECHNICAL BRIEF: RECOVERY CYCLE
A model black liquor formulation for use in development and evaluation of membranes for concentrating weak black liquor
Scott A. Sinquefield

»**COVER CREDIT**: Researchers Kankkunen et al. studied black liquor nozzles using simple water spraying experiments, taking into account nozzle type, spray opening angle, velocity, and mass distribution (p. 95). Among other findings, nozzle geometry was found to greatly affect spray characteristics. The methods or measurement results presented can be used to compare nozzles for different purposes and to inform nozzle design.

TAPPI JOURNAL
WWW.TAPPI.ORG

Editor-in-Chief
Douglas W. Coffin coffindw@miamioh.edu
+1 513 529-0771

Associate Editor
Peter W. Hart peter.hart@westrock.com
+1 409 276-3465

Editorial Director
Monica Shaw mshaw@tappi.org
+1 770 367-9534

PRESS Manager
Jana Jensen jjensen@tappi.org
+1 770 209-7242

Webmaster
Trina Heath theath@tappi.org
+1 770 209-7416

***TJ* EDITORIAL BOARD**

Brian N. Brogdon, FutureBridge Consulting & Training LLC
brian.brogdon@gmail.com, +1 678 581-9114

Douglas W. Coffin, Miami University
coffindw@miamioh.edu, +1 513 529-0771

Mahendra Doshi, Doshi and Associates
mahen@aol.com, +1 920 832-9101

Marc Foulger, Valmet
marc.foulger@valmet.com +1 315 767-2920

Peter W. Hart, WestRock
peter.hart@westrock.com, +1 409 276-3465

Carl J. Houtman, USDA Forest Products Laboratory
choutman@fs.fed.us, + 1 608 231-9445

Vamsi Jasti, Ahlstrom-Munksjo Nonwovens LLC
jvamsik1@gmail.com, +1 818 585-3524

Lucian Lucia, North Carolina State University
lucian.lucia@gmail.com, +1 919 889-7059

John A. Neun, John A. Neun LLC
john.neun@gmail.com, +1 518 275-8139

Jim Niemiec, Jim Niemiec Consulting LLC
jim.niemiec@outlook.com, +1 715 213-4766

Steven P. Ottone, Omya
steven.ottone@omya.com, +1 919 641-7854

Gaurav Pranami, Imbed Biosciences
gpranami@imbedbio.com, +1 515 230-7005

Arthur Ragauskas, Oak Ridge National Laboratory
aragausk@utk.edu

Seshadri Ramkumar, Texas Tech University
S.Ramkumar@ttu.edu, +1 806 742-4567

Gregg Reed, Imerys
gregg.reed@imerys.com, +1 478 553-5747

Gerard J.F. Ring, University of Wisconsin—Stevens Point
gerrryring@wi-net.com, +1 715 592-3732

Scott Rosencrance, Kemira Chemicals
scott.rosencrance@kemira.com, +1 770 429-2753

Paul Wiegand, NCASI
pwiegand@ncasi.org, +1 919 941-6417

Junyong Zhu, USDA Forest Products Laboratory
jzhu@fs.fed.us, +1 608 231-9520

Join TAPPI *today!*
TAPPI JOURNAL is a free benefit of TAPPI membership, and is only available to members. To join TAPPI, to renew your TAPPI Membership, or to learn about other valuable benefits, visit www.tappi.org.

TAPPI, 15 Technology Parkway S., Suite 115, Peachtree Corners, GA 30092, publishes *TAPPI JOURNAL* monthly.

ATTENTION PROSPECTIVE AUTHORS: All papers published are subject to *TAPPI JOURNAL's* peer-review process. Not all papers accepted for review will be published. Before submitting, check complete author guidelines at http://www.tappi.org/s_tappi/doc.asp?CID=100&DID=552877.

Statements of fact and opinions expressed are those of individual authors. TAPPI assumes no responsibility for such statements and opinions. TAPPI does not intend such statements and opinions or construe them as a solicitation of or suggestion for any agreed-upon course of conduct or concerted action of any sort.

Copyright 2022 by TAPPI, all rights reserved. For copyright permission to photocopy pages from this publication for internal or personal use, contact Copyright Clearance Center, Inc. (CCC) via their website: www.copyright.com. If you have questions about the copyright permission request process, please contact CCC by phone at +1 978 750-8400. To obtain copyright permission to use excerpts from this publication in another published work, send your specific request in writing to Editor, TAPPI JOURNAL, 15 Technology Parkway S., Suite 115, Peachtree Corners, GA 30092, USA; or by fax to +1 770 446-6947. Send address changes to TAPPI, 15 Technology Parkway S., Suite 115, Peachtree Corners, GA 30092, USA; Telephone +1 770 446-1400, or FAX +1 770 446-6947. www.tappi.org

Editorial

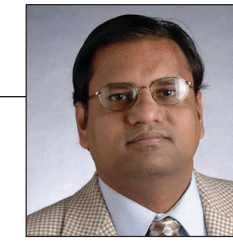

SESHADRI RAMKUMAR
TAPPI Journal Editorial Board

Innovation: How useful is it?

Innovation has become a genuine buzz word to promote one's product or company, to highlight its strength, and to enhance its visibility. The use of words like novel, innovative, etc., help with marketability, enhance economic strength, and elevate initial public offering (IPO) status. Genuine innovation helps with improving lifestyles, health, the environment, and the economy.

In their book, *How Google Works*, Eric Schmidt and Jonathan Rosenberg state that innovation is "production and implementation of novel and useful ideas." As you may note from the previously stated view, thoughts leading to products and processes that alter the ways we do things for the better signify true innovation. Innovation need not be just novel products alone. Any development in processes or implementation of new methods for carrying out an activity, whether on the shop floor or in our lives, is also innovation, with varied levels of novelty.

The innovation process

While it is not feasible to teach or provide a textbook model to innovate, groundwork towards being creative and innovative can be planned and later implemented. Innovation can be broadly categorized as: 1) incremental, and 2) disruptive. It is not necessary that every innovation needs to be totally disruptive and, in a way, erase the established ways of doing an activity or carrying out business. However, such disruptive developments will have broader impacts on society and the end-user community.

For instance, the internet revolutionized the way we communicate and created the IT revolution. Subsequently, social media platforms and search engines sprang up, changing the way we live. Google uses its improved search algorithms to significantly enrich the search process, which is an incremental development. As stated previously, even modest developments in processes and activities can have a great influence on society and change the way we live. Leaders in the field of innovation consider innovations that provide solutions to big problems and/or cater to the broader needs of society as having a good chance of success in the marketplace.

In addition to finding a panacea to pressing needs, even providing easy ways to tackle an activity will be well accepted. Innovation basically arises when there is competition, dire need for new solutions, and lack of resources for carrying out things in the same old-fashioned ways. Israel is a good example of being a leader in innovation. The need to have advanced products for national security and scarcity of water has led Israel to be an innovation leader with many startups. For example, Israel is a world leader in water desalination technology and an exporter of defense technologies to countries like India.

With resources being scarce, innovative approaches are needed to support R&D endeavors in academia and research organizations.

R&D investments and innovation

Research can be broadly categorized as: 1) basic, 2) applied, and 3) translational. Federal and state governments have roles to support basic and mission-linked applied research. These will lead to "lab-to-reality" in due course, resulting in economic growth. While basic research programs in industry have been downsized, domestic and international collaborations will help all stakeholders to strategically use their resources to grow the research and development (R&D) sector.

Strong support for research by stakeholders is necessary to advance any field and the related industries within it. With resources being scarce, innovative approaches are needed to support R&D endeavors in academia and research organizations. Collaborating with industry, supporting commercialization, and encouraging startups are a few successful approaches to move the R&D sector

forward. Many universities like Texas A&M and Texas Tech University are recognizing patents as important contributions towards academic tenure. Commercialization provides financial rewards to the institutions and inventors, as well as professional recognition. The National Academy of Inventors, a nationally recognized association in the United States, recognizes inventors from academia with fellowships and senior memberships. Many universities have been creative in spearheading the startup culture by providing free licensing for university intellectual property (IP) for its students, as it results in job creation, economic growth, and more importantly, alumni support.

Multidisciplinary research involving different fields such as engineering, mathematical modeling, biomedicine, and sustainable materials is being encouraged to find solutions to complex problems. This has been the model of The Institute of Environmental and Human Health (TIEHH) at Texas Tech University, which resulted in developing and commercializing nonwoven products, such as a sulfur mustard decontamination wipe, FiberTect, and cotton-based oil absorbent wipes.

In speaking about innovation, Professor Ronald Kendall, founding director of TIEHH stated that "innovation is critical for any great organization to move forward to address new challenges and create solutions to those challenges. For instance, even with the COVID pandemic, we have seen tremendous innovation in the United States to develop vaccines, therapeutics, personal protective equipment, and strategies to better maintain our health and economy despite the pandemic."

R&D in paper and advanced textiles sectors

The paper and textiles sectors are good examples to showcase how planning and strategic approaches help to take challenges and convert them into opportunities.

When the paper industry faced challenges due to the growth in e-communication, the industry strengthened its investments in applications such as hygiene and packaging. Sustainability, recycling, and improvements in design aspects continue to provide new opportunities.

Similarly, when the textiles sector was challenged due to shifts in manufacturing from developed economies to other regions of the world, the textiles industry focused on advanced fields such as nonwovens and technical textiles. These sectors play important roles in developing absorbent hygiene products and industrial and medical textiles. During these COVID-19 times, such products have been lifesavers, and these sectors of the advanced textiles industry have gained tremendous momentum.

Proper and planned investments in research, creating global partnerships, and effective communication with the public and policymakers will enable the industry to move forward and garner much support for research and development.

With challenges come different opportunities, and our industry is not a stranger to such scenarios. Proper and planned investments in research, creating global partnerships, and effective communication with the public and policymakers will enable the industry to move forward and garner much support for research and development. As emphasized by Professor Kendall, "the process of innovation in any organization is critical to the future success and contribution that organization can make to the society of the United States as well as other societies around the world."

Indeed, innovation in different forms is an important component of a growth equation. **TJ**

Ramkumar is a past chair of TAPPI's NET Division and a professor of Nonwovens and Advanced Materials at Texas Tech University, in Lubbock, TX, USA.

Furnishing autohydrolyzed poplar weakly alkaline P-RC APMP to make lightweight coated base paper

BO ZHANG, KAILI WU, QINGXI HOU, TONGBAO JIANG, WENWEN ZHANG, KAISHENG LUO, AND WEI LIU

ABSTRACT: This work investigated the effects of autohydrolysis pretreatment severity on poplar (*Populus tomentosa Carr.*) woodchips used to make a type of high-yield pulp (HYP) known as preconditioning followed by refiner chemical treatment, alkaline peroxide mechanical pulp (P-RC APMP). It also investigated the ratios for partially replacing sodium hydroxide (NaOH) with magnesium oxide (MgO) in the high-consistency (HC) retention stage of the P-RC APMP process on the obtained HYP's properties.

The results show that the pretreatment severity of autohydrolysis at combined hydrolysis factor (CHF) = 10.77 and the 50 wt% ratio for partially substituting NaOH with MgO were the optimum conditions for making lightweight coated (LWC) base paper. Compared to the conventional P-RC APMP, the optimized P-RC APMP had similar bulk and higher tensile, burst, and tear indices, as well as opacity, but a slightly lower ISO brightness. When the optimized P-RC APMP and commercial softwood bleached sulfate pulp (SBKP) were blended to make LWC base paper, the most favorable pulp furnish was comprised of 50% optimized P-RC APMP and 50% commercial SBKP. The obtained LWC base paper handsheet had better bulk, and its other properties could also meet the requirements of LWC base paper.

Application: In the manuscript, poplar woodchips were subjected to autohydrolysis pretreatment with different levels of intensity, and then the autohydrolyzed woodchips were used to make P-RC APMP by partially substituting NaOH with MgO in the HC retention stage. Finally, the obtained P-RC APMP was blended with commercial SBKP to make LWC base paper. The present work investigated the optimum conditions for the autohydrolysis pretreatment, substitution ratio of NaOH by MgO, and adding a proportion of the P-RC APMP in the pulp furnish.

High-yield pulp (HYP) has the characteristics of high yield, good bulk, and good optical properties. In the pulping process, it has the advantages of less chemical dosage; less capital investment (about 60% of the amount required for chemical pulping); wide sources of raw materials; more uses in paper and paperboard products; and less effluent pollution (generally only 10%–15% of that from chemical pulp) [1-3]. Therefore, use of HYP has been rapidly growing since the 1980s, and it is now one of the main pulps used in the paper industry in the 21st century, especially in China.

Among HYPs, preconditioning followed by refiner chemical treatment, alkaline peroxide mechanical pulp (P-RC APMP) is favored by many scholars and pulp and paper mills because of its characteristics as a high-efficiency process and for clean pulping. P-RC APMP is currently a popular type of HYP with an ISO brightness of 60%–85% and Canadian freeness of 100–600 mL. It is mostly used to make lightweight coated (LWC) paper and multilayer board (core layer) [4]. In the conventional P-RC APMP pulping process, due to the strong alkalinity of sodium hydroxide (NaOH), some part of wood components (mainly hemicellulose) will be dissolved away, leading to decreased pulp yield and increased chemical oxygen demand (COD) in the pulping effluent. Some studies have shown that substituting a magnesium base for a sodium base in a high-yield pulping process can ameliorate the previously mentioned issue [5-7]. Even so, some amount of hemicellulose is still dissolved in the pulping effluent. How can we solve this problem?

A biorefinery refers to the conversion of lignocellulosic biomass into fuel ethanol, biomass power, biogas, and biomass materials after particular treatments [8-10]. Among the biomass pre-extraction methods, autohydrolysis is a green, economic, and promising approach and is usually applied for isolation of the hemicellulose from lignocellulosic biomass [11-15]. From the paper industry's point of view, on the one hand, the pretreated lignocellulosic biomass can be used as raw material for pulping, the COD load in the pulping effluent will be greatly decreased, and the energy consumption of the pulp refining will be reduced [16]. On the other hand, the extracted hemicellulose can be further isolated and purified for high value-added applications. This demonstrates the concept of combining the biorefinery and the pulp and paper industry [17-20].

CHF	Control	2.78	10.77	24.54
Autohydrolysis temperature, K	-	393.15	413.15	433.15
Autohydrolysis time, min	-	30	30	20
CHF = combined hydrolysis factor.				

I. Autohydrolysis condition and the corresponding CHF.

With the continuous economic development and the continuous improvement of people's living standards, the demand for paper, especially printing paper grades, has increased. At present, LWC paper is widely used in a variety of commercial printing materials due to its characteristics of low basis weight, high bulk, high opacity, and excellent printing effects. Base paper is the basis material of coated paper. Although the coating process can improve some properties of base paper, the quality of coated paper is greatly affected by the properties of its base paper [21,22]. In the production of LWC base paper, not only is chemical pulp with long fibers and good strength needed to ensure good operational performance, but also HYP with good bulk and optical properties for providing good stiffness and optical properties.

The present work explored the preparation of P-RC APMP from poplar (*Populus tomentosa Carr.*) woodchips after autohydrolysis pretreatment for improving the pulp's physical and strength properties. Meanwhile, in the high-consistency (HC) retention stage of the P-RC APMP, magnesium oxide (MgO) was used to partially replace NaOH as the alkali source to reduce the COD in the pulping effluent. The optimum pulping conditions were then selected according to the properties of autohydrolzed woodchips and the resultant P-RC APMP. The P-RC APMP obtained under optimum conditions and commercial softwood bleached kraft pulp (SBKP) were blended to make LWC base paper handsheets, and the physical properties of the handsheets were determined for selecting the optimum pulp furnish. The present work aims to maximize the use of the main components of wood raw materials. That is, some amount of the hemicellulose in wood raw materials can be collected for high value-added applications, and the rest can be further used to make P-RC APMP for LWC base paper production.

MATERIALS AND METHODS

Materials

The poplar (*Populus tomentosa Carr.*) woodchips were obtained from a paper mill in Shandong province, China. After removing the bark, knots, and rotten parts, the selected woodchips were washed, then air dried, and finally collected in a sealed plastic bag to equilibrate their moisture content for later use.

Pre-steaming and autohydrolysis pretreatment

Both pre-steaming and autohydrolysis pretreatment of the poplar woodchips were conducted in an upright rotary digester (Model 2615, KRK Co. Ltd.; Tokyo, Japan). Deionized water and 600 g of equivalently oven-dried poplar woodchips were mixed at a liquid-to-solid ratio of 4:1 (L/kg) and then added into the digester. After the digester was heated to 90°C for 30 min to imitate a pre-steaming process in practical production, it was heated to the temperature required by the autohydrolysis pretreatment and maintained for a corresponding time. After completing the autohydrolysis pretreatment, the woodchips were taken out from the digester and then washed using deionized water until the filtrate was neutral.

In the present work, the combined hydrolysis factor (CHF) was used for quantifying the intensity of autohydrolysis pretreatment, which is shown below [23]:

$$CHF = t \times \exp\left(25.6 - \frac{11000}{T}\right) \quad (1)$$

where t is autohydrolysis time in min, and T is the temperature in Kelvin. The autohydrolysis pretreatment conditions are listed in **Table I**.

Screw extrusion and impregnation

The autohydrolyzed woodchips were extruded with a screw extruder (JS30, Shandong Wenrui Papermaking Machinery Co. Ltd.; Anqiu, China) at a compression ratio of 4:1.

The extruded woodchips were then collected in a polyethylene bag, and the polyethylene bag was placed in a water bath at a temperature of 80°C for pre-heating. The first-stage impregnation of the P-RC APMP process was carried out according to the following conditions: 0.3% NaOH, 0.1% diethylenetriaminepentaacetic acid (DTPA), 30% consistency, and 80°C for 30 min. All chemical dosages were based on the weight of oven-dried woodchips.

After the impregnated woodchips were extruded a second time with the same extruder at a compression ratio of 4:1, the extruded woodchips were put into a polyethylene bag once again and then placed in a water bath for the second-stage impregnation. The impregnation conditions were as follows: 3% NaOH, 3.5% hydrogen peroxide (H_2O_2), 3% sodium metasilicate (Na_2SiO_3), 0.05% DTPA, 25% consistency, and 80°C for 60 min.

Sample Number	CHF	Ratio of Partially Substituting NaOH with MgO, wt%
1#	-	0
2#	-	25
3#	-	50
4#	2.78	0
5#	2.78	25
6#	2.78	50
7#	10.77	0
8#	10.77	25
9#	10.77	50
10#	24.54	0
11#	24.54	25
12#	24.54	50

CHF = combined hydrolysis factor; NaOH = sodium hydroxide; MgO = magnesium oxide; P-RC APMP = preconditioning followed by refiner chemical treatment, alkaline peroxide mechanical pulp.

II. Corresponding CHF and substitution ratio of NaOH by MgO in the high-consistency (HC) retention stage of P-RC APMP.

Refining and high-consistency retention stage

The first-stage refining was conducted in a KRK refiner (BR30-300CB; Tokyo, Japan) with a 0.8 mm plate gap at 25% consistency. The corresponding CHF and substitution ratio of NaOH by MgO in the high consistency (HC) retention stage of P-RC APMP are listed in **Table II**.

Latency, screening, and beating

The refined P-RC APMP underwent the latency treatment at 4% pulp consistency at 95°C for 30 min. After the latency treatment was completed, the pulp was screened using a screener (Model 535, Lorentzen & Wettre Co. Ltd.; Kista, Sweden) with 0.15 mm slot size. The screened P-RC APMP was further beaten at 10% pulp consistency using a PFI mill (P40110.E000, PTI Inc.; Vorchdorf, Austria) to a CSF of approximately 255 mL.

Handsheet preparation and property measurement

After disintegrating the beaten pulp with a disintegrator (Model 1107, Lorentzen & Wettre Co. Ltd.) for 5000 revolutions, the handsheets were made on a standard sheet former (7407S, British Pulp Evaluation Apparatus, Mavis Engineering Ltd.; UK) according to ISO Standard 5269-1:2005 "Pulps — Preparation of laboratory sheets for physical testing — Part 1: Conventional sheet-former method." The pulp ratio of the optimized P-RC APMP to SBKP for making LWC base paper is listed in **Table III**.

Sample	P-RC APMP, wt%	SBKP, wt%
PS0-10	0	100
PS2-8	20	80
PS3-7	30	70
PS4-6	40	60
PS5-5	50	50
PS6-4	60	40
PS7-3	70	30
PS8-2	80	20

P-RC APMP = preconditioning followed by refiner chemical treatment, alkaline peroxide mechanical pulp; SBKP = softwood bleached sulfate pulp.

III. Preparation conditions for the lightweight coated (LWC) base paper handsheets made with P-RC APMP and SBKP.

The obtained handsheets were placed in a room with 23 ± 1°C and 50 ± 1% relative humidity for 4 h, and then the properties of the handsheets were tested [24] in accordance with ISO Standard 5270:2005 "Pulps — Laboratory sheets — Determination of physical properties."

Analysis of surface and cross-section morphology

The surface and cross-section morphology of the LWC base paper handsheets were observed by using the scanning electron microscope (SEM) (JSM-IT300L, JEOL Ltd.; Tokyo, Japan).

RESULTS AND DISCUSSION

Effects of autohydrolysis severity and MgO substitution on bulk and optical properties

The effects of autohydrolysis severity and substitution of NaOH for MgO in the HC retention stage on the bulk and optical performance of the obtained poplar P-RC APMP were studied. In the production of paper or paperboard, the use of HYP can increase the bulk of the product so as to improve its stiffness and can reduce pulp consumption and production cost. **Figure 1** shows the effects of autohydrolysis pretreatment and substitution ratio of NaOH by MgO on the bulk, ISO brightness, and opacity of the P-RC APMP. It can be seen from Fig. 1a that under the selected experimental conditions, with the increase in severity of autohydrolysis pretreatment, the bulk of the pulp significantly decreased. This is because the fibers become much closer due to the exposure of more free hydroxyl groups on the cellulose [25]. However, with the increase of the substitution proportion of NaOH by MgO, the bulk of the resultant pulp increased. This is mainly attributed to the de-

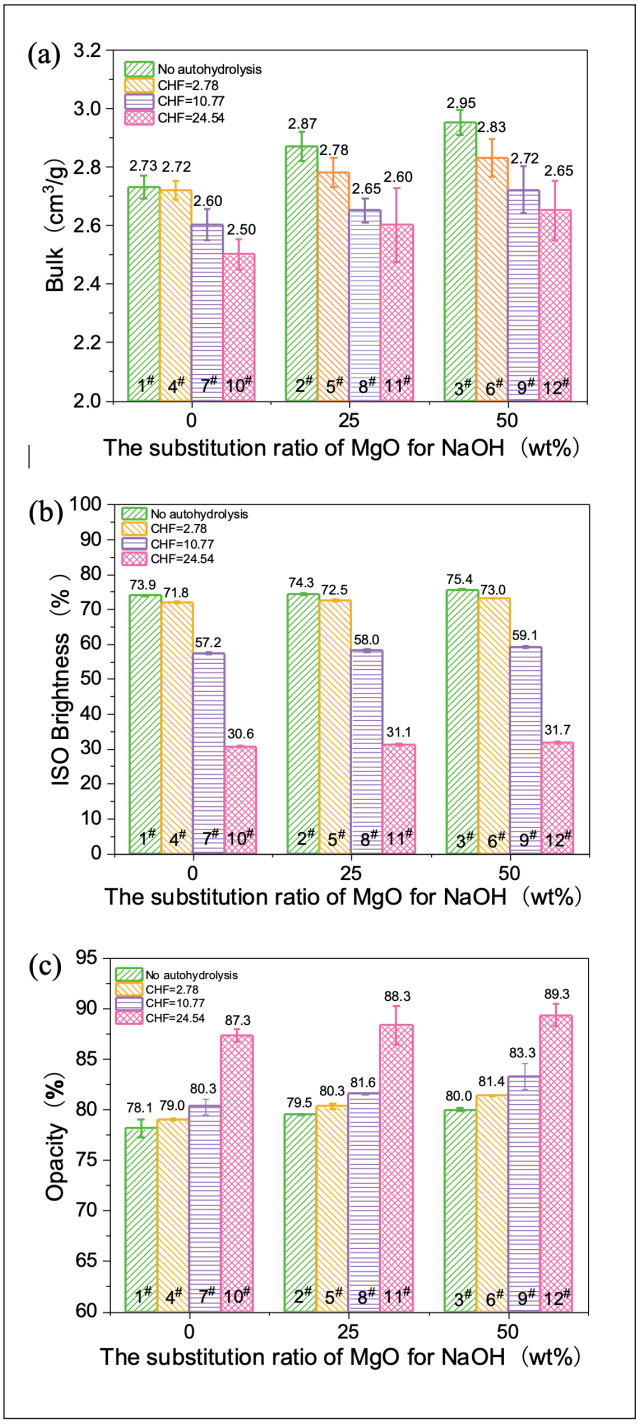

1. Effects of the autohydrolysis pretreatment and substitution proportion of sodium hydroxide (NaOH) by magnesium oxide (MgO) on bulk and optical properties of the resultant preconditioning followed by refiner chemical treatment, alkaline peroxide mechanical pulp (P-RC APMP): (a) bulk; (b) ISO brightness; and (c) opacity (CHF = combined hydrolysis factor).

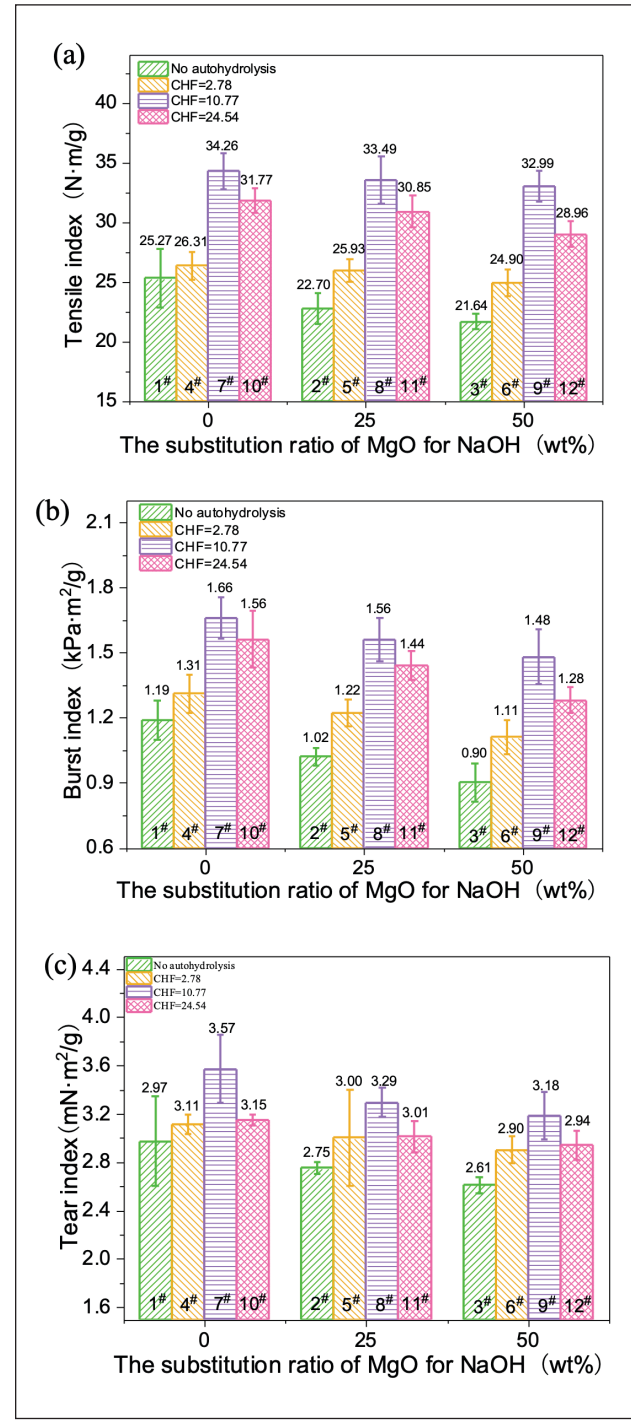

2. Effects of autohydrolysis pretreatment and substitution proportion of NaOH by MgO on the strength indices of the resultant P-RC APMP: (a) tensile index; (b) burst index; and (c) tear index - test edit.

crease of alkalinity in the bleaching process, leading to the decreased degree of fibrillation and the weakening of the bonding strength between pulp fibers. After autohydrolysis pretreatment, the bulk of the pulp with MgO replacing 50 wt% NaOH was not significantly raised (only 4%–6%). This indicated that autohydrolysis pretreatment could improve the bonding strength of the pulp fibers even if the alkalinity of the bleaching environment was weakened in the HC retention stage of P-RC APMP, which led to a decrease in the growth rate of the pulp bulk.

Raising the brightness can improve the appearance and printing performance of paper. The influence of autohydrolysis pretreatment and the substitution proportion of NaOH by MgO on the brightness of the resultant P-RC APMP is shown in Fig. 1b. It can be found that the ISO brightness of the pulp pronouncedly decreased as the severity of autohydrolysis pretreatment increased. This is because the high pretreatment temperature and acidic conditions resulted in the change of chromogenic groups in lignin, such as the lignin condensation reaction [26]. However, with the increase of the substitution proportion of NaOH by MgO, the ISO brightness of the pulp was slightly increased due to the weakened alkaline blackening effect that usually happens in the bleaching process of HYPs [27].

The opacity of paper indicates the resistance of paper to light transmission, which is the main factor that determines whether the paper will have strike-through after printing. Figure 1c shows the effect of autohydrolysis pretreatment and substitution proportion of NaOH by MgO on the opacity of the pulp. Under the selected experimental conditions, the opacity of the pulp greatly increased by raising the CHF and the substitution proportion of NaOH by MgO. Although the opacity of the pulp was higher than 85% when CHF = 24.54, the ISO brightness was too low (only about 31%) to be suitable for making LWC base paper. When CHF = 2.78 or CHF = 10.77, the opacity of the pulp was higher than 79%, and the bulk and ISO brightness were higher than 2.6 cm^3/g and 57%, respectively.

Effects of autohydrolysis severity and MgO substitution on strength properties and formation index

The strength of the pulp is an important index for LWC base paper. The influence of autohydrolysis pretreatment and substitution proportion of NaOH by MgO on the strength properties of the pulp were investigated, as shown in **Fig. 2**. It can be found that the tensile index (Fig. 2a), burst index (Fig. 2b), and tear index (Fig. 2c) all reached their maximum value at CHF = 10.77 under the selected experimental conditions.

Paper formation is an important performance index. Formation has an effect on the appearance, strength, print quality, and optical performance of paper, as well as the papermaking performance of a paper machine. In this work, effects of the autohydrolysis severity and the substitution proportion of NaOH by MgO on the formation index were investigated, and the results are shown in **Fig. 3**. It can be seen in Fig. 3 that under the same MgO substitution ratio, the formation index showed an increasing and then a decreasing trend as CHF increased from 0 to 24.54. When CHF increased up to 24.54, the formation index rapidly dropped, which was similar to the change of the strength property of the pulp. However, the formation index also changed with the increase of the substitution proportion of NaOH by MgO. The pulp with a CHF 10.77 had the biggest change as the substitution proportion of NaOH by MgO rose from 25 wt% to 50 wt%, but only a 3.2% increase (from 144.2 to 148.8), demonstrating that the substitution proportion of NaOH by MgO had little impact on the formation of pulp.

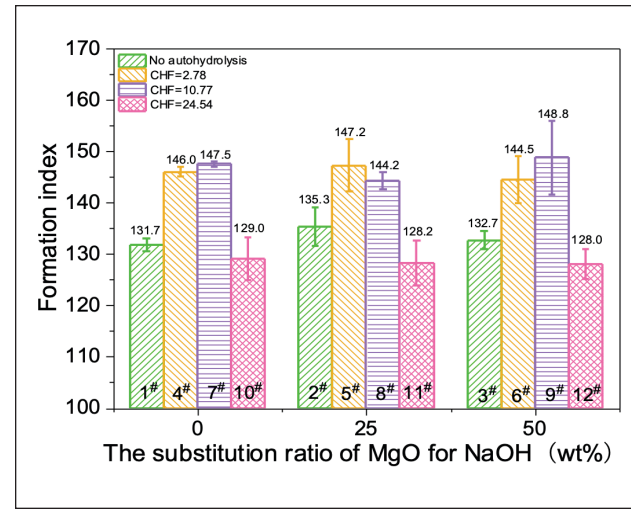

3. Effects of autohydrolysis pretreatment and substitution proportion of NaOH by MgO on the formation index of the resultant P-RC APMP.

Partially replacing NaOH with MgO can significantly improve the bulk and ISO brightness of pulp. When the substitution ratio was 50%, the bulk and ISO brightness of the pulp were 8.1% and 2.0% higher than those of the pulp without substitution. Compared to the pulp without autohydrolysis pretreatment, the opacity of the pulp with CHF = 24.54 increased by 11.8%, and the tensile, burst, and tear indices of the pulp with CHF = 10.77 increased by 35.6%, 39.5%, and 20.2%, respectively. Autohydrolysis pretreatment could improve the opacity and strength index of the pulp, and the CHF had a more significant impact on all the pulp quality variables than the substitution ratio of NaOH by MgO. The decrease in ISO brightness and bulk of the pulp caused by autohydrolysis pretreatment could be partly compensated by partially substituting NaOH by MgO.

From the comprehensive analyses of the previously mentioned results, it can be concluded that CHF 10.77 and 50 wt% substitution of NaOH by MgO (i.e., Sample 9#) would be the most appropriate condition for producing the P-RC APMP used subsequently to make LWC base paper. **Table IV** shows further comparison of the properties of the optimized poplar P-RC APMP, poplar P-RC APMP without NaOH substitution at CHF=10.77, and the conventional one. It can be easily seen that the optimized poplar P-RC APMP in this work had higher bulk, ISO brightness, and opacity, but other properties were lower in comparison with the poplar P-RC APMP without NaOH substitution at CHF=10.77. It also had similar bulk, lower ISO brightness, and other properties that were better in

Sample	CHF	Ratio of Substituting NaOH with MgO, wt%	Freeness, mL	Bulk, cm^3/g	ISO Brightness, %	Opacity, %	Tensile Index, N·m/g	Burst Index, $kPa·m^2/g$	Tear Index, $mN·m^2/g$	Formation Index
1#	-	0	725	2.73	73.9	78.1	25.27	1.19	2.97	131. 7
2#	-	25	680	2.87	74.3	79.5	22.70	1.02	2.75	135.3
3#	-	50	731	2.95	75.4	79.9	21.64	0.90	2.61	132.7
4#	2.78	0	741	2.72	71.8	79.0	26.31	1.31	3.11	146.0
5#	2.78	25	727	2.78	72.5	80.3	25.93	1.22	3.00	147.2
6#	2.78	50	727	2.83	73.0	81.4	24.90	1.11	2.90	144.5
7#	10.77	0	741	2.60	57.2	80.3	34.26	1.66	3.57	147.5
8#	10.77	25	740	2.65	58.0	81.6	33.49	1.56	3.29	144.2
9#	10.77	50	783	2.72	59.1	83.3	32.99	1.48	3.18	148.8
10#	24.54	0	669	2.50	30.6	87.3	31.77	1.56	3.15	129.0
11#	24.54	25	672	2.60	31.1	88.3	30.85	1.44	3.01	128.2
12#	24.54	50	660	2.65	31.7	89.3	28.96	1.28	2.94	128.0

CHF = combined hydrolysis factor; NaOH = sodium hydroxide; MgO = magnesium oxide.

IV. Characteristics of the P-RC APMPs with and without autohydrolysis pretreatment of poplar woodchips.

comparison with the conventional poplar P-RC APMP. As for the weak point in the ISO brightness of the P-RC APMP, it can be remedied to a certain extent during the subsequent coating process for LWC base paper.

Optimization of poplar P-RC APMP ratio in the pulp furnish

Although coating can improve the surface appearance and optical and printing properties of LWC paper, the base paper properties will ultimately affect the final performance of the obtained LWC paper [28]. An LWC paper needs lower basis weight, better printability, and better strength performance, and usually uses HYP and chemical pulp as the pulp furnish. This is because using P-RC APMP in the LWC base paper production not only can save the use of chemical wood pulp, but can also improve the bulk and opacity of the paper, thus improving the paper printability. In this work, different proportions of the optimized poplar P-RC APMP (i.e., sample 9#) and SBKP were selected as the pulp furnish, and the detailed properties of the resultant handsheets are listed in **Table V**.

Comprehensively, considering the bulk, ISO brightness, opacity, and strength properties of the LWC base paper handsheets, sample PS5-5, which was made with 50 wt% P-RC APMP (i.e., pulp sample 9#) and 50 wt% SBKP, would be the most appropriate pulp furnish for making the LWC base paper. The PS5-5 improved the bulk and opacity of the handsheets to a large extent, based on meeting the needs of ISO brightness and strength properties for LWC base paper, wich is very beneficial to the performance of LWC base paper. Compared to the bulk, opacity, and formation index of sample PS0-10, which was made with 100% SBKP (or control sample), those of sample PS5-5 were increased by 10.2% to 2.17 cm^3/g, 18.2% to 78.67%, and 4.7% to 136.8, respectively. Although the ISO brightness of the handsheet with PS5-5 was only 70.8%, this problem could be remedied by the subsequent coating technology. Therefore, it can be concluded that the optimized pulp furnish (i.e., PS5-5) can meet the requirements for making LWC base paper.

SEM observation of the LWC handsheets with 50 wt% optimized poplar P-RC APMP and 50 wt% SBKP

Figure 4 shows the SEM images of the surface and cross section of the LWC base paper handsheets made with pulp sample PS0-10 and pulp sample PS5-5. It can be clearly seen in Fig. 4a and 4b that the handsheets both presented a similar surface topography, because the top layer (Fig. 4b) was almost full of the long softwood fibers, although there was 50 wt% P-RC APMP in the pulp furnish PS5-5. The well-distributed SBKP fibers could enable the LWC base paper to exhibit good strength performance due to the good strength of the fibers themselves and the good bonding strength between them. As for the cross-section struc-

Sample	P-RC APMP, wt%	SBKP, wt%	Basis Weight, g/m²	Bulk, cm³/g	ISO Brightness, %	Opacity, %	Tensile Index, N·m/g	Burst Index, kPa·m²/g	Tear Index, mN·m²/g	Formation Index
PS0-10	0	100	58.40	1.97	88.0	66.6	55.51	4.37	12.64	130.7
PS2-8	20	80	58.10	2.04	78.2	69.0	50.47	3.83	11.26	134.2
PS3-7	30	70	57.96	2.08	75.1	74.6	45.31	3.34	10.81	137.6
PS4-6	40	60	57.35	2.06	72.2	75.7	44.33	2.92	9.40	141.2
PS5-5	50	50	58.58	2.17	70.8	78.7	41.05	2.74	9.23	136.8
PS6-4	60	40	58.64	2.21	68.0	80.2	38.65	2.33	8.51	139.0
PS7-3	70	30	57.65	2.23	66.8	81.4	35.54	1.97	6.75	146.6
PS8-2	80	20	58.15	2.22	65.4	82.2	33.53	1.80	6.04	147.1

P-RC APMP = preconditioning followed by refiner chemical treatment, alkaline peroxide mechanical pulp; SBKP = softwood bleached sulfate pulp.

V. Properties of the LWC base paper handsheets made with different addition amount levels of poplar P-RC APMP and SBKP.

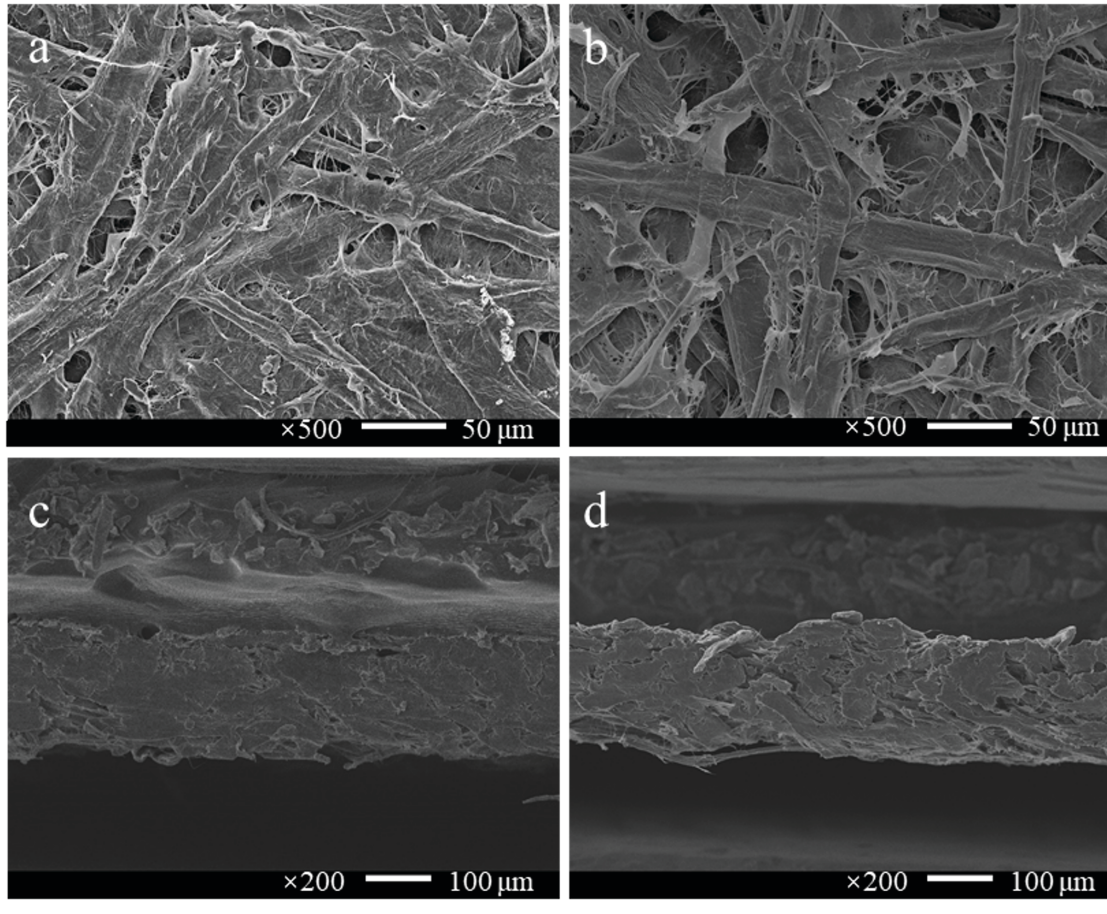

4. Scanning electron microscope (SEM) images of the lightweight coated (LWC) base paper handsheets as follows: surface images of handsheet samples (a) PS0-10 (×500) and (b) PS5-5 (×500); and cross-section images of handsheet samples (c) PS0-10 (×200) and (d) PS5-5 (×200).

ture of the LWC base paper handsheets, the one with PS5-5 (Fig. 4d) was much looser than that with PS0-10 (Fig. 4c) because of the addition of P-RC APMP in the pulp furnish, which resulted in the LWC base paper handsheet with a higher bulk and opacity.

CONCLUSIONS

This work investigated the effects of autohydrolysis pretreatment severity on poplar (*Populus tomentosa Carr.*) woodchips used to make P-RC APMP, along with the effects of ratios for partial substitution of NaOH with MgO in the P-RC APMP's HC retention stage on pulp properties. The results indicate that autohydrolysis pretreatment can significantly improve the opacity and strength index of pulp, and partially replacing NaOH with MgO can clearly increase the bulk of pulp. The CHF had more significant impact on all the pulp quality variables than the substitution ratio of NaOH by MgO. The decrease of ISO brightness and bulk of the pulp caused by autohydrolysis pretreatment can be partly compensated by partially substituting NaOH by MgO. From the point of view of making LWC base paper, the most appropriate condition for producing autohydrolyzed poplar P-RC APMP could be achieved, which is CHF 10.77 for the poplar autohydrolysis pretreatment and 50 wt% substitution of NaOH by MgO in the HC retention stage of P-RC APMP.

The optimized P-RC APMP and SBKP were selected as the pulp furnish to make the LWC base paper handsheets. After comprehensively considering the bulk, opacity, ISO brightness, strength properties, and formation index of the obtained handsheets, the optimized pulp furnish, that is, 50 wt% prepared poplar P-RC APMP and 50 wt% SBKP, can be achieved. **TJ**

ABOUT THE AUTHORS



*B. Zhang**



*Wu**



Hou

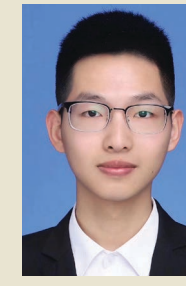

Jiang

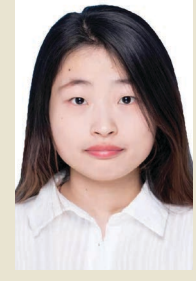

W. Zhang



Lou



Liu

We chose this topic to research because we wanted to try using preconditioning followed by refiner chemical treatment, alkaline peroxide mechanical pulp (P-RC APMP) instead of traditional high-yield pulp (HYP) to make lightweight coated (LWC) base paper. Many researchers that have focused on autohydrolysis pretreatment are mainly studying the characteristics of the liquid phase. What we have been studying is the combination of the solid phase of autohydrolysis pretreatment and P-RC APMP with magnesium alkali partially replacing sodium alkali, which takes full use of the advantages of the two processes to prepare LWC base paper.

The most difficult aspect of this research was how to regulate and control the properties of the resultant pulp. The decrease in the brightness of the obtained pulp could be partially compensated by adding softwood-bleached sulfate pulp (SBKP) in the final pulp furnish.

We found that autohydrolysis pretreatment can significantly improve the opacity and strength index of pulp, and partially replacing NaOH with MgO can obviously increase the bulk of pulp. The CHF had a more significant impact on all of the pulp quality variables than the substitution ratio of NaOH by MgO. Our most interesting finding was that the P-RC APMP process not only can make full use of woodchips, but can also significantly decrease the chemical oxygen demand (COD) load of the pulping effluent.

The pulping method proposed in this study not only can make full use of woodchips, but also can significantly decrease the COD load of the pulping effluent, which can bring additional benefits for pulp mills. Our next step is to further optimize the pulping process of P-RC APMP in order to make the pulp widely acceptable for making many paper or paperboard grades.

B. Zhang is a Master's student, Wu* is a Ph.D. candidate, Hou is professor, Jiang is a Master's student, Zhang is a Master's student, Luo is a Master's student, and Liu is associate professor at Tianjin Key Laboratory of Pulp and Paper, Tianjin University of Science & Technology, Tianjin, China. Email Hou at qingxihou@tust.edu.cn.*

** B. Zhang and Wu contributed equally to this work.*

LITERATURE CITED

1. Chen, H.Z. and Liu, Z.H., *Biotechnol. J.* 10(6): 866(2015).
2. Colodette, J.L., Longue, D., Pedrazzi, C., et al., *Ind. Eng. Chem. Res.* 50(4): 1847(2011). https://doi.org/10.1021/ie101799y.
3. Engstrom, G. and Morin, V., *Nord. Pulp Pap. Res. J.* 9(2): 106(1994). https://doi.org/10.3183/npprj-1994-09-02-p106-110.
4. Gao, Y., Rajbhandari, V., Li, K.C., et al., *TAPPI J.* 7(4): 4(2008).
5. Han, S., Liu, W., Wu, S.S., et al., *J. Ind. Eng. Chem.* 21: 121(2015). https://doi.org/10.1016/j.jiec.2014.02.013.
6. He, Z.B., Wekesa, M., and Ni, Y.H., *TAPPI J.* 3(12): 27(2004).
7. Hronich, J.E., Martin, L., Plawsky, J., et al., *J. Ind. Microbiol. Biotechnol.* 35(5): 393(2008). https://doi.org/10.1007/s10295-008-0333-x.
8. Hua, X., Tanguy, P.A., Li, R., et al, *TAPPI J.* 79(5): 112(1996).
9. Liu, W., Han, S., Xu, N.P., et al., *Ind. Eng. Chem. Res.* 53(8): 2897(2014). https://doi.org/10.1021/ie4037752.
10. Mao, H., Genco, J.M., Yoon, S.H., et al., *J. Biobased Mater. Bioenergy* 2(2): 177(2008). https://doi.org/10.1166/jbmb.2008.309.
11. Narron, R.H., Chang, H.M., Jameel, H., et al., *ACS Sustainable Chem. Eng.* 5(11): 10763(2017). https://doi.org/10.1021/acssuschemeng.7b02716.
12. Nitsos, C.K., Choli-Papadopoulou, T., Matis, K.A., et al., *ACS Sustainable Chem. Eng.* 4(9): 4529(2016). https://doi.org/10.1021/acssuschemeng.6b00535.
13. Li, Y., Liu, W., Hou, Q., et al., *Ind. Eng. Chem. Res.* 53(20): 8366(2014). https://doi.org/10.1021/ie500637a.
14. Hou, Q., Wang, Y., Liu, W., et al., *Bioresour. Technol.* 169: 155(2014). https://doi.org/10.1016/j.biortech.2014.06.091.
15. Nuström, M., Pykäläinen, J., and Lehto, J., *Pap. Puu* 75(6): 419(1993).
16. Hou, Q., Liu, L., Liu, W., et al., *Ind. Eng. Chem. Res.* 53(45): 17843(2014). https://doi.org/10.1021/ie503244b.
17. Sumi, Y., Hale, R.R., Meyer, J.A., et al., *Tappi* 47(10): 621(1964).
18. Sun, X.Q., Hou, Q.X., Zhang, B.X., et al., *TAPPI J.* 16(6): 332(2017). https://doi.org/10.32964/TJ16.6.331.
19. Sundberg, A., Pranovich, A., and Holmbom, B., *J. Wood Chem. Technol.* 20(1): 71(2000). https://doi.org/10.1080/02773810009349625.
20. Udy, D.J., *Pulp Pap. Can.* 68(8): 71(1994).
21. Van Heiningen, A., *Pulp Pap. Can.* 107(6): 38(2006).
22. Wang, M., Hong, M.W., and Huo, H., *Environ. Res. Lett.* 2(2): 024001(2007). https://doi.org/10.1088/1748-9326/2/2/024001.
23. Wyman, C.E., *Annu. Rev. Energy Environ.* 24: 189(1999). https://doi.org/10.1146/annurev.energy.24.1.189.
24. Wyman, C.E., *Biotechnol. Prog.* 19(2): 254(2003). https://doi.org/10.1021/bp025654l.
25. Xu, E.C., *Pulp Pap. Can.* 102(2): 44(2001).
26. Sood, Y.V., Tyagi, S., Tyagi, R., et al., *Indian J. Chem. Technol.* 17(4): 309(2010).
27. Yu, G., Yano, S., Inoue, H., et al., *Appl. Biochem. Biotechnol.* 160(2): 539(2010). https://doi.org/10.1007/s12010-008-8420-z.
28. Zhu, W., Houtman, C.J., Zhu, J.Y., et al., *Process Biochem.* 47(5): 785(2012).https://doi.org/10.1016/j.procbio.2012.02.012.

ABOUT THIS PAPER

Cite this article as:
Zhang, B., Wu, K., Hou, Q., et al., *TAPPI J.* 21(2): 71(2022). https://doi.org/10.32964/TJ21.2.71

DOI: https://doi.org/10.32964/TJ21.2.71

ISSN: 0734-1415

Publisher: TAPPI Press

Copyright: ©TAPPI Press 2022

About this journal

Utilization of kraft pulp mill residuals

TORSTEN MEYER

ABSTRACT: Kraft pulp mills produce on average about 100 kg of solid residuals per metric ton of pulp produced. The main types of mill waste are sludge from wastewater treatment plants, ash from hog fuel boilers, dregs, grits, and lime mud from causticizing plants and lime dust from lime kilns. Of these, about half is disposed of in landfills, which highlights the need and potential for waste recycling and utilization.

Sludge is either incinerated in hog fuel boilers to generate steam and power or used in various forms of land application, including land spreading, composting, or as an additive for landfill or mine waste covers. The majority of hog fuel boiler ash and causticizing plant residues is landfilled. Alkaline residuals can be conditioned for use in land application, manufacture of construction materials, and production of aggregates for road work.

This technical review summarizes residuals utilization methods that have been applied in pulp and paper mills at demonstration- or full-scale, and therefore may act as a guide for mill managers and operators whose goal is to diminish the costs and the environmental impact of waste management.

Application: This technical review provides information about industrial-scale applications of residuals utilization, and therefore may act as a guide for mills that are seeking to implement waste reduction or utilization programs.

The global annual production of kraft pulp has been steadily increasing and is now about 145 million metric tons [1]. It is expected to continue growing for the next few years [2,3]. With an average residuals generation of 0.1 metric tons per air-dried metric ton of pulp, the waste generated at kraft pulp mills amounts to approximately 14.5 million metric tons globally. Most of the waste consists of sludge from wastewater treatment, ash from biomass combustion, green liquor dregs, lime mud, and slaker grits from causticizing (**Table I**).

Diverting waste from landfills and finding strategies for utilization have increasingly become important environmental and social considerations in kraft mill operations. Therefore, many mills are conducting residuals utilization programs in order to reduce the amount of waste disposed of in landfills. For example, UPM in Finland is currently implementing a zero-waste program with the goal to avoid any waste disposal in landfills by 2030 [9]. Other pulp and paper producing companies, such as Stora Enso and International Paper, have also implemented aggressive waste reduction programs aimed at minimizing landfill disposal [10,11].

Recent reviews have summarized numerous important scientific and engineering studies that have demonstrated

	Wastewater Treatment Plant Sludge	Wood Ash	Lime Mud	Dregs	Grits
Amount	49 (0.5–270), kg wet/o.d. metric ton of pulp[1]	34 (2.2–107), kg/o.d. metric ton of pulp[1]	12 (0.1–560), kg/a.d. ton of pulp[5]	6.6 (0.01–120), kg/a.d. ton of pulp[5]	3 (0.01–40), kg/a.d. ton of pulp[5]
pH	6.6–8.2[2]	10.4 (9.0–13.5)[4]	11.4 (8.4–13.0)[1]	10.8 (9.5–12.1)[1]	12.5 (12.2–12.7)[1]
Nitrogen, g/kg	29 (1.4–41)[3]	1.5 (0.2-7.7)[4]	1.8[1]	2.7 (1.6–4.2)[1]	2.2 (1.3–5.0)[1]
Phosphorous, g/kg	3.4 (1.2–5.8)[3]	5.3 (1-14)[4]	2.8 (1.1–5.7)[1]	0.67 (0.13–1.2)[1]	0.81 (0.23–1.7)[1]
Potassium, g/kg	1.4 (0.4–6.0)[3]	26 (1-130)[4]	0.44 (<0.2–1.2)[1]	4.6 (0.33–12)[1]	2.7 (1.3–6.0)[1]
Calcium, g/kg	30 (2.7–90)[3]	150 (25-330)[4]	380 (280–500)[1]	190 (35–320)[1]	360 (340–390)[1]
Magnesium, g/kg	0.65 (0.11–1.0)[3]	10 (1-25)[4]	6.2 (2.4–10.4)[1]	23 (5.8–43)[1]	7.2 (3.7–10)[1]

[1][4, and references therein], [2][5, and references therein], [3][6], [4][7, and references therein], [5][8 and references therein].

I. Amounts and composition of kraft pulp mill residuals. Amounts of waste are median values, and all others are mean values (except pH of wastewater treatment plant sludge). Numbers in brackets are ranges (o.d. = ovendry; a.d. = air dry).

the utilization potential of sludge, ash, and causticizing plant residues in agricultural settings and various environmental engineering applications [5,12,13]. The majority of these studies have investigated utilization methods on a laboratory or pilot scale, and the associated results cannot be directly translated to full-scale operation. Upscaling of these methods is often challenging and requires tailoring the methods to the specifics of the waste generated at a mill, as well as the market conditions for the waste.

Full-scale applications are often not reported in technical or scientific publications and can therefore not easily serve as a reference to other mills that seek to implement residuals utilization programs. Therefore, this technical review is an attempt to fill this gap, while focusing on applications that have been previously applied at pulp and paper mills on an industrial scale.

SLUDGE UTILIZATION

The median sludge production is 49 kg wet/ovendry (o.d.) metric ton of pulp [4]. The main types of sludges generated at pulp and paper mills are biosludge (waste activated sludge) and primary sludge. Primary sludge is generated when solids settle in primary clarifiers and mainly contains fibers. Biosludge is generated as a result of biological wastewater treatment and contains mainly bacterial biomass and lignocellulosic material. Only about 20% of the sludge generated in pulp and paper mills worldwide is disposed of in landfills, whereas at least 25% is beneficially used by means of land application [14,15].

Land application of sludge

Biosludge and primary sludge are suitable for land application because of high organic matter and nutrient contents. Biosludge contains notable concentrations of nitrogen and phosphorous because these nutrients are added to the activated sludge treatment system and partially end up in the sludge. The carbon (C): nitrogen (N) ratio of biosludge usually ranges from about 5:1 to 20:1 [16], which is suitable for plant growth. Primary sludge can provide other benefits to soils, such as improving the soil structure by means of aggregate formation and enhancement of the water infiltration rate. Adding primary sludge to kaolinitic soils improves aeration and water permeability. Sandy soils benefit from the high nutrient holding capacity and the high moisture holding capacity of primary sludge [16]. Primary sludge may also be applied for erosion control and roadside vegetation growth [17].

One of the most significant challenges of land application is the high C:N ratio of the primary sludge, which can lead to nitrogen deficiency in the soil. In this case, nitrogen may become immobilized within the tissue of soil microorganisms and is therefore unavailable for plant uptake. Composting of the sludge or the addition of nitrogen can alleviate this deficiency. In order to provide a balanced nutrient supply, a Canadian mill has added 2.7 kg of nitrogen per dry ton of sludge for land application [18]. Other potential problems with sludge application are related to odor, herbicide ineffectiveness, and the stimulation of weed competition [19]. In most cases, sludge has been reported to be non-hazardous with respect to heavy metal contamination and toxicity, as determined by the Toxicity Chemical Leaching Procedure [4,20]. Also, according to a leachability study on metals in paper mill sludge, the majority of heavy metals are more tightly bound to the sludge matrix and is less likely to leach [21]. Nevertheless, heavy metal concentrations in mill sludge can vary over several orders of magnitude [4], and in some cases, high concentrations can constitute a significant environmental risk. Therefore, prior to land application, sludge composition analyses and leachability tests should be implemented.

Sludge can be land applied either as dewatered sludge with a solids content of 15%–40% or as thickened sludge with a solids content of 3%–8%. The advantage of the thickened sludge is that it can be sprayed using conventional manure spraying technology. However, due to the larger volume of thickened sludge, the transportation costs usually allow land application only within 50–100 km around the mill.

Composting mill sludge can enhance its fertilizing value by reducing the C:N ratio and increasing the nitrogen availability, as well as increasing the cation exchange and moisture holding capacity. Mill residuals including sludge have been mixed with other types of waste to produce more balanced compost, including food waste, manure, municipal biosolids, yard trimmings, and waste from the pharmaceutical and textile industries [16].

Several pulp mills in Alberta, Canada, deliver their biosludge and primary sludge to surrounding farms. The land application of sludge not only can save farmers costs for nitrogen fertilizers, but also improves soil structure and water holding capacity. The sludge only needs to be applied once every several years because the nitrogen in the sludge is present mainly in the organic form, which is released slowly [20]. Turning mill sludge into product can result in different types of benefits. For example, sludge and bark from a Chilean mill are utilized as vegetable substrates, which has led to waste disposal cost savings, decrease in landfilling, and a reduction in ash generation [22]. Several mills in Ontario, Canada, utilize most of their sludge in agriculture and silviculture, as well as for soil rehabilitation. The sludge application has shown to reduce the use of commercial fertilizer with a potential saving of $250/hectare (ha) for a crop of corn [23]. In a large-scale field study in Quebec, Canada, a combination of paper mill biosolids and alkaline residuals (calcitic lime, lime mud, wood ash) was applied on crop land over the course of nine years in various amounts and mixtures [24]. The application turned out to be beneficial to crop growth because of the nutrients contained in the waste. Adverse environmental effects were not found, unless the application of sludge exceeded

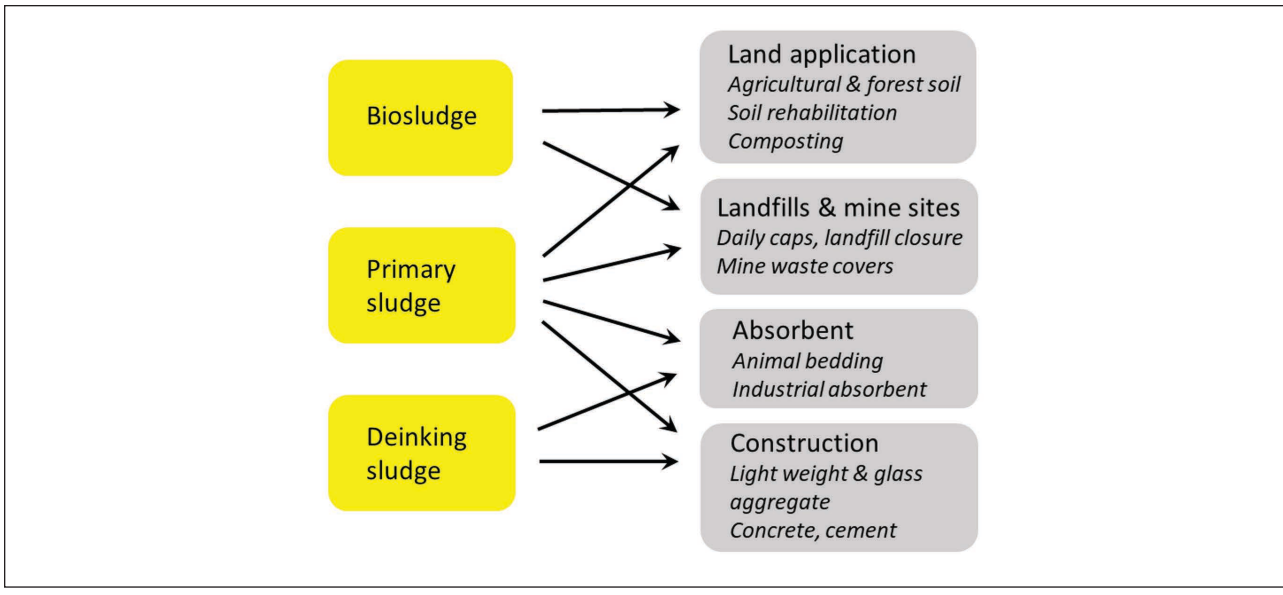

1. Mill sludges and previously applied utilization methods.

60 metric tons wet ha^{-1} yr^{-1}, which then caused significant nitrate leaching.

Landfill and mine site amendments

Mill sludge has been incorporated into manufactured soils to be used as landfill capping material and as mine site amendments (**Fig. 1**). As an example, sludge from two kraft mills in Michigan, USA, have been tested for use as covers on mining waste rock stockpiles to provide organic matter and nutrients and to help establish self-sustaining plant growth [25]. In another case, sludge from a mill was used as cover for copper uranium tailings. The sludge application provided for vegetation growth and cut the sludge disposal costs at this mill in half [26].

Similar to agricultural applications, various types of mill wastes are often mixed to improve the soil properties and fulfill engineering requirements. Mixtures consisting of biosludge, wood waste, and fly ash were used as barrier layers for the closure of two landfills at a coastal mill in British Columbia, Canada. The low hydraulic conductivity of the waste mixture led to improved erosion stabilization and at the same time provided a growing medium for plants [27]. Other advantages of using sludge in barrier layers of landfill caps are its higher flexibility compared to compacted clay and a lower bearing pressure imposed on the waste material [28].

Absorbents

Primary sludge from pulp and paper mills has been used to produce animal bedding and litter, while requiring minimal processing prior to application [29]. Sludge from several mills in New York State, USA, has been applied as bedding at cow farms. Prior to application, the sludge is amended with cement kiln dust to facilitate drying and inhibit bacterial growth. After usage, some farmers reuse the material as soil fertilizer [30]. Primary sludge has also been used for the production of cat litter, after being sanitized, deodorized, dried, and pelletized [31]. The sludge may also be used in the production of industrial oil absorbents [29].

Construction material

Since sludge contains notable amounts of silicon, aluminum, and iron, it can be used as an ingredient in the production of glass aggregate. A company in Wisconsin, USA, has used sludge from several nearby paper mills to produce glass aggregate [32] that can be used in floor tiles, abrasives, roofing shingles, asphalt, and decorative landscaping [16]. Because sludge contains organic matter, the heat of combustion supplements the energy required in the glass aggregate production [32]. In a similar application, sludge and fly ash were mixed and used to produce lightweight aggregate that can be applied in concrete masonry, landscaping, and geotechnical applications [16].

Mill primary sludge can be utilized as an addition to concrete, where it can have several benefits, including improved durability, increased pumpability of the liquid concrete, and reduced shrink and freeze-thaw related cracking, as well as improved salt-scaling resistance [33].

Other applications

Sludge from mills in the Netherlands and Slovenia has been utilized to produce anti-dust material for coal-fired power plants and ore stockpiles [29,34]. Sludge storage, transport, and application can be facilitated by drying and pelletizing to reduce volume and odor. This is also beneficial in applications where mill sludge is used as an additive to produce pellets that are applied as a fuel supplement [33]. Mill sludge has also been used to produce granules that act as carrier material for plant pesticides. Because the product is dust-

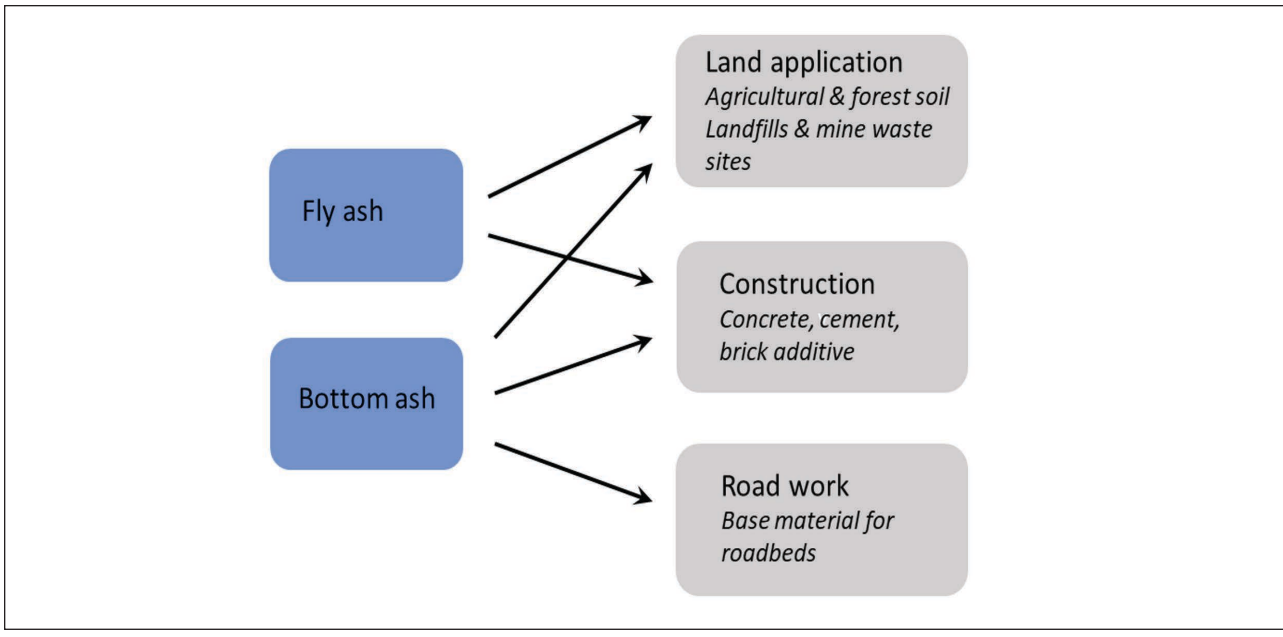

2. Previously applied utilization methods for bottom ash and fly ash.

free and attrition resistant, it may have a benefit over other conventional pesticide carriers [31].

ASH UTILIZATION

Ash from biomass (hog fuel) boilers has a pH ranging between 9.0 and 13.5, and on average, about 30–50 kg are generated per metric ton of pulp. Ash usually contains high concentrations of calcium, potassium, phosphorous, and magnesium, which are important nutrients that make it suitable as a soil supplement. However, ash can also contain undesirable metals such as arsenic, cadmium, and selenium [33], which may make it unsuitable for land application. Bottom ash and fly ash are often treated and utilized separately because of their different properties. Bottom ash has a higher bulk density and a lower carbon content. It also contains less dioxin and furans compared to fly ash [35 and references therein]. The unburned carbon content in wood ash ranges between 5% and 50% [36], and a high carbon content may be detrimental to some construction-related applications such as the manufacture of concrete [36]. The composition of ash from biomass boilers depends on the type of the biomass burned and the location of the mill. Fly ash from coastal mills usually contains notably larger concentrations of dioxins and furans [35], which may prevent certain forms of land application. In North American mills, approximately two-thirds of the generated hog fuel boiler ash is disposed of in landfills, with one-third being used in land application or other beneficial ways [19].

Land application

Biomass boiler ash is suitable for land application for several reasons. It contains valuable nutrients that are important for plant growth, and its high calcium content helps stabilize the soil pH. Pulp mills that grow their own trees for use in pulping often utilize their biomass boiler ash during re-forestation. Most kraft pulp mills in Brazil apply their boiler ash on fast-growing eucalyptus trees, which require a constant nutrient supply. Due to its high pH, boiler ash can also be used as a liming agent. The challenges of land application are the high reactivity and solubility of the ash, leading to a fast release of nutrients. To address these challenges, the ash may be pelletized with a binder that can help regulate the release of nutrients [37]. Also, the application of granulated ash on a forest owned by a Finnish mill [38] has been shown to be a suitable method to reduce the amount of landfilled waste. Heavy metal concentrations in wood ash are usually considered non-hazardous [39], and detrimental effects of land application on soil health and microbial community seem to be minimal [40]. However, the metal concentrations and the leaching behavior vary, and elevated levels of some metals may pose an environmental risk. In a leachability study by Pöykiö et al. [41], cadmium appeared to be the most mobile metal in fly ash, pointing to its potential bioavailability.

Boiler ash has been used as part of manufactured soil for the application at mine waste sites, for landfill covers, and for waste solidification/stabilization [19] (**Fig. 2**). As an example, wood ash from a Swedish mill is used as hardener in filling mine cavities [42]. Mine cavities require large amounts of material; therefore, low-quality ashes that cannot be used as fertilizer are used for this purpose [37]. In another application, fly ash from a mill in Maine, U.S., is used as a stabilizing material at a landfill. Injection of limestone during boiler operation for sulfur dioxide (SO_2) emission control generates a product that is suitable for this purpose [43].

Composting additive

Wood ash is particularly suitable as feedstock for composting because it provides nutrients to the compost, it reduces moisture, acts as a bulking agent, reduces odor, and darkens the product [16]. A darker color is beneficial during spring application on agricultural land by absorbing more heat. Biosludge and ash in compost mixtures complement each other. Ash provides alkalinity and certain nutrients (calcium, magnesium, potassium), whereas biosludge provides other nutrients (nitrogen, phosphorous), as well as organic matter. Another potential benefit of composting ash-sludge mixtures is that they have shown to notably decrease the concentrations of dioxins during the composting process [44].

Construction material

Due to its high mineral content, ash has been applied as an additive for the manufacture of construction material such as concrete, cement, and bricks. Ash addition to concrete may improve its durability and saltwater erosion resistivity. However, for these types of applications, the carbon content of the ash must be below about 6% [16]. Because of the different properties of bottom ash and fly ash, the bottom ash of a Brazilian kraft mill is used for cement production, whereas the fly ash, high in potassium, is transported to nearby farmers [45]. Utilization of ash is often diversified, depending on the demand for certain applications. Ash from several pulp mills in Norway is used in the production of concrete and bricks, as well as for road construction [46]. Ash has also been used as an additive in the production of controlled low-strength material (CLSM) for structural fill, foundation support, and pavement bases [19].

Road work

Ash from mills has been used for road construction, stabilization, and embankments [19], which is beneficial when the ash is high in aluminum, iron, and silicon oxides. Because of its higher density and lower carbon content, bottom ash is commonly used as a base material in roads [37]. As an example, ash from several of a Finnish pulp and paper company's mills is utilized for forest road construction. Adding wood ash to wet soil has been shown to create a hard foundation that can substitute for crushed stone in roadwork [47]. Ash from sludge incineration at a mill in Sweden also appeared to be applicable for building of forest roads and for use as a binder in asphalt [48].

Activated carbon

Fly ash containing a relatively large fraction of unburned carbon (~30%) is suitable for the production of activated carbon. The product can be used as an absorbent of colors and odors [16].

GREEN LIQUOR DREGS UTILIZATION

Dregs are solid particles removed from green liquor by settling or filtering. They consist mostly of char (carbon) and compounds of calcium, sodium, magnesium, and sulfur. Dregs are highly alkaline, with a pH of 9.5–12.1. On average, about 5–15 kg dregs are generated per metric ton of product.

Land application

Dregs can be beneficial as a soil supplement due to their alkalinity and high calcium and magnesium contents. Dregs can have a similar liming effect as commercial limestone [49]. However, one of the main challenges of soil application is the high sodium content of dregs. The sodium adsorption ratio (SAR) is often used to assess the suitability of dregs for land application. The SAR considers the concentration of sodium on the one hand and the concentrations of calcium and magnesium on the other hand; high concentrations of the latter two elements are beneficial to the soil. In order to diminish the negative effects of sodium, mills have mixed dregs with other types of mill waste prior to soil application. Mixtures consisting of dregs and grits are typically applied at about 6 tons/ha land for liming purposes [8]. Mills transport the residuals to the farmers, and benefit from the extended lifetime of their landfills. Another potential utilization method involves drying and pelletization of dregs/lime mud mixtures, which may then be applied on agricultural land. The pellets limit the leachability of sodium due to a smaller specific surface area [50].

Dregs as mine site amendments

Long term effects of mining operations include the formation of acid mine drainage in sulfide-laden mine waste sites [51]. Dregs have been applied as part of manufactured soils for the capping of mine sites. In a large demonstration scale project, dregs from Swedish pulp and paper mills were mixed with till and applied on a mine site to prevent acid rock drainage. The mixture acts as a sealing layer while preventing oxidation of the mine waste, infiltration of water, and leaching of heavy metals [52]. Challenges of dregs application are its stickiness and low shear strength. This may prevent engineering applications that involve providing weight support for a protective layer on top of the dregs or the application in a sloped sealing layer without the risk of sliding [53].

Construction material

The relatively high calcium, silicon, aluminum, and iron contents make causticizing residues suitable as additives for cement production and as fine aggregate in hot-mixed asphalt. However, most of the sodium and sulfur need to be washed off prior to application [33]. There are numerous examples of application of dregs in earthworks. In a mill in Finland, the dregs are incinerated, and the resulting ash is utilized for soil construction projects [54]. At another mill, dregs/fly ash mixtures were utilized for the construction of a load-bearing storage field [55]. Also, dregs and ash from several kraft mills in the United States were used to produce

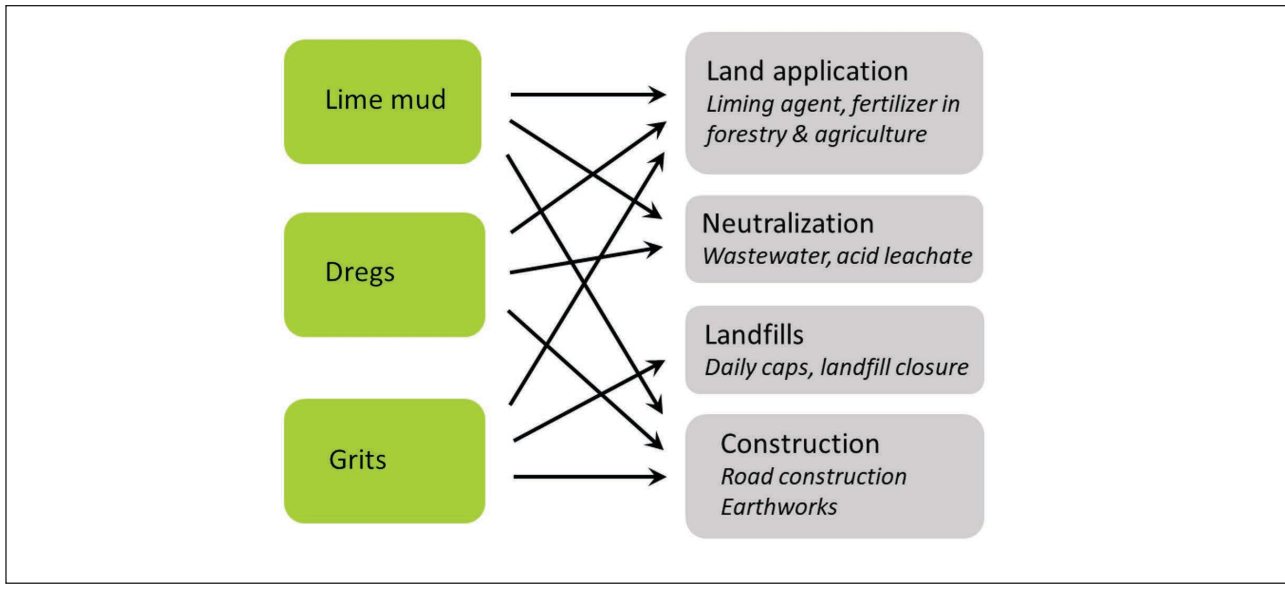

3. Previously applied utilization methods for causticizing residues.

"AshCrete," a product applied in various earthwork projects [56]. Pulp and paper companies increasingly implement residuals utilization programs that include causticizing residues. A European pulp and paper mill consortium has conducted demonstration projects to investigate applications of lime mud as a concrete filler and dregs and grits as aggregates for asphalt pavements, as well as dregs as a sealing layer for mine waste deposits [57].

Dregs as a neutralizing agent

Dregs are used for pH adjustment and stabilization. One mill in Finland has used its dregs for neutralization of acidic mill wastewater [42]. Another Finish mill has tested dregs utilization for the neutralization of acidic gases and to remove sulfur dioxide by the calcium carbonate contained in the dregs [54].

LIME MUD UTILIIZATION

A small portion of lime mud, typically in the form of lime dust from lime kilns, is purged from the lime cycle in order to control accumulation of non-process elements. Lime mud is alkaline (pH 8.4–13.0) and consists mainly of calcium carbonate.

The most common application of lime mud is as a soil amendment on agricultural lands (**Fig. 3**). The high pH of lime mud helps adjust the pH of crop soil, allowing for better absorption of nutrients. It has shown to provide a better yield for the forage crop alfalfa used in dairy farming [58]. The calcium carbonate equivalence (CCE) of lime mud is higher than that of dregs/grits mixtures. In agriculture, lime mud is usually applied at a rate of 2.5 tons/ha land [8]. This type of waste is also applied in forestry. Mixtures of lime mud and ash from a mill in Portugal are utilized as fertilizer in oak, pine, and eucalyptus forestlands [48].

Other applications include the usage as an additive for the construction of roads and for soil stabilization. Lime mud from several U.S. mills was used as an additive to manufactured soil to improve the soil bearing capacity, which is beneficial for the construction of roads and parking lots [8].

Also, a variety of other different utilization methods have been reported, including use as an additive for the production of topsoil or potting mix and as a constituent for cement production [8]. Similar to dregs, lime mud has been shown suitable for pH control of mill wastewater. Mahmood and Paice [59] refer to several Canadian kraft mills that add lime mud to their aerated stabilization basins for pH adjustment.

One of the challenges of using lime mud is related to the recovery and the conditioning of the lime mud prior to utilization, i.e., the dredging from mill holding ponds and the drying and pulverization in order to enable distribution with conventional dry lime spreaders. Another challenge may be the relatively low concentration of magnesium in lime mud and grits. Therefore, long-term application as a liming agent may cause magnesium deficiencies in the soils [4].

SLAKER GRITS UTILIZATION

Grits constitute the settleable material in the slaker, and they consist mostly of calcium carbonate with some calcium hydroxide, sodium, magnesium, and aluminum compounds. On average, about 5 kg of grits are generated per metric ton of pulp.

Grits are alkaline (pH 12–13), and therefore have been utilized for liming purposes on agricultural and forest land. As an example, grits, dregs, and sludge from a Brazilian

Type of Residual	Application	Potential Benefits and Requirements
Sludge	Land application	Biosludge: adds nitrogen, phosphorous, and organic matter to soil; cost savings for sludge dewatering/disposal. Primary sludge: enhanced soil structure, water infiltration, and moisture and nutrient holding capacity (depending on the type of soil). Composted sludge: lower carbon (C): nitrogen (N) ratio, higher nitrogen availability, and larger cation exchange and moisture-holding capacity. Low C:N ratio, odor, and heavy metal concentrations are required.
	Landfills and mine sites	Adds organic matter and nutrients for self-sustaining plant growth.
Ash	Land application	Adds soil nutrients, including calcium, potassium, phosphorous, and magnesium; pH stabilization. Composting additive: ash reduces moisture/odor and acts as a bulking agent. Low heavy metal and dioxin/furan concentrations are required.
	Construction material, road work	High mineral content is beneficial for concrete, cement, and brick production; bottom ash (high density, low carbon content) is suitable as a base material in roads — creates hard foundation in combination with soil. Low carbon content is required.
Dregs	Land application	Adds calcium and magnesium to soils; used as a liming agent. Low sodium adsorption ratio is required.
	Construction material	High mineral content is beneficial for cement and fine aggregate production; dregs/ash mixture is suitable as a base material for earthworks. Low sodium and sulfur content is required.
Lime mud	Neutralizing agent	Stabilizes pH of agricultural and forest soil due to high alkalinity (liming agent); pH control in mill wastewater treatment systems.
	Road construction	Improves road stability and bearing capacity.
Grits	Land application and landfills	pH stabilization of agricultural and forest soil (liming agent); suitable as an additive for landfill covers.
	Road construction	Grits/sand mixtures are beneficial for roadbed stabilization, particularly when affected by heavy truck traffic.

II. Summary of the main benefits and requirements of residuals utilization.

mill are used for soil fertilization and pH control in forestry [60]. Grits are also suitable as a soil additive for daily landfill covers, where it helps to control blowing litter, animals, and insects [33]. In another reported application, lime mud, grits, and dregs from a mill in the United States were marketed for various uses, including strip mine reclamation [8]. Because of the potential leaching behavior of sulfur, alkali metals, and alkaline earth metals from grits, a leachability assessment might be necessary prior to application on soil [61].

Grits are particularly suitable for application in road construction. Mixtures consisting of sand and grits from a kraft mill were used for the construction of roads affected by heavy-truck traffic. As a result, the roads require less maintenance than unpaved roads using native soils. Also, grits have a better liquid holding capacity, which makes certain dust suppression techniques more effective [33]. Other examples include the application of grits from a U.S. mill in roadbed underlayment [58] and the utilization of sand/grits mixtures as a road stabilizer at a mill in Chile [22].

CHALLENGES OF MILL RESIDUALS UTILIZATION

There are several challenges related to the utilization of mill residuals. One of the main challenges is the large day-to-day variations of the physical and chemical properties of the waste. In particular, applications of mill waste for the manufacture of construction material require a consistent

quality in terms of mineral and organic matter content. Markets must be available for the mill waste that are reliable on a longer-term basis in terms of the required quantity and cost. Also, the geographical vicinity to the companies that utilize the waste is important to keep transport costs at a minimum.

Potential long-term liabilities related to waste utilization programs are often a concern to mills. Future changes of environmental regulations may lead to the shutdown of a beneficial use program or a liability for cleanup of a site where mill wastes were previously applied.

The implementation of mill residuals utilization programs must comply with environmental health and safety regulations at the mill and must be economically viable. If the utilization method is more costly than the conventional method of disposal, an implementation will likely not take place.

Contamination of waste, such as heavy metals and organic contaminants, in sludge or ash can also prevent utilization.

Regulations for the beneficial use of mill residuals vary widely among countries and local governments. In Canada and the United States, some of the parameters analyzed for consideration of land application of residuals are metal concentrations, pH conditions, pathogens, vector attractiveness, dioxin/furan concentrations, C:N ratio, sodium adsorption ratio, and odor. Also, the permit process often requires the investigation of site-specific parameters related to various soil properties and the distance to surface water and groundwater.

SUMMARY

Currently, about half of all residuals generated in kraft pulp mills are landfilled. Mill waste is most suitable for land application, road building, earthworks, and construction (**Table II**). However, every utilization strategy has to be tailored to the specific conditions at the mill, including waste type and amount and the quality and variations in waste composition. Further, long-term residuals utilization programs require reliable market conditions in terms of supply and demand.

A substantial portion of the sludge generated in pulp and paper mills is put to some use, either by incineration or various forms of land application, including land spreading, composting, or adding to landfill or mine waste covers. However, the majority of the alkaline wastes (ash and causticizing residues) are currently landfilled. Wood ash is suitable for land application in agriculture and forestry because it is rich in nutrients such as potassium, calcium, and phosphorus, and because it provides alkalinity for pH stabilization. Ash can also be used for the manufacture of building material such as concrete, cement and bricks, as well as for road and earth construction. The alkalinity of lime mud, dregs, and grits has been harnessed for the purpose of neutralizing acidic effluents or acid leachate. The combination of alkalinity and nutrients has led numerous mills to apply their lime mud and dregs in agricultural settings. Grits have been shown to be useful as an additive for construction and road building material, as well as for landfill covers.

Some of the challenges to utilize mill waste are large day-to-day variations in the amount and composition. Also, the transport and the geographical vicinity to the waste recipients are important aspects of feasibility. Potential utilization as a soil amendment requires long-term toxicology and leachability assessments. Other challenges may be related to the chemical composition of the waste, such as low nitrogen content in sludge or high sodium content in dregs. **TJ**

ACKNOWLEDGEMENTS

This work is part of the industrial research consortium project "Effective Energy and Chemical Recovery in Pulp and Paper Mills – II" at the University of Toronto, supported by Andritz, Arauco, Babcock & Wilcox, Canadian Kraft Paper, Cenibra, Clyde Bergemann, CMPC, ERCO Worldwide, FITNIR, FPInnovations, Georgia Pacific, International Paper, Irving, KFS, Klabin, Meadow Lake, Mercer, NORAM, Rayonier, Resolute, Sappi, Södra, Stora Enso, Suzano, Valmet, and WestRock. The author would also like to acknowledge the support of the Natural Sciences and Engineering Research Council of Canada (NSERC) and Cette Recherche a été Financée par le Conseil de Recherches en Sciences Naturelles et en Génie du Canada (CRSNG), [IRCPJ 517715 -16]. Special appreciation goes to Honghi Tran of the University of Toronto for his comments and advice.

LITERATURE CITED

1. U.N. FAO, *Yearbook of Forest Products 2019*, Food and Agriculture Organization of the United Nations, Rome, 2021.
2. Data Bridge Market Research "Global bleached kraft pulp market — industry trends and forecast to 2028," Data Bridge Market Research, Pune, India, April 2021.
3. Aryan, V. and Kraft, A., *J. Cleaner Prod.* 280: 124616(2021).
4. Camberato, J.J., Vance, E.D., and Someshwar, A.V., "Composition and land application of paper manufacturing residuals," in *Agricultural Uses of Byproducts and Wastes*, ACS Symp. Ser. 668 (J.E. Rechcigl and H.C. MacKinnon, Eds.), American Chemical Society, Washington, DC, 1997, pp. 185-202.
5. Simão, L., Hotza, D., Raupp-Pereira, F., et al., *Cerâmica* 64: 443(2018).
6. McGovern, J.N., Berbee, J.G., Bockheim, J.G., et al., *Tappi J.* 66(3): 115(1983).
7. Risse, M., "Best management practices for wood ash as an agricultural soil amendment," Bulletin No. 1142, The University of Georgia Cooperative Extension, Athens, GA, USA, 2013.
8. Thacker, W.E., "Beneficial use of by-product solids from the kraft recovery cycle," Technical Bulletin No. 931, National Council for Air and Stream Improvement, Cary, NC, USA, 2007.

9. UPM, *Aiming Higher with Biofore: Annual Report 2016, Sustainability Report*, UPM, Helsinki, 2016.
10. Stora Enso, "Sustainability,"in *Stora Enso Annual Report*, Stora Enso, Helsinki, 2018.
11. International Paper, *2017 Global Citizenship Report*, International Paper, Memphis, TN, USA, 2017.
12. Kinnarinen, T., Golmaei, M., Jernström, E., et al., *J. Cleaner Prod.* 133: 953(2016). https://doi.org/10.1016/j.jclepro.2016.06.024.
13. Quina, M.J. and Pinheiro, C.T., *Appl. Sci.* 10: 2317(2020). https://doi.org/10.3390/app10072317.
14. Fisher International, "The 2012 global PPI water benchmark report (2014 update)," Fisher International Inc., Norwalk, CT, USA, 2012.
15. Fisher International, "The 2016 global PPI water benchmark report," Fisher International Inc., Norwalk, CT, USA, 2016.
16. Bird, M. and Talberth, J., "Waste stream reduction and re-use in the pulp and paper sector," Washington State Department of Ecology Industrial Footprint Project, Project Task 5.1, Center for Sustainable Economy, Santa Fe, NM, USA, 2008.
17. Thacker, B., "Road-related applications of paper industry byproducts," *2012 Workshop on Sustainable Resource Management in Transportation*, NCASI/Western Michigan University, Cary, NC/Kalamazo, MI, USA, 9 July 2012.
18. Jean, M., "Paper mill residuals: free soil amendment available to Upper Peninsula farmers," Michigan State University, MSU Extension Field Crops, East Lansing, MI, USA, 11 January 2017.
19. Upton, B. and Lama, I., "Beneficial use resources available from NCASI (with 2014 AF&PA and NCASI data)," National Council for Air and Stream Improvement, Cary, NC, 2017.
20. Kryzanowski, T., "Sludge — a success story for Whitecourt-area farmers," *Alberta Farmer Express*, 18 March 2015.
21. Kuokkanen, T., Nurmesniemi, H., Pöykiö, R., et al., *Chem. Speciation Bioavailability* 20(2): 111(2008). https://doi.org/10.3184/095422908X324480.
22. Arauco, *Sustainability Report 2014*, Arauco, Santiago, Chile, 2014.
23. Velema, G., *Pulp Pap. Can.* 105(7): T150(2004).
24. Gagnon, B. and Ziadi, N., *Can. J. Soil Sci.* 92: 917(2012). https://doi.org/10.4141/cjss2012-026.
25. Koski, A.E., "Reclamation of waste rock stock piles utilizing paper mill residuals at Cliffs Michigan mining company, *National Meeting American Society Mining Reclamation*, ASMR, Lexington, KY, USA, 2005 p. 627.
26. Hargreaves, J., Lock, A., Beckett, P., et al., *Can. J. Soil. Sci.* 92: 203(2012). https://doi.org/10.4141/cjss2010-056.
27. SYLVIS, "Evaluation of paper mill sludge for use as a landfill cover barrier," SYLVIS, New Westminster, BC, Canada, 2018. Available [Online] https://www.sylvis.com/our-work/evaluation-paper-mill-sludge-use-landfill-cover-barrier <11Feb2022>.
28. NCASI, "Compilation of alternative landfill cover experience using wastewater treatment plant residuals," Technical Bulletin No. 900, National Council for Air and Stream Improvement, Cary, NC, 2005.
29. CEPI, "Novel bio-based products from side streams of paper and board production," Report No. 604187, REFFIBRE European Community's 7th Framework Programme, Confederation of European Paper Industries, Brussels, 2016.
30. Post, P., "Recycled paper offers affordable bedding alternative," *Lancaster Farming*, 26 October 2013.
31. Wiegand, P.S. and Unwin, J.P., *TAPPI J.* 77(4): 91(1994).
32. Myers, J.F. and Carroll, T.W., "Field experience of processing paper mill sludge in a slagging boiler, *Recycl. Symp. Proc.*, TAPPI Press, Atlanta, 1999.
33. RMT, "Beneficial use of industrial by-products," prepared for NCASI, RMT Inc., Huntertown, IN, USA, 2003.
34. *GreenPort*, "No waste, just resources at the port of Koper," *GreenPort*, 16 February 2015.
35. Elliott, A. and Mahmood, T., *TAPPI J.* 5(10): 9(2006).
36. Thacker, W.E., "Management of by-product solids generated in the pulp and paper industry," Report, National Council for Air and Stream Improvement, Cary, NC, 2004.
37. IEA, "Options for increased use of ash from biomass combustion and co-firing," IEA – Bioenergy, Task 32: Biomass Combustion and Co-firing, Internationl Energy Agency, Paris, 2018.
38. UPM Kymi, "Environmental Performance in 2016," UPM Kymi, Kouvola, Finland, 2016.
39. Cherian, C. and Siddiqua, S., *Sustainability* 11: 4394(2019). https://doi.org/10.3390/su11164394.
40. Noyce, G.L., Fulthorpe, R., Gorgolewski, A., et al., *Appl. Soil Ecol.* 107: 368(2016). https://doi.org/10.1016/j.apsoil.2016.07.006.
41. Pöykiö, R., Nurmesniemi, H., Perämäki, P., et al., *Chem. Speciation Bioavailability* 17: 1(2005). https://doi.org/10.3184/095422905782774964.
42. Nurmesniemi, H., Pöykiö, R., Keiski, R.L., *Waste Manage.* 27: 1939(2007). https://doi.org/10.1016/j.wasman.2006.07.017.
43. Catalyst, S*ustainability Report 2015*, Catalyst Paper Corp., Richmond, VA, USA, 2015.
44. Hackett, G.A.R., Easton, C.A., and Duff, S.J.B., *Bioresour. Technol.* 70: 217(1999). https://doi.org/10.1016/S0960-8524(99)00048-6.
45. Cenibra, personal communication, 2019.
46. Norske Skog, *Annual Report 2016*, Norske Skog, Oslo, 2016.
47. Töyssy, S., "Ash is a major waste fraction with many possibilities for utilization," UPM, Helsinki, 7 September 2016.
48. CEPI, "Resource efficiency in the pulp and paper industry," Confederation of European Paper Industries, Brussels, 2018.
49. Pöykiö, R., Nurmesniemi, H., Kuokkanen, T., et al., *Environ. Chem. Lett.* 4: 37(2006). https://doi.org/10.1007/s10311-005-0031-0.
50. Mahmoudkhani, M., Richards, T., and Theliander, H., *Process Saf. Environ. Prot.* 82(B3): 230(2004). https://doi.org/10.1205/095758204323065993.
51. Sartz, L., Hamilton, I., Mácsik, J., et al., "Green liquor dregs from pulp and paper industry used in mine waste management: a symbiosis project (GLAD) between two Swedish base industries," in *Mine Water & Circular Economy, Vol. II* (C. Wolkersdorfer, L. Sartz, M. Sillanpää, and A. Häkkinen, Eds.), Lappeenranta University of Technology, Lappeenranta, Finland, 2017, pp. 862-868.
52. Back, S., "Killing two birds with one stone," *Paper Advance*, Blog, 4 January 2016.
53. Mäkitalo, M., Maurice, C., Jia, Y., et al., *Minerals* 4: 330(2014). https://doi.org/10.3390/min4020330.
54. Töyssy, M., "The moist green liquor dregs are a recycling challenge," UPM, Helsinki, 14 December 2016.
55. UPM Kaukas, *Environmental Performance*, UPM Kaukas, Kaukas, Finland, 2011.

56. Hill, M., Saviello, T., and Groves, S., *J. Ind. Ecol.* 6(1): 107(2002). https://doi.org/10.1162/108819802320971669.
57. Paperchain project, European Union's Horizon 2020 Research and Innovation Programme, Grant No. 730305, European Union, Brussels, 2019.
58. Sappi, *Group Sustainability Report*, Sappi, Johannesburg, South Africa, 2017.
59. Mahmood, T. and Paice, M., *J. Environ. Eng. Sci.* 5: 383(2006). https://doi.org/10.1139/s05-047.
60. Cenibra, *Sustainability Report*, Cenibra, Belo Oriente, MG, Brazil, 2016.
61. Pöykiö, R., Dahl, O., Nurmesniemi, H., et al., *J. Environ. Occup. Sci.* 4(1): 22(2015). https://doi.org/10.5455/jeos.20150114041516.

ABOUT THIS PAPER

Cite this article as:
Meyer, T., *TAPPI J.* 21(2): 83(2022).
https://doi.org/10.32964/TJ21.2.83

DOI: https://doi.org/10.32964/TJ21.2.83

ISSN: 0734-1415

Publisher: TAPPI Press

Copyright: ©TAPPI Press 2022

About this journal

ABOUT THE AUTHORS

This topic was selected for study because mills are increasingly interested in diverting residuals from landfills and establishing beneficial use programs. The most difficult part of this work was to find information about current and previous applications of mill waste utilization, because these are usually not reported in technical and scientific publications. This challenge was addressed by searching for reports from organizations that support the forest products industry, reading sustainability reports from pulp and paper companies, and having personal communications with mill personnel.

The most surprising part of this study was to learn that there is a wide variety of utilization methods that have been applied by mills, and that there is often not much known about the successes or failures of these programs. Mill personnel will find this review helpful when considering options for diverting residuals from landfills.



Meyer

Torsten Meyer is senior research associate at the Pulp & Paper Centre, University of Toronto, Toronto, ON, Canada. Email Meyer at torsten.meyer@utoronto.ca.

Experiments and visualization of sprays from beer can and turbo liquor nozzles

ARI KANKKUNEN, SANTERI KOIVISTO, KARI SAARI, MIKA JÄRVINEN, JAMES BIGGS, AND ANDREW JONES

ABSTRACT: Industrial scale swirl-type black liquor nozzles were studied using water as the test fluid. Simple water spraying experiments were found to be very beneficial for studying and comparing nozzles for black liquor spraying. These kinds of experiments are important for finding better nozzle designs.

Three nozzle designs were investigated to understand the functional differences between these nozzles. The pressure loss of nozzle 1 ("tangential swirl") and nozzle 3 ("turbo") were 97% and 38% higher compared to nozzle 2 ("tangential swirl"). Spray opening angles were 75°, 60°, and 35° for nozzles 1, 2, and 3, respectively. Video imaging showed that the nozzles produced sprays that were inclined a few degrees from the nozzle centerline. Spray pattern-nation showed all the sprays to be asymmetric, while nozzle 2 was the most symmetric. Laser-Doppler measurements showed large differences in spray velocities between nozzles. The spray velocity for nozzle 1 increased from 9 m/s to 15 m/s when the flow rate was increased from 1.5 L/s to 2.5 L/s. The resulting velocity increase for nozzle 2 was from 7 m/s to 11 m/s, and for nozzle 3, it was from 8 m/s to 13 m/s. Tangential flow (swirl) directed the spray 6°–12° away from the vertical plane. Liquid sheet breakup mechanisms and lengths were estimated by analyzing high speed video images. The liquid sheet breakup mechanism for nozzle 1 was estimated to be wave formation, and the sheet length was estimated to be about 10 cm. Sheet breakup mechanisms for nozzle 2 were wave formation and sheet perforation, and the sheet length was about 20 cm. Nozzle 3 was not supposed to form a liquid sheet. Nozzle geometry was found to greatly affect spray characteristics.

Application: Spray properties are experimentally characterized. Knowledge of spray opening angle, velocity, and mass distribution can be used to compare different nozzles for better char bed, fouling, and emissions control. Spray characteristics can be adapted for computational fluid dynamics (CFD) modeling.

The dominant method of spraying black liquor into a recovery boiler is via the use of "splash-plate" nozzles. While this has generally been found to be the most effective method of spray formation, there are some cases where alternative liquor nozzles have demonstrated improved recovery boiler operating characteristics.

Alternative nozzles that have been used include: "U" and "V" jet nozzles supplied by Combustion Engineering; "swirl-cone" nozzles also supplied by Combustion Engineering; "wedge nozzles" supplied by Babcock & Wilcox (Akron, OH, USA); "tangential swirl" nozzles (beer cans) used by Andritz (Graz, Austria), Crenshaw Machine Systems (Bay Minette, AL, USA), and Clyde Industries (Atlanta, GA USA); and "turbo" nozzles supplied by Crenshaw Machine Systems.

A majority of these alternative designs have fallen out of common use due to four main reasons:

1. The superiority of the "splash-plate" design, especially at higher liquor percent solids when utilizing stationary firing methods.
2. Most Combustion Engineering two level air systems boilers have now been retrofit, thus eliminating the need for the fine (low average diameter) sprays produced by U jet, V jet, and swirl-cone nozzles.
3. Firing of higher percent solids on recovery boilers.
4. The increased size of recovery boilers.

There are two notable exceptions: the tangential swirl nozzle (colloquially referred to as a beer can nozzle) has found increasing acceptance, and the turbo nozzle has also been shown to result in improved recovery boiler operation. These designs are certainly not universally applicable across all situations, but they have found success primarily when applied to older and smaller recovery boilers, burning both oxidized and unoxidized black liquor. It is not entirely clear why they have resulted in improved operation, as the characteristics of the sprays produced by these nozzles are not well understood.

The two most important characteristics of a spray produced by a liquor nozzle are the mean diameter and the trajectory (distribution of droplet speed and direction). The droplet size distribution once normalized by the average diameter has been shown to be relatively invariant for all nozzle types by Adams [1]. The performance of a nozzle when used on a recovery boiler will be determined by these two important characteristics, and these characteristics are determined by the properties of the black liquor and by the geometry of the nozzle.

In general, the improvements that have been seen relate to the increased fraction of the spray that is fired di-

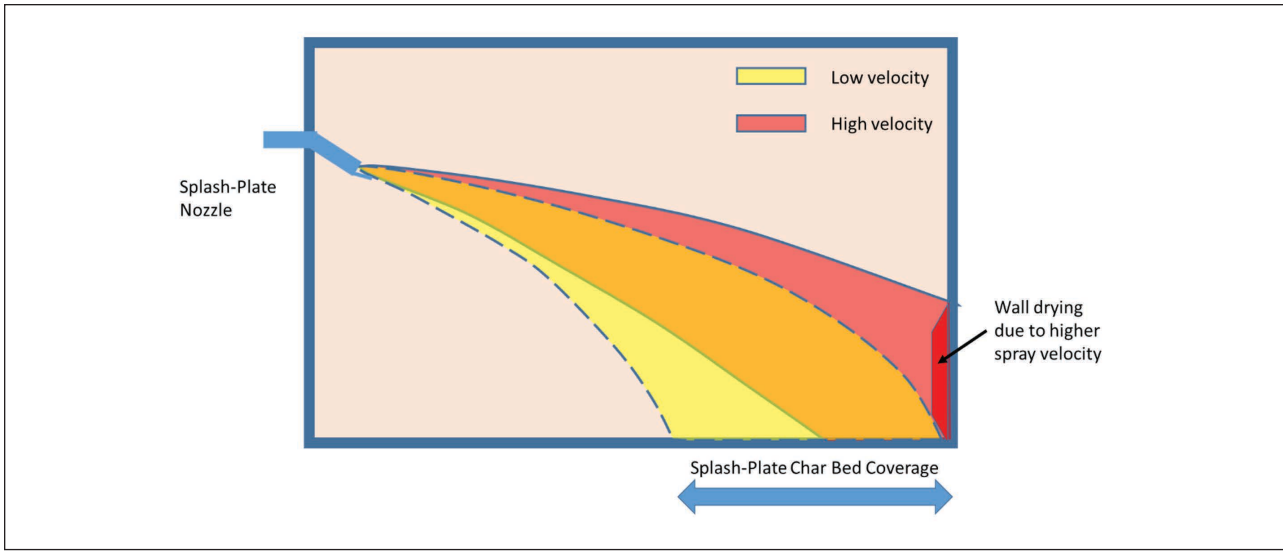

1. Splash-plate operation at different spray velocities.

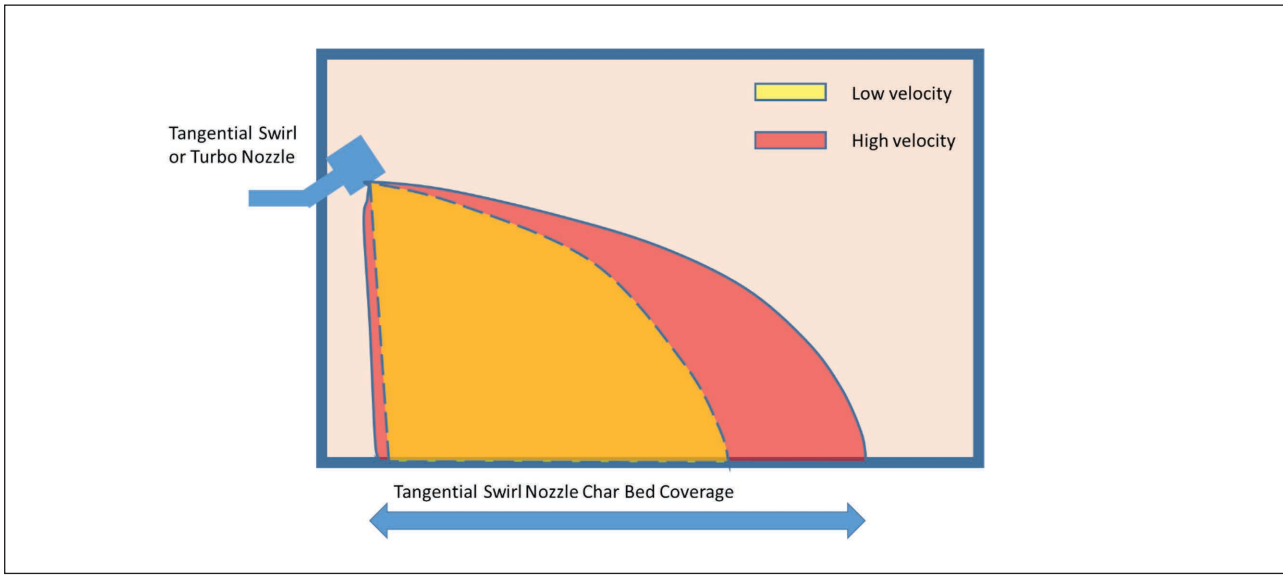

2. Tangential swirl nozzle operation at different spray velocities.

rectly onto the char bed, rather than utilizing wall drying. Splash-plate nozzles are typically fired horizontally or with a slightly downward trajectory. Consider a situation where liquor temperature is increased to induce additional flashing: this will both decrease droplet size and increase the penetration distance of the spray into the furnace (as the spray velocity will increase). If this spray was impinging directly in front of the opposite wall, then increasing the temperature could result in sprays that then reach the opposite wall; this is a particular problem on small recovery boilers, as shown in **Fig. 1**. Spray nozzles that produce a spray that is directed downward towards the char bed will have far less influence on the amount of wall drying (**Fig. 2**).

By avoiding wall drying, a few benefits can be obtained:

1. A higher fraction of the fuel is delivered to the hearth. In the case of older recovery boilers, this generally results in a hotter char bed that improves the rate of combustion and reduces the release of sulfur. Lowering sulfur dioxide (SO_2) and total reduced sulfur (TRS) emissions.
2. Char falling from the walls can plug smelt spouts. If wall drying is reduced, then smelt spout pluggage can be reduced.
3. Large "shelves" of char falling from the walls causes instability in the lower furnace (changes to air demands, char bed piling, etc.), which can result in difficulties minimizing the excess air used on the recovery boiler.

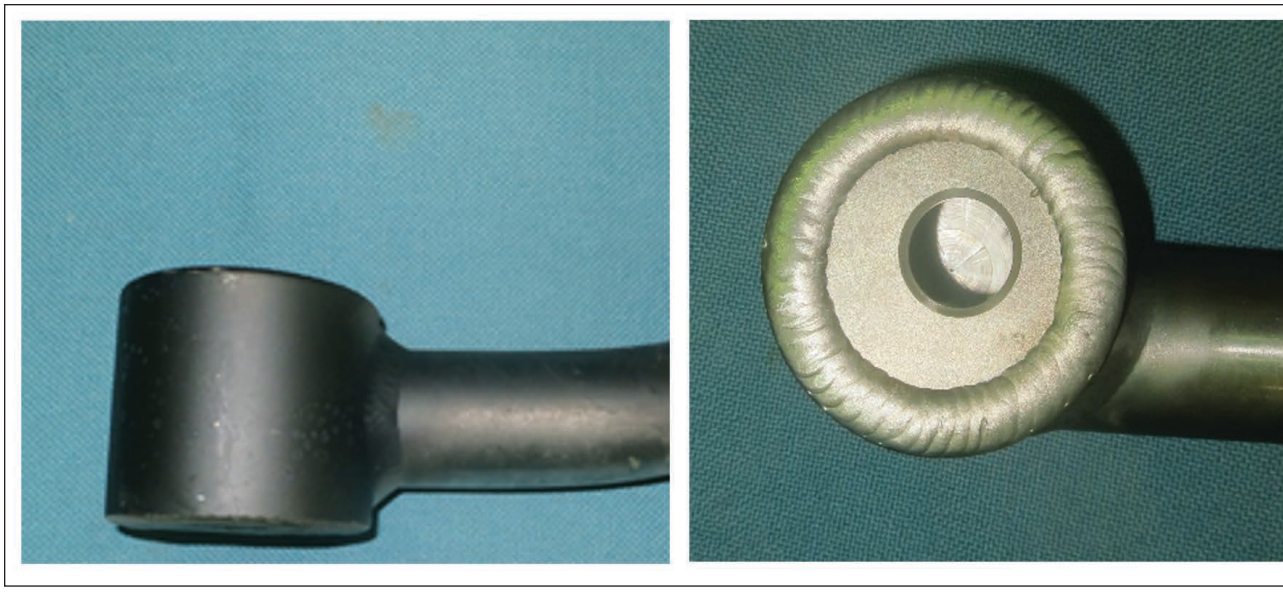

3. Nozzle 1: tangential swirl with pipe inlet.

A downward trajectory of the liquor will also tend to reduce carryover; this can then result in reduced rates of upper furnace fouling. The benefit is then in reduced water washes and/or sootblowing steam usage.

Directing a spray downward onto the char bed does have a potential drawback; if the spray becomes coarse (larger average diameter), then there is a risk of overloading a region of the char bed with partially combusted black liquor drops. This could result in excessive char bed growth or "blackout," where excessive moisture causes local loss of ignition. Experience has shown that this is a very rare occurrence with these nozzles, perhaps even less than with splash-plate nozzles. It is not entirely clear why this is the case. One possibility is that the droplet size produced by these nozzles tends to vary less with changes in black liquor properties. Another is that fouling of these nozzles seems to be less of a problem in operation. A splash-plate nozzle, when fouled, can have a very poor spray and produce a large "stringy" ligament that falls directly to the char bed that is known as a root-cause of char bed excessive growth and blackouts.

The understanding of the impact of nozzle geometry can be examined independently of the properties of black liquor by testing the performance of these nozzles using water. The properties of water can be precisely controlled, and thus the test fluid is removed from the source of variability when seeking to understand the test results. Clearly, this will not give a full picture of the performance of these nozzles in recovery boiler application, but the goal of this effort was to seek to understand fundamental differences between these nozzles vs. the large body of information gathered on splash-plate nozzles from similar tests (e.g., Kankkunen et al. [2]).

Only two earlier literature mentions around beer can nozzles were found. Kardio et al. [3] studied the effect of beer can nozzles, substituting two of six splash-plate nozzles in a furnace. They found an increase in the temperature of the char bed. Jameel and Pingel [4] have presented a patent application for a variable orifice beer can nozzle that provides variable spray patterns.

There is a need for a simple and easily reproducible method for comparing nozzles for black liquor spraying. Measurements with real black liquor are expensive, and differences between black liquors and spraying practices may hinder proper comparisons between nozzles. In addition, simple water experiments allow inexpensive studies of the changes in the spray characteristics caused by geometrical differences in nozzle design. Therefore, a measurement campaign using water as the test liquid was carried out with three swirl type nozzles.

METHOD

Test nozzles

Three nozzles for black liquor spraying were tested by spraying water as the test fluid. Two of the nozzles were typical tangential swirl nozzles with a swirl chamber just before the nozzle exit orifice. The third nozzle was called a turbo nozzle. In this nozzle type, the swirling motion was produced by guide vanes located near the nozzle exit.

All the test nozzles had a similar inlet pipe with R1 1/4 thread, which was connected to the same size inlet assembly with sensors for pressure, temperature, density, and volume flow rate measurements. The inner and outer diameters of the inlet pipe were 32 mm and 42 mm, respectively. The length of each nozzle was about the same, 21 cm + swirl chamber. The nozzles were painted black to avoid laser light reflection. Furthermore, the exit orifice was beveled in all nozzles, consistent with normal fabrication methods.

Figure 3 shows nozzle 1. One of this nozzle's prominent features is the straight inlet to the swirl chamber. The

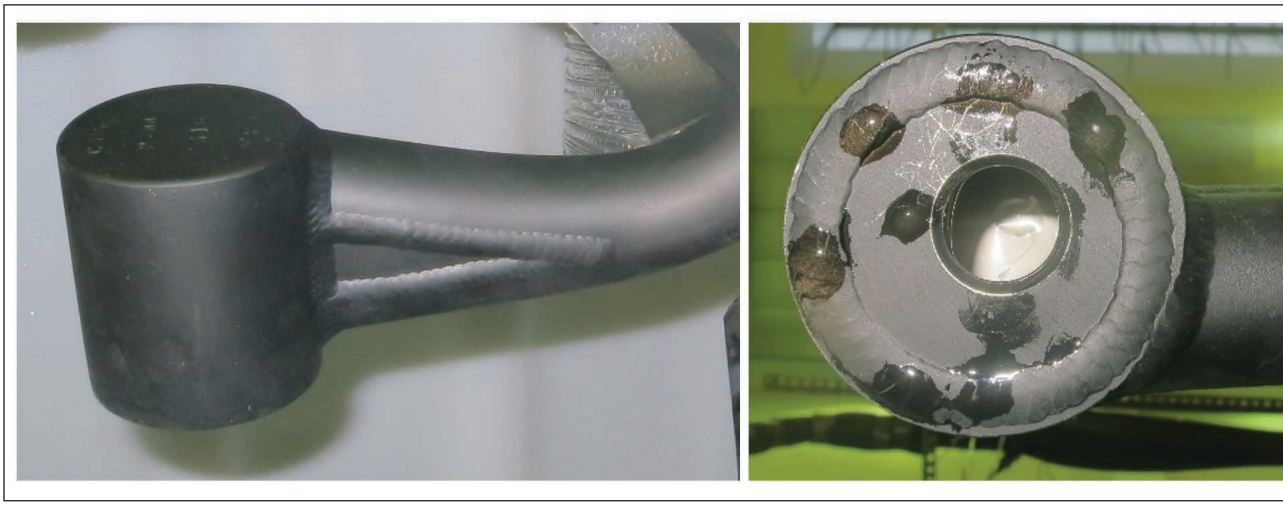

4. Nozzle 2: tangential swirl with expanding inlet.

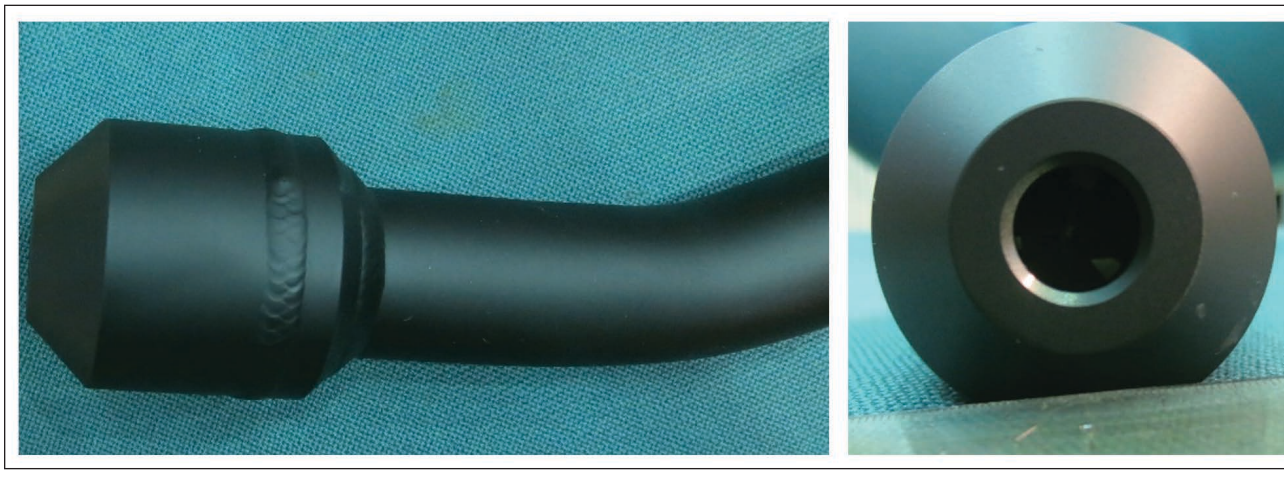

5. Nozzle 3: turbo nozzle.

outside height of the swirl chamber was 65 mm and the outside diameter was 75 mm. The inside height of the chamber was 48 mm. The inlet was located to the right side of the swirl chamber, thus producing a swirling motion to the liquid. The exit orifice diameter was 22 mm.

Figure 4 shows nozzle 2. This nozzle had an expanding inlet to the swirl chamber. The height of the expanding inlet was about 77 mm at the highest. The outside height of the swirl chamber was 82 mm, and the outside diameter was 72 mm. The inside height of the chamber was 65 mm. As in nozzle 1, the inlet was on the right-hand side of the swirl chamber. The exit orifice diameter of the swirl chamber was 22 mm.

Figure 5 shows nozzle 3, which was totally different in comparison to the other two nozzles. In nozzle 3, the liquid enters the swirl chamber from above. The swirling motion is produced by the liquid guide vanes inside the swirl chamber. The height of the swirl chamber was about 77 mm, and the outside diameter was 72 mm. The exit orifice diameter was 17 mm, and the exit orifice was located in the centerline of the swirl chamber.

The main differences between tangential swirl nozzles A and B were the size and the shape of inlet pipe and the size and shape of swirl chamber. Nozzle A had a widening inlet pipe, which decreases the velocity of liquid injected to the swirl chamber. In addition, the swirl chamber of nozzle A was higher and wider compared to nozzle B.

Experiments

The nozzles were tested using water as the test fluid. The nozzle was fixed to a nozzle stand, which allowed control of the height and inclination angle of the nozzle. Nozzles were positioned carefully so that the nozzle spraying axis was downwards. **Figure 6** presents the nozzle assembly with pressure and temperature sensors, along with other relevant dimensions.

The image width for high-speed imaging was fixed at 40 cm and the frame rate was always 2000 frames per second, which allowed for systematic velocity measurements of the studied sprays. The resolution of the video was 1024

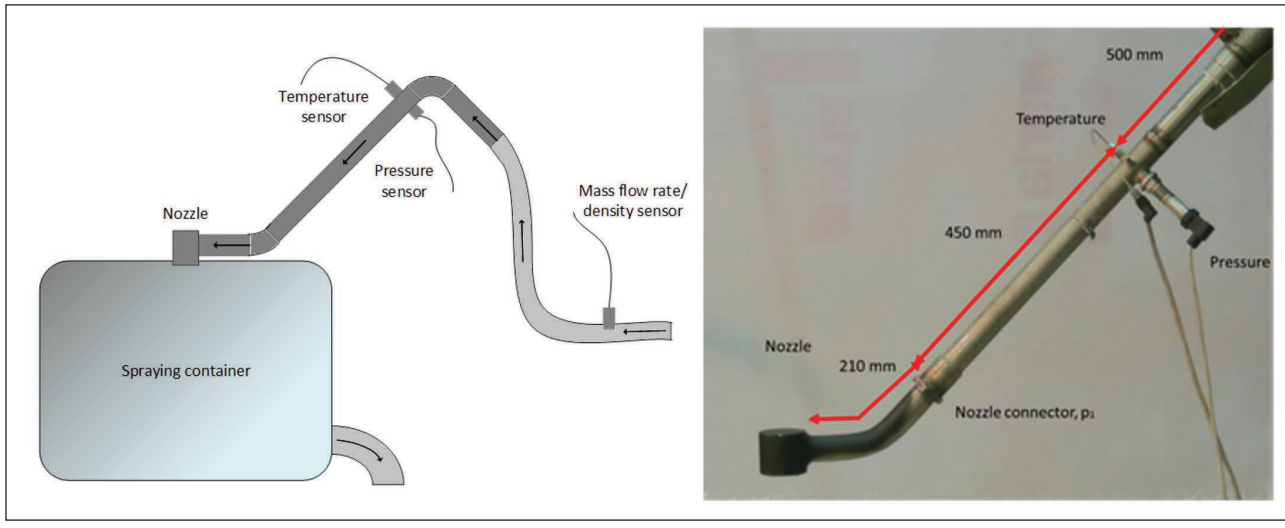

6. Spraying setup and instrumentation.

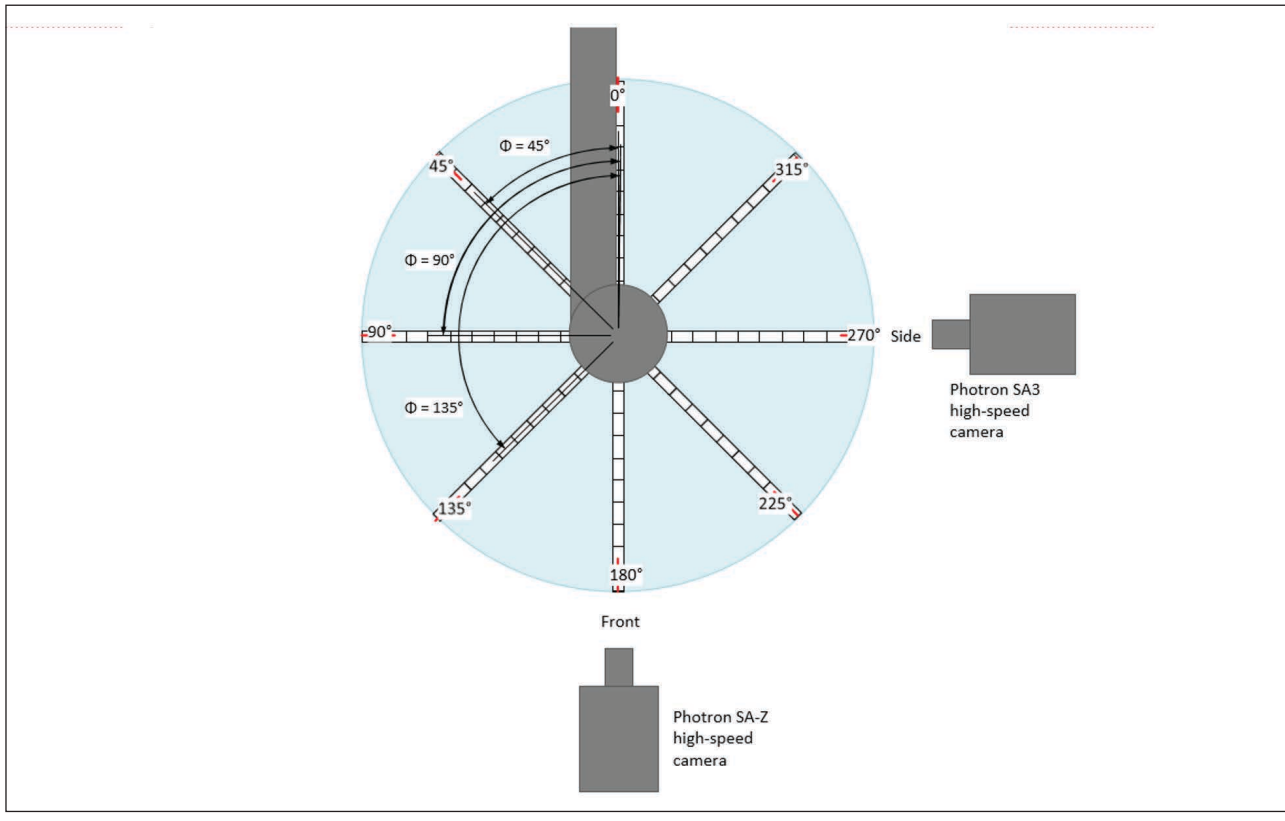

7. Camera placement and the coordinate system for patternation and laser doppler anemometer (LDA) measurements (downward view).

to 1024 pixels. Efficient LED lightning was used to allow a short exposure time, which varied between 10–50 µs for each video recording.

Figure 7 shows the coordinate system used and the placement of the high-speed cameras. The angle coordinate of 0° was chosen to be behind the nozzle inlet. The spray behavior was observed from two directions. The front camera was located at the angle of 180° and the side camera at the angle of 270°. The angular position of the patternator (φ) was defined based on the location of the left-hand side of the patternator.

Pressure drop vs. volumetric flow rate

Test nozzles were connected to a nozzle base with a length of 95 cm and an inside diameter of 36 mm. Liquid pressure was measured 45 cm before the nozzle connector. Pressure was reduced to the connector between the nozzle and nozzle assembly (Fig. 6). Thus, the pressure at the connector

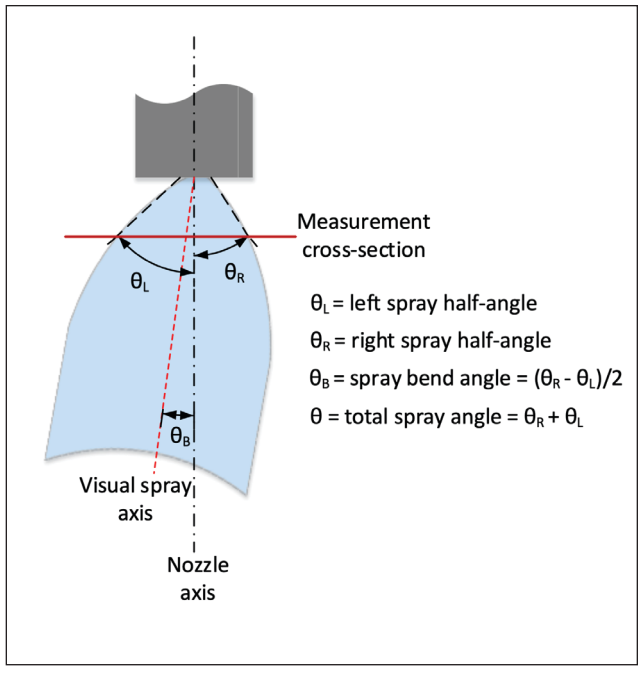

8. Definitions for spray half angles, spray bend angle, and total spray angle.

(p1) represents the pressure drop in the actual nozzle part, which is removable from the nozzle base. The flow rate was measured with a 2-in. Coriolis mass flow meter (Schlumberger; Houston, TX, USA).

Opening angle

Two high-speed cameras were used to obtain spray cone angles, velocities, and breakup mechanisms. A FASTCAM SA-Z (Photron; Tokyo) viewed the spray from the front and a FASTCAM SA3 (Photron) viewed the spray from the side (Fig. 7). Having two camera locations allowed measurements of 4 half-angles. Opening angles were measured at the distance of 4 cm below the nozzle orifice. This was achieved with a MatLab (Mathworks; Natick, MA, USA) code, which detected the edges of the spray in each frame of the video.

The total spray angle consists of the two measured half-angles (θ_L and θ_R), which denote the spray angles on the left-hand and the right-hand sides, as shown in **Fig. 8**.

Mechanical patternation

Spray liquid distributions were measured at different circumferential angles with a spray patternator. The patternator had 11 slots on both sides of the center. It was rotated around its center axis to measure at 8 different angles (Fig. 7). The collected radial distributions were reduced to circumferential liquid distribution by summing the volumes collected by each vessel in the patternator. The patternator was located 21 cm and 20 cm below the nozzle orifice for nozzles 1 and 2, respectively. For nozzle 3, the patternator was located 50 cm below the nozzle.

Spray velocity

The spray velocity was measured with an Aerometrics (Sunnyvale, CA, USA) laser doppler anemometer (LDA). An LDA measures a small point where two laser beams form a fringe pattern. The velocity was measured 40 mm below the nozzle. The velocities were measured at coordinates of 45°, 135°, 225°, and 315°. An example of the LDA measurement is shown in **Fig. 9**.

The alignment angle of 38° was used for all nozzle 1 and 2 measurements and the angle of 28° for nozzle 3 measurements. These angles are assumed to be orthogonal compared to the liquid sheet, when the measurable velocity components are parallel to the liquid sheet. Two orthogonal velocity components were measured when moving horizontally through the liquid sheet. The total velocity vector along the liquid sheet and the direction (swirl) angle between the total velocity and the vertical direction of the liquid sheet were calculated based on these two velocity components.

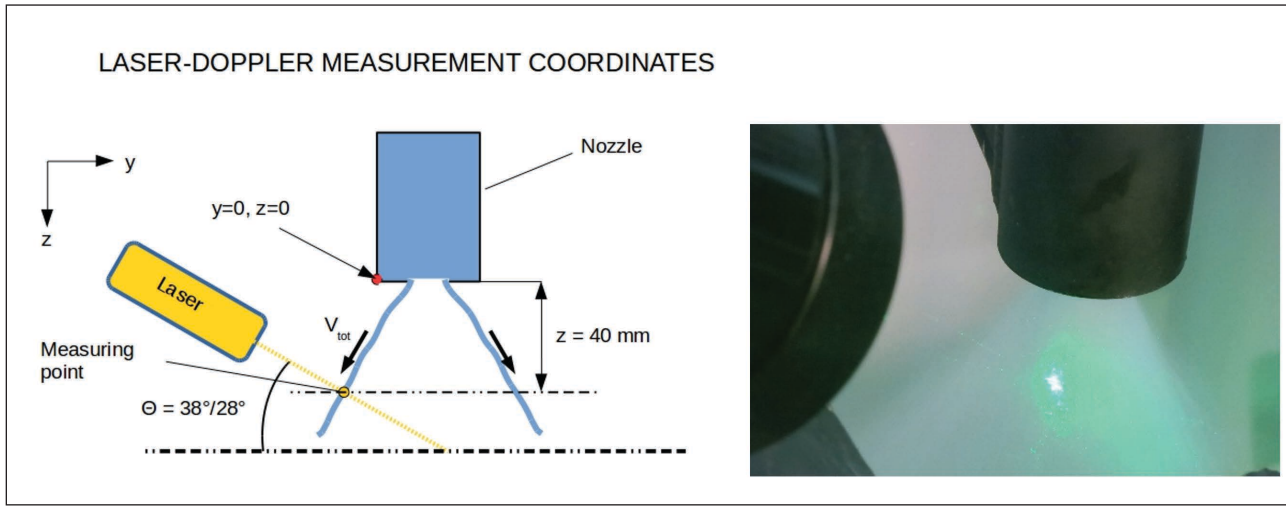

9. Measurement coordinate system of the LDA measurements and total velocity vector.

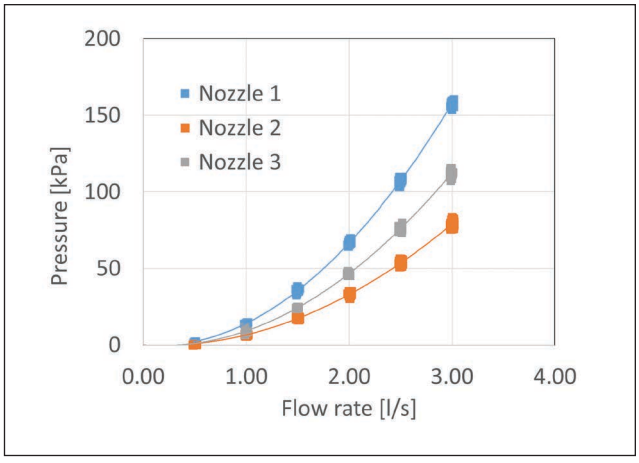

10. Differential pressure as a function of flow rate for nozzles 1, 2, and 3.

RESULTS AND DISCUSSION

Differential pressure vs. volumetric flow rate

The differential pressure curves in **Fig. 10** show that nozzle 2 had the smallest pressure drop of the three nozzles. This could be attributed to the expanding inlet channel, which reduces flow resistance by allowing a smooth entry into the swirl chamber. Conversely, the highest pressure drop was encountered with nozzle 1, where the entrance to the swirl chamber was abrupt. In the case of nozzle 3, the differential pressure curve is in between the curves of the other two nozzles. The pressure loss of nozzle 1 and 3 were 97% and 38% higher, respectively, compared to nozzle 2.

Opening angle

Figure 11 shows the measured spray angle data and the calculated average spray angles for each of the three noz-

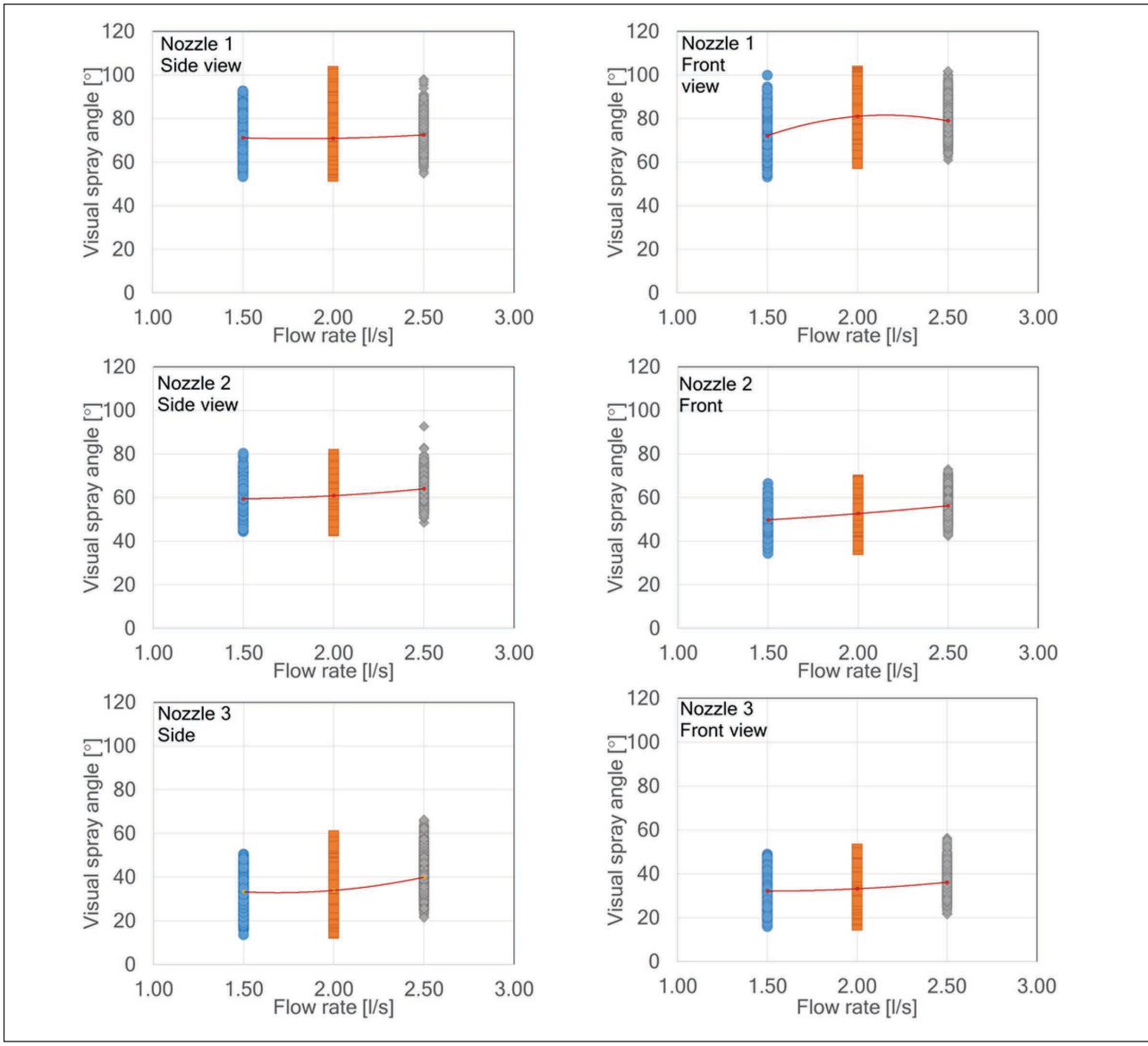

11. Spray opening angles from the front and side views for nozzles 1, 2, and 3 as a function of flow rate (p.i. = patternation index).

	Front View			Side View		
Flow rate, L/s	1.50	2.00	2.50	1.50	2.00	2.50
θ_B Nozzle 1	-5.4°	-4.4°	-4.9°	1.0°	0.6°	0.4°
θ_B Nozzle 2	-0.4°	-0.5°	-2.1°	3.1°	2.3°	2.9°
θ_B Nozzle 3	3.1°	2.5°	3.1°	2.0°	2.0°	1.5°

I. Average spray bend angles (θ_B) for nozzles 1, 2, and 3 from the front and the side view at flow rates of 1.50–2.50 L/s.

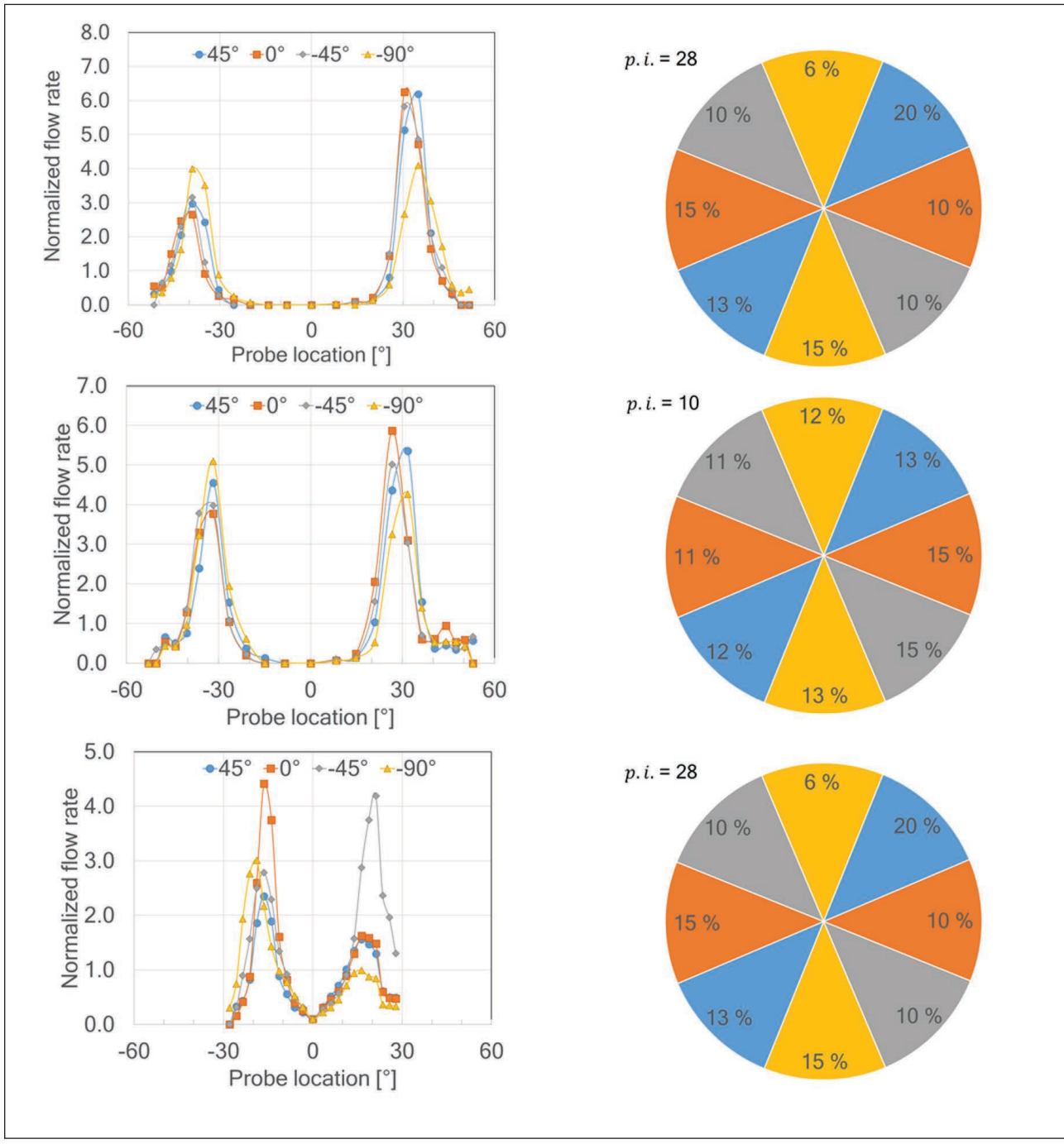

12. Radial and circumferential liquid distributions with flow rate of 2.0 L/s.

zles. The results indicated that nozzle 1 produced the widest spray angles. This can be explained by considering the effect of the straight inlet channel, which increases the tangential velocity component of the flow entering into the swirl chamber. For nozzle 2, the expanding inlet decreases the tangential velocity, thus producing a narrower spray. For nozzle 3, the flow enters the swirl chamber from above, which yields the narrowest total spray angle.

The average of the total spray angle θ varied between 70° and 80° for nozzle 1. The average of the total spray angle was slightly less for nozzle 2, between 50° and 60°. Nozzle 3 had the smallest total spray angle, between 30° and 40°. The range of total spray fluctuation was wide for each nozzle. The range is presented by the blue, yellow, and grey markers in Fig. 11.

The results from high-speed photography indicated only minor bending of the spray. In fact, the largest θ_B was encountered with nozzle 1, where from the front view, the spray was inclined roughly 5° to the left. For the other cases, the spray appears to be quite straight with θ_B less than 3.1° in either direction. These results are shown in **Table I**.

Liquid distribution in spray angles

Figure 12 shows the volume flow distributions for nozzles 1, 2, and 3. The radial and circumferential liquid distributions are shown on the left-hand and right-hand side in each figure at a flow rate of 2.0 L/s. The symmetry of the spray pattern is represented with the patternation index (p.i.), which describes the deviation from ideal distribution. For example, for an eight sector measurement, the ideal would be 12.5 % of flow in each sector. In this case, a sector getting 20 % of flow would have a deviation of 7.5 %. The patternation index is then the sum of the deviations from this ideal for all of the sectors. The normalized flow rate is obtained by dividing the flow rate to each collecting vessel with the total collected flow rate across all the patternator positions for a given flow rate.

The results indicate that nozzle 2 was clearly better in terms of the spray symmetry than nozzles 1 and 3. For each nozzle, the spray symmetry increased as a function of flow rate. For example, going from 1.50 to 2.50 L/s, the patternation indexes decreased by 22.7%–50.0%. Nozzle 3 not only exhibited poorer symmetry, but also had a larger percentage of the flow collected in the middle portion of the patternator. Conversely, nozzles 1 and 2 had only a small amount of flow in the middle due to the better hollow cone flow.

Velocity measurements

The average spray velocities were calculated based on the measurements within the liquid sheet. The average velocities along the liquid sheet for nozzle 1 are between 9 m/s and 15 m/s, for nozzle 2 between 7 m/s and 12 m/s, and for nozzle 3 between 7.5 m/s and 13.5 m/s when the flow rate varies between 1.5 L/s and 2.5 L/s. The average velocities

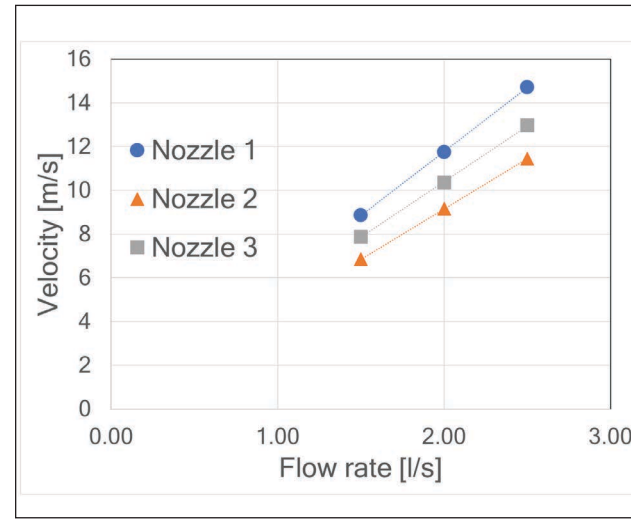

13. Average spray velocities.

for nozzles 1, 2, and 3 are presented in **Fig. 13**. The velocity was measured in 4 different spray locations to study velocity distribution with varying spray angles. The velocity variation for different measuring angles was smallest for nozzle 1 and highest for nozzle 3.

The LDA measured two rectangular velocity components along the spray (liquid sheet), which were used to define the total velocity vector along the liquid sheet at each measuring point. This vector defines the rotation angle of the spray. The swirl direction of the flow for nozzle 1 was about 10° inclined because of tangential flow. Consequent inclinations for nozzles 2 and 3 were 12° and – 6°. Flow rates did not affect the swirl direction angles.

Liquid sheet breakup

The water flow in the inlet pipe before the swirl chamber could be calculated as turbulent for all cases. Although the swirl chamber may have allowed some space for decreasing turbulence (nozzles 1 and 2), turbulence was still visually detected in the liquid sheet exiting the nozzles. For nozzle 3, the guiding vanes might have increased the turbulence inside the swirl chamber. Example images of the spray appearance are presented in **Fig. 14**.

Nozzles 1 and 2 form a conical thinning sheet, which breaks up and forms ligaments and droplets. The main sheet breakup mechanism for nozzle 1 was wave formation. The sheet breakup mechanism for nozzle 2 was both wave formation and sheet perforations.

Although nozzle 3 did not form a clear liquid sheet, the centrifugal force directed the liquid into a conical shape. Being essentially different compared to tangential swirl type nozzles and splash-plate nozzles, nozzle 3 may be appropriate for special cases. The droplet size is probably larger than can be produced with nozzles 1, 2, or splash-plate nozzles when the spraying practice is similar for these nozzles. Small opening angles allow deeper penetration compared to nozzles 1 and 2.

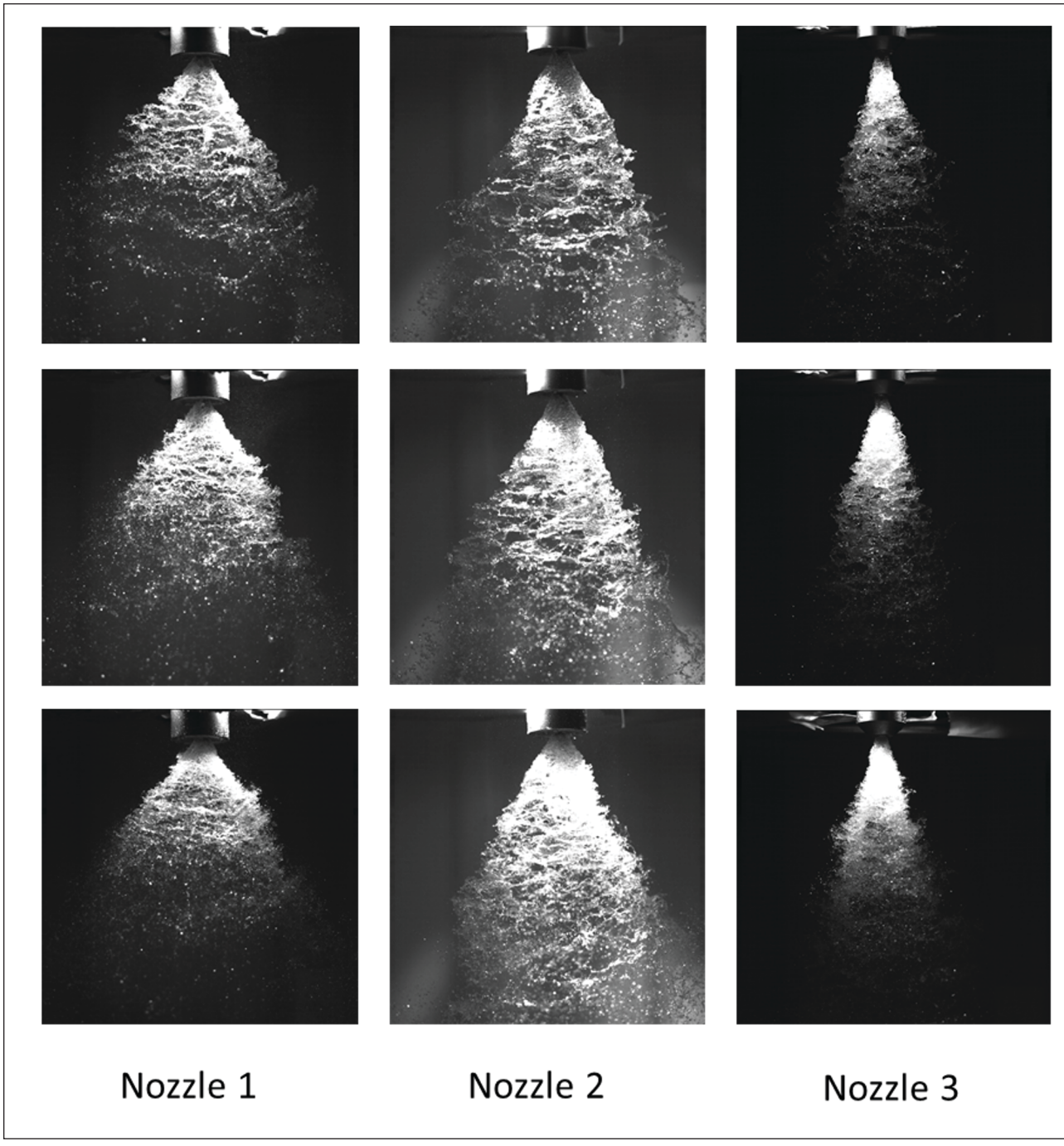

14. Spray breakup. Flow rate increases downwards (1.5 L/s, 2.0 L/s, and 2.5 L/s).

The hollow cone shape causes thinning of the liquid sheet when the distance from the nozzle is increased. This leads to the eventual breakup of the sheet at a certain distance from the nozzle, which is referred to as the breakup length. The estimation for breakup length for nozzle 1 was on average between 8 cm to 12 cm below the nozzle. The breakup length for nozzle 2 was on average 15 cm to 25 cm. The liquid breakup location for nozzle 3 could not be properly estimated, but droplet formation was estimated to begin 20 cm below the nozzle. At constant flow rate, short breakup length leads to large droplets, because the liquid sheet is thick when droplet formation begins. Therefore, nozzle 2 is supposed to form the smallest droplets.

CONCLUSIONS

Simple water spraying experiments were found to be very beneficial for studying and comparing nozzles for black liquor spraying. These kinds of experiments are important for finding better nozzle designs. Appropriate nozzles for black liquor spraying are essentially different compared to

nozzles for any other purpose, mostly because of the large size needed for high flow rates and for large droplets. The experiments here were carried out for rates of 1.5 L/s, 2 L/s, and 2.5 L/s, which are typical values for these nozzle sizes with exit orifice diameters of 22 mm and 17 mm.

The pressure loss of tangential swirl nozzle 1 and nozzle 3 (turbo) were 97% and 38% higher, respectively, compared to tangential swirl nozzle 2. This was an unexpected result and must be considered in nozzle design. The exit orifice area of nozzle 3 was only 60% of the exit orifice area of nozzles 1 and 2. Nevertheless, the pressure loss of nozzle 3 was between pressure losses of nozzles 1 and 2. High pressure loss increases pumping expenses.

The spray opening angel for nozzle 1 was roughly 75°, and for nozzle 2, the opening angle was 60°. Nozzle 3 had smallest opening angle at only 35°. Opening angles slightly increased when flow rate was increased. A large opening angle distributes the spray smoothly to the char bed, but it easily leads to spraying the furnace walls. A small opening angle may increase spray penetration and allows precise targeting to the char bed.

An interesting finding was that the spray of nozzle 1 was asymmetric concerning both bend angle and spray patternation. Video images showed that the spray centerline was inclined by 5° from the nozzle centerline. Interestingly, the inclination for nozzle 2 was only 3°, but toward a different direction. Nozzle 3 was inclined by 3°. Flow rates did not affect the inclination.

ABOUT THIS PAPER

Cite this article as:
Kankkunen, A., Koivisto, S., Saari, K., et al., *TAPPI J.* 21(2): 95(2022). https://doi.org/10.32964/TJ21.2.95

DOI: https://doi.org/10.32964/TJ21.2.95

ISSN: 0734-1415

Publisher: TAPPI Press

Copyright: ©TAPPI Press 2021

About this journal

Spray patternation showed that liquid was distributed unevenly to different spray directions. When liquid distribution was divided into eight sectors, the minimum and maximum volumes for nozzle 1 were 9% and 16%, respectively, at opposite sectors. For nozzle 2, minimum and maximum volumes were 11% and 15% at opposite sectors. Nozzle 3 had its minimum and maximum liquid volumes in contiguous sectors, 6% and 20%. The most symmetric was nozzle 2 with a patternation index of 10, and the most asymmetric was nozzle 3 with a patternation index of 28. Increased flow rates decreased asymmetry for all nozzles.

The spray velocity measured by LDA for nozzle 1 increased from 9 m/s to 15 m/s when flow rate was increased with a 67% larger exit orifice area.

For mills, the methods or measurement results presented here can be used to compare nozzles for different purposes. As a next step, similar measurements with black liquor or with an analogous substitute fluid should be carried out.

ABOUT THE AUTHORS

The pulp and paper industry needs a better understanding of black liquor spray nozzles, and industrial-size, swirl-cone nozzles had not been properly characterized by modern methods before this study.

We found that the liquid distribution of spray angles was difficult to measure because of the very large variations in spray distribution. A high number of small, controllable inlets and the potential to rotate the collector enabled reliable measurements.

We discovered that there are significant differences between nozzles. An interesting finding was that the pressure loss of the nozzle with the smallest exit orifice was less than the pressure loss of a nozzle

Kankkunen is research engineer, Koivisto is research assitant, Saari is laboratory manager, and Järvinen is professor at Aalto University, Espoo, Finland. Biggs is research and development manager at Crenshaw Machine Systems, Bay Minette, AL, USA. Jones is senior engineering Fellow at International Paper in Loveland, OH, USA. Email Kankkunen at ari.kankkunen@aalto.fi.


Kankkunen


Koivisto


Saari


Järvinen


Biggs


Jones

from 1.5 L/s to 2.5 L/s. Consequently, for nozzle 2, the velocity increased from 7 m/s to 11 m/s. Velocities for nozzle 3 increased from 8 m/s to 13 m/s. The velocity increase was in all cases linear with increasing flow rate.

The swirl direction of the flow for nozzle 1 was about 10° inclined because of tangential flow. Consequent inclinations for nozzles 2 and 3 were 12° and – 6°. Flow rates did not affect the swirl direction angles.

Liquid sheet breakup was studied. Nozzles 1 and 2 formed a liquid sheet, which then broke up into ligaments and droplets. Liquid sheet lengths were estimated to be on average 10 cm for nozzle 1 and 20 cm for nozzle 2. Nozzle 3 was not supposed to form a liquid sheet. Nozzle 2 was assumed to form the smallest droplets based on the liquid sheet breakup location.

A lot of differences between nozzles could be detected by water tests. The spray opening angle, the pressure difference, and the velocity were significantly different for these three nozzles. Sprays were not directed along the centerline of the nozzle, and spray mass distributions were asymmetric.

Further studies should be carried out to find similar nozzle properties under in-furnace conditions when spraying black liquor. In-furnace measurements allow many other spray characteristics to manifest, like droplet size and spray trajectories. **TJ**

LITERATURE CITED

1. Adams, T.N., Ed., *Kraft Recovery Boilers*, 1st Edn., TAPPI Press, Atlanta, GA, USA, 1997.
2. Kankkunen, A., "Understanding of black liquor sprays," in *Continuous Development of Recovery Boiler Technology – 50 Years of Cooperation in Finland*, Finnish Recovery Boiler Committee, Helsinki, 2014.
3. Karidio, I. and Uloth, V., "Impact of black liquor firing characteristics on recovery boiler operation," *7th Black Liquor Colloq.*, Jyväskylä, Finland, 2006.
4. Jameel, I. and Pingel, K., U.S. pat. 2011248095 (Apr. 18, 2011).

A model black liquor formulation for use in development and evaluation of membranes for concentrating weak black liquor

SCOTT A. SINQUEFIELD

ABSTRACT: As part of a larger program to develop robust membranes for concentrating weak black liquor prior to the evaporation step, several commercially available membranes were tested for suitability in this application. Given the variation in kraft black liquor for various wood species, the mill-to-mill variations, and the challenges of obtaining fresh samples, the need became apparent for a synthetic reference black liquor that would allow any membrane developer to test a new prototype membrane and compare the results with others.

We present a formulation for a model black liquor (MBL) similar to real kraft black liquor in the composition of the major species that can be formulated from readily available reagents. The MBL was tested with two commercial membranes and resulted in similar levels of lignin retention as the real black liquor. It also showed similar viscosity behavior to real black liquor as a function of solids content.

Application: A recipe for a model black liquor is presented for use in developing and testing robust membranes for concentrating black liquor. The use of a common reference liquor allows developers to directly compare prototype membrane performance to that of other commercial or prototype membranes.

In 2016, Agenda 2020 (now APPTI) [1] identified kraft black liquor (BL) evaporation alternatives as one of five research areas of greatest potential benefit to the industry. APPTI identified membrane-based concentration as the most viable approach [1]. If the weak black liquor leaving the digester could be dewatered from nominally 15 wt% solids to 30 wt% solids before the evaporators, the industry-wide savings are estimated at 23 trillion BTU/year [1]. The remaining water would then be removed with existing evaporators to bring the BL to the 65%–85% solids specification for the given mill.

Beyond the immediate goal of reducing the energy required to concentrate BL, advanced robust membranes would have the potential to fractionate the constituents of BL to produce streams that can be used as feedstocks for production of value-added products. For example, a stream rich in hydroxy acids, resin acids, and lower molecular weight (acetic and formic) acids could be catalytically deoxygenated and converted to higher-molecular weight products such as biofuels, lubricants, and other products. Lignin and hemicellulose could also be fractionated into ranges of molecular weight that are more suitable for producing high-value nanomaterials. Membrane-based BL concentration has been considered since the 1980s [2]. However, the high solids content, pH, and temperature of BL present a very harsh environment for the commercially available nanofiltration and reverse osmosis membranes.

Weak BL enters the evaporators at 90°C and pH from 11.5–13. While some advanced polymer-based nanofiltration membranes are rated for higher pH, it usually limits them to temperatures well below 70°C. There are ceramic membranes rated for 200°C and above, but their high capital cost and lower solute rejection makes them unsuitable for this application. Furthermore, simply rejecting lignin is not enough: any viable membrane process should also reject most of the smaller species (hydroxy acids, salts) at the pH and temperature ranges of BL. These limitations notwithstanding, a market search was done to identify robust commercial membranes for potential use with black liquor, albeit at temperatures below 70°C. A number of candidate commercial membranes were tested with a softwood black liquor using a smaller-scale pilot membrane test facility housed at Georgia Institute of Technology's Renewable Bioproducts Institute (RBI) in Atlanta, GA, USA. Typically, in all types of BL-related research, the BL samples are obtained from a kraft mill. However, shipping restrictions on hazardous materials have grown more stringent over the years, making acquisition of fresh samples a challenge. There is also the issue of considerable BL variation between mills, since there are different wood feedstocks and pulping process variants in use. Thus, it would be useful to have a reference model black liquor that could be easily pre-

pared in-house by any membrane developer or testing laboratory, and then used extensively in the early stages of development and evaluation of candidate membranes. This would also allow direct performance comparisons between different membranes to be tested by different laboratories. If a new membrane performs well with the MBL, it could move on to subsequent testing with real black liquor in laboratory and mill environments.

METHODS

Our goal is to create a MBL that can be made in a laboratory without extensive experience with BL and using easily available constituents. There are many organic reagents that are only sold in gram-sized amounts for analytical calibration, and they usually come at a very high price per gram. The MBL presented here is made from readily available and reasonably priced components. Adams [3] gives the overall solids composition of black liquor shown in **Table I**.

Similar considerations guided the selection of the other chemicals. After considerable experimentation, we have produced the model liquor formulation shown in **Table II**. The source and product code number are listed for each chemical, so that identical chemicals can be purchased or an equivalent option from another source can be determined. The components are mixed with distilled or deionized water to achieve the desired 15%–30% total solids, depending on the final concentration of liquor that is to be used in testing of membranes. Hydrate water should be taken into account. No special procedures are required other than thorough mixing.

Lignin is the organic glue that binds the cellulose fibers together in the wood. It is partially broken down and dissolved in the pulping process but still retains a polymeric structure. It was purchased as a market chemical, also known as Indulin AT (Ingevity; North Charleston, SC, USA). The hydroxy acids category represents many compounds spanning a broad range of molecular weights. They originate from dissolution and degradation of hemicelluloses and some degraded cellulose in the pulping process. The viscosity of the model liquor should be close to that of the real black liquor, as viscosity is expected to affect membrane performance at higher solids content. The most abundant extractive acids in black liquor are steric, oleic, linoleic, and linolenic [4]. For MBL formulation, we use oleic acid, because it is the only one that is commonly available as a reagent. For softwood liquor, there is also a subset of acids called resin acids, of which the major ones are levopimeric, neoabietic, and abietic. Abietic acid is the most readily available and is used for MBL formulation. Galactan is a polymeric form of galactose found in hemicellulose. It is sold over the counter as a dietary supplement. We use it to model the bulk of the hydroxy acid fraction shown in Table I. Acetic acid was selected to model the lower molecular weight spe-

Chemical Species	Wt%	Elemental	Wt%
Alkali lignin	30–45	C	34–39
Hydroxy acids	25–35	H	3–5
Extractives	3–5	O	33–38
Acetic acid	5	Na	17–25
Formic acid	3	S	3–7
Methanol	1	K	0.1–2
Inorganic Sulfur	3–5	Cl	0.04–0.2
Sodium	15–20	Other	0.1–0.3

I. Dry-basis composition ranges of softwood black liquor [3].

Chemical	Grams	Wt%	Source	Product Code
NaOH (anhydrous)	8	8.51	EM Chemicals	CAS 1310-73-2
Na_2CO_3 (anhydrous)	10	10.64	Sigma-Aldrich	CAS 6132-02-1
Na_2SO_4 (anhydrous)	10	10.64	Acros	CAS 7757-82-6
KCl (anhydrous)	1	1.06	JT Baker	CAS 7447-40-7
Acetic acid	8	8.51	EM Chemicals	CAS 64-19-7
Abietic acid	2	2.13	Alfa Aesar	CAS 514-10-3
Oleic acid	1	1.06	Fisher	CAS 112-80-1
Galactan (powder)	20	21.27	Premier Research	Galactan
Lignin (powder)	33	35.11	Sigma-Aldrich	CAS 8068-05-1
Methanol	1	1.06	Fisher	CAS 67-56-1
Dry Total	94	100.00		
Water	532.7	to achieve 15% solids liquor		

NaOH = sodium hydroxide; Na_2CO_3 = sodium carbonate; Na_2SO_4 = sodium sulfate; KCl = potassium chloride.

II. Model black liquor composition (dry basis).

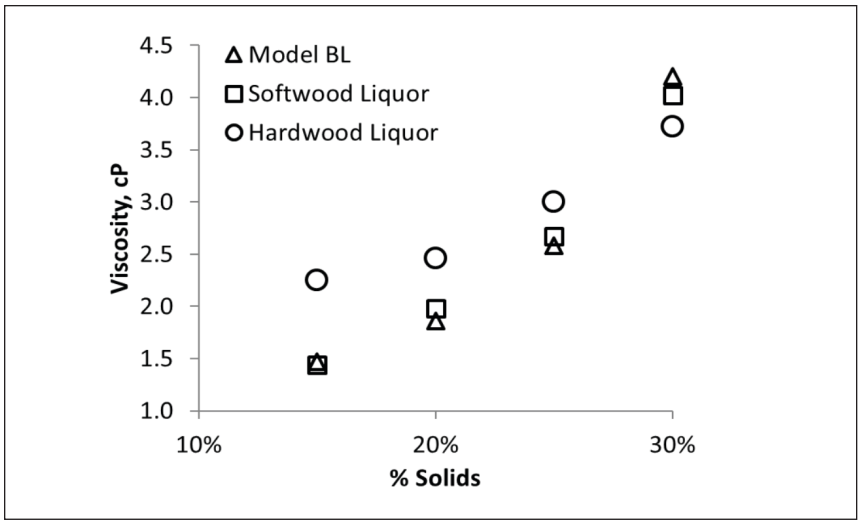

1. Viscosity behavior of model black liquor (MBL) and real liquors at 50°C.

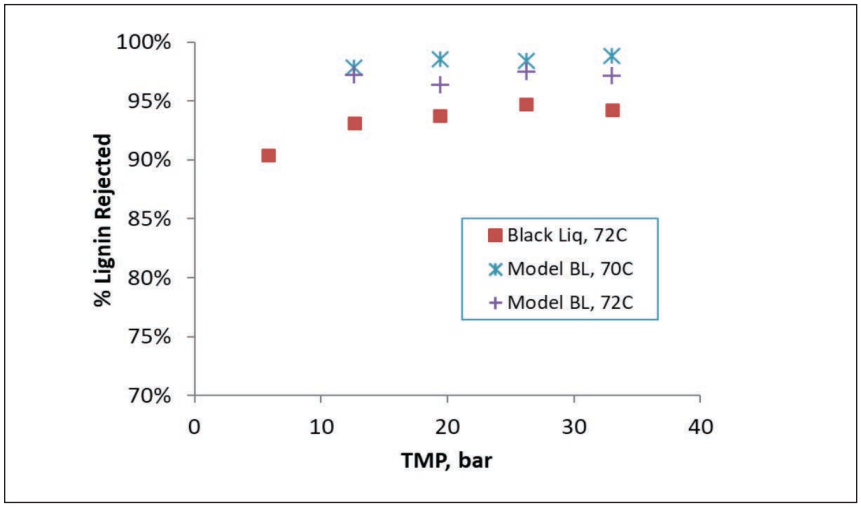

2. Lignin rejection for model and real black liquor through a Microdyn-Nadir NP030 membrane (TMP = transmembrane pressure). Cross flow velocity = 0.64 m/s.

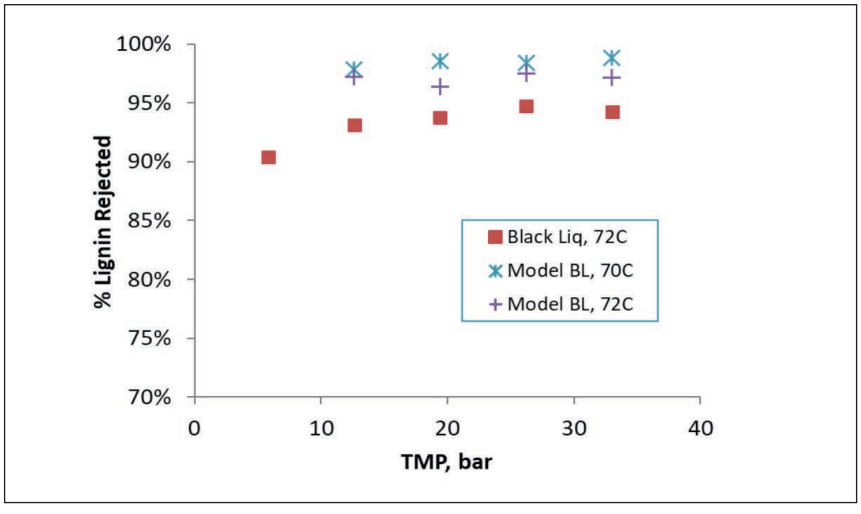

3. Lignin rejection for model and real black liquor through a Koch SelRO MPS-36 membrane. Cross flow velocity = 0.64 m/s.

cies. This is in addition to the actual amounts of acetic acid found in black liquor. The lignin fraction was set at about 35%.

Black liquor contains organic compounds spanning a wide range of molecular weight, which interact to produce non-Newtonian viscosity behavior. **Figure 1** shows the results of viscosity measurements over the range of solids content that membranes would be expected to operate in. The MBL was tested against a hardwood and a softwood liquor at 50°C using a Brookfield LVDV-I Prime viscometer (Brookfield Engineering; Middleboro, MA, USA). The viscosity vs. solids behavior of the MBL is quite close to that of the real liquors.

A membrane separation system for concentration of weak black liquor prior to evaporation would most likely consist of at least two stages: an initial nanofiltration (NF) stage to retain the heavy and medium weight organic compounds, followed by a tighter NF or reverse osmosis (RO) stage to retain most of the inorganic compounds and the lightest organic compounds [2]. A search of commercial membranes revealed a short list of NF membranes nominally suitable for testing with black liquor. Weak black liquor feeds the evaporators at temperatures as high as 90°C, which would rule out all polymer NF membranes. Therefore, we allow for the possibility of cooling the weak liquor to below 70°C for the membrane concentrators and then reheating the concentrated liquor before sending it the evaporators. Counterflow heat exchange would allow for much of the lost heat to be recovered if necessary.

No RO membranes were found sufficiently robust to warrant testing with black liquor. Therefore, the MBL was only benchmarked using lignin rejection in NF membranes. Lignin is the largest organic species in BL and also the most abundant. It is also easily detected by ultraviolet-visible (UV-VIS) absorbance spectroscopy, and it is a convenient measure of performance for the initial nanofiltration stage. We

benchmarked the MBL against two of the tested NF membranes. **Figure 2** shows the lignin rejection in a Microdyn-Nadir NP030 flat sheet NF membrane (Microdyn-Nadir; Wiesbaden, Germany), which is a polyethersulfone (PES) membrane on a polyethylene support and has a rated molecular weight cut-off (MWCO) in the range of 500–600 Daltons. The lignin rejection from MBL at 67°C is quite close to that from real BL. **Figure 3** shows similar results using a Koch SelRO flat sheet MPS-36 (Koch Separation Solutions; Wilmington, MA, USA), a proprietary thin film composite membrane that is rated at 1000 Daltons. In this case, the observed lignin rejection for the MBL is slightly higher than for the real liquor, but it is still quite reasonable and follows the same trends with transmembrane pressure (TMP).

We have used only lignin rejections for membrane benchmarking in this work. Rejections of other species were not measured/benchmarked, since the MWCOs of the two membranes (500–1000 Daltons) would lead to a very low rejection of the other species in both MBL and real BL. Thus, the rejections of these species are not meaningful as a benchmark. Nevertheless, these species (Table II) are still important for simulating the other characteristics of real BL (e.g., viscosity, as seen in Fig. 1), and will become more useful in benchmarking when higher-performance membranes are sought to be tested.

ABOUT THIS PAPER

Cite this article as:
Sinquefield, S., *TAPPI J.* 21(2): 109(2022). https://doi.org/10.32964/TJ21.2.109

DOI: https://doi.org/10.32964/TJ21.2.109

ISSN: 0734-1415

Publisher: TAPPI Press

Copyright: ©TAPPI Press 2021

About this journal

CONCLUSION

The present MBL formulation proposed here exhibits similar viscosity and membrane permeation (e.g., lignin rejection) behavior compared to a real softwood black liquor. The MBL also mimics the pH of real BL. While the exact rejection values for lignin and other species will differ somewhat from real black liquors, the MBL will be a useful tool for initial evaluations of existing and new membranes for suitability in BL concentration applications. The MBL components are readily available and inexpensive and only require mixing together thoroughly with purified water to prepare the MBL, thus eliminating the need to acquire black liquor from a mill for early-stage research and development efforts. **TJ**

ACKNOWLEDGEMENTS

We gratefully acknowledge the support of this work by a consortium consisting of the Renewable Bioproducts Institute at Georgia Institute of Technology, Domtar Corporation, Kapstone Paper and Packaging (now part of WestRock), International Paper, SAPPI, and WestRock. Dr. Alan Rudie of the USDA Forest Products Laboratory also provided valuable input.

LITERATURE CITED

1. Agenda 2020, "Black liquor concentration technology roadmap," Agenda 2020 Technology Alliance, 2016.
2. Kevlich, N.S., Shofner, M.L., and Nair, S., *Sep. Sci. Technol.* (52)6: 1070(2017). https://doi.org/10.1080/01496395.2017.1279180.
3. Adams, T.N., Frederick, W.J., Grace, T.M., et al., *Kraft Recovery Boilers*, TAPPI Press, Atlanta, 1997.
4. Rudie, A., USDA Forest Products Laboratory, personal communication.

ABOUT THE AUTHOR

This study was part of a larger project funded by a consortium of pulp and paper companies. We found that by defining a reference black liquor, membrane performance can be compared by different research labs or membrane manufacturers.

The most difficult aspect of this research was deciding on a small number of compounds to simulate a substance that is composed of hundreds of compounds. To do so, pulping and recovery experts were consulted.

We propose a tool that allows membrane developers to easily test membranes without having to obtain real black liquor. It was interesting to see the close agreement in viscosity behavior between the model and real liquor.

Mills would benefit from the implementation of robust membranes for concentrating black liquor from 15% to about 35%, as the energy savings is substantial. Our next step is continued development and optimization of the robust membranes for black liquor.



Sinquefield

Sinquefield is a senior research engineer at the Renewable Bioproducts Institute, Georgia Institute of Technology, Atlanta, GA, USA. Email Sinquefield at scott.sinquefield@rbi.gatech.edu.

TAPPI JOURNAL
WWW.TAPPI.ORG
THE PAPER AND PACKAGING INDUSTRIES' TECHNICAL RESOURCE
MARCH 2022 | VOL. 21 NO.3



PAPERMAKING **127**
Numerical investigation of the effect of ultrasound on paper drying
Munevver Elif Asar, Zahra Noori, and Jamal Yagoobi

PAPERMAKING **143**
Predicting strength characteristics of paper in real time using process parameters
Shivamurthy Modgi and Kamala Rajan

PAPERMAKING **157**
The Shendye-Fleming OBA Index for paper and paperboard
Awadhoot Shendye, Paul D. Fleming III, Alexandra Pekarovicova, Veronika Husovska, and Kiran Deshpande

WASTEWATER TREATMENT **167**
Considerations in managing wastewater odor at pulp and paper operations
Amanda Johansen Mattingly, Paul Wiegand, and Robert Sackellares

TAPPI Journal NOW FULLY OPEN ACCESS

March 2022

TABLE OF CONTENTS VOL. 21 NO. 3

121 EDITORIAL
Unlock the gates! *TAPPI Journal* moves to fully Open Access research for all
Monica Shaw

127 PAPERMAKING
Numerical investigation of the effect of ultrasound on paper drying
Munevver Elif Asar, Zahra Noori, and Jamal Yagoobi

143 PAPERMAKING
Predicting strength characteristics of paper in real time using process parameters
Shivamurthy Modgi and Kamala Rajan

157 PAPERMAKING
The Shendye-Fleming OBA Index for paper and paperboard
Awadhoot Shendye, Paul D. Fleming III, Alexandra Pekarovicova, Veronika Husovska, and Kiran Deshpande

167 WASTEWATER TREATMENT
Considerations in managing wastewater odor at pulp and paper operations
Amanda Johansen Mattingly, Paul Wiegand, and Robert Sackellares

»**COVER CREDIT**: TAPPI has announced that *TAPPI Journal* content is now fully Open Access to all, increasing visibility and engagement for authors and providing an unobstructed view for researchers, students, and other interested parties (p. 123).

TAPPI JOURNAL
WWW.TAPPI.ORG

Editor-in-Chief
Douglas W. Coffin coffindw@miamioh.edu
+1 513 529-0771

Associate Editor
Peter W. Hart peter.hart@westrock.com
+1 409 276-3465

Editorial Director
Monica Shaw mshaw@tappi.org
+1 770 367-9534

PRESS Manager
Jana Jensen jjensen@tappi.org
+1 770 209-7242

Webmaster
Trina Heath theath@tappi.org
+1 770 209-7416

***TJ* EDITORIAL BOARD**

Brian N. Brogdon, FutureBridge Consulting & Training LLC
brian.brogdon@gmail.com, +1 678 581-9114

Douglas W. Coffin, Miami University
coffindw@miamioh.edu, +1 513 529-0771

Mahendra Doshi, Doshi and Associates
mahen@aol.com, +1 920 832-9101

Marc Foulger, Valmet
marc.foulger@valmet.com +1 315 767-2920

Peter W. Hart, WestRock
peter.hart@westrock.com, +1 409 276-3465

Carl J. Houtman, USDA Forest Products Laboratory
choutman@fs.fed.us, + 1 608 231-9445

Vamsi Jasti, Ahlstrom-Munksjo Nonwovens LLC
jvamsik1@gmail.com, +1 818 585-3524

Lucian Lucia, North Carolina State University
lucian.lucia@gmail.com, +1 919 889-7059

John A. Neun, John A. Neun LLC
john.neun@gmail.com, +1 518 275-8139

Jim Niemiec, Jim Niemiec Consulting LLC
jim.niemiec@outlook.com, +1 715 213-4766

Steven P. Ottone, Omya
steven.ottone@omya.com, +1 919 641-7854

Gaurav Pranami, Imbed Biosciences
gpranami@imbedbio.com, +1 515 230-7005

Arthur Ragauskas, Oak Ridge National Laboratory
aragausk@utk.edu

Seshadri Ramkumar, Texas Tech University
S.Ramkumar@ttu.edu, +1 806 742-4567

Gregg Reed, Imerys
gregg.reed@imerys.com, +1 478 553-5747

Gerard J.F. Ring, University of Wisconsin—Stevens Point
gerrryring@wi-net.com, +1 715 592-3732

Scott Rosencrance, Kemira Chemicals
scott.rosencrance@kemira.com, +1 770 429-2753

Paul Wiegand, NCASI
pwiegand@ncasi.org, +1 919 941-6417

Junyong Zhu, USDA Forest Products Laboratory
jzhu@fs.fed.us, +1 608 231-9520

Join TAPPI *today!*
TAPPI JOURNAL is a free benefit of TAPPI membership, and is only available to members. To join TAPPI, to renew your TAPPI Membership, or to learn about other valuable benefits, visit www.tappi.org.

TAPPI, 15 Technology Parkway S., Suite 115, Peachtree Corners, GA 30092, publishes *TAPPI JOURNAL* monthly.

ATTENTION PROSPECTIVE AUTHORS: All papers published are subject to *TAPPI JOURNAL's* peer-review process. Not all papers accepted for review will be published. Before submitting, check complete author guidelines at http://www.tappi.org/s_tappi/doc.asp?CID=100&DID=552877.

Statements of fact and opinions expressed are those of individual authors. TAPPI assumes no responsibility for such statements and opinions. TAPPI does not intend such statements and opinions or construe them as a solicitation of or suggestion for any agreed-upon course of conduct or concerted action of any sort.

Copyright 2022 by TAPPI, all rights reserved. For copyright permission to photocopy pages from this publication for internal or personal use, contact Copyright Clearance Center, Inc. (CCC) via their website: www.copyright.com. If you have questions about the copyright permission request process, please contact CCC by phone at +1 978 750-8400. To obtain copyright permission to use excerpts from this publication in another published work, send your specific request in writing to Editor, TAPPI JOURNAL, 15 Technology Parkway S., Suite 115, Peachtree Corners, GA 30092, USA; or by fax to +1 770 446-6947. Send address changes to TAPPI, 15 Technology Parkway S., Suite 115, Peachtree Corners, GA 30092, USA; Telephone +1 770 446-1400, or FAX +1 770 446-6947. www.tappi.org

Editorial



MONICA SHAW | EDITORIAL DIRECTOR
mshaw@tappi.org

Unlock the gates! *TAPPI Journal* moves to fully Open Access research for all

TAPPI and the *TAPPI Journal* (*TJ*) Editorial board and staff are pleased to announce that *TJ*'s content is now immediately open access (OA), with no embargoes. In 2020, the journal had adopted a hybrid OA model wherein its peer-reviewed research was free to TAPPI members for one year and then became free to all on the one-year anniversary of a research paper's publishing date. Now, research is immediately accessible to all, increasing visibility and engagement for authors and providing an unobstructed view for researchers, students, and other interested parties.

At TAPPI's Board of Director's meeting in February, Peter Hart, associate editor of *TAPPI Journal* and also a member of TAPPI's Board of Directors, gave a presentation on the benefits of the journal being fully OA, including the fact that its research would serve to advance science and engineering by easily circulating through a broader community that studies the industry.

According to Hart, the move to full OA was unanimously supported by the TAPPI Board. The TAPPI Board wanted to stress the value of *TJ*'s fully peer-reviewed content as a reliable source for industry information, especially for students in the field who frequently search online, as well as the fact that there is no charge for this access or for publishing authors. This sentiment was summarized by TAPPI Board Member Karyn Biasca, professor and chair of the Paper Science and Chemical Engineering Department at the University of Wisconsin – Stevens Point.

"The fact that *TAPPI Journal* is peer-reviewed means that the papers contain reliable technical information. Having these materials available in an open-access format is invaluable. "

– **KARYN BIASCA**, TAPPI Board Member

"The fact the *TAPPI Journal* is peer-reviewed means that the papers contain reliable technical information," said Biasca. "Having these materials available in an open-access format is invaluable. When our students search the internet for literature sources for term papers and design projects, they often find articles that look like good sources but have incorrect information. The variability in technical accuracy concerns me as an instructor and a technical professional in the paper industry. TAPPI should emphasize the peer-review process used before acceptance for publication and the reliability of the information in the journal."

"Our authors are eager to get their research out there. We are confident this move will not only help improve exposure to their research, but also the use and application of the important research contained in each issue, as well as increasing submissions."

– **DOUG COFFIN**, *TAPPI Journal* Editor-in-Chief

Open Access fuels scientific advancements

For a number of years, there has been a push for online journal content in general to be either partially or fully OA so that more institutions and individuals can take full advantage of scholarly literature without a subscription or society membership. The primary idea behind OA journals is that they serve to accelerate scientific advances through greater access to the latest research and to improve online searchability without "gated" content.

Also, many authors, particularly those from academia and research institutions, prefer to publish

their articles in OA journals, because it allows for an author's discoveries and findings to be easily accessed and cited by fellow peers working in their fields.

"The *TAPPI Journal* Editorial Board is very excited about this change," said Doug Coffin, *TJ*'s Editor-in-Chief. "Our authors are eager to get their research out there. We are confident this move will not only help improve exposure to their research, but also the use and application of the important research contained in each issue, as well as increasing submissions."

Many research studies have indicated OA articles receive a significant advantage in terms of the number of citations they receive. More citations serve to improve the visibility of the science, as well as the reputation of a journal. The OA format also helps researchers meet their funding and grant application requirements.

A number of major platforms and publications are transitioning to OA by adopting various types of models, hybrid and otherwise, although many of these require additional fees from authors and readers. These include platforms and organizations like Elsevier, The Royal Society, and American Chemical Society, to name a few.

Additional OA benefits for authors in *TAPPI Journal*

A major advantage for authors who publish in *TJ* is that the are not charged a page or publication fee for their OA research papers. Also, as in the past, the copyright remains with the author.

In addition, authors are considered for the *TJ* Best Research Paper Award and $2,000 Honghi Tran Prize, which is assessed each year by the *TJ* Editorial board and awarded at TAPPICon.

Prospective authors from academic and research institutions, as well as speakers who present scientific papers at TAPPI and other conferences, are encouraged to submit their research for peer review and consideration for publication in *TJ*. You can submit your research through our online system at tappi.org/tjsubmit. **TJ**

For information on publishing in TAPPI Journal*, contact mshaw@tappi.org or tjournal@tappi.org.*

2022 TAPPI Fellows Class includes three members of *TAPPI Journal* Editorial Board



Lucian Lucia



Seshadri Ramkumar

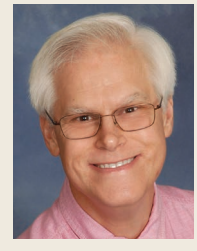

Gregg Reed

In March, TAPPI announced it would bestow the title of Fellow on ten new members, three of whom currently serve on the *TAPPI Journal* Editorial Board: Lucian Lucia, Seshadri Ramkumar, and Gregg Reed.

Fellow is an honorary title bestowed on a small percentage of TAPPI's membership and is given to individuals who have made extraordinary technical or service contributions to the industry and/or the Association. The following is the full list of individuals who were named 2022 TAPPI Fellows:

- Garnet Bremner, Global Technical Specialist, Nalco
- Scott Frasca, Technical Sales Representative, MiniFIBERS, Inc.
- Lucian Lucia, Ph.D., Professor, North Carolina State University
- Kim Nelson, Ph.D., CTO Nanocellulose, GranBio USA
- Tim Patterson, Ph.D., Research Fellow, Solenis
- Seshadri Ramkumar, Ph.D., Professor, Texas Tech University
- Gregg Reed, Ph.D., Technical Manager, Imerys
- Guenter Schubert, Dr. rer. nat., Foil Converting, Senior Scientist R&D, Speira
- Douglas Singbeil, Industrial Sector Leader – Bioproducts, FPInnovations
- Doug Sweet, P.E., President, Doug Sweet & Associates, Inc.

This prestigious group will be honored May 1, 2022, at the Fellows Luncheon during TAPPICon, April 30-May 4, in Charlotte, NC, USA.

Numerical investigation of the effect of ultrasound on paper drying

MUNEVVER ELIF ASAR, ZAHRA NOORI, AND JAMAL YAGOOBI

ABSTRACT: The paper drying process is very energy inefficient. More than two-thirds of the total energy used in a paper machine is for drying paper. Novel drying technologies, such as ultrasound (US) drying, can be assessed numerically for developing next-generation drying technologies for the paper industry.

This work numerically illustrates the impact on drying process energy efficiency of US transducers installed on a two-tiered dryer section of a paper machine. Piezoelectric transducers generate ultrasound waves, and liquid water mist can be ejected from the porous media. The drying rate of handsheet paper in the presence of direct-contact US is measured experimentally, and the resultant correlation is included in the theoretical model.

The drying section of a paper machine is simulated by a theoretical drying model. In the model, three scenarios are considered. In the first scenario, the US modules are positioned in the dryer pockets, while in the second scenario, they are placed upstream of the drying section right after the press section. The third case is the combination of the first and second scenarios. The average moisture content and temperature during drying, enhancement of total mass flux leaving the paper by the US mechanism, total energy consumption, and thermal effect of heated US transducers are analyzed for all cases. Results show that the application of the US can decrease the total number of dryer drums for drying paper. This numerical study is based on the US correlation obtained with the US transducer direct-contact with the paper sample. Thus, future work should include US correlation based on a non-contact US transducer.

Application: In this paper, for the first time, the effect of the application of a US mechanism in a multi-cylinder dryer section is numerically investigated. The results of this study aim to uncover the potential impact of US drying on a paper machine.

Approximately 420 million metric tons of paper were manufactured worldwide in 2018 [1]. Even with modern technologies, papermaking involves an immensely energy-intensive drying operation, which has a great economic significance and contributes to climate change [2]. The energy consumed during the paper drying process corresponds to around 70% of the energy used in papermaking, or by a paper machine [1]. According to the U.S. Department of Energy's report published in 2015 [3], the use of novel drying technologies in paper drying can save 64 trillion Btu annually across the nation's pulp and paper industry. Thus, the effect of enhancing the paper dewatering methods is crucial.

Approximately 90% of paper produced is dried by multi-cylinder dryers [4,5], consisting of 20–120 dryer drums. Paper gets dried by traveling through heated and rotating cast-iron cylinders. Generally, the dryer drums are internally heated by condensing steam, which transfers heat mainly through the conduction mode of heat transfer. Paper entering the drying section has a dry-basis moisture content in the range of 0.82–1.86 after being pressed in the pressing section [6]. Linerboard paper is the most produced paper type in the United States, corresponding to almost one-third of the produced paper in the United States in 2010 [3]. Linerboards are widely used to manufacture corrugated boxes [3]. Therefore, this study focuses on the drying of linerboard paper.

Various researchers studied heat and mass transfer in porous media and paper drying. Nissan and Hansen [7] were one of the first who simulated paper drying, and they divided a dryer drum into four phases, with each phase having a set of boundary conditions. Yagoobi et al. [8] simulated free-water removal during paper drying. That study simultaneously solved transient energy and mass conservation equations in the thickness direction of the paper, considering water vapor fluxes by diffusion and liquid water fluxes by convection. Later, Asensio and Seyed-Yagoobi [9] improved the model by adding the impact of porosity and thickness changes during drying and used better contact conductance correlations between paper and dryer drum surface. Seyed-Yagoobi et al. [10] combined a gas-fired infrared emitter with multiple dryer drums for various grades of paper. They stated that the model was giving [9] predicted experimental data from pilot machine trials very well. Using the same model, paper drying with single and two-tiered dryer configurations was studied numerically, and no significant differences were found between them [11]. In addition, Hoshi et al. [12] demonstrated a transient 1D drying model for paper, placed in between a hot dryer roll and a canvas. This study modeled the water inside and outside

the cell membranes of the wood fiber and treated vapor movement by diffusion and advection and liquid water movement by capillary forces. Similarly, Lu and Shen's model [6] considered convection and capillary transport for liquid fluxes and convection and diffusion transport for water vapor and air fluxes. They verified the model against the data obtained from a working paper machine. Furthermore, Sadeghi and Douglas [13] provided a validated paper drying simulator for cylinder dryers, impingement air dryers, and hybrid dryer configurations for the full range of paper grades. Asensio et al. [14] compared three different paper drying models. A review of main paper drying models can be found in Sadeghi [15]. Overall, most drying models utilize the volume-averaging approach detailed by Whitaker [16]. Few studies [9-11,17-19] have incorporated paper's structural changes during drying into their model, since porosity and thickness changes affect the temperature, moisture variation, and liquid and vapor fluxes during drying.

Wet samples can be dried by ultrasonic waves when the sample is in direct contact or in proximity with an ultrasound-emitting piezoelectric transducer. Piezoelectric transducers generate ultrasound by efficiently converting electric energy to mechanical vibrations. This vibrational energy induces instabilities on the liquid-air interface, and consequently, liquid water mist can be ejected from the porous media [20]. The porous media dries as water mist leaves the boundaries due to the applied ultrasound. In a recent study, Zhang and Abatzoglou [21] extensively reviewed fundamentals, applications, and potentials of ultrasound-assisted drying. They discussed the various ultrasonic phenomena, such as the sponge effect, acoustic streaming, local oscillations, atomization, and thermal effect. These phenomena can enhance mass and heat transfer in the drying of porous media. This study also mentioned the effect of ultrasound on drying efficiency. Furthermore, Peng et al. [20] experimentally investigated the ultrasonic drying of fabrics, using piezoelectric crystal and mesh-type transducers. They verified the capillary wave theory with their data on the atomization of droplets. They reported that the ultrasound-assisted drying process is composed of two modes: water atomization and thermal evaporation. The characterization of these modes depends on the transducer, fabric type, and operating conditions. Patel et al. [22] utilized multiple ultrasonic transducers for fabric drying experiments, and they concluded that ultrasound performed better at higher initial moisture contents for a given applied power. Dupuis et al. [23] studied direct-contact ultrasonic drying with fabrics and presented their non-dimensional equation for ultrasonic dewatering that depended on the surface area of the cloth and transducer acceleration.

Ultrasound-assisted drying can be considered as a novel drying technology for the pulp and paper industry. Thus far, ultrasound (US) drying has mainly been studied for fabric and food products. Therefore, there is a need for studies focusing on the application of the US mechanism within the drying section of a paper machine. In this paper, for the first time, the effect of the application of a US mechanism in a multi-cylinder dryer section is numerically investigated. The results of this study aim to uncover the potential impact of US drying on a paper machine where a direct-contact US correlation is used as a starting point. Direct-contact US results will pave the way for the fundamental understanding of the US mechanism.

THEORETICAL MODEL

The drying section of a papermaking machine is simulated by a theoretical drying model, developed by Asensio and Seyed-Yagoobi [9] for simulating conventional steam-heated, multi-cylinder drying of paper. The model predicts moisture and temperature profiles inside the paper and describes uncoated paper in a two-tiered dryer configuration, as shown in **Fig. 1** (without the US modules). The model is transient and one-dimensional in space (in thickness). Changes in porosity and paper shrinkage due to moisture and temperature variations during drying were considered as described by Asensio and Seyed-Yagoobi [9]. The effect of ultrasound on paper drying was captured by altering the original boundary conditions provided by Asensio and Seyed-Yagoobi [9]. Mass and energy conservation are the governing equations of the model where heat flux, liquid flux, and vapor flux are calculated by Fourier's, Darcy's, and Fick's Laws. For the complete set of governing equations and boundary conditions, one can consult Asensio and Seyed-Yagoobi [9] to fully understand the current study's modeling. The capillary pressure correlation of linerboard [24] is used in the model instead of using a correlation for wood in the original model. A list of the terminology referenced in the following sections is given in the Appendix.

Boundary conditions

Nissan and Kaye [25] divided cylinder drying into four phases, according to the location of interest on a dryer drum. Four drying phases can be seen in Fig. 1. The model developed by Asensio and Seyed-Yagoobi [9] utilizes this four-phase model, which is described as follows.

In Phase I, the bottom surface of the paper sheet is in contact with the dryer surface, and the top surface of the paper sheet is open to ambient air and thus permits evaporation from the top surface. In Phase II, the bottom surface is in contact with the dryer surface. However, the top surface is in contact with felt (porous sheet) rather than being open to ambient air without any restriction, as compared to Phase I. Phase III is similar to Phase I. In Phase IV, the paper travels between two dryer drums and is not in contact with any surface on either top or bottom. Evaporation can occur from both sides of the paper. When paper travels from the beginning of Phase I to the end of Phase IV for a given drum, it completes its residence time for that dryer

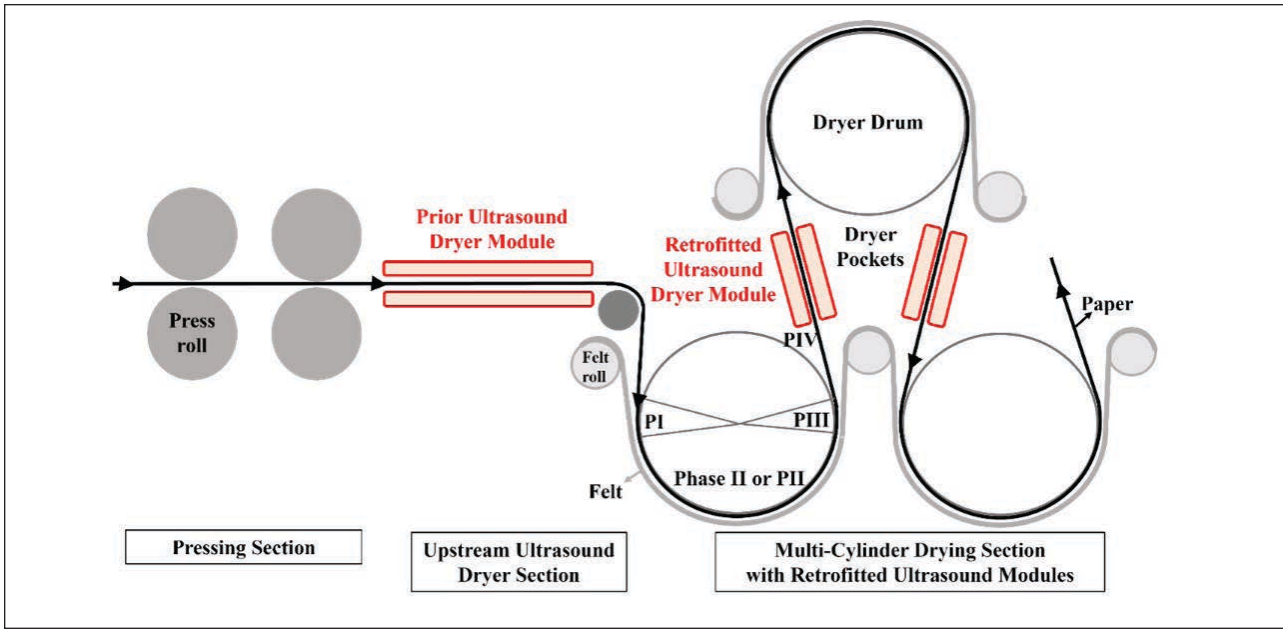

1. Press and dryer section with addition of prior and retrofitted ultrasound (US) dryer modules (in red), along with nomenclature for the four phases of drying,

and moves to another dryer drum until it is dry. Note that top (z=Z) and bottom (z=0) nodes were not located at the physical boundaries; instead, they were located a half-step size into the paper. This approach was also used in the original model by Asensio and Seyed-Yagoobi to simplify the numerical model and is acceptable for small step sizes in thickness direction [9]. This numerical study placed ultrasound modules in the middle half of Phase IV and just before the drying section. If an ultrasound module exists at a location between the dryers or before the drying section, the boundary conditions at that location need to be altered. Here, the effect of ultrasound on the drying mechanism was studied by adding a liquid flux term to the boundary condition equations. This is needed because the water mist generated by the US is in liquid form. Physically, the ejected mist has to leave the porous media from the open boundaries. Enforcing liquid flux at the open boundaries (when the US is applied) will ensure that the liquid mist leaves the paper. Note that the liquid flux at the boundaries not only affects the boundary nodes but also affects the temperature, saturation, moisture content, liquid, and vapor fluxes of the interior nodes as well. This additional liquid flux ($J_{w,o}$), was determined experimentally and described in the "Methodology" section. By utilizing $J_{w,o}$, mass and energy boundary conditions at the bottom boundary (z=0) in Phase IV are updated, as shown in Eq. 1 and Eq. 2. The effect of US can be seen by the second term on the right hand side in Eq. 1 and the fifth term on the right hand side in Eq. 2. The enthalpy for liquid water (H_w) was used in the energy boundary condition when representing the energy leaving the porous media due to the exiting mist.

$$\frac{\partial M}{\partial t} = \frac{1}{\Delta z}(-J_{w,i} - J_{w,o} - J_{v,i} - J_{v,o}) \tag{1}$$

$$\left(c_w \rho_w s\varepsilon + c_f \rho_f (1-\varepsilon)\right)\frac{\partial T}{\partial t} = \frac{1}{\Delta z}\left(k_{eff}\frac{\partial T}{\partial z} - J_{v,i}H_v - J_{w,i}H_w - J_{v,o}H_v - J_{w,o}H_w - h(T - T_a)\right) \tag{2}$$

Similarly, with the presence of ultrasound, the boundary conditions for Phase IV at the top boundary (z=Z) should be updated and are:

$$\frac{\partial M}{\partial t} = \frac{1}{\Delta z}(+J_{w,i} - J_{w,o} + J_{v,i} - J_{v,o}) \tag{3}$$

$$\left(c_w \rho_w s\varepsilon + c_f \rho_f (1-\varepsilon)\right)\frac{\partial T}{\partial t} = \frac{1}{\Delta z}\left(-k_{eff}\frac{\partial T}{\partial z} + J_{v,i}H_v + J_{w,i}H_w - J_{v,o}H_v - J_{w,o}H_w - h(T - T_a)\right) \tag{4}$$

Drying performance during the prior US modules is found using the same governing equations and boundary conditions described above, corresponding to the modified Phase IV boundary condition. In other words, in the prior US section, the length of the phases I, II, and III is zero because there is no dryer drum in the prior US section. The paper experiences the boundary conditions corresponding to the modified Phase IV while passing through the prior US section. Also, to better compare with the baseline case, $J_{v,o}$ term is considered zero at both boundaries while paper

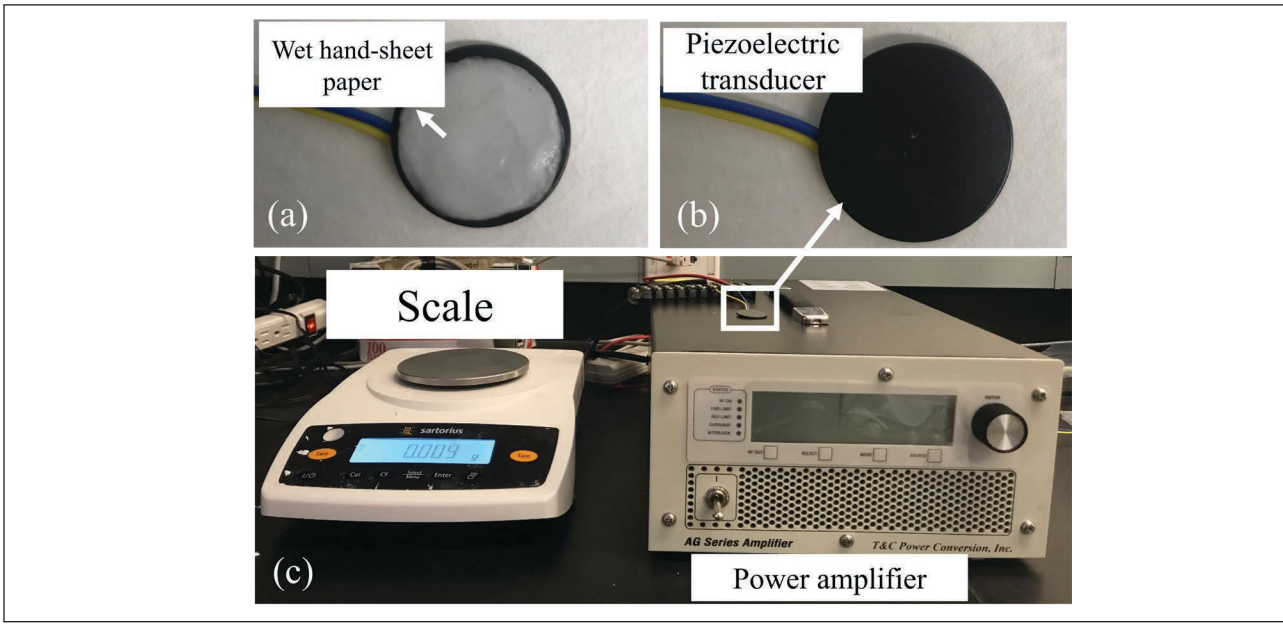

2. Experimental setup for direct-contact US drying experiments: (a) wet handsheet paper on the transducer, (b) a piezoelectric transducer; and (c) the overall setup, including a scale, a power amplifier, and a transducer.

passes through prior US modules. In addition, the temperature of the surrounding air during the prior US section is assumed to be equal to the temperature of the sheet exiting the pressing section. This is an acceptable assumption, because no heat is applied during the prior US section.

METHODOLOGY

Experimental US drying rate correlation

An experimental US drying rate correlation is input into the theoretical drying model to assess the performance of US modules installed on a paper drying machine. This section discusses how this experimental drying rate correlation was obtained. **Figure 2** shows the major components of the experimental setup for direct-contact ultrasound-assisted drying where the fresh 2-cm diameter handsheet papers were used. The preparation of the samples follows TAPPI Standard Test Method "Forming handsheets for physical tests of pulp (Reaffirmation of T 205 sp-02)," and the pressed handsheets have an initial dry basis moisture content (DBMC) of 1.49. Note that there was a slight difference from TAPPI Standard T 205 sp-02 in the final size of the paper. To achieve the smaller paper sizes, short cylindrical molds (with internal diameter=2 cm) were placed before fully opening the sheet maker cylinder's gates very fast (the last step of the sheet-making process according to TAPPI Standard T 205 sp-02 before couching and pressing). The ultrasound drying experiments are conducted at 3W of load power and 1.7 MHz frequency, which corresponds to the manufacturer-specified resonance frequency of the transducer. The sample's top surface is open to the ambient air during the experiments, whereas the bottom surface is in direct contact with the transducer. However, this contact ceased shortly, at every 10 s, when the sample was brought to the scale for weight measurement. The effect of this loss of contact on the drying performance is ignored. The ambient is a standard laboratory environment at ~19°C (with ~50% relative humidity). The experiments are repeated ten times, averages are taken, and the maximum standard deviation of moisture content is within 4% over the entire drying time during the experiments.

Figure 3a represents the average DBMC, where Fig. 3b shows the corresponding drying rate with respect to drying time for conditions in **Table I**. The drying rate was estimated by taking a derivative of DBMC and multiplying it with basis weight (BW). The derivate was taken by second-order central differencing. Generally, higher moisture content levels result in higher drying rates because more water is available for the ultrasound to generate mist. Other researchers also observed similar results. Patel et al. [22] reported that ultrasound performed better at higher initial moisture contents for a given applied power. Also, the drying rate is relatively lower than the

BW	Pressing	$WBMC_{init}$	$DBMC_{init}$	s_{init}	Fiber Type	th_{fin}	Sample Area
204 g/m²	Applied	0.65	1.86	0.74	Unrefined softwood	0.6 mm	3.08 cm²

I. Parameters for handsheet papers used in the experiments. See Appendix for terms.

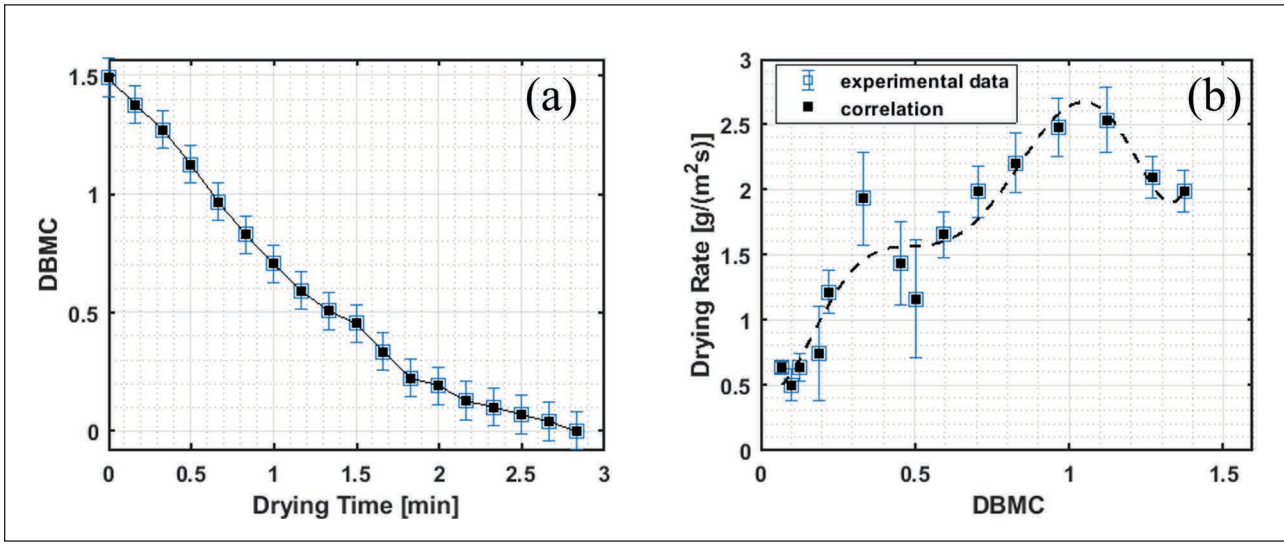

3. Experimental data showing experimental drying curve (a) and drying rate (b) of handsheet paper when in contact with the US transducer (DBMC=dry basis moisture content).

neighboring points at the beginning of drying. This corresponds to the DBMC range of 0.9–1.4. These regions can be called the combined warmup-drying zone due to the initial warm-up of the transducer (and sample) and ultrasonic misting. The increase of drying rate at the early stages of drying can be attributed to this combined warmup-drying zone. That is because the drying rate increases when the sample temperature increases due to decreasing the water viscosity and increasing the vapor saturation pressure.

A drying rate correlation can be found that is a function of the average DBMC and given in Eq. 5. This correlation is also plotted in Fig. 3b. This is the experimental US drying rate correlation (Eq. 5) that is combined with the numerical model, which is based on the combined thermal and ultrasound effects. The effect of transducer thermal load was analyzed and is given in the "Results" section. In addition, this correlation is for unrefined softwood. Thus, using refined paper may yield slightly different results due to the differences explored in Park et al. [26]. It was shown that the beating of fibers changes the fibrillation of the surface [26,27], free water/bound water regions, and freeness [26].

$$\begin{aligned} &\textit{Drying Rate correlation} \\ &= 5.87x10^{-11}(\overline{DBMC}[\%])^6 \; - \; 2.40x10^{-8}x(\overline{DBMC}[\%])^5 \\ &+ 3.62x10^{-6}x(\overline{DBMC}[\%])^4 \; - 0.000248x(\overline{DBMC}[\%])^3 \\ &+ \; 0.007x(\overline{DBMC}[\%])^2 \; - 0.053x(\overline{DBMC}[\%]) \\ &+ \; 0.585\left[\frac{kg}{m^2 s}\right], \end{aligned} \tag{5}$$

$$R^2 = 0.97 \text{ for } 0.07 \leq \overline{DBMC} \leq 1.38$$

Numerical analysis

Highly coupled governing equations and the given set of boundary conditions were solved numerically via MATLAB (Mathworks; Natick, MA, USA) using finite difference methods. For time marching, a fully explicit Euler method was used. Time-derivative terms were discretized with first-order finite differencing. The discretization of spatial derivatives was second-order differencing. The model used 12 nodes across the thickness and found a solution at every 0.25 ms to generate the mesh size and time-step size-independent solutions.

The same BW and bone-dry thickness values as the handsheet paper in the experiments were inserted into the numerical simulation. Moreover, numerical simulations were run until DBMC=0.2, because the theoretical model simulated free water removal, not bound water removal, during multi-cylinder drying. Reardon et al. [28] stated that the transition to bound water from free water happens at DBMC <~0.3, while Schennerberger et al. [29] had results of vaporization energy showing that a threshold at DBMC=0.2 is reasonable for focusing on the free water removal region.

RESULTS

The summary of the studied cases is given in **Table II**, whereas the placement of the US modules is illustrated in Fig. 1. Even though the correlation used is for the direct-contact US and the placement of the US modules may introduce some challenges, both retrofitted and prior US cases are studied to illustrate the potential impact of the application of US mechanism in a paper machine. Note that a wrap or "w" is equivalent to the total length of Phases I-IV for the selected dryer, or 5.26 m. Figure 1 shows the prior US cases as a horizontal section, but the prior US section can consist of wraps to conserve space. De-wetting of the cases is predicted for the operating conditions given in **Table III**. It is important to note that most results are based on theoretical calculations.

Cases	Description	Retrofitted US	Prior US
Baseline	Multi-cylinder dryer drums with no US modules.	No	No
R_US_all	Retrofitted US on every dryer at middle-half of every Phase IV.	Yes	No
R_US_first19	Retrofitted US at middle-half of Phase IV for the first 19 dryers.	Yes	No
P_US_10w	US modules installed prior to dryer drum section with a length of 10 wraps.	No	Yes
P_US_5w	US modules installed prior to dryer drum section with a length of 5 wraps.	No	Yes
P_US_5w + R_US_first10	US modules installed prior to dryer drum section with a length of 5 dryer wraps followed by retrofitted US at middle-half of Phase IV for the first 10 dryers.	Yes	Yes

II. Summary of cases (US = ultrasound).

Operating Conditions		Value	Unit
Paper	Basis weight, *BW*	204	g/m^2
	Initial dry-basis moisture content, $DBMC_{init}$	1.00	-
	Initial wet-basis moisture content, $WBMC_{init}$	0.5	-
	Initial saturation, s_{init}	0.41	-
	Bone-dry thickness, th_{final}	0.6	mm
	Fiber/cellulose density, ρ_f	1500	kg/m^3
	Initial temperature	45	°C
	Permeability	$8x10^{-16}$	m^2
	Specific heat	1340	J/(kgK)
Air	Temperature, T_a (dryer section)	85	°C
	Temperature, T_a (upstream of dryer section)	45	°C
	Humidity ratio	0.12	-
	Sheet speed	6.00	m/s
	Cylinder diameter	1.829	m
	Cylinder surface temperature, T_{su}	120	°C
Machine	Phase I length	0.188	m
	Phase II length	3.089	m
	Phase III length	0.188	m
	Phase IV length	1.794	m
	Length of US modules in Phase IV (if retrofitted)	0.897	m
	Felt tension	3 (17)	kN/m (pli)

III. Operating conditions for numerical simulation.

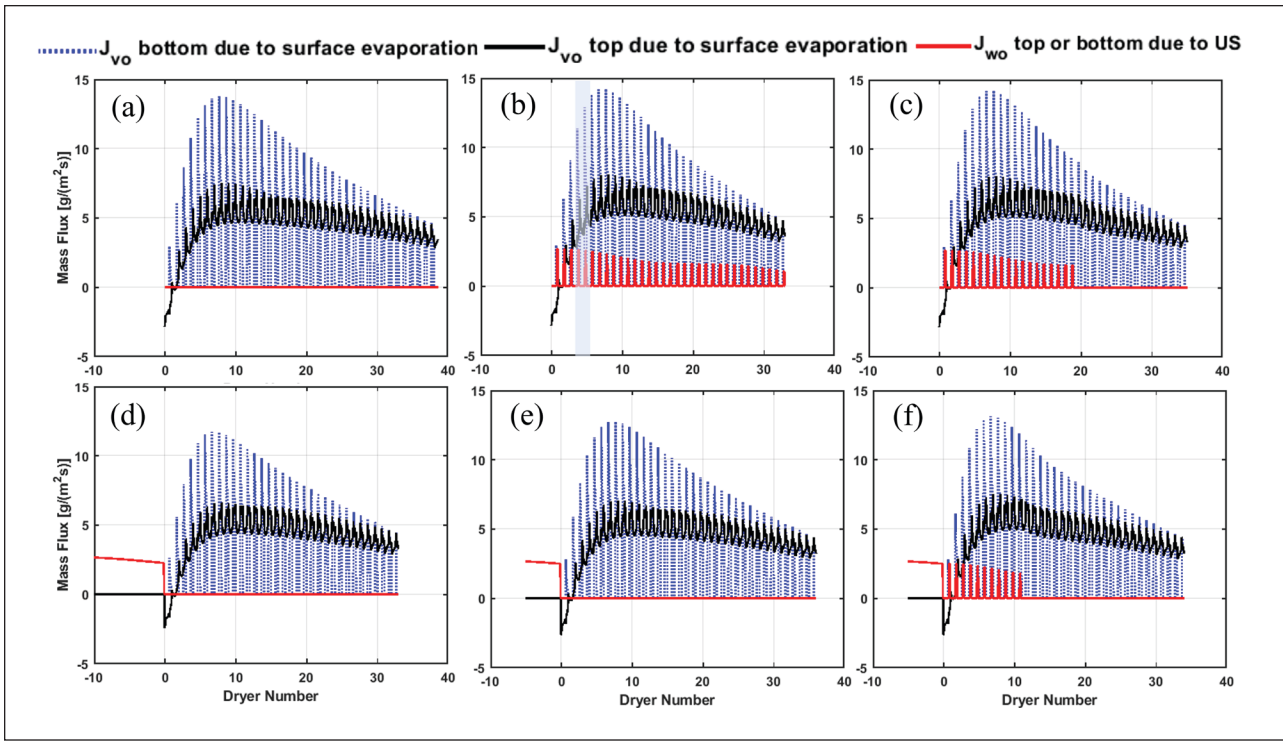

4. Numerical data comparing vapor and liquid mass fluxes that exit the paper vs. dryer number for cases: (a) baseline; (b) R_US_all; (c) R_US_first19; (d) R_US_select; (e) P_US_10w; (f) P_US_5w + R_US_first10. A zoomed version is given in Fig. 5a.

Figure 4 shows the comparisons of water vapor and liquid water fluxes exiting the paper for all the studied cases in Table II. Comparing these fluxes is critical, because the drying rates strongly depend on the mass exiting from the boundaries. The vapor flux due to evaporation ($J_{v,o}$) is illustrated for both the top (z=Z) and bottom (z=0) surfaces. The bottom surface (z=0) is always the surface on the dryer side, and the top surface (z=Z) is on the air side, although the paper flips due to the two-tiered configuration of the paper machine. When the dryer number is negative, it does not correspond to actual dryer drums, but instead, it corresponds to the prior US modules upstream of the dryer drum section. Figure 4a is for the baseline case, and liquid fluxes are zero because there is no US applied. In addition, the vapor flux exits from the bottom boundary (dryer side) are always greater than that of the top boundary (air side), because the bottom node is closer to the dryer and has higher temperatures. Both vapor fluxes increase with time/dryer number in the beginning due to increases in the sheet temperature. This is followed by a decline due to the decreased moisture availability of the surfaces. Note that, at the very early stages of drying, the vapor flux is negative because the surrounding air temperature is higher than the initial sheet temperature, and moisture in air condensates on the paper sheet. This is because the partial pressure of water vapor in ambient air is higher than the saturation pressure of water at sheet temperature when the paper sheet is relatively colder than the ambient humid air.

Figure 4b shows the mass flux comparisons for the retrofitted US case where **Fig. 5a** is a zoomed section of the shaded region of the plot shown in Fig. 4b. As seen in Fig. 4b, $J_{v,o}$ at z=0 is only non-zero when it is in Phase IV, because in other phases, the bottom surface is in contact with the dryer surface, and surface evaporation is blocked. At the beginning of Phase IV, the evaporation at z=0 is relatively high and then drops, as the surface's moisture availability decreases. On the other hand, $J_{v,o}$ at z=Z is always non-zero because the top surface allows for evaporation at all drying phases. At z=Z and in Phase II, $J_{v,o}$ values were multiplied with a factor of 0.8 due to the presence of felt, and the drop in $J_{v,o}$ can be clearly identified from Fig. 5a. Moreover, in Fig. 4b, the solid red line representing the water flux ($J_{w,o}$) due to US $J_{w,o}$ was determined using the experimental drying rate correlation, using corresponding average DBMC at a given time. From the drying rate curve, shown in Fig. 3b, the maximum $J_{w,o}$ value is about 2.5 g/(m²s), which is lower than the evaporation mass fluxes at almost all of the drying section.

For a better comparison, a comparison factor in total mass flux leaving the boundaries is plotted in Fig. 5b. The factor is denoted as C_j and shown in Eq. 6. It represents the percent ratio of total $J_{w,o}$ to $J_{v,o}$ on both sides of the paper. In other words, C_j is the moisture removal rate by liquid form divided by the moisture removal rate by the vapor form. Because $J_{w,o}$ estimation uses the averaged DBMC, the value for a given time's $J_{w,o}$ value is the same for both sides of the paper. Therefore, the numerator in

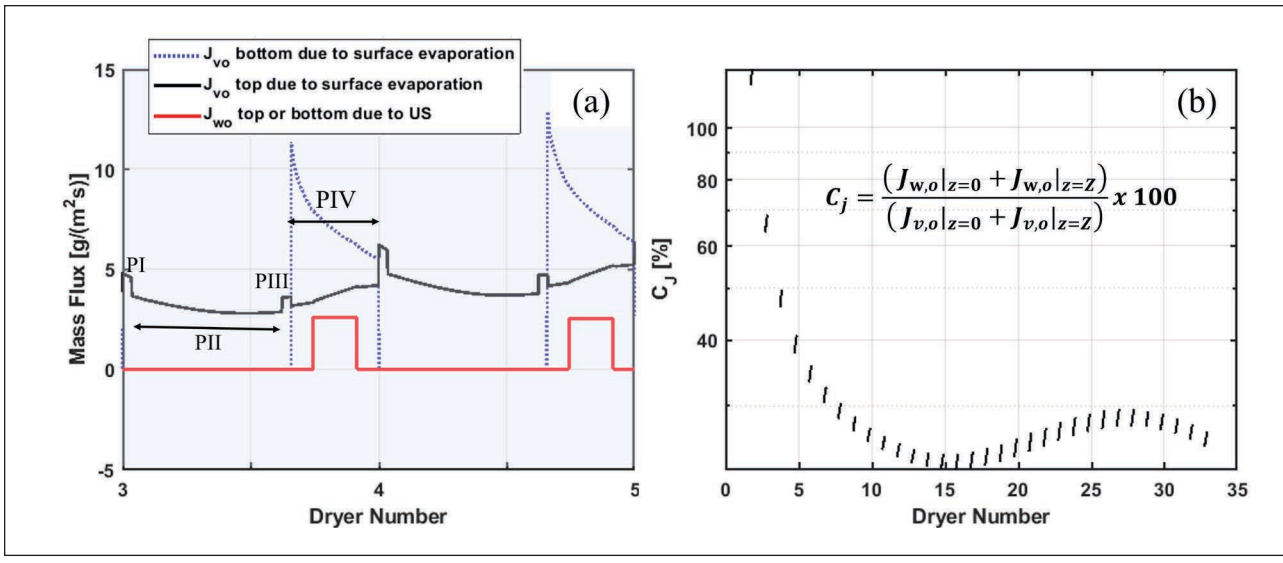

5. Numerical data showing vapor and liquid mass flux comparison vs. dryer number: (a) zoomed image for the shaded area in Fig. 4b; and (b) mass flux comparison at the boundaries for the retrofitted US case (R_US_all).

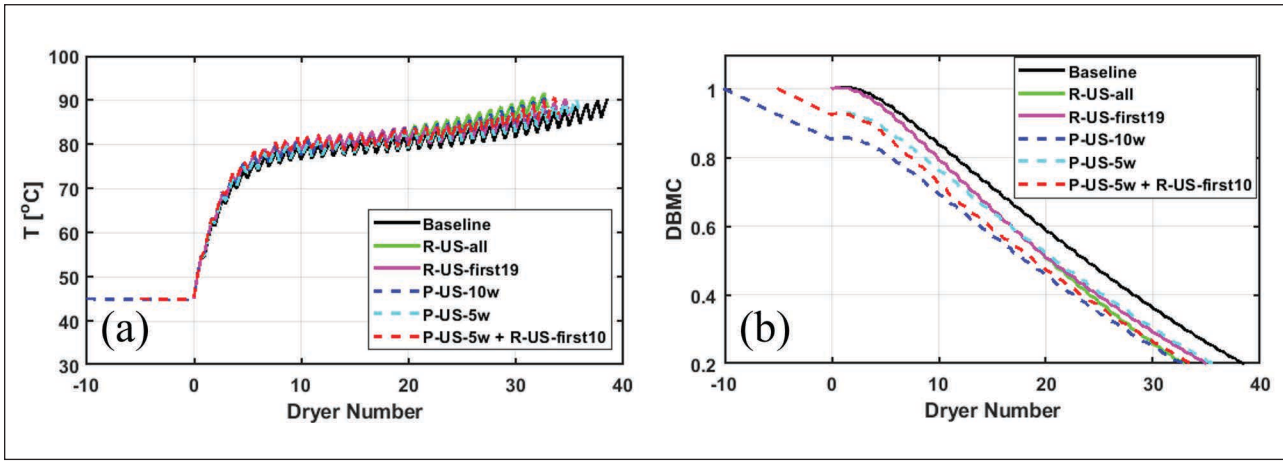

6. Numerical data: (a) average temperature, and (b) average dry-basis moisture content of paper sheet during drying.

Eq. 6 is twice that of $J_{w,o}$ to account for both sides of the paper. C_j is non-zero only when the US is applied and is remarkably high at the first couple of dryers. It starts to decay afterward as the sheet temperature is high enough to allow for much higher surface evaporation fluxes. Towards the end of the drying section, although $J_{w,o}$ is on the decline, C_j rises slightly. This increase in C_j is due to decreases in $J_{v,o}$ because of the limited moisture availability at the boundary nodes for surface evaporation. Although C_j is about 22%–30% when it is non-zero, it is zero most of the drying length because the US is applied on only the middle-half section of Phase IV. Moreover, an average comparison ratio ($\overline{C_j}$) can be calculated by Eq. 7, where t' is the time when paper reaches $\overline{DBMC}$ =0.2 and is 8.9% for R_US_all case.

$$C_j = \frac{(J_{w,o}|_{z=0} + J_{w,o}|_{z=Z})}{(J_{v,o}|_{z=0} + J_{v,o}|_{z=Z})} x\ 100 = \frac{2\ x\ J_{w,o}|_{z=0\ or\ Z}}{(J_{v,o}|_{z=0} + J_{v,o}|_{z=Z})} x\ 100 \quad (6)$$

$$\overline{C_j} = \frac{\int_{t=0}^{t'} (J_{w,o}|_{z=0} + J_{w,o}|_{z=Z})\ dt}{\int_{t=0}^{t'} (J_{v,o}|_{z=0} + J_{v,o}|_{z=Z})\ dt} x\ 100 \quad (7)$$

In the R_US_first19 case, US modules are only retrofitted in the first half of the paper machine. The comparison of the mass fluxes of R_US_first19 is given in Fig. 4c. As expected, after the 19th dryer, R_US_first19 has slightly different vapor flux values than R_US_all. Moreover, Fig. 4d-f demonstrates the cases with prior US modules and

Cases	Total Length of US Modules, m	Average Comparison Ratio ($\bar{C}j$), %	Decrease in Dryer Number	Decrease in Dryer Number, %	Energy Ratio
R_US_all	29.60	8.9	6	15.4	0.67
R_US_first19	17.04	5.8	4	10.3	0.69
P_US_10w	52.6	24.9	6	15.4	0.38
P_US_5w	26.3	11.3	3	7.7	0.38
P_US_5w + R_US_first10	35.27	15.6	5	12.8	0.47

IV. Summary of the results for all cases.

a prior US case when combined with the retrofitted US at the beginning of the dryer drum, respectively. As mentioned previously, surface evaporation is canceled in the model before the dryer drum section to make a fair judgment between the baseline model and the prior US cases.

Figure 6a shows the average temperature of all the cases studied. Alternating boundary conditions for different stages of drying cause fluctuating temperature curves. Sheet temperature increases when the paper is in contact with the hot dryer surface during Phases I, II, and III. On the other hand, sheet temperature reduces in Phase IV because the pocket temperature is lower than the sheet temperature, except at the first dryer drum. The decrease in temperatures during Phase IV is also a result of elevated evaporation rates, considering that both surfaces are available for surface evaporation. Furthermore, the application of the US slightly changes the paper's temperature compared to that of the baseline case. This is expected because the non-zero liquid fluxes at the boundaries not only affect parameters at the boundaries, but also change the internal dynamics of the porous medium, such as local moisture content, vapor and liquid fluxes, etc.

Figure 6b shows the average dry-basis moisture content until DBMC=0.2 for all cases. Prior US modules help to have a drier paper onset of the cylinder dryer section. For example, for P_US_10w, the DBMC of paper reduces to ~0.85 from 1.0 after the paper passes through the prior US section. In addition, for all cases, the paper's initial temperature is lower than the surrounding air temperature, and moisture condensates on relatively cold paper. This results in an increase in DBMC at the very early stages in the cylinder-dryer section. Furthermore, all US cases result in a decrease in the required number of dryers.

Decrease in required dryer numbers and total length of US modules, average comparison ratios ($\bar{C}_j$), and energy ratios are tabulated in **Table IV**. Energy ratio compares the US cases to the baseline case and is given in Eq. 8. At a given location or time (t) during the drying process, the difference between the mass of water ($\Delta\bar{M}|t$) is calculated between the baseline and US cases. The numerator of the energy ratio is the energy consumed to evaporate $\Delta\bar{M}|t$ using the dryer drums with an efficiency (η_{dryer}) of 0.65 [30,31]. Whereas the denominator corresponds to the total energy consumed by the US modules using an ultrasonic power based (P_{US}) based on the load power and ultrasonic power efficiency (η_{US}) of 0.85. (The current ultrasonic power efficiency was not optimized; however, an optimal design efficiency of ~0.85 can be readily achievable [32].) Therefore, if the energy ratio of a certain US case at the end of drying is higher than 1, that US case consumes less energy to de-wet the same amount of water than the dryer drums, and vice versa.

$$Energy\ Ratio = \frac{\frac{(\Delta\bar{M}|_t)\cdot H_{fg}}{\eta_{dryer}}}{\frac{\int_{t=0}^{t} P_{US}\,dt}{\eta_{US}}} = \frac{\frac{(\Delta\overline{DBMC}|_t \cdot BW)\cdot H_{fg}}{\eta_{dryer}}}{\frac{\int_{t=0}^{t} P_{US}\,dt}{\eta_{US}}} \quad (8)$$

The key findings using Table IV and Fig. 6b can be summarized as follows; however, it should be noted that these results are limited to operating conditions and the contact US correlation considered in this study.

- All US cases result in a decrease in required dryer numbers up to 15% (R_US_all and P_US_10w). This finding means that the sheet speed can be increased with the application of the US mechanism when the total number of dryers is kept constant. In other words, if a paper machine adopts US modules, the machine's throughput can be increased by applying the US mechanism.
- Retrofitted US cases can be an advantage to enhance drying, especially for dryer- or space-limited machines.
- Overall, the energy ratio for all the US cases is less than 1. This means that the US requires more energy to dry a moist paper than the baseline case. This implies that the atomization requires more power to vibrate the liquid and generate liquid mist that escapes from the paper than the baseline drying method.

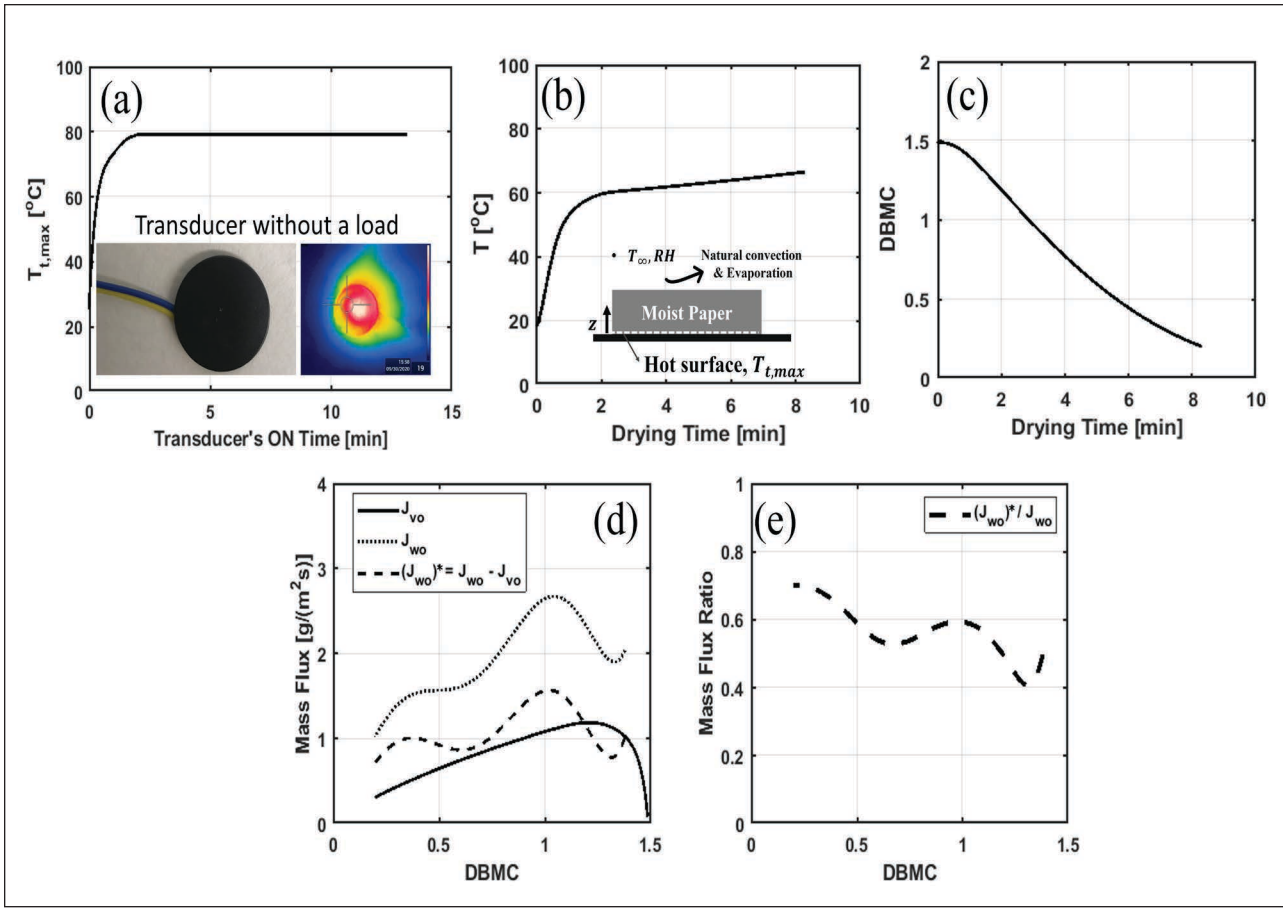

7. Experimental data (a) and numerical data (b-e): (a) maximum measured surface temperature of the transducer ($T_{t,max}$); (b) average temperature of the moist paper when it is placed on a hot surface with $T_{t,max}$; (c) drying curve of the moist sample in (b); (d) vapor flux ($J_{v,o}$) exiting the moist porous medium and liquid flux ($J_{w,o}$) and corrected liquid flux ($(J_{w,o})^*$) for comparison; and (e) mass flux ratio ($(J_{w,o})^*) / J_{w,o}$).

- R_US_all and P_US_10w result in the same decrease in dryer number, although R_US_all's US section is much shorter. This implies that P_US_10w can give an excellent headstart for drying the paper, but the great enhancement at the beginning is not carried on until the end of the dryer drum section. In addition, P_US_10w has a much lower energy ratio than R_US_all.
- Although perhaps it would practically be easier to add prior US modules to a paper machine, it will not be as effective in decreasing the required dryer number (increasing the sheet speed) while decreasing the energy consumption.
- When ten retrofitted US modules are added to P_US_5w, $\overline{Cj}$ and decrease in dryer number are increased, as expected. Also, the energy ratio is increased because retrofitted cases have a higher energy ratio than the prior US module cases.
- When the prior US section's length is doubled, $\overline{Cj}$ and the decrease in dryer number are doubled without compromising the energy ratio. A similar conclusion can be made for the retrofitted US cases.

Proportions of thermal effects and US phenomena

In contrast to non-contact US, drying rate estimated by the direct-contact US contains the thermal effects of the transducer. To assess the overall contribution of the thermal load of the heated transducer to the experimental drying rate correlation ($J_{w,o}$), a numerical analysis is performed. First, the transducer's surface temperature is measured with an IR camera while there is no load on the US transducer. In **Fig. 7a**, the maximum temperature of the transducer is plotted with respect to the transducer's ON time. Then, drying of a moist paper was simulated when it was placed on a "regular" hot plate with a transient surface temperature of $T_{t,max}$. The same governing equations are used as Asensio and Seyed-Yagoobi [9] but with altered boundary conditions to capture the fixed temperature at the bottom and the natural convection and evaporation at the top surface with T_∞=19°C. The convective heat transfer is estimated by the natural convection correlations [33] of a horizontal isothermal surface.

The average temperature and DBMC of the moist paper placed on the hot plate are shown in Fig. 7b and Fig. 7c. As expected, the sample's average temperature follows a

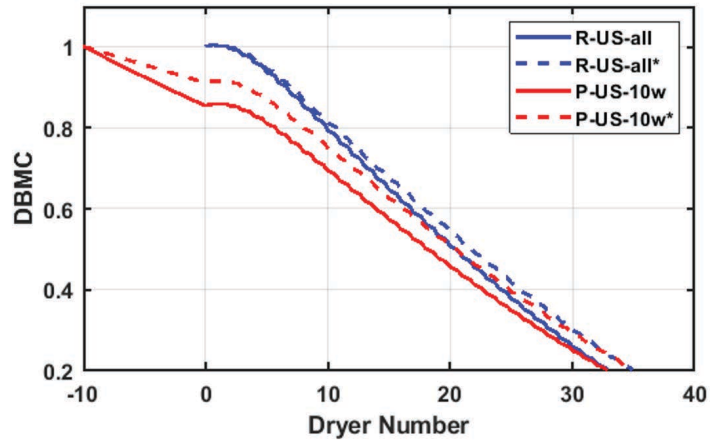

8. Numerical data: DBMC vs. dryer number for US cases with (solid line) and without (dashed line) thermal effect adjustment in the US liquid flux equation.

similar but delayed increase with time compared to the "hot plate" temperature. Figure 7d shows the vapor mass flux that exits the porous medium due to surface evaporation ($J_{v,o}$) at the top surface with respect to DBMC. From the initial DBMC of 1.5 to 1.25, during the initial heat-up period, the $J_{v,o}$ increases as expected. After that, $J_{v,o}$ monotonically declines because of the decrease in the moisture availability at the surface. On the same plot, the original liquid flux ($J_{w,o}$) correlation due to in-contact ultrasound was also plotted for comparison. By a rough estimation, the adjusted liquid flux ($J_{w,o}$)* can be estimated by ($J_{w,o}$) – ($J_{v,o}$) to exclude the thermal effects. To compare the proportions of thermal effects and ultrasound mechanism, ($J_{w,o}$)' is divided by ($J_{w,o}$) and the resultant ratio is called mass flux ratio, as shown in Fig. 7e. The higher the mass flux ratio, the lower the thermal effects on the magnitude of the liquid flux. Overall, the mass flux ratio is around 0.6. Note that this estimation for thermal effects does not explain the possible attenuation of US due to the space between the paper sheet and the transducer when more practical non-contact US is used.

Retrofitted and prior US cases were simulated using the updated liquid flux, ($J_{w,o}$)* and results are shown in **Fig. 8** and **Table V**. The $\overline{C}_j$ of new results (R_US_all* and P_US_10w*) are decreased because of the mitigated liquid flux values. However, both R_US_all* and P_US_10w* still show a 10% enhancement in drying compared to the baseline case. In addition, both cases' energy ratio deteriorates, because the drying performance becomes less effective with the same energy input. It is essential to mention that the paper experienced bulging (lift-off of paper while drying under no pressure) during the US experiments. Therefore, this analysis is an overprediction of the transducer's thermal effects.

CONCLUSIONS

To demonstrate the potential impact of an ultrasound (US) mechanism on paper drying, a numerical study was conducted to simulate a two-tiered configuration of the dryer section on a paper machine in the presence of installed US modules. A US drying rate correlation was used to represent the US drying and was obtained experimentally where the US transducers were in direct contact with the paper samples. A previously validated theoretical model of paper

Cases	Average Comparison Ratio ($\overline{Cj}$), %	Decrease in Dryer Number, %	Energy Ratio
R_US_all	8.9	15.4	0.67
R_US_all*	5.4	10.3	0.39
P_US_10w	24.9	15.4	0.38
P_US_10w*	13.9	10.3	0.23
* Excluding thermal effects in the US drying rate correlation.			

V. The effect of US transducer thermal loads on the numerical model results for selected cases.

drying was adopted, and boundary conditions were adjusted to incorporate the effect of ultrasound using the US drying rate correlation. The US dryer modules were placed in the pockets and/or just upstream of the dryer drum section. It is important to mention that most of the conclusions related to dryers are based on the numerical model, and placing US modules into a paper machine could have some challenges. However, as a novel drying method, US needed to be explored in the field of paper drying to demonstrate the possible impact.

The average moisture content and temperature during drying, moisture removal rates by liquid (due to the US) and vapor forms, and total energy consumption were analyzed for all cases. Results show that the application of US decreases the total number of dryer drums for drying paper. For example, with US modules installed in every pocket, the total mass flux leaving the paper could be increased by up to ~9%, resulting in 15% fewer dryers required to remove the free water from the paper. This means that the paper's sheet speed can be increased for a given dryer number, and throughput can be increased. Furthermore, the scenario where the US modules are installed upstream of the dryer drum section has a much higher drying performance compared to the baseline case at the beginning of drying. Overall, retrofitted US cases seem to have a better drying performance and lower energy consumption than prior US cases. Also, US retrofitting may be a benefit for dryer-limited machines. In addition, thermal effects in the experimental US drying rate correlation were de-coupled or corrected. The corrected correlation was used to generate the effect of the thermal load of the transducer on the paper machine results. With the use of adjusted US correlation, the effect of US reduced to 10% from 15%.

As mentioned previously in this study, the US drying correlation was obtained with a US transducer in direct contact with the paper sample. Direct-contact US transducers are not applicable for a paper drying machine due to the possible breaking and tearing of paper. Thus, future work should apply ultrasound correlation obtained for a non-contact US transducer. In addition, the US drying rate should also be acquired for other types of fibers and other operating conditions, such as transducer load power and US frequency. **TJ**

ACKNOWLEDGEMENTS

This study was financially supported by the U.S. Department of Energy Office of Advanced Manufacturing under Award Number DE-EE0009125 and the Center for Advanced Research in Drying (CARD), a U.S. National Science Foundation Industry University Cooperative Research Center. CARD is located at Worcester Polytechnic Institute and the University of Illinois at Urbana-Champaign (co-site).

LITERATURE CITED

1. Statista, "Production volume of paper and cardboard worldwide from 2008 to 2018," Statista, Hamburg, 2020. Available [Online] https://www.statista.com/statistics/270314/production-of-paper-and-cardboard-in-selected-countries/ <25 Dec 2020>.
2. Shirkole, S.S. and Mujumdar, A.S., *Drying Technol.* 38(14): 1817(2020). https://doi.org/10.1080/07373937.2020.1822080.
3. Miller, T., Kramer, C., and Fisher, A., "Bandwidth study on energy use and potential energy saving opportunities in U.S. pulp and paper manufacturing," U.S. Department of Energy, Washington, DC, 2015.
4. Stenström, S., *Drying Technol.* 38(7): 825(2019). https://doi.org/10.1080/07373937.2019.1596949.
5. Mujumdar, A.S., *Handbook of Industrial Drying*, Dekker, New York, 1987.
6. Lu, T. and Shen, S., *Appl. Therm. Eng.* 27(8-9): 1248(2007). https://doi.org/10.1016/j.applthermaleng.2006.11.005.
7. Nissan, A. and Hansen, D., *AIChE J.* 6(4): 606(1960). https://doi.org/10.1002/aic.690060420.
8. Seyed-Yagoobi, J., Bell, D., and Asensio, M., *J. Heat Transfer* 114(2): 538(1992). https://doi.org/10.1115/1.2911313.
9. Asensio, M.C. and Seyed-Yagoobi, J., *J. Energy Resour. Technol.* 115(4): 291(1993). https://doi.org/10.1115/1.2906435.
10. Seyed-Yagoobi, J., Sikirica, S.J., and Counts, K.M., *Drying Technol.* 19(3-4): 639(2001). https://doi.org/10.1081/DRT-100103940.
11. Asensio, M. and Seyed-Yagoobi, J., *Tappi J.* 75(10): 203(1992).
12. Hoshi, Y., Kuno, H., Takeshita, K., et al., *J. Heat Transfer* 30(2): 77(2001). https://doi.org/10.1002/1523-1496(200103)30:2<77::AID-HTJ1>3.0.CO;2-3.
13. Sadeghi, M. and Douglas, W.M., "From tissue to linerboard: validation of a microscale simulator for single technique and hybrid dryers," *Proc. Int. Drying Symp., 14th*, Unicamp Publishing House, Sao Paulo, 2004.
14. Asensio, M.C., Seyed-Yagoobi, J., Lehtinen, J.A., et al., *Drying Technol.* 13(4): 945(1995). https://doi.org/10.1080/07373939508916992.
15. Sadeghi, M., "Modeling and simulation of transport phenomena in paper drying," Ph.D. thesis, McGill University, Montreal, 2003.
16. Whitaker, S., *Adv. Heat Transfer* 13: 119(1977). https://doi.org/10.1016/S0065-2717(08)70223-5.
17. Coumans, W., "Transport parameters and shrinkage in paper drying," in *Drying 94* (V. Rudolph and R.B. Keey, Eds.), Elsevier, Amsterdam, 1994.
18. Harrmann, M. and Schulz, S., *Drying Technol.* 8(4): 667(1990). https://doi.org/10.1080/07373939008959910.
19. Karlsson, M. and Stenström, S., *Drying Technol.* 23(1-2): 165(2005). https://doi.org/10.1081/DRT-200047951.
20. Peng, C., Ravi., S., Patel, V.K., et al., 125: 498(2017). https://doi.org/10.1016/j.energy.2017.02.138.
21. Zhang, Y. and Abatzoglou, N., *Chem. Eng. Res. Des.* 154: 21(2020). https://doi.org/10.1016/j.cherd.2019.11.025.
22. Patel, V.K., Reed, F.K., Kisner, R., et al., *J. Therm. Sci. Eng. Appl.* 11(2): 021008(2019). https://doi.org/10.1115/1.4041596.

23. Dupuis, E.D., Momen, A.M., Patel, V.K., et al., *Appl. Energy* 235: 451(2019). https://doi.org/10.1016/j.apenergy.2018.10.100.
24. Asensio, M.C., "Transport phenomena during drying of deformable, hygroscopic porous media: Fundamentals and applications," Ph.D. dissertation, Texas A&M University, College Station, TX, USA, 1999.
25. Nissan, A. and Kaye, W., *Tappi* 38(7): 385(1955).
26. Park, S., Venditti, R.A., Jameel, H., et al., *Carbohydr. Polym.* 66(1): 97(2006). https://doi.org/10.1016/j.carbpol.2006.02.026.
27. Maloney, T. and Paulapuro, H., *J. Pulp Pap. Sci.* 25(12): 430(1999).
28. Reardon, S., Davis, M., and Doe, P., *Drying Technol.* 17(4-5): 655(1999). https://doi.org/10.1080/07373939908917563.
29. Schneeberger, M., Leuk, P., Hirn, U., et al., "The heat of sorption in paper drying — an investigation of measurement methods and influence of pulp parameters," in *Advances in Pulp and Paper Research, Trans. XVth Fund. Res. Symp., Cambridge*, 2013 (S.J. l'Anson, Ed.), FRC, Manchester, 2018, pp. 469-492.
30. Kong, L., Hasanbeigi, A., and Price, L., *J. Cleaner Prod.* 122: 5(2016). https://doi.org/10.1016/j.jclepro.2015.12.116.
31. Rahnama Mobarakeh, M., Santos Silva, M., and Kienberger, T., *Energies* 14(4): 1161(2021). https://doi.org/10.3390/en14041161.
32. Patel, V.K., "Ultrasonic clothes dryer," U.S. Department of Energy Office of Energy Efficiency & Renewable Energy, Washington, DC, 2019. Available [Online] https://www.energy.gov/sites/default/files/2019/05/f62/bto-peer-2019-ornl-ultrasonic-clothes-dryer.pdf <08March2022>.
33. Incropera, F.P., DeWitt, D.P., Bergman, T.L., et al., *Principles of Heat and Mass Transfer*, 6th edn., John Wiley & Sons, Hoboken, NJ, 2006.

ABOUT THIS PAPER

Cite this article as:
Asar, M.E., Noori, Z., and Yagoobi, J., *TAPPI J.* 21(3): 127(2022). https://doi.org/10.32964/TJ21.3.127

DOI: https://doi.org/10.32964/TJ21.3.127

ISSN: 0734-1415

Publisher: TAPPI Press

Copyright: ©TAPPI Press 2022

About this journal

APPENDIX

The following is a list of terms used in this paper:

BW	Basis weight, kg/m²
c	Specific heat, J/(kgK)
C_j	Comparison ratio; moisture removal rate by the liquid form/moisture removal rate by the vapor form
C_j	Average comparison ratio
$DBMC$	Dry basis moisture content; weight of water/weight of dry fibers
$\overline{DBMC}$	Average DBMC across thickness direction
D_v	Vapor diffusivity, m²/s
h_i	Interface thermal contact conductance, W/(m²K)

ABOUT THE AUTHORS

Ultrasound (US)-assisted drying can be considered as a novel drying technology for the pulp and paper industry. Thus far, US drying has mainly been studied for fabric and food products. Therefore, there is a need for studies focusing on the application of the US mechanism within the drying section of a paper machine.

In this paper, for the first time, the effect of the application of a US mechanism in a multi-cylinder dryer section is investigated numerically. The most difficult aspect of this research was assessing the US drying mechanism compared to the baseline case.

It was interesting to find that for the operating conditions (experimental and numerical), the ultrasound's atomization requires more power to vibrate the liquid and generate liquid mist to escape from the paper than the baseline drying method.

Through our research, we found that ultrasound can increase the drying performance of a paper machine for mills. Also, retrofitted ultrasound modules can be a great fit for dryer-limited paper machines.



Asar



Noori



Yagoobi

This numerical study is based on the US correlation obtained with the US transducer in direct contact with the paper sample. Thus, future work should include US correlation based on a non-contact US transducer.

Asar is graduate research assistant; Noori is graduate research assistant; and Yagoobi is professor at the Center for Advanced Research in Drying, Multi-Scale Mass and Heat Transfer Laboratory, at Worcester Polytechnic Institute, Worcester, MA, USA. Email Asar at masar@wpi.edu.

H_{fg}	Enthalpy of vaporization of water, J/kg
k_m	Mass transfer coefficient, kg/(m²s)
η_{dryer}	Efficiency of multi-cylinder dryer section
$\eta_{transducer}$	Transducer efficiency
Δz	Step size or distance between two nodes, m
H	Enthalpy, J/kg
J	Mass flux, kg/(m²s)
K	Permeability, m²
k	Thermal conductivity, W/(m K)
M	Mass of liquid water in paper sheet, kg/m³
MW	Molecular weight, kg/kmol
P	Power, W/m²
P	Pressure, Pa
P_US	Prior US module/case where US modules are placed prior to the dryer drum section
$PI\text{-}PIV$	Phase I to IV of drying
q''	Heat flux, W/m²
R_US	Retrofitted US module/case
s	Saturation; volume of liquid/volume of voids
T	Temperature, K
t	Time, s
th	Thickness of paper sheet, m
US	Ultrasound
w	Length that is equivalent to the total length of Phases 1-4 for the selected dryer or 5.2 6m
$WBMC$	Wet basis moisture content; weight of water/total weight
y	Mole fraction
Z	Paper thickness, m
z	Axis across the thickness of paper sheet
ε	Porosity; volume of voids/total volume
ρ	Density, kg/m³

Superscript

(_)*	Excluding thermal effects or adjusted

Subscripts

a	Air
ap	Apparent
atm	Atmosphere
ca	Capillary
eff	Effective
f	Fiber
fin	Final (bone-dry)
$init$	Initial (inlet of dryer section)
max	Maximum
su	dryer surface
t	transducer
v	water vapor
v,o	water vapor to exterior
va	Vapor in air
w	Liquid water
w,o	Liquid water to exterior

Predicting strength characteristics of paper in real time using process parameters

SHIVAMURTHY MODGI AND KAMALA RAJAN

ABSTRACT: Online paper strength testing methods are currently unavailable, and papermakers have to wait for manufacture of a complete reel to assess quality. The current methodology is to test a very small sample of data (less than 0.005%) of the reel to confirm that the paper meets the specifications. This paper attempts to predict paper properties on a running paper machine so that papermakers can see the test values predicted in real time while changing various process parameters.

This study was conducted at a recycled containerboard mill in Chicago using the multivariate analysis method. The program provided by Braincube was used to identify all parameters that affect strength characteristics. Nearly 1600 parameters were analyzed using a regression model to identify the major parameters that can help to predict sheet strength characteristics. The coefficients from the regression model were used with real-time data to predict sheet strength characteristics.

Comparing the prediction with test results showed good correlation (95% in some cases). The process parameters identified related well to the papermaking process, thereby validating the model. If this method is used, it may be possible to predict various elastic moduli (E11, E12, E22, etc.) in the future as the next step, rather than the traditional single number "strength" tests used in the containerboard industry, such as ring crush test (RCT), corrugating medium test (CMT), and short-span compression strength test.

Application: The information presented in this paper is useful for operators to track sheet properties as the paper is being made. It also helps them to understand the effect of each parameter change they make in their day-to-day operation and how it impacts sheet quality.

The only way to measure destructive strength properties of paper today is after it is made by testing it in the laboratory, either using bench top equipment or using automated testing machines. Every jumbo reel takes at least 30–40 min to build, depending on machine speed and various other factors. Conditioning of paper samples and testing takes 15–20 min. During this period, the paper continues to be manufactured without papermakers knowing if it meets customer specifications. If, for instance, this paper does not meet the specifications, then it has to be either downgraded or discarded, thereby resulting in losses for mills. Also, only 0.005% of the total paper is typically tested and that, too, is on the top of the jumbo reel. It is assumed that the paper manufactured during the production of a jumbo reel has not changed in its structure or composition and will produce the same results as it does on top of the reel. This is an assumption on which paper is being manufactured and sold today. However, there could be numerous changes in the papermaking process that might affect the paper quality, either positively or negatively. These changes cannot be traced and related to the sheet properties at present. In a recycled paper mill, these variations might be huge in magnitude, such as, for example, variations in raw material being fed on the furnish conveyors.

Traditionally, the only method of knowing continuous real-time sheet properties was limited to using a scanner that measures basis weight, moisture, caliper, brightness, color, and some special scanners measuring tensile stiffness orientation (TSO) angle. In addition to this, the variation in testing from laboratory to laboratory and person to person will introduce certain errors to mills, as all mills add a safety factor to meet grade specifications. Attempts have been made in the past to utilize real-time adaptive predictions for process and quality optimization to make informed decisions, detect changes, and tune by machine learning principles [1]. Other researchers have used modeling to reduce testing in the mills, mainly by using predictive models after the paper is made. Once the paper is made, the models predict the sheet strength properties that can be used to sell paper. The periodic testing of the paper by technicians ensures the models are in line with the testing equipment. These types of models have reduced testing frequencies and improved quality decision-making. However, this method is not as preventive as the models, because when applied, the paper has already been made [2]. There are also attempts using an online sensor in the scanner to measure extensional stiffness. Due to some unknown reasons, this sensor has not been widely implemented to date [3]. Other research involved in modeling

uses sheets produced on the machine with various process variables and studies in the laboratory. Then, using modeling, this method relates these properties to the paper machine process as to what major variables affect the sheet properties, including press loading, refining energy, freeness, etc. The results were verified with laboratory measurements and experimentation [4]. The combination of laboratory experimentation data and actual sheet tensile strength measurement were also used to potentially predict tensile strength of paper. But without integrating dynamic paper machine conditions, the models are ineffective. Simulations have been used to imitate dynamic conditions for input into tensile strength models [5]. There are other equipment suppliers who use advanced laboratory results for fiber furnish by conducting high-definition image analysis of fiber fibrillation, fiber length distribution, fines content, freeness, and other key morphology to use as soft sensors in dynamic conditions for predicting sheet strength properties. These strength parameters are then compared with the automated paper laboratory and correlated with paper machine process parameters like refining energy, rush/drag, chemical additions, etc., to predict the sheet properties. However, these soft sensors are expensive and need dedicated manpower to maintain and calibrate them [6].

The objective of this paper is to predict sheet strength properties in real time using dynamic paper machine process parameters. The method applies statistical analysis and papermaking knowledge to arrive at simple mathematical models that will allow operators to achieve sheet strength properties that meet customer specifications in real time. Another advantage of this method is that the sheet strength property is continuously derived in real time, thereby ensuring the quality is met throughout the process of making a jumbo reel.

METHODOLOGY

Alsip MiniMill (Alsip, IL, USA) was originally built in 1969 as a newsprint/fine paper mill and was converted to manufacture containerboard in 2015 with a clear vision that it will produce the highest quality containerboard in the United States with the help of a "data-driven culture." The project vision included significant investment in measurement of process variables; a high level of focus on paper physics; automated testing on ABB L&W Autoline 400 (ABB; Zurich, Switzerland); and an integrated quality database by Siemens (Munich, Germany) and Panther (Vancouver, WA, USA) that allows advanced statistical analysis by a software firm such as Braincube (Issoire, France). These are the pre-requirements for the mill's methodology. Prior to implementation, it also requires thorough understanding of the mill's design parameters all the way down to pump curves and equipment capacities.

The offline testing of paper was conducted using bench top equipment for ring crush test (RCT), Concora corrugating medium test (Concora), and short-span compression strength test (SCT). The tensile stiffness index machine direction/cross-machine direction (TSI MD/CD) ratio was obtained through the mill's ABB L&W Autoline products. **Figure 1** shows the Autoline equipment installed in the mill to measure basic paper properties like basis weight, moisture, porosity, TSI, and tensile stiffness orientation (TSO). **Figure 2** shows the Concora tester (ABB L&W Crush Tester Code 248) along with the fluter (Concora Medium Fluter, Liberty Engineering; Roscoe, IL, USA) for the flat crush test of corrugating medium. TAPPI Standard Test Method T 809 om-06 "Flat crush of corrugating medium (CMT test)" is used to measure Concora. The ABB L&W Crush Tester is also used to measure RCT using TAPPI T 818 "Ring crush of paperboard (flexible beam method)." The SCT is performed using an ABB L&W Compressive Strength Tester to measure compressive strength of the corrugating medium according to TAPPI T 826 "Short span compressive strength of containerboard."



1. ABB L&W Autoline automated paper and board testing system used by the Alsip MiniMill.

A very simplistic method was used to develop the predictive models for sheet strength properties. Six months of data from each strength property that was tested using bench top equipment or ABB Autoline was collected, along with the process parameters when the paper was manufactured. The ABB Autoline measures the entire width of the sheet for every reel at 12 points. So, each property for the reel is an average of 12 points across the width of the paper machine. For RCT and SCT, the mill takes an average of 12 points across the width of the paper machine. The values used for developing the model are an average of 12 points across the width of the paper machine. Approximately 1600 variables in the process are used to conduct a multivariate analysis using Braincube software. Process variables from the pressure transmitter, consistency transmitters, flow transmitters, freeness analyzers, and so forth are collected every minute in the database. The multivariate analysis statistically provides process parameters that highly impact

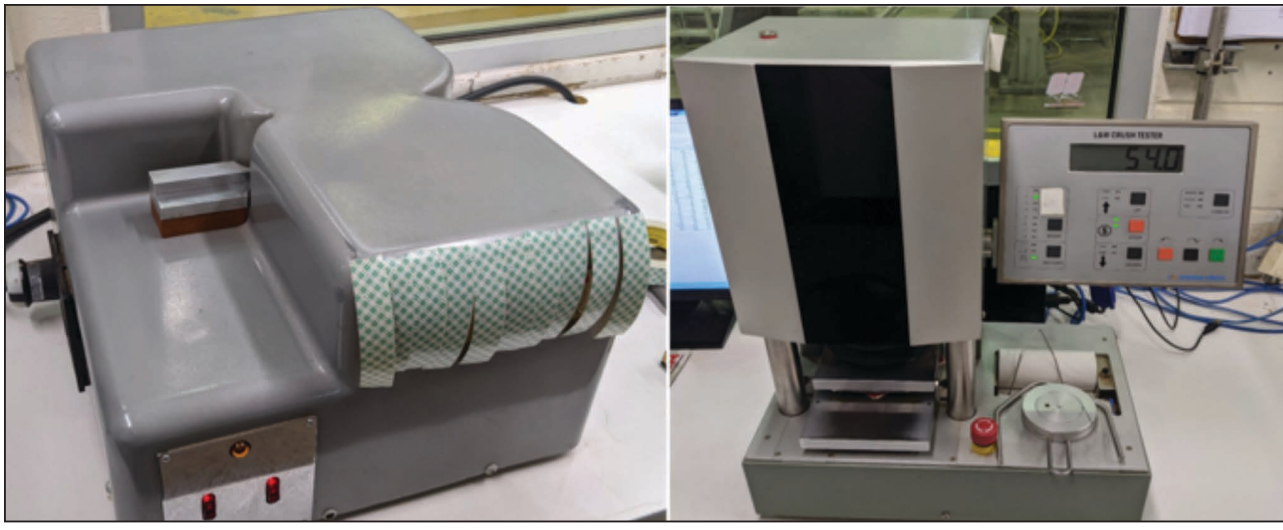

2. ABB L&W fluter (left) and ring crush test (RCT)/Concora tester (right) used by the Alsip MiniMill.

the sheet property being analyzed. Papermaking and paper engineering knowledge is then applied to these process parameters to ensure they make sense. Some data cleaning is required to eliminate blanks or unrecorded entries. The high impact process parameters are selected based on papermaking knowledge and statistics. These parameters are then subjected to multivariate regression analysis. From the statistics, it becomes possible to identify the parameters that have a linear relation to the sheet property under study. This method is iterative, as only the parameters that meet the 95% confidence limits are selected for further analysis. With these coefficients, it is now possible to arrive at an equation that will help to predict the sheet property. Each process variable's coefficients are then used in real time with the process parameter to arrive at the predicted sheet property. The predicted sheet property value is compared to the actual value after the laboratory testing to determine the coefficient of determination (R^2) value to validate the accuracy of the model. Error calculations are also performed to ensure the results are well within the 10%–15% range seen in laboratory-to-laboratory and person-to-person testing variation.

The error percent notifies mill personnel when the predicted model moves away from the actual value, thereby showing when the model needs to be carefully examined. These equations are then entered into the mill's live database to examine whether it can accurately predict the properties. By trending the calculated sheet property with the operator tested property, it was evident that the mill had a model that could accurately predict the sheet properties. Observing the process parameters, it became easy to see how the sheet property changed with process changes. The process parameters used to develop the model were indicative of whether the paper would meet the specifications for the grade. The data was validated for the past data from the historian and also the present ongoing manufacturing data. From both the trends, it became evident that that the mill was able to predict sheet strength properties accurately. This process also identified the key parameters and their operating ranges to meet the sheet quality requirements.

RESULTS AND DISCUSSION

Ring crush test prediction

Ring crush test is one of the main quality parameters that is measured in the mill's process and is used to grade paper. The mill would benefit greatly if it could control and predict this sheet property when the paper is being manufactured. The operators perform RCT every reel and enter it into the mill quality system with the timestamp for when the reel was produced. Six months of the process data during the manufacture of the reels in real time is used to perform multivariate analysis and use the top parameters that can predict the RCT. **Figure 3** shows the correlation between the actual values tested by the operator using laboratory equipment on the X-axis compared to the predicted value through statistical analysis on the Y-axis. The data clearly show a strong correlation between the lab-measured value and the value obtained by the mill's model. The R2 value was 0.95, which shows that the model used to predict RCT is reliable and accurate. The graph shows a grouping of two major data points, mainly due to the different grades manufactured at the mill. Moreover, one single model was able to predict all the grades manufactured on the machine.

The major parameters that showed a strong correlation to predict RCT are shown in **Table I**. Basis weight, headbox static head, rush/drag, and wet suction box-1 vacuum on the Fourdrinier table were the major parameters that affect RCT. It is evident that the sheet strength will always depend on basis weight, which forms the basic structure. The wet-suction box-1 vacuum on the Fourdrinier table is the vacuum element on the mill's Fourdrinier table where the sheet consolidates ("dry line"). It is also evident how the headbox operations are important in obtaining the desired RCT by controlling the rush/drag for fiber orientation and headbox

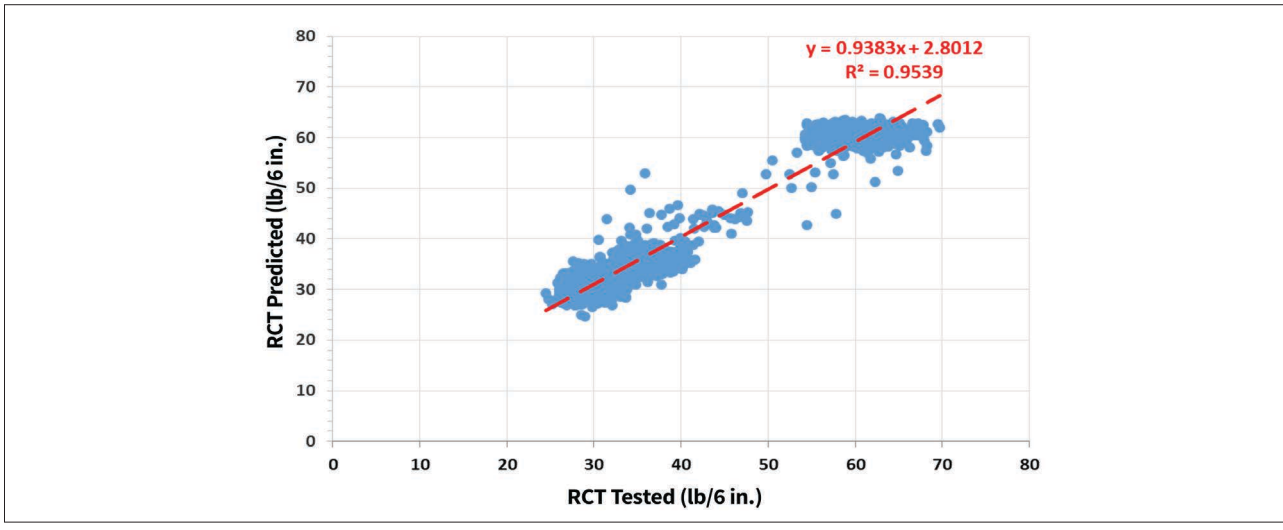

3. Correlation between RCT tested in the laboratory vs. RCT predicted using the model.

Parameters	Influence/Impact
Basis weight average	+ High
Wet suction box No. 1 vacuum	+ High
Rush/drag value	+ Medium
Headbox static head control	- Low

I. Process parameters that affect RCT.

static head for headbox flows. The combination of all these process parameters will ensure the mill achieves the desired RCT. Note that a strong correlation of refining energy or freeness as a parameter that affects RCT was not seen. The refining energy applied at this mill is a constant, and hence was not a major factor in developing RCT.

Once the model for RCT was developed, the operators could manipulate the corresponding variables to achieve the required RCT target for the grade. Also, when making process changes for any reason, they can see the impact of each variable and the trend of RCT to ensure it is in the right direction. The operators also have trends available for watching these individual variables with statistical pro-

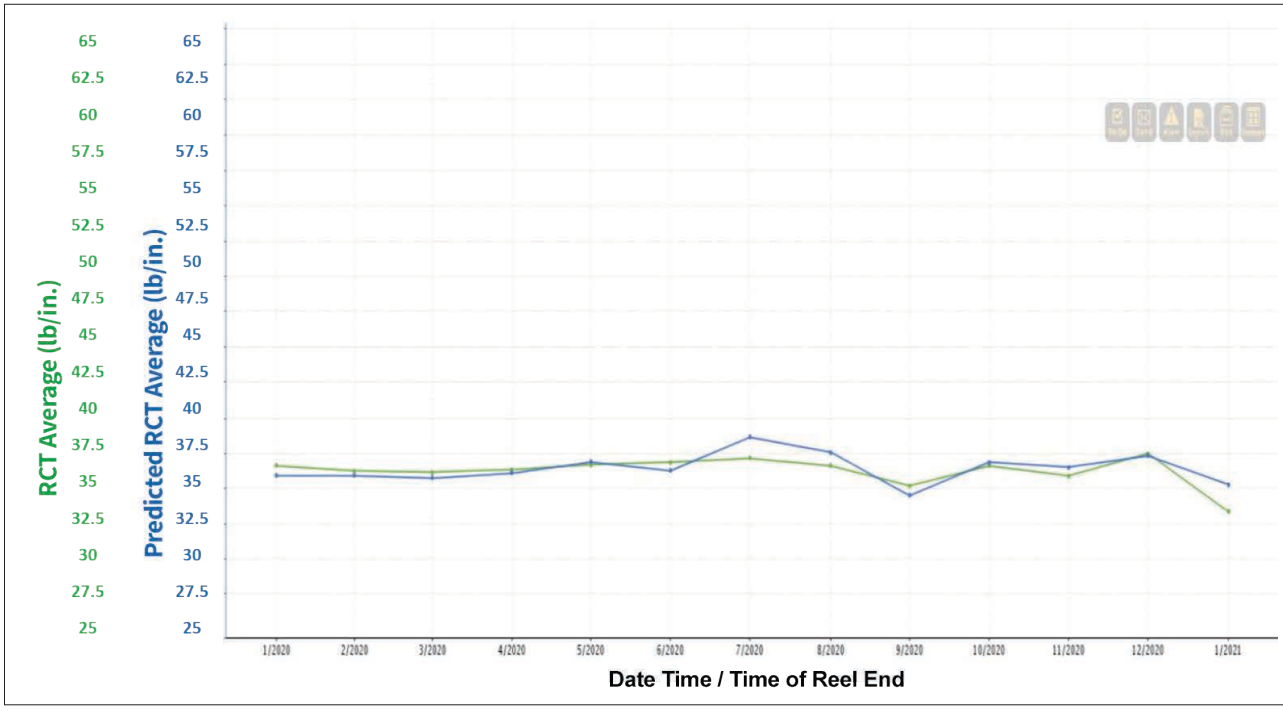

4. Trend between RCT tested in laboratory vs. RCT predicted using the model.

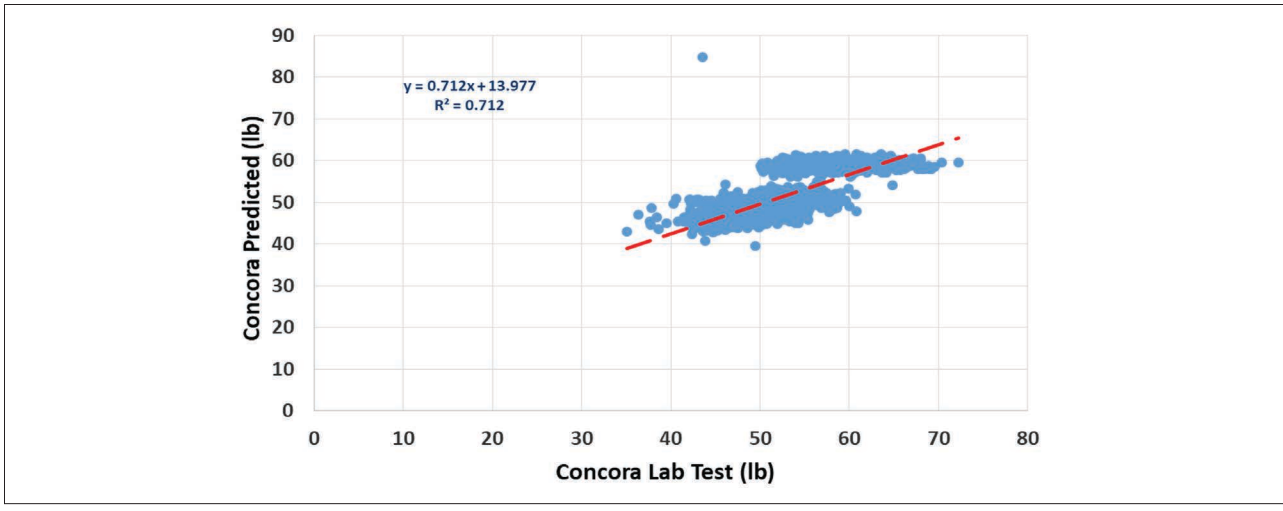

5. Correlation between Concora tested in the laboratory vs. Concora predicted using the model.

cess control charts to ensure they are within the parameters to achieve the grade specifications. This has also helped the mill to optimize various items, such as basis weight and steam usage per ton, to obtain the desired results, leading to consistent operations and cost reduction. This makes quality decisions easier for achieving the desired RCT for the entire reel, for example. One result achieved using these models and their variables was to avoid "over-refining," which affects drying and production rates. The predicted RCT from its variables has resulted in increased speed and optimized basis weight and prevented unnecessary refining energy use.

Comparing the predicted calculated values for a one-year period, it was evident that the model accurately predicts the RCT (**Fig 4**). This accuracy is enough to guide the operators in real time to control and make changes to the process to achieve desired results. They can also troubleshoot RCT problems before the entire reel is manufactured by making necessary changes to the right process parameters to achieve the grade targets. This model also guides them if the changes made are in the right direction. This type of prediction not only helps the mill to meet grade specifications all the time and make prime paper but also optimizes basis weight, reduces refining energy, and increases throughput.

Table II shows the statistics for a period of one year. This confirms that the RCT-predicted value through the mill's models can be used reliably. This statistic represents 9900 reels manufactured during the period.

Concora flat crush of corrugating medium prediction

Concora, as evaluated by TAPPI T 809 om-06, is another important paper property for the mill that is used to meet grade specifications. For grades where the CD property RCT and MD property Concora are both requirements for meeting grade specifications, it becomes imperative for the mill's operators to watch and control these properties to optimize the results. Since both of these properties are attained at the cost of each other, it is a constant challenge to balance between MD and CD direction sheet properties.

Figure 5 shows the correlation between the actual Concora values tested by the operator in the lab on the X-axis compared to the predicted value using the mill's statistically derived model on the Y-axis from real-time process parameters on the paper machine. The R^2 value of 0.71 shows that the model can reliably predict Concora using the real-time process parameters. The mill believes that the R^2 value is slightly lower due to laboratory variation in testing Concora.

With recycled furnish, it becomes more challenging due to the inherent variability of wastepaper, as the process is highly dependent on variations in the raw material used. In order to help the operators, the Concora predictor is used to guide operators to ensure the mill meets grade specifications. With the multivariate analysis, it was found that Concora is dependent on more process variables compared to the RCT. All the process variables were machine parameters. **Table III** shows the process

	Minimum	Maximum	Average	Deviation	1st quartile	Median	3rd quartile
Predicted RCT	32	36.2	33.9	1	33.2	33.8	34.4
Laboratory RCT	30.9	35	33.7	0.997	33.4	34.1	34.2

II. Statistical comparison of laboratory test values vs. predicted values for RCT.

Parameters	Influence/Impact
Bone-dry basis weight +	+ High
Headbox static head control +	+ High
Second press draw +	+ Medium
Rush/drag value -	+ Low
Paper machine dilution screen accepts pressure indication -	- Low
Suction pick-up roll-holding zone vacuum -	- Medium
Headbox stilling chamber pressure -	- High

III. Process parameters that affect Concora or flat crush medium test (CMT).

variables that have impact on Concora and are used in the model to predict Concora on the paper machine. The major parameters that showed the influence on the Concora test were basis weight, headbox operations, and suction pick-up (PU) roll holding zone vacuum. As stated earlier, basis weight will always be the major parameter that affects sheet strength.

It was also evident how headbox operations were important to control the fiber orientation to achieve Concora values. The mill's paper machine is equipped with a dilution headbox where the paper machine (PM) dilution screen feeds the low consistency (LC) header. It was observed that when the dilution screen accepts pressure was high (>46 PSIG), we would see a drop in the Concora values. Dropping this pressure by 2 PSIG saw an increase in Concora values. Investigating this further, it was evident that the design of the ModuleJet headbox (Voith; Heidenheim, Germany) confirms that it affects the fiber orientation, based on the description in the patent [7]. This PM dilution screen controlled the pressure on the LC header of the headbox, which in turn maintained the differential pressure between the LC header and stilling chamber; the higher the differential pressure, the greater the disturbance in fiber orientation. The second press draw also appeared as an important parameter for obtaining Concora; the higher the draw, the higher the Concora, until the sheet breaks. The second press draw is where the sheet is transferred to the second press with a sheet solids of 37%–38%. Here, the sheet is still consolidating, and any pull at this point changes the fiber orientation and lowers TSI CD strength. This helps to improve Concora only if the force is not enough to cause a sheet break or weak spots in the sheet. The first press is a Valmet (Espoo, Finland) Combi Press (ceramic roll against PU roll nip). The holding zone vacuum is important, because this determines how the sheet is sealed and how the water is drained in the first press section. This also impacts the sheet solids coming out of the press section. This is the only open draw on the paper machine. Again, the refiner outlet freeness or refiner specific energy did not show up as an influential process parameter. This

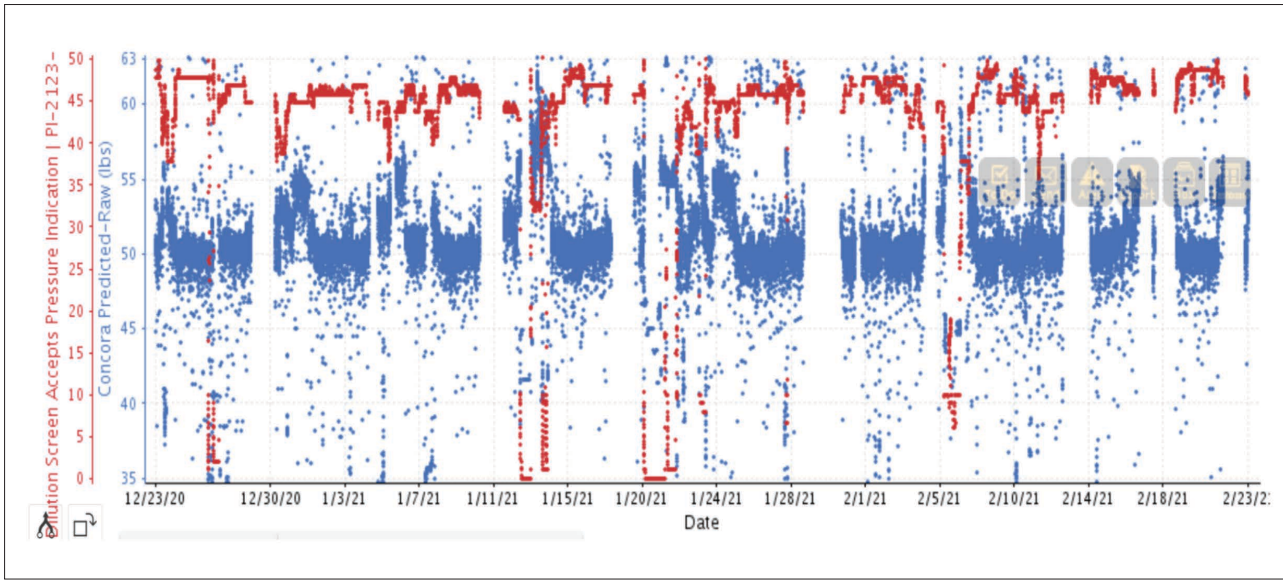

6. Data showing the influence of the mill's low consistency header pressure on Concora.

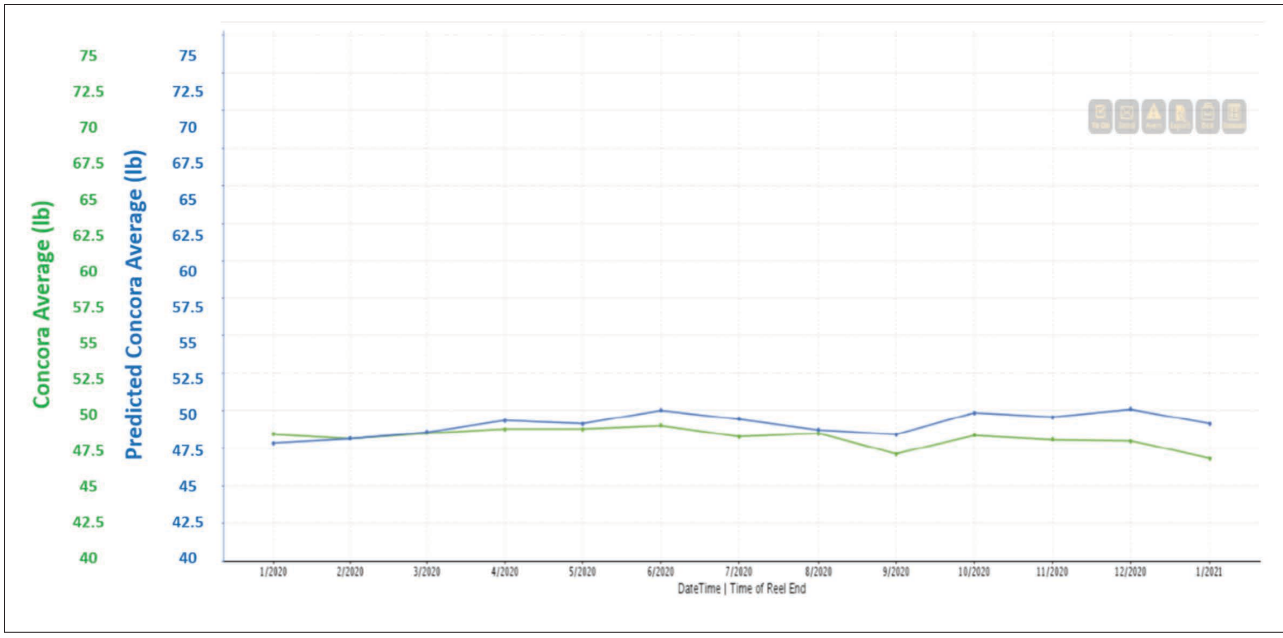

7. One-year trend for laboratory-tested Concora values vs. the predicted Concora values derived from the model.

shows that the mill's sheet properties might not be directly affected by the refining process, because this refining process is stable, with minimal changes. However, the vacuum on the suction PU roll was a factor that shows some relation with refining. However, by using other variables like PM dilution screen pressures, which can be manipulated using the LC header recirculation flow, the mill was able to produce the desired Concora values. This eliminated the use of high refining energy, which impacted the mill's drying rates.

Based on the predicted parameters for influencing Concora, **Fig. 6** shows one of these parameters that negatively influences Concora. As the paper machine dilution screen accepts pressure increases, feeding the LC dilution header of the headbox increases, the Concora decreases and vice versa. This pressure increase or decrease can be managed by using the LC header recirculation valve. This parameter is now used to maintain the Concora specifications. Prior to developing these models, increasing refining energy and increasing recirculation flow of the refined stock were the ways to maintain Concora. This resulted in adverse effects on the paper machine drying capacity, leading to slowdown of the paper machine. Statistical modeling with papermaking knowledge proves to meet Concora specifications, and at the same time, improve productivity.

Figure 7 shows a one-year trend for laboratory-tested Concora values vs. the predicted Concora values derived from the model. It can be clearly seen that the predicted models accurately follow the trend, but the actual values might differ slightly due to various reasons, including variation in paper testing. It can be concluded that the mill was able to predict the Concora values using process parameters.

Table IV shows the statistics for measured values of Concora and the predicted value for 9900 reels manufactured during the period. This confirms that the Concora predicted value from the mill's models can be reliably used.

Short span compression test prediction

By further investigating sheet properties, the mill was also able to develop a statistical model for predicting SCT using process parameters. There were several iterations to the model to arrive at the right model based on statistical interpretation and papermaking knowledge. The SCT was found to be dependent on only two variables; namely, basis weight and rush/drag. All the other variables had negligible or no impact on the outcome of SCT. This might also be machine dependent and process dependent and vary from mill to mill and machine to machine.

Figure 8 shows the correlation between SCT tested on bench top equipment and that was obtained with the

	Minimum	Maximum	Average	Deviation	1st quartile	Median	3rd quartile
Predicted Concora	47.8	50.1	49.1	0.688	48.4	49.1	49.6
Laboratory Concora	46.8	49	48.2	0.601	48	48.4	48.5

IV. Statistical comparison of laboratory test values vs. predicted values for Concora.

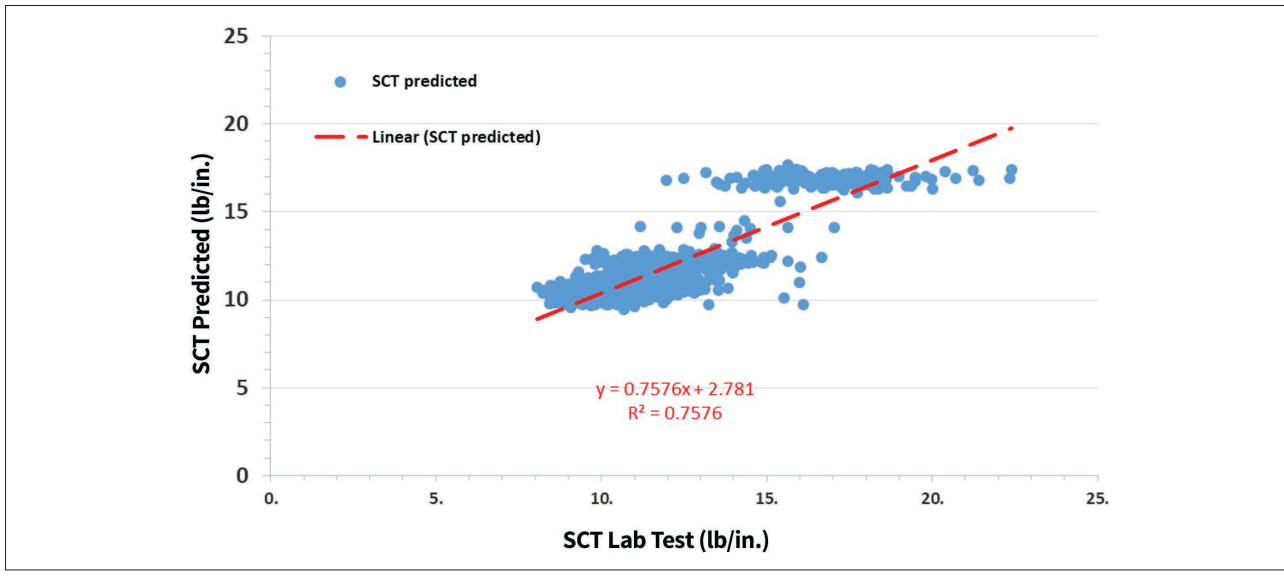

8. Correlation between laboratory-tested short-span compression strength test (SCT) values vs. SCT predicted using the model.

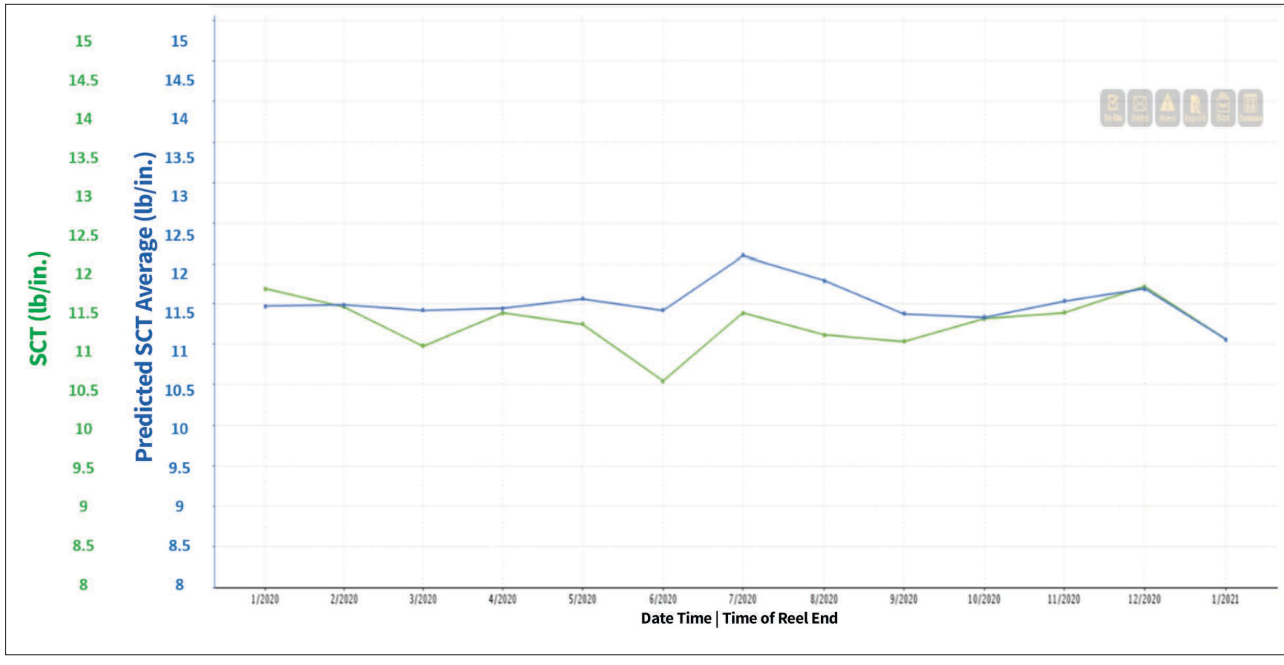

9. One-year trend for laboratory-tested SCT values vs. the predicted SCT values derived from the model.

mill's predicted model. The R^2 value of 0.76 shows that the model can accurately predict the SCT value using process parameters. Comparing RCT and SCT, which are both CD-oriented tests, it was surprising to see that more variables are required to predict RCT compared to SCT. The explanation for this difference is unknown, as the same parameters were used for multivariate analysis and also during the same period. The R^2 value of 0.758 suggests that this is a reliable model.

Figure 9 shows the trend for a period of one year using laboratory-tested data and predicted values from our model. It is also important to note that the mill does not test SCT values for every reel. Based on these trends, it can be concluded that the mill's model can reliably predict SCT values.

Table V shows the statistics for laboratory-measured and predicted values of SCT for 3500 reels manufactured during a period of one year. This confirms that the SCT predicted value through the models can be reliably used.

Tensile stiffness index ratio prediction

Further applying the methodology, the mill looked at the process parameters affecting TSI MD/CD ratio. **Table VI** shows the process parameters that affect TSI MD/CD ratio. It was found that the TSI MD/CD ratio was dependent on the machine draws, low vacuum on the fourdrin-

	Minimum	Maximum	Average	Deviation	1st quartile	Median	3rd quartile
Predicted SCT	11.06	12.1	11.52	0.24	11.38	11.47	11.57
Laboratory SCT	10.5	11.7	11.3	0.305	11	11.3	11.4

V. Statistical comparison of laboratory test values vs. predicted values for short-span compression strength test (SCT).

Parameters	Influence/Impact
Second press draw percentage +	+ High
Basis weight average +	+ Medium
Step foil box No. 3 separator vacuum +	+ Low
Machine speed +	+ Low
First press draw percentage -	- Low
Rush/drag value -	- Low
Suction pick-up roll-holding zone vacuum -	- Low
After-dryer draw percentage -	- High
Wet suction box No. 1 separator vacuum -	- High
Headbox stilling chamber pressure indication -	- High

VI. Process parameters that affect tensile stiffness index machine direction/cross-machine direction (TSI MD/CD) ratio.

ier table, and headbox operations. In fact, one of the draws was the mill's long open draw between the pre-dryer section and after-dryer section due to the absence of the old size press. The model developed showed satisfactory correlation and was dependent on 10 variables. The R^2 value was slightly lower at 0.61. The mill believes that the lower TSI MD/CD is due to the challenge to meet both CD direction strength RCT and MD direction strength Concora. The model would predict more accurately if CD strength and MD strength are maintained independently of each other. **Figure 10** shows the correlation between the laboratory-tested TSI MD/CD ratio using Autoline with that calculated using the mill's statistical model.

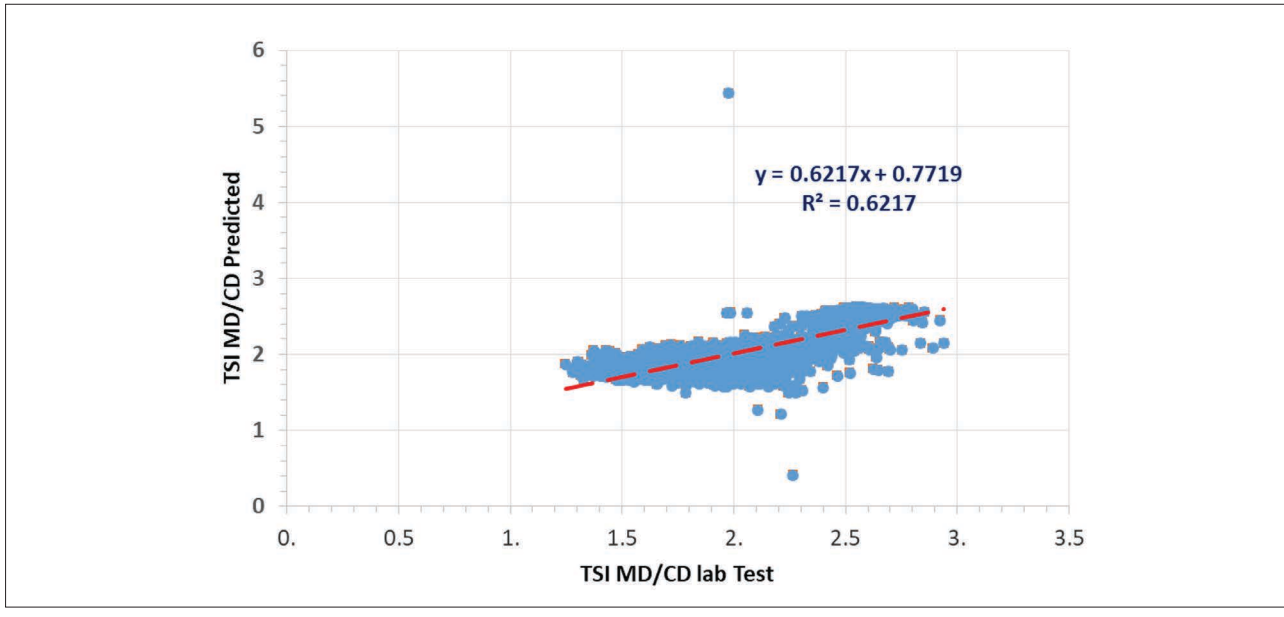

10. Correlation between TSI MD/CD ratio in the laboratory vs. TSI MD/CD predicted using the model.

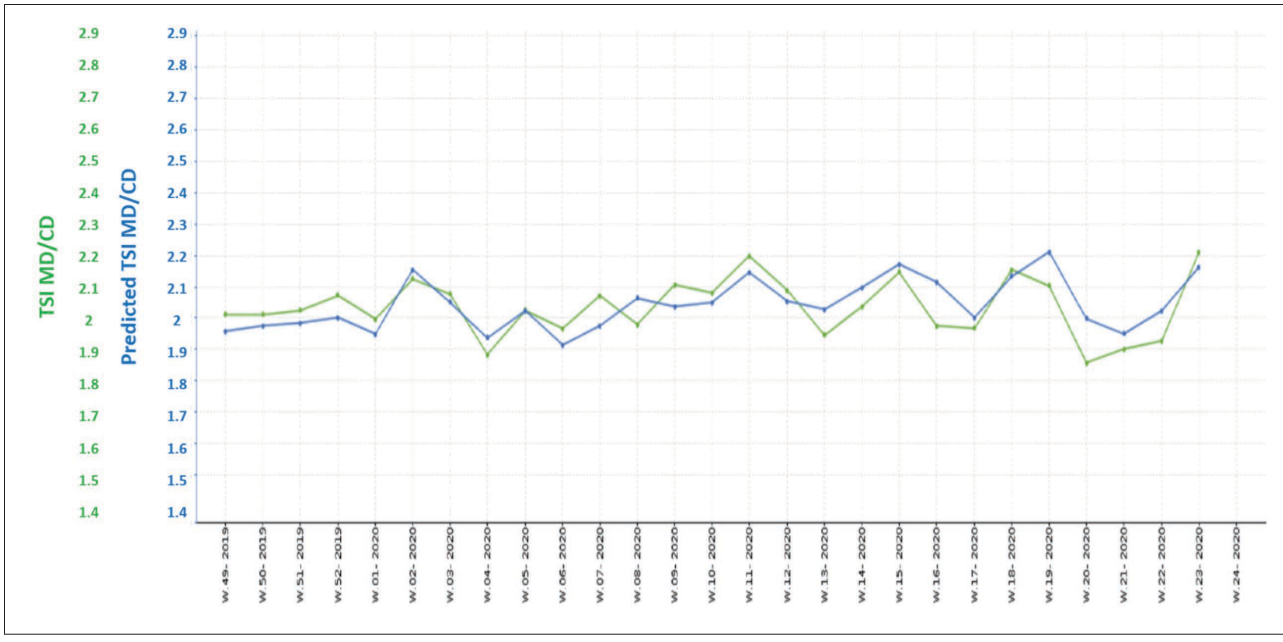

11. Trend between TSI MD/CD ratio in the laboratory vs. TSI MD/CD predicted using the model.

	Minimum	Maximum	Average	Deviation	1st quartile	Median	3rd quartile
Predicted TSI MD/CD	1.98	2.15	2.06	0.049	2.01	2.05	2.11
Laboratory TSI MD/CD average	1.9	2.21	2.25	0.701	1.97	2.06	2.11

VII. Statistical comparison of laboratory test values vs. predicted values for TSI MD/CD.

Figure 11 compares the six-month trend between TSI MD/CD ratio in the laboratory to that obtained by the predicted statistical model. Most of the time, the trend is identical, but the magnitude varies slightly.

Table VII shows the statistics for laboratory-measured and predicted value of TSI MD/CD for 9900 reels manufactured during a period of one year. This confirms that the TSI MD/CD predicted value through the mill's models can be reliably used.

Key performance indicators

The authors gained confidence in the methodology used for predicting sheet strength properties using multivariate analysis. To take it to the next level, the began to apply the same principles to identify the major process indicators that govern key performance indicators (KPIs). The KPIs studied were stock preparation production rates, refiner freeness, press uhle box flows, freshwater flows, production rates, etc. It was evident that these parameters could be accurately modeled and predicted in real time. The major advantage of performing this modeling was to identify the key process parameters that control or affect these KPIs. Controlling these key process parameters using statistical process control will lead to better quality, improved cost, and increased productivity. The mill is now in the process of controlling these process parameters using statistical process control to reap these benefits.

CONCLUSION

In order to improve quality, cost, and productivity, there is a need to use a "data driven decision-making" process in the manufacturing environment in real time. This paper demonstrates the use of statistical data combined with subject matter expertise to achieve desired results. The major focus of this project continues to provide real-time data to the operators and tools to control and optimize the papermaking process. Process parameters obtained using this method resulted in a perfect guide for operators to ensure the process is optimized to provide the best quality to customers and reduce costs by improving efficiency. Further applying this methodology to predict KPIs resulted in improved cost and productivity. **TJ**

ACKNOWLEDGMENTS

Authors thank the mill management team and operations team in helping to execute these findings in the mill. It is with sincere thanks we acknowledge the effort of the Alsip MiniMill India team for helping with data processing.

LITERATURE CITED

1. Rechtin, C., Ranjan, C., Lewis, A., et al., *TAPPI J.* 18(11): 679(2019).
2. Pankonin, B. and Jimmerson, D., "Mill experiences with on-line ultrasound-based stiffness measurements," *TAPPI Eng. Conf.*, TAPPI Press, Atlanta, 1999.
3. Reed, W. and Brown, T., "Mill use of on-line stiffness/strength sensor," *Process Prod. Qual. Conf.*, TAPPI Press, Atlanta, 1999.
4. Jones, G.L. and Petaja, P.H., "Optimization of linerboard properties through performance attribute modelling and simulation of a two ply papermachine," *Papermakers Conf.*, TAPPI Press, Atlanta, 1994, p. 275.
5. Garg, P. and Scott, W.E., "Potential application of predictive tensile strength models in paper manufacture: Part I – Development of a predictive tensile strength model from the Page Equation," *Papermakers Conf.*, TAPPI Press, Atlanta, 2001.
6. Fralic, G., Virtanen, P., Viitamäki, T., et al., "Using automation to predict and control board strength properties in real-time," *PaperCon*, TAPPI Press, Peachtree Corners, GA, USA, 2017.
7. Graf, E.X. and Haltinner, D.A., U.S. pat. 6,083,351 (Jul. 4, 2000).

ABOUT THIS PAPER

Cite this article as:
Modgi, S., and Rajan, K., *TAPPI J.* 21(3): 143(2022).
https://doi.org/10.32964/TJ21.3.143

DOI: https://doi.org/10.32964/TJ21.3.143

ISSN: 0734-1415

Publisher: TAPPI Press

Copyright: ©TAPPI Press 2022

About this journal

ABOUT THE AUTHORS

In this study, we were trying to understand the interactions of various process parameters and how they affect sheet strength. What are the tools that the operators need to watch to stay on quality all the time? We decided to use statistics and papermaking knowledge to arrive at a conclusion.

There are some researchers who have tried to use process parameters for predicting sheet strength, but everyone's methodology is different. Here, we provide a simplistic tool to develop these models, which can be modified if any process changes happen.

Arriving at the model and selecting the parameters from the statistical analysis was a challenge. We had to dive deep into papermaking knowledge to ensure the statistics matched with papermaking theory.

The most surprising part of this finding was the R^2 values for our models. We did not imagine that these values would work out this well, as any industrial data correlations have very low R^2 values.

The tool described here is very simple to use and can be adopted by any mill if it has a good data historian. With this tool, we are not waiting for the paper reel to be manufactured to know the sheet strength. Loss of paper due to poor quality can be avoided.

Mills can also use this tool for tracking not just quality, but also various KPIs. We are seeing great success with this method.

Modgi is technical quality manager for Domtar's packaging mill in Kingsport, TN, USA. Rajan is president of Alsip MiniMill LLC in Alsip, IL, USA. Email Rajan at krajan@alsipminimill.com.



Modgi



Rajan

The Shendye-Fleming OBA Index for paper and paperboard

AWADHOOT SHENDYE, PAUL D. FLEMING III, ALEXANDRA PEKAROVICOVA, VERONIKA HUSOVSKA, AND KIRAN DESHPANDE

ABSTRACT: We are proposing a new one-dimensional scale to calculate the effects of optical brightening agents (OBA) on the bluish appearance of paper. This index is separate from brightness and whiteness indices.

In the paper industry, one-dimensional scales are widely used for determining optical properties of paper and paperboard. Whiteness, tint, brightness, yellowness, and opacity are the most common optical properties of paper and paperboard. Most of the papers have a blue cast generated by addition of OBA or blue dyes. This blue cast is given because of the human perception that bluer is whiter, up to a certain limit. To quantify this effect, it is necessary to determine how much blue cast paper and paperboard have.

As the printing industry follows the ISO 3664 Standard for viewing, which has a D50 light source, this also plays a very important role in showing a blue cast. Color perception is based on light source and light reflected from an object. The ultraviolet (UV) component in D50 interacts with OBA to provide a reflection in the blue region of the visible spectrum.

Use of a UV blocking filter results in measurements without the effect of emission in the blue region. This difference is used in determining the OBA effect in the visible range of the paper. This equation is known as the Shendye-Fleming OBA Index.

Application: The new OBA index proposed here provides a new one-dimensional scale for measuring the effect of OBAs.

In the paper and printing industries, the whiteness of paper is very important. The perception of color depends on the type of light source used for viewing. In the printing industry, D50 is used as the standard illuminant. The D50 illuminant approximately represents horizon daylight [1,2,3]. In the paper industry, illuminant "C" [4] is used for the calculation of color values. Practically, illuminant C is not a readily available light source for viewing conditions. As a result, the CIE discontinued illuminant C and replaced it with D65 [1,2,5]. The difference between these two illuminants is that D65 is richer in the ultraviolet (UV) region than illuminant C [6].

Ideally, the illuminant used for calculation and its corresponding light source should be used for visual inspection of paper. This would allow for better correlation between color scales and perception of color. For our experiments, a D50 (CRI [7]-95) was used because the majority of paper made for the printing industry and printing is viewed under a D50 illuminant. A D65 (CRI-90) was also tested because it, too, is used as a daylight illuminant [1].

The lightness value of a coated paper has an impact on the perception of paper whiteness. In the CIE L*a*b* color space, theoretically, a paper with color values of a*=0 and b*=0 with a lightness value (L*) of 100 are accounted as standard white, although paper white always has some tint. If the amount of tint increases, white is no longer standard white. So, it is important to define a boundary where white is no longer white, but is a light shade of color. Measurement numbers should match what the eyes perceive.

One-dimensional color scales

In assessment of optical properties of color of a material, many one-dimensional color scales are used. Brightness, whiteness, and yellowness are common one-dimensional scales used to specify optical properties of paper or other white substrates.

Optical brightening agents (OBA) are widely used in paper to provide a blue cast, but there is no index available to measure the effect of an OBA in the blue region of the visible spectrum. When a sample of white paper is considered, it may have a bluish tint or a creamy tinge to it. This is because it is very difficult to create a cast-free white paper that will reflect all the colors of the spectrum equally. The ideal white spectrum is a straight line of spectrum in the visible range with full refection. A blue white shade reflects in shorter wavelengths more than in red and green regions of light, while a cream white or yellowish white shade absorbs more light in the blue region. So, to quantify, a change in reflection in the blue region of visible light, caused by excitation of OBA from a UV component of light, needs a new one-dimensional color scale.

Brightness of paper

Papers containing OBA require ultraviolet radiation in light source in wavelengths below 400 nm. This causes excitation of the OBA and the emission of light in the blue region of the visible spectrum. It brings the peak reflectance wavelength to around 457 nm, the exact wavelength at which brightness is measured according to TAPPI Standard Test

Method T 452 "Brightness of pulp, paper, and paperboard (directional reflectance at 457 nm)." TAPPI T 525 "Diffuse brightness of paper, paperboard and pulp (d/0) – ultraviolet level C" measures brightness using a geometry instrument. TAPPI Test Method T 534 "Brightness of clay and other mineral pigments (d/0 diffuse)" also employs a geometry instrument, as does TAPPI T 646 "Brightness of clay and other mineral pigments (45/0)." As brightness is measured at 457 nm, which is in the blue region, an OBA is added to the paper to increase the apparent "reflection" in that region. Thus, the addition of the OBA helps to increase the measured brightness of paper. The limitation of brightness in accounting for the effect of OBA is that brightness is measured only at a particular wavelength and does not consider the entire spectrum affected by OBA excitement. This limitation is covered by the Shendye-Fleming OBA Index.

Whiteness of paper

TAPPI T 560 measures "CIE whiteness and tint of paper and paperboard (d/0 geometry, C/2 illuminant/observer)," and TAPPI T 562 om-10 measures "CIE whiteness and tint of paper and paperboard (45/0 geometry, C/2 illuminant/observer)." Both have an equivalent method in ASTM E313 "Standard practice for calculating yellowness and whiteness indices from instrumentally measured color coordinates."

TAPPI T 560 and T 562 use illuminant C, which has a correlated color temperature of 6774 K. CIE has discontinued illuminant C and recommended replacing it with D65. The TAPPI Standards have not been updated, so C illuminant is still used. The method for calculating CIE whiteness is given in the "CIE whiteness formula" section of this paper.

The Fleming-Aksoy whiteness [8,9] formulas N_{FA} and W_{FA} have been proposed to cover some limitations of the CIE formula. These are further discussed in the "Fleming-Aksoy whiteness formulae" section of this paper.

WHITENESS FORMULAE

Illuminants

An illuminant is a set of numbers defined by a relative spectral power distribution that may or may not be physically realizable as a source [10,11]. Illuminant and light source are distinctly different concepts:

- An illuminant is defined by mathematical data, which are used in colorimetric calculations.
- A light source is a physical source, which emits electromagnetic radiation in the visible region.

Not all illuminants have physical light sources. Light sources are made by targeting illuminant data, and the difference between target (illuminant) and light source is characterized by the color-rendering index [7].

All illuminant data are published by CIE. **Table I** is a summary of those discussed in this work [12]. These CIE standard illuminants are also described in the following sections.

Illuminant	Temperature, K	Simulating Source
A	2856	Tungsten/incandescent
C	6774	North sky daylight
D_{65}	6504	North sky daylight
D_{50}	5000	Daylight

I. Summary of CIE illuminant data discussed in this work [12].

CIE Standard Illuminant C

The CIE Standard Illuminant C [4,13] is derived from Illuminant A, a standard based on a tungsten-filament source (2856 K). It was originally chosen because this light source was the basis of incandescent lighting in the 20th century and early 21st century. Illuminant C, based on early daylight or overcast sky sources, has a correlated color temperature of 6774 K. According to CIE recommendations [5], illuminant C should be replaced with Illuminant D65 (a noontime daylight, discussed further in the next section). The paper industry still uses C, as TAPPI Standards have not been updated.

CIE "D" Series of illuminants

The method of calculation for the CIE "D" series of illuminants [1,14] is based on a correlated color temperature, and D65 is recommended by CIE [5] as a standard illuminant. It represents daylight at noon with a color temperature of 6504 K. Also, D50 has been adopted by the graphic arts industry in the United States as a standard illuminant, and it represents horizon sunlight with a color temperature of 5000 K.

ISO 13655 and OBA

The ISO 13655:2009 Standard "Graphic technology – Spectral measurement and colorimetric computation for graphic arts images" defines measurement conditions for use with a 0/45 geometry spectrophotometer and was released around 2010. This standard defined measurement conditions for light sources used in the spectrophotometer, and we have used it in our method for measuring papers with high OBA content. This standard defines four color measurement modes:

- **M0** – This measurement condition uses the tungsten lamp as per old spectrophotometers. This light source contains less UV and does not show much impact due to OBA in measurements.
- **M1** – This is the new mode based on D50 lighting. This light source used in the spectrophotometers contains a UV component, and it is designed to have better visual-numerical correlation under ISO 3664:2009 "Graphic technology and photography – viewing conditions" as the illuminate to accurately measure printed results on papers with high OBA content.

- **M2** – This measurement uses a UV cut filter, which is the replacement for the current UV instruments. Adding all these modes in a single instrument eliminates the need for keeping different instruments.
- **M3** – To avoid dry back effect in measurement of density, a polarization filter is used. This measurement mode defines use of a polarization filter for measurement of wet printed sheets.

Selection of the correct measurement conditions for measurement is important. Also, selection of measurement conditions for measurement of optical properties of paper plays an important role in visual-numerical correlation.

ISO 3664 and OBA

The ISO 3664:2009 Standard "Graphic technology and photography – viewing conditions" defines viewing conditions for viewing of color and printed images for the printing industry. The light source spectrum and its intensity play an important role in perception of color. ISO 3664 specifies using D50 illuminant as a reference to make light sources and viewing conditions for viewing printed images. These new light sources are much closer to the amount of UV energy present in reference D50 viewing conditions and are thus closer to typical M1 measuring conditions so that we get a better correlation between visual assessment and measurement of color.

In ISO 3664, various parameters are defined for creating a standard viewing condition. When paper contains an OBA and it is viewed under the ISO 3664 viewing condition, the UV component of D50 light source interacts with the OBA and increases apparent "reflection" of light in the blue region. This causes the substrate to look bluer. ISO 3664, which specified increased levels of UV activity in D50 graphic arts lighting, gives a standard that is closer to "real" daylight. At the same time, D50 exposes even more strongly some of the problems caused by the mismatch between OBA-free proofing papers and OBA-containing printing papers.

ISO 15397 OBA specification

The ISO/DIS 15397:2014 Standard "Graphic technology – Communication of graphic paper properties" specifies the list of relevant properties of paper substrates to be communicated between the paper and printing industries. This standard recommends to specify brightness, CIE whiteness, gloss, color measurement, and fluorescence along with mechanical properties of paper. Here, the fluorescence component is calculated as the difference between the whiteness/brightness measured with a source of light having a UV-content corresponding to the chosen illuminant vs. that where that excitation band is absent. Specification of OBA on a one-dimensional scale will help fluorescence caused by OBA in paper to define properties of paper affected by reflection of light.

ISO 2470 and OBA

The ISO 2470-1:2016 Standard "Paper, board and pulps – Measurement of diffuse blue reflectance factor – Part 1: Indoor daylight conditions (ISO brightness)" specifies a method for measuring the diffuse blue reflectance factor (ISO brightness) of pulp, paper, and paperboard. This is an indication of the amount of OBA present in the substrate, expressed as a percentage. As per this standard, brightness is measured at wavelength 420 nm (but with total UV blockage). The delta UV is the difference between both values. If, in the case of fluorescent samples, measurements are made with a filter with a cutoff wavelength of 420 nm placed in the light beam, it is possible to determine the ISO brightness of the non-fluorescent substrate and thus to calculate the contribution of the fluorescent whitening agent to the ISO brightness:

$$\Delta UV\ (\%) = R_{457} - R_{420} \quad (1)$$

where:
R_{457} = brightness at 457 nm (red/green cutoff)
R_{420} = brightness at 420 nm (UV cutoff)

The biggest limitation of this standard is that the UV affects the sample measurement throughout the 400 nm to 550 nm region. The amount of fluorescence effects in this region impacts visual perception, and yet there is no fluorescence effect over at least a portion of that region. So, the calculation method of ISO 2470 has poor visual numerical correlation for the ISO 3664 viewing condition.

OBA and color reproduction

Process color inks are transparent and measured as the amount of light reflected from print that passes through specific filters. The color gamut [15] of print is based on the ink and substrate combination. The International Color Consortium (ICC) White Paper 14 (2005) summarizes CIE Publication 163 (2004) [16], which says that "the results indicate and quantify that the fluorescence of the substrate can be measured in both solid ink areas and halftone ink areas, with the effect being far larger in the latter." This means the colors reproduced by papers with and without OBA are different, and the methods to predict or correct the OBA effects are important for color reproduction.

CIE whiteness formula

The TAPPI Standard Test Method T 562 om-10 is used to calculate whiteness for paper. The CIE whiteness formula is based on the belief that bluer is whiter. The CIE recommended an equation for whiteness in 1981 [17]. This formula was inspired by the work of Ganz [18,19]. It uses the CIE chromaticity coordinates of the sample and illuminant along with the Y tristimulus value [20].

The CIE whiteness formula is used for the relative evaluation of whiteness by the same instrument and without

reference to a white scale. This system of equations does not clarify whether the whiteness has any component of blueness or yellowness. Evaluations with the formula are significantly improved if the sample illumination is stabilized and fitted as closely as possible to a desired illuminant. This also improves the matching of different measurement instruments for whiteness, but the tint deviation or hue value can still not be adequately matched.

A restriction of the CIE formula is that samples should not differ greatly in tint and fluorescence. The formulae produce relative, not absolute, whiteness assessments. It would seemingly be adequate for commercial use in many cases. However, a method that considers bluer to be whiter may not match visual perception if the blueness becomes so high that the sample is no whiter, but instead a light shade of blue. Again, the measuring instruments must have illumination resembling daylight.

If the sample illumination is stabilized, assessments with the CIE formulas are significantly improved, and samples to be compared do not have to be measured at the same time. This also improves the matching of different measuring instruments for whiteness. The remaining problem is that tint deviation or hue value can still not be adequately matched to that of visual perception.

In 2009, the CIE formed TC1-77, "Improvement of the CIE-whiteness and tint equations," as recommended by Joanne Zwinkels [21]. Among the issues raised by Zwinkels were factors such as:

1. Measurement geometry
2. Illumination
3. Limited range of validity
4. CIE whiteness limits

EXPERIMENTAL

Fleming-Aksoy whiteness formulae

Recently, Aksoy proposed two new whiteness formulas [8] based on a combination of theoretical and empirical considerations. One formula, N_{FA}, corresponds to a maximum whiteness at the perfectly reflecting diffuser, i.e., zero chroma in the CIE L*a*b* space [16] (or HunterLab space).

The other formula, W_{FA}, is based on the assumption that observers prefer a more "blue" white, but only if it is not too blue. Thus, a local maximum in whiteness is expected. The coefficients in W_{FA} were determined from the CIE formula by requiring that the two formulas have the same value and derivatives with respect to a* and b* at zero chroma (a*=b*=0) for a given Y (or L* value).

These formulae are given by [8,9]:

$$N_{FA} = L^*\left(1/2\right)^{(C/C_0)^2} \quad (2)$$

and

$$W_{FA} = Y\left(1/2\right)^{[a^*(a^*-2a_1^*)+b^*(b^*-2b_1^*)]/C_2^2} \quad (3)$$

where $C = (a^{*2}+b^{*2})^{1/2}$ is the chroma and C_0 and C_2 are characteristic chroma values determined from the boundary region of applicability defined by inequalities from the definition of CIE whiteness [20]. The a_1^* and b_1^* variables are the coordinates for the local maximum whiteness at constant lightness Y (or L*). They are determined by equating the corresponding derivatives of W_{FA} and W_{CIE} with respect to a_1^* and b_1^* to one another. The expressions are:

$$a_1^* = \alpha(Y_n/Y)^{4/3}C_2^2/(200\ln 2) \text{ and} \quad (4)$$

$$b_1^* = -\beta(Y_n/Y)^{4/3}C_2^2/(200\ln 2) \quad (5)$$

where:
$\alpha = 3x_n(900y_n - 800z_n)/500$ and $\beta = 3z_n(800x_n + 1700y_n)/200$, with Y_n, x_n and y_n being the illuminant luminance and chromaticity values. The W_{FA} formula shows good agreement with observer surveys [9].

Proposed equation for the OBA Index

The proposed equation for the Shendye-Fleming OBA Index is:

$$\text{Shendye} - \text{Fleming OBA Index} = 100 * \left[\frac{\int_{400nm}^{550nm} d\lambda\left(\left(R(M1)-R(M2)\right)*D50\right)}{\int_{400nm}^{550nm} d\lambda D50}\right] \quad (6)$$

The Shendye-Fleming OBA Index can be used with any spectrophotometer with ISO 13655 M1 and M2 measurement modes having 0/45 instrument geometry like the i1pro2 (X-Rite; Grand Rapids, MI, USA), eXact (X-Rite), or Techkon (Techkon; Königstein, Germany) spectrophotometers used in the printing industry. It uses illuminant data of D50. A normalization constant is derived from illuminant data from beginning of the blue region to 550 nm, so it does not require separate hardware like a Ciba-Geigy scale or Laetus fluorescence sensor. As the concept is based on measurement of the fluorescent effect in the visible region, it can also be called Shendye-Fleming Fluorescent Index.

Applications of Shendye-Fleming OBA Index

Application of the OBA index is for use in the paper and paperboard industry as a quality control tool. The Shendye-Fleming OBA Index can be used to compare blue cast between two papers in production. It can also be used for comparing the amount of OBA added between two papers.

As the Shendye-Fleming OBA Index uses D50 illuminant along with M1 and M2 measurement conditions, it gives a better visual-numerical correlation under the ISO 3664 viewing condition for comparing OBA of the paper. The blue cast of paper plays a very important role in color reproduction, as it has an impact on color appearance and measurements. The Shendye-Fleming OBA Index can help in color management to determine the impact of OBA on blue and yellow colors on a device profile.

Substrate	CIE L*a*b* (M1)	CIE L*a*b* (M2)	CIE WI (Tint)	WFA	S-F FI
Calibration tile	92.08, 1.09, -0.55	92.08, 1.09, -0.55	82.77(-1.84)	82.77	0
Tissue paper	95.12, -0.32, 3.09	95.11, -0.31, 3.19	75.17(-0.97)	74.57	0.15
Corrugated white paperboard	86.08, 0.95, 0.70	85.99,0.23, 3.44	65.21(-2.37)	63.95	1.85
Coated recycled paperboard	91.13, 0.06, -0.01	91.04, -0.63, 1.73	82.21(0.34)	81.89	1.89
Coated paper	92.20, 0.63, -5.47	92.05, -0.05, -1.43	104.34(1.74)	91.85	3.19
Bristol board	92.33, 2.79, -6.89	92.08, 1.09, -0.55	110.87(-1.63)	88.52	4.99
Copier paper	93.31, 3.08, -10.08	93, 0.46, -1.28	126.17(-0.38)	94.16	7.14

CIE L*a*b* = CIE-defined color space; CIE WI = CIE whiteness; WFA = Fleming-Aksoy whiteness; S-F FI = Shendye-Fleming Fluorescent Index.

II. Shendye-Fleming OBA Index of different substrates.

RESULTS AND DISCUSSION

The Shendye-Fleming OBA Index was calculated for various substrates and a comparison was conducted. Optical brighteners are also known as fluorescent whitening agents, so the Shendye-Fleming OBA Index can also be called as Shendye-Fleming Fluorescent Index and can be denoted as "S-F FI" or "S-F OBA Index."

In **Table II**, M1 measurements are used along with D50/2 illuminant/observer combination to calculate CIE whiteness and Fleming-Aksoy whiteness. The CIE tint value is given in brackets, along with CIE whiteness (CIE WI).

Table II shows that the white calibration tile of the spectrophotometer has an OBA index of zero, as no OBA is used while manufacturing calibration material for a spectrophotometer. Tissue paper has no added OBAs, so its OBA index, at 0.15, is close to zero. The CIE L*a*b* values are calculated by D50/2 with M1 (UV component present) and M2 (UV component filtered out) measurement conditions and are shown in Table II. These show that the greater the difference between M1 and M2 measurements in the CIE b* value, the higher the OBA index number. A greater difference in the Shendye-Fleming OBA Index is indicative of higher OBA levels. As paper has a higher amount of OBA, it gets a bluer cast, and the Fleming-Aksoy whiteness formula shows paper is no whiter and reduces its whiteness value. This observation can be related to the Shendye-Fleming OBA Index to determine at which OBA index the Fleming-Aksoy formula shows higher whiteness. This way, the Shendye-Fleming OBA Index can be used for determining the correct amount of OBA in paper manufacturing and can become a good quality control index for OBA dosage monitoring as well.

The reflectance graph of the calibration tile of the spectrophotometer in **Fig. 1** shows there is no difference in M1

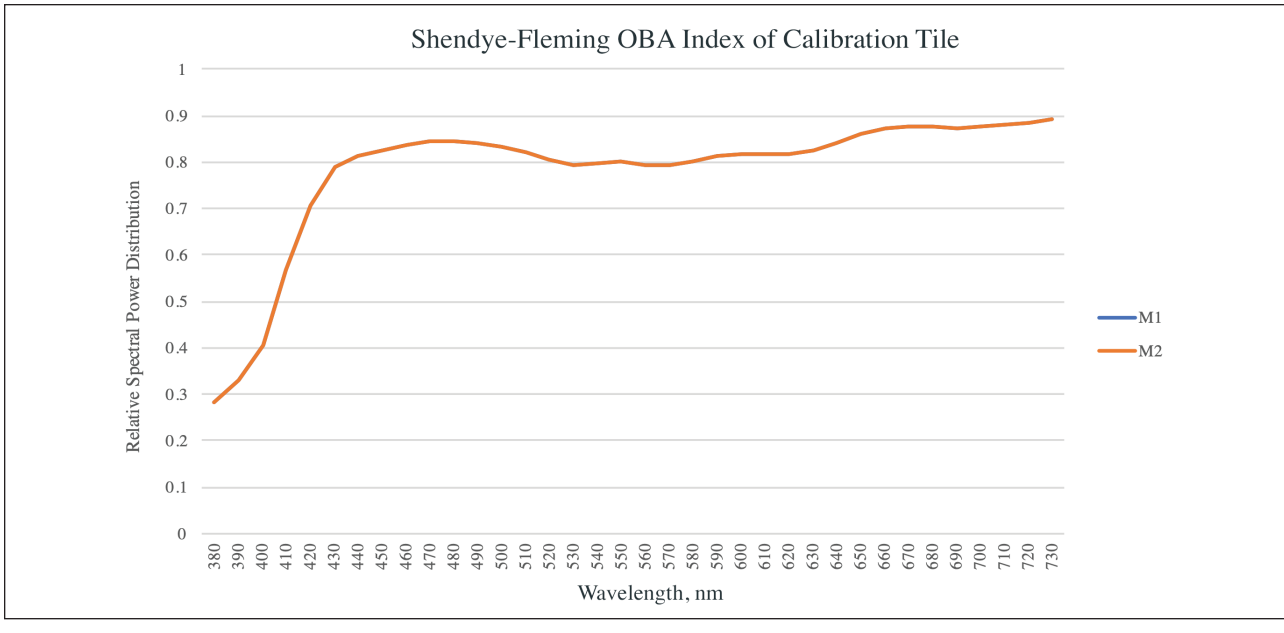

1. Reflectance graph of calibration tile by M1 and M2 measurements.

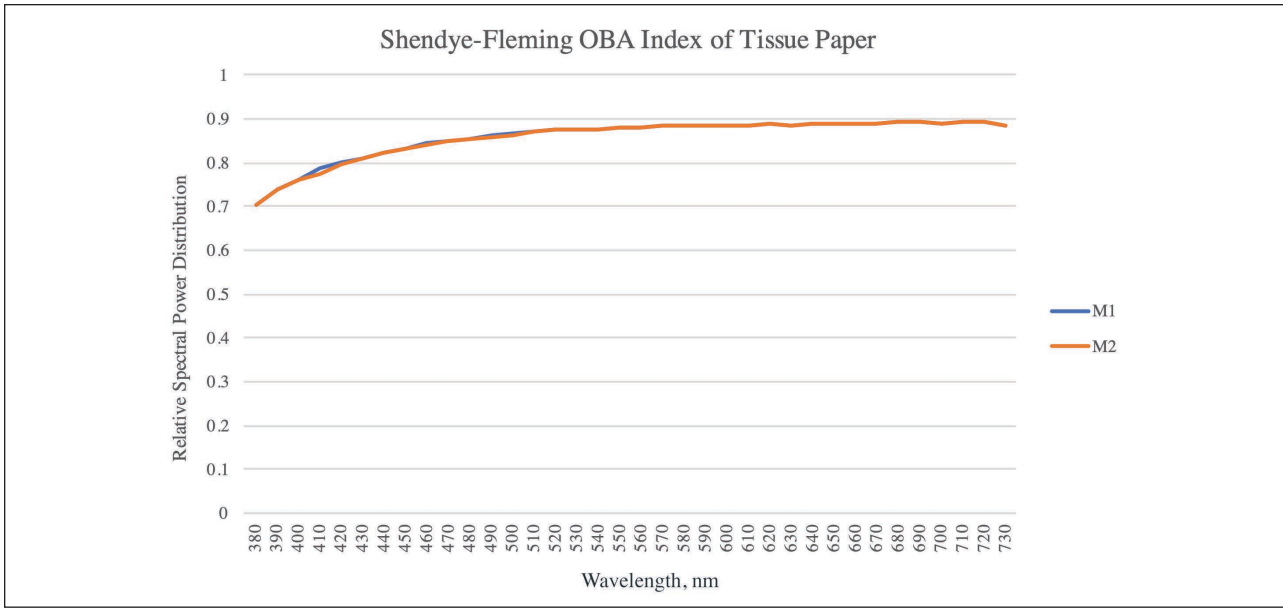

2. Reflectance graph of tissue paper by M1 and M2 measurements.

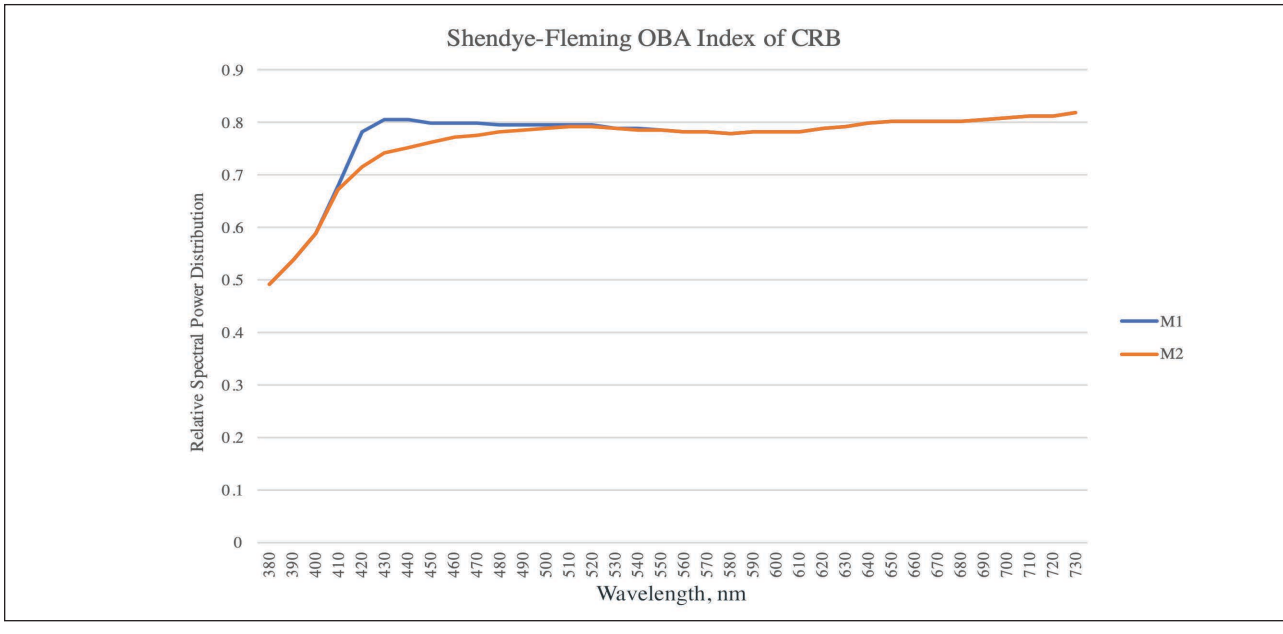

3. Reflectance graph of coated recycled paperboard (CRB) by M1 and M2 measurements.

and M2 measurements. No OBA is added in the calibration tile, as it is a requirement for the calibration standard; as a result, the OBA index is zero.

Tissue paper has a very short shelf life and color or high whiteness or brightness is not required. As it is not printed, no OBA is added in tissue paper. Tissue paper is bleached to appear white. This can cause a very small difference in M1 and M2 measurements, which results in an OBA index of 0.15 (**Fig. 2**). The OBA index of tissue paper is very small and close to zero.

A recycled paperboard requires a white coating to provide printable surface. In paper coatings, small amounts of OBAs are added to provide blue cast, as this coating cannot provide high lightness and whiteness due to the recycled nature of paperboard. **Figure 3** shows a small amount of OBA added to coated recycled paperboard.

This Bristol board has a CIE b* value of -6.89 by M1 measurement, which shows it has a good amount of OBA added for blue cast (**Fig. 4**). The difference between CIE b* value of M1 and M2 of solid bleached sulfate (SBS) pulp is 6.34, which shows a higher Shendye-Fleming OBA Index value of 4.99.

Copier paper uses a lot of OBA to give blue cast to the paper. More emission in the blue region also gives higher

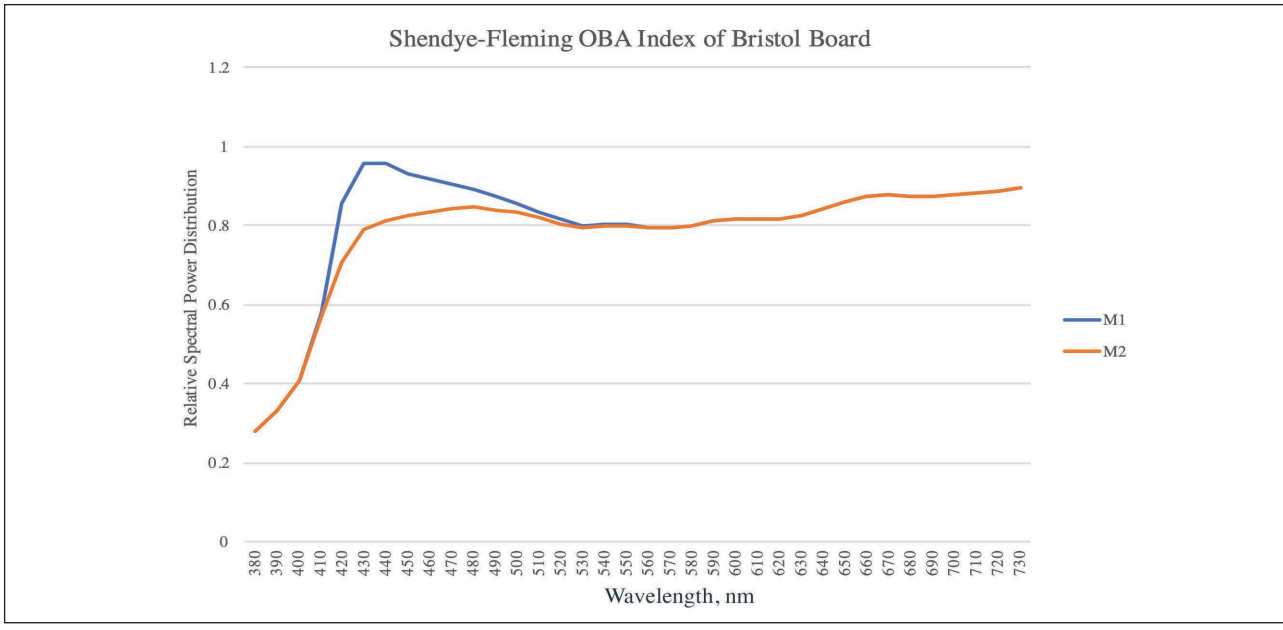

4. Reflectance graph of Bristol board by M1 and M2 measurement.

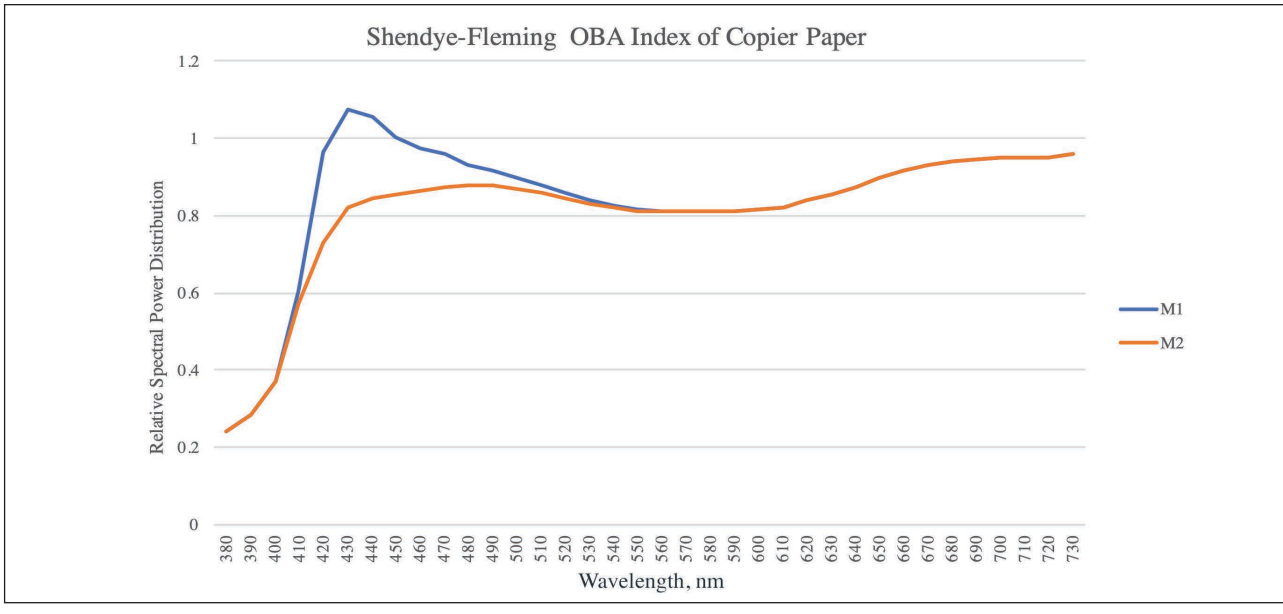

5. Reflectance graph of copier paper by M1 and M2 measurements.

brightness, as brightness of paper is measured at 457 nm. **Figure 5** shows the reflectance graph of copier paper by M1 and M2 measurements. The difference between M1 and M2 measurements of CIE b* value for copier paper is 8.8, which is very high. The Shendye-Fleming OBA Index for copier paper is 7.14. This demonstrates that different amounts of OBA can impart different blue casts to paper, and it can be measured and compared using the Shendye-Fleming OBA Index. There were several attempts made using the b* value, but if we have to compare two papers just for OBA with b* values close to one another, then Δb* is not enough. This is because b* values can come from blue tint printed on paper during proofing for paper background simulation or even blue dye used in paper, which is not fluorescent in nature. Paper could be bluish but not necessarily have OBA. It could be bluish because of blue dye or ink printed on it. When L*a*b* values are calculated, the entire spectrum from 400 nm to 700 nm is used, so the b* value has data from the green and red region of the spectrum, which is not affected by OBA. Also, b* values are impacted by selection of measurement mode; M0, M1 and M2; illuminant (D50, D65, etc.); and observer (2° and 10°) used to calculate L*a*b* values.

Currently, the paper and printing industries are not on

the same page for using illuminant and observer. The paper industry uses illuminant C or D65 and 10° settings, but the printing industry uses D50 and 2° settings. As a result, the b* value is not good for OBA comparison.

In our equation, we are using the fluorescence property of OBA, and only the spectral area affected by OBA is under consideration. This avoids illuminant and observer differences between the print and paper industries so that both industries can use Shendye-Fleming OBA Index, as it is purely spectral based and uses CIE illuminant D50 for normalization to align with ISO 3664 and ISO 13655. That is why the Shendye-Fleming OBA Index equation is an accurate one-dimensional scale for the effect of OBA in visual perception of color.

In the paper and printing industries, several attempts have been made to measure the effect of OBA on the visual appearance of paper. The OBA in paper plays an important role in color management, color perception, and security printing. Most printers and paper manufacturers have spectrophotometers, so we developed this one-dimensional scale using spectrophotometric data. This means that printers and paper manufacturers do not have to invest in new hardware. The one-dimensional scale supports the following applications:

1. Paper mills can use it as a quality control tool for batch-to-batch comparison.
2. Printers can use it to compare two different papers for OBA amount.
3. In color management, proofing paper is required to be brighter, whiter, and with more OBA than printing paper. Therefore, printers can use the Shendye-Fleming OBA Index, along with brightness and whiteness formulas, for selection of proofing paper.
4. By knowing the amount of OBA in paper, printers can select the correct measurement mode for color management.
5. Paper used in security printing should not have any OBA, as it interferes with UV-fluorescent features. The Shendye-Fleming OBA Index can be used to identify OBA-free paper.

The Shendye-Fleming OBA Index will help paper manufacturers and printers, as it derived by considering existing standards like ISO 3664 used for standard viewing conditions and ISO 13655 used in color measurement.

CONCLUSIONS

The Shendye-Fleming OBA Index was successfully implemented for evaluation of the OBA's effect on the blue tint of paper. This index will benefit OBA manufacturers, paper manufacturers, and printers.

- The Shendye-Fleming OBA Index can be calculated for any white paper with M1 and M2 measurement mode by 0/45 or 45/0 geometry spectrophotometer.
- The Shendye-Fleming OBA Index calculates the difference between M1 and M2 measurements from 410 nm to 550 nm.
- The CIE whiteness has no relationship to the Shendye-Fleming OBA Index.
- The difference between CIE b* values and M1 and M2 measurements can be correlated with this index. The higher the difference in b*, the higher the OBA index.
- The Shendye-Fleming OBA Index and the Fleming-Aksoy whiteness formula can be used together for evaluating whiteness of paper.
- The Shendye-Fleming OBA Index is compatible with ISO 3664 viewing conditions, as it uses D50 illuminant and M1 measurement conditions.
- A higher OBA index number is indicative of a higher level of OBA added to the paper.

Future work on the Shendye-Fleming OBA Index

This research provides a basis for further research on the Shendye-Fleming OBA Index. Further research will benefit the paper industry in standardizing procedures for the OBA index as a standard method, allowing users to:

- Obtain reflectance data for M1 and M2 from a d/8 geometry spectrophotometer with specular mode included to calculate OBA index.
- Calculate Fleming-Aksoy whiteness and Shendye-Fleming OBA Tint Index with a 0/45 geometry instrument and d/8 geometry instrument to determine optimized OBA levels for whiteness. Reductions in OBA dosage are often possible.
- Conduct psychophysical tests for the OBA index under ISO 3664 viewing conditions.

Implementation

For commercial use of Shendye-Fleming OBA Index, software called "ColorScale" has been developed and is available for use [22]. With this software, whiteness and OBA index may be calculated for comparison between two papers. **TJ**

LITERATURE CITED

1. Judd, D.B., MacAdam, D.L., Wyszecki, G., et al., *J. Opt. Soc. Am.* 54(8): 1031(1964). https://doi.org/10.1364/JOSA.54.001031.
2. Wyszecki, G., *J. Opt. Soc. Am.* 58(2): 290(1968). https://doi.org/10.1364/JOSA.58.000290.
3. CIE, CIE 51.2-1999 (including Supplement 1-1999), "A method for assessing the quality of daylight simulators for colorimetry," Commission Internationale de l'Eclairage (International Commission on Illumination), CIE Central Bureau, Vienna, 1999.
4. Davis, R. and Gibson, K.S., *Filters for the Reproduction of Sunlight and Daylight and the Determination of Color Temperature"* (No. 114), U.S. Government Printing Office, Washington, DC, 1931. https://doi.org/10.6028/NBS.MP.114.
5. CIE, *CIE l5th Session, Proc.*, Vol. A (CIE 11A), 1963, p. 25, Commission Internationale de l'Eclairage (International Commission on Illumination), CIE Central Bureau, Paris, 1964.
6. Green P. and MacDonald L.W., *Colour Engineering: Achieving Device Independent Colour*, Wiley, Hoboken, 2002, p. 25.
7. Judd D. and Wyszecki G., *Color in Business, Science, and Industry*, 2nd edn., Wiley, Hoboken, 1975, pp. 362-372.

8. Aksoy, B., "Effect of coating additives on the rheological and optical properties of coated papers," Ph.D. dissertation, Western Michigan University, Kalamazoo, MI, USA, 2004. Available [Online] http://scholarworks.wmich.edu/dissertations/1081 <21March2022>.
9. Shendye, A., Aksoy, B., Fleming III, P.D., et al., *TAPPI J.* 15(5): 339(2016). https://doi.org/10.32964/TJ15.5.339.
10. Berns, R., *Billmeyer and Saltzman's Principles of Color Technology*, 3rd edn., Wiley, Hoboken, 2000, p. 7.
11. Shendye, A., Fleming III, P.D., and Pekarovicova, A., *Proc. Annu. Tech. Meet., Tech. Assoc. Graphic Arts, 62nd*, Technical Association of the Graphic Arts, Chicago, 2010, p. 471.
12. CIE, *ILV: International Lighting Vocabulary*, 2nd edn., CIE S 017/E:2020, Commission Internationale de l'Eclairage (International Commission on Illumination), CIE Central Bureau, Vienna. https://doi.org/10.25039/S017.2020.
13. Berger-Schunn, A., *Practical Color Measurement,* Wiley, Hoboken, 1994, p. 165.
14. Wyszecki, G. and Stiles, W.S., *Color Science: Concepts and Methods, Quantitative Data and Formulae*, Wiley, Hoboken, 2000, pp. 143-156.
15. Chovancova-Lovell, V. and Fleming III, P.D., *TAPPI J.* 8(2): 4(2009).
16. ICC, "Summary of CIE Publication 163: 'The effects of fluorescence in the characterization of imaging media'," White Paper 14, International Color Consortium, Reston, VA, USA, April 2005.
17. CIE, "Recommendations on uniform color spaces, color-difference equations, psychometric color terms," Supplement No. 2 of CIE Publication No. 15 (E-1.3.1), 1971, Commission Internationale de l'Eclairage (International Commission on Illumination), CIE Central Bureau, Paris, 1978.
18. Ganz, E., *Appl. Opt.* 15(9): 2039(1976). https://doi.org/10.1364/AO.15.002039.

ABOUT THIS PAPER

Cite this article as:
Shendye, A., Fleming III, P., Pekarovicova, A., et al., *TAPPI J.* 21(3): 157(2022). https://doi.org/10.32964/TJ21.3.157

DOI: https://doi.org/10.32964/TJ21.3.157

ISSN: 0734-1415

Publisher: TAPPI Press

Copyright: ©TAPPI Press 2022

About this journal

19. Ganz, E., *Appl. Opt.* 18(17): 1073(1979). https://doi.org/10.1364/AO.18.001073.
20. CIE, *Commission Internationale de l'Eclairage Proceedings, 1931*, Cambridge University Press, Cambridge, England, 1932.
21. Zwinkels, J., "Evaluation of whiteness," Report R1-46, *CIE Division 1 Meet.*, Commission Internationale de l'Eclairage (International Commission on Illumination), CIE Central Bureau, Vienna, 2009.
22. Shendye, A., "Self-generated absorption filter based optical densitometry calculations for expanded gamut and spot color printing on paperboard for packaging applications and proposed OBA index," Ph.D. dissertation, Western Michigan University, Kalamazoo, MI, USA. Available [Online] https://scholarworks.wmich.edu/dissertations/3184 <20March2022>.

ABOUT THE AUTHORS

We studied this topic because there is no OBA index available for easy use. Our study was different than previous ones because we introduce a new mathematical formula. Deriving this new equation was the most difficult aspect of our study, but we found that it is possible to solve current problems with the new Shendye-Fleming OBA Index.

For mills, the Shendye-Fleming OBA Index would be a simple and easy quality assurance tool to use. Our next step is to implement this method at a mill.

Shendye is technical development engineer at The Challenge Printing Company in Clifton, NJ, USA. Fleming III is professor and Pekarovicova is professor in the Department of Chemical and Paper Engineering, Western Michigan University, Kalamazoo, MI, USA. Husovska is owner at Pressburg LLC in Kalamazoo, MI, USA. Deshpande is global senior color expert – color management at Siegwerk (UK) Ltd., Swadlincote, UK. Email Shendye at ashendye@gmail.com.



Shendye



Fleming III



Pekarovicova

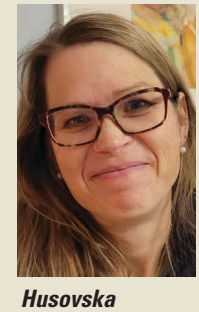

Husovska



Deshpande

Considerations in managing wastewater odor at pulp and paper operations

AMANDA JOHANSEN MATTINGLY, PAUL WIEGAND, AND ROBERT SACKELLARES

ABSTRACT: Many pulp and paper mills are, at least periodically, faced with the release of odors that can migrate offsite and be considered a nuisance by nearby residents. At chemical pulp mills, perceptible odors associated with reduced sulfur compounds (RSCs) are common, many of which are highly perceptible owing to their low odor thresholds. As releases of RSCs and other odorous substances from production processes are progressively controlled, the proportional contribution from wastewater treatment systems to areal odors can increase.

This review paper summarizes important fundamentals of odor generation, source identification, and control. Common odorous substances are identified, and mechanisms for their generation are summarized. Approaches for measuring odorous substances are detailed to enable more effective management, and various odor control strategies are discussed.

Application: This article reviews the fundamentals of odor generation, sources of odor, potentially offending substances, and the basis for control at pulp and paper mills. Approaches for identifying odorous substances, their origins, and means for their control are provided.

While odor associated with reduced sulfur compound (RSC) emissions from pulping processes is well understood, managing odor in wastewater, from wastewater treatment systems and from other sources, is considerably more challenging. Indeed, as progress has been made in reducing process-related sources of odor, wastewater-related odors have the potential to be a proportionally greater contributor to overall mill odor impacts. At many locations, the encroachment of residential populations nearer to mill properties has increased public awareness of odor, and these social forces have mandated a redoubling of efforts to minimize mill odors.

Odors can originate from a variety of process areas throughout the mill, with an equally disparate range of substances contributing to the odor. The behavior of odorous substances in ambient air or in combination with other airborne substances can affect the identification of odor sources, and the odor thresholds for different substances can range widely, as does the ability of human observers to detect and interpret related odors. All these matters further complicate efforts to develop and maintain an aggressive odor control program.

It is not surprising that the best means for managing mill-related odors are site-specific and highly dependent on the ability of mill staff to obtain a comprehensive understanding of the specific causes of odor and viable control strategies for minimizing odor. This article reviews the fundamentals of odor sources and potentially offending substances at manufacturing sites. It focuses on means for addressing challenges in identifying odor sources and substances and for the minimization of related odors. Steps in the process are detailed in this article and include: discussion of odorous substances common at some pulp and paper mills; mechanisms by which these substances are generated; process units frequently associated with their generation; and control approaches that may apply to various processes and odorous substances.

The information provided, coupled with a more detailed treatment of certain topics that may be found in the referenced documents, will provide a framework for initiating or refining an effective odor management program. Among the many documents providing more detail on managing wastewater odors are NCASI [1], WEF [2], and Cook and Hoy [3]. The interested reader is encouraged to examine these publications.

COMMON ODOROUS SUBSTANCES

Odorous compounds can come from many sources in mill environments, including the pulp mill, paper mill, wood pile, bark pile, strong waste pond, primary clarifier, sludge dewatering area, biological treatment system, receiving waters, landfill, leachates, and others [4]. Potentially odorous substances include: process additives; compounds generated during manufacturing; process-generated compounds derivatized, decomposed, or rearranged in effluent treatment; and products of anaerobic decomposition.

Reduced sulfur compounds (RSCs) are a collection of sulfur compounds that have been reduced (gained electrons in an oxidation-reduction reaction) and are commonly comprised mostly of hydrogen sulfide (H_2S), methyl mercaptan, dimethyl sulfide, and dimethyl disulfide [5]. Because sulfur compounds are utilized in pulping processes (e.g.,

sodium sulfide in kraft pulping, sulfite in sulfite pulping), sulfur is available for a variety of transformations that can occur during processing and wastewater treatment. Such RSCs as methyl mercaptan (MeSH), dimethyl sulfide (DMS), dimethyl disulfide (DMDS), and dimethyl trisulfide (DMTS) are formed during kraft pulping by the reaction of sulfide with the methoxy groups of lignin via nucleophilic substitution reactions [6]. Sulfate in process wastewaters can be converted to hydrogen sulfide via sulfate-reducing bacteria.

Organic acids are any organic compounds with acidic properties. These most commonly include carboxylic acids (COOH group) and phenolic alcohols (OH group). Of those relevant to treatment of pulp and paper mill wastewater, volatile fatty acids (VFAs) and aldehydes result from anaerobic decomposition of carbohydrates (in cellulose) and proteins (in biomass). Volatile fatty acids (such as acetic, propionic, and butyric acids) can contribute to odor in recycled paper mill systems and paper [7]. O'Connor et al. [8] indicated that odors associated with effluent treatment system residuals at chemical and non-chemical mills were due to products of anaerobic decomposition, including VFAs, p-cresol, indole, and skatole. Extractives released during wood processing and pulping, such as terpenes, are volatile and poorly soluble, and they can also contribute to odor.

Odors are often related to RSCs, as demonstrated in a multi-mill odor study reported in 2004 [4]. Compounds that were associated with odors at all sites included in this study were RSCs, terpenes, aldehydes, ketones, and alcohols. The VFAs were detected but not associated with odors [4]. In addition to RSCs and VFAs, a variety of other odorous compounds have been found in chemical pulp mill effluents, including formic acid, ammonia, sulfur dioxide, and nitric oxide [9]. A study conducted to estimate airborne concentrations of odorous compounds from wastewater treatment

Compound	Odor Description	Human Odor Detection Threshold, (mg/m^3)[b]
Reduced Sulfur Compounds		
Hydrogen sulfide	Rotten eggs	0.0007–0.01
Methyl mercaptan	Rotten eggs, sulfur-like, pulp mill	0.00004
Dimethyl sulfide	Rotten vegetables, sour milk	0.0025–0.01
Dimethyl disulfide	Rotten eggs, burnt rubber	0.0001–0.03
Dimethyl trisulfide	Putrid/rancid, rotten eggs, burnt rubber	0.007
3-(methylthio)-1-propene	Rotten vegetables, burnt rubber	Not available
1-(methylthio)-1-propene	Match strike, skunk	Not available
Ethyl methyl disulfide	Not listed	0.062
Volatile Fatty Acids		
Acetic acid	Vinegar	0.025–5.0
Propanoic acid (propionic acid)	Pungent/rancid	0.003–0.89
Butyric/isobutyric acid	Rancid butter	0.0004–3.0
Valeric/isovaleric acid	Rancid cheese	0.00012–0.1
Caproic/isocaproic acid	Goat or limburger cheese	0.04–0.52
2-methylbutyric acid	Rancid, fatty	0.3
Terpenes		
Alpha-pinene	Medicinal, chemical	0.016
Beta-pinene	Rotten vegetables, skunk-like	140 ppb in water
Limonene	Woodsy	0.01
p-cymene	Medicinal, like a hospital	0.012
Others		
Acetaldehyde	Solvent-like	0.0002
4-methyl-2-pentanone (MIBK)	Sweet, vanilla, phenolic	0.3
Guaiacol	Phenolic, floral at low concentration	0.0025
Skatole	Fecal	0.001

[a] Sources: [12,13,14].
[b] Detection thresholds in air (unless otherwise stated); ranges are shown where reported values differ significantly.

I. Odorous compounds identified in pulp and paper mill wastewater treatment plants[a].

lagoons at kraft pulp mills identified acetic acid, propionic acid, thiophenol, furfuraldehyde, 2-furan methanol, camphor, 2-butoxyethanol, and others [10]. These compounds are known to have relatively low odor thresholds. Gas chromatography olfactory mass spectrometry (GC/O-MS) was used during an initial industry investigation to help identify compounds in various pulp and paper mill wastewaters that were associated with odors. Based on these investigations and information found in the literature, the main compounds identified as contributing to odors emitted from pulp and paper mill wastewater treatment plants (WWTPs) are summarized in **Table I**, along with odor descriptions and odor threshold data [3,10,11]. The odor detection threshold is defined as the odor intensity distinguishable from the background and not the threshold at which odor becomes objectionable.

MECHANISMS RESULTING IN GENERATION OF ODOROUS SUBSTANCES

Reduced sulfur compounds are primarily formed in the kraft pulping process and may be present in wastewater at kraft mills or semichemical mills utilizing a sulfur-based pulping liquor. In kraft pulping, RSCs, including methyl mercaptan, dimethyl sulfide, and dimethyl disulfide, are inadvertently generated during the pulping and recovery processes. Odor formation is proportional to the methoxyl content and sulfur concentration in the pulping system. Hardwood pulp contains more methoxyl groups than softwood pulp. Consequently, if all other conditions remain the same, hardwood pulping produces more methyl mercaptan and dimethyl sulfide than softwood pulping. Overall, approximately 2.3%–2.5% of the sulfur charged to the digester is converted to organic sulfides. Therefore, reducing the net sulfur charge reduces the formation of RSCs, while cooking at higher sulfidity increases the generation of RSCs. Increasing the duration and/or temperature of cooking results in a higher generation of RSCs, although temperature has less of an effect on softwoods than hardwoods [15].

Inorganic H_2S is not formed during kraft cooking due to the high pH [16]. Instead, it is formed in subsequent processes such as brownstock washing and black liquor storage when the black liquor pH decreases. A considerable amount of H_2S is formed during black liquor evaporation when the pH of the black liquor decreases down to 10 or even lower [15]. Besides the RSCs generated during kraft pulping and black liquor evaporation that end up as noncondensable gases (NCGs) and condensates, these compounds are also generated during kraft chemical recovery operations. These operations include black liquor combustion in recovery furnaces, black liquor oxidation, lime generation in lime kilns, smelt dissolution in dissolving tanks, and tall oil acidulation in tall oil reactors [15].

Chemical fate and transport of sulfur compounds in the WWTP are summarized in **Fig. 1** [1]. The processes include volatilization, reduction (dissimilatory and assimilatory), oxidation (chemical and biological), and mineralization [17,18]. The mechanisms of sulfide generation in wastewater systems may be numerous and complex, but most literature sources indicate that the primary mechanism is dissimilatory sulfate reduction. This biologically mediated reaction occurs under conditions that can develop in many pulp and paper wastewater treatment systems: high temperatures, high biological oxygen demand (BOD) and sulfate loads, and an absence of energetically favorable electron acceptors such as oxygen or nitrate [18,19]. These conditions are likely to occur in anoxic sections of the treatment system [17,20], such as primary settling units, the front end of aerated units, and sludge deposits.

Both chemical and biological sulfide oxidation can occur

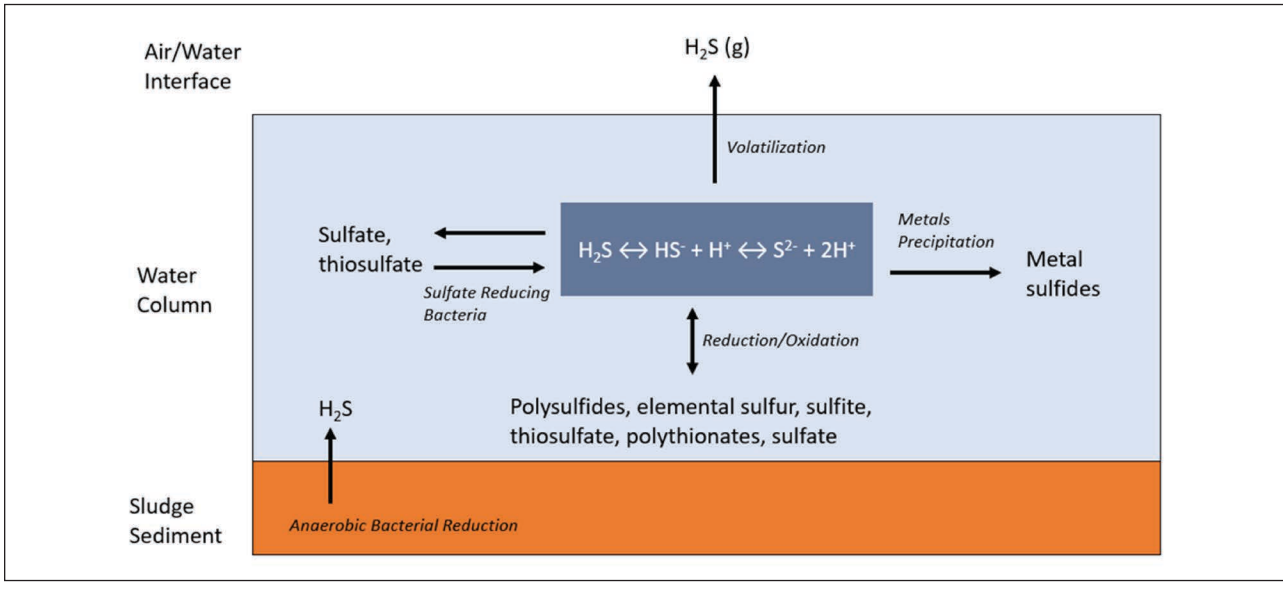

1. Major sulfide transitions in the wastewater treatment plant.

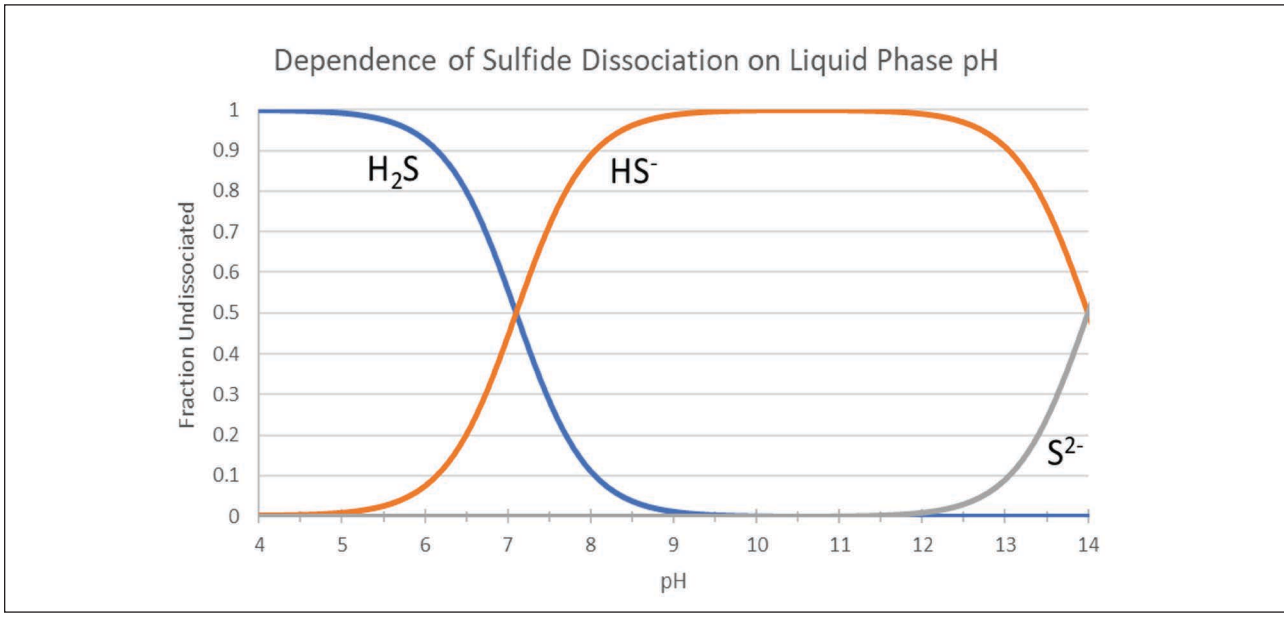

2. Dependence of sulfide dissociation on liquid phase pH [31].

in the WWTP. Chemical oxidation can be slower than biological oxidation [17,20], and is influenced by pH, temperature, reactant concentration ratios, ionic strength, and other factors, such as the presence of transition metal catalysts. The resulting products (e.g., sulfate, elemental sulfur) depend on these factors. Biological oxidation occurs via sulfur-oxidizing bacteria that use sulfide, elemental sulfur, thiosulfate, or other partially reduced oxides of sulfur as a source of energy, producing sulfate. Organic compounds that contain sulfur can be decomposed by heterotrophic microorganisms that incorporate some of the sulfur and release some as sulfide. The sulfur-containing organic compound is reduced to MeSH, which in turn is hydrolyzed biochemically to methyl alcohol and sulfide [20].

Anaerobic conditions also promote the formation of other odor-causing compounds, such as VFAs through fermentation. The VFAs are byproducts released from the oxidation of glucose in fermentative bacteria [21]. These VFAs can contribute to odor but can also play a role in sulfide generation by providing substrate for sulfate-reducing bacteria (SRB), which produce hydrogen sulfide [1].

COMMON SOURCES OF WASTEWATER ODOR

The wastewater treatment system unit operations most commonly identified as sources of odorous emissions are the ones that have the potential for biologically anoxic or anaerobic conditions. These include unit processes with high-strength wastewater and limited oxygen supply, such as equalization basins, primary treatment units, or the front sections of aeration basins [22]. Aeration basins where foul condensates are introduced have increased potential for odor generation due to the high BOD concentrations and presence of reduced sulfur compounds. In front aeration zones with very high BOD concentrations, it can be difficult to provide enough oxygen to maintain a measurable dissolved oxygen concentration using conventional aeration. Hydraulic conditions also play a role. In a system with plug flow hydraulics, the BOD at the front of the aeration basin is higher due to less dilution. Other common sources are facultative lagoons, e.g., inadequately aerated stabilization basins or polishing ponds where anoxic conditions prevail and secondary clarifiers where the accumulated sludge is excessive.

Unstabilized sludge is also a potential significant odor source, especially when it is being handled (e.g., turning, spreading, moving). Unstabilized sludge experiences shear when processed by conveyance or dewatering equipment, releasing proteins that degrade to odorous compounds such as mercaptans [23]. Unstabilized sludge being stored can experience anoxic/anaerobic conditions, leading to odor emissions, as well.

TECHNIQUES FOR MEASURING ODOROUS SUBSTANCES IN WASTEWATER

Among the many potentially frustrating aspects of odor management are the subjective nature of odor descriptors, the within and between individual variability of odor sensitivities, and the thresholds at which perceptible odors become objectionable. The application of various analytical methods to measure odorous substances originating in wastewater can alleviate some of these issues by allowing perceptions of odor to be correlated with quantitative measures of odorous constituents.

Several methods for measuring forms of reduced sulfur compounds are available, owing to the frequency at which these substances significantly contribute to perceived odor. Among them is the use of sulfide ion detection tubes. These tubes are relatively simple to use and can yield valid results

when sulfide concentrations in wastewater are greater than 1 mg/L [24]. If more sensitivity is required, Standard Method 4500-S^{2-} -D [25] and HACH 8131 [26] are laboratory wet chemistry methods. These methods use methylene blue as an indicator and have a sensitivity in the 10 ug/L range for total sulfides, H_2S, bisulfide (HS^-; hydrosulfide), and certain metal sulfides in wastewater. If there is a need to analyze for other common reduced sulfur substances (i.e., methyl mercaptan, dimethyl sulfide, and dimethyl disulfide), NCASI has developed Method RSC-02.02 [27,28] with a sensitivity of around 20 ug/L for these substances.

It is important to distinguish hydrogen sulfide from total sulfide (TS) measurements. Sulfide determinations are, by necessity, "method-defined" because sulfide assumes various forms, depending on sample pH (**Fig. 2**), temperature, ionic strength, and the biological constituents present in the matrix [29]. Analytical results for total sulfide should be considered as dissolved H_2S plus HS^- plus acid-soluble metallic sulfide and sulfide weakly associated with organics in the sample. Metallic and organic sulfides may be present in pulp mill wastewaters and may, but do not always, serve as sources of hydrogen sulfide. Most metallic sulfides would not be a significant source of hydrogen sulfide under normal wastewater treatment facility operating conditions, because they are mostly insoluble in water and require a strong acid to increase the solubility [30]. Sulfide (S^{2-}) would also be considered a component of total sulfide but is present in negligible amounts unless sample pH is extremely basic.

If VFAs are suspected of contributing to odor, the analytical methods described by Cook and Hoy [3,11] and NCASI [32] have been used for investigative purposes. A more elaborate procedure for identifying and quantifying numerous odorous substances in pulp and paper mill wastewaters using GC/O-MS was also developed by NCASI [33].

APPROACHES FOR CONTROLLING ODOR

The Water Environment Federation (WEF) divides control approaches into several types under two categories: "reactive," meaning responding after odorous compounds are formed; or "proactive," meaning preventing or minimizing the generation of odorous compounds. In most cases, successful odor management programs operate in the proactive category.

Suppression of anoxic/anaerobic conditions

A primary example of a proactive strategy is the suppression of anoxic or anaerobic conditions. As noted previously, some odorous substances, particularly reduced sulfur compounds, can be biologically generated when oxygen supplies are insufficient to support the demand by biomass oxidizing organic materials. Thus, odor can often be effectively controlled by increasing the dissolved oxygen level in the treatment unit. Most reduced sulfide-related odor can be prevented if a measurable residual dissolved oxygen concentration is maintained in the water column of the treatment unit. The NCASI experience [34] is that 0.1–0.5 mg/L of oxygen is adequate, while WEF [2] suggests 0.5 to 1.0 mg/L. Relatedly, an appreciable reduction of sulfate to H_2S does not occur in wastewaters with an oxidation-reduction potential greater than about -150 mV [1].

The energy needed for cell growth in bacterial communities typical of secondary wastewater treatment is most often supplied by chemical oxidation reactions involving the transfer of electrons from an electron donor to an electron acceptor. The electron donors and acceptors can be either organic or inorganic compounds, and the electron acceptor can be present within the cell (fermentative metabolism) or obtained from outside the cell (respiratory metabolism). Each electron donor and acceptor pair has a standard reduction potential (E_0'), which is a measurement of the tendency of a substance to donate or accept electrons, measured in volts, compared with that of a reference substance (e.g., hydrogen [H_2]). These pairs are often organized on a redox tower that organizes pairs with the most negative E_0' on the top and pairs with the most positive E_0' at the bottom. The difference between E_0' of a donor and acceptor pair is the $\Delta E_0'$, and pairs with larger $\Delta E_0'$ will have a greater amount of energy released in the net reaction [21]. **Table II** shows a small redox tower with $\Delta E_0'$ calculated for the oxidation of glucose to carbon dioxide (CO_2) using

Redox Couple	E_0', V	$\Delta E_0'$ for Oxidation of Glucose, V
CO_2/glucose	-0.43	N/A
SO_4^{2-}/H_2S	-0.22	+0.21
Fe^{3+}/Fe^{2+}	+0.2 (pH = 7)	+0.63
NO_3^-/NO_2^-	+0.42	+0.85
0.5 O_2/H_2O	+0.82	+1.25

E_0' = electron standard reduction potential; $\Delta E_0'$ = E_0' difference between donor and acceptor pair; CO_2 = carbon dioxide; SO_4^{2-} = sulfate ion; H_2S = hydrogen sulfide; Fe^{3+}= ferric ion; Fe^{2+} = ferrous ion; NO_3^- = nitrate; NO_2^- = nitrite; O_2 = oxygen; H_2O = water.

II. Redox tower [21].

a variety of electron acceptors. The greatest amount of energy to be gained is from reaction with oxygen, followed by nitrate, iron, and then sulfate.

The most energetically favorable reactions proceed first and thus, in the wastewater treatment process, oxygen will be used up first. When dissolved oxygen is depleted, the bacteria will move onto nitrate and iron. In the absence of both oxygen and nitrate, a sulfate-reducing community (producing hydrogen sulfide) will dominate in wastewaters with high sulfate concentrations. Hydrogen sulfide generation can be reduced by ensuring an adequate supply of oxygen and/or nitrate (both energetically favorable electron acceptors). In the secondary treatment process, this can be accomplished by adding more aeration. If additional aeration is not possible, a short-term solution (but more expensive) is the dosage of calcium nitrate or oxygen injection at a point of good mixing, either near a surface aerator or in the inlet pipe to the aeration basin. The amount of oxygen or nitrate to be added should be determined based on the BOD load to the system. An alternative approach is the redistribution of organic loads, such as split feed.

Oxygen addition can take many forms, including conventional aeration, pure oxygen, and Speece cones. In addition to the suppression of SRB growth, dissolved oxygen works by reacting rapidly with hydrogen bisulfide. Conventional aeration, in some cases, can be inadequate to maintain aerobic conditions, such as in front ends of aerated stabilization basins (ASBs) where high strength streams such as foul condensates are sometimes introduced. Pure oxygen has been applied via a liquid oxygen tank and a system that includes a storage vessel, vaporizer, piping, process controls, and a means of diffusing the gas into the wastewater. While effective in areas where conventional aeration is inadequate or in areas where wastewater travels through non-aerated vessels or pipes, safe handling practices are required due to increased combustion risk [1]. Adding oxygen to wastewater treatment units that are stagnant by design, such as primary clarifier and settling lagoons, is more involved, but there are several ways to introduce the oxygen into the influent of the treatment unit. Several mills have achieved ~50 % oxygen transfer by injecting oxygen into the discharge line of the lift pumps feeding the primary clarification unit. Much higher transfer rates (~90%) are achievable using commercial injection units [35,36]. The sludge beds within primary clarifiers and settling basins are often sources of anoxic or anaerobic biological activity. Therefore, this method is often combined with removing the accumulated sludge more rapidly from these units. The application of these methods has been reported to substantially reduce hydrogen sulfide emission rates [37,38]. Speece cones have been used to add oxygen to concentrations much higher than saturation, allowing additional oxygen to be available downstream of the cone location [38].

Nitrate addition usually consists of a storage tank (for either sodium or calcium nitrate), metering pump, piping, and valves. In addition to the use of nitrate to prevent sulfate reduction, it can also be used to remove H_2S from wastewater by biochemical conversion of sulfide to sulfate. The average stoichiometry reported in the literature ranges from 0.6 to 4.5 mg nitrate/mg sulfur (NO_3^- /mg S), with a sulfide elimination of 90% to 100% [18]. Nitrate addition has been used to address odor from anaerobic conditions in settling lagoons, dewatered sludge storage piles, equalization basins, and primary clarifiers [1].

Disinfection

An alternative, proactive option for controlling odor in wastewater collection and primary treatment systems is to impede biological activity, thereby ceasing the production of biologically mediated odorous substances. A practice used at recovered fiber mills, some of which recycle clarified water from the primary clarifier back into the mill, is the use of disinfectants in the primary clarifier feed or upstream in stock storage chests or in the wastewater collection system. Common disinfectants are sodium hypochlorite (also an oxidant) and proprietary biocides. Biocides are often used in conjunction with other odor reduction techniques to address odors at recycled paper mills [1]. Care must be taken, however, to ensure that residual disinfectants or biocides are not present in inhibitory concentrations in waters sent for secondary biological treatment.

Control of wastewater pH

Hydrogen sulfide is a weak dibasic acid that disproportionates in wastewater according to Eq. 1:

$$H_2S \rightleftharpoons H^+ + HS^- \rightleftharpoons 2H^+ + S^{2-} \quad (1)$$

Of the sulfur species shown, only H_2S is volatile. The reaction is affected by the pH of the wastewater (Fig. 1), temperature, and ionic strength. As shown in Fig. 2, the release of hydrogen sulfide from wastewaters is only significant at pH levels below 7.5–8. Thus, for mills addressing odor related to H_2S, managing wastewater pH is critically important to reducing emissions. Adjustment of pH with a target of 7.5 has been used in combination with nitrate addition to reduce sulfide odors associated with settling ponds during temporary upset conditions [1].

Chemical oxidation

Chemical oxidation of odorous substances in wastewater is considered a reactive approach in that it is designed to reduce odorous substances that are already present or have formed. The two oxidants most commonly used for this purpose are elemental oxygen and hydrogen peroxide. Both offer the advantage of no or innocuous reaction byproducts. In clean water, the chemical oxidation of hydrogen bisulfide by these chemicals is slow. In most wastewaters, however, oxygen oxidizes hydrogen bisulfide to sulfate very rapidly [39,40].

Control Method	Application	Average Sulfide Reduction[a]
Ferric chloride ($FeCl_3$)	Sludge dewatering, prior to primary clarifier	70%
Ferrous chloride ($FeCl_2$)	Force main	~95%
Ferrous sulfate ($FeSO_4$)	Foul condensate header	~60%
Hydrogen peroxide (H_2O_2)	Foul condensate	79%, 39%
Sodium hypochlorite (NaClO)	Foul condensate	75%
Potassium permanganate ($KMnO_4$)	Sludge dewatering	~90%
Oxygen (O_2)	Primary clarifier inlet	~70 – 99%
Increased aeration HP	ASB	Reduced odor complaints
Sodium nitrate ($NaNO_3$)	Settling lagoon, sludge dewatering	~90% eliminated odor complaints
Calcium nitrate ($CaNO_3$)	Paper machine sewer	Reduced odor complaints
Caustic for pH control	Settling pond prior to ASB	Reduced odor complaints
Anthraquinone and pulping modifications	In digester	40%
Biostimulants	ASB lagoon	Reduced sulfide concentrations and odor complaints
Organic scavengers	Primary clarifier, sludge press	>90%
Enzyme blockers	Sludge thickener mix box	Reduced sulfide and odor
Organic neutralizers	Emergency spill basin	80%
Biocides	Paper system	~40% reduction in VFAs

[a] Values are for sulfide unless otherwise noted.
ASB = aerated stabilization basin; VFAs = volatile fatty acids.

III. Summary of odor control methods.

Hydrogen peroxide is commonly used in the municipal wastewater treatment industry to oxidize H_2S (aqueous) to sulfate or elemental sulfur, depending on the pH [2]. An advantage of this approach is that it can potentially oxidize other odorous compounds, e.g., VFAs [1] and methyl mercaptan [41]. A disadvantage is that the chemical is expensive, potentially hazardous, and subject to U.S. Department of Homeland Security rules and regulations. It can also be consumed by fiber and other constituents in the effluent. Another common oxidant is potassium permanganate ($KMnO_4$), which has been used to oxidize H_2S to potassium sulfate (alkaline conditions) or elemental sulfur (acidic conditions) [1]. A disadvantage of $KMnO_4$ is that it is often more expensive than hydrogen peroxide.

Other oxidants, which also act as disinfectants, include hypochlorite, chlorine dioxide (if available at the facility), and peracetic acid. Hypochlorite is relatively inexpensive but has the potential drawback of creating halomethane byproducts, including chloroform. Chlorine dioxide cannot be purchased in quantity and transported and, therefore, is only practically available if it is already being manufactured on site for use in chemical pulp bleaching. Peracetic acid is a peroxy acid produced by combining acetic acid and hydrogen peroxide. It is commonly used as a disinfectant, but its use for odor control is not common, owing to its expense. Dosage rates of oxidants should be established using bench-scale testing [23].

Capture and scrub

Capturing odorous gases from wastewater treatment units and treating them is another reactive approach that can be feasible, though rarely for units with a large surface area. For example, primary clarifiers can be covered and the off-gases collected and treated [2]. There are several methods for treating off-gases, including wet scrubbing, carbon absorption, and bio-filtration. Such options are capital intensive and create additional safety and maintenance challenges. Furthermore, this approach does not prevent the formation of odor problems downstream of the treatment unit.

Emerging approaches

There are several areas where improvements are being made. For example, new methods have been developed for adding oxygen to lagoons. At least one aeration equip-

ment supplier, Aeration Industries, offers a blower-assisted directional aerator where it is possible to decouple the blower and add oxygen [42]. This approach could be attractive when oxygen is not routinely needed. Another area of continued emergence is the use of advanced oxidation reactions to treat contaminants in wastewater [43]. At least one company, ORIN Technologies, uses a proprietary, non-hazardous catalyst to increase the effectiveness of dissolved oxygen or hydrogen peroxide when controlling odors in mill wastewater and sludge treatment systems [41]

SUMMARY AND CONCLUSIONS

Odor management at pulp and paper mills is challenging, owing to the existence of numerous potential odor sources, identification of odorous substances and their origins, human perceptions, and the complexity associated with implementing control strategies. The information presented in this review is intended to assist mill staff with meeting these challenges by providing a fundamental understanding of the origins of odorous substances and opportunities for managing process units such that odorous substances are not formed, not released as gasses, or controlled in another fashion to minimize or eliminate offsite transfer. **Table III** provides a summary of various control strategies, many of which are described in detail in an NCASI review [1]. **TJ**

LITERATURE CITED

1. NCASI, "Summary of industry experience with odor minimization at wastewater treatment plants," 2008a, Technical Bulletin No. 0949, National Council for Air and Stream Improvement, Cary, NC, USA, 2008.
2. WEF, *Odor Emissions and Control for Collection Systems and Water Resource Recovery Facilities*, Manual of Practice 25, 2nd edn., Water Environment Federation, Alexandria, VA, USA, 2020.
3. Cook, D.L. and Hoy, D.R., "Analytical techniques for investigating odors at pulp and paper facilities: Preliminary results," *TAPPI Environ. Conf.*, TAPPI Press, Atlanta, 2003.
4. NCASI, *Understanding Odor From Wastewater Treatment Systems*, Webcast, National Council for Air and Stream Improvement, Cary, NC, USA, 2004.
5. Smook, G.A., *Handbook for Pulp and Paper Technologists*, 2nd edn., Angus Wilde Publications, Bellingham, WA, USA, 1992.
6. Biermann, C.J., *Handbook of Pulping and Papermaking*, 2nd edn., Academic Press, San Diego, 1996.
7. Davis, C.K. and Smith, K.S., *Pulp Pap.* 75(12): 42(2001)
8. O'Connor, B.I., Buchanan, B.E., and Kovacs, T.G., *Pulp Pap. Can.* 101(2): 57(2000).
9. Goyer, N. and Lavoie, J., *AIHAJ* 62(3): 330(2001). https://doi.org/10.1080/15298660108984635.
10. Lange, C.R. and Christiansen, J. "Characterization of odors originating from pulp and paper wastewater lagoons," *TAPPI Int. Environ. Conf.*, TAPPI Press, Atlanta, 2004.
11. Cook, D.L. and Hoy, D.R., "What's that smell? Analytical measurements for odorous compounds in pulp and paper mill wastewaters," *Proc. Water Environ. Fed.*, Water Environment Federation, Alexandria, VA, USA, 2008, p. 55. https://doi.org/10.2175/193864708788807727.
12. Verschueren, K., *Handbook of Environmental Data on Organic Chemicals*, 2nd edn., Van Nostrand Reinhold, New York, 2001.
13. Ruth, J.H., *AIHA J.* 47(3): A-142(1986). https://doi.org/10.1080/15298668691389595.
14. Van Gemert, L.J. and Nettenbreijer, A.H., *Compilation of Odour Threshold Values in Air and Water*, Rijksinstituut voor Drinkwatervoorziening (RID), Voorburg, The Netherlands, 1977.
15. NCASI, "Formation, release and control of reduced sulphur compounds from kraft pulp and paper facilities," 2008b, Technical Bulletin No. 0952, National Council for Air and Stream Improvement, Cary, NC, USA, 2008.
16. McKean, W.T., Hrutfiord, B.F., and Sarkanen, K.V., *Tappi* 48(12): 699(1965).
17. Tooke, D.L., "Sulfur transport and fate in a pulp mill wastewater treatment system," Ph.D. dissertation, University of Montana, Missoula, MT, USA, 2006.
18. Zhang, L., De Schryver, P., De Gusseme, B., et al., *Water Res.* 42(1-2): 1(2008). https://doi.org/10.1016/j.watres.2007.07.013.
19. Delgado, S., Alvarez, M., Rodriguez-Gomez, L.E., et al., *Water Res.* 33(2): 539(1999). https://doi.org/10.1016/S0043-1354(98)00223-1.
20. ASCE, *Sulfide in Wastewater Collection and Treatment Systems*, American Society of Civil Engineers, New York, 1989.
21. Madigan, M.T., Bender, K.S., Buckley, D.H., et al. *Brock Biology of Microorganisms*, 15th edn., Pearson Education, New York, 2018.
22. Crawford, R.J., Crapo, A.M., and Jain, A.K., "Reduced sulfur compound and methane emissions from kraft pulp and paper mill wastewater treatment plants," *Proc. Water Environ. Fed.*, Water Environment Federation, Alexandria, VA, USA, 2008, p. 777. https://doi.org/10.2175/193864708788808168.
23. Tchobanoglous, G., Stensel, H.D., Tsuchihashi, R., et al., *Wastewater Engineering: Treatment and Resource Recovery*, 5th edn., McGraw Hill Education, New York, 2014.
24. NCASI, "Evaluation of sulfide ion detector tubes for determining sulfide concentrations in pulp and paper mill wastewaters," Special Report No. 05-01, National Council for Air and Stream Improvement, Cary, NC, USA, 2005.
25. AWWA, WEF, and APHA, "Standard Test Method 4500-S^2—D methylene blue method," in *Standard Methods for the Examination of Water and Wastewater*, 23rd edn., American Water Works Association, Water Environment Federation, and American Public Health Association, Washington, DC, 2017.
26. HACH, "Sulfide, USEPA methylene blue method," HACH Method 8131, Hach Company, Loveland, CO, USA, 2018.
27. NCASI, "Development and application of a method for measuring reduced sulfur compounds in pulp and paper mill wastewaters," 2007a, Technical Bulletin No. 0933, National Council for Air and Stream Improvement, Cary, NC, USA, 2007.
28. NCASI, "Method RSC-02.01 Reduced sulfur compounds by direct injection GC/PFPD," in *NCASI Methods Manual*, National Council for Air and Stream Improvement, Cary, NC, USA, 2007.
29. NCASI, "The presence, fate, and ecological significance of hydrogen sulfide in pulp and paper mill effluents," Technical Bulletin No. 0997, National Council for Air and Stream Improvement, Cary, NC, USA, 2012.

30. Moeller, T., Bailar Jr., J.C., Kleinberg, J., et al., *Chemistry with Inorganic Qualitative Analysis*, Academic Press, New York, 1980. https://doi.org/10.1016/B978-0-12-503350-3.50004-4.

31. Snoeyink, V.L. and Jenkins, D., *Water Chemistry*, John Wiley & Sons, New York, 1980.

32. NCASI, *Process Water Quality and Water Reuse Practices at Low- and Zero-Discharge Recycled Paperboard Mills*, Technical Bulletin No. 796, National Council for Air and Stream Improvement, Cary, NC, USA, 1999.

33. NCASI, "Investigating odorous compounds in pulp and paper mill wastewater treatment plants using gas chromatography olfactory mass spectroscopy," Special Report No. 09-05, National Council for Air and Stream Improvement, Cary, NC, USA, 2009.

34. Palumbo, J.E., Brown, L.C., and Stratton, S.C., *J. Environ. Eng.* 136(10): 1171(2010). https://doi.org/10.1061/(ASCE)EE.1943-7870.0000248.

35. Kim, S.Y., Garcia, H.A., Lopez-Vazquez, C.M., et al., *Process Saf. Environ. Prot.* 139: 171(2020). https://doi.org/10.1016/j.psep.2020.03.026.

36. ECO2 Oxygen Technologies, "ECO2 SuperOxygenation system design: Literary references," ECO2 Oxygen Technologies, Indianapolis, 2022. Available [Online] https://eco2tech.com/wp-content/uploads/Tech-Bulletin-Oxygen-Demand-and-Solubility-Calculations.pdf <25March2022>.

37. BlueInGreen, "Odor control," BlueInGreen LLC, Fayetteville, AR, USA, 2021. https://www.blueingreen.com/odor-control <25March2022>.

38. Speece, R.E. and Clidence, D., *Water Environ. Technol.* 18(3): 60(2006).

39. Sackellares, R.W., Barkley, W.A., and Hill, R.D., *J. Water Pollutt. Control Fed.* 59(10): 877(1987).

40. Mahmood, T., Banerjee, S., and Sackellares, R.W., *Water Sci. Technol.* 40(11-12): 289(1997). https://doi.org/10.2166/wst.1999.0724.

ABOUT THIS PAPER

Cite this article as:
Mattingly, A.J., Wiegand, P., and Sackellares, R., *TAPPI J.* 21(3): 167(2022). https://doi.org/10.32964 TJ21.3.167

DOI: https://doi.org/10.32964/TJ21.3.167

ISSN: 0734-1415

Publisher: TAPPI Press

Copyright: ©TAPPI Press 2022

About this journal

41. Baures, M., personal communication, ORIN Technologies, Ettrick Town, WI, USA, 2021.

42. Mathour, A. and Rafiuddin, A., "Oxygen injection systems provide emergency aeration, D.O. management," *Responsible Seafood Advocate*, Global Seafood Alliance, Portsmouth, NH, USA, June 2005. Available [Online] https://www.globalseafood.org/advocate/oxygen-injection-systems-provide-emergency-aeration-d-o-management/ <25March2022>.

43. Hermosilla, D., Merayo, N., Gascó, A., et al., *Environ. Sci. Pollut. Res.* 22: 168(2015). https://doi.org/10.1007/s11356-014-3516-1.

ABOUT THE AUTHORS

NCASI supports mills having a variety of wastewater operations questions, and this paper provides a useful summary for pulp and paper mills dealing with odor-related challenges. Collectively, NCASI has 70-plus years of experience with operational troubleshooting of wastewater treatment systems. This work pulls together information from the literature and our own experience and summarizes important tools and approaches for developing and implementing odor management programs.

The most challenging aspect of compiling this information was attempting to address the very wide variety of potential odor sources, offending substances, and wastewater treatment configurations that exist in the pulp and paper industry.

Odor control has always been part of most mill environmental management programs. Odor issues in the forest products industry have been recognized for some time, so the evolution of solutions using progressively more modern techniques is most interesting.

As mill process odors are reduced, preventing odor generation at the wastewater treatment plant becomes more important. The information provided in this paper is intended to be directly actionable by mill staff tasked with developing or overseeing odor management programs. The next steps for this research include following up on the use of identified emerging approaches.



Mattingly



Wiegand



Sackellares

Mattingly is research engineer and Wiegand is vice president at the National Council for Air and Stream Improvement (NCASI), Cary, NC, USA. Sackellares is senior industrial water engineer, GHD, Duluth, GA. Email Mattingly at amattingly@ncasi.org.

TAPPI JOURNAL
WWW.TAPPI.ORG
THE PAPER AND PACKAGING INDUSTRIES' TECHNICAL RESOURCE
APRIL 2022 | VOL. 21 NO.4

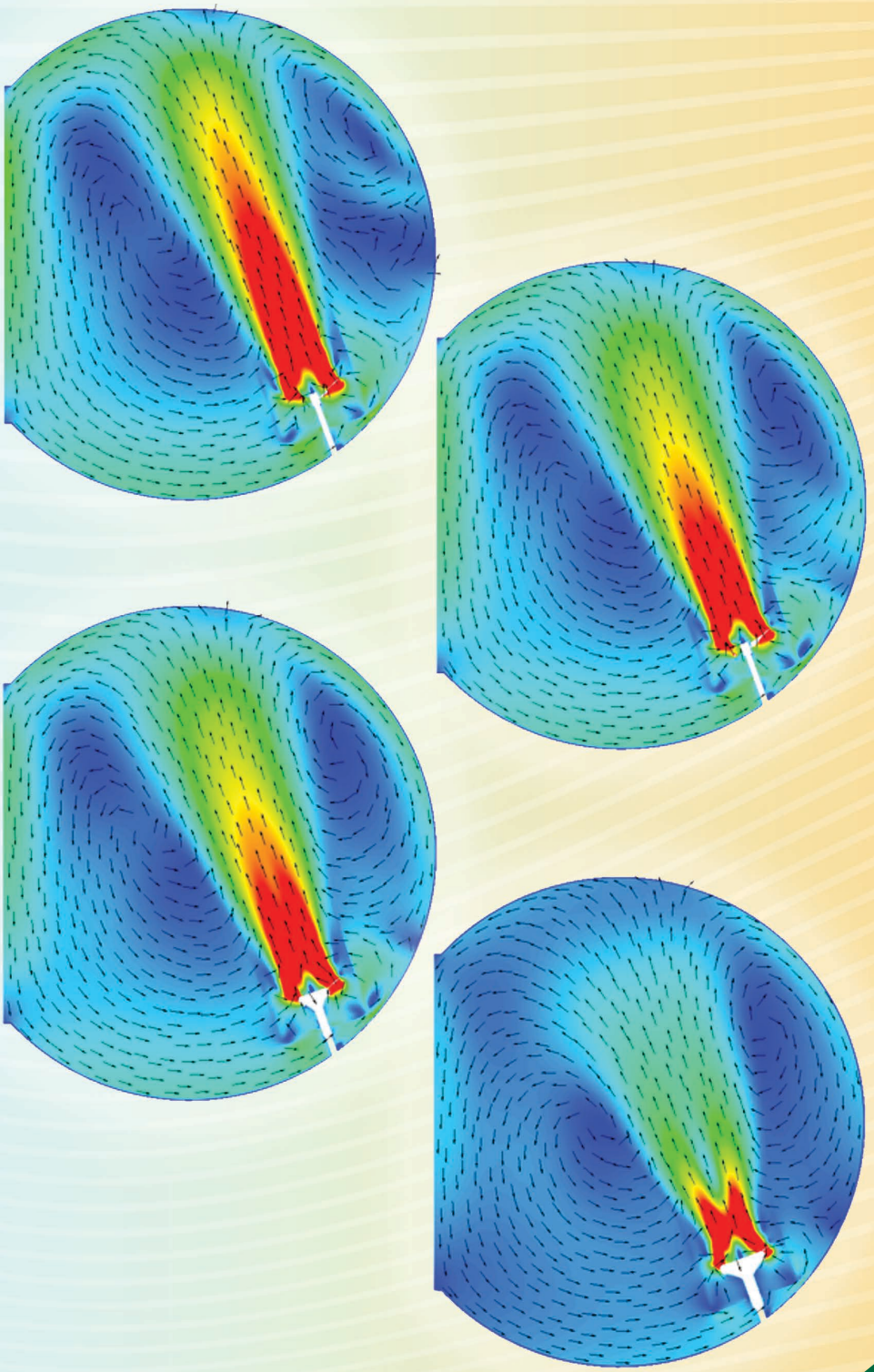

PULPING 189
Effects of agitator blade scaling on mixing in dissolving tanks
Patrick Gareau, Markus Bussmann, and Nikolai DeMartini

PAPERMAKING 203
Comparative study of guar gum and its cationic derivatives as pre-flocculating polymers for PCC fillers in papermaking applications
Indrasena Ghosh, Chhaya Sharma, and Rita Tandon

CELLULOSE 219
Ultrastructural behavior of cell wall polysaccharides
Dietrich Fengel

PAPERMAKING 229
The chemistry of aluminum salts in papermaking
Thomas R. Arnson

TAPPI Journal NOW FULLY OPEN ACCESS

April 2022

TABLE OF CONTENTS VOL. 21 NO. 4

185 EDITORIAL
"Didn't know we knew that" – Rediscovering the fundamentals
Paul Wiegand

189 PULPING
Effects of agitator blade scaling on mixing in dissolving tanks
Patrick Gareau, Markus Bussmann,and Nikolai DeMartini

203 PAPERMAKING
Comparative study of guar gum and its cationic derivatives as pre-flocculating polymers for PCC fillers in papermaking applications
Indrasena Ghosh, Chhaya Sharma, and Rita Tandon

219 CELLULOSE
Ultrastructural behavior of cell wall polysaccharides
Dietrich Fengel

229 PAPERMAKING
The chemistry of aluminum salts in papermaking
Thomas R. Arnson

»**COVER CREDIT**: University of Toronto researchers Gareau, Bussmann, and DeMartini created a 3D model to study mixing impacts from hard calcium carbonate scale on agitators in smelt dissolving tanks (p. 189). Cover image shows a flow field comparison of clean and mildly scaled agitators (top, left-right) and ones with moderate and extreme scaling (bottom, left-right), the latter of which can reduce average tank fluid velocity by 35%.

TAPPI JOURNAL
WWW.TAPPI.ORG

Editor-in-Chief
Douglas W. Coffin coffindw@miamioh.edu
+1 513 529-0771

Associate Editor
Peter W. Hart peter.hart@westrock.com
+1 409 276-3465

Editorial Director
Monica Shaw mshaw@tappi.org
+1 770 367-9534

PRESS Manager
Jana Jensen jjensen@tappi.org
+1 770 209-7242

Webmaster
Trina Heath theath@tappi.org
+1 770 209-7416

***TJ* EDITORIAL BOARD**

Brian N. Brogdon, FutureBridge Consulting & Training LLC
brian.brogdon@gmail.com, +1 678 581-9114

Douglas W. Coffin, Miami University
coffindw@miamioh.edu, +1 513 529-0771

Mahendra Doshi, Doshi and Associates
mahen@aol.com, +1 920 832-9101

Marc Foulger, Valmet
marc.foulger@valmet.com +1 315 767-2920

Peter W. Hart, WestRock
peter.hart@westrock.com, +1 409 276-3465

Carl J. Houtman, USDA Forest Products Laboratory
choutman@fs.fed.us, + 1 608 231-9445

Vamsi Jasti, Ahlstrom-Munksjo Nonwovens LLC
jvamsik1@gmail.com, +1 818 585-3524

Lucian Lucia, North Carolina State University
lucian.lucia@gmail.com, +1 919 889-7059

John A. Neun, John A. Neun LLC
john.neun@gmail.com, +1 518 275-8139

Jim Niemiec, Jim Niemiec Consulting LLC
jim.niemiec@outlook.com, +1 715 213-4766

Steven P. Ottone, Omya
steven.ottone@omya.com, +1 919 641-7854

Gaurav Pranami, Imbed Biosciences
gpranami@imbedbio.com, +1 515 230-7005

Arthur Ragauskas, Oak Ridge National Laboratory
aragausk@utk.edu

Seshadri Ramkumar, Texas Tech University
S.Ramkumar@ttu.edu, +1 806 742-4567

Gregg Reed, Imerys
gregg.reed@imerys.com, +1 478 553-5747

Gerard J.F. Ring, University of Wisconsin—Stevens Point
gerrryring@wi-net.com, +1 715 592-3732

Scott Rosencrance, Kemira Chemicals
scott.rosencrance@kemira.com, +1 770 429-2753

Paul Wiegand, NCASI
pwiegand@ncasi.org, +1 919 941-6417

Junyong Zhu, USDA Forest Products Laboratory
jzhu@fs.fed.us, +1 608 231-9520

Join TAPPI *today!*
TAPPI JOURNAL is a free benefit of TAPPI membership, and is only available to members. To join TAPPI, to renew your TAPPI Membership, or to learn about other valuable benefits, visit www.tappi.org.

TAPPI, 15 Technology Parkway S., Suite 115, Peachtree Corners, GA 30092, publishes *TAPPI JOURNAL* monthly.

ATTENTION PROSPECTIVE AUTHORS: All papers published are subject to *TAPPI JOURNAL's* peer-review process. Not all papers accepted for review will be published. Before submitting, check complete author guidelines at http://www.tappi.org/s_tappi/doc.asp?CID=100&DID=552877.

Statements of fact and opinions expressed are those of individual authors. TAPPI assumes no responsibility for such statements and opinions. TAPPI does not intend such statements and opinions or construe them as a solicitation of or suggestion for any agreed-upon course of conduct or concerted action of any sort.

Copyright 2022 by TAPPI, all rights reserved. For copyright permission to photocopy pages from this publication for internal or personal use, contact Copyright Clearance Center, Inc. (CCC) via their website: www.copyright.com. If you have questions about the copyright permission request process, please contact CCC by phone at +1 978 750-8400. To obtain copyright permission to use excerpts from this publication in another published work, send your specific request in writing to Editor, TAPPI JOURNAL, 15 Technology Parkway S., Suite 115, Peachtree Corners, GA 30092, USA; or by fax to +1 770 446-6947. Send address changes to TAPPI, 15 Technology Parkway S., Suite 115, Peachtree Corners, GA 30092, USA; Telephone +1 770 446-1400, or FAX +1 770 446-6947. www.tappi.org

Editorial



PAUL WIEGAND
TAPPI Journal
Editorial Board

"Didn't know we knew that" — Rediscovering the fundamentals

Access to today's extensive electronic information archives is certainly an amazing feat of technology. Nonetheless, it can sometimes be difficult to find pulp and paper industry process-specific resources that are easily digestible and tailored to help us in our day-to-day work. This brief editorial is intended to help address a portion of this challenge by pointing out some resources that might be less familiar to some of the industry's newer staff yet contain important information that can be applied in everyday operations at pulp and paper mills.

Review articles accelerate learning curve

An example of one type of resource appeared in the March 2022 issue of *TAPPI Journal*. In this case, the title of the article was "Considerations in managing wastewater odor at pulp and paper operations." If you perused it, you will have realized that it is one of several articles of a similar type published in recent years and that my fellow editors and I refer to as "review articles." These types of articles appear in *TAPPI Journal* from time to time and are intended to provide a high-level overview of the practical fundamentals needed to either improve one's ability to properly control and operate a process or to effectively troubleshoot and improve process operations. Articles like this are purposely designed to accelerate the learning curve for new-to-position technical and operational staff at mills, and as a refresher for more seasoned staff.

In looking over *TAPPI Journal* issues published in the past decade, it occurred to me that not all the review articles are easily identified by their title. Thus, it seemed worthwhile to highlight some of them, and these are identified in **Table I**. Indeed, important operational concepts are part of virtually every article published in this journal, but those listed in the table

Topic	Issue	DOI
Anthraquinone	October 2014	https://doi.org/10.32964/tj13.10.23
Beneficial utilization of mill residuals	February 2022	https://doi.org/10.32964/tj21.2.83
Brownstock washing	February 2013, January 2014, and March 2014	https://doi.org/10.32964/tj12.2.69 https://doi.org/10.32964/tj13.1.9 https://doi.org/10.32964/tj13.3.55
Corrosion	May 2018	https://doi.org/10.32964/tj17.5.253
Eucalyptus pulps	June 2015	https://doi.org/10.32964/tj14.6.353
"Green" lime kiln fuels (I and II)	May 2020	https://doi.org/10.32964/TJ19.5.263 https://doi.org/10.32964/TJ19.5.271
Green liquor scale formation	October 2018	https://doi.org/10.32964/tj17.10.571
High kappa pulping	October 2014	https://doi.org/10.32964/tj13.10.33
Paper machine performance and conductivity	October 2017	https://doi.org/10.32964/tj16.10.567
Smelt runoff phenomena	January 2015	https://doi.org/10.32964/tj14.1.41
Soda loss and conductivity	February 2017	https://doi.org/10.32964/tj16.2.65
Wastewater aeration	June 2015	https://doi.org/10.32964/tj14.6.405
Wastewater nutrient management	November 2014	https://doi.org/10.32964/tj13.11.9

I. Selected review articles published in* TAPPI Journal *2012 to present.

have a broader purpose that many will find helpful as they operate or observe process operations throughout the mill.

Outside of *TAPPI Journal* and TAPPI Conference Proceedings, there are a number of other long-proven and electronically accessible resources that some newer mill staff may not yet be aware of and more seasoned staff may have forgotten. Among them are library archives maintained specifically on forest products industry topics. These include the libraries kept at the Forest Products Laboratory in Madison, WI, [1] and the Renewable Bioproducts Institute at Georgia Institute of Technology in Atlanta that maintains the previous holdings of the Institute of Paper Science and Technology [2]. A pulp and paper research database referred to as PaperChem is also maintained and is accessible at several university libraries, including North Carolina State University [3], Georgia Tech, and others.

Finally, I'd be remiss to not mention a few journals that have a long history of publishing pulp and papermaking research. These include *Nordic Pulp* and *Paper Research Journal* [4], *Journal of Wood Chemistry and Technology* [5], *BioResources* [6], and *Holzforschung* [7]. The list of resources mentioned here is certainly not comprehensive but does represent a good starting place when searching for pulp and paper process-specific information. **TJ**

Paul Wiegand is a member of the TAPPI Journal *Editorial Board and is vice president, Water Resources and Laboratory Operations, for the National Council for Air and Stream Improvement (NCASI) in Cary, NC, USA.*

References

1. https://usforestserv.on.worldcat.org/discovery
2. https://smartech.gatech.edu/handle/1853/123
3. https://www.lib.ncsu.edu/databases/paperchem
4. https://www.degruyter.com/journal/key/npprj/html?lang=en
5. https://www.tandfonline.com/journals/lwct20
6. https://bioresources.cnr.ncsu.edu/
7. https://www.degruyter.com/journal/key/hfsg/html

Effects of agitator blade scaling on mixing in dissolving tanks

PATRICK GAREAU, MARKUS BUSSMANN, AND NIKOLAI DEMARTINI

ABSTRACT: Hard calcium carbonate scale often forms on the agitators in smelt dissolving tanks. The effects of this scale on mixing are not well understood. While mixing in tanks has often been modeled in the literature, there have been no studies involving agitator scaling.

To better understand the impact of agitator scaling on hydrodynamics and tank concentrations, a steady state, three-dimensional (3D) model has been developed for a smelt dissolving tank at a kraft pulp mill. In this work, four cases are compared: an agitator with no scaling, mild scaling, moderate scaling, and extreme scaling. The extreme scaling case is representative of scale buildup on a dissolving tank agitator that was significant enough that the agitator had to be stopped and cleaned. The reduction in the agitator fluid jet velocity is relatively small for the mild and moderate scaling cases, but it becomes more significant for the extreme scaling case, for which the results indicate that the mixing of the smelt with the weak wash is likely poor and that there would thus be a risk of smelt pooling.

Application: A smelt dissolving tank model has been developed to predict how tank hydrodynamics and smelt concentrations respond to the presence of agitator scaling.

Causticizing plants in kraft pulp mills frequently suffer from hard calcium carbonate scale formation on the smelt dissolving tank agitators, walls, and floor, as well as in the downstream pumps, pipelines, and other green liquor handling equipment [1]. As scale builds up on an agitator, it can eventually bridge between the blades. The scaling illustrated in **Fig. 1** is an example of extreme scaling in which the agitator had to be shut down, removed, and cleaned because it was no longer possible to maintain the required rotational speed without significant vibrations and very high pump amps. The scale in this case is thickest near the center of the agitator, whereas the blade tips are relatively clean. Scaling also covers the shaft. Although a certain amount of scale will inevitably build up on the agitators, unmanaged scaling may cause insufficient tank mixing, in addition to vibrations due to mass imbalance, increased motor load due to the mass of the scale, and damage to the agitator packing or mechanical seal. For side wall agitators, damage to the packing or seal leads to reliability and safety issues. While many tanks have backup steam agitators to deal with agitator failure, these are only a short-term solution, as it is not known how long tanks can be operated under these conditions.

In a smelt dissolving tank, droplets of shattered molten smelt from the recovery boiler fall into the tank, interact with weak wash, and dissolve to produce green liquor. Agitators promote the mixing in the tank, which is critical to rapid dissolution of the smelt and ideally prevents the smelt from settling to the bottom of the tank. Good smelt dissolution and avoidance of smelt pooling is needed to avoid loud, violent, and potentially dangerous smelt-water interactions, such as during smelt runoffs [2,3].



1. Severe agitator scaling.

Cho [4] recently studied the effects of agitator configurations on the hydrodynamics and outlet concentrations in a cylindrical smelt dissolving tank to determine ideal design and operating conditions. That study used MixIT, a commercial computational fluid dynamics (CFD) software for simulating tank mixing. It was found that positioning agitators away from the outlet reduces outlet concentration fluctuations and low-velocity regions (i.e., "dead zones") where smelt might pool. It also indicated that tanks with three

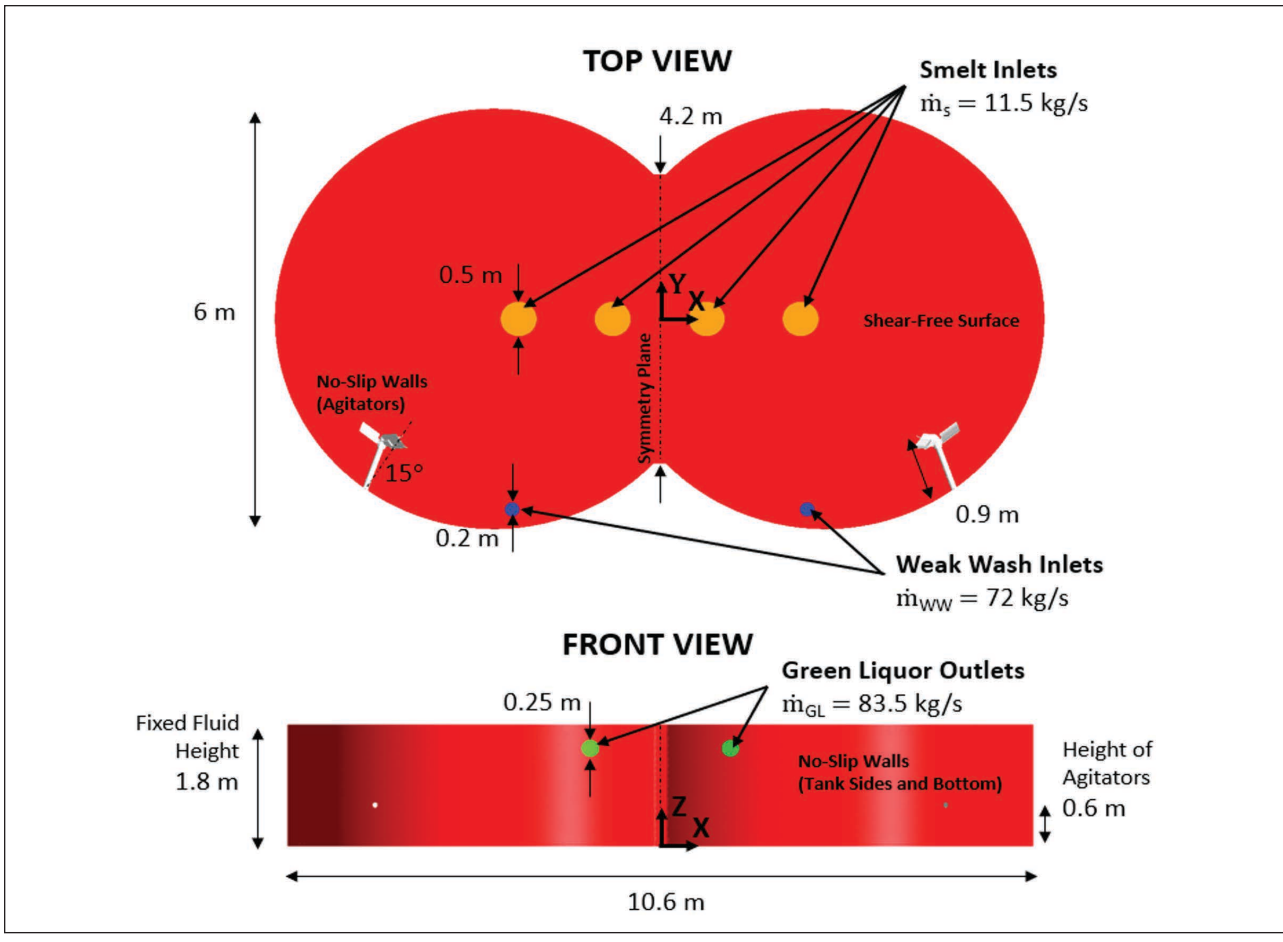

2. Model geometry and boundary conditions.

impellers could perform better than tanks with only two, although a poorly configured three-impeller tank could perform worse than a well configured two-impeller tank.

Although no other numerical studies of mixing in smelt dissolving tanks were found in literature, there have been several numerical studies of mixing tanks in general, usually involving cylindrical tanks with either top-entry [5-9] or side-entry [10-12] agitator configurations. The topics and purposes of these studies are all widely varied. For example, Madhania et al. [10,12] compared different turbulent and mixing model couplings for the mixing of two miscible liquids with large viscosity differences in a conical-bottomed cylindrical tank and the resulting mixing times obtained with the standard and realizable k-ε turbulence models. Torotwa and Ji [5] compared flow and homogeneity for four impeller designs (anchor, sawtooth, counterflow, and Rushton turbine). Zamankhan [6] studied the dissolution of multi-sized sodium formate granules in a baffled laboratory-scale tank. Hernández-Jaramillo et al. [11] simulated flow distribution in a crude oil storage tank. Zadravec et al. [9] examined the effect of the rotating domain size in a multiple reference frame modeling approach on numerical accuracy compared to experimental results. Cao et al. [7] developed a model for predicting the dissolution of spray-dried detergent powder, linking the dissolution behavior of bulk particles to the input power of the mixing system. Finally, Pakzad et al. [8] characterized the performance of a Scaba 6SRGT impeller for the mixing of non-Newtonian pseudoplastic fluids with a yield stress in laminar and transitional flow regimes.

The turbulence and mixing models that are used impact the numerical accuracy and computational cost. The Multiple Reference Frame model [13] was frequently used in the previously mentioned studies [5,8,9,10-12]. It is less accurate than the alternative Sliding Mesh model [14], but it is much less computationally expensive and allows for time-averaged steady-state solutions. Turbulence models included the standard k-ε [5,10,12]; realizable k-ε [10,12]; RNG k-ε [11]; k-ω-based shear stress turbulence [9]; and large-eddy simulation [6,10], with the latter being the most computationally expensive.

The objective of this work was to develop a CFD smelt dissolving tank model to determine how agitator scaling affects the hydrodynamics in the tank. Four cases are compared that range in degree of agitator scaling: clean agitators (i.e., no scaling), mild scaling (no bridging between blades), moderate scaling (bridging between blades), and extreme scaling (bridging between blades and more cover-

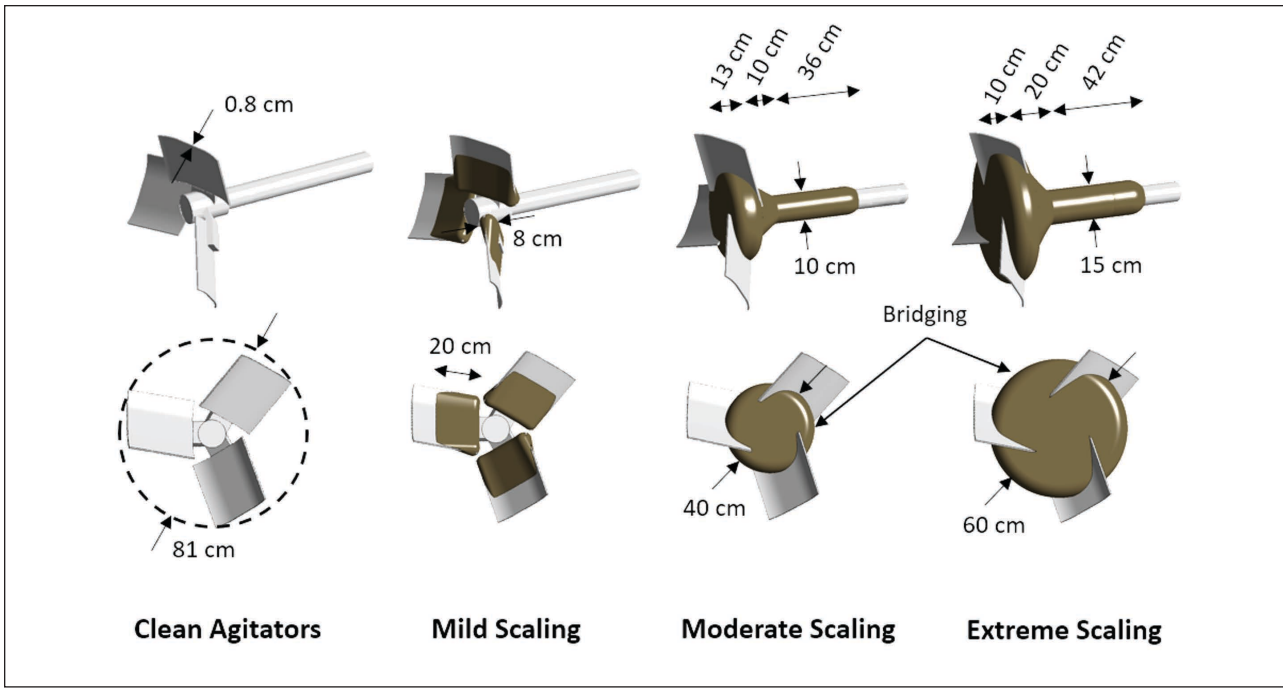

3. Agitator and scaling geometry.

age of blades). Velocity profiles for the four cases provide an indication of the extent to which mixing is affected. As described in the next section, smelt is treated as a liquid stream with twice the density of water [15], and then the density of the mixture of the weak wash and smelt are used to identify areas of relatively poor mixing.

COMPUTATIONAL METHODOLOGY

A steady state, three-dimensional (3D) model has been developed for a uniquely shaped industrial dissolving tank with side-entry agitators (**Fig. 2**). The tank resembles a peanut shell from above. Only the inside of the tank (i.e., the fluid domains and agitators) was modeled. The maximum length and width of the computational domain are 10.6 m and 6 m, respectively. A fixed height of 1.8 m was assumed for the fluid. Smelt was treated as a liquid miscible with water. Four smelt inlets, with a combined mass flow rate of $\dot{m}_S$= 11.5 kg/s, and two weak wash inlets, with a combined mass flow rate of $\dot{m}_{WW}$ = 72 kg/s, are located on the top surface of the domain. Two green liquor outlets, with a combined mass flow rate of $\dot{m}_{GL}$= 83.5 kg/s, are located on the front wall of the tank. The following material properties were assumed for weak wash and smelt: $\rho_{WW} = \rho_{water} = 1000$ kg/m^3, $\rho_{smelt} = 2\rho_{water} = 2000$ kg/m^3, and $\mu_{WW} = \mu_{smelt} = \mu_{GL} = 9.637\times10^{-3}$ kg/m-s. Shear-free conditions were imposed on the free surface and no-slip conditions on the tank walls and agitators. The agitators are offset 15° from the wall normal and are located 0.6 m from the bottom of the tank.

The geometry of the agitators and scaling from each case are given in **Fig. 3**. The mild scaling case has equal amounts of scaling on each blade that are thickest near the shaft of the agitator and then taper off about halfway up the blades. For the moderate and extreme scaling cases, the scale bridges the blades and covers the shaft. The extreme scaling case approximates the scaling shown in Fig. 1.

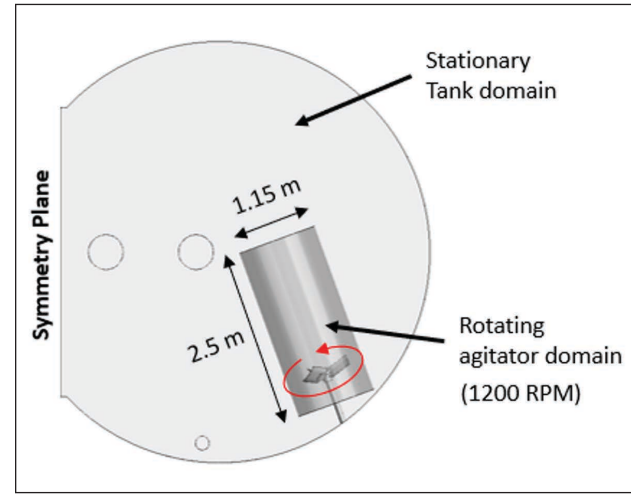

4. Multiple reference frame model setup.

The commercial, trademarked CFD software ANSYS Fluent was used to run the simulations. Preliminary simulations of the entire tank confirmed a symmetry about the tank center, and so thereafter, we modeled just the right half of the tank to reduce computational costs. Mixing was modeled with the Multiple Reference Frame model [13]. **Figure 4** shows the model setup. The tank was separated into a rotating agitator domain and a stationary domain for the remainder of the tank. Flow was solved in each subdomain in its corresponding reference frame. The rotating domain rotates at the speed of the agitator, 1200 rpm,

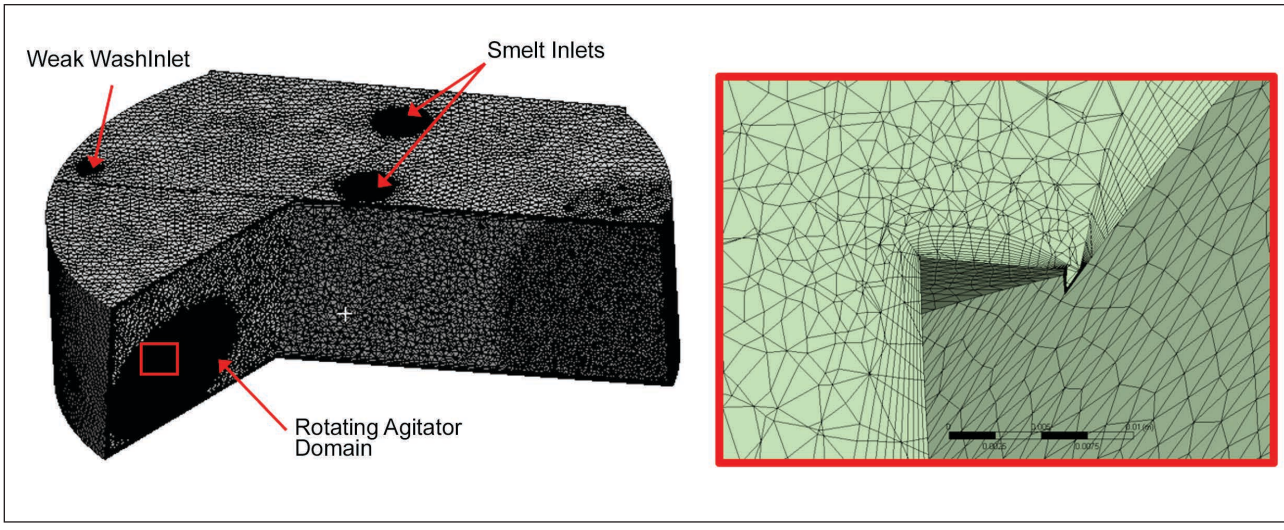

5. Cut-out view of the extreme scaling case mesh (left) and a zoom-in view of the agitator surface (right) prior to conversion to a polyhedral mesh.

which was kept constant even with scale up, as is done in practice. Although the rotating domain diameter was maximized to improve model accuracy, as was found in [9], the bottom of the tank posed an upper limit.

The realizable k-ε model was used to model turbulence. This model is a variation of the standard k-ε model and is more suitable for flows featuring strong streamline curvature, vortices, and rotation [16]. The curvature correction option and Menter-Lechner wall treatment were also used (see [16] for more information on turbulence modeling). For simplicity, the complex smelt-weak wash interaction described in [2,3] was not modeled.

Smelt concentration in the tank was modeled with the homogeneous multiphase mixture fraction model using an implicit formulation for the volume fractions of the miscible weak wash and smelt phases and the dispersed interface option because of the low loading of the smelt phase and to reduce computational cost (see [17] for more information on multiphase modeling).

The governing equations were spatially discretized in ANSYS Fluent with the following schemes: PRESTO! for pressure, second order upwind for momentum and turbulence, and QUICK for the multiphase volume fraction. The pressure-based solver and the SIMPLEC pressure-velocity coupling scheme were used. See [18] for detailed solver theory.

RESULTS AND DISCUSSION

Mesh independence and a convergence study

Meshes composed of tetrahedral cells were constructed for the right-half domain of each case using ANSYS Meshing. For example, **Fig. 5** shows the mesh used for the extreme scaling case. The mesh was refined at the inlets and outlet, the interfaces between rotating and stationary domains, and the agitator. Local refinements were also made within the rotating domain and the jet impingement region on the wall opposite the agitator. Mesh inflation was used on the walls

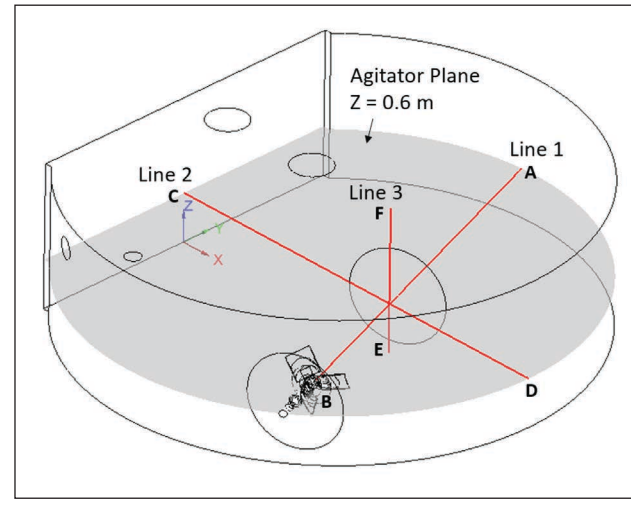

6. Three lines along which velocities are compared. Line 1 is co-linear with the agitator rotational axis. Line 2, also residing in the agitator plane, spans from the tank center to the opposite side wall. Line 3 is perpendicular to the agitator plane and passes through the intersection point of Lines 1 and 2.

and agitators (5 and 10 layers, respectively). Polyhedral meshes tend to be more efficient than tetrahedral meshes [19]; thus, once imported into ANSYS Fluent, the tetrahedral meshes were converted to meshes composed of polyhedral cells using the built-in Fluent conversion feature, reducing cell count by a factor of approximately 5. The prism cells in the inflation layers were preserved in the process.

A mesh study was conducted on the extreme scaling case to determine an appropriate level of mesh refinement, which was assumed to then apply for all the other cases. Three polyhedral meshes were compared: A, B, and C with 1.99 M, 3.71 M, and 6.29 M cells, respectively. To compare the three cases, velocities were examined along three lines illustrated in **Fig. 6**. **Figures 7–9** show the fluid velocities along those lines. Mesh independence is not fully

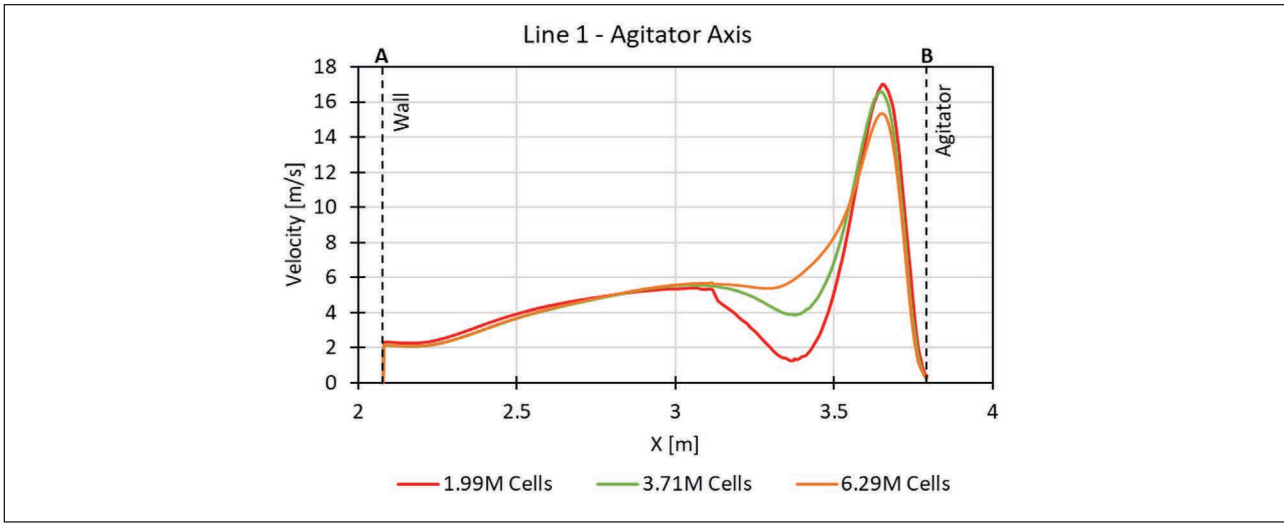

7. Mesh study velocity comparison along Line 1 from Fig. 6.

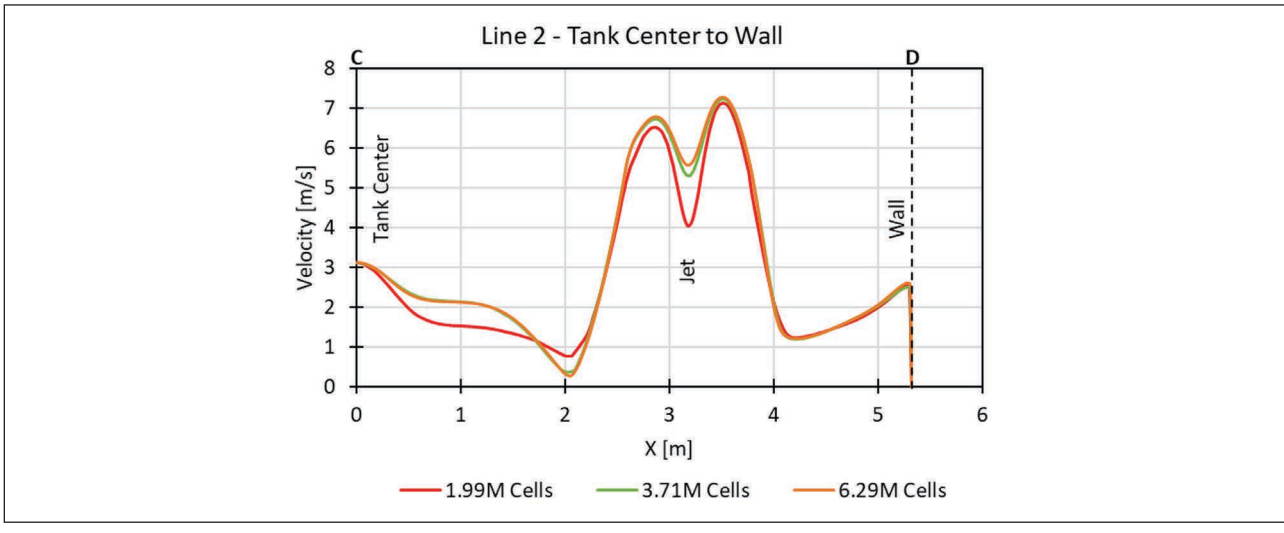

8. Mesh study velocity comparison along Line 2 from Fig. 6.

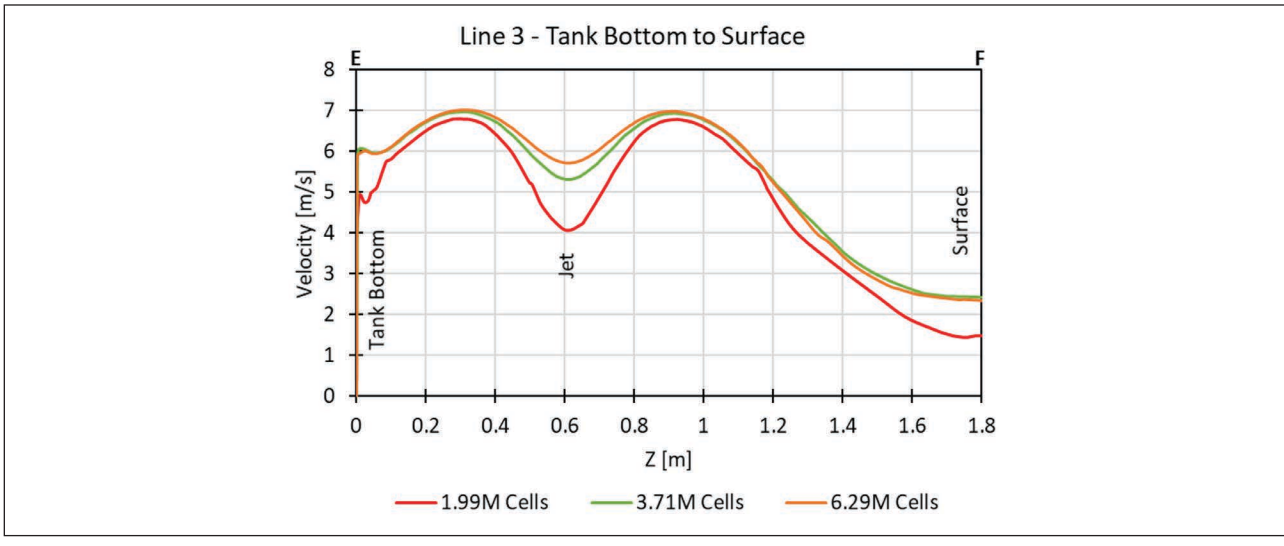

9. Mesh study velocity comparison along Line 3 from Fig. 6.

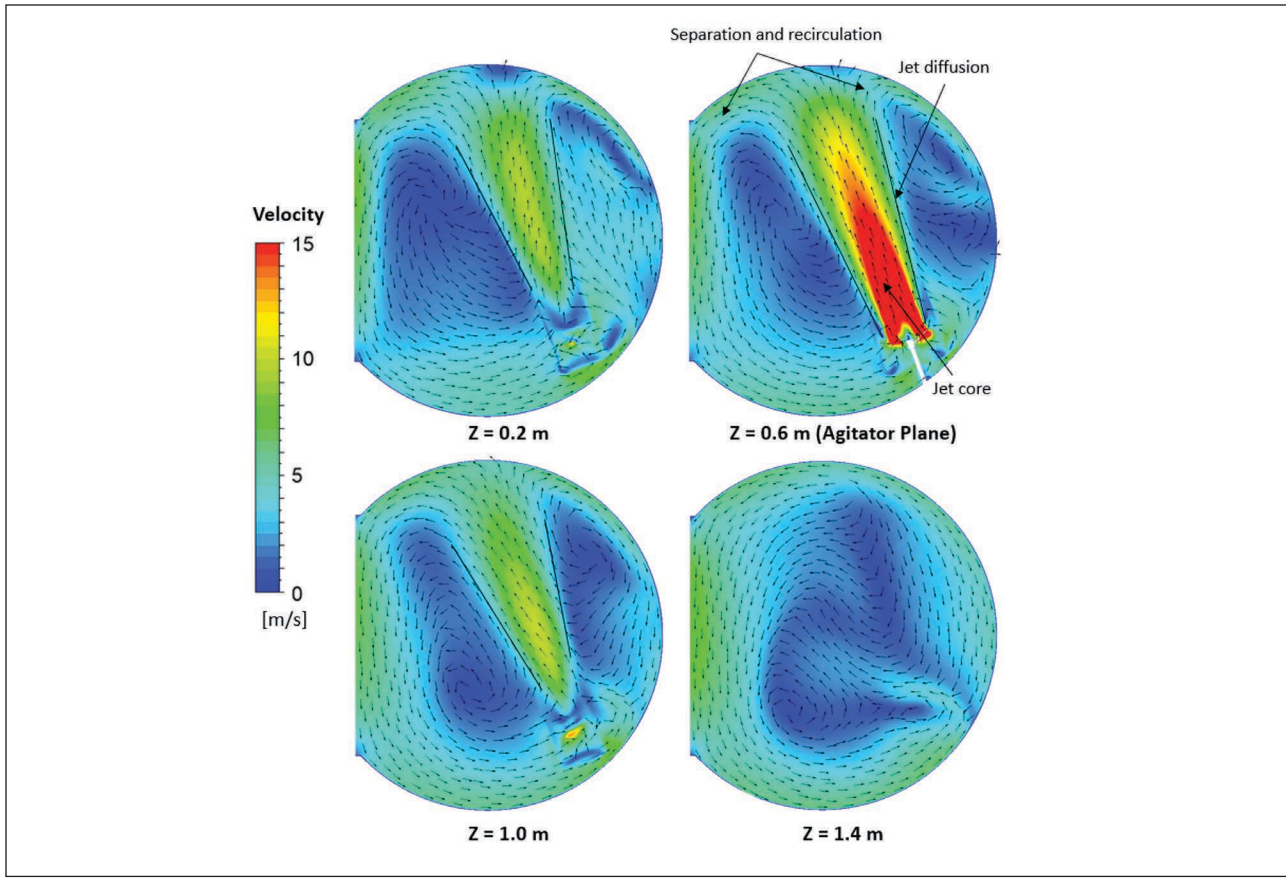

10. Clean agitator flow fields at Z = 0.2, 0.6, 1.0, and 1.4 m elevations from the bottom of the tank.

reached with Mesh B (3.71 M cells), as can be seen when comparing meshes B and C. Nevertheless, it was decided to proceed with this level of mesh refinement for the scaling study, because simulations took significant amounts of time to run and reach convergence. Based on these results, mesh-related inaccuracy is expected to be highest near the agitators but minimal throughout most of the tank.

Although there were no problems in achieving convergence for the extreme scaling case and clean agitator case, there were oscillations in the solutions for the other two cases, despite significant efforts to remove them. For example, modifying the turbulence model would sometimes resolve the issue for one case but create issues for others. It was ultimately decided to accept the oscillations, since velocities would only fluctuate locally within ±10% or less. Results for the mild and moderate scaling presented in what follows are the mean of these oscillations.

Scaling study

Effects on velocity

The clean agitator creates a high velocity jet that diffuses outward radially as it moves away from the agitator and impinges on the wall facing it (**Fig. 10**). The jet then separates and recirculates along the walls back toward the agitator, and some of the recirculated flow is drawn back into the jet. Eddies can be seen in the dark blue low-velocity regions. The agitator axis is at Z = 0.6 m and highest velocities are naturally seen at this level. At Z = 0.2 m and Z = 1.0 m, similar flow fields are obtained, although the jet is more diffuse and has a lower velocity due to the distance from the jet core. In these planes, the flow in the jet is also skewed to the right and left, respectively, due to the counterclockwise rotation imposed by the agitator. At Z = 1.4 m, the jet is very diffuse, although the recirculating flow pattern from the jet impingement is still present.

Figures 11 and 12 show similar flow fields for all the degrees of agitator scaling. The scaling reduces the jet velocity, as is apparent by the shorter high velocity red regions in the jet core at Z = 0.6 m with increased scaling. The regions outside of the jet also have lower velocities for the extreme scaling case compared to the other three, at both Z = 0.6 m and 1.0 m.

The average velocities in the tank (**Table I**) can be used to quantify the global impact of scaling on the dissolving tank hydrodynamics. With clean agitators, the average velocity in the tank is 4.00 m/s. This is reduced by 2.5%, 6.2%, and 35.2% due to mild, moderate, and extreme scaling, and so the overall effect is only pronounced for the extreme scaling case. It is interesting to note that the mild and moderate cases impact the velocities in similar ways, despite the bridging that is pres-

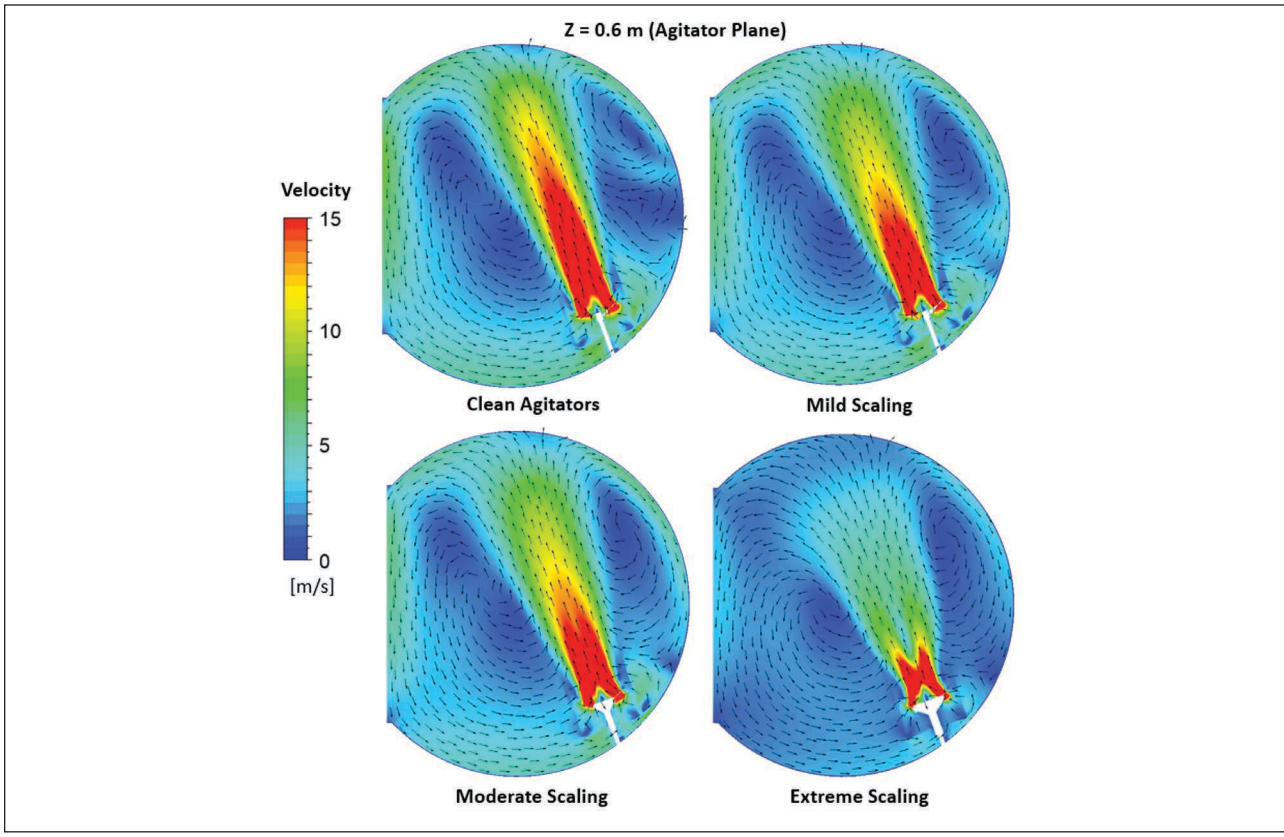

11. Flow field comparison of each scaling case at an elevation of Z = 0.6 m from the bottom of the tank (i.e., the agitator plane).

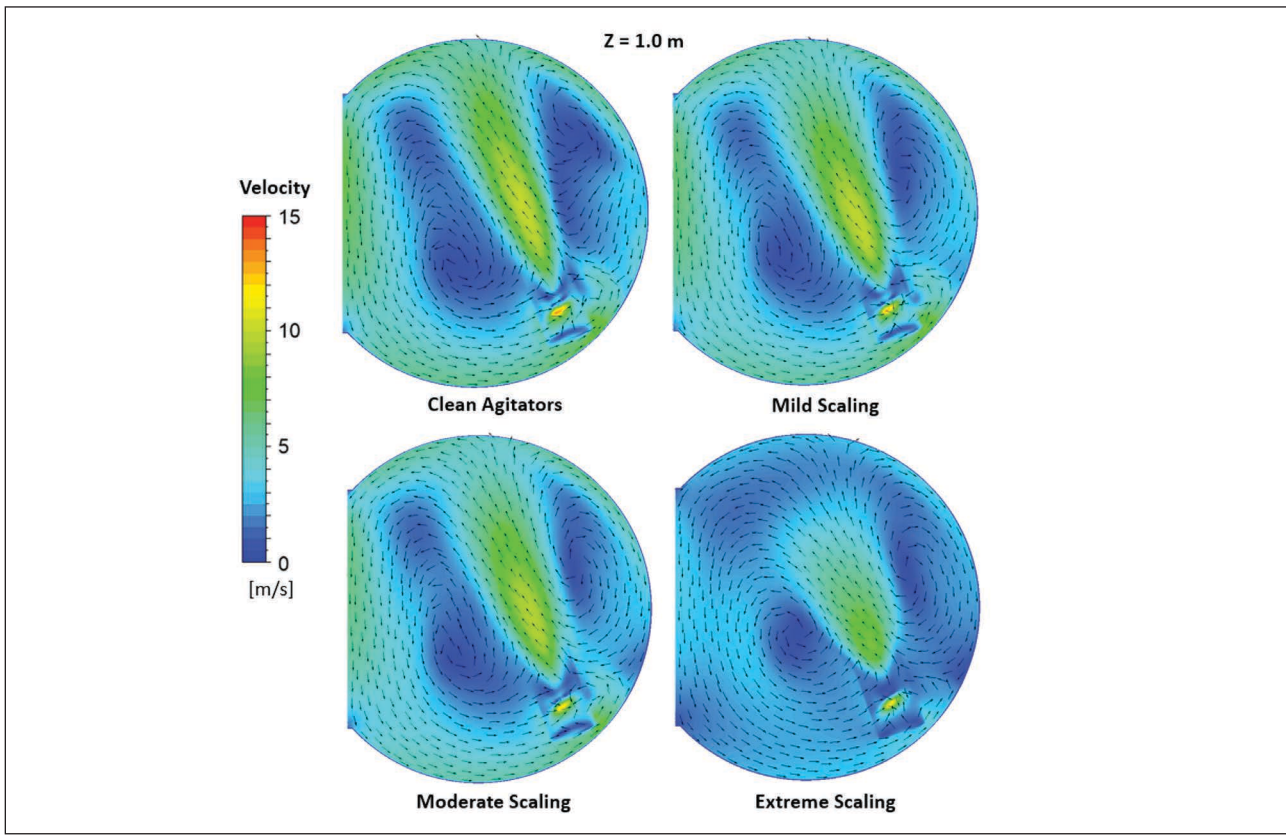

12. Flow field comparison of each scaling case at an elevation of Z = 1.0 m from the bottom of the tank.

Case:	Clean Agitator	Mild Scaling	Moderate Scaling	Extreme Scaling
Tank average velocity, m/s	4.00	3.90	3.75	2.59
Velocity reduction, %	--	2.5	6.2	35.2

I. Reduction of average velocities in the tank from scaling.

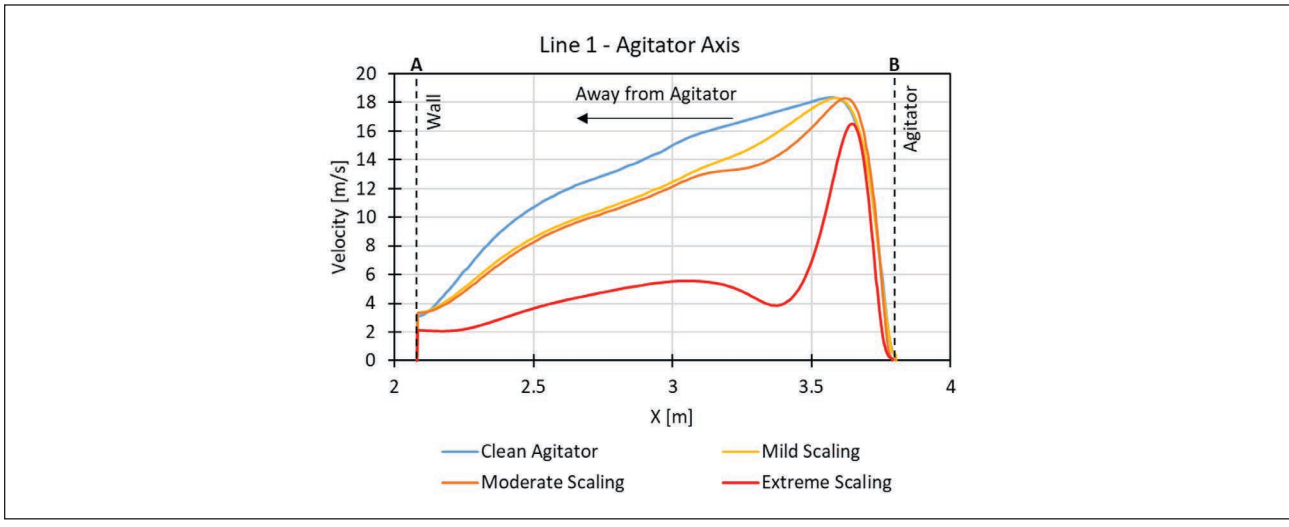

13. Velocity comparison of each scaling case along Line 1 from Fig. 6.

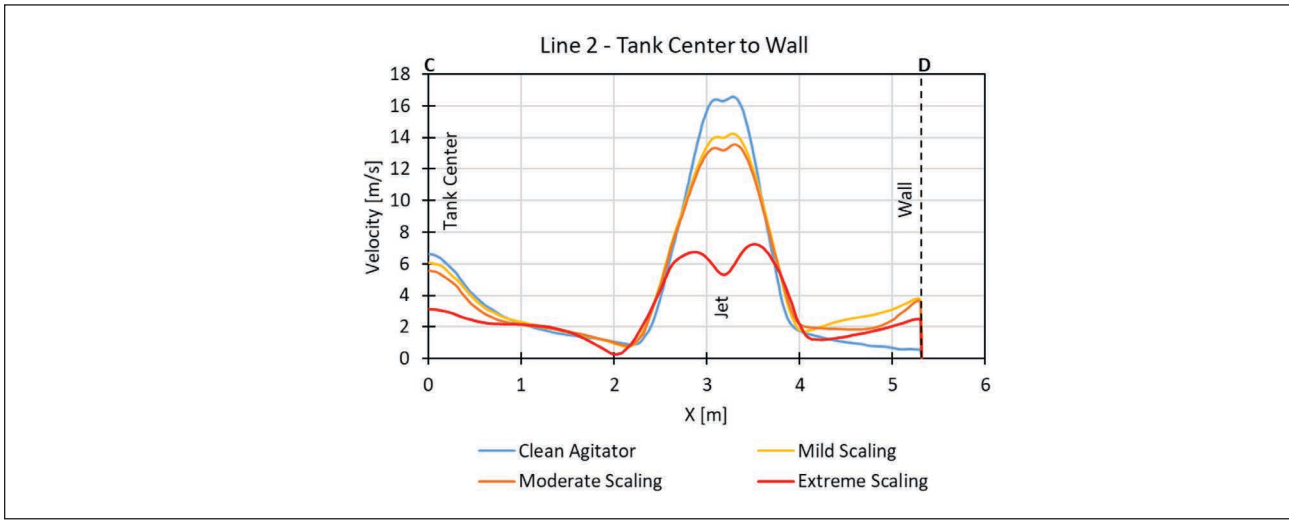

14. Velocity comparison of each scaling case along Line 2 from Fig. 6.

ent on the moderate scaling case. The similarity could be due to the relatively small blade spans in either case.

To quantitatively compare the four cases, velocities are plotted along Lines 1-3 from Fig. 6 shown earlier (**Figs. 13–15**). The peak jet velocity near the agitator at X = 3.79 m is similar for all four cases: ~16.5 m/s for the extreme scaling case and ~18.3 m/s for the other three cases (Fig. 13). The velocity decays very rapidly by X = 3.4 m for the extreme scaling case, whereas the other three cases show a more gradual velocity gradient along the line.

Perpendicular to the jet, velocities are generally lower as the scaling increases, particularly within the jet (**Fig. 14**). It is interesting to note that this is not the case near the wall, where velocities are higher with some scaling (the mild scaling case has the highest local velocity).

The effect of scaling on the diffusion of the jet is pronounced when looking at the vertical axis line, which is 1.79 m from the agitator (**Fig. 15**). Velocities are all very similar near the bottom of the tank. Near the free surface, the velocity is about the same for the clean agitator, mild, and moderate scaling cases, ~0.8 m/s, whereas it is higher for the extreme scaling case, ~2.4 m/s.

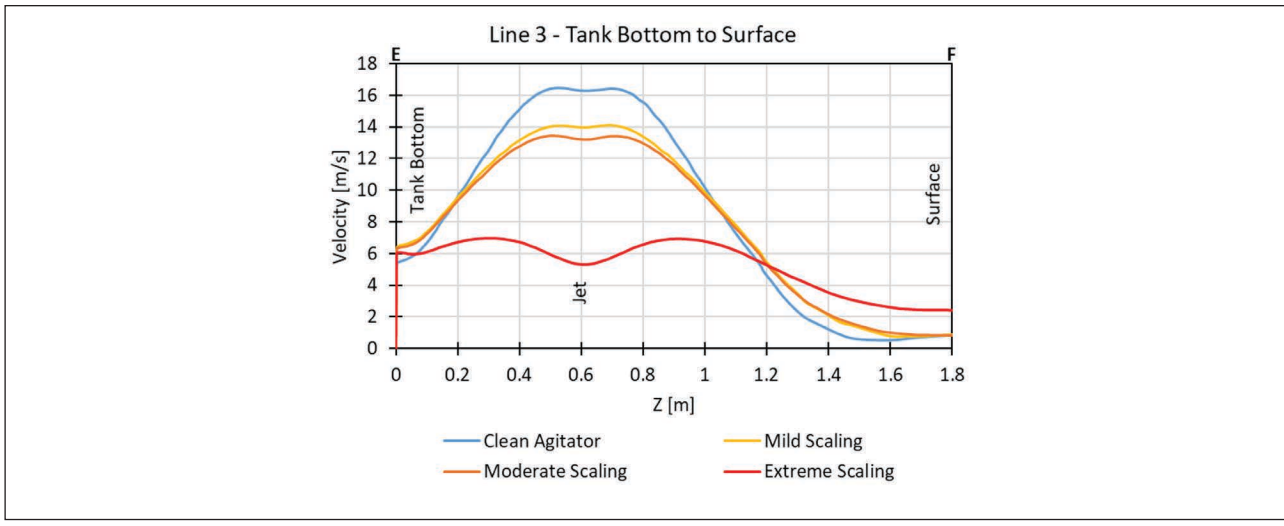

15. Velocity comparison of each scaling case along Line 3 from Fig. 6.

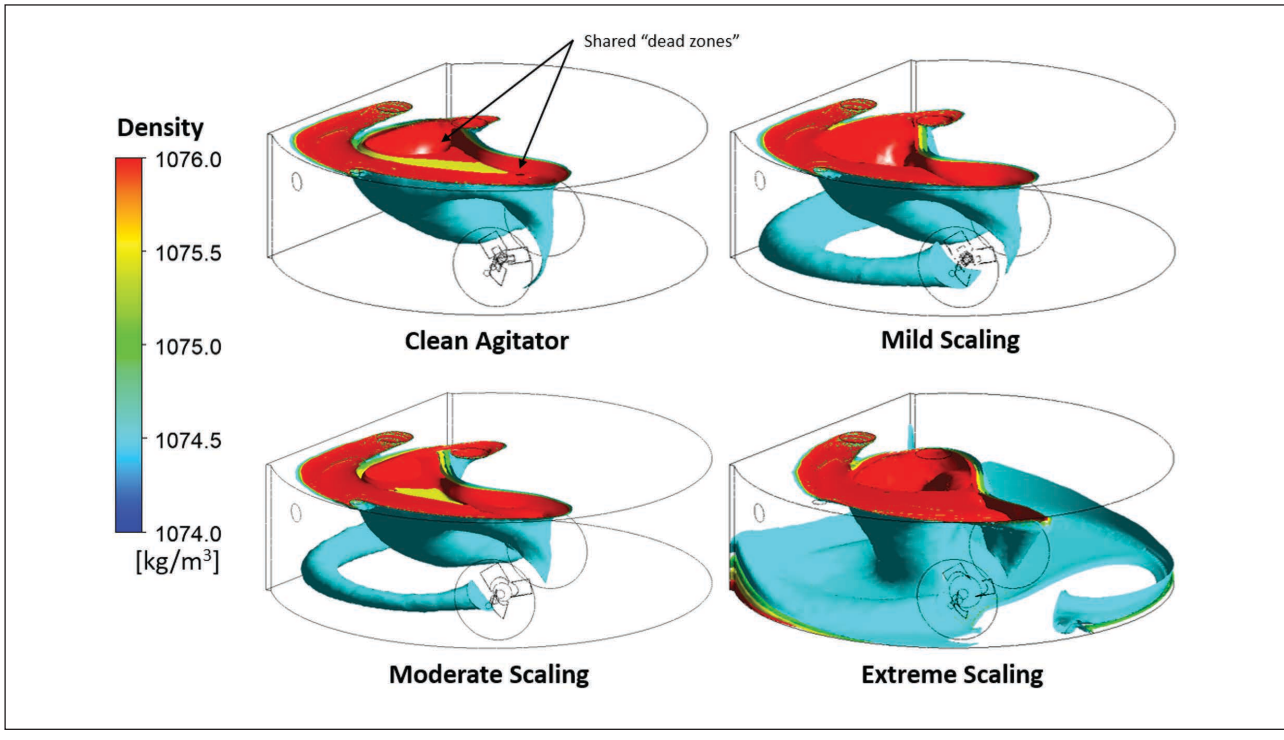

16. Isosurfaces of above average density in the tank due to higher smelt concentration.

Effects on smelt mixing

The multiphase model tracked the volume fractions of the smelt and weak wash phases throughout the tank, and overall densities were computed based on the volume fractions. Since smelt is denser than weak wash, higher smelt concentrations are denoted by regions of higher overall density. The average overall density in the tank is 1074.4 kg/m³ for all the cases, and the resulting variances are very small due to the long residence times and considerable agitation. Four density isosurfaces, corresponding to 1074.5, 1075, 1075.5, and 1076.0 kg/m³, allow for visualization of the extent of mixing of the weak wash and smelt in all cases (**Fig. 16**). Regions encapsulated by these surfaces have higher smelt concentrations. Near the smelt inlets, smelt concentration is obviously highest. The recirculated flow from the jets then sweeps the smelt towards the agitators and into "dead zones" that are shared by all four cases. These dead zones thus have higher smelt concentrations, which coincide with the findings of Cho [4]. The bottom of the tank has higher smelt concentrations for all three scaling cases, but this is especially pronounced for the extreme scaling case. Acknowledging that smelt-water interaction is

more complicated than modeled here and thus actual smelt concentrations might look somewhat different, the results nevertheless indicate that in the extreme scaling case, mixing of smelt with weak wash is diminished, which may imply a risk of smelt pooling.

CONCLUSIONS

The results presented in this paper strongly indicate that by the time an agitator scales to the degree that it needs to be taken down due to excessive vibration or the limitations of pump amps, it is likely no longer mixing sufficiently. What is harder to quantify is when mixing is no longer adequate between the moderate case and extreme case. The next step in this research will be to better account for smelt-water interaction, including smelt droplet cooling and dissolution, which will better define the conditions for which smelt droplets begin to reach the bottom of the tank and pool, rather than dissolve. Additional modeling work is also needed to better understand what limits the strength of the jet so that some more general guidelines on agitator scaling can be provided. Lastly, additional modeling work is needed to identify the source of the oscillations seen in the mild and moderate scaling cases.

ABOUT THIS PAPER

Cite this article as:
Gareau, P., Bussmann, M., and DeMartini, N., *TAPPI J.* 21(4): 189(2022). https://doi.org/10.32964/TJ21.4.189

DOI: https://doi.org/10.32964/TJ21.4.189

ISSN: 0734-1415

Publisher: TAPPI Press

Copyright: ©TAPPI Press 2022

About this journal

ACKNOWLEDGEMENTS

This work is part of the industrial research consortium project Effective Energy and Chemical Recovery in Pulp and Paper Mills - III at the University of Toronto supported by Andritz, Arauco, Babcock & Wilcox, Canadian Kraft Paper, Cenibra, Clyde Bergemann, CMPC, FITNIR, FPinnovations, Georgia Pacific, International Paper, Irving, KFS, Klabin, Mercer, Rayonier, Sappi, Södra, Stora Enso, Suzano, Valmet, and WestRock. We would also like to acknowledge

ABOUT THE AUTHORS

Hard calcium carbonate scale often forms on the agitators in smelt dissolving tanks, and the effects of this scale on mixing are not well understood. A steady state, 3D model has been developed for a smelt dissolving tank at a kraft pulp mill to better understand the impact of agitator scaling on hydrodynamics and tank concentrations. While mixing in tanks has often been modeled in the literature, there have been no studies involving agitator scaling.

Modeling mixing in an industrial-scale tank is computationally expensive. Thus, finding the right balance between model accuracy and computational expense was the most difficult aspect of this research, which was addressed through a literature review of other mixing tank models and by trying different models during the model development stage.

Flow fields were obtained for four cases (clean agitators and mild, moderate, and extreme scaling), showing that mixing is negatively impacted by agitator scaling, particularly for the extreme scaling case, in which a 35% reduction in the average fluid velocity in the tank resulted.

The results presented in this paper strongly indicate that by the time an agitator scales to the degree that it needs to be taken down due to excessive vibration or the limitations of pump amps, it is likely no longer mixing sufficiently, which may lead to smelt pooling. With the information presented here, mills can have better knowledge of the degree to which mixing is impacted by agitator scaling and when it needs to be shut down for removal and cleaning. The next step in this research will be to better account for smelt-water interaction, including smelt droplet cooling and dissolution, which will better define the conditions for which smelt droplets begin to reach the bottom of the tank and pool, rather than dissolve.

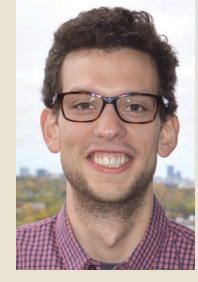

Gareau



Bussmann



DeMartini

Gareau is an MASc graduate and Bussmann is professor and chair of the Department of Mechanical & Industrial Engineering at the University of Toronto, Toronto, Canada. DeMartini is associate professor in the Department of Chemical Engineering & Applied Chemistry at the University of Toronto, Toronto, Canada. Email Bussmann at markus.bussmann@utoronto.ca.

the support of the Natural Sciences and Engineering Research Council of Canada (NSERC), [IRCPJ 517715 -16]. Cette recherche a été financée par le Conseil de recherches en sciences naturelles et en génie du Canada (CRSNG), [IRCPJ 517715 -16].

LITERATURE CITED

1. Giglio, A., Björk, M., Wadsborn, R., et al., *TAPPI J.* 19(8): 387(2020). https://doi.org/10.32964/TJ19.8.387.
2. Jin, E., Bussmann, M., and Tran, H., *TAPPI J.* 14(6): 385(2015). https://doi.org/10.32964/TJ14.6.385.
3. Jin, E., "Smelt droplet-water interaction in the kraft recovery boiler dissolving tank," Ph.D. thesis, University of Toronto, Toronto, 2017.
4. Cho, D., "Computational fluid dynamics modeling of dissolving tank hydrodynamics," MASc thesis, University of Toronto, Toronto, 2020.
5. Torotwa, I. and Ji, C., *Designs* 2(1): 2010010(2018). https://doi.org/10.3390/designs2010010.
6. Zamankhan, P., *Chem. Eng. Technol.* 33(3): 508(2010). https://doi.org/10.1002/ceat.200900347.
7. Cao, H., Amador, C., Jia, X., et al., *Chem. Eng. Res. Des.* 114: 108(2016). https://doi.org/10.1016/j.cherd.2016.08.012.
8. Pakzad, L., Ein-Mozaffari, F., Upreti, S.R., et al., *Can. J. Chem. Eng.* 91: 90(2013). https://doi.org/10.1002/cjce.21616.
9. Zadravec, M., Basic, S., and Hribersek, M., *J. Eng. Sci. Technol.* 2(2): 126(2007).
10. Madhania, S., Cahyani, A.B., Nurtono, T., et al., *IOP Conf. Ser.: Mater. Sci. Eng.* 316: 012014(2018). https://doi.org/10.1088/1757-899X/316/1/012014.
11. Hernández-Jaramillo, D.C., Nieto-Londoño, C., Álvarez-Sarmiento, N., et al., *Iteckne* 12(1): 25(2014). https://doi.org/10.15332/iteckne.v12i1.818.
12. Madhania, S., Fathonah, N.N., Kusdianto, et al., *MATEC Web Conf.* 333: 02003(2021). https://doi.org/10.1051/matecconf/202133302003.
13. ANSYS, "Chapter 9: Modeling flows with moving reference frames," in *ANSYS Fluent, 19.1, Help System, User Guide*, ANSYS Inc., Canonsburg, PA, USA, 2019, pp. 997-1020.
14. ANSYS, "Chapter 10: Modeling flows using sliding and dynamic meshes," in *ANSYS Fluent, 19.1, Help System, User Guide*, ANSYS Inc., Canonsburg, PA, USA, 2019, pp. 1021-1142.
15. Lin, Z., "Characterizing smelt shattering in recovery boilers," Ph.D. thesis, University of Toronto, Toronto, 2014.
16. ANSYS, "Chapter 4: Turbulence," in *ANSYS Fluent, 19.1, Help System, Theory Guide*, ANSYS Inc., Canonsburg, PA, USA, 2019, pp. 39-140.
17. ANSYS, "Chapter 17: Multiphase flows," in A*NSYS Fluent, 19.1, Help System, Theory Guide*, ANSYS Inc., Canonsburg, PA, USA, 2019, pp. 505-652.
18. ANSYS, "Chapter 21: Solver theory," in *ANSYS Fluent, 19.1, Help System, Theory Guide*, ANSYS Inc., 2019, pp. 679-740.
19. ANSYS, "Chapter 17: Generating polyhedral meshes," in *ANSYS Fluent, 19.1, Help System, User Guide*, ANSYS Inc., Canonsburg, PA, USA, 2019, pp. 267-272.

Comparative study of guar gum and its cationic derivatives as pre-flocculating polymers for PCC fillers in papermaking applications

INDRASENA GHOSH, CHHAYA SHARMA, AND RITA TANDON

ABSTRACT: In this work, gums from guar seeds were evaluated as a potential precipitated calcium carbonate (PCC) filler pre-flocculant to induce functional filler in papermaking applications. In recent years, guar has been considered one of the promising wet-end additives due to its abundance, rich source of hemicellulose content, and biodegradability. However, application of guar gum in filler pretreatment methods for producing high ash paper has scarcely been reported.

In this paper, the flocculating ability of three types of guar gum was established with charge analysis and turbidity (NTU) of the system at 1% and 5% for each gum: native gum (NG) having a degree of substitution (DS) of 0, and cationic gums having a DS value of 0.07 (CL) and 0.15 (CH). It was interesting to observe that even at a 5% dose of NG, the charge density of PCC did not deviate much from the initial values. The system carried a weak negative charge, resulting in an unstable colloidal suspension that led to PCC-PCC particle bridging. On the other hand, the operative mechanism of CL and CH during adsorption and PCC flocculation was predicted to be charge neutralization and electrostatic-patch formation, accompanied by particle bridging. Note that CL, with a maximum 47.5% reduction in residual turbidity of PCC at a 1% dose, was much more efficient in doing so than the other two gums; NG had a 40% maximum reduction in residual turbidity at a 5% dose and CH had a maximum 30% reduction at a 1% dose. Later on, floc formation and structure were correlated with optical and field emission scanning electron microscopy (FE-SEM) images.

In the next set of trials, paper properties were determined by varying the different gum dosages from 0.2% to 5% at a constant dose of 20% filler. It is also noteworthy to mention that with 1% CL (low DS) dose, PCC retention increased by 39%, which also enhanced the tensile, tear, burst, and opacity properties by 11%, 19%, 5%, and 4.4%, respectively, without significantly affecting the bulk properties. Further, wide-angle X-ray diffraction (XRD) analysis and Fourier transform infrared (FTIR) analysis revealed that pre-flocculating PCC with a 1% gum dose did not induce any change in crystalline transformation. Based on observation, it was found that cationic gums with low DS values are a better choice for maximizing the strength of paper while maintaining bulk and high opacity when pre-flocculation is adopted to increase the filler retention in paper.

Application: This work aims to identify the flocculation mechanism of PCC with guar gum and its derivatives in order to establish pre-flocculated filler slurries prior to stock addition. The most important contribution from the study is selection of the optimum degree of substitution (DS) value, which is crucial when adopting pre-flocculation technologies that later affect strength of paper and filler retention.

Utilization of biobased resources in filler modification technology has been an active field aimed at overcoming the drawback of paper strength failure at high filler addition [1]. As per knowledge, since fillers are inert and are incapable of making bonds with cellulose fibers, modifying their surfaces with a hydroxyl group containing polysaccharides can conquer their disadvantages and add beneficial attributes to retention and strength properties. In this respect, considerable works have already been reported with starch, cellulose, chitosan, and their derivatives. With successful commercialization of this technology, which has found potential practical solutions for the papermaking industry, researchers are now focusing on new biodegradable polymers as filler modifiers [2-4].

Given growing challenges, the emerging utility of gum and its different chemically modified derivatives has motivated various sectors in India to intensify research on new applications for them, including the sectors of paper, textile, petroleum recovery, and pharmaceuticals [5]. Seed gums are one of the richest sources of renewable functional hemicellulosic biopolymers and are relatively low-cost biodegradable polymers. Guar gum is one of those gums that is commercially available in India, Pakistan, and the southwestern United States. It is a water-soluble

polysaccharide that mainly consists of D-mannopyranose rings with galactopyranose side branching units [6]. Since consumption of starch in the paper industry is very common, physiochemical properties of starch and guar gum may be important aspects to consider. The highly branched structure amylopectin in starch confers relatively higher molecular weight of the polymer compared to gum and is only soluble in hot water, while gum is soluble in cold water [7-9]. However, solubility of gum can be hastened by heating but generally degrades at high temperature. Additionally, starch in its native state is not very favorable for papermakers, as it tends to undergo retrogradation that results in viscosity instability, making processability difficult [7]. On the other hand, viscosity of guar in water is unaffected by pH change and salts, thus providing easy control of guar dispersion [9].

In available literature, guar has been established as a wet-end retention aid chemical that improves the paper's physical and mechanical properties by regulating the flocculation state during the papermaking process [6,10]. The conformation of guar gum in aqueous solution adopts a random coiled structure with extensive intermolecular hydrogen bonding between unsubstituted mannose ring and large hydrodynamic volume [11,12]. During the kraft pulping process, large portions of inherent hemicellulose in wood chips are unintentionally removed, which gum supplements as a bonding material in the later stage of paper formation. In addition to its gluing property, its thickening and gel forming properties are advantageous in manufacturing high-quality paper grades [13]. Guar gum derivatives, especially cationic guar products, have replaced native gum for many years, and their viability in papermaking has been explored by many authors. Interaction of cationic guar with pulp and fines has been thoroughly studied through adsorption phenomenon, indicating that electrostatic forces were added advantages in addition to hydrogen bonding that resulted in improved strength of paper [14,15]. It is also interesting to note that cationic guar-based retention aid systems outperformed cationic starch in ash retention and formation properties [16]. Deposition of stickies is another problem during the papermaking process, and it has been observed that cationic guar having a degree of substitution (DS) value lower than cationic starch was superior in controlling stickies [17]. On the other hand, precipitated calcium carbonate (PCC) is the most common filler used in the paper industry, and the alkaline pH of PCC may be attributed to hydrolysis of carbonate ions [18].

Application of gum in filler pretreatment has rarely been reported. One patent disclosed by Fairchild revealed that cationic PCC treated with 1% anionic xanthan gum was enough to promote sufficient flocculation of PCC, which aided in improving filler retention, internal Scott bond, and strength properties [19]. To date, studies on guar gum-mediated filler pre-flocculation have not reported elsewhere, although extensive research on starch in pre-flocculation technology has been reported [20-22]. Therefore, this study involves comparative experiments on pre-flocculation of PCC with native guar gum, including its derivatives, and their implications for paper handsheets.

MATERIALS AND METHODS

Materials

Native and HIBOND-brand cationic guar gums were given as sample gifts from Hindustan Gum & Chemicals Ltd. (Bhiwani, Haryana, India). Industrial PCC was procured from local paper mills in India. Chemicals were used without any further purification. Detailed properties of different types of gums and PCC are described in **Table I**. Bleached hardwood pulp with initial 17°SR was obtained from an integrated paper mill in India.

Methods

Preparation of PCC and different gum dispersions

The PCC slurry was dispersed at 10% consistency with mechanical stirrer at 2000 rpm for at least 2 h prior to pre-flocculation. It was then diluted to 3% consistency before addition of gums. Then, 0.5% native gum was freshly cooked in distilled water at 80°C for 1 h in a water jacketed vessel equipped with continuous stirring. Cationic gums were stirred at 500 rpm with a magnetic stirrer in water at ambient temperature to form 1% gum dispersions. Homogeneous dispersion of gums was transferred to other beakers for subsequent use in pre-flocculation.

Pre-flocculation of PCC with native gum and cationic gums

Pre-flocculation was carried out while stirring the PCC slurry at 500 rpm for all samples prepared. Freshly prepared gums were gradually added in the slurry at different dosage levels, ranging from 1%–5% on the basis of ovendry (o.d.) PCC, and total time of pre-flocculation was fixed at 5 min. Final consistency of pre-flocculated PCC in all the samples was maintained at 3.5% by adding 7 g of PCC in 200 mL of water. The as-prepared samples were directly used further for papermaking application.

Characterization

FTIR and XRD

For characterization of pre-flocculated and untreated fillers, several sets of experiments were performed. Samples were dried for 24 h at 40°C to form dried powders before Fourier transform infrared (FTIR) spectrophotometry analysis with a PerkinElmer (Waltham, MA, USA) spectrophotometer and wide-angle X-ray diffraction (XRD) analysis with a Rigaku (Tokyo) Ultima IV diffractometer. For FTIR analysis, samples were diluted with potassium bromide (KBr) to form pressed pellets, and absorption spectra were collected in a transmission mode conducting 16 scans at a resolution of 4 cm^{-1} between 4000 and

Trade Name	Native Guar	HIBOND GCP-31	HIBOND GCP-15	PCC
Stock concentration, %	0.5	0.5	0.5	10
Degree of substitution, DS	0	0.07	0.15	-
Molecular weight, g/mole	12×105	5.5×105	5×105	-
Nature of charge	Anionic	Cationic	Cationic	Anionic
Titrated volume for charge neutralization, mL	1.85	1.6	2.9	0.25
Charge density, μeq/g	-1728.97	1739.13	2932.85	-9.8
Brookfield viscosity (cps) @ 1%	5500	1100	1200	-
pH	7	7	7.5	11.2

I. Characteristics of native gum, cationic gums with 0.07 and 0.15 degree of substitution, and precipitated calcium carbonate (PCC) filler.

500 cm^{-1}. The XRD analysis was performed at a scan rate of 4°/min over a range of 2θ=5°–80°. The operating voltage was 40 kV with a current of 30 mA. The radiation source was nickel-filtered CuKα (λ=1.5406 Å) [4].

Charge determination and turbidity analysis

Surface charge and electrophoretic mobility of filler slurry was determined by zetasizer using a ZetaPlus zeta potential analyzer (Brookhaven; Holtsville, NY, USA). For that, filler slurries were diluted to 0.1% followed by ultrasonication before testing. Colloidal charge densities of fillers and gums were also calculated with particle charge detector (PCD) from BTG/Mutek [23]. The instrument applies a titration method where 0.001 N standard solution of polydiallyldimethylammonium chloride (PDADMAC) and polyethene sodium sulfonate (PES-Na) were used as cationic and anionic titrants, respectively. Also, a 10 mL of the sample containing 0.01 g was kept constant for all samples. The streaming potential and volume of the titrant (cationic/anionic) required to reach the point of zero charge (i.e., streaming current= 0 mV) were noted for each experiment. Charge density was calculated from the following equation:

$$Q = \frac{V \times C}{M} \quad (1)$$

where Q is expressed in eq/g; V is the consumed titrant volume in L; C is the concentration of titrant in eq/L; and M is the solid content in grams in 10 mL volume. For turbidity analysis, 1% of all filler slurries were kept for 24 h after pretreatment in a stationary manner [24]. The supernatants were analyzed for turbidity through a 2100AN turbidity meter (Hach; Ames, IA, USA) at an NTU ranging from 0–10,000. It gave an indication of deposition efficiency on PCC for different gums, with higher turbidity values corresponding to lower deposition efficiency.

Microscopic analysis and particle size determination

Image analysis through optical microscope (B1 Series, Motic; Hong Kong) was done by diluting the filler slurries to 1% and then spreading them on the glass slides, which was followed by air drying. Imaging was performed at 10x and 40x, respectively. It is important to efficiently study the basic characteristics of the microstructure; therefore, morphological and textural studies of PCC flocs were carried out with a MIRA 3 (TESCAN; Brno, Czechia) field-emission scanning electron microscope (FE-SEM) operated at a voltage of 8–10 kV. The as-prepared PCC flocs (0.2%) were again diluted, and one drop was taken on a small piece of glass slide and dried for 24 h at 40°C to obtain discrete flocs under the microscope. The floc size and distribution were also analyzed by FE-SEM and calculated from ImageJ Basics opensource software [25].

Handsheet preparation and characterization

Dried pulps were first beaten in a laboratory Hollander beater to a level of 38°SR and then disintegrated at a pulp consistency of 1% for 10 min at 3000 rpm. Pulp slurry was then diluted to 0.4% prior to the addition of treated and untreated fillers. For papermaking experiments, gum dosages were varied from 0.2% to 5% for the treatment of o.d. PCC filler during pre-flocculation. The pre-flocculated PCC filler loading was kept constant at 20% based on o.d. pulp. The stock suspension was then mechanically stirred at 400 rpm for 5 min and transferred to a batch laboratory sheet former so as to achieve a target basis weight of 70 g/m^2 according to the TAPPI Standard Test Method T 205 sp-02 "Forming handsheets for physical tests of pulp." The handsheets were then conditioned in a humidity chamber at 23°C±1°C and relative humidity 50±2% before testing. Filler dose was kept constant at 20% based on o.d. pulp. For filler retention, ash in the paper was estimated by incinerating paper sheets at

525°C as per TAPPI T 211 om-93 "Ash in wood, pulp, paper and paperboard: combustion at 525°C." Thus, filler retention was calculated from the following equation:

$$Filler\ retention = \frac{Ash\ in\ filled\ paper(g) - Ash\ in\ unfilled\ paper\ (g)}{Amount\ of\ total\ filler\ added\ (g)} \times 100 \quad (2)$$

The various paper properties that were evaluated according to TAPPI procedures are summarized in **Table II**, as is the testing equipment from L&W (ABB Lorentzen & Wettre; Zurich) and Konica Minolta (Chiyoda City, Tokyo). Bulk was calculated from caliper. All experiments were carried out three times, and the bars shown in certain figures that follow present the standard deviation on each side of the mean value. The internal structure of the paper was analyzed through FE-SEM. It provides an idea about filler distribution and how the distribution can affect fiber-filler-fiber bonding, which can then be correlated with paper properties.

As mentioned earlier, pre-flocculation behavior of PCC was studied with native guar and its two cationic derivatives by varying the dosages of gums through various analytical tools.

RESULTS AND DISCUSSION

Characteristics of different gum and PCC fillers

Table I describes the characteristics of underivatized guar and its cationic derivatives, along with PCC filler. The concentration for all the gum solutions was kept at 0.5% for ease of handling the stock solution. The nature of native gum resulted in high solvation, which was responsible for a much higher increase in solution viscosity compared to cationic gums [12]. However, chemical modification in the guar backbone consequently reduces the molecular weight and viscosity, as reported elsewhere [12,26]. Generally, cationic derivatives are obtained by grafting quaternary amine groups through reaction of hydroxyl group present in galactose side chains [27]. Slightly less molecular weight is evident at higher DS of cationic gum. Though natural gum is considered to be non-ionic and neutral [28], in the present study, native guar exhibits anionic character, as shown by charge density value, that may be due to the fractions of uronic acid derivatives, as claimed by some authors [23,27,28]. On the other hand, higher DS represents more cationic charge density of the guar samples. As we can see, the pH of all the gums show a neutral value. The PCC filler at 10% consistency is slightly anionic at its initial high alkaline pH, as reported in another study [29.] In our previous study, the industrial PCC shows similar absorption spectra as revealed in the current work. The presence of OH and CH species may confer the presence of some added organic additives as dispersants during the manufacturing process [29].

Effect of pre-flocculation on residual turbidity and system charge

Pre-flocculation of PCC with 1% and 5% dose of each gum was carried out to study their effects on charge analysis and residual turbidity after flocculation, as presented in **Table III**. With native gum, the change in charge density of PCC was not very significant, even at a 5% dose, and pre-flocculated PCC dispersion showed slightly weak negative charge. This was in accordance with the zeta potential values that demonstrate almost near neutral negative charge at 5% dosage. Moreover, low values of zeta potential suggest unstable colloidal dispersion of PCC, which arises due to particle–particle aggregation that overcomes the electrical double-layer repulsive forces. According to Dejaguin-Landau-Verwey-Overbeek (DLVO) theory, stable colloidal dispersion can be obtained from the energy barrier between the particles that results from interaction of van der Waals

Paper Properties	TAPPI Standard Test Method	Instrument Model
Tensile index	T 494 om-01 "Tensile properties of paper and paperboard (using constant rate of elongation apparatus)"	SE 060 (L&W)
Tear index	T 414 om-98 "Internal tearing resistance of paper (Elmendorf-type method)"	SE 009 (L&W)
Burst index	T 403 om-97 "Bursting strength of paper"	SE 181 (L&W)
Air permeability	ISO 5636-3 "Paper and board — Determination of air permeance (medium range) — Part 3: Bendtsen method"	SE 166 (L&W)
Roughness	T 538 om-01 "Roughness of paper and paperboard (Sheffield method)"	SE 164 (L&W)
Caliper	T 411 om-15 "Thickness (caliper) of paper, paperboard, and combined board"	SE 050A (L&W)
Brightness	T 452 om-08 "Brightness of pulp, paper and paperboard (directional reflectance at 457 Nm)"	CM 3630 (Konica Minolta)
Opacity	T 425 om-01 "Opacity of paper (15/d geometry, illuminant A/2*, 89% reflectance backing and paper backing)"	CM 3630 (Konica Minolta)

II. Paper testing methods and instrument model.

Sample	Titrated Volume, mL	Streaming Potential, mV	Charge Density, µeq/g	Zeta Potential, mV	Mobility, (µ/s)/(V/cm)	Turbidity, NTU
PCC	0.25	-221	-9.82	-2.21	-0.19	40
PCC+1%NG	0.35	-267	-17.11	-2.43	-0.19	32
PCC+5%NG	0.5	-282	-24.39	-3.86	-0.30	28
PCC+1%CL	0.9	69	45.00	2.93	0.29	21.6
PCC+5%CL	1.3	125	260.85	6.13	0.55	34.5
PCC+1%CH	0.8	92	153.11	13.09	1.03	24.4
PCC+5%CH	1.45	207	287.41	16.17	16.17	35.6

PCC = precipitated calcium carbonate; NG = native gum with a 0 degree of substitution (DS); CL = cationic gum with a 0.07 DS; CH = cationic gum with 0.15 DS.

III. Charge analysis and residual turbidity after flocculation with 1% and 5% of each gum.

attractive forces and the electrostatic double layer [30]. This phenomenon definitely implies the flocculating ability of native guar through a bridging mechanism.

It is noted that both PCC and gum carry negative charge, and hence no electrostatic charge interactions could have developed between the two. The higher molecular weight as compared to two cationic gums indicates that the chain length was long enough to extend loops and tails beyond the electrical double layer when certain segments of the biopolymer adsorbed onto a PCC particle. In that case, the potential for a single chain to adsorb on more than one particle becomes obvious. Conceptually, strong van der Waals forces overcame the electrostatic repulsive forces between the PCC and guar gum, leading to aggregation of PCC particles and their entrapment in the physical network of the random coiled structure of gum. It can also be helpful to consider effects related to entropy. Polymers in solution have only limited degrees of freedom, which implies that when the polymers adsorb onto surfaces, very little freedom is lost. However, if the adsorption displaces some small molecules from the surface, then the total amount of freedom within the system increases, which makes the final condition more energetically favorable. This explains why polymers tend to adsorb, even when there is not any charge attraction. Adsorption and flocculation of kaolinite particles by high molecular weight anionic polyacrylamide was based on bridging theory when non-electrostatic attractive forces were dominant, even if repulsion existed between the two like-charged surfaces [30,31]. In this case, it might also be possible that columbic interactions prevailed between positively charged calcium ions and negatively charged etheric O atoms in guar gum [32], as the weak calcium binding ability of gum has been previously discussed in other literature [33]. According to a reported mechanism for adsorption of various organic additives containing hydroxyl group on calcium carbonate, hydrogen bonding is the dominant force among all non-electrostatic interactions [34]. Based on this hypothesis, it may be assumed that guar gum could also form a hydrogen bond between the OH group in its backbone and oxygen atom of carbonate anions in PCC. Similarly non-ionic polyvinyl alcohol was able to adsorb on a calcium carbonate surface via hydrogen bond formation [35]. With 1% and 5% dosage of NG, residual turbidity of PCC after flocculation was decreased by 20% and 30%, respectively, as initial turbidity for PCC was found to be 40 NTU. This implies that 1% of gum was not enough to attain the saturated adsorbed layer on PCC, and bare surfaces were still there to accommodate gum macromolecules at a 5% dose of gum. Turbidity removal of dolomite suspension by increased gum concentration was also seen, and flocculation was noted to be slightly narrower at a higher concentration of gum [18].

In earlier research, PCC was found to be strongly flocculated by non-ionic polyacrylamide due to its high intrinsic viscosity and molecular weight that was sufficient to cover the inter-particular distance between PCC particles [36]. Higher turbidity reduction (48%) with 1% CL might be associated with flocculation through the combined effect of charge neutralization and particle bridging. The effect of conformational change and charge densities in biopolymeric flocculants on the flocculation mechanism has been explained in detail elsewhere [37]. In fact, a 1% dose could reverse the zeta potential values to positive by screening PCC-PCC repulsion, as seen in Table III. Cationic gum with DS 0.07 might have adsorbed with a conformation having loops and tails that facilitated bridging afterwards. At high dosage (5%), zeta potential continued to increase with increases in turbidity, indicating re-stabilization of the system due to steric stabilization between the charged particles of PCC.

On the other hand, when pre-flocculation was carried out with 1% CH, turbidity reduction was less compared to CL and imparted more cationicity to the system. It might be assumed that the electrostatic-patch mechanism was operative during adsorption and flocculation of high charge gum. It was expected that gum polyelectrolytes with high

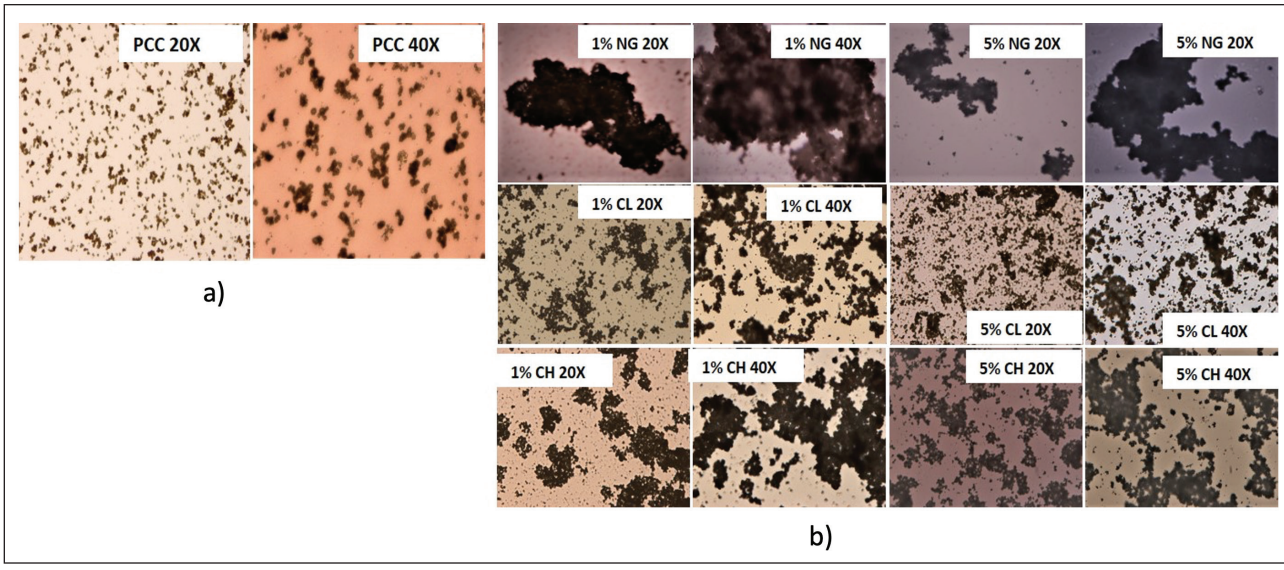

1. Optical microscopic images of (a) native precipitated calcium carbonate (PCC) at 20x and 40x magnification, and (b) aggregated PCC particles with different gums at 20x and 40x magnification.

charge density adsorbed in a flat manner on the negative sites of the solid PCC surface due to a strong electrostatic interaction that led to net positive charge on the adsorbed layer in patches. Then, flocculation might have been promoted by the positive area's interaction with negative sites on the bare surface of another PCC particle. A highly cationic system was obtained at 5% dosage, shifting the system towards more stability. Mechanistic interpretation is available with high and low charge gum-induced flocculation of a colloidal dispersion in the papermaking system [14,15].

Image analysis of PCC flocs upon pre-flocculation

The micrographs shown in **Fig. 1** depict how flocs formed by 1% NG gum are denser and bigger in size compared with flocs formed by 1% CL and CH. This proves the higher effectiveness of native guar gum in bridging PCC particles. Moreover, from this image, it seemed that flocs produced by high charge gums are relatively larger than low charge gum-induced flocs. At 5% dosage, PCC aggregation was reduced for all the gums and was found to be more pronounced in the case of cationic gums. This reduction in aggregation can then be well correlated with the increase in zeta potential values relating to re-stabilization of the PCC particles. Pre-flocculation of fillers has been well demonstrated with image analysis in many studies [38,39]. According to the work of Roger Gaudreault and his co-workers, at a high dosage of polymer, floc size may be determined on the basis of the competitive nature of polymer adsorption and filler aggregation [40]. Initially, flocs might have formed before the polymer could reach saturation, and the subsequent adsorption prevented further floc growth and bridging due to electrostatic repulsion.

Effect of pre-flocculation on particle size of PCC

Figure 2 introduces the floc distribution of pre-flocculated PCC for three different gums and the corresponding FE-SEM images for each distribution. Use of FE-SEM has been employed by researchers to obtain floc size and distribution in the flocculation process [25,40].

Upon flocculation with native gum, the average particle size of PCC was almost double the size of un-flocculated PCC, which was relatively greater when compared with the other two cationic gums. Therefore, optical images of the flocs are well validated with particle size measurements from FE-SEM analysis. However, pre-flocculation with high charge cationic gum produced slightly larger flocs (1.6 times) compared to low charge cationic gums (1.3 times) than the original PCC. In earlier reports, the authors reported that the larger floc size of PCC could be obtained with high charge starch (DS 0.13) compared to low charge starch (DS 0.07) [41]. Overwhelmingly, the mean size reduction in the floc in case of low charge starch was due to low bridging efficiency in comparison to high charge starch. Similar interpretation can also be concluded from our study. Another possibility is that steric stabilization was more pronounced in the case of low charge gum at 1% dosage, which may be due to an unexpected distribution of charges. As reported, fillers with larger particle size and broad floc size distribution would be more easily retained and provide less negative impact on tensile strength [42].

Effect of pre-flocculation on paper properties

The effects of different gum dosages in filler modification on filler retention, filler bondability, and paper tensile strength are shown in **Fig. 3**. The maximum increase in filler retention was observed at 0.5%, 0.2%, and 1% for NG, CH, and CL gum, respectively. For NG gum, after 8.5% reduction at 1%, it remained almost unaffected at a higher dose. High charge gum (CH) showed the same level of filler retention up to 1%, which then became

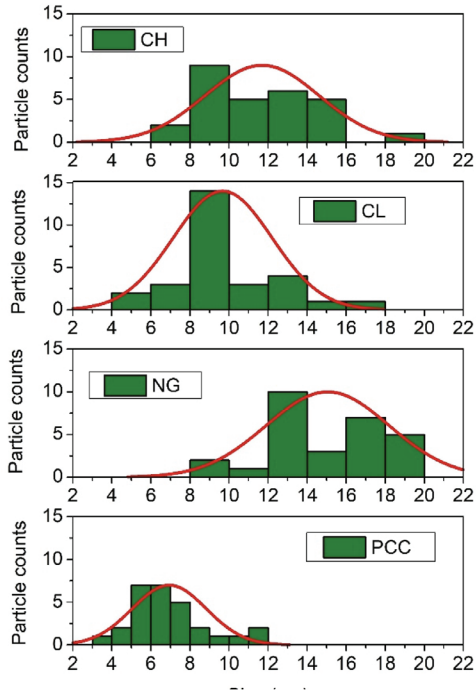

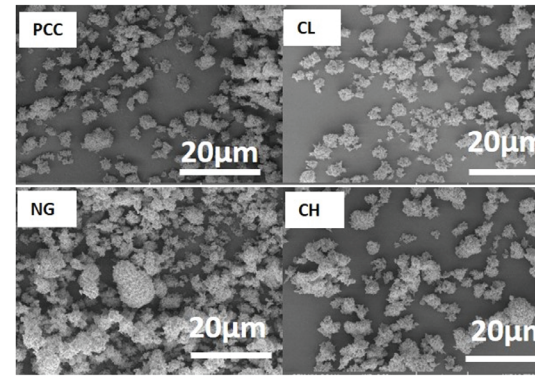

	Particle Mean size µm
PCC	6.93± 1.89
NG	15.04±3 .14
CL	9.67± 2.53
CH	11.69± 2.91

2. Particle size distribution of native and pre-flocculated PCC and their corresponding field-emission scanning electron microscope (FE-SEM) images and average particle size. Gum dosage was 1% on PCC for all samples. NG is native gum having a 0 degree of substitution (DS); CL is cationic gum having a 0.07 DS; and CH is cationic gum with 0.15 DS.

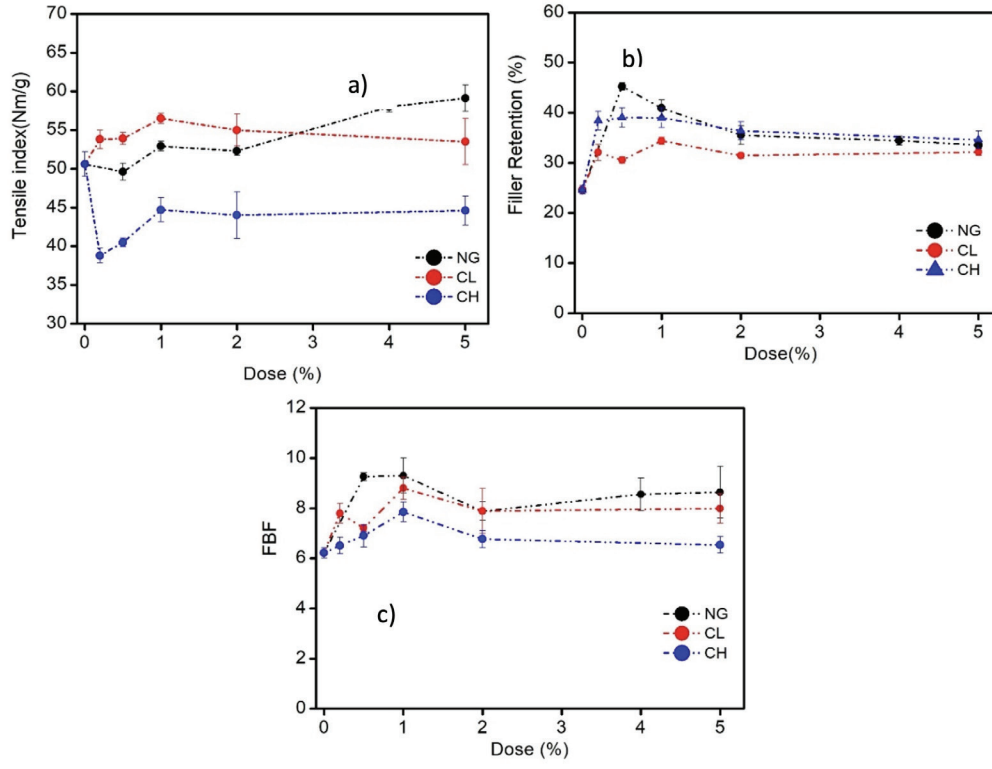

3. Effect of total gum dosage during pre-flocculation on (a) tensile strength, (b) filler retention, and (c) filler bonding ability factor (FBF) of paper.

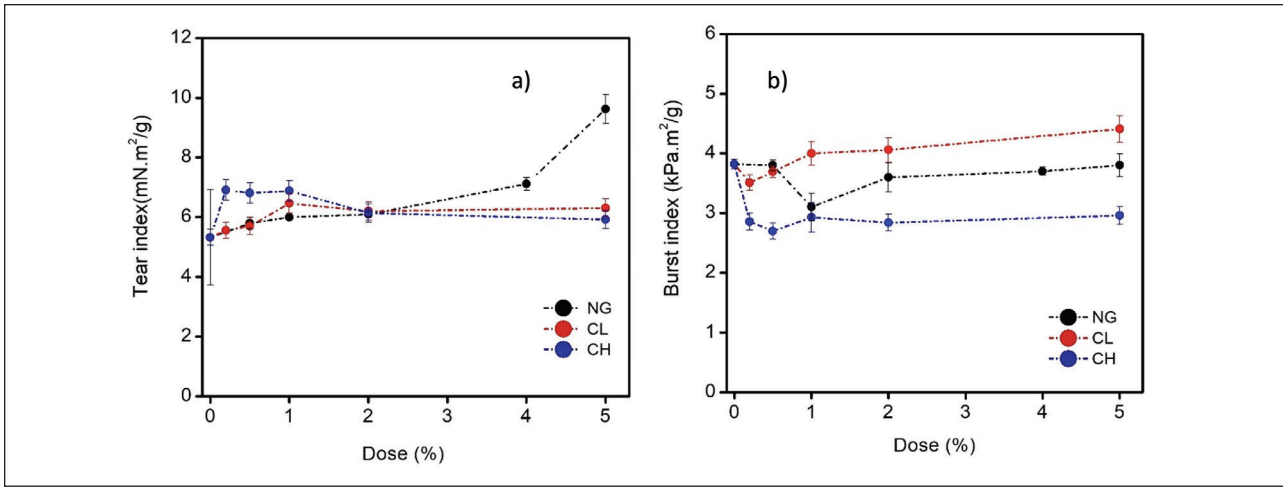

4. Effect of total gum dosage during pre-flocculation on (a) tear index and (b) burst index of paper.

slightly reduced at 2% and maintained a constant value at 5% dose. Low charge gum (CL), on the other hand, seemed to be favorable at 1%, which then reduced to 9.5% beyond that. Overall, in the studied range of doses, CL provided lower retention ability for fillers compared to NG and CH gums.

Notably, maximum tensile index was found at 1% irrespective of all types of gum samples, and CH gums achieved the least tensile strength. While there was a decreased trend observed for CL and CH at a higher dose, NG gums improved the paper strength with increased dose. However, it might be possible that at low dose, maximum fiber flocculation could have taken place, leading to a nonuniform sheet and decreased tensile strength. Based on the tensile index and retention properties, filler bondability with cellulose fiber was assumed to be more in the case of NG, followed by CL and CH, as depicted in Fig. 3c. In earlier reports [22,24,43], the concept has been put forth that fillers pre-flocculating with different polymers, such as starch, chitosan, and CPAM, form large aggregates that are easily retained at high ash levels, without massive loss in paper strength properties. However, the effects of charge densities in pre-flocculating polymers on the filler modification process may have a direct impact on paper properties, which has rarely been discussed in earlier literature. Therefore, in this study, it is revealed that the effectiveness of filler treatment and its successive application in paper formation is dependent on total dosage, as well as charge densities, of the gums.

Jun Fan and his co-workers considered total dosage of starch as one of the critical parameters in the filler modification process that could impart characteristic features to paper [44]. The enhanced retention ability of native guar gum may be explained from the optical images in Fig. 1, which prove its higher bridging efficiency towards PCC to induce superior flocculation performance between 0.5% and 5% dose. Comparing the cationic gums in terms of retention properties, CH provided the best results, revealing its superior aggregation ability to CL, as demonstrated by the images. A reduction in this parameter after a certain dose, as specified for each gum, may be due to the charge characteristics and colloidal stability of the aggregates, which can be supported with zeta potential and turbidity values. Even optical images captured at a 5% dose of each gum disclose the tendency to form smaller aggregates in contrast to low gum dosages. From 0–2% dosage, the highest tensile strength achieved with CL may have a direct relationship with charge densities that predicts that adsorbed molecules of low charge gum on PCC interact with fibers to form bridges between fiber-filler-fiber with its protruding loops and tails through electrostatic interactions. On the other hand, a much flatter conformation of high charge gum on the PCC surface was less capable of forming bonds between fibers due to a rigid and expanded structure, thus inhibiting the tensile strength of paper. At higher concentration, as soon as the charge neutralization of negatively charged fibers occurred and adsorbed molecules reached a saturation point, charge reversal might have limited further gum adsorption due to electrostatic repulsive forces between the surface and polymer. More adverse effects were noticed for CH gum. The effect of charge densities of starch and the cationic polyacrylamide CPAM on retention and strength properties have previously shown similar results [45,46]. In the case of native guar gum (NG), hydrogen bonding is more effective over repulsive forces and was the primary cause for increased tensile strength at a high dose. On the other hand, CH imparted more tear strength to paper compared with native and CL gums, with only a 0.2% dose required for filler flocculation. Tear strength generally decreases when interfiber bonding increases, which is because the paper becomes more brittle when bonding increases. Therefore, it follows that the CH system proving least effective as a bonding agent gave the highest tear strength at a low gum dosage. Pre-flocculation with CL could marginally improve the tear strength, while underivatized gum at a 5% dose

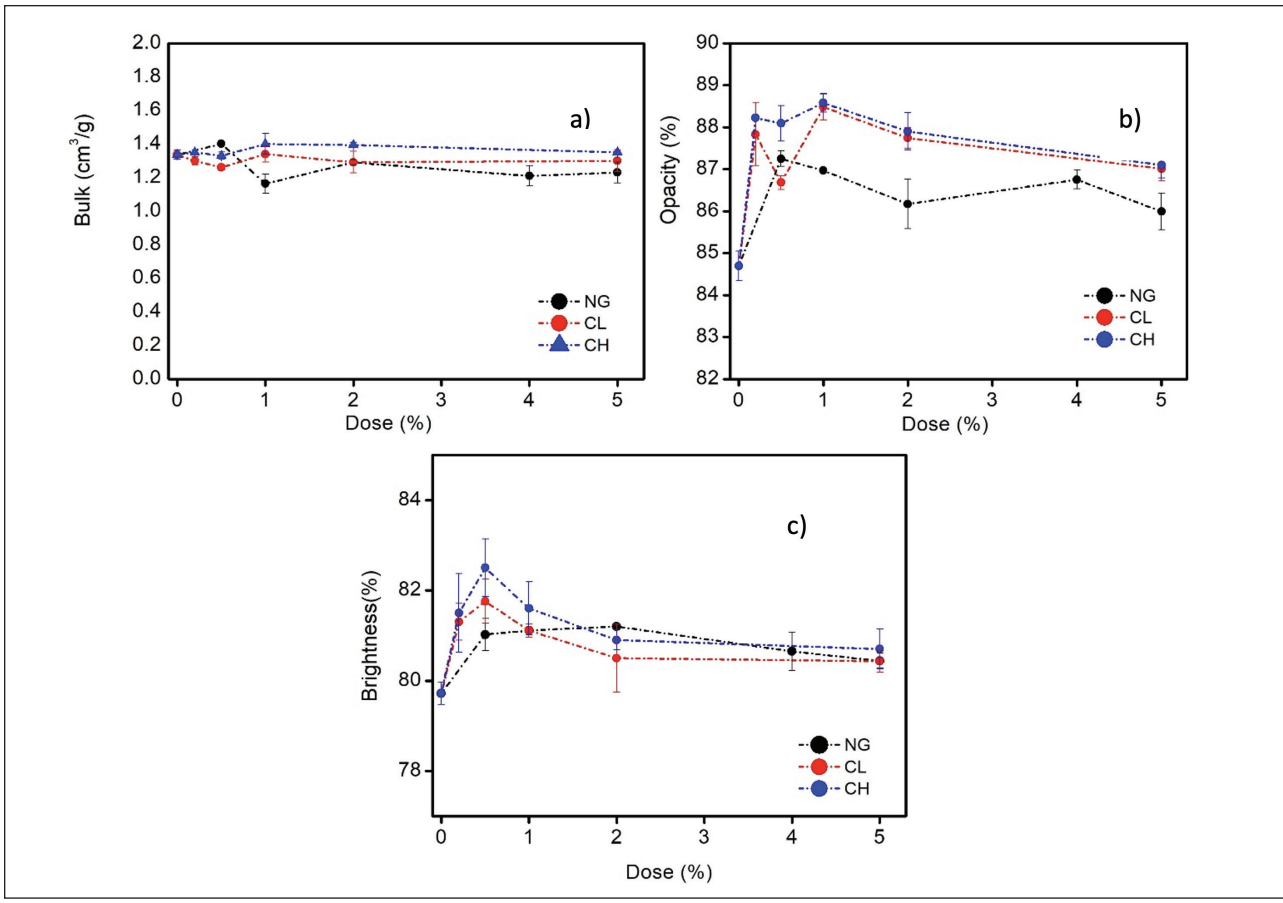

5. Effect of total gum dosage during pre-flocculation on (a) bulk, (b) opacity, and (c) brightness of paper.

showed a pronounced effect, with an increase in tear index of 75%. When PCC flocs were pre-flocculated, more surface areas of fibers were exposed for fiber bonding per unit mass of paper. This might have increased the effective fiber length, which is beneficial for tear index [42]. The authors indicated that the primary size of PCC particles in filler pretreatment are crucial for tear properties of paper [47]. Bursting strength displays a similar trend as tensile index, as shown in **Fig. 4**.

The bulking effect was also studied, revealing that paper integrated with cationic gums induced PCC pre-flocs that were more bullky at a higher dose of gum when compared to native gum. The CH gave the highest bulk, ranging from 1.35–1.4 cm³/g, followed by CL and native gum. The result was 1.33 cm³/g for native PCC, which reduced to 1.16–1.2 cm³/g when the NG dose increased from 0.5%–5%. The lower bulk associated with NG may be ascribed to a high filler bonding ability factor (FBF) and large, dense flocs. A dense structure results when the fibers are able to easily slide past each other. Native guar can be expected to have that effect, reducing the coefficient of friction between wet fibers. In general, low bulk or high apparent density is responsible for high strength of paper, as reported by various authors [22,39,48]. For CL, a marginal effect can be observed, which varied from 1.26–1.34 cm³/g. Bulky sheets with CH tended to produce low strength paper, which is again in accordance with previous studies [49]. A larger particle size compared with CL might have lower packing ability that distributed the particles laterally in the interfiber spaces of the fiber-fiber domain. The effect of particle distribution in the sheet on bulk has been previously discussed [50]. Increased bulk and improved strength were also noted with loose structured composite flocs having more air voids during co-flocculation of fines and fillers [51]. Recently, it was revealed that if the particles are rigid enough to resist compressive strength during the papermaking process, high bulk may be obtained [49]. It may be assumed that paper with CH-induced PCC flocs has a tendency to have a porous structure, as bulk is interrelated with porosity [52].

Other important properties, like optical properties of opacity and brightness, were studied. The initial opacity of PCC was 84.69%, which increased by 3%–4% for all gum samples, with cationic gums showing higher opacity in the range of doses studied. High opacity indicates better light scattering efficiencies and bulk, as can be corroborated from the results in **Fig. 5**. Although this has been previously demonstrated in studies [42,43], Ming He and his co-workers [53] showed, to the contrary, that nanofibril-

	Tensile Index, Nm/g	Tear Index, mN.m²/g	Burst Index kPa.m²/g	FBF	Bulk, cm³/g	Filler Retention, %	ISO Brightness, %	Opacity, %	Scattering Coefficient
Unfilled	59.69	5.40	4.20	NA	1.34	0.00	77.40	82.20	33.98
PCC	50.63	5.40	3.80	6.21	1.33	24.60	79.70	84.70	40.6
NG	52.92	6.00	3.10	9.30	1.16	40.90	81.10	87.00	47.57
CL	56.54	6.46	4.00	8.80	1.34	34.40	80.60	88.50	49.04
CH	44.73	6.99	2.93	7.85	1.40	39.00	81.60	88.60	53.91

FBF = filler bonding ability factor; PCC = precipitated calcium carbonate; NG = native gum with a 0 degree of substitution (DS); CL = cationic gum with a 0.07 DS; CH = cationic gum with 0.15 DS.

IV. Paper properties determined at 1% dosage (based on o.d. PCC) of each gum. The PCC loading in pulp was kept constant at 20%.

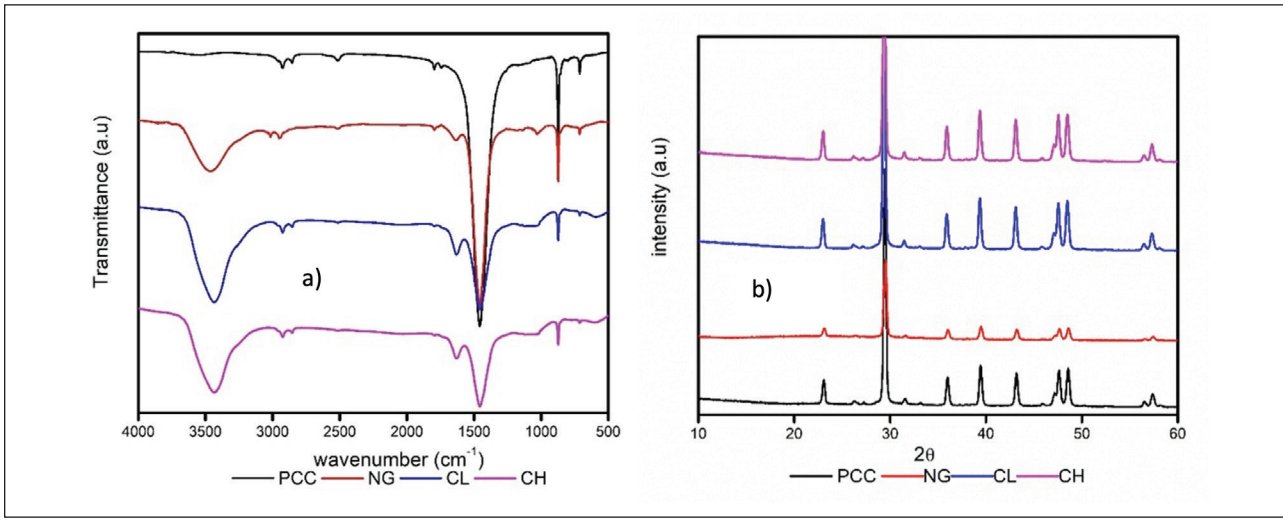

6. (a) Fourier transform infrared (FTIR) and (b) wide-angle X-ray diffraction (XRD) analysis of native PCC and pre-flocculated PCC obtained from treatment with 1% dosage (based on o.d. PCC) of each gum.

lated cellulose starch-modified PCC composites produced dense paper with higher opaqueness compared to unmodified PCC. In this case, it was observed that beyond 1%, opacity started to decrease with increased dose. Similarly, brightness with native PCC was 79%, which increased for all the gums in the range 0–0.5%. Slightly lower brightness was obtained with CL gum, which might be interconnected with lower PCC retention. Enhancement in paper brightness with high ash content was justified by several authors [3,22,39]. A rather diversified impact was observed with pre-flocculated fillers on paper brightness and opacity. Cheng and his co-workers [54] reported the positive impact of derivatized chitosan-modified PCC on paper's optical properties, whereas CPAM pre-flocculated lime mud decreased the optical properties of paper [55]. Pre-flocculated talc with amphoteric starch was found to increase opacity with decreased brightness properties [39]. It might be a reason that when gum dosage was increased, brightness reduced to a certain level due to interference of gum, as the refractive index of gum is around 1.35, which is less than cellulose pulp (1.5–1.6) [56]. On balance, a 1% gum dosage was preferred, considering the retention properties and other properties that were compared and tabulated in **Table IV**.

Further, the crystal identification of native PCC in the presence of gums is evident from FTIR data in **Fig. 6a** and XRD data in Fig. 6b. These techniques were extensively studied in evaluating the various polymorphs of calcium carbonate [57,58]. The typical infrared (IR) spectrum of PCC in this study reveals calcite polymorphs assigned by following carbonate absorption bands at 1456 cm^{-1}, 872 cm^{-1}, and 712 cm^{-1} [4]. These are related to asymmetric stretch vibration ($v3$), out of plane deformation ($v2$), and in-plane bending of C-O bonds ($v4$), respectively. Other bands that appear at 2923 cm^{-1} and 2853 cm^{-1} are designated for CH stretch, with a band of very low intensity at 1798 cm^{-1} in native PCC, which is very similar to the spectrum produced for pure calcium carbonate in other studies [59]. When NG was used as a flocculant, a broad band appeared at 3443 cm^{-1}, corresponding to OH stretching vibration of hydroxyl groups of gum.

However, many sharp peaks were observed in cationic

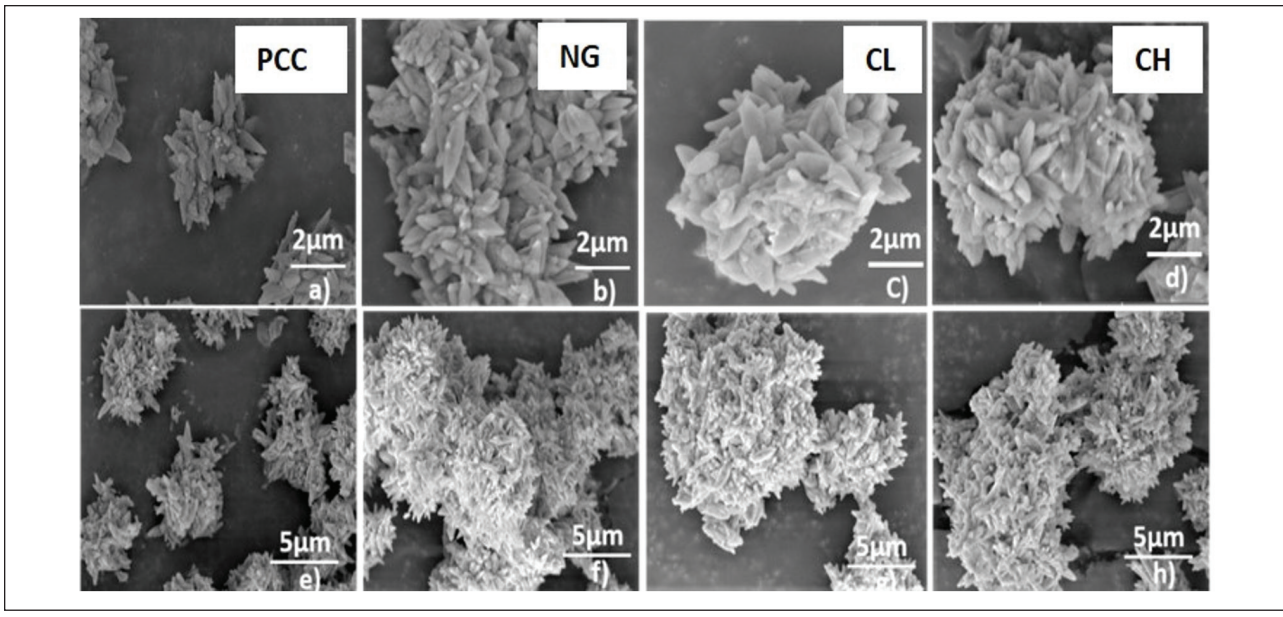

7. The FE-SEM images of native PCC and pre-flocculated PCC obtained from treatment with a 1% dose (based on o.d. PCC) of each gum.

gum-flocculated PCC samples. The spectra of NG-flocculated PCC displayed a characteristic small broad peak at 1630 cm^{-1} related to the carboxylic structure in the guar backbone. This peak became intensified and sharper in the case of cationic gums. The characteristic peak of carbonate CO^{3-} appeared to be broad due to the overlapping band of cationic guar gums, as the peaks at 1648 cm^{-1} and 1419 cm^{-1} in cationic gums represent – $N^{+}(CH_3)_3$ ions [60].

Evidently, these findings reflect physical adsorption of underivatized and derivatized guar gums on PCC, as was also predicted for adsorption of poly (diallyldimethylammonium chloride) (PolyDADMAC) on kaolin particles [61]. In addition, it is clear that pre-flocculation with gum did not induce any crystal transformation. This was later supported with XRD. The diffraction peak 2θ at 23.0° (112), 29.4° (104), 35.9° (110), 47.5° (018), and 28.5° (116) were identified as calcite polymorphs in native PCC. Positioning of the peaks are analogous in all the pre-flocculated samples, implying no change in crystal transformation, but traces of gum could not be identified though XRD. Gum-modified PCC showed similar results as reported in the literature [4]. The calcite crystals of native PCC exhibit scalenohedral morphology, as seen in FE-SEM micrographs from **Fig. 7**. Pre-flocculating with gums, irrespective of their variants, might preserve the structural and morphological hierarchy. It is also notable that flocs were more aggregated in the NG sample (i.e., the number of particles in each floc was more compared to CL and CH). Figures 7c and 7d revealed that with increasing DS values of gum, floc structures were created with small internal microvoids in aggregates. These optically-active pores might be responsible for better performance in light scattering ability and opacity of sheets having CL- and CH-mediated flocs (see Table IV). It was found that dense or porous aggregates could be created with the same flocculants during pre-flocculation, depending on their macromolecular structure and charge densities [42]. They also suggested that internal microvoids were beneficial for optical properties of paper. In order to study the distribution of flocs in mineral-filled paper sheets and also to validate the effect of flocs on filler-fiber-filler bonding, SEM micrographs were analyzed with native and different pre-flocculated PCCs.

A number of native/untreated PCC aggregates distributed in the cellulosic network were less retained compared to pre-flocculated fillers at the same level of PCC dose (20%) based on o.d. fiber. It is clearly identified from **Fig. 8** that PCC in its native state tended to disperse itself in the interfiber spaces through mechanical entrapment, but was mostly located on interfiber surfaces, thus negatively affecting the fiber bonding. In the case of pre-flocculated fillers, much larger aggregated flocs distributed themselves not only in the gaps between fibers, but also adsorbed onto the fiber surfaces. It has also been proposed in the past that the agglomerated PCC can also be retained through a filtration mechanism and might end up in a location that contributes to filler retention [62]. In the case of high DS gum, heterogeneous aggregates were distributed much more irregularly, leading to localization of the flocs. This might be related to lower tensile strength of paper containing PCC-CH flocs. Compared to paper containing NG, more voids could be observed when cationic gums were used as flocculants, with a higher number of microvoids existing in aggregates produced by CH. It is therefore assumed that during the process of sheet consolidation, the cellulosic fibrillar network restrained from shrinkage, thus creating a large number of pores and micropores, which are apparently important for high bulk and opacity [42,53]. Thus, like starch pre-flocculated fillers as reported in past studies, gum as a pre-flocculant could effectively increase the bridg-

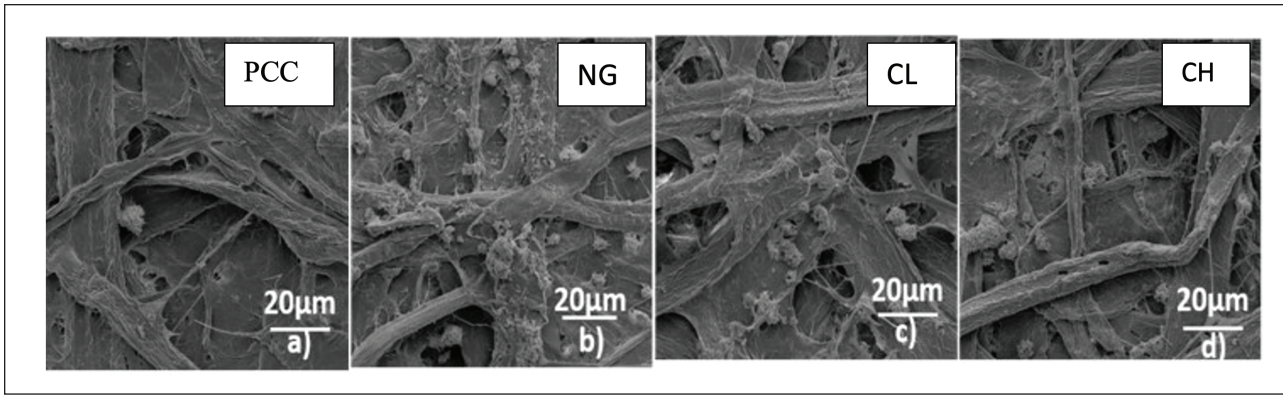

8. The FE-SEM images of native PCC and pre-flocculated PCC at 20% filler dose (based on o.d. fiber). Total gum dosage on PCC is 1%.

ing between fiber-filler-fiber bonding due to its adhesive nature. The gluing quality of guar in papermaking is mainly attributable to its hydroxyl polar groups and electrostatic forces when cationic moieties are introduced into the guar backbone. Therefore, they would have a mutual attraction towards a negatively charged hydroxyl group containing cellulose fiber, which establishes fiber-filler-gum-fiber bonding that further increases the PCC retention and paper strength. The initial studies show that guar gum has a significantly high potential in pre-flocculation technology as an alternative to starch; however, resistibility of pre-flocculated flocs against dynamic shear forces is important criteria to consider for future work, as filler retention is directly related to the intensity of floc strength.

CONCLUSIONS

This preliminary study indicated that optimum dosage and choice of particular gum grades were crucial in pre-flocculation technology that produced different floc structures, which ultimately were responsible for paper sheet properties. The study also revealed that DS values should be an important parameter that must be carefully chosen when cationic gums are considered. For industrial application, high bulk in paper is always preferable, unless it is detrimental to the strength properties. Through this association, we observed that high DS cationic guar produced paper with increased bulk and optical properties at high ash content, but strength properties were reduced to a greater extent. Therefore, we must conclude that cationic gums with low DS values are a better choice for maximizing the strength of paper, while maintaining bulk and higher opacity, when pre-flocculation is adopted to increase the filler retention in paper. So, notably, gum may be considered as an alternative potential biopolymer to starch when using a pre-flocculation method. **TJ**

ACKNOWLEDGEMENT

The research grant for the present work was supported by Ministry of Human Resource Development (MHRD), Government of India.

LITERATURE CITED

1. Kuusisto, J.E. and Maloney, T.C., *BioResources* 10(2): 3277(2015). https://doi.org/10.15376/biores.10.2.3277-3292.
2. Fatehi, P., Shen, J., Hamdan, F.C., et al., *Carbohydr. Polym.* 92(2): 2103(2013). https://doi.org/10.1016/j.carbpol.2012.11.046.
3. El, A., Khiari, R., Bettaieb, F., et al., *Appl. Clay Sci.* 101: 626(2014). https://doi.org/10.1016/j.clay.2014.09.032.
4. Xie, W., Song, Z., Liu, Z., et al., *Carbohydr. Polym.* 150: 114(2016). https://doi.org/10.1016/j.carbpol.2016.05.010.
5. Kumar, S., Sharma, B.R., and Hissaria, M., "Cationic guar gum–A binding force in paper manufacturing," Special report, *Chemical Weekly*, 19 May 2009.
6. Barua, P., Rahaman, A., and Mahanta, D., *IPPTA Q. J. Indian Pulp Pap. Tech. Assoc.* 8: 19(1996).
7. Özden, Ö. and Sönmez, S., *Res. Rev. Eng.* 2019: 207(2019).
8. Domene-López, D., García-Quesada, J.C., Martin-Gullon, I., et al., *Polymers* 11(7): 1(2019). https://doi.org/10.3390/polym11071084.
9. Eldaw, G.E., "A study of guar seed and guar gum properties (*Cyamopsis tetragonolabous*)," M.Sc. thesis, University of Khartoum, Sudan, 1998.
10. Liu, Z., Li, X., and Xie, W., *PLoS One* 12(2): 1(2017). https://doi.org/10.1371/journal.pone.0171326.
11. Khouryieh, H.A.M., "Rheological characterization of xanthan-gum mixtures in dilute solutions," Ph.D. dissertation, Kansas State University, Manhattan, KS, USA, 2006.
12. Garcia Vidal, C.A, "Molecular weight effects in guar gum adsorption and depression of talc," MASc. thesis, University of British Columbia, Vancouver, 2013.
13. Agro Gums, "Useful properties of guar gum," Blog, Agro Gums, Ahmedabad, India, 20 December 2012. Available [Online] https://www.agrogums.com/blog/useful-properties-of-guar-gum/ <18April2022>.
14. Lee, J.Y., Lee, H.L., and Youn, H.J., *TAPPI J.* 4(10): 15(2005).
15. Rojas, O.J. and Neuman, R.D., *Colloids Surf., A* 155(2-3): 419(1999). https://doi.org/10.1016/S0927-7757(99)00040-0.
16. Ham, C.H. and Lee, H.L., *J. Korea Tech. Assoc. Pulp Pap. Ind.* 40(3): 1(2008).
17. Lijun, W., Fu-shan, C., Li-juan, Q., et al., *China Pulp Pap.* 25(1):17 (2006).

18. Pawlik, M. and Laskowski, J.S., *Can. J. Chem. Eng.* 84(5): 532(2006). https://doi.org/10.1002/cjce.5450840504.
19. Fairchild, G.H., U.S. pat. 5,458,679 (Oct. 17, 1995).
20. Chen, N., Wang, L., Wen, J., et al., *Nord. Pulp Pap. Res. J.* 35(1): 89(2019). https://doi.org/10.1515/npprj-2019-0047.
21. Yang, H., Qiu, L., Qian, X., et al., *BioResources* 8(4): 5449(2013). https://doi.org/10.15376/biores.8.4.5449-5460.
22. Yu, Y., Xue, G., Gu, C., et al., *J. Appl. Polym. Sci.* 129(5): 2692(2013). https://doi.org/10.1002/app.38992.
23. Fatehi, P., Hamdan, F.C., and Ni, Y., *Carbohydr. Polym.* 94(1): 531(2013) https://doi.org/10.1016/j.carbpol.2013.01.081.
24. Huang, X., Shen, J., and Qian, X., *Carbohydr. Polym.* 98(1): 931(2013). https://doi.org/10.1016/j.carbpol.2013.07.024.
25. Nasim, T., Panda, A.B., and Bandyopadhyay, A., *Int. J. Biol. Macromol.* 58: 140(2013). https://doi.org/10.1016/j.ijbiomac.2013.03.069.
26. Gao, J. and Grady, B.P., *Ind. Eng. Chem. Res.* 57(22): 7345(2018). https://doi.org/10.1021/acs.iecr.8b00782.
27. Pal, S., Mal, D., and Singh, R.P., *J. Appl. Polym. Sci.* 105(6): 1(2007). https://doi.org/10.1002/app.26440.
28. Banerjee, S., Abdulsattar, Z.R., Agim, K., et al., *Petroleum* 3(3): 384(2017). https://doi.org/10.1016/j.petlm.2017.04.002.
29. Ghosh, I., Sharma, C., and Tandon, R., *SN Appl. Sci.* 2(9): 1(2020). https://doi.org/10.1007/s42452-020-03313-w.
30. Dwari, R.K. and Mishra, B.K., *Int. J. Min. Sci. Technol.* 29(5): 745(2019). https://doi.org/10.1016/j.ijmst.2019.06.001.
31. Nasser M.S. and James, A.E., *Sep. Purif. Technol.* 52(2): 241(2006). https://doi.org/10.1016/j.seppur.2006.04.005.
32. Elkholy, A.E., El-Taib Heakal, F., Rashad, A.M., et al., *J. Pet. Sci. Eng.* 166: 263(2018). https://doi.org/10.1016/j.petrol.2018.03.019.

ABOUT THIS PAPER

Cite this article as:
Ghosh, I., Sharma, C., and Tandon, R., *TAPPI J.* 21(4): 203(2022). https://doi.org/10.32964/TJ21.4.203

DOI: https://doi.org/10.32964/TJ21.4.203

ISSN: 0734-1415

Publisher: TAPPI Press

Copyright: ©TAPPI Press 2022

About this journal

33. Ha, Y.W., Thomas, R.L., Dyck, L., et al., *J. Food Sci.* 54(5): 336(1989). https://doi.org/10.1111/j.1365-2621.1989.tb05986.x.
34. Hakim, S.S., Olssson, M.H.M., and Sorenson, H.O., *Sci. Rep.* 7(1): 1(2017).
35. Kim, I.W., Robertson, R.E., and Zand, R., *Cryst. Growth Des.* 5(2): 513(2005). https://doi.org/10.1021/cg049721q.
36. Sakaguchi, K. and Nagase, K., *J. Soc. Chem. Ind., Jpn.* 69(6): 1199(1966). https://doi.org/10.1246/nikkashi1898.69.6_1199.
37. Vajihinejad, V., Gumfekar, S.P., Bazoubandi, B., et al., *Macromol. Mater. Eng.* 304(2): 1800526(2019). https://doi.org/10.1002/mame.201800526.
38. Chauhan, V.S. and Bhardwaj, N.K., *Nord. Pulp Pap. Res. J* 28(2): 248(2013). https://doi.org/10.3183/npprj-2013-28-02-p248-256.
39. Yoon, S. and Deng, Y., *J. Appl. Polym. Sci.* 100(2):1032(2006). https://doi.org/10.1002/app.23007.

ABOUT THE AUTHORS

High ash content papers with improved paper properties are always preferable to papermakers for minimizing production costs, but at the same time, technologies adopted for ash retention face challenges. Therefore, we did fundamental research on guar gum as a pre-flocculating polymer for PCC fillers, as it had not been conducted before. From a physicochemical point of view, it resembles that of starch in biodegradability, adhesive properties, and strength enhancement. The hemicellulosic property of gum is an added advantage, making it a potential alternative polymer to starch in pre-flocculation technology.

Previously, most of the research has been performed using starch. Though gum has been proven as a strength additive for paper, it still finds room in pre-flocculation technology.

Our research showed that guar gum has a high potential for increasing filler retention with less detrimental effects to paper strength properties. It was interesting to find that the degree of substitution (DS) plays a critical role in pre-flocculation technology when considering cationic derivatives of gum.



Ghosh



Sharma



Tandon

For mills, choice of the right DS when using cationic gum derivates as a PCC pre-flocculant is critical. Our next step is to evaluate floc strength against shear forces.

Ghosh is research scholar and Sharma is professor in the Department of Paper Technology, IIT Roorkee, Saharanpur Campus, Saharanpur, Uttarpradesh, India. Tandon is senior scientist, retired, at Central Pulp and Paper Research Institute, Saharanpur, Uttarpradesh, India. Email Sharma at chhaya.iitr@gmail.com.

40. Gaudreault, R., Di Cesare, N., van de Ven, T.G.M., et al., *Ind. Eng. Chem. Res.* 54(24): 6234(2015). https://doi.org/10.1021/acs.iecr.5b00818.
41. Sang, Y. and Englezos, P., *Colloids Surf., A* 414: 512(2012). https://doi.org/10.1016/j.colsurfa.2012.07.019.
42. Song, S., Liang, J., Li, L., et al., *Nord. Pulp Pap. Res. J.* 33(4): 603(2018). https://doi.org/10.1515/npprj-2018-0044.
43. Mohamadzadeh-Saghavaz, K., Resalati, H., and Ghasemian, A., *Chem. Pap.* 68(6): 774(2014). https://doi.org/10.2478/s11696-013-0513-7.
44. Fan, J., Li, T., Ren, Y., et al., *Ind. Crops Prod.* 97: 417(2017). https://doi.org/10.1016/j.indcrop.2016.12.048.
45. Mahanta, D. and Rahman, A., *Indian J. Chem.* 25A: 825(1986).
46. Liu, Q., Li, J., and Xu, W., *17th IAPRI World Conf. Packag.*, International Association of Packaging Research Institutes (IAPRI), East Lansing, MI, USA, 2010, p. 35.
47. Chauhan, V.S. and Bhardwaj, N.K., *Lignocellulose* 1(3): 241(2012).
48. Lourenço, A.F., Gamelas, J.A.F., Zscherneck, C., et al., *Ind. Eng. Chem. Res.* 52(14): 5095(2013). https://doi.org/10.1021/ie3035477.
49. Kang, D.S., Han, J.S., Choi, J.S., et al., *ACS Omega* 5(25): 15202(2020). https://doi.org/10.1021/acsomega.0c01179.
50. Hubbe, M.A. and Gill, R.A., *TAPPI Pap. Summit – Spring Tech. Int. Environ. Conf.*, TAPPI Press, Atlanta, 2004, p. 141.
51. Zhang, M., Li, Q., Song, S., et al., *BioResources* 11(3): 7406(2016). https://doi.org/10.15376/biores.11.3.7406-7415.
52. Song, X., Shangguan, W., Zhang, L., et al., *BioResources* 13(3): 6631(2018). https://doi.org/10.15376/biores.13.2.2411-2423.
53. He, M., Cho, B.U., and Won, J.M., *Carbohydr. Polym.* 136: 820(2016). https://doi.org/10.1016/j.carbpol.2015.09.069.
54. Chen, Z., Li, C., Song, Z., et al., *BioResources* 9(4): 5917(2014). https://doi.org/10.15376/biores.9.4.5917-5927.
55. Peng, Y., He, B., and Zhao, L., *J. Appl. Polym. Sci.* 132(11): 41640(2015). https://doi.org/10.1002/app.42788.
56. Yousif, M.E., Mohamed, B.E., and AE, E., *J. Food Process. Technol.* 8(2): 1000656(2017). https://doi.org/10.4172/2157-7110.1000656.
57. Toffolo, M., Regev, L., Dubernet, S., et al., *Minerals* 9(2): 121(2019). https://doi.org/10.3390/min9020121.
58. Xu, B. and Poduska, K.M., *Phys. Chem. Chem. Phys.* 16(33): 17634(2014). https://doi.org/10.1039/C4CP01772B.
59. Tatzber, M., Stemmer, M., Spiegel, H., et al., *Environ. Chem. Lett.* 5(1): 9(2007). https://doi.org/10.1007/s10311-006-0079-5.
60. Kaur, J. and Kaur, G., *Polym. Adv. Technol.* 29(12): 3035(2018). https://doi.org/10.1002/pat.4424.
61. Sun, W., Liu, W.L., and Hu, Y.H., *J. Cent. South Univ. Technol.* 15(3): 373(2008). https://doi.org/10.1007/s11771-008-0070-3.
62. Gill, R.A., in *Applications of Wet-End Paper Chemistry* (C.O. Au and I. Thorn, Eds.), Springer, Dordrecht, 1995, pp. 54-75. https://doi.org/10.1007/978-94-017-0756-5_4.

Ultrastructural Behavior of Cell Wall Polysaccharides

DIETRICH FENGEL

Abstract: Studies on the behavior of wood polysaccharides inside and outside the cell wall were carried out under varying conditions using the electron microscope in combination with physico-chemical methods to gain new information on the supermolecular structure of the polysaccharides. Several fractions containing different polyoses were obtained by fractionation of the alkali extract of holocellulose. Isolated polyoses are at least partially able to arrange themselves in fibrillar elements. After delignification, the cellulose is recognizable within the cell wall as microfibrils with an average diameter of about 250 Å. However, these fibrillar units seem to be rather unstable as they can easily be split into units 120 Å in diameter by chemical treatment. After partial hydrolysis, isolated cellulose shows more subunits about 30 Å in diameter at higher magnification. Moreover, the more sensitive portions of the fibrils in the longitudinal direction are attacked by partial hydrolysis, and these portions seem to grow with increasing duration of the hydrolysis. Fractionation of cellulose isolated from thermally treated wood shows that the chain fragments are multiples about 300 Å in length. A tentative model of the supermolecular arrangement of the cellulose in relation to the other cell wall components is presented.

Keywords: Softwoods · Hardwoods · *Picea abies* · *Fagus sylvatica* · Electron microscopy · Cell wall · Cell structure · Fibrils · Microfibrils* · Cellulose · Polysaccharides · Hemicelluloses · Carbohydrates · Xylan · Mannan · Degree of polymerization

CONSIDERABLE information on the ultrastructural organization of the plant cell wall and the supermolecular arrangement of the cell wall components, in particular of cellulose, has been obtained with the electron microscope. However, some ultrastructural features were clarified by indirect methods such as X-ray diffraction (*1*) and light birefringence (*2*) several years before the first electron microscope was constructed (*3*). The X-ray studies gave evidence that the cellulose chains are arranged in monoclinic lattices (*4*). In addition, it was found that the ordered regions build up higher-level systems in the longitudinal as well as in the lateral direction. Several such systems have already been seen in the electron microscope but it has not yet been possible to resolve single polysaccharide molecules although modern high-performance instruments have a resolution power down to 3 Å.

This paper reports results obtained during the study of polyoses and cellulose from wood, primarily by electron microscopical observation but supplemented by other chemical and physical methods. It is an attempt to combine a series of results, some of which have been published previously, others quite new, into a model of the supermolecular organization of the cell wall polysaccharides.

MATERIALS AND METHODS

The basic material for investigation was air-dried wood meal from spruce (*Picea abies* Karst.) and from beech (*Fagus sylvatica* L.). The samples were extracted for 6 hr with methanol-benzene and delignified with sodium chlorite at 70°C (*5*). The polyoses were extracted from holocellulose by treatment with 5 and 24% potassium hydroxide in two stages under a nitrogen atmosphere, followed by precipitation with ethanol and acetic acid (*5*). The two alkali-soluble fractions could each be further subdivided into three other fractions by treatment with water and ethanol according to the scheme of fractionation previously described (*6*).

DIETRICH FENGEL, Univ.-Dozent, Head of Division for Wood Chemistry and Ultrastructure Research of the Institute for Wood Research and Wood Technology, University of Munich, West Germany.

The partial hydrolysis of the cellulose was carried out by boiling the samples in an excess (about 100 times the weight) of 20% sulfuric acid for 1 or 5 hr.

In special cases, the wood meal was thermally pretreated by heating at different temperatures in the range of 100 to 200°C for 24 hr (*7*).

The samples used for metal shadowing were generally suspended in 80% ethanol; those used for negative staining were suspended in buffer solution (pH 7). The suspensions were precipitated by ultrasonic atomizing onto copper grids bearing a collodium film. The specimens were stained by shadowing with platinum at an angle of 20° at a high vacuum or by negative staining with a 1% phosphotungstic acid (PTA) solution or a 1% uranyl acetate solution for 15 min. The specimens were examined in an AEG-Zeiss EM 8/IV, in a Siemens Elmiskop 1, and in a Siemens Elmiskop 101.

For the determination of the average degree of polymerization, the viscosity of cellulose in cadoxene (*8*) was measured in a capillary viscosimeter.

For chain length fractionation, solutions of cellulose nitrate in acetone were precipitated in stages with acetone-water according to the method of Philipp and Linow (*9*). The degree of polymerization was determined by measuring the viscosity of each fraction in acetone solution in a capillary viscosimeter. The curves of chain length distribution were calculated by adding up the percentage weight of the single fractions according to Schulz (*10*).

RESULTS AND DISCUSSION

Polyoses

One of the most striking properties of the wood components, from the analytical point of view, is their intimate mixing with one another within the cell wall. Consequently, they cannot be separated quantitatively without incurring changes. Only a small amount of polyoses can be removed intact by means of water extraction, e.g., the galactans from larch wood (*11*) and part of the xylans in hardwoods (*12*). Even careful removal of lignin from finely milled wood by extraction with dioxane results in a decrease in the degree of polymerization (DP) (*13*). The main portion of the polyoses must be isolated from holocellulose by means of alkali extraction.

By the method applied in this study, two alkali-soluble fractions containing polyoses and one alkali-insoluble fraction containing alpha cellulose were obtained. The subsequent fractionation of the two polyose fractions resulted in six more fractions. The composition of each separate fraction was determined by paper chromatography of the totally hydrolyzed product.

Polyose Fraction A2 contained the highest percentage of the total alkali-soluble polysaccharides. Thus, Fraction A2 from beechwood contained about 73% and Fraction A2 from sprucewood about 52% of the total. Paper chromatographic identification of the constituents of these fractions revealed that Fraction A2 from beechwood consists of rather pure xylan while Fraction A2 from sprucewood con-

sists of a mixture of glucomannan and arabinoxylan (*6*). The same mixture is found in a different fraction from sprucewood, termed B2, which amounts to about 20% of the total alkali-soluble polysaccharides.

In the electron microscope, the abovementioned fractions show fibrillar elements (Figs. 1 and 2). Contrary to the fraction from beechwood, the fibrils in the two fractions of sprucewood polyoses are partially veiled by an amorphous-looking substance (Fig. 2). Here "amorphous" is used in the sense of "structureless," i.e., substances appearing amorphous in the electron microscope may show a lattice order when submitted to X-ray or electron diffraction. From the similarity of the shape to that of the polyose fraction from beechwood and from the changes taking place in the polyose fractions from sprucewood during heating of wood (*7*, *14*), it is concluded that the fibrils consist of arabinoxylan and the amorphous-looking substance consists of glucomannan. The amorphous shape of the glucomannan on the electron micrographs should not lead to the assumption that it is in fact without any structure. There is some evidence that the amorphous-looking substance in sprucewood Fractions A2 and B2 consists of very fine fibrils (Fig. 2) which can barely or not at all be resolved under conditions prevailing in this study (metal-shadowed specimens, microscope of relatively low resolution power). This question will be solved by further studies with an instrument of high resolution power, as already used for some details in the observation of cellulose. A distinctly fibrillar mannan was isolated in one fraction from sprucewood which, however, amounted to only about 0.5% of the alkali-soluble polysaccharides (Fig. 3).

A highly interesting change of the

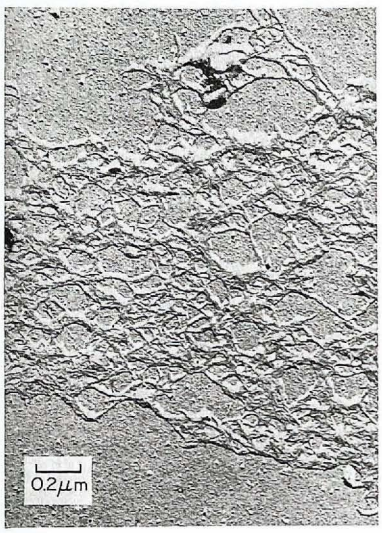

Fig. 1. Polyose Fraction A2 from beechwood containing fibrillar xylan. Platinum-shadowed.



Fig. 2. Polyose Fraction A2 from sprucewood containing fibrillar arabinoxylan and amorphous-looking glucomannan. In several places, the smooth areas are resolved into fine fibrillar structures. Platinum-shadowed.

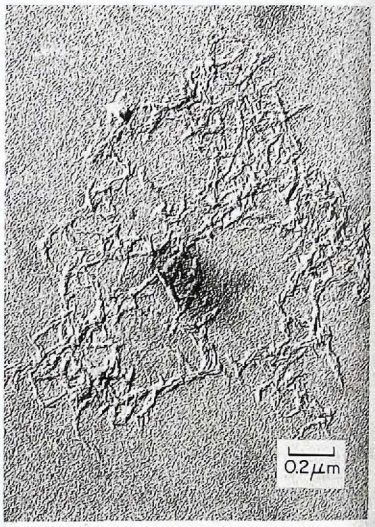

Fig. 3. Polyose Fraction B1 from sprucewood containing fibrillar glucomannan. Platinum-shadowed.

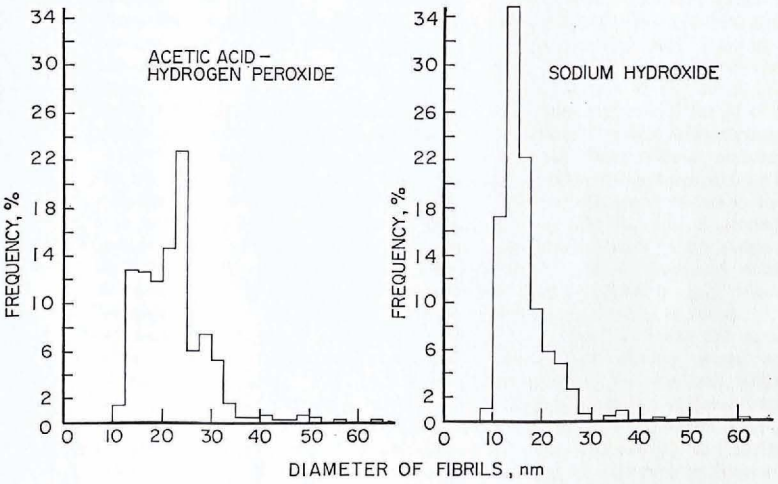

Fig. 4. Diameters of fibrils in the S1 of delignified sprucewood fibers after treatment with acetic acid-hydrogen peroxide (1:1, 60 min, 70°C) and with sodium hydroxide (5%, 10 min, 20°C).

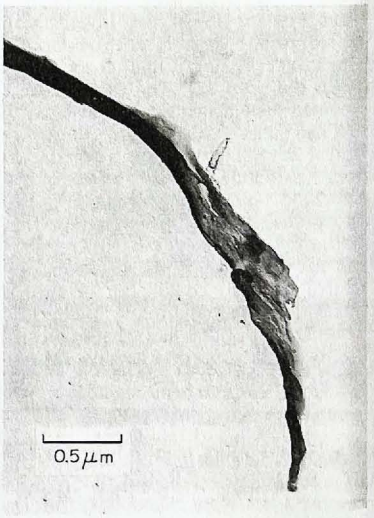

Fig. 5. Cell wall fragment of sprucewood meal after delignification. Platinum-shadowed.

CITE THIS PAPER: Fengel, D., *Tappi* 53(3): 497(1970). https://doi.org/10.32964/TJ53.3.497.

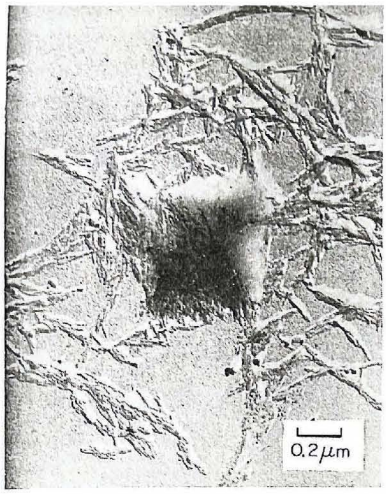

Fig. 6. Partially hydrolyzed cellulose (20% H_2SO_4, 5 hr, 100°C) from sprucewood. The fibrillar fragments are arranged in various lateral aggregates. Platinum-shadowed.

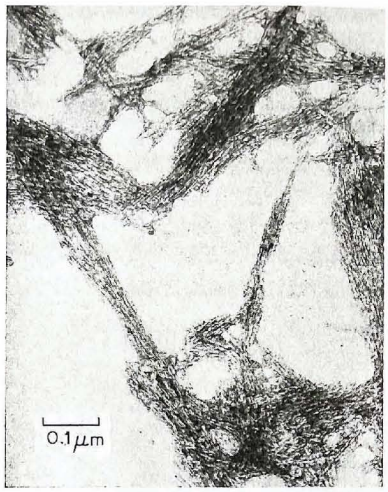

Fig. 7. Partially hydrolyzed cellulose (20% H_2SO_4, 5 hr, 100°C) from sprucewood. The light-colored lines are elementary fibrils of about 30 Å in diameter. Negative stained with uranyl acetate.



Fig. 8. Partially hydrolyzed cellulose (20% H_2SO_4, 5 hr, 100°C) from sprucewood. The fibrillar fragments are subdivided in longitudinal direction (arrows). Platinum-shadowed.

fraction from sprucewood containing fibrillar mannan can be observed if the wood is thermally treated prior to the isolation of the polyoses. After heating the wood for 24 hr at various temperatures, this fraction, termed B1, showed the most striking increase in percentage of all alkali-soluble polysaccharide fractions. While the percentages of the other fractions vary more or less with treatment temperatures between 120 and 200°C, there is a strong increase in fraction B1 to about 21% of the wood at temperatures between 150 and 200°C (*14*). The higher the treatment temperature, the higher is the content of glucan in Fraction B1. The glucan originates from the cellulose cleaved during the thermal treatment of wood. Thus, the main decomposition products of the cellulose are found in Fraction B1. From this, it may be concluded that the mannan fibrils in this fraction from untreated wood are parts of the mannan which cannot be separated from the alpha cellulose by alkali-extraction and which is known as "resistant" mannan.

From the fibril-forming behavior of the xylan and of at least a portion of the mannan after their isolation from wood, it is assumed that the molecules of these polyoses are mainly oriented in the direction of the cellulose fibrils within the cell wall. Moreover, the intimate association of part of the mannan with the cellulose, the behavior of the cellulose fibrils under the influence of different chemical treatments, and the partial chemical bonding between polyoses and lignin lead to the conclusion that the polyose molecules are predominantly arranged around the larger and between the smaller fibrillar units of the cellulose. This concept implies a combination of the ideas of Preston (*15*) and of Marchessault (*16*) concerning the arrangement of polyoses in relation to the cellulose fibrils. The various side groups of the polyose molecules probably prevent the same strict orientation as shown by the cellulose molecules. Meier and Welck (*17*) studied the association of the polyoses with the cellulose fibrils in the electron microscope, but their observations gave no definite information.

Cellulose

Within the plant cell wall, the molecular chains of cellulose are arranged in systems at various levels of magnitude. The cell wall itself can be regarded as the highest-level system. It is built up from fibrillar units which are called "microfibrils" and whose diameters measure about 250 Å. The microfibrils, however, do not seem to be very stable units since they can easily be split into smaller units within the fiber wall, e.g., by treatment with alkali. Figure 4 shows the result of measurements of the fibril units within ultra-thin sections of the S1 of delignified sprucewood fibers. After treatment of the cellulose fibers with a mixture of acetic acid and hydrogen peroxide, a maximum for fibril diameters occurs in the range of 225 to 250 Å, and a second, smaller maximum occurs in the range of 125 to 150 Å. After treatment with sodium hydroxide, there is only one maximum in the range of 125 to 150 Å.

The basic material for the isolation of cellulose during wood analysis is wood meal, i.e., the cell walls are disintegrated and the various reactions take place in these fragments (Fig. 5). In the electron microscope, the isolated cellulose can be observed as fragments of the cell wall. The fibrillar structure, however, is only clearly recognizable after an acid treatment since it is covered by amorphous cellulose material created in the various isolation steps. After partial hydrolysis, specimens of isolated cellulose show lateral fibrillar aggregates of various dimensions (Fig. 6). The diameter of a single fibril measures about 120 Å.

It is concluded from these observations that fibrils of about 120 Å in diameter are constant units within the cell wall and that they are subunits of the microfibrils.

Some years ago, cellulose fibrils about 30–35 Å in diameter were detected in meristematic tissue and bacteria slime by several authors (*18*). Frey-Wyssling and Mühlethaler (*19*) termed these smallest cellulose units "elementary fibrils." At higher magnification and higher resolution power in negative-stained specimens of partially hydrolyzed cellulose from wood, fibrillar elements about 30 Å in diameter also become visible (Fig. 7). This observation proves that the elementary fibrils are also order systems of the cellulose in wood (*20*).

On the other hand, electron micrographs of partially hydrolyzed cellulose also show a subdivision of the fibrillar elements in the longitudinal direction. This subdivision is recognizable in several places in Fig. 8. Since this picture is taken from a platinum-shadowed specimen, the interspaces between the longitudinal units seem to be holes or notches, i.e., the fibrillar units had been attacked at regular distances by the acid. After negative staining, the fibrils are visible in the form of white dotted lines (Fig. 9); consequently, the interspaces are more accessible to the staining material than the fibrillar units which show up as white. At high magnification, it is obvious that the bright units are often of a more or less rectangular shape and that these units as well as the more accessible interspaces are structured. In Fig. 10, there is a highly interesting area within the framed

CITE THIS PAPER: Fengel, D., *Tappi* 53(3): 497(1970). https://doi.org/10.32964/TJ53.3.497.



Fig. 9. Partially hydrolyzed cellulose (20% H_2SO_4, 5 hr, 100°C) from sprucewood. The fibrillar elements have a beaded appearance. Negative stained with phosphotungstic acid (PTA).

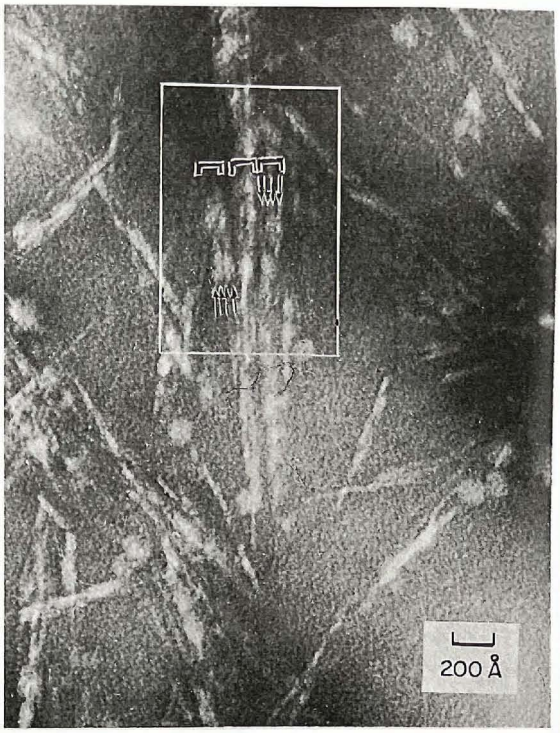

Fig. 10. Partially hydrolyzed cellulose (20% H_2SO_4, 5 hr, 100°C) from sprucewood. The high-magnification photo shows fibrils which are subdivided into darker and lighter zones. Within the framed field, there are three 120-Å units (in brackets) which are built up of four elementary fibrils in lateral direction (arrows). Negative stained with PTA.

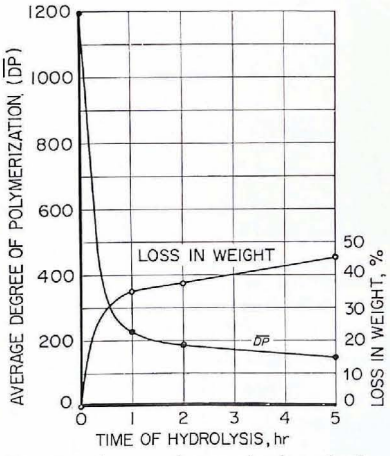

Fig. 11. Average degree of polymerization and loss in weight of cellulose from sprucewood as a function of time of hydrolysis.

field. The structural details are indicated by arrows. Three fibrillar fragments about 120 Å in diameter, each subdivided into four fibrillar units about 30 Å in diameter, are recognizable. Within the less accessible regions, the 30-Å subunits seem to be thicker and seem to contact each other so that they cannot be completely discerned. The lengths of the less accessible regions after 5 hr of hydrolysis with sulfuric acid measure about 150 Å.

Early in the thirties, a decay of the fibrillar elements into shorter pieces in chemically treated cellulose was observed with the aid of the light microscope (*21*). Later studies with the electron microscope and measurements of DP resulted in observation of different lengths of fibrillar units of partially hydrolyzed cellulose, depending on the origin of the specimen and the reaction conditions. The respective values in the literature range from 60 to 2500 Å (*22*).

During the present study, the "leveling-off DP" (*23*) was reached after 1 hr of acid treatment of the cellulose samples (Fig. 11). Between 1 and 5 hr of treatment, there is only a slight decrease in the $\overline{DP}$ value.

For more detailed information, chain-length fractionation was also performed. Figure 12 shows the integral distribution curve of the DP of cellulose treated with 20% sulfuric acid for 1 hr. The DP decreases continually from about 200 to about 40. The steepest part is within the range $\Sigma m_p = 40$ and $\Sigma m_p \approx 0$ with a DP value of about 40–50, i.e., there is a considerable portion of cellulose chains about 200–250 Å in length.

The fractionation of cellulose hydrolyzed for 5 hr with sulfuric acid resulted in the main portion of cellulose chains having a DP below 40, i.e., the chains are shorter than 200 Å. In this low DP range, however, the applied method of determination no longer gives exact values. Nevertheless, it may be assumed that there is a good agreement of these results and of the chain length measured in the electron micrographs at about 150 Å from the less accessible regions of cellulose hydrolyzed for 5 hr.

In several cases, the less accessible regions of the fibrillar fragments are separated from one another and are visible as grains on the micrographs (Fig. 13). As these particles are the result of fragmentation of cellulose fibrils, they would consist of short cellulose chains which are still oriented in a parallel arrangement. This consideration is further supported by the observation that these particles are able to rearrange themselves in new fibrillar units. The newly formed fibrils are oriented in parallel systems (Fig. 14) or grow in the shape of whiskers (Fig. 15).

In addition to the heterogenous acid hydrolysis, cellulose was decomposed by heating. The behavior of the cellulose was studied as part of an extensive study on the changes taking place in the wood during heating (*7*, *24*). The heating results in a strong decrease of the cellulose content between 120 and 200°C, determined as the alkali-insoluble fraction.

CITE THIS PAPER: Fengel, D., *Tappi* 53(3): 497(1970). https://doi.org/10.32964/TJ53.3.497.

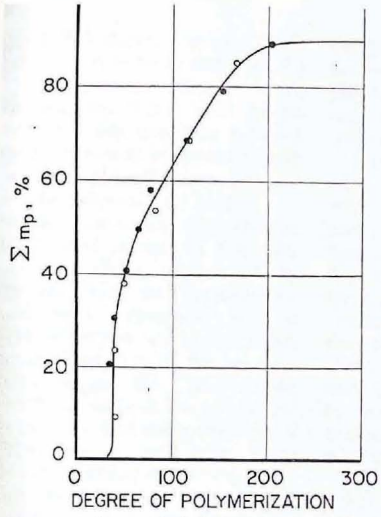

Fig. 12. Curve of chain length distribution of cellulose hydrolyzed for 1 hr with 20% H_2SO_4 at 100°C as a result of two different fractionations.

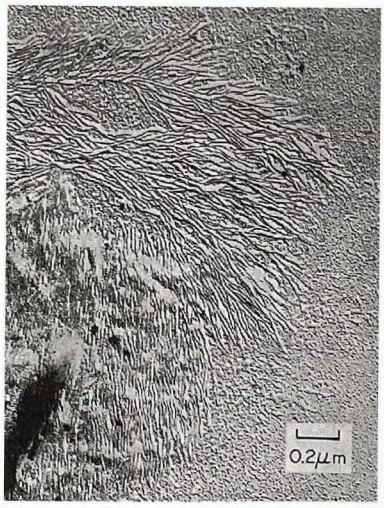

Fig. 13. Partially hydrolyzed cellulose (20% H_2SO_4, 1 hr, 100°C) from sprucewood. Very short fragments are deposited on the supporting films. Platinum-shadowed.



Fig. 14. Partially hydrolyzed cellulose (20% H_2SO_4, 1 hr, 100°C) from sprucewood. Newly formed fibrillar systems. Platinum-shadowed.

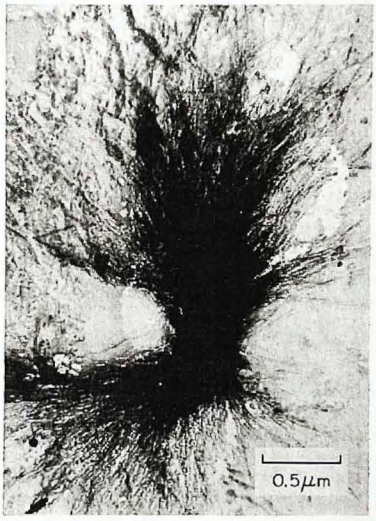

Fig. 15. Partially hydrolyzed cellulose (20% H_2SO_4, 5 hr, 100°C) from sprucewood; reaggregation of fibrillar fragments in the shape of a whisker. Platinum-shadowed.

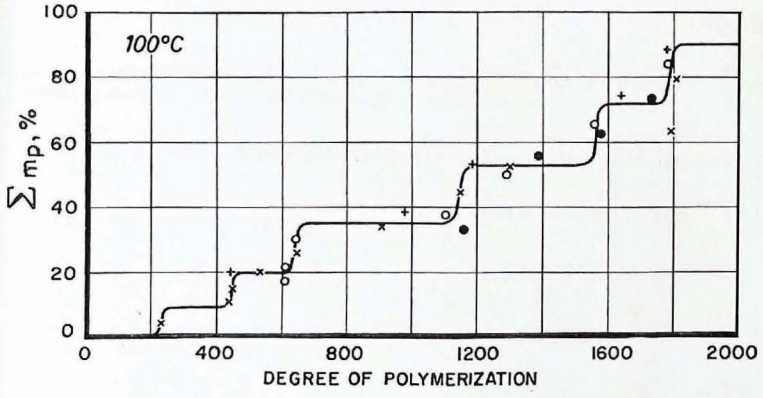

Fig. 16. Curve of chain length distribution of cellulose isolated from sprucewood, heated for 24 hr at 100°C, as a result of four different fractionations.

Within the temperature range of 120 to 200°C, there is also a decrease in the average DP. If there are sensitive regions equidistant from one another within the cellulose fibrils, one would assume that the thermally induced cleavages occur in these regions.

The cellulose isolated from wood which had been heated for 24 hr at 100, 120, 150, 180, and 200°C was submitted to a chain-length fractionation. As an example, Fig. 16 shows the chain-length distribution of cellulose isolated from wood heated at 100°C for 24 hr. The results of the fractionation of all tested celluloses are compiled in Table I. The DP values represent kinks in the distribution curves. In curves of three or four samples of different treatment temperature, there are various kinks in the same DP range. As shown in the bottom row, there is evidence that all DP values are multiples of about 60. This result leads to the conclusion that the thermally induced cleavage of the cellulose chains occurs at certain distances which are multiples of about 300 Å.

CONCLUSIONS

Although many points are still open to question, these findings can be projected in a model from which the observations may be interpreted satisfactorily. A model of this kind should not be considered final, but may be varied and supplemented if subsequent observations prove it necessary. It is on this basis that the tentative model of the supermolecular organization of the polysaccharides within the cell wall presented below should be considered.

The molecular chains of the polysaccharides are able to form fibrillar units or to arrange themselves in the direction of fibrillar units. The formation of well-ordered fibrils is a known property of the cellulose molecules. The smallest fibrillar units which were detected as constant elements 30–35 Å in diameter in various lower and higher plants are called "elementary fibrils." These elementary fibrils are densely packed into higher units 120 Å in diameter. There must be interfaces between the elementary fibrils, otherwise they could not be separated in such a uniform manner by chemical treatment. The recently published observations of Heyn (*25*) showed that in the natural swelling state of the wood cell wall, the elementary fibrils are visible even without chemical treatment. It is assumed that the interfaces between the elementary fibrils are formed by less-ordered cellulose chains and by polyose chains. From the fibril-forming properties of isolated polyoses, it is concluded that these molecules are oriented in the direction of the cellulose fibrils within the cell wall.

The next higher-level system is represented by the "microfibrils" which are

built up of 120-Å fibrils. The microfibril unit does not seem to be as stable as the two lower systems since the microfibrils are easily split into 120-Å units by an alkali treatment; the interfaces between these units are assumed to consist mainly of polyoses. The microfibrils in turn are surrounded by polyoses and lignin.

The graphic projection of these findings is shown in cross section in Fig. 17a. The elementary fibrils represented by framed square fields are bordered by narrow interfaces containing only a few polyose molecules within the 120-Å units. The main portion of the polyoses is deposited around the 120-Å fibrils, within as well as without the microfibril unit. It is assumed that the movement of water within the cell wall takes place mainly in the interfaces containing polyoses; processes such as shrinkage and swelling occur preferentially within these interfaces. At the surface of the microfibrils, the polyoses are in intimate contact with the lignin, thus in these places chemical bonds between lignin and polysaccharides (*13*, *26*) exist. Nevertheless, polyoses may also be deposited within the lignin in varying quantities in different cell wall layers (*27*).

Figure 17b shows a longitudinal view of a 120-Å fibril, with additional consideration of the results of hydrolytic and thermal decomposition. In this section plane, the 120-Å unit is built up of four elementary fibrils. The chain-length measurement of cellulose from thermally treated wood leads to the conclusion that there are sensitive regions located about 300 Å from each other. In the model, the sensitive regions are outlined by dashed lines. Data on the structural character of these regions cannot, however, be given.

There have been many models published in recent years showing a rather different arrangement of the cellulose molecules in the sensitive or accessible regions. Some of the models (*28*) are based on the observations o f Keller (*29* and Fischer (*30*) stating that under special conditions macromolecules are able to form chain-folds. Other models show chains running through the accessible regions in an irregular and/or crossing-over arrangement (*31*). However, in most of the models the accessible zones are very conspicuous so that they should be easily visible in the electron microscope. Generally, in the untreated state the elementary fibrils can be observed as smooth stretched strings. Heyn (*25*, *32*) observed a beaded appearance of the elementary fibrils after freeze-drying the samples.

Loosely arranged accessible zones should presumably give the separated fibrils a high flexibility. In reality, the elementary fibrils seem to be very stiff and as Mühlethaler (*33*) demonstrated, they cannot be bent except in a large radius. It is, therefore, assumed that the sensitivity of certain regions of the elementary fibrils is not caused by a disarrangement of the whole system at that point. Deviation of a few molecules from the complete order causing a lattice defect and/or the presence of molecular chain ends is believed to be a sufficiently good reason for a special sensitivity. A very slight reduction of the lattice order in the accessible regions of regenerated cellulose is assumed to occur by Kiessig (*34*) from the results of X-ray low-angle investigations. Also, Ruck (*35*) concluded from results of mercerizing studies on cellulose that the molecular chains in the accessible regions show only slight deviations from the lattice order. The cross-section model of the cellulose fibrils of Ruck (*36*) considers only the distribution of the extractives and makes no reference to the polyoses.

At the sensitive regions, the cellulose fibrils are also attacked during chemical treatments such as partial acid hydrolysis. The sensitive regions are highly accessible to staining materials and these accessible regions evidently grow toward the less accessible regions, depending on reaction conditions. The influence of a chemical attack on the sensitive regions is indicated by dashed arrows in Fig. 17b.

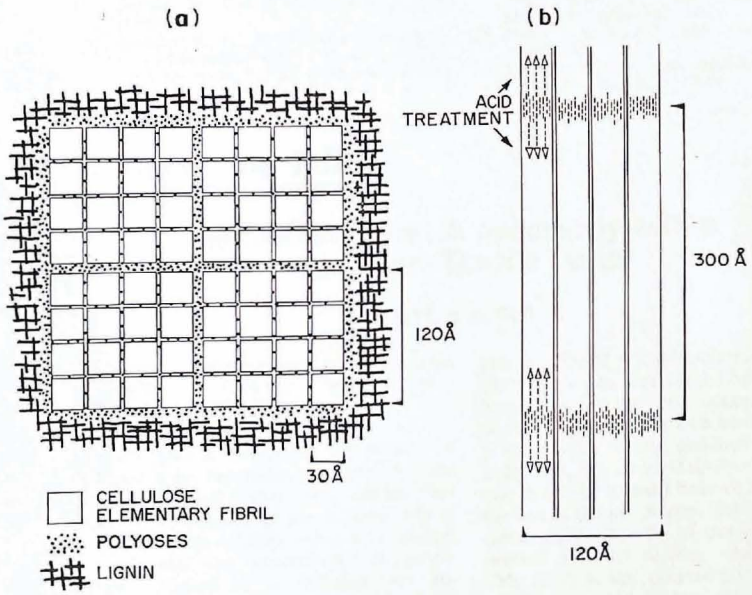

Fig. 17. Model of the ultrastructural organization of a microfibril within the wood cell wall in cross section (a) and model of a 120-Å fibril in longitudinal section (b).

LITERATURE CITED

1. Nishikawa, S. and Ono, S., *Proc. Math. Phys. Soc. Tokyo* **7**: 131 (1913); Herzog, R. O. and Janke, W., *Ber. Deut. Chem. Ges.* **53**: 2162 (1920).

Table I. Chain Length Fractionation of Cellulose Isolated from Thermally Treated Wood

Temperature, °C	*DP values of kinks in the distribution curves*													
20	...	220	300	400	...	...	...	...	...	930	...	...	...	1770
100	...	230	...	...	450	...	...	...	...	...	1160	...	1560	1780
120	...	...	...	380	...	...	...	730	...	...	1220	1420		
150	...	...	300	...	460	...	630	...	830	...	1190	1380		
180	110	220	....	360	...	560	...	...	...	...	1210	1430		
200	130	220	310	410	...	590								
Multiple × mean factor	2 × 60	4 × 55	5 × 60	6 × 64	7 × 65	9 × 64	10 × 63	12 × 61	13 × 64	15 × 62	19 × 63	23 × 61	25 × 62	28 × 63

CITE THIS PAPER: Fengel, D., *Tappi* 53(3): 497(1970). https://doi.org/10.32964/TJ53.3.497.

2. Ambronn, H., *Kolloid-Z.* **20:** 173 (1917).
3. Knoll, M. and Ruska, E., *Ann. Physik* **12:** 607 (1932).
4. Meyer, K. H. and Mark, H., *Chem. Ber.* **61:** 953 (1928); Mark, H. and Meyer, K. H., *Z. Physik. Chem.* **B2:** 115 (1929).
5. Wise, L. E., Murphy, M., and D'Addieco, A. A., *Paper Trade J.* **122:** 35 (1946).
6. Fengel, D., *Holz, Roh- Werkstoff* **24:** 98 (1966); *Svensk Papperstid.* **70:** 70 (1967).
7. Fengel, D., *Holz, Roh- Werkstoff* **24:** 9 (1966).
8. Jayme, G. and Kleppe, P., *Papier* **15:** 6 (1961).
9. Philipp, B. and Linow, K. J., *Zellstoff Papier* **14:** 321 (1965).
10. Schulz, G. V., *In* "Methoden der Organischen Chemie" (E. Müller, *Ed.*), Stuttgart, Thieme Verlag, 1955, Vol. III/1, p. 445. *See also*, Vollmert, B., "Grundriss der Makromolekularen Chemie," Berlin, Göttingen, Heidelberg, Springer Verlag, 1962, p. 259.
11. Adams, G. A., *Tappi* **40** (9): 721 (1957); Roudier, A. and Eberhard, L., *Bull. Soc. Chim. France:* 844 (1963); Aspinal, G. O., Actes Symp. Intern. de Grenoble, 1964, p. 89.
12. Timell, T. E. and Zinbo, M., *Tappi* **50** (4): 195 (1967); Timell, T. E., *Wood Sci. Technol.* **1:** 45 (1967).
13. Freudenberg, K., *Science* **148:** 595 (1965).
14. Fengel, D., *Svensk Papperstid.* **72:** 209 (1969).
15. Preston, R. D., *In* "Cellular Ultrastructure of Woody Plants" (W. A. Coté, Jr., *Ed.*), Syracuse, N. Y., Syracuse University Press, 1965, p. 1.
16. Marchessault, R. H., Actes Symp. Intern. de Grenoble, 1964, p. 287; Marchessault, R. H., Settineri, W., and Winter, W., *Tappi* **50** (2): 55 (1967).
17. Meier, H. and Welck, A., *Svensk Papperstid.* **68:** 878 (1965).
18. Günther, I., *J. Ultrastructure Res.* **4:** 304 (1960); Mühlethaler, K., *Beih. Z. Schweiz. Forstverein* No. 30: 55 (1960); Ohad, I., Danon, D., and Hestrin, S., *J. Cell Biol.* **12:** 31 (1962); Schnepf, E., *Planta* **67:** 213 (1965).
19. Frey-Wyssling, A. and Mühlethaler, K., *Makrom. Chem.* **62:** 25 (1963).
20. Fengel, D., *Papier* **21:** 635 (1967).
21. Farr, W. K., *J. Appl. Phys.* **8:** 228 (1937); Wergin, W., *Holz, Roh- Werkstoff* **2:** 97 (1939).
22. Kinsinger, W. G. and Hock, C. W., *Ind. Eng. Chem.* **40:** 1711 (1948); Morehead, F. F., *Textile Res. J.* **20:** 549 (1950); Rånby, B. G., *Discussions Faraday Soc.* No. 11: 158 (1951); *Tappi* **35** (2): 53 (1952); Hess, K., Mahl, H., and Gütter, E., *Kolloid-Z.* **155:** 1 (1957); Krässig, H. and Käppner, W., *Makrom. Chem.* **44/46:** 1 (1961).
23. Battista, O. A., *Ind. Eng. Chem.* **42:** 502 (1950).
24. Fengel, D., *Holz, Roh- Werkstoff* **24:** 98, 529 (1966); **25:** 102 (1967); "Die Einwirkung hoher Temperaturen bis 200°C auf Struktur und chemische Bestandteile von Nadelholz," Habilitationsschrift, Universität München, 1968.
25. Heyn, A. N. J., *J. Ultrastructure Res.* **26:** 52 (1969).
26. Freudenberg, K. and Harkin, J. M., *Chem. Ber.* **93:** 2814 (1960).
27. Fengel, D., *Wood Sci. Technol.* **3:** 203 (1969).
28. Tønnesen, B. A. and Ellefsen, Ø., *Norsk Skogind.* **14:** 266 (1960); Dolmetsch, H., *Kolloid-Z.* **176:** 63 (1961); Manley, R. St. J., *Nature* **204:** 1155 (1964); Marx-Figini, M. and Schulz, G. V., *Biochim. Biophys. Acta* **112:** 81 (1966); Bittiger, H. and Husemann, E., *Papier* **23:** 17 (1969).
29. Keller, A., *Phil. Mag.* **2:** 1171 (1957); *Makrom. Chem.* **34:** 1 (1959).
30. Fischer, E. W., *Z. Naturforsch.* **12a:** 753 (1957).
31. Hermans, P. H., *Kolloid-Z.* **83:** 71 (1938); Hess, K., Mahl, H., and Gütter, E., *Kolloid-Z.* **155:** 1 (1957); Dolmetsch, H. and Dolmetsch, H., *Papier* **22:** 1 (1968).
32. Heyn, A. N. J., *J. Cell Biol.* **29:** 181 (1966).
33. Mühlethaler, K., *Beih. Z. Schweiz. Forstverein* No. 30: 55 (1960).
34. Kiessig, H., *Papier* **12:** 117 (1958); **22:** 261 (1968); *Norelco Rept.* **7:** 99 (1960).
35. Ruck, H., *Papier* **16:** 703 (1962).
36. Ruck, H., *Papier* **21:** 697 (1967); **22:** 701 (1968).

RECEIVED FOR REVIEW July 28, 1969.

ACCEPTED Nov. 2, 1969.

Expanded version of a paper presented at the International Seminar, "Physical and Chemical Properties of Wood Fibers," of the Technical Association of the Pulp and Paper Industry, held in Appleton, Wis., May 12–15, 1969.

The author is very grateful to Dr. N. S. Thompson for kindly presenting this paper at the Seminar.

The chemistry of aluminum salts in papermaking

ABSTRACT
Alum and related aluminum salts are used extensively in a variety of papermaking operations. The versatility of these aluminum additives stems from the ability of the various aluminum species to adsorb and interact with the other materials in the papermaking system. Underlying these interactions is the aqueous chemistry of the aluminum ion. A review of the current views on the aqueous chemistry of the aluminum ion and papermaking aluminum chemistry is presented. Application of the aqueous aluminum equilibria to aluminum adsorption and alum–rosin sizing are also discussed.

KEYWORDS
Aluminum compounds
Aluminum sulfate
Additives
Papermaking

Thomas R. Arnson*
The Institute of Paper Chemistry, P.O. Box 1039, Appleton, Wis. 54911

Papermaker's alum, aluminum sulfate, has long been used in the manufacture of paper and paperboard. Alum and related aluminum salts (sodium aluminate and aluminum chloride) are used extensively in a variety of papermaking operations including: sizing, curing of wet strength resins, pH and pitch control, drainage, and retention of nonfibrous additives. However, even with its widespread use, our fundamental knowledge of alum's interactions with other materials in the papermaking system is inadequate.

A major factor which has inhibited the progress of investigations of these interactions is the complicated chemistry of the aluminum ion in aqueous solutions. Under the conditions used in the papermaking system, the aluminum ion can form a multitude of species including the simple trivalent cation, various hydroxo-aluminum complexes, and the insoluble aluminum hydroxide precipitate. The following overview is intended to highlight some of the newer views on the aqueous chemistry of the aluminum ion. With this information, it is possible to better define the type of aluminum species existing in the papermaking system and the type of interactions that are occurring. A general review on the uses of alum in papermaking will not be included as this subject has been covered in recent reviews by Davison (*1*) and Wortley (*2*).

*Current address: Eastman Kodak Co., Rochester, N.Y. 14650.

Aluminum in the papermaking system

The primary source of aluminum for most papermaking systems is aluminum sulfate [$Al_2(SO_4)_3 \cdot 14H_2O$] (*1, 2*). Sodium aluminate ($NaAlO_2$) (*3, 4*) and aluminum chloride ($AlCl_3 \cdot 6H_2O$) (*5*) are also used as sources of aluminum for certain special applications. Regardless of the source, aluminum salts are added to the papermaking system based on the dry mass of the pulp such as lb/ton of pulp. This convention is not, however, used in studies on the aqueous chemistry of the aluminum ion, where the amount of aluminum is expressed on a mass per mass or volume of water basis such as parts per million (ppm) or moles per liter (*M*); in addition, only part of the aluminum remains in solution while a large portion is adsorbed onto the fibers. Therefore, only an estimated aluminum concentration can be calculated from the dry mass addition rate. An estimated initial concentration of aluminum per unit of water volume calculated for a typical range of alum addition rates and pulp consistencies is shown in Table I. These values show good agreement with those of Avery (*5*), who measured the dissolved aluminum concentration in numerous papermaking systems and found a range of 2–60 ppm Al.

The pH of a papermaking system using aluminum salts can range from slightly alkaline to acidic. However, most systems operate at pH 4.0–5.5 because many of the benefits of having aluminum in the system are obtained in this pH range (*1*).

Aqueous chemistry of aluminum

The diversified chemical activity of the aluminum ion in aqueous solutions is a result of its high charge, 3^+, and small ionic radius (0.50 Å), which yields a high-charge density (*6, 7*). In order to reduce its high-charge density, the aluminum ion acts as a Lewis acid electron pair acceptor and complexes with neutral or anion molecules which are referred to as a ligand. The strength or stability of the aluminum–ligand bond is governed by the ability of the ligand to give up electrons, by the receptivity of the aluminum ion for the

I. Relationship between alum addition and aluminum concentration

Alum[a] addition		Pulp consistency,	Aluminum[b] concentration	
%	lb/ton	%	M	ppm
1	20	0.3	1×10^{-4}	2.7
1	20	3.0	1×10^{-3}	27.0
2	40	0.3	2×10^{-4}	5.4
2	40	3.0	2×10^{-3}	54.0

[a] As $Al_2(SO_4)_3 \cdot 14H_2O$. [b] Estimated initial concentration per unit volume of water.

electrons, and by the ability of the ligand to occupy more than one coordination site with a stable ring structure development.

It is well recognized (*1, 6, 7*) that the aluminum cation complexes with six ligands to form an octahedral structure as seen in Fig. 1. However, newer concepts on metal ion complex formation (*6–9*) indicate that aluminum and other multivalent cations have two coordination spheres referred to as the inner and outer spheres. The octahedral structure is used to describe the orientation of the ligands only in the inner coordination sphere. Veillard (*9*) has indicated that 12 waters of hydration exist in the outer coordination sphere and are oriented by the waters of hydration in the inner sphere.

In relatively dilute solutions as would exist in the majority of papermaking systems, the aluminum cation forms complexes with H_2O, OH^-, SO_4^{2-}, $H_2PO_4^-$, $C_2O_4^{2-}$, and R–COO^-, but not with Cl^-, NO_3^-, or ClO_4^- (*1, 10–13*). R–COO^- represents an ionized carboxyl group available from the pulp, size precipitate, anionic polyacrylamide, or other anionic papermaking additives. These ligands will be discussed as two groups, one including only H_2O and OH^- (aluminum hydrolysis) and the other comprised of the remaining ligands.

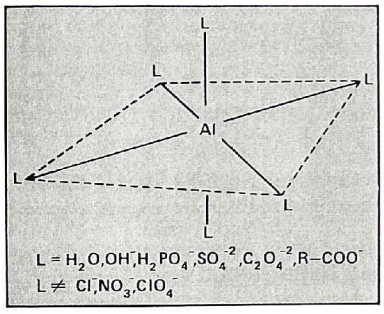

1. General complexing behavior of the aluminum cation in dilute solutions.

Aluminum hydrolysis

When an aluminum salt of a noncomplexing anion (Cl^-, NO_3^-, ClO_4^-) is dissolved in an aqueous medium, the simple trivalent, hydrated cation is the sole aluminum species only at pH < 3.0 (*14*). Above this pH, the replacement of a water ligand with a hydroxide group in the inner coordination sphere starts to become significant. This is referred to as hydrolysis, and the reaction is shown in Fig. 2, Eq. 1. The hydrolysis reaction is really a summation of two reactions where the hydroxyl ion shifts the equilibrium in favor of the hydrolyzed species by removing the protons from solution (*15*).

$$Al^{3+} + H_2O \rightleftharpoons AlOH^{2+} + H^+$$
$$H^+ + OH^- \rightleftharpoons H_2O$$
$$\overline{Al^{3+} + OH^- \rightleftharpoons AlOH^{2+}}$$

As the hydroxide ion concentration increases, $AlOH^{2+}$ and other hydroxoaluminum complexes are formed. Too often this change in the chemical equilibrium is incorrectly shown by a series of mononuclear complexes as illustrated in Fig. 2, Eqs. 2–5. The aluminum ion in aqueous solutions is amphoteric and does form significant amounts of $AlOH^{2+}$, $Al(OH)_3$ and $Al(OH)_4^{1-}$. However, it has been demonstrated by many workers (*16–21*) that aluminum hydrolysis does not occur by a simple mononuclear process. Rather, the hydrolysis complex, $AlOH^{2+}$, is in equilibrium with polynuclear complex species. Polynuclear species are formed when the mononuclear aluminum complex species are linked to each other by the hydroxyl bridging process called olation (*10, 11, 22*) (see Fig. 2, Eq. 6).

An extension of the olation process leads to the formation of higher-order polynuclear species. The exact number and formula of the polynuclear species is uncertain because their formation is significantly affected by aging (*14, 16, 22*), high temperatures (*10, 14, 16, 22*), and aluminum concentration (*10*). With most investigations (*17, 18, 23, 24*), the experimental conditions are limited to freshly prepared, dilute solutions of aluminum salts at room temperature. Under these conditions, potentiometric titration analysis (*17–21, 23–25*) and coagulation experiments (*16, 26*) have been the main investigative methods used to study the structure of the polynuclear species.

Grunwald and Fong (*23*) and Turner (*19*) interpreted their titration data to show evidence of the dimer, $Al_2(OH)_2^{4+}$, although Turner's calculations indicate that only a maximum of 1% of the aluminum would exist as this species. Several higher-order polynuclear species have been proposed by workers using potentiometric titration analysis: $Al_6(OH)_{15}^{3+}$ (*20*), $Al_7(OH)_{17}^{4+}$ (*21*), $Al_{13}(OH)_{32}^{7+}$ (*25*), and $Al_{14}(OH)_{35}^{7+}$ (*17*). Using potentiometric titration data and coagulation experiments, Matijevic and coworkers (*16, 26*) indicate that the charge of the polynuclear species should be +4 and proposed $Al_8(OH)_{20}^{4+}$ to be the correct formula.

Therefore, prior to the work of Hayden and Rubin (*24*), one concluded from the literature that the most probable aluminum species existing in a freshly prepared, dilute solution of a noncomplexing anion aluminum at room temperature would be Al^{3+}, $AlOH^{2+}$, $Al(OH)_3$, $Al(OH)_4^{1-}$, one or more higher-order polynuclear species, and possibly the dimer, $Al_2(OH)_2^{4+}$.

The work of Hayden and Rubin (*24*) is probably the most complete study of aluminum hydrolysis and precipitation to date. It provides the basis for a new and more precise description of the equilibrium between the aluminum ion and its hydrolysis products. Hayden and Rubin concluded that their experimental data could only explain the presence of five aluminum species: Al^{3+}, $AlOH^{2+}$, $Al_8(OH)_{20}^{4+}$, $Al(OH)_3$, and $Al(OH)_4^{1-}$. Noticeably, their solution to the aluminum aqueous equilibria is similar to other workers in the field, and yet it is more precise in suggesting only one polynuclear species, $Al_8(OH)_{20}^{4+}$.

The distribution of the aluminum species as a function of pH is shown in Fig. 3. The broad region of aluminum hydroxide precipitation at pH 5–9 and the predominance of Al^{3+} and $Al(OH)_4^{1-}$ at the extremes of this pH range agree well with other workers (*14, 27*). The mononuclear species, $AlOH^{2+}$, exists in limited amounts, less than 10% of the total aluminum. Conversely, a significant amount of aluminum goes to form the polynuclear species, but only over a

$$[Al(H_2O)_6]^{3+} = YH_2O \leftrightharpoons [Al(OH)_Y(H_2O)_{6-Y}]^{(3-Y)+} + YH_3O^+ \quad (1)$$

$$[Al(H_2O)_6]^{3+} + H_2O \leftrightharpoons [Al(OH)_2(H_2O)_5]^{2+} + H^+ \quad (2)$$

$$[Al(OH)(H_2O)_5]^{2+} + H_2O \leftrightharpoons [Al(OH)_2(H_2O)_4]^{1+} + H^+ \quad (3)$$

$$[Al(OH)_2(H_2O)_4]^{1+} + H_2O \leftrightharpoons [Al(OH)_3(H_2O)_3]^{0} + H^+ \quad (4)$$

$$[Al(OH)^3(H_2O)_3]^{0} + H_2O \leftrightharpoons [Al(OH)_4(H_2O)_2]^{1-} + H^+ \quad (5)$$

$$2\left[(H_2O)_4Al\begin{matrix}OH\\H_2O\end{matrix}\right]^{2+} \leftrightharpoons \left[(H_2O)_4Al\begin{matrix}H\\O\\O\\H\end{matrix}Al(H_2O)_4\right]^{4+} + 2H_2O \quad (6)$$

2. Equations.

CITE THIS PAPER: Arnson, T.R., *Tappi* 65(3): 125(1982). https://doi.org/10.32964/TJ65.3.125.

II. Concentration of soluble aluminum species at pHp = 0.05

Aluminum concentration, M	*Species concentration*, M		
	Al^{3+}	$AlOH^{2+}$	$Al_8(OH)_{20}^{4+}$
2.5×10^{-4}[a]	1.26×10^{-4} (0.51)[c]	2.00×10^{-5} (0.08)	1.29×10^{-5} (0.41)
5.0×10^{-4}[b]	2.47×10^{-4} (0.49)	3.11×10^{-5} (0.06)	2.77×10^{-5} (0.44)

[a]pH = 4.75. [b]pH = 4.65. [c]Fraction of total aluminum.

narrow pH region. The polynuclear species is in equilibrium with the precipitate, so the maximum concentration of $Al_8(OH)_{20}^{4+}$ occurs at the pH of precipitation formation—the pHp.

As previously mentioned, most papermaking systems using aluminum salts are maintained between pH 4.0 and 5.5. The distribution of aluminum species as a function of pH for this pH region is shown in Fig. 4. It is possible to consider three distinct regions for the pH range from 4.0 to 5.5. One region is at the lower values of pH where Al^{3+} and $AlOH^{2+}$ are the only species. Another region is at the middle of the narrow pH band where the polynuclear species forms but below the pHp. Here, the aluminum species, Al^{3+}, $AlOH^{2+}$, and $Al_8(OH)_{20}^{4+}$, are soluble, and most of the aluminum exists as Al^{3+} or $Al_8(OH)_{20}^{4+}$. However, since there are eight aluminum atoms for every polynuclear molecule, the concentration of $Al_8(OH)_{20}^{4+}$ is about the same as $AlOH^{2+}$ and considerably less than the concentration of the trivalent cation (Table II). Finally, there is a region above the pHp which is dominated by the formation of the colloidal aluminum hydroxide precipitate. Although the precipitate is written as a neutral species, $Al(OH)_3$, it exists as a positively charged species up to pH 8.5–9.0 due to the adsorption of the hydrolysis products onto the precipitate (*1*, *31*).

The distribution of the complex aluminum species is a function of aluminum concentration as well as pH (Fig. 5 and Table II). The three arbitrary regions still exist, but the curves have shifted somewhat. As the aluminum concentration is raised, the polynuclear species is formed at a lower pH and in increasing amounts. Also, the pHp moves to a lower pH. The data from Hayden and Rubin illustrate an important point: when studying the solution or adsorption properties of aluminum salts, you must consider the pH and aluminum concentration of the system together as interrelated, dependent variables.

Aluminum complexes with other anions

The formation of metal ion complexes in aqueous solution with ligands other than the hydroxide ion is known to occur by a stepwise release of water molecules from the hydration shell of the ions (*8*). The mechanism, referred to as the Eigen-Tamm mechanism (*28*), is:

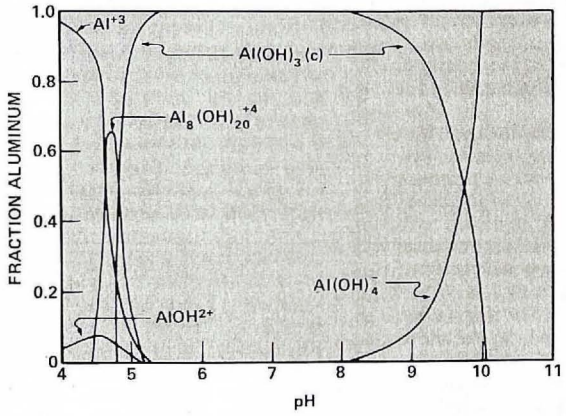

3. Distribution of aluminum species as a function of pH at pH 4–11 ($5.0 \times 10^{-4}M$).

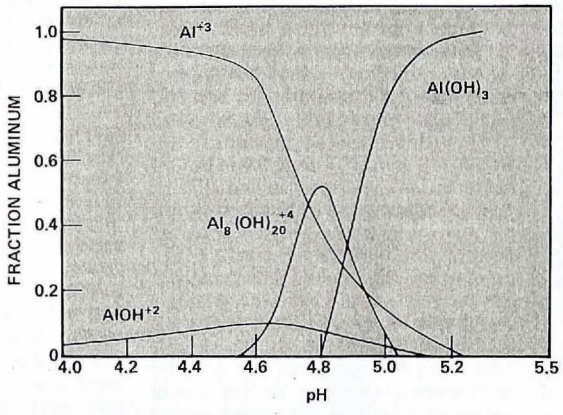

4. Distribution of aluminum species as a function of pH at pH 4.0–5.5 ($2.5 \times 10^{-4}M$).

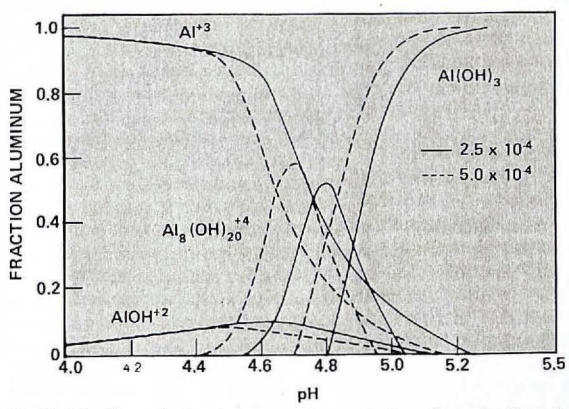

5. Distribution of aluminum species as a function of pH and aluminum concentration at pH 4.0–5.5.

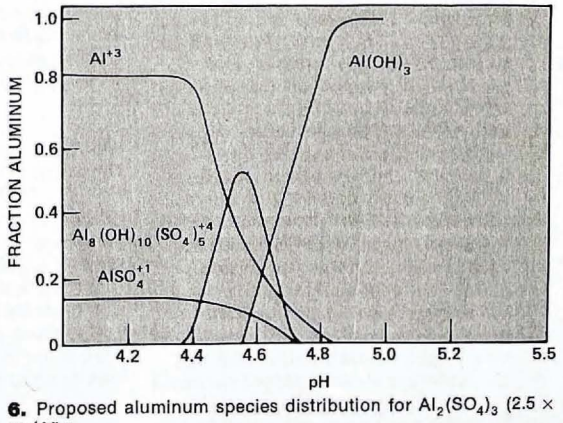

6. Proposed aluminum species distribution for $Al_2(SO_4)_3$ ($2.5 \times 10^{-4}M$).

III. Effect of sulfate ion on the minimum pH of formation of the aluminum hydroxide precipitate (pHp)

Aluminum concentration, M	pHp	
	$AlCl_3$	$Al_2(SO_4)_3$
1.0×10^{-4}	4.90	4.65
2.5×10^{-4}	4.80	4.55
5.0×10^{-4}	4.70	4.45
1.0×10^{-3}	4.65	4.25

$$M^{m+} + L^{n-} \rightleftharpoons M^{m+}(S)L^{n-} \rightleftharpoons ML^{(m-n)+} \quad (7)$$

M^{m+} and L^{n-} represent the hydrated metal ion and ligand, respectively; M^{m+} (S) L^{n-} stands for the "outer-sphere complex" where the hydration shell of the metal ion separates the metal ion and ligand; $ML^{(m-n)+}$ represents the "inner-sphere complex" where the ligand is bonded directly to the metal ion.

The distribution between these forms is a function of the type of ligand, the solution concentration of the metal ion and the ligand, and the equilibrium stability constants. In dilute solutions, fluoride and the bidentate ligands (oxalate, malonate, citrate, and tartrate) form inner-sphere complexes (*13*); sulfate, formate, and acetate exist mainly as outer-sphere complexes (*18, 29, 30*), while chloride, nitrate, and perchlorate have no tendency to complex with aluminum (*32*). As alum is the primary source of aluminum used in papermaking, the complexing behavior of aluminum with the sulfate ion is of special interest.

Below pH 4.0, both direct spectroscopy evidence (*13, 29*) and other experimental studies (*33, 34*) indicate that a portion of the Al^{3+} complexes with the sulfate ion to form the $AlSO_4^+$ complex. In dilute solutions, 90–99% of the $AlSO_4^+$ complex will exist as an outer-sphere complex (*18, 29*).

Above pH 4.0, where aluminum hydrolysis is a significant factor, there is little, if any, agreement on the formation of basic aluminum sulfate complexes. Stryker and Matijevic (*35*) reviewed the proposed formulations for the sulfate hydroxo-aluminum complexes. Most of the complexes were suggested to be neutral or negatively charged, such as $Al(OH)SO_4$, $Al_2(OH)_4SO_4$, $[Al(OH)SO_4]_2$, and $[Al(OH)_2SO_4]^-$. From their own work on the coagulation of lyophobic sols, Stryker and Matijevic indicated that the charge on the active complex is +4 and proposed the $Al_8(OH)_{10}(SO_4)_5^{4+}$ complex. However, they could not exclude the formation of a series of complexes containing various numbers of sulfate ions. The hydrolysis and precipitation studies on Hayden and Rubin (*24*) support the contention that soluble and insoluble sulfatohydroxoaluminum species are formed. Specifically, their data indicated a +4-charged species along with a species of lower charge being formed in the region of maximum hydrolysis.

In contrast with the previously mentioned investigations, DeBruyn and coworkers (*18*) found no evidence of basic aluminum sulfate complexes forming before the precipitation of aluminum sulfate solutions. Ow (*34*) also indicated that sulfate ion does not complex with hydroxoaluminum complexes above pH 4.0. The difference between these two views may not be easily resolved because most of these studies were done using potentiometric titration analysis, and in order to study metal ion anion complexing by this technique, the anion must hydrolyze to a certain extent (*24*). The sulfate ion does not hydrolyze in this pH range and, therefore, no detectable pH change will occur with an aluminum–sulfate interaction.

Complexing anions also affect the precipitation of aluminum hydroxide. Thomas and coworkers (*10, 11*) were among the first to show that various complexing anions significantly affect the precipitation of aluminum hydroxide. They found that the stability of the aluminum complex affected the pH of maximum precipitation depending on whether the anion was incorporated into the precipitate or displaced by the hydroxide ion.

Hayden and Rubin (*24*) indicate that the pHp is influenced in the same way. If the anion complexes with aluminum and is displaced by hydroxide ions in forming aluminum hydroxide, the pHp will move to a higher pH. If the anion is incorporated into the precipitate forming a mixed salt, the pHp will be shifted to a lower pH. When the sulfate ion concentration is similar to the aluminum ion concentration, the latter situation appears to occur as seen from experimental data by Hayden and Rubin (*24*) in Table III.

Thus, with complexing anions such as the sulfate anion, the aqueous aluminum chemistry cannot be described as precisely as with the noncomplexing anions. However, an estimation of the equilibria for alum in the papermaking system can be made with the following considerations:

1. At low pH prior to extensive hydrolysis, the equilibrium is primarily between Al^{3+} and $AlSO_4^+$ (*36*).

2. A mixed complex polynuclear species of higher charge is formed prior to precipitation. The parallel adsorption behavior of $AlCl_3$ and $Al_2(SO_4)_3$ observed by Arnson (*36*) strongly implies the formation of a polynuclear species. Matijevic and Stryker (*35*) have proposed the mixed polynuclear species, $Al_8(OH)_{10}(SO_4)_5^{4+}$.

3. The alum equilibria are similar to those proposed by Hayden and Rubin for noncomplexing anions.

4. The pH of precipitation (pHp) at a given alum concentration occurs in accordance with values observed by Hayden and Rubin (Table III).

An example of the proposed alum equilibria is shown in Fig. 6. As with $AlCl_3$ (Fig. 5), the proposed alum equilibria would be expected to shift to lower pH with an increase in the aluminum concentration.

Application

With an improved understanding of the aluminum aqueous equilibria, papermakers can begin to control and predict the interactions of aluminum species with other materials in the papermaking system. The following examples show how the Hayden and Rubin equilibria have been applied to the adsorption of aluminum on cellulosic fibers (*36*) and aluminum–rosinate sizing (*37*).

Aluminum adsorption

Arnson (*36*) studied the adsorption of aluminum by oxidized cellulosic fibers from dilute solutions of aluminum chloride and aluminum sulfate. A comparison of the aluminum adsorption and the aluminum aqueous equilibra for $AlCl_3$ is shown in Fig. 7. The initial aluminum concentrations, 2.5×10^{-4} *M* or 6.8 ppm Al^{3+} and 1.0×10^{-3} *M* or 27 ppm Al^{3+}, are typical of what would be found in a papermaking system (Table I).

The adsorption of aluminum at both concentrations shows a distinct pattern characterized by a sharp increase in the adsorption between pH 4 and 5. A similar pattern has been observed by other workers (*38–40*). It is important to note that the increase in adsorption occurs before the pHp and coincides with the formation of the polynuclear species. The importance of the aqueous aluminum chemistry and its controlling factors, pH and aluminum concentration, to aluminum adsorption can be clearly seen.

There is a significant difference in the aluminum adsorption behavior of the various aluminum species. In the trivalent cation region, the adsorption is relatively low and independent of the aluminum concentration. The polynuclear species has a higher level of adsorbed aluminum and concentration dependence. Finally, the adsorption in the precipitate region is greater than the other two and is dependent on the aluminum concentration present in the system.

The adsorption data in Fig. 7 also illustrate the importance of controlling the pH independent of the aluminum salt addition. Consider the amount of

CITE THIS PAPER: Arnson, T.R., *Tappi* 65(3): 125(1982). https://doi.org/10.32964/TJ65.3.125.

adsorbed aluminum at pH 4.5 for the two aluminum concentrations. At $2.5 \times 10^{-4} M$, Al^{3+} is the primary species and the adsorption is 0.15–0.20 mg of aluminum/g of cellulose. At the higher concentration, a significant amount of the aluminum exists as the polynuclear species, and the adsorption is over 1.0 mg of aluminum/g of cellulose. Thus, two different papermaking systems, both controlled to pH 4.5 but with different amounts of alum, can have quite different aluminum species and interactions.

A comparison of the aluminum adsorption for aluminum chloride and alum at an aluminum concentration of 2.5×10^{-4} M is shown in Fig. 8. The adsorption of aluminum from an alum solution has the same pattern as the aluminum chloride, although the sulfate curve breaks upward before the chloride curve. This difference is predicted by the observed influence that the sulfate ion has on the aqueous equilibria according to Hayden and Rubin. At these sulfate concentrations, the pHp is lowered 0.25–0.40 pH units, as seen in Table III.

Aluminum–rosinate sizing

The application of the Hayden and Rubin equilibria to aluminum–rosinate sizing has been made by Crow (*37*), who studied various properties of aluminum–rosinate precipitate and sized papers using both aluminum chloride and aluminum sulfate. He found that the type of aluminum species and the presence of sulfate ions had a significant influence on the properties studied. An example of the effect of alum and the various aluminum species on rosin retention is shown in Fig. 9. The best sizing results were obtained in the presence of sulfate ions and with either the trivalent cation or the aluminum hydroxide precipitate.

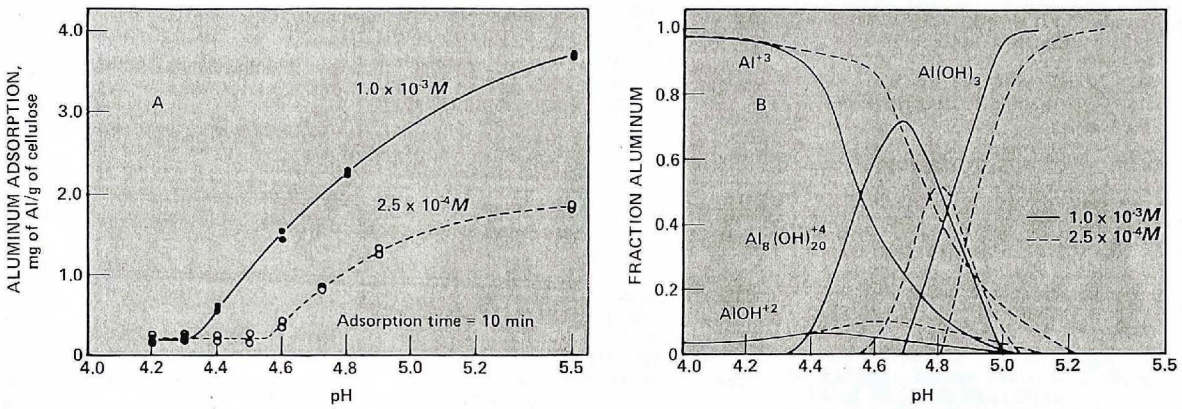

7. Left: aluminum adsorption as a function of pH and aluminum concentration for $AlCl_3$. Right: distribution of aluminum species as a function of pH and aluminum concentration for $AlCl_3$.

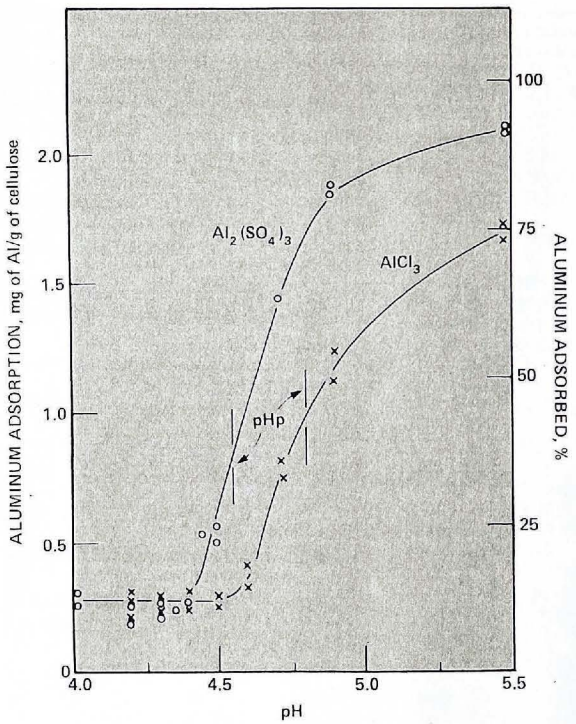

8. Comparison of aluminum adsorption for $AlCl_3$ and $Al_2(SO_4)_3$ ($2.5 \times 10^{-4} M$). Solid vertical lines denote the pH of precipitate formation (pHp) for each aluminum salt.

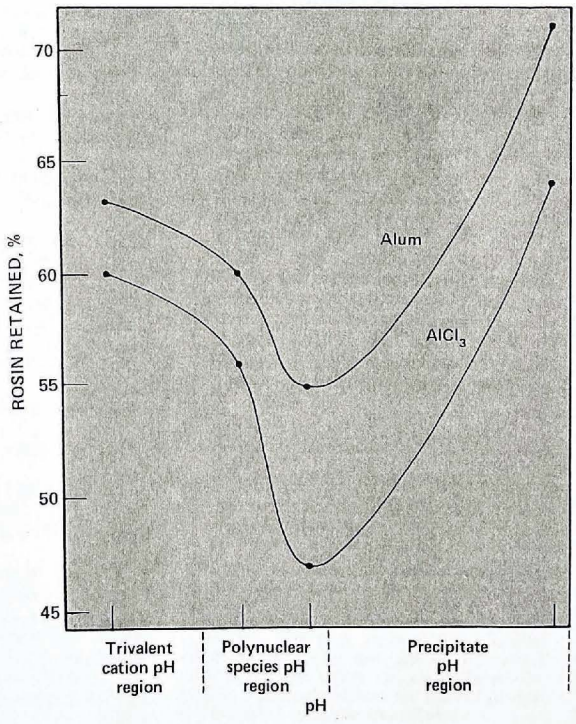

9. Percent rosin retained as a function of pH for $AlCl_3$ and $Al_2(SO_4)_3$ ($4.6 \times 10^{-3} M$).

Sodium aluminate

Thomas (*3*) and Davison (*1*) have both discussed the use and benefits of using sodium aluminate as a partial replacement for alum in the papermaking system. Essentially, sodium aluminate provides means to introduce aluminum into the papermaking system without the sulfate anion. The use of sodium aluminate may therefore be especially applicable to mills that have tightly closed white water systems and observe a high buildup of dissolved solids.

The aqueous aluminum equilibria of a papermaking system using sodium aluminate can also be described with the previously mentioned equilibria, provided that the pH and aluminum and sulfate concentrations of the system are known. Control of pH independently of the aluminum salt addition would be expected to be important for good control of the system.

Literature cited

1. Davison, R.W., "Alum and Related Materials in Papermaking," TAPPI C.A. Report 57, TAPPI PRESS 1975, p. 71.
2. Wortley, B.H., "Papermaker's Alum," *1979 Retention and Drainage Seminar Notes*, TAPPI PRESS, p. 29.
3. Thomas, R.A., Jr., "Sodium Aluminate in Paper Manufacture," *1979 Retention and Drainage Seminar Notes*, TAPPI PRESS, p. 29.
4. Porter, C.C., and Lane, W.H., *Tappi* **32**(10): 456 (1949).
5. Avery, L.P., "The Quantitative Alum Analysis of a Papermaking Furnish and the Effect of Alum on Retention," *1977 Course Notes—Retention and Drainage Technology in Paper Manufacturing*, TAPPI PRESS, p. 32.
6. Stumm, W., and Morgan, J.J., *Aquatic Chemistry*, Ch. 6, Wiley-Interscience, New York, 1970, p. 238.
7. Hunt, J.P., *Metal Ions in Aqueous Solutions*, W.A. Benjamin, Inc., New York, 1963.
8. Margerum, D.W., Cayley, G.R., Weatherburn, D.C., and Pagenkopf, G.K., "Kinetics and Mechanism of Complex Formation and Ligand Exchange," in *Martell's Coordination Chemistry*, Vol. 2, ACS Monograph 174, Washington, D.C., American Chemical Society, 1978, pp. 1–220.
9. Veillard, H., *J. Am. Chem. Soc.* **99**(22): 7194 (1977).
10. Thomas, A.W., *Tech. Assoc. Papers* **18**: 242 (1935).
11. Marion, S.P., and Thomas, A.W., *J. Colloid Sci.* **1**: 221 (1946).
12. Salmon, T., and Wall, E.W., *J. Chem. Soc.*: 1128 (1958).
13. Akitt, J.W., "Nuclear Magnetic Resonance Spectroscopy in Liquids Containing Compounds of Aluminum and Gallium," in *Moody's Annual Reports on NMR Spectroscopy*, Academic Press, London, 1972, pp. 465–542.
14. Baes, C.F., Jr., and Mesmer, R.E., *The Hydrolysis of Cations*, Wiley-Interscience, New York, 1976, pp. 112–123.
15. Sienko, M.J., and Plane, R.A., *Chemistry*, third edition, McGraw-Hill, New York, 1966, p. 377.
16. Matijevic, E., Janauer, G.E., and Kerker, M., *J. Colloid Sci.* **19**: 333 (1964).
17. Turner, R.C., *Can. J. Chem.* **54**: 1528 and 1910 (1976).
18. DeBruyn, P.L., DeHek, H., and Stol, R.J., *J. Colloid Interface Sci.*, **51**(3): 449 (1975); **57**(1): 115(1976); **64**(1): 72(1978).
19. Turner, R.C., *Can. J. Chem.* **53**: 2811 (1975).
20. Brosset, C., Biedermann, G., and Sillen, L.G., *Acta Chem. Scand.* **8**: 1917 (1954).
21. Biedermann, G., *Svensk. Kem. Tidskr.* **76**: 362 (1962).
22. Gimblett, F.G.R., *Inorganic Polymer Chemistry*, Butterworths, London, 1963, pp. 77–110.
23. Grunwald, E., and Fong, D., *J. Phys. Chem.* **73**: 650 (1969).
24. Hayden, P.L., and Rubin, A.J., "Systematic Investigation of the Hydrolysis and Precipitation of Aluminum (III)," in *Rubin's Aqueous-Environmental Chemistry of Metals*, Ann Arbor Science, Ann Arbor, 1974, p. 317.
25. Aveston, J., *J. Chem. Soc.*: 4438 (1965).
26. Matijevic, E., *J. Colloid Interface Sci.* **43**(2): 217 (1973).
27. Stumm, W., and O'Melia, C.R., *J. Am. Water Works Assoc.* **60**: 514 (1968).
28. Eigen, M., and Tamm, K., *Z. Elektrochem.* **66**(2): 93 (1962).
29. Volokhov, Y.A., Eremin, N.I., and Mironov, V.E., *Issled Ob. Neorgan. Tekhnolo.* 258–61 (1972) (IPC Translation, T-1833).
30. Rauh, H., and Knoche, W., *Ber. Bunsenges. Phys. Chem.* **83**: 518 (1979).
31. Matijevic, E., and Brace, R., *J. Inorg. Nucl. Chem.* **35**: 3691 (1973).
32. Hester, R.E., Plane, R.A., *Inorganic Chem.* **3**: 769 (1964).
33. Stryker, L.J., and Matijevic, E., *J. Phys. Chem.* **73**(5): 1484 (1979).
34. Ow, S.K., "Investigation of the Role of Sulfate Ions in the Reaction Between Tetrahydrabietic Acid Monolayers and Aluminum Ions," Doctoral Dissertation, The Institute of Paper Chemistry, Appleton, Wis., 1974.
35. Stryker, L.J., and Matijevic, E., *J. Colloid Interface Sci.* **22**: 68 (1966).
36. Arnson, T.R., "The Adsorption of Complex Aluminum Species by Cellulosic Fibers from Dilute Solutions of Aluminum Chloride and Aluminum Sulfate," Doctoral Dissertation, The Institute of Paper Chemistry, Appleton, Wis., 1980.
37. Crow, R.D., "The Influence of pH and Sulfate Ions on the Rosin Sizing of Paper," A-291 Independent Study, The Institute of Paper Chemistry, Appleton, Wis., 1980.
38. Jaycock, M.J., and Pearson, J.L., *Svensk Papperstid.* **78**(5): 167 (1975) and **78**(8): 289 (1975).
39. Linke, W.F., *Tappi* **45**(4): 326 (1962).
40. Reynolds, W.F., and Linke, W.F., *Tappi* **46**(7): 410 (1963).

The financial support of the Institute of Paper Chemistry and its member companies during the author's thesis work is gratefully acknowledged. Special thanks to R. A. Stratton, J.W. Swanson, and L. J. Stryker for their advice and counsel while at IPC. The author also acknowledges the support of professional development and permission to publish by the Eastman Kodak Co.

Based on a paper published in *1981 Sizing Short Course Notes*, a TAPPI PRESS publication.

CITE THIS PAPER: Arnson, T.R., *Tappi* 65(3): 125(1982). https://doi.org/10.32964/TJ65.3.125.

TAPPI JOURNAL
WWW.TAPPI.ORG
THE PAPER AND PACKAGING INDUSTRIES' TECHNICAL RESOURCE
MAY 2022 | VOL. 21 NO.5



PAPERMAKING 247
Development of paper quality parameter measurement in China
Lianhua Hu and Jin Ma

PULPING 259
Improving refining efficiency with deflocculation
Dwight Anderson and Len Schuster

PAPERMAKING 271
Web instability in the open draw and the impact on paper machine efficiency
Frédéric Parent, Daniel Ricard, J. David McDonald, and Richard J. Kerekes

PAPERMAKING 283
The effect of component removal upon the porous structure of the cell wall of wood. II. Swelling in water and the fiber saturation point
J.E. Stone and A.M. Scallan

TAPPI Journal NOW FULLY OPEN ACCESS

MAY 2022

TABLE OF CONTENTS VOL. 21 NO. 5

243 EDITORIAL
Reflections on the Page equation, laboratory work, and new concepts
Gerard J.F. Ring

247 PAPERMAKING
Development of paper quality parameter measurement in China
Lianhua Hu and Jin Ma

259 PULPING
Improving refining efficiency with deflocculation
Dwight Anderson and Len Schuster

271 PAPERMAKING
Web instability in the open draw and the impact on paper machine efficiency
Frédéric Parent, Daniel Ricard, J. David McDonald, and Richard J. Kerekes

283 PAPERMAKING
The effect of component removal upon the porous structure of the cell wall of wood. II. Swelling in water and the fiber saturation point
J.E. Stone and A.M. Scallan

»**COVER CREDIT**: Authors Anderson and Schuster introduce a novel refiner plate modification that improves refining efficiency by mitigating the adverse effects of flocs generated in refining (p. 259). Mill results show nominally 15% gross refining energy reduction when incorporated into a refiner plate design.

TAPPI JOURNAL
WWW.TAPPI.ORG

Editor-in-Chief
Douglas W. Coffin coffindw@miamioh.edu
+1 513 529-0771

Associate Editor
Peter W. Hart peter.hart@westrock.com
+1 409 276-3465

Editorial Director
Monica Shaw mshaw@tappi.org
+1 770 367-9534

PRESS Manager
Jana Jensen jjensen@tappi.org
+1 770 209-7242

Webmaster
Trina Heath theath@tappi.org
+1 770 209-7416

***TJ* EDITORIAL BOARD**

Brian N. Brogdon, FutureBridge Consulting & Training LLC
brian.brogdon@gmail.com, +1 678 581-9114

Douglas W. Coffin, Miami University
coffindw@miamioh.edu, +1 513 529-0771

Mahendra Doshi, Doshi and Associates
mahen@aol.com, +1 920 832-9101

Marc Foulger, Valmet
marc.foulger@valmet.com +1 315 767-2920

Peter W. Hart, WestRock
peter.hart@westrock.com, +1 409 276-3465

Carl J. Houtman, USDA Forest Products Laboratory
choutman@fs.fed.us, + 1 608 231-9445

Vamsi Jasti, Ahlstrom-Munksjo Nonwovens LLC
jvamsik1@gmail.com, +1 818 585-3524

Lucian Lucia, North Carolina State University
lucian.lucia@gmail.com, +1 919 889-7059

John A. Neun, John A. Neun LLC
john.neun@gmail.com, +1 518 275-8139

Jim Niemiec, Jim Niemiec Consulting LLC
jim.niemiec@outlook.com, +1 715 213-4766

Steven P. Ottone, Omya
steven.ottone@omya.com, +1 919 641-7854

Gaurav Pranami, Imbed Biosciences
gpranami@imbedbio.com, +1 515 230-7005

Arthur Ragauskas, Oak Ridge National Laboratory
aragausk@utk.edu

Seshadri Ramkumar, Texas Tech University
S.Ramkumar@ttu.edu, +1 806 742-4567

Gregg Reed, Imerys
gregg.reed@imerys.com, +1 478 553-5747

Gerard J.F. Ring, University of Wisconsin—Stevens Point
gerrryring@wi-net.com, +1 715 592-3732

Scott Rosencrance, Kemira Chemicals
scott.rosencrance@kemira.com, +1 770 429-2753

Paul Wiegand, NCASI
pwiegand@ncasi.org, +1 919 941-6417

Junyong Zhu, USDA Forest Products Laboratory
jzhu@fs.fed.us, +1 608 231-9520

Join TAPPI *today!*
TAPPI JOURNAL is a free benefit of TAPPI membership, and is only available to members. To join TAPPI, to renew your TAPPI Membership, or to learn about other valuable benefits, visit www.tappi.org.

TAPPI, 15 Technology Parkway S., Suite 115, Peachtree Corners, GA 30092, publishes *TAPPI JOURNAL* monthly.

ATTENTION PROSPECTIVE AUTHORS: All papers published are subject to *TAPPI JOURNAL's* peer-review process. Not all papers accepted for review will be published. Before submitting, check complete author guidelines at http://www.tappi.org/s_tappi/doc.asp?CID=100&DID=552877.

Statements of fact and opinions expressed are those of individual authors. TAPPI assumes no responsibility for such statements and opinions. TAPPI does not intend such statements and opinions or construe them as a solicitation of or suggestion for any agreed-upon course of conduct or concerted action of any sort.

Copyright 2022 by TAPPI, all rights reserved. For copyright permission to photocopy pages from this publication for internal or personal use, contact Copyright Clearance Center, Inc. (CCC) via their website: www.copyright.com. If you have questions about the copyright permission request process, please contact CCC by phone at +1 978 750-8400. To obtain copyright permission to use excerpts from this publication in another published work, send your specific request in writing to Editor, TAPPI JOURNAL, 15 Technology Parkway S., Suite 115, Peachtree Corners, GA 30092, USA; or by fax to +1 770 446-6947. Send address changes to TAPPI, 15 Technology Parkway S., Suite 115, Peachtree Corners, GA 30092, USA; Telephone +1 770 446-1400, or FAX +1 770 446-6947. www.tappi.org

Editorial

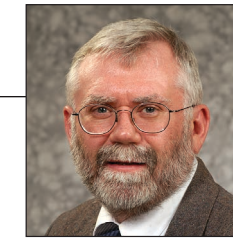

GERARD J.F. RING
TAPPI Journal
Editorial Board

Reflections on the Page equation, laboratory work, and new concepts



PEER-REVIEWED | PAPER STRUCTURE

The hyperbolic theory of light scattering, tensile strength, and density in paper

GERARD J.F. RING

ABSTRACT: The hyperbolic theory of light scattering, tensile strength, and density in paper describes a sheet of paper as a matrix of cellulose with a characteristic material strength and open and closed pores dispersed through the cellulose, forming solid foam. This paper presents two principle hyperbolic equations. The first describes the conservation of tensile strength and the second describes the conservation of mass as functions of light scattering. Three additional equations are derived. The first relates tensile strength to sheet density, the second relates light scattering to total pore volume, and the third relates tensile strength to total pore volume. The conservation of tensile strength equation varies with processing for a given cellulose pulp. Variable refining levels at constant levels of web pressing produce separate curves for each web pressing level. Correspondingly, variable wet-pressing levels produce separate curves for each level of constant refining. Hydrolyzing pulps or cutting fibers to shorten the average degree of cellulose polymerization shifts the curves to lower tensile strengths. The conservation of mass equation results in a single curve, regardless of processing or reduction in the degree of cellulose polymerization. The concept of relative bonded area measurement using light scattering as developed by Ingmanson and Thode is shown to be invalid for paper by this hyperbolic theory. The validity of relative bonded area by any technique is also questioned.

Application: Hyperbolic theory represents a simplified concept of paper structure, opening the door for innovative research and developmental investigations.

Light scattering, tensile strength, and density are shown to be functionally related by rectangular hyperbolas whose asymptotes are parallel to their axes. Rectangular hyperbolas are important in science because they are the product of two variables that equal a constant of physical significance [1]. In rectangular hyperbolas, one variable describes the quality of the physical system (processes) while the other is proportional to the system's size (extensive) [2]. An example is the ideal gas law where a constant energy isotherm is the product of gas pressure and volume. Another example is the product of density and volume equating the mass of an incompressible material.

In both hyperbolic equations presented in this paper, light scattering is the extensive variable because increasing the area of the sheet will increase the total amount of scattered light. The constant of the tensile/light-scattering (TS) hyperbola will be shown to be dimensionally consistent with energy, while the constant of the density/light-scattering (DS) hyperbola will be shown to be dimensionally consistent with mass. These hyperbolas are remarkable because they are origin-shifted into the third Cartesian quadrant; thus, additional constants are included in these equations to account for the displacement of the origin.

By combining the TS hyperbola with the DS hyperbola (eliminating the light scattering variable) a tensile/density (TD) hyperbola is produced. The DS hyperbola can be combined with a density/pore-volume (DV) hyperbola to produce a pore-volume/light-scattering (VS) hyperbola. Finally, the TS hyperbola can be combined with the VS hyperbola to produce a tensile/pore-volume (TV) hyperbola.

This family of hyperbolas describes the tensile failure of paper as a simple function of pore volume and the tensile strength of cellulose at its maximum density. The constant of fiber properties (measured after pulping) of length, coarseness, fiber strength, and fiber-to-fiber bonding strength are not necessary about with fiber conditions such as the degree of compaction, kinking, and curling [3]. Paper is treated not as a structure composed of hydrogen-bonded fibers but as a cellulosic material with air pores randomly dispersed throughout [4]. By this definition, paper is an example of the general category of colloidal materials known as solid foams [5].

Relative bonded area (RBA) will be shown to be a parameter of TS hyperbolas and not an estimate of pointal bonding between fibers [6]. This paper will also demonstrate that the Shallhorn-Karnis [11], and the Page [12] equations can be simplified to TS hyperbolas, thus eliminating unnecessary fiber property variables in these theories.

Shear bag models ignore the effects of processing on pulp fibers. In contrast, TS hyperbolas incorporate both pulp refining and wet pressing as sheet densification pathways using the calculated hyperbolic constants. Hence, a TS hyperbola describes the change of state that a sheet undergoes as a particular process produces a denser and stronger sheet. Refining TS hyperbolas may or may not be collinear with wet pressing hyperbolas. DS hyperbolas for a given pulp are all collinear regardless of either refining or wet pressing.

NOVEMBER 2011 | VOL. 10 NO. 10 | TAPPI JOURNAL 9

PAPER PHYSICS | TAPPI JOURNAL REPRINT 1969

B. H. PAGE

A Theory for the Tensile Strength of Paper

OCTOBER 2019 | VOL. 17 NO. 10 | TAPPI JOURNAL 579

I began teaching paper physics to undergraduates in the late 1980s when the recognized giants in the field were still actively debating their subjects in the literature and scientific conferences. Many of these scientists visited the Department of Paper Science and Engineering at the University of Wisconsin–Stevens Point (UWSP) to present lectures of their subjects for videotaping. The list of presenters included James Clark, Alfred Nissan, Johannes Van den Akker, and Derek Page, among others. These video tapes were collected as a series titled "Personalities in paper" that included not only their lectures, but personal interviews where they discussed their careers and accomplishments.

My academic background at that time was centered on cellulose chemistry and not paper physics, so I was very appreciative of having those videotapes as resources during my course development. I chose to structure my course beginning with the fiber properties (length, coarseness, and strength), followed by the paper properties, notably tensile strength. The best way to bring fiber properties together with paper properties was the famous Page equation, which was published in *TAPPI Journal* 52(4): 674(1969) and reprinted in the October 2018 issue.

Fiber properties vs. paper properties in the lab

Around the same time, UWSP had just built a new Paper Science wing for the Science building, and my task was to outfit our paper testing laboratory with both fiber and paper testing capabilities. Hence, I was able to complement my lectures with actual laboratory data. But, as the data accumulated over time, it became apparent that fiber properties didn't predict paper properties. Most notably, fiber dimensions as measured by fiber length analyzers remained virtually constant during a beater run, whereas tensile strength varied greatly.

These results were problematic, because they disrupted the logic of my lectures and the meaningfulness of the laboratory sessions. Engineering students are quick to point out this type of discrepancy. Subsequent laboratory work concentrated on the remaining fiber property, shear bond strength.

But things didn't go well with shear bond strength either. Increasingly, this fiber property was appearing to be constant in value, most likely due to its fundamental association with the strength of hydrogen bonds. This realization left one undeniable conclusion: light scattering and tensile strength were the only two variables in the Page equation.

During this time, I enjoyed many productive interactions with Derek Page at TAPPI courses and conferences. I especially enjoyed being at his lecture commemorating the 25th anniversary of the Page equation, where both he and Alfred Nissan politely listened to my thoughts about measuring shear bond strength.

Refining, the Page equation, and a hyperbolic theory

A year after this anniversary, during one of his technical seminars, Dr. Page presented the audience with a series

of slides demonstrating that refining destroys the original structure of a fiber, producing a sheet that becomes progressively more transparent and denser. I was astounded not because this was an unexpected result, but because I finally realized that the underlying assumptions of the Page equation can never be met with a pulp that has undergone refining or beating. Hence, initial fiber properties are not predictors of subsequent sheet properties, because the extent of change incurred by the fiber during refining is unpredictable.

In 1996, I sent Derek a detailed letter demonstrating that when you remove all fiber property parameters from his equation, leaving only the light scattering coefficient and tensile strength, his equation becomes the exact regressor line through the plot of light scattering vs. tensile strength data. Dr. Page quickly responded to my letter with a phone call expressing his impatience with me and then sent me an article that would ostensibly refute my observations. It didn't. But this article turned out to give me the necessary information to identify the Page equation as a hyperbola and publish my Hyperbolic Theory article in *TAPPI Journal* (Vol. 10, No. 11, 2011).

In 2014, Derek published a delightful and memorable book of essays titled *The Curious Mind of a Would-be Humorist*. According to Amazon, I am a verified purchaser of his book, albeit one of the few reviewers. Soon after my review was posted, I received an email from Derek. We pleasantly communicated on a number of items and in his deft way he let me know that he had read my Hyperbolic Theory article. **TJ**

Editor's Note:

Gerard "Gerry" J.F. Ring, Ph.D., is professor emeritus at the University of Wisconsin-Stevens Point and a member of the TAPPI Journal *Editorial Board. Gerry's research, "The hyperbolic theory of light scattering, tensile strength, and density in paper," was chosen as the* TAPPI Journal *Best Research Paper for 2011. At that time, Editorial Board Member Terry Bliss, Ph.D., said: "Gerry's paper challenges giants of the paper physics community (Page, Shallhorn, Ingmanson, de Ruvo, etc.) and ties everything together neatly, using their own previously published data. Most likely it will launch a generation of new dissertations as others seek to test it."*

Development of paper quality parameter measurement in China

LIANHUA HU AND JIN MA

ABSTRACT: Paper quality parameters are important indicators of paper production, such as paper moisture, basis weight, ash content, strength, and so on. This study focuses on the online measurement methods and development of paper basis weight, moisture, and ash measuring.

First, the measurable paper parameters and quality control system products in China are analyzed. Then, the basis weight measurement methods, accuracy, and development are given in the range of 10~1000 g/m^2. Third, the distinction between infrared and microwave methods for moisture measurement is discussed. Finally, the ash measurement is introduced.

Production and consumption of tissue paper in China have continually increased during the past decade. Near-infrared light technology is mature for the measurement of paper parameters in the range of 10~200 g/m^2 basis weight. However, the near-infrared online measurement of tissue paper is not widely used, and few tissue paper lines are equipped with this type of quality control system in China. Therefore, technology for near-infrared measurement of basis weight has a great potential market in the field of tissue paper production. This article analyzes the future development trend of near-infrared light in tissue paper basis weight measurement and summarizes the difficulties in near-infrared light measurement of tissue paper basis weight.

Application: Different measurement methods suitable for measuring basis weight, moisture, and ash of various paper types are summarized in this paper. The near-infrared light measurement method is suitable for the measurement of tissue paper, but influences such as ambient temperature and humidity interference, along with onsite dust, need to be overcome.

Measurement of paper quality parameters plays an important role in the study and production of paper. It is the guarantee for controlling the quality of paper production. The main quality parameters of the paper are moisture, basis weight, ash, paper strength, etc. [1]. For these parameters, paper mills can measure almost all of them off line in laboratories under the Chinese National Standard. These offline methods have high accuracy advantages, but the detection process is complicated, the test time is long, and the paper may be damaged. To solve the shortcomings of offline measurement methods, non-destructive online measurement methods are widely used in the measurement of paper quality parameters. The commonly used non-destructive online paper measurement methods mainly include the near-infrared light method, β-ray method, X-ray method, γ-ray method, and microwave measurement method. With the development of the paper industry, more and more domestic enterprises in China have begun to pay more attention to the production requirements related to paper quality, and they have also put forward higher requirements for the paper quality control system (QCS). This paper primarily summarizes the application of some non-destructive online measurement methods for paper quality parameters. By comparing the advantages and disadvantages of various measurement methods, the trend of near-infrared light in the measurement of low basis weight paper in the future is mentioned, and the problems that need to be solved are put forward.

With the advent of the era of a "low carbon economy," the development trend of paper with low basis weight is becoming more and more prominent. However, the reduction of the paper basis weight will lead to a decrease in the opacity and stiffness of the paper, and the binding ability between the fibers will be weakened. It is important to improve paper strength by adding inorganic fillers, adding polymers in pulp, surface sizing, surface dissolution, nanofiber coating, and so on. Therefore, the detection of paper strength is also an important factor to ensure the quality of paper. Because this article mainly just introduces the online measurement method and online paper strength testing methods that are currently unavailable, papermakers still must wait for the manufacture of a complete reel to assess quality.

ONLINE MEASUREMENT METHOD FOR PAPER QUALITY PARAMETERS

Paper quality parameters include paper moisture, base weight, ash, thickness, smoothness, paper strength, and transparency [2]. The QCS provides the possibility to realize online monitoring of paper quality parameters. At present, the international QCS system suppliers in China are Valmet, Voith, Honeywell, and ABB [3-5]. The Chinese QCS

Parameter \ Supplier	Valmet	Honeywell	ABB	Voith	Zhejiang Shuangyuan	Gundam Measurement and Control	Haitian Measurement and Control
Basis weight	√	√	√	√	√	√	√
Moisture	√	√	√	√	√	√	√
Ash	√	√	√	√	√	√	√
Thickness	√	√	√	√	√	√	
Transparency	√	√	√	√	√		
Smoothness	√	√	√	√	√		

I. Paper parameters measured by international and Chinese quality control system (QCS) suppliers.

Parameter \ Method	A	B	C
Basis weight	Infrared light	Isotope β-rays	Isotope γ-rays
Moisture	Infrared light	Microwave method	Charge transfer method
Ash	X-ray		

II. Online measurement methods for paper parameters.

system suppliers include Zhejiang Shuangyuan, Gundam, and Haitian. **Table I** shows the measurable paper parameters of international and Chinese QCS suppliers [6-8].

The two most important paper quality parameters are moisture and basis weight. Whether these two parameters meet outlined standards determines the product rating of the paper. Paper basis weight refers to the content of fiber per unit area of paper, and paper moisture refers to the moisture content per unit area of the paper [9]. **Table II** shows the commonly used online measurement methods for paper quality parameters.

Summarizing the measurement methods for various paper quality parameters shows that non-contact online measurement methods have been widely used in paper production. The yield and quality of the paper can be improved by using a high-performance QCS corresponding to the measurement method, and it is significant in terms of reducing energy and raw material consumption [10].

RESEARCH ON PAPER QUALITY PARAMETER MEASUREMENT METHODS

Basis weight measurement

The basis weight of paper is used for evaluating the quality of the paper. Generally, the basis weight of the paper needs to be maintained within the tolerances specified by the standard. If the basis weight of the paper is higher than the index specified in the standard, it will lead to a waste of pulp. If the basis weight is lower than the index specified in the standard, there will be more problems in the coiling process and the rewinding conversion process of the paper. If the basis weight of the paper is not uniform, the printing font is not clear and paper is wasted. Although the accuracy of paper basis weight detection has been improved by combining basis weight sensors with advanced controls [11], it is still challenging to use it widely in measurement of certain paper grades. The detection accuracy of the international basis weight sensor is ±0.5 g/m² in the measurement process for the basis weight range of 12~20 g/m². The measurement accuracy of the basis weight in the range of 150~1500 g/m² is expressed as a percentage. The current international basis weight sensor has a detection accuracy of ±1.0% for the basis weight in the range of 150~1500 g/m² [12].

Research on basis weight measurement in China mainly focuses on the paper basis weight range of 50~1500 g/m². Hu [13-15] studied the basis weight measurement of high-basis weight paperboard. Beta rays were chosen for paper basis weight measurement, because beta rays penetrate paper according to Bell's Law. The basis weight sensor range automatic identification fusion framework is designed to improve measurement accuracy through data fusion technology. **Figure 1** shows the working diagram of the basis weight sensor measurement.

G. Li et al. [16] put forward suggestions for the selection of the energy of the paper basis weight radioactive source. The ^{147}Pm is the best radioactive source through comparing sensitivity and statistical error, and it is usually selected for measurement of the basis weight ranging from 10 g/m² to 200 g/m². In addition, the ^{85}Kr radioactive source is often chosen for the basis weight range between 20~1000 g/m². **Table III** shows the β-ray source parameters currently applicable to paper measurements.

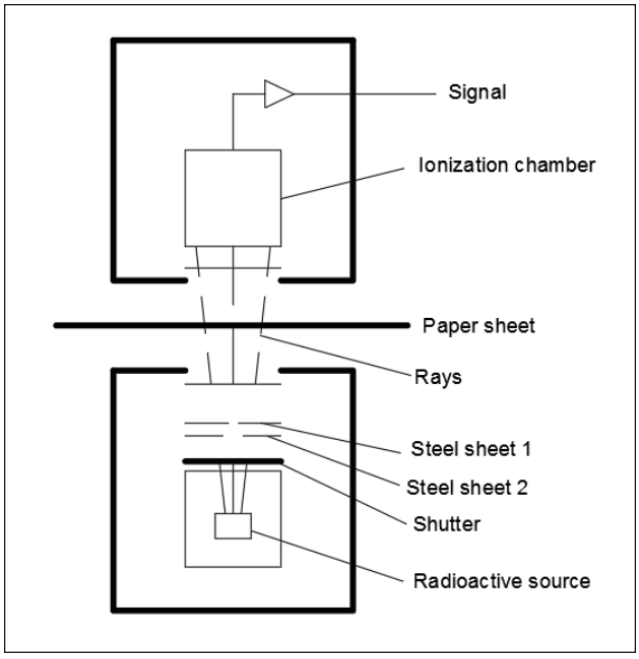

1. Schematic diagram of the basic weight sensor.

Y. Li et al. [17] proposed a pre-amplification digital method of β ionization chamber to measure the energy of β ray after penetrating the paper. The Butterworth filter was used by Zhou to process the signal in the process of paper basis weight signal processing [18]. Because temperature drift is an important factor affecting the accuracy of paper basis weight measurement, Sun et al. [19] proposed a compensation method for the temperature drift in the measurement process. When QCS technology failed to meet the detection requirements in China, Tang et al. and Wang et al. [3,4] improved the detection accuracy by researching and transforming the imported QCS system.

Some researchers have also used infrared, gamma rays, and other methods to conduct research in the measurement of paper basis weight. Li [20] developed a method to simultaneously measure the basis weight and moisture of paper with near-infrared light. This measurement method is mainly used in the basis weight range of 400~600 g/m². In addition, this method has high measurement accuracy and low comprehensive cost, and it solves the technical problem of simultaneous measurement of paper basis weight and moisture. This near-infrared measurement method also has some technical problems that need to be solved. For example, the measurement accuracy of the sensor is affected by onsite dust, and the thicker paper has poor infrared light penetration ability.

The combined measurement method of isotope and charge method was adopted by Hou et al. to simultaneously measure paper basis weight and moisture [21]. The basis weight measurement of paper is based on the principle that the absorption of beta rays obeys the law of exponential decay. The principle of paper moisture measurement is to generate polarization charges according to the polarization of polar media in an electric field. The amount of polarized charge is measured by the method of charge transfer, and the relationship between the polarized charge and the moisture of the paper is analyzed to calculate the moisture content of the paper.

The backscattering method of low-energy γ-rays was used by Hou et al. [22] to study the measurement of paper basis weights ranging from 50 g/m² to 500 g/m². The measurement principle is based on the dependence of the interaction of the low-energy γ-rays with the paper on the atomic number. The basis weight of the paper can be determined by measuring the backscattered intensity of low-energy γ-rays proportional to the mass absorption coefficient, which can meet the requirements of measurement accuracy. The errors generated by this measurement method are mainly the unevenness of paper samples, laboratory errors, instrument errors, and so on.

By comparing several different paper basis weight measurement methods, the most mature application in the paper basis weight measurement process is still the isotope measurement method, which can be widely used in the paper basis weight range of 10~1000 g/m². However, this method generates radiation during paper basis weight measurement. Therefore, near-infrared light measurement methods are increasingly used in the measurement of paper basis weight, especially in low basis weight paper. However, the environmental temperature, humidity, and dust factors have a major influence on the basis weight measurement of tissue paper. As a result, the near-infrared light measurement method is not widely used to measure tissue basis weight.

Moisture measurement

The moisture of the paper is another important indicator of paper quality. If the moisture content of the paper is too high, the bonding strength between the paper fibers will decrease, and if the moisture content is too low, the rigidity of the paper will increase and become brittle [11]. Therefore, ensuring stability of the moisture content of the paper

Radioactice Source	^{14}C	^{147}Pm	^{85}Kr	^{204}Tl	^{90}Sr
Beta ray energy, MeV	0.153	0.285	0.57	0.76	2.27
Half-life, a	50.3	2.62	10.7	3.13	28.1
MeV = mega electron-volt; a = anniversary.					

II. Online measurement methods for paper parameters.

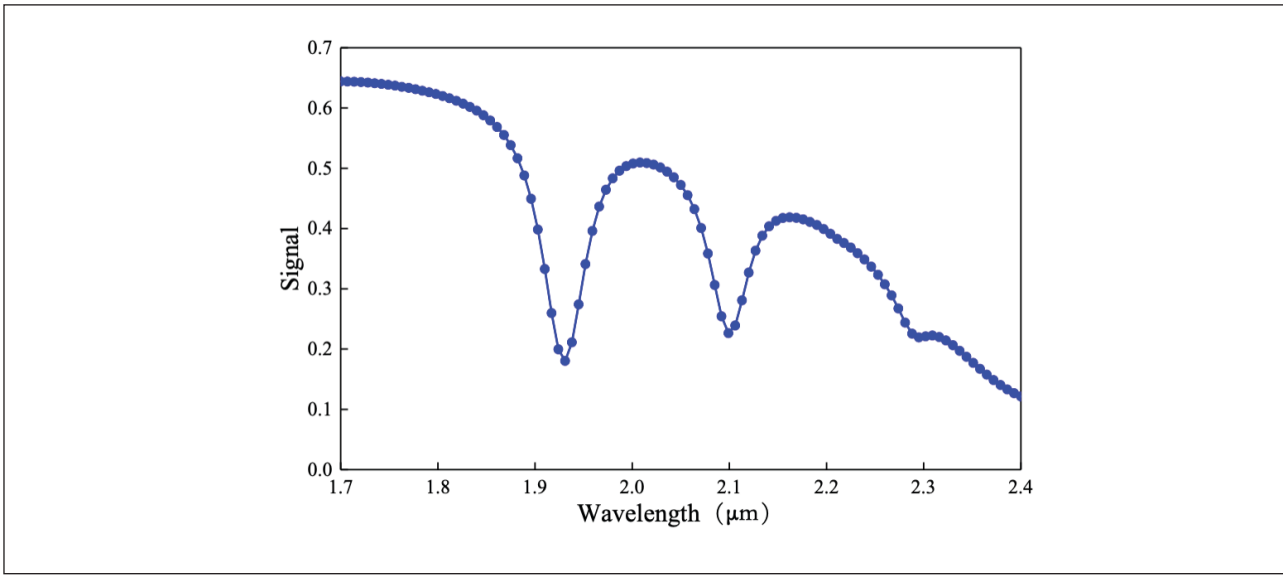

2. Typical infrared spectrum of paper.

is a basic requirement for ensuring paper quality. The real-time distribution of paper moisture can be more comprehensively reflected through online measurement of paper moisture, which is the basis of a paper quality control system. Currently, infrared and microwave methods are mainly used in the online measurement of paper moisture. The infrared method to measure paper moisture is primarily based on the principle that water molecules selectively absorb infrared light. As shown in **Fig. 2**, the measurement of moisture in paper is based on the specific absorption properties of water for near-infrared light at a wavelength of 1.94 μm, where the radiative transmission at this wavelength is compared with the intensity at a wavelength of 1.83 μm to obtain the moisture content. The 1.83 μm wavelength signal is not affected by moisture in the paper, but will be weakened by other factors and can be used as a reference signal for moisture measurement. In this process, when moisture absorbs infrared light, the paper also absorbs infrared light. The principle of microwave measurement of paper moisture is that the moisture in the paper will affect the characteristic parameters of the microwave resonant cavity, and then the moisture measurement is completed.

Infrared light measurement methods are mostly used to measure the moisture of paper with a basis weight of less than 100 g/m². Because infrared light has a poor measurement effect on thick paper, microwave measurement is often used to measure the moisture of paper with a basis weight greater than 200g/m² or even higher.

The absorption of near-infrared light by paper moisture can be expressed as:

$$E_{1.94}=E_{0e}^{-KM} \quad (1)$$

where E_0 is the incident infrared energy of 1.94 μm, K is the absorption coefficient of the paper, and M is the moisture content of the paper. The moisture in the paper sheet has four absorption bands in the infrared band, which are 1.18 μm, 1.46 μm, 1.94 μm, and 2.92 μm, respectively. At present, 1.94 μm is mainly used as the measurement wavelength, because the absorption peak of water molecules in the 1.94 μm band is relatively large, and the detection sensitivity is high.

Ye and Sun [23] proposed a new type of optical measurement system for paper moisture with high basis weight that can be used in paper moisture measurement with a basis weight less than 500 g/m². It mainly uses different lenses for modulation and retains the double-half integrating sphere structure of other moisture meters to improve the system's infrared radiation receiving efficiency. In the measurement of paper moisture with a basis weight of 150~350 g/m² and more than 450 g/m², the stable output can be obtained by using this measuring system. Dong [24] studied the method of measuring paper moisture and basis weight based on near-infrared light, which is mainly used in the measurement process for cardboard paper with a basis weight range of 0~350 g/m². According to this measurement principle, a near-infrared moisture quantitative measuring instrument that does not require a cooling structure is adopted. Multireference, multibeam measurement, and automatic compensation techniques are used in this measuring instrument, so the paper moisture measurement stability is improved. In addition, the influence of external factors, such as dust in the environment and moisture in the air, is eliminated, and the measurement accuracy is improved.

Kangasrääsiö [25] studied the integrity of the infrared light online moisture measurement system based on the multireference infrared light principle. The prepared reference is sealed between two glass plates in this measure-

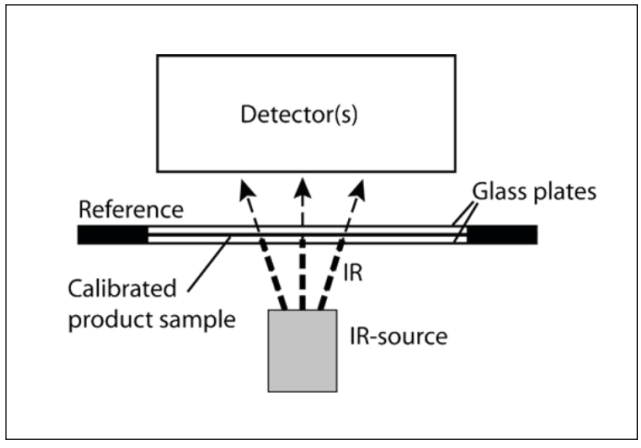

3. Basic calibration of online moisture measurement based on infrared transmission.

ment system, as shown in **Fig. 3**. The thermal expansion coefficient of the glass plate is low, and the infrared light has high transparency in the glass plate. The moisture content of the reference sample ranges from 1.7% to 15%, and the paper basis weight ranges from 35 g/m² to 375 g/m². The results show that the moisture measurement error of different measurement systems can be reduced to less than 0.5% by employing a traceable method in the basic calibration process. Taking this approach improves the integrity of the online moisture measurement system and reduces the need for continuous laboratory testing.

There are some defects in the infrared light measurement system. First, thicker paper cannot be measured on line with infrared light, because the infrared light penetration ability is poor. Second, the infrared probe cannot stably work, because the paper has high impurity content and dust interference. In addition, the optical components are easily heated, which affects the service life of the sensor.

Liu [26] studied the related technology of microwave measurement of paper moisture content by comparing the problem of infrared light measurement. This measurement technology is mainly used in paper with a basis weight of 400~600 g/m² and with a moisture range of 3%~15%. Part of the energy is lost in the process of the microwave passing through the paper, and the energy loss increases as the moisture content of the paper increases. Paper moisture not only absorbs energy but also reflects microwave energy, both of which can measure moisture content. This microwave measurement system can be applied to the moisture measurement of high basis weight paper through experimental studies. This measurement technology not only has the advantages of high real-time performance, good sensitivity, strong anti-interference energy, stable measurement results, and so forth, but it also has a wide measurement range and has a relatively broad potential in the field of online moisture measurement in industrial production.

In summary, infrared light measurement is currently often used in the measurement of paper moisture in a basis weight range of less than 200 g/m². It can be found that infrared light is widely used in the measurement of low basis weight paper. In the measurement of high basis weight paper, the microwave paper moisture measurement system is often used because of the poor penetration of infrared light in thick paper.

Ash measurement

In the processes of paper research and production, paper ash is also an important quality indicator. To improve the stability of paper quality, factors such as pulp slurry ratio, paper filler types, and changes in the properties of the filler itself cause the fluctuation of paper ash content to be reduced. In some papermaking enterprises, the ash content of the paper is appropriately increased and the amount of paper fiber is reduced. Therefore, the detection and control of paper ash have become an important link in the process of paper production and scientific research [27]. The traditional method of measuring paper ash requires a long measurement time, tedious steps, and requires burning the paper. Relevant researchers have proposed some chemical methods and improvements in traditional combustion methods to solve the shortcomings of traditional combustion methods, but these measurement methods are all contact measurements, which destroy paper filler components. The paper ash online measurement method not only improves the measurement accuracy and efficiency but also can control the production in real time and reduce the consumption of pulp. Relevant scientific research institutions and papermaking enterprises have developed the rapid detection of paper ash by ray method based on the online measurement of paper ash [28]. The main offline ray methods for the determination of paper ash are X-ray diffraction (XRD) and X-ray fluorescence (XRF) spectrometry. The principle of XRF spectroscopy (XRF) is to irradiate X-rays on paper, and each component element in the exciting paper will emit X-ray fluorescence. Also, X-ray fluorescence emitted by different elements has specific energy characteristics or wavelength characteristics. The energy and quantity of the emitted fluorescence are measured by the detection system to obtain measurement signals, and the collected signals are converted into the types and contents of various elements in the paper through the instrument software. However, the principle of XRD spectroscopy is to measure the diffraction peaks of the paper sample within a certain diffraction angle range, which is mainly used to determine the structure of the sample.

Commonly used ray methods for online measurement of paper ash content are X-ray tube measurement method, X-ray, and γ-rays method with isotope ^{55}Fe as the radioactive source.

Gu et al. developed a soft X-ray transmission intensity measurement method. The principle of this method is that

when the X-ray penetrates the paper, the law of attenuation of the ray intensity conforms to Bell's law [29]. Ou et al. developed a paper ash meter using the isotope ^{55}Fe as the X-ray radiation source [30]. The ash content of 28 different types of calcium carbonate and talc-filled paper was determined using this ash meter. The measurement results show that the error of 26 of the 28 measurement data obtained by this paper ash meter is less than 0.5%, which fully meets production requirements. Based on the selective absorption characteristics of low-energy X-rays passing through paper, Feng et al. designed an online paper ash measuring instrument using the isotope ^{55}Fe as a γ-ray radiation source [31]. After the field operation test, the measurement error of the measuring instrument is less than 1%, which meets the requirements of online detection of paper ash content. Using X-ray radiated from ^{55}Fe passing through the change of paper absorption intensity to measure ash content, Xiao used the ash sensor produced by Impact Company to detect the ash content of paper in a paper mill, and the measurement error was less than 1% [32]. Hofman proposed a method that can measure the ash content in paper products [33]. This method primarily obtains the relative content of each ash component by rapidly changing the energy level of the X-ray and comparing it with the basic physical parameters.

Guo et al. developed a paper ash online detector by using the absorption characteristics of substances to γ-rays [34]. After testing, the measurement range of paper ash content is 1%~30%, and the measurement accuracy is ±0.5%. This measuring instrument is suitable for paper basis weights ranging from 20 g/m² to 150 g/m², and the response time is less than 50 ms.

In the field of online measurement of paper ash, X-ray measurement is currently the main method, although this method has shortcomings, including the high precision required of the measurement device, high requirements related to environment where it is used, and the small application range. However, the measurement time is short, the measurement accuracy is high, and the cost is low. According to actual production needs, the appropriate ray method is applied to measure the ash content of the paper, which can improve the production efficiency of the enterprise.

DEVELOPMENT TRENDS IN INFRARED LIGHT FOR MEASURING TISSUE QUALITY

With growth in population and rapid development of the economy, the consumption of paper and cardboard has increased in China. From 2011 to 2020, the average annual growth rate of production was 1.41% in China, and the average annual growth rate of consumption was 2.17% [35].

New, efficient, and environmentally-friendly technical equipment is used in papermaking enterprises. It will inevitably save energy and reduce consumption, improve the environment, and improve economic efficiency [36,37]. Measurements of parameters such as basis weight and moisture are usually taken from paper rolls due to the lower speed of previous paper machines. According to the traditional method for paper parameter measurement, the whole measurement process is quite cumbersome, and the obtained results vary widely due to the large uncertainty of manual operation [38]. If the basis weight and moisture content of the paper are to be measured in real time and comprehensively, it is necessary to realize the online detection of paper quality parameters. Only in this way can field operators and quality inspectors keep abreast of the production status of the paper machine and solve problems in a timely manner. **Table IV** shows common measurement methods for paper basis weight and moisture in different basis weight ranges.

The basis weight of tissue paper is mainly in the range of 10~20 g/m². In this range, infrared light and ^{147}Pm radioactive source are often used to measure the basis weight online. The ^{147}Pm radioactive source is used in the process of making tissue because of its good sensitivity, but it is limited because of the radioactive measurement method.

Voith has developed a nonradioactive sensor (the LSC type TecoSens sensor) specifically for tissue machines that simultaneously measures the moisture content and fiber content of the tissue paper. It uses an infrared moisture sensor that measures infrared absorption at four wavelengths and has a baseline correction function. The use of such a sensor minimizes the influence of environmental factors or paper color on the measurements [39]. Paper fiber weight and moisture can be simultaneously measured with the Valmet IQ Fiber sensor developed by Valmet. This sensor has replaced the traditional nuclear basis weight

Method \ BW, g/m²	Tissue Paper 10-20	Glossy Paper 18-40	Writing Paper 45-80	Coated Paper 80-400	Corrugated Paper 120-200	White Cardboard 230-450	Packaging Paper 250-1000
Infrared light	√	√	√	√	√		
Microwave				√	√	√	√
^{147}Pm	√	√					
^{86}Kr			√	√	√	√	√

IV. Commonly used online measurement methods for paper in different basis weight (BW) ranges.



4. Onsite dust accumulation.

analyzer by improving the infrared technology, and it has been successfully installed in more than 140 tissue machines worldwide [40]. The high-efficiency infrared fiber quality sensor (HPIR-FW) introduced by ABB can measure paper fiber quality, paper web moisture, and paper web temperature at the same time while using only one infrared instrument. The sensor avoids numerous complicated procedures because no radioisotopes are used for the measurements [41].

The OUMDS-III intelligent near-infrared paper basis weight and moisture measuring instrument was developed by Liyuan Science and Technology in Xi'an, Shaanxi Province, China. This sensor is suitable for online dynamic continuous measurement of the basis weight and moisture of various types of paper in paper mills and paper processing lines. Also, it can realize automatic control of paper basis weight and moisture by connecting with other control equipment. The measurement range of paper basis weight is 10~400 g/m², and the measurement range of paper moisture is 0%~20%.

Infrared light also has many issues in the measurement of tissue paper. The dust disturbance at the production site, the ambient temperature and humidity, the speed of the paper machine, and the transmission effect of the sensor are all factors that affect the measurement results of near-infrared light. The dust at the production site is mainly composed of paper wool from the shedding of fine fibers during the wrinkling process of paper and dust in the air. **Figure 4** shows the accumulation of dust on the scanning frame.

Figure 5 shows the results of measuring the basis weight of 16 g/m² paper by near-infrared light before and after removing dust from the sensor platform. Future research in the use of near-infrared light for measuring tissue basis weight will focus on how to minimize the dust impacts on infrared light transmission and the impact of ambient temperature and humidity on the measurement process.

As shown in **Fig. 6**, the production of tissue paper in 2020 was 10.8 million tons in China, an increase of 7.46% over the previous year; the consumption was 9.96 million tons, an increase of 7.10% over the previous year. From 2011 to 2020, the average annual growth rate of production was 4.45%, and the average annual growth rate of consumption was 4.43% [35]. In the next ten years, it is expected that the consumption of tissue paper will reach about 50 million tons around the world, and the possibility of meeting this prediction is very high [42]. With the increasing production and consumption of tissue, papermaking enterprises have greater demand for paper basis weight and moisture measurement equipment. Infrared

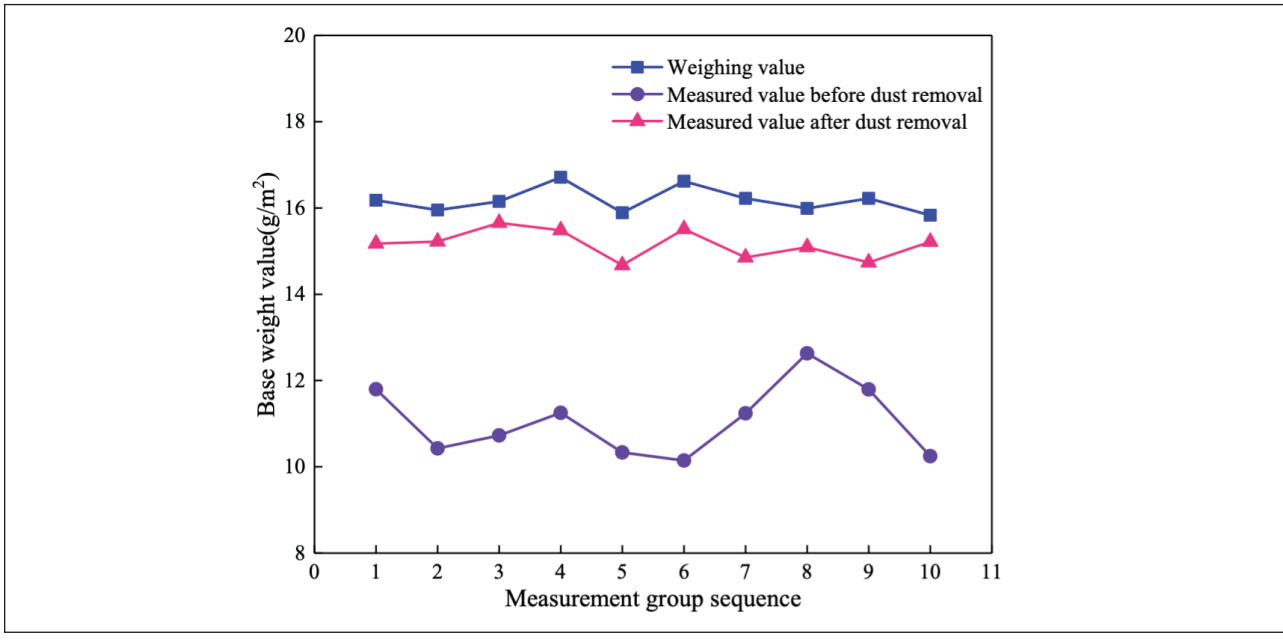

5. Basis weight value of near-infrared light measurement before and after dust removal.

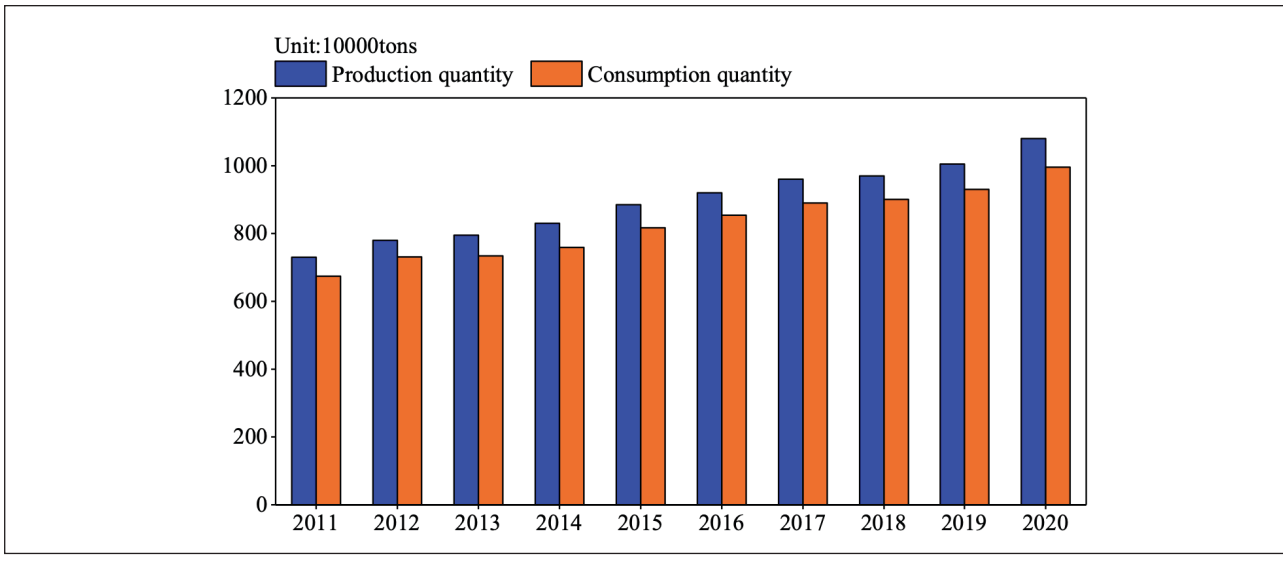

6. Production and consumption of tissue in China from 2011 to 2020.

light online measurement of paper parameters shows good development potential in the field of tissue.

The application of QCS in tissue paper production is relatively simple. However, because the manufacture of tissue has its own characteristics, the QCS system cannot relax the standards in terms of operation speed, control performance, and environmental characteristics [43]. To further enhance the performance of the QCS system, the control of the transverse basis weight of the paper machine has been improved by optimizing the scanning measurement method [44]. To meet the needs of different production scales, products covering various production scales from small to large will be formed in terms of system scale and structure [45,46]. The QCS system has been improved into a networked, integrated, and intelligent system, which is of great strategic significance to papermaking enterprises [47,48].

CONCLUSION

Quality parameter measurement plays a pivotal role as part of the paper production process. Online measurement of paper quality parameters will continue to be the trend in tissue paper production in the future, and there will be significant improvements. In this research article, the application of near-infrared, β-ray, X-ray, γ-rays, and microwave measurement methods in the field of paper parameter measurement are compared. The measurement of the basis weight of paper in the range of 40~200 g/m² is better with ^{85}Kr, and the measurement of the basis weight of paper in the range of 10~40 g/m² is better with ^{147}Pm. However, these two methods are not economical for measuring basis weight and cause radiation contamination. Infrared light measurement is also widely used in the measurement of low basis weight paper. However, the temperature, humidity, and field dust in the production environment have a major influence on the results in the measurement of tissue paper by near-infrared light. Measurement accuracy can be significantly improved by overcoming these interference factors. Near-infrared light measurement of paper basis weight will be widely used in tissue paper production.

Future research can be devoted to the improvement of factors such as onsite dust interference, sensor light-emitting temperature, and ambient temperature and humidity during infrared light measurement. This will provide a better technical guarantee for papermaking enterprises to improve process accuracy and paper quality. It is also an inevitable requirement for enterprises to enhance market competition and to improve production efficiency and economic benefits. **TJ**

ACKNOWLEDGEMENTS

The authors gratefully acknowledge the fund of Shaanxi University of Science and Technology (BJ15-19) and the Youth Innovation Team of Shaanxi Universities.

LITERATURE CITED

1. Chen, Y., Du, S., and Yuan, Z., "Fast detection of quality parameters of finished products based on near-infrared spectroscopy," *Chin. J. Anal. Lab.* (10): 112(2013).
2. Wang, M., Sun, Y., Tang, W., et al., *Pulping and Papermaking Process Measurement and Control System and Engineering*, Chemical Industry Press, Beijing, 2003.
3. Tang, W., Wang, M., and Chen, Y., "The realization of an imported QCS transformation," *China Pulp Pap.* 23(7): 27(2004).
4. Wang, M., Tang, W., Chen, Y., et al., "Imported B/M meter transformation (1)—Analysis and simulation of transmission algorithm," *J. Shaanxi Univ. Sci.* 22(1): 66(2004).
5. Wu, X. and Xue, X., "Introduction of Honeywell Quality Control System (QCS) in the paper industry," *Technol. Innovation Appl.* 3(25): 67(2013).
6. Anon., "Honeywell 4000 scanner system manual 6510020200," Honeywell International, Charlotte, NC, USA.

7. Anon., "Voith launched a new generation of sensor technology," *China Pulp Pap. Ind.* 41(8): 75(2020).
8. Anon., "Honeywell Da Vinci operators manual," Honeywell International, Charlotte, NC, USA.
9. Zhou, L., *Printing Design*, Huazhong University of Science and Technology Press, Wuhan, China, 2008.
10. Chen, X., "Research on multi-motor synchronous control system of paper machine division drive," Ph.D. dissertation, Shandong University, Jinan, China, 2009.
11. Zhong, J., "Design of an online detection system for paper parameters based on Python," Ph.D. dissertation, Chang'an University, Xi'an, China, 2019.
12 Hu, L., Li, X., and Tang, W., "A large-scale high-precision basis weight sensor," *China Pulp. Pap.* 30(02): 46(2011).
13. Hu, L., Li, X., and Tang, W., "Research on using β-ray to accurately measure the basis weight of paper," *Nucl. Electron. Detect. Technol.* 33(7): 869(2013).
14. Hu, L.H., Li, X.P., and Tang, W., *Appl. Mech. Mater.* 511-512: 185(2014). https://doi.org/10.4028/www.scientific.net/AMM.511-512.185.
15. Hu, L., "Research on on-line accurate measurement technology of basis weight and thickness of high basis weight cardboard," Ph.D. dissertation, Shaanxi University of Science and Technology, Xi'an, China, 2015.
16. Li, G., Hou, Y., Zhou, D., et al., "The selection of radioactive source intensity in paper basis weight detection," *Nucl. Electron. Detect. Technol.* 29(5): 1189(2009).
17. Li, Y., Hou, Y., Xiao, D., et al., "Application of pre-amplification digitization of β ionization chamber in paper basis weight measurement," *Instrum. Test. Technol.* 29(3): 71(2010).
18. Zhou, Q. and Han, J., "Paper basis weight signal processing based on Butterworth filter," *China Pulp Pap.* 25(9): 27(2006).
19. Sun, Y., Zhou, Q., and Wang M., "Research and improvement on the temperature drift of domestic basis weight meter," *China Pulp Pap.* 24(9): 29(2003).
20. Li, W., "Near-infrared paper basis weight moisture measurement method," China pat. CN1800825 (Jul. 12, 2006).
21. Hou, Y., Li, Y., Li, G., et al., "Research on integrated measurement of paper basis weight and moisture," *Instrum. Test. Technol.* 29(4): 60(2010).
22. Hou, Y., Su, H., Gao, H., et al., "Research on the measurement of paper basis weight by low-energy γ-ray backscattering method," *Nucl. Electron. Detect. Technol.* 21(2): 148(2001).
23. Ye, W. and Sun, Y., "Infrared optical system for measuring moisture in high basis weight paper," *Laser Infrared* 30(04): 230(2000).
24. Dong, P., "Research on paper moisture and basis weight measurement technology based on near infrared rays," Ph.D. dissertation, Changan University, Xi'an, China, 2009.
25. Kangasrääsiö, J., *Measurement* 44(10): 1937(2011). https://doi.org/10.1016/j.measurement.2011.08.024.
26. Liu, Y., "Research on on-line measurement technology of paper moisture content based on microwave cavity," University of Electronic Science and Technology of China, Chengdu, China, 2013.

ABOUT THIS PAPER

Cite this article as:
Hu, L. and Ma, J., *TAPPI J.* 21(5): 247(2022).
https://doi.org/10.32964/TJ21.5.247

DOI: https://doi.org/10.32964/TJ21.5.247

ISSN: 0734-1415

Publisher: TAPPI Press

Copyright: ©TAPPI Press 2022

About this journal

ABOUT THE AUTHORS

This research primarily focuses on the measurement of tissue paper basis weight with near-infrared (NIR) light and the difficulties in this measurement process. The most challenging aspect of this study was the summary analysis of paper parameter measurement methods, including the sorting out of some measurement methods. The problems with obtaining NIR measurement of tissue paper basis weight in China were addressed through careful analysis.

We found that while paper basis weight measurement methods are well established, tissue basis weight measurement needs further development. We also discovered that the measurement error of NIR light in the actual production of tissue paper is reduced by compensating for the algorithm of ambient temperature and humidity, as well as designing a mechanical dust-removing device for a scanning frame.

Our main focus for the next step in this study is how to reduce the influence of temperature, humidity, and dust on NIR light measurement, primarily concentrating on the measurement algorithm and mechanical design.

Hu is associate professor and Ma is a Master's student in the College of Mechanical and Electrical Engineering, Shaanxi University of Science and Technology, Xi'an, Shaanxi Province, China. Email Ma at majin2@sust.edu.cn.



Hu



Ma

27. Li, Q., Zhang, M., Song, S., et al., "Paper ash content rapid determination device and method," *China Pulp Pap.* 34(04): 56(2015).
28. Hu, L., Lu, X., and Ma, J., *BioResources* 15(1): 2096(2020).
29. Gu, J. and Sun, Y., "On-line detection of paper ash content and development of ash content meter," *Trans. China Pulp Pap.* (00): 19(1993).
30. Ou, X., "Research on paper ash meter," *Proc. Autom. Instrum.* 19(7): 4(1998).
31. Feng, D. and Sun, Y., "On-line measuring instrument for paper ash content," *Acta Metrologica Sinica* 19(1): 52(1998).
32. Xiao, Z., "On-line detection and control of paper ash content," *China Pulp Pap.* 31(09): 45(2012).
33. Hofman, G.J., U.S. pat. 7,376,215 B2 (May 20, 2008).
34. Guo, W., Wang, R., Huang, X., et al., "Paper ash content online detector," *Techniques of Automation and Applications* (02): 37(1996).
35. Anon., "China paper industry 2019 annual report," *China Pulp Pap. Ind.* 41(11): 16(2020).
36. Chen, K. and Zhang, X., "Several issues on the independent innovation strategy research of my country's pulp and paper equipment manufacturing industry," *China Pulp Pap. Ind.* 27(6): 6(2006).
37. Cao, Z., "Retrospect and prospect of China's paper industry," *China Paper Newsletters* (06): 10(2006).
38. GB/T 451.2-2002 "Determination of basis weight of paper and cardboard," National Standard of the People's Republic of China.
39. Voith, "Fiber weight and moisture without radioactive source," *Prof. Papermaking* 9(2): 36(2012).
40. Valmet, "Valmet launches IQ Range for quality control," *Paper Asia* 31(5): 14(2015).
41. ABB, "ABB introduces new HPIR-FW sensor to reduce energy and fibre costs," *Paper Asia* 28(6): 38(2012).
42. Uutela, E., "Global household paper consumption development trend forecast," *China Pulp Pap. Ind.* 41(11): 60(2021).
43. Wen, X., "Discussion on the performance of basis weight moisture control system," *China Pulp Pap.* 21(5): 63(2002)
44. Raunio,J.-P. and Ritala, R., *J. Process Control* 72: 74(2018). https://doi.org/10.1016/j.jprocont.2018.09.012.
45. Huang, L., Huang, X., and Zhao, Z., "Analysis of advantages and development trend of paper quality control system," *Mech. Electr. Eng. Technol.* 50(01): 19(2021).
46. Luo, Z., Huang, Y., Xie, Q., et al., "Application and development of automation control system in energy-saving transformation of paper industry," *Pop. Sci. Technol.* 21(10): 35(2019).
47. Li, Q., "Design of papermaking quality control system based on industrial Ethernet," Ph.D. dissertation, Chongqing University, Chongqing, China, 2013.
48. Chen, G., Zhang, K., and Ma, C., "Paper quality control based on Siemens control system," *Pap. Pap. Making* 28(05): 60(2009).

Improving refining efficiency with deflocculation

DWIGHT ANDERSON AND LEN SCHUSTER

ABSTRACT: The ability to load a refiner requires the formation of a fiber mat between opposing refiner bars. One of the consequences of this is the formation of flocs that persist through the refiner grooves and exit the refiner. These flocs interfere with sheet strength, requiring additional energy to make up the strength deficit. In addition, flocs can initiate string formation, resulting in machine efficiency issues such as cross-machine profile deterioration and the downtime required to correct it.

Novel refiner plate modifications have been shown to improve refining efficiency in otherwise identical refiner plates. Energy savings are typically around 15% of gross refining energy on the basis of the treated stock, although much higher reductions have also been seen. Addressing this previously underappreciated flaw in conventional refining enables greenhouse gas reduction and other benefits related to sheet strength and machine efficiency.

Application: Conventional refining of softwood and old corrugated containers (OCC) is compromised by the creation of flocs. A novel refiner plate modification counteracts this, making refining more energy efficient. The improvement in refining efficiency is typically greater than can be achieved through no-load reduction. Additional research could yield further optimization.

Refining of low consistency stock continuously forms flocs in the gap between the rotor and the stator. The fate of these flocs is different, depending partly on fiber morphology. Hardwood flocs, for example, are easily broken during refining, but softwood flocs are stronger and do not break as easily with refining [1]. Floc formation in the gap between opposing refiner bars is necessary to accomplish refiner loading. This gap is typically a few tenths of millimeters, which is several times the width of individual fibers. El-Sharkawy et al. [2] used the onset of net power application in refining as the indication of when fibers were trapped in the refining gap and therefore susceptible to refining action. They showed how pulp properties affect floc formation and how flocs interact with the refiner plate design and rotational speed to affect the onset of refining and the development of fibrillation and fiber shortening during refining. El-Sharkawy et al. also measured the size and stability of flocs moving through a flow channel similar to a refiner groove. They found that flocs are temporarily elongated in the direction of flow, but flocs made of long, coarse fibers are larger and retain their size, while flocs of shorter, less coarse fibers had their size eroded through a flow channel. Lundin et al. [3] further quantified the effect of the thickness of the fiber mat trapped between the opposing refiner bars and showed how it depends on consistency and refiner speed. It is one of the two critical parameters in their model, the other being the fraction of the bar that traps fibers.

Flocs strong enough to survive refining have the potential to affect sheet properties. The strength of flocs can vary widely. Van de Ven differentiates between coherent flocs and incoherent flocs [4]. Coherent flocs are so strong that they are permanent, while incoherent flocs are weaker and are broken up in the papermaking process. Van de Ven points out that coherent flocs are susceptible to growing as they come into contact with individual fibers, and they are detrimental to paper properties. It is also known that shives are detrimental to paper strength [5]. Shives are similar to coherent flocs in that they present a nonuniformity in a sheet. A difference, however, is that shives can consist of uncooked wood, for example, because shives are defined as the mass reject fraction of a screening process. A floc, on the other hand, is defined by its morphology as being composed of individual fibers that are mechanically and/or chemically bonded with each other. We might expect coherent flocs and shives to decrease sheet strength through a similar mechanism, since they both present a nonuniformity in the sheet.

MILL ANALYSIS OF SHIVE AND FLOC MORPHOLOGY

A mill with two uncoated freesheet machines was equipped with a Valmet MAP fiber analyzer (Valmet; Espoo, Finland) that monitored freeness, fiber morphology, and shives. Both machines used a majority of hardwood, but they reinforced their sheets with softwood. During a paper machine performance audit, a multivariate analysis hinted that what the fiber analyzer described as “shives” played a significant role in refining performance and strength development. In particular, an entity designated on this apparatus

	Before Refiners, ppm	After Two Refiners, ppm
Paper Machine #1	24	7048
Paper Machine #2	24	8988

I. Softwood floc quantification before and after two stages of refining on each paper machine.

as a "wide shive" was prominent in differentiating performance. A "wide shive" was classified as having a width greater than 150 µm and a length from 0.3 mm to 40 mm. The "shive" designation in this term is appropriate in the sense that the fiber analyzer prepared the sample with dilution and agitation, mimicking what could have been done in a screening step such as is done in shive measurements. As it turns out, however, the "wide shives" were in fact flocs: they were aggregates of individual fibers. We will refer to these as flocs from here on. They do not primarily come from the pulp mill. They are mostly generated during refining. **Table I** shows the quantification of flocs across the softwood refiners, and **Fig. 1** shows the average floc level throughout the two machines. The machines have the same overall schematic and very similar floc profiles.

The bleached hardwood pulp was lower than the softwood pulp in flocs before refining, and flocs did not increase after hardwood refining. Although the softwood flocs after refining only appear to constitute approximately 8000 ppm of the softwood pulp, the actual floc content could be greater. The floc definition used by the fiber analyzer does not count all flocs that might affect strength development, such as roughly spherical flocs of 150 µm or less. **Figure 2** shows stock samples before and after the first and second stages of softwood refining on Paper Machine #2. The samples must be diluted to approximately 0.1% to 0.2% consistency to see the flocs clearly, and that process of dilution breaks up the looser flocs. The remaining flocs, however, appear to be dense and roughly spherical.

The last refiner on each of these machines was a Beloit SA400 conical refiner. The last refining position in a machine is commonly known as a "tickler" refiner because it is the final means to apply refining energy before the machine. A tickler typically applies a moderate amount of power. These refiners, however, were almost always un-

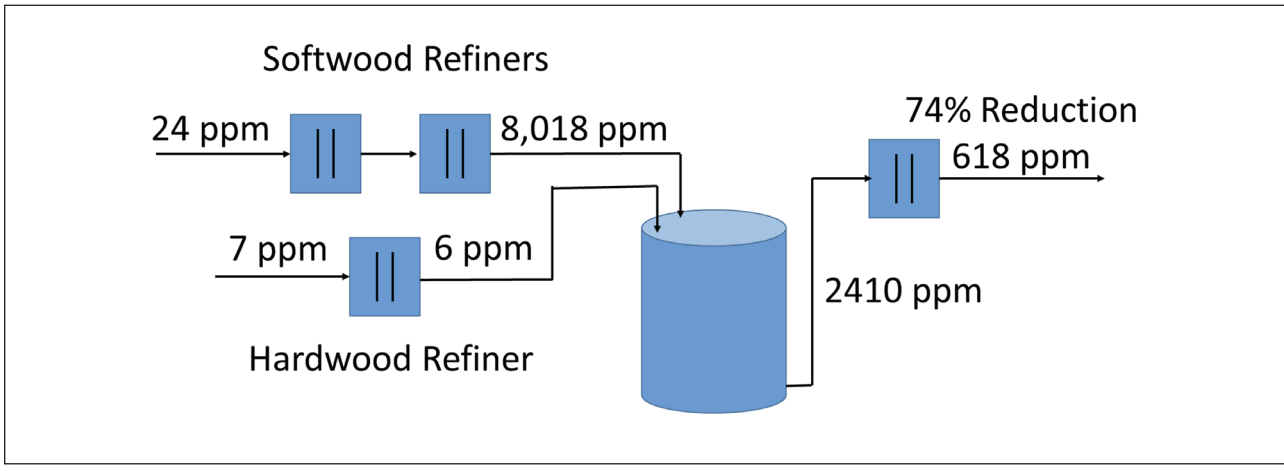

1. Schematic of each paper machine showing average levels of flocs.

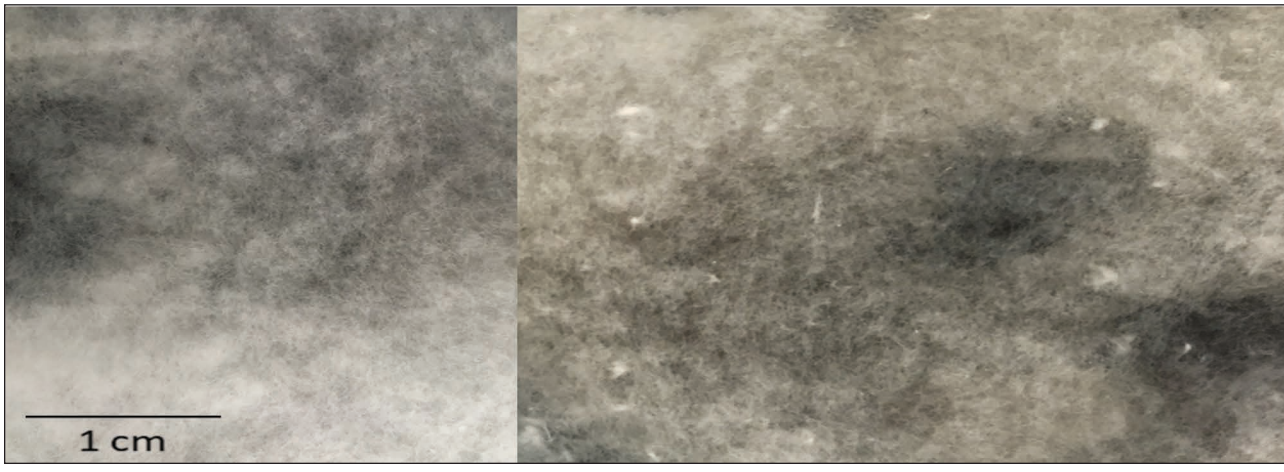

2. Bleached softwood pulp before (left) and after (right) two stages of refining.

	Flocs Into Tickler*, ppm	Flocs Out of Tickler, ppm	Floc Reduction (%)
Paper Machine #1	2118	395	81%
Paper Machine #2	2701	842	69%
* Estimated from softwood/hardwood stock blend.			

II. Floc reduction across unloaded tickler refiners.

loaded. Even unloaded, these refiners operated at a significant energy cost. It turns out this cost was easily justified. Whenever the operators turned the ticklers off, the sheet quality would suffer from poor formation. Could this formation be related to the flocs made during softwood refining? A measurement of flocs going into the tickler refiners was not available, but it could be estimated from the flocs in the outlets of the softwood and hardwood refiners on the basis of the 30% softwood/70% hardwood flow ratio, assuming minimal changes in an intermediate chest. Given this assumption, the unloaded tickler refiner reduced flocs by 74% on average between the two machines. **Table II** compares the flocs at the inlets and outlets of the tickler refiners. In both cases, the tickler refiners were being operated near their no-load power.

The floc reduction in Table II assumes there is no significant change in flocculation in the thick stock system after the refiners. This seems reasonable to expect. A quick check was done with another mill's uncoated freesheet machine with a semi-quantitative method to assess the relative amount and strength of flocculation. Approximately 0.5 o.d. grams of never-dried fiber were added to 500 mL of water in a 7-3/8 in. diameter flat-bottom bowl and agitated at slow speed with a magnetic stir bar. Stirring was paused after 30 s, 1 min, 2 min, and 4 min so that manual counts could be made of flocs visible to the unaided eye. **Figure 3** compares the blend chest and machine chest samples after 30 s of agitation with this protocol. It was necessary to do some agitation to begin to see the structure of the flocs and differentiate them from the well-dispersed or loosely flocculated fibers. The ideal amount of agitation would represent the subsequent mixing of the thin stock system. We do not know what amount of mixing this would be, but some point within the 4-min protocol should be close to this. Very little difference between these two chests is visually apparent, even though the machine chest sample represents one more stage of mixing and pumping at nominally 4% consistency. We see no reason to doubt that the flocculation of 4% consistency stock after the refiners is somewhat stable.

Counting both the larger, looser flocs and the smaller, denser flocs is tedious and imprecise, but it does seem to

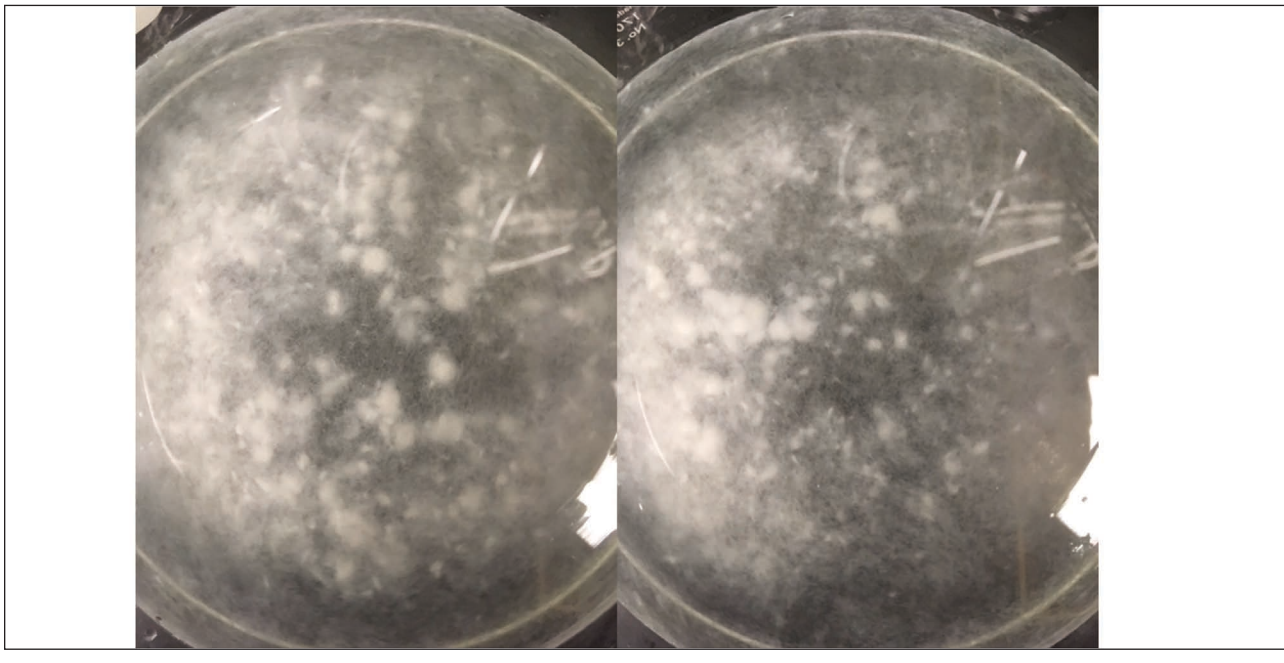

3. Blend chest (left) and machine chest (right) outlet samples, diluted to 0.1% and agitated for 30 s. There is little apparent difference in the flocculation in spite of the machine chest being a subsequent chest.

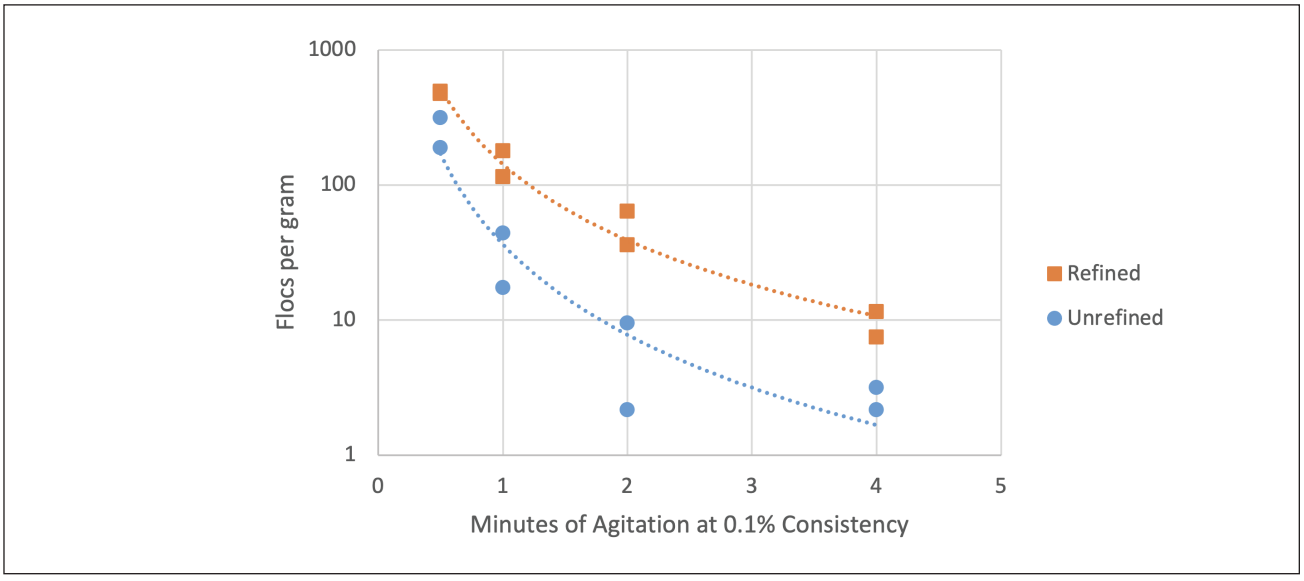

4. Manual floc counts after dilute agitation.

be capable of differentiating between refined and unrefined samples. Unrefined softwood samples have lower flocs than the refined softwood samples at all levels of agitation, often by nearly an order of magnitude as seen in **Fig. 4**. This also illustrates that these flocs are capable of being dispersed with a few minutes of agitation at 0.1% consistency. This consistency is lower and the duration is longer than the time a floc spends in a headbox, but the degree of turbulence in a headbox is typically greater. The survival rate of the flocs through the papermaking process is therefore uncertain.

REMOVING FLOCS

Deflocculating concept

We have demonstrated that just as softwood flocs are created faster than they are destroyed during refining, they are destroyed faster than they are created (if they are created at all) in an unloaded refiner. The shear forces of an unloaded refiner must therefore be suited to reducing flocculation. Following each refiner with an unloaded refiner would be a costly proposition. It would also allow only one plate gap for deflocculating, whereas it might be that different plate gaps are suitable for deflocculating different sizes and types of flocs. As was seen in Fig. 3, there is a large range of sizes, from large flocs a few millimeters in diameter, to small dense flocs just over 150 µm in diameter, and possibly smaller flocs that are not visually apparent without magnification. Refiner parameters such as bar width can influence floc size, but the size range in Fig. 3 was generated with a single set of refining conditions. The floc size distribution represents a degree of randomness inherent to the formation and release of flocs from the refining bar gap.

A refiner plate modification (D-Floc-It™ technology) [6] has been disclosed elsewhere [7,8] that provides for a range of shear forces to be applied at the exit of a disc or conical refiner for the purpose of deflocculating the pulp as it emerges from a refiner. It is advantageous to deflocculate as soon as possible after refining for several reasons. First, it is possible that dense flocs could seed the formation of strings or larger flocs [4]. The mill where the flocs were quantified had significant stringing in the screens, with strings that were more than a centimeter in length. While strings might primarily form around screens, their tendency to form could be influenced by the presence of dense flocs. Second, when flocs are disrupted prior to entering another refiner, the stock is free to form new flocs between the bars of the subsequent refiner. Work on compression refining indicated that if a handsheet is not re-formed between successive compressive impacts, multiple impacts had little effect on the strength [9]. If, however, the handsheet is formed again between impacts, each successive impact contributes to the strength of the handsheet. In the same way, if a floc formed in a refiner enters a subsequent refiner bar gap intact, that impact would be analogous to a repeated compression on a handsheet that is not re-formed. Deflocculation at the refiner outlet, however, would be analogous to re-forming the handsheet in the compression refining study, thus enabling further strength development. Third, deflocculating in the refiner with a refiner plate modification can be done without capital and without the energy burden of additional unit operations. In fact, as we shall see, refining energy efficiency increases when deflocculation is incorporated into refining.

The new deflocculation zone concept typically occurs on the outer 1 to 2 in. (0.025 to 0.051 m) of circumference of a refiner plate. It consists of a gradually widening plate gap towards the outer circumference, as shown in **Fig. 5**. The expanding gap imparts a range of shear forces intended to disrupt flocs. As the plates wear and bar heights de-

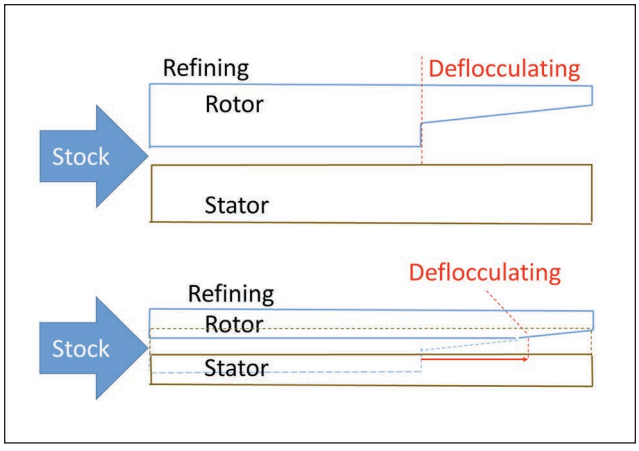

5. Sketch (not to scale) of the modified bar geometry at the outlet of the rotor that constitutes a deflocculating zone. When the plates are new (top), the step in rotor bar height that initiates the deflocculating zone is enough to ensure no more refining occurs. As the bars wear (bottom), the bar height decreases, increasing the length of the refining zone and decreasing the length of the deflocculating zone.

crease, the beginning of the deflocculation zone moves radially outward over the life of the plate, as shown in the bottom of Fig. 5. In doing so, the refining intensity decreases slightly as the cutting edge length increases. If the refining intensity is close to the optimum level, this is immaterial. If, however, the refining intensity is far from optimum, a refiner plate with this kind of a deflocculation zone has the added benefit of being able to indicate the direction of change in intensity needed.

First mill results

The first mill trial of a deflocculating refiner plate (also known as a "defloccer") was performed on a linerboard machine in the southeastern United States. This machine typically operates two 54 in. (1.372 m) double disc refiners in parallel for the base ply, and refines 100% pine kraft pulp at about 105 kappa number. The top ply typically operates a single 42 in. (1.067 m) double disc refiner on the same furnish. The floc content of this high-yield pulp appeared much lower than the bleached pulps we had previously seen, but this particular machine was a good candidate for deflocculation because it had a longstanding problem of strings plugging the base headbox tubes. Every nine to twelve days, the cross-machine direction profiles would deteriorate to the point that the machine would need to be taken down to flush the headbox tubes that were filled with strings such as shown in **Fig. 6**.

The trial was done in two steps. First, one of the parallel base refiners had the legacy 54 in. (1.372 m) refiner plate replaced with an underhung 50 in. (1.270 m) refiner plate that did not have a deflocculating zone. In doing this, the bar width decreased from 0.119 in. (3.02 mm) to 0.095 in. (2.41 mm), and the cutting edge length was similar. There was some perception that this decreased the degree of the



6. Strings removed from the base headbox.

headbox plugging somewhat, but it was still necessary to shut down to clean out the headbox as before. After three months of operating this way, the trial defloccer replaced the other parallel legacy 54 in. (1.372 m) plate set. The trial defloccer was a 54 in. (1.372 m) plate consisting of a refining zone identical to the 50 in. (1.270 m) plate in the parallel refiner, plus a two inch (0.051 m) circumferential outer radius designed to deflocculate the stock. The stator had full height bars for all 54 in. (1.372 m) of the plate diameter, but the rotor had a deflocculating zone that began at a radius of 25 in. (0.635 m) from the center of the plate, at which point the bar height stepped down by 0.7 mm. From this point outward, the bars were tapered with a decreasing bar height with a 3° angle to the full 27 in. (0.686 m) radius of the plate.

This first defloccer eliminated a long-standing machine liability. Since putting it in, the mill went from about twelve days to over a year and a half without needing to shut down to clean the headbox, and it is not certain that something else did not cause that rare plugging event. In spite of the less visible flocs in high-yield pine pulp, the defloccer is effective at reducing string formation. The 50 in. conventional plate operating in parallel with the trial plate was changed to the same 54 in. deflocing pattern at the midpoint of the original defloccer's life, and both refiners have had defloccers ever since.

Since this first trial, two machines in two other mills have also reported improved headbox cleanliness with defloccers. The headbox plugging reduction is interesting because it demonstrates something significant is happening, but refining efficiency is relevant to all machines. We can measure refining efficiency as energy reduction with all other variables held constant. Energy reduction is the most conservative valuation. Depending on bottlenecks and needs, it can be exchanged for more valuable properties, such as reduced basis weight, reduced chemical additives, higher yield, lower cost fiber, or higher speed, for example. Taken as an energy benefit, however, the reduc-

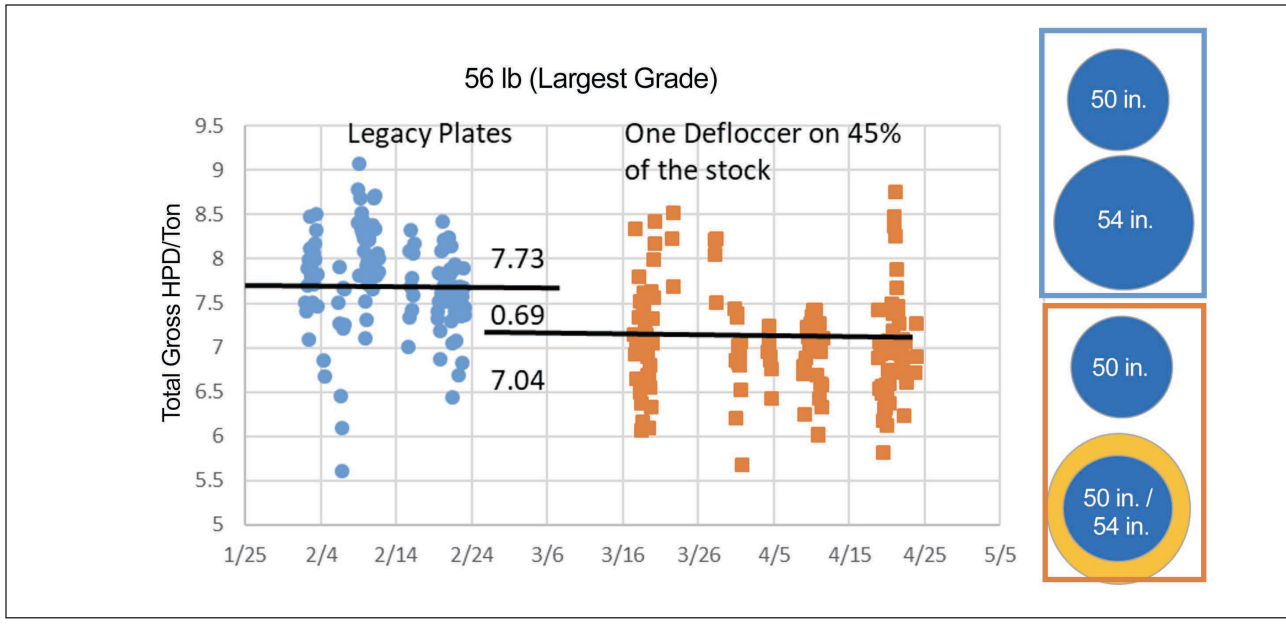

7. Energy savings on the largest grade with the first set of deflocculating refiner plates (defloccers) indicates 9% gross energy reduction on the whole sheet with only one defloccer refining 45% of the stock. The previous plates were a 50 in. underhung and 54 in. full size plate shown in the blue box on the right. The orange box on the right shows the defloccer replaced the 54 in. refiner with a 50 in. refining diameter and a 54 in. total diameter plate that included a 2-in.-wide circumferential deflocking zone.

tion in purchased electricity also contributes toward Class 2 emission reduction.

Based on comparisons made around the times of the plate changes, the conventional underhung 50 in. plate appears to have not saved refining energy and in fact might have increased energy demand slightly by 0.07 horsepower days per short ton (hpd/ton) on the whole sheet compared to the legacy 54 in. plate it replaced. The 54 in. trial defloccer plate, however, when it replaced the 54 in. legacy plate, appears to have saved 0.69 hpd/ton on the whole sheet on the largest grade, 56 lb., as shown in **Fig. 7**. This is ten times greater than the no-load reduction from applying the deflocculating zone to what was previously part of the refining zone. Results were similar on other grades.

Refining energy efficiency is conventionally improved by decreasing no-load energy or achieving a more optimal refining intensity. In these cases, the benefit achieved on one refiner manifests itself as an average energy reduction across the whole sheet. Conversely, the energy change in the whole sheet can be attributed to the im-

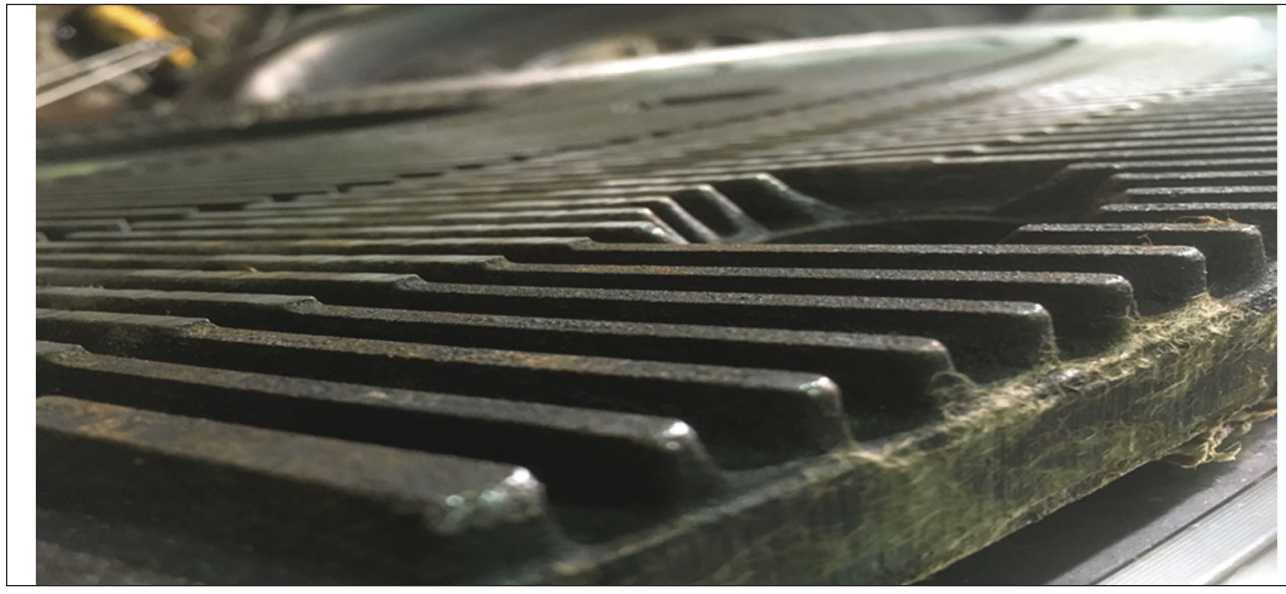

8. First experimental plate with a deflocking zone designed for only partial plate life for diagnostic purposes. This picture shows the step down and slightly sloped outer 2 in. of the rotor after 8 days of run time.

		Total Gross HPD/Ton			
Basis Weight, lb/1000 ft²	No. of Refiners	Zero Defloccers	One Defloccer	Savings	Savings (if all refiners were defloccers)
33	2	3.41	3.36	0.05	3%
36	2	3.42	3.18	0.24	14%
40	2	2.2	1.85	0.35	32%
45	2	2.27	1.77	0.50	44%
33	3	3.96	3.75	0.21	16%
34	3	4.11	4.00	0.11	8%
35	3	8.12	7.76	0.36	13%
				Average:	**19%**

III. OCC refining benefit.

proved refiner, all else being equal. The improvement with the defloccer, however, is not in the refining per se. The 50 in. refining zone was the same in the defloccer and the 50 in. underhung plate. The improvement was also not from no-load. The no-load difference between a 54 in. conventional plate and a 54 in. defloccer is an order of magnitude less than the energy savings observed. The efficiency must come from the interaction of the deflocculated stock with the sheet. For this reason, the benefit of deflocculating might not scale linearly with the proportion of stock treated. Nevertheless, it is informative to represent the energy reduction in this way to be able to compare results from different applications with different percentages of stock treated and to relate results to conventional methods of improving refining energy efficiency. Normalizing the 9% energy reduction by the 45% of the stock that was treated with the defloccer results in a 20% energy reduction of the whole sheet, extrapolating the same results to 100% deflocced stock.

From our current perspective after having implemented dozens of defloccers, this turns out to be fairly typical. The median energy savings we have seen in general is 15% of the gross refining energy on the total sheet, prorated by the percentage of deflocculated stock. One of the features of the machine depicted in Fig. 7 is that refining is controlled by a vacuum box on the Fourdrinier. Thus, the refining energy reduction reflects the increased vacuum capability developed by the deflocculated stock, perhaps as a result of liberating individual fibers from flocs. With deflocculation, the refining energy is lowered to maintain the original vacuum setpoint.

The deflocculating zone used in this first trial differs from later practice. **Figure 8** shows the first experimental plate after eight days of use. Notice the significant bar height at the outer edge. This was done on a trial basis so that the deflocculating zone would wear away partway through the plate life. Later versions have included a steeper taper that enables deflocculating capability for the entire life of a plate. No loss of benefits has been detected with full-life defloccers. For more than two years, this mill has run all low consistency refiner plates on both machines with full-life defloccers.

Additional mill trials

The initial applications focused on softwood because long softwood fibers are most prone to make flocs. It turns out we also see a refining energy reduction on old corrugated containers (OCC). A 100% recycled containerboard machine in the United States uses either two or three refiners at a time. The following analysis segregates comparisons by the number of refiners used. The mill has four refiners available, all of them being 42 in. (1.067 m) double disc refiners running plates with similar cutting edge lengths for both the baseline period and the trial period with the defloccer. The defloccer was installed on one of the two base refiners in parallel. Frequent sampling of the refiners in parallel suggested the defloccer produced a lower CSF stock with less refining energy. As before, however, the most meaningful comparison is the grade-by-grade comparison of the gross specific energy on the total sheet. **Table III** shows this, comparing the full life performance of a single set of defloccer refiner plates to over a month of data from the previous conventional plates. The average basis weights, machine speeds, and STFI short span compression test (STFI-SCT) were identical for the baseline period (zero defloccers) and the trial period with one defloccer. The average Mullen for the defloccer trial increased 4%, however, and on corrugating medium grades, Concora increased 2%. If the refining had been run to constant net specific energy, it is likely that STFI-SCT would have been higher as well.

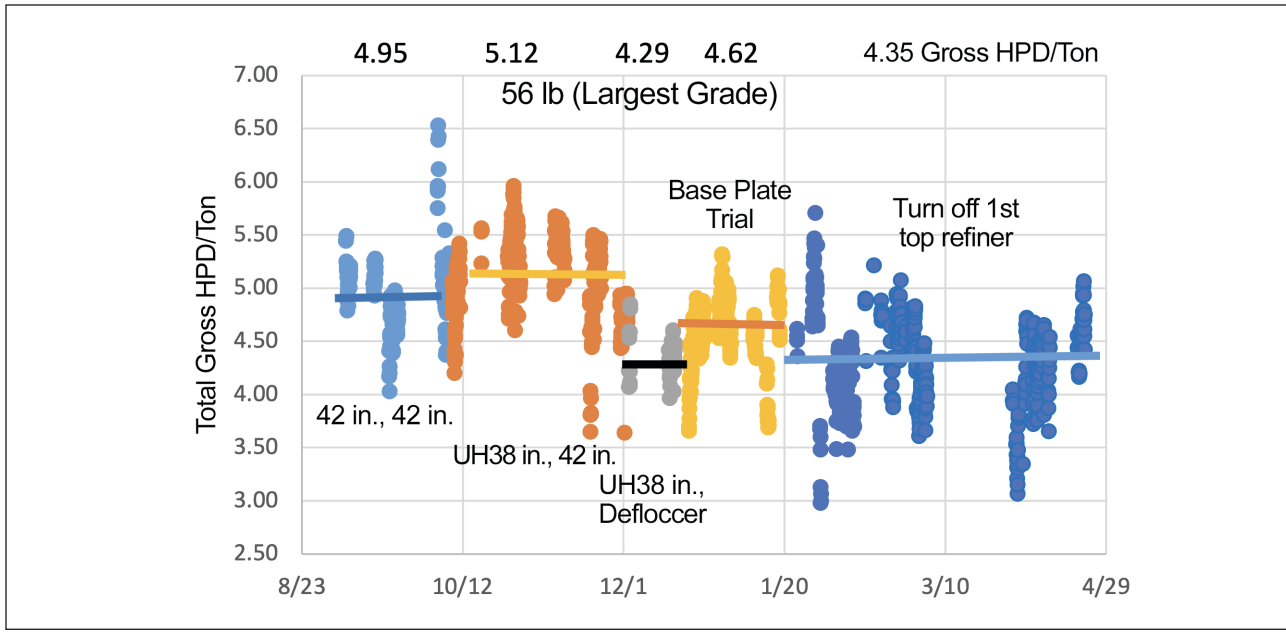

9. Series of refiner trials shown for a grade that represents half of this paper machine's production.

Measuring refining energy differences from refiner trials with precision is often challenging because of variability in the process and the pulp, but the energy benefit in Table III is consistently favorable. The right column extrapolates the benefit to using defloccers on all refiners. Interestingly, the 19% reduction in gross specific energy is about the same as for the softwood linerboard example mentioned previously.

One additional example is interesting, because it gives insight into the mechanism of the energy savings. A softwood linerboard machine in the southeastern United States was operating a top ply with two refiners in series. Each of these refiners operated at about 60% to 70% of full motor load. A defloccer was put in the second of these refiners. A series of plate changes was made in close consultation with a refiner plate supplier to contrast conventional ways of reducing refining energy to reducing energy with a defloccer. The baseline period, in September, had both top refiners with conventional 42 in. (1.067 m) plates, as shown in **Fig. 9**. This figure represents a single grade that constitutes approximately half of this machine's production. The first change, in October and November, was to put a 38 in. underhung plate into the first top refiner. We did not see an energy decrease from this, and in fact energy use increased from 4.95 to 5.12 gross hpd/ton. Next, a defloccer was added in the second top refiner. It had the same 38 in. refining zone as the underhung refiner, but a 2 in.circumferential defloccing zone was added. We averaged much lower, at 4.29 gross hpd/ton. While this was still running, a conventional trial plate was installed on the base ply, but the average energy use increased from 4.29 to 4.62 hpd/ton. In late January, the mill decided to turn off the underhung top refiner and only use the defloccer in the top ply, resulting in a decrease to 4.35 gross hpd/ton on the whole sheet. All of the averages of the five periods noted in Fig. 9 are statistically different with 95% confidence, except for the third and fifth periods. These are not statistically different from each other, but they are lower than all other periods.

The defloccer is the only plate trialed that showed evidence of decreased energy use. The magnitude of energy reduction shows us that the defloccer on the top ply is affecting the sheet as a whole, not just the top ply refining energy. For example, look at the transition from the second to the third periods of trials, as the defloccer first went in. The total gross specific energy decreased by 0.83 hpd/ton (5.12 to 4.29) on the whole sheet, but the top ply refining itself actually increased slightly, from 15.06 to 15.42 gross hpd/ton. Half of the 15.42 gross hpd/ton being run on the top ply in the third period was due to the refiner with the defloccer. In other words, a defloccer operating at 7.7 gross hpd/ton on 10% of the total sheet (0.77 hpd/ton on the total sheet) reduced refining energy by 0.83 hpd/ton on the total sheet. The defloccer is effectively saving over 100% of the energy used by the defloccing refiner. Clearly, 100% energy reduction would not be possible on 100% of the sheet. This calculation demonstrates that the energy reduction mechanism is related to something that goes beyond the refiner itself. This defloccer must be building the sheet more efficiently. Even a small amount of deflocculated fiber can interact with the rest of the sheet to bring about a stronger sheet, thereby requiring less refining. A factor that might have supported this level of improvement could include a very high recirculation rate of 57% through the top ply refiner. Repeated passes through the refiner likely produced more flocs than is common.

CONCLUSIONS

Conventional refining of softwood, OCC, and perhaps other pulps results in the formation of flocs that are detrimental to strength and are therefore detrimental to refining efficiency. A refiner plate modification based on the ability of an unloaded tickler refiner to reduce flocs has been demonstrated to save nominally 15% of gross specific refining energy in the total sheet, prorated by the percentage of treated stock. This modification has also been demonstrated to improve headbox cleanliness by reducing the flocs that initiate fiber stringing.

Fiber morphology is most commonly measured on well-dispersed, dilute pulps so that single fibers can be isolated for measurement. The current work shows the importance of understanding the impact of flocs under the conditions they are present on a paper machine. Likewise, refining efficiency and the development of sheet strength on a paper machine are strongly affected by this phenomenon. While the solution investigated is straightforward and well-proven, a greater understanding of this phenomenon could lead to additional optimization in this nascent field. **TJ**

LITERATURE CITED

1. Lumiainen, J.J., in *Papermaking Part 1, Stock Preparation and Wet End*, Fapet Oy, Helsinki, 2000, Chap. 4.
2. Khalil El-Sharkawy, K., Haavisto S., Koskenhely, K., et al., *BioResources* 3(2): 403(2008).
3. Lundin, T., Batchelor, W., and Fardim, P., *TAPPI J.* 7(7): 15(2008).
4. van de Ven, T.G.M., "Interactions between fibers and colloidal particles subjected to flow," *Annu. Trans. Nord. Rheol. Soc.* 14: (2006).
5. Soszynski, R.M. and Seth. R.S., *Int. Packag. Conf. Proc.*, *Conex '85*, Beijing, 1985, Vol. 2, p. 590.
6. ©2022 International Paper Company. All rights reserved. D-Floc-It is a trademark of International Paper Company, used with permission.
7. Anderson, D.E., U.S. pat. 10,794,003 B2 (Oct. 6, 2020).
8. Anderson, D.E., U.S. pat. 11,001,968 B2 (May 11, 2021).
9. Goosen, D.R., Olson, J.A., and Kerekes, R.J., *J. Pulp Pap. Sci.* 33(2): 110(2007).

ABOUT THIS PAPER

Cite this article as:
Anderson, D. and Schuster, L., *TAPPI J.* 21(5): 259(2022). https://doi.org/10.32964/TJ21.5.259

DOI: https://doi.org/10.32964/TJ21.5.259

ISSN: 0734-1415

Publisher: TAPPI Press

Copyright: ©TAPPI Press 2022

About this journal

ABOUT THE AUTHORS

Others have noted the formation of flocs in refining before, but not much attention has been given to its consequence or remedy. A confluence of fortuitous observations gave us insight into both of these.

Refining improvements are often focused on reducing no-load or optimizing fiber properties. Not much attention has been paid to the effect of flocculation in refining. To our knowledge, this is the first effort at identifying the effect of refiner-generated flocs and finding a remedy for them.

We found some interesting results with handsheets, but they were inconsistent. We have concluded that the handsheet making process itself, much like fiber morphology measurement, involves agitation and therefore degradation of flocs. Because of this, we have focused on the paper machine's response as our measure of success.

We discovered that, although we work in a mature industry, new opportunities can be found outside of existing paradigms. The elimination of headbox plugging with the very first trial set of plates was a pleasant surprise.

Almost any mill that is interested in saving refining energy or debottlenecking refiners could benefit by implementing this technology. If the mill is happy with their current refiner plates, all the better. This can be added to most refiner plates without significantly affecting refining itself.



Anderson



Schuster

Although we are focused on completing replication in our company, further optimization might be possible with an improved fundamental understanding. We will look for opportunities to leverage research into this phenomenon.

Anderson is manager of Innovative Technology Development at International Paper in Puyallup, WA, USA. Schuster is principal scientist at International Paper in Loveland, OH, USA. Email Anderson at dwight.anderson@ipaper.com.

Web instability in the open draw and the impact on paper machine efficiency

FRÉDÉRIC PARENT, DANIEL RICARD, J. DAVID MCDONALD, AND RICHARD J. KEREKES

ABSTRACT: Paper is most likely to break in the first open draw on a paper machine where it is unsupported, wettest, and weakest. Tension is applied to peel the web from the roll surface, as well as minimize web flutter in the open draw. The average tension is well below the breaking point and is often set by adjusting the speed difference between the press and the next machine element by visually observing the behavior of the web. However, machine direction variations caused by instabilities in the paper machine can cause tension swings that exceed the strength of the web.

Measurement of the web's release point from press rolls on pilot and commercial paper machines was used to identify the cause of tension instabilities. Variations in the speed of the paper machine drives and the work of adhesion from the press roll surface were identified as key factors. Fluctuations of paper moisture, which affects the elastic modulus and strength of the web, appear to be less important.

Application: Measurement of the release point of the web from a press roll can be used to identify tension stability problems in the open draw and the source of web breaks. Paper machine drive stability and the web adhesion to the press roll surface are possible problem areas.

Web breaks on paper machines commonly occur in the first open draw where paper is wettest and weakest. The strength of the web in the first open draw is a critical factor in determining ultimate machine speed and therefore production. A key principle of new machine design has been to move the open draw farther down the machine, where the web is drier and stronger. This has been accomplished using pick-up felts at the couch and clustering press rolls to support the web through two or three press nips. In modern paper machines, the first open draw is typically between the last press and the dryer. For lightweight grades such as tissue, the web is entirely supported until it is dry-creped off the yankee dryer. For some heavier grades, the draw between press section and dryers has been closed on a few machines using transfer felts or belts [1-3]. Another approach has been to reduce moisture content before the first open draw by shoe presses. Despite these advances, many paper machines today still have an open draw between the last press and the dryer. Consequently, there remains a need to mitigate web breaks in this zone.

Because webs adhere to press rolls, tension must be applied to peel the web from the roll surface. Web adhesion to the press roll is a function of surface topography and chemistry, as well as operational factors such as web solids, temperature, and paper machine speed [4-8]. Online tension measurements on a pilot press [4] and pilot paper machines [9-11] have been used to study the behavior of the web in the open draw and calculate the work of adhesion under commercial conditions.

Given the importance of the open draw on paper machine operation, several theoretical models have been proposed [12-16], but they remain to be confirmed by experimental studies. For example, Edvardsson and Uesaka [16] showed the critical importance of the release point and its sensitivity to operational and material variations, but this is yet to be demonstrated under commercial conditions.

A laser camera has been used on a commercial paper machine to measure the distance between a fixed point and the web position near the release point from a press roll [7]. This distance was used to measure the effect of draw, basis weight, furnish composition, and chemistry on the web's behavior in the open draw [7]. In our study, we have extended this technique by deriving equations that relate this distance to strain and tension in the web. This technique has been used on pilot and commercial paper machines to identify and rectify the cause of disturbances that can lead to web breaks.

ANALYSIS

Breaks occur when web tension exceeds web rupture strength. Tension and variation in tension are difficult to measure on operating paper machines. To overcome this, we have taken an indirect approach based on the following picture of cause and effect.

The primary operating variable in this problem is web draw (stretch, [%]), attained by setting differential roll speeds. In practice, draws are set to provide a suitable tension often well below the average breaking point of the web, to avoid web flutter and instabilities. In addition to

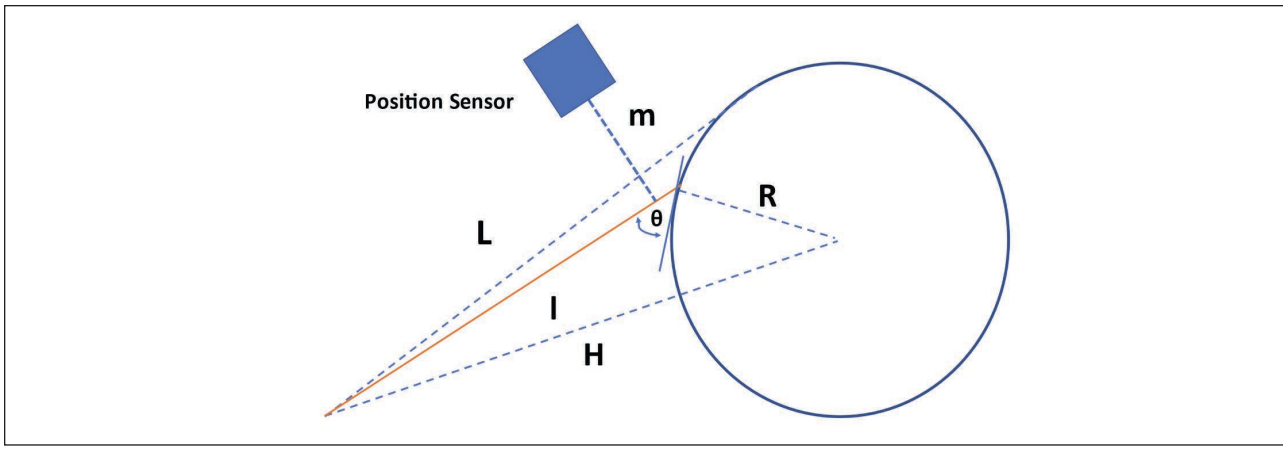

1. A laser position sensor was used to measure the distance to the web in the open draw. The measurement can be used to calculate the release angle, θ, and release point. This configuration is for the open draw between the third and fourth press on the FPInnovations pilot paper machine. The draw length is l, R is the radius of the press roll, H is the distance from the center of the press roll to the next stage, and L is the maximum possible draw length.

draw, tension is governed by the web modulus E and thickness t:

$$T = Et\varepsilon \tag{1}$$

Web tension and work of adhesion, W, set the angle of release, θ, according to the Rifkin equation (first term in Eq. 2). At high speeds, an additional force is required to turn the web at the peel point. This force is determined by the web mass per area, M, and the speed of the machine, V. The resulting peel equation is:

$$T = \frac{W}{1-\cos\theta} + MV^2 \tag{2}$$

For this tension, the web self-positions on the roll to give the required release angle θ in Eq. 2. This release point sets the length of the draw, l, to a fixed-point downstream point (for example, the nip of first dryer), as shown in **Fig. 1**. For the machine speeds considered in this paper, the MV^2 term is second order and was not included in subsequent calculations. Above 2000 m/min, which is higher than that of the fastest machines with an open draw before the dryers, the MV^2 term becomes important and may be a barrier to higher machine speeds.

In typical operation, angle θ is small, and changes in this angle are sufficiently small to be described by derivatives such as $d\theta$ and dT. These can be calculated by measuring the change in distance dm near the release point (Fig. 1).

The change in the release angle expressed in differential form is:

$$d\theta = \frac{-\theta^3}{4W} t(Ed\varepsilon + \varepsilon dE) + \frac{\theta}{2W} dW \tag{3}$$

The effect of $d\theta$ on dT is given by:

$$dT = \frac{-W\sin\theta}{(1-\cos\theta)^2} d\theta + \frac{1}{(1-\cos\theta)} dW \approx \frac{-4W}{\theta^3} d\theta + \frac{2}{\theta^2} dW \tag{4}$$

We note that the previous equations can also be expressed in terms of time derivatives

In this study, angle $d\theta$ is calculated from the measured change in distance of the web near the release point, dm, as shown in Fig 1. The relationship between dm and $d\theta$ is derived in the Appendix:

$$d\theta = \frac{dm}{l[1+\frac{R\theta}{L}]} \tag{5}$$

The sensor and setup employed to measure dm is described in the following section.

EXPERIMENTAL PROGRAM

Measurements of dm were made on the presses of a pilot paper machine and on two commercial machines using a displacement sensor accompanied by measurements of moisture content and draw.

Equipment

Position sensor

The position sensor is a charge coupled device (CCD) long-range laser displacement sensor, the Keyence LK-G150 (Keyence; Osaka, Japan). It has high resolution (0.5 um) and high accuracy (±0.05%). The position sensor is aimed at a fixed point on the web near the release point, as shown in **Fig. 2**.

Portable solids content sensor

Local moisture content was measured with a portable IR sensor (MCA 1420, Fibro System; Stockholm, Sweden). Because its output depends linearly on distance from the web,

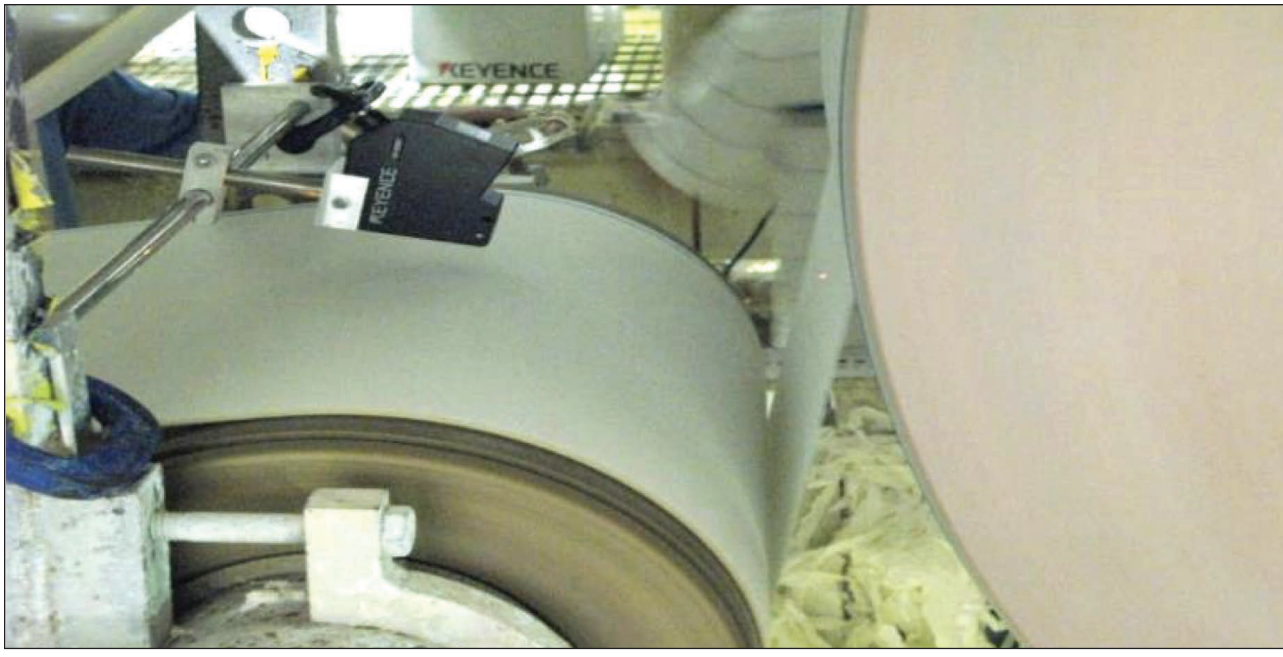

2. The position sensor aimed near the web release point on the third press of the FPInnovations pilot paper machine.



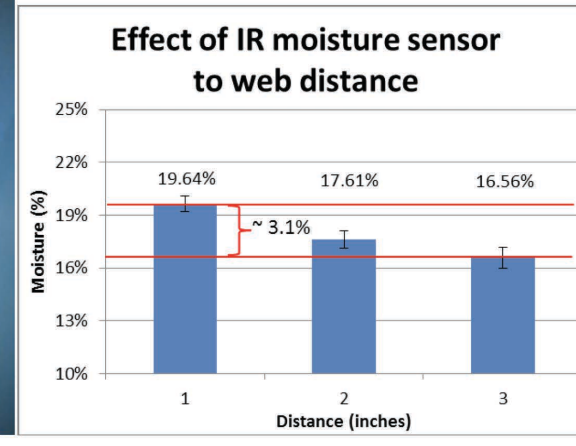

3. Portable infrared moisture sensor positioned in the open draw of a commercial fine paper machine. Shown also is the effect of distance between the sensor and paper surface on moisture measurement.

as shown in **Fig. 3**, it was situated next to the position sensor. Simultaneous measurement of distance and moisture permitted a linear correction to account for changes in distance.

Speed sensor

A contactless laser speed sensor (Beta laser, NDC Technologies; Dayton, OH, USA) based on Doppler frequency shift was used to measure web speed (**Fig. 4**). The speed difference from two sensors before and after a press nip were used to calculate the draw.

Test program

Effect of drive instability: pilot paper machine

This work was carried out on the FPInnovations pilot paper machine, which is described elsewhere [17]. Measurements were made between the third and fourth press during periods of good and poor stability (breaks). **Figure 5** shows the time-varying draw and release point. The two discontinuities in the latter signify breaks. There was little variance in the moistures, but significant variance in the draws. The problem was traced to vacuum fluctuations in the uhle box that caused the speed of the



4. Non-contact laser speed sensor for velocity measurement.

fourth press felt and hence the press to vary.

A frequency analysis shown in **Fig. 6** confirmed that the vacuum fluctuations had the same frequency as the release fluctuations. Once the uhle box problem was corrected, release variations were eliminated and so were breaks, as shown for the good runnability case in Fig. 5.

Effect of drive instability: mill press section

In this case, a fine paper machine experienced breaks in the open draw, but the cause was unclear. Our measurements indicated that moisture content was stable, but there were significant variations in release angle. This suggested draw variations. The source was diagnosed to be the flywheel on the drive after the couch. Replacing this flywheel reduced the release angle variations by 55%, as shown in **Fig. 7**. Consequently, draw variations and web breaks were reduced.

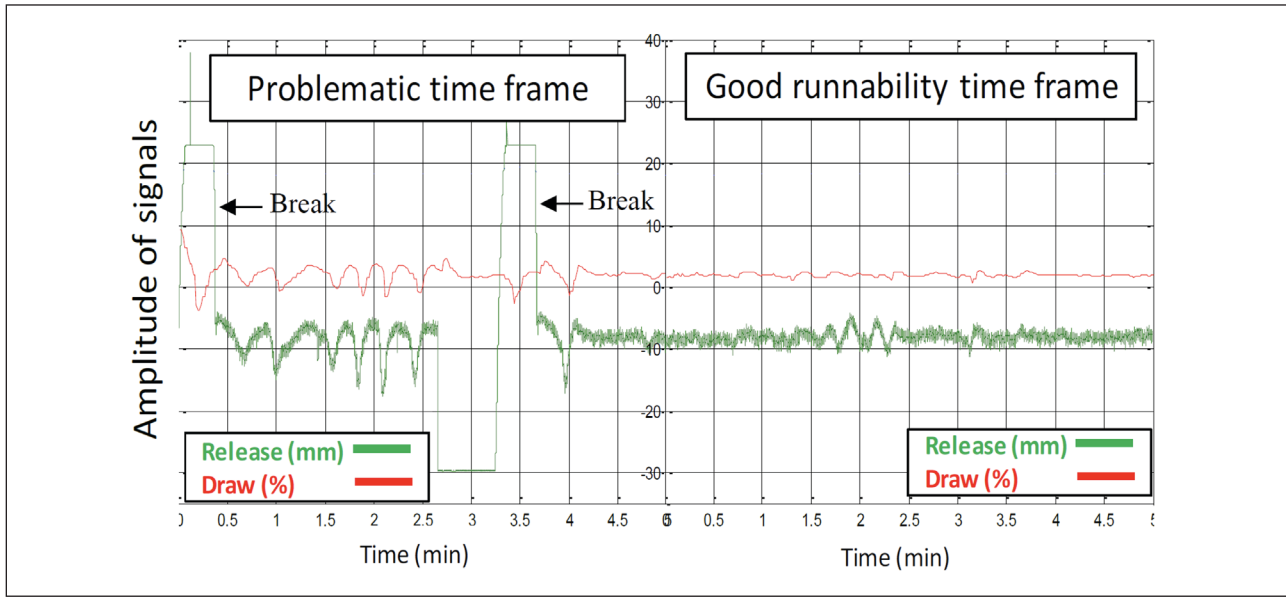

5. Measurements of release point and draw on a pilot paper machine during periods of poor and good runnability.

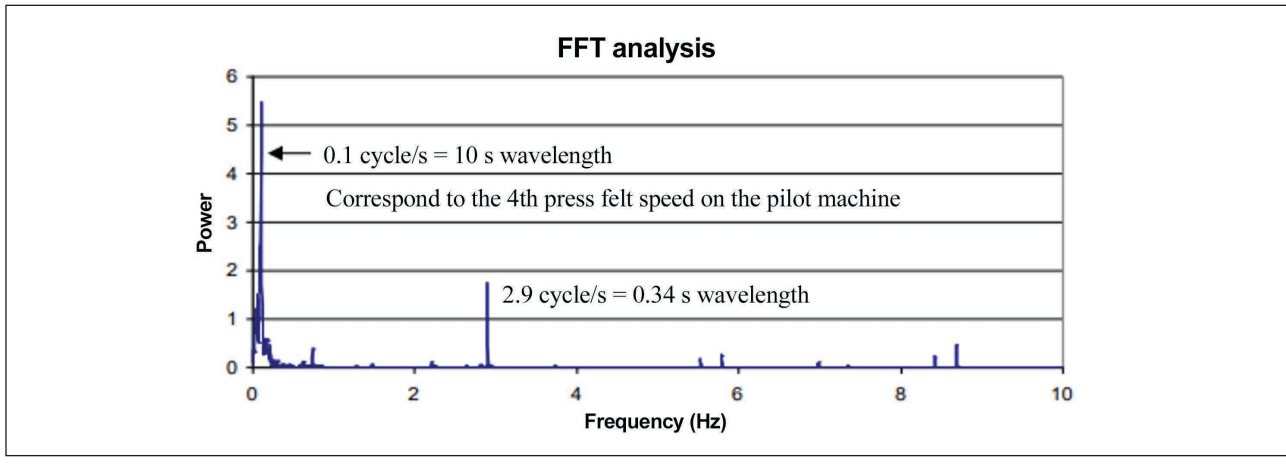

6. Fast Fourier transform (FFT) frequency analysis of release angle measurement shows cyclic variations caused by malfunctioning uhle box.

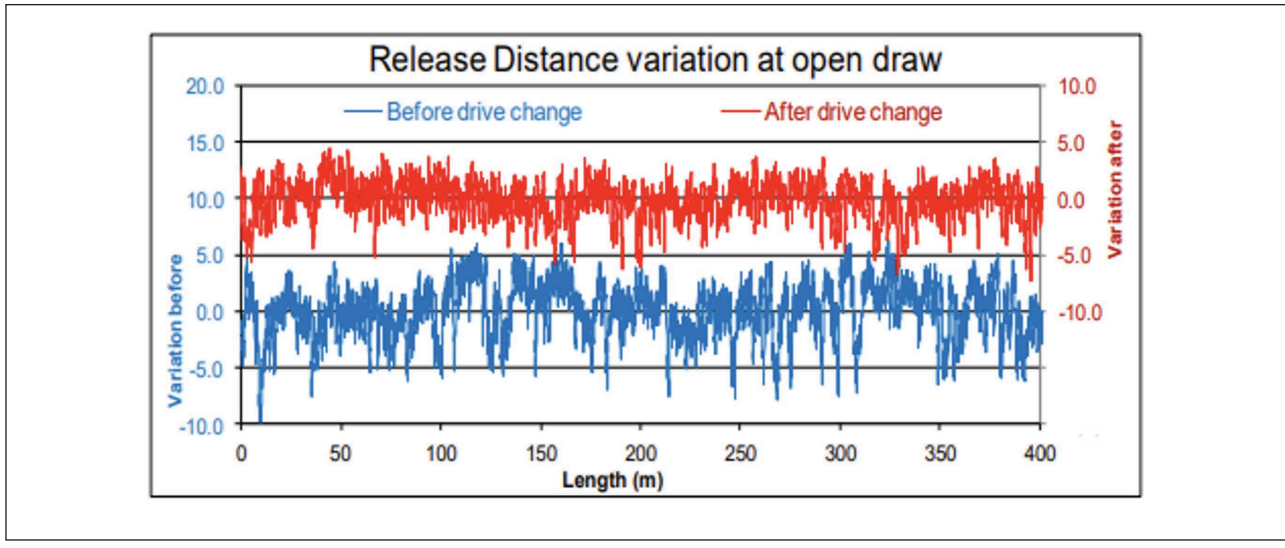

7. Release point variation was reduced after changing the drive flywheel by reducing the drive speed fluctuations.

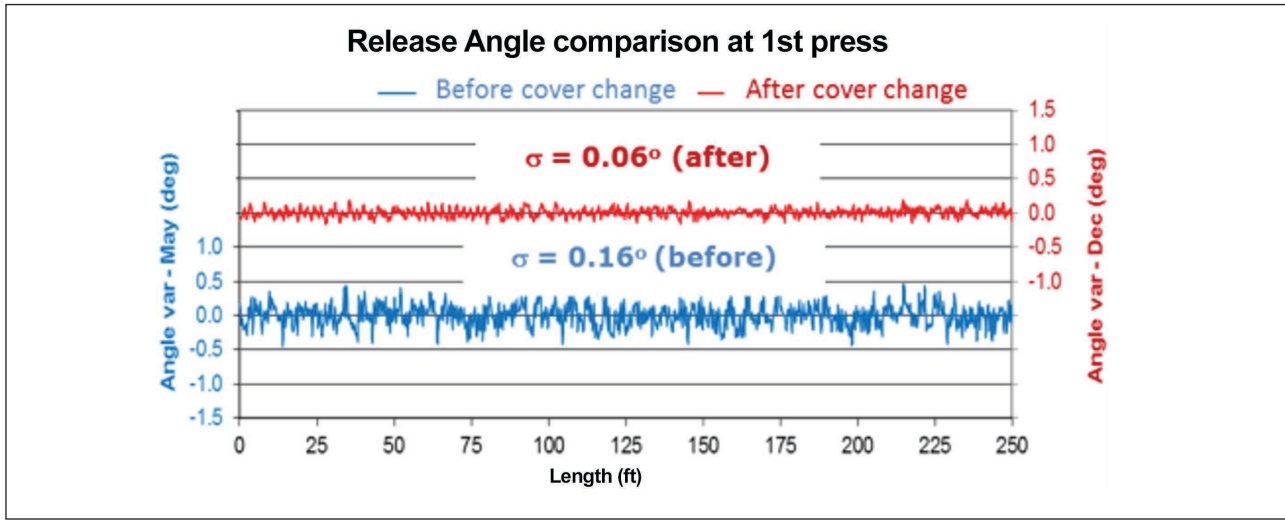

8. Replacing the press roll cover reduced the release angle variation.

Effect of work of adhesion

Work of adhesion, *W*, plays a key role in the link between release angle and tension (Eq. 2). Each roll cover has a unique value of *W* that can change over periods of time as the roll is worn or cleaned.

A fine paper machine was experiencing over 20 breaks per day at the first press open draw. The mill made a number of changes in the wet end, including replacing the cover of the first press roll, which significantly decreased the release angle variation, as shown in **Fig. 8**. There are two possible reasons for this outcome. First, a larger work of adhesion would reduce the release point variation caused by unsteady draw or moisture (first term in Eq. 3). Second, fewer sticky deposits that cause uneven stick/release would also reduce release point variation (second term in Eq. 3). Our measurements did not allow us to distinguish between the two mechanisms.

There was also a small decrease in moisture variability, but this was not correlated with draw variability.

Effect of web modulus of elasticity

Machine direction modulus governs the relationship web between tension and draw. Moisture content is a major factor determining modulus, but the relationship is complex, depending on speed and draw size. Measurements on the fine paper machine shown in **Fig. 9** and **Fig. 10** exhibited no correlation between draw and moisture, perhaps because the moisture changes were too small to produce measurable changes in draw and release angles.

Web moisture will affect machine direction modulus, but determining this relationship is challenging. The modulus of wet webs is speed dependent, and reaching commercial machine speeds in laboratory measurements is difficult. To address this issue, we used tension vs. draw

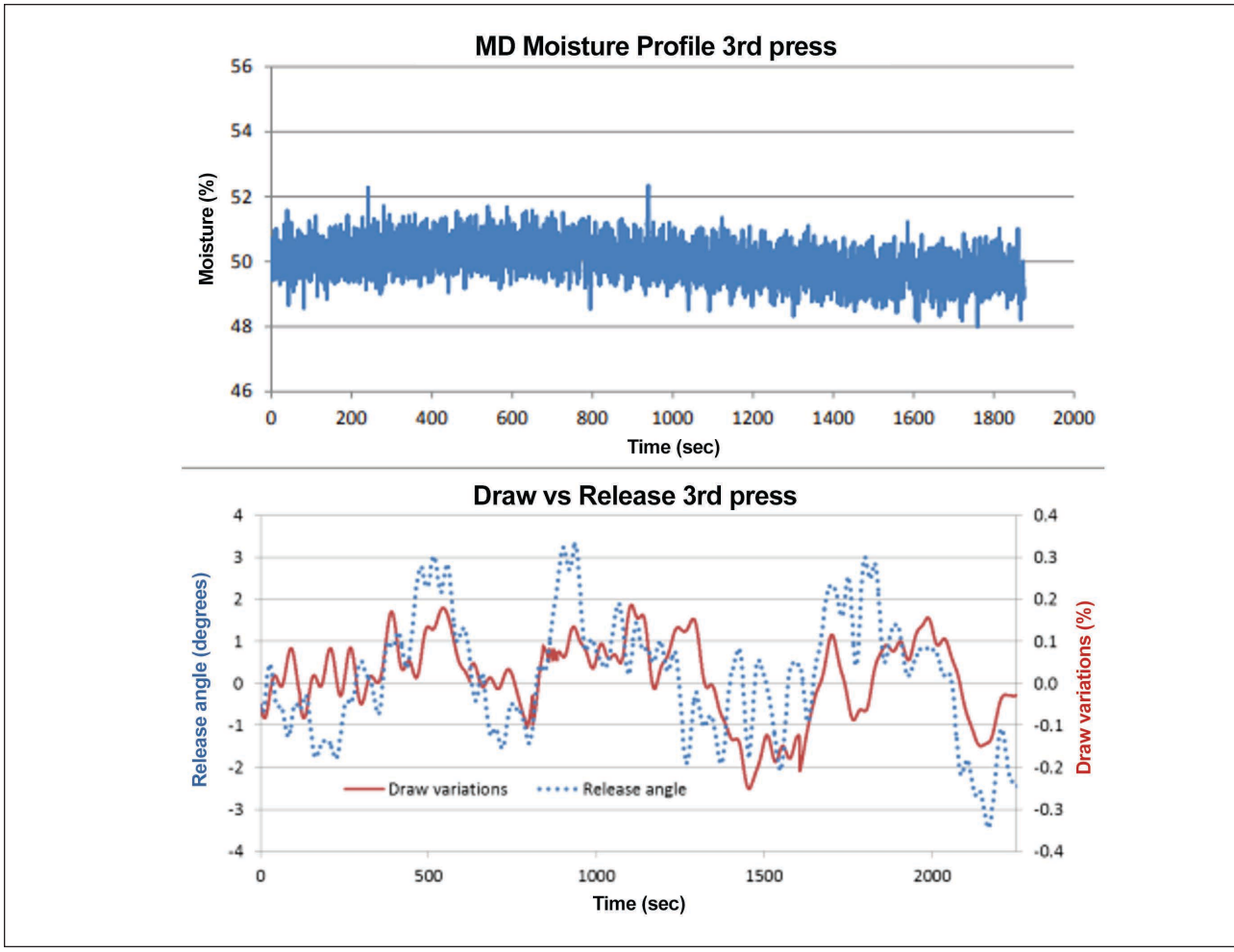

9. Draw and release angle in the open draw after the third press on a fine paper machine. The draw and release angle follow a similar pattern, as expected from Eq. A4 in the Appendix. The variation in machine-direction (MD) moisture does not affect the release angle or draw.

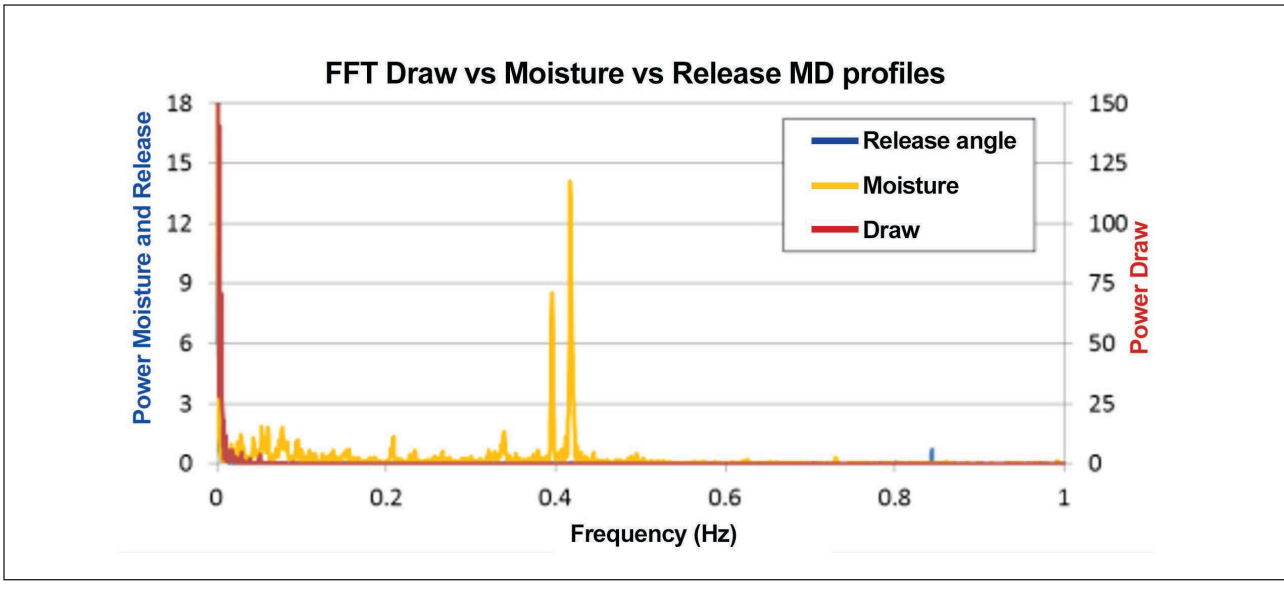

10. Frequency profiles for MD moisture, release angle, and draw after the third press on a fine paper machine. The cyclic variations in moisture do not appear in the release angle or draw.

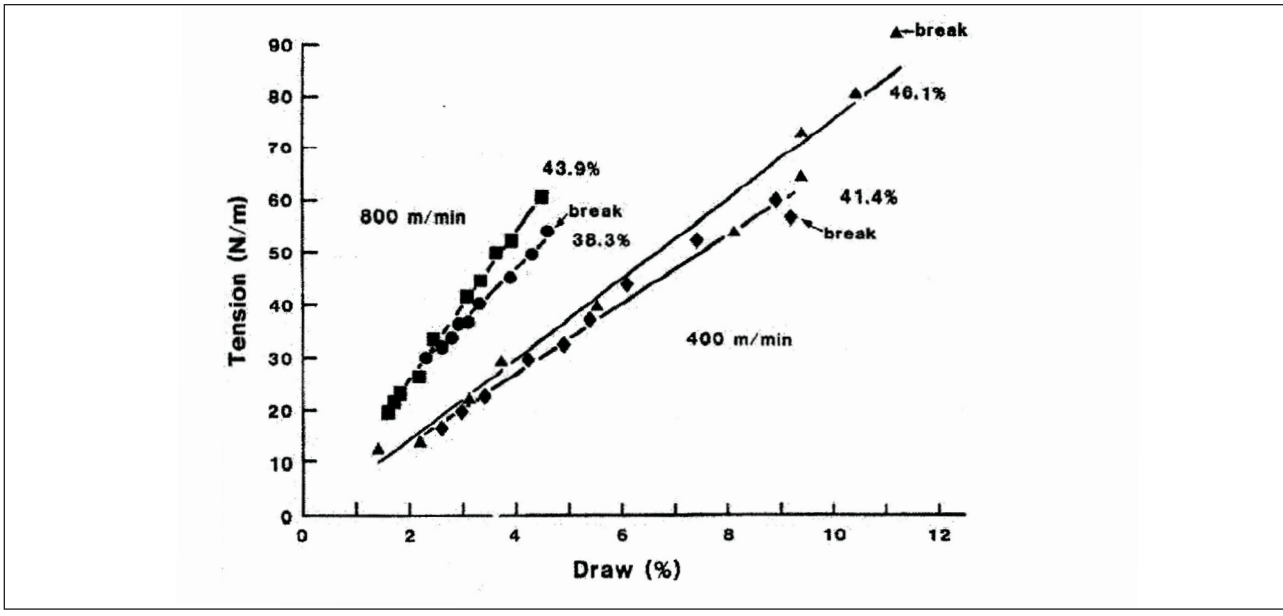

11. Pilot machine measurements of tension and draw for a newsprint furnish [11].

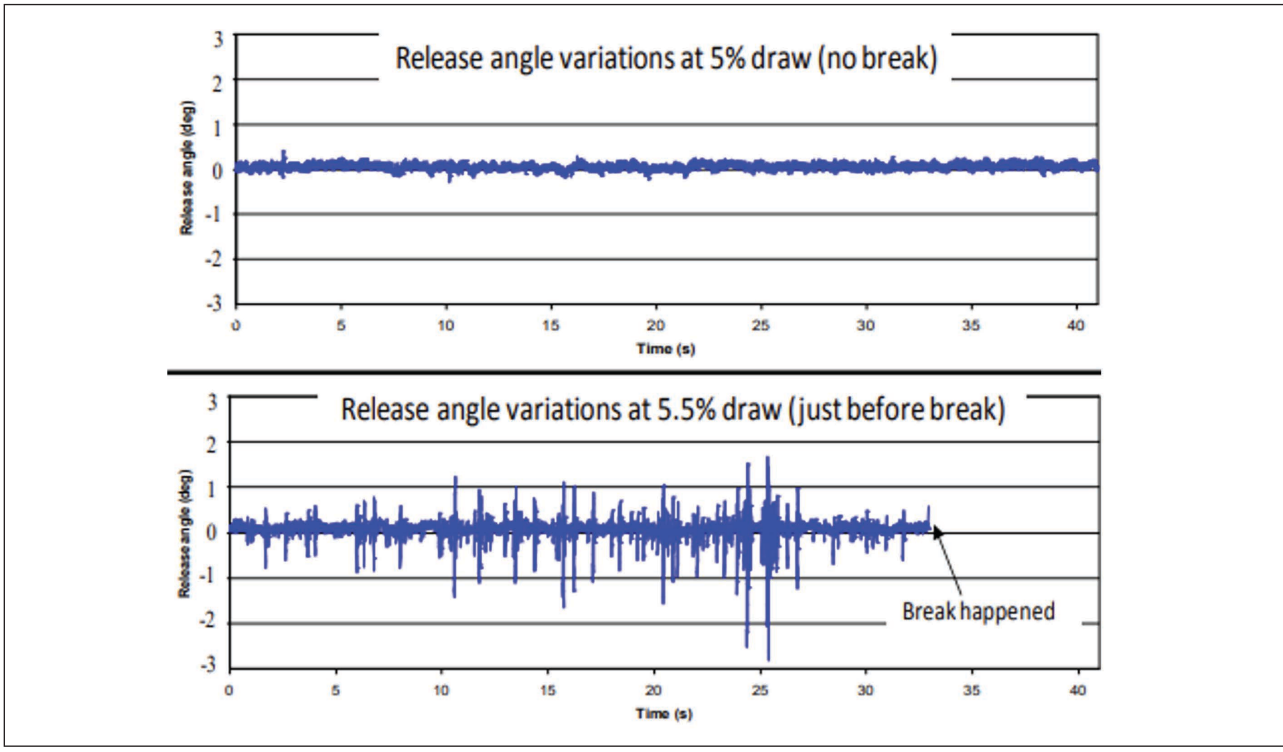

12. Release angle variations in the first open draw on the FPInnovations pilot paper machine increased dramatically when the draw was increased from 5% to 5.5%.

measurements from a pilot paper machine for a newsprint furnish to determine the modulus at several different conditions [11]. As shown in **Fig. 11**, increasing the paper machine speed or increasing the web solids increases the slope of the tension vs. draw lines, which is proportional to the web modulus (Eq. 1).

The relative effect of draw vs. moisture variation on the web tension at 800 m/min is shown in the following calculation. In Fig. 11, the slopes of the tension vs. draw lines are 11.8 N/m and 13.3 N/m for web solids of 38.3% and 43.9%, respectively. Consider a draw of 3.5%, which is safely below the breaking point of the web, at an average moisture of 44%. In Fig. 9, the draw variation is 0.4%, which would cause a tension variation of 5.3 N/m. On the other hand, the moisture variation was 2%, which would cause the tension to change by 1.8 N/m. This means that the ef-

fect of the moisture (modulus) change on draw or release point is below the detection limit of the equipment. This explains why the measured variation in web moisture does not appear as a variation in Figs. 9 and 10. However, potentially larger variations in moisture caused by press barring or by variations in basis weight could cause measurable changes in release point or angle. However, these variations would cause greater problems than draw and tension variations.

Effect of draw

The effect of draw was also studied on the pilot paper machine. As shown in **Fig. 12**, increasing a draw from 5% to 5.5% significantly increased variations in the release angle and thereby tension. This value exceeded the threshold beyond which the draw became unstable and chaotic, displaying aperiodic variations in release point [18]. This higher tension combined with greater variability from the increased draw caused a break.

SUMMARY AND CONCLUSIONS

In the open draw of the press section, variations in draw, moisture content, and roll-web adhesion can lead to web tension instability and breaks. Measurements of the varying distance between the web near the release point and the press roll using a non-contacting sensor were used to calculate variations in release angle. This technique was demonstrated on a pilot machine and two commercial paper machines.

ABOUT THIS PAPER

Cite this article as:
Parent, F., Ricard, D., McDonald, J., et at., *TAPPI J.* 21(5): 271(2022). https://doi.org/10.32964/TJ21.5.271

DOI: https://doi.org/10.32964/TJ21.5.271

ISSN: 0734-1415

Publisher: TAPPI Press

Copyright: ©TAPPI Press 2022

About this journal

Large release angle variations and consequent web breaks were linked to speed-induced draw variations and web-roll adhesion changes resulting from a roll cover change.

This technique shows promise as a new tool to troubleshoot web breaks in the open draw of press sections. **TJ**

LITERATURE CITED

1. Pirinen, T. and Banecki, R., *PaperAge* 1-2: 24(2008).
2. McDonald, J.D., Daunais, R., Pikulik, I.I., et al., *Pulp Pap. Can.* 92(3): 75(1991).
3. McDonald, J.D., Daunais, R., Pikulik, I.I., et al., *TAPPI J.* 80(7): 115(1997).
4. Pikulik, I.I., McDonald, J.D., and Aïtcin, P.C., *Pulp Pap. Can.* 94(4): T108(1993).

ABOUT THE AUTHORS

We studied this topic because web breaks in the press section can have a significant impact on paper machine efficiency. Tension and web adhesion measurements to press rolls on high-speed pilot machines have shown that web breaks in the press section are the result of complicated, non-linear processes. Because web breaks are often infrequent events, monitoring must be done over long time periods to pinpoint the cause.

We discovered that paper machine drive stability and the adhesion of the web to the press roll surface are critical factors. Surprisingly, we found that although web moisture variation affects both paper modulus and strength, it appears to have a minimal effect on the web in the open draw.

For mills, measurement of the release point of the web from the press roll can be used to quantify instability in the open draw and as a tool to identify the source of the problem. This technique is available to help solve wet-end break problems on commercial paper machines.



Parent



Ricard



McDonald



Kerekes

Parent is research engineer and Ricard is senior scientist, Pulp and Paper Innovations Group, at FPInnovations in Pointe-Claire, QC, Canada. McDonald is president, JDMcD Consulting in Vaudreuil-Dorion, QC, Canada. Kerekes is professor emeritus at the University of British Columbia, Pulp and Paper Centre, Vancouver, BC, Canada. Email Parent at frederic.parent@fpinnovations.ca.

5. Thompson, C.B., McDonald, J.D., and Pikulik, I.I., *Pulp Pap. Can.* 98(10): T357(1997).
6. Alastalo, A., Neimo, L., and Paulapuro, H., *TAPPI J.* 82(6): 175(1999).
7. Hättich, T., Häyrynen, P., and Berg, M., *Pap. Puu* 82(6): 393(2000).
8. Ahrens, F., Patterson, T., Mueller, S., et al., *Braz. J. Chem. Eng.* 22(2): 217(2005). https://doi.org/10.1590/S0104-66322005000200008.
9. Osterberg, L., *Sven. Papperstidn.* 65(6): 222(1962).
10. Pye, I.T., Daunais, R., and Batty, R.C., *J. Pulp Pap. Sci.* I(1): J145(1985).
11. McDonald, J.D., Pikulik, I.I., and Daunais, R., *J. Pulp Pap. Sci.* 14(3): J53(1988).
12. Wahren, D., *Tappi* 64(3): 89(1981).
13. Kurki, M., Vestola, J., Martikainen, P., et al., "The effect of web rheology and peeling on web transfer in an open draw," *4th Int. Conf. Web Handling*, Oklahoma State University, Stillwater, OK, USA, 1997.
14. Karlsson, M., Ed., Papermaking Science and Technology. 9 Part 2, Papermaking - Drying, Finnish Paper Engineers' Association/TAPPI, Fapet Oy, Helsinki, 2000, pp. 369-430.
15. Edvardsson, S. and Uesaka, T., "System stability of the open draw section and paper machine runnability," in *Advances in Pulp and Paper Research, Oxford 2009, Trans. of the XIVth Fund. Res. Symp. Oxford*, 2009 (S.J. I'Anson, Ed.), pp. 557-575, FRC, Manchester, 2018.
16. Edvardsson, S. and Uesaka, T., *J. Appl. Mech.* 77(2): 1-1(2010). https://doi.org/10.1115/1.3197425.
17. Pikulik, I., Berry, R., and McDonald, D., *Pulp Pap. Can.* 101(10): 34(2000).
18. Strogatz, S.H., *Nonlinear Dynamics and Chaos*, Perseus Books Publishing, New York, 1994.
19. Rivlin, R.S., *Paint Technol.* 9: 215(1944).

APPENDIX

Relationship between peel angle, release point, and draw length

Variations in peel angle and release point of a web from a press roll are indications of instability in an open draw. Here, we derive the relationship between peel angle and key factors affecting stability, such as draw, moisture content, and web tension. We then relate peel angle to the distance, dm, measured by the technique in this paper.

A generic open draw between a press roll and the next machine component is shown in **Fig. A1**. The radius of the press roll is R, and the distance from the center of the roll to the next machine element is *H*. The draw length is *l* and its maximum, *L*, is tangent to the press roll. As the peel angle increases from zero at the maximum draw length to $\pi/2$ radians at the point where *H* intersects the roll surface, the draw length decreases from *L* to *H-R*. The relationship between release point and release angle can be determined by extending *l* to form a right-angle triangle with a radial line, as shown in Fig. A1.

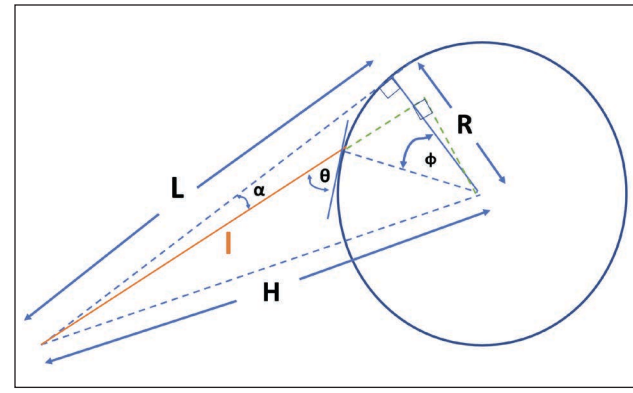

***A1. The draw length* l *is shown in orange. The maximum draw length* L *is tangent to the press roll surface. The distance between the center of the press roll and the downstream nip drawing the web is* H*. The release angle of the web from the roll is* θ.

From geometry, the draw length is:

$$l = H\cos\left[arcsin\left[\frac{R}{H}sin(90-\theta)\right]\right] - Rcos(90-\theta) \quad \text{(A1)}$$

$$l = R\sqrt{\frac{H^2}{R^2} - [cos\theta]^2} + Rsin\theta \quad \text{(A2)}$$

$$dl = Rcos\theta d\theta\left[1 + \frac{sin\theta}{\sqrt{\left(\frac{H^2}{R^2} - [cos\theta]^2\right)}}\right] \quad \text{(A3)}$$

For small peel angles, θ:

$$dl = R\left[1 + \frac{R\theta}{L}\right]d\theta \quad \text{(A4)}$$

The change in draw length is proportional to the change in peel angle and a factor consisting of roll diameter, maximum draw length, and angle of release.

Relationship between sensor measurement distance and peel angle

The sensor measures the change in distance *dm* to the web's surface near the release point.

$$dm = ld\alpha \quad \text{(A5)}$$

$$d\alpha = d\varphi = \frac{dl}{R} \quad \text{(A6)}$$

Substituting Eq. A6 into Eq. A4:

$$dm = l\left[1 + \frac{R\theta}{L}\right]d\theta \quad \text{(A7)}$$

The variation in the measured position of the web is proportional to the variation in peel angle and a factor consisting of the roll radius, maximum draw length, peel angle, and the draw length.

Factors that affect the release angle

In steady-state, the tension in the web is governed by Hooke's law:

$$T = Et\varepsilon \tag{A8}$$

and the Rivlin peel equation [19]:

$$T = \frac{W}{1-\cos\theta} \tag{A9}$$

where T is the tension, E is the machine direction modulus, ε is the strain, W is the work of separation of the web from the press roll surface, t is the thickness of the web, and θ is the separation angle.

For small changes in strain and modulus,

$$dT = t(Ed\varepsilon + \varepsilon dE) \tag{A10}$$

and release angle and work of separation:

$$dT = \frac{-W\sin\theta}{(1-\cos\theta)^2}d\theta + \frac{1}{(1-\cos\theta)}dW \tag{A11}$$

Substituting Eq. A10 into Eq. A11 gives an equation for incremental change in release angle:

$$d\theta = \frac{-(1-\cos\theta)^2}{W\sin\theta}t[Ed\varepsilon + \varepsilon dE] + \frac{(1-\cos\theta)}{W\sin\theta}dW \tag{A12}$$

For small release angles, where the average tension is large and the web is susceptible to breaking, Eq. A12 can be approximated by:

$$d\theta = \frac{-\theta^3}{4W}t[Ed\varepsilon + \varepsilon dE] + \frac{\theta}{2W}dW \tag{A13}$$

This assumes that the tension in the entire open draw changes instantaneously with changes in ε.

The variation of the release angle with time depends on the stability of the drives, the work of adhesion, and the MD modulus of the paper, which in turn depend on web moisture and thickness.

J. E. STONE
and A. M. SCALLAN

The Effect of Component Removal Upon the Porous Structure of the Cell Wall of Wood. II. Swelling in Water and the Fiber Saturation Point

The fiber saturation point is defined as the amount of water contained within the water-saturated cell wall. Previous techniques for the determination of the fiber saturation point of wood and pulp fibers are criticized and it is suggested that the values of about 0.3 g/g frequently quoted in the literature are too low. Two entirely independent methods for finding the true fiber saturation point are presented and the results by both methods are in agreement. The fiber saturation point of air-dried and re-swollen black sprucewood was found to be 0.4 g/g rising to 1.2 g/g as the wood was pulped by the kraft process to progressively lower yields. A method of calculating the relative changes in water-swollen cell wall thickness from changes in the fiber saturation point is given, and the changes brought about by kraft pulping are calculated and discussed in terms of cell wall structure.

Keywords: Cell wall · Cell structure · Cell wall thickness · Data · Fibers · Saturation · Moisture content · Swelling · *Picea* · Softwoods

THE word "swelling" applied to an assemblage of fibers such as wood or wood pulp is very vague. The situation is best discussed with reference to a simple diagram such as Fig. 1, where three fibers are shown lying across one another to form a system in which water can be held in various ways. The walls of the fibers consist of a gel of carbohydrate and lignin that can take up water and thereby increase in volume after the manner of any gel material. Recent work (*1*) has indicated that in the dry state the walls are essentially nonporous and, hence, it follows that in the wet state the walls are swollen above their dry volume by an amount equal to the volume of water that they contain. This volume will be denoted V_c. The fiber walls enclose lumens, which will hold a certain volume of water V_L depending upon the morphology of the fibers and the state of lumen collapse. The external surfaces of fibers, particularly after beating, contain a "pile" of microfibrils that can entrap a volume of water V_F, and finally the interstices between a number of fibers form a capillary system that will hold a volume of water V_I.

Many of the methods used to measure the swelling of pulp fibers actually measure a composite of V_c, V_L, V_F, and V_I. The amount of each included in the quantity of water per gram of fiber depends not only upon the method used but also upon the experimental conditions adopted within the particular method. This is true of the permeability technique for measuring the swollen specific volume, the use of dilatometry for measuring swelling and the determination of the centrifugal water retention value. Consequently, when the total water held by the fiber system is found by these methods to have been increased by a given process, e.g., by beating, it is impossible to determine whether the increase was due to external fibrillation, cell wall swelling, or lumen expansion. It would be extremely useful in the analysis of beating to be able to make such a distinction.

J. E. STONE, Head, Division S., and A. M. SCALLAN, Physical Chemist, Pulp and Paper Research Institute of Canada, 570 St. Johns Rd., Pointe Claire, Quebec, Canada.

As part of a comprehensive and continuing study of the pore structure within the water-swollen cell wall of wood and pulp fibers (*1–4*),[1] it became important to have accurate information on the total amount of water that can be held by the wall; that is to say, the quantity V_c above. Upon examination of the literature, it soon became apparent that the measurement of V_c is by no means straightforward. Methods such as the ones mentioned above, which include water other than cell wall water, cannot be used. The direct approach of making microscopic measurements of cell wall dimensions in the wet and the dry state, although laborious and susceptible to error, has been applied to cotton and viscose (*6*) but has not yet been applied to wood pulp fibers. A method involving the determination of the amount of nonfreezing water at some temperature below 0°C exists (*7*), but the application of this method has been limited and the exact temperature to be employed is uncertain. The nonsolvent water technique using sodium thiosulfate as solute (*8*) is unsuitable because the molecule is both small and an electrolyte. (More will be said about this technique later.)

Our first approach to the solution of the problem was via the so-called "fiber saturation point" (FSP). This is a term introduced by Tiemann (*8*) in 1906 to describe the moisture content of wood when all the water from the gross capillary structure has been removed but no water has been removed from the cell walls. It is a term that has since been extended to other cellulosic fibers. The fiber saturation point is thus effectively V_c, and the term will be used throughout this paper to imply this. In the case of wood, the FSP has been obtained by plotting some property, such as mechanical strength, electrical conductivity, or heat of wetting, against moisture content as the sample is progressively dried, and observing the point of inflexion where water starts to leave the cell wall. The methods and results have been reviewed by Stamm (*9*), and values of about 0.3 g/g are found for many wood species. Another technique for measuring the fiber saturation point, and one that is applicable to all materials regardless of their physical form, is the measurement of the water sorbed by the material at various relative vapor pressures of water. The extrapolation of this water sorption isotherm from the highest relative vapor pressure readily obtainable by a saturated salt solution (0.95) to a relative vapor pressure of unity has been taken as the fiber saturation point (*10*). The results obtained by this method have also been reviewed by Stamm, and again values of about 0.3 g/g have been obtained, not only for wood but also for holocellulose, hemicellulose, lignin, and cotton and wood pulps of various yields, both beaten and unbeaten.

Although the value of 0.3 g/g has been widely quoted for many years, it has become increasingly apparent that it could not be correct. We first suspected this as a result of a study (*3*) of the drying of a bleached spruce sulfite pulp, in which, at various stages of the drying process,

[1] J. E. Stone and A. M. Scallan, unpublished work.

the water that remained was removed by solvent exchange (water to methanol, methanol to pentane) followed by evaporation of the final solvent. When the surface areas of the resulting aerogels were determined by nitrogen adsorption, it was found that the surface area of about 100 m^2/g remained constant down to a moisture content of 1.0 g/g, after which there was a progressive loss of surface down to complete dryness, when the surface area was less than 1 m^2/g. Since by far the greatest part of the 100 m^2/g is associated with surfaces within the cell wall (*3*), the onset of its disappearance during drying must coincide with the onset of water loss from inside the wall. This would therefore suggest an FSP of 1.0 g/g for the pulp studied, as opposed to the literature value of 0.3 g/g. Apart from the low value attributed to the fiber saturation point, we also question its constancy from material to material. As wood is first pulped and then beaten, considerable changes take place in physical properties; one might therefore expect changes in something as fundamental as the amount of water within the cell wall.

In order to clarify the situation, we decided to measure the fiber saturation point using two independent methods. The first method was the water sorption isotherm, which is one used by most previous authors. However, particular attention was paid to the measurement and interpretation of water sorption in the region of high relative vapor pressures. Neglect of this region proved to be the cause of error in most earlier investigations, as the following reasoning and later results will show.

When a water-saturated porous body is progressively equilibrated at a series of lower and lower partial pressures of water vapor, water will evaporate from the pores in order of decreasing size. The relationship between the radius of a pore and the relative vapor pressure at which the pore[2] loses its water is given by the Kelvin equation:

$$\log_e(p/p_0) = \frac{-2\gamma M}{rdRT} \qquad (1)$$

where

p/p_0 = relative vapor pressure
γ = surface tension of water
M = molecular weight of water
r = radius of curvature of the water surface, and also the radius of the capillaries if these are of circular cross section
d = density of water
R = gas constant
T = absolute temperature

If we now consider wood and pulp fibers, the majority of the capillaries fall into two size groups: the lumens and the cell wall pores. These differ in magnitude by a factor of at least 10 but probably more. The smallest lumens are about 5 μ in radius, whereas the largest cell wall pores must certainly be less than 1 μ and probably less than 0.1 μ in radius, considering that the cell wall itself is only a few microns thick. This suggests that there is likely to be a plateau or a point of inflexion in the desorption isotherm corresponding to the size gap between the final emptying of the lumens and the onset of the emptying of the cell wall pores. The moisture content at which this occurs would then be the fiber saturation point. Examination of Table I, in which the values of p/p_0 corresponding to various radii are given, suggests that this plateau or point of inflexion, if it exists, will be found below $p/p_0 = 0.9999$ and possibly above $p/p_0 = 0.9900$. Fortunately, there is now a method by which such high relative vapor pressures of water can be obtained quite readily, and this method, which employs a porous plate, has been adopted for the present study.

In view of the importance of having accurate data available on the swelling of cell wall substance, and the rather serious discrepancy between reported values and those that it was suspected might arise from the present study, it was felt desirable to employ a second and entirely independent method of measurement. The method chosen is based upon a modification of the nonsolvent water technique used by Samuelson to measure the total amount of water in swollen rayon fiber (*11*). In this method, a weighed quantity of fibers of known moisture content is placed in a known amount of a dilute aqueous solution of polymer, with the polymer molecules of such a size that they are too large to enter cell wall pores. From the change in concentration of the polymer solution brought about by the presence of the fibers, it is possible to calculate the amount of water taken up by the cell walls. This method of determining the fiber saturation point is superior to others in that the grosser structure of the sample is not involved, and also because the fibers are immersed in free water when the measurement is made and not partially dried as in most methods. Its limitation is that the concentration changes are usually quite small, and an accurate method of determining concentration must be available. It is also necessary to check that the polymer is chemically inert toward the fibers and is not physically or chemically adsorbed on the surface.

It may be stated that values for the fiber saturation point have been obtained by the two techniques that are in excellent agreement with one another. They are, as suspected, substantially higher than the frequently reported value of 0.3 g/g. Because our primary interest was in the structure of the cell wall of wood and the way in which it changes during conversion to pulp, rather than in the FSP of a specific wood or pulp sample, it was decided to follow the change in FSP during the kraft pulping of sprucewood to a series of progressively lower yields. The results proved to be unexpected and unusually interesting.

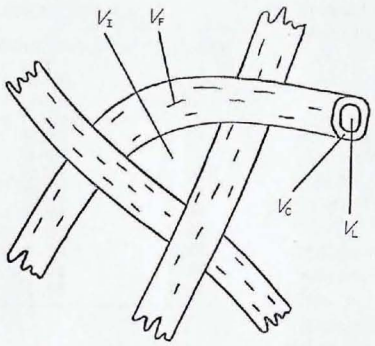

Fig. 1. Ways in which water may be held by fibers.

Table I. Calculations Based on the Kelvin Equation at 25°C

Relative vapor pressure of water, p/p_0	*Effective capillary radius, μ*
0.99999	106
0.9999	10.6
0.999	1.06
0.99	0.106
0.98	0.052
0.95	0.020
0.50	0.0015

EXPERIMENTAL

Preparation of Wood and Pulp Samples

The wood used was air-dried black spruce (*Picea mariana*) in the form of microtome cross sections 100-μ thick and 2 cm^2 in area. When examined as wood (100% yield), the sections were soaked in water for several weeks before use.

Samples of pulp were required also in the form of microtome sections, and these were prepared by subjecting wood microtome sections to a pulping procedure. In order to prevent disintegration during cooking and subsequent washing, the wood sections were placed individually between layers of cotton cloth. This method of cooking microtome sections has been described previously (*12*). The composition of the kraft liquor and the cooking conditions were also the same as reported previously (*12*). The yields and lignin contents are included in Table II. The cooked and washed sections were kept

[2] This is for a pore in a rigid material. Presumably, with a pore in a viscoelastic material like cellulose, which is nonporous (*1*) once it is completely dry, a drop in p/p_0 results in the pore losing some of its water and collapsing to the size in equilibrium with the new relative vapor pressure.

CITE THIS PAPER: Stone, J.E. and Scallan, A.M., *Tappi* 50(10): 496(1967). https://doi.org/10.32964/TJ50.10.496

Table II. Fiber Saturation Point of Kraft Cooked Spruce

Sample	Yield, %	Lignin, %	Fiber saturation point, g/g: Pressure plate[a]	Fiber saturation point, g/g: Nonsolvent water
K0	100	27.0	0.40	0.42
K20	92.4	27.3	0.67	0.70
K35	89.0	27.6	0.74	(0.66)
K50	80.0	28.5	0.86	0.92
K65	77.8	28.2	0.94	0.94
K80	70.4	25.2	1.06	1.08
K95	61.6	19.3	1.16	1.22
K110	53.4	12.3	1.21	1.28
K125	48.7	6.5	1.14	1.21

[a] Water retention at $p/p_0 = 0.9975$ (50 psi).

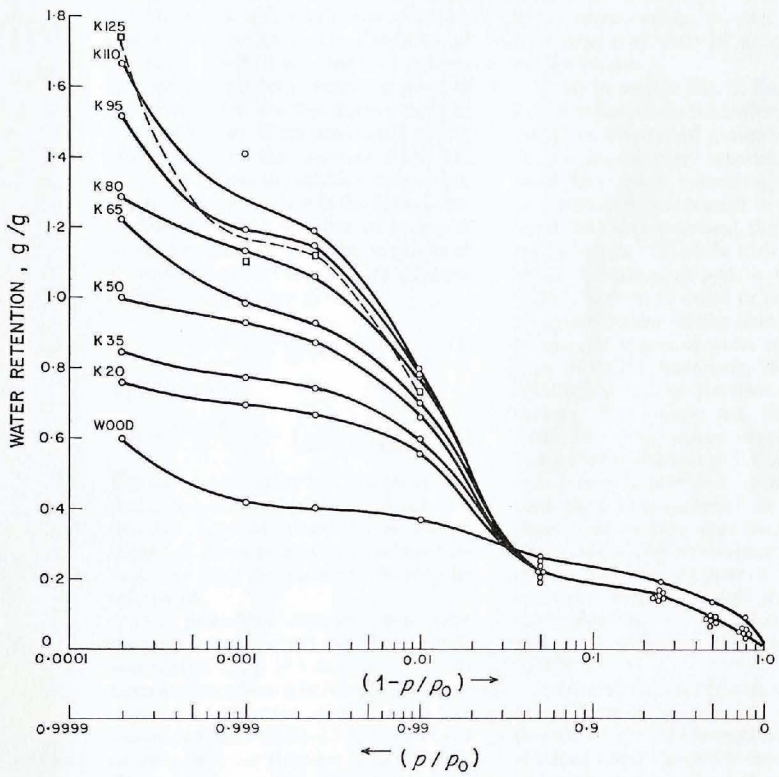

Fig. 2. Water desorption isotherms of wood and kraft cooked microtome cross sections.

immersed in water between the layers of cotton cloth until they were used.

In the nonsolvent water experiments, either microtome sections or ordinary pulp fibers were used because the physical shape of the sample was immaterial.

Fiber Saturation Point from the Desorption Isotherm

The water retained by samples upon desorption to relative vapor pressures in the 0.9999–0.9900 range was determined by the porous plate technique developed for soil moisture studies. This method was first used in studies of pulp fibers by Barkas (*12*) and, more recently, has been used extensively by Robertson (*13*). The procedure consists of placing a wet sample of the material to be tested upon a wet porous ceramic plate[3] and applying a gas pressure above the sample. The gas pressure tends to force the water from the sample through the plate, and is opposed by the surface tension forces of the water within the capillaries of the sample. Where the surface tension force is less than the gas pressure, i.e., in the larger capillaries, the water is forced out of the sample; where the surface tension forces are higher than the gas pressure, i.e., in the smaller capillaries, the water remains within the sample. The relationship between the applied pressure P and the critical radius r is given by

$$P = \frac{2\gamma}{r} \qquad (2)$$

Once equilibrium has been reached, all pores larger than the critical radius calculated from Eq. (2) for a particular pressure will be free of water, and the relative vapor pressure of the gas above the sample will be that calculated from a substitution of the critical radius into Eq. (1). The time to reach equilibrium is usually a matter of days, after which time the pressure is released.

In order to provide as simple and as unambiguous a capillary system as possible, and thereby to increase the chance of obtaining an easily interpretable isotherm, fiber samples in the form of microtomed cross sections were used. Such sections contain no large amount of interfiber pores and the lumens are fully accessible to the receding menisci, which are the bottlenecks represented by the pits eliminated. For each point on the desorption isotherm, duplicate samples, each consisting of ten microtome sections held between the two strips of cotton cloth in which they were cooked, were placed upon the pressure plate. The gas pressure was then applied and the samples were left for at least a week. It had previously been found that the presence of the cotton cloth did not affect the equilibrium moisture content of the samples; however, it did make the sections easier to handle and better contact was made with the plate. Once equilibrium was reached, the pressure was released, the upper strips of cloth were removed from the samples, and the samples were rapidly transferred to weighing bottles and weighed wet and oven dry to give their moisture contents. Sets of samples were treated at 4, 20, 50, and 200 psi, giving four points for each pulp, corresponding to relative vapor pressures of 0.9998, 0.9990, 0.9975, and 0.9900.

In order to measure the amount of water held by a sample at relative vapor pressures below 0.95 (0.95, 0.75, 0.44, and 0.22 were actually used), a sample in the form of one or two very wet microtome sections was placed in the pan of a Cahn recording electro microbalance mounted within a desiccator. The atmosphere within the desiccator was adjusted to $p/p_0 = 0.95$ by placing within the desiccator a vessel containing a saturated solution of potassium nitrate. When the recorder showed that the sample had reached a constant weight (usually in at least 24 hr), the weight was noted and the saturated solution of potassium nitrate was quickly replaced by one of sodium chloride. The procedure was repeated with salt solutions of lower and lower relative vapor pressures, and eventually the dry weight of the sample was determined by replacing the

[3] The actual apparatus used the "15 Bar Ceramic Plate Extractor, Cat. No. 1500," produced by the Soil Moisture Equipment Co., Santa Barbara, Calif.

last salt solution by phosphorus pentoxide. The moisture content at each relative vapor pressure was then calculated and the isotherm plotted.

The Fiber Saturation Point by the Nonsolvent Water Technique

Recent work has shown that the water-soluble molecules of dextran 110[4] are so large that they cannot enter the cell wall pores of kraft cooked black spruce (*5*). If very wet fibers are immersed in a dilute aqueous solution of this material, the water associated with the fibers over and above the fiber saturation point will dilute the solution, whereas the water within the cell wall will not. Thus, if δ_s is the fiber saturation point in grams of water per gram of dry fiber, and if the wet fibers consist of p grams of dry fibers associated with q grams of water, the presence of the wet fibers will dilute the solution by $q - p\delta_s$ grams of water. If c_i is the initial concentration of the solution in grams of solute per gram of solution, w grams of this solution added to the fibers will have a final concentration given by:

$$c_f = \frac{w}{w + (q - \delta_s p)} c_i \qquad (3)$$

or, rearranging

$$\delta_s = \frac{w + q}{p}\left[1 - \left(\frac{w}{w + q}\right)\left(\frac{c_i}{c_f}\right)\right] \qquad (4)$$

Hence, by measuring the change in concentration of a known weight of polymer solution brought about by a known weight of fibers of known moisture content, the fiber saturation point may be calculated.

The procedure followed was very simple. Into a small weighing bottle was placed 1.0 g of wet pulp or microtome sections from a batch of previously determined moisture content. To this was added just sufficient 1% dextran 110 solution to cover the sample (3.5–5.0 g). The mixture was then allowed to stand for 1–3 days with periodic shaking, after which 1 ml of solution was withdrawn with a syringe and injected into the narrow bored 10-cm cell of a Zeiss photoelectric precision polarimeter reading to 0.005°. Previous experiments had shown that the optical rotation was proportional to the concentration of the dextran 110, and, hence, the ratio of the rotation of the stock solution to that of the solution taken from the sample after standing was taken as equal to c_i/c_f. The wavelength used was 436 nm, because of the higher sensitivity at this lower wavelength than at the more conventional wavelength of 578 nm. For each pulp, δ_s was determined at least in duplicate, and the average values are recorded in Table II.

[4] Dextran 110 has a mol. wt. of 110,000 and was obtained from Pharmacia, Uppsala, Sweden.

RESULTS

The complete desorption isotherms for spruce and eight pulps of different yields are shown in Fig. 2. The method of plotting the data requires some explanation. If isotherms are plotted against p/p_0 on a linear scale, the points at high relative vapor pressures are extremely congested, and there is a strong temptation to extrapolate the isotherm to $p/p_0 = 1$, which, as stated earlier, is misleading. A suitable method of plotting the data is to plot water retention against the function $(1 - p/p_0)$ on a logarithmic scale (*14*). The values of p/p_0 corresponding to each value of $1 - p/p_0$ may then be denoted on an extra abscissa.

It can be seen in Fig. 2, that there are indeed inflexions in the isotherms as predicted on theoretical grounds. The inflexions are not very marked in certain cases, but, taken collectively, they can be considered real enough to justify the belief that they represent the fiber saturation points. There is little to choose between readings at $p/p_0 = 0.9999$ and 0.9975, and so, in order to obtain some numerical values for the fiber saturation points, the values of water retention at $p/p_0 = 0.9975$ have been taken somewhat arbitrarily as the fiber saturation points. The values are recorded in Table II. Very strong support for relating these inflexions to the fiber saturation points is provided by the nonsolvent data also recorded in Table II. Here it can be seen that the amount of water inaccessible to dextran 110, which may be taken to be the amount of water contained within the cell wall, is virtually identical with the volume of water associated with the fibers at $p/p_0 = 0.9975$.

Returning to Fig. 1, it is readily apparent from an examination of the isotherms why other investigations have obtained lower values for the fiber saturation point using the water desorption isotherms with data obtained at partial pressures of 0.95 and below. Extrapolation of the isotherms from 0.95 either to 1.00 in a linear plot or to 0.999 in a logarithmic plot will necessarily give low values for the fiber saturation point, because the step in the isotherm above 0.96 is bypassed. Also, because the isotherms for all the pulps regardless of yield follow a very similar path below $p/p_0 = 0.95$, an extrapolation from this value gives a single fiber saturation point for all pulps. It is only by actually measuring the water contents in regions of high partial pressure that valid values can be obtained.

The results in Table II are plotted in Fig. 3, and it is clear that the fiber saturation point is strongly affected by pulping in that it generally increases with decreasing yield. At all yields, the values are much higher than the 0.3 g/g that has been widely quoted. The value of 0.4 g/g for wood has been confirmed recently by others examining Sitka spruce by the nonsolvent water technique (*15*). Values of over 1.0 g/g for low yield pulps have been suggested by Robertson (*15*), although in his work the measurement of water retention at high relative vapor pressures was made on fiber pads. Therefore, because of the presence of interfiber pores in these samples (largely absent in the microtome sections used in the present work), the exact fiber saturation point was somewhat uncertain.

DISCUSSION

The primary purpose of this study was to learn a little more about the interior of the cell wall of water-swollen fibers as lignin and hemicellulose are removed from within it. We recently studied these changes by the N_2 adsorption technique, which showed that the surface area and pore volume increase rapidly as material is removed from sprucewood and reaches a maximum at about 70% yield and drops as the yield is reduced to 50% (*2*). The investigation reported here has shown that the total amount of water in the cell wall increases several fold over this same range of pulp yield; therefore, it is now possible to put together these two sets of data and discuss their meaning in terms of structure.

The first thing that must be appreciated is that as wood is pulped to lower and lower yields, the average weight of a single fiber decreases, so that a gram of pulp contains more and more fibers. For structural studies it is necessary to examine how the quantity of water associated with a fixed number of fibers, rather than with 1 g of pulp, varies with yield. To do this, the fiber saturation point can be multiplied by the yield, and the quantity of water thus obtained is that associated with N fibers, where N is the number of fibers in 1 g of wood. The result is shown in Fig. 4(a). The change in the volume of the solid materials of 1 g of wood can also be calculated as it is pulped: it is 0.667 cm^3 at the start [the reciprocal of dry cell wall density, i.e., 1.5 g/cm^3 (*1*)] and drops to half this value at 50% yield. This change is depicted in Fig. 4(b). Since the water-swollen cell wall is comprised only of solid material plus water, it follows that by adding Fig. 4(a) and Fig. 4(b) we obtain the upper curve in Fig. 4(c), which is the variation with yield in the total cell wall volume of the fibers in 1 g of wood.

Figure 4(c) refers to the volumetric changes in the cell wall of N fibers. Obviously, the volumetric changes in the cell wall of a single fiber follow the same pattern on a reduced scale. How are these volumetric changes reflected in changes in the dimensions of the fiber? It is well known that a fiber stays ap-

 CITE THIS PAPER: Stone, J.E. and Scallan, A.M., *Tappi* 50(10): 496(1967). https://doi.org/10.32964/TJ50.10.496

Table III.

Yield, %	*Total pore volume,[a] FSP in ml/g*	*Macro-pore volume,[b] ml/g*	*Micro-pore volume,[c] ml/g*
100	0.41	0.01	0.40
92.4	0.68	0.04	0.64
89.0	0.70	0.08	0.62
80.0	0.89	0.27	0.62
77.8	0.94	0.33	0.61
70.4	1.07	0.54	0.53
61.6	1.19	0.63	0.56
53.4	1.24	0.55	0.69
48.7	1.17	0.57	0.60

[a] Average of pressure plate and nonsolvent water data Table II.
[b] As measured by nitrogen adsorption (2) with graphical interpolation to permit comparison at the same yield.
[c] The difference between columns 2 and 3.

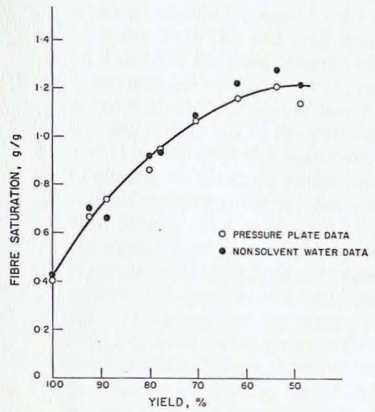

Fig. 3. Fiber saturation point of kraft cooked pulps.

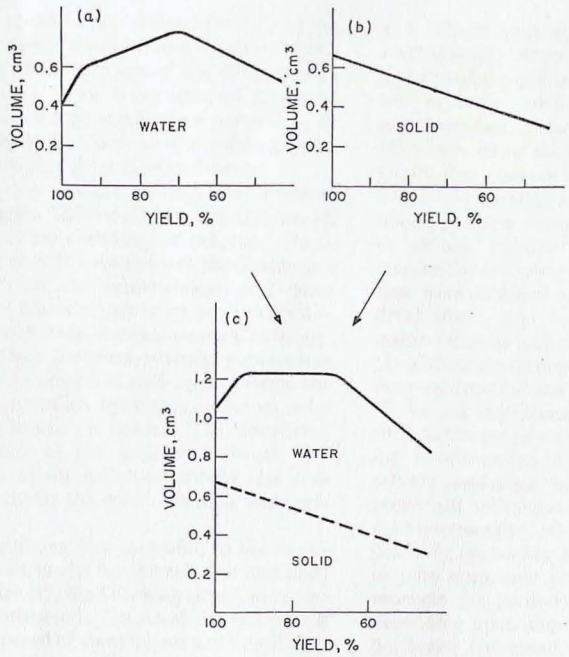

Fig. 4(a). Volume of water in the cell walls of N fibers. (b). Volume of solid in the cell walls of N fibers. (c). Total volume of the cell walls of N fibers.

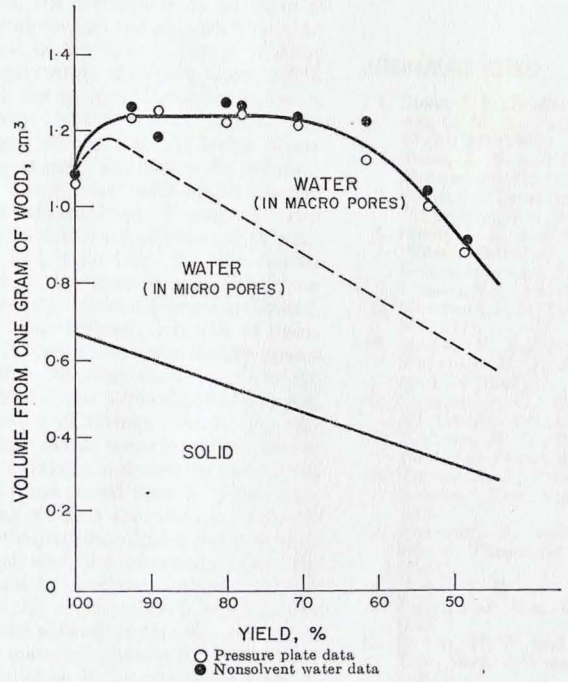

Fig. 5. Volumetric changes brought about by pulping 1 g black spruce by the Ural V process.

proximately the same length throughout the pulping process; therefore, these volumetric changes must be due to changes in cross-sectional area. There are two possible ways this may occur; The first is a change in the diameter of the fiber, and the second is a change in the thickness of the cell wall. Microscopic observations made by us on microtome cross sections revealed that any changes in the cell wall brought about either by drying or by pulping were (where detectable) seen as changes in cell wall thickness. Changes in diameter to account for the same amount of volumetric change would have been readily observed, but they were not. We must therefore conclude that any volumetric changes shown in Fig. 4(c) are to a good approximation directly proportional to changes in thickness of the water-swollen cell wall.

It can be seen that, as the first few percent of wood substance are removed, there is a small but significant rise in cell wall thickness. This may be a general phenomenon or it may be because the wood used for the initial point on the curve had been dried before these experiments, and the simple soaking in water at room temperature that it had received before test was not sufficient to swell the wood to its never-dried state. The samples at lower yields had all received some treatment with warm pulping liquor, which could have returned the cell wall to its original dimensions. It is a matter that needs further study.

The most interesting feature of Fig. 4(c) is the constancy of cell wall thickness from 95% down to 70% yield, which implies that, as solid material is removed from the cell wall, the space previously occupied by the material fills with water, with the volume of the pores created equal to the volume of solid material removed. Below 70% yield, the situation changes and we are no longer dealing

with a porous body of fixed external dimensions being eroded away from inside; instead, the porous body starts to shrink.

Before this discussion is continued, it is necessary to introduce the data derived from the first part of this study (*2*). In that work, the volume of pores within the cell wall was measured by nitrogen adsorption and by mercury intrusion on a series of kraft pulps prepared under similar conditions to those reported in the present work. Since these techniques cannot be applied in the presence of water, the pulps were solvent-exchange-dried from the never-dried state before the determinations. This procedure is commonly thought to remove the water from the cell wall while retaining its water-swollen structure. If this is the case, the pore volume after solvent exchange should be equal to the volume of water that the cell wall contained. In Table III the pore volumes obtained in the first part of this work (*2*) are compared with the volumes of water within the cell wall found in the present work, and it is seen that the pore volumes, as measured by nitrogen adsorption after solvent-exchange drying, are considerably lower. The comparison confirms our recent suspicions of the inadequacy of solvent-exchange drying for preserving exactly the swollen cell wall structure (*4*). In this paper we suggested that only a fraction of the pores in the water-swollen cell wall were retained after solvent-exchange drying, and these were termed macro-reticular pores in the belief that they were larger in size than those collapsed by the procedure (the micro-reticular pores). More recent work confirms their relative sizes (*5*). Let us therefore examine the collected data with these ideas in mind; i.e., that the fiber saturation point (in ml/g) represents the total pore volume, that the pore volume found after solvent exchange represents the volume of larger pores, and that the difference between these two volumes represents the volume of smaller pores.

In Table III it is seen that the micro-reticular pore volume per gram of pulp is fairly independent of yield throughout the kraft cook (apart from wood, but this anomaly has been discussed before). This constancy is interesting but misleading and a better understanding is obtained if the micro-reticular pore volume is multiplied by yield. When this is done the micro-reticular pore volume per fixed number of fibers decreases as the cook proceeds. In Fig. 5 the water in the cell wall has been subdivided into that contained within macro-reticular pores and that contained within micro-reticular pores. From this diagram it is clear that to a first approximation the water within the cell wall of wood fibers is contained wholly within small or micro-reticular pores. As the wood is pulped, larger or macro-reticular pores are progressively created not only at the expense of a volume of solid material but also at the expense of the micro-porous system. This latter concept might be visualized as small pores combining to form larger pores as the solid material separating them is eroded away.

It is possible to link the physical changes outlined above to what is known about the chemistry of pulping. Pulping consists essentially of the dissolution of lignin and hemicellulose, and, since these materials are in an amorphous disordered state, it seems reasonable to suggest that the micro-reticular pore system is to be identified with spaces within the water-swollen lignin-hemicellulose macromolecular network. The disordered portion of the cellulose network (*ca.* 30% of the cellulose) should also contribute to the micro-reticular pore system.

Applying this reasoning to the multilamella model for the cell wall described earlier (*3*), the following situation can be hypothesized. In wood the cell wall is composed of many layers concentric with the cell axis. These layers or lamellas are alternately cellulose-rich and lignin-hemicellulose-rich. In the cellulose-rich layers, the cellulose is in the form of microfibrils and the microfibrils are arranged in the form of sheets. During the early stages of pulping, down to 70% yield, the layers of lignin hemicellulose dissolve away, which reduces the amount of material containing micro-reticular pores and leaves the cellulose-rich layers intact with macro-reticular pores between them. During what may be termed the second phase of pulping, from 70% yield down, the cross-linking effect of the lignin is progressively removed, the cellulose network is released, and, being released, it is able to move. This it does in such a way that the spaces between lamellas start to close up, macro-reticular pore volume is lost, and the cell wall shrinks. As to why the cellulose should move in such a manner that shrinkage is caused as soon as the restrictions placed upon it by the cross-linking of lignin are removed, it can be hypothesized that during the growth of the cell wall, the intussusception of lignin and hemicellulose imposes a strain upon the system, which expands the cellulose network so that the removal of these materials permits the reversion of the cellulose to its strain-free state in which the total volume of the system is smaller.

The usefulness and significance of classifying pores into macro-reticular and micro-reticular may well be questioned in view of the artificial and arbitrary nature of the solvent exchange procedure used for making the division, and the fact that this procedure causes considerable shrinkage, pore loss, and undoubtedly many structural changes within the cell wall. We recognize this, and believe that structural studies of water-swollen fibers should always be performed, if possible, while the fibers are still saturated with water. Our most recent studies, to be published shortly, have been based on this belief and have shown that there is a continuous distribution of pore sizes in water-swollen cellulose, ranging from virtually zero up to several hundred angstroms. Our reasons for including data in this paper that were obtained on solvent exchange dried fibers, and for using the terms macro-reticular and micro-reticular are: (1) to show that solvent exchange drying does *not* preserve the total pore volume; (2) to link the present data with earlier work that used solvent drying for studying water-swollen fibers; (3) because solvent exchange is used for certain important techniques, particularly electron microscopy; (4) because, in a porous body containing a wide distribution of pore sizes, any procedure that will separate the pores into two categories, depending upon their response to some particular treatment, becomes a useful tool for obtaining additional information about the system.

LITERATURE CITED

1. Stone, J. E., Scallan, A. M., and Aberson, G. M. A., *Pulp Paper Mag. Can.* 67 (5): 263 (1966).
2. Stone, J. E. and Scallan, A. M., *J. Polymer Sci. Part C* 11: 13 (1965).
3. Stone, J. E. and Scallan, A. M., *Pulp Paper Mag. Can.* 66 (8): 407 (1965).
4. Stone, J. E. and Scallan, A. M., *In* "Consolidation of the Paper Web," F. Bolam, Ed., Tech. Sect. BP and BMA, London, Vol. 1: 145 (1965).
5. Morehead, F. F., *Textile Res. J.* **17 (2):** 96 (1947).
6. Magne, F. C., Portas, H. J., and Wakeham, H. J., *J. Am. Chem. Soc.* 69: 1896 (1947).
7. Champetier, G., *Compt. Rend.* **195:** 280 (1932); **195:** 499 (1932).
8. Tiemann, H. D., Bull. No. 70 U. S. Dept. Agr. Forest Serv., 1906.
9. Stamm, A. J., "Wood and Cellulose Science," New York, Ronald Press, 1964.
10. Anderson, B. and Samuelson, O., *Svensk Papperstid.* 61 (23): 1001 (1958).
11. Stone, J. E. and Clayton, D. W., *Pulp Paper Mag. Can.* 61 (10): 474 (1960).
12. Barkas, W. W. and Hallan, R., *Proc. Tech. Sect. BP and BMA* **34:** 289 (1953).
13. Robertson, A. A., *Tappi* **48** (10): 568 (1965).
14. Tarkow, H., Feist, W. C., and Southerland, C. F., *Forest Prod. J.* 16(10): 61 (1966).
15. Robertson, A. A., *In* "Consolidation of the Paper Web," F. Bolam, Ed., Tech. Sect. BP and BMA, London, Vol. 1, p. 90 (1965).

RECEIVED March 1, 1967. Revised May 9, 1967. Presented at the 52nd Annual Meeting of the Technical Association of the Pulp and Paper Industry, held in New York, N. Y., Feb. 19–23, 1967.

 CITE THIS PAPER: Stone, J.E. and Scallan, A.M., *Tappi* 50(10): 496(1967). https://doi.org/10.32964/TJ50.10.496

TAPPI JOURNAL
WWW.TAPPI.ORG
THE PAPER AND PACKAGING INDUSTRIES' TECHNICAL RESOURCE
JUNE 2022 | VOL. 21 NO.6



RECOVERY CYCLE **301**
Effects of rings on flow and temperature in lime kilns
Patrick Gareau, Markus Bussmann, Nikolai DeMartini, and Honghi Tran

PAPERMAKING **313**
Water chemistry challenges in pulping and papermaking – fundamentals and practical insights: Part 1: Water chemistry fundamentals and pH
Przemyslaw Pruszynski, Lebo Xu, and Peter W. Hart

PAPERMAKING **327**
Rewet suppression through press felt engineering
Sumner Dudick, Dennis W. Hess, and Victor Breedveld

CELLULOSE **335**
The influence of the fine structure of cellulose on the action of cellulases
Curtis S. Walseth

TAPPI Journal NOW FULLY OPEN ACCESS

June 2022

TABLE OF CONTENTS VOL. 21 NO. 6

297 EDITORIAL
TAPPI's 2022 Nanotechnology Conference convenes in Finland
J.Y. Zhu

301 RECOVERY CYCLE
Effects of rings on flow and temperature in lime kilns
Patrick Gareau, Markus Bussmann, Nikolai DeMartini, and Honghi Tran

313 PAPERMAKING
Pulping and papermaking – fundamentals and practical insights: Part 1: Water chemistry fundamentals and pH
Przemyslaw Pruszynski, Lebo Xu, and Peter W. Hart

327 PAPERMAKING
Rewet suppression through press felt engineering
Sumner Dudick, Dennis W. Hess, and Victor Breedveld

335 CELLULOSE
The influence of the fine structure of cellulose on the action of cellulases
Curtis S. Walseth

»**COVER CREDIT**: Researchers Dudick, Hess, and Breedveld discovered that introducing a stiff spacer to the felt-web interface preserves void volume during pressing (p. 327). This causes water channels that would otherwise span the gap to break, preventing a flow path for rewet. By recording video of their bench-top process, the researchers can show this mechanism in operation.

TAPPI JOURNAL
WWW.TAPPI.ORG

Editor-in-Chief
Douglas W. Coffin coffindw@miamioh.edu
+1 513 529-0771

Associate Editor
Peter W. Hart peter.hart@westrock.com
+1 409 276-3465

Editorial Director
Monica Shaw mshaw@tappi.org
+1 770 367-9534

PRESS Manager
Jana Jensen jjensen@tappi.org
+1 770 209-7242

***TJ* EDITORIAL BOARD**

Brian N. Brogdon, FutureBridge Consulting & Training LLC
brian.brogdon@gmail.com, +1 678 581-9114

Douglas W. Coffin, Miami University
coffindw@miamioh.edu, +1 513 529-0771

Mahendra Doshi, Doshi and Associates
mahen@aol.com, +1 920 832-9101

Marc Foulger, Valmet
marc.foulger@valmet.com +1 315 767-2920

Peter W. Hart, WestRock
peter.hart@westrock.com, +1 409 276-3465

Carl J. Houtman, USDA Forest Products Laboratory
choutman@fs.fed.us, + 1 608 231-9445

Vamsi Jasti, Ahlstrom-Munksjo Nonwovens LLC
jvamsik1@gmail.com, +1 818 585-3524

Lucian Lucia, North Carolina State University
lucian.lucia@gmail.com, +1 919 889-7059

John A. Neun, John A. Neun LLC
john.neun@gmail.com, +1 518 275-8139

Jim Niemiec, Jim Niemiec Consulting LLC
jim.niemiec@outlook.com, +1 715 213-4766

Steven P. Ottone, Omya
steven.ottone@omya.com, +1 919 641-7854

Gaurav Pranami, Imbed Biosciences
gpranami@imbedbio.com, +1 515 230-7005

Arthur Ragauskas, Oak Ridge National Laboratory
aragausk@utk.edu

Seshadri Ramkumar, Texas Tech University
S.Ramkumar@ttu.edu, +1 806 742-4567

Gregg Reed, Imerys
gregg.reed@imerys.com, +1 478 553-5747

Gerard J.F. Ring, University of Wisconsin—Stevens Point
gerrryring@wi-net.com, +1 715 592-3732

Scott Rosencrance, Kemira Chemicals
scott.rosencrance@kemira.com, +1 770 429-2753

Paul Wiegand, NCASI
pwiegand@ncasi.org, +1 919 941-6417

Junyong Zhu, USDA Forest Products Laboratory
jzhu@fs.fed.us, +1 608 231-9520

Join TAPPI *today!*

TAPPI JOURNAL is a free benefit of TAPPI membership, and is only available to members. To join TAPPI, to renew your TAPPI Membership, or to learn about other valuable benefits, visit www.tappi.org.

TAPPI, 15 Technology Parkway S., Suite 115, Peachtree Corners, GA 30092, publishes *TAPPI JOURNAL* monthly.

ATTENTION PROSPECTIVE AUTHORS: All papers published are subject to *TAPPI JOURNAL's* peer-review process. Not all papers accepted for review will be published. Before submitting, check complete author guidelines at http://www.tappi.org/s_tappi/doc.asp?CID=100&DID=552877.

Statements of fact and opinions expressed are those of individual authors. TAPPI assumes no responsibility for such statements and opinions. TAPPI does not intend such statements and opinions or construe them as a solicitation of or suggestion for any agreed-upon course of conduct or concerted action of any sort.

Copyright 2022 by TAPPI, all rights reserved. For copyright permission to photocopy pages from this publication for internal or personal use, contact Copyright Clearance Center, Inc. (CCC) via their website: www.copyright.com. If you have questions about the copyright permission request process, please contact CCC by phone at +1 978 750-8400. To obtain copyright permission to use excerpts from this publication in another published work, send your specific request in writing to Editor, TAPPI JOURNAL, 15 Technology Parkway S., Suite 115, Peachtree Corners, GA 30092, USA; or by fax to +1 770 446-6947. Send address changes to TAPPI, 15 Technology Parkway S., Suite 115, Peachtree Corners, GA 30092, USA; Telephone +1 770 446-1400, or FAX +1 770 446-6947. www.tappi.org

Editorial

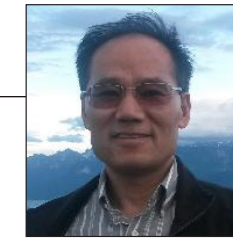

J.Y. ZHU
TAPPI Journal
Editorial Board

TAPPI's 2022 Nanotechnology Conference convenes in Finland

TAPPI's International Conference on Nanotechnology for Renewable Materials was finally held in person this past June 13-17 in Helsinki, and more than 200 attendees gathered to participate in the 36-session program. A total of 24 countries were represented at the event and more than one-third of attendees were first-time participants.

I personally enjoyed the conference very much in terms of the venue, technical content, and other activities. I had a great time thanks to the technical program committee, local organizing committee, and of course the excellent support from our great TAPPI staff. I heard similar comments from many attendees. In this column, I'd like to review some highlights from the event.



There were more than 200 attendees at TAPPI's International Conference on Nanotechnology for Renewable Materials that was held June 13-17 in Helsinki.

VTT/ Aalto University tour

The Monday, June 13, tour of VTT and Aalto University was outstanding. We visited the new VTT facility (away from their Otaniemi main campus, Espoo) dedicated to biomass utilization, specifically for producing textile fibers, cellulose nanomaterials, and biofuels. The facility is newly established, especially their scale-up cellulose nanofibers (CNF) production facility. VTT is now able to accomplish two things: (1) high solids (30%) CNF (most likely microfibrillated cellulose [MFC]) production using high solids endoglucanase treatment of bleached pulp fibers, and (2) continuous MFC film production. The work is very impressive. I had the opportunity to discuss in detail with their CNF production manager, Panu Lahtinen, about potential collaboration in producing lignin containing CNF, as I have known him for several years since the last TAPPI nanotechnology conference in Helsinki.

We then visited Aalto University (originally called HUT or TKK) for lunch. This was my first visit since I left Aalto in 2016 for my Fulbright program. There have been many changes at Aalto. First of all, the Metro is completed and operational, and it is very convenient to get to Aalto from downtown Helsinki. The new School of Art, Design, and Architecture has finally moved into a new building on the Otaniemi campus (next to the Metro). The new building was designed by Aino and Alvar Aalto themselves. Also, renovation of the Dipoli Event and Conference Facilities is now complete. There is still a lot of construction going on within the campus, and there are many more new buildings next to the campus for housing startup companies. After lunch, we visited the textile lab at the School of

Art, Design, and Architecture. To see how different pattens were made in weaving machines was really fascinating. I have not seen this type of machine since the one my mom used when I was a child.

We also quickly visited the ion cell pilot plant in the Department of Bioproducts and Biosystems, which had been renovated after I left in 2016. The Ioncell process was developed by retired Professor Herbert Sixta, the host of my Fulbright program at Aalto. The process uses ionic liquid developed by Professor Ilkka Kilpeläinen at the University of Helsinki to solubilize cellulose for production of textile fibers. The ionic liquid is very robust and can solubilize thermomechanical pulp (TMP) and old newspapers without delignification. The spun fibers have excellent properties. Professors Sixta and Kilpeläinen were selected as the winner of the 2022 Marcus Wallenberg Award for this work.

Conference sessions

The International Conference on Nanotechnology for Renewable Materials had three parallel tracks, and all were well attended. As a matter of fact, two session rooms were a bit smaller and were always crowded. My session attendances were mainly in cellulose nanomaterials (CNM) production and utilization for papermaking. I found that there have been significant advances in these areas. Below are specific observations:

- There were several papers on ***high solids CNF (or MFC) production through enzymatic treatment*** from VTT, the University of British Columbia, and others. I believe that high solids production can remove one major barrier for CNF transportation and application in composites.
- It appears ***barrier coating using MFC*** has made its way into commercial products. Marc Foulger of Valmet presented their newly designed surface coating applicator for installation on a commercial paper machine.
- Empa presented that ***coating fruits with CNF*** significantly improves their freshness, especially bananas. This is a very interesting application for CNM. A similar application was presented by Washington State University to use CNF coating for preventing on-tree damage from frost/freezing.
- The ***student rapid fire session*** was really fired up. Each student was given 5 minutes (including Q&A) to summarize their poster. I really enjoyed this session and chose certain posters to visit for specific questions afterwards.
- The ***plenary sessions*** by special guests were well attended.
- The food and drinks provided for breaks and lunches were very good for networking, and the conference banquet was outstanding, with dancing after the awards ceremony.

According to TAPPI, the most attended presentations included:

- Session 2: Paper & Packaging — "Cellulose-based biofoam for temperature-controlled packaging" — ***Xiao Zhang, Washington State University***
- Session 5: Paper & Packaging — "Cellulose nanofiber coatings for food packaging applications" — ***Gilberto Siqueira, Empa***
- Session 20: Renewable Production — "Methods to produce dry nanoscale cellulose nanocrystal powders: Challenges and opportunities" — ***Douglas Gardner, University of Maine***

Upcoming nano activities

On Tuesday, June 28, from 9:00 am to 10:00 am (ET), TAPPI will host a free webinar on "*Cellulose nanocrystals in cementitious systems – Pilot and commercial scale*" from Sean McAlpine. McAlpine is chief technical officer for Blue Goose Biorefineries Inc., a manufacturer of cellulose nanocrystals. He will discuss what improvements the addition of cellulose nanocrystals (CNC) to cementitious systems have made on a number of fresh and hardened properties.

Previous work has reported benefits from CNC use in cementitious systems that include improved strength, viscosity, and barrier properties. These improvements can provide fundamental improvements in the performance of concrete structures, while decreasing their carbon footprint. **TJ**

J.Y. Zhu is a member of the TAPPI Journal *Editorial Board and is research general engineer at the USDA Forest Products Laboratory in Madison, WI, USA.*

Effects of rings on flow and temperature in lime kilns

PATRICK GAREAU, MARKUS BUSSMANN, NIKOLAI DEMARTINI, AND HONGHI TRAN

ABSTRACT: A steady state, two-dimensional (2D) axisymmetric model has been developed to help understand how rings form and grow in a typical lime kiln. Rings of varying length, thickness, and geometry at the front and back faces were modeled to study the effects on flue gas flow and temperature.

The results show that ring growth causes the gas velocity to increase and insulates the adjacent refractory, resulting in a lower kiln shell temperature. The results also reveal the formation of recirculation zones immediately downstream of the rings, as well as temperature deviations upstream and downstream of the rings that might promote recarbonation and further ring growth. The model was applied to a kiln from a kraft mill with front-end and mid-kiln rings and good agreement was obtained between the measured and predicted kiln shell temperatures, providing confidence in the modeling.

Application: A lime kiln model has been developed to predict how gas flow and kiln temperatures respond to the presence of ring deposits and may provide insights into how rings form and grow.

Ring formation is a common problem in lime kiln operation. Rings can impact the ability of lime kilns to operate continuously and meet mill demands for lime recovery. Ideally, a kiln will operate for at least a year between shutdowns for maintenance. However, in extreme cases, rapid ring formation can lead to a costly unplanned shutdown in less than a month from a clean start. Moreover, rings can have undesired effects related to gas flow, temperature, combustion, dusting, product quality, and production capacity [1,2].

Rings can form in the cold end of the kiln (often called mud rings); middle of the kiln (mid-kiln rings); and in the hot end (front-end rings). Several factors are known to promote ringing in the different regions of a lime kiln, including high soda and high moisture content in the lime mud feed, the burning of high sulfur-containing fuels, poor flame characteristics, low feed-end temperatures, and unstable kiln operation [2]. Of these, high soda content and unstable kiln operations are often considered the most important [1].

Mid-kiln ring formation is thought to begin with particle adhesion on the exposed refractory surface, which makes a soft lime (calcium oxide; CaO) layer that subsequently becomes hard upon reacting with carbon dioxide (CO_2) in the flue gas [1]. Ring hardening through recarbonation of lime ($CaO + CO_2 \rightarrow CaCO_3$) is known to occur when temperatures drop to below ~800°C. The high sodium content in the lime mud promotes the adhesion of particles to the kiln wall, since sodium compounds, mainly sodium carbonate (Na_2CO_3) and sodium sulfate (Na_2SO_4), melt at around 800°C. Temperature fluctuations in the kiln can then cause the adhered lime to recarbonate and form a harder deposit that is not easily eroded by the tumbling motion of the bed, leading to the initial formation of a stable ring. Each newly adhered layer will insulate the existing layer, driving the recarbonation reaction and promoting further ring growth.

Despite this earlier research, ring growth is still not fully understood, because it is difficult to examine ring formation and measure local conditions in an operating kiln. Simulations are a more practical option for studying local conditions. Computational fluid dynamics (CFD) can be used to model and predict gas flow and heat transfer within a kiln. It has been used extensively over the years for improving the design and operation of rotary kilns with promising results (e.g., [3,4]), although it has never been used to study the effects of rings.

In this work, we use CFD to predict flue gas flow and temperatures inside lime kilns with rings as a function of ring length and thickness, ring location, and ring geometry at the front and back faces. The computational methodology is presented first, followed by the model validation against shell temperature measurements of an actual kiln, and finally results are given on the effect of the various ring geometry parameters.

COMPUTATIONAL METHODOLOGY

A steady state, two-dimensional (2D) axisymmetric lime kiln and ring model has been developed to characterize a typical kiln. The trademarked commercial CFD software ANSYS Fluent (Ansys; Canonsburg, PA, USA) was used to run the simulations. The realizable k-ε model, a non-premixed combustion model, and a discrete ordinates model were used to model turbulence, combustion, and radiation,

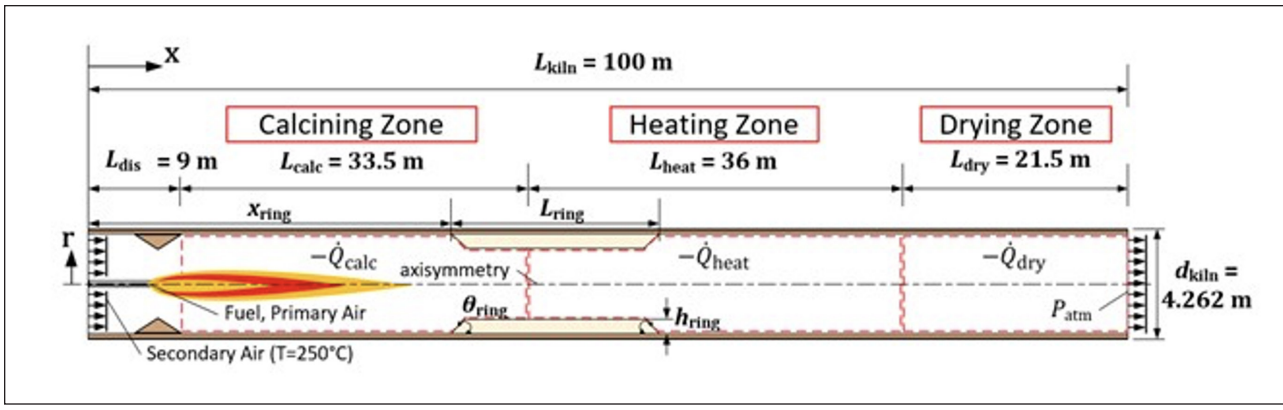

1. Model geometry and boundary conditions.

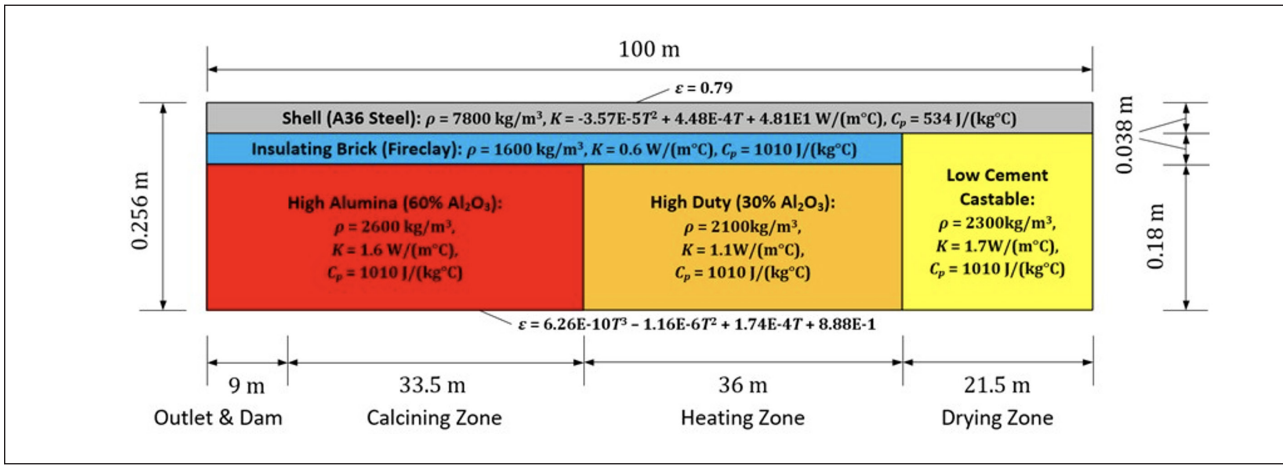

2. Model refractory and shell configuration.

respectively. The bed geometry and flow are not modeled due to the 2D axisymmetric geometry, although a bed heat sink model was developed to account for the drying, heating, and calcining of lime. A simple model was developed to describe ring composition based solely on temperature. Since rings grow relatively slowly, any part of the ring above/below the recarbonation temperature, 800°C, is assumed to be calcium oxide/calcium carbonate ($CaO/CaCO_3$), respectively, which in turn affects the density and thermal conductivity of the ring. The governing equations are discretized in Fluent with the PRESTO! (PREssure STaggering Option) scheme for pressure and second order upwinding for all other equations. A pressure-based solver and coupled pressure-velocity coupling scheme were used to solve the equations. See [5] for detailed solver theory.

The geometry and boundary conditions of the modeled kiln are shown in **Fig. 1**. A concentric methane (CH_4) burner is assumed for simplicity, with separate inlets for fuel, primary air, and heated secondary air. Although the bed is not modeled, a discharge dam is present to account for its effects on gas flow. The kiln interior is divided into four zones where drying, heating, calcining, and discharging of the bed take place; the lengths of these zones were determined based on values in literature [6]. The bed heat sink model prescribes average heat losses in each of the first three zones (approximately 7.63, 5.56, and 15.33 MW, respectively), based on kiln operating conditions and a global conservation of energy analysis. Although the total heat losses are assumed constant in each simulation, their distribution changes due to the rings. The geometry of a ring is described by the four variables illustrated in Fig. 1: ring starting position, x_{ring}; ring length, L_{ring}; ring thickness, h_{ring}; and the geometry of the ring front and back faces, as characterized by the angle, θ_{ring}. Ring thickness was varied from 25.1 to 93.8 cm (corresponding to reductions of cross-sectional area of 25% to 75%). The geometry at the front and back of a ring was varied by considering angles from 15° to 75°. The combined heat loss by mixed convection and radiation to the surroundings was modeled by imposing thermal boundary conditions on the shell exterior.

The simplified double brick refractory and shell configuration is illustrated in **Fig. 2**, and is based on a typical layout given in [6]. The operating conditions of the modeled kiln are listed in **Table I**.

The following material properties were assumed for the ring: for density, ρ_{CaO} = 1512 kg/m³, ρ_{CaCO_3} = 2700 kg/m³; for specific heat capacity, $C_{p,CaO} = C_{p,CaCO_3}$ = 1000 J/(kg°C); for thermal conductivity, K_{CaO} = 3.46E-7T^2 -1.00E-3T +1.48

Operating Conditions	
Capacity	350 metric tons of CaO/day
Fuel type	CH_4
Excess O_2	2.9%
Primary air ratio	15%
Mean gas outlet temperature	275 ± 10°C
CaO = calcium oxide; CH_4 = methane; O_2 = oxygen.	

I. Modeled kiln operating conditions.

W/(m°C) [7], $K_{CaCO_3} = 0.33 + 672.36/(301+T)$ W/(m°C) [7]; and for emissivity, $\varepsilon_{CaO} = \varepsilon_{CaCO_3} = 5.45E\text{-}7T^2 - 1.18E\text{-}3T + 1.01$ [8]. Additional geometry, boundary conditions, and other modeling details can be found in [9].

RESULTS AND DISCUSSION

Model validation

Figure 3 shows results of a model validation, comparing predicted kiln shell temperatures to those of a kiln at a kraft mill operated by one of the companies that supported this research [10]. The real shell temperature data was measured with an infrared scanner prior to shutdown of the kiln for ring removal. The kiln has a length of approximately 100 m, outer diameter of 3.3 m, and lime capacity of 236 metric tons/day.

The geometry of the mid-kiln ring was approximated based on available sketches by the mill. No information on the smaller front-end ring was available, and so it was not modeled. Overall, the agreement between the predicted and measured kiln shell temperatures is very good. For the most part, the predicted shell temperatures are within 25°C, 35°C, and 40°C of the measured values in the calcining, heating, and drying zones, respectively. Where the unmodeled front-end ring is situated, the shell temperature is overpredicted by ~45°C. Along the mid-kiln ring, the shell temperature is somewhat underpredicted. There could be several reasons for this, including the simplified ring modeling, ring geometry approximation, assumed material properties, thermal boundary conditions imposed, and 2D axisymmetric limitations. Despite the modeling simplifications, the trends in temperature are reasonably well captured, the shell temperature is overall well predicted, and as a result, the model was considered validated.

Effect of ring thickness

To assess the impact of ring geometry and location on gas flow and heat transfer, rings were characterized by prescribing the four variables shown earlier in Fig. 1; namely, the ring starting position, x_{ring}; ring length, L_{ring}; ring thickness, h_{ring}; and the geometry of the ring front and back faces, as characterized by the angle, θ_{ring}. In this section, the effect of thickness of a mid-kiln ring is studied. It is assumed that the mid-kiln ring starts at a location 35 m from the front end (x_{ring} = 35 m) and has a length L_{ring} = 20 m. The θ_{ring} is set to 45°. The ring thickness, h_{ring}, is varied between 25.1, 54.9, and 93.8 cm, corresponding to kiln interior cross-sectional area reductions (A.R.) of 25%, 50%, and 75%, respectively.

Streamline plots of gas flow through the three mid-kiln ring cases are shown in **Fig. 4**. Up until the location where the ring starts, the gas flow is largely unaffected; streamlines are smooth and horizontal, and velocity profiles are practically identical. However, as the gas flow enters the opening of the ring, it converges and speeds up as the area decreases. At the exit of the ring, flow separation occurs. The gas flow exits the ring opening in an expanding jet

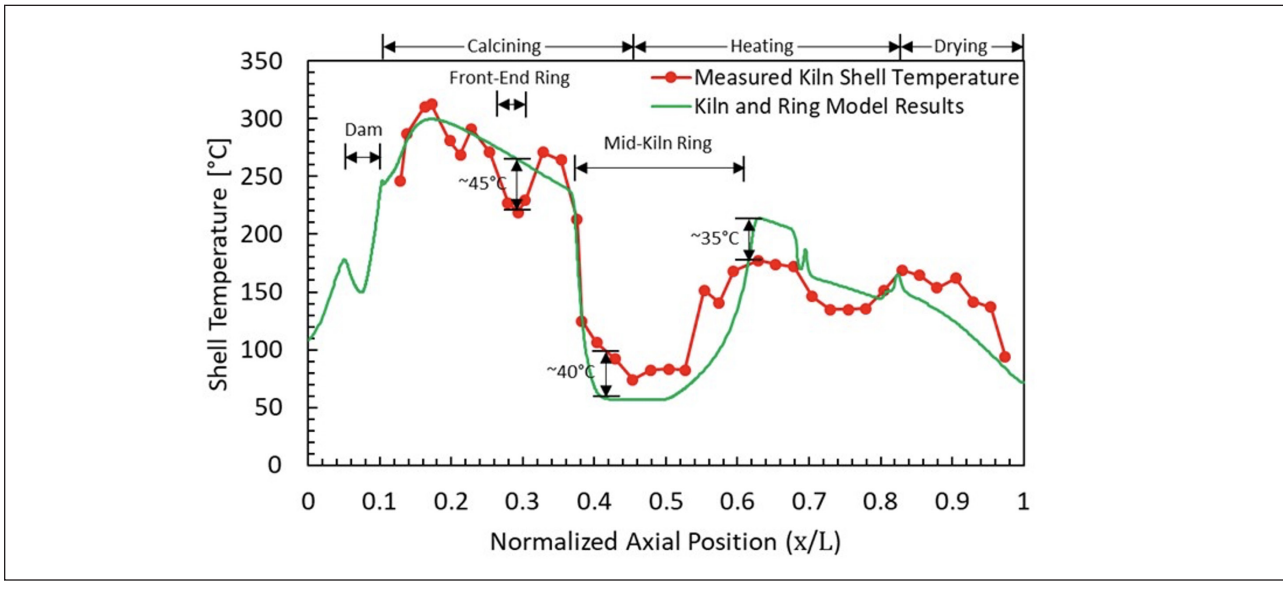

3. Measured kiln shell temperature versus kiln and ring model results.

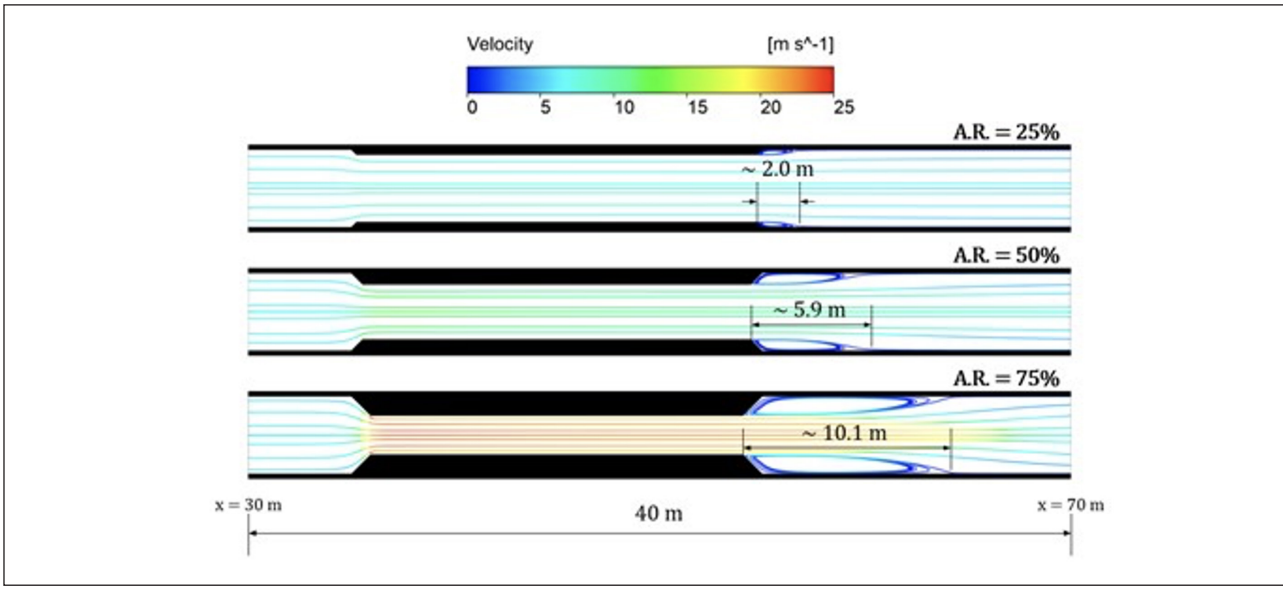

4. Streamline plots of flow through mid-kiln rings of increasing thickness. A.R. is the cross-sectional area reduction.

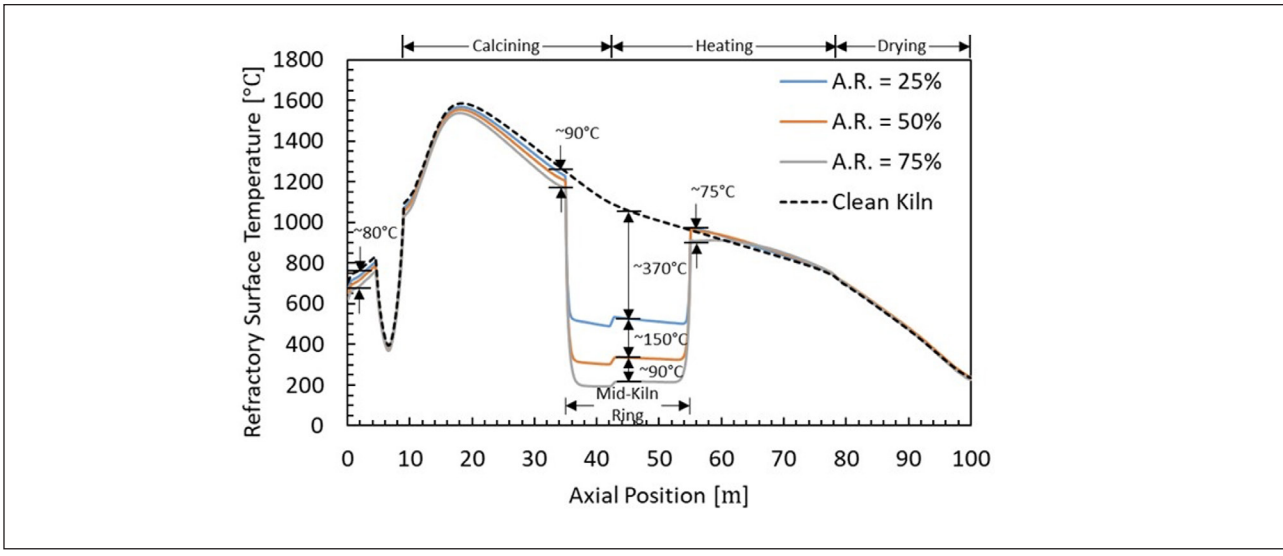

5. Refractory surface temperature changes with increasing mid-kiln ring thickness.

stream, while recirculation zones are formed adjacent to the ring and exposed refractory surface. These recirculation zones are about as thick as the ring and increase in length with increasing ring thickness: for A.R. = 25%, 50%, and 75%, the recirculation zones span ~2.0, 5.9, and 10.1 m, respectively. Overall, the acceleration of the gas flow may affect dust levels in the kiln, because higher velocity flow is more likely to entrain more dust particles from the bed.

The temperature profiles of the refractory surface (i.e., the interface between the refractory and flue gas/ring) for a clean kiln and each of the three mid-kiln ring cases are shown in **Fig. 5**. For the clean kiln case, the temperature reaches a peak in the calcining zone approximately where the flame ends, and then decreases with distance from the burner at a roughly steady rate in each of the calcining, heating, and drying zones. Apart from where the ring is located, similar trends are observed for the three other cases. Upstream of the ring, the refractory surface temperature decreases with increasing ring thickness; this effect is most prominent at locations adjacent to the ring and in the kiln discharge region, where temperatures vary by ~90°C and ~80°C, respectively. By contrast, downstream of the ring, about 65 m from the lime discharge, the refractory surface temperature increases with increasing ring thickness, although to a much lesser degree. Directly adjacent to the ring, temperatures vary by ~75°C, and the thickest ring case yields the lowest local temperature. This can be explained by the recirculation zones that form as the gas flow exits the ring, which have a direct impact on the local convective heat transfer. When comparing the upstream

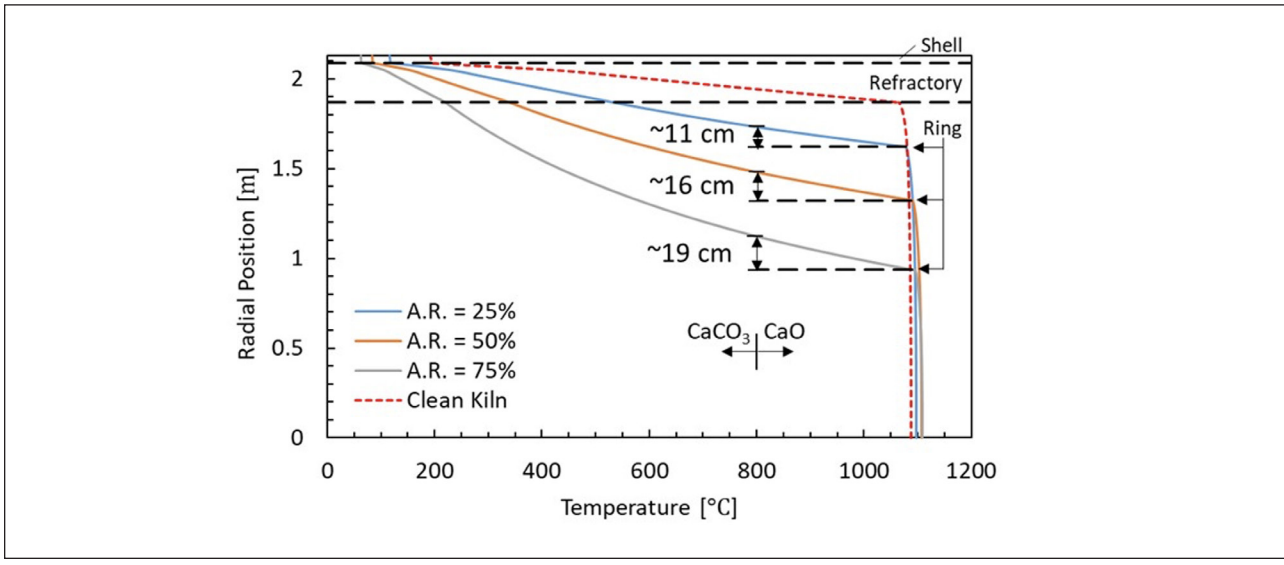

6. Radial temperature profile from the kiln centerline to the shell, as a function of mid-kiln ring thickness. The axial position is at the midpoint of the mid-kiln ring (x = 45 m).

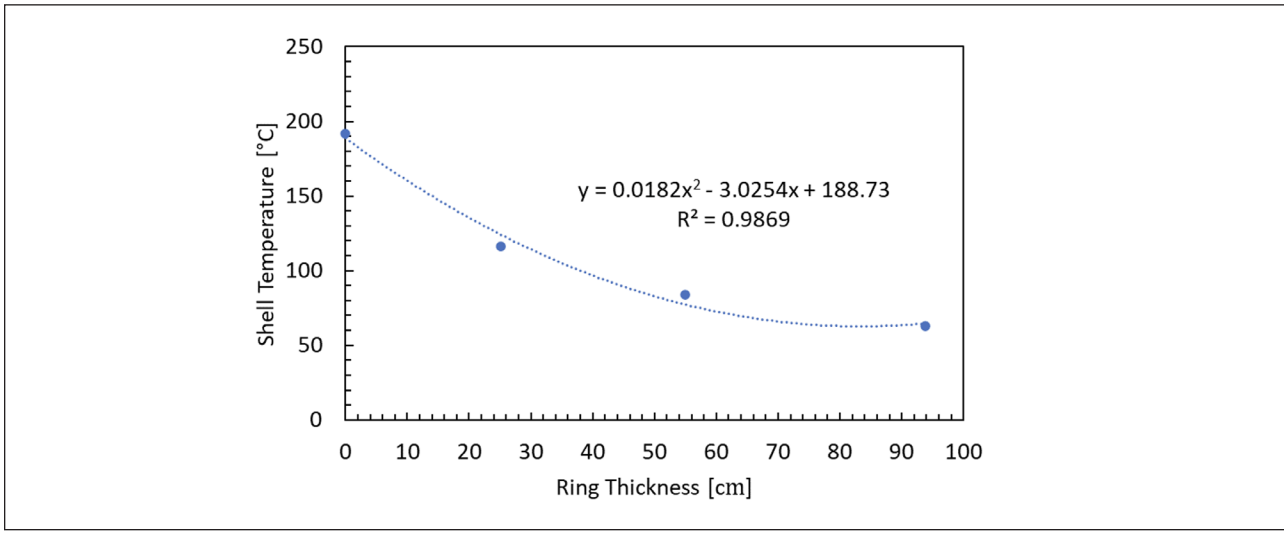

7. Shell temperature plotted against mid-kiln ring thickness. The axial position is at the midpoint of the mid-kiln ring (x = 45 m). The dashed line and equation shown are for a second-order polynomial fit.

and downstream effects on refractory surface temperature, it seems that ring growth is more likely to occur upstream where temperatures tend to decrease, and recarbonation would thus be promoted. Finally, the most prominent temperature variations occur along the lengths of the rings due to insulation effects. Interestingly, the temperature of the refractory surface decreases less with increasing ring thickness. For example, with each incremental area reduction, the changes in temperature at the midpoint of the rings are ~370°C, 150°C, and 90°C, respectively, despite the ring thickness roughly doubling each time. This is due to the strong insulating effect of the ring, which should be accounted for when correlating changes in shell temperature to ring thickness.

These insulation effects are shown more clearly in **Fig. 6**, where radial temperature profiles are plotted at the midpoint of the mid-kiln ring. The refractory, shell, ring, and gas boundaries are indicated. As can be seen, the surfaces exposed to the gas all have similar temperatures, but within the ring, refractory, and shell, temperatures decrease with increasing ring thickness at any given radial position. As was shown earlier, the refractory surface temperature drops to a lesser degree with each increase in ring thickness. The same is true at any radial position, including the shell exterior. Thus, an initial small ring will cause a relatively large drop in shell temperature, whereas each additional increment of area reduction brought on by ring growth will result in relatively smaller drops in temperature. This result has important implications on using shell temperature monitoring to assess ring growth. To illustrate, **Fig. 7** shows the shell temperature plotted against mid-kiln ring thickness and a second-order polynomial fit with good

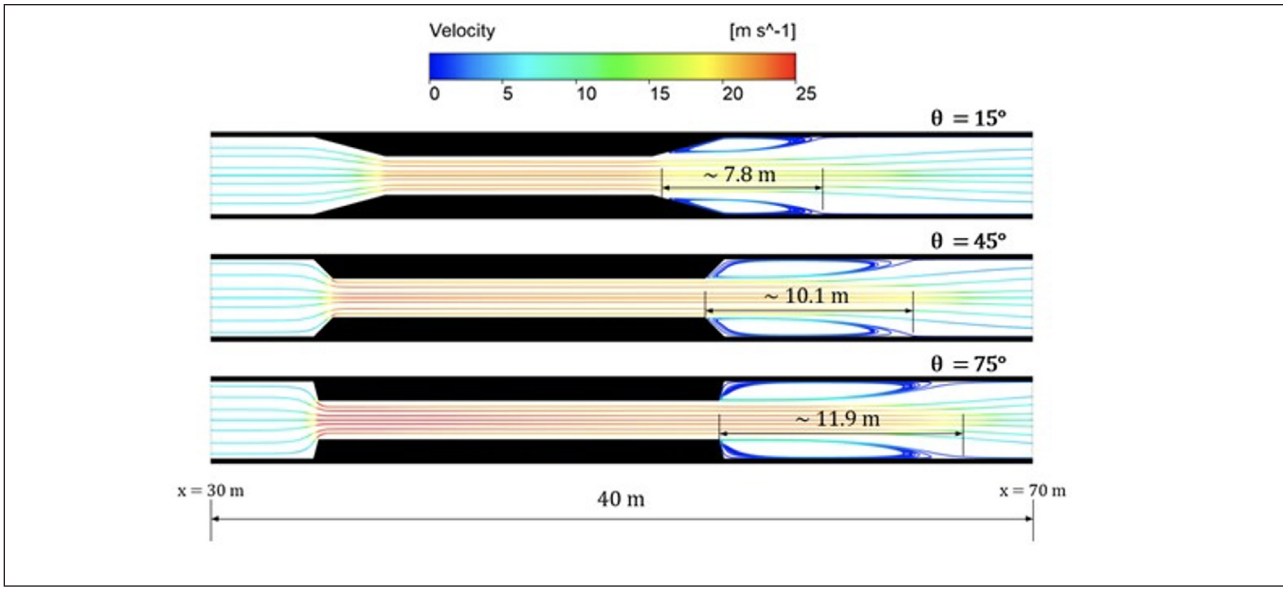

8. Streamline plots of flow through mid-kiln rings of varying front and back face angles.

agreement. The same methodology can be used to construct a similar profile for estimating ring thickness in other kilns.

The recarbonation front position in each ring is also marked in Fig. 6 and corresponds to the distance from the surface of each ring to where the temperature is 800°C (i.e., the point at which CaO transitions to $CaCO_3$). Note that the distance to the recarbonation front equal to ~11, 16, and 19 cm for the A.R. = 25%, 50%, and 75% cases, respectively, varies little with increasing ring thickness. However, the ratio of recarbonated $CaCO_3$ to CaO (on a per-area basis) increases with increasing ring thickness; the ratios are 58%, 74%, and 85% for the A.R. = 25%, 50%, and 75% cases, respectively. This means that the composition of the ring contains increasingly more recarbonated $CaCO_3$ as it grows, making it harder.

Effect of the geometry of the front and back faces of the ring

As the temperatures just upstream and downstream of a ring are a strong function of ring thickness, as shown in Fig. 5, here we consider the effect of varying the ring front and back faces, as characterized by the angle θ_{ring}. A mid-kiln ring with x_{ring} = 35 m, L_{ring} = 20 m, and h_{ring} = 93.8 cm (A.R. = 75%) is assumed, while θ_{ring} is varied between 15°, 45°, and 75°. A thick ring was chosen to accentuate the difference between the three cases. Streamline plots of flow through the three cases are shown in **Fig. 8**. The flow is still largely unaffected upstream of the ring, and very similar jet and recirculation phenomena occur in all three cases. However, as θ_{ring} increases, the flow converges and accelerates more quickly, as expected, and slightly higher velocities are attained in the ring channel. Downstream of the ring, the jet stream expands more slowly and the recirculation zone length increases with increasing θ_{ring}. Recirculation zone lengths are ~7.8, 10.1, and 11.9 m for θ_{ring} = 15°, 45°, and 75°, respectively.

The refractory surface temperatures for these cases and for a clean kiln are shown in **Fig. 9**. Differences in refractory surface temperature are negligible upstream of the ring and along the ring, except at the front and back faces. Downstream of the ring, the effect of the back face angle on flow and temperature is unclear. Immediately downstream of the rings, the refractory surface temperatures vary by ~90°C for the three cases. Temperatures relative to the clean kiln case decrease when θ_{ring} = 45° and 75°, but increase for the θ_{ring}= 15° case. Yet further downstream, the temperatures are all higher than those of the clean kiln, although the refractory surface temperature of the 45° case approaches that of the clean kiln significantly sooner than those of the other two cases. Overall, the effects of varying the front and back faces on temperature are relatively small, especially upstream of the ring.

Effect of ring location

Front-end, mid-kiln, and mud rings are studied in this section. It is assumed that: front-end rings have x_{ring} = 10 m and L_{ring} = 8 m; mid-kiln rings still have x_{ring} = 35 m and L_{ring} = 20 m; and mud rings have x_{ring} = 70 m and L_{ring} = 8.5 m. In each case, θ_{ring} = 45° and h_{ring} = 54.9 cm (A.R. = 50%). Streamline plots of flow through the three ring types are shown in **Fig. 10**.

As in previous cases, the gas flow converges and accelerates as it passes through the ring. In each case, the gas flow exits the ring as an expanding jet stream, forming a recirculation zone adjacent to the ring and refractory surface. The flow through and downstream of the mid-kiln and mud rings are very similar (e.g., the recirculation zone

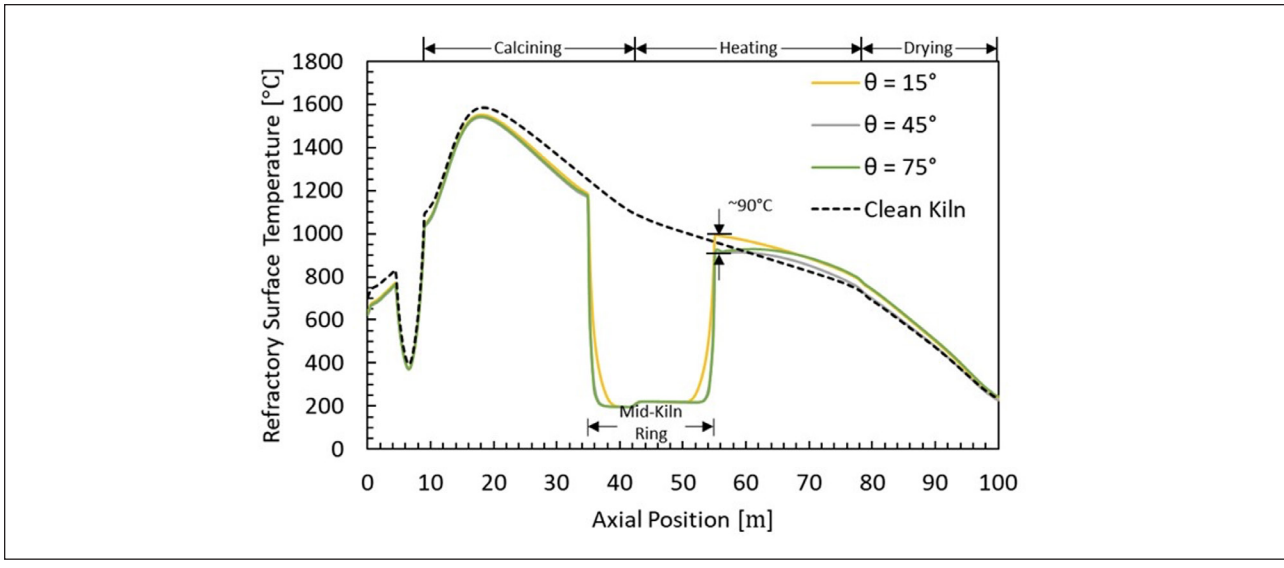

9. Gas-side refractory surface temperature profiles for mid-kiln rings with varying front and back face angles.

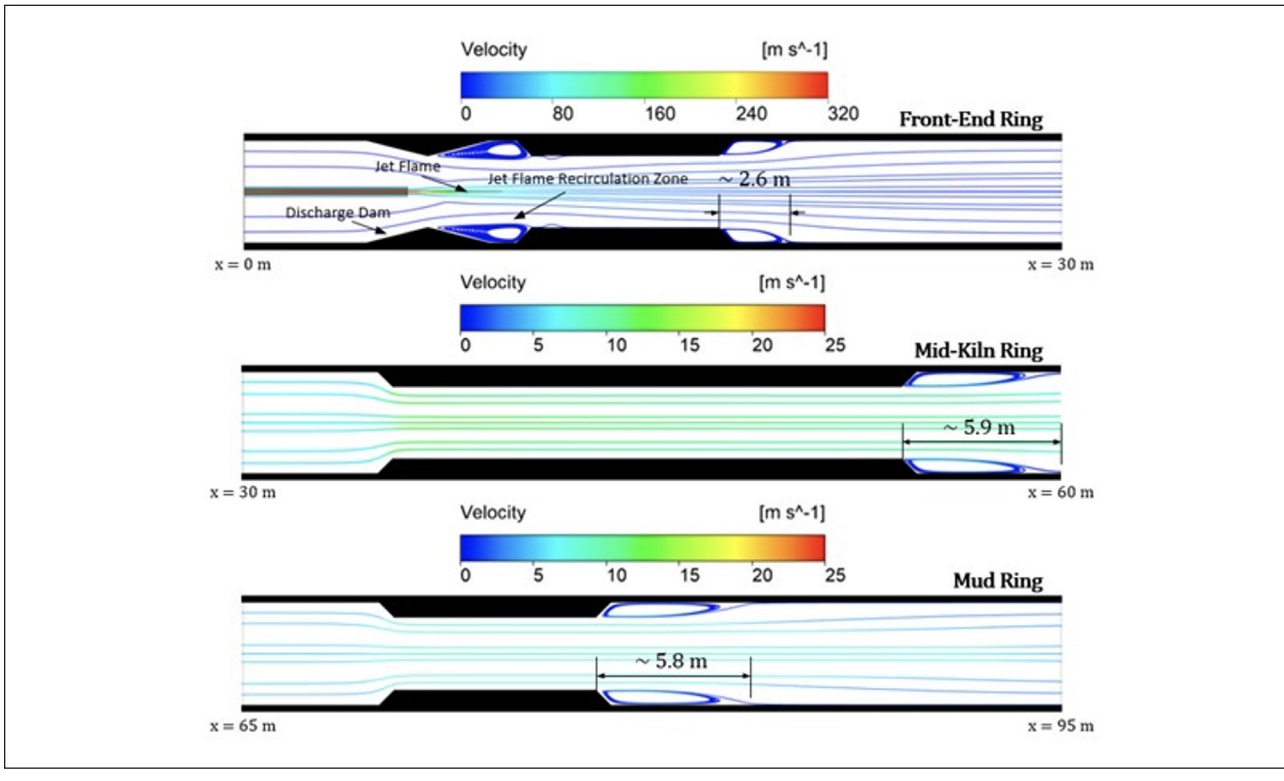

10. Streamline plots of flow through front-end, mid-kiln, and mud rings.

lengths are 5.8 m and 5.9 m), because the upstream flow conditions are very similar for both rings, as they are located far downstream of the burner.

On the other hand, due to the proximity to the burner, front-end rings can have a direct impact on the upstream jet flame recirculation zones, which helps to shape and stabilize the flame. As a result, the jet flame recirculation zone is approximately half its normal length. Front-end rings are therefore much more likely to affect burner operation and result in unsteady flames. Downstream of the front-end ring, the jet expansion and recirculation zones still occur, although they are much shorter; for example, the length of the recirculation zone is only ~2.6 m, which is less than half that of the other two rings. Therefore, downstream of a front-end ring, flow recovers from the disturbance caused by the ring in a shorter distance. Note that the local gas temperature impacts the local gas density and velocity, and therefore the recirculation zones to a certain degree.

The refractory surface temperature for each of the three ring types and for a clean kiln is shown in **Fig. 11**. The

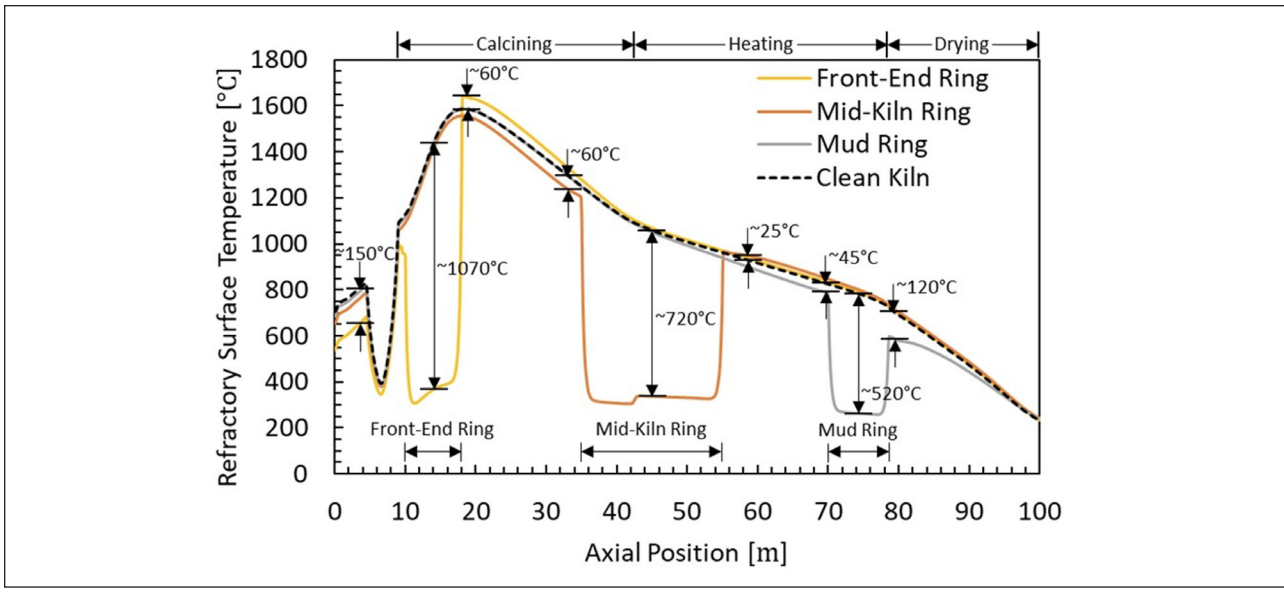

11. Gas-side refractory surface temperature profiles for front-end, mid-kiln, and mud rings.

refractory surface temperature decreases upstream of each ring. It decreases by a similar amount for the mid-kiln and mud ring, ~60°C and ~45°C, respectively, whereas it decreases significantly more for the front-end ring, ~150°C in the discharge region. Downstream of the front-end and mid-kiln rings, the temperatures increase by ~60°C and ~25°C, whereas downstream of the mud ring, the temperature decreases by ~120°C. Once more, the most prominent drop in refractory surface temperature occurs along the span of each ring due to insulation effects. Although the three rings share the same thickness, the temperature drops are different, primarily due to the different local gas temperatures and refractory bricks. For the front-end, mid-kiln, and mud rings, the temperature drops at the mid-section of each ring are ~1070°C, 720°C, and 520°C, respectively. Thus, ring location affects the extent to which the refractory and shell are insulated, which will affect how one uses shell temperature measurements to estimate ring thickness.

CONCLUSIONS

A steady state, 2D axisymmetric lime kiln model has been developed to assess the effect of ringing on gas flow and heat transfer. Rings are characterized by their position within the kiln, length, thickness, and geometry of the front and back faces. Prominent effects of the rings are the increase in gas velocity caused by the reduction in cross-sectional area of the kiln and the insulation of the refractories and shell. For a mid-kiln ring, the change in the location of the recarbonation front is relatively small in the axial direction, but larger in the radial direction, indicating that the thermal driving force for recarbonation increases as the ring grows, which can promote ring hardening. Moreover, the results show that ring growth results in increasingly smaller changes in shell temperature, which must be accounted for by mills using measured shell temperature to estimate ring growth.

Another finding is that gas recirculation zones always form downstream of a ring. These recirculation zones can become long (over 10 m). Their length is affected more by ring thickness than by the face angle at the end of the ring. The formation of these recirculation zones in turn impacts the refractory surface temperature immediately downstream of the ring; hotter temperatures are observed for the front-end and mid-kiln rings, whereas cooler temperatures are observed for the mud ring. The formation of these recirculation zones supports the idea that significant amounts of lime could be carried from the bed at the front of a ring, because of the higher gas velocities that result, and deposited behind the ring, causing further recarbonation and ring growth. Finally, front-end rings can disrupt the upstream jet recirculation zone and destabilize the flame, which in turn can result in undesirable temperature fluctuations in the kiln. **TJ**

ACKNOWLEDGEMENTS

This work is part of the industrial research consortium project Effective Energy and Chemical Recovery in Pulp and Paper Mills - III at the University of Toronto supported by Andritz, Arauco, Babcock & Wilcox, Canadian Kraft Paper, Cenibra, Clyde Bergemann, CMPC, FITNIR, FPInnovations, Georgia Pacific, International Paper, Irving, KFS, Klabin, Mercer, Rayonier, Sappi, Södra, Stora Enso, Suzano, Valmet, and WestRock. We would also like to acknowledge the support of the Natural Sciences and Engineering Research Council of Canada (NSERC), [IRCPJ 517715 -16]. Cette recherche a été financée par le Conseil de recherches en sciences naturelles et en génie du Canada (CRSNG), [IRCPJ 517715 -16].

LITERATURE CITED

1. Tran, H., Mao, X., and Barham, D., *J. Pulp Pap. Sci.* 19(4): J167(1993).
2. Tran, H. and Barham, D., *Tappi J.* 74(1): 131(1991).
3. Elattar, H., Stanev, R., Specht, E., et al., *Comput. Fluids* 102: 62(2014). https://doi.org/10.1016/j.compfluid.2014.05.033.
4. Georgallis, M., Nowak, P., Salcudean, M., et al., *Can. J. Chem. Eng.* 83: 212(2005). https://doi.org/10.1002/cjce.5450830208.
5. ANSYS, "Chapter 21: Solver theory," in *ANSYS® Fluent, 19.1, Help System, Theory Guide*, Ansys Inc., 2019, pp. 679–740.
6. Gorog, J.P., "Selection of refractory bricks for use in lime sludge kilns," *Corrosion in the Pulp and Paper Industry and Biorefineries*, Georgia Institute of Technology, Atlanta, 2014.
7. Silva, M., "Experimental investigation of the thermophysical properties of new and representative materials from room temperature up to 1300°C," Ph.D. thesis, Otto von Guericke University Magdeburg, Madeburg, Germany, 2009.
8. Sandaka, G., "Calcination behavior of lumpy limestones from different origins," Ph.D. thesis, Otto von Guericke University Magdeburg, Madeburg, Germany, 2016.
9. Gareau, P., "A CFD study of the effects of rings on flow and temperature in lime kilns," MASc thesis, University of Toronto, Toronto, Canada, 2020.
10. Keim, E., Zuñiga, J., and Tran, H., *TAPPI J.* 19(7): 345(2020). https://doi.org/10.32964/TJ19.7.345.

ABOUT THIS PAPER

Cite this article as:
Gareau, P., Bussmann, M., DeMartini, N., et al., *TAPPI J.* 21(6): 301(2022). https://doi.org/10.32964/TJ21.6.301

DOI: https://doi.org/10.32964/TJ21.6.301

ISSN: 0734-1415

Publisher: TAPPI Press

Copyright: ©TAPPI Press 2022

About this journal

ABOUT THE AUTHORS

Ring formation is a common problem in lime kiln operation that can impact the ability of lime kilns to operate continuously and meet mill demands for lime recovery. A lime kiln model was developed to predict how gas flow and kiln temperatures respond to the presence of ring deposits, which may provide insights into how rings form and grow.

Accurate modeling was the most difficult aspect of this research. It was addressed by validating the modeled kiln shell temperature profile against that of a kiln from industry, and good agreement was obtained.

We discovered that ring growth causes the gas velocity to increase and the kiln shell temperature to decrease due to insulation. The formation of recirculation zones immediately downstream of the rings, as well as temperature deviations upstream and downstream of the rings, that might promote recarbonation and further ring growth, were also discovered. Moreover, the thermal driving force for recarbonation increases as a mid-kiln ring grows, which can promote ring hardening.

The results show that ring growth results in increasingly smaller changes in shell temperature, which must be accounted for by mills using measured shell temperature to estimate ring growth. Mills can use the introduced model for modeling their kilns.

Possible next steps in this study are further model development to add phenomena currently not taken into account, such as dusting or a fully three-dimensional (3D) model with bed flow, and transient studies.

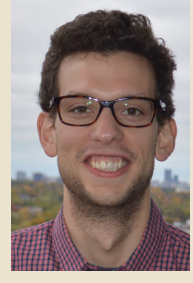

Gareau



Bussmann



DeMartini



Tran

Gareau is an MASc graduate and Bussmann is professor and chair of the Department of Mechanical & Industrial Engineering at the University of Toronto, Toronto, ON, Canada. DeMartini is assistant professor and Tran is professor emeritus in the Department of Chemical Engineering & Applied Chemistry at the University of Toronto. Email Bussmann at markus.bussmann@utoronto.ca.

Water chemistry challenges in pulping and papermaking – fundamentals and practical insights: Part 1: Water chemistry fundamentals and pH

PRZEMYSLAW PRUSZYNSKI, LEBO XU, AND PETER W. HART

ABSTRACT: Water is an essential component of the papermaking process. Nevertheless, papermakers often overlook its importance compared to fibers and chemical additives. A better understanding of water properties and chemical interactions associated with water at the wet end leads to a sound foundation for high-quality paper production and smooth operation. Not all fresh water and process water is the same. Fresh water varies from mill to mill, primarily due to the location and availability of water sources. Some industrial trends, such as enhancing water conservation and production yield, gradually shift process water quality over time.

The current work serves as a primer on water and water chemistry fundamentals to help the papermaker prepare for the future challenges of increased contamination of process water associated with reduced fresh water usage. This paper focuses on basic water chemistry definitions and discusses the impact of pH on wet-end operation. It is clear that pH is a fundamental factor that directly affects the process and impacts other factors relevant to the papermaking process. It is crucial to understand what pH represents, how it is measured, how to select the proper pH and carefully control it, and how to closely maintain the process at target setpoints. Understanding the sensitivity of operation to pH change will lead to an appropriate focus on these issues. In addition to basic theory, we also review onsite experience and practical mill cases. It is imperative to stress that, although critical, pH is not the only chemical parameter impacting papermaking operations. Other factors, such as ionic concentration measured by conductivity, surface, soluble charge, and hardness, are critical and will be discussed in Part II of this series. As pH is a primary and independent factor that impacts various forms of charge and conductivity, the authors decided to start the current series of papers by discussing pH.

Application: By gaining comprehensive and fundamental understanding on how pH affects wet end chemistry, mills can be better prepared to address water challenges and obtain more efficient operation.

The paper industry is experiencing a rapid loss of experienced technical and operations personnel. Well-seasoned papermakers and engineers are retiring and taking decades of experience away from the mills. Younger engineers, scientists, and operators are being rapidly promoted into positions of authority without their predecessors' years of operational experience. Even though the new generation of papermakers is well-educated in engineering and scientific fundamentals, it is beneficial for them to understand how crucial water chemistry and pH control are for papermaking.

The impact of water on the papermaking process depends on multiple water quality parameters, such as conductivity, surface, soluble charge, suspended and dissolved solids, acidity/alkalinity, oxidation reduction potential (ORP), hardness, and pH. The current series attempts to provide a primer where important water/wet-end chemistry concepts that occasionally fool even experienced people are collected and explained. The present work focuses on the importance of water chemistry and pH. The reason pH is so important is that it impacts the performance of the entire sheet forming and additive processes. Poor machine performance may result if pH and its impacts are not well controlled and understood. Additional water properties and their impact on papermaking and wet end chemistry will be reviewed in the second paper in this series.

In the last 30 years, the industry has experienced a wave of significant changes in the pH of operations. Many papermaking processes have moved from acid grades utilizing large quantities of alum, rosin sizing, and kaolin clays to alkaline woodfree calcium carbonate-filled grades of paper and neutral pH applications specific to mechanical pulps. These pH conversions illustrate the importance of pH, as they required a significant effort to develop chemical technologies that operate at higher pH values.

For both virgin and recycled mills, changes in pulp quality represent another significant contributor to shifting water quality. Cost considerations, quality requirements, process washing limitations, grade development requiring new pulp sources, and water use reduction have increased pulp's impact on the overall process water quality.

Water is an essential component of the papermaking

process, although it is not a part of the final product. It serves as a medium for the dilution and transportation of papermaking solids to allow the formation of a uniform sheet of paper/paperboard. Water facilitates many processes involving fiber development and delivery of chemical additives and serves as a medium for several chemical and mechanical interactions associated with papermaking. After the diluted papermaking slurry is prepared and delivered to the headbox (typical consistency 0.5%~1%), the essence of making paper becomes water removal. This removal process starts as physical filtration on the forming section of paper machine and continues in the press and dryer sections. In the papermaking process, water is primarily recirculated and, with every pass, becomes contaminated with soluble and colloidal materials that negatively impact the papermaking process. Part of the process water needs to be replaced with fresh water. More fresh water addition means more sewered water must be treated in the effluent treatment plant. A significant part of fresh water addition is the energy required to maintain the required process water temperature. Therefore, reducing the amount of fresh water used per ton of the product, besides reducing an environmental footprint, reduces the cost of fresh water and its treatment, reduces the cost of effluent treatment, and saves a significant amount of energy. Current industrial trends have forced papermakers to attempt to do more to make consistently high-quality products with often declining fiber quality and less fresh water. There is little room for deviation from chemical best practices if quality and productivity are attainable goals. The paper machine's chemical environment needs to be optimum and stable. In addition, potential incompatibilities between different chemicals should be well understood and avoided or reduced [1].

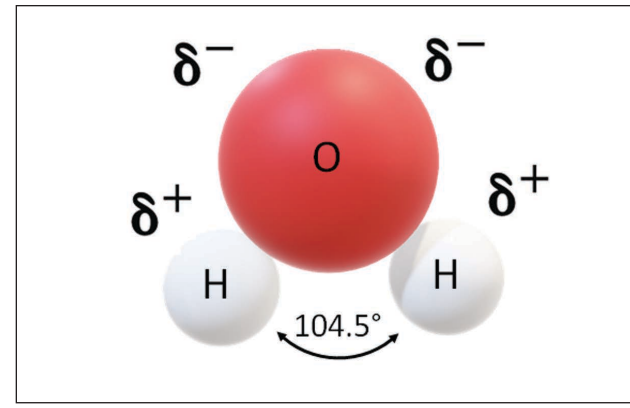

1. Structure of water molecule.

The papermaker must adequately select and control the paper machine's wet-end chemistry. These decisions must include the intricate relationships between various wet end parameters. Such decisions are only possible if the fundamentals of wet-end chemistry are understood. Recently, a paper was published dedicated solely to conductivity [2], including basic definitions, typical values, impact on machine performance, and available control strategies. Based on this paper's significant interest level, the authors decided that a review of fundamental water properties and related wet end chemistry would be of value to the industry. Herein, basic definitions, typical values, relationships between discussed parameters, best practices, and control strategies associated with water fundamentals are reviewed.

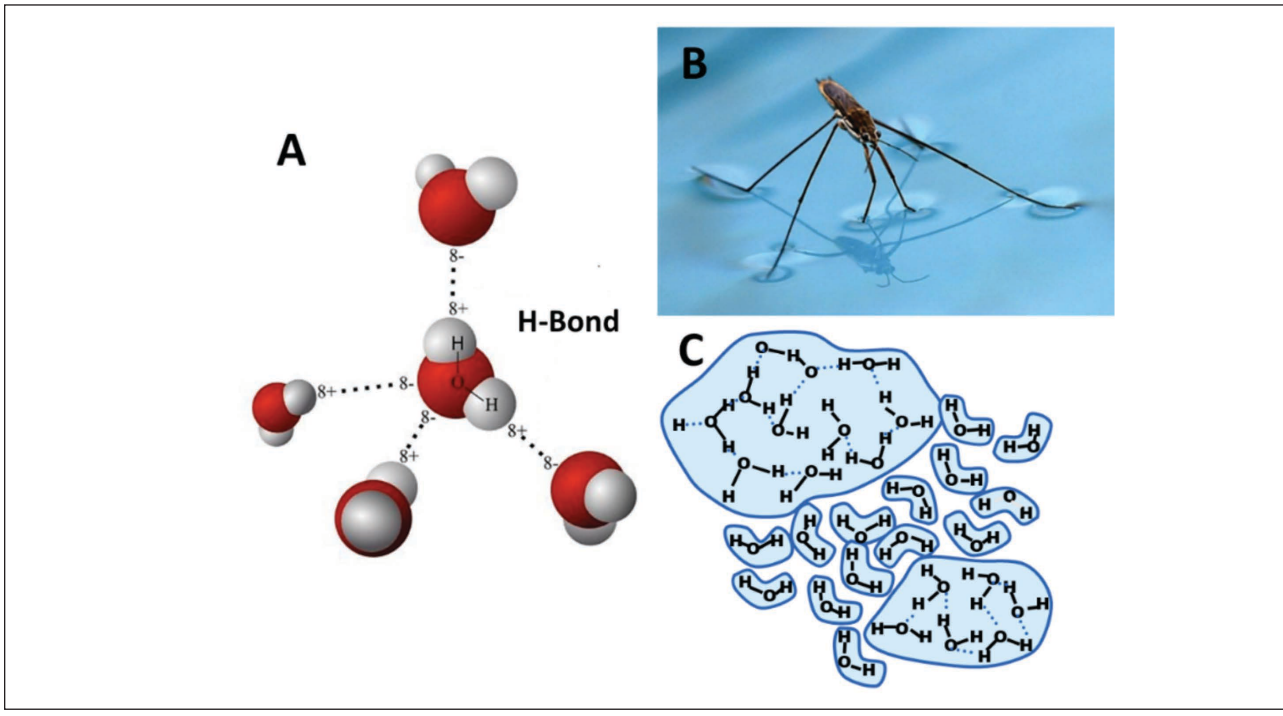

2. Hydrogen bond between water molecules (A), high water surface tension (B), and water molecular organization (C).

WATER CHEMISTRY BASICS

Water is a ubiquitous compound around us. It is abundant, covering about 71% of our planet's surface area. It is critical for life, occupying about half the volume inside biological cells, and crucial for most industrial processes, including pulping and papermaking. Though people use water every day, few realize it exhibits several unique properties. Water (H_2O) has a molecular weight (MW) of 18 g/mole. It has stronger intermolecular interactions than other substances made of molecules with equivalent sizes, molecular weight, and geometry. For example, hydrogen sulfide (H_2S) (molecular weight of 34 g/mole) or carbon dioxide (CO_2) (molecular weight of 44 g/mole) are gases under room conditions due to their lower cohesive force.

An example of water's unique "packing" property is its unusual volumetric anomaly, with the density of water's solid form (ice) being lower than its liquid form (water). This anomaly explains why ice forms on top of rivers and lakes rather than sinking to the bottom and results from the liquid phase being more organized than the solid form of water. The strong organization of water molecules in their liquid form has relatively high surface tension, melting point, boiling point, and heat capacity. As a result, ice floats on the water surface and melts under pressure, making skating possible.

It is beneficial to review water's molecular structure to understand water properties better. There has been a continuous effort, even recently, to explore water molecular coordination and arrangements [3-5]. A water molecule consists of two hydrogen atoms and one oxygen atom. These three atoms are connected in sequence as H-O-H, with a bond angle of 104.5° (**Fig. 1**). Since oxygen is strongly electronegative, it attracts electrons, shared with hydrogen atoms, to form bonds. As a result, the oxygen side (of a water molecule) bears a partial negative charge, and the hydrogen side carries a partial positive charge. This molecular polarity makes water an excellent polar solvent to disperse cellulosic material and papermaking additives, such as cellulose derivatives, starch, polymer compounds, and inorganic salts.

The hydrogen bond, a term often used when explaining interactions in the papermaking process, is another feature that makes water unique. The oxygen atom in one water molecule has excellent, unhindered access to a hydrogen atom in other nearby water molecules. The simple molecular structure makes it possible to develop a relatively strong interaction, defined as a hydrogen bond (**Fig. 2A**). The hydrogen bond is responsible for water's organization and unique properties, including high boiling point, high specific density, and high surface tension (Fig. 2B). The hydrogen bond organizes water molecules, packing more molecules in a defined volume (Fig. 2C), making liquid water density higher than ice.

pH — proton (hydrogen ion) concentration

Pure water dissociates into a proton (H^+) and hydroxyl anion (HO^-). This dissociation takes place in the presence of and is driven by the contribution of other water molecules, best represented by Eq. 1:

$$H_2O + H_2O \rightleftharpoons H_3O^+ + HO^- \quad (1)$$

In pure water, the concentrations of both ions are identical and equal to 10^{-7} mol/L. The product of both concentrations is, therefore, constant and equal to:

$$[H_3O^+][HO^-] = 10^{-14} \quad (2)$$

Since the concentration of both water ions is constant, once we know the concentration of one of these ions, we can easily find the other ion's concentration. Equation 3 defines pH value:

$$pH = -\log[H_3O^+] \quad (3)$$

Acids and bases

Acids are substances that, in water, provide additional H_3O^+ ions. Acids have the H atom attached to oxygen or another highly electronegative atom. This electronegative character of the atom (A) directly linked to a hydrogen atom makes the bond A-H highly polarized, with electrons shifted towards the A and away from H atoms. This polarization of the H-A bond is responsible for interactions with water dipoles, referred to as hydration (**Fig. 3**).

If the energy released from interaction with water dipoles, called hydration, exceeds the energy of the A-H bond, the complete dissociation of this bond occurs, leading to hydrated ions A^- and H_3O^+. This process is called dissociation. Since H^+ interacts with a water molecule to form H_3O^+, the formula (H^+-H_2O) reflects water's role in this process.

There are two major classes of acids:

- Strong acids: All molecules of strong acids undergo complete dissociation into H_3O^+ and A^- when placed in water. There is no undissociated form of strong acid left in the solution. Therefore, there is no equilibrium between dissociated and undissociated states of the acids. The concentration of H_3O^+ equals the initial concentration of the acid if the acid has one H atom capable of dissociation. Therefore, if we prepare a $1x10^{-3}$ M solution of strong, monoprotic acid (e.g., hydrochloric acid [HCl]), the concentration of the H_3O^+ ion will also be $1x10^{-3}$ M. The pH of this solution would be equal to 3.
- Weak acids: All acids that do not wholly dissociate when dissolved in water are weak acids. For weak acids, there are both forms, dissociated and undissociated, existing in equilibrium. The concentration of H_3O^+ is smaller than the concentration of the acid. To calculate the concentration of H_3O^+ ion, we need to know the dissociation constant of the weak acid, K_a:

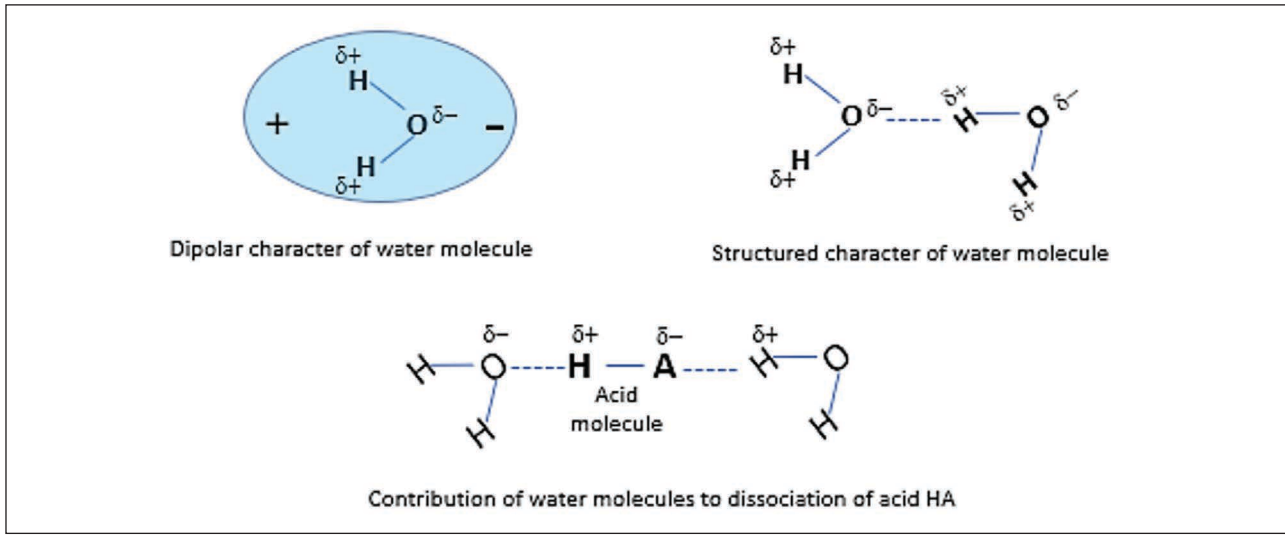

3. Dipolar character of water, water structure, and interaction with polar and ionic species leading to dissociation.

$$K_a = \frac{[H_3O^+][A^-]}{[HA]} \quad (4)$$

where: $[H_3O^+]$, $[HA]$, and $[A^-]$ are equilibrium concentrations of hydronium ion, dissociated, and undissociated acid, respectively. A specific K_a value for each weak acid is often presented as a pK_a (Eq. 5). This equation is a measure of the strength of the weak acid:

$$pK_a = -logK_a \quad (5)$$

Equation 4 and K_a value do not apply to strong acids since they fully dissociate, and no undissociated form is available in the equilibrium.

The most common weak acid group in papermaking is the carboxylic group (-COOH), with the approximate pK_a = 4.8. It is worth stating that the pK_a value for the same acid function may differ based on neighboring groups in the molecule. In general, electron-withdrawing groups increase the acid strength (lower pK_a value), and electron-donating groups lower the strength of the acid (higher pK_a value).

Practical aspects of pH control

Based on Eq. 1:

$$[H_3O] = K_a \frac{[HA]}{[A-]} \quad (6)$$

$$-\log[H_3O^+] = -logK_a - log\frac{[HA]}{[A-]} \quad (7)$$

$$pH = pK_a - \log\frac{[HA]}{[A^-]} \quad (8)$$

Equation 8 is known as the Henderson–Hasselbach equation. It allows for a fundamental understanding of how advanced the dissociation is at a given pH for any weak acid if we know its pK_a value. Since dissociation of weak acids is also a source of charge in papermaking systems, this equation provides information about the system's charge development. It is interesting to conclude that for the situation where $[HA]=[A^-]$, midpoint for the dissociation process, Eq. 5 becomes:

$$pH = pK_a \quad (9)$$

Based on Eq. 9, we can draw some conclusions:

- For any weak acid, the $pH = pK_a$ value represents a situation where the concentration of acid form (HA) and its anionic form (A) are equal (half-point of the ionization).
- When $pH = pK_a - 1$: $\frac{[HA]}{[A^-]} = 10$ (10)
  - lowering *pH* by one from the pK_a value increases the concentration of acid (no charge) by ten-fold.
- When $pH = pK_a + 1$: $\frac{[HA]}{[A-]} = 0.1$ (11)
  - increasing *pH* by one from the pK_a value increases the concentration of dissociated form (anionic charge) by ten-fold.

Based on Eq. 10 and Eq. 11, we can conclude that the change between 10% and 90% ionization of weak acid occurs in the range of two pH units, $pH = pK_a \pm 1$. The complete ionization process (1%~99%) occurs in the range:

$$pK_a - 2 \le pH \le pK_a + 2 \quad (12)$$

with the steepest change of ionization located close to $pH = pK_a$.

Since the H^+ concentration has a logarithmic relationship with pH units, a slight shift in pH value represents a significant change in H^+ concentration (1 pH unit change = 10 times $[H^+]$ concentration change). Additionally, changing pH in a different pH scale range requires different amounts of acid or base. Reducing pH requires ten times more base

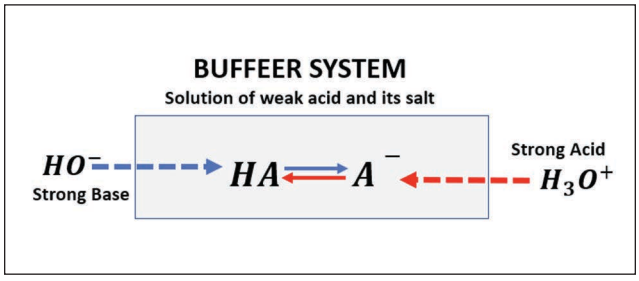

4. The model explanation of the buffer system.

with every pH unit going down. For example, correcting pH from 3 to 2 requires 10,000 times more strong acid than the pH change between 7 to 6. These facts stress the importance of tight pH control for smooth machine operation and the performance of chemical additives. The best practice in pH control on many large, fast paper machines is to operate with variations within ± 0.1 units range from the target pH.

Besides total acid usage, it is also essential to properly design the dosing method of pH control acid or base to maintain a desired control of pH. For example, using diluted acid is better than adding concentrated acid. Split, multipoint dosing is better than one-point massive dosing. Higher acid flow velocity than stock flow velocity and good mixing is also essential. Designing a good control loop requires a well-operating pH sensor and the use of the proper algorithm that correlates the required dosage of acid or base with the observed pH of the treated stream. Sulfuric acid, phosphoric acid, sulfamic acid, and CO_2 are most commonly used to reduce the pH. Caustic soda, sodium bicarbonate, and sodium carbonate are most often used when correction to higher pH is desired. The application of CO_2 has recently become increasingly more important, primarily in thick stock applications, because it allows pH reduction in the systems using calcium carbonate fillers, with minimum hardness development [6]. This technology, known as ADALKA, allows a mill to effectively reduce the pH of alkaline stock to about 7.2–7.4 and is very important for grades operating with mechanical pulps that experience significant brightness losses at higher pH.

Buffering

Equation 8 explains buffering—a fundamental property of solutions containing a weak acid and its conjugate anion. Buffering reflects resistance to pH change on the addition of strong acid or strong base. The addition of strong acid, or strong base, to the solution containing buffer components resists a sharp shift in pH until either the weak acid or its anion ceases to exist. Adding strong acid or strong base does not directly increase or decrease the concentration of H_3O^+ ion but changes HA and A^- ratio in the equilibrium (Eq. 8). This effect reduces the total impact of adding a strong acid or strong base on pH. **Figure 4** illustrates the mechanism of pH buffering of weak acid/anion solutions. Hydronium ions (red arrow) from added strong acid do not impact pH directly. Instead, they react with a weak acid's anion (A^-) and increase HA concentration. Similarly, hydroxyl anion (OH^-) from an added strong base does not impact pH directly but reacts with the weak acid (HA), increasing the anionic A^- form concentration.

The buffer performs best in the range of pH close to the pK_a value of the weak acid. Therefore, for carboxylic acid ($-COOH$) with pK_a~4.8 (in acetic acid pK_a = 4.75 at 25°C, pK_a = 4.78 at 50°C) [7], pH between 3.8–5.8 represents the best performance range.

Various forms of calcium carbonate, precipitated calcium carbonate (PCC) or ground calcium carbonate (GCC), fresh or introduced with recycled fiber, present an essential buffering system. The bicarbonate ion (HCO_3^-) can consume added acid, prevent pH drop, and form unstable carbonic acid, decomposing to H_2O and CO_2. Since CO_2 evolves from the system, this buffer is irreversible.

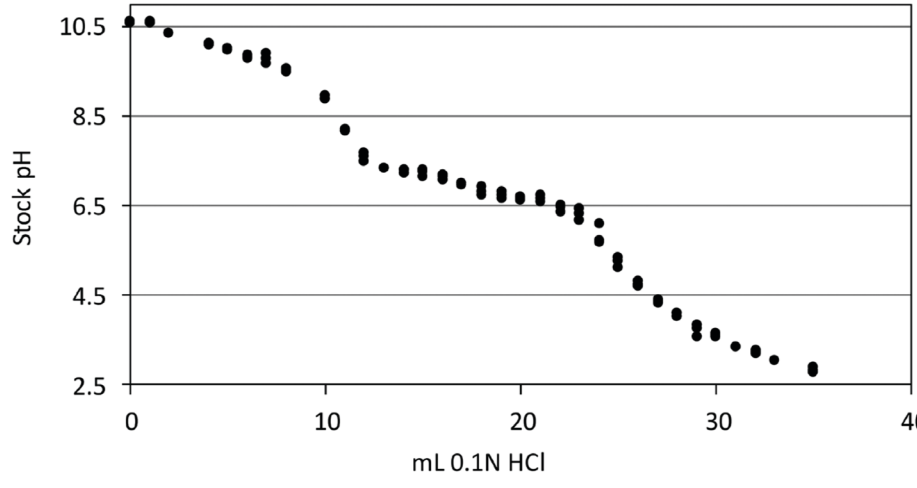

5. The pH Curve for 1 gram of unbleached pine fiber (kappa number 25) diluted to 0.5% consistency and titrated in the presence of fiber with 0.1N HCl. Data from [8].

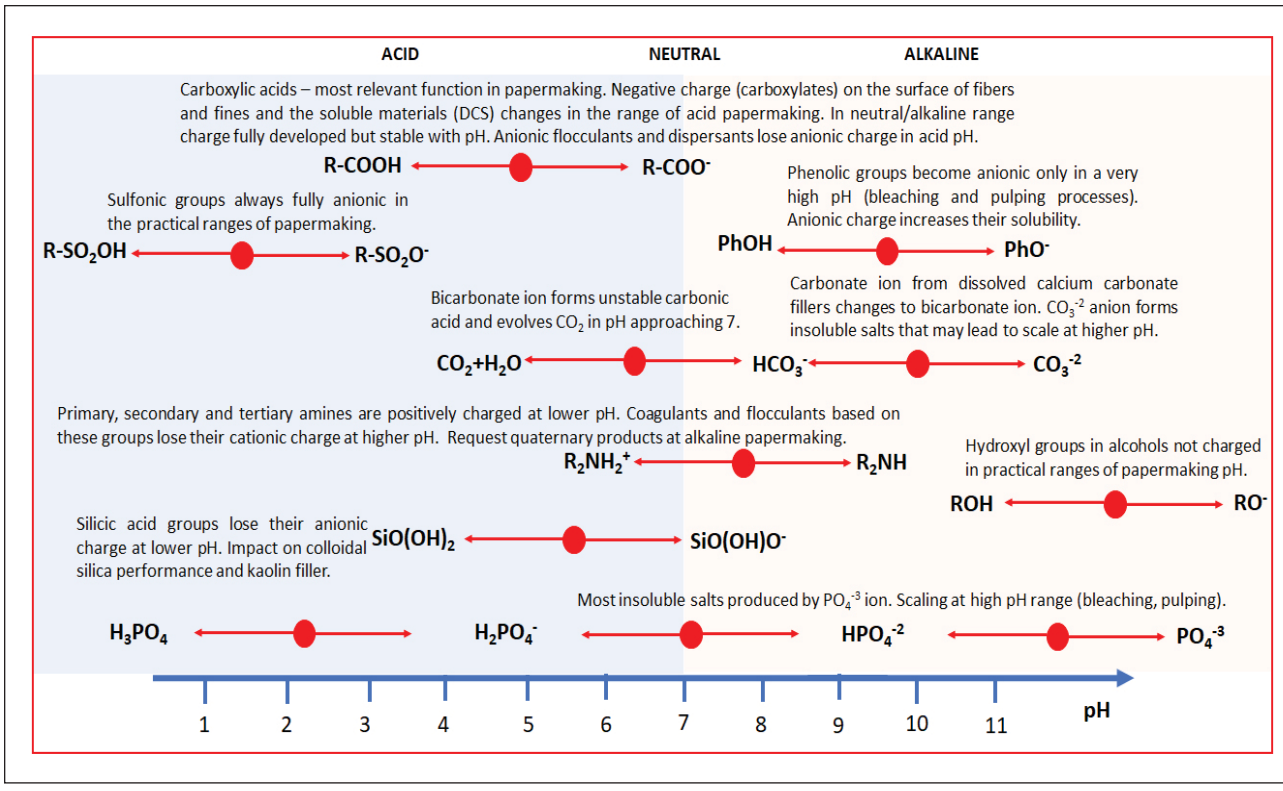

6. Most relevant weak acid systems and pH ranges of their dissociation reaction.

It is essential to know that the pulp fiber itself impacts buffering. Due to acidic groups with different acidity (pK_a values), pulps may buffer an impact of added strong acid or base around the pH close to the pK_a value. What groups are present on the pulp depends on the pulping technology, lignin content, wood species, etc. Being aware of the pulp buffering ranges and capacity may be very helpful in designing the pH control loop in the mill. **Figure 5** shows the titration curve of the pulp suspension, revealing the presence of two buffering groups as the semi-plateau regions in the plot of stock pH as a function of the amount of 0.1N HCl added [8].

Practical implications

It is significant for paper machines operating in the acid pH range that most of the conversion between charged and uncharged forms of the carboxylic acid functions occurs in the pH range of their operation. This pH sensitivity dictates special requirements for pH control to prevent sudden system charge changes.

Figure 6 presents the position of pK_a values and pH ranges for 10% and 90% dissociation for most of the weak acids relevant to papermaking. We also included general comments reflecting on the practical impact of a given acid group's dissociation on the papermaking process. It is essential to mention that the pK_a of any acidic group may change significantly based on its chemical environment. Functional groups that donate electrons (-OH, $-NH_2$, $-OCH_3$) make acid weaker, increasing its pK_a value. On the other hand, groups that are capable of withdrawing electrons ($-NO_2$, -CN, C=O) from acidic bonds undergoing dissociation make acids stronger, decreasing their pK_a value. Using potentiometric titration, Laine [9] measured the pK_a values on the surface of kraft fiber. These pK_a values varied between pK_a = 3.4 for uronic acid in hemicellulose to pK_a = 5.5 for acid groups in lignin. These values may be different for the soluble acidic species. For our discussion, the authors selected pK_a = 5 for carboxylic acids in the soluble form.

Controlling pH in a papermaking system is the most fundamental process control activity. It is essential for retention, drainage, deposit control, scale prevention, sizing, and strength development; wet-end chemistry truly starts with a proper pH control strategy. Controlling pH requires knowledge of the pH change observed with the addition of a strong acid or strong base. **Figure 7** illustrates that pH drop due to strong acid addition is minimized in the presence of substances that consume hydronium ions. How any given system responds to acid addition cannot be predicted based solely on pH but must be checked experimentally by titration with a standardized HCl solution to determine the system's *alkalinity*.

Similarly, weak acid presence reduces the impact of a strong base on pH and represents system *acidity*. The pH value does not predict how a system responds to pH correction, due to a lack of a direct relationship between weak acid or base concentrations and pH. Alkalinity and acidity

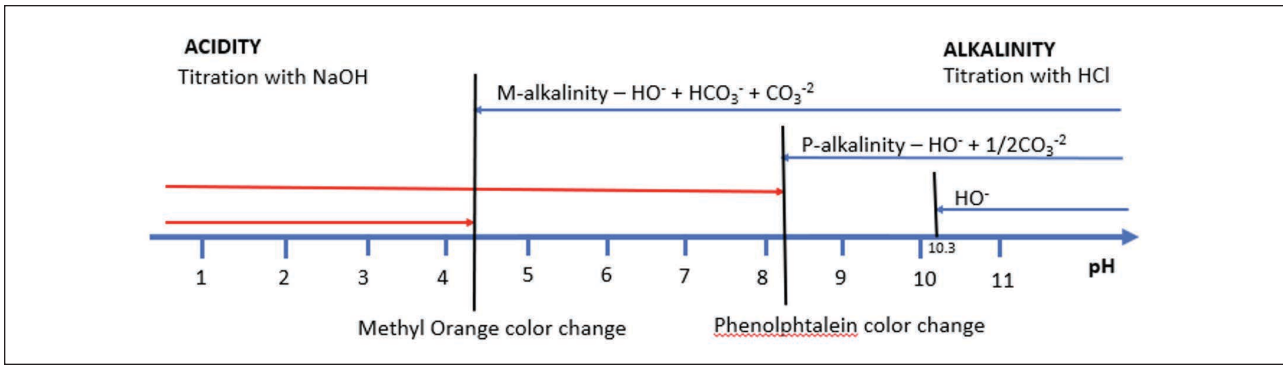

7. Concepts of acidity and alkalinity of the system.

must be measured empirically by titration with strong acid or strong base. Figure 7 illustrates the concepts and measurement of the *acidity* and *alkalinity* of the system.

CHARGE DEVELOPMENT IN THE PAPERMAKING PROCESS

Carboxylic acid groups (-COOH), with the pK_a of about 5, are the most significant source of anionic charges. As discussed earlier (Eq. 8), the steepest part of the dissociation curve coincides with the pH equal to the pK_a value. Equation 8 explains why acid papermaking, with a pH close to 5, represents a unique sensitivity of charge development due to pH variability, making the need for proper pH control of critical importance. **Figure 8** illustrates anionic charge development for carboxylic (-COOH) and sulfonic ($-SO_2OH$) groups. Neighboring acid functionalities impact their dissociation, and the actual curves may be slightly flatter. The higher the pH, the more anionic a papermaking system can be.

The sulfonic, hydroxyl, and phenolic groups do not significantly affect charge or charge variability in papermaking systems. The sulfonic group is much more acidic (pK_a <1) and will practically always fully dissociate in the range of papermaking pH. Therefore, it fully contributes to the overall negative charge at any pH but not to charge variability. Hydroxyl group (OH) (pK_a >14) and phenolic (pK_a~10) groups are much weaker acids, and their dissociation takes place at very high pH values that are not practical for papermaking, except for some pulping processes.

Practical considerations

The follow is a list of some practical considerations related to charge development:

- pH is an essential factor affecting stability for grades operating in an acid pH range.
- Neutral (pH = 6.8–7.4) and alkaline (pH = 7.5–8.2) papermaking systems are always more anionic but far less sensitive to the pH-induced variability of charge than grades operating in an acid pH range.

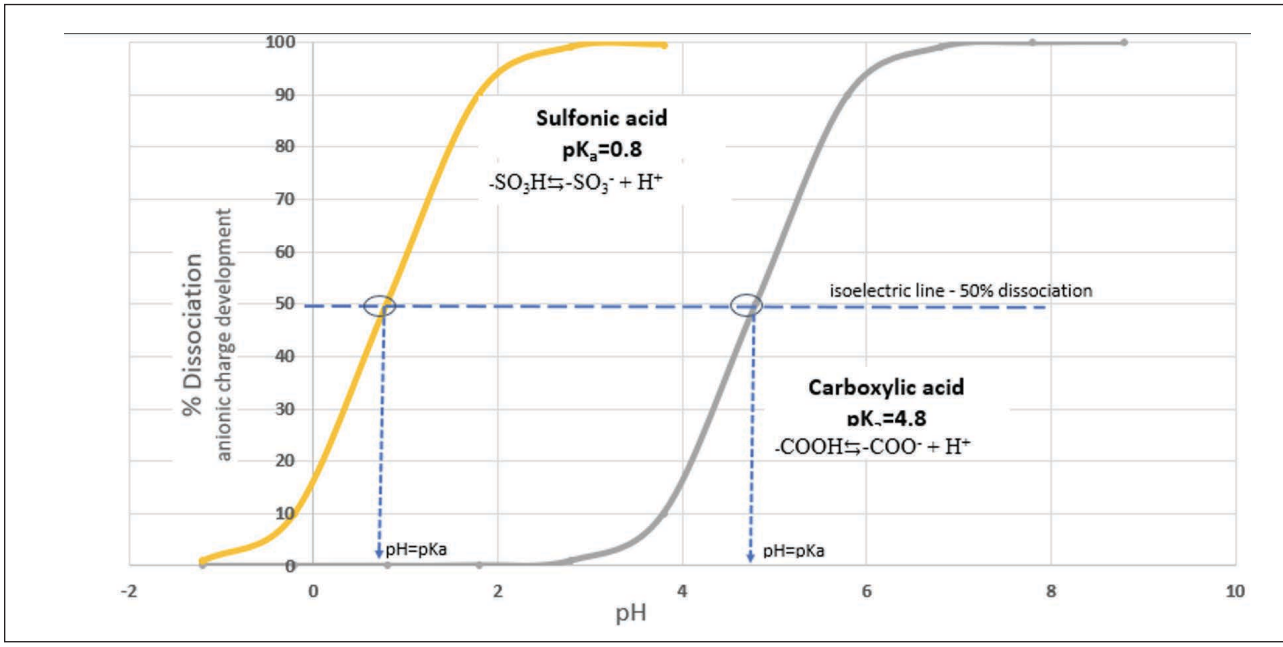

8. Theoretical dissociation curves for single carboxylic acid (pK_a=5) and sulfonic acid (pK_a=1) groups.

- The solubility of organic materials increases with elevated pH. Charged species are more soluble in water. Thus, exposing the fiber (especially high yield mechanical fiber) to higher pH increases soluble organic materials concentration. These materials are known collectively as dissolved and colloidal substances (DCS) and present challenges to cationic papermaking additives, including cationic starches.
- The level and variability of detrimental anionic substances (DCS) affect the performance and stability of retention and drainage polymers.
- The level and variability of surface charge of papermaking elements leads to variation in adsorption of additives, fiber swelling, strength, and water retention values. The impact of pH on the fiber swelling, strength, and drainage can be significantly reduced at higher conductivity levels. Higher pH increases the internal negative charge of the fiber and increases its swelling and water retention value (WRV).
- Fiber swelling associated with higher pH stock around pH 8 to 9.5 is also beneficial for fiber strength development during the refining process. Refining at lower pH results in excessive fiber shortening, while operating at a higher pH level increases refining energy demand to obtain a target freeness or strength property.
- Changes in the amount of the anionic charge alter the stability of colloidal dispersions of pitch and stickies material. Changes in this repulsive stabilizing force explain the well-known pH shock trigger to massive pitch or sticky deposits. Understanding that a lower pH reduces the anionic charge and that the gradient of charge loss is the highest around $pH = pK_a$ of the carboxylic group, one could define downward pH change, reaching pH <5 as the worst type of "pH shock." Although very important, pH shock is not the only trigger of deposit formation. Other chemical and mechanical factors such as hardness, conductivity, and shear contribute to this problem, which we will discuss in our later paper from this series. However, it is essential that papermakers closely analyze pH range and pH variation in the case of deposit problems. It is crucial to avoid the local pH variation around addition points of acidic materials as a potential source of initial colloidal destabilization.
- Anionic additives, including anionic retention polymers and dispersants, experience a loss of anionic charge at a lower pH. In the products with anionic charge derived from carboxylic acid groups, this anionic charge loss will be significant at pH <5, leading to performance deterioration. This loss of performance determines pH limits for applying anionic polymers. Anionic polymers are an excellent choice for neutral or alkaline operations, where their full anionic charge is displayed. It is important to remember that charge on the polymeric chain of flocculants (cationic or anionic) and its impact on adsorption are primarily responsible for maintaining their extended conformation in solution and improved bridging capabilities. Loss of this charge or lowering the repulsive interaction between the same charges results in coiling of flocculant molecules, decreasing their effective length and reducing their bridging capabilities.
- Most cationic additives get a positive charge from various amine functionalities and may be pH-dependent. For primary, secondary, and tertiary amines, the cationic charge from the related ammonium salt comes from the amine protonated form (Eq. 13):

$$RNH_2\,(\text{base}) + H^+ \rightleftharpoons RNH_3^+\,(\text{acid}) \qquad (13)$$

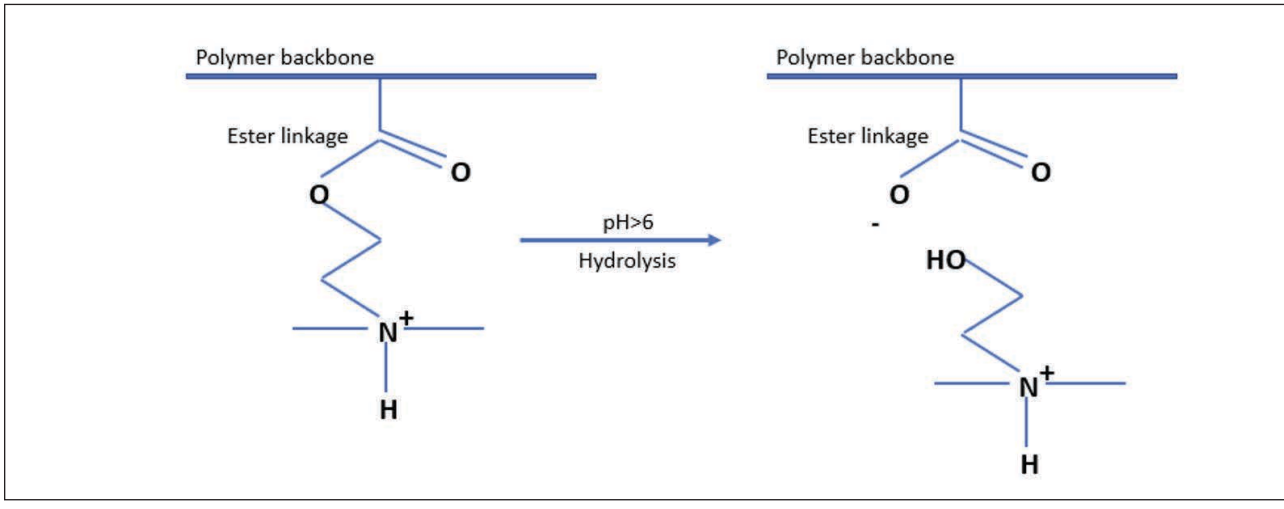

9. Hydrolysis of the ester bond in cationic flocculant leads to charge loss as a cationic charge of the substituent is replaced by an anionic charge. This reaction occurs faster at higher pH and a higher temperature—lower pH for storing flocculant solution.

This equilibrium and charge development (Eq. 13) depends on the amine's strength as a base as described by the pK_a of the ammonium salt ($pK_{a\ RNH3+}$). Typical values for aliphatic amines that resemble molecules used to produce the cationic flocculants (dimethylamino-ethyl acrylate) have pK_a~10. In the practical range of papermaking, the charge on these amines is relatively resistant to higher pH levels. However, an ester bond's hydrolysis connecting amine function to the polymer chain undergoes hydrolysis with apparent charge loss [10] (**Fig. 9**):

Other typical coagulants based on ethylene imine chemistry, pK_a = 8.04 [7], are more sensitive to deprotonation and charge loss. One may see the difference in fixation performance at pH 6.5 and higher. In one interesting case of a newsprint machine operating with a blend of TMP and recycled fiber, loss of charge of coagulant related to the conversion from acid to neutral pH led to significant loss of paper machine efficiency from increased calender stack deposition [11-12].

Cationic additives with the quaternized amine functionality (R_4N^+) carry a cationic charge independent of protonation, as they do not undergo acid-base equilibrium. Therefore, the charge density of quaternary ammonium salts practically does not depend on pH. The authors strongly recommend, especially for alkaline operations (pH = 8 and higher), quaternized amines as cationic additives (fixatives, starches) for the best performance level and stability.

IMPACT OF pH ON SOLUBILITY OF $CACO_3$ REACTIVE FILLERS

Another aspect of pH control involves the impact on the systems using various forms of calcium carbonate ($CaCO_3$) fillers. Calcium carbonate, although generally insoluble, shows slight solubility in water, as illustrated by its low solubility product, $K_{spCaCO3}$ = 6x10^{-9}), leading to the formation of Ca^{+2} and CO_3^{-2} (carbonate) ions. Carbonate ion undergoes a series of pH-dependent equilibriums (**Fig. 10**), leading to unstable carbonic acid (H_2CO_3) and CO_2 gas evolution.

The evolution of CO_2 makes this process irreversible and results in the accumulation of Ca^{+2} ions. Increasing pH will not correct the resulting increase in water hardness, and the papermaker should pay careful attention to avoiding lower pH areas, either system-wide or locally. This process includes selecting the proper pH of operation, well-designed feed points of acidic additives, and control over microbiological issues that could lead to local pH drops. Good broke management in $CaCO_3$ containing papers and excellent microbiological treatment of broke has proven beneficial in several mill applications. The authors strongly recommend adding the routine of frequent and regular hardness measurement of the broke stream containing calcium carbonate filler to detect local pockets of microbiological activity in the tower. Papermakers must pay special attention when controlling pH using acids or adding acidic additives to avoid localized pH drops. The best practices are diluting the acid and selecting the feed point where $CaCO_3$ filler consistency is low. The concern for excessive hardness development also led to CO_2-based pH control technology [6]. This technology is an excellent way of reducing pH to pH~7.4 without significant hardness development. If pH <7.4 is targeted, it becomes increasingly difficult (cost-wise) to reach the target pH due to carbonic acid's weak character. A pH control with CO_2 is used in the thick stock area of the pulping and paper machine systems. Its value is evident in the presence of calcium carbonate fillers.

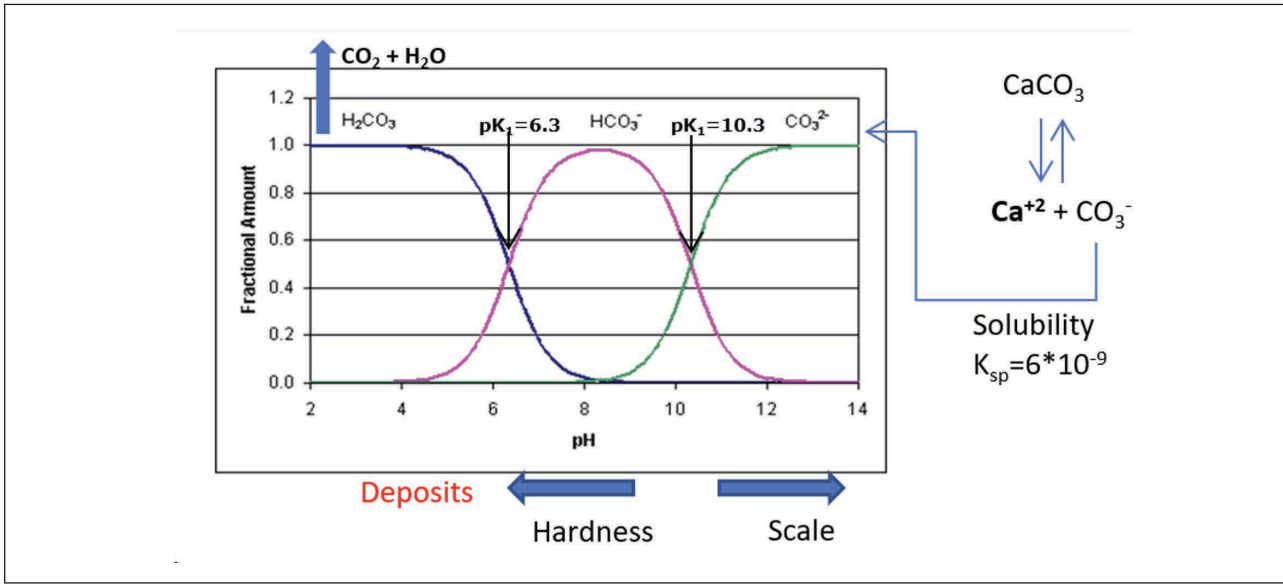

10. The pH equilibria of carbonate ion. Solubility of $CaCO_3$ fillers supplies carbonate ion (CO_3^{-2}). As we lower pH value, carbonate ion exists in equilibrium with bicarbonate ion (HCO_3^-) and hypothetical carbonic acid (H_2CO_3) that decomposes to CO_2 and water. Since CO_2 leaves the system, it leads to the gradual dissolution of $CaCO_3$ and the buildup of hardness in the system.

The addition of strong mineral acid could lead to filler yield losses with corresponding hardness increase development, potentially leading to deposits and scaling.

IMPACT OF pH ON SOLUBILITY OF FATTY AND RESIN ACIDS

Fatty and resin acid constituents are a part of natural extractives. These materials are typically a part of the outer layer of colloidal pitch particles, remaining in direct contact with the water phase and stabilizing the particles against agglomeration. This process occurs at a much lower pH level for resin acids than for fatty acids. At higher pH, the increasing anionic charge on the carboxylic groups of these acids increases their solubility. At pH = 7, close to 50%–80% of the resin acids dissociate [13]. The need for additional energy to free the hydrophobic chain of fatty acids from the hydrophobic interior of pitch particles significantly increases the colloidal pK_a value for fatty acids [12]. The presence of resin acids and fatty acids in the soluble form creates an opportunity to precipitate their salts with Ca^{+2} and Mg^{+2} as an alternative mechanism for pitch deposition.

IMPACT OF pH ON BRIGHTNESS CONTROL

Mechanical pulps undergo the well-known alkaline yellowing process at higher pH levels. Alkaline yellowing is related to chemical changes in the structure of lignin. Therefore, it is a problem almost exclusively associated with high-yield, wood-containing pulps like thermomechanical (TMP), stone groundwood (SGW), and pressurized groundwood (PGW), as well as recycled newsprint to a lesser extent. Although the degree of alkaline darkening also depends on the wood species, it is a universal problem for all mechanical grades.

The trend toward higher pH, driven by the desire to utilize calcium carbonate fillers, increases the potential for brightness loss of mechanical pulps. It was estimated that the change from acid to neutral pH operation results in losing about two brightness points [14]. The increased sheet strength at higher pH compensates for this initial brightness loss by applying higher brightness $CaCO_3$ fillers (PCC or GCC) and a high filler content target. Accommodating calcium carbonate fillers in the furnish requires a minimum pH of 6.8–7.2. A special acid-resistant PCC grade was developed for mechanical grades, offering lower hardness generated at neutral pH but not widening the application range significantly. Any higher pH level may result in unnecessary brightness losses that will require increased dosages of bleaching chemicals.

Figure 11 summarizes the pH sensitivity for mechanical grades using virgin fiber and calcium carbonate fillers. The sensitivity of the brightness of mechanical pulps to pH differs between wood species and brightening technologies. Allison and Graham discuss the alkaline darkening phenomenon and its mechanisms for Radiata pine-based pulps [15]. Even one point of brightness loss for high brightness mechanical pulps translates to significantly increased bleaching costs (up to $10/ton) and consequent excessive contamination of the wet end. With this in mind, it is crucial to understand that mechanical pulp-containing grades, especially virgin pulps, require operating at the narrow band of pH to control calcium carbonate dissolution (pH >6.8) and reduce the impact on brightness (pH <7.2).

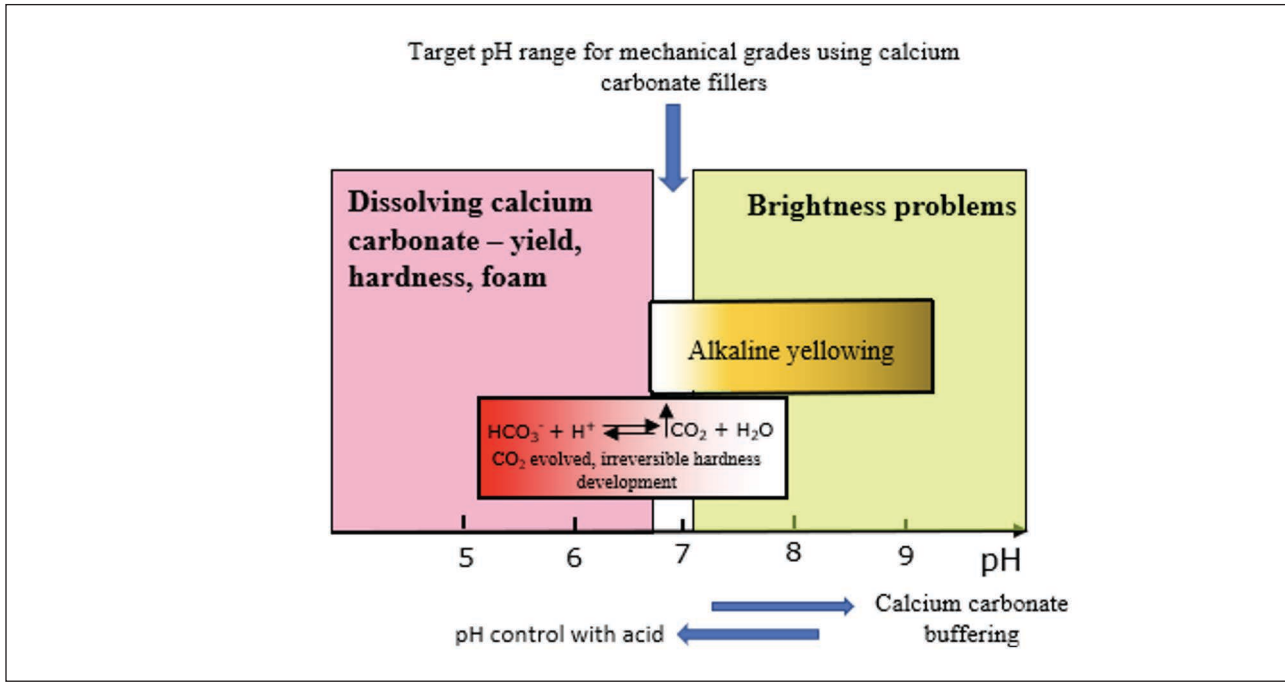

11. The pH range for mechanical grades with calcium carbonate fillers. Natural buffering by bicarbonate ion needs to be controlled by accurate acid addition to prevent pulp yellowing without triggering excessive hardness development.

It is worth mentioning that brightness sensitivity is lower for recycled mechanical furnish, allowing operation up to pH = 7.8.

IMPACT OF pH ON HYDROLYSIS REACTIONS IN PAPERMAKING

Organic compounds containing carbonyl functions (C=O), such as esters, amides, acetals, and ketenes, undergo a reaction with water (hydrolysis) that is most effectively catalyzed with bases, particularly by HO^- ion. This family of reactions is called base-catalyzed hydrolysis. The concentration of HO^- ion increases with pH, making hydrolysis reaction faster at higher pH. An example of the relevant papermaker reaction is alkenyl succinic anhydride (ASA) hydrolysis, which leads to the loss of sizing response and formation of the dicarboxylic acid and deposits [16]. The formation of the dicarboxylic acid is a competing reaction to actual sizing development through a reaction with the fiber. Hydrolysis of ASA is an unproductive pathway, leading to losses of efficiency, generation of a de-sizing dicarboxylic acid, and increasing potential for deposition of its calcium salts. This hydrolysis reaction generally defines the upper pH range for uncoated freesheet grades since brightness concerns, typical for mechanical grades, do not apply to bleached chemical pulps. Exceeding a pH of 8.0–8.2 for these grades coincides with reduced sizing effectiveness and deposit formation. As discussed earlier, the formation of deposits in these cases would increase with some local pH drops (e.g., from microbiologically driven pH drops in broke towers), resulting in a higher hardness level. Running ASA sizing at higher pH without deposits may be possible at low hardness levels, but lowering pH to the best practices range will slow ASA hydrolysis down and increase its efficiency. Other alkaline hydrolysis reactions relevant to papermaking include alkyl ketene dimer (AKD) sizing application, generation of pectic acids contributing to soluble anionic trash, and free fatty and resin acids from their esters.

CONCLUSIONS

Water is an essential element in the papermaking process. Due to its molecular structure and polarity, water offers unique solvent properties. It makes water an ideal medium to disperse cellulose fiber and promote hydrogen bond development. Water is also an excellent solvent for various organic and inorganic materials. Water dissociates, forming hydrated proton (H_3O^+) and hydroxyl anion (HO^-). Concentrations of both these ions are interrelated and typically expressed by pH value. Process pH is the most crucial water chemistry parameter affecting the properties of cellulose fiber and additives, both process and functional. The pH indirectly affects charge properties in terms of surface charge and charge demand. The pH conditions also affect retention, drainage, strength, water absorption, deposits, sheet defects, and scale. Finding proper pH to satisfy the often-conflicting needs of the previously-listed applications is the most complex chemistry decision facing papermakers. It seemed essential to these authors to assist papermakers by collecting the basics of acid-base interactions, basic definitions, and intricate ways pH influences their operations. A sound understanding of these basic principles will build more attention to selecting the optimal and stable pH value for their process.

Not all papermaking systems are equally sensitive to pH levels and their variability. Based on the discussion in this paper, one can quickly identify papermaking systems where pH control is of essential importance to machine performance and product quality. As a minimum, papermakers need to measure pH in the headbox or tray water. We recommend that pH measurements be performed continuously online and correlated with relevant paper machine performance data and product quality. Over time, the analysis of generated data will provide information on the sensitivity of the given papermaking system to pH and the optimum pH range. Determination of the sources of pH variation and an effort to eliminate them should then take a preference over the aggressive pH control approach. An online, automatic pH control loop should be developed to provide the final pH level control and stability control. The importance of this approach may vary between grades. Papermakers could miss potential gains from addressing pH issues without initial pH monitoring and correlation efforts.

SUGGESTED READING

As we prepare this paper, TAPPI Press is completing the first printing of a new textbook, *Process Chemicals for Papermaking*, edited by Martin A. Hubbe and Scott Rosencrance. Chapter 2 by Temple Ballard, John Williamson, and William Tuck covers "Influent water: Starting with the right water." Other relevant chapters include Chapter 3, "Charge control agents, acids, and bases: Aiming for balanced conditions" by Martin A. Hubbe and Chapter 7, "Wastewater treatment: Making sure it ends well" by Angeles Blanco, Ana Balea, Borja Ojembarrena, Daphne Hermosilla, Antonia Gasco, and Carlos Negro. **TJ**

LITERATURE CITED

1. Pruszynski, P. and Gratton, R., "Wet-end chemical applications: Paper machine chemical environment and interactions between chemical additives," in *Advances in Papermaking Wet End Chemistry Application Technology* (M. Hubbe and S. Rosencrance, Eds.), TAPPI Press, Peachtree Corners, GA, USA, 2018.
2. Xu, L., Pruszynski, P., and Hart, P., *TAPPI J.* 16(10): 567(2017). https://doi.org/10.32964/TJ16.10.567.
3. Luzar, A. and Chandler, D., *Nature* 379: 55(1996). https://doi.org/10.1038/379055a0.
4. Dill, K.A., Truskett, T.M., Vlachy, V., et al., *Annu. Rev. Biophys. Biomol. Struct.* 34: 173(2005). https://doi.org/10.1146/annurev.biophys.34.040204.144517.

5. Brini, E., Fennell, C.J., Fernandez-Serra, M., et al., *Chem. Rev.* 117: 12385(2017). https://doi.org/10.1021/acs.chemrev.7b00259.
6. Jansson, A-C., "Carbon dioxide based applications for optimization of calcium carbonate containing papermaking processes," *PAPTAC Annu. Meet., 95th*, PAPTAC, Brossard, QC, Canada, 2009, p. 429.
7. Dean, J.A., *Lange's Handbook of Chemistry*, 14th edn., McGraw-Hill, New York, 1992.
8. Hart, P.W and Rudie, A.W., *The Bleaching of Pulp*, 5th edn., TAPPI Press, Atlanta, 2012, p. 156.
9. Lovgren, L.J., Stenius, P., and Sjoberg, S., *Colloids Surf., A* 88(2-3): 277(1994). https://doi.org/10.1016/0927-7757(94)02834-6.
10. Ekberg, R. and Wagberg, L., *J. Appl. Polym. Sci.* 38(2): 297(1989). https://doi.org/10.1002/app.1989.070380211.
11. Dechandt, A., Watkins, T., and Pruszynski, P., *Appita J.* 57(1): 13(2004).
12. Richardson, D., Waller, N., Parsons, T., et al., "Optimization of neutral papermaking wet end chemistry for pitch-free newsprint manufacture," *Appita Annu. Conf. Proc., 57th*, APPITA, Macleod, Vic, Australia, 2003, p. 219.
13. McLean, D., Vercoe, D., Stack, K., et al., *Appita J.* 58(5): 362(2005).
14. Evans, B. and Slozer, M., "Neutral groundwood papers: Practical and chemical aspects," *Int. Pap. Coat. Chem. Symp., 5th*, PAPTAC, Brossard, QC, Canada, 2003.
15. Allison, R. and Graham, K., *J. Pulp Pap. Sci.* 16(1): 28(1990).
16. Farley, C.A. and Wasser, R., in *The Sizing of Paper* (W.F. Reynolds, Ed.), TAPPI Press, Atlanta, 1989, p. 54.

ABOUT THIS PAPER

Cite this article as:
Pruszynski, P., Xu, L., and Hart, P.W., *TAPPI J.* 21(6): 313(2022). https://doi.org/10.32964/TJ21.6.313

DOI: https://doi.org/10.32964/TJ21.6.313

ISSN: 0734-1415

Publisher: TAPPI Press

Copyright: ©TAPPI Press 2022

About this journal

ABOUT THE AUTHORS

Water chemistry is a fundamental topic for wet-end additives and operation. Many new engineers do not fully understand these fundamentals, so we are attempting to provide a useful review to assist them as they start their new careers. This review highlighted current industry trends (more recycled content, more closed water systems, and higher percentage of young employees). An earlier work focused on conductivity, and future work will address other fundamental areas.

As water chemistry has a broad impact on wet-end additives and operation, the author team was comprised of members from both the chemical supplier side and papermaker side to provide a comprehensive view and knowledge in this review.

Through this study, we gained a greater appreciation for the importance of basic/fundamental factors with broad impacts. It is always interesting to revisit how much a small pH change in the papermaking pH range can alter chemical performance.

With this review, mills gain a comprehensive view of how water affects wet-end additives and how to make optimal use of them. The work highlights the need for good pH control. It also can function as a good training resource for new employees.

Our next step is to put the knowledge in this review paper to work and to develop the next paper in our wet-end chemistry series.



Pruszynski

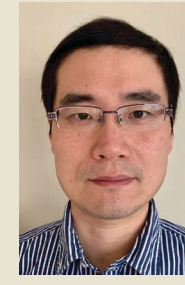

Xu



Hart

Pruszynski is technical director and owner at Pruszynski Paper Chemistry Consulting LLC, Naperville, IL, USA. Xu is senior research scientist/engineer and Hart is director, Fiber Science and Innovation, at WestRock in Richmond, VA, USA. Email Xu at lebo.xu@westrock.com.

Rewet suppression through press felt engineering

SUMNER DUDICK, DENNIS W. HESS, AND VICTOR BREEDVELD

ABSTRACT: Due to the immense energy and associated financial cost of drying paper, achieving a drier web entering the dryers is a key objective in paper manufacture. One major research thrust has been finding a way to increase press solids by mitigating or eliminating rewet in the press section. For decades, solutions to this problem have remained elusive.

In this work, we develop a novel approach that significantly reduces rewet by rupturing the liquid channels between felt and web. We illustrate the effects that altering the mechanical and surface properties of the press felt matrix have on the stability of these liquid channels. In a laboratory-scale platen press, a 40% reduction in the residual water of 120 g/m^2 southern bleached softwood kraft (SBSK) pulp handsheets after pressing was observed, corresponding to an increase in press solids from 48% to 61%. For reference, pressing under identical conditions with paper blotters, in which minimal rewet is presumed to occur, resulted in 64% solids. Furthermore, we observed enhanced dewatering across a range of basis weights, applied pressures, and felt types. In addition to measuring the solids content of pressed sheets, we capture and analyze video evidence of the mechanisms at play in our improved dewatering technology.

Application: This work describes a novel approach to prevent rewet in the press section. The authors hope that the papermaking community will use these insights to design press fabrics that increase the energy efficiency of the mill.

Since the 1960s, papermakers have been aware that reflux of water to the sheet after pressing compromises the efficiency of mechanical dewatering [1]. Efforts to improve press section performance by mitigating rewet have included primary strategies such as creating a hydrophobic barrier within the felt [2], including superhydrophilic regenerated cellulose filaments [3]; adding angular filament profiles in the fabric [4]; placing one-way valves in the felt that open and close with applied pressure [5], including a low porosity flow control layer in the felt [6]; and designing ever finer batt filaments to combat the capillary forces in the sheet [7]. For various physical and practical reasons, many of these approaches have been limited in the results they deliver when tested on production paper machines. Still, the previous decades have seen tremendous progress in pressing technology. With improved fabric designs and extended nips, the state of the art can achieve up to 55% solids after pressing on certain grades. Although longer dwell times have pushed press sections close to achieving minimum equilibrium moisture in-nip, rewet continues to be a major challenge.

We propose a new approach to mitigating rewet that relies on placing a stiff, porous spacer at the felt surface, such that direct contact between the felt and the paper web is reduced. Doing so decouples felt-web separation from decompression exiting the nip. When the spacer layer is well-designed, fluid channels connecting the paper and felt are destabilized; they break, resulting in fully dewatered paper that has no contact with the felt, all before the layers are pulled apart. When the expanding paper, upon decompression, creates a capillary driving force for reflux of water towards the sheet, pathways for water flow have been disrupted, and rewet is avoided.

EXPERIMENTAL METHODS

Wet handsheets were prepared at different basis weights from southern bleached softwood kraft (SBSK) pulp, which was obtained as dry lap and resuspended in water. The handsheet protocol followed the TAPPI Standard Test Method "Forming handsheets for physical tests of pulp," up until pressing. Instead of pressing, the wet webs were adjusted to a moisture ratio (MR) of 3 (25% solids) to simulate the couch solids on a paper machine. The MR and solids content are defined by the mass composition of water and fiber in the sheet:

$$MR = \frac{m_{water}}{m_{fiber}} \qquad solids = \frac{m_{fiber}}{m_{fiber} + m_{water}}$$

The wet web was then pressed against various felt configurations in a benchtop screw press (**Fig. 1**). A force sensor allows the applied stress to be measured and controlled. One primary advantage of using a platen press is that the imposed pressure gradient is essentially unidirectional. This simplifies the problem of analyzing flow in three di-



1. Screw press used for dewatering trials. Shown from bottom to top: the bottom platen, paper, press felt, top platen, force sensor, and screw press.

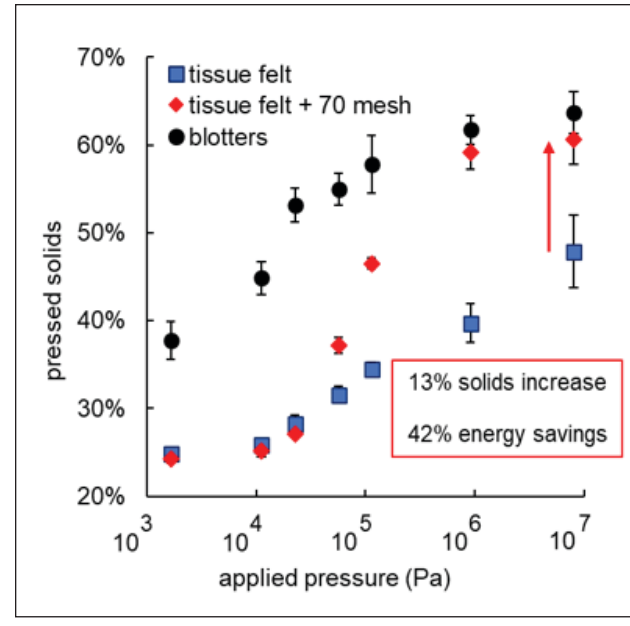

2. Pressed solids of 120 g/m² southern bleached softwood kraft (SBSK) pulp handsheet vs. applied pressure for various pressing conditions: (blue squares) commercial tissue felt, (black circles) stack of dry blotters that represents limit of maximum drying, and (red diamonds) tissue felt with metal #70 mesh.

mensions—which is already complicated by the heterogeneity of the materials involved. The paper is pressed three times at a given pressure to simulate the sequence of nips on the machine, to reduce variation introduced from control of the initial moisture ratio, and to show the limits of enhanced dewatering. Following pressing, the moisture content of the paper was determined by comparing the weight to that after oven drying at 105°C for 8 h.

RESULTS

The impact of sandwiching a mechanically stiff layer between the press felt and web is illustrated in **Fig. 2**. In this case, a commercially available #70 stainless-steel mesh was used as the stiff spacer layer (red data series). The blue series, which represents pressing with a commercial tissue felt, serves as the base case. The black series, in which the paper is pressed with a thick stack of blotters, shows the upper limit of solids that can be realized at a given pressure in the absence of rewet. At low pressures, no mechanical dewatering is done; the blotters' result improved solids because of the strong capillary forces they exert. As pressure is increased, more water is expelled from the web, resulting in higher press solids. At pressures relevant to industrial conditions (7 MPa), the web is significantly deformed, resulting in dewatering. The presence of a stiff spacer layer enhances the dewatering potential of the press felt, as seen in the transition of the red series from the blue series to the black series. Pressing has shifted to a scenario where limited rewet occurs. An improvement of 13% solids from 48% to 61% corresponds to a 40% reduction in the residual moisture content of the sheet. That translates to a 42% reduction in the dryer load, assuming the sheet is dried to 95% solids.

To illustrate how sandwiching a spacer between the felt and web improves dewatering, we videographed the paper and felt as they were pressed. **Figure 3** depicts frames from these videos. Fluorescent dye was added to the water so that it would be easily detectable under the microscope. The brighter a region, the more water it contains. As time progresses from left to right, the pressure is increased, then reduced. A stark difference can be observed between pressing only with the felt (top row of images) and with the mesh-added felt (bottom row). Initially, both start the same: the (wet) paper is very bright, and there is no water in the felt. Upon compression, water is driven from the sheet into the felt. Here, the mechanism of the technology can be seen; the mesh layer destabilizes liquid bridges between the paper and felt. In the top images, a continuous bright channel spans the paper and felt. Upon decompression, water flows back through this channel, rewetting the paper. In the bottom row, the liquid bridges snap once water is transported into the felt. Upon decompression, there is no path for water to rewet the paper. After pressing, water has moved from the paper into the felt, regardless of the felt configuration. With the mesh-added felt, however, the paper is noticeably drier.

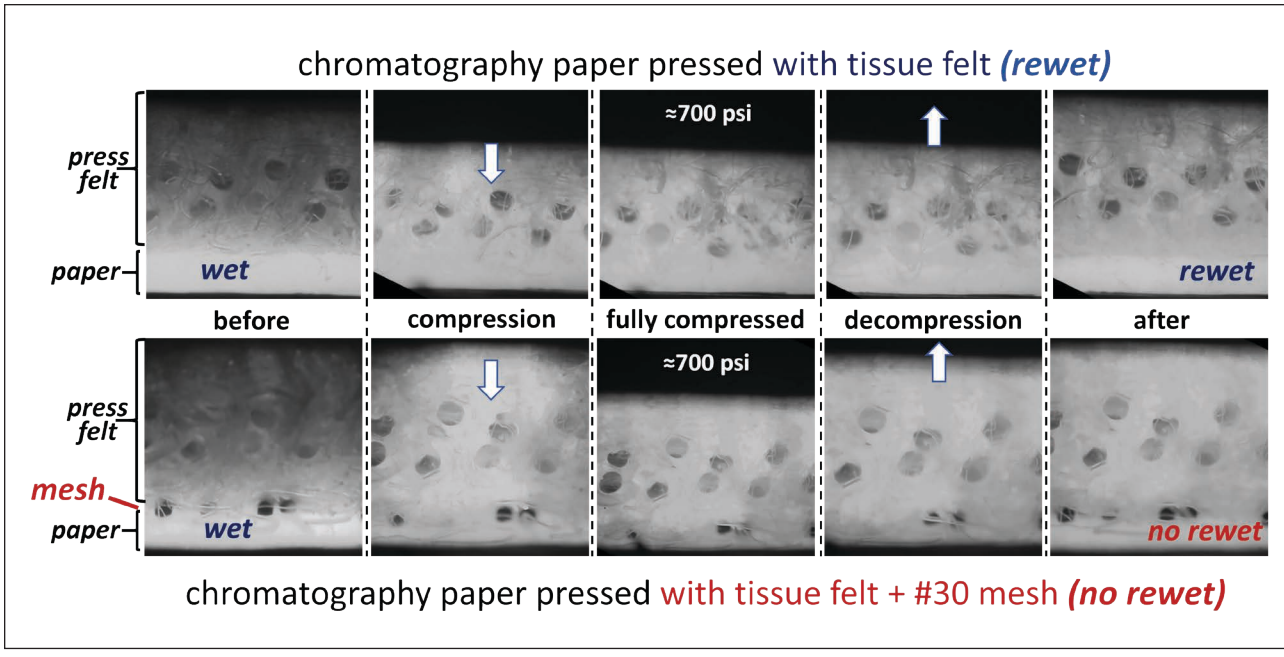

3. Still images from videos taken during the pressing of wet chromatography paper (initial solids 25%) up to maximum pressure of ~5 MPa with: (top) commercial felt, and (bottom) commercial felt plus #30 mesh (wire thickness 165 µm; openings 681 µm). Sideview image with fluorescently labeled water; greater brightness indicates larger amounts of water present.

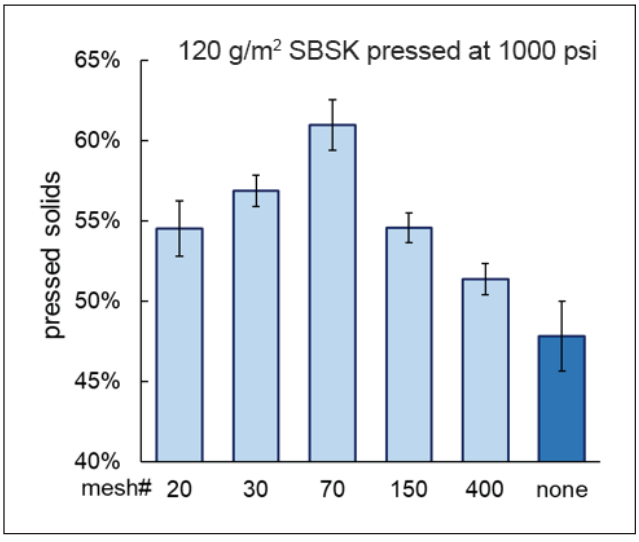

4. Effect of mesh size on press solids. The dimensions of the spacer layer have a significant impact on dewatering. A mid-size mesh balances tradeoffs between gap thickness, pressure distribution, and sheet contact.

Effect of mesh size

The dimensions of the spacer layer have a significant effect on the stability of liquid channels between the felt and paper. The pressed solids obtained with different commercially available meshes between the felt and paper are shown in **Fig. 4**. The solids appear to go through a maximum as the mesh size is changed; this suggests a certain tradeoff between various contributions. If the mesh number is too low (thick wires and large openings), the pressure applied to the sheet will not be uniform. Also, there is a greater volume of fluid within the liquid bridges (i.e., mesh openings). When these bridges are disrupted, more fluid can return to the sheet. On the other hand, high mesh numbers have small mesh openings that are similar in size to the filament and pore sizes already present in the felt. If the gap is too small, the liquid bridges are less likely to break, and the mesh-added felt system begins to resemble the felt alone. The optimum mesh size depends on the basis weight of the sheet, since deformation of the paper web into the spacer pores affects the gap height and, thus, liquid breakup.

Effect of basis weight

Figure 5 shows a Sweet plot of the moisture ratio obtained at different basis weights. Reassuringly, the technology is effective over a wide range of basis weights. At high basis weight, the effect of reducing rewet on solids is lower because rewet constitutes a lower fraction of the sheet's mass. At lower basis weights, the spacer layers that were used did not perform as well as hoped. Two factors likely contribute. First, issues with pressure uniformity introduced by a stiff layer are exacerbated by a thinner sheet. Second, there is likely not enough water initially in the sheet to fill the open spaces in the mesh and span the gap introduced by the spacer. For low basis weight sheets, the design of the spacer will have to be optimized beyond these standard meshes to effectively mitigate rewet.

Sweet plots enable regression to estimate the rewet and equilibrium moisture in the press [7]. Plotting moisture ratio vs. inverse basis weight produces a line whose slope

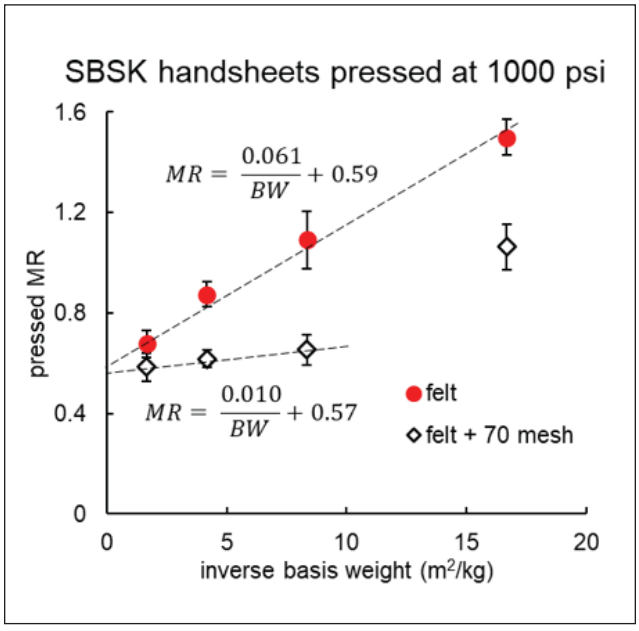

5. Effect of basis weight (BW) on dewatering. The technology is effective over a range of basis weights, reducing rewet by a factor of 6 (MR = moisture ratio).

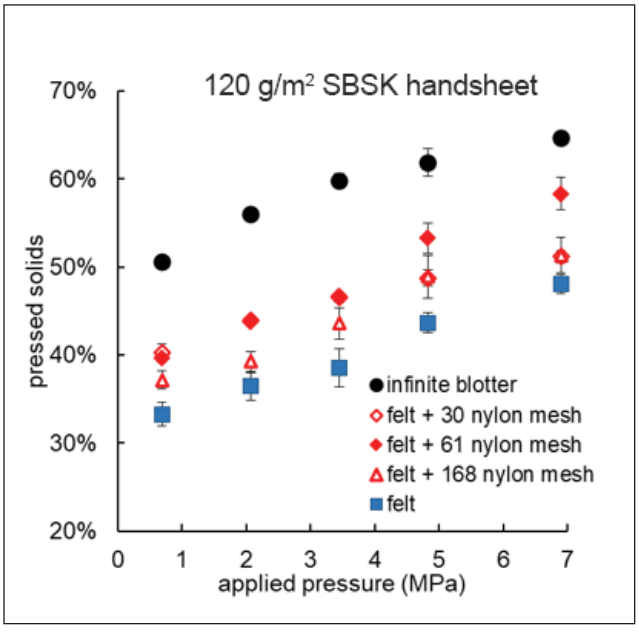

6. Enhanced dewatering observed with nylon meshes. The medium-size mesh (#61) performs best of the ones tested, for reasons previously discussed. Two of the mesh series, #30 and #168, fall on top of one another.

is equal to the rewet and whose intercept is equal to the equilibrium moisture ratio of the paper. For reasons mentioned previously, the data point of mesh-added felt at lowest basis weight was excluded from the regression, because its dewatering is not fully representative of liquid channel breakup. As expected, the series share the same intercept, because equilibrium moisture of the sheet should only depend on the furnish properties and pressure applied—not

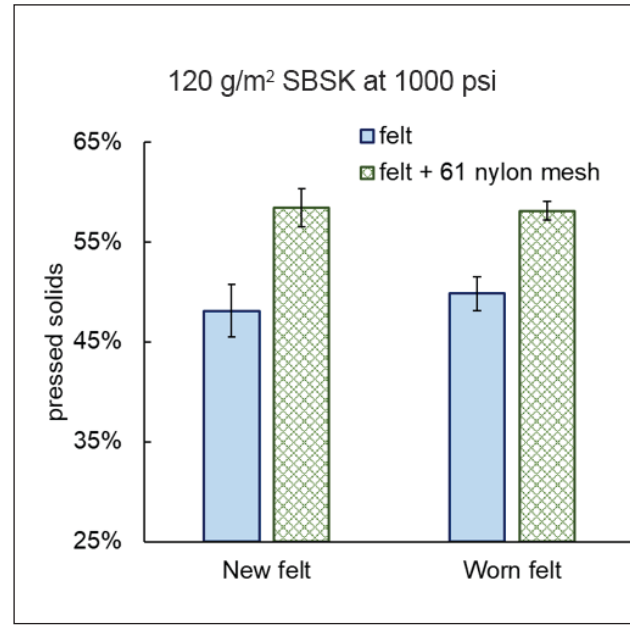

7. Enhanced dewatering observed with new and used tissue felts.

the felt characteristics. The series have different slopes, however, suggesting that rewet has been reduced from 61 g/m² to 10 g/m² by adding the mesh. These values display excellent agreement with those of the rewet values suggested by Fig. 2, 62 g/m² and 9.6 g/m².

Nylon meshes

For reasons of safety and wear, metal structures would be difficult to implement in a paper machine press nip. Metal materials, however, should not be necessary to achieve the desired liquid bridge breakup. Provided that the spacer layer is sufficiently stiff to resist significant deformation under nip loads, the approach should work well. Given that stress applied in the nip is around 10 MPa, any material that has a stiffness (i.e., elastic modulus) of at least 1 GPa will likely work. Fortunately, there are many candidate materials that satisfy this criterion. Among them, nylon meshes are a natural choice, as nylon is already used in press fabrics.

Figure 6 shows the enhanced dewatering performance that nylon meshes add to a commercially available felt. Similar to the effect demonstrated with metal meshes, we observed lower residual water in the sheet after pressing when the spacer layer is included. Once more, the dimensional parameters of the spacer layer have a significant impact on the mitigation of rewet. Compared to pressing with the felt alone, each of the mesh-added felts showed at least some improvement in press solids. The greatest improvement was seen with the medium-sized mesh, implying that there is an opportunity to optimize the design of the spacer layer beyond the commercially available meshes. As in Fig. 2, the gap between the

blue and red series highlights the progress already made in developing this technology. The gap between the red and black series corresponds to the opportunity to further optimize this process. Although less improvement was seen with the nylon meshes compared to metal meshes, this is more indicative of only testing three structures, which is less likely to capture the optimum value.

Different felts

Because the technology works by disrupting the fluid phase, improved dewatering should be observed regardless of what felt is used, or in what condition the felt may be. **Figure 7** shows results obtained from pressing a 120 g/m^2 SBSK handsheet at 1000 psi (7 MPa) with new and used felts. Addition of a mesh improved dewatering in both cases. The used felt appears to have marginally better dewatering ability, compared to the new felt. However, this is only because the new felt has not been sufficiently well conditioned. Overall, it is encouraging to see that the technology has high potential to work over the lifetime of the felt.

ECONOMIC IMPACT

The financial value of reducing rewet comes in two main ways: energy savings and increased production. By removing more water in the press section, less has to be dried later—a notoriously intensive and costly process. Reducing the drying load by 40% would result in an enormous reduction in energy. Assuming that, in the base case, energy devoted to drying the sheet costs about US$20/finished ton, the impact on energy savings would be US$8/finished ton. In application, the control/base case—pressing with conventional press fabric—could perform better than suggested by experiments on the platen press, simply due to dynamics. Even if the drying load were only reduced by 10%, energy savings would still be about US$2/finished ton, an attractive value for technology that is essentially drop-in.

The value that could be created from increased production in debottlenecking the dryers is more difficult to estimate. For those mills currently struggling with dryer limitations, marginal profitability attained with higher production volume could be at least as valuable as energy savings. The analysis is complicated by other process streams that would then become production-limiting. In theory, reducing the dryer load by 40% could result in up to 40% increase in production for this case. However, in practice, upstream processes engineered around the initial dryer limitation would quickly become new bottlenecks. Understanding how reducing energy use in the dryers results in higher production requires a detailed analysis that would have to be performed on a mill-by-mill basis. Additionally, the economic considerations complicate quickly. Significant increases in production, especially those that can be realized sector-wide, are likely to affect the pricing—and thus, profitability—of marginal tons.

FUTURE WORK

Additional work is needed to improve the design of the spacer layer. One limitation of working with commercially available meshes is that the thickness (gap size) and mesh opening width cannot be varied independently. For breaking water channels, we hypothesize that more slender openings relative to gap thickness would be preferable. Another disadvantage of the commercial samples is the mesh geometry itself. Because of the filaments' cylindrical profile, some water is likely getting trapped near the paper surface. This could potentially be avoided by choosing a different pore geometry in the spacer.

Another limitation of using meshes is their roughness, which creates two main problems. The first is sheet smoothness. Placing a mesh between the web and the felt negatively impacts sheet smoothness, although the exact extent of the effect—which will ultimately depend on drying and potential calendering—is difficult to assess in our current laboratory setup. The second potential problem with roughness created by mesh weave is that it creates larger channels along the interface of the web. When the applied pressure gradient is unidirectional, such as in our platen press, this presents no issue. However, once machine-direction pressure gradients are introduced, such as might be observed in a nip, dewatering could be severely compromised. Both these problems could be resolved by engineering a spacer layer with high surface smoothness and stiffness that is matched to the felt and web, while maintaining appropriate dimensions for channel breakup.

Assessing the effect of the spacer's surface wettability is an ongoing study. Although the primary function of the spacer is mechanical, we have observed there is potentially a marginal improvement from making the pore walls of the spacer more hydrophobic. How this may interact with the time scales and pressure gradients in a nip vs. platen press will have to be determined.

Overall, designing structures with the goal of controlling liquid channel rupture is a new paradigm for press fabric design and suggests an encouraging future for this body of work.

CONCLUSIONS

Enhanced dewatering can be realized by severing the liquid channels that would otherwise span the felt-web interface. One, mechanical, way of accomplishing this is to introduce a stiff, porous spacer between the felt and web. Doing so effectively changes the boundary conditions of the interface while it is in the nip. Because the mechanism works by disrupting the fluid phase, it should only be indirectly influenced by other parameters in the system like nip load, pulp furnish, or press fabric. This means that application is likely to be wide-ranging, although we do expect some of the design optimization to depend on paper grade. While there is additional work to be done, initial results of this approach are promising. Improved dewatering observed

on the laboratory scale, coupled with a preliminary economic analysis, shows that structures that destabilize liquid channels at the felt-web interface have enormous potential in paper manufacture. **TJ**

ACKNOWLEDGEMENTS

The authors would like to thank AstenJohnson for providing all felts used in this study. We would also like to thank the Renewable Bioproducts Institute at Georgia Institute of Technology for funding the work.

LITERATURE CITED

1. Wahlström, P.B., *Pulp Pap. Mag. Can.* 70(10): T349(1969).
2. Johnson, M.C. and Schultz, G.V., U.S. pat. 5,372,876 (Dec. 13, 1994).
3. Despault, M.P. and Patterson, B.S., U.S. pat. 7,138,037 B2 (Nov. 21, 2006).
4. Hansen, R.A., U.S. pat. 7,128,810 B2 (Oct. 31, 2006).
5. Busker, L.H. and Daane, R.A., U.S. pat. 3,840,429 (Oct. 8, 1974).
6. Beck, D.A., U.S. pat. 7,323,087 B2 (Jan. 29, 2008).
7. McDonald, J.D. and Kerekes, R.J., *TAPPI J.* 16(2): 81(2017). https://doi.org/10.32964/TJ16.2.81.

ABOUT THIS PAPER

Cite this article as:
Dudick, S., Hess, D.W., and Breedveld, V., *TAPPI J.* 21(6): 327(2022). https://doi.org/10.32964/TJ21.6.327

DOI: https://doi.org/10.32964/TJ21.6.327

ISSN: 0734-1415

Publisher: TAPPI Press

Copyright: ©TAPPI Press 2022

About this journal

ABOUT THE AUTHORS

We chose to research rewet in the press section because of the immense energy savings that could be realized with enhanced dewatering. This research complements developments in press nip design, which have previously attained close to equilibrium moisture in-nip. Our fabric designs have the unique potential to fully realize the value of this technology by mitigating the effect of rewet.

The most difficult aspect of this research was visualizing the flow of water in the felt/paper system. This was addressed largely with the expertise of the corresponding author's background.

We discovered that rethinking some basic assumptions can lead to great leaps in engineering. Our most interesting result was that adding a stiff spacer can lead to better dewatering.

Mills would benefit from this research's energy savings in the dryer section and increased production. The next step is to design our own spacers, considering the impacts on sheet smoothness, wear, permeability, and multidimensional flow.



Dudick



Hess



Breedveld

Dudick is graduate researcher, Hess is professor emeritus, and Breedveld is professor in the school of Chemical & Biomolecular Engineering and Renewable Bioproducts Institute at Georgia Institute of Technology, Atlanta, GA, USA. Email Breedveld at victor.breedveld@chbe.gatech.edu.

The Influence of the Fine Structure of Cellulose on the Action of Cellulases

CURTIS S. WALSETH

In the hydrolysis of cellulose with enzymes of *Aspergillus niger* at 47°C., it was shown that a great decrease in the rate occurred in the late stage of the reaction, usually with considerable cellulose still remaining undissolved. The most important factor contributing to this lowered rate was shown to be a decrease in the reactivity of the residual cellulose during the course of the reaction, but the activity of the enzyme solution itself decreased somewhat during the course of the reaction. Inactivation of the enzyme by heat and inhibition by the presence of glucose were both shown to contribute to the loss in activity, with the former being somewhat more important. As the enzymic hydrolyses progressed the moisture regain values for the undissolved residues decreased. This is evidence that amorphous regions were attacked most rapidly and that this preferential removal of amorphous cellulose was the reason for the decrease in reactivity of cellulose noted during the course of the enzymic hydrolysis. The relative content of amorphous cellulose, as indicated by moisture regain values, was shown to be the main factor which could account for the great differences that were observed in the ease and extent of decomposition of various celluloses by enzymes. A striking difference between the nature of acid and enzymic hydrolysis of cellulose was detected. By means of enzymic treatment, it was found possible to dissolve a considerable portion of a cellulose sample, but still to retain a relatively high degree of polymerization in the residual cellulose, whereas an acid hydrolysis, which results in any appreciable loss in weight, decreases the degree of polymerization of undissolved cellulose to a very low level. The most likely explanation for the difference lies in the relative size of the two hydrolytic agents and their consequent ability to penetrate the cellulose fine structure.

CURTIS S. WALSETH, Graduate Student, The Institute of Paper Chemistry, Appleton, Wis.; present address, Weyerhaeuser Timber Co., Pulp Div., Longview, Wash.

IN A previous paper (*1*), it was shown that the enzymic hydrolysis of cellulose is characterized by a very rapid reaction rate in the initial stage, followed by a decrease to a low and virtually constant rate in the later stage, usually with considerable cellulose still remaining undissolved. The difficulty of attainment of complete enzymic hydrolysis of cellulose has previously been reported by Karrer (*2*), who also pointed out the extreme variability of different celluloses with respect to ease of hydrolysis, from native cellulose (which is extremely resistant) to some of the more reactive regenerated celluloses. In the present work the causes of these phenomena are considered. In addition, the effect of enzymic action upon the undissolved cellulose residues from the hydrolysis reactions, as reflected by measurements of the degree of polymerization and the moisture regain, was considered, since no direct evidence was available concerning this effect. This information should be of assistance in interpreting the kinetics and general nature of the enzymic hydrolysis of cellulose.

TAPPI Journal revisits relevant research



The above paper by Curtis S. Walseth is another in *TAPPI Journal*'s series of recently digitized classic papers from the archives. According to J.Y. Zhu of the *TAPPI Journal* Editorial Board and the USDA Forest Products Laboratory, Walseth "carefully designed a set of very simple experiments to illustrate the contributing factors of decreasing cellulose hydrolysis in the late stage of enzymatic hydrolysis. The results indicate that the relatively rapid hydrolysis of disorder cellulose, which leaves a high crystalline cellulose fraction, is the main factor to decrease cellulose hydrolysis at a late stage. Crystalline cellulose is much more difficult to access than disorder cellulose by enzymes."

In the May issue, we also presented another classic paper from 1967, "The effect of component removal upon the porous structure of the cell wall of wood. II. Swelling in water and the fiber saturation point." By J.E. Stone and A.M. Scallan, this study illustrates the concept of a solute exclusion technique for determining fiber saturation point. According to J.Y. Zhu, "this concept is the basis for using solute exclusion to determine fiber pore size distributions when using a set of molecules of different sizes to probe fiber pores. The solute exclusion technique remains the reliable, quantitative, and low-cost technique for fiber pore size distribution today."

In the future, we will digitize and publish more such historical papers as selected by the *TAPPI Journal* Editorial Board, along with providing their DOI information at the bottom of pages.

EXPERIMENTAL

Materials and Methods

Enzyme Source. The source of cellulase used in this investigation was a commerically available, unpurified preparation from *Aspergillus niger*, which was reported previously as Emulsin A (*1*). It is produced by the Rohm and Haas Co. and designated by them as Enzyme 19AP. The dry emulsin was extracted with cold water, and clear solutions were obtained by centrifuging and then filtering the supernatant solution through a Pyrex fritted-glass filter (F porosity). The solids content of the filtered solution was determined by drying 1- or 2-ml. aliquots of the solution *in vacuo* over calcium chloride. A mat of glass wool in the bottom of the weighing bottle prevented loss from foaming upon evacuation. The solids content in grams per 100 ml. is referred to as "enzyme" concentration, although considerable materials other than cellulases undoubtedly were present.

Cellulose Substrates. Three celluloses having reactivities distributed over a wide range were used as substrates in this investigation. One was shredded Hercules purified cotton linters, designated as *Cellulose A*, which exhibited a relatively high resistance to enzymic attack. The other two celluloses were products of the swelling of cellulose A in cold 85% phosphoric acid. A product of a 10-minute swelling period was designated as *Cellulose B*, and that of a 2-hour period as *Cellulose C*. The details of the preparation of celluloses B and C were described in the previous paper (*1*). Cellulose C had the highest reactivity and that of cellulose B was intermediate cellulose A and cellulose C.

Enzymic Hydrolyses. Hydrolysis reactions were carried out in general, according to the procedure which was described previously (*1*), with the exception that the extent of hydrolysis was evaluated exclusively by gravimetric determinations of the amount of undissolved cellulose. The previously reported "5-hour test" conditions were used as the standard conditions of this investigation, except for any variation required by the purpose of a particular experiment, which will be indicated. The standard conditions are listed below:

Cellulose (oven-dry), g.	0.58–0.60
Cellulose concentration, %[a]	3.00
Enzyme concentration, %[b]	1.00
pH (acetate buffer)	4.5
Total acetate molarity	0.16
Temperature, °C.	47

[a] Grams per 100 ml. of solution.
[b] Grams of solids extracted from the emulsin per 100 ml. of solution.

Moisture Regain. The property of cellulose referred to subsequently as *moisture regain* is the equilibrium moisture content of the cellulose, approached from the dry side, attained at 50% relative humidiy and 73°F.

The procedure was as follows: After the cellulose residue from an enzymic treatment had been filtered on a Pyrex fritted-glass crucible and completely washed with water, it was washed with acetone to remove the water. The cellulose residue was then dried over sulphuric acid at 1 to 2 mm. for at least 24 hours. The crucibles containing the cellulose were exposed to the controlled atmosphere until the cellulose had attained constant weight. The cellulose was then dried in a vacuum oven at 50°C. and reweighed. The equilibrium moisture content of the conditioned cellulose was calculated as the percentage of the air-dry weight.

Degree of Polymerization. The determinations of the degree of polymerization were carried out according to a method similar to that described by Atchison (*3*). According to this method, the cellulose is converted into cellulose nitrate and the nitrate is dissolved in acetone. The intrinsic viscosity of this solution is determined and the degree of polymerization calculated according to the Staudinger equation (*4*), using for K_m the value of 11×10^{-4}. Celluloses which were to be evaluated for the degree of polymerization were not dried at a temperature higher than 50°C.

Effect of Various Factors on the Reaction Kinetics

In the studies of the rate of hydrolysis, a marked decrease in the rate was observed in the later stages of the reaction. It was desired to evaluate the relative effects of certain factors which were considered to be possible causes for the decreased rate. These factors were (1) a decrease in the average reactivity of the cellulose resulting from the removal of its more accessible portions, (2) inactivation of the enzyme by heat, and (3) inhibition of the enzyme action by the accumulated reaction products (glucose). The effects of these factors were isolated according to the procedure described below and the results are reported in Fig. 1.

A 50.25-gram (oven-dry basis) sample of cellulose B was subjected to hydrolysis by a 1% enzyme solution at 3% cellulose concentration for 72 hours. The residual cellulose (Cellulose B-72) and the hydrolyzate (hydrolyzate A) were then separated, and hydrolyzate A was tested for activity immediately by a rate of hydrolysis determination on fresh samples of cellulose B. Simultaneously, rate determinations were made using two "synthetic" compositions simulating hydrolyzate A. Both were identical in enzyme concentration and pH; one had been subjected to a reaction temperature of 47°C. along with hydrolyzate A, but contained no D-glucose, whereas the other contained D-glucose equivalent to the cellulose which had dissolved in hydrolyzate A, but had not been subjected to the heating period. All rates were compared with that of a fresh enzyme solution on samples of cellulose B, under the standardized conditions. The various hydrolysis rate curves for a period of 24 hours are plotted in Fig. 1.

Cellulose B-72 was washed thoroughly with water, acetone, and ether. It was then air dried at room temperature. The yield was 32.35 grams (oven-dry basis), a loss in weight from the original sample of 35.6%. The rate of hydrolysis of cellulose B-72, using fresh enzyme solution, was then determined at both 3.0 and 1.9% cellulose concentration, the latter being the concentration which existed when cellulose B-72 and hydrolyzate A were separate. The results at 3.0% concentration are plotted in Fig. 1. However, in order that it may be shown in its proper relation, the data for 1.9% concentration are superimposed as a dotted curve on the curve for cellulose B of Fig. 2. In order to determine the capability of cellulose B-72 for reactivation, a 5-gram portion was reactivated by the phosphoric acid treatment according to the original condi-

 CITE THIS PAPER: Walseth, C.S., *Tappi* 35(5): 233(1952). https://doi.org/10.32964/TJ35.5.233

tions of the preparation of cellulose B. This reactivated product was termed cellulose B-72R. The rate of hydrolysis was then determined for this cellulose with fresh enzyme solution under the standardized conditions. Moisture regain values of 5.45 and 8.06% were obtained for cellulose B-72 and cellulose B-72R, respectively.

Effect of Enzymic Action on Undissolved Cellulose

The moisture regain and the degree of polymerization were determined on cellulose residues from hydrolysis rate determinations on celluloses A, B, and C, according to the following plan.

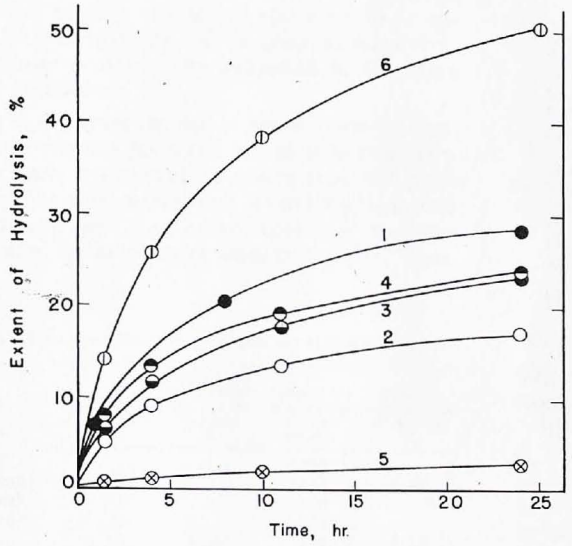

Fig. 1. Effects of various factors on the kinetics of enzymatic hydrolysis

(1) Cellulose B and fresh enzyme solution (control); (2) cellulose B and hydrolyzate A; (3) cellulose B and "synthetic" hydrolyzate A (heated); (4) cellulose B and "synthetic" hydrolyzate A (glucose added); (5) cellulose B-72 and fresh enzyme solution; (6) reactivated cellulose B-72R and fresh enzyme solution.

The rate of hydrolysis determinations was carried out under the standard conditions which have been listed, except that sufficiently large cellulose samples were used to allow the determination of the moisture regain, the degree of polymerization, and the loss in weight of the residues. In addition, the effect at the reaction temperature of 47 °C. of water alone and of buffer solution alone (0.16 *N* total acetate, pH 4.5) on the degree of polymerization was determined for each of the celluloses.

A comparison was also made, for each cellulose, of the degree of polymerization resulting from enzymic and acid treatments which had produced comparable losses in weight.

Information was available (*5*) in the case of cellulose A for the selection of acid hydrolysis conditions which would approximately duplicate the 6.68% loss in weight which that cellulose had sustained by the maximum enzymic treatment of 144 hours. This treatment, applied to all three celluloses, involved heating at 100 °C. with 0.25 *N* sulphuric acid (at 1% cellulose concentration) for 48 hours. The loss in weight and the degree of polymerization were then determined by the usual methods.

The results of this study are presented for cellulose A in Table I, for cellulose B in Table II, and for cellulose C in Table III. The curves of extent of hydrolysis as a function of time are presented in Fig. 2 for the three celluloses.

DISCUSSION

The rates of hydrolysis of three cellulose materials (A, B, and C) under similar conditions by an enzyme preparation from *Aspergillus niger* are shown in Fig. 2. Cellulose A is purified cotton linters, and celluloses B and C are samples of A swollen with phosphoric acid. Detailed data are given in Tables I, II, and III. Although the hydrolyses are similar in that they consist of a rapid phase followed by a slow phase, the rates and extent of the rapid phase differ markedly for the several celluloses. The decrease in rate in the second phase cannot be ascribed entirely to an inactivation of the enzyme, for, as shown by the dotted curve, the rate of attack of the residual cellulose is only slightly increased when the residual material is separated and resuspended in fresh enzyme solution.

The cause of the slowing down of the rate of hydrolysis was investigated by a series of experiments with cellulose B and illustrated in Fig. 1. The typical curve for cellulose B and fresh enzyme is shown in curve 1.

The residual material when retreated with fresh enzyme solution is only slowly hydrolyzed (curve 5), but when it is reactivated by a swelling teatment with phosphoric acid, it becomes quite reactive again (curve 6).

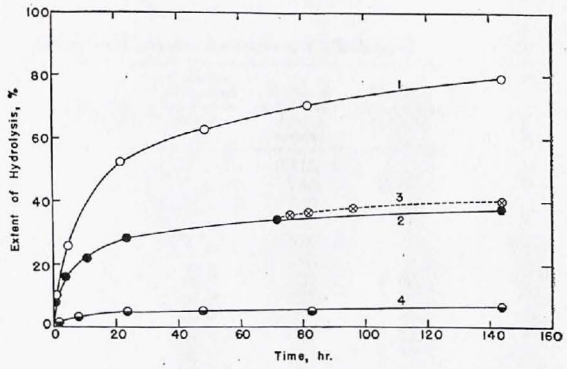

Fig. 2. Rate of enzymatic hydrolysis of various celluloses

The enzyme solution removed from the cellulose at the period of slow hydrolysis is still quite active when added to a fresh sample of the original cellulose (curve 2) but not quite as active as originally (curve 1). The decrease in activity seems to result from a partial inactivation of the enzyme, because when a portion of the enzyme solution is kept for 72 hours at 47 °C. before addition to the cellulose sample (curve 3), the rate of hydrolysis is less than with the fresh enzyme solution. However, the hydrolysis products also

exert an inhibiting influence, since the rate is slower in the presence of added D-glucose (curve 4).

These results indicate that the principal reason for the slowing down of the hydrolytic reaction is the removal of easily accessible portions and the accumulation of difficultly accessible (presumably crystalline) portions. However, inhibition by glucose formed in the hydrolytic reaction and inactivation of the enzyme exert significant but minor influences. It does not appear that the minor differences in the degree of polymerization of these materials (1385 to 1215; see Tables I, II, and III) can be enough to account for the great differences in the rates of enzymic hydrolysis. External surface area or particle size would also seem to be excluded as the principal cause of variation in reactivity, since the three products were subjected to the same mechanical treatments.

Reaction rate curves similar to those given in Figs. 1 and 2 are commonly observed for cellulose reactions. They have been interpreted as arising from the presence of amorphous (reactive) and crystalline (inactive) regions and have been used in the "chemical" methods of estimation of the amounts of these materials. Thus,

Table I. Effect of Enzyme Action on Cellulose A

Nature of treatment	*Reaction time, hr.*	*Cellulose solubilized (by loss in weight), %*	*Degree of polymerization of residue*	*Moisture regain value of residue, %*
Untreated	...	...	1385	...
Water blank[a]	24	...	1140	5.58
Buffer blank	1	...	1320	...
Buffer blank	24	...	1225	...
Enzyme	1/2	1.32	1135	5.19
Enzyme	2	1.69	1195	5.01
Enzyme	8	3.17	1245	5.01
Enzyme	24	4.81	1120	4.91
Enzyme	48	5.35	...	5.33
Enzyme	83	5.44	...	4.92
Enzyme	144	6.68	1105	5.35
Acid	48	6.34	105	...

[a] pH of suspension after 24 hours—7.2 (pH of distilled water—6.0).

Nickerson (*7*), using an acid hydrolysis method, obtained values of 6, 10, and 21% for the amorphorus fractions of purified cotton linters, wood pulp, and viscose rayon, respectively. The periodic acid oxidation method of Goldfinger, Mark, and Siggia (*8*) has likewise given a value of 6% for the amorphous fraction of cotton linters. Philipp, Nelson, and Ziifle (*9*) obtained, by the acid hydrolysis method, a value of 12% for the amorphous content of purified cotton linters, and values ranging from 17 to 31% for various rayons.

If the late portions of the curves in Fig. 2 are extrapolated back to zero time, the intercepts on the ordinate give values of approximately 5, 30, and 60% for the amorphous fraction of celluloses A, B, and C, respectively. The value for cellulose A (shredded cotton linters) is similar to that obtained in the chemical methods mentioned above.

The capacity of celluloses to take up water vapor is reflected in the amount of moisture absorbed under standardized conditions and is known as the moisture regain value. This value is also used as a measure of the amounts of amorphous and crystalline materials. Hermans (*6*), for example, has obtained values for the content of amorphous cellulose by the water-vapor sorption method which agree favorably with his results by density measurements and optical methods. By these physical methods, he obtained values of about 40% for the amorphous fraction of native cotton,

Table II. Effect of Enzyme Action on Cellulose B

Nature of treatment	*Reaction time, hr.*	*Cellulose solubilized (by loss in weight), %*	*Degree of polymerization of residue*	*Moisture regain value of residue, %*
Untreated	...	...	1310	...
Water blank[a]	24	...	1120	6.30
Buffer blank	1	...	1300	...
Buffer blank	48	...	1180	...
Buffer blank	120	...	1290	...
Enzyme	1/4	3.7	830	5.62
Enzyme	1	7.9	920	5.42
Enzyme	4	16.1	900	5.08
Enzyme	11	22.0	1020	5.02
Enzyme	24	28.2	900	4.99
Enzyme	72	34.2	1005	5.31
Enzyme	144	37.6	1080	5.43
Acid	48	8.3	80	...

[a] pH of suspension after 24 hours—6.2 (pH of distilled water—6.0).

50% for wood pulps, and about 75% for many different regenerated or hydrate celluloses.

In Tables I, II, and III, it is shown that celluloses A, B, and C had moisture regain values of 5.58, 6.30, and 9.37%, respectively, in order of increasing extent of swelling and of ease of hydrolysis. Also, it should be noted that, as the enzymic hydrolyses proceeded toward their maximum extent, the moisture regain values for the residues were all reduced to a common range of about 5.0 to 5.4%. It is shown in curve 5

Table III. Effect of Enzyme Action on Cellulose C

Nature of treatment	*Reaction time, hr.*	*Cellulose solubilized (by loss in weight), %*	*Degree of polymerization of residue*	*Moisture regain value of residue, %*
Untreated	...	...	1215	...
Water blank[a]	24	...	740	9.37
Buffer blank	1	...	850	...
Buffer blank	5	...	785	...
Buffer blank	16	...	820	...
Buffer blank	48	...	765	...
Enzyme	1/6	3.6	525	7.95
Enzyme	1/2	6.3	370	7.81
Enzyme	1	10.0	375	7.60
Enzyme	5	25.6	315	7.18
Enzyme	22	52.4	275	6.72
Enzyme	49	62.7	270	6.68
Enzyme	82	70.5	295	6.47
Enzyme	144	79.3	...	5.25
Acid	48	13.9	40	...

[a] pH of suspension after 24 hours—6.4 (pH of distilled water—6.0).

of Fig. 1 that the residue (cellulose B-72) which resulted from a partial enzymic hydrolysis of cellulose B was very resistant to further hydrolysis and had a moisture regain value of 5.45%. However, when this residue was subjected to the swelling action of cold 85% phosphoric acid, the resulting product (cellulose B-72R) was again easily hydrolyzed by the enzyme,

 CITE THIS PAPER: Walseth, C.S., *Tappi* 35(5): 233(1952). https://doi.org/10.32964/TJ35.5.233

as shown by curve 6, and had a moisture regain value of 8.06%. Thus, the increase in ease of hydrolysis brought about by the swelling action appears to be directly related to the amorphous content of the cellulose.

As noted above, the "chemical" and "physical" methods give different results for the amounts of amorphous cellulose. This difference is difficult to explain. It would appear that any cellulosic surface which is accessible to water vapor in the water-vapor sorption method would likewise be accessible to the hydrogen (or hydronium) ion in an acid hydrolysis method, since the volume of a proton is practically negligible (*10*). Several possible explanations might be proposed for the low values of the amorphous content obtained by the chemical methods. Liquid water or reagent molecules may penetrate only partially certain portions of the amorphous regions which would be determined as amorphous by the water-vapor sorption method. An enzymic hydrolysis would probably represent an extreme case, because of the presumed large size of the catalyst molecules.

The possibility that recrystallization of amorphous cellulose may take place during the course of a reaction also may account for the lower results by chemical methods. Partial recrystallization of amorphous cellulose has been shown to take place upon heating in water under certain conditions (*11*). According to Brenner, Frilette, and Mark (*12*), the "chemical" methods may give erroneous results as a result of crystallization of chains liberated during hydrolysis. The data obtained in the present work for untreated cotton linters agree with those obtained with other "chemical" methods, although the conditions are quite different. If crystallization of chain ends occurred, the agreement of the results would be coincidental. In any case, it was shown in this work that crystallization of the unhydrolyzed material did not occur under these conditions, because swollen cotton linters kept for 16 hours at 47 °C. in the buffer mixture showed the same rate of attack by enzymes before and after the treatment.

The values for degree of polymerization in Tables I, II, and III show a striking difference between the effects of enzymic and acid hydrolysis upon the undissolved cellulose. For conditions of enzymic and acid hydrolysis which produced approximately equal losses in weight of cellulose A (Table I), the residue from the enzymic treatment retained a degree of polymerization of about 1100, whereas the acid residue had a value of only 105. With cellulose B (Table II), the difference becomes even more striking because, under the same conditions of hydrolysis, a 37.5% loss in weight resulted from the enzymic action, compared with only 8.3% for the acid treatment*; yet the residue from the enzymic action retained a degree of polymerization of about 1000, more than tenfold that of the residue from the acid hydrolysis. Thus, for cellulose A and cellulose B, the enzymic treatments resulted in degree of polymerization values which are only very slightly lower than those attained by water or buffer treatments alone. †

With cellulose C (Table III), the same general difference is still noted for the two types of treatments, but, in this case, the enzymically treated cellulose did not maintain a degree of polymerization as high as in the other two cases, but fell to slightly less than 300. This result might be expected in view of the extreme sensitivity of this cellulose, indicated by the fact that the water blank and buffer blank treatments alone reduced the degree of polymerization of this cellulose from 1215 to about 800.

The relative lack of effect of enzymic treatments on the degree of polymerization of cellulose residues concurrent with considerable loss in weight indicates that the cellulose in regions accessible to the large enzyme molecule may be rapidly and completely reduced to soluble products. When all readily accessible cellulose is dissolved, the hydrolysis, as evidenced by glucose production, still proceeds, but presumably takes place only on the surfaces of crystallites or inaccessible regions, with rapid and complete solution of each chain molecule as it becomes exposed in turn at the crystallite surface. In this manner, hydrolysis could proceed to glucose with only a fleeting existence in the system of any intermediate dextrins or short-chain fragments. In the case of acids, on the other hand, the active catalyst could penetrate the cellulose structure to a much greater extent and hydrolyze glucosidic bonds at points from which short fragments perhaps could not easily diffuse out of the cellulose structure.

It might be suggested that the rapid production of glucose without a great lowering in the degree of polymerization may indicate that the enzyme attacks the cellulose chains only at the ends, rather than at random over the entire length. No experiments were performed specifically to test this possibility, but the low value of 830 which resulted from the first 15 minutes of hydrolysis of cellulose B would indicate that a random attack took place immediately in the most accessible regions and that enough shortened chains were produced to have the effect of lowering the degree of polymerization significantly. Complete dissolution of these shortened chains could then take place quickly to leave only the longer chains in the inaccessible regions, and the degree of polymerization would rise again to the value of about 1000.

The observed differences between acids and enzymes should be of practical interest, for it means that the more reactive areas of cellulose may be removed by the action of enzymes without producing much chain degradation of the residual materials.

* That is, conditions which gave equal losses in weight of cellulose A samples did not give equal losses with the more reactive cellulose B.

† The water and buffer blank residues, rather than the untreated celluloses, are considered the legitimate bases for comparison of the degree of polymerization of the enzyme residues. It is difficult to explain the decreases in degree of polymerization which were produced by water and by buffer treatments. Since the pH measurements made on the water blanks after the heating period, all showed only slight increases from the value for distilled water, the degradation effect could not have been caused by acids retained in the cellulose.

LITERATURE CITED

1. Walseth, C. S., *Tappi* 35, No. 5: 228–233 (May, 1952).
2. Karrer, P., *Kolloid-Z.* 52: 304–319 (1930).
3. Atchison, Joseph E., *Paper Trade J.* 116, No. 22: 23–34 (T.S. 243–254) (June 3, 1943); *Tech. Assoc. Papers* 26: 233–244 (1943).
4. Staudinger, H., and Mohr, Rolf, *Ber.* 70B: 2296–2309 (1937).
5. Shockley, W. H., Personal communication, 1947.

6. Hermans, P. H., "Contributions to the Physics of Cellulose Fibers." Amsterdam, Elsevier, 1946, 221 pp.
7. Nickerson, R. F., *Ind. Eng. Chem.* 34: 1480–1485 (1942).
8. Goldfinger, G., Mark, H., and Siggia, S., *Ind. Eng. Chem.* 35: 1083–1086 (1943).
9. Philipp, Howard J., Nelson, Mary L., and Ziifle, Hilda M., *Textile Research J.* 27: 585–596 (1947).
10. Stillwell, Charles W., "Crystal Chemistry," especially p. 57. New York, McGraw-Hill Book Co., 1938, 431 pp.
11. Hermans, P. H., and Weidinger, A., *J. Am. Chem. Soc.* 68: 2547–2552 (1946).
12. Brenner, F. C., Frilette, V., and Mark, H., *J. Am. Chem. Soc.* 70: 877 (1948).

RECEIVED March 10, 1952. A portion of a thesis presented in partial fulfillment of the requirements of The Institute of Paper Chemistry for the degree of Doctor of Philosophy from Lawrence College, Appleton, Wis., June, 1948. This work was carried out under the direction of W. W. Pigman.

 CITE THIS PAPER: Walseth, C.S., *Tappi* 35(5): 233(1952). https://doi.org/10.32964/TJ35.5.233

TAPPI JOURNAL
WWW.TAPPI.ORG
THE PAPER AND PACKAGING INDUSTRIES' TECHNICAL RESOURCE
JULY 2022 | VOL. 21 NO.7

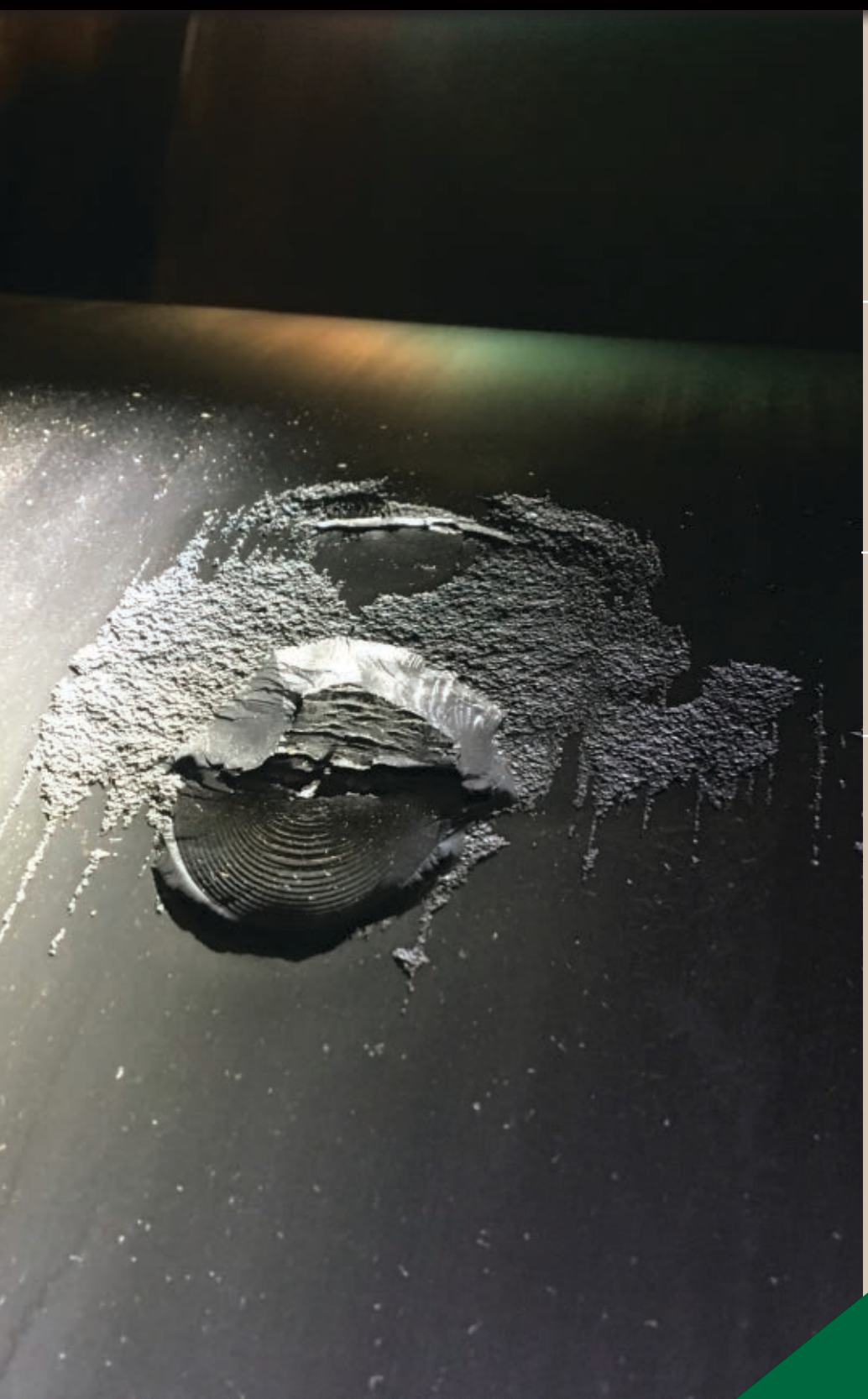

BLEACHING 353
Using bleaching stage models for benchmarking softwood ECF bleach plants
Brian N. Brogdon

PULPING 365
On the usage of online fiber measurements for predicting bleached eucalyptus kraft pulp tensile index — an industrial case
R.B. Demuner, C.A. Faria, A.A.R. de Almeida, and P.N. Pignaton

PAPERMAKING 377
Calender barring review with experiences
Jake Zwart

CELLULOSE 387
Investigation of the cellulose-water relationship by the pressure plate method
A.A. Robertson

TAPPI Journal NOW FULLY OPEN ACCESS

July 2022

TABLE OF CONTENTS VOL. 21 NO. 7

349 EDITORIAL
A closer look at the 2021 *TAPPI Journal* Best Research Paper
Monica Shaw

353 BLEACHING
Using bleaching stage models for benchmarking softwood ECF bleach plants
Brian N. Brogdon

365 PULPING
On the usage of online fiber measurements for predicting bleached eucalyptus kraft pulp tensile index — an industrial case
R.B. Demuner, C.A. Faria, A.A.R. de Almeida, and P.N. Pignaton

377 PAPERMAKING
Calender barring review with experiences
Jake Zwart

387 CELLULOSE
Investigation of the cellulose-water relationship by the pressure plate method
A.A. Robertson

»**COVER CREDIT**: Researcher Zwart explored the history of barring from self-excited vibration in the calender stack, as well as its causes and solutions (p. 377). The cover image shows damage to a roll cover from vibration when the nip load was roughly double the design nip load, resulting in removal of rubber from the cover.

TAPPI JOURNAL
WWW.TAPPI.ORG

Editor-in-Chief
Douglas W. Coffin coffindw@miamioh.edu
+1 513 529-0771

Associate Editor
Peter W. Hart peter.hart@westrock.com
+1 409 276-3465

Editorial Director
Monica Shaw mshaw@tappi.org
+1 770 367-9534

PRESS Manager
Jana Jensen jjensen@tappi.org
+1 770 209-7242

***TJ* EDITORIAL BOARD**

Brian N. Brogdon, FutureBridge Consulting & Training LLC
brian.brogdon@gmail.com, +1 678 581-9114

Douglas W. Coffin, Miami University
coffindw@miamioh.edu, +1 513 529-0771

Mahendra Doshi, Doshi and Associates
mahen@aol.com, +1 920 832-9101

Marc Foulger, Valmet
marc.foulger@valmet.com +1 315 767-2920

Peter W. Hart, WestRock
peter.hart@westrock.com, +1 409 276-3465

Carl J. Houtman, USDA Forest Products Laboratory
choutman@fs.fed.us, + 1 608 231-9445

Vamsi Jasti, Ahlstrom-Munksjo Nonwovens LLC
jvamsik1@gmail.com, +1 818 585-3524

Lucian Lucia, North Carolina State University
lucian.lucia@gmail.com, +1 919 889-7059

John A. Neun, John A. Neun LLC
john.neun@gmail.com, +1 518 275-8139

Jim Niemiec, Jim Niemiec Consulting LLC
jim.niemiec@outlook.com, +1 715 213-4766

Steven P. Ottone, Omya
steven.ottone@omya.com, +1 919 641-7854

Gaurav Pranami, Imbed Biosciences
gpranami@imbedbio.com, +1 515 230-7005

Arthur Ragauskas, Oak Ridge National Laboratory
aragausk@utk.edu

Seshadri Ramkumar, Texas Tech University
S.Ramkumar@ttu.edu, +1 806 742-4567

Gregg Reed, Imerys
gregg.reed@imerys.com, +1 478 553-5747

Gerard J.F. Ring, University of Wisconsin—Stevens Point
gerrryring@wi-net.com, +1 715 592-3732

Scott Rosencrance, Kemira Chemicals
scott.rosencrance@kemira.com, +1 770 429-2753

Paul Wiegand, NCASI
pwiegand@ncasi.org, +1 919 941-6417

Junyong Zhu, USDA Forest Products Laboratory
jzhu@fs.fed.us, +1 608 231-9520

Join TAPPI *today!*
TAPPI JOURNAL is a free benefit of TAPPI membership, and is only available to members. To join TAPPI, to renew your TAPPI Membership, or to learn about other valuable benefits, visit www.tappi.org.

TAPPI, 15 Technology Parkway S., Suite 115, Peachtree Corners, GA 30092, publishes *TAPPI JOURNAL* monthly.

ATTENTION PROSPECTIVE AUTHORS: All papers published are subject to *TAPPI JOURNAL's* peer-review process. Not all papers accepted for review will be published. Before submitting, check complete author guidelines at http://www.tappi.org/s_tappi/doc.asp?CID=100&DID=552877.

Statements of fact and opinions expressed are those of individual authors. TAPPI assumes no responsibility for such statements and opinions. TAPPI does not intend such statements and opinions or construe them as a solicitation of or suggestion for any agreed-upon course of conduct or concerted action of any sort.

Copyright 2022 by TAPPI, all rights reserved. For copyright permission to photocopy pages from this publication for internal or personal use, contact Copyright Clearance Center, Inc. (CCC) via their website: www.copyright.com. If you have questions about the copyright permission request process, please contact CCC by phone at +1 978 750-8400. To obtain copyright permission to use excerpts from this publication in another published work, send your specific request in writing to Editor, TAPPI JOURNAL, 15 Technology Parkway S., Suite 115, Peachtree Corners, GA 30092, USA; or by fax to +1 770 446-6947. Send address changes to TAPPI, 15 Technology Parkway S., Suite 115, Peachtree Corners, GA 30092, USA; Telephone +1 770 446-1400, or FAX +1 770 446-6947. www.tappi.org

Editorial



MONICA SHAW | EDITORIAL DIRECTOR
mshaw@tappi.org

A closer look at the 2021 *TAPPI Journal* Best Research Paper



Bliss

Each year, the *TAPPI Journal* Editorial Board honors the best of the journal's content by nominating and voting for the *TAPPI Journal* Best Research Paper, which is ultimately selected based on scientific merit, innovation, creativity, and clarity. The winning paper is awarded in the successive year to allow time for nominations from the Editorial Board and assessment of the nominated papers from the preceding year.

The winning paper for 2021 was "Application of foamed additives to the surface of wet handsheets," authored by Terry Bliss with co-authors Mingxiang Lou and Matthew Nicholas—all of Solenis LLC. At Solenis, Bliss is a research fellow, Luo is a global market development manager, and Nicholas is a process research engineer. The foam additives research appeared in the January 2021 issue and is available as an open access download. Bliss accepted the Best Research Paper honors and Honghi Tran *TAPPI Journal* Best Research Paper Prize at TAPPICon in May of this year.

"The work combines foam form concepts with optimization of chemical additive application," said Editorial Board Member Scott Rosencrance of the winning paper. "Extending the window of operation for some specialty additives can allow continued evolution of wet-end system configurations, ultimately resulting in acceleration of commercial implementation of emerging production processes and grades."

In a recent conversation with *TAPPI Journal,* Bliss discussed some of the aspects of the Best Research Paper.

How difficult was it to devise and construct the wet handsheet coating apparatus? What was the process and about how long did it take to get it "right" for the experiments?

We went through three major revisions of our second concept over a nine-month period. We worked on a bench scale method of generating foam suitable for the application at the same time.

The 200 g/L foam density was the magic number for the trials. Would it be similar on an actual paper machine or does that remain to be seen?

The bench scale coater is limited to 200 g/L minimum foam density to keep it pourable. When you make foam in a small beaker, it must fall into the center of the beaker by gravity to circulate. Lower density foam also risks damage to the wet sheet when it is spread to a target thickness. In full scale or even pilot paper machine applications, we envision a pressurized foam generator that would have a bit more flexibility, as has been demonstrated by others.

How long did evaluating 100 foaming agents take? What are your predictions, if any, about what foaming agent(s) could achieve real-world application?

It took longer to get the samples than to test them. As shown in Figure 4 [below] in the paper, only a few tests at different concentrations are needed to eliminate most of the candidates, as the amount of foaming agent required is too high to be practical. The

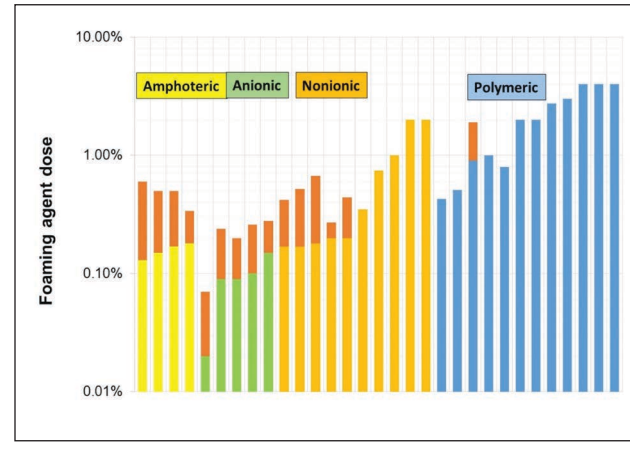

4. Minimum effective dose of various foaming agents needed to produce 300 g/L (lower bar) and 200 g/L (dark orange upper bar) foam density. The color of the lower bar identifies the type of foaming agent. Some foaming agents could not reach 200 g/L foam density at any dose.

	Dry Tensile	Wet Tensile	Wet/ Dry	Dry Stretch, %	Wet Stretch, %	Dry TEA	Wet TEA
0.21% WE, clean	9%	31%	31%	11%	2%	30%	34%
0.16% FA, clean	24%	116%	116%	27%	85%	65%	318%
0.21% WE, dirty	5%	17%	12%	-6%	-6%	2%	17%
0.16% FA, dirty	25%	129%	83%	24%	112%	46%	374%
Average SD, as %	6.8%	28.0%		11.5%	11.4%	18.3%	16.6%
WE = wet-end; FA = foam-assisted; SD = standard deviation; TEA = tensile energy absoprtion.							

II. Color gradation chart for 100 g/m² recycled linerboard (RLB) handsheets diluted and formed with addition of clean vs. dirty water, for a structured PAM, for wet-end (WE) and foam-assisted (FA) addition. Values shown are percent over the control (untreated) value. Average SD is the average of the SD of each condition's values divided by the condition's value.

	Dry Tensile	Wet Tensile	Wet/ Dry	Dry Stretch	Wet Stretch	Dry TEA	Wet TEA	Porosity	Water Drop
Structured PAM 1	16%	68%	45%	9%	34%	28%	129%	-12%	25%
Structured PAM 2	16%	132%	99%	15%	108%	35%	408%	-3%	89%
PVAm 1	26%	420%	311%	17%	169%	45%	1154%	2%	426%
PVAm 2	16%	282%	230%	8%	165%	27%	873%	-17%	134%
PVAm 3	29%	404%	292%	29%	193%	60%	1198%	8%	385%
GPAM 1	19%	97%	66%	21%	61%	37%	196%	-7%	-38%
GPAM 2	31%	261%	176%	36%	183%	71%	896%	-3%	-21%
Amphoteric PAM 1	24%	33%	8%	33%	17%	56%	48%	-11%	-29%
Average SD, as %	11.3%	7.8%		11.4%	13.0%	15.4%	22.0%	7.2%	12.0%
PAM = polyacrylamide; PVAm = polyvinylamines; GPAM = gloxalated polyacrylamides; SD = standard deviation; TEA = tensile energy absoprtion.									

III. Dry strength additive screening results. Values shown are percent over the control (untreated) value. Average SD is average of the SD of each condition's values divided by the condition's value.

remaining candidates were tested in more depth. We continue to evaluate candidates to this day. Since most additives are cationic, the anionics and nonionics tend to be more compatible.

Can you summarize the significance of the data in Tables II and III [shown above] in the paper?

Both of these tables show useful information that can be produced with the handsheet foam coating technique. Table II shows that dissolved components commonly found in recycled linerboard white water can interfere with the effectiveness of some wet-end applied dry strength additives, but do not interfere with the same dry strength additives added in foam onto the wet sheet. Table III shows that the handsheet coating application technique can be used to compare the effectiveness of foamed addition of a wide range of dry strength additives.

What sort of equipment do you envision for applying foamed additives on actual paper machine? How far away would you estimate any machine trials of this technology?

Let's say much larger than our handsheet setup! I would like to see this discussed in future submissions. As a scientist I don't like to make commercial timeline predictions.**TJ**

Using bleaching stage models for benchmarking softwood ECF bleach plants

BRIAN N. BROGDON

ABSTRACT: Steady-state bleaching delignification and brightening models were used to gauge how well elemental chlorine-free (ECF) bleach plants were using chlorine dioxide to bleach 25-kappa softwood brownstocks. Case 1 examined the $D_0(EOP)D_1$ portion of Mill 1's five-stage sequence that brightens the pulp to 86% ISO. Case 2 studied the $D_0(EO)D_1$ portion of Mill 2's four-stage sequence, which brightens the pulp to 82% ISO, and Case 3 re-examined the same bleach plant several years after it made improvements around the extraction stage. The models highlighted days in the previously mentioned cases where high bleach usage occurred, presumably because of high brownstock and/or extraction washer carryover, and days where bleach usage was normal. In Case 2, the model estimated that 10 kg of the 44 kg chlorine dioxide/metric ton pulp consumed in bleaching was likely reacting with washer carryover sources; approximately two-thirds of this extra consumption was assumed to be reacting with extraction filtrate. Changes that Mill 2 made (Case 3) reduced the unproductive chlorine dioxide usage from 10 to 5 kg/metric ton pulp. When the delignification and brightening models were simultaneously solved, the models predicted somewhat different optimized distributions of chlorine dioxide to D_0 and D_1 vs. actual values used in bleach plants. However, the forecasted chlorine dioxide totals agreed with the actual values when washer carryover sources were considered. This study showed the bleaching models could be used as hypothetical benchmarks for softwood ECF bleach plants.

Application: Multistage models are used to identify how much chlorine dioxide is being used inefficiently, which can infer how much brownstock and/or extraction washer carryover is occurring with $D_0(EO)D_1$ or $D_0(EOP)D_1$ sequences. The models can show if brownstock and/or extraction washing is problematic, or if certain shower water sources at the washers are beneficial or detrimental to overall bleach usage.

Kraft pulp mills constantly strive to identify process inefficiencies to decrease overall manufacturing costs. Over the past twenty years since ECF bleaching was adopted in North America, approximately 60% to 70% of the variable cost to manufacture bleached kraft pulp can be traced back to the wood consumed [1,2]. Pulping and bleaching chemicals can account for between 15% and 25% of this cost, with the balance ascribed to energy usage (i.e., steam and electricity). Nearly one-half to two-thirds of the chemical cost for elemental chlorine-free (ECF) bleaching is attributed to chlorine dioxide used [1,2]. Hence, methods to reduce chlorine dioxide usage or to improve its effectiveness are often the focus of bleach plant optimization.

Several key factors affect overall chlorine dioxide consumption and efficiency during ECF bleaching [3-10]. An example is the kappa number of the pulp entering the bleach plant. Pulps with higher kappa numbers need higher chlorine dioxide charges in the chlorine dioxide delignification (D_0) stage than pulps with lower kappa numbers [1,3,7,10]. If the kappa feeds swing from high to low values within minutes to hours, then the pulp will be inconsistently delignified in the D_0 stage unless the chlorine dioxide dosage is accordingly adjusted. Historically, this issue is addressed by the over-application of chlorine dioxide in the D_0 to dampen variations in the pulp's post-extraction kappa number. Another factor that affects chlorine dioxide efficiency to delignify (D_0) and brighten (D_1 and D_2) softwood kraft pulps is pH [7-9,11]. The ideal pH for delignification (2.5 to 3.0 pH) is typically lower than for brightening (4.0 pH).

A third factor affecting chlorine dioxide consumption is the carryover into the D stages, whether from the brownstock or post-oxygen washers, or the first extraction stage (typically (EO) or (EOP)) [3-8,11]. Dissolved organic solids entering the bleach plant with the unbleached or oxygen-delignified pulp consume chlorine dioxide in the D_0 stage, which otherwise reacts with the lignin in the pulp. Likewise, dissolved organic solids from the first extraction stage contribute to excess chlorine dioxide consumption in the D_1, which leads to a poor brightness response. Several issues can cause excessive extraction carryover, ranging from washer performance issues, filtrate management schemes, shower water application, shower water source, etc.

Finally, optimized ECF bleaching is affected by how much chlorine dioxide is proportioned to delignification and brightening [1-6,10]. Some bleach plants over-charge the D_0 stage at the front end of the sequence to circumvent making sizeable adjustments to the back end to control pulp brightness. Although this approach attains or exceeds the final brightness specification, it comes at the expense of high chlorine dioxide usage. This is because of the inefficient incremental reductions of the pulp's kappa number

at the higher D_0 charges and the negligible D_1 brightness gains of the very low kappa pulps after extraction.

Two common inefficiencies reported for bleach plants with high chemical costs are the carryover from the brownstock or post-oxygen delignification washers, and the first extraction stage washer [3-6,11-15]. Newly developed in-line sensors can now quantify the organic part of these carryover sources [16-18], which can be used to adjust chlorine dioxide charges to the D stages. However, many mills do not measure this variable in real-time, particularly after the extraction washers. Pulp mills follow brownstock washer losses using conductivity measurements, which detect inorganic components (e.g., sodium ion [Na^+]). Mills use conductivity as a surrogate measure of the organic load caused by the brownstock carryover [16]. Several published audits [3-6] use bleaching data from laboratory studies, based on either the mill's pulp or an appropriate reference, to determine if excess chlorine dioxide is being used in D_0 and D_1 stages. Regrettably, it is difficult to locate literature studies that are analogous to the bleach plant, or it cost too much time and money to conduct detailed laboratory studies on the mill's brownstock. Data obtained by these approaches are often limited to a specific kappa number entering the D_0 and D_1 stage unless the laboratory study incorporated this variable into the experimental design [1,10]. Another issue often overlooked in laboratory or published studies is how variable washer carryover loads to both D stages affect overall bleach plant efficiency.

An alternative approach to evaluating bleach plant performance is to use a computer spreadsheet to model the bleach sequence [19,20] as a hypothetical point of reference. Generalized steady-state models for ECF delignification (e.g., D_0(EO), D_0(EOP), etc.) and brightening (e.g., D_1 and D_2) have been developed for softwood kraft pulps. These hypothetical models have been tuned based on published laboratory bleaching data. The advantages of these models are that they can consider how bleaching delignification is affected if chlorine dioxide charge, oxidant-reinforced extraction conditions, or entering pulp kappa number is altered, or how D_1 brightness is affected by bleach charge and extracted kappa number of the pulp. Further refinements [21,22] now allow the models to examine how brownstock washer and extraction carryover affect chlorine dioxide consumption in the D stages, as well as how bleaching delignification and brightening are affected at a fixed bleach charge.

In this investigation, the in-line sensor data collected from two southern U.S. bleach plants are examined. These kraft mills bleach southern pine brownstocks with ECF sequences. Spreadsheet models for bleaching delignification and brightening are employed to determine how effectively chlorine dioxide is being used in the D stages, as well as to infer how much brownstock and extraction washer carryover is occurring. These analyses will illustrate the usefulness of these spreadsheet models as tools for identifying and quantifying bleach plant inefficiencies.

METHODOLOGY

Daily average, sensor-measured data were collected over an approximately three-week period from two southern U.S. bleach plants. At these mills, automated in-line sensors are used to measure and monitor stream properties (e.g., kappa number, pulp brightness, pH, etc.) as part of their process control. During the data collection, the mills operated at relatively stable production rates with no major process upsets in the kraft pulp mill and bleach plant. It was assumed that the in-line sensors were well maintained and calibrated. Specific developments of the D_0(EO) or D_0(EOP) delignification and D_1 brightening models are covered in previous publications [19-22].

The bleaching delignification model is:

$$Kappa_1 = \frac{Kappa_0}{\left(\frac{x_0}{2A} + 1\right)^2} \quad (1)$$

where $Kappa_0$ is the brownstock kappa number, x_0 (% chlorine dioxide [ClO_2] on oven-dried pulp) is the chlorine dioxide used in the D_0 stage, and $Kappa_1$ is the post-extracted kappa number. The tuning parameter, A (% ClO_2), is calculated by:

$$A = 1.294 - 0.00560 \cdot T - 0.122 \cdot P \quad (2)$$

where T (°C) is the temperature of the (EO) or (EOP) stage and P (% hydrogen peroxide [H_2O_2] on oven-dried pulp) is the peroxide used in oxidant-reinforced extraction. This tuning parameter has an estimated standard error of approximately ±0.014.

The D_1 brightening model is:

$$B_{D1} = 92 - \frac{\beta_1}{x_1 + \frac{\beta_1}{92 - B_E}} \quad (3)$$

where x_1 (% ClO_2 on oven-dried pulp) is the chlorine dioxide used in the D_1 stage, B_E (% ISO) is the post-extracted pulp brightness, and B_{D1} (% ISO) is the post-D_1 brightness. The constant, 92% ISO, is the estimated brightness limit for a U.S. southern pine kraft pulp (i.e., predominantly loblolly and shortleaf pine). This asymptote is predicated on the unbeaten light scatting coefficient for this kraft pulp (ca. 28 to 30 m^2/kg) and the light absorption coefficient for lignin-free cellulose fibers (ca. 0.10 m^2/kg) [23]. The β_1 tuning parameter (% ClO_2•% ISO) is determined from the post-extracted kappa number entering the D_1 by the revised expression:

$$\beta_1 = 4.67 \cdot Kappa_1 - 7.66 \quad (4)$$

where the estimated standard errors for the slope and ordinate intercept terms are approximately ±0.12 and ±0.57, respectively [23].

Bleaching Model	Input Variables (Averaged Mill Data)	Calculated Variable (Prediction)	Calculated vs. Averaged Mill Value
D_0(EO) or D_0(EOP) Delignification (Eqs. 1 & 2)	*T, P,* x_0, $Kappa_0$	$Kappa_1$	Brownstock carryover (C.O.) to D_0 if Calculated $Kappa_1$ < Mill's $Kappa_1$
	T, P, $Kappa_0$, $Kappa_1$	x_0	Difference represents ClO_2 consumed by C.O.
	T, P, x_0, $Kappa_1$	$Kappa_0$	Difference represents C.O. (as kappa units)
D_1 Brightening (Eqs. 3 & 4)	$Kappa_1$, x_1, B_E	B_{D1}	Extraction C.O. to D_1 if calculated B_{D1} > Mill's B_{D1}
	$Kappa_1$, B_E, B_{D1}	x_1	Difference represents ClO_2 consumed by C.O.
	x_1, B_E, B_{D1}	$Kappa_1$	Difference represents C.O. (as kappa units)

I. Calculations of predicted variables based on different model inputs from daily-averaged bleach plant data, as well as comparisons of the predictions to the mill values to approximate washer carryover.

Bleaching Model	Calculated Variable (Prediction)	Estimated Uncertainty
D_0(EO) or D_0(EOP) Delignification (Eqs. 1 & 2)	$Kappa_1$	±0.2 kappa units
	x_0	±0.12% to ±0.15% ClO_2 on o.d. pulp
	$Kappa_0$	±1.7 to ±2.2 kappa units
D_1 Brightening (Eqs. 3 & 4)	B_{D1}	±0.6% to ±0.8% ISO points
	x_1	±0.11% to ±0.24% ClO_2 on o.d. pulp
	$Kappa_1$	±0.2 to ±0.3 kappa units

II. Estimated uncertainty in the calculated variables from the bleaching models.

In the initial analysis (**Table I**), Eqs. 1 to 4 were used to calculate $Kappa_1$ and B_{D1} based on the inputs of daily-averaged $Kappa_0$, x_0, B_E, and x_1 values, as well as the oxidant-reinforced extraction stage conditions. These calculated values were compared to the mill's daily-averaged extracted kappa and post-D_1 brightness to determine if washer carryover was affecting D_0 and D_1 stage performance. If the model predictions for $Kappa_1$ and B_{D1} were better than the mill's extracted kappa and post-D_1 brightness, then further analyses were performed on the daily-averaged mill data. In these cases, Eqs. 1 to 4 were algebraically manipulated to solve for other predicted quantities (Table I), such as x_0 or $Kappa_0$ for bleaching delignification, and x_1 or $Kappa_1$ for D_1 brightening. These calculated quantities were compared to the daily-averaged mill data to estimate the entering washer carryover as wet kappa units, or chlorine dioxide consumed in D_0 or D_1 by entrained washer filtrate in the pulp [3-6,15,22]. Uncertainties in the model predictions (**Table II**) are approximated using the propagation of errors method [24]. Uncertainties in the model input variables were based on data from an ECF bleaching study [25] for a typical softwood kraft brownstock.

In the second analysis, the system of equations for delignification (Eqs. 1 and 2) and brightening (Eqs. 3 and 4) were solved simultaneously to find the values of x_0 and x_1 subjected to the constraint that the total chlorine dioxide used (i.e., $x_0 + x_1$) was minimized. The calculations used the mill's daily average values for $Kappa_0$ (brownstock kappa) and B_{D1} (D_1 brightness) and either included or excluded carryover contributions (determined from the earlier analysis). Linear relationships of extracted brightness (B_E) versus $Kappa_1$ (specific to each mill) were used to calculate B_{D1}. The equations were incorporated into a spreadsheet software program (Excel, version 2016; Microsoft, Redmond, WA, USA). The spreadsheet's solver routine (which employs an iterative process) was used to minimize the total chlorine dioxide charge needed to obtain B_{D1}.

Estimations of brownstock carryover into the D_0 stage were based on the model calculations of excess chlorine dioxide used. One kg saltcake/metric ton pulp carryover was assumed to consume approximately 0.3 kg chlorine dioxide/metric ton pulp, whereas 1 kg of chemical oxygen demand (COD)/metric ton pulp carryover was assumed to react with 0.2 kg chlorine dioxide/metric ton pulp [21]. Model extraction carryover expressed as kg COD was calculated based on the relation [26]:

$$Model's\ Extraction\ Filtrate\ COD\ (\text{kg/t pulp}) = 4.5 \cdot (Model's\ Filtrate\ Kappa\ on\ pulp) + 2.4 \quad (5)$$

RESULTS

Overview

Analyses with the models were performed on the sensor-measured data from two U.S. bleach plants using southern pine kraft pulps. Both fiber lines use ECF sequences to bleach the brownstocks. Mill 1 uses a five-stage sequence to produce an 88% ISO brightness pulp. Mill 2 uses a four-stage sequence to attain an 86% ISO pulp. Data analyses in this study focused on the first three stages of each mill's bleach sequence. Case 1 examines the bleach plant of Mill 1 where the D_1 target is 86% ISO, whereas Case 2 investigates Mill 2, which has a D_1 target of 82% ISO. Case 3 re-examines the bleach plant of Mill 2 several years after the mill made changes around the oxidant-reinforced extraction stage. In all cases, the D_0 stages operated with zero chlorine dioxide residuals, and the D_1 stages operated with trace vat residuals (ca. ≤ 0.05 g ClO_2/L).

Case 1: Mill 1 with D_0(EOP)D_1 (86% ISO)

Figure 1 presents the daily averages from the D_0(EOP)D_1 portion of the bleach plant at Mill 1 (Case 1), along with analyses with Eqs. 1 and 2 to model D_0(EOP) delignification and Eqs. 3 and 4 to model D_1 brightening. In Fig. 1A, the brownstock kappa number entering the D_0 ranged from 21 to 29 (an overall average of 24.5). Kappa factor (KF) is defined as the percentage of D_0 chlorine dioxide used (expressed as active chlorine) on o.d. pulp per kappa unit of the entering brownstock. The D_0 operated with an approximate 0.30 KF, which yielded pulps that had extracted kappa numbers between 3 and 4.2. The D_0(EOP) model under-predicted the D_0 stage KF when solved for the chlorine dioxide (x_0) charge, with the other inputs being from the mill data. Discrepancies between the mill's KF and the model ranged from about 0 (e.g., days 13 to 16) to 0.09 (e.g., day 7). Similarly, when the delignification model was solved for the extracted kappa ($Kappa_1$) in Fig. 1B, it forecasted lower values, by 0.3 to 0.9 kappa units, vs. the mill. In several instances, it was suspected that brownstock carryover affected D_0 stage performance. For example, on days 7 to 10, the model-calculated carryover is consuming about 0.07 KF units, which is equivalent to about 0.67% chlorine dioxide on pulp. Subsequently, on days 11 to 20, the model-calculated carryover was minimal, as the excess chlorine dioxide consumption was low (ca. 0.19% ClO_2 on pulp).

Comparing Mill 1's D_1 stage to the brightening model is illustrated in Fig. 1C. During the observation period, the brightness varied between 84.0% and 87.5% ISO (an overall average of 85.9% ISO). Calculated brightness values were mostly congruent with the mill values (days 4 to 13), except for days 2, 14, and 17 to 20. During these days, the model showed that the brightness should have been 1 to 3 points higher. Inputting the mill's data on extracted kappa ($Kappa_1$) and D_1 brightness (B_{D1}) into the model and solving for the chlorine dioxide charge (x_1), it was presumed that approximately 0.63% chlorine dioxide was being consumed by (EOP) filtrate on these high-usage days. However, benchmarking the D_1 mill data with the hypothetical model showed that the calculated (EOP) carryover was nominal because of the low excess of chlorine dioxide being consumed in the D_1 stage most of the time. The amount of bleach consumed on these good days was about 0.14% on pulp, which was within the uncertainty error of the model (±0.23% ClO_2 on pulp for this case).

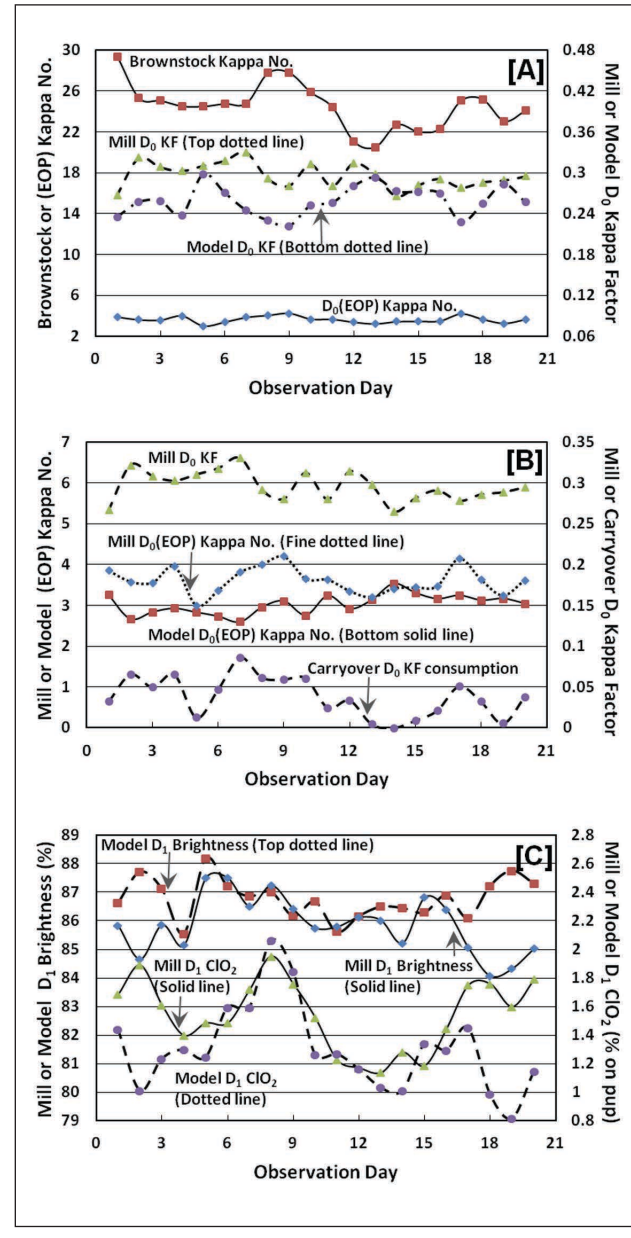

1. Comparing the daily averages of the D_0(EOP)D_1 partial sequence of Mill 1 to the D_0(EOP) delignification model (A and B) and the D_1 brightening model (C).

Case 2: Mill 2 with D_0(EO)D_1 (82% ISO)

Figure 2 presents the daily averages from the D_0(EO)D_1 portion of the bleach plant at Mill 2 (Case 2), which are compared to the predictions from the bleaching delignifi-

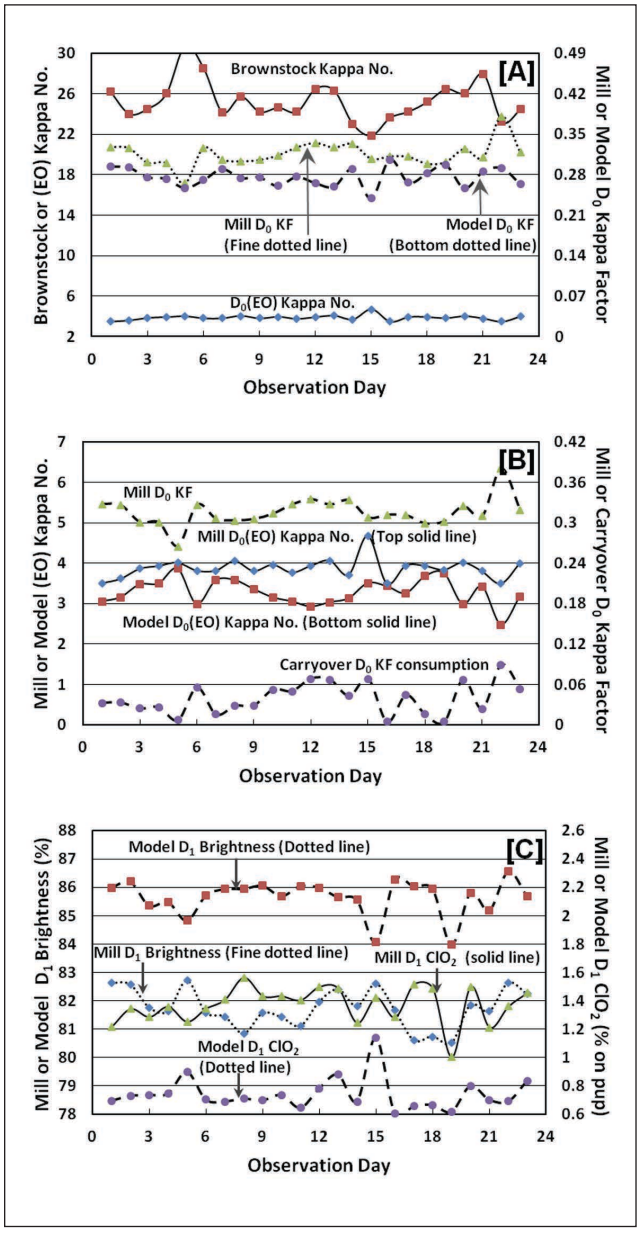

2. Comparing the daily averages of the D_0(EO)D_1 partial sequence of Mill 2 to the D_0(EO) delignification model (A and B) and the D_1 brightening model (C).

cation and brightening models. The brownstock kappa ranged from 22.0 to 31.7 (an overall average of 25.3; Fig. 2A). The mill's D_0 KF remained stable between 0.30 to 0.33, which yielded extracted kappa numbers between 3.6 and 4.0. The D_0(EO) delignification model (Eqs. 1 and 2) forecasted a continual KF charge between 0.26 and 0.29. These KF values were lower by about 0.04 KF units vs. the mill's values (Fig. 2B). In addition, the delignification model predicted lower (EO) kappa numbers than the actual values. These differences were relatively small (by 0.38 kappa units) during days 1 to 5, but were high (by 0.89 kappa units) during days 10 to 15. During this time, it was deduced that nearly 20% of the mill's D_0 KF is being consumed by brownstock carryover, or about 0.55% chlorine dioxide on pulp. Where the model and mill KF values were nearly identical (e.g., days 1 to 5 and 7 to 9), the carryover consumption was calculated to be 0.03 KF units (0.24% chlorine dioxide on pulp), which was 55% less than on days 10 to 15.

The D_1 stage data from Mill 2 were compared to the brightening model (Fig. 2C). The mill's brightness cycled between 80.4% and 82.8% ISO (an overall average of 81.7% ISO). The model predicted much higher D_1 brightness levels around 86.0% ISO, which was at the mill's brightness specification after exiting the fourth bleaching stage. The mill's D_1 stage used 1.20% to 1.50% chlorine dioxide on pulp (an overall average of 1.37%). When the model computed the chlorine dioxide charge (x_1) needed to reach the daily brightness values, the model predicted chlorine dioxide levels to be between 0.60% and 0.90% on pulp, which was about 45% lower than the mill's values. It was suspected that carryover of (EO) filtrate appreciably affected the brightening and chlorine dioxide consumption in the D_1. The model estimated the wet or apparent kappa number entering the D_1 ($Kappa_1$). Model-derived (EO) kappa values were between 4.9 to 7.0, which were approximately 1.9 kappa units higher than the mill's (EO) values shown in Fig. 2B (Mill 2's D_0(EO) kappa no.).

Case 3: Mill 2 with D_0(EOP)D_1 (82% ISO)

Figure 3 shows the daily averages from the D_0(EOP)D_1 portion of the bleach plant at Mill 2 (Case 3). Here, the observation period happened several years after Case 2. During that time, the bleach plant converted its (EO) stage to an (EOP) stage (ca. 0.5% peroxide on o.d. pulp), increased the stage's temperature by approximately Δ10°C, and discontinued extraction washer filtrate as shower water at the D_0 washer. Also displayed in Fig. 3 are the comparisons to the bleaching delignification and brightening models.

The brownstock kappa number entering the D_0 (Fig. 3A) had a somewhat lower variation than Case 2, generally between 20.1 and 26.5 (an overall average of 23.6). Likewise, the mill's D_0 KF was reduced to between 0.24 and 0.28, which afforded extracted kappa numbers of 4.0 (except for days 11 to 14). Lower D_0 KF values were predicted by the delignification model, usually between 0.20 and 0.25. When using the model to predict the extracted kappa numbers, it yielded values around 3.4 (Fig. 3B). It was inferred that 14% of the applied bleach, or approximately 0.33% chlorine dioxide on pulp, was in excess and was likely being consumed by brownstock carryover. This suggested that there were relatively low amounts of brownstock washer filtrate entering the bleach plant.

The D_1 brightening model was used to evaluate the D_1 stage at Mill 2 (Case 3). Actual brightness values varied between 80.0% and 83.0% ISO, whereas the model values ranged from 81.0% and 84% ISO. The amount of chlorine dioxide the mill used in D_1 was between 0.80% and 1.0%

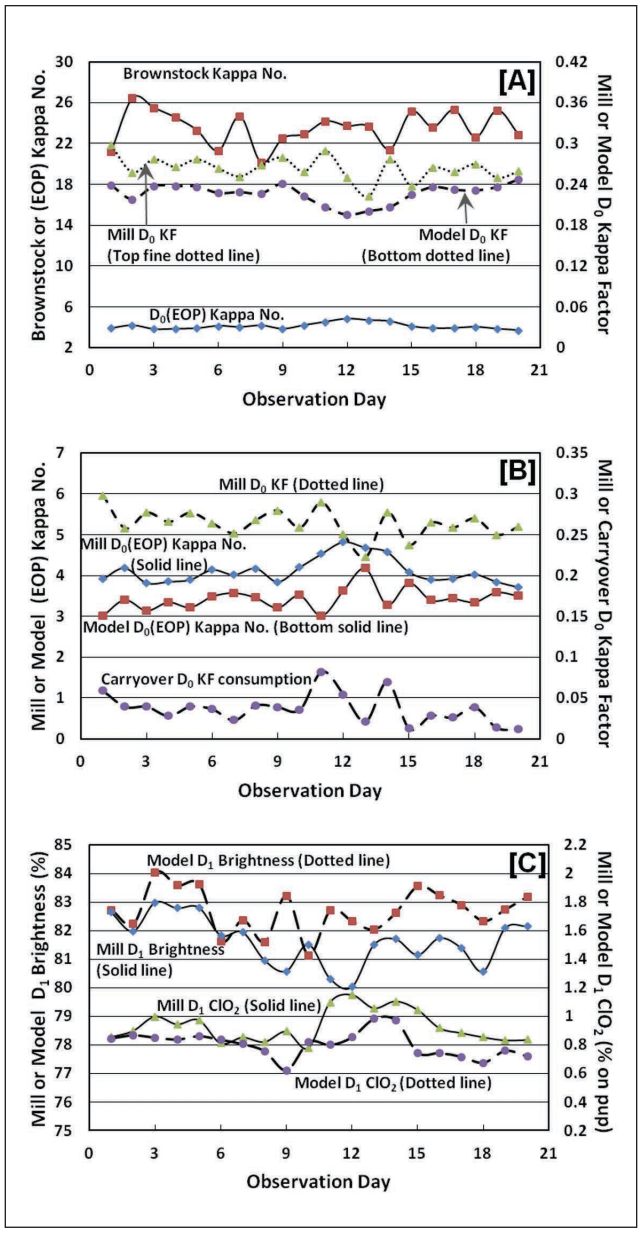

3. Comparing the daily averages of the $D_0(EOP)D_1$ partial sequence of Mill 2 (several years after Case 2) to the $D_0(EOP)$ delignification model (A and B) and the D_1 brightening model (C).

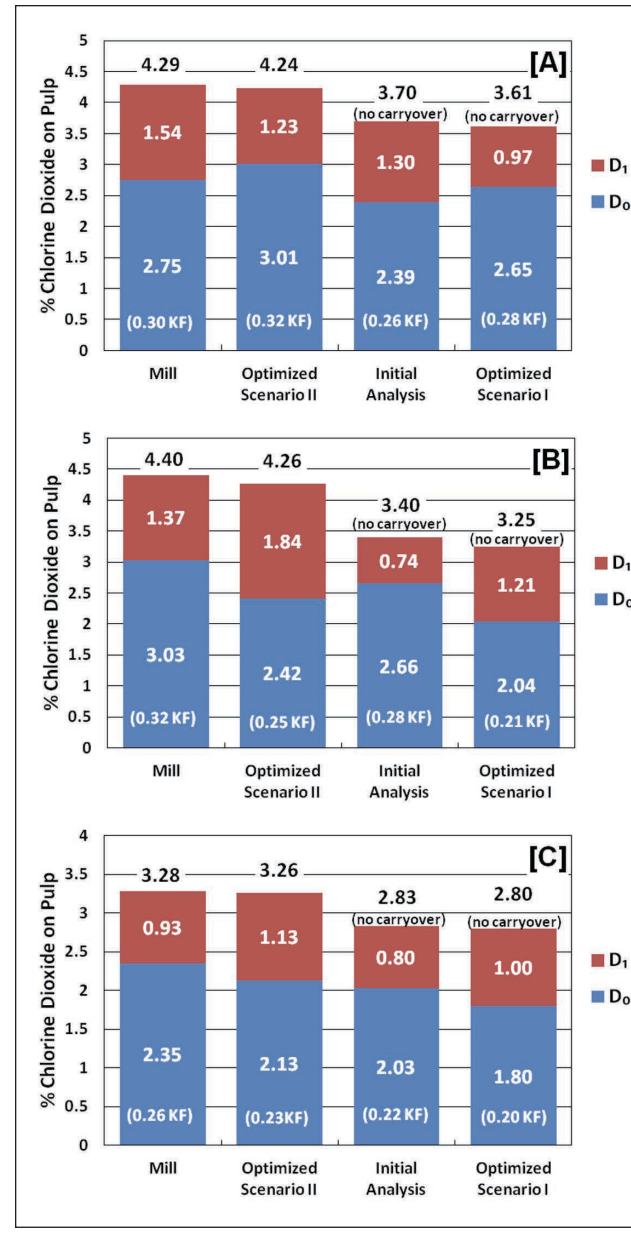

4. Comparing overall averages of chlorine dioxide used in D_0 and D_1: (A) Case 1 — $D_0(EOP)D_1$; (B) Case 2 — $D_0(EO)D_1$; and (C) Case 3 — $D_0(EOP)D_1$. Optimized scenarios are results from coupled delignification and brightening models that (I) excluded or (II) included brownstock and extraction carryover. Initial analysis is the result from earlier analysis of mill data to each model separately. Total chlorine dioxide is listed above the columns.

on most days (except days 11 to 15). The brightening model forecasted somewhat lower chlorine dioxide usage, generally around 0.80% on pulp. For Case 3, unlike Case 2, the calculated excess in D_1 bleach consumption (ca. 0.11% chlorine dioxide on pulp) was within the model's uncertainty error. This observation implied that (EOP) carryover was having a negligible impact on D_1.

Optimized chlorine dioxide distribution

Another round of analyses was conducted on the three cases to find the optimized chlorine dioxide distribution between the delignification and brightening stages. Both models were solved simultaneously to find the chlorine dioxide used in each stage (x_0 and x_1) where the total bleach used (i.e., $x_0 + x_1$) was the lowest. Calculations were done for individual days; afterward, an overall average was determined from the individual calculations. In one of these scenarios, the bleach consumption caused by brownstock and extraction carryover (determined from the initial analysis) was included. The results are shown in **Fig. 4**.

The predicted total charges for Optimized Scenario II, which included brownstock and extraction carryover ef-

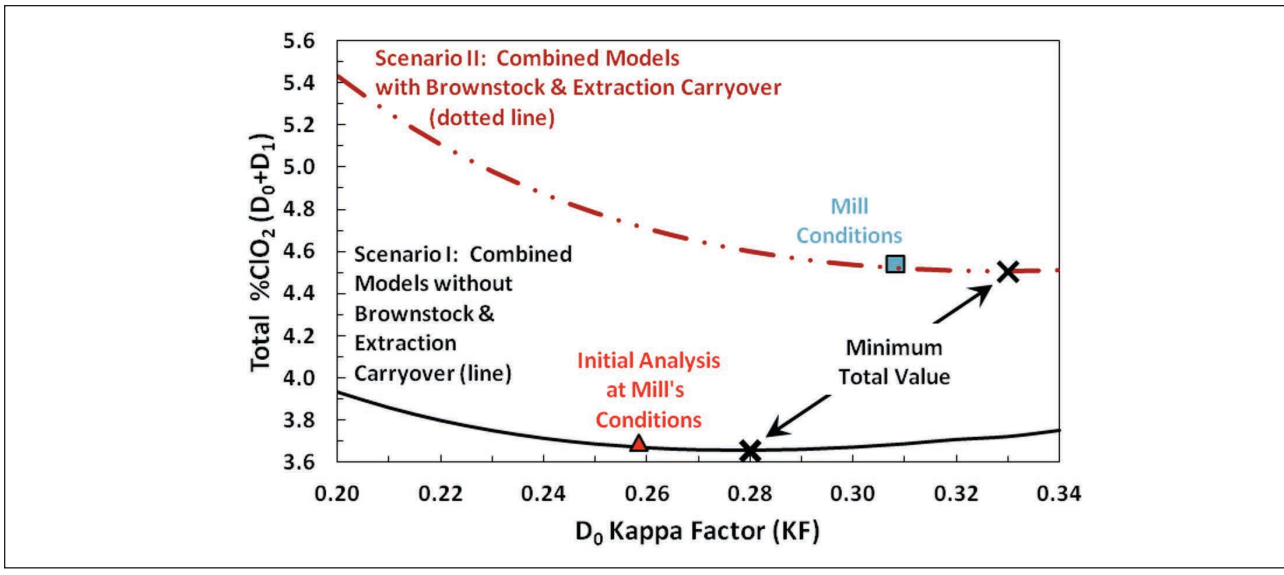

5. Total chlorine dioxide used vs. D_0 kappa factor calculated by the coupled delignification and brightening models (Scenario I and II) for day 3 of Case 1. Optimized values denoted by × symbol. The ■ symbol denotes actual mill data and the ▲ symbol denotes earlier analysis with the models separately.

fects, were remarkably close to the mills' values for all three cases. Likewise, the forecasted total charges for Optimized Scenario I were very close to the values from the initial analysis. In most instances, the small differences in totals from the scenarios to their respective counterparts are within the uncertainty error of the combined models (±0.16% to ±0.28% total chlorine dioxide on pulp). Noted discrepancies are the distributions of chlorine dioxide used in D_0 and D_1. In Case 1, the optimized runs had more chlorine dioxide going to D_0. For Cases 2 and 3, the optimized runs had less chlorine dioxide going to D_0 and more going to D_1.

DISCUSSION

The previous analyses showed that the bleaching models for softwood pulps (Eqs. 1 to 4) could be used as a hypothetical reference to determine how well a mill's D_0 and D_1 stages are using chlorine dioxide. In the cases examined, the actual D_0 stages required an additional 0.33% chlorine dioxide on pulp than was predicted by the delignification model. If assumed brownstock carryover is causing the excess bleach demand, a widespread issue identified in mill surveys [3,5,11-14], then the carryover can be approximated based on stoichiometric relationships [21] at 11 kg saltcake/metric ton pulp or 17 kg COD/metric ton pulp. These model estimates are comparable to the historical averages measured around the timeframe of Case 2 (9.8 kg saltcake/metric ton pulp) and the average recorded during Case 3 (13 kg saltcake/metric ton pulp). The model predicted that the brownstocks, on nominal days, were bleaching as if the pulps' kappa was 4.7 kappa units higher than the measured values. These predictions parallel measured carryover values (2.5 to 7.5 kappa units) reported for Scandinavian bleach plants [27], as well as for mills using in-line dissolved lignin sensors (1.6 to 12 kappa units) [28,29]. The model highlighted days where the extra bleach demand exceeded the typical levels, such as days 7 to 10 in Case 1 (Fig. 1B). Here, the analysis revealed that there was an added demand of 0.67% chlorine dioxide on pulp, and that the brownstock kappa was 9.9 kappa units higher than the measured value. This approximated to 22 kg saltcake/metric ton pulp or 34 kg COD/metric ton pulp of brownstock carryover into the D_0 stage.

Likewise, the D_1 brightening model could estimate how much extra chlorine dioxide is being used and how much extraction filtrate is contributing to the bleach demand. For Cases 1 and 3, the D_1 appeared to use an extra 0.1% to 0.2% chlorine dioxide on pulp vs. the model's predictions. In these cases, the estimated carryover contributed a 0.45-unit higher extracted kappa load (ca. 4.4 kg COD/metric ton pulp, from Eq. 5). These observations implied that the bleach plants had adequate extraction stage washing on most days. Case 2 represented the other extreme. Here, the mill's D_1 appeared to have a surplus bleach demand of 0.60% chlorine dioxide on pulp vs. the model. The carryover approximated to 1.9 kappa units (or 11 kg COD/metric ton pulp). High extraction carryover levels of 1.5 to 2.0 kappa units are somewhat common and have been measured during bleach plant audits in the literature [3,4,6]. Other audits [5,11] have measured carryover levels as high as 5.4 to 13 kappa units. When Mill 2 made changes around its extraction stage (Case 2 vs. Case 3), the estimated carryover was reduced from 1.9 to 0.42 kappa units. It was speculated that most of this reduction was caused by the mill eliminating extraction filtrates as a D_0 shower water source. Prior spreadsheet simulations with a hypothetical ECF bleach plant [30]

showed 30% to 40% reductions in extraction carryover (expressed as kappa units) when this filtrate is not used at the D_0 washer. This publication showed the buildup of dissolved organic solids in the recycled water circuits around the extraction stage and its washer when extraction filtrate is used at the D_0 washer.

An interesting finding from this study regards the distribution of chlorine dioxide between the two D stages vs. the overall total. Predictions from the combined models that considered carryover suggested different chlorine dioxide dosages to be used at D_0 and D_1 than the actual values (Fig. 4, column 1 vs. 2). However, the total amount was nearly identical for both. This observation is attributed to the broad minimum for various D_0 KFs computed from the models, as is illustrated in **Fig. 5** for a typical day in Case 1. In all three cases, it seemed that the process control systems were balancing the chlorine dioxide charges between D_0 and D_1 close to the optimum when considering the washer carryover loads into these stages.

Comparing the mill cases in this study with the hypothetical bleaching models revealed how well the ECF bleach plants are utilizing their chlorine dioxide. In Cases 1 and 3, the $D_0(EOP)D_1$ portions of the bleach plant are operating reasonably well with only 4 to 6 kg chlorine dioxide/metric ton pulp (overall) being inefficiently used. About 50% to 70% of that extra consumption was presumed to be caused by brownstock carryover. It is improbable in these cases that brownstock washing can be improved without increasing the dilution factors used. This adjustment would increase steam costs at the black liquor evaporators, which likely negates any economic savings realized in bleaching [31,32]. The approximated extraction carryover levels in the three cases examined, which ranged from 4.4 to 11 kg COD/metric ton pulp, are on par with the measured levels reported in a survey of Canadian bleach plants [15]. Computed carryover for Cases 1 and 3 is similar to the Canadian bleach plants that measured low COD levels in the pulp feeds to D_1 (i.e., 3 to 5 kg COD/metric ton pulp). On the other hand, the approximated carryover for Case 2 is similar to the Canadian bleach plants that have high COD levels in their extracted pulps, namely 11 to 17 kg COD/metric ton pulp. Case 2 required an additional 10 kg chlorine dioxide/metric ton pulp (overall) vs. what the bleach models predicted. The bulk of this excess bleach usage (>6 kg/metric ton pulp) was presumed to be caused by high extraction carryover.

CONCLUSIONS

Multistage models were used as hypothetical references to determine how efficiently the $D_0(EOP)D_1$ and $D_0(EO)D_1$ partial sequences at two southern U.S. bleach pants utilize chlorine dioxide to bleach southern pine kraft brownstocks. Daily averages of bleach plant data (from in-line sensor measurements) were obtained from the two mills and analyzed by the models. The models highlighted days where the D_0 and/or D_1 stages were using excessively high levels of chlorine dioxide, which was believed to be caused by washer carryover entrained in the pulp feeds. Mill 1 with $D_0(EOP)D_1$ was determined to have nominal levels of brownstock and extraction washer carryover, similar to low-cost Canadian bleach plants; the mill consumed an extra 5 kg chlorine dioxide/metric ton pulp vs. the hypothetical models. Mill 2 with $D_0(EO)D_1$ had a similar predicted brownstock carryover to D_0 as Mill 1 but had a very high predicted extraction carryover to D_1, which resulted in 10 kg chlorine dioxide/metric ton pulp being wasted. When Mill 2 converted its $D_0(EO)D_1$ to $D_0(EOP)D_1$ and discounted the use of extraction filtrates as D_0 shower water, the mill diminished its excess bleach demand of 10 kg chlorine dioxide/metric ton pulp to 5 kg chlorine dioxide/metric ton pulp. Although the coupled models predicted different distributions of chlorine dioxide between D_0 and D_1 stages than what the mills used, the total amounts were accurately predicted when washer carryover loads were considered. This study showed that the bleaching models could be used as hypothetical benchmarks to evaluate how efficiently chlorine dioxide is used in ECF bleach plants. **TJ**

ACKNOWLEDGEMENTS

Parts of this work were presented at the 2022 PAPTAC PaperWeek Virtual Conference (February 7-11, 2022) and will also appear at the 2022 TAPPI PEERS Conference (October 30–November 2, 2022). The author thanks the reviewers for their constructive criticism and suggestions for improving this submission during the peer-review process.

LITERATURE CITED

1. Hart, P.W. and Connell, D., *TAPPI J.* 5(4): 23(2006).
2. Brogdon, B.N., *TAPPI J.* 9(9): 47(2010). https://doi.org/10.32964/TJ9.9.47.
3. Earl, P.F., "Bleach plant best practices and optimization," *Annu. Meet. - Pulp Pap. Tech. Assoc. Can., 102nd*, PAPTAC, Brossard, QC, Canada, 2016, p. 978.
4. Santos, R.B., Hart, P.W., Pryke, D.C., et al., *TAPPI J.* 15(9): 581(2016). https://doi.org/10.32964/TJ15.9.581.
5. Pryke, D.C. and Nylen, K., "Progress toward 'best in class': A summary of bleaching chemical consumption reduction and optimization," *TAPPI Eng., Pulping Environ. Conf.*, TAPPI Press, Atlanta, 2006.
6. Steelreath, E., Earl, P.F., and Vanderheide, J., "Bleach plant optimization at the Resolute Forest Products Coosa Pines mill," *TAPPI PEERS Conf.*, TAPPI Press, Peachtree Corners, GA, USA, 2014.
7. Connell, D. and Carmichael, S., "Chlorine dioxide as a delignifying agent," in *The Bleaching of Pulp* (P.W. Hart and A.W. Rudie, Eds.) 5th edn., TAPPI PRESS, Atlanta, 2012, Chap. 3.
8. Connell, D. and Carmichael, S., "Chlorine dioxide as a brightening agent," in *The Bleaching of Pulp* (P.W. Hart and A.W. Rudie, Eds.) 5th edn., TAPPI PRESS, Atlanta, 2012, Chap. 8.

9. Hart, P. and Connell, D., *TAPPI J.* 7(7): 8(2008).

10. Brogdon, B.N., "Multistage bleach pant modeling, and optimization," in *The Bleaching of Pulp* (P.W. Hart and A.W. Rudie, Eds.) 5th edn., TAPPI PRESS, Atlanta, 2012, Chap. 12.

11. Lunn, R., *Pulp Pap. Can.* 102(3): 46(2001).

12. Pryke, D.C. and Reeve, D.W., *TAPPI J.* 80(5): 153(1997).

13. Pryke, D.C. and Earl, P.F., "Softwood bleaching practices in Canada: Analysis of the 2003 PAPTAC Bleaching Committee 'best practices' survey," *TAPPI Eng., Pulping Environ. Conf.*, TAPPI Press, Atlanta, 2005, Session 50-2.

14. Towers, M. and Turner, P.A., "Survey of bleach plant washing practices in Canadian mills," *Pulp Washing Conf.*, CPPA/TAPPI, Brossard/Atlanta, 1996, pp. 23-29.

15. Earl, P.F. and Schofield, M., "Pulp washing after the first extraction stage: A survey of Canadian mills," *Annu. Meet. - Pulp Pap. Tech. Assoc. Can., 93rd,* PAPTAC, Brossard, QC, Canada, 2007.

16. Andersson, N., Wilke, C., Biazzo, T., et al., *Pulp Pap. Can.* 116(1): 18(2015).

ABOUT THIS PAPER

Cite this article as:
Brogdon, B., *TAPPI J.* 21(7): 353(2022).
https://doi.org/10.32964/TJ21.7.353

DOI: https://doi.org/10.32964/TJ21.7.353

ISSN: 0734-1415

Publisher: TAPPI Press

Copyright: ©TAPPI Press 2022

About this journal

17. Van Fleet, R., Morningred, D., Padasak, S., et al., "Bleach load: A new inline sensor-based improvement for bleach plant advanced control," *TAPPI PEERS Conf.*, TAPPI Press, Peachtree Corners, GA, USA, 2012, p. 622.

ABOUT THE AUTHORS

The purpose of this study was to illustrate how developed models of bleaching stages (e.g., *TAPPI J.* 14(2): 93(2015) and *TAPPI J.* 15(3): 178(2016)) can analyze softwood bleach plant data to find inefficiencies. The generalized models for bleaching delignification and first brightening stages were based on published laboratory data, where the conditions were highly controlled. Prior evaluations showed the models' predictions were normally better than the actual plant data. One explanation for the discrepancy is that the models did not account for bleach consumption caused by washer carryover, a common occurrence in mill operations. I hypothesized that predicted vs. actual values could offer information about wasted bleach consumption and estimated washer carryover loads to bleaching stages. This premise is examined in this study.

One challenge I encountered regarded the preliminary raw mill data analysis. The data had to be examined to rule out other factors that might account for bleaching inefficiencies besides washer carryover, such as suboptimum pH values, large swings in production rates, and faulty in-line sensor readings. Another factor needing consideration was that the bleach plant data was in the same measured units as the models' inputs were based, such as ISO brightness and oven-dried (o.d.) kilograms or metric tons.

One interesting finding I encountered was regarding the data analysis of Mill 2 from two different periods (Case 2 and Case 3). Predictions of the brightening model were much better than the data in Case 2 (Fig. 2), whereas the predictions were much closer to the actual data in Case 3 (Fig 3). When examining my notes when the data were collected, I discovered Mill 2 had changed its shower water source used at the D_0 washer. In Case 2, the mill used dirtier shower water at this location, namely extraction washer filtrate. This resulted in higher amounts of dissolved organics building up in the water circuits around the extraction stage, which resulted in higher washer carryover into the D_1 stage. The model showed that when the mill changed the post-D_0 shower water to a cleaner source, the amount of wasted chlorine dioxide decreased by 50%.



Brogdon

Many mills do not regularly check washer carryover entering the D_0 and D_1 stages. Process engineers could use the bleach stage models to examine their bleach plant data to estimate how much chlorine dioxide is used effectively, and to infer how much washer carryovers are contributing to bleaching inefficiencies. The models could quantify how well defoamers and/or washing aids are reducing washer carryover and are affecting bleaching operations. Alternatively, the models could be integrated into a broader spreadsheet program to evaluate how changes in shower water sources at washers affect chlorine dioxide consumption.

Future work will examine whether developed hardwood models for bleaching delignification and brightening can be similarly used.

Brogdon is president of Future Bridge Consulting Services LLC in Marietta, GA, USA. Email Brogdon at Brian.Brogdon@gmail.com.

18. Andersson, N., Wilke, C., Biazzo, T., et al., *TAPPI J.* 13(10): 39(2014). https://doi.org/10.32964/TJ13.10.39.
19. Brogdon, B.N., *TAPPI J.* 11(3): 31(2012). https://doi.org/10.32964/TJ11.3.31.
20. Brogdon, B.N., *TAPPI J.* 12(2): 17(2013). https://doi.org/10.32964/TJ12.2.17.
21. Brogdon, B.N., *TAPPI J.* 14(2): 93(2015). https://doi.org/10.32964/TJ14.2.93.
22. Brogdon, B.N., *TAPPI J.* 15(3): 178(2016). https://doi.org/10.32964/TJ15.3.178.
23. Brogdon, B.N. and Lucia, L.A., *TAPPI J.* 20(3): 186(2021). https://doi.org/10.32964/TJ20.3.186.
24. Taylor, J.R., "Propagation of uncertainties," in *An Introduction to Error Analysis: The Study of Uncertainties in Physical Measurements*, 2nd edn., University Science Books, Sausalito, CA, USA, 1997, Chap. 3.
25. Runge, T.M., "The chemistry of alkaline extraction between chlorine dioxide stages," Ph.D. dissertation, Institute of Paper Science and Technology, Atlanta, 1998.
26. Jain, S., Mortha, G., and Calais, C., *J. Pulp Pap. Sci.* 35(3-4): 100(2009).
27. Blomberg, L., Järvinen, R., Talka, E., et al., "Organic carry-over in kraft pulp and bleaching discharges," *TAPPI Pulping Conf.*, TAPPI Press, Atlanta, 1990, p. 217.
28. Wilke, C., Andersson, N., van Fleet, R., et al., *TAPPI J.* 15(3): 167(2016). https://doi.org/10.32964/TJ15.3.167.
29. de Oliveira, M.H., "Bleach plant advanced controls – An approach using model predictive control (MPC)," *ABTCP Int. Pulp Pap. Congr., 51st, X IberoAm. Congr. Pulp Pap. Res.*, Associação Brasileira Técnica de Celulose e Papel (ABTCP), São Paolo, Brazil, 2018.
30. Brogdon, B.N. and Lucia, L.A., *TAPPI J.* 17(11): 621(2018). https://doi.org/10.32964/TJ17.11.621.
31. Hart, P.W., *TAPPI J.* 10(7): 37(2011). https://doi.org/10.32964/TJ10.7.37.
32. Hart, P.W., "Impact of washer performance upon other parts of the mill," in *Brownstock Washing: Fundamentals and Practices* (P.W. Hart and M.T. Brown, Eds.), TAPPI PRESS, Peachtree Corners, GA, USA, 2017, Chap. 17.

On the usage of online fiber measurements for predicting bleached eucalyptus kraft pulp tensile index — an industrial case

R.B. DEMUNER, C.A. FARIA, A.A.R. DE ALMEIDA, AND P.N. PIGNATON

ABSTRACT: Cellulose pulp's physical-mechanical properties are determined by laboratory tests obtained from prepared handsheets. However, this procedure is time intensive and presents a lead time until the results are available, hindering its utilization for monitoring and decision-making in a pulp mill. In this context, developing real-time solutions for physical-mechanical properties prediction is fundamental.

This work applied a mathematical modeling approach to develop a soft sensor for tensile index monitoring. The mathematical model considers online morphology measurements obtained from the last bleaching stage outlet stream and important process variables for tensile index prediction. The results obtained are satisfactory compared to laboratory results, presenting a mean absolute percentual error of 2.5%, which agrees with the laboratory testing method's reproducibility.

Application: This paper presents the use of online morphology information to predict pulp physical-mechanical properties in real-time measurements.

Bleached eucalyptus kraft pulps (BEKP) are used in different paper product applications due to their unique physical-mechanical characteristics. For instance, in printing and writing applications, technical requirements for short fibers are related to improved printability, high bulk, high opacity, and high tensile index [1]. In tissue applications, the technical requirements are mainly related to softness and high bulk [2].

The fiber properties and other papermaking raw materials influence the properties of the end product. The wood supply and its processing in pulp mills are determinants [1,3]. The wood supply influences fiber morphology and chemical aspects. In this sense, the eucalyptus fiber morphology is peculiar. For instance, the fiber length is shorter than other species and narrowly distributed. The fiber coarseness is lower than other pulp fibers available on the market. Consequently, the fiber population is high. Additionally, the eucalyptus fiber's collapsibility is low due to a relatively high wall thickness [4]. Natural variation in wood supply is expected, which influences the morphological characteristics and, consequently, the pulp properties.

The relationship between fiber morphology and paper physical-mechanical properties has been a research topic for a long time. Page (1969) [5] developed a theoretical model for the paper tensile index. The fiber length and fiber width positively impacted tensile index, while coarseness affected it negatively. Additionally, the zero-span, the breaking stress of bonds, and the relative bounded area are other variables that influence the tensile index.

Page et al. (1985) [6] showed the effects of fiber deformation on pulp properties. For instance, increasing the fiber curliness decreases tensile index. This effect is related to reducing the actual fiber length used for bonding. One interesting point to highlight is that fibers are straight in wood. Thus, fiber deformation occurs during pulping processes. According to Page et al. [6], fiber deformation occurs due to mechanical and chemical effects' synergic actions. The mechanical effects may be unintentional and can happen, for instance, during high consistency pumping. Regarding the fiber deformation due to chemical effects, its occurrence has been reported during pulp bleaching in the caustic extraction stage [6].

Some research has been done using fiber morphology and other properties to predict pulp physical-mechanical properties. For instance, Horn (1978) [7] presented equations based on fiber morphology to predict hardwood fibers' properties. The main important variables considered were fiber length, length/cell wall thickness ratio, and fibril angle. In this study, eucalyptus fibers were not considered in the evaluation. Demuner et al. (1991) [8] presented a study on different species and hybrids of eucalyptus. It was concluded that wood basic density, fibers per gram, and pulp pentosans content were the main variables related to pulp physical-mechanical properties. Pulkkinen et al. (2008) [9] evaluated the correlation between fiber morphol-

ogy and water retention value (WRV) and its impacts on physical-mechanical properties in eucalyptus fibers. Sundblad (2018) [10] applied previously developed models (e.g., Page (1969) [3] and Axelsson (2009) [11]) and estimated its parameters to fit models to laboratory data.

From the works mentioned earlier, fiber morphology is an important characteristic in describing pulp's physical-mechanical properties. Correlation and model development were already present in the literature. However, laboratory results are typically employed, and a limited number of samples are considered. Also, the performance of the models in an industrial application was not reported.

The traditional laboratory method of assessing pulp physical-mechanical properties is based on a beating device, such as the Norwegian Paper and Fiber Research Institution (PFI) mill device. Given different pre-established beating levels, the handsheets are formed and their physical-mechanical properties are evaluated at each level [12].

In pulp mills, these tests are done once or twice a week in the laboratory [13] and express the potential of pulps for papermaking, as the paper properties that might be produced on a paper machine are also dependent on paper production processes. Indeed, keeping the physical-mechanical properties stable in a pulp mill is important, consequently minimizing a source of variability for paper production.

However, due to the lead time of the conventional laboratory methodology, the results are available a few days after the pulp production time. Thus, the conventional method is not suitable for applications that aim to help decision-making during the production time.

It would be convenient and helpful to use the unbeaten fiber information available to predict pulp physical-mechanical properties, such that the potential of pulps for papermaking would be available. In this sense, Horn [7] showed that the unbeaten fiber morphology correlates well with physical-mechanical properties obtained from unbeaten and beaten fibers. Theoretically, it can be explained by hardwood pulp's physical-mechanical properties being primarily dependent on the characteristics involved in developing fiber-to-fiber bond potential, such as fiber flexibility.

Therefore, the present work offers a complete methodology to develop a soft sensor to predict the BEKP tensile index based on morphology and online measurements of process variables. This work also presents the results applied to an industrial operation of a large pulp mill placed in Brazil for over one year.

METHODOLOGY

Materials and methods

This section describes the methods applied to the tensile index soft sensor development. **Figure 1** presents the simplified process diagram and the positions of the measurements. After the dryer machine (dried pulp sheets), pulp samples were taken to assess their physical-mechanical properties by laboratory testing.

The pulp was disintegrated, beaten at 1500 revolutions in a PFI mill device, and the handsheets were formed and tested in the mill quality control laboratory. The methodologies considered are also presented in **Table I**. From the procedure described before, it was possible to obtain the tensile index at 1500 PFI revolutions, which was considered as the soft sensor output.

An online instrument for morphology measurement was installed at the bleaching plant outlet, which means that the morphology of never-dried pulp at a consistency of approximately 10% is sampled by the measuring device. New morphology information is available every 15 min. In terms of measurement technology, the fibers are analyzed through an optical method based on image analysis. A fiber suspension sample is collected from the bleaching plant outlet by an automatic sampler and sent to the measuring device. The samples are diluted in a dilution chamber using demineralized water in order to achieve very low consistency (0.004%–0.01% for hardwood pulps, according to ISO 16015-2 [2014] "Pulps — Determination of fibre length by automated optical analysis — Part 2: Unpolarized light method") suitable for fiber measurements. The sample then flows through the measurement cell, which measures only the amount of light received by the camera imaging cell. Due to scattering optics, the incident light is scattered from or absorbed by fibers in its path, and only the light that is not scattered will reach the camera. Therefore, the amount of light that does not reach the camera is equal to the particle area. This measuring concept allows the measurement of up to several million fibers, allowing repeatability of 1.5% for the average fiber length [14]. Based on image analysis, algorithms are applied to calculate morphology properties,

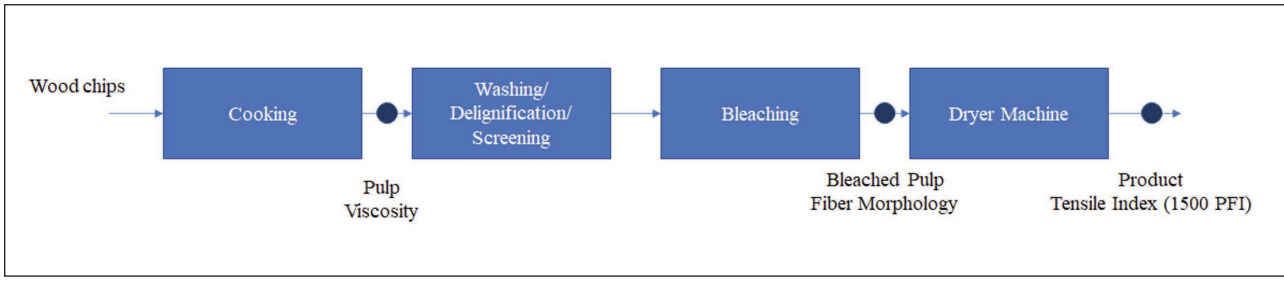

1. Simplified process diagram with measurements and sampling positions.

Analysis	Method
Morphology (fiber length & width)	ISO 16065-2 "Pulps — Determination of fibre length by automated optical analysis — Part 2: Unpolarized light method"
Laboratory wet disintegration	ISO 5263-1 "Pulps — Laboratory wet disintegration — Part 1: Disintegration of chemical pulps"
PFI beating	ISO 5264-2:2011 "Pulps — Laboratory beating — Part 2: PFI mill method"
Handsheet formation	ISO 5269-1:2005 "Pulps — Preparation of laboratory sheets for physical testing — Part 1: Conventional sheet-former method"
Tensile index test	ISO 1924-3:2005 "Paper and board — Determination of tensile properties — Part 3: Constant rate of elongation method (100 mm/min)"
Viscosity	ISO 5351:2010 "Pulps — Determination of limiting viscosity number in cupri-ethylenediamine (CED) solution"

I. Methods applied in laboratory and online equipment.

such as length, width, coarseness, fiber per gram, kinks, shape, mean kink angle, fines, and distributions thereof. The information generated by the equipment is then sent to the mill distributed control system (DCS) and process information management system (PIMS), where historical data can be consulted. Regarding the operating principle and specification details of morphology measurement equipment, the authors refer to ISO 16015-2 (2014), which establishes a standard for automated morphology measurements by optical sensors.

From the measurements obtained from the equipment, the following morphology information was considered for model development: mean fiber length (arithmetic), length weighted mean length, fiber width, fiber coarseness, fines, curl, mean kinks, and mean kinks angle.

In addition, the digester pulp viscosity was also considered a predictor variable. The viscosity is based on laboratory measurements. Table I presents the applied methodologies in this study.

Data acquisition and pretreatment

The tensile index results were measured daily, considering a composite sample from an interval of one hour of production, with a sampling time of 20 min. It means that three samples were collected during one hour on a given day, and this composite sample was tested.

To correlate the measured tensile index of the product to past process steps (e.g., bleaching and cooking), the retention time of each step was calculated based on the tank's volume and current level, pulp suspension consistency, and production rate of each step. The retention time value is considered as a lag, such that the morphology and viscosity data need to be time-shifted based on it.

Based on the sampling date and time of the product (pulp sheet), the corresponding morphology information at the bleaching plant outlet and pulp viscosity at the digester outlet are obtained based on the calculated retention time. This procedure can be interpreted as data synchronization, and it was applied to each product sampling instant available, which is always associated with a tensile index result.

The resulting dataset is a matrix of 363 lines (which represents the number of tensile index results) and nine columns, which represent the following variables: mean fiber length (arithmetic), length weighted mean length, fiber width, fiber coarseness, fines, curl, mean kinks, mean kinks angle, and pulp viscosity, which are considered as potential predictors for model development.

The resulting dataset represents a year of the mill operation and considers the pulp properties' natural variability, primarily related to the wood source. Also, model robustness is encouraged by sampling across the daily conditions, which may encompass different conditions and is not limited to a given operational condition of the mill.

Model development

The dataset previously obtained was randomly split, such that 70% of the data (254 points) is considered for model training (calibration) and the remaining 30% of the data (109 points) for model testing (validation). The data were scaled using a standardization scaler, such that the resulting data is centered on its average (zero mean) and scaled by its standard deviation. Mathematically, it can be written as follows:

$$x_{scaled,j} = \frac{x_j - \bar{x}_j}{\sigma_j} \quad (1)$$

where $x_{scaled,j}$ is the standardized j-th variable (j =1,…,m), m is the number of variables, x_j is the original j-th variable

(without standardization), $\bar{x}_j$ is the j-th variable average value, and σ_j is the j-th variable standard deviation. For the sake of notation, this work considers the notation using the variable x for the predictor variables and y for the output (response) variable.

The data scaling step, here considered the standardization, is important due to the differences in the order of magnitude of the variables considered in the dataset. Thus, after standardization, the variables become dimensionless and in the same order of magnitude. Additionally, linear regression also allows for obtaining the standardized regression coefficients.

Multivariable linear regression was considered and implemented in Python code based on *Sklearn* library [15]. Thus, the model can be written as follows:

$$y^m_{scaled} = \sum_{j=1}^{m} \beta_j \, x_{scaled,j} \tag{2}$$

where y^m_{scaled} is the model output, here considered the standardized tensile index, and β_j is the regression model coefficient associated with the j-th variable.

In order to keep only independent variables in the dataset, a multicollinearity test was applied to remove variables that are strongly linearly related. In this test, the correlation matrix of the predictor variables is evaluated. If one pair of independent variables has more than 0.9 correlation, one of these variables is removed, preferably the one with a lower correlation to the output variable. The correlation evaluation was based on Pearson correlation coefficients.

Subsequentially, the model is trained using a backward feature elimination to select only statistical meaning variables based on a significance level of 0.05 for model parameters. The algorithm starts with all possible predictor variables and fits the model. The predictor variables' coefficients' significance values (p-value) are calculated, and the highest p-value is identified. If this value is greater than the predefined significance level, the corresponding predictor variable is removed from the training dataset. This procedure is repeated until all predictor variables' significance values are statistically significant.

The model coefficients are obtained by the maximum likelihood estimation problem [16], leading to a weighted least squares problem, such that the following objective function is minimized:

$$F_{obj} = \sum_{i=1}^{n_{train}} \frac{(y_i^m - y_i^{exp})^2}{\sigma_i^2} \tag{3}$$

where n_{test} is the test dataset size, y^m and y^{exp} are the tensile index predicted by the model and the laboratory data, and σ_i^2 is the i-th variance, which corresponds to the experimental error (variance) obtained in the i-th laboratory result.

In Eq. 3, it is important to notice that it corresponds to a generalization of the least-square problem. If the variance of each experiment is the same, the resulting objective function is equivalent to an ordinary least-square problem. In this work, the least-square objective function is assumed.

For model validation, the mean absolute percentual error (MAPE) was evaluated as model metrics, which is calculated as follows:

$$MAPE\ (\%) = \frac{100}{n_{test}} \sum_{i=1}^{n_{test}} \frac{|(y_i^m - y_i^{exp})|}{y_i^{exp}} \tag{4}$$

where $|\cdot|$ is the absolute value operator and n_{test} is the test dataset size. In Eq. 4, it is important to notice that the MAPE is calculated based on the tensile index value without scaling. Therefore, it represents the relative error itself, enabling the comparison of the model error to the laboratory reproducibility error.

Also, the model predictions were compared to the laboratory method based on a paired t-test considering the test dataset. The paired t-test is used to verify if the mean difference between pairs of measurements is zero. This test aims to validate if the method under development is equivalent to a reference method. In this case, this test is applied to compare the tensile index model predictions to the laboratory data. The authors refer to Montgomery [16] for details of the paired t-test.

In the paired comparison, the i-th paired difference is calculated as follows:

$$d_i = y_i^m - y_i^{exp} \tag{5}$$

The expected value of the difference is:

$$\mu_d = E(d_i) = \mu_m - \mu_{exp} \tag{6}$$

where μ_d is the expected value of the difference, E(·) is the expected value operator, and μ_m and μ_{exp} are the expected value of the model and laboratory results.

The null hypothesis is described as follows:

$$H_0: \mu_d = 0 \tag{7}$$

$$H_1: \mu_d \neq 0 \tag{8}$$

The test statistic for this hypothesis is:

$$t_0 = \frac{\bar{d}}{s_d/\sqrt{n_{test}}} \tag{9}$$

where t_0 is the t statistics, $\bar{d}$ is the average of the differences, and s_d is the standard deviation of differences.

The average and standard deviation of differences are

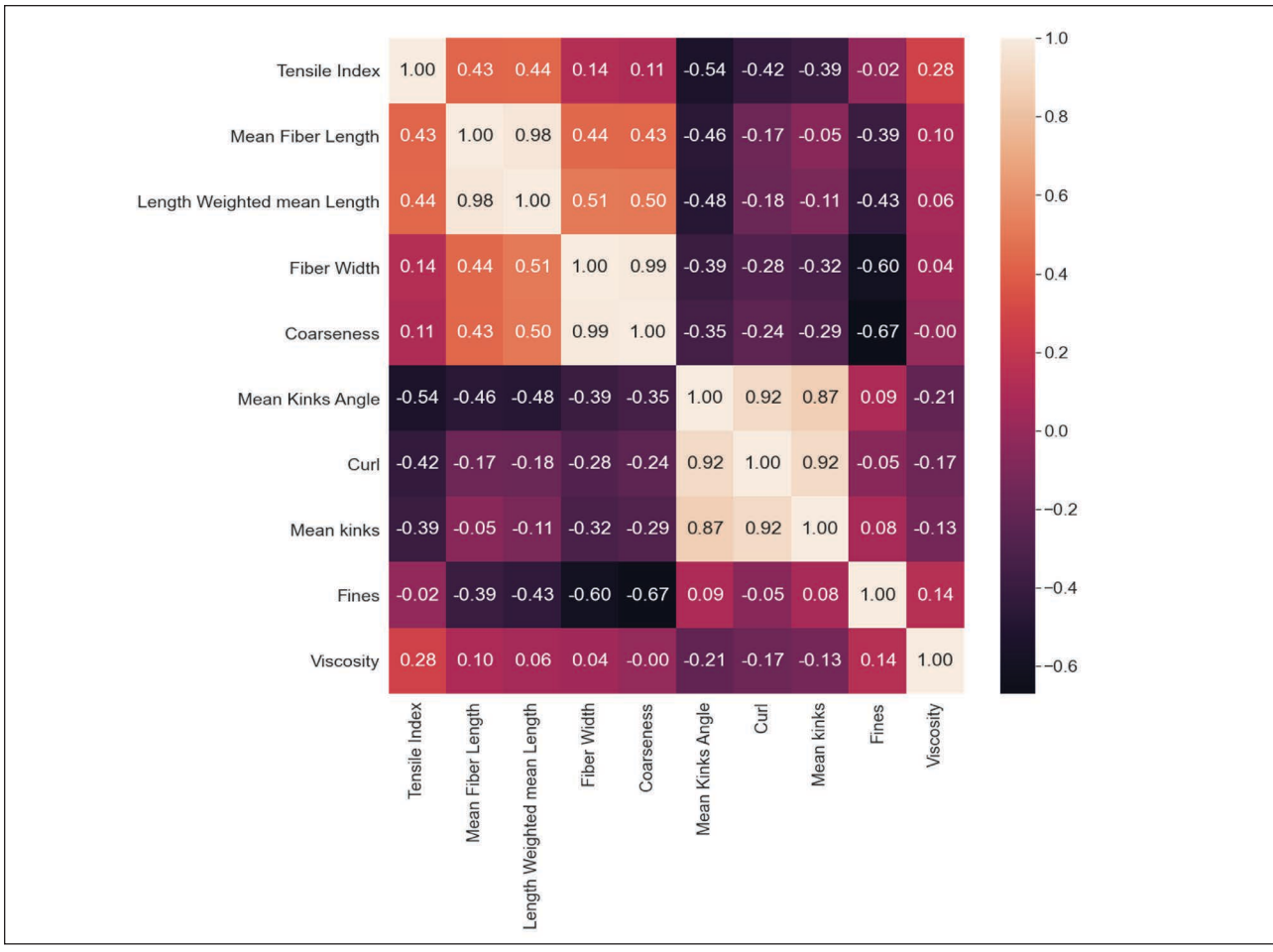

2. Correlation analysis of fiber properties and tensile index. All variables are scaled following standardization.

calculated as follows:

$$\bar{d} = \frac{1}{n_{test}} \sum_{i=1}^{n_{test}} d_i \tag{10}$$

$$s_d = \sqrt{\frac{\sum_{i=1}^{n_{test}} (d_i - \bar{d})^2}{n_{test} - 1}} \tag{11}$$

H_0: $\mu_d = 0$ is rejected if $|t_0| > t_{critical}$, where $t_{critical}$ is the t-student value obtained for a significance level α and n_{test} – 1 degrees of freedom.

Additionally, the F-test is also applied to verify the regression model overall significance. The F-statistics is calculated as follows [17]:

$$F_{statistics} = \frac{MSR}{MSE} \tag{12}$$

where *MSR* and *MSE* are the mean sum of squares due to regression and the mean squared errors calculated as follows:

$$MSR = \frac{\sum_{i=1}^{n_{test}} (y_i^m - \overline{y_i^{exp}})^2}{p} \tag{13}$$

$$MSE = \frac{\sum_{i=1}^{n_{test}} (y_i^m - y_i^{exp})^2}{n_{test} - p - 1} \tag{14}$$

where p is the number of model coefficients, and $\overline{y_i^{exp}}$ is the average value of laboratory results.

In the F-test, if $F_{statistics} > F_{critical}$, the regression model presents overall significance. In this test, $F_{critical}$ is obtained from the F-distribution with a significance level of 0.05 and degrees of freedom equal to p and $n_{test} - p - 1$.

RESULTS AND DISCUSSION

Correlation analysis

The correlation between fiber properties and tensile index is presented in **Fig. 2**. It is possible to notice that the mean kink angle, curl, shape, and mean kinks have a negative impact on the tensile index. Indeed, these effects were already identified in the literature, and using the available

Variable	Coefficient	Standard Error	p-value
Mean kink angle	-0.3550	0.060	0.000
Length weighted fiber length	0.2435	0.061	0.000
Pulp viscosity	0.2474	0.056	0.000

II. Model coefficients, standard errors, and p-values. The coefficients are related to standardized variables.

online technology, it was also possible to see this effect. Additionally, the fiber length and viscosity correlate positively with tensile. The viscosity effect could be interpreted as a higher cooking selectivity, preserving carbohydrates and probably integrity of fibers. The effect of fiber length could be interpreted as a higher effective length for bonding. Also, the correlation between the tensile index and the variable's fines content, coarseness, and fiber width were low. Regarding the low correlation between fines and tensile index, as the morphology data is related to the unbeaten pulp, these fines are primary fines, which have a minor impact on the tensile index compared to secondary fines.

When analyzing the correlation among predictor variables, it can be noticed that the mean fiber length (arithmetic) and length weighted mean length are strongly correlated. It can be justified because these properties are based on the fiber length and are only calculated by different mathematical expressions. The same behavior can be noticed in fiber width and coarseness. It can be explained that coarseness depends on fiber weight, which depends on fiber width and cell wall thickness. Regarding the fiber shape variables, it can be noticed that there is a strong correlation among mean kinks angle, curl, and kinks, which is expected, as these variables describe fiber deformations.

Model training

After analyzing the correlation matrix, some variables were eliminated to avoid multicollinearity among predictor variables. The remaining variables in the matrix are the length weighted mean length, fiber width, mean kinks angle, fines, and pulp viscosity.

The multivariable linear model was fitted using the backward feature elimination procedure. The selected variables and their coefficients are presented in **Table II**.

From Table II, it can be noticed that only three variables were selected, which are: mean kinks angle, length weighted mean length, and pulp viscosity. Analyzing the coefficient signals shows that the mean kinks angle affects the tensile index negatively, while length weighted mean length and pulp viscosity affect the tensile index positively. This result agrees with the correlation matrix presented in Fig. 2. Also, as expected, due to the backward feature

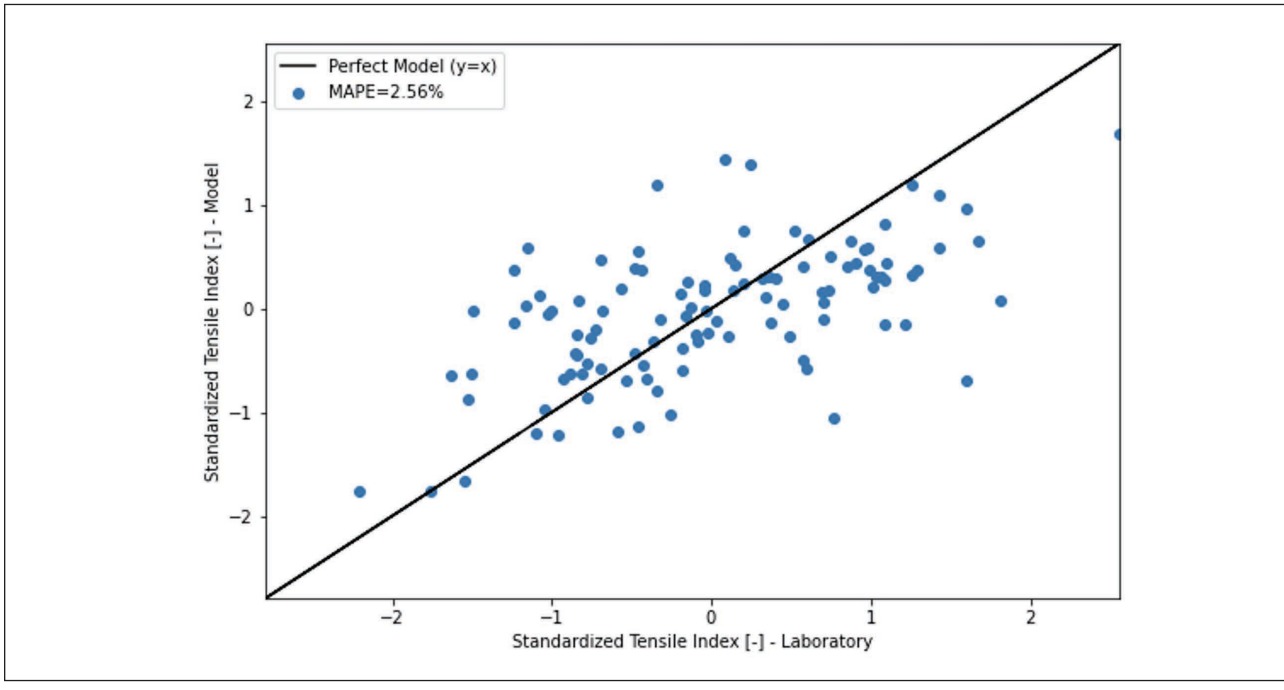

3. Scatter plot of tensile index – model prediction and laboratory data in test dataset (time independently). MAPE is the mean absolute percentual error.

Mean of Differences	Standard Deviation of Differences	Standard Error of Differences	95% Confidence Interval of the Difference		t-statistics	p-value	Degrees of Freedom
			Lower	Upper			
-0.025	0.752	0.072	-0.144	0.094	0.34	0.72	108

III. Paired t-test applied for model predictions and laboratory method.

elimination, the p-value of each coefficient is below the significance value of 0.05 selected in this work.

Model validation

The scaled model prediction results against laboratory data are presented in **Fig. 3**. The predictions are calculated using the test (validation) dataset, which comprises 30% of the data gathered during a year of operation. The test dataset represents approximately three months of operation. It is important to highlight that Fig. 3 is time independent, showing an overall tendency of the validation period.

Analyzing Fig. 3 shows that the data is distributed along the perfect model line (y=x), which tends to fit the laboratory data. In the test dataset, a MAPE=2.56% was obtained. Here, it is worthwhile to mention that the laboratory method, ISO 1924-3 (2005) "Paper and board — Determination of tensile properties — Part 3: Constant rate of elongation method (100 mm/min)," indicates a reproducibility range of 2%–4%, depending on the paper grade [17]. Thus, the model developed showed an error comparable to the conventional method error.

Additionally, a paired t-test was carried out to compare model predictions and laboratory data. **Table III** presents the results obtained in the paired t-test.

From Table III, it is possible to notice that a mean difference of -0.025 is obtained, with a confidence interval that contains zero. It means that, statistically, the mean of differences can be null, such that there is no difference between model and laboratory results averages. It can also be confirmed by the p-value that is higher than 0.05 (significance level). It means that the null hypothesis of identical averages cannot be rejected.

The regression model overall significance was assessed using an F-test. In the test data set, the calculated $F_{statistics}$ was 25.81, while the $F_{critical}$ = 3.24, considering a significance level of 0.05 and degrees of freedom of 3 (number of coefficients) and 105. Thus, as $F_{statistics}$ is greater than $F_{critical}$, it was concluded that the model has overall significance.

The time trend of scaled model prediction and laboratory results is presented in **Fig. 4**, which represents the predicted and laboratory tensile index results in the overall dataset (training and testing) and can be interpreted as almost one year of operation of the mill, as the tensile index

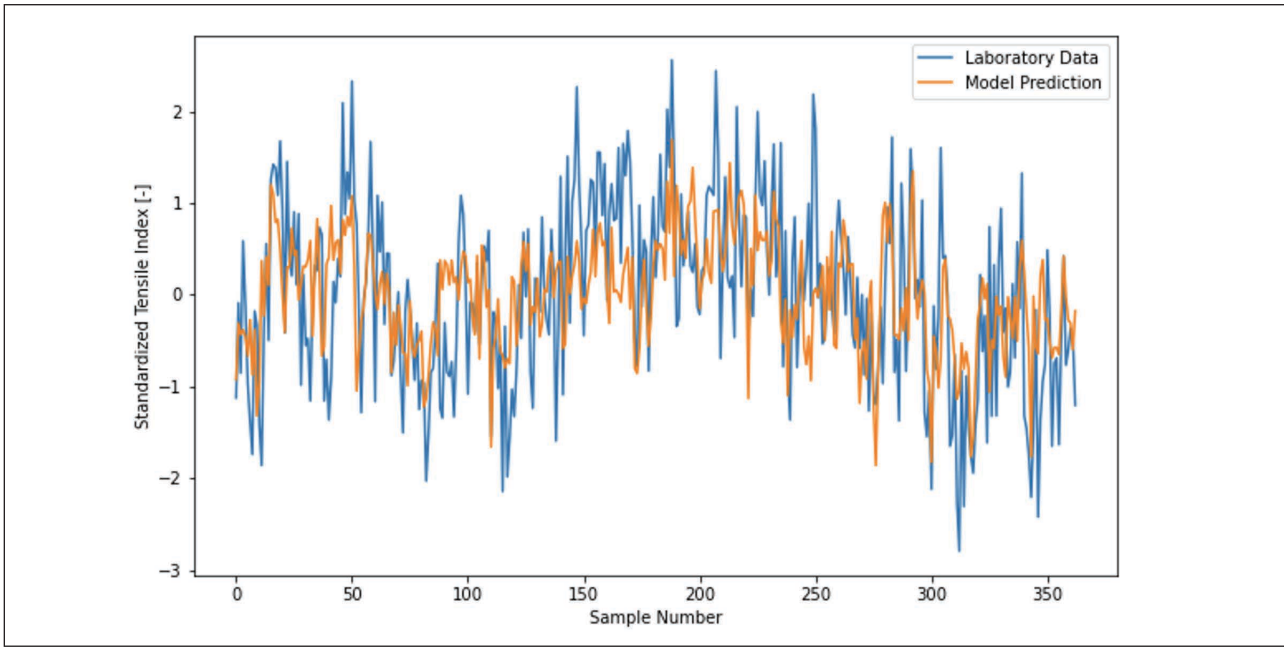

4. Time evolution of model predictions and laboratory data during a period of one year of operation.

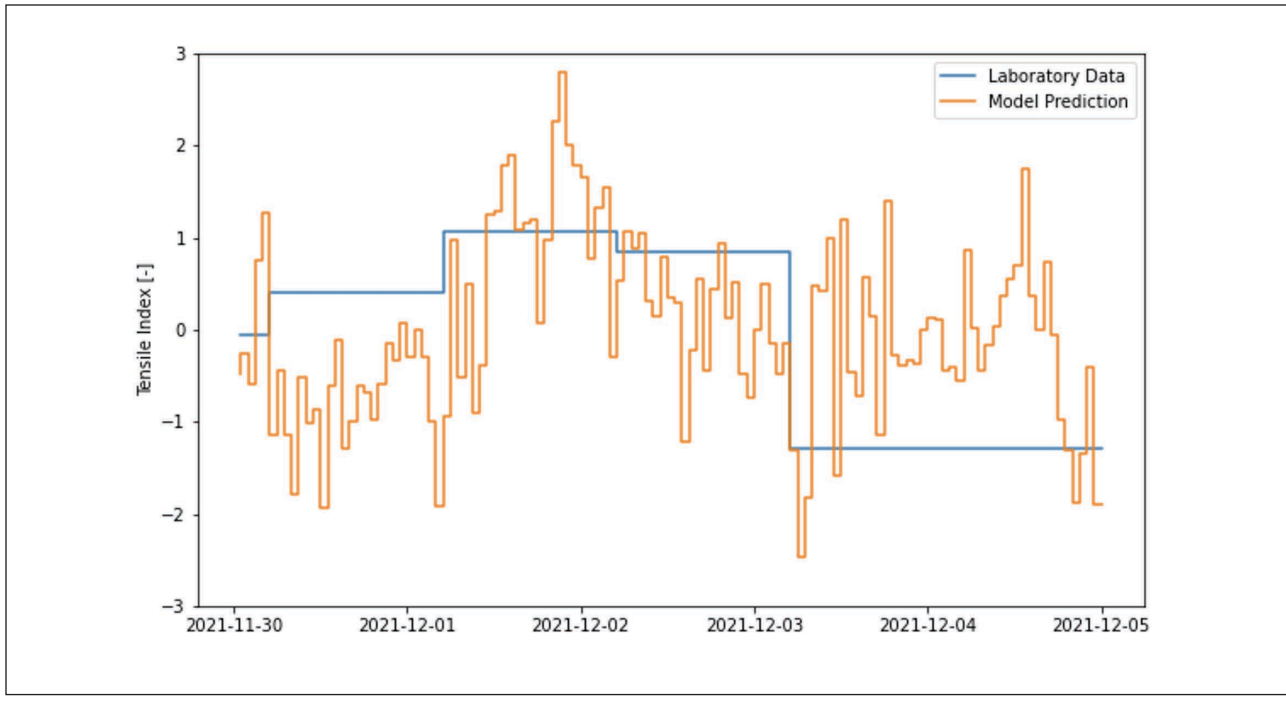

5. Tensile index laboratory data and model predictions during a period of one week.

results are obtained on a daily basis. Analyzing Fig. 4 shows that the model predictions follow the laboratory data trends. There are some results peaks that the model cannot predict, which can be related to external variables that are not measured or considered by the model. However, the model can predict the trends of tensile, which is important for process understanding and its usage for decision-making.

One of the most important advantages of developing a soft sensor is data availability. As mentioned before, typically, physical-mechanical tests are carried out a few times during a week. By using a soft sensor, it is possible to achieve a higher frequency. **Figure 5** presents the scaled laboratory data and model predictions for one week.

By analyzing Fig. 5, it is possible to verify that model prediction at the time of the laboratory sampling agrees with laboratory results. It is also worth mentioning that the laboratory results are available at least six hours after the production time. In that sense, the soft sensor enables results on an hourly basis. Furthermore, using model predictions also enables verifying how the tensile index varies between the interval of laboratory results. This information also enables development of control actions and decision-making in a pulp mill aimed at tensile index variability reduction.

Discussion

Three variables were selected and identified as statistically significant regarding the fitted model: mean kink angle, length weighted mean length, and pulp viscosity. Although these variables are a consequence of wood source and process influences, this information could be further investigated to identify process variables strongly correlated to the model features. Thus, a causality map could be built aiming to leverage the tensile index.

The model predictor variables were identified through a data-driven strategy. The obtained relationships are also influenced by the conditions of mill processes and wood source. Direct extrapolation of this model to another mill needs to be carefully done since the output may be biased due to the differences in raw material and processes. However, it is important to mention that the identified variables agree with the theoretical foundation present in the literature and its effects. Thus, the variables are not limited to a specific mill, but corrections in model coefficients should be necessary when applied to another mill.

In this work, a considerable time range was considered for model development. A total of 363 tensile index results were considered, representing one year of mill operation, as the laboratory results are obtained daily. It means that natural variation of wood source and conditions of processes are considered.

Although validated by statistical tests, the model predictions presented an opportunity for accuracy improvement, especially in cases of tensile index peaks. It means that morphological variables do not fully explain the tensile index, and some additional information should be considered in the model. For instance, fiber chemical information, such as pentosans content, was found in the literature [8] as a variable of influence.

Despite the opportunity for accuracy improvement, the developed model can follow the tensile index trend, with a response time much faster than the laboratory results.

The main advantage of this model is data availability, which enables the mill operation to identify the tensile index fluctuations and take actions to minimize variability.

The following steps of this research intend to include fiber chemical properties into the model to improve its accuracy, as well as identification of key process variables aimed at minimizing tensile index variability. Moreover, variations in the wood mix due to the eucalyptus growth cycle need to be followed over time, and there is the need for a model recalibration due to these seasonal changes.

CONCLUSIONS

This work developed a soft sensor for predicting tensile index using online morphology measurements, such as mean kink angle, length weighted mean length, and the pulp viscosity. These variables agree with the theoretical foundation present in the literature and its effects. This work shows that the model mean average percentual error is equivalent to laboratory method reproducibility. Also, the averages of the soft sensor prediction results were equivalent to the laboratory results averages based on a paired t-test and overall model significance, which was assessed by an F-test. The results also showed an improvement in terms of data availability when using the soft sensor. **TJ**

LITERATURE CITED

1. Fiserová, M. and Gigac, J., *Cellul. Chem. Technol.* 45(9-10): 627(2011).
2. Cotterill, P. and Macrae, S., *TAPPI J.* 80(6): 82(1997).
3. Tomkins, M.R., Gilbert, W., and Trung, T., *TAPPI J.* 17(4): 207(2018). https://doi.org/10.32964/TJ17.04.207.
4. Demuner, B.J. and Claudio-da-Silva Jr., E., "Eucalyptus: Today's preferred short-fiber pulp," in *The World of Market Pulp* (H. Nanko, A. Button, D. Hillman, et al., Eds.), WOMP LLC, Appleton, WI, USA, 2005.
5. Page, D.H., *Tappi* 52(4): 99(1969).
6. Page, D.H., Seth, R.S., Jordan, B.D., et al., "Curl, crimps, kinks and microcompressions in pulp fibres — their origin, measurements and significance," in *Papermaking Raw Materials, Trans. of the VIIIth Fund. Res. Symp. Oxford, 1985*, (V. Punton, Ed.), FRC, Manchester, 2018, pp. 183–227.
7. Horn, R.A., "Morphology of pulp fiber from hardwoods and influence on paper strength," USDA Forest Service Research Paper, Forest Products Laboratory, Madison, WI, USA, 1978.

ABOUT THIS PAPER

Cite this article as:
Demuner, R.B., Faria, C.A., de Almeida, A.A.R., et al., *TAPPI J.* 21(7): 365(2022).
https://doi.org/10.32964/TJ21.7.365

DOI: https://doi.org/10.32964/TJ21.7.365

ISSN: 0734-1415

Publisher: TAPPI Press

Copyright: ©TAPPI Press 2022

About this journal

ABOUT THE AUTHORS

In this work, we developed a tensile index soft sensor based on online fiber measurements, which express the potential for papermaking of the pulp. The most challenging aspect of this research was getting accurate information from the process and treating it to generate information. We applied statistics tools for data treatment and mathematical modeling to develop the soft sensor.

From this research, we found the contributions of fiber morphology and process variables to strength. The soft sensor's main benefit is the availability of results compared to traditional laboratory measurements

The next steps for this research are related to incorporating fiber chemical properties into the model to improve its accuracy and identify key process variables aimed at minimizing tensile index variability.



Demuner

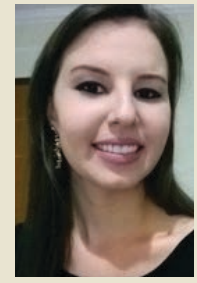

Faria



de Almeida



Pignaton

Demuner is quality manager at Suzano S/A and is based in Mato Grosso do Sul, MS, Brazil. Faria is a graduate student at Universidade Federal de Uberlândia in Uberlândia, MG, Brazil. De Almeida is quality manager at Suzano S/A in Três Lagoas, MS, Brazil. Pignaton is executive quality manager at Suzano S/A and is based in Aracruz, ES, Brazil. Email Demuner at rafael.demuner@suzano.com.br.

8. Demuner, B.D., Vianna Doria, E.L., Claudio-da-Silva Jr., E., et al., "The influence of eucalypt fiber characteristics on paper properties," *Int. Pap. Phys. Conf.*, TAPPI Press, Atlanta, 1991.
9. Pulkkinen, I., Alopaeus, V., Fiskari, J., et al., *O Papel* 69(10): 71(2008).
10. Sundblad, S., "Predictions of pulp and paper properties based on fiber morphology," Master's thesis, Royal Institute of Technology (KT), Stockholm, Sweden, 2015.
11. Axelsson, A., "Fibre based models for predicting tensile strength of paper," Master's thesis, Luleå University of Technology, Luleå, Sweden, 2009.
12. Popil, R., *Physical Testing of Paper*, Smithers Group Company, Shawbury, UK, 2017.
13. Alanen, M., Poukka, A., and Kouivuniemi, I., WO. Pat. 2014/009605 A1 (January 16, 2014).
14. Keinanen, P., Piirainen, E., Maatta, J., et al., "New ways to manage drainability, fibre properties and shive content of the pulp," *Appita Annu. Conf. Exhib., 60th*, Appita, Bundoora, VIC, Australia, 2006, p. 503.
15. Pedregosa, F., Varoquaux, G., Gramfort, A., et al., *J. Mach. Learn. Res.* 12: 2825(2011).
16. Montgomery, D.C., *Design and Analysis of Experiments*, 2nd edn., Wiley, New York, 1984.

Calender barring review with experiences

JAKE ZWART

ABSTRACT: Excessive calender vibration affects all styles of calender stacks from single to multi-nip, all hard rolls, or a combination of hard and soft rolls. Calender vibration can be forced vibration or self-excited vibration. Forced vibration occurs at the first few harmonics of the calender roll rotational speeds and is caused by imbalance, misalignment, eccentricity, etc. Self-excited vibration, the focus of this paper, occurs at higher frequencies.

Feedback paths for self-excited vibration must be understood in order to ameliorate the problem. This is presented in the context of the historical development of the theory of self-excited feedback mechanisms, followed by a survey of self-excited feedback mechanisms in various types of calender stacks. Methodology to determine which feedback path is present and techniques to control or eliminate the resulting vibration follow. To obtain a flavor of the types of problems faced and practical remedial actions, a variety of experiences with barring issues are provided.

Application: This paper provides background information on the history of calender barring on a calender stack, along with the factors that contribute to the problem and resolutions to the problem.

Calender barring is vibration of calender rolls resulting in caliper variations with accompanying gloss and opacity variations. This paper focuses on calender vibration due to self-excited vibration and not the forced vibration due to typical rotating equipment phenomena such as imbalance, misalignment, eccentricity, etc. Self-excited vibration starts when random disturbances excite a resonance in the calender, resulting in caliper variations in the paper and/or barring marks on the roll, which act as an excitation source after a time delay.

A simple contrived example that is useful for understanding the self-excited concept is the playground swing. When the force of a push on the swing is in phase with the velocity of the swing, the amplitude of the swing increases. When the force is applied out of phase with the velocity, the amplitude quickly decreases. Here, the person pushing on the swing mimics the time-delay feedback mechanism.

Self-excited vibration is not unique to calender stacks. The machine tool industry is plagued with this problem, with early research funded and performed by Cincinnati Milacron [1] in the 1950s, going right up to modeling a 5-axis milling machine [2] in modern times. The steel industry faces similar problems where the word chatter is used instead of barring in rolling mills. Press section vibration can also be the result of self-excited vibration. Time delay differential equations [3] are the fundamental equations used to model all self-excited vibrations.

Calender barring in multi-nip hard roll stacks has been recognized in papermaking literature for a long time, with the first reference being a private communication between Bercel [4] and an E.B. Eddy employee in 1950, with the first written papers [5-7] dating back to the early 1960s. In 1966, the MASc thesis of Davidson [8] shows the feedback paths we know today were still under debate. In the early days Bowater Technical Services contributed greatly to the understanding of calender barring. By 1975, Parker [9] gave a good summary, indicating calender barring was well understood, which was echoed by Cotgrove [10] a decade later. Their summary is included in the next section under caliper feedback and corrugated surface feedback for multi-nip hard calenders.

CALENDER BARRING VIBRATION FEEDBACK MECHANISMS

The feedback mechanism for self-excited vibration is a variation induced by the process, which then acts on the same process as an excitation after a time delay. A forced vibration, on the other hand, is intrinsic in the system and acts without a time delay.

Multi-nip hard roll calender with caliper feedback

We can think of each calender roll in a multi-nip stack as a rigid mass with vertical translational motion, with the paper in the nip acting as both a spring and a damper. This system yields one natural frequency per roll. The lowest natural frequency occurs when all of the rolls move in phase with no relative movement between the rolls, resulting in no caliper variations. For the remainder of the natural frequencies, assuming the damping is viscous, the rolls will be in phase or out of phase with neighboring rolls. The out of phase motion between adjacent rolls results in caliper variations.

An impulsive disturbance excites all frequencies, with the response proportional to the amplitude of its natural frequencies. Thus, the response is sinusoidal vibrations at the resonant frequencies of the stack, resulting in sinusoidal

caliper variations. Any caliper variation induced by an upper nip will travel to the lower nips, acting as an excitation after a time delay. If the caliper is increasing as the rolls in the lower nips are moving apart, the vibration is sustained or increases. Stated quantitatively, this occurs when there are an integer-plus-one-quarter (N+1/4) wavelengths between an upper and lower nip. Conversely, if the rolls are moving towards each other when the caliper is increasing, the force acts to reduce the vibration level. The number of wavelengths between nips is controlled by the calender offsets. The offset is defined as the machine direction centerline distance of the rolls relative to the fixed roll, usually the king roll. Most calenders can extend or retract the pivot arms. On older A-frame calender stacks, shims are used to offset the rolls.

This type of self-excited multi-nip hard roll calender barring can start or stop instantaneously with a change in machine operating conditions. Important operating conditions are the machine speed and the parameters that change the stiffness of the paper in the nip. Fortunately for many machines, these parameters are relatively constant.

The investigation of the actual behavior of paper in a nip has been modeled by Browne [11]. Shelley [12] inverted this model to determine the nonlinear stiffness properties of the paper in the nip, and then used the stiffness to solve for barring in the time domain using time delay differential equations [3]. His four-roll stack model indicated changing calender speed could induce or prevent barring.

Bercel [4] created a model of the vertical vibration of a calender stack in which the vibration along the length of the roll was considered. Melnick [13] used finite element methods to extend the standard calender offset calculation procedure by creating a two-dimensional model of the dynamics of a calender stack. This is used to generate a set of roll offsets to counter the tendency to vibrate.

Corrugated surface on hard calender roll feedback

All paper furnishes have some level of abrasiveness. Fillers such as precipitated calcium carbonate (PCC) and ground calcium carbonate (GCC) greatly add to the abrasiveness, increasing calender roll wear. The wear rate is proportional to the nip load.

If the resonant frequency is at an integer multiple of the roll rotational speed, the wear will occur at the same circumferential location and will eventually wear a corrugation pattern into the calender roll. The wear rate will increase exponentially until it is limited by system nonlinearities. Consistent with other research in self-excited vibration, Parker [8] found that the bar marks on the roll rotate slowly around the circumference of the roll.

Single-nip soft calender thermal barring

Chinn [14] discusses the effect of thermal barring on a soft roll in a press section where vibration causes a circumferential temperature variation, which in turn results in modulus variations around the circumference of the roll. The modulus variation in the cover then acts as the exciter in the nip. Chinn also discusses the anomalous vibration characteristics of polymers that act as nonlinear springs in the nip.

Single-nip soft calender creep barring

Polymers exhibit creep, a time dependent behavior governed by the relaxation time constant [15]. The increased deformation at the circumferential location where the rolls are closest together in the vibration cycle takes time to fully recover due to the time-dependent behavior. Before this recovery is complete, the partially deformed roll enters the nip again, with the remaining nonuniform deformation acting as the excitation force. It is probable that the relaxation time constant and thermal barring act in tandem.

Peripherally drilled rolls

Peripherally drilled rolls, when heated, induce a nonuniform thermal expansion to form a polygon shape, with a difference in roll radii of 2–3 µm [16] when the roll surface temperature reaches 200°C. In most calenders, the effect will be more modest, as they have lower surface temperatures. This is an exciter for forced vibration, and to the author's knowledge has never been associated with barring problems.

STEPS TO RESOLVE BARRING ISSUES

Measurement of barring

Barring is typically detected by high vibration, noise, and sheet quality variations. Quantifying the vibration has mainly been determined by one of two methods. The first is measuring the paper properties. This is best achieved by taking a butt roll of paper and measuring the caliper and gloss variations with an offline profiler such as the Tapio Paper Machine Analyzer [17]. The caliper gauge of an online scanner can also be used in single point if the frequency response is sufficient for the frequencies present. Since caliper reduction and gloss formation occur in tandem, many early papers mention a gloss sensor to measure barring on the machine [10], as it has extremely good frequency response.

Severity	Vibration Velocity, mm/s rms
Very severe	10
Severe	5
Moderate	2
Acceptable	1
Good	0.5

I. Calender roll vibration severity.

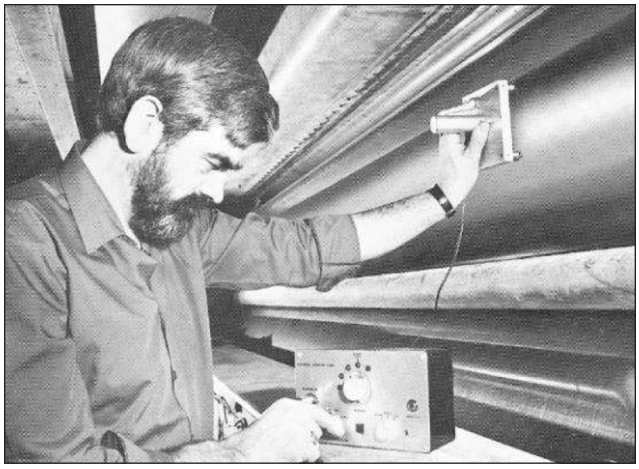

1. Bowater Technical Services (BTS) electronic curvature gauge.

Effect/Roll Condition	Size of Corrugation, peak to peak
Very severe barring	Over 20 µm (0.0008 in.)
Severe barring	Over 10 µm (0.0004 in.)
Moderate barring	Over 5 µm (0.0002 in.)
Seen in paper	2.5 µm (0.0001 in.)
Reground roll target	Less than 1.0 µm (0.00004 in.)
New roll condition	Less than 0.5 µm (0.00002 in.)

II. Hard roll corrugation severity.

The second commonly used method is to measure the vertical vibration of the calender roll bearing housings. **Table I** shows a table for the vibration severity on the calender roll bearings. One of the shortfalls of measuring the vibration on the bearing housings is the assumption that the bearing housing vibration is identical to the roll vibration. Ideally, the roll vibration should be measured directly. Kiviluoma [18] discusses a number of methods for measuring the roll vibration, citing their advantages and failings. He then develops a method to overcome the shortcomings, using an accelerometer mounted on a sliding base.

More recently, video operating deflection shape analysis [19] and motion amplification [20] show promise to resolve this problem as well. With these techniques, one must ensure sufficient resolution to measure micrometer level displacements at the frequencies of interest.

Corrugations on a calender roll were first measured by Parker [21] using a dial indicator mounted on a platform with feet held against the roll. Bowater Technical Services (BTS) refined this technique by replacing the dial indicator with a displacement sensor and a primitive display called the electronic curvature gauge as shown in **Fig. 1**.

Corrugation severity on a roll

BTS [22] gives a range of amplitudes of corrugations in a roll with the corresponding severity, as shown in **Table II**. FPInnovations has more recently confirmed these results in several documented case studies [23].

Distinguishing between barring sources

The best approach to resolving a calender barring issue is to ensure the problem is understood. Understanding the different characteristics of the vibration between the feedback due to the paper caliper variations and a corrugated roll is crucial. **Table III** gives a number of indicators to determine the type of feedback for a multi-nip stack. For a single-nip stack, there is no feedback path through caliper variation.

Step-by-step diagnostic procedure

With this background, the following procedure will aid in determining which feedback path is causing the barring problem:

1. Review what is known about the barring phenomena.
   a. Does it come and go with grade and/or speed changes?
   b. Has it been increasing slowly over time?
   c. Have paper samples been tested on a Tapio or other offline profiler to obtain the magnitude and frequency of barring?

Symptom	Caliper	Barred Roll
Barring frequency at an integer multiple of a roll rotational frequency		Yes
Barring has roll running speed sidebands		Yes
Vibration increases steadily (or exponentially) over the course of days, weeks, or months		Yes
Barring will stop or start instantaneously	Yes	
Barring frequency is not an integer multiple of a roll rotational frequency	Yes	
Measured barring on a calender roll with a barring gauge is greater than 1 µm p-p		Yes

III. Feedback source for multi-nip stack.

d. Have single point caliper or gloss measurements been taken from the online scanner? Take care with the frequency response of online gauges.

2. Take vibration measurements and analyze using Table I and Table III.
   a. *Ideal measuring procedure* — Take vibration measurements on each bearing housing simultaneously with tachometer readings from each roll using a multi-channel vibration data acquisition system along with the paper caliper and/or paper gloss readings.
   b. *Normal measurement procedure* — Take vertical vibration measurements at barring frequencies, using a predictive maintenance vibration data collector to obtain spectra from each calender roll bearing along with the rotational speed of the calender rolls.
   c. Perform these measurements on a scheduled basis.
3. If the problem is paper caliper feedback:
   a. Generate optimum offsets for the grade manufactured most often, at normal operating speed. This requires information about the calender stack and the vibration spectra from the calender roll bearings.
4. If the problem is indicative of calender roll corrugations:
   a. Utilize a barring gauge to determine the barring level on the calender rolls in the existing stack and ensure there is no residual barring on rolls being changed into the stack.
5. Single-nip stack — Vibration is at a harmonic of roll rotational speed (caliper feedback is not present).
   a. Permanently corrugated roll:
      • Vibration is present immediately upon startup.
   b. Creep or thermal feedback:
      • No vibration at startup, but increases during operation, possibly taking an hour to build up.
      • Take infrared temperature measurement of cover.

Caliper feedback

A calender roll is offset when its machine direction position is not directly above the king roll. This changes the paper wrap length from the nip above the roll to the nip below the roll, which in turn affects the number of wavelengths of caliper variation from one nip to the next.

To determine the offsets, first a dynamic model of the calender stack is required. An N-roll calender stack is modeled as an N-degrees of freedom (DOF) system with the paper in the nip acting as both the spring and damping. The model requires the mass, damping, and spring constants of the system. The roll masses are obtained from the engineering drawings or by weighing the rolls. The spring constants are determined from the natural frequencies. Since the vertical vibration is the motion that imparts the caliper variation and barring occurs at the natural frequencies of the calender stack, the natural frequencies are determined from the barring frequencies using the vertical vibration on the calender roll bearing housings, or the gloss or caliper spectra, while the machine is in normal operation. The damping value is assumed.

Any parameter affecting the amount of paper and its density in the nip affects the paper spring constant and thus changes the dynamic model. According to the calendering equation developed by Crotogino [24], the parameters that control the paper bulk (inverse of density) exiting from the nip are the ingoing bulk, furnish, nip load, machine speed, harmonic mean of the roll radii, mid-nip web temperature, and web moisture content. Of these, and assuming a reasonably constant furnish, the most sensitive parameters will be the ingoing bulk (caliper/basis weight) and the nip load. Speed also affects the caliper, but even more importantly, it affects the travel time of the paper from one nip to the next.

Caliper variations induced in an upper nip can act as an exciter in all of the subsequent nips. However, intermediate nips will diminish the magnitude of the caliper variation, and this needs to be accounted for in the model. Each natural frequency that is contributing to the barring problem is included in the model. In practice, the lowest barring frequency for a multi-nip hard calender is normally in the 80–90 Hz vicinity.

Once a dynamic model of the calender stack has been created, it is used to determine the optimum set of offsets. As the roll offsets are changed, the nip-to-nip wrap length also varies. The offsets giving a wrap length of N+3/4 (N is an integer) wavelengths of caliper variations between one nip and the next are ideal. Mathematically, this is determined by finding the global minimum of the regenerative tendency, where the regenerative tendency is the positive work (dot product of force and displacement) done in a nip for all the natural frequencies.

Because conditions change over time, and since the diameter of each calender roll is unique, offset calculations are recommended for every stack change for problem machines.

Corrugated roll

If the feedback path has been determined to be a barring pattern on the rolls, then the rolls must be removed and reground to remove this pattern. The barring amplitude should be measured both before and after the roll grind to ensure that there is no invisible residual barring in the roll. If the roll life is short, then the abrasiveness of the furnish needs to be checked.

The barring pattern on a roll slowly rotates around the roll in one direction if the barring is getting more severe, and in the opposite direction if the barring is reducing in severity. This can be used as an early warning indicator of a change in barring severity with an appropriate online monitoring system installed.

Damping

Another potential resolution for calender barring regardless of the feedback path is to add damping to the system. An industrial damper [25] is available that is used extensively on single-nip soft calenders with low nip load on tissue machines. The Vibrosoft swimming roll [26] has built-in damping designed into the swimming roll portion. Its damping frequency range is 20–80 Hz but is most effective at 40–60 Hz. This limits its usefulness for typical barring problems where the problem frequencies tend to be 80 Hz and higher. Bearing systems with integral damping [27,28] are another means to add damping in principle. These dampers are only likely to work on the king roll and not with the calender rolls on pivoting arms.

CASE STUDIES

This section provides some brief vignettes of barring experienced by different mills. Most are for multi-nip hard calenders, some are for different types of calenders, and a few are from other areas of the paper machine, as they are enlightening.

Offsetting calender rolls

A paper machine with a 5-roll calender stack was experiencing calender barring. The mill decided to trial offsets provided from multiple vendors and found the offsets from different vendors varied and the performance of the offsets were not all equal. This variation is likely due to the large number of factors that must be accounted for in modeling calender barring. Implementing offsets from the preferred vendor has controlled the vibration from the calender stack, with the vibration normally staying within 1 mm/s at barring frequencies.

Newsprint calender stack

A newsprint calender stack was having barring problems to such an extent that nearby offices were uncomfortable due to barring noise. The tone (frequency) of the sound changed with operating conditions. A vibration survey was performed in which the vibration and rotational speed of all the calender rolls were simultaneously measured.

The barring on the rolls was measured with a barring gauge developed by Spectrum Technologies (Puslinch, ON, Canada). While some variations were found, there was not an integer number of corrugations in a revolution, nor did the roll corrugation wavelength coincide with the barring wavelength, confirming that the rolls were not the feedback path for the self-excited vibration.

On the first day of measurements, the 45 g/m² paper showed the dominant vibration was at 127 Hz, with an amplitude of 2.5 mm/s on the bearing housings. Listening to the sound while walking along the calender catwalk, the noise was much louder at the center of the machine than at the drive or tending sides.

The measurements were repeated the next day on 48.8 g/m² paper. This time the main frequency present was 218 Hz with a peak amplitude of 10–15 mm/s on the bearing housings. The sound was much higher at the ends than at the center of the machine.

When operating deflection shapes were taken near the pivot pin assembly, differential movement was detected. This led to the suspicion of excessive looseness at that location, and recommendations were made to resolve the problem.

Offsets were generated for this machine that alleviated the barring problem.

After a number of years, the vibration level on the calender stack started to increase. Measurements taken by the predictive maintenance crews showed the vibration increasing with time over the course of a month. This indicated the rolls were becoming corrugated and needed regrinding.

Online supercalender barring

A mill was having barring problems on an online supercalender. When they learned about offsetting calender rolls in conventional hard-nip calender stacks, they moved the fly rolls to see if changing the nip-to-nip paper length would help. This change resulted in improved runnability [29].

Impact of breaker stack use

A newsprint mill was normally operating with very little barring with a 6-roll calender stack while the breaker stack was in operation. As soon as the breaker stack was lifted, the calender started barring, with calender vibration levels increasing by about two orders of magnitude. When the top calender roll was subsequently lifted, the barring immediately stopped.

This type of barring is regenerative feedback through paper caliper variations, showing paper properties are important in determining barring propensity.

Paper abrasives

A groundwood sulfite mill had a history of barring. At different times, the bar marks could be seen across the face of the roll, at the center only, at the roll ends only, and even at one end but not the other. The bars were usually spaced at 3/8 in. to 3/4 in. apart.

Items that improved stack life were:

- Moving the intermediate swimming roll to the top position and changing the load relief settings, combined with operators adjusting edge relief to control barring.
- Improved calender roll grinding.
- Installation of cleaners to remove groundwood grit.
- Replacement of the entire stack rather than just the barred roll.
- Implementing offsets predicted from a mathematical model; this produced limited results, likely because the feedback path was through calender roll wear rather than paper caliper.

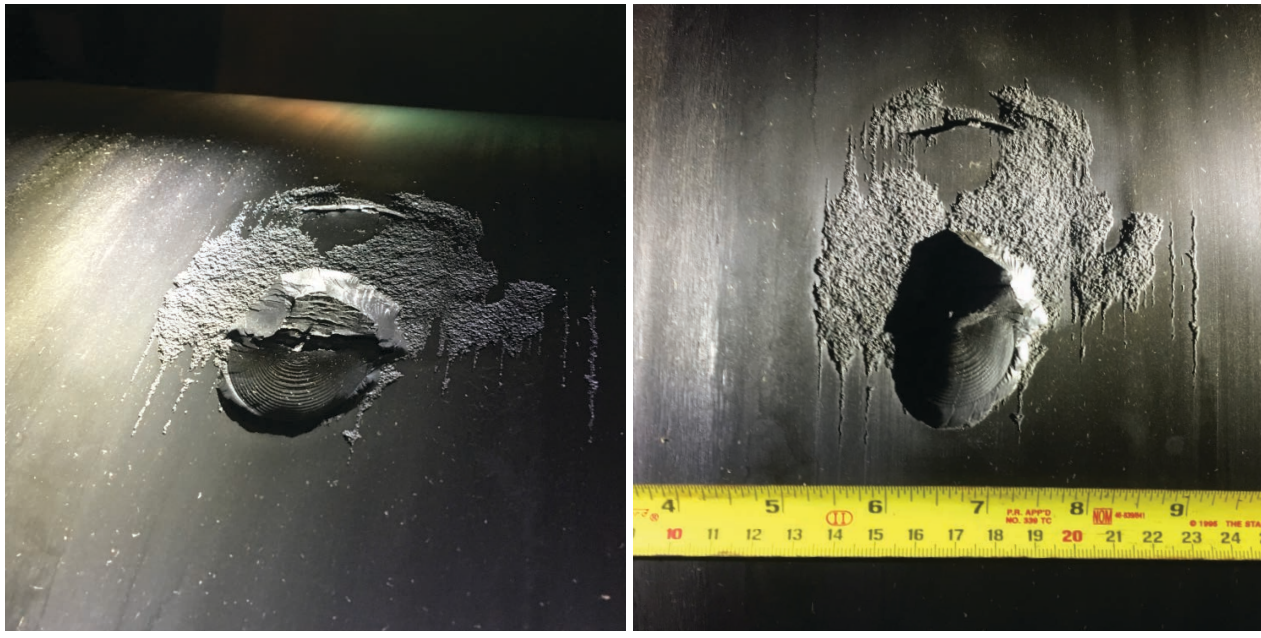

2. Damage to roll cover, including chunks of cover removed due to barring.

- Using an electronic curvature gauge on every shutdown to monitor the condition of the rolls; freshly ground rolls were also checked to ensure no residual barring was present.
- Monitoring the vibration on the roll bearing housings.

At the beginning of this process, stack life was often as little as 3–4 weeks. Once complete, stack life was 4–7 months.

Single nip with covered roll

In a single nip of a covered pressure roll without crown compensation against a dryer can, a trial was performed to find the optimum nip loading. When the nip load went to roughly double the design nip load, the vibration increased drastically at 6x roll rotational speed, resulting in damage to the rubber cover, with some locations having pieces of rubber removed from the cover, as shown in **Fig. 2**. The damaged locations were uniformly spaced around the circumference.

The rubber cover could handle a uniform CD nip load without a problem, but as the nip load increased, the loading became nonuniform, with increased loading near the edge. Once the nip load at the edge reached a critical value, the cover could not recover its original material properties before reentering the nip, resulting in hot spots at the edge of the roll, as measured with an infrared camera. These hot soft spots acted as an exciter the next time they entered the nip, increasing the temperature to the point of failure.

Soft nip calender barring

A soft nip calender stack with low nip loads was prone to barring. The barring frequencies occurred at 5, 6, and 7 times the covered roll rotational frequency, depending upon machine speed and operating conditions. Both vibration and cover temperature were monitored.

When the nip load was increased, the vibration increased first, followed by a cover temperature increase and thermal barring on the cover. The vibration and temperature frequencies were identical, confirming a thermal barring problem — or a combined creep and thermal barring problem.

Additional damping at each end of the roll was used to eliminate the barring.

Dryer gear mesh frequency

Vibration measurements around a calender stack prone to barring found the dryer gear mesh frequency coincided with a barring frequency. The mill removed the closest idler gear and found no improvement.

One of the calender natural frequencies coincided with the dryer gear mesh frequency, and the dryer gear mesh frequency was part of the ambient vibration exciting the resonance. The remaining ambient vibration with the idler gear removed was sufficient to excite the vibration.

After the installation of a new multistage screen to remove grit, and the use of calculated offsets, the barring was greatly reduced.

CONCLUSIONS

This paper reviews the history of calender barring literature, putting barring into a solid theoretical context. When properly understood, self-excited vibration is not as daunting as when it is first encountered. Specific symptoms can

be used to determine which feedback path is present.

If the problem is feedback through caliper variations, offsetting the rolls is an effective way to manage the vibration. New offsets are calculated for each stack change.

Dampers are extensively used on lightly loaded soft calenders used in the tissue industry.

If the problem is feedback through calender roll corrugations, a barring gauge is an excellent method to measure the corrugations on the roll and provide guidance on when the stack should be changed. An online monitoring system is suggested to determine if the corrugation pattern is becoming worse over time.

With these strategies, barring issues are successfully managed. **TJ**

ABOUT THIS PAPER

Cite this article as:
Zwart, J., *TAPPI J.* 21(7): 377(2022).
https://doi.org/10.32964/TJ21.7.377

DOI: https://doi.org/10.32964/TJ21.7.377

ISSN: 0734-1415

Publisher: TAPPI Press

Copyright: ©TAPPI Press 2022

About this journal

LITERATURE CITED

1. Brown, D.L., "Grinding dynamics," Ph.D. thesis, University of Cincinnati, Cincinnati, OH, 1976.
2. Comak, A., "Mechanics, dynamics and stability of turn-milling operations", Ph.D. thesis, University of British Columbia, Vancouver, 2018.
3. Anon., "Delay differential equation," Wikipedia page, Wikimedia Foundation, San Francisco. Available [Online] *https://en.wikipedia.org/wiki/Delay_differential_equation* <14July2022>.
4. Bercel, E., *Tappi* 62(11): 93(197).
5. Wahlstrom, P.B., Larsson, K.O., and Asklof, C.A., "Calender barring, its mechanism and possible elimination," *Pulp Pap. Mag. Can.* 64(4): T205(1963).
6. Pye, I.T., *Pulp Pap. Mag. Can.* 64(4): T194(1963).
7. Howe, B.I. and Cosgrove, J.C., *Pulp Pap. Mag. Can.* 64(6): T259(1963).
8. Davidson, R.W., "A study of calender barring through analog simulation," MASc thesis, University of Maine, Orono, 1966.
9. Parker, J.R. and Epton, J.B.A., *Pulp Pap. Can.* 76(10): T308(1975).
10. Cotgrove, L.B., "Calender barring – causes and cures," *Pulp and Paper Mill Equipment*, February 1988.
11. Browne, T.C., "Viscoelastic properties of paper in a calender nip," Ph.D. dissertation, McGill University, Montreal, August, 1994.
12. Shelley, S., Zwart, J., and Fournier, A., "New insights into calender barring prevention," *Annu. Meet. - Can. Pulp Pap. Assoc., Tech. Sect., 83rd*, CPPA, Montreal, 1997.
13. Melnick, R.M., Zwart, J., Zu, J.W., et al., "Comprehensive modelling of a calender stack for prediction of offsets," *Annu. Meet. - Can. Pulp Pap. Assoc., Tech. Sect., 83rd*, CPPA, Montreal, 1997.
14. Chinn, F., *Pulp Paper Can.* 100(1): 11(1999).
15. Karttunen, A.T and von Hertzen, R., *J. Sound Vib.* 330(16): 3959(2011).
16. Zaoralek, M., "Improved high temperature calender roll," *Prepr. Pap., Annu. Meet. - Can. Pulp Pap. Assoc., Tech. Sect.*, 1991, Preprints B, p. 107.
17. Anon., "Tapio PMA & TS Profiler," Tapio Technologies, Espoo, Finland. Available [Online] *https://tapiotechnologies.com/tapio_pma_ts_profiler/* <14July2022>.
18. Kiviluoma, P., "Method and device for in situ runout measurement of calender thermo rolls," Ph.D. dissertation, Helsinki University of Technology, Helsinki, 2009.

ABOUT THE AUTHOR

I chose to study this topic because it is an ongoing area of concern in paper mills, and a broad overview paper giving insight is important for younger engineers. This paper is a survey of the existing research into calender barring, stressing the reasons for barring and what can be done to eliminate or minimize its effect. It concentrates on giving the mill engineer an intuitive understanding and ways to diagnose the problem.

The most difficult aspect of this study was validating some of the modeling assumptions by taking mill measurements of the vibration. Personally, I discovered that research into calender barring has mostly been accomplished within my lifetime. Also interesting was that the calender barring model to predict offsets works surprisingly well, despite some of the assumptions seemingly being violated.

Mills that experience calender barring (and press barring, though that is not the focus of this paper) can use the results of this paper to understand what is happening and where they can go for help. The next step in this research is to measure the difference between the bearing housing vibration and the roll vibration. Another next step is a proper modal test, or at a minimum an operating modal test, on a calender stack.



Zwart

Zwart is principal at Spectrum Technologies in Puslinch, ON, Canada. Email Zwart at jake.zwart@spectrum-tec.com.

19. Schwarz, B., Richardson, S., Tyler, J., et al., "Post-processing ODS data from a vibration video," *IMAC XXXVIII*, Society for Experimental Mechanics, Bethel, CT, USA, 2020.
20. Hay, J., "Motion amplification: A new way to visualize and measure dynamic systems and structures utilizing video cameras," *IMAC XXXVIII*, Society for Experimental Mechanics, Bethel, CT, USA, 2020.
21. Parker, J.R., *Pap. Technol.* 6(1): T1(1965).
22. Cotgrove, L.B., "The B.T.S. electronic curvature gauge," personal communication, 28 November 1989.
23. Parent, F. and Hamel, J., "Calender residual barring correction during roll grinding," *TAPPI PaperCon*, TAPPI Press, Atlanta, 2010.
24. Crotogino, R.H., Hussain, S.M., and McDonald, J.D., *J. Pulp Pap. Sci.* 9(11): TR128(1983).
25. Anon., "Industrial damper systems," Xcite Systems, Cincinnati. Available [Online] *https://xcitesystems.com/industrialdampersystems-2/* <14July2022>.
26. Cameron, D., Voith Appleton, personal communication, 15 July 2022.
27. Anon., "Voith winder upgrades," Voith, Heidenheim, Germany. Available [Online] *https://voith.com/corp-en/papermaking/winder-upgrades.html* <14July2022>.
28. Anon., "Integral squeeze film damper," Waukesha Bearings, Waukeshaw, WI, USA. Available [Online] *https://www.waukbearing.com/en/products/fluid-film-bearings/integral-squeeze-film-damper.html* <14July2022>.
29. Morgan, B. and Charron, J., "Irving Paper PM1 speed increase," *Annu. Meet. - Pulp Pap. Tech. Assoc. Can., 103rd*, PAPTAC, Montreal, 2017.

A. A. ROBERTSON

Investigation of the Cellulose-Water Relationship by the Pressure Plate Method

The water retention properties of papermaking fibers have been investigated by a "pressure plate" technique which permits a measurement of equilibrium moisture contents of pulp samples at precisely controlled relative vapor pressures between 0.99 and 1.00. This range encompasses the water contents of interest in papermaking from the table to the middle of the drier section. Water retention isotherms are drawn and are satisfactorily related to desorption isotherms which have been reported in the literature. Isotherms for a variety of pulps are reported. These are related to the papermaking properties of the fibers and show the effects of wood species, cooking method, pulp yield, bleaching, drying, and beating on the cellulose-water relationship.

THE swelling and water retention properties of pulp fibers are of basic importance in papermaking. The flow and drainage behavior are affected by the volume of the swollen fibers; the efficacy of the pressing and drying operations depends on the mechanism and extent of water retention; the shrinkage or anisotropic strains in the drying web reflect changes in the fibers due to water removal.

When a fiber suspension is drained to form a mat, a great deal of water is removed by simple drainage. Additional water can be removed by suction, by pressing, or by a combination of the two. However when the concentration of the fibers reaches 30 or 40%, a resistance to further water removal by mechanical means is built up and further drying must be accomplished by heat and evaporation.

Except for a small amount (0.04–0.06 g/g fiber) of molecularly held water, the water which is held by the fibers is believed to be capillary water held in pores or voids in the fibers, held between fibers, or held on the surface of fibers by fibrillae.

It has been our purpose for some time (*1*, *2*) to measure the water retention properties of cellulose fibers in those ranges of moisture content which are important in papermaking. The final objective is to be able to assess the amounts of water held by the various fiber elements—lumina, walls, fibrillated surfaces—and to determine the se-

A. A. ROBERTSON, Physical Chemistry Div., Pulp and Paper Research Institute of Canada, Montreal, Que.

Obtaining water retention ability in the papermaking cycle: *TAPPI Journal* revisits relevant research


The chemistry of aluminum sa in papermaking

The Effect of Component Removal Upon the Porous Structure of the Cell Wall of Wood. II. Swelling in Water and the Fiber Saturation Point

Over the years, *TAPPI Journal* has provided a wealth of information that is helpful to those in both new and established positions in our industry. In many of its regular meetings, *TAPPI Journal*'s Editorial Board has noted the importance of certain "classic" papers that are as important and relevant today as ever, but may only be available through libraries and institutions. To keep these valuable papers in circulation and accessible to the industry, TAPPI is digitizing papers selected as valid and relevant to today's research environment by the Editorial Board.

The above paper by A.A. Robertson is one such research paper. J.Y. Zhu of the *TAPPI Journal* Editorial Board and the USDA Forest Products Laboratory selected this classic paper because the water retention ability in cellulosic fibers under different water vapor pressures is critically important to understand dewatering and drying in papermaking.

"This study described a pressure plate method to measure water retention by cellulose fibers at high vapor pressure conditions that were not possible to measure at the time of this paper's publication in 1965," said Zhu. "By combining existing data, Robertson obtained fiber water retention ability in the entire papermaking cycle, from dewatering and pressing to drying."

You can find more such historical papers in recent issues of *TAPPI Journal*, along with their associated DOI information.

quence in which the water is removed and the effect of its removal on the properties of the fiber and the web. One requirement was for a method which would permit a measurement of the equilibrium water retention of pulp fibers over a range of forces of water removal.

The measurement of moisture retention of cellulose fibers as a function of the relative vapor pressure has been a classical method for investigating the cellulose-water relationship in both the textile and papermaking fields. However, because of experimental difficulties primarily related to temperature control and the time required to reach equilibrium, the equilibrium is difficult to establish at high relative vapor pressures ($p/p_o > 0.95$), and data in this region are uncertain. Since papermaking operations of great interest occur at moisture contents corresponding to higher relative vapor pressures than this, it is desirable to increase the reliability of the method in this region.

This paper describes one approach to this problem. It is based on the measurement of the water retention of a pad of moist fibers when the water is under a measurable hydrostatic tension.

METHOD

The hydrostatic tension technique has had a long history and has had varied applications. It was applied to the measurement of the water retention properties of soils by Richards in 1928 (*3*) to textile fibers by Preston in 1952 (*4*) and by Barkas to pulp fibers in 1953 (*5*).

In the simplest form of the method, a wet sample of the material to be tested is brought into contact with a wet, porous plate, usually ceramic or of sintered glass, and a hydrostatic tension is applied through a column of water to the reverse side of the plate. The water retention at specified tensions can then be determined (*1*). One of the limitations of the apparatus is the maximum tension which can be applied without air being drawn through the plate. Even if the plate has very fine pores, the pressure differential attainable by suction below the plate is normally only one atmosphere.

However, the method can be considerably extended by using extremely fine-pore plates or membranes and increasing the differential across the plate by applying pressure on the top.

APPARATUS

The apparatus used in this study is commercially available[1], and was developed primarily by and for soil investigators. It is shown schematically in Fig. 1.

In the pressure vessel a ceramic plate (*B*) is mounted. A metal gauze (*C*) and a rubber diaphragm (*D*) are sealed to the plate. An opening from the sealed side of the plate to the atmosphere is provided by tubing (*E*) which passes through the wall of the pressure vessel.

The porous ceramic plate is saturated with water and one or more saturated pads of fibers (*G*) are placed on the upper surface with good contact made between the pad and the plate. The pressure vessel is closed, and nitrogen from a gas bottle (*H*) is admitted to the required pressure. Water is progressively expelled from the pad through the plate, the gap formed by the gauze, and the tube. The time required to attain equilibrium is determined by trial and depends on the thickness of the pad, the nature of the fiber (which determines the mobility of the water), and the distance the water must migrate. It is of the order of days.

After it is considered that equilibrium has been reached, the pressure is released, the vessel is opened, and the samples are weighed wet and dry. The procedure is repeated at other pressures until a curve of water retention versus pressure is obtained (Fig. 2). The upper pressure with the present apparatus is 15 atm. and is limited by the porosity of the ceramic plate.

The amounts of water measured correspond, on the basis of past experience (*1*, *2*), to almost fully swollen fibers down to moisture contents lower than those at which interfiber bonding occurs.

DISCUSSION

At equilibrium the hydrostatic tension in the plate-sample system is everywhere the same. This tension is theoretically related to the curvature of the water surface, or meniscus, and the relative vapor pressure above the curved surface, and these consequently are also everywhere the same.

Table I. Calculations Based on the Kelvin Equation (Temperature, 25°C)

Relative vapor pressure	*1 − RVP*	*P, dynes/sq cm*	*r, cm*
0.999990	10^{-5}	1.36×10^{4}	1.06×10^{-2}
0.99990	10^{-4}	1.36×10^{5}	1.06×10^{-3}
0.9990	10^{-3}	1.37×10^{6}	1.05×10^{-4}
0.990	10^{-2}	1.38×10^{7}	1.04×10^{-5}
0.98	2×10^{-2}	2.77×10^{7}	5.19×10^{-6}
0.95	5×10^{-2}	7.04×10^{7}	2.04×10^{-6}
0.90	10^{-1}	1.45×10^{8}	1.00×10^{-6}
0.80	0.20	3.06×10^{8}	4.70×10^{-7}
0.70	0.30	4.90×10^{8}	2.94×10^{-7}
0.60	0.40	7.01×10^{8}	2.05×10^{-7}
0.50	0.50	9.51×10^{8}	1.51×10^{-7}

1 psi = 6.89×10^{4} dynes/sq cm
1 atm = 1.013×10^{6} dynes/sq cm
1 bar = 1.00×10^{6} dynes/sq cm
1 cm Hg = 1.333×10^{4} dynes/sq cm

The relationship of these quantities is given by the Kelvin equation:

$$\ln p/p_o = \frac{-2\gamma M}{rdRT}$$

where

p/p_o = relative vapor pressure
γ = surface tension of water
M = molecular weight of water
r = radius of curvature of the water surface
d = density of water
R = gas constant
T = absolute temperature

and an equation relating the hydrostatic tension P with the surface tension and the radius of curvature r.

$$P = \frac{-2\gamma}{r}$$

With these two equations it is possible to make the calculations required to compile Table I.

With the pressure plate apparatus it is possible to exert maximum tensions of 1.5×10^{7} dynes/sq cm corresponding to a relative vapor pressure of something less than 0.990 and a radius of curvature of about 0.1 μ.

It is necessary to note that the menisci existing in a porous medium are not spherical and the radius of curvature is not to be identified with the radius of circular capillaries. The radius of curvature, r, required by the equation when applied to porous media is the harmonic mean of the two principal radii of curvature which exist at any point on the interface. At equilibrium the value of the equivalent radius r is the same everywhere in the system, although its component curvatures vary.

The mechanism by which equilibrium is reached cannot yet be discussed quantitatively. At low tensions and high moisture contents, equilibrium will be attained primarily by capillary conductivity, that is, by flow of liquid water from the pad to the plate or from regions of low meniscus curvature to high. However as moisture contents decrease, the capillary movement becomes very slow, and it is assumed

[1] Soil Moisture Equipment Co., Santa Barbara Calif.

 CITE THIS PAPER: Robertson, A.A., *Tappi* 48(10): 568(1965). https://doi.org/10.32964/TJ48.10.568

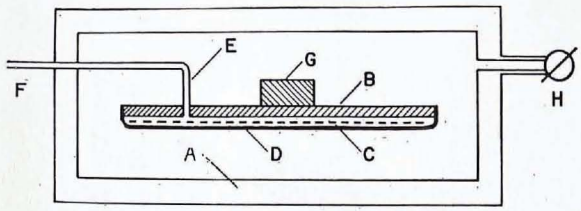

A—pressure vessel
B—ceramic plate
C—metal gauge
D—rubber diaphragm
E—tubing
F—opening in vessel
G—fiber pad
H—gas bottle

Fig. 1. Schematic diagram of the pressure plate apparatus

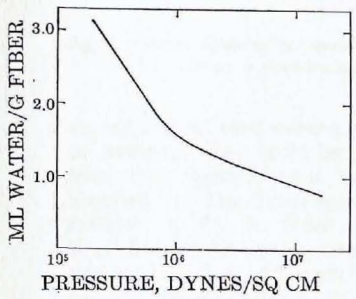

Fig. 2. Typical water retention curve plotted as a function of pressure: undried unbeaten spruce sulfite pulp

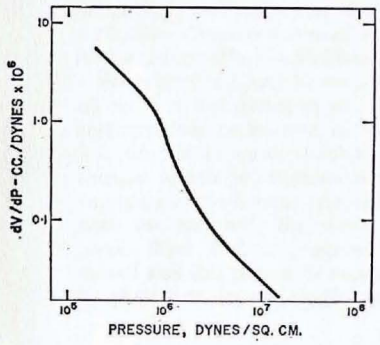

Fig. 3. Differential plot of Fig. 2—logarithmic

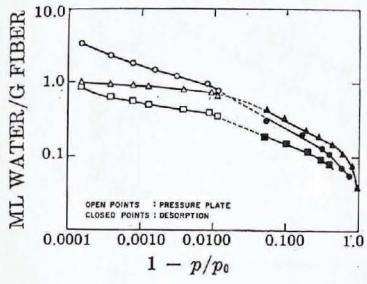

Fig. 4. Comparison of pressure plate data with desorption isotherms from the literature (8–10): O = sulfite pulp, unbleached, beaten; △ = viscose rayon; □ = cotton linters

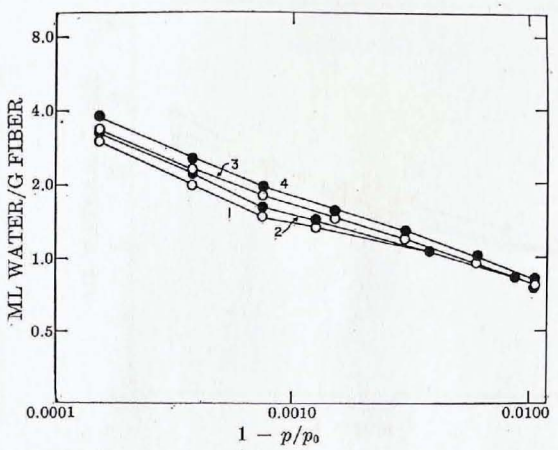

Fig. 5. Water retention isotherms: 1—unbeaten kraft; 2—unbeaten sulfite; 3—beaten kraft; 4—beaten sulfite

that evaporation-condensation processes contribute increasingly to the attainment of equilibrium (*1*, *2*).

The release of pressure at the end of the run is an occasion for the introduction of an uncertain error. The water vapor is vented with the nitrogen and a relatively dry atmosphere exists. The samples have an opportunity to dry out somewhat before they can be removed to weighing bottles.

The range of pressures employed is dictated by both experimental and theoretical considerations. At pressures or suctions below 2×10^5 dynes/sq cm, the water retained by the pad includes amounts of interfiber capillary water which may vary with the formation, structure, and mechanical properties of the pad. The measurement therefore is less clearly related to the amount of water associated with individual fibers. Barkas (*6*) has, in fact, used the porous plate technique in this low tension region to investigate the bulk moduli of the fiber structure and to attempt the determination of the elastic properties of the pad. The upper pressure limit of about 1.5×10^7 dynes/sq cm is limited by the porosity of the plate, the construction of the apparatus, and the slowness with which equilibrium is attained. Extension of the method to higher pressures by using porous membranes rather than ceramic plates is being considered.

The decrease in water held by the fiber pad as the hydrostatic tension is increased may be related to two processes. One is a collapse of the fiber structure. This general collapse includes the collapse of the fiber on its lumen, the drawing-down of external fibrillae onto the fiber surface, the collapse of the porous fibrillar wall to a denser structure (*7*), and the flattening or pulling together of fibers at interfiber crossings. The second mechanism permitting water loss is the emptying of noncollapsing pores and capillary spaces. As the tension is increased menisci retreat into pores or re-entrants and water is removed until the equilibrium curvature is established.

Because of the collapse of the pad and fiber structure as the tension is increased and because of the complicated geometry of a porous medium, any attempt to calculate pore sizes, pore size distributions, or surface areas of pores from the change of water retention with tension is invalid. However, it is frequently observed that the water retention isotherm for pulp fibers shows a rapidly changing slope in the neighborhood of pressures of $0.6–1.5 \times 10^6$ dynes/sq cm (Fig. 3). This pressure corresponds to a relative vapor pressure near 0.9990 and an equivalent radius of curvature of 1.0–2.4 μ. This last figure suggests that the rapidly decreasing negative slope of the curve is related to the end of changes at the fiber level, e.g., emptying or collapse of the lumen, and the transfer of phenomena to capillary spaces of smaller dimensions.

The range of relative vapor pressures covered by the present technique complements the range covered by conventional methods for obtaining desorption isotherms. It should therefore be possible to consolidate the data from both into a single curve. Such an attempt is made in Fig. 4 for a beaten unbleached sulfite pulp, for viscose rayon and for cotton linters. The desorption data are for similar fibers and are taken from Campbell (*8*), Staples (*9*), and Stamm and Woodruff (*10*), respectively.

The correspondence is reasonably good and the continuous curve obtained suggests that any fiber saturation point must depend on some rather arbitrary definition. Plotting water content versus ln $(1 - p/p_o)$ tends to remove the temptation to extrapolate to a relative vapor pressure of 1.0 for a fiber saturation value.

In earlier studies of the cellulose-water relationship, the hypothesis was ad-

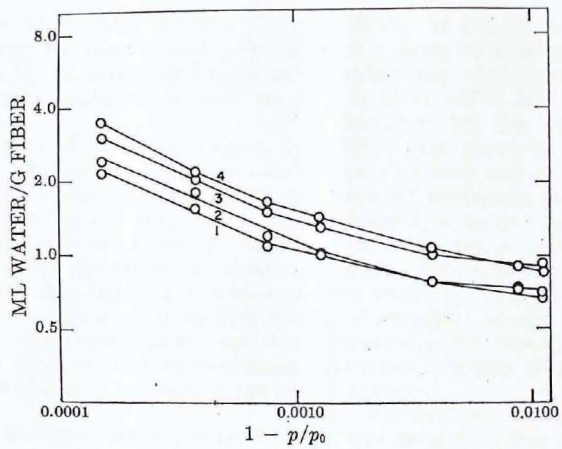

Fig. 6. Water retention isotherms: 1—air-dried kraft; 2—air-dried sulfite; 3—undried kraft; 4—undried sulfite

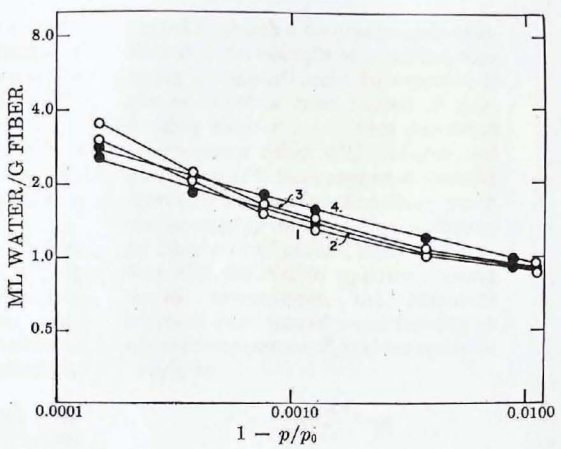

Fig. 7. Water retention isotherms: 1—unbleached kraft; 2—bleached kraft; 3—unbleached sulfite; 4—bleached sulfite

vanced that the total water immobilized by immersed fibers could be calculated from their hydrodynamic volume as obtained by the liquid permeability method (*1*, *2*). In those studies a single hydrostatic tension measurement was made at 2×10^5 dynes/sq cm (3 psi) to obtain further information. The difference between the associated water measured by the two methods was considered to indicate the collapsibility of the fiber structure under surface tension forces in an air-intruded pad. The difference was greater if the pulps were never-dried, beaten, thin-walled, well delignified, and otherwise deformable, while the difference was small or absent for nondeformable, nonfibrillated fibers.

By extension it may be supposed that up to 7×10^5 dynes/sq cm (10 psi), corresponding to radii of curvature of 2 μ, the loss of water is related to the collapse of external fibrillation and the emptying of the lumen. As higher tensions are imposed, the water in the porous fiber wall is progressively removed and this process is accompanied by partial or complete collapse of the porous structure. This mechanism obtains through the range of the present technique and into the range of tensions which are more conveniently obtained by desorption methods.

APPLICATION

The water retention properties of pulp fibers differ depending upon the origin and treatment of the pulp. Several pulps subjected to different treatments have been investigated by this method and the corresponding isotherms are given in Figs. 5–11. The limited number of samples suggests that the results shown here should not be generalized without caution. The isotherms are plotted logarithmically with $(1 - p/p_o)$ as the independent variable.

Figure 5 depicts the isotherms for unbeaten and beaten kraft and sulfite pulps, never-dried, from the same wood (black spruce). The sulfite appears to hold more water than the kraft both before beating (curves *1* and *2*) and after beating to 400 CSF (curves *3* and *4*). The differences become less marked as the tension is increased, and at the lowest relative vapor pressure attainable the differences between beaten and unbeaten fibers is slight, thus confirming the findings of Campbell (*3*) and others based on desorption isotherms.

The water retention differences between beaten and unbeaten pulps are most discernable near $(1 - p/p_o) = 0.0008$, corresponding to radii of curvature of 2 μ. The curves for unbeaten pulp (curves *1* and *2*) show some appreciable curvature, while the curves for beaten pulp (*3* and *4*) show a more linear behavior. This difference could be interpreted as indicating a smoother transition of the retention phenomena from fiber to fibrillar dimensions.

Figure 6 shows the effect of drying on unbeaten, unbleached kraft and sulfite pulps. Curves *1* and *2* are the isotherms for once-dried krafts and sulfite pulps, respectively. The corresponding isotherms for the undried pulps are shown as *3* and *4*. The pulps are similar but not identical to those in Fig. 5. The drying was at room tem-

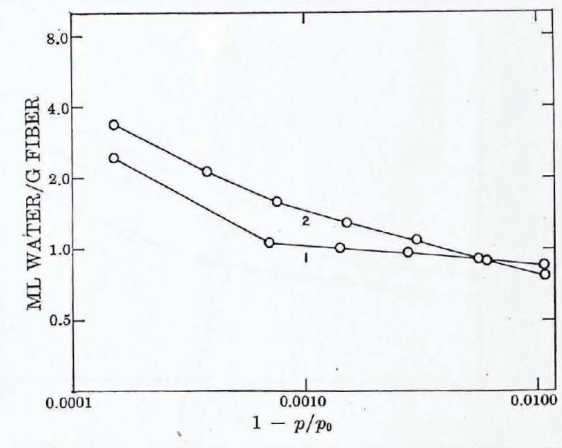

Fig. 8. Water retention isotherms: 1—high-yield kraft; 2—high-yield sulfite

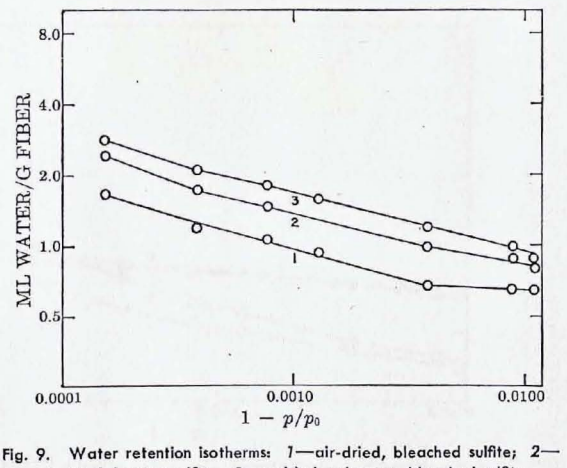

Fig. 9. Water retention isotherms: 1—air-dried, bleached sulfite; 2—air-dried, beaten sulfite; 3—undried, unbeaten, bleached sulfite

 CITE THIS PAPER: Robertson, A.A., *Tappi* 48(10): 568(1965). https://doi.org/10.32964/TJ48.10.568

perature over $CaCl_2$ (~30% RH). The water retention of both pulps is reduced by air drying, and again the sulfite pulp continues to hold more moisture.

The effect of bleaching is shown in Fig. 7. The isotherms for unbleached kraft and sulfite pulp are shown as curves *1* and *3*, and the corresponding bleached pulps are *2* and *4*. Sulfite maintains its greater water retention properties after bleaching as compared with kraft. The shape of the isotherms has changed—straightened out—but whether this is attributable to a change in deformability or geometry is not yet known.

The difference between samples of high-yield kraft and sulfite pulp is shown in Fig. 8. Both pulps have been beaten for the same time. The 73% yield sulfite (curve *2*) holds more water and is continuously deformable over the whole range of pressures. In fact, its behavior is not greatly different from a low yield pulp. The 70% yield kraft which is a stiff, nonfibrillating, noncollapsing fiber (curve *1*) loses water at low tensions—presumably from the noncollapsing lumen—and then loses very little more over the remainder of the range.

The effect of beating dried pulp on its water retention is shown in Fig. 9. An air-dried bleached sulfite pulp has an isotherm represented by curve *1*. A mild beating (1000 revolutions in the PFI mill) increases the water retention through the whole range (curve *2*), and the water retention properties of the pulp approach that of the never-dried pulp (curve *3*). The behavior here is to be contrasted with that in Fig. 5, in which the effect of beating a never-dried pulp was relatively minor. The isotherms here are well separated, although they appear to be converging at the highest tensions.

A drying process which is more drastic than air drying produces additional effects. In Fig. 10 an isotherm (curve *1*) is shown for an unbleached unbeaten sulfite pulp which has been treated for 16 hr at 105°C and 95% RH. The isotherms for the corresponding air-dried pulp (curve *2*) and never-dried pulp (curve *3*) may be compared. The marked decrease in water retention is believed to be due to a relaxation of swelling or recovery stresses in the fiber during heat treatment (*11*). A pulp so treated shows decreased swelling on reimmersion which becomes more marked as the time or temperature or relative humidity of the treatment is greater.

The isotherms for other tested cellulosic fibers differ from those for papermaking fibers in that the retention is considerably lower over most of the range. Figure 11 shows the isotherms for cotton linters (curve *1*), acetate grade dissolving pulp (curve *2*), viscose (curve *3*), and linters swollen in 17.5% alkali (curve *4*). The curves for viscose and alkali-treated linters are flat, presumably indicating a relatively compact, incompressible structure without pores or voids in the size range corresponding to the range of applied tensions. The curves for untreated linters and dissolving pulp (curves *1* and *2*) have a shape similar to those for papermaking fibers, although at a much lower level; this can be interpreted as indicating a lumen and fibrillar wall structure that viscose, for example, lacks.

SIGNIFICANCE

The technique described in this paper is related to some extent to earlier methods for assessing cellulose-water relationships. The congruity of pressure plate measurements and desorption isotherms has been shown in Fig. 4. The agreement is considered reasonably good in view of the differences in samples.

Agreement with other methods depends on how closely the systems concerned approach a thermodynamic equilibrium. An example of a method with which agreement could be expected is the calorimetric measurement of nonfreezing water in a wet fiber sample at temperatures below 0°C. Magne and co-workers (*12*) have suggested that the lowered freezing point of capillary water can be roughly estimated by combining an integrated Clausius Clapeyron equation with the Kelvin equation. Using several assumptions, the minimum radius of curvature of water freezing at a given temperature, T, is given approximately by

$$r = \frac{2\gamma M T_0}{d\Delta H(T_0 - T)}$$

where

ΔH = molar heat of fusion
T_o = normal freezing point, °K.

Using this equation, r was calculated for the temperatures at which nonfreezing water was measured (*13*). The relative vapor pressure or capillary tension can be calculated for the same values of r but at 25°C. Thus, nonfreezing water at −4.5°C corresponds approximately to water held under a tension of about 5×10^7 dynes/sq cm or at $(1 - p/p_o) = 0.036$.

This value, corresponding to about 50 atm, is beyond the tensions presently available in the apparatus, but the extrapolation of pressure plate data as in Fig. 4 produces consistent results (Table II).

The results suggest the possibility that the measurement of nonfreezing water or nonfreezing benzene by precision calorimetry might be used to measure pore size distributions of cellulose fibers within an appropriate range.

The water retention isotherms obtained in this work are determined by molecularly bound water, capillary-condensed water, occluded water, water held by fibrillation, and interfiber water. So far it does not appear to be possible

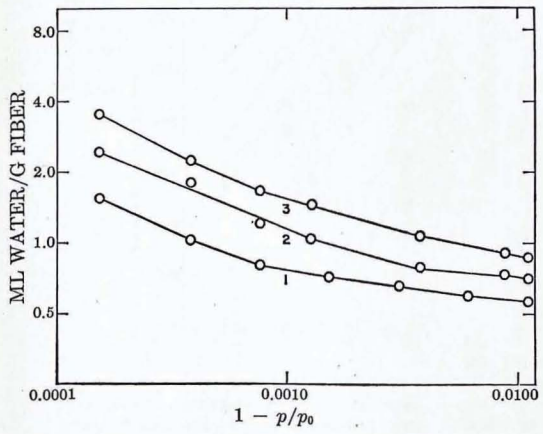

Fig. 10. Water retention isotherms: *1*—air-dried pulp, heat treated at 105°C, 95% RH for 16 hr; *2*—air-dried sulfite; *3*—never-dried sulfite

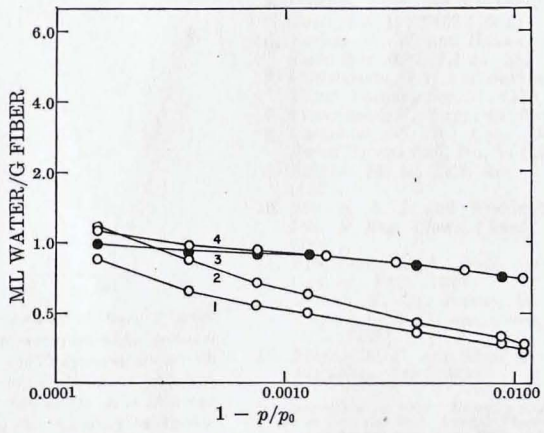

Fig. 11. Water retention isotherms: (1) cotton linters; (2) acetate grade dissolving pulp; (3) viscose rayon; (4) alkali-treated linters

to distinguish clearly the amounts of each by an equilibrium method. However, the mobilities of water held in the different ways are presumably different and dynamic nonequilibrium methods may be devised to estimate the quantity of each. One such test which appears to be useful for research purposes is the dye migration test (*1*, *2*), particularly when coupled with a hydrostatic tension test or other equilibrium measurement.

The relation of the water retention isotherm to the papermaking properties of pulps is not yet clear, but some qualitative observations may be made. In Fig. 12 the physical properties of handsheets prepared from 16 pulps are compared. Four pulps were treated in four specific ways:

I. Untreated
II. Lightly beaten (1000 revs. in PFI mill)
III. Sample I air-dried
IV. Sample III lightly beaten

The four pulps were unbleached kraft (*A*), bleached kraft (*B*), unbleached sulfite (*C*), and bleached sulfite (*D*).

The corresponding water retention values at $(1 - p/p_o) = 7.6 \times 10^{-4}$ (1.03×10^6 dynes/sq cm) are given in Fig. 13. A similarity is apparent, but no quantitative correlation is possible. The beating of never-dried pulp increases the strength properties. A similar increase in water retention is shown at this tension level. The air drying of the pulps reduces the strength properties and water retention, and partial recovery is obtained by light beating. However, the recovery of strength properties is more complete than is the recovery of water retention. Both the strength properties and water retention suggest that unbleached pulps (*A* and *C*) are less responsive to drying and beating than are the bleached pulps (*B* and *D*).

Thus, although strength properties cannot be quantitatively related to water retention properties when a variety of pulps are compared, it is clear that mechanical treatments (beating, drying) affect strength and water retention in the same direction. When chemically different (kraft, sulfite, bleached, unbleached) pulps are compared, unbeaten and undried, no correlation of strength and water retention is yet clear.

Table II. Comparison of Capillary Water Measured as Nonfreezing Water at −4.5°C and as Water Retained at $p/p_o = 0.964$ (Extrapolated)

	As nonfreezing water, ml/g [Magne and Skau (13)]	*As water retained, ml/g (Fig. 4)*
Viscose	0.39, 0.41	0.45
Alkali-swollen linters	0.41, 0.45	(0.45)
Cotton	0.19, 0.22, 0.21	0.23

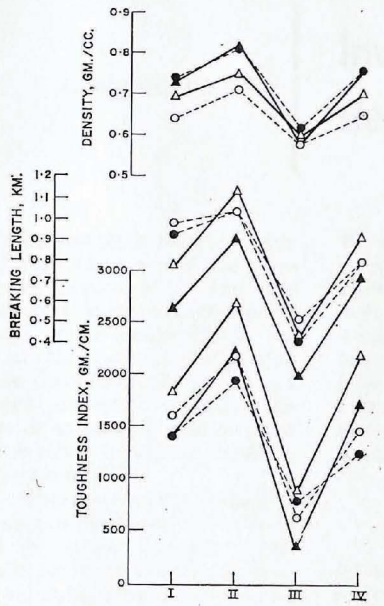

Fig. 12. Physical properties of handsheets from 4 pulps—○ unbleached kraft; △ bleached kraft; ● unbleached sulfite; ▲ bleached sulfite—each having the following treatments: I—untreated; II—light beating; III—air-dried; IV—air-dried, light beating

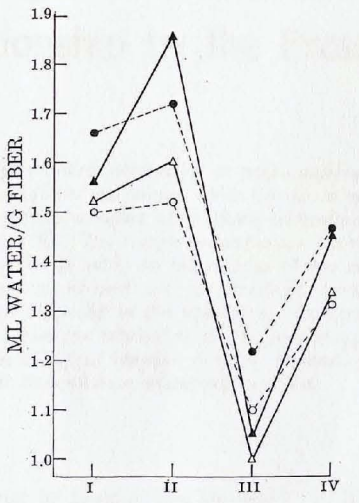

Fig. 13. Water retention of the 16 pulps (Fig. 12) measured at a relative vapor pressure of 0.99924 (1.03×10^6 dynes/sq cm or 15 psi). ○ = unbleached kraft; △ = bleached kraft; ● = unbleached sulfite; ▲ = bleached sulfite—each having the following treatments: I—untreated; II—light beating; III—air-dried; IV—air-dried, light beating.

SUMMARY AND CONCLUSIONS

The pressure plate technique appears to give reliable and significant data concerning the cellulose-water or fiber-water relationship over the range of water contents which is of interest in papermaking, that is, from the saturated condition down to water contents which are typical of the middle of the drier section. Throughout this region, water is held by capillary forces, and the differences between isotherms for different pulps are dependent on differences in the morphology, fibrillation, porosity, and collapsibility of the fibers, with possible contributions by noncellulosic hydrophilic materials which may be present.

The technique measures the equilibrium or minimum retention at a specified force of water removal. The measurements therefore may not be directly relevant to the processes of papermaking since these processes characteristically involve nonequilibrium phenomena which occur in response to transient forces associated with rapidly varying conditions inherent in table roll or foil drainage, suction boxes, suction couch compartments, press nips, and alternating hot surface and free evaporating drying. For quantitative prediction of behavior under such dynamic conditions, practical tests which more closely simulate the process must presumably be devised.

The determination of the cellulose-water relationship for relative vapor pressures between 0.99 and 1.00 complements earlier studies of desorption isotherms obtained by evaporation into controlled environments. The comparison of isotherms obtained from different pulps permits some conclusions to be drawn concerning the effects of wood species, cooking method, pulp yield, bleaching, drying, and beating.

LITERATURE CITED

1. Robertson, A. A., *Tappi* **42**: 969 (1959).
2. Robertson, A. A., *Svensk Papperstid.* **66**: 477 (1963).
3. Richards, L. A., *J. Agr. Res.* **37**: 719 (1928).
4. Preston, J. M. and Nimkar, M. V., *J. Text. Inst.* **43**: T402 (1952).
5. Barkas, W. W. and Hallan, R., *Proc. Tech. Sect. BPBMA* **34**: 289 (1953).
6. Christensen, G. N. and Barkas, W. W., *Trans. Faraday Soc.* **51**: 130 (1955).
7. Moorehead, F., *Tappi* **46**: 524 (1963).
8. Campbell, W. B., *Can. Dept. Int. Forest Service Bull.* No. 84 (1933).
9. Staples, M. L., *Text. Res. J.* **28**: 950 (1958).
10. Stamm, A. J. and Woodruff, S. A., *Ind. & Eng. Chem. (Anal.)* **13**: 836 (1941).
11. Robertson, A. A., *Pulp Paper Mag. Can.* **65**: T161 (1964).
12. Magne, F. C., Portas, H. J., and Wakeham, H., *J. Am. Chem. Soc.* **69**: 1896 (1947).
13. Magne, F. C. and Skau, E. L., *Text Res. J.* **22**: 748 (1962).

Received Oct. 29, 1964. Revised May 12, 1965. Presented at the 50th Annual Meeting of the Technical Association of the Pulp and Paper Industry, held in New York, N. Y., Feb. 21–25, 1965.

 CITE THIS PAPER: Robertson, A.A., *Tappi* 48(10): 568(1965). https://doi.org/10.32964/TJ48.10.568

TAPPI JOURNAL
WWW.TAPPI.ORG
THE PAPER AND PACKAGING INDUSTRIES' TECHNICAL RESOURCE
AUGUST 2022 | VOL. 21 NO.8

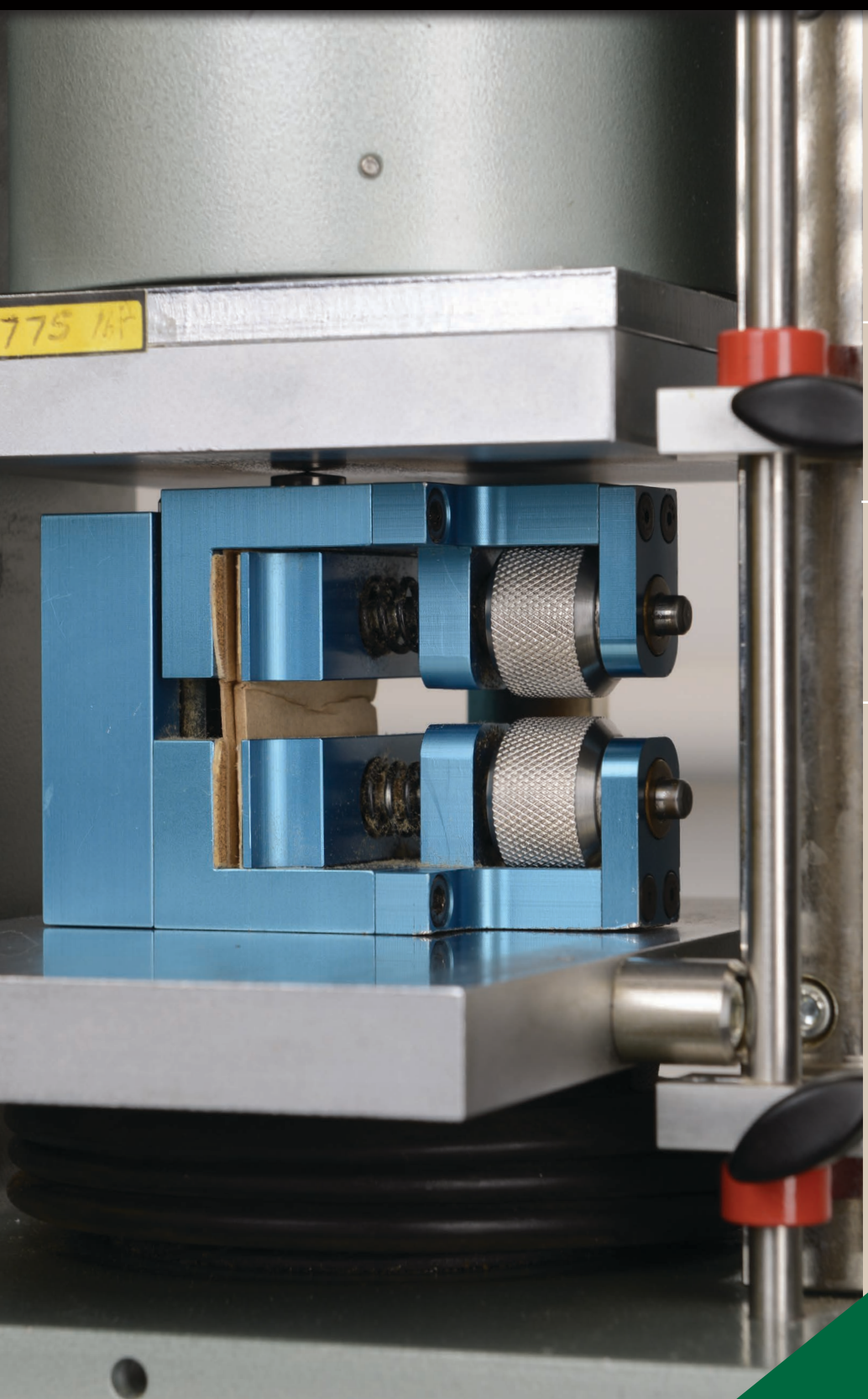

RECOVERY CYCLE **405**
A feasibility study of using the organic Rankine cycle for power generation from the flue gases of recovery boilers
Seyed Javad Amirfakhri

CORRUGATED BOXES **418**
Edge crush testing methods and box compression modeling
Benjamin Frank and Douglas Cash

RECOVERY CYCLE **435**
Causes of poor dregs settling in a green liquor clarifier
Torsten Meyer, Heather Munn, and Honghi Tran

CELLULOSE **445**
The creep properties of paper
J.P. Brezinski

TAPPI Journal NOW FULLY OPEN ACCESS

August 2022

TABLE OF CONTENTS VOL. 21 NO. 8

401 EDITORIAL
Impacts from using recycled pizza boxes in furnish: *TAPPI Journal*'s runner-up to 2021 Best Research Paper
Monica Shaw

405 RECOVERY CYCLE
A feasibility study of using the organic Rankine cycle for power generation from the flue gases of recovery boilers
Seyed Javad Amirfakhri

418 CORRUGATED BOXES
Edge crush testing methods and box compression modeling
Benjamin Frank and Douglas Cash

435 RECOVERY CYCLE
Causes of poor dregs settling in a green liquor clarifier
Torsten Meyer, Heather Munn, and Honghi Tran

445 CELLULOSE
The creep properties of paper
J.P. Brezinski

»**COVER CREDIT**: Researchers Benjamin Frank and Douglas Cash explore the importance of identifying and developing optimal test methods to measure compressive strength of corrugated materials (p. 418). Cover photo of a clamped edge crush test specimen courtesy of Packaging Corporation of America (PCA). This photo was used for the 75th Anniversary Edition of the *Fibre Box Handbook* from the Fibre Box Association.

TAPPI JOURNAL
WWW.TAPPI.ORG

Editor-in-Chief
Douglas W. Coffin coffindw@miamioh.edu
+1 513 529-0771

Associate Editor
Peter W. Hart peter.hart@westrock.com
+1 409 276-3465

Editorial Director
Monica Shaw mshaw@tappi.org
+1 770 367-9534

PRESS Manager
Jana Jensen jjensen@tappi.org
+1 770 209-7242

***TJ* EDITORIAL BOARD**

Brian N. Brogdon, FutureBridge Consulting & Training LLC
brian.brogdon@gmail.com, +1 678 581-9114

Ravi Challa, Suominen Corporation
Ravi.Challa@suominencorp.com, +1 843 680 2586

Douglas W. Coffin, Miami University
coffindw@miamioh.edu, +1 513 529-0771

Mahendra Doshi, Doshi and Associates
mahen@aol.com, +1 920 832-9101

Marc Foulger, Valmet
marc.foulger@valmet.com +1 315 767-2920

Peter W. Hart, WestRock
peter.hart@westrock.com, +1 409 276-3465

Carl J. Houtman, USDA Forest Products Laboratory
choutman@fs.fed.us, + 1 608 231-9445

Vamsi Jasti, Ahlstrom-Munksjo Nonwovens LLC
jvamsik1@gmail.com, +1 818 585-3524

Lucian Lucia, North Carolina State University
lucian.lucia@gmail.com, +1 919 889-7059

John A. Neun, John A. Neun LLC
john.neun@gmail.com, +1 518 275-8139

Jim Niemiec, Jim Niemiec Consulting LLC
jim.niemiec@outlook.com, +1 715 213-4766

Steven P. Ottone, Omya
steven.ottone@omya.com, +1 919 641-7854

Gaurav Pranami, Imbed Biosciences
gpranami@imbedbio.com, +1 515 230-7005

Arthur Ragauskas, Oak Ridge National Laboratory
aragausk@utk.edu

Seshadri Ramkumar, Texas Tech University
S.Ramkumar@ttu.edu, +1 806 742-4567

Gregg Reed, Imerys
gregg.reed@imerys.com, +1 478 553-5747

Gerard J.F. Ring, University of Wisconsin—Stevens Point
gerryring@wi-net.com, +1 715 592-3732

Scott Rosencrance, Kemira Chemicals
scott.rosencrance@kemira.com, +1 770 429-2753

Paul Wiegand, NCASI
pwiegand@ncasi.org, +1 919 941-6417

Junyong Zhu, USDA Forest Products Laboratory
jzhu@fs.fed.us, +1 608 231-9520

Join TAPPI *today!*
TAPPI JOURNAL is a free benefit of TAPPI membership, and is only available to members. To join TAPPI, to renew your TAPPI Membership, or to learn about other valuable benefits, visit www.tappi.org.

TAPPI, 15 Technology Parkway S., Suite 115, Peachtree Corners, GA 30092, publishes *TAPPI JOURNAL* monthly.

ATTENTION PROSPECTIVE AUTHORS: All papers published are subject to *TAPPI JOURNAL's* peer-review process. Not all papers accepted for review will be published. Before submitting, check complete author guidelines at http://www.tappi.org/s_tappi/doc.asp?CID=100&DID=552877.

Statements of fact and opinions expressed are those of individual authors. TAPPI assumes no responsibility for such statements and opinions. TAPPI does not intend such statements and opinions or construe them as a solicitation of or suggestion for any agreed-upon course of conduct or concerted action of any sort.

Copyright 2022 by TAPPI, all rights reserved. For copyright permission to photocopy pages from this publication for internal or personal use, contact Copyright Clearance Center, Inc. (CCC) via their website: www.copyright.com. If you have questions about the copyright permission request process, please contact CCC by phone at +1 978 750-8400. To obtain copyright permission to use excerpts from this publication in another published work, send your specific request in writing to Editor, TAPPI JOURNAL, 15 Technology Parkway S., Suite 115, Peachtree Corners, GA 30092, USA; or by fax to +1 770 446-6947. Send address changes to TAPPI, 15 Technology Parkway S., Suite 115, Peachtree Corners, GA 30092, USA; Telephone +1 770 446-1400, or FAX +1 770 446-6947. www.tappi.org

Editorial



MONICA SHAW | EDITORIAL DIRECTOR
mshaw@tappi.org

Impacts from using recycled pizza boxes in furnish: *TAPPI Journal*'s runner-up to 2021 Best Research Paper



Ashok Ghosh

The runner-up to the 2021 *TAPPI Journal* Best Research Paper was "Incorporation of post-consumer pizza boxes in the recovered fiber stream: Impact of grease on finished product quality." From Ashok Ghosh, Peter Hart, Adele Panek, Tran Nguyen, and Meredith Dooley of WestRock, the goal of this paper was to demonstrate how used pizza boxes can contribute to a circular economy where the industry recycles the products it makes as part of the overall manufacturing process. The paper was assessed as runner-up by the *TAPPI Journal* Editorial Board based on its scientific merit, innovation, creativity, and clarity.

The runner-up paper appeared in the March 2021 issue, which is available as an open access download. In a recent conversation with *TAPPI Journal*, first author Ghosh discussed some of the rationale and approach for studying used pizza boxes as a viable furnish.

What prompted you to undertake studying the acceptability of post-consumer pizza boxes in the recycle stream?

We could see in the media that there were lots of opinion pieces about why the boxes aren't acceptable for recycling. These articles weren't based on a scientific approach, so we decided to take a deep dive. We started with a mass balance, looking at the assumption that 100% of pizza boxes were recycled and what percentage that would be of total OCC [old corrugated containers]. We found that this percentage is just 2.5%.

We knew that the fibers used to make pizza boxes are of good quality, as WestRock is a major producer of them. We then started studying where the grease is coming from in used pizza boxes, such as the base, or toppings, like cheese and meat. We undertook a huge study looking at how to determine grease levels in the boxes. Once we had the average grease level and the percent pizza boxes in OCC, we went to the lab and designed a set of experiments.

The idea was always to get this information out to the public, but as a first step, we needed to get it out within the industry at large. We provided the study to AF&PA, where the various industry members were able to review it. After the industry peer-review, AF&PA issued a statement about the recyclability of pizza boxes. The next step was to submit the paper to a peer-reviewed journal, as we did with *TAPPI Journal*. We wanted to establish a rigorous scientific basis on which to draw conclusions rather than express opinions. We wanted to make sure the community at large, MRFs [material recycling facilities], paper manufacturers, converters, etc., knew the facts.

Are you surprised that no one has taken a more scientific approach to the subject until now?

I think the issue was down to resource availability, because it takes time to pull together a multi-faceted study and then address the questions brought up by the reviewers.

It took us around two months, working on and off, to gather the market data. Determining the average grease content involved setting up a lab methodology and finding the right people for pizza box collections, imaging, and so forth. Defining the percent of pizza boxes as part of OCC and average grease level ended up taking almost as long as the lab work.

Were the MRFs willing to participate in the study?

Yes, and some of them were part of Westrock, which helped. What we were trying to get from MRFs was independent confirmation of our findings on grease levels. We asked that, for a period of a couple of days, they

take out all the pizza boxes from the OCC bales and take pictures. Then we ran image processing to independently confirm our results from physical sampling.

The boxes used in your study had 8% by weight grease content. What was the significance of that number?

Paper strength comes from hydrogen bonding between fibers. We know that grease, like oil, is hydrophobic and disrupts the inter-fiber bonding. We added oil, at different contents, to fiber and studied the effect of oil versus strength reduction. We drew the curves for burst strength, short span compression, ZDT, and tensile strength with increasing ratio of greasy fiber, as shown in Figures 16-19 in the paper.

The market data informed us that pizza boxes account for approximately 2.5% of OCC, assuming 100% of pizza boxes are recycled. For grease content, we bought a lot of pizzas to determine the grease content in boxes. We also developed a correlation between grease content and images of the used pizza boxes. The average grease level in pizza boxes was found to be around 2%, with a high limit of 8% grease.

On average we can expect 2% grease level in pizza boxes, and the pizza boxes are about 2.5% of the OCC stream. We also reviewed the worst-case scenario of 5% pizza boxes in the OCC stream, with 8% grease content. The data showed that the grease levels in question do not impact strength or other properties in significant enough amounts to be a huge concern.

Are there microbiological concerns with recycling pizza boxes?

Although our study did not address this, we do show that pizza boxes are a relatively small percent of OCC. Also, the pizza boxes become part of the overall board furnish. The pizza boxes will not all be recycled to only make more pizza boxes, so this is not a closed-loop buildup of grease.

For a recycle mill using low quantities of water, there is buildup of dissolved and colloidal materials, so we need to deal with biological growth. An example of food for bugs is starch, which is commonly used as a papermaking strength aid and as glue in the corrugation process. Grease content of pizza boxes in the overall OCC stream is a relatively small component. **TJ**

Ghosh is senior process specialist at WestRock in Richmond, VA. You can hear more from Ghosh about WestRock's pizza box study as part of TAPPI Connect's Ask the Expert series on Friday, September 9, from 10am to 12pm EDT. For a link to the event, visit the Open Forum page on September 9.

IN MEMORIAM



Darren Keith Swales, Ph.D., died Tuesday, August 16, 2022, surrounded by his loved ones after a short but fierce battle with cancer. He was born on June 17, 1966, in Clitheroe, England. For his entire professional life, Darren worked in the field of paper chemicals. Most recently, he was the Director of Sales with Plasmine Technology Inc., headquartered in Pensacola, FL. He was a graduate of Loughborough University with a Ph.D. in Colloidal Chemistry (1991) and a B.Sc. Hons. in Analytical Chemistry (1988).

Darren held a Licentiate from the Royal Society of Chemistry and was inducted as a TAPPI Fellow in 2016. Additionally, he held the roles of Secretary, Vice-Chair, and Chair of both the Papermaking Additives Committee and the Paper and Board Division of TAPPI, as well as the Chair of the Technical Program Committee for two TAPPICon conferences. Darren was a published author whose body of work includes many patents, journal articles, and book chapters. He also was active as an instructor for many technical courses offered by TAPPI, including the "Introduction to wet end chemistry" course offered annually at TAPPI headquarters.

When he wasn't working and learning, Darren loved hunting, fishing, and the outdoors. He spent many hours sitting in a tree or out on the lake. He is survived by his wife Erika, of 25 years, and children, Ella, Hana, and L.J. Darren was dedicated to his family and friends, always the life and soul of the party, and he and Erika loved to entertain.

A feasibility study of using the organic Rankine cycle for power generation from the flue gases of recovery boilers

SEYED JAVAD AMIRFAKHRI

ABSTRACT: Almost 415 tons/h of flue gases with a temperature of 160°C are released to the atmosphere from the recovery boiler of a pulp mill with capacity of 1000 air dried (a.d.) metric tons of pulp per day. This is a large waste heat stream that can be used to generate power, to decrease the operating costs of a pulp mill, and to save carbon dioxide (CO_2) emissions.

In this work, the feasibility of using an organic Rankine cycle (ORC) with ammonia as the working fluid to generate power from the flue gases of recovery boilers is studied. CHEMCAD and Taguchi methods are used for simulation of the process and for optimization of operating conditions, respectively. The temperature of the ammonia and flue gases at the exit of evaporator, exit pressure of the pump and turbine, and the degree of subcooling of ammonia at the exit of the condenser are five operating parameters that are manipulated to optimize the process. Three different scenarios are defined: minimizing the net power cost, maximizing the ORC efficiency, and maximizing the net profit. Different aspects of these scenarios, such as net power generation, cost, efficiency, and CO_2 emission savings are discussed, and optimum operating conditions are reported.

Application: This work presents the application of an organic Rankine cycle as a waste heat recovery system to generate electric power from flue gases of recovery boilers at pulp mills.

Waste heat recovery systems (WHRS) have received a great deal of attention during the last two decades for two main reasons. For one, they increase overall efficiency of industrial processes. Efficiency is defined as desired output to required input, and WHRS can be used to increase desired output in terms of useful energies such as electric power. Secondly, WHRS can decrease greenhouse gas emissions. In comparison with conventional power plants that are responsible for 37% of the global carbon dioxide (CO_2) emissions [1], power generation from waste heat streams can be a zero emission process. One should note that fossil fuels are the primary energy sources to generate electric power. For instance, coal and natural gas were used to generate 66% of the electric power in the United States in 2015 [2]. WHRS are alternative clean energy sources that can be used to diminish our dependency on fossil fuels.

According to a study conducted by the U.S. Department of Energy, 20%–50% of the heat loss in different industrial processes can be recovered [3]. Organic Rankine cycle (ORC), Kalian cycle, phase change material engine, and Stirling cycle are some examples of WHRS [4]. Currently, ORC is one of the best technologies for recovering waste heat streams with low temperatures. It can be used to generate electricity from heat sources with temperatures as low as 100°C [5]. Flue gases of aluminum production plants [6], flue gases of diesel engines [7], wastewaters of deep-sea mining [8], and flue gases of cement kilns [9] are some examples of waste heat streams that can be recovered with an ORC.

The ORC is a vapor/two-phase cycle that consists of evaporator, turbine, generator, condenser, and pump [10] (**Fig. 1**). A working fluid with a low boiling temperature absorbs heat from a waste heat stream in the evaporator. As a result, the working fluid is converted to superheated vapor at the exit of the evaporator. The superheated vapor generates shaft work in the turbine by expansion. The working fluid then rejects heat in the condenser and returns to the evaporator by the pump. Finally, shaft work is converted to electric power in the generator.

Among members of the International Energy Agency, pulp and paper is one of the more energy-intensive industries that uses 5% of total industrial energy [1]. Flue gases of recovery boilers with a temperature around 160°C are one of the waste heat streams in pulp mills. As the main objective of this work, ORC with ammonia as the working fluid is simulated in CHEMCAD chemical process simulation software (Chemstations; Houston, TX, USA) to generate electric power from flue gases of a recovery boiler. Three scenarios are defined, and the Taguchi method is used to find optimal operating conditions.

ORGANIC RANKINE CYCLE

Figure 1 shows different components of the ORC studied in this work. Ammonia is selected as working fluid for several

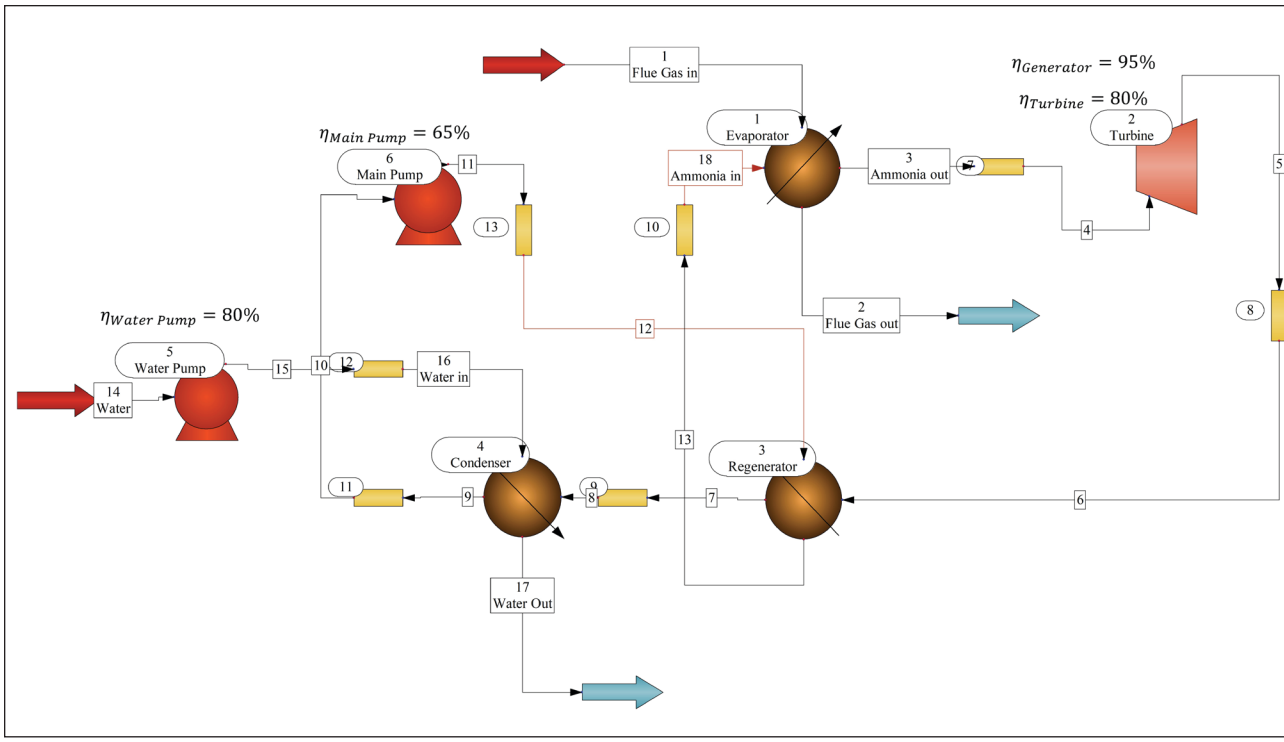

1. The organic Rankine cycle (ORC) flowchart: 1: evaporator, 2: turbine, 3: regenerator, 4: condenser, 5: cooling water pump, 6: main pump, and 7-13: pipes. Shaft work generated in the turbine is then converted to electric power in a generator (not shown here).

reasons. For one, its global warming potential (GWP) is zero as compared to other refrigerants, such as R-134a with a GWP of 1300 and R236fa with a GWP of 9400 [12]. Ammonia is also an environmentally friendly fluid, with an ozone depletion potential (ODP) of zero [13]. Moreover, ammonia has a high heat of vaporization, high specific heat, and low cost [14]. Ammonia, on the other hand, has a low occupational exposure limit (OEL) of 25 ppm [15]. Hence, its application is limited to outdoor areas and specific indoor areas.

The heat source is the flue gases of a recovery boiler with a mass flow rate and temperature of 415 tons/h and 160°C, respectively. The flue gases are generated in a recovery boiler of a pulp mill with a capacity of 1000 air dried (a.d.) tons of pulp per day. It consists of 17.4 wt% water (H_2O), 2.4% oxygen (O_2), 19.6% carbon dioxide (CO_2), and 60.6% nitrogen (N_2), with a dew point of 74°C [16]. Presence of hygroscopic salts such as sodium bisulfate ($NaHSO_4$) and sodium carbonate (Na_2CO_3) increases the dew point of flue gases [17]. For instance, $NaHSO_4$ can absorb water vapor from flue gases 15°C above the dew point of pure water. Hence, to avoid acid formation, a minimum temperature of 95°C is used for flue gases in this work. This temperature is much higher than the dew point of flue gases (74°C).

To increase thermal efficiency of the cycle, the possibility of using a regenerator before the condenser is studied. Ammonia is preheated in this regenerator and then sent to the evaporator. Efficiency of pumps, turbine, and regenerator are presented in Fig. 1.

SIMULATION AND OPTIMIZATION

CHEMCAD software (Chemstations; Houston, TX, USA) is used to simulate the process. The modified L16 orthogonal array of the Taguchi method and the signal-to-noise ratio (S/N) analysis are used, respectively, to design the 16 experiments and to optimize the process [18]. The ammonia temperature at the exit of the evaporator (AT), the flue gas temperature at the exit of the evaporator (FT), the exit pressure of the pump (PP), the exit pressure of the turbine (TP), and the degree of subcooling of ammonia at the exit of the condenser (DOS) are five operating conditions to optimize the process. **Table I** presents five different levels of these parameters. **Table II** presents all 16 runs of this work based on the modified L16 orthogonal array of the Taguchi method. The process is simulated in CHEMCAD based on this table, and data are collected for optimization.

The analysis of variance (ANOVA) is employed to find the most and the least important parameters to minimize the net power cost, to maximize the ORC efficiency, and to maximize the net profit [18,19]. The S/N analysis is used to find the optimum value of operating conditions [19]. First, the mean square deviation (MSD) is determined for all 16 runs. To minimize the net power cost, a smaller quality characteristic (QC) is desired, resulting in $MSD = \frac{\sum_{i=1}^{n} y_i^2}{n}$ where y_i is the net power cost in the ith run. On the other hand, to maximize the ORC efficiency and the net profit, a bigger QC is preferred, resulting in $MSD = \frac{\sum_{i=1}^{n} 1/y_i^2}{n}$. Then, signal-to-noise ratio is calculated for all 16 runs using S/N=-10log (MSD). Finally, the mean S/N is calculated for all four levels of the

Parameter	Level 1	Level 2	Level 3	Level 4
Ammonia temperature in the exit of evaporator (AT), °C	100	110	120	130
Flue gas temperature in the exit of evaporator (FT), °C	95	105	115	125
Pressure in the exit of the main pump (PP), bar	35	40	45	50
Pressure in the exit of the turbine (TP), bar	13	16	19	22
Degree of subcooling of ammonia in the exit of condenser (DOS), °C	1	2	3	4

I. Operating parameters and their different levels.

Run	Level					Run	Level				
	AT	FG	PP	TP	DOS		WF	FG	PP	TP	DOS
1	1	1	1	1	1	9	3	1	3	4	2
2	1	2	2	2	2	10	3	2	4	3	1
3	1	3	3	3	3	11	3	3	1	2	4
4	1	4	4	4	4	12	3	4	2	1	3
5	2	1	2	3	4	13	4	1	4	2	3
6	2	2	1	4	3	14	4	2	3	1	4
7	2	3	4	1	2	15	4	3	2	4	1
8	2	4	3	2	1	16	4	4	1	3	2

II. Design of experiments based on the Taguchi method.

operating parameters. The level with maximum S/N is selected as the optimum value of that operating parameter.

Cost estimation

The cost estimation tool of CHEMCAD is used to find the equipment and installation costs. All three heat exchangers are shell and tube with an installation factor of 2. Stainless-steel 304 is used for all equipment and piping to decrease the corrosion rate. An installation factor of 2.8 and 1.5 is considered for pumps and turbine, respectively. Engineering and piping are assumed to be 3% and 7%, respectively, of the total equipment and installation cost. These data are used to determine the capital cost (which is the combination of equipment, installation, piping, and engineering cost) after applying the federal Business Energy Investment Tax Credit (ITC). The ITC for waste energy recovery property that has a maximum capacity of 50 MW or less is 26% in 2022 [20].

The capital cost is then used to determine depreciation based on 10 years of lifetime of the equipment and operating hours of 7200 h/year (Eq. 1). The operating cost is calculated by combining the maintenance (2% of the capital cost) and ammonia cost. Finally, the net power cost is determined by combining the depreciation and operating cost (Eq. 2). The net profit is calculated from the difference between annual net cash flow and annual depreciation (Eq. 3).

$$Depreciation\left(\frac{\$}{kWh}\right) = \frac{capital\ cost\ (\$)}{equipment\ lifetime\ (year) \times Annual\ electricity\ generation\ \left(\frac{kWh}{year}\right)} \quad (1)$$

$$Net\ power\ cost\left(\frac{\$}{kWh}\right) = Depreciation\left(\frac{\$}{kWh}\right) + operating\ cost\left(\frac{\$}{kWh}\right) \quad (2)$$

$$Net\ profit\left(\frac{\$}{year}\right) = annual\ net\ cash\ flow\left(\frac{\$}{year}\right) - annual\ depreciation\left(\frac{\$}{year}\right) \quad (3)$$

The power required for the pumps is supplied from the power generated in the cycle. As a result, the utility cost of ORC is assumed to be negligible. The net power, which is defined as the difference between power generated in the cycle and power required for the pumps, is used for all calculations. According to the most recent data released by the U.S. Energy Information Administration, the industrial electricity cost in the United States ranges from 4.8 cents/kWh at the Palo Verde hub in the Southwest to 13.3 cents/kWh at the ISO New England internal hub [21]. The industrial

electricity cost at the MISO Illinois hub in the Midwest, which is 9.5 cents/kWh, is selected for the cost estimation. This region has one of the highest numbers of paper mills in the US. The net present value (NPV) is determined using an 8% discount rate.

RESULTS AND DISCUSSION

Figure 2 presents the capital cost, including equipment and installation, piping, and engineering, required for all 16 runs. According to this figure, heat exchangers are the most expensive equipment and account for more than 70% of the total capital cost. This can be due to the low deriving force of heat transfer (temperature gradient) between the hot and cold fluids in the heat exchangers. For run 13, for instance, a maximum temperature gradient of 54°C and 17°C exists in the evaporator and condenser, respectively. On the other hand, a maximum temperature gradient of 67°C and 25°C is observed in the evaporator and condenser, respectively, for run 16. These higher temperature gradients can explain the lower capital cost required for run 16 in comparison with run 13. For runs 1, 2, 3, 4, 7, 8, and 10, the regenerator is useless due to the low temperature gradient between hot and cold ammonia (<5°C). As a result, the regenerator is excluded for these runs.

Figure 3 presents the net power cost and net power generated in the cycle for all 16 runs. The ORC efficiency

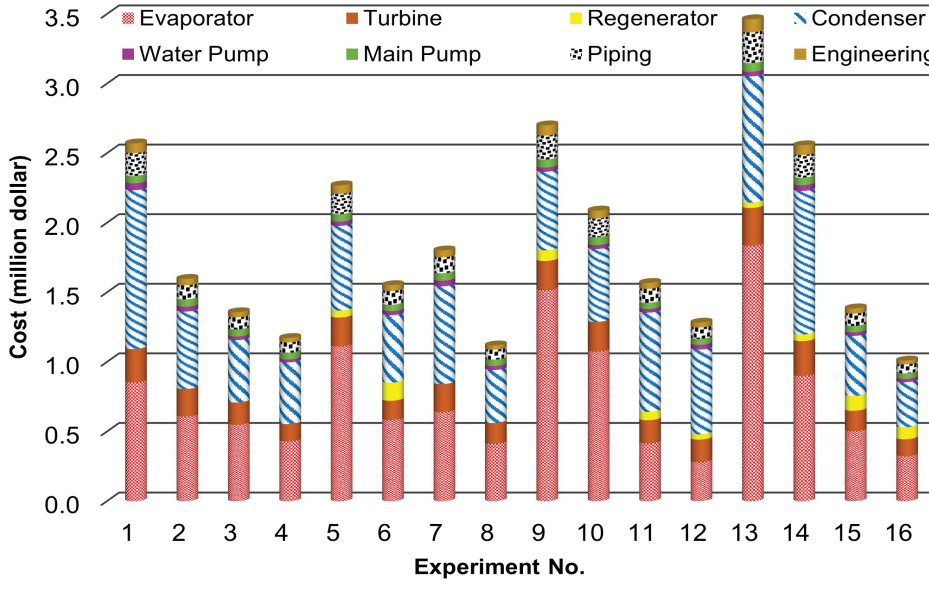

2. The capital cost (equipment and installation, piping, and engineering) of all 16 runs without considering the federal Business Energy Investment Tax Credit (ITC).

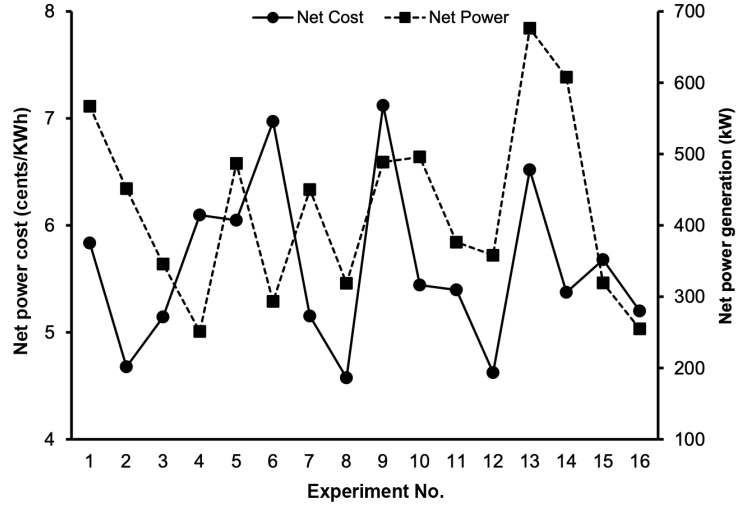

3. The net power cost (cents/kWh) and the net power generation (MW) of all 16 runs

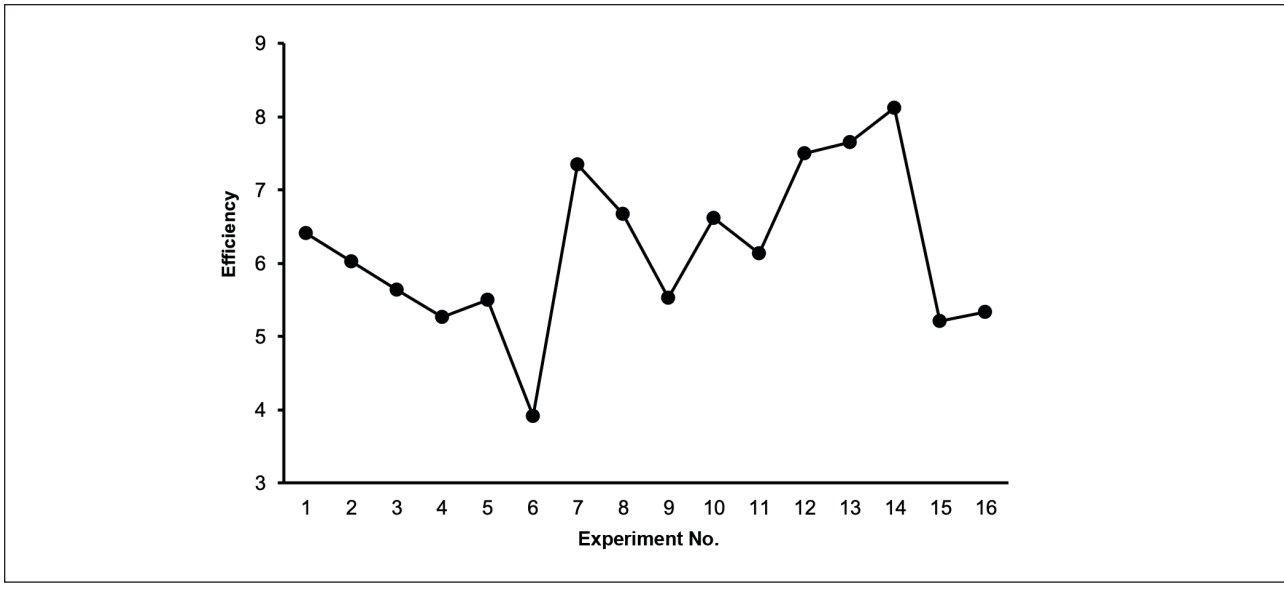

4. Efficiency of the organic Rankine cycle (ORC) for all 16 runs.

varies between 3.9% and 8.1% (**Fig. 4**). Data obtained in this section are used to evaluate three different scenarios in the next section after applying the ITC.

First scenario: Minimization of the net power cost

The net power cost is the combination of equipment depreciation and operating cost required to run the cycle (Eqs. 1 and 2). The results of ANOVA indicate that the exit pressure of the turbine and the temperature of flue gases at the exit of the evaporator are the most important parameters to minimize the net power cost. On the other hand, the temperature of ammonia at the exit of evaporator is the least important parameter. **Table III** presents the optimum value of the operating parameters to minimize the net power cost after applying the S/N analysis. According to the results, ammonia, and flue gases should exit the evaporator at minimum and maximum temperatures, respectively, to minimize the costs. Under the optimum conditions, the temperature gradient between the cold and hot fluids in the evaporator is 85°C, which is much higher than all other 16 runs. Despite this maximum driving force between cold and hot fluid, the temperature difference in the cold side ($T_{C,out} - T_{C,in}$) and hot side ($T_{b,in} - T_{b,out}$) is a minimum. As a result, under these conditions, both heat transfer rate and power generation decrease.

The ORC cycle is run in CHEMCAD under the optimum operating conditions obtained for this scenario. As a result, a net power cost of 4.1 cents/kWh is obtained, which is lower than all other 16 runs presented in Fig. 3. The total capital cost required for this scenario is $0.66 million, which leads to an annual profit of $0.11 million. The regenerator is ineffective due to the small temperature difference between hot and cold ammonia (ΔT=0.2°C). In comparison with the average CO_2 emissions from U.S. natural gas power plants (549 g CO_2/kWh) [22], using the ORC can lead to savings of 1.39 kiloton CO_2 generation annually.

The net power generation and ORC efficiency is 290 kW and 6.1%, respectively. Comparison between power generated in this scenario and data presented in Fig. 3 reveals that the net power of this scenario is among the minimum powers reported in this work. The internal rate of return (IRR) and NPV of this scenario are 23.9%, and $0.54 million, respectively

Parameter	Value
AT, °C	100
FT, °C	125
PP, bar	40
TP, bar	16
DOS, °C	1

III. The optimum operating conditions to minimize the net power cost.

Parameter	Value
AT, °C	130
FT, °C	95
PP, bar	50
TP, bar	13
DOS, °C	1

IV. The optimum value of operating parameters to maximize the organic Rankine cycle (ORC) efficiency.

Second scenario: Maximization of the ORC efficiency

Efficiency is calculated as the ratio of the net power generated in the cycle to the heat transferred in the evaporator. According to the ANOVA results, ammonia pressure at the exit of the turbine is the most important parameter to maximize the ORC efficiency. On the other hand, temperature of flue gases at the exit of the turbine and degree of subcooling of ammonia at the exit of condenser are the least important parameters. The results of S/N analysis to maximize the ORC efficiency are presented in **Table IV**. Using these parameters, an ORC efficiency of 8.4% is obtained, which is the maximum value obtained in this work. On the other hand, the total capital cost required for this scenario is $2.82 million, which is much higher than the $0.89 million of the previous scenario. This leads to a net power cost of 6.5 cents/kWh and annual profit of $0.16 million. The net power generated in the cycle is 745 kW. The regenerator is excluded from the cycle due to the negligible temperature gradient between hot and cold ammonia. In comparison with the U.S. natural gas power plants, this scenario can lead to a reduction of 3.6 kilotons of CO_2 emissions per year. Data obtained in this scenario leads to an IRR and NPV of 8.1% and $0.014 million, respectively.

Parameter	Value
AT, °C	130
FT, °C	105
PP, bar	40
TP, bar	13
DOS, °C	1

V. The optimum value of operating parameters to maximize the net profit.

Third scenario: Maximization of the net profit

The net profit is the difference between the net cash flow and depreciation (Eq. 4). The ANOVA results indicate that the fluid pressure at the exit of the turbine is the most important parameter to maximize the net profit. On the other hand, the ammonia temperature at the exit of evaporator and the degree of subcooling of ammonia at the exit of the condenser are the least important parameters.

Table V presents the optimum conditions to maximize the net profit based on the results of S/N analysis. Contrary to the previous two scenarios, the regenerator is

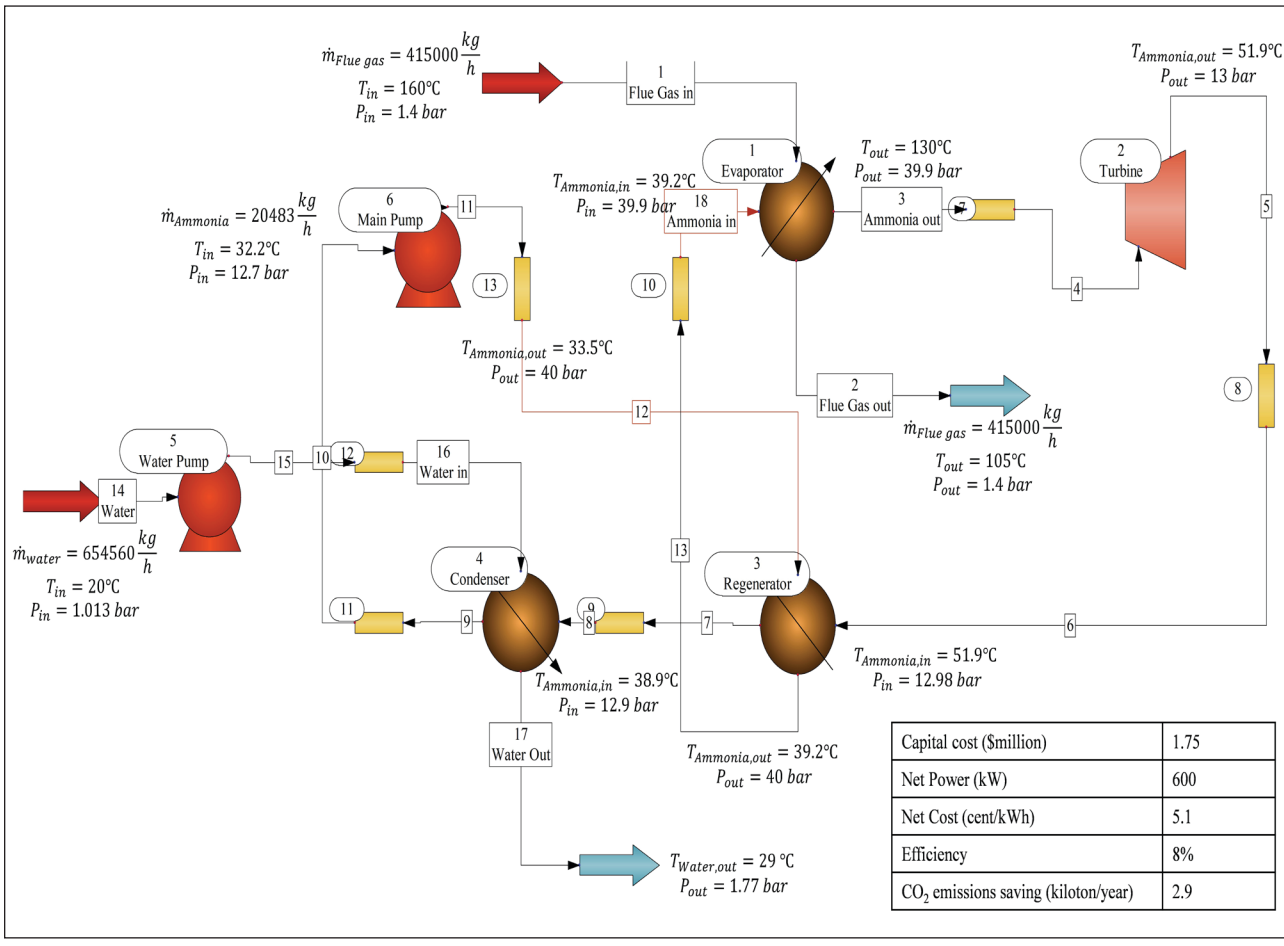

Capital cost ($million)	1.75
Net Power (kW)	600
Net Cost (cent/kWh)	5.1
Efficiency	8%
CO_2 emissions saving (kiloton/year)	2.9

5. Process flow diagram of the best scenario based on maximum profit.

Parameter	Evaporator	Regenerator	Condenser
Amount of equipment	5	1	4
Diameter (m) × Length (m)	1.07×3.05	0.34×4.88	0.59×6.1
Number of tubes	1609	146	1878
Tube outside diameter, mm	6.35	19	9.52
Overall coefficient in service $(\frac{W}{m^2.K})$	295.8	479.7	629.9
Total heat transfer area	480.5	41.8	1361.7
Fluid velocity in shell, m/s	21.27	0.5	0.12
Fluid velocity in tube , m/s	3.36	21.8	1.77

VI. Summary of the design parameters for heat exchangers in the third scenario.

	Scenario 1	Scenario 2	Scenario 3
Capital cost, $ million	0.66	2.82	1.75
Net power generation, kW	289	743	600
Net power cost, cents/kWh	4.1	6.5	5.1
ORC efficiency	6.1	8.4	8
CO_2 emissions savings, kilotons/year	1.39	3.6	2.9
Net cash flow, $ million/year	0.18	0.44	0.37
Annual depreciation, $ million/year	0.07	0.28	0.18
Annual net profit, $ million	0.11	0.16	0.19
IRR	23.9%	8.1%	17.1%
NPV, $ million	0.54	0.014	0.71
ORC = organic Rankine cycle; CO_2 = carbon dioxide; IRR = internal rate of return; NPV = net present value.			

VII. Summary of the data obtained for all three scenarios (scenario 1: minimizing the net power cost; scenario 2: maximizing the ORC efficiency; scenario 3: maximizing the net profit).

efficient and can be used for the preheating of cold ammonia. The capital cost required for this scenario is $1.75 million, which is lower than the second scenario. The net power generation in the cycle is 600 kW and results in a net power cost of 5.1 cents/kWh. It leads to an annual net profit of $0.19 million, which is higher than the first and the second scenarios. The thermal efficiency of the ORC under these conditions is 8%, which is close to the maximum efficiency obtained for the second scenario. The results indicate that 2900 tons of CO_2 can be saved annually in comparison with the natural gas power plant. The IRR and NPV of this scenario are 17.1% and $0.71 million, respectively. **Figure 5** presents the process flow diagram of this scenario. The design parameters of heat exchangers are presented in **Table VI**.

CONCLUSION

Waste heat of recovery boiler flue gases at pulp mills can be successfully recovered to generate electric power in an ORC with ammonia as the working fluid. According to the ANOVA results, ammonia pressure at the exit of the turbine is the most important parameter to optimize the process. A summary of the results obtained for three scenarios studied in this work is presented in **Table VII**. The net power cost of all three scenarios is much lower than the industrial electricity cost of the MISO Illinois hub in the Midwestern United States [21]. Although the efficiencies are below 10%, they are still in the typical range of the ORC efficiencies (6%–18%) [23,24]. According to this table, the first scenario can be selected when minimum capital cost, minimum net power cost, and maxi-

mum IRR are the main targets. However, one should note that the efficiency, net power generation, and net profit of this scenario is lower than the other two scenarios. The second scenario presents the maximum efficiency and net power generation. However, its capital cost and net power cost are maximum as well. This scenario has the minimum IRR and NPV among these three scenarios. Data presented in Table VII suggest that the third scenario can be selected as the best option due to several reasons. First, this scenario presents the maximum net profit and NPV. Moreover, its efficiency is close to the maximum ORC efficiency reported in this work. Finally, it has a reasonable net power cost that is close to the minimum value reported for the first scenario. **TJ**

ABOUT THIS PAPER

Cite this article as:
Amirfakhri, S., *TAPPI J.* 21(8): 405(2022).
https://doi.org/10.32964/TJ21.8.405

DOI: https://doi.org/10.32964/TJ21.8.405

ISSN: 0734-1415

Publisher: TAPPI Press

Copyright: ©TAPPI Press 2022

About this journal

LITERATURE CITED

1. Majedi, H., Fathian, H., Nikbakht-Shahbazi, A., et al., *Water Resour. Manage.* 35(8): 2685(2021). https://doi.org/10.1007/s11269-021-02860-0.
2. Squalli, J., *Energy* 127: 479(2017). https://doi.org/10.1016/j.energy.2017.03.156.
3. Meinel, D., Wieland, C., and Spliethoff, H., *Appl. Therm. Eng.* 63(1): 246(2014). https://doi.org/10.1016/j.applthermaleng.2013.11.016.
4. Cruz, I., Wallén, M., Svensson, E., et al., *Energies* 14(24): 8499(2021). https://doi.org/10.3390/en14248499.
5. Anastasovski, A., Rasković, P., and Guzović, Z., *Energy Convers. Manage.* 221: 113175(2020). https://doi.org/10.1016/j.enconman.2020.113175.
6. Castelli, A.F., Elsido, C., Scaccabarozzi, R., et al., *Front. Energy Res.* 7: 44(2019). https://doi.org/10.3389/fenrg.2019.00044.
7. Mondejar, M.E., Andreasen, J.G., Pierobon, L., et al., *Renewable Sustainable Energy Rev.* 91: 126(2018). https://doi.org/10.1016/j.rser.2018.03.074.
8. Chen, R., Deng, S., Zhao, L., et al., *Appl. Energy* 305: 117719(2022). https://doi.org/10.1016/j.apenergy.2021.117719.
9. Fierro, J.J., Escudero-Atehortua, A., Nieto-Londoño, C., et al., *Int. J. Thermofluids* 7-8: 100040(2020). https://doi.org/10.1016/j.ijft.2020.100040.
10. Loni, R., Mahian, O., Markides, C.N., et al., *Renewable Sustainable Energy Rev.* 150: 111410(2021). https://doi.org/10.1016/j.rser.2021.111410.
11. Kong, L., Hasanbeigi, A., and Price, L., *J. Cleaner Prod.* 122: 5(2016). https://doi.org/10.1016/j.jclepro.2015.12.116.
12. Öhman, H., *Energy* 48(1): 227(2012). https://doi.org/10.1016/j.energy.2012.02.074.
13. EPA, "Protection of stratospheric ozone: New listings of substitutes; changes of listing status; and reinterpretation of unacceptability for closed cell foam products under the significant new alternatives policy program; and revision of Clean Air Act Section 608 Venting Prohibition for Propane," in *40 CFR Part 82* (EPA, Ed.), RIN:2060-AS802016, Document Number:2016-25167, U.S. Environmental Protection Agency, Washington, DC, 2016.
14. Tchanche, B.F., Papadakis, G., Lambrinos, G., et al., *Appl. Therm. Eng.* 29(11-12): 2468(2009). https://doi.org/10.1016/j.applthermaleng.2008.12.025.

ABOUT THE AUTHORS

Waste heat recovery systems (WHRS) for electricity generation from sources with temperatures below 200°C have received a great deal of attention in recent years. This work concentrates on the application of the organic Rankine cycle (ORC) for power generation from flue gases of recovery boilers at pulp mills in the United States. The process is simulated using CHEMCAD software. The operating parameters are optimized using the Taguchi method. This information is used to discuss the technical aspects, cost estimation, and environmental benefits of using the ORC.

Through this study, it was found that the heat exchangers account for more than 70% of the total capital cost of the ORC due to the small deriving force of heat transfer (temperature gradient) in the heat exchangers. Moreover, the ORC can be used to generate electricity at prices lower than the whole industrial electricity price at the MISO Illinois hub in the Midwest.

Paper companies can use the ORC to increase the overall efficiency of their mills, while also decreasing greenhouse gas emissions and increasing mill profits. As the next step, I will work to improve the efficiency of the process, as it is still lower than 10%.



Amirfakhri

Amirfakhri is assistant professor in the Department of Paper Science and Engineering and Chemical Engineering at the University of Wisconsin–Stevens Point in Stevens Point, WI, USA. Email Amirfakhri at samirfak@uwsp.edu.

15. Rappe, K.G., Alexander, L., Wahl, J.H., et al., "NUCON vapor abatement unit performance on Hankford Tank Farm chemicals of potential concern," Technical Report, U.S. Department of Energy, Office of Scientific and Technical Information, Oak Ridge, TN, 2018. https://doi.org/10.2172/1545580.
16. Adams, T., Frederick, W.J., and American Paper Institute Recovery Boiler Research and Development Subcommittee, *Kraft Recovery Boiler Physical and Chemical Processes*, American Paper Institute, New York, 1988.
17. Vainio, E., Laurén, T., DeMartini, N., et al., *J. Sci. Technol. For. Prod. Processes* 4(6): 14(2014).
18. Amirfakhri, S.J., *Process Integr. Optim. Sustain.* 6(2): 275(2022). https://doi.org/10.1007/s41660-021-00209-z.
19. Roy, R.K., *Design of Experiments Using the Taguchi Approach: 16 Steps to Product and Process Improvement*, John Wiley & Sons Inc., New York, 2001.
20. Sherlock, M.F., "The energy credit or energy investment tax credit (ITC)," Report# IF10479, 7th edn., U.S. Congressional Research Service (CRS), Washington, DC, 2021.
21. EIA, "Short-term energy outlook: Summer 2022 electricity industry outlook," U.S. Department of Energy, Washington, DC, May 2022.
22. de Gouw, J.A., Parrish, D.D., Frost, G.J., et al., *Earth's Future* 2(2): 75(2014). https://doi.org/10.1002/2013EF000196.
23. Jafary, S., Khalilarya, S., Shawabkeh, A., et al., *J. Cleaner Prod.* 281: 124552(2021). https://doi.org/10.1016/j.jclepro.2020.124552.
24. Matuszewska, D. and Olczak, P., *Energies* 13(6): 1499(2020). https://doi.org/10.3390/en13061499.

Edge crush testing methods and box compression modeling

BENJAMIN FRANK AND DOUGLAS CASH

ABSTRACT: While multiple test procedures have been developed to assess the inherent compressive strength of corrugated materials (edge crush test, ECT), limited work has explored the appropriateness of each in the context of box compression modeling. This study incorporates a variety of real-world samples, highlighting the varying challenges different ECT methods face in measuring the intrinsic compressive resistance of combined corrugated board. We examine each of these methods as inputs for different types of models, as well as discuss the propagation of measurement variation through the modeling effort. By highlighting the cases in which a given ECT method no longer proves to be an optimal parameter in box compression strength modeling, we explore how we might better measure this material property.

Application: This work highlights the importance of identifying and developing more optimal test methodologies to measure the inherent compressive strength of corrugated materials (ECT).

Corrugated boxes contain and protect their contents throughout the distribution environment and are used to package the vast majority of goods sold and transported commercially. Container performance is impacted by how the distribution environment acts on the box, and in a stacking and storage situation (e.g., warehouse) box compressive strength (typically measured by a top-to-bottom compression strength test, BCT) is the key performance metric. Since the invention of the box, researchers have attempted to generate predictive equations for box compression strength to provide robust estimations without requiring the actual production and testing of each order or every box. Modeling approaches relying on fundamental properties, as well as first-principle mechanics, offer the promise of enabling package optimization and "right sizing" packaging to meet distribution needs, ideally providing the opportunity to perform cost-benefit analyses of packaging. The "McKee equation" is the most common closed form box compression model used in the industry [1], though many others have been developed using both closed form mechanics-based approaches [2] and numerical simulations [3-5]. For all these models, the inherent material strength of the board structure contributes most significantly to box strength [6-8]. We attempt to evaluate this property by measuring the edge crush strength of the combined corrugated board (edge crush test, ECT).

The industry has developed several different edge crush tests, and it may be confusing even for those experienced with corrugated packaging to identify which method is best for a given situation. The most common North American certification process for boxes, the conforming (circular) box manufacturer's certificate (BMC), specifies the use of TAPPI Standard Test Method T 811 "Edgewise compressive strength of corrugated fiberboard (short column test)" as the referee method for determining the ECT of boxes used for shipping (ISO 13821 "Corrugated fibreboard — Determination of edgewise crush resistance — Waxed edge method" is similar). Significant development work underlies this test in its attempt to measure intrinsic compression strength, particularly in the context of the BMC rules [9]. For this specific application the "best ECT method" is clear; it is the one required by the governing specification. However, that does not automatically imply that the same test is best for other applications. Many manufacturing operations measure ECT to control or optimize their processes and assure they meet customers' performance requirements, and the best method in this case might be one that is easiest to use and achieves "reasonably repeatable" results. In this context, North American box plants often use TAPPI Test Method T 839 "Edgewise compressive strength of corrugated fiberboard using the clamp method (short column test)," where carefully cut square pieces are tested with edges clamped to prevent the results from being influenced by the effect of loading on the edges. This approach simplifies the testing process by eliminating the waxing and reconditioning steps and by providing a single specimen height for all materials. In Europe, operations commonly use ISO 3037 "Corrugated fibreboard — Determination of edgewise crush resistance (unwaxed edge method)" (FEFCO 8 "Edgewise crush resistance of corrugated fiberboard" is similar), an even simpler testing approach that avoids the time-consuming sample edge waxing and reconditioning of the T 811 method as well as the hassles involved in a clamping approach. ISO 3037 tests a short unwaxed specimen by directly loading on the cut edges. Other methods (e.g., TAPPI T 838 "Edge crush test using neckdown," JIS Z 0403-2 "Corrugated fibreboard — Part 2: Determination of edgewise crush resistance") re-

quire test pieces where the width of the specimen has been substantially reduced at a point midway between the loading edges, again to induce failure away from those edges. Each of these different methods has distinct advantages and applicability in their specific applications, but it is not clear from their descriptions which best captures the inherent material strength of the board structure. From a model, mechanics, and estimation perspective, the "best ECT method" would provide the strongest correlation with what we actually care about when using boxes — box performance. Ideally, it would also have the smallest variation in the measurement (within a single laboratory operation and between laboratories in the industry). If a method had very narrow variation but did not relate to BCT particularly well, it would not be very helpful, as it would not facilitate "robust" package performance estimations.

These different methods each have sample preparation and measurement steps that can impact the results. Loading the sample directly, whether waxed or not, requires very tight specifications on the parallelism and cutting quality of the loading edges [10,11]. Clamping can cause damage to the specimen, reducing its load carrying capacity [12]. Loading on an unreinforced edge typically causes curling of the paper at the edge, which leads to failure at the edge rather than in the sample body and thus may not be representative of the inherent material strength of the bulk structure [10,13,14]. Because of these challenges and others, these various ECT measurement approaches often produce different test values for the same materials [11,15-23]. Historical discussions across the industry failed to achieve consensus [24-26] as to which may best assess strength, and the question has not been addressed by more recent finite element analysis of the ECT process [5] or full field strain measurement [27]. Each ECT approach can be used to create models predicting BCT, provided that the formula to predict BCT values from ECT results is based on data from the ECT method being used. But the accuracy of the different models, based on the failure mechanics of the different tests, has not been well studied in the literature. As noted by Urbanik in 1990 [26], "a more complete critique of superior tests would need to involve comparisons using identical materials."

In this paper, we leverage a data set of 118 single-wall boxes to explore the correlation of ECT measurement with box compression and to assess model quality. For each box, we measured ECT using multiple methods, which are described further in the following sections. Along with measurements for bending stiffness, caliper, and other parameters, this data set provides a unique opportunity to explore different measurement and modeling approaches, serving to highlight which method better captures the inherent material strength required by structurally relevant models. In parallel, we explore the impact of measurement variation to guide future research into improved ECT measurement techniques.

METHODS

This research, and any comparative assessment of testing approaches, critically relies on the specifics of the testing process. All testing discussed in this paper was performed after preconditioning of the sample materials in a dry (~25% relative humidity [RH]) environment, followed by conditioning the materials at 23°C/50% RH, in line with the requirements of TAPPI T 402 "Standard conditioning and testing atmospheres for paper, board, pulp handsheets, and related products." Randomized sampling across each lot of commercially produced boxes assured that our different measurements were representative of the respective materials.

We assessed BCT following TAPPI T 804 "Compression test of fiberboard shipping containers." As the rotation of the minor flaps into the box can impact the measured compression load, all boxes were sealed using hot melt glue to immobilize the minor flaps during loading and were tested on a fixed platen compression tester. We regularly checked and maintained equipment parallelism at 1:2000 or better, tighter than required by the standard, to minimize the impact on BCT due to differences in platen parallelism [2,28]. Each reported BCT value represents an average of 10 individual measurements.

We measured board caliper following TAPPI T 411 "Thickness (caliper) of paper, paperboard, and combined board" with a foot pressure of 7.3 psi in line with that standard. Other caliper measurement standards call out different pressures, and since combined board is compressible, these standards can produce different values when measuring the same combined board [29]. This can be particularly relevant when evaluating boxes that may have experienced damage from the fabrication process. Each reported caliper value represents an average of 20 individual measurements.

Bending stiffness measurements were performed following TAPPI T 836 "Bending stiffness, four point method" using the 4-point bending stiffness tester developed by L&W (and presently sold by ABB; Zurich). For many boxes in this study, we were able to evaluate the bending stiffness at the standard span for single-wall board, 200 mm. For boxes too small in one or both dimensions for testing at 200 mm, we tested at either 150 mm or 100 mm and scaled the results following the literature [30]. Each reported bending stiffness value, in either the machine or cross machine direction, averages 10 individual measurements, half with the sample bent to be concave to the double-back side and half concave to the single-face side. Root mean square (RMS) bending, used in some models, is the square root of the product of the bending stiffness in the two principal directions.

All ECT specimens were cut using a dual blade cutter with rigidly mounted single beveled blades, with the unbeveled side producing the loading edge of the sample specimens [11]. Using single beveled blades for all sample loading edges assures similar parallelism across the different test materials examined. We verified this parallelism with occasional measurements of random specimens for all test methods. As noted previously and described in the in-

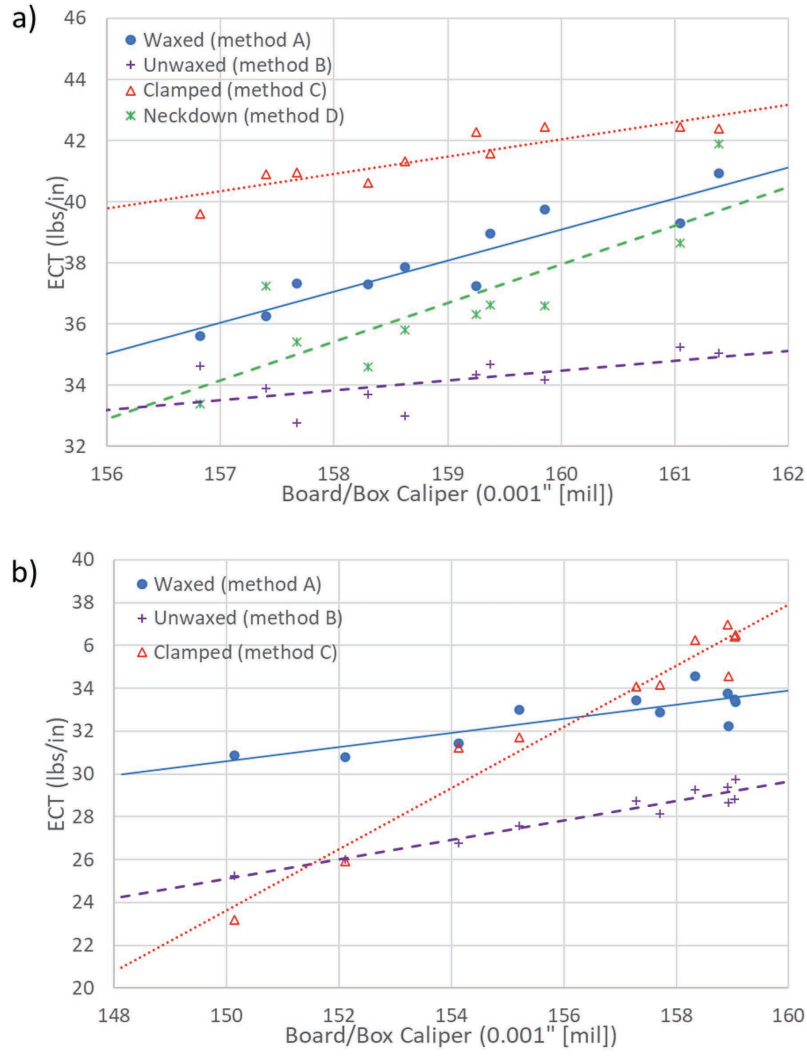

1. Edge crush test (ECT) measurements using different methodologies on boxes crushed various amounts during the production process. The lines indicate best fit relationships between ECT and box caliper for each method. Each data point is an average of 10 individual measurements, with a typical standard deviation in ECT of 1–2 lb/in. For a) the combined board used a heavy medium while b) involved board using a lighter medium.

troductory information for both ISO 3037 and ISO 13821, the variety of methods currently in practice for the determination of edgewise crush resistance can be generally classified into four groups:

A. Methods in which the edges of the test specimens are waxed to prevent the test results from being influenced by edge effects, such as ISO 13821 and TAPPI T 811. In this study, all specimens were 2 in. long, with C-flute board specimens cut 1.5 in. high and B-flute board specimens cut 1.25 in. high, following the TAPPI protocol.

B. Methods in which carefully cut rectangular test pieces are tested without any special treatment to prevent failure at the loading edges, including ISO 3037 and FEFCO 8. In line with those methods, samples in this study were cut 4 in. long and 1 in. high and tested without any further modifications. We identified curling of the papers at the loading edges as the failure mode for most materials, supporting the observation that this approach likely does not measure the actual intrinsic compressive strength of the corrugated structure [13]. We include this testing approach in the present study given the prevalence of this test methodology in the worldwide industry.

C. Methods in which carefully cut rectangular pieces are tested with edges clamped to prevent the results from being influenced by edge effects, such as TAPPI T 839. Following TAPPI T 839, samples in this study were cut 2 in. long and 2 in. high and tested using the clamping fixture produced by Emerson Apparatus (Gorham, MA, USA).

D. Those methods in which the shape of the test piece is reduced, or "necked down," in the center of the specimen, including TAPPI T 838 (based on work at the USDA Forest Products Laboratory [31]) and JIS Z-0403-2 (where the necked down sample is tested in a clamping fixture). Reducing the width of the specimen in the center increases the stress on the specimen in that area, forcing failure to the necked down zone and away from the specimen edges.

Examining test data using these four approaches on two lots of material crushed by different amounts during the fabrication process (**Fig. 1a** and **Fig. 1b**) highlights not only the significant difference in absolute values produced by these diverse testing approaches but also the different relationship these methods have to board damage (which occurs from crushing the board in its thickness direction, either in the box fabrication process or in erecting and use).

While this study incorporates data from ECT methods A, B, and C above, we were unable to reliably generate consistent, undamaged specimens in line with method D. However, we added an additional ECT approach to this study (method E), preparing 2 in. x 2 in. square samples in line with the clamping method (C) but then waxing those edges in line with the waxed method (A) before testing those specimens in the clamping fixture. The hardened wax should conceptually keep the samples from further crushing by the clamps (resulting in a significant shift in properties, Fig. 1) [12]. Method E is not useful as an expedited evaluation approach (since it incorporates both the waxing stage and the time required to execute clamping), but we will find below that it is helpful in separating/identifying contributions from different specimen failure mechanics.

Data set

In this study, we examine a diverse set of regular slotted cartons (RSCs) produced across a range of North American box plants for use in commerce. These include a mix of B-flute and C-flute boxes with lengths from 7.25–24 in., widths from 4.75–20.75 in., and depths from 5–26.5 in. We combine both B and C flute boxes when modeling in this study, as the literature [7] indicates that these single-wall boxes have the same general failure dynamics. Box perimeters were normally distributed with a mean of about 52 in. Average box depth was about 10 in. The ECT values (lb/in.) measured following method A ranged from ~25–75 lb/in. and BCT values ranged from 350–1160 lb. Given the variety in linerboard and corrugating medium grammages used for these different containers, this data set is assumed to be broadly representative of boxes in general. We did not conclusively determine the nominal grades of the component papers of all the different materials tested, nor the level of recycled or virgin content in each of the boxes. However, these factors are not input parameters in box estimation models; while perhaps desirable for future analyses, these are not relevant to the current study beyond indicating an expected change from one box to another where the grades or weights were known. Dimensional and physical property data on each box set examined in this study were collected from the boxes themselves, incorporating printed and unprinted areas in rough proportion to the level of print on the boxes, and are available in the Appendix.

Each method of ECT assessment has its own challenges, and we tried to incorporate boxes in our data set that would highlight those challenges. Though specimen heights for the waxed approach (A) are intended to achieve pure compression, that may not be the case for some unbalanced board combinations, as when sample caliper has

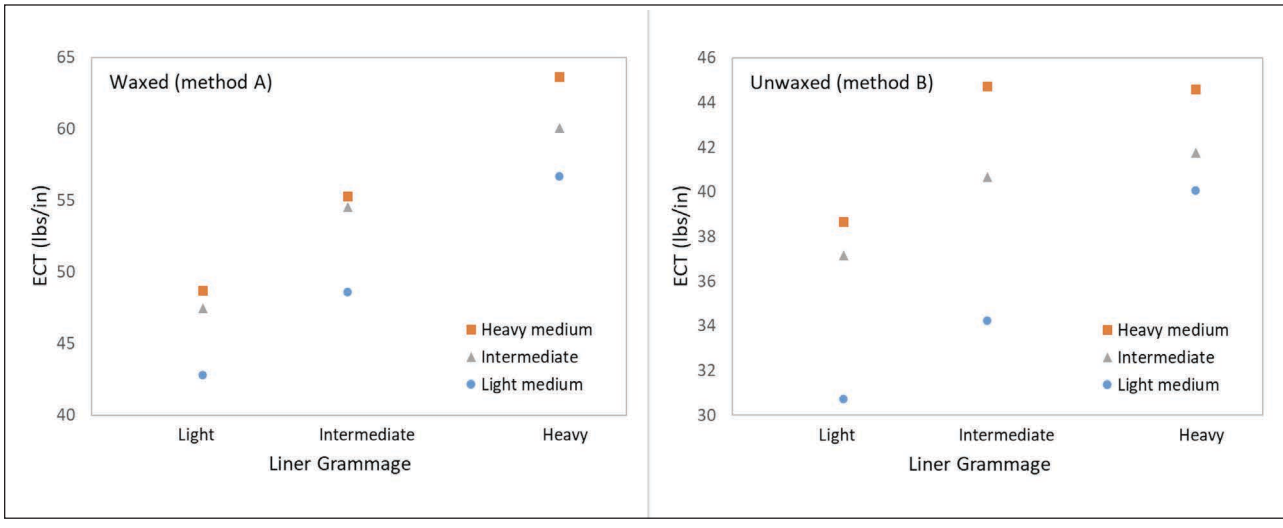

2. Corrugated boxes made by combining relatively light, intermediate, and heavy liners with light, intermediate, and heavy medium. For the waxed ECT method, strength increases linearly both as linerboard weight (and strength) increases and as corrugating medium weight (and strength) increases. For the unwaxed method, this is not the case. Data from samples 26–33 in the Appendix.

been dramatically reduced due to crush or when material bending stiffness is particularly low due to light liners [32]. Our data set thus includes crushed boxes and boxes with light liners (particularly for B-flute). For method B, the degree of edge curl may depend in part on the specific papers used, and in particular on the ratio of the strengths or weights of the linerboard and medium (**Fig. 2**). Our data set includes two groups of boxes (samples 26–33 in C-flute and 109–114 in B-flute) where the component weights (strengths) varied for the same box size. As we observed in Fig. 1, the impact of board damage (crush) in the converting process can also influence the different ECT tests in different ways. Because we sampled materials "from commerce," some boxes in this study likely experienced more converting damage than others. For one set of materials (samples 54–61), we systematically and significantly varied the amount of crush the board experienced in the box fabrication process, and we collected several additional groups of material where we evaluated the same box under more than one level of converting impact. All these different subsets of data were included to allow us to probe the appropriateness of each test method relative to the others across a wide range of boxes one might expect, given the natural variation of the box making process, and to highlight the responses of the different ECT methods.

Variation

Testing variation plays a critical role in our ability to develop robust models [33]. The less variation we have in measured properties, the better we know the values measured, and the more precise our models will be. Distinct from model accuracy, which would assess whether the model estimate is on target, variation impacts the amount of uncertainty around the estimated value. The best models would be on target and have a relatively low window of uncertainty around them. Since model uncertainty stems in part from measurement variation of the parameters that go into the model, if two ECT methods both assess the system in the same way and have similar correlations with the physical behavior leading to box failure, then the one with the lowest variation would result in the better model.

For our data set, we can calculate the average coefficient of variation (COV; percent variation, or standard deviation in the measurement divided by the average value) of the various properties measured, as well as their median values (**Table I**). If the uncertainty in measurement is randomly distributed about the average, we would expect the mean (average) and median values to be the same. Differences between them indicate the influence of skew in the sampled materials, typically arising from:

- Physical limitations on the boxes in the data set (e.g., there is a limit to how small a box dimension can be), leading to an uneven distribution of box sizes and strengths given that boxes in commerce are not evenly distributed (e.g., most boxes tend to be specific sizes to facilitate palletization).
- Variation of a physical property, part of which is of fixed size (e.g., due to test equipment) and part proportional to the magnitude of the measurement.
- Property changes through converting (e.g., crush increases COV for most properties), and the data set has an uneven distribution of damaged boxes.

	Perimeter	Caliper	RMS Bending	BCT
Mean	0.50%	1.09%	10.73%	4.51%
Median	0.48%	0.78%	8.35%	4.30%

RMS = root mean square; BCT = top-to-bottom compression strength test.

I. Average percentage variation (COV, the standard deviation of the measurement divided by the value) for physical properties used in box modeling across the 118 boxes in the data set.

	Waxed (A)	Unwaxed (B)	Clamped (C)	Wax in Clamp (E)
Mean	4.35%	4.97%	4.68%	4.23%
Median	4.07%	4.70%	4.13%	3.93%

II. Average percentage variation (COV) for the four edge crush test (ECT) methods studied across the 118 boxes in the data set.

We see this skew at some level in most physical properties, indicating that the measurement variations incorporated in this study are not uniformly distributed. In practice, for most parameters, we have a limited number of samples with particularly large COVs that shift the mean value somewhat from the median.

Despite all the challenges around sample preparation [11], the waxed ECT methods (A and E) have the lowest level of variation (COV, **Table II**) in our data. The mean values for methods A, C, and E are statistically similar, with overlapping confidence intervals. The values for methods B and C are also statistically similar to each other. We would expect ECT values with similar levels of variation to result in BCT estimations with similar levels of variation if the methods captured failure mechanics in the same way. We might also expect the lowest level of variation to produce the best fit. The difference between the mean and median values implies that something in each testing approach increases the measurement variation for a subset of the samples, skewing the distribution. As discussed previously, we intentionally selected samples to challenge each method and potentially enhance this skew. The larger the difference, the more significant it is across the population.

MODELS

The literature contains a wide range of closed form models for box compression strength [1,2,7,34-37]. For this study, we report on fits for just a few empirical models with their roots in first-principle mechanics, recognizing that even this simple modeling approach, based on a few measured parameters, remains challenged and challenging [38].

As a baseline, we start with the most common simplified form of the McKee equation [1]:

$$BCT = a * ECT * (c * p)^{\frac{1}{2}} \quad (1)$$

which relies on parameters relatively easily (and commonly) measured in a box plant: caliper (c) and box perimeter (p). Parameter a is a free fitting constant resulting from fitting the general model and is unique to each particular ECT test approach in combination with caliper and perimeter. McKee et al. arrived at this equation from their fundamental functional form (Eq. 3 below) by observing a relationship between ECT and caliper on the one hand and bending stiffness on the other, and by then rounding their exponent to simplify the calculations.

It is straightforward to approximate the expected variation in the calculated BCT based simply on the variation in each of the input parameters [33]. We can approach this in two ways: either by calculating the expected variation overall based on the mean value for the variation in each test (using the data from Tables I and II), or by using the same methodology to calculate the expected uncertainty for each box in the data set and then averaging those values. As we would expect from the differences in the means and medians in Tables I and II, the first approach should provide a slightly lower value for the COV estimate, because the high-end tail of the distribution for each property disappears when looking just at the averages. The advantage of using the average of the estimates for each box is that we can then also calculate a confidence interval on that estimate if we assume that the distributions are reasonably normal. We find, as expected, that the estimates based on the average value for each physical property included in the model are within the confidence interval calculated from the averages of each individual item in the data set (**Table III**). The confidence intervals in Table III also provide a sense of scale for when differences between two values, for example models generated using different ECT methods, become meaningful. As would be expected given the principles of error propagation, where we propagate the variances (squares of the COVs) of the inputs through the model to estimate the uncertainty of the output (BCT), the ECT methods with higher variation produce estimates of box compression strength that have higher COVs and wider confidence intervals around their estimates. Note that for the three established formal test methods (A, B, and C), the confidence interval is tightest and the average is lowest for method A, ECT on edge-waxed specimens.

The values in Table III are estimated average variance ranges between the actual BCT measured and what we would predict from the best fit of the data to Eq. 1. Differences arise entirely because of the measurement variations in the input parameters. We can compare these to the actual sum-squared error values for the best fit model to the functional form. (Other methods, including minimizing the absolute average error, the percent error, etc., provide qualitatively similar results with similar trends and are not discussed further here.) Each modeling approach and each method of measuring ECT generates a different value for parameter a, none of which match the value in the literature, which is unsurprising given prior literature summaries of data from multiple sources [7]. This highlights the importance of the specific data set in setting model parameters and the challenge of finding a universal equation to fit all data across the industry.

Where the actual model error (these sum-squared errors) is similar to what we would expect based on the propagated variation from average properties, we might assume that the model is capturing the physics to the best of its ability and all our model error is based primarily or entirely on measurement noise. In that case, the total uncertainty/error/noise in the model estimate can be attributed to variation in the input measurements. However, where the actual error of the best fit model is notably higher than what we would expect based on measurement noise, that implies there is an additional factor causing the deviation. The resulting model does not estimate as well as we would expect, because it is missing something in the physics or mechanics accounted for by the measurements.

	Waxed (A)	Unwaxed (B)	Clamped (C)	Wax in Clamp (E)
Estimate of the average COV (Eq. 1)	7.7%	8.4%	8.1%	7.5%
Average of the estimated COV (Eq. 1)	7.9%	8.7%	8.4%	7.8%
CI on estimated COV (Eq. 1)	0.4%	0.6%	0.6%	0.4%

III. Calculated variations in the estimates for BCT using two different approaches (see text) based on Eq. 1. Estimate of the average coefficient of variation (COV) is based on the mean variation in the input properties, while the average of the estimated COVs is the average of the calculations done for each individual box, with the confidence interval (CI) calculated for that average.

	Waxed (A)	Unwaxed (B)	Clamped (C)	Wax in Clamp (E)
Model sum-squared error	7.9%	10.8%	8.8%	7.7%
Model error-variation estimate	0.2%	2.4%	0.7 %	0.2%

IV. Best fit model variation based on Eq. 1, and comparison of the best fit model variation to the estimate of the average COV (Table III).

As anticipated from the level of variation in the tests themselves, when examining the existing test methods (A, B, C), the best fit model (with the lowest average difference between the estimated and actual BCT) in either approach occurs when we use method A, the waxed ECT test (**Table IV**). These models minimize the sum-squared deviation between the predictions based on the input parameters and the actual box strengths, calculated independently for each ECT method, and thus produce different values for the parameter a for each ECT method. The difference between the average of the best fit model and what we would expect from measurement variation is very close to zero for the fit generated using method A, and is within the confidence interval of the calculation of the expected variation based on the variation in the measurements themselves (Table III). By contrast, methods B and C have differences that are larger than the confidence intervals in the variations of the modeling fits and that are substantial relative to the values themselves. Put another way, while the clamp method (C) should provide an estimate of similar quality to that provided by the waxed method based on variation in the tests themselves, it does not. This implies that across the full set of 118 sampled materials, the ECT method does not capture the inherent material strength correctly for its need in the function form of the McKee equation (Eq. 1). While the unwaxed method (B) has more inherent variation, the deviation even from that higher variation is quite significant. Thus, the failure modes of specimens in these tests do not relate as well to box failure dynamics as the failure mode in the wax test (A).

In Tables II-IV, we have also included method E, where the specimen is waxed before clamping. The mean variation in that testing approach is similar to, but even lower, than that in the original wax test (method A). Subsequent calculations of the COV expected from the model (Table III) and actually found in the best fit model (Table IV) are slightly more accurate than method A. Since method E uses the same clamping fixture as method C, we might conclude that the problem with the clamp method is not the loading dynamics of the clamping mechanism itself. Rather, it likely arises because of the clamping pressure discussed previously and in the literature, which further damages any material that might be crushed from processing, artificially lowering the ECT value (Fig. 1). The crushed samples included among the 118 boxes in the data set highlight this problem. If we wanted to fix this approach, we could look to hardness [39-41] and identify the compressive forces a sample can support in its thickness direction at the hardness peak. We might then adjust our spring force so that the force applied even to a damaged specimen remains below the load the sample can support at the hardness deflection, even in the case of damaged samples. This might be fruitful for future exploration, if we can find a way to adjust the method to reduce the COV and better align behavior under crushing with the TAPPI T 811 results. By contrast, it is not clear how we could adjust method B to bring the failure mode in line. Those samples often fail by curling of the papers at the loaded edges, a load resistance mechanism clearly distinct from compression of papers or combined board. There are no opportunities for edge curl in the failure process of a box, and thus method B appears out of line with the failure mechanism captured in the structure of the model (Eq. 1).

While bending stiffness is not typically measured at a box plant, we included it in our testing in order to also examine the simplified model that incorporates bending:

$$BCT = a * ECT^{3/4}(RMSBending)^{1/4}p^{1/2} \quad (2)$$

as well as McKee's original model based on fundamental mechanics, with assumptions to enable closed form calculation:

$$BCT = a * ECT^{b} * (RMSBending)^{1-b} * p^{2b-1} \quad (3)$$

The RMS bending stiffness testing has a much higher variation than caliper measurements (Table I), and we might expect as a result that the variation in BCT calculation would thus be higher. However, Eqs. 2 and 3 have a correspondingly smaller impact from the variation in the ECT measurement, as well as lower contributions from bending variation than from caliper variation, and the overall estimate of COV is lower for Eq. 2 than for Eq. 1 (**Table V**). (For more detail on this calculation, see [33].) As with our fits to Eq. 1, in fitting Eq. 2 each ECT method was used in an independent calculation to find a best fit model and estimate of COV, resulting in different parameters for a and b for each method. We find that the best fit models using each of the ECT testing methods in Eq. 2 are more accurate, with lower variations, when we use

	Waxed (A)	Unwaxed (B)	Clamped (C)	Wax in Clamp (E)
Estimate of the average COV (Eq. 2)	7.5%	7.9%	7.7%	7.4%
Model sum-squared error (Eq. 2)	7.6%	9.7%	8.3%	7.4%
Model sum-squared error (Eq. 3)	7.6%	9.2%	8.2%	7.3%

V. Calculated variations in the estimates for BCT (based on mean values of testing variation), measured variation of BCT for Eq. 2, and measured variation in BCT for Eq. 3.

bending stiffness data instead of board caliper. Bending stiffness clearly does a better job at capturing the physics of failure than board caliper. While caliper "captures" the mass distribution of the liners in the board as a first order assessment of the moment of inertia of the material, measured bending stiffness more thoroughly captures the multiple contributions to material rigidity. Though we cannot get a clean, closed-form estimate of the propagated variation from the testing process for the full McKee equation (Eq. 3), we find further improvement in model quality. However, even with Eq. 3, the difference between the actual model error and the error estimate based on propagation of the error of the respective tests is larger than the confidence interval around the calculation for ECT method B.

We also examined the much more complex model developed by Urbanik and Frank [7] that, by removing the assumptions of McKee et al., better captures the mechanics at failure, especially for boxes that are particularly deep, shallow, or of significant aspect ratio. However, few of the boxes in this data set had aspect ratios substantially above two, few were particularly deep compared to the size of their panels, and fewer than 5% were expected to fail in a completely inelastic mode. Thus, the added physics captured by the more fundamental approach did not meaningfully impact the overall results, and in particular, did not provide additional insight on the contribution of the failure mechanism of the ECT test itself to the assessment of box performance.

Different methods of attempting to measure a given physical property do not necessarily provide the same level of model robustness, particularly (as we see here) when it comes to assessing inherent material strength (ECT). Much of the effort over the years has focused on adjusting the functional form (for a closed form model) or modeling approach (e.g., finite element analysis [FEA]) to create an assessment method that better represents the data, whether gathered from a single testing facility, as in the present study, or across multiple sources. These various approaches are all empirical, typically from first-principle mechanics, but with missing components that might explicitly account for unbalanced structures, torsional stiffness [42,43], or other factors. Model inaccuracy is usually attributed to the lack of completeness of the approach. Here, we see confirmation [33] that the impact of variation in our measurements themselves can be, and often is, the limiting factor on model quality. No amount of computer-aided mechanical modeling or adding more parameters to a closed form model can overcome the variation in the parameters we are using. As we strive to do a better job estimating package performance, we need to improve all the physical assessments we all rely on, particularly for the intrinsic compressive strength, reducing their inherent variability to the limit of what is possible given the nature of our materials.

CONCLUSIONS

Testing variation plays a critical role in our ability to develop robust models. The less variation we have, the better we know the values measured and the more precise our models will be. The best models would be on target and have a relatively low window of uncertainty around them. The BCT estimations based on the traditional waxed ECT test (TAPPI T 811) have lower variation than the other standard test methods examined. This test allows us to produce the most precise models, where the limits on modeling accuracy are almost entirely accounted for by variation in the underlying physical tests. By contrast, the average BCT estimation error when using other common ECT methods is larger than what we would calculate based on the testing variation alone, indicating a systematic problem with the relationship between the underlying test methods and the model's functional form. Using a waxed sample in the clamping fixture identifies the clamping pressure itself as the source of additional uncertainty/inaccuracy in the resulting models using the clamp test, and highlights edge curl as the likely source of added inaccuracy from unwaxed methods. These insights point to additional approaches we might take in the development of even better assessments of the inherent material strength of corrugated board. **TJ**

APPENDIX

The dimensional and physical property data on each box set were examined in this study, collected from the boxes themselves and incorporating printed and unprinted areas in rough proportion to the level of print on the boxes. See pages 428-433 for this data.

LITERATURE CITED

1. McKee, R.C., Gander, J.W., and Wachuta, J.R., *Paperboard Packag.* 48(8): 149(1963).
2. Frank, B., *Packag. Technol. Sci.* 27(2): 105(2014). https://doi.org/10.1002/pts.2019.
3. Fadiji, T., Coetzee, C.J., Berry, T.M., et al., *Biosyst. Eng.* 174: 20(2018). https://doi.org/10.1016/j.biosystemseng.2018.06.015.
4. Mrówczyński, D., Knitter-Piątkowska, A., and Garbowski, T., *Materials* 15(3): 720(2022). https://doi.org/10.3390/ma15030720.
5. Park, J., Park, M., Choi, D.S., et al., *Appl. Sci.* 10(19): 6716(2020). https://doi.org/10.3390/app10196716.
6. Batelka, J.J., *Corrugating Int.* 2(4): 163(2000).
7. Urbanik, T.J. and Frank, B., *Wood Fiber Sci.* 38(3): 399(2006).
8. FBA, *Edge Crush Test: Application and Reference Guide for Combined Board*, Fiber Box Association, Itasca, IL, USA, 2011.
9. Kroeschell, W.O., *Tappi J.* 67(10): 56(1984).
10. Eriksson, L., "A review of the edge crush test," *Boxboard Containers*, March 1979.
11. Loza, J., Cash, D., and Frank, B., *TAPPI J.* 17(4): 219(2018). https://doi.org/10.32964/TJ17.04.219.
12. Frank, B., "Revisiting clamped ECT," *Corrugating Int.*, Summer 2007, p. 7.
13. ISO 3037, "Corrugated fibreboard — Determination of edge-wise crush resistance (unwaxed edge method)," Introduction, International Standards Organization, Geneva.
14. Ernst, U. and Graf, E., *Papier* 45(9): 549(1991).
15. Frank, B., "Which ECT?," *Corrugating Int.*, August 2003, p. 3.
16. IPC, "An investigation of testing methods for determination of the ultimate edgewise compression behavior of corrugated board. Part VI. A comparison of various test methods on commercially-made corrugated board," IPC Project 1940-4, Institute of Paper Chemistry, Appleton, WI, USA, June 1962.
17. Schrampfer, K.E. and Whitsitt, W.J., *Tappi J.* 71(10): 65(1988).
18. Frank, B., *Corrugated Today* 2(3): 52(2006).
19. Popil, R.E., *BioResources* 7(2): 2553(2012). https://doi.org/10.15376/biores.7.2.2553-2581.
20. Dimitrov, K. and Heydenrych, M., *South. For.* 71(3): 227(2009). https://doi.org/10.2989/SF.2009.71.3.7.919.
21. Bormett, D.W., "Predicting edgewise compressive strength," *Boxboard Containers*, November 1986.
22. Du Plooy, A.B.J., "Edgewise compression strength of corrugated board," in *CSIR Special Report*, HOUT 462, National Timber Research Institute, Council for Scientific and Industrial Research (South Africa), Pretoria, 1987.
23. Stott, R.A., *Appita* 29(1): 29(1975).
24. Stott, R.A., *Tappi J.* 71(1): 57(1988).
25. Koning, J.W., *Tappi J.* 71(10): 62(1988).
26. Urbanik, T.J., *Tappi J.* 73(10): 263(1990).

ABOUT THIS PAPER

Cite this article as:
Frank, B. and Cash, D., *TAPPI J.* 21(8): 418(2022).
https://doi.org/10.32964/TJ21.8.418

DOI: https://doi.org/10.32964/TJ21.8.418

ISSN: 0734-1415

Publisher: TAPPI Press

Copyright: ©TAPPI Press 2022

About this journal

ABOUT THE AUTHORS

Across the industry, we still wrestle with the different ECT methods in use. It can be hard to explain to customers what their differences are and why. This study was our effort to better understand and resolve the challenge, and it builds on our previous work around box compression modeling and test method assessment. In many ways, it pulls those efforts together.

Generating a robust data set was challenging and time consuming. Many of the prior research articles on this topic came out of efforts to understand the input data parameters and generation process.

Through this study, we discovered many things, including how important it is to define up front what we intend to achieve when developing a test method. It can be very hard to clarify or "clean up" discrepancies once the test methods are in active use. Our most interesting finding was that the original ECT method seems to be the most robust of those in common practice.

Box plants and their customers can benefit by understanding the methods we use in the industry, and by basing discussions regarding specifications on a solid foundation. Our next step is to figure out how to further reduce variation in our systems so that we can continue to improve models and predictive approaches.

Frank is director of Materials Research and Innovation for Packaging Corporation of America in Mundelein, IL, USA. Cash is senior data analyst with Norvax LLC in Chicago, IL, USA. Email Frank at bfrank@packagingcorp.com.



Frank



Cash

27. Garbowski, T., Knitter-Piatkowska, A., and Marek, A., *Materials* 14(19): 5768(2021). https://doi.org/10.3390/ma14195768.
28. Anon., "TAPPI FISCOTEC Committee meeting minutes," TAPPI, Atlanta, 6 April 2011. Available [Online] https://www.tappi.org/content/040611M-FISCOTEC-Committee-with-AppendixA-BCT-Parallelism.pdf <03Aug2022>.
29. Frank, B., "Caliper or weighted caliper for evaluating boxes," *Corrugating Int.*, October 2004, p. 3.
30. Cash, D. and Frank, B., *TAPPI J.* 19(8): 419(2020). https://doi.org/10.32964/TJ19.8.419.
31. Koning, J.W., *Tappi J.* 69(1): 74(1986).
32. Wilson, C.J. and Frank, B., *TAPPI J.* 8(6): 24(2009). https://doi.org/10.32964/TJ8.6.24.
33. Frank, B. and Kruger, K., *TAPPI J.* 20(4): 231(2021). https://doi.org/10.32964/TJ20.4.231.
34. Wolf, M., *Package Eng.* 7(3): 66(1972).
35. Shick, P.E. and Chari, N.C.S., *Tappi* 48(7): 423(1965).
36. Challas, J., Schaepe, M., and Smith, C.N., "Predicting package compression strength geometry effect," IPST Project 3806, Final Report, Institute of Paper Science and Technology, Georgia Institute of Technology, Atlanta, 1994.
37. Maltenfort, G.G., Ed., *Performance and Evaluation of Shipping Containers*, Jelmar Publishing, Plainview, NY, USA, 1989.
38. Coffin, D., *TAPPI J.* 14(8): 537(2015).
39. Fürst, T. and Gerards, P., *Rev. ATIP* 70(2): 15(2016).
40. Cash, D. and Frank, B., *TAPPI J.* 18(3): 161(2019). https://doi.org/10.32964/TJ18.3.161.
41. Anon., "CEPI Containerboard takes a new approach to standardization," *Nachhaltige Papierwirtschaft (Fibers in Progress)*, 14 February 2017. Available [Online] https://bit.ly/3zWxZ4u [from German] <04Aug2022>.
42. Chalmers I.R., *Appita J.* 59(5): 357(2006).
43. Popil, R.E., Coffin, D.W., and Habeger, C.C., *Appita J.* 61(4): 307(2008).

CORRUGATED BOXES

	Inside Dimensions			Caliper (n=10)		ECT Method (lb/in.)							
						TAPPI T 811 (n=10)		TAPPI T 839 (n=10)		TAPPI T 839 Waxed (n=10)		FEFCO (n=10)	
Sample #	L	W	D	Avg	STD	Avg	STD	Avg	STD	Avg	STD	Avg	STD
1	12 5/8	9 1/4	7 7/8	159.46	1.60	39.10	1.51	43.89	2.13	44.82	2.38	27.64	2.15
2	12 3/4	8 5/8	12	161.77	4.50	49.80	1.55	43.49	2.27	48.85	2.27	32.94	0.82
3	18 1/4	12 1/8	6 1/4	163.54	1.73	51.91	3.92	54.04	0.65	54.59	2.16	37.49	2.46
4	16 5/8	7	12	155.67	2.92	46.40	1.64	54.02	2.34	54.19	1.74	34.69	1.55
5	17	14 1/4	11 3/8	148.69	4.29	33.83	1.48	34.68	3.03	35.71	2.29	26.65	1.25
6	13 1/2	11 7/8	9 7/8	160.41	7.59	63.49	2.60	65.53	3.66	62.41	3.71	50.86	2.87
7	12 1/4	9 1/2	5 1/4	158.21	0.55	37.97	1.47	40.15	2.69	39.71	2.16	28.19	1.87
8	18 1/4	9 1/8	8 1/4	112.19	3.43	35.84	3.65	37.64	1.81	40.04	1.98	31.48	2.30
9	19 3/8	12 3/4	9 3/4	120.25	0.31	42.08	1.66	45.20	1.87	43.92	1.98	33.34	0.82
10	12 1/8	12	6 1/4	161.06	0.43	50.23	1.79	51.77	2.16	52.41	1.99	36.80	2.01
11	15 5/8	12 3/4	9 1/2	171.37	0.55	67.07	2.61	66.99	2.11	69.96	2.16	47.98	2.22
12	15 3/4	7 3/8	8 1/2	160.61	1.13	40.37	1.52	42.86	0.90	41.83	2.11	28.41	1.36
13	15 1/2	9 3/4	12 1/2	150.78	0.82	27.40	1.50	28.12	1.13	29.13	1.38	22.48	1.66
14	13	11 7/8	14	150.45	2.33	34.96	1.85	39.05	1.24	40.55	1.85	27.34	1.23
15	16 1/2	12 3/4	12 7/8	155.01	1.40	38.71	1.82	40.04	1.63	41.61	2.10	27.63	1.45
16	12 1/8	12	8 1/4	157.42	1.08	40.40	1.19	41.90	1.51	41.76	1.04	29.59	1.85
17	7 1/4	7	7 7/8	116.01	3.31	40.99	2.74	45.26	2.08	44.75	4.07	32.23	1.66
18	10 3/8	6 1/2	10	152.45	4.83	39.30	1.68	38.08	1.89	39.76	1.92	27.48	2.27
19	9	7 3/8	9 1/4	154.49	4.48	33.99	1.65	31.26	4.00	35.75	2.28	24.80	1.71
20	13 1/8	11 1/8	6 3/8	156.30	2.91	45.36	2.73	50.31	2.14	52.48	2.72	34.36	3.67
21	12 1/2	10 1/2	7 1/4	159.25	2.40	42.07	1.89	48.16	2.21	49.82	1.67	32.15	1.02
22	13 7/8	10 7/8	6 5/8	174.04	0.96	65.95	2.14	67.15	2.72	71.20	2.42	45.86	1.90
23	18	7 1/4	11 3/4	150.73	0.86	38.60	1.68	40.70	1.37	39.41	3.12	30.77	1.33
24	17 1/2	9 3/4	9 1/8	151.40	1.44	40.66	1.69	39.86	1.85	42.92	1.30	28.79	0.68
25	16 1/8	12 1/8	10 3/8	160.58	0.32	54.55	1.14	54.30	3.03	57.55	1.93	40.67	0.83
26	16 1/8	12 1/4	10 3/8	155.75	2.15	48.63	1.05	50.97	1.51	49.60	2.00	34.23	1.44
27	16 1/8	12 1/8	10 3/8	161.35	0.95	56.68	2.78	57.08	3.28	60.43	2.83	40.08	2.38
28	16 1/8	12 1/8	10 3/8	162.14	2.22	55.30	1.50	57.27	1.99	56.36	2.62	44.74	1.43
29	16 1/4	12 1/4	10 3/8	151.71	1.62	42.79	1.69	43.28	1.75	43.66	1.70	30.74	2.45
30	16 1/8	12 1/8	10 3/8	156.90	0.71	47.44	1.53	47.39	2.57	47.34	2.70	37.15	1.52
31	16 1/8	12 1/8	10 3/8	164.72	0.90	60.08	2.40	62.12	1.09	57.05	3.55	41.77	3.72
32	16 1/8	12 1/8	10 3/8	160.01	0.62	48.69	1.84	52.99	1.65	52.86	1.70	38.65	2.26
33	16 1/4	12 1/8	10 3/8	167.42	0.33	63.66	1.29	64.98	2.33	64.84	2.81	44.59	2.96
34	15 1/2	7 1/2	7 1/2	153.50	1.38	36.52	1.50	36.95	1.56	37.21	1.41	27.13	1.27
35	15 5/8	11 3/4	10 1/8	154.99	1.75	37.56	1.72	36.45	2.13	38.69	1.22	28.03	1.33
36	15 1/2	7 1/2	7 1/2	154.60	1.60	39.20	1.55	37.37	2.16	38.22	1.45	30.18	1.51
37	15 5/8	11 3/4	10 1/8	157.01	2.22	39.11	1.41	38.17	2.05	39.15	1.02	27.49	1.54
38	14 1/8	10 1/8	10 3/8	157.90	1.40	39.90	1.80	40.80	2.80	43.05	2.17	28.40	2.10
39	14 1/8	10 1/8	10 3/8	156.50	3.10	41.80	1.80	41.90	2.20	43.88	2.72	31.70	2.30
40	12	9 1/8	9 1/4	155.18	1.19	40.84	1.52	41.64	1.85	38.51	1.80	32.11	1.92

	Bending Stiffness 200mm (actual or scaled)						BCT (lb) (n=10)		Deformation (in.) (n=10)	
	CD Bend (Nm) (n=10)		MD Bend (Nm) (n=10)		RMS Bending (lb-in.) (n=10)					
Sample #	Avg	STD	Avg	STD	Avg	STD	Avg	STD	Avg	STD
1	6.25	0.38	10.50	0.59	71.67	5.93	571	29	0.393	0.016
2	8.43	0.52	11.84	1.76	88.44	14.20	706	16	0.404	0.019
3	9.15	1.74	16.31	3.77	102.28	24.24	1050	49	0.437	0.012
4	7.65	0.25	13.71	0.92	90.64	6.80	687	36	0.436	0.034
5	5.17	0.21	9.62	0.45	62.42	3.90	497	26	0.302	0.022
6	6.84	0.20	15.93	1.18	92.36	7.36	901	61	0.423	0.008
7	6.16	1.17	7.51	1.48	54.63	8.36	681	24	0.352	0.012
8	3.07	0.09	4.64	0.22	33.40	1.86	480	11	0.279	0.010
9	4.92	0.12	5.74	0.39	47.00	3.37	600	35	0.296	0.008
10	6.48	1.38	12.38	2.10	73.37	12.82	770	14	0.446	0.015
11	11.14	0.29	17.81	0.56	124.66	5.08	1100	40	0.543	0.011
12	6.86	0.36	14.74	1.19	88.97	8.54	620	21	0.365	0.010
13	3.47	0.16	6.71	0.85	42.69	5.74	407	25	0.378	0.011
14	5.66	0.22	9.10	0.45	63.50	3.98	585	28	0.371	0.014
15	5.77	0.16	12.80	0.89	76.04	5.69	586	27	0.409	0.010
16	6.62	0.33	10.19	0.96	72.72	7.79	522	30	0.374	0.015
17	3.36	0.92	7.02	1.61	36.94	6.63	395	22	0.281	0.019
18	5.52	0.14	11.53	1.22	70.58	7.71	487	31	0.355	0.066
19	4.66	0.16	9.85	1.07	59.92	6.87	387	17	0.344	0.037
20	6.64	0.30	12.07	1.00	79.24	7.49	593	29	0.404	0.006
21	6.95	1.05	10.75	1.79	70.77	9.20	619	23	0.417	0.010
22	11.64	0.66	25.15	1.14	151.41	10.98	1110	45	0.497	0.010
23	5.96	0.19	9.45	0.32	66.40	3.08	614	33	0.361	0.014
24	5.74	0.15	8.89	0.28	63.25	2.59	512	27	0.407	0.013
25	8.56	0.24	12.31	0.69	90.85	5.71	878	48	0.512	0.012
26	7.95	0.31	11.88	1.44	86.04	10.98	802	51	0.479	0.011
27	9.82	0.33	15.09	0.72	107.69	6.28	934	93	0.522	0.021
28	8.66	0.20	12.71	0.81	92.84	6.25	941	50	0.508	0.016
29	7.24	0.22	8.61	0.47	69.86	4.37	765	52	0.454	0.012
30	8.03	0.39	9.98	0.45	79.23	5.26	823	26	0.493	0.010
31	10.26	0.43	14.87	0.25	109.30	4.95	864	69	0.501	0.008
32	8.28	0.24	9.78	0.57	79.65	5.15	869	21	0.493	0.008
33	10.59	0.30	16.06	0.78	115.39	6.51	1163	75	0.538	0.008
34	5.32	1.28	9.90	1.45	58.36	9.27	463	9	0.338	0.012
35	5.95	0.57	10.13	0.64	68.71	7.84	526	13	0.312	0.009
36	5.03	1.19	13.92	3.04	67.62	14.71	477	15	0.354	0.012
37	5.49	0.31	13.79	0.46	76.98	5.07	523	11	0.335	0.014
38	5.60	0.20	10.76	0.75	68.71	5.38	548	8	0.380	0.020
39	5.57	0.23	11.02	0.75	69.37	5.56	580	18	0.380	0.010
40	5.95	0.09	10.70	0.76	70.59	5.13	540	22	0.376	0.009

CORRUGATED BOXES

	Inside Dimensions			Caliper (n=10)		ECT Method (lb/in.)							
						TAPPI T 811 (n=10)		TAPPI T 839 (n=10)		TAPPI T 839 Waxed (n=10)		FEFCO (n=10)	
Sample #	L	W	D	Avg	STD	Avg	STD	Avg	STD	Avg	STD	Avg	STD
41	12 1/8	8 1/4	9 7/8	155.88	2.64	38.93	1.39	40.50	2.00	38.43	2.56	30.29	1.80
42	14 1/8	10	8 7/8	152.97	2.07	34.23	2.39	36.38	2.32	36.56	2.00	27.14	1.89
43	13 1/4	9 1/2	6 1/2	160.69	2.60	51.21	3.61	52.55	3.15	54.71	5.23	35.67	1.43
44	17 1/2	9 7/8	6 1/2	157.43	1.13	40.50	1.92	41.70	1.67	43.18	1.53	34.43	1.12
45	12	9 5/8	7 1/8	152.04	2.02	36.65	1.40	42.45	2.30	40.36	2.40	28.80	1.56
46	11 1/2	7 1/8	5 5/8	148.51	2.97	39.98	1.67	33.14	4.76	39.72	3.24	27.43	3.88
47	13 3/8	10	9	149.84	0.77	50.42	1.54	57.47	1.65	56.10	2.79	41.11	2.12
48	7 7/8	7	10	148.66	4.31	50.86	2.25	51.59	2.95	56.05	2.44	38.22	1.60
49	18 1/8	16 1/4	10 3/8	157.13	1.79	42.05	1.54	34.37	1.62	39.09	1.02	32.36	1.54
50	18 1/8	16 1/4	10 3/8	157.45	1.26	43.03	1.33	34.97	2.32	40.77	2.10	31.65	1.32
51	24	18 7/8	20 1/8	134.55	2.40	36.05	1.62	30.90	2.44	36.41	1.05	27.14	2.11
52	10 3/4	7 1/4	7 3/4	155.78	1.45	39.13	1.71	38.88	2.05	38.93	1.87	28.05	2.07
53	11 7/8	4 3/4	7	143.54	3.52	40.65	2.65	40.09	2.34	40.99	2.90	25.28	2.76
54	15 1/2	11 5/8	10 1/8	155.69	1.19	38.01	1.43	36.87	0.94	36.87	1.96	24.88	2.93
55	15 1/2	11 3/4	10 1/8	154.29	0.97	35.36	0.86	34.18	1.95	34.91	1.28	24.98	2.56
56	15 1/2	11 3/4	10 1/4	148.09	0.91	33.99	1.74	31.10	1.20	34.41	1.31	24.08	1.74
57	15 1/2	11 5/8	10 1/4	151.98	1.17	35.07	1.66	32.61	0.99	34.63	1.24	23.17	1.95
58	15 1/2	11 3/4	10 1/4	155.99	0.83	37.86	1.67	36.21	1.47	38.90	1.61	26.64	1.55
59	15 1/2	11 5/8	10 1/4	156.66	1.54	36.53	1.20	38.47	1.96	38.35	0.70	25.78	1.71
60	15 1/2	11 3/4	10 1/4	156.64	0.86	37.50	1.52	38.28	1.59	40.82	1.67	25.57	2.04
61	15 1/2	11 3/4	10 1/4	155.83	1.08	35.58	1.95	34.72	0.84	37.81	0.55	25.00	1.37
62	15 7/8	11 7/8	10 3/8	162.07	1.26	57.84	2.08	58.55	2.07	57.77	1.91	40.55	4.80
63	15 7/8	11 3/4	10 3/8	162.10	1.27	56.61	1.91	55.90	1.72	59.00	2.23	39.52	1.56
64	15 7/8	11 7/8	10 1/4	157.86	1.02	58.02	1.97	58.19	1.73	58.49	2.00	39.36	3.15
65	17 7/8	7 5/8	6 3/4	114.42	1.67	37.33	2.36	40.61	2.06	42.21	1.52	30.33	1.21
66	11 5/8	8 5/8	21 1/4	114.25	0.67	38.69	2.01	41.99	1.53	40.40	0.92	32.27	1.66
67	13	9 1/2	10 7/8	119.70	1.41	56.17	2.14	58.94	2.14	62.34	1.52	41.40	1.49
68	17 1/4	10 1/8	14	152.99	2.19	34.94	1.52	34.64	1.48	34.76	1.24	24.72	0.94
69	18 7/8	7 5/8	18 3/8	145.36	1.88	34.16	1.22	34.19	2.97	35.51	1.91	36.00	1.75
70	23 1/4	15 5/8	8 3/4	123.73	0.71	55.81	1.85	59.67	1.76	64.65	2.66	41.30	2.88
71	10 3/4	10 1/2	7	122.92	0.67	56.15	2.53	58.13	2.08	60.90	1.36	43.13	1.74
72	19 3/4	11 3/4	6 1/2	116.09	3.10	48.86	3.08	52.35	1.83	52.96	2.53	33.32	0.88
73	22 1/4	17 5/8	22 1/4	151.30	1.09	37.42	1.81	39.29	3.74	42.35	2.84	28.46	1.46
74	15 5/8	13 1/8	21 3/4	158.90	0.91	44.67	2.27	45.74	1.98	43.37	2.31	31.11	1.85
75	15 3/4	9 3/8	9 1/8	160.46	1.38	51.48	1.22	54.55	6.11	53.17	2.66	43.54	1.93
76	15 1/4	11	13 1/8	129.30	0.90	69.09	2.97	70.35	1.98	70.47	2.20	54.12	2.30
77	15 1/8	11	13 1/8	118.98	0.56	47.52	1.24	48.44	1.46	47.26	2.20	36.78	0.87
78	17	15 3/4	14 1/8	121.42	0.16	51.14	1.69	54.05	1.24	51.21	1.78	42.09	1.23
79	19 1/2	12 7/8	12 7/8	120.59	0.31	50.43	1.41	53.04	1.18	50.44	1.91	41.87	0.32
80	13 3/4	11 3/4	13 3/8	159.17	1.48	49.83	2.44	52.06	2.58	56.08	2.43	36.20	1.89

		Bending Stiffness 200mm (actual or scaled)						BCT (lb) (n=10)		Deformation (in.) (n=10)	
		CD Bend (Nm) (n=10)		MD Bend (Nm) (n=10)		RMS Bending (lb-in.) (n=10)					
	Sample #	Avg	STD	Avg	STD	Avg	STD	Avg	STD	Avg	STD
	41	6.18	0.16	11.02	0.93	73.05	6.42	516	36	0.375	0.011
	42	5.29	0.12	9.32	0.52	62.13	3.75	455	14	0.326	0.014
	43	9.36	2.00	14.38	2.53	96.95	20.03	763	23	0.369	0.014
	44	7.15	1.30	9.17	1.08	66.08	7.41	685	12	0.405	0.008
	45	6.19	1.20	10.82	2.21	72.43	20.41	569	20	0.301	0.014
	46	5.19	0.97	8.94	1.64	60.30	15.74	478	26	0.239	0.019
	47	7.67	0.41	13.12	0.88	88.80	7.66	721	32	0.436	0.012
	48	6.96	1.39	13.11	2.32	84.52	22.54	605	39	0.367	0.019
	49	5.52	0.45	12.34	0.79	73.03	7.52	615	61	0.365	0.032
	50	5.99	0.43	15.42	0.83	85.09	7.62	713	26	0.414	0.015
	51	4.89	0.13	8.40	0.70	56.71	4.94	681	54	0.360	0.030
	52	5.89	1.22	9.91	1.75	67.61	18.35	515	20	0.295	0.025
	53	6.11	1.19	9.49	1.67	67.42	17.75	462	9	0.246	0.010
	54	5.62	0.21	8.52	0.61	61.23	4.90	597	19	0.386	0.016
	55	5.67	0.16	8.05	0.76	59.79	5.88	594	39	0.383	0.013
	56	5.25	0.14	7.60	0.58	55.91	4.49	554	35	0.367	0.013
	57	5.91	0.20	7.69	1.22	59.70	9.64	579	25	0.377	0.014
	58	5.71	0.10	9.17	0.45	64.04	3.29	601	30	0.389	0.012
	59	5.92	0.17	8.31	1.06	62.10	8.09	598	33	0.394	0.014
	60	5.92	0.19	8.38	0.64	62.35	5.13	625	10	0.396	0.006
	61	5.76	0.27	8.55	0.63	62.12	5.40	598	27	0.389	0.010
	62	8.32	0.35	18.35	0.36	109.39	5.13	850	26	0.377	0.013
	63	8.49	0.24	14.49	0.58	98.13	4.83	1087	17	0.463	0.009
	64	7.50	0.31	16.98	0.40	99.89	4.76	1007	82	0.406	0.018
	65	4.59	1.15	5.62	1.01	44.95	13.87	409	20	0.258	0.054
	66	2.88	0.31	6.37	0.37	37.92	4.62	456	25	0.286	0.011
	67	4.91	0.54	8.11	0.74	55.85	7.95	675	17	0.370	0.009
	68	5.51	0.17	9.80	0.78	65.03	5.56	611	21	0.386	0.010
	69	5.35	0.29	9.33	0.24	62.56	3.78	490	34	0.307	0.022
	70	4.63	0.55	9.88	0.74	59.86	8.37	941	35	0.505	0.040
	71	5.52	1.35	10.83	1.34	68.47	18.76	709	36	0.307	0.015
	72	4.18	1.15	6.93	1.32	47.65	15.95	700	15	0.252	0.007
	73	6.16	0.15	8.62	0.73	64.47	5.66	721	45	0.434	0.024
	74	6.82	0.28	13.77	0.67	85.76	5.45	698	48	0.429	0.018
	75	7.49	0.23	12.72	0.50	86.38	4.33	758	39	0.466	0.010
	76	6.12	0.35	12.56	1.06	77.58	7.90	875	29	0.383	0.010
	77	3.14	0.27	8.05	0.39	44.51	4.43	618	25	0.336	0.012
	78	3.52	0.14	8.30	0.47	47.86	3.28	631	27	0.330	0.012
	79	3.36	0.12	8.42	0.53	47.08	3.39	671	24	0.349	0.012
	80	8.43	0.23	14.60	0.43	98.18	3.93	774	20	0.400	0.018

CORRUGATED BOXES

	Inside Dimensions			Caliper (n=10)		ECT Method (lb/in.)							
						TAPPI T 811 (n=10)		TAPPI T 839 (n=10)		TAPPI T 839 Waxed (n=10)		FEFCO (n=10)	
Sample #	L	W	D	Avg	STD	Avg	STD	Avg	STD	Avg	STD	Avg	STD
81	13 3/4	11 3/4	13 3/8	164.18	1.10	52.92	2.60	59.15	1.19	60.66	1.86	45.83	0.81
82	13 3/4	11 3/4	13 3/8	161.42	0.83	46.35	1.93	50.53	1.93	53.85	2.09	35.90	0.90
83	14 7/8	10 1/8	26 1/2	139.25	1.33	28.85	1.74	26.38	2.75	27.99	1.10	20.08	1.03
84	19 3/8	10 1/8	6 1/4	161.99	2.36	51.34	3.36	45.06	5.88	54.94	3.42	34.92	2.14
85	18 1/8	9	24 1/4	151.98	1.29	36.29	3.00	37.49	1.39	37.76	2.18	25.60	1.61
86	16 1/8	11 1/4	8 1/4	162.41	0.94	48.69	2.04	52.94	1.67	55.29	2.23	34.50	1.70
87	8 5/8	7 7/8	9 1/4	155.56	3.45	42.06	1.71	40.75	1.75	43.80	2.91	31.45	1.25
88	8 1/2	7 5/8	7 1/8	148.98	0.81	37.33	1.33	38.97	1.38	39.70	1.82	24.38	1.24
89	9 1/4	8	7 3/4	166.15	4.25	65.52	3.67	61.08	1.89	67.42	4.41	47.07	1.74
90	14 5/8	11 1/2	9 1/8	170.25	0.92	72.09	1.82	70.31	2.94	74.27	1.14	55.29	1.22
91	14 5/8	11 1/2	9 1/8	169.56	1.24	71.28	1.79	70.13	2.46	72.41	1.40	52.42	1.07
92	14 5/8	11 1/2	9 1/8	169.08	1.04	74.27	2.67	72.57	2.43	72.41	2.87	54.34	1.01
93	14 5/8	11 1/2	9 1/8	168.92	1.49	73.05	3.10	73.43	3.02	76.50	1.95	56.65	1.25
94	14 5/8	11 1/2	9 1/8	170.32	1.36	68.52	1.92	69.09	2.85	68.70	1.85	49.93	1.17
95	14 5/8	11 1/2	9 1/8	169.14	1.42	69.86	2.63	68.78	3.01	71.14	2.11	49.12	1.50
96	14 5/8	11 1/2	9 1/8	171.91	0.89	70.57	2.93	70.63	2.92	72.25	1.59	54.76	1.38
97	14 5/8	11 1/2	9 1/8	170.41	1.25	70.94	2.45	72.81	2.37	70.53	2.64	54.20	0.65
98	14 5/8	11 1/2	9 1/8	167.02	1.31	63.79	1.77	62.94	1.79	61.27	2.65	47.11	0.76
99	14 5/8	11 1/2	9 1/8	166.51	1.54	64.03	1.87	62.15	2.51	63.66	1.99	46.38	1.96
100	23	17 1/4	14 7/8	148.52	1.20	29.91	1.15	31.43	1.53	34.93	1.37	22.63	0.92
101	12 1/8	9	6	148.70	1.47	31.59	1.66	32.71	1.15	34.43	1.67	22.41	0.85
102	18	9 1/4	15 7/8	144.02	0.95	29.81	1.67	31.17	1.29	33.63	1.28	19.94	0.94
103	13 1/2	11	5	110.44	0.19	31.20	1.72	34.33	1.78	32.06	0.90	27.16	0.66
104	12 1/8	13 1/4	10 1/2	160.18	0.66	38.73	1.35	40.11	0.94	41.07	1.43	28.43	0.59
105	12 1/8	13 1/4	10 1/2	159.37	0.39	37.60	1.36	39.76	1.40	39.60	0.51	28.16	0.66
106	12 1/8	13 1/4	10 1/2	159.60	0.89	39.70	1.29	41.54	0.97	41.68	1.13	29.37	0.40
107	12 1/8	13 1/4	10 1/2	141.94	0.92	33.10	3.41	31.50	4.93	31.25	2.23	23.35	0.76
108	12 1/8	13 1/4	10 1/2	141.81	8.01	32.40	2.03	27.08	3.76	33.13	3.20	22.17	1.19
109	16 1/2	8	11	117.37	0.35	42.99	1.34	45.36	1.36	45.68	1.11	33.07	1.24
110	16 1/2	8	11	115.64	0.37	39.78	1.44	43.06	0.93	41.44	0.97	31.62	1.18
111	16 1/2	8	11	113.02	0.41	33.14	1.45	36.29	0.84	34.79	1.13	27.00	0.67
112	16 1/2	8	11	115.02	0.22	36.14	1.07	38.45	0.99	37.43	0.64	29.20	1.18
113	16 1/2	8	11	110.63	0.19	29.91	1.00	31.96	0.71	31.60	0.83	23.91	0.52
114	16 1/2	8	11	108.65	0.18	27.64	0.96	29.48	0.62	29.53	0.40	21.76	0.62
115	20 1/8	12 1/4	8 3/8	161.00	3.60	54.90	3.20	55.30	2.20	59.56	1.53	44.25	1.47
116	20 1/8	12 1/4	8 3/8	155.10	3.50	58.20	2.20	57.20	2.50	62.06	1.70	46.34	1.38
117	14	14	14	149.02	0.67	33.50	2.35	35.68	1.49	39.31	1.19	32.14	2.04
118	22	20 3/4	20	156.26	2.28	36.15	2.84	38.99	1.08	39.50	1.55	31.31	1.47

	Bending Stiffness 200mm (actual or scaled)						BCT (lb) (n=10)		Deformation (in.) (n=10)	
	CD Bend (Nm) (n=10)		MD Bend (Nm) (n=10)		RMS Bending (lb-in.) (n=10)					
Sample #	Avg	STD	Avg	STD	Avg	STD	Avg	STD	Avg	STD
81	8.91	0.27	15.37	0.60	103.57	5.12	897	42	0.432	0.012
82	7.80	0.40	13.75	0.56	91.65	5.99	708	25	0.359	0.016
83	3.54	0.10	7.32	0.22	45.09	1.87	393	26	0.340	0.020
84	4.69	1.05	13.01	1.70	69.13	17.96	976	30	0.401	0.019
85	6.00	0.22	10.05	0.25	68.73	3.07	590	38	0.340	0.010
86	8.46	0.32	13.58	0.70	94.86	6.04	994	28	0.472	0.015
87	6.11	0.99	9.66	1.73	67.97	16.42	479	16	0.414	0.053
88	5.40	1.01	9.50	1.50	63.37	15.56	460	18	0.304	0.026
89	10.61	1.30	17.10	2.36	119.23	21.98	829	24	0.386	0.007
90	10.70	0.74	24.50	1.38	143.31	12.83	1087	48	0.435	0.010
91	10.13	0.56	24.25	1.04	138.72	9.67	961	43	0.448	0.016
92	10.51	0.63	25.27	1.61	144.23	12.60	1038	60	0.440	0.014
93	10.53	0.65	23.71	1.38	139.86	11.87	996	59	0.428	0.010
94	10.47	0.83	23.30	1.91	138.20	15.79	970	34	0.444	0.011
95	10.91	0.80	21.46	2.00	135.38	16.08	922	44	0.434	0.009
96	10.59	0.54	25.23	1.13	144.68	9.78	1067	56	0.467	0.011
97	10.36	0.69	25.09	1.08	142.68	11.32	1016	41	0.464	0.010
98	9.67	0.43	23.46	1.14	133.27	8.79	972	58	0.423	0.012
99	9.90	0.46	22.86	1.35	133.13	10.01	947	48	0.422	0.011
100	4.45	0.12	9.17	0.51	56.50	3.45	665	30	0.373	0.008
101	5.61	1.34	10.92	0.67	69.29	17.14	506	11	0.310	0.020
102	4.56	0.16	8.33	0.68	54.55	4.84	484	21	0.318	0.013
103	7.44	1.64	2.75	0.22	40.05	9.36	418	18	0.236	0.022
104	6.73	0.44	12.57	0.44	81.39	6.00	688	26	0.396	0.012
105	6.25	0.23	11.77	0.49	75.90	4.22	716	18	0.415	0.016
106	6.39	0.18	12.33	0.26	78.55	2.78	769	19	0.415	0.013
107	4.80	0.62	9.93	1.26	61.08	11.00	512	15	0.328	0.008
108	4.96	0.11	9.77	0.98	61.60	6.35	496	24	0.349	0.019
109	3.28	0.03	5.37	0.15	37.12	1.08	546	16	0.234	0.008
110	3.17	0.12	5.05	0.14	35.40	1.66	510	22	0.211	0.009
111	2.47	0.04	4.56	0.14	29.69	1.03	409	20	0.210	0.012
112	2.57	0.04	4.67	0.09	30.65	0.79	431	10	0.195	0.009
113	2.22	0.05	4.24	0.09	27.16	0.85	362	15	0.183	0.013
114	2.16	0.17	4.28	0.15	26.93	2.27	347	18	0.183	0.019
115	14.82	0.54	9.74	0.30	106.34	5.06	1038	37	0.383	0.005
116	12.03	0.74	9.93	0.68	96.69	8.91	1008	24	0.364	0.007
117	9.32	0.42	4.92	0.17	59.90	3.42	599	46	0.355	0.022
118	12.04	0.75	7.03	0.46	81.43	7.31	598	71	0.372	0.021

Causes of poor dregs settling in a green liquor clarifier

TORSTEN MEYER, HEATHER MUNN, AND HONGHI TRAN

ABSTRACT: A study was conducted to examine the most likely parameters responsible for poor dregs settling at a kraft mill over a 2.5-year period, using multivariate data analysis (MVDA) and machine learning (ML) techniques. The dregs settling behavior seems to be seasonally influenced, implying that wood quality variation can be a factor. The results from the MVDA/ML analysis show that poor dregs settling is correlated to incomplete combustion and/or low load conditions in the recovery boiler, low sulfidity in the causticizing plant, and high flow in the green liquor–weak wash cycle. Compositions of dregs and black liquor were also examined to identify correlations with impaired dregs settling. The results show that poor dregs settling strongly correlates with high silicon (Si) content in dregs and moderately correlates with high iron (Fe) and high aluminum (Al) contents, and with low bulk density in dregs. For mills that experience dregs settling or green liquor filtering issues, regular compositional analyses of dregs, green liquor, weak wash, and black liquor are recommended in order to monitor the dynamics of silicon and other constituents in the recovery cycle.

Application: This paper provides evidence to support several reasons for poor dregs settling in a green liquor clarifier. The insights gained and the information provided may help mills that have been experiencing persistent dregs settling issues.

Poor dregs settling in green liquor clarifiers is a persistent problem in many kraft pulp mills. It makes green liquor and lime mud "dirtier," increases char and non-process element (NPE) contents in the lime mud, and results in impaired liquor and lime mud filtering.

While the root causes of poor dregs settling are not known, several possible reasons have been proposed. Empie et al. [1] reported that the presence of small magnesium hydroxide ($Mg(OH)_2$) particles caused poor dregs settling. Taylor [2] attributed the problem to the presence of an inorganic gelatinous material in the dregs with a high silicon-to-aluminum (Si-Al) molar ratio. This ratio was about 2:1 during normal settling, but increased to 5:1 during a poor settling period. The gel appeared to be an amorphous magnesium silicate with a density only slightly higher than that of the green liquor. Also, during normal settling periods, the dregs contained more lime mud and thus had a higher density, which helped improve settling. In a study on black liquor gasification, poor dregs settling was observed when the gasifier was operated at a low air-to-fuel ratio, leading to an increase in char content in the resulting smelt and the associated decrease in dregs density [3]. Lidén [4] suggested that explosive smelt–water interaction in the dissolving tank could break down char, produce fine particles, and thus deteriorate the settling behavior of the dregs in the clarifier. He also further suggested that mills that use magnesium sulfate ($MgSO_4$) in the oxygen delignification process may experience elevated magnesium levels in the black liquor, and as a result, deteriorated dregs settling.

A systematic study was conducted to investigate the root causes of poor dregs settling experienced in the causticizing plant at the Irving Pulp and Paper (IPP) mill in Saint John, NB, Canada, using both multivariate data analysis (MVDA) and machine learning (ML) analysis methods. The objective was to identify the most likely mill and recovery boiler operating parameters responsible for episodes of poor settling in a green liquor clarifier at IPP. This paper first discusses the mill experience and the methodology used in this work, as well as the key results and implications for mill operation.

EXPERIENCE AT IRVING PULP AND PAPER

The chemical recovery plant at IPP consists of an evaporation plant with six effects and a high-solids concentrator (HSC) that produces strong black liquor at 74% dry solids, a Babcock & Wilcox (Akron, OH, USA) recovery boiler that burns on average 3.9 million lb/day of virgin black liquor dry solids (BLDS), a causticizing plant, and a lime kiln. Soap is not separated from black liquor and is burned together with the liquor in the recovery boiler. The raw green liquor flows from the smelt dissolving tank to the surge tank, and then to the green liquor clarifier (**Fig. 1**). The underflow of the clarifier, containing the settled dregs, is pumped to the dregs centrifuge to concentrate the dregs content from 10% to 25%. The resulting dregs are washed and further dewatered on a pre-coat dregs filter.

At IPP, the settling performance of the dregs in the clarifier is measured daily using a conventional Imhoff cone test method. The method involves measuring the volume of solids in one liter of sample that settles to the bottom of

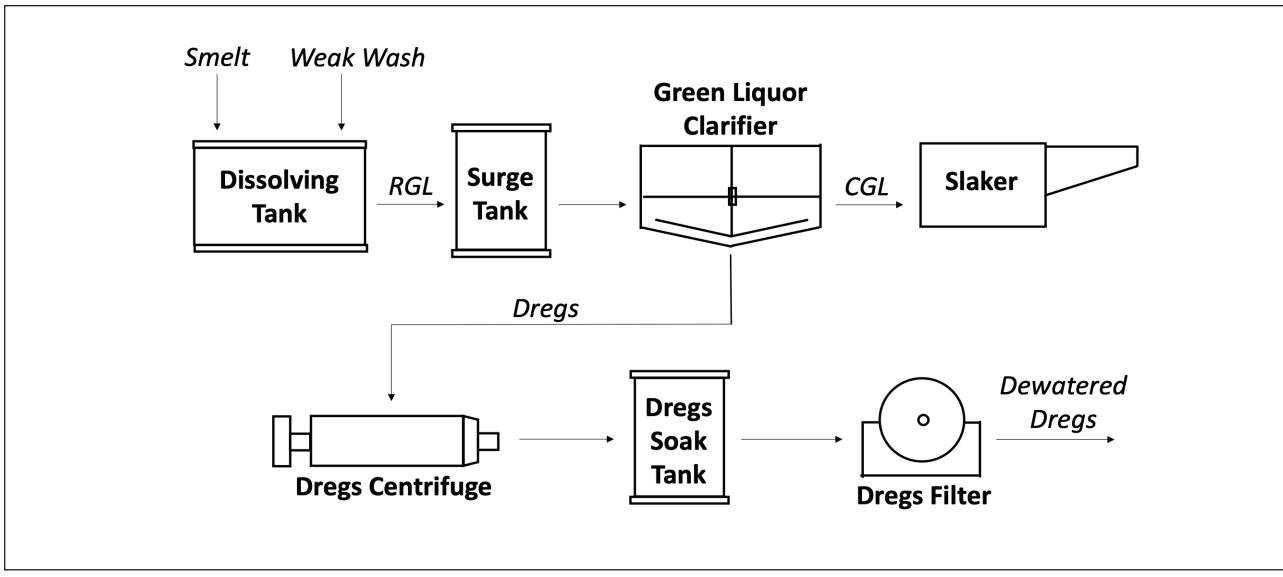

1. Process flow scheme (RGL = raw green liquor, CGL = clarified green liquor).

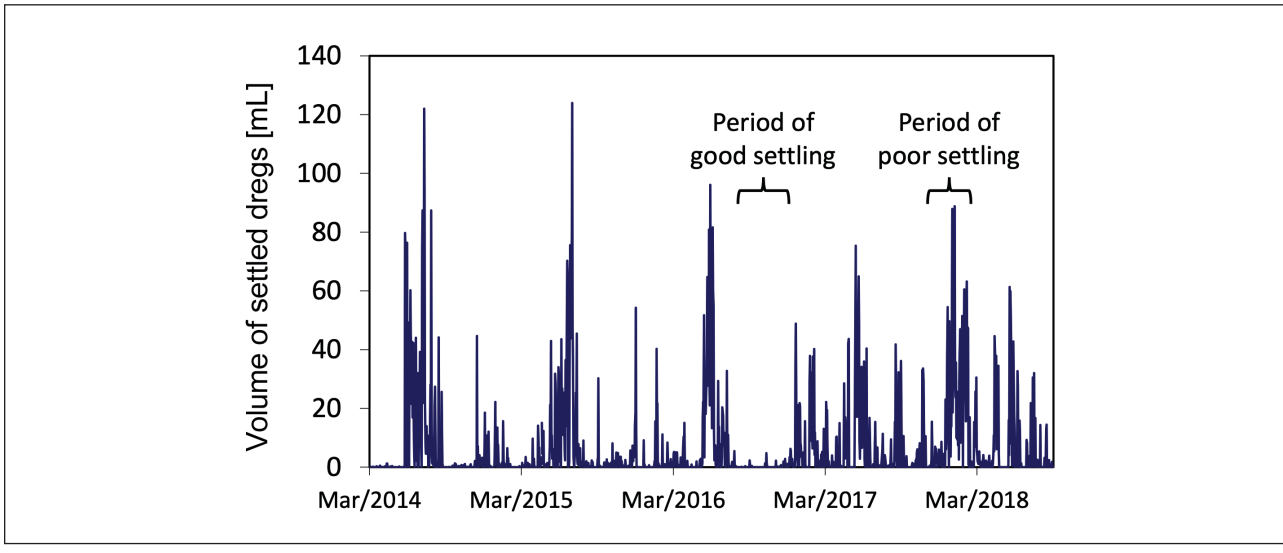

2. Performance of dregs settling in samples collected after the green liquor clarifier. High values mean poor settling.

the Imhoff cone during a specified time period. The samples are taken at the exit of the green liquor clarifier. If the volume of settled dregs is small, the settling performance is considered good. A large dregs volume indicates poor settling. **Figure 2** shows the dregs settling behavior in the green liquor clarifier over a 4.5-year period. The plot shows periods of good settling behavior (low volume of settled dregs) that lasted several months, as well as periods of poor settling (large volume of settled dregs) that lasted several weeks or months.

Poor dregs settling is usually accompanied with poor dregs filtering, causing the pre-coat to build up faster, thus requiring the filter cloth to be replaced more often. Also, poor dregs settling can lead to more frequent ringing problems in the lime kiln.

METHODOLOGY

Mill process data

Daily averaged data of 200-plus operating parameters over a 2.5-year period were collected from the evaporation plant, the recovery boiler, and the causticizing plant at IPP. Compositions of dregs, lime mud, and black liquor were also examined to determine if they have any correlations with poor dregs settling. Softwood, mixed hardwood, and maple were used for pulping during the period. The pulping cycle usually involved 14 days of softwood pulping, followed by 5 days of mixed hardwood pulping, and 9 days of maple pulping. Depending on the type of wood used for pulping, the recovery boiler operating conditions varied. These included air distribution, flow rates, temperatures, and pressures. This makes it difficult to identify correlations be-

tween those parameters and the dregs settling behavior. Therefore, additional subparameters were created that only contain data related to pulping of one specific type of wood; i.e., these subparameters contain either data generated during softwood pulping, mixed hardwood pulping, or maple pulping.

Multivariate data analysis

The MVDA program SIMCA version 15 (MKS Umetrics; Umeå, Sweden) was used to perform an orthogonal partial least squares discriminant analysis (OPLS-DA), which is a linear regression-based classification method. This software has been applied and described in detail in previous studies where operating data related to the recovery cycle in pulp mills were investigated [5-7]. The parameter "Volume of settled dregs after the clarifier" (Fig. 2) was used as target parameter to distinguish between good settling and poor settling. Prior to the analysis, the parameter was converted to a two-class parameter. The "Class A" days were days when the volume of settled dregs in the Imhoff cone was 0 ml (48% of all days), while "Class B" days were days when the volume of settled dregs was > 0 ml (52% of all days). The discriminant analysis identifies and ranks the process parameters that have the highest discriminatory power, i.e., those that distinguish the days with good dregs settling (Class A) from the days with poor settling (Class B).

Machine learning methods

Numerous parameters, including the parameter "Volume of settled dregs after the clarifier" are not normally distributed; i.e., the parameter values are not distributed in form of a bell-shaped curve. In this case relationships between the parameters are nonlinear. Because OPLS-DA is based on linear regression, interpretation of the results becomes less reliable as non-linearity increases. In order to complement the OPLS-DA, several machine-learning algorithms were applied to the dataset. The open-source machine learning tool Weka (version 3.8.4) was used for these analyses. Of the tested algorithms, Random Forest and Naïve Bayes were found to be the most successful techniques in predicting the dregs settling behavior, based on the available process parameters.

Since Random Forest uses a nonlinear classification system to generate a multitude of decision trees, it is fundamentally a different approach to identify relationships between operating parameters and dregs settling, compared to the regression-based OPLS-DA. The predictive power of each of the individual variables is calculated based on the parameter importance index. This index is related to the number of times that a variable is used to split a node in all of the decision trees, weighted by the number of instances (i.e., days of mill operation) that it splits. Prior to the analysis, a correlation-based feature selection method was applied, and only the 40 most important parameters were used for the prediction. By applying separate training and testing datasets, Random Forest correctly classified 87% of all instances; i.e., 87% of all days of operation were correctly assigned as either days of good dregs settling or days of poor settling. The receiver operating characteristic (ROC) was 0.79, which is considered a relatively high value. The ROC value is a performance measure of discriminability between two classes achieved with a particular machine-learning algorithm. Results from Naïve Bayes and the MVDA were used to confirm whether an individual parameter is larger or smaller during days of poor settling.

Dregs composition analysis

Samples of dregs, lime mud, and grits were analyzed on a monthly basis, and samples of green liquor and black liquor were analyzed on an occasional basis for over 30 elements, bulk density, ash and moisture content, pH, conductivity, percentage loss after combustion at 550°C, and particle size distribution. Lignin and soap contents in the black liquor were also analyzed. Each dregs composition parameter was individually correlated to the volume of settled dregs measured using the Imhoff cone settling test.

Sample extraction and analysis were carried out by a commercial laboratory. Samples were air dried and pulverized, and a portion of each was digested according to the EPA Method 3050B [8]. The resulting solutions were analyzed for the elements using inductively coupled plasma-mass spectrometry (ICP-MS). Silicon (Si) was determined by ICP-MS after sodium peroxide fusion of the sample. Total carbon (C) and sulfur (S) were determined using a carbon/sulfur analyzer with combustion/infrared analysis.

Settling Behavior	Si	Al	Fe	Ca	Mg	Mn	P	Na	K	Mg/Al Ratio	Si/Al Ratio
Poor	10.7 (±3.2)	3.7 (±0.8)	3.1 (±0.9)	220 (±45)	37 (±8)	17 (±4)	1.7 (±0.4)	36 (±23)	4.2 (±1.9)	10.2 (±1.7)	3.0 (±0.8)
Good	5.5 (±2.0)	2.7 (±1.0)	2.3 (±0.8)	240 (±41)	42 (±10)	19 (±5)	2.2 (±0.6)	31 (±23)	4.2 (±3.7)	17.1 (±4.6)	2.2 (±0.9)

Si = silicon; Al = aluminum; Fe = iron; Ca = calcium; Mg = magnesium; Mn = manganese; P = phosphorus; Na = sodium; K = potassium.

I. Average concentrations (out of 29 measurements) and standard deviations of the main elements during periods of poor vs. good dregs settling (g/kg), and the average Mg/Al and Si/Al ratios. (Note: Poor settling was defined by a volume of settled dregs after the clarifier of ≥5 ml, as measured with the settleable solids test.)

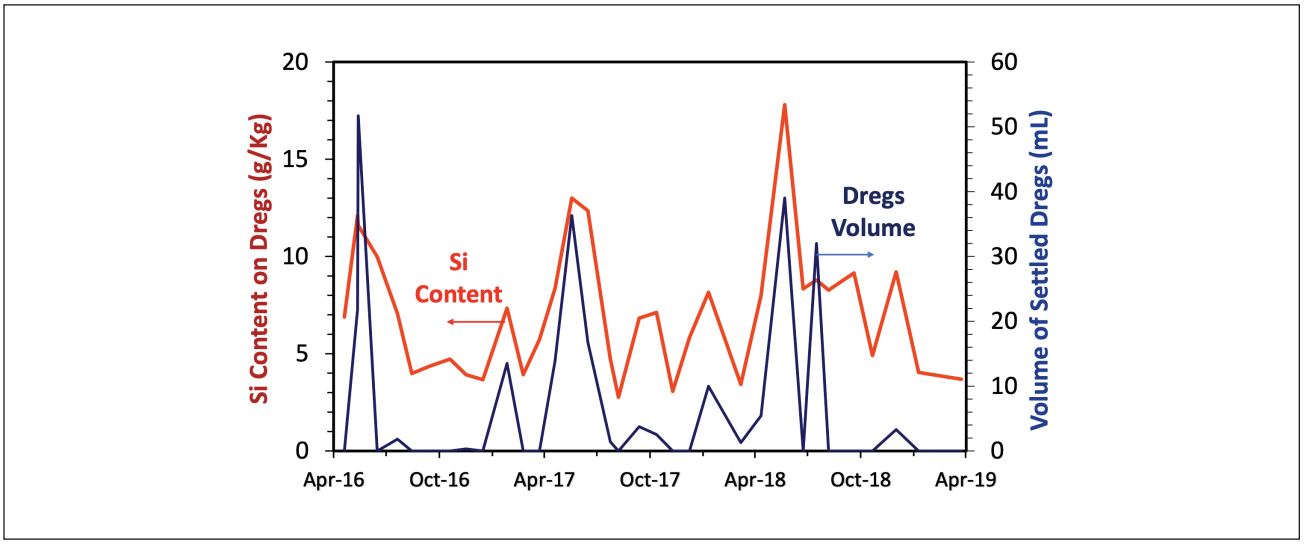

3. Poor dregs settling vs. silicon (Si) content in dregs (r=0.77, confidence level >99.9%; r is the Pearson correlation coefficient).

RESULTS AND DISCUSSION

Compositions of dregs, lime mud, and black liquor

During periods of poor dregs settling, the composition of dregs changes significantly (**Table I**). The dregs composition and correlation analysis revealed a strong correlation between poor dregs settling and Si content in dregs (**Fig. 3**). Poor settling is also moderately correlated to high aluminum (Al) content, high iron (Fe) content, and low bulk density in dregs (**Table II**). Although the Si/Al ratios in the dregs in this study are similar to those reported by Taylor [2], ranging between 1.2 and 4.6, there is only a moderate correlation between the Si/Al ratio and poor dregs settling (r = 0.43).

Besides concentrations in dregs, the concentrations of several metals in lime mud are also correlated well with dregs settling. For example, poor dregs settling is correlated to high Al (r=0.59, Conf.>99.9%) and Fe contents (r=0.58, Conf.>99.9%), as well as weakly correlated to high Si content (r=0.39, Conf.>95%) in the lime mud (r is the Pearson correlation coefficient; Conf. is the confidence level).

Table III shows correlations between poor dregs settling and compositional parameters of black liquor. These parameters are concentrations of Si, Al, Fe, lignin, and soap. Using the SIMCA software, the parameters were lagged by 3 to 8 days, meaning that the correlations involve a time shift between the composition of black liquor and poor dregs settling. For example, there is a strong correlation (r=0.90) between high soap content in black liquor and poor dregs settling three days later. Apparently, a few days prior to periods of poor dregs settling, concentrations of Si, Al, Fe, and soap in black liquor are higher, and concentrations of lignin are lower. Partially soluble elements such as Si and Al can accumulate in the green liquor/weak wash cycle until sufficiently high concentrations lead to precipitation and purging, along with the dregs and the lime mud [9]. Higher soap and lower lignin contents may refer to temporary changes in wood quality and/or cooking conditions.

Seasonal variation

Figure 4 shows the monthly averaged volume of settled dregs after the clarifier for over 4.5 years. Episodes of poor dregs settling are not equally distributed over the course of the year, and they rather seem to be seasonally influenced. During late spring/early summer (May to July), as well as early winter (December and January), dregs settling was poor in almost all investigated years. On the other hand, during late summer/early fall (August to November), the settling was good for most of the time. This seasonal variation implies that the dregs settling may be to some extent influenced by the wood species used for pulping or by operational changes at the mill as a result of wood variability.

The Si content in wood can range over three orders of magnitude, depending on the type of the tree (wood species), the part of the tree, and the geological conditions [10].

	Si	Al	Fe	Bulk Density	Mg/Al Ratio	Si/Al Ratio
Correlation values	0.77	0.47	0.58	-0.43	-0.55	0.43

Si = silicon; Al = aluminum; Fe = iron; Mg = magnesium.

II. Correlations between poor dregs settling and dregs composition. Correlations are significant at the confidence level >95% (N = 29).

Time Delay, days	Si	Al	Fe	Lignin	Soap
3	**0.77**	**0.95**	**0.94**	**-0.91**	**0.90**
4	0.58	**0.68**	0.58	-0.52	**0.68**
5	0.51	**0.78**	**0.72**	**-0.67**	**0.82**
6	**0.77**	**0.89**	**0.84**	**-0.85**	**0.88**
7	**0.67**	**0.77**	**0.76**	**-0.84**	**0.79**
8	**0.73**	**0.95**	**0.94**	**-0.95**	**0.93**

Si = silicon; Al = aluminum; Fe = iron.

III. Pearson correlations (r values) between black liquor parameters and poor dregs settling 3 to 8 days later. Correlations in bold text are significant at the confidence level of 95% (N = 11).

Also, the content of resin-like compounds or pitch is seasonally influenced. The latter compounds affect the content and composition of organics in black liquor, and hence black liquor combustibility [7].

Multivariate data and machine learning analyses

The MVDA and ML analyses were conducted to identify operating parameters that are related to dregs settling behavior. A discriminant analysis (OPLS-DA) was implemented to identify the parameters that distinguish the days of good settling from the days of poor settling (**Fig. 5**), while Random Forest analyses (ML) were conducted to identify parameters that have the strongest relationship to poor dregs settling (**Fig. 6**). Figures 5 and 6 show only parameters that have the strongest relationship to poor dregs settling, out of 200-plus operating parameters. There is a relatively large degree of consistency between the parameters in both figures, which confirms their relationship to the dregs settling behavior.

Poor dregs settling is related to low solids content of the dregs cake after the dregs filter (Fig. 5) and low solids concentration in the dregs cake after centrifuging (Figs. 5 and 6). Low solids content in the dewatered dregs suggests the difficulty in dewatering the dregs during periods of poor settling. Also, the volumes of settled dregs from samples taken after the surge tank and after the clarifier are correlated. If the green liquor from the surge tank entering the clarifier has a high dregs content, a somewhat larger portion of dregs will likely also exit the clarifier.

The white liquor sulfidity in the causticizing system is lower during periods of poor dregs settling. At a given total titratable alkali (TTA), a lower sulfidity liquor contains more carbonate and less sulfide, and hence, has a higher density than a higher sulfidity liquor. This is because the

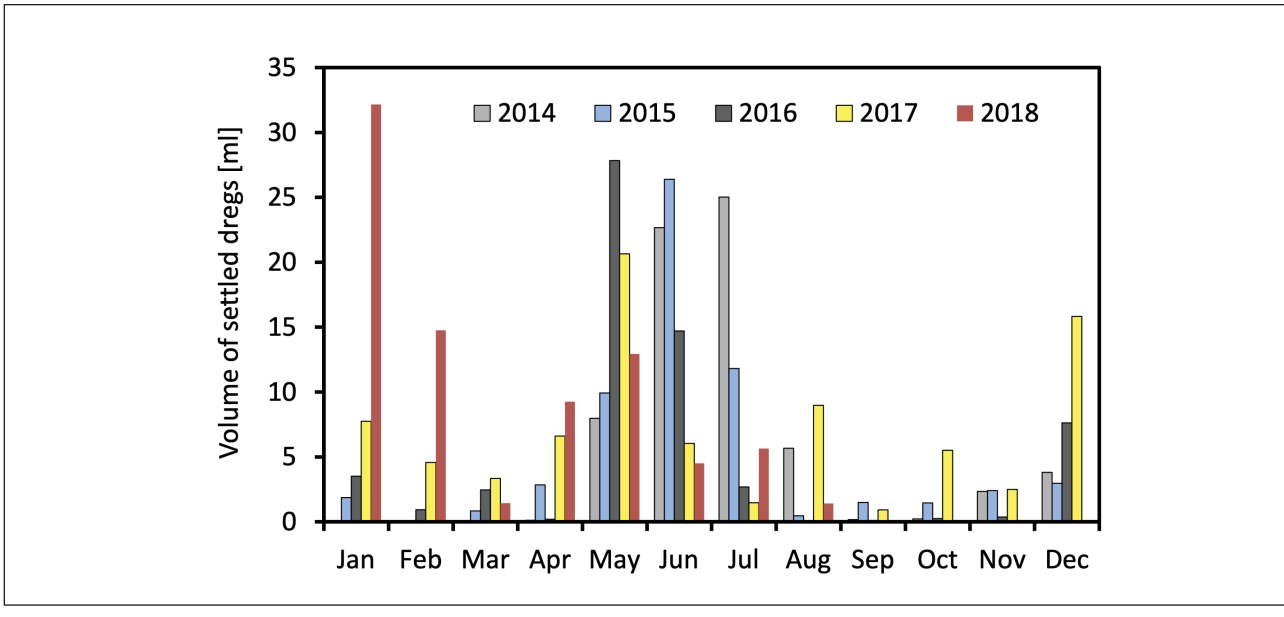

4. Monthly average volume of settled dregs after the clarifier. High values mean numerous days within a month with deteriorated dregs settling.

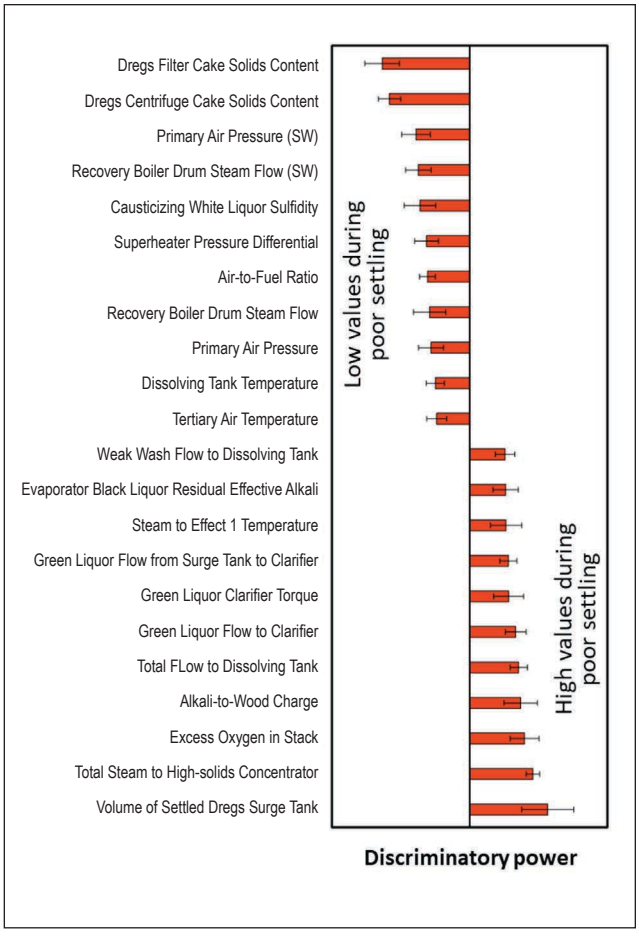

5. Parameters with the highest discriminatory power between days of good settling and days of poor settling. Parameters at the right side of the middle axis of the column chart have high values during days of poor settling, and parameters to the left have low values. Longer bars mean that the parameters distinguish between good and poor settling more strongly. "SW" means only data generated during softwood pulping were used.

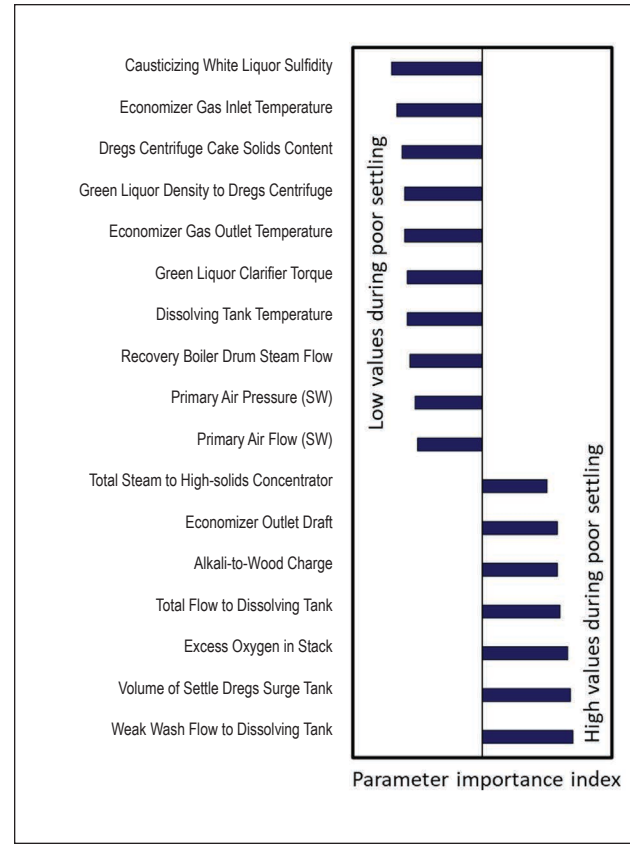

6. Most important parameters as calculated with Random Forest. Naïve Bayes and multivariate data analysis (MVDA) results were used to distinguish between positive and negative parameter relationship. "SW" means only data generated during softwood pulping were used.

density of sodium carbonate (Na_2CO_3) is 2.54 g/cm³, which is much larger than the density of sodium sulfide (Na_2S) at 1.86 g/cm³. A higher density liquor gives more buoyancy and hence makes it more difficult for dregs to settle.

The results also show that poor dregs settling is correlated with the operation of a lower primary air pressure and lower steam production in the recovery boiler, lower temperatures in the economizer, lower air-to-fuel ratio, and higher excess oxygen in the stack. All of these imply that the boiler was operated at either a low black liquor firing load condition and/or under an incomplete combustion condition that results in an increased char content in dregs.

Poor dregs settling is also correlated to increased steam consumption in the high-solids concentrator (HSC) within the evaporation plant. This implies the difficulty in achieving the targeted black liquor solids content due to increased boiling point rise or decreased organic/inorganic ratio of the liquor. The high alkali-to-wood charge during poor settling periods, as indicated in Figs. 5 and 6, can lead to a boiling point rise and the associated increase in steam requirement. Also, high soap content in the black liquor (Table III) during times of poor settling can lead to increased foaming, reduced heat transfer, and lower evaporation efficiency.

Poor dregs settling is also related to higher flow rates to the dissolving tank and green liquor clarifier, as well as lower temperatures in the dissolving tank (Figs. 5 and 6). Increased flow through the clarifier can lead to enhanced solids carryover, and a larger volume of settled dregs after the clarifier. A lower liquor temperature in the dissolving tank can also increase green liquor density and buoyancy, leading to poorer settling.

It is important to note that some of these correlations are not necessarily cause-effect relationships; i.e., the target parameter and the correlated process parameters may only be associated because of their dependency on other, unidentified processes.

Sources of silicon

Silicon is derived mostly from wood, makeup lime, and the silicon-based defoamer used in brownstock washers. Chem-

ical analysis performed on three samples of wood chips showed that they contain on average 300 (±105) mg/kg (dry). Using this Si content in wood, the amount of Si entering the mill via wood was estimated to be about 0.5 kg of Si per metric ton of pulp produced.

Using compositional data and the amounts of the makeup lime used, the amount of Si entering the recovery cycle via makeup lime is 0.1 kg/metric ton pulp. Finally, assuming an Si content of 14% in the applied polydimethylsiloxane defoamer (personal communication with supplier), and by using data about the defoamer application during brownstock washing, the amount of Si entering the mill via defoamer is about 0.05 kg/metric ton pulp. Therefore, the largest contribution of Si introduced into the mill that may affect the dregs settling is by far from wood, and to some smaller extent, from makeup lime and defoamer.

CONCLUSIONS

Multivariate data and machine learning analyses as well as a composition analysis of dregs were conducted to identify parameters that are responsible for impaired settling in the green liquor clarifier. While the main causes of the poor settling are not entirely clear, there is evidence to support several reasons for poor dregs settling issues at IPP.

The poor dregs settling in the clarifier is closely associated with the high Si content in dregs. It is also, to some extent, seasonally influenced due to changes in the wood chip quality. The settling behavior is also related to the operating conditions in the recovery boiler and the causticizing plant. Poor settling is correlated to low primary air pressure, low economizer temperature, and low steam production in the recovery boiler, particularly during softwood pulping, as well as high excess oxygen in the stack. These operating conditions indirectly imply that poor dregs settling is more likely to occur when the recovery boiler is operated at a low furnace temperature and/or under incomplete combustion conditions. Poor dregs settling is also correlated to lower sulfidity in the causticizing system, which may be related to the higher density and buoyancy force in low sulfidity–high carbonate liquor, and the associated difficulties to settle dregs.

For mills that experience poor dregs settling problems, it is important to monitor the composition of dregs, black liquor, green liquor, and weak wash on a regular basis. The information can help identify the main causes of the problem. **TJ**

ABOUT THIS PAPER

Cite this article as:
Price, C. and Hubbe, M., *TAPPI J.* 21(8): 435(2022).
https://doi.org/10.32964/TJ21.8.435

DOI: https://doi.org/10.32964/TJ21.8.435

ISSN: 0734-1415

Publisher: TAPPI Press

Copyright: ©TAPPI Press 2022

About this journal

LITERATURE CITED

1. Empie, H.J., Ellis, M., and Amundsen, M., "Fundamentals of dregs removal," Project F01707 Final Progress Report to the Member Companies of the Institute of Paper Science and Technology, U.S. Environmental Protection Agency (1971) "Laboratory procedures – analysis for wastewater treatment plant operators," EPA Water Programs – Region VII, Kansas City, MO, USA, 1999.

ABOUT THE AUTHORS

We chose this topic because poor dregs settling is a common problem in many kraft pulp mills, and it is part of our expertise. This research complements previous work in our group on the settling and filtering properties of dregs as influenced by black liquor burning conditions. The most difficult part of the study was to identify data analysis methods with which the dregs settling behavior can be predicted well.

The study showed that dregs settling issues can have a variety of different reasons. The most interesting result was that the dregs settling behavior seems to be seasonally influenced, which points to variations in wood quality or operational changes as a result of these variations.

Mills that experience poor dregs settling may benefit from this work by gaining a better understanding of some of the potential causes, which might help to develop strategies for mitigation.



Meyer



Munn



Tran

Meyer is senior research associate and Tran is professor emeritus in the Department of Chemical Engineering & Applied Chemistry at the University of Toronto, Toronto, ON, Canada. Munn is process engineer at Irving Pulp and Paper Ltd., Saint John, NB, Canada. Email Meyer at meyer.torsten@yahoo.com.

2. Taylor, K., *TAPPI J.* 12(9): 29(2013). https://doi.org/10.32964/TJ12.9.29.

3. Landälv, I., Stare, R., Yuan, J., et al., "Advancement of high temperature black liquor gasification technology," Final Technical Report DE-FC26-04NT42259 (P.I. Brown, Proj. Dir.), U.S. Department of Energy, Washington, DC, 2008. Available [Online] https://www.osti.gov/servlets/purl/973572 <05Aug2022>.

4. Lidén, J., *Int. Chem. Recovery Conf.*, TAPPI Press, Atlanta, 1995, p. A291.

5. Versteeg, P. and Tran, H.N., *TAPPI J.* 8(11): 22(2009).

6. Jones, A.K., Wagoner, J., Michaelson, T., et al., "Use of multivariate analysis to understand the root causes of premature smelt spout failures on recovery boilers," *Int. Chem. Recovery Conf.*, TAPPI Press, Peachtree Corners, GA, USA, 2014.

7. Meyer, T., Goel, R., Chowdhury, A., et al., *J-FOR* 7(2): 53(2018).

8. EPA, "Method 3050B: Acid digestion of sediments, sludges, and soils," Revision 2, U.S. Environmental Protection Agency, Washington, DC, 1996.

9. Doldán, J., Poukka, O., Salmenoja, K., et al., *O Papel* 72(7): 47(2011).

10. Cornelius, J.-T., Ranger, J., Iserentant, A., et al., *Biogeochemistry* 97: 231(2010). https://doi.org/10.1007/s10533-009-9369-x.

The Creep Properties of Paper

J. P. BREZINSKI

The creep properties of alpha-pulp handsheets were determined at various constant tensile loads and relative humidities for the purpose of clarifying the prerupture mechanical behavior of paper. Included in this investigation were studies of first-creep properties, creep recovery, mechanical conditioning and primary creep, the dependence of creep behavior on handsheet solid fraction, and the relative permanence of nonrecoverable deformations. It was concluded that the delayed creep deformation of the handsheets was of at least two general types which were separated in time and varied in their recoverability and dependence on relative humidity. The general patterns of first-creep behavior could be described by the formation of master creep curves. The creep behavior does not appear to be reconcilable with rate-controlling mechanisms of deformation which embrace macroscopic reorientations of the fibers in the sheet or the rupture of fiber-fiber bonds.

In the manufacture of paper, one has some control of the mechanical properties and structural characteristics of the finished product. Consequently, the relations between paper properties and processing variables have become an important industrial problem. Paper is classified mechanically as a viscoelastic material. Its prerupture response to stress may be characterized by immediate elastic deformations, which are considered to occur instantaneously with the application of load; delayed elastic deformations, which are distributed in time and are recoverable within reasonable periods of time after removal of load; and delayed nonrecoverable deformations, also distributed in time, but not recoverable within reasonable periods of time following load removal. In recent years, increased attention has been directed toward the prerupture mechanical behavior of paper, chiefly by means of the load-deformation test, and increased use has been made of load-deformation data in evaluating variables in the manufacture of pulp and paper. Interpretation of load-deformation data, however, is difficult because of the arbitrary time-controlled sequence of load or deformation development common in such tests. In addition, an interpretation of the prerupture mechanical behavior of paper has been hampered by a general inability to precisely describe the structure of paper. Basically, an understanding of the mechanical behavior of paper is contingent on relating its mechanical properties to its structure.

One may consider the mechanical properties of paper to be functions of sheet structure and fiber property variables, where the sheet structure variables depend on the formation of a sheet for their existence. It has not been possible, however, to completely separate and define those variables by independent methods, and both are normally considered at the same time. It is axiomatic that the response of any material to an external stress should be ultimately relatable to the molecular structure and the precise shape of the solid parts of the specimen. The complex void pattern of paper precludes the specification of a solid shape factor, and paper is too frequently treated as an entity rather than an assembly of formerly discrete elements of fibrous materials. Studies of the mechanical properties of papermaking fibers present severe experimental difficulties. As a result, the problem of relating the mechanical properties of paper to molecular structure, fiber property variables, sheet structure, etc., is largely academic. Nevertheless, the approach to the overall problem should be based on the knowledge that such relationships must exist.

In studying the mechanical properties of paper, it is first necessary to describe the patterns of mechanical behavior as fundamentally as possible with emphasis on the interrelationships between load, deformation, and time; and to interpret those patterns of behavior in terms of the rate-controlling mechanisms of deformation. This essentially was the purpose of the present study. The constant-load tensile creep test was selected to describe the mechanical behavior of paper, since the variables of deformation, load, and time are separated effectively with a minimum of experimental difficulty. Following the preliminary investigations of creep and recovery, creep properties were determined for handsheets of different solid fractions produced by varying the degree of beating and wet pressing. The dependence of creep properties on relative humidity was also investigated.

THE VISCOELASTIC PROPERTIES OF PAPER

The first descriptions of the viscoelastic behavior of paper were drawn almost entirely from the load-deformation test. The work of Gibbon (*1*) and Farebrother (*2*) established that the early deformation in a load-deformation test was largely elastic, but that at higher loads, the specimen was more easily deformable in a manner indicating flow. The later deformation was largely nonrecoverable. It was noted that the deformation in subsequent load-unload cycles after the first was almost entirely recoverable and that a marked hysteresis existed in the load-unload curves. The shape of the load-deformation curve suggested that the mechanical behavior of paper could be described in terms of a yield stress or yield zone of stress. Steenberg's (*3*) earlier studies of the load-deformation properties of paper indicated that the load-deformation curve depended on numerous factors related to the manner of sheet preparation, the external test conditions, the rate of testing, and the previous mechanical history of the specimen. The nonrecoverability of large portions of the first deformation of paper was attributed to a superficial invisible creping of the fibers which was removed to varying degrees in the first

J. P. Brezinski, Graduate Student, The Institute of Paper Chemistry, Appleton, Wis.; present address, Minnesota & Ontario Paper Co., International Falls, Minn.

tests. This concept was somewhat similar to those proposed by Gibbon (*1*), Mason (*4*), and others, which consider macroscopic unkinking or uncurling of the fibers in the sheet as the principle mechanism of the nonrecoverable deformation. Rance (*5*, *6*), however, proposed that the nonrecoverable deformation of paper was due to the rupture of fiber-fiber bonds, which occurred at an ever-increasing rate until termination of the test by rupture of the specimen. The time-dependency of the delayed deformation was attributed to frictional sliding of fiber over fiber following bond ruptures plus possible additional elastic contributions because of redistributed stresses during straining. As evidence in support of this view, Rance presented creep curves of paper at several constant loads which rose rapidly in deformation (on the semilogarithmic plot) at various times of loading. The tensile load to cause rupture decreased linearly with the logarithum of the time of its application; this effect was also demonstrated by Jacobsen (*7*). Nordman, Gustafsson, and Olofsson (*8*) observed increases in the specific scattering coefficient of paper with increasing deformation, which they attributed to the rupture of fiber-fiber bonds. Haward (*9*, *10*) found reductions in the tensile strength of cellulose acetate under load which were greater at higher loads and longer times of application. The nonrecoverable deformation could be recovered in large measure, however, by heating the specimen. The loss of strength was not recovered. It has not been demonstrated, however, that internal damage of high polymers is a rate-controlling mechanism of deformation, nor that it accounts for the nonrecoverable portion of a given deformation.

The effect of rate of straining on the load-deformation curve was studied by Broughton and Matlin (*11*) and Andersson and Sjoberg (*12*). The slope of the initial straight line of the load-deformation curve was not affected by rate of straining. The initial slope, therefore, was taken as a measure of the apparent elastic modulus of paper. The slope of the final straight line which frequently is noted and the load at rupture increased slightly with greater rates of deformation. The relatively small increases are in contrast with much larger expected increases if the deformation versus initial stress relationship were linear. In the mechanical-conditioning studies of Ivarsson (*13*), it was found that numerous load-unload cycles are required before paper can be considered mechanically conditioned in the sense that the curves of successive load-deformation cycles become identical.

Andersson and Berkyto (*14*) studied the effect of relative humidity and temperature on the load-deformation properties of paper. Rather abrupt increases in response occurred with increasing relative humidity (reached by adsorption) between 60 and 70% R.H. Both the initial and final slopes of the load-deformation curve and the tensile strength decreased with increasing relative humidity. An increase in temperature (dry specimens) had the effect of increasing the time-rate of deformation at constant load. Most of the previous studies of the prerupture mechanical properties of paper deal with first tests in which large portions of the first deformation are nonrecoverable. Less attention has been directed toward the immediate elastic and delayed elastic deformations of paper. Ivarsson and Steenberg (*15*) tested paper in load-deformation tests after mechanical conditioning in an attempt to fit the recoverable delayed response to the theory of Halsey, White, and Eyring (*16*). This theory, discussed later by Halsey (*17*), relates the recoverable delayed deformation to molecular mechanisms based on the dimensions of a molecular flow unit and a kinetic rate constant, which in turn is related to an "energy of activation" for transfer of flow units. It was concluded that the theory would apply at least qualitatively to mechanically conditioned paper.

Attempts have been made to describe the viscoelastic properties of paper by mechanical spring and dashpot combinations (*3*, *13*, *15*), which will respond in a manner similar to paper in mechanical tests. Andersson, Ivarsson, Nissan, and Steenberg (*18*) attempted to characterize the viscous nature of paper in terms of the apparent viscosity of the dashpot fluid of a mechanical model. In general, mechanical model analogies are useful in describing the mechanical behavior of high polymers, but contribute little toward an interpretation of the deformation mechanisms. Kubat (*19*, *20*) studied the stress relaxation of paper at varying levels of initial deformation and stress reached in load-deformation tests. The rate of stress relaxation was dependent on the manner of arriving at the initial conditions corresponding to zero time in the stress relaxation test, which complicated an interpretation of the results. It appeared that the stress might relax to varying finite values at lower relative humidities, but would relax to zero stress at higher relative humidities.

Van den Akker (*21*) suggested that the problem of relating the mechanical properties of paper to the structural characteristics of the sheet might be approached profitably by the development of a special statistical mechanics which essentially considered the response of the sheet to be associated with the response of the fibers. He argued that the deformation of paper could not be due in large degree to viscoelastic contributions of the zones of bonding because of their very small thickness. He also pointed out that stress distribution effects would be of extreme importance in a structurally heterogeneous material such as paper, and that it is unwise to consider paper as an entity when approaching a problem of this type.

The difficulty in interpreting the results of load-deformation tests, and the lack of a sound description of the viscoelastic behavior of paper have not enabled a critical analysis of the somewhat controversial hypotheses which have been proposed to account for the mechanisms of deformation under tensile load.

EXPERIMENTAL METHODS AND APPARATUS

The Creep Tester

A creep tester was designed and built for this work. It employed simple dead-weight loading and a micrometer-driven electrical contact device to detect and measure the relative displacement of a pair of clamps. A schematic drawing of a single unit is shown in Fig. 1. Six units were mounted on a single frame.

The framework consisted of horizontal and parallel upper and lower support bars which were fixed in

 CITE THIS PAPER: Brezinski, J.P., *Tappi* 39(2): 116(1956). https://doi.org/10.32964/TJ39.2.116

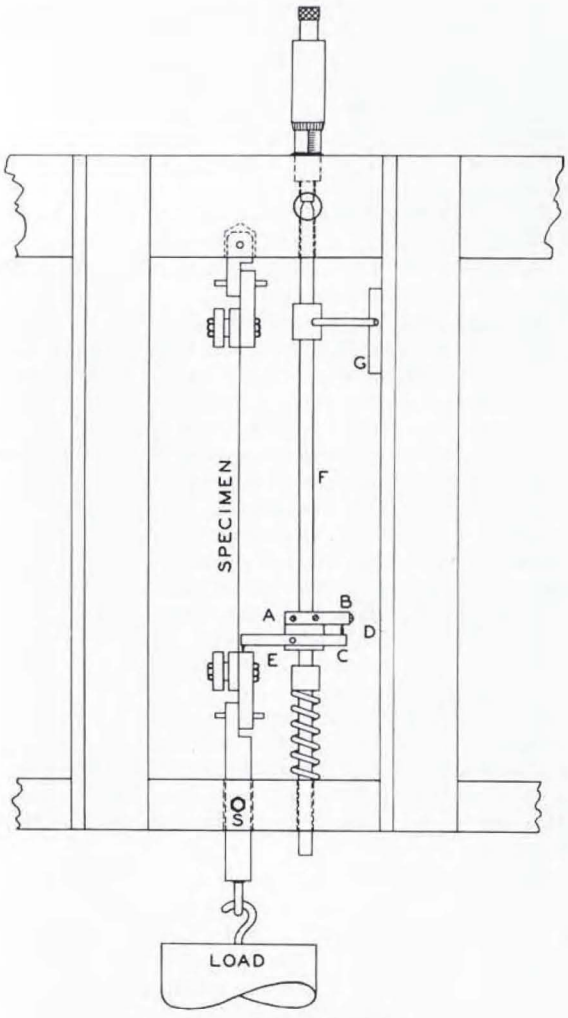

Fig. 1. Creep testing unit

position by pairs of angle-iron struts at 6-in. intervals. This assembly essentially formed an open trussed beam of considerable rigidity. The upper clamp was pinned to a short length of 1/2-in. diameter rod which was milled flat at one end as shown in Fig. 1. This supporting rod fitted freely into a hole in the bottom of the upper support bar and was pinned in position. The pins are at right angles to each other and form a universal joint which permits alignment of the upper clamp in the direction of the load. The lower clamp was pinned to a section of 1/2-in. rod which passed through a hole in the lower support bar. A hook was fixed to the lower end of this rod to receive the load. The lower clamp could hang freely from the specimen or could be supported by means of the set screw S to remove all load from the specimen.

A micrometer head was soldered in position at the top of the upper support bar. A 1/4-in. diameter shaft F was mounted for free vertical movement as an extension of the micrometer screw. The shaft was spring loaded to maintain contact with the micrometer screw and was fitted with a pin which could slide against an edge of the guide block G and prevent its rotation. The electrical contact device was mounted on the extension shaft opposite the lower clamp. It consisted of three main parts. The body block A fitted over and was secured to the extension shaft. A brass block B was firmly attached to the body block but was insulated for electrical isolation from the remainder of the apparatus. The unbalanced lever arm C was free to rotate in a vertical plane about a cantilever pin fulcrum which fitted closely in a horizontal hole in the body block. A needle was soldered at each end of the lever arm to point in opposite vertical directions. The needle D was normally in contact with the polished undersurface of block B and completed an electrical circuit between that block and the frame. The needle at the other end of the lever arm was in position to contact the polished top surface of the lower clamp. Rotation of the micrometer drives the entire unit vertically. When needle contact is made with the lower clamp, the electrical circuit is broken. The completion or interruption of the electrical circuit was detected with a milliammeter, and the corresponding micrometer reading indicated the position of the lower clamp. The upper clamp showed no significant change in position with loading; hence, the deformation of the specimen was measured directly by the change in position of the lower clamp. The lower clamp assembly was balanced about the center line of the specimen, and relative changes in specimen lenght could be measured accurately to the nearest 0.01%.

One set of six units was enclosed in a cabinet to enable conditioning of the atmosphere at relative humidities other than 50%. The framework base was set in wax to level the apparatus and minimize vibrational disturbances.

Preparation of Specimens

Commercial softwood alpha pulp was used in the preparation of all handsheets. The pulp was beaten

Table I. Description of Alpha Pulp Handsheets[a]

Handsheet No.	*Schoppec-Riegler pulp freeness ml.*	*Wet pressure, p.s.i.*	*Caliper, in. × 1000*	*Basis weight, g./sq. in. × 1000*	*Calculated solid[b] fraction, %*	*Estimated[b,c] apparent elastic modulus, kg./sq. mm.*
23	620	50	3.1	3.69	48.1	1000
28–33	620	50	3.2	3.64	45.0	1000
36	620	200	2.8	3.61	51.6	1050
42	620	800	2.6	3.51	54.1	1100
47	775	10	5.0	3.91	31.7	700
48	775	50	3.9	3.87	40.6	800
50	775	400	3.0	3.77	50.6	860
55	425	50	3.0	3.83	51.7	1150

[a] Properties determined at 50% R.H. and 73°F.
[b] Based on an assumed fiber density of 1.5 g./cc.
[c] Determined by low-load static tests.

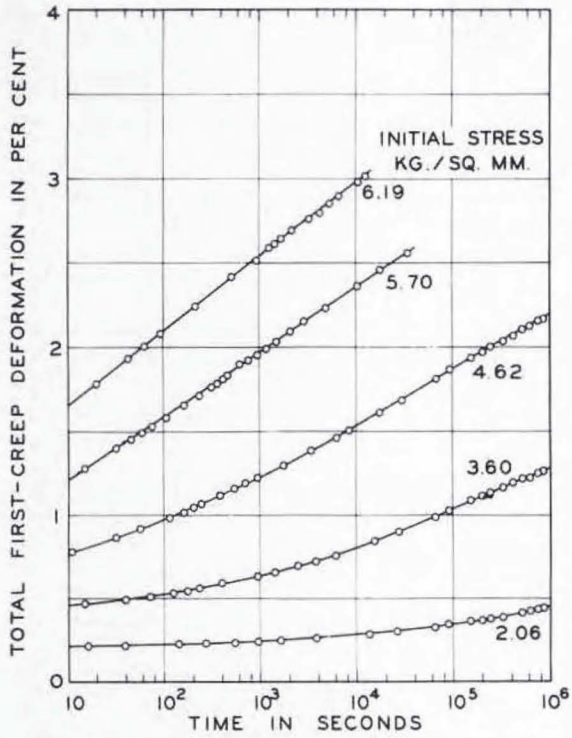

Fig. 2. First-creep curves of handsheet 23

to desired levels in a Valley laboratory beater, essentially following TAPPI Standard T 200 m-45. All handsheets were formed on a 17-in. square sheetmold to an approximate basis weight of 40 lb. per ream (25 × 40–500). The newly formed wet sheets were couched off the wire with blotters and transferred to metal plates. After wet pressing at the desired pressure for 5 min., each sheet was taped to the plate along its edges and air dried to TAPPI standard conditions of 50% R.H. and 73°F. Shrinkage during drying was negligible. Specimens were razor-cut to 1-in. widths and 12-in. lengths and weighed individually. To account for differences in basis weight, all creep loads were converted to average initial stresses based on calculated average solid cross sectional areas of each specimen. Calculation of the initial stress was made using the specimen weights at standard conditions and assuming an average fiber density of 1.5 grams per cc. The same density was used in calculating handsheet solid fractions. The characteristics of the handsheets used in this study are given in Table I.

Creep Testing Procedures

The clamps were removed from the apparatus for insertion of specimens. A jig was used to provide alignment of the specimens in the clamps and to obtain constant initial lengths of 10 in. at standard conditions. The clamps and specimen were reinserted in the creep test unit and an initial micrometer reading was taken under a tension of 300 grams provided by the lower clamp assembly. Small loads in the range of 100 to 300 grams were applied and removed at approximately 10-sec. intervals. The small reversible deformations which occurred were used to correct the initial micrometer reading to zero tension. The measurements also provided estimates of the apparent elastic modulus. In starting a creep test, a deadweight load was applied manually within a period of about 0.5 sec. Time was recorded from the instant of load application and first readings were normally obtained after about 10 sec. of elapsed time. Creep recovery curves were obtained by rapid removal of the load and supporting of the lower clamp assembly to allow zero-load recovery. Time was recorded from the instant of load removal, and first readings were taken with a 300-gram load on the specimen after about 100 sec. to minimize any effect of this small load on the recovery curve. All tests were run at 73 ± 0.4°F. The tests at 50% R.H. were run in a temperature and humidity-controlled room with normal relative humidity variations of about ± 1% in long-duration tests. Tests at other relative humidities were run in an enclosed cabinet provided with an external air circulation system. Air was bubbled through saturated salt solutions for control of the relative humidity. All relative humidity measurements were made with electric hygrometer elements, which were calibrated over saturated salt solutions using the equilibrium relative humidity values reported by Wink (*22*).

RESULTS AND DISCUSSION

First-Creep Properties

Typical first-creep curves of alpha-pulp handsheets are shown in Fig. 2. The tests were run on specimens from handsheet 23 at standard conditions of 73°F. and 50% R.H. The range of loads was approximately 26 to 84% of the tensile strength determined in a load-deformation test at a constant deformation rate of

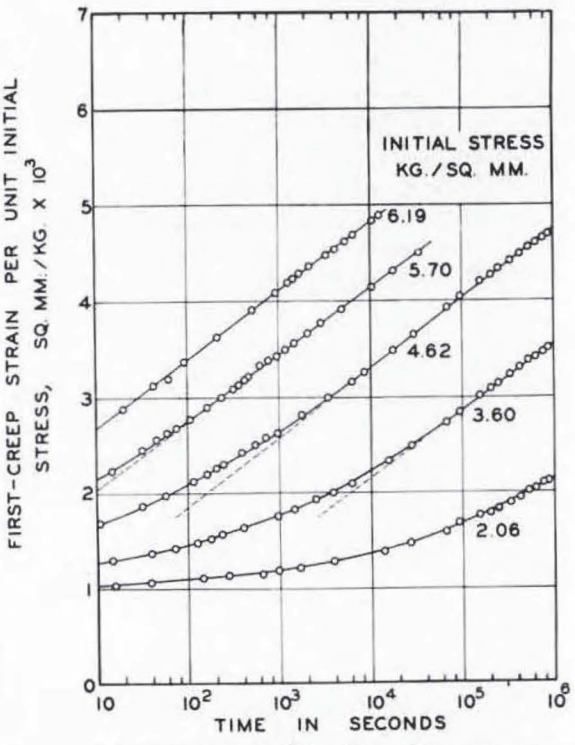

Fig. 3. First-creep curves of handsheet 23 on a deformation per unit initial stress basis

 CITE THIS PAPER: Brezinski, J.P., *Tappi* 39(2): 116(1956). https://doi.org/10.32964/TJ39.2.116

1% per min. Duplicate tests agreed to within 5% in deformation at the same initial stresses and times. The tests were discontinued at 864,000 sec. unless terminated earlier by rupture of the specimen.

The exact deformation-time relationships in first-creep tests varied with the creep load; however, general patterns of behavior were noted which were consistent in all first-creep tests. For example, in the test at 3.60 kg. per sq.mm., creep in the first two decades of log time could be described by an exponential equation

$$y/L_0 = Bt^a + C \quad (1)$$

where

y = total first-creep deformation, in.
L_0 = initial specimen length, in.
t = time of loading, sec.

and B, a, and C are constants. With continued time of loading, the creep rate declined more rapidly than was consistent with equation 1. Creep enters a transitional zone where simple mathematical equations could not be applied to describe the relationship between deformation and time. Following this transitional zone, which may embrace two or more decades of log time, the deformation-time relationship became linear on the semilogarithmic plot and could be described by a logarithmic equation

$$y/L_0 = K \log t + C' \quad (2)$$

where K and C' are constants. At low initial stresses, the creep curves could be described by exponential equations over the entire experimental time interval, whereas at higher initial stresses only logarithmic creep was observed within the experimental time interval. A broad span of log time is required to identify exponential, transitional, and logarithmic creep at a single initial stress.

The exponent, a, of equation 1 was equal to 0.23 in tests at initial stresses of 3.60 and 2.06 kg. per sq.mm. and could not be determined at higher initial stresses. The constant, K, of equation 2 was linearly proportional to initial stress and extrapolated to zero at zero initial stress. For these specimens, K divided by initial stress was nearly constant at 7.0×10^{-4} sq.mm. per kg. The constant C of equation 1 is mathematically equivalent to the immediate elastic deformation. The apparent elastic modulus calculated from equation 1 at the two lower initial stresses was approximately

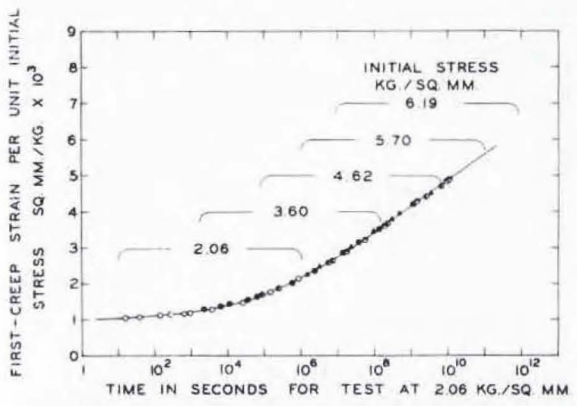

Fig. 4. Master creep curve of handsheet 23

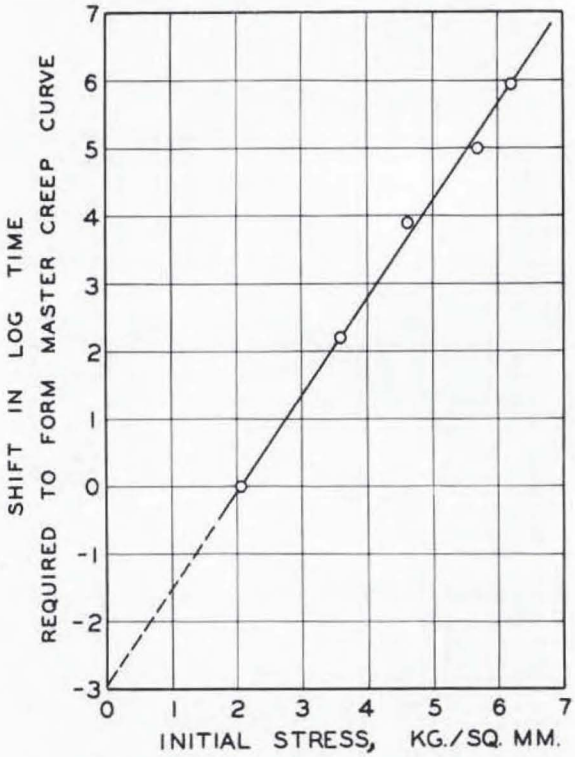

Fig. 5. Shifts in log time required to form master creep curve of handsheet 23 versus initial stress

1050 kg. per sq.mm., which checked well with values estimated from the small reversible deformations between initial stresses of 0.31 to 0.62 kg. per sq.mm. Other constants in these equations relate principally to the position of the creep curves along the time axis and do not determine the curve shape.

The total first-creep deformation at constant times of loading bears an extremely nonlinear relationship to initial stress. The deformation increases rapidly with increasing initial stress. Estimated yield stresses derived from total first-creep deformation versus initial stress curves are functions of the time of loading, and it is felt that the yield-stress concept is not useful in describing or interpreting the creep properties of paper. At the higher initial stresses, a considerable amount of the total first-creep deformation occurs prior to the experimental time interval. The earlier deformation could not be measured directly in this study, nor could it be estimated by extrapolation. It was noted, however, that one of the effects of increasing initial stress was a shift of the various kinds of response, defined by the deformation-time relationships, toward earlier times. This suggests that exponential and transitional creep may also occur at the higher stresses but at times prior to the experimental time interval. Similarly, logarithmic creep may be expected at longer times of loading in tests at low initial stresses. There was no indication of any deviation from logarithmic creep prior to rupture in the tests at the two higher initial stresses. In other tests of up to 48-day duration, no departure from logarithmic creep was noted. Hence, it is assumed that logarithmic creep represents

the limiting type of response in the long-duration regime.

The concept of a single generalized or master creep curve formed by the combination of the creep curves at different initial stresses proved useful in describing the effect of initial stress on the creep behavior of paper. This concept was explored by Catsiff, Alfrey, and O'Shaughnessy (*23*) in creep tests of nylon. After appropriate adjustment of some of the creep curves by expansion in deformation, they were able to form a single master creep curve of nylon by shifting the curves obtained at different loads along both the deformation and time axes until the curves coincided in the regions of overlap. Thus, the creep curve at any load described only a portion of the total creep response which was considered to be defined by the entire master creep curve. The requirements for forming a master creep curve suggested that one of the effects of increasing creep load was a speeding up of the response to stress.

The construction of a master creep curve from the various creep curves of Fig. 2 was relatively simple. Each creep curve was first reduced in deformation by a factor of the initial stress. These reduced curves, shown in Fig. 3, coincided well in the regions of overlap when shifted along the log-time axis. The time axis of the creep test at 2.06 kg. per sq.mm. was selected arbitrarily as the time axis of the master creep curve shown in Fig. 4. The brackets identify experimental time intervals of 10 to 10^6 sec. at the various initial stresses. The required timeshifts in decades of log time to form the master creep curve were linearly related to initial stress as shown in Fig. 5. A shift of about 1.45 decades of log time was required per unit initial stress. The effect of increasing initial stress in first-creep tests of these handsheets, therefore, may be described as a stress proportional increase in deformation plus a stress proportional shift in log time of the curves toward shorter times.

The manner by which a master creep curve can be constructed is determined empirically. The requirements may be simple, but their significance will depend on their possible interpretation in terms of the mechanisms of response to stress. Even if such interpretation cannot be made, the master creep curve is useful in describing the relationships between deformation, initial stress, and time, and forms an excellent description of the viscoelastic nature of paper. By inference from the master creep curve, the amount of any kind of response, as described by a particular deformation-time relationship, is linearly related to initial stress. If the master creep curve could be used to extrapolate the creep curves at any initial stress to shorter and longer times, it is seen that the immediate elastic deformation will be linearly related to initial stress, and that the creep curves at all initial stresses will begin with exponential creep, followed by transitional creep, and then by logarithmic creep. The nonlinearity of the deformation versus initial stress relationships, which suggests an apparent yield stress, is a consequence of a linear increase in amount of response with increasing initial stress superposed on a stress-proportional speeding up of the response relative to the long-time axis.

The first-creep behavior of alpha-pulp handsheets demonstrates a degree of ideality in the deformation-initial stress-time relationships, which appears to be consistent with rate-controlling molecular mechanisms of deformation. The results do not appear to be reconcilable with either rate-controlling macroscopic mechanisms of deformation or large changes in stress distribution during the course of the creep tests. Any significance which might be attached to a particular relationship between deformation and time lies in the mechanisms of deformation that determine the rates of creep within the range where the relationship is applicable. Unfortunately, first-creep data alone do not provide sufficient information to enable an interpretation of creep behavior in terms of the individual mechanisms of deformation.

The Relationship Between Creep and Load-Deformation Tests

The possibility of relating the results of creep and load-deformation tests is of practical interest, since the load-deformation curve is easily obtained in comparison to the time and effort involved in creep studies. In seeking a possible interrelation between creep and load-deformation data, the concept of a mechanical equation of state appeared promising. Findley (*24*) was able to derive a mechanical equation of state from creep data which was useful in describing the behavior in load-deformation tests. The mechanical equation of state concept is essentially based on the principle that the creep rate at constant external test conditions is dependent on the existing load and deformation and is independent of the path followed in arriving at a given load and deformation. This concept was tested using the creep data of handsheet 23 and a load-deformation curve obtained at a constant rate of deformation of 1% per min.

The creep rate was determined at various times in the load-deformation test by subtracting the rate of immediate elastic deformation from the constant test rate of deformation. The rates of immediate elastic deformation were determined from calculated rates of loading (the slopes of tangents to the load-time curve) and an apparent elastic modulus, which was determined from the slope of the initial straight line of the load deformation curve and was assumed to be constant throughout the test. The creep rates of the load-deformation test and those obtained from creep test data showed excellent agreement when compared at equivalent total deformations and loads. Estimates of the work done in arriving at the same total deformation at equivalent higher loads differed by more than 20% in the two types of tests. The creep rates in the load-deformation test occurred at relatively short times in creep tests at the corresponding loads. It was not determined whether good agreement in creep rate–load-deformation data would also occur in longer-duration tests. On the basis of this limited study, however, it was felt that paper may obey an apparent mechanical equation of state principle in first tests. Hence, an analysis of load-deformation data in terms of creep rate–load-deformation relationships may be very useful, since such relationships may prove to be independent of the arbitrary rate of testing over rather wide ranges.

If a substance responds mechanically in accordance with a mechanical equation of state, it may be assumed that the same kinds of deformation occur at the lower

 CITE THIS PAPER: Brezinski, J.P., *Tappi* 39(2): 116(1956). https://doi.org/10.32964/TJ39.2.116

Table II. First-Creep and First-Recovery Tests of Handsheet 42

Calculated initial stress, kg./sq. mm.	3.80	4.87	4.90	5.95	5.95	5.95	5.95
Duration of first-creep test, sec.	10,000	10,100	347,000	5	100	1990	20,000
Total first-creep deformation, %	0.65	1.23	1.90	1.03	1.46	1.95	2.37
Total first-creep strain per unit initial stress, sq. mm./kg. $\times 10^3$	1.71	2.52	3.88	1.73	2.45	3.28	3.99
Extrapolated total first recovery, deformation, %	0.54	0.83	0.92	0.83	1.06	1.12	1.14
Total first-recovery strain per unit initial stress, sq. mm./kg. $\times 10^3$	1.42	1.70	1.88	1.39	1.78	1.88	1.91

loads as at the higher loads and that the concept of a speeding up of the response with increasing load is substantiated in part. If the mechanical equation of state were shown to be applicable to first tests of paper over wider ranges of time and rates of deformation, it may provide substantial evidence that changes in structure of the specimen with increasing deformation are unlikely to be relatable to macroscopic mechanisms of deformation.

First-Recovery Properties

The nature of the first-creep response can be described in part by the relative recoverability of successive increments of first-creep deformation. The recoverability of first-creep deformations is illustrated in Table II by seven tests of handsheet 42, in which recovery curves of long duration were obtained at no load following first-creep tests at different loads and times of loading. The recovery curves were normally sigmoidal on the customary semilogarithmic plot. Recovery continued over extended periods of time, and it was necessary to extrapolate the recovery curve to zero slope at long times to obtain a measure of the total possible recovery deformation. The shape of the recovery curves, however, indicated that the nonrecoverable deformation could be considered permanent at the test conditions of temperature and relative humidity. In Fig. 6, the extrapolated total first-recovery deformation is plotted versus the total first-creep deformation with both quantities expressed as total strain per unit initial stress. The point representing the immediate application and removal of load will fall on the dotted line of 100% recovery at a level defined by the reciprocal of the apparent elastic modulus, if it is assumed that the immediate elastic deformation is linearly related to initial stress. The experimental points represent creep tests of different initial stresses and durations. All of the points, however, essentially describe the same curve. Therefore, in tests at any initial stress the early increments of delayed first-creep deformation were about 60% recoverable. As creep entered the transitional zone, the percentage of recovery decreased steadily until at the onset of logarithmic creep further increments of first-creep deformation were almost entirely nonrecoverable. Thus, a limiting value of total first-recovery deformation is reached at about the onset of logarithmic creep in tests at any initial stress and is linearly related to initial stress. The first-recovery behavior demonstrated here was typical of all first tests of alpha-pulp handsheets. It should be pointed out that recoverability is a function of total first-creep strain per unit initial stress prior to logarithmic creep and is not directly a function of test duration. If percentage of recovery in first tests could be used as a measure of the structural change in the creep test, the structural change would depend on the existing total deformation and initial stress at the end of the creep test. These recovery data tend to substantiate an earlier observation that alpha-pulp handsheets apparently obey a mechanical equation of state principle in first tests. Percentage of recovery, however, cannot be a measure of structural change after logarithmic creep begins.

There was some indication in other data obtained in this study that the total first-recovery deformation may fall below the limiting value in tests of very long duration particularly at higher relative humidities. It also could not be demonstrated that increments of deformation in second and third creep tests, at times greater than the onset of logarithmic creep in first tests, would be totally nonrecoverable. It is felt that in first-creep tests at constant initial stress, the limiting value in total recovery deformation with time of loading is evidence of an interdependence of different mechanisms of response to stress and that logarithmic creep deformation may have an inhibitory effect on recovery.

Mechanical Conditioning and Primary Creep

A specimen is normally said to be mechanically conditioned when the deformations in subsequent tests at the same or lower loads and at times equal to less than those of the first (mechanical conditioning) test are largely recoverable within reasonable periods of time at the test conditions. The recoverable delayed deformation of creep tests is termed primary creep; the nonrecoverable component is termed secondary creep. A study of the primary creep properties of paper is essentially a study of mechanical conditioning. Primary creep behavior is frequently analyzed in terms of compliance with the superposition principle of Boltzmann (*25*). In essence, this principle states that the deformation at time due to a complex sequence of load application or removal should equal the simple summation of the deformations which would have occurred at that instant if each load application or removal were an independent test which continued over an indefinite period of time. Creep recovery is considered to be identical in nature to primary creep except that it is of opposite sign. Obviously the principle cannot be expected to apply if some part of the creep deformation is nonrecoverable. Leaderman (*26*) points out that polymers which obey the superposition principle will have identical creep and recovery curves over most of the experimental time interval in long-duration tests whether creep is a linear or nonlinear function of load.

Multiple-cycle tests of 24-hr. duration in creep and

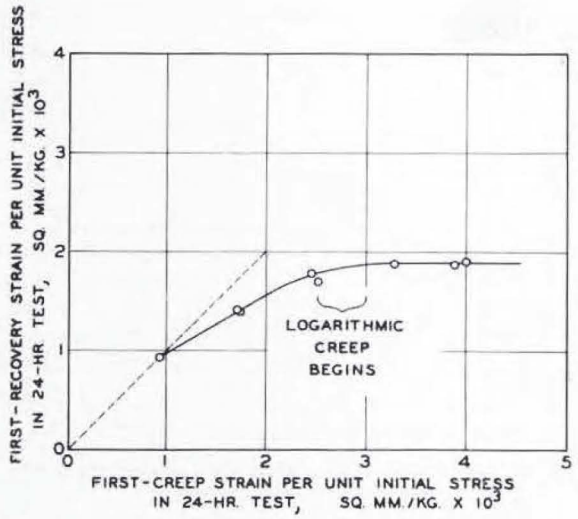

Fig. 6. Relation between total first-creep and total extrapolated first-recovery strain per unit initial stress (handsheet 42)

recovery where chosen to investigate the mechanical conditioning effect and primary creep. The creep loads were normally held constant in tests of a single specimen and recovery curves were obtained at no load. The principal effect noted in these tests was that the primary creep decreased in both rate and amount during the first few long-duration cycles. The creep curves and the recovery curves each approached similarity in shape in cycles after the third or fourth. However, even when this point was reached, the recovery curves were lower in total deformation than the preceding primary creep curves over the entire experimental time interval in tests at higher initial stresses. At relative humidities below about 65%, the recovery curves were approximately parallel to the creep curves, but at higher relative humidities, the recovery curves were generally steeper than the primary creep curves. At low initial stresses, however, the creep and recovery curves of long-duration tests were nearly identical indicating agreement with the superposition principle.

It was not possible to accurately determine the effect of initial stress on primary creep response due to the dependency of primary creep on the extent of mechanical conditioning. Generally, the total 24-hr. first-recovery deformation was over 90% of the total possible recovery following 24-hr. creep tests and was a good approximation of the primary creep deformation in 24 hrs. at the same creep load. Consequently, throughout the remainder of this study, total 24-hr. first-recovery deformations are used as estimates of the total primary creep deformation in 24 hr.

A typical example of primary creep and recovery behavior in 24-hr. multiple-cycle tests is shown in Fig. 7 in a series of tests on a single specimen of handsheet 32 at 83% R.H. The total 24-hr. first-creep deformation at an initial stress of 3.65 kg. per sq.mm. was 3.02% and the total 24-hr. first-recovery deformation was 1.03%. Two more cycles of creep and recovery were run at the same creep load before the cyclic tests of Fig. 7 were begun in order of decreasing initial stress. The greater disagreement with the superposition principle at the higher initial stresses is evident. The rise in the creep curve at 3.65 kg. per sq.mm. after 10^4 sec. is due to nonmechanically conditioned behavior. It was also noted that there was little difference in the relative delayed deformations between 10 and 10^4 sec. in the tests at 3.65 and 2.92 kg. per sq. mm. Such reduced stress dependency in relative delayed deformation was noted only at the higher relative humidities and initial stresses. Similar behavior was reported by Leaderman (*26*) for nylon and for viscose rayon at higher relative humidities. Leaderman postulated that behavior of the type shown in Fig. 7 at the higher initial stresses was due to crystallite growth during the creep test and melting of the stress-induced crystallite growth during the recovery period. Crystallization was advanced as the reason for noncompliance with the superposition principle. The same mechanisms may be suggested for paper with reversible crystallization accounting for the logarithmic primary creep.

Primary creep curves at different initial stresses in tests at standard conditions were of the same general form as the first-creep curves. It appeared that master creep curves could be constructed from primary creep curves by the stress-proportional technique described earlier. The principle differences, however, lie in the decreased magnitude of the deformation and reduced nonlinearity of the creep deformation to initial stress relationships. The latter effect was manifested by smaller timeshift requirements for the formation of master primary-creep curves. The requirements could not be determined accurately because of the dependency of primary creep on the extent of mechanical condi-

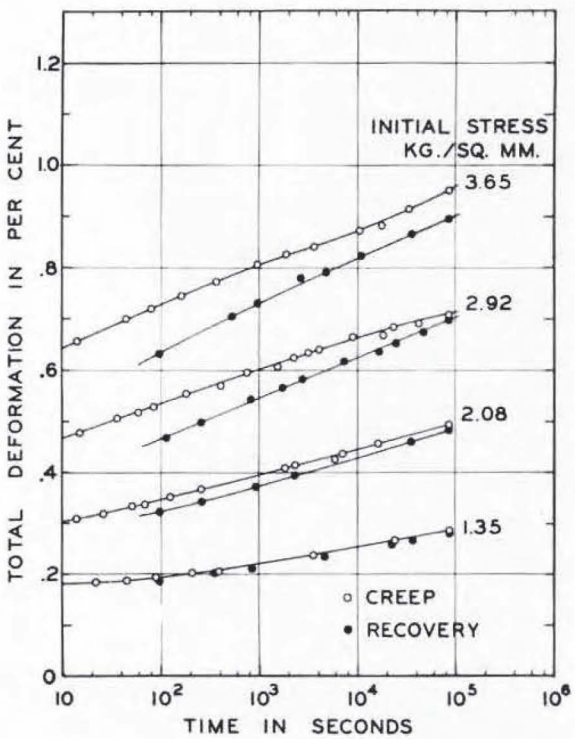

Fig. 7. Primary creep and recovery curves at 83% R.H. (handsheet 32)

CITE THIS PAPER: Brezinski, J.P., *Tappi* 39(2): 116(1956). https://doi.org/10.32964/TJ39.2.116

tioning. The similarity of primary and first-creep behavior suggests that logarithmic first-creep deformation may represent crystallite growth which is largely nonrecoverable and results in an inhibition of recovery.

Dependence of Creep Properties on Sheet Structure

Handsheets of different solid fraction were produced by different degrees of beating and wet pressing. It was felt that such changes in solid fraction would represent changes in sheet structure with a minimum effect on fiber properties. Changes in solid fraction by beating and wet pressing were calculated to affect chiefly the distribution and extent of bonding between fibers. Solid fraction was useful in characterizing the sheet structure in the absence of more fundamental variables. The creep properties of the various handsheets were determined at standard conditions principally in 24-hr. multiple cycle tests. A double-logarithmic plot of the total 24-hr. first-creep deformation versus initial stress is shown in Fig. 8 for handsheets described in Table I.

It may be noted that a change in solid fraction has the effect of shifting the curves along the log-stress axis without significantly changing their shape. As a first approximation, the handsheets differed in the initial stresses required to reach specified total first-creep deformations in given periods of time. At constant solid fraction, increased beating resulted in decreased deformation in tests of the same duration and initial stress. The first increments of beating

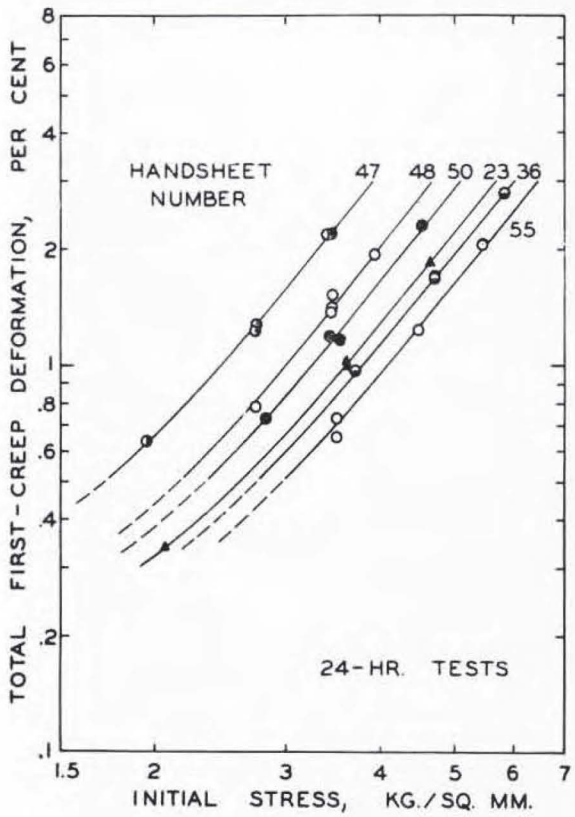

Fig. 8. Total 24-hr. first-creep deformation versus initial stress for handsheets of different solid fraction

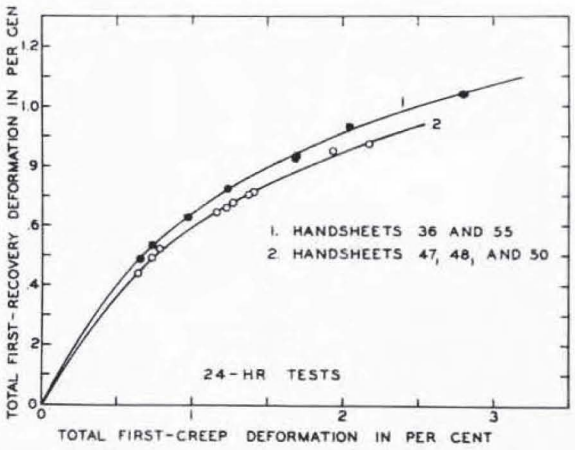

Fig. 9. Total first-creep versus total first-recovery deformations in 24-hr. tests

appear to produce the greatest effect. Increases in solid fraction by wet pressing were very effective in decreasing the creep response in the lower solid-fraction range, but similar changes in solid fraction were much less effective at higher values.

The shapes of the first-creep curves were roughly the same at comparable levels of total first-creep deformations. It appeared that the mechanisms of deformation may be basically the same for all handsheets.

A comparison of the first-recovery curves indicated near identity in shape at comparable levels of total first-recovery deformation. This suggested that the slight differences in shape of the first-creep curves may be due to differences in nonrecoverable deformation. A plot of the total 24-hr. first-recovery deformations versus the total 24-hr. first-creep deformations is shown in Fig. 9 for all handsheets. The percentages of recovery in 24-hr. tests were identical at equal total deformations for all handsheets prepared from 775 ml. S.-R. freeness pulp despite the fact that the solid fraction varied from 31.6 to 50.6% and large differences existed in the initial stresses required to reach equivalent levels of total creep deformation. The recoverability of given creep deformations was only slightly greater for the handsheets prepared from 620 and 425-ml. S.-R. freeness pulps. The differences in percentage of recovery with beating may be due to differences in structural change during drying. It seems unlikely that differences in stress distribution could account for differences in recoverability with beating but not with wet pressing. There is little doubt, however, that the distribution of the curves of Fig. 8 along the log-stress axis is the result of differences in stress distribution between handsheets.

It was possible to construct master creep curves from the first-creep curves of any handsheet of this study in tests at 50% R.H. using the technique described earlier. All of the master creep curves were of the same general type shown in Fig. 4 and, as a first approximation, the master creep curves were related to each other by simple shifts along the two coordinate axes of a double-logarithmic plot.

There were significant differences, however, in the timeshift requirement to form the master creep curves.

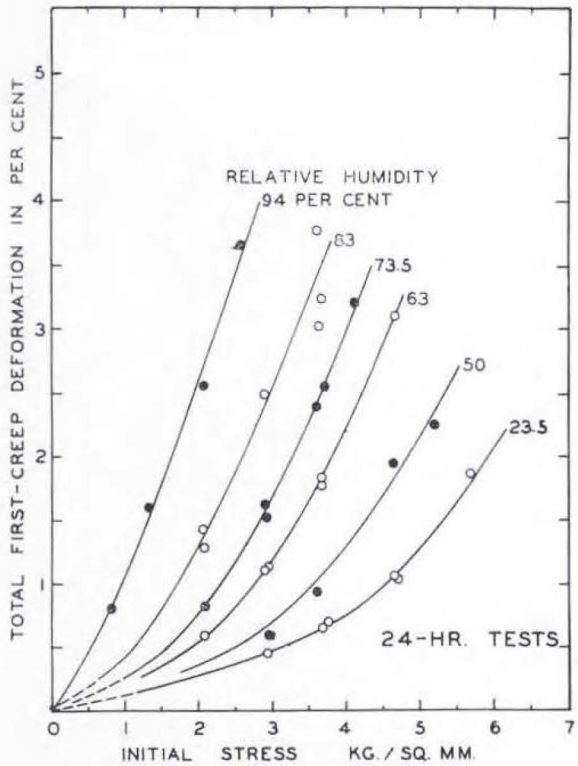

Fig. 10. Total first-creep deformation in 24 hr. versus initial stress at various relative humidities

A timeshift of approximately 2.2 decades of log time per unit initial stress was required for all handsheets prepared from 775-ml. S.-R. freeness pulp, compared to about 1.45 for all other handsheets. The timeshift requirement was not affected by changes in solid fraction due to wet pressing, but was reduced considerably with the first increments of beating. The timeshift requirement is a measure of the nonlinearity of total first-creep deformation to initial stress relationships but is not a sole index of that nonlinearity. It is suggested that the required timeshift to form a master creep curve becomes greater with greater degrees of molecular disorder in the polymer and that a reduction in the required timeshift with beating may correlate with greater molecular alignment due to a greater inhibition of shrinkage in drying the handsheets prepared from the more highly swollen pulps.

The implications of these results were not entirely clear. It may be stated categorically that the master creep curve concept applies to handsheets of widely different solid fraction, and that the principle effect of solid fraction may be expressed by differences in the initial stress required to reach specified total deformations at equal times in either first-creep or first-recovery tests. Differences in stress distribution may be of basic importance in explaining the differences in prerupture mechanical behavior with changing sheet structure.

The Dependence of Creep Properties on Relative Humidity

The mechanical properties of paper are known to be strong functions of relative humidity. It is generally accepted that the adsorption of water by cellulose occurs essentially in the amorphous regions with subsequent decreased intermolecular bonding and increased spacing between molecules. The manner in which creep properties vary with specimen moisture content may aid in the separation and definition of the mechanisms of response to stress.

Creep tests of 24-hr. duration followed by 24-hr. recovery tests were run at relative humidities of 23.5, 50, 63, 73.5, 83, and 94% on specimens of handsheets 28 through 33. The tests at 50% R.H. were run on specimens taken directly from storage. The relative humidity of 94% was reached by adsorption from 50% R.H., and all other relative humidities were reached by adsorption from 12% R.H. Adsorption from lower relative humidities had no significant effect on creep behavior at 50% R.H. compared to tests on specimens taken directly from storage. This study, therefore, essentially represents tests at relative humidities reached by adsorption. The approximate specimen moisture content versus relative humidity data are summarized in Table III.

Plots of the total 24-hr. first-creep deformations versus initial stress shown in Fig. 10 illustrate the wide variations in creep response as a function of relative humidity. The shapes of the curves are dependent on the duration of the creep tests. This is partly indicated by comparing the curves of Fig. 10 with plots of the relative delayed deformation (between 10 and 86,400 sec.) versus initial stress shown in Fig. 11. At higher relative humidities and initial stresses, the relative delayed deformations become less dependent on initial stress and continued increases in total first-creep deformation occur largely before 10 sec. Similar behavior was reported earlier in primary creep tests at 83% R.H.

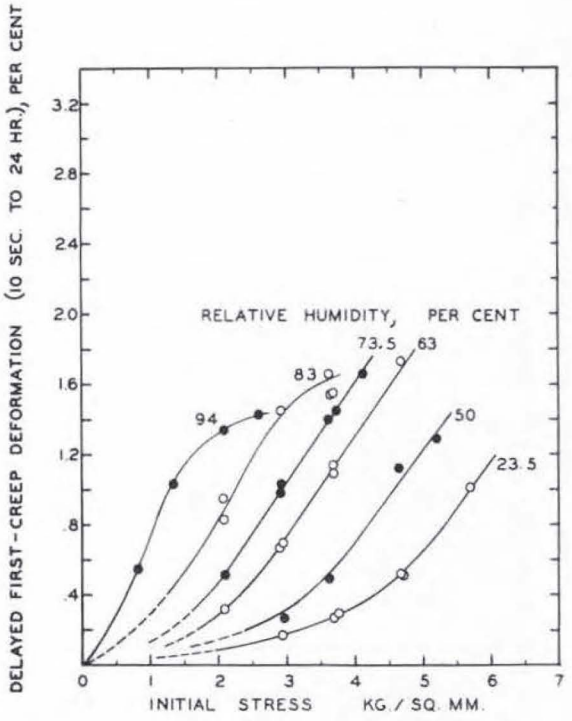

Fig. 11. Relative delayed deformation versus initial stress at various relative humidities

CITE THIS PAPER: Brezinski, J.P., *Tappi* 39(2): 116(1956). https://doi.org/10.32964/TJ39.2.116

Table III. Specimen Moisture Content versus Relative Humidity in Creep Tests at 73°F.

Relative humidity, %	*Specimen moisture content, % (oven-dry basis)*	
	Absorption series	*Desorption from 97.8% R.H.*
23.5	4.6	4.7
50	7.4	8.0
63	8.5	10.4
73.5	10.4	12.6
83	14.0	16.1
94	21	
97.8	24	

Master creep curves could be constructed by the technique described earlier from the first-creep curves at either 23.5, 50, or 63% R.H. with excellent agreement in the regions of overlap. The chief differences in the master creep curves were in the greater strain per unit initial stress values at the higher relative humidities. The timeshift requirement per unit initial stress was lower at 23.5 and higher at 63% R.H. compared to values at 50% R.H. At 73.5% R.H., disagreement in the regions of overlap became evident. This became worse at higher relative humidities. At 94% R.H., the creep curves could be combined into a master creep curve with fair accuracy by merely shifting the curves along the time axis without prior adjustment in deformation. The inability to construct master creep curves by the method described earlier is due to the reduced dependency of delayed response on initial stress at the higher relative humidities as indicated in Fig. 11. It was noted that at higher relative humidities and initial stresses, the shape of the first-creep curves prior to logarithmic creep were concave downward on the semilogarithmic plot. This curve shape was never observed at lower relative humidities, and suggests the possibility of at least two types of response in first-creep tests, which vary in different ways with increasing relative humidity at higher values.

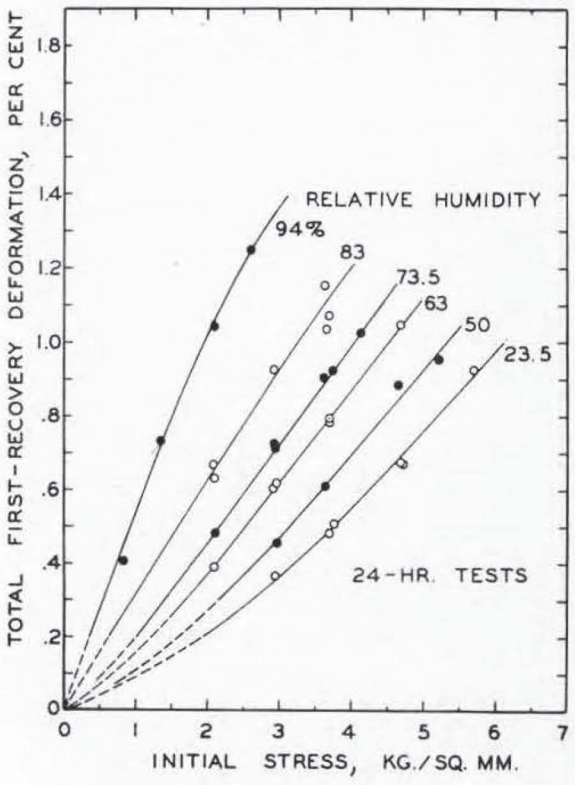

Fig. 12. Total first-recovery deformation in 24 hr. versus initial stress at various relative humidities

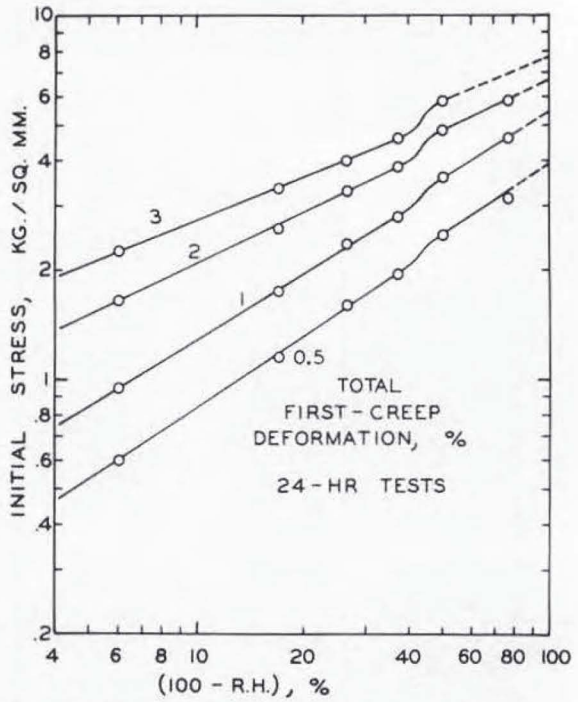

Fig. 13. Initial stress required to reach specified total first-creep deformations in 24 hr. versus (100 − R.H.)

The total 24-hr. first-recovery deformation versus initial stress curves are shown in Fig. 12. The shapes of these curves are also dependent on the test duration. The curves are concave upward at the lower relative humidities principally because the duration of the first-creep tests was insufficient to approach the limiting value of total recovery deformation at the lower initial stresses. If the duration of the first-creep tests were sufficiently long to approach the limiting value in total recovery at all initial stresses, the curves would approach straight lines of greater slope at higher relative humidities. Basically, there was a linear relationship between the limiting value of total first-recovery deformation and initial stress at all relative humidities.

Changes in the recoverability of total first-creep deformations with relative humidity were rather involved since the changes depended on the extent of deformation. It was noted that minimums in the percentage of recovery occurred between 70 and 80% R.H. when the total 24-hr. first-recovery deformations exceeded 0.6% and that the percentage of recovery increased rapidly from 60 to 50% R.H. The latter change correlated with rather sharp breaks in curves relating total 24-hr. first-creep deformations to relative humidity at constant initial stress. These breaks in response are illustrated most conveniently by double-logarithmic plots of the initial stress required to reach specified total 24-hr. first-creep deformations versus 100 minus the relative humidity in per cent (see Fig.

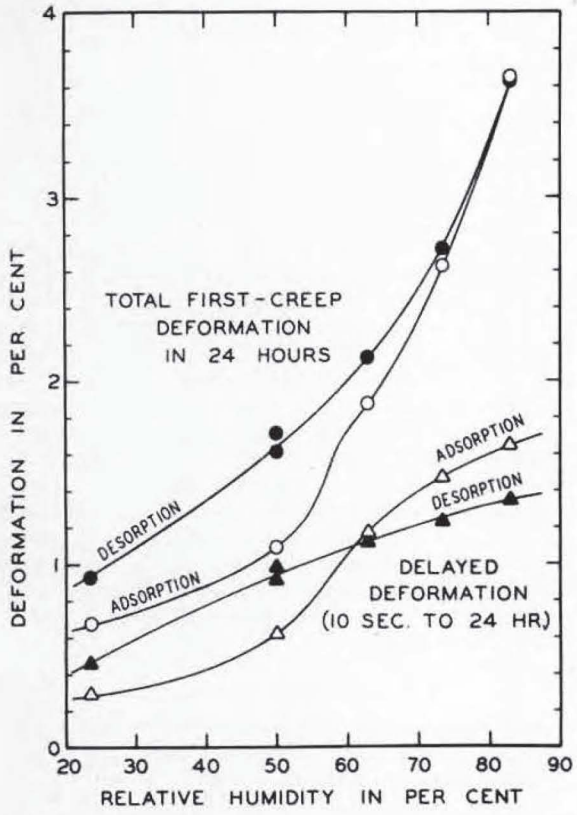

Fig. 14. Comparison of first-creep response at 3.75 kg. per sq. mm. before (adsorption) and after (desorption) humidification

13). The sharp rise in initial stress did not occur in similar plots for total first-recovery deformation, and, therefore, is attributable to the nonrecoverable component of the first-creep deformation. Similar breaks in response were reported by Andersson and Berkyto (*14*) in load-deformation response versus relative humidity for machine-made papers. In their work, the breaks occurred between 60 and 70% R.H. and were greatest for machine-direction specimens. The breaks in response are toward a reduced percentage of nonrecoverable deformation at the lower relative humidities. In a sense, a reduced percentage of nonrecoverable deformation can be considered as "partial mechanical conditioning." As a general rule, it was noted that mechanical conditioning was effective at relative humidities below those of the mechanical conditioning test, but the effect was destroyed progressively as the relative humidity was increased to higher values. For these specimens, the "partial mechanical conditioning" effect might occur as a result of structural changes during drying.

Creep Behavior of Humidified Specimens

In order to determine the reasons for the break in the first-creep response versus relative humidity curves, six specimens of handsheet 29 were subjected to a relative humidity of about 97% for a period of 48 hr. Specimens were then tested in 24-hr. first-creep and first-recovery tests at various lower relative humidities reached by desorption. The specimen moisture contents are given in Table III. In all tests, the initial stress was 3.75 kg. per sq. mm. A comparison of the results with those obtained before humidification at the same initial stress is shown in Fig. 14 and illustrates the principal effects of humidification. The comparisons of Fig. 14 are made on a relative humidity basis and would differ slightly if made on a moisture-content basis. The conclusions, however, will remain the same. Large increases in the total 24-hr. first-creep deformation occur at the lower relative humidities with little change at the higher values. The humidification treatment effectively eliminated the abrupt change in creep behavior at 50 to 60% R.H. The total 24-hr. first-recovery deformation increased by about 0.1% at all relative humidities indicating that most of the increased total first-creep deformation was non-recoverable. It may be noted in Fig. 14 that the relative delayed deformation between 10 and 86,400 sec. was markedly affected by the humidification treatment. The differences are also reflected in the slopes of the logarithmic-creep portions of the first-creep curves. The first-creep curves of the humidified specimens at 3.75 kg. per sq.mm. are shown in Fig. 15. The slopes were the same between 50 and 83% R.H. Logarithmic creep did not occur in 24 hr. at 23.5% R.H., and it was not determined whether the slope was the same at this lower relative humidity. Before humidification, however, the slopes were lower at relative humidities below about 55% and greater thereafter with a rapid increase in slope between 50 and 63% R.H. (see Table IV). This similarity of slope for the humidified specimens indicates that the rate of logarithmic creep may be basically independent of relative humidity over a rather wide range. The dependence of slope on relative humidity before humidification may be ascribed to changes in specimen structure of an irreversible nature with increasing relative humidity. Structural changes with increasing relative humidity may result in the breaks in first-creep response shown in Fig. 13. The creep response prior to logarithmic creep increases in amount and is also shifted toward earlier times with increasing relative humidity at constant initial stress. Hence, logarithmic creep and the preceding creep response (largely exponential

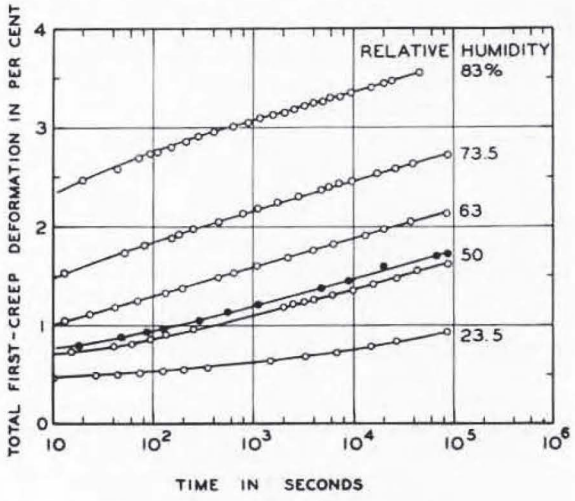

Fig. 15. First-creep curves of humidified specimens at 3.75 kg. per sq. mm. and various relative humidities

CITE THIS PAPER: Brezinski, J.P., *Tappi* 39(2): 116(1956). https://doi.org/10.32964/TJ39.2.116

Table IV. Slopes of Logarithmic First-Creep Curves versus Relative Humidity

Relative humidity	Slope, sq. mm./kg. × 10^4 Before humidification	After humidification
23.5	6.0	
50	7.1	7.6
63	8.7	7.7
73.5	9.7	7.7
83	10.1	7.7

creep) are revealed as two different kinds of response by their different relative humidity dependence.

It seems most plausible that a mechanism of deformation which is unaffected by changes in specimen moisture content would involve changes in the crystalline structure. It should be pointed out that greater deformations are reached in tests at the higher relative humidities before logarithmic creep begins and the similarity of the slope of this portion of the creep curve becomes evident. The fact that the specimens may be in different structural states when logarithmic creep begins, however, does not appear to be inconsistent with the possibility of crystallite growth as the mechanism of logarithmic-creep deformation. It is felt that the earlier deformation is largely due to changes in molecular configuration in the amorphous areas of the polymer.

The Relative Permanence of Nonrecoverable First-Creep Deformations

It was stated earlier that the nonrecoverable deformation in first-creep tests must be considered permanent at the test conditions of temperature and relative humidity. Leaderman (*26*) demonstrated that large portions of the nonrecoverable deformations in first-creep tests of silk, viscose rayon, and cellulose acetate could be recovered by steaming the specimens at no load and redrying. This ultimate recoverability of previously nonrecoverable deformations by plasticization is sufficient evidence to preclude the possibility of viscous flow as the mechanism of deformation. The relative permanence of the nonrecoverable deformations of paper can be tested by subjecting the specimens to high relative humidities followed by desorption to the test humidity. Humidification treatments are arbitrary in time, temperature, and moisture content. It is presumed that the extent of additional recovery due to humidification will be a function of these variables.

An illustration of humidification recovery is provided by the following series of tests on a specimen of handsheet 55 at standard conditions. Before testing, the specimen was subjected to a relative humidity of 97.8% (over a saturated solution of potassium sulphate (*27*)) for 12 hr. at no load. Upon reconditioning at 50% R.H., a net shrinkage of 0.48% occurred, which represents a recovery of "residual strain." A 24-hr. creep test at 3.49 kg. per sq.mm. and 50% R.H. yielded a total deformation of 1.13%. The total recoverable deformation in 7 days was 0.62%, which was substantially complete recovery at the test conditions. A second humidification treatment at 97.8% for 24 hr. increased the total recovery to 1.08% measured at 50% R.H. The entire process was repeated three more times with almost complete recovery of the creep deformation measured at the test conditions after the humidification treatment. A 24-hr. creep test at 4.50 kg. per sq.mm. accounted for a total creep deformation of 1.58%. The total recovery in 5 days was 0.83%, which was increased to 1.51% by humidification. Similar tests on another specimen at 5.45 kg. per sq.mm. indicated that an increase in the total recovery deformation from about 1 to 1.9% would occur with humidification compared to a total creep deformation of about 2.3%. The total recovery after humidification accounts for practically all of the first-creep deformation to the onset of logarithmic creep and a part of the logarithmic-creep deformation. The bulk of the logarithmic-creep deformation, however, appeared to be resistant to recovery by humidification treatments of the type described. It is suggested that the deformation which is recoverable by humidification is largely retarded configurational elastic response, whose recovery was inhibited at the test conditions by the formation of a metastable molecular structure. Humidification recovery occurs most readily following tests at low relative humidities where strong inter-molecular bonding is present. Humidification is less effective in providing for increased recovery in tests at higher relative humidities.

LITERATURE CITED

1. Gibbon, E. R., *Paper Makers' Assoc. Gt. Brit. Ireland, Proc. Tech. Sect.* 25: 199–210 (1944).
2. Farebrother, T. H., *Paper Makers' Assoc. Gt. Brit. Ireland, Proc. Tech. Sect.* 25: 216–220 (1944).
3. Steenberg, Borje, *Svensk Papperstidn.* 50, No. 15: 346–350 (Aug. 15, 1947).
4. Mason, S. G., *Pulp Paper Mag. Can.* 49, No. 3: 207–214, 221 (1948).
5. Rance, H. F., *Paper Makers' Assoc. Gt. Brit. Ireland, Proc. Tech. Sect.* 29: 449–469 (1948).
6. Rance, H. F., *In* Meredith's "Mechanical Properties of Wood and Paper," Part B, Amsterdam, North-Holland Publishing Company, 1953. 298 p.
7. Jacobsen, P. M. H., *Worlds' Paper Trade Rev.* 134: 150, 152, 155–156 (1950).
8. Nordman, Lars, Gustafsson, Charley, and Olofsson, Goran, *Paper and Timber (Finland)* 34, No. 3: 47–52 (1952).
9. Haward, R. N., *Trans. Faraday Soc.* 38: 394–403 (1942).
10. Haward, R. N., *Trans. Faraday Soc.* 39: 267–280 (1943).
11. Broughton, Geoffrey, and Matlin, N. A., *Tappi* 34, No. 11: 493–497 (1951).
12. Andersson, Olle, and Sjoberg, Lars, *Svensk Papperstidn.* 56, No. 16: 615–624 (Aug. 31, 1953).
13. Ivarsson, Bertil, *Svensk Papperstidn.* 51, No. 17: 383–388 (Sept. 15, 1948).
14. Andersson, Olle, and Berkyto, Edward, *Svensk Papperstidn.* 54, No. 13: 437–444 (July 15, 1951).
15. Ivarsson, Bertil, and Steenberg, Borje, *Svensk Papperstidn.* 50, No. 18: 419–432 (Sept. 30, 1947).
16. Halsey, G., White, H., Jr., and Eyring, H., *Textile Research J.* 15: 295–311 (1945).
17. Halsey, G., *J. Appl. Phys.* 14, No. 5: 1072–1097 (1947).
18. Andersson, O., Ivarsson, B., Nissan, A. H., and Steenberg, B., *Paper Makers' Assoc. Gt. Brit. Ireland, Proc. Tech. Sect.* 30: 43–56 (1949).
19. Kubat, J., *Naturwissenschaften* 39, No. 5: 107 (1952).
20. Kubat, J., *Svensk Papperstidn.* 56, No. 17: 670–675 (Sept. 15, 1953).
21. Van den Akker, J. A., *Tappi* 33, No. 8: 398–402 (1950).
22. Wink, Willmer A., *Ind. Eng. Chem., Anal. Ed.* 18: 251–252 (1946).
23. Catsiff, Ephraim, Alfrey, Turner, Jr., and O'Shaughnessy, M. T., *Textile Research J.* 23, No. 11: 808–820 (1953).
24. Findley, W. N., *Soc. Plastics Engr. J.* 6, No. 10: 13–16 (Dec., 1950); *Engineering Index* p. 900 (1951).
25. Boltzmann, L., *Pogg. Ann. Physik* 7: 624 (1876).
26. Leaderman, Herbert, "Elastic and Creep Properties of Filamentous Materials and Other High Polymers," Washington, D. C., The Textile Foundation, 1943. 278 p.
27. Bobb, Franklin, Unpublished work, 1953.

Portions of this paper were presented at the American Chemical Society symposium on "The Rheology of Cellulose Fibers and Sheets," New York, N. Y., Sept., 1954.

TAPPI JOURNAL
WWW.TAPPI.ORG
THE PAPER AND PACKAGING INDUSTRIES' TECHNICAL RESOURCE
SEPTEMBER 2022 | VOL. 21 NO.9



NONWOOD PULPING **469**
Development of reinforced paper and mitigation of the challenges of raw material availability by utilizing Areca nut leaf
Kishan K. Jaishwal, Izhar Alam, and Chhaya Sharma

LIGNIN **479**
Economic and competitive potential of lignin-based thermoplastics using a multicriteria decision-making method
Cédric Diffo Téguia, Nima Ghavidel Mehr, Wolfgang G. Glasser, and Paul R. Stuart

PULPING **497**
Fiber-based characterization of pulp refining
Richard J. Kerekes and J. David McDonald

PAPER PHYSICS **507**
The mechanism of bonding
W. Boyd Campbell

TAPPI Journal NOW FULLY OPEN ACCESS

September 2022

TABLE OF CONTENTS VOL. 21 NO. 9

465 EDITORIAL
Ravi Challa brings tissue, nonwovens, and operational expertise to *TJ* Editorial Board
Monica Shaw

469 NONWOOD PULPING
Development of reinforced paper and mitigation of the challenges of raw material availability by utilizing Areca nut leaf
Kishan K. Jaishwal, Izhar Alam, and Chhaya Sharma

479 LIGNIN
Economic and competitive potential of lignin-based thermoplastics using a multicriteria decision-making method
Cédric Diffo Téguia, Nima Ghavidel Mehr, Wolfgang G. Glasser, and Paul R. Stuart

497 PULPING
Fiber-based characterization of pulp refining
Richard J. Kerekes and J. David McDonald

507 PAPER PHYSICS
The mechanism of bonding
W. Boyd Campbell

»**COVER CREDIT**: Researchers Diffo Téguia et al. explore the market and technical drivers for use of lignin in bio-based thermoplastic products, such as these eating utensils (p. 479). They also assess lignin-based thermoplastics against previously studied phenolic resins and polyurethane foams.

TAPPI JOURNAL
WWW.TAPPI.ORG

Editor-in-Chief
Douglas W. Coffin coffindw@miamioh.edu
+1 513 529-0771

Associate Editor
Peter W. Hart peter.hart@westrock.com
+1 409 276-3465

Editorial Director
Monica Shaw mshaw@tappi.org
+1 770 367-9534

PRESS Manager
Jana Jensen jjensen@tappi.org
+1 770 209-7242

***TJ* EDITORIAL BOARD**

Brian N. Brogdon, FutureBridge Consulting & Training LLC
brian.brogdon@gmail.com, +1 678 581-9114

Ravi Challa, Suominen Corporation
Ravi.Challa@suominencorp.com, +1 843 680 2586

Douglas W. Coffin, Miami University
coffindw@miamioh.edu, +1 513 529-0771

Mahendra Doshi, Doshi and Associates
mahen@aol.com, +1 920 832-9101

Marc Foulger, Valmet
marc.foulger@valmet.com +1 315 767-2920

Peter W. Hart, WestRock
peter.hart@westrock.com, +1 409 276-3465

Carl J. Houtman, USDA Forest Products Laboratory
choutman@fs.fed.us, + 1 608 231-9445

Vamsi Jasti, Ahlstrom-Munksjo Nonwovens LLC
jvamsik1@gmail.com, +1 818 585-3524

Lucian Lucia, North Carolina State University
lucian.lucia@gmail.com, +1 919 889-7059

John A. Neun, John A. Neun LLC
john.neun@gmail.com, +1 518 275-8139

Jim Niemiec, Jim Niemiec Consulting LLC
jim.niemiec@outlook.com, +1 715 213-4766

Steven P. Ottone, Omya
steven.ottone@omya.com, +1 919 641-7854

Gaurav Pranami, Imbed Biosciences
gpranami@imbedbio.com, +1 515 230-7005

Arthur Ragauskas, Oak Ridge National Laboratory
aragausk@utk.edu

Seshadri Ramkumar, Texas Tech University
S.Ramkumar@ttu.edu, +1 806 742-4567

Gregg Reed, Imerys
gregg.reed@imerys.com, +1 478 553-5747

Gerard J.F. Ring, University of Wisconsin—Stevens Point
gerrryring@wi-net.com, +1 715 592-3732

Scott Rosencrance, Kemira Chemicals
scott.rosencrance@kemira.com, +1 770 429-2753

Paul Wiegand, NCASI
pwiegand@ncasi.org, +1 919 941-6417

Junyong Zhu, USDA Forest Products Laboratory
jzhu@fs.fed.us, +1 608 231-9520

Join TAPPI *today!*
TAPPI JOURNAL is a free benefit of TAPPI membership, and is only available to members. To join TAPPI, to renew your TAPPI Membership, or to learn about other valuable benefits, visit www.tappi.org.

TAPPI, 15 Technology Parkway S., Suite 115, Peachtree Corners, GA 30092, publishes *TAPPI JOURNAL* monthly.

ATTENTION PROSPECTIVE AUTHORS: All papers published are subject to *TAPPI JOURNAL's* peer-review process. Not all papers accepted for review will be published. Before submitting, check complete author guidelines at http://www.tappi.org/s_tappi/doc.asp?CID=100&DID=552877.

Statements of fact and opinions expressed are those of individual authors. TAPPI assumes no responsibility for such statements and opinions. TAPPI does not intend such statements and opinions or construe them as a solicitation of or suggestion for any agreed-upon course of conduct or concerted action of any sort.

Copyright 2022 by TAPPI, all rights reserved. For copyright permission to photocopy pages from this publication for internal or personal use, contact Copyright Clearance Center, Inc. (CCC) via their website: www.copyright.com. If you have questions about the copyright permission request process, please contact CCC by phone at +1 978 750-8400. To obtain copyright permission to use excerpts from this publication in another published work, send your specific request in writing to Editor, TAPPI JOURNAL, 15 Technology Parkway S., Suite 115, Peachtree Corners, GA 30092, USA; or by fax to +1 770 446-6947. Send address changes to TAPPI, 15 Technology Parkway S., Suite 115, Peachtree Corners, GA 30092, USA; Telephone +1 770 446-1400, or FAX +1 770 446-6947. www.tappi.org

Editorial



MONICA SHAW | EDITORIAL DIRECTOR
mshaw@tappi.org

Ravi Challa brings tissue, nonwovens, and operational expertise to *TJ* Editorial Board

Editor's Note: *This column is part of a series that profiles the background and expertise of* TJ*'s editorial board members. These volunteer members spend long hours overseeing the peer review process and contributing to* TJ*. TAPPI would like to express its gratitude to the editorial board members for their hard work and willingness to share their expertise with the forest products community.*

— Monica Shaw, Editorial Director

TAPPI and the *TAPPI JOURNAL* (*TJ*) editorial staff would like to welcome a new member to the *TJ* Editorial Board, Ravi Challa, Ph.D., who is Research & Development (R&D) manager for Suominen Corporation at the company's Bethune, SC, facility. There, his primary focus is new product development on wetlaid nonwovens paper machines, from maintaining mature technologies and innovation to discovering patterns in paper machine shutdowns and executing nonwovens product development trials.



New member of* TAPPI Journal *Editorial Board, Ravi Challa, Ph.D.

Prior to joining Suominen, Ravi was a process engineer and an eTAD technology platform engineer at Georgia-Pacific in Crossett, AR, from 2015 through 2020. As a corporate process engineer, he worked to advance and commercialize the company's proprietary eTAD technology, as well as to support R&D efforts for new product trials at both the Crossett and Port Hudson, LA, facilities. In his process engineer role there, Ravi's focus included power boilers, chemical recovery, evaporator fouling, and chemical cost optimization. Ravi started his career as a process engineer in the pharmaceutical industry for a few years in India, after which he pursued graduate engineering programs in the United States.

Ravi received his Ph.D. in Biological Engineering from the University of Illinois at Urbana Champaign in 2015, completing a dissertation on "Characteristics of heat transfer fouling of thin stillage using model thin stillage and evaporator concentrates." As a research assistant in the university's Department of Agricultural and Biological Engineering, he published both peer-reviewed journal papers and papers for engineering conferences. Ravi published additional papers as a graduate research assistant at Mississippi State University, where he received his M.S. in Biological Engineering. He also holds a B.S. in Chemical Engineering from Sri Venkateswara University in India. In addition to his publications as a research assistant, Ravi is a published patent author.

In his job, Ravi enjoys a balance between R&D efforts in the lab and work in the field, and he hopes to bring that experience to bear as a member of the *TJ* Editorial Board.

"As a Ph.D. scientist with several years of manufacturing experience—not just R&D alone—in the tissue and pharmaceutical industries, process engineering experience helps me judge whether the ideas/solutions proposed in technical papers are sustainable in the paper industry," said Ravi. "My training as a scientist allows me to interpret technical information irrespective of the difficulty levels and novelty. To improve the technical quality of any research article, it is important that reviewers check both the quality of the scientific research and also whether the research results may ultimately be pragmatic to implement in production plants."

TAPPI and industry involvement

Ravi joined TAPPI in 2016, and one of his primary reasons for joining was the content in *TAPPI Journal*. He currently works on the TAPPI Dust Mitigation Committee, serving as secretary since 2021. He said that membership helps him "understand current trends in the paper industry" through offerings like TAPPI's *Tissue360°* magazine and newsletter, other publications, committee meetings, and conferences. Ravi is especially excited now to both share his expertise and learn through being a member of the *TJ* Editorial Board.

"Having served as a peer reviewer for several international journals, I enjoy reading technical articles," he said, "and being on the *TJ* Editorial Board will further enhance my technical reading and help build a perspective on the current trends in the paper industry."

Ravi is also a previous member of the American Institute of Chemical Engineers, American Institute of Agricultural and Biological Engineers, and American Association of Cereal Chemists. In addition, he is a full member of the Sigma Xi Scientific Research Honor Society.

Industry perspectives

For Ravi, the biggest technological and research changes he's seen since joining the industry relate to increased focus on sustainability and data analytics. However, he sees some roadblocks for the industry in approaching these trends.

"The paper industry is drifting towards environmental sustainability, but the industry is unfortunately not equipped with the right tools and personnel to match the market trends," said Ravi. "Also, there still exists a gap between operations and data scientists, and this makes it hard to implement data analytics for applied solutions in paper plants, which produce lots of data. It's no surprise that most data scientists don't know what a former or pickup function is in paper manufacturing. Data scientists with no manufacturing experience will slow down technology advancements that truly benefit the organization."

Informed by a background that began outside the paper industry, Ravi does see challenges to the industry going forward that relate to research, the right talent, and calculated operational decisions. As for research, he finds that the paper industry is not always known for being transparent to academic scientists. In addition, the remote location of mills makes it difficult to attract talent, making professionals with advanced education like Ph.D. degrees scarce.

On the operations side, better knowledge of machine and operating conditions are needed to make technology advancements, as is a better understanding by those who do possess such knowledge as to the bottom-line impacts from targeted improvements.

"While it's an advantage to have experienced papermakers on the team, their observations need to be translated to tangible results that benefit the organization and make a difference in the annual balance sheet," Ravi said.

On a personal note, Ravi enjoys volunteering for his local Lions Club, which is part of an international community service organization. His hobby is microscopes, which has proven a useful interest in his career assignments.

"I like microscopes and received professional training to conduct sample analysis on several large-scale microscopes like SEM and TEM during my grad school programs," said Ravi. "When I started my first job in the paper industry, this very hobby helped me innovate and implement sustainable solutions to significantly improve paper machine clothing life." **TJ**

Development of reinforced paper and mitigation of the challenges of raw material availability by utilizing Areca nut leaf

KISHAN K. JAISHWAL, IZHAR ALAM, AND CHHAYA SHARMA

ABSTRACT: Paper industries are facing a raw material crisis and searching for alternate raw materials that may be able to help mitigate the issue. Many industries use agro-waste as a raw material, irrespective of it having low bleachability and poor mechanical strength.

Areca nut leaf (ANL) is a nonwood-based material that may be acceptable as an alternate source of raw material that contains 61.5% holocellulose and 13.6% lignin, which is comparable to other agro-wastes and hardwood pulps. Kraft anthraquinone pulping with 20% active alkali as sodium oxide (Na_2O), 25% sulfidity, and 0.05% anthraquinone produced 15 kappa pulps with about 38.5% pulping yield. The bleachability of ANL pulp was good, and 83.5% ISO brightness could be achieved using the $D_0(EOP)D_1$ bleaching sequence. The ANL fiber has 33.8% better tensile, 54.5% better tear, and 15.2% better burst index than hardwood fiber. Similarly, 60.4% better tensile, 56.5% better tear, and 21.7% better burst index were observed in ANL than in wheat straw. Thus, the study revealed that Areca nut leaf can be used as an alternative raw material for papermaking, as well as to improve the physical property of paper products by blending it with inferior quality pulp.

Application: Areca nut leaf was used in this study as a potential raw material for papermaking, with good pulping and bleachability. The paper properties were also good as compared to other agricultural residues and hardwood pulp, so Areca nut fiber pulp can be used in place of hardwood to improve the physical properties of paper products, as agro-based paper industries are using hardwood pulp to improve its strength.

The Areca nut plant is commonly known as a palm plant and is cultivated for producing betel nut in tremendous quantities. The plant is grown in the coastal region of tropical countries in Asia and East Africa. India, Kerala, Assam and other places are major producers of areca nut and generate a huge amount of plant waste that is being burned or disposed of in the open field. This causes serious environmental problems of harmful gases (carbon monoxide, carbon dioxide, methane gas, etc.) because of burning and biodegradation in the open field. Thus, the present investigation was carried out for the utilization of Areca nut leaf (ANL). By utilizing ANL fiber, open field burning can be minimized, and the struggle for raw materials in the paper industry can be reduced.

The Areca nut plant has a very large evergreen leaf that whorls around the top of the stem. The ANL has a tubelike sheath at the base that is open at one side at maturity. The ANL fiber is a rich source of α-cellulose. Earlier works have shown that ANL fibers contain 75% or 66% α-cellulose [1,2]. Compared to the Areca nut husk fibers, which contain only 34%–35% cellulose, Areca seeds are found to have high cellulose content [3]. There is very little literature on the use of ANL fibers, especially in pulp and paper. Various reinforced polymer composite materials have been developed using the higher cellulose content of ANL fiber [1,4-5]. Researchers have worked on the use of Areca leaf sheets by blending them with wastepaper in a different proportion for developing paperboards with high resistance to water absorption and good tear and tensile strength [6]. Methods were developed for the utilization of Areca nutshells by softening their fiber through microbial treatment of the material. These methods can be commercially applied for developing value-added products likes textiles, viscose, and polyesters [7]. Areca leaf sheaths were noticed as potential sources for extracting high crystalline nanocellulose fibers with about 72% cellulose content [8]. Areca nutshell was used as a raw material for making pulp, and bleaching was done with hydrogen peroxide to make handmade colored art paper [9]. Areca leaf sheath has traditionally been used to develop disposable plates and dishes as a sustainable packaging material in India for decades [10]. Based on the literature, no work has been reported on the extraction of pulp fibers by kraft pulping and elemental chlorine-free (ECF) bleaching, as well as its blending with other agro-residue pulp for developing improved mechanical strength properties of paper products.

The current work evaluated ANL as a new raw material for paper manufacturing, keeping in mind that paper-based industries are facing a series of problems related to raw material availability and strength development in paper products. The whole Areca nut leaf was used to generate pulp via the kraft pulping process. Bleachability of the pulp was investigated using ECF bleaching. The strength properties of bleached pulp were determined, along with the comparative strength properties of other fibers, e.g., hardwood and wheat straw pulps. Successful utilization of ANL would provide an additional raw material for the paper manufacturing industries, as well as for improving the quality of the paper product in terms of strength properties.

MATERIALS AND METHODS

Areca leaf was collected from agricultural lands in the urban areas of western Uttar Pradesh, India. Raw materials were chopped to about 2–3 cm in length, wet cleaned with hot water, and air dried to remove absorbed water. Chopped and cleaned materials were stored at room temperature for further investigation. An active alkali (AA) solution of 100 g/L was prepared by dissolving sodium hydroxide (NaOH) and sodium sulfide (Na_2S) in distilled water; sulfide was maintained at 25%.

Chemical proximate analysis

Determination of the chemical components of the material was done by following regular laboratory procedures as per the TAPPI Standard Test Methods specified in **Table I**. To facilitate the analysis, the samples needed to be ground in a Wiley mill to make dust, and the moisture content of the dust material was measured as per standard.

Pulping

Kraft pulping of ANL was done to produce about 15 kappa pulps. Cooking was performed in a rotary digester having four stainless steel bombs of 100-gm ANL chip capacity on ovendry basis. The measured weight of the material was taken in this bomb, and to optimize the AA, different doses were charged with 0.05% of anthraquinone as a cooking aid that was added to the alkali. A 4:1 liquid-to-solid ratio was maintained through the addition of water after the alkali was charged. The bombs were placed into a digester that was full of water as a heating medium. Cooking was done at a fixed 165°C temperature for 60 min, excluding the time to achieve this temperature from ambient, which was 60 min (time to temperature). The conditions are presented in **Table II**. Targeted kappa numbers were achieved by keeping all the conditions the same, except AA charges. After cooking, black liquor was collected to analyze residual AA, and the pulp was thoroughly washed with hot and cold tap water to remove incorporated black liquor from the pulps. The washed unbleached pulp was kept in a polyethylene bag and stored in a refrigerator for further analysis of pulping yield and kappa number.

Parameter	Cooking Condition
AA, as Na_2O, on o.d. ANL	16%–22%
Sulfidity	25%
Anthraquinone, on o.d. ANL	0–0.05%
Liquid-to-solids ratio	4:1
Temperature	165°C
Time to temperature	60 min
Time at temperature	60 min
AA = active alkali; Na_2O = sodium oxide; ANL = Areca nut leaf.	

II. Cooking conditions during kraft pulping.

Bleaching

The unbleached pulp was bleached using an ECF bleaching sequence of $D_0(EOP)D_1$ to get the maximum possible brightness of the pulp. Here, D_0 stands for the delignification stage, which includes chlorine dioxide (ClO_2) used to react with the remaining lignin; and (EOP) is the extraction stage, which includes sodium hydroxide, oxygen, and hydrogen peroxide together in the same stage to remove chlorinated and oxidizing lignin products from the pulp. It also

Test Parameter	Standard Test Method
Solvent extractive	TAPPI T 204 cm-97 "Solvent extractives of wood and pulp"
1% alakali solubility	TAPPI T 212 om-02 "One percent sodium hydroxide solubility of wood and pulp"
Holocellulose	Wise, Murphy, and D'Addieco [11]
Lignin	TAPPI T 222 om-06 "Acid-insoluble lignin in wood and pulp"
Ash	TAPPI T 211 om-12 "Ash in wood, pulp, paper and paperboard: combustion at 525°C"
Silica	TAPPI T 245 cm-07 "Silicates and silica in pulp (wet ash method)"

I. Standards followed during the chemical analysis of Areca nut leaf (ANL).

Parameter	Bleaching Stage		
	D_0	(EOP)	D_1
Temperature, °C	50–55	80	75
Time, min	40–45	90	180
Consistency, %	5	10	10

III. Bleaching conditions used in different stages.

helps to reactivate the remaining lignin for the next oxidation stage, D_1, which is the bleaching or oxidizing stage for the remaining lignin with ClO_2 to get higher pulp brightness. During the delignification stage, the dose of ClO_2 was optimized by applying different kappa factors to the pulp. The ClO_2 dose in the D_1 stage was also optimized to achieve high brightness of the pulp with minimum loss of chemicals during this stage. Chlorine dioxide bleaching (D_0 and D_1) was performed in polyethylene terephthalate jars, and the temperature throughout treatment was maintained in a water bath. The alkaline extraction (EOP) phase was performed in an electrically-heated reactor under pressurized conditions. After every bleaching stage, the pulp was thoroughly washed with distilled water to remove residual chemicals and reaction products. The process conditions followed at every stage of the bleaching are depicted in **Table III**.

Refining of pulp and handsheet preparation

The unbleached and bleached pulps obtained were refined according to TAPPI Standard Test Method T 248 sp-00 "Laboratory beating of pulp (PFI mill method)" in a PFI mill to reach 450 ± 25 mL freeness level. For the blending study, unbleached and bleached hardwood and wheat straw pulp were also refined to get the same freeness level. Preparation of handsheets of 60 ± 2 g/m² for all samples and blends of the samples in different proportions using a British handsheet former were needed to determine all physical properties of the paper and were performed as per TAPPI T 220 sp-06 "Physical testing of pulp handsheets." Afterwards, the handsheets were kept at 27 ± 2°C temperature and 65 ± 5% relative humidity for about 24 h as per ISO 187:1990 "Paper, board and pulps—Standard atmosphere for conditioning and testing and procedure for monitoring the atmosphere and conditioning of samples" before further analysis of physical properties.

Parameter	Present Study	[8]	[12]	[13]
Extractives, %	12.7	1.51	10.86	0.72
Holocellulose, %	61.5	85.7	60.4	73.3
Lignin, %	13.6	12.8	16.6	19.6
Ash, %	10.4	--	10.9	—

IV. Chemical composition of Areca nut leaf (ANL) fibers.

RESULTS AND DISCUSSION

Assessment of chemical components

The chemical composition of natural fibers varies with their place of origin. The main components found in the natural fibers are lignin, holocellulose (cellulose and hemicellulose), and a small amount of pectin and extractives. The chemical composition of ANL fibers were measured and are depicted in **Table IV**. It was noted that ALN contains more than 60% of hollocelluose in its fibrous mass and is approximately comparable to the other materials, which are frequently used by the paper industry, as listed in **Table V**.

Active alkali dose optimization during pulping

Unbleached 15 ± 1 kappa number pulps were generated using different doses of AA with and without the cooking aid, 0.05% anthraquinone, during pulping with all other conditions (e.g., sulfidity, temperature, time, and liquid-to-solid ratio) held constant. As shown in **Table VI**, 20% AA as Na_2O was needed to produce the targeted 15 kappa pulp of 38.8% yield with 1.1% rejects. It was observed that, by adding a cooking aid, a 15%–20 % kappa reduction can be achieved for the same AA charge and that pulping yield increased by 7%.

Optimization of dosages of ClO_2 during the D_0(EOP)D_1 stage

The first stage of a bleaching sequence is known as the delignification stage (D_0-stage), as most of the residual lig-

Parameter	Areca Leaves (present study)	Rice straw [14]	Wheat Straw [15]	Bagasse [13]	Hardwood [16]
Extractives, %	12.7	3.4	3.2	–	1.8
Holocellulose, %	61.5	66.6	72.7	51–72	83.6
Lignin, %	13.6	13.2	19.9	27–32	25.7
Ash, %	10.4	12.7	5.2	1.5–5	1.4

V. Comparison of chemical content with other agro-waste material.

Parameter	Ex-1	Ex-2	Ex-3	Ex-4	Ex-5	Ex-6
AA, %	16	18	20		22	
Pulping additives, %	–	–	–	0.05	–	0.05
Residual AA, g/L	2.6	4.1	5.1	5.6	6.5	9.6
pH, black liquor	11.6	11.8	12.1	12.0	12.4	12.3
Kappa number	29.9	25.8	18.0	15.2	14.4	11.5
Unscreened pulp yield, %	39.1	38.8	35.9	38.5	33.8	36.2
Reject, %	1.7	1.5	1.2	1.1	1.0	0.9

VI. Active alkali (AA) dose optimization for targeted kappa pulp.

Particular	Ex-1	Ex-2	Ex-3	Ex-4	Ex-5
Kappa no.	15.0				
D_0-Stage (retention time: 45 min; temperature: 55°C; consistency: 5%)					
Kappa factor	0.15	0.20	0.23	0.25	0.30
ClO_2 added, %	0.86	1.14	1.31	1.42	1.71
End pH	2.5	2.4	2.6	2.4	2.6
Residual ClO_2, ppm	2.4	6.1	10.5	15.9	35.2
ClO_2 consumed, %	99.5	99.0	98.7	97.9	96.1
(EOP)-Stage (H_2O_2: 0.5%; temperature: 75°C; time: 90 min; end pH: 10.5)					
Brightness, % ISO	61.5	63.2	65.4	65.8	65.9
(EOP) kappa number	2.2	1.9	1.6	1.5	1.5

VII. Optimization of chlorine dioxide (ClO_2) charge at D_0 stage.

nin is removed at this stage. Different kappa factors were tested to optimize the ClO_2 charge, and a kappa factor of 0.23 was determined to be the optimum ClO_2 charge, as shown in **Table VII** and **Fig. 1**. The dotted line in Fig. 1 represents the tangent drawn on the curves of X-Y plane, and the point of intersection of the tangent is shown as the optimum kappa factor. Chlorine dioxide optimization at the D_1 stage was carried out by applying various doses of the chemicals from 0.5%–2.0% on the ovendry pulp for four different sets, as shown in **Table VIII**. In the final bleaching with ClO_2, a maximum brightness of about 83% ISO was achieved, and no further improvement in the brightness of pulp was observed beyond 1.0% dose of the chemical. As a result, a 1.0% dose of ClO_2 was determined to be the optimum value in the final stage of the $D_0(EOP)D_1$ bleaching sequence. Our finding to achieve this brightness is of great importance, as an earlier study showed a maximum of 69.2% brightness with 17.07% hydrogen peroxide bleaching [9].

Measurement of physical properties of pulp handsheets

The physical properties of handsheets of the unbleached and bleached ALN, wheat straw, and hardwood pulps of the same freeness level and basis weight were measured to compare their behavior, as presented in **Table IX** and **Table X**. All the physical properties of ANL pulp handsheets were found to be higher than wheat straw and hardwood pulp handsheets. It was calculated that 39.3% and 2.1% higher tensile index was observed for ANL sheets than for wheat straw and hardwood, respectively, in the case of unbleached pulp handsheets. However, in the case of bleached pulp handsheets, tensile index for ANL sheets was observed at about 60.4% and 33.8% higher than for wheat straw and hardwood, respectively, as shown in Table X. Similarly, the tear index of ANL pulp handsheets was observed 49.2% and 39.7% higher than wheat straw and hardwood pulp handsheets, respectively, in the case of unbleached pulp sheets; in the case of bleached pulp

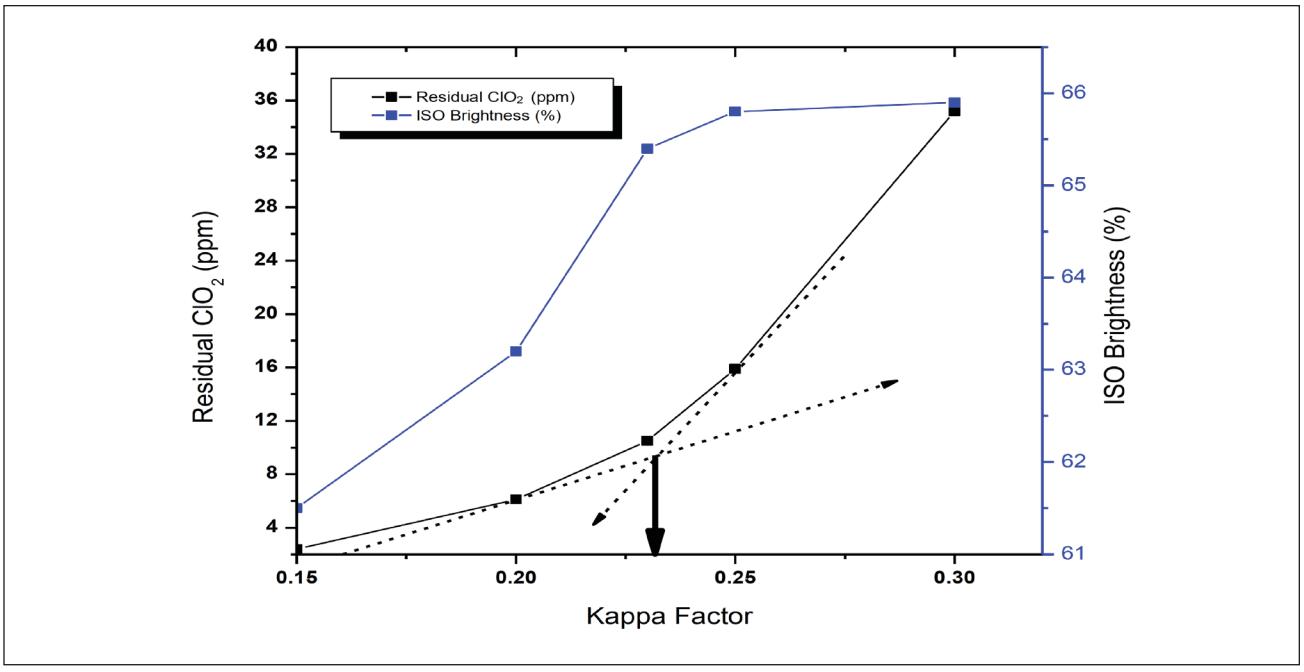

1. Residual chlorine dioxide (ClO_2) and ISO brightness (%) of pulp vs. kappa factor curve.

Particular	Results			
Kappa no.	**15**			
D_0-Stage (temperature: 55°C; time: 45 min; cy: 5%)				
Kappa factor			0.23	
ClO_2 added, %			1.31	
End pH			2.6	
Residual ClO_2, ppm			10.5	
ClO_2 consumed, %			98.7	
(EOP)-Stage (temperature: 75°C; time: 90 min; cy: 10%)				
NaOH added, %	2.07			
H_2O_2 added	0.5			
Final pH	10.7			
H_2O_2 consumed, %	94.4			
Brightness, % ISO	65.2			
(EOP) kappa number	1.5			
D_1-Stage (temperature: 75°C; time: 180 min; cy: 10 %)				
ClO_2 added, %	0.5	1.0	1.5	2.0
Final pH	3.4	3.6	3.2	3.6
Residual ClO_2, ppm	90.0	60.0	594	445
ClO_2 consumed, %	99.1	97.5	95.1	92.5
Brightness, %	80.2	83.1	83.4	83.1
CIE whiteness	79.2	82.4	82.8	82.4

ClO_2 = chlorine dioxide; NaOH = sodium hydroxide; H_2O_2 = hydrogen peroxide.

VIII. Optimization of chlorine dioxide (D_1) dose for D_0(EOP)D_1 bleaching of pulp.

Parameter	Areca Leaves	Wheat Straw	Hardwood
CSF, mL (before refining)	715±10	760±10	800±10
CSF, mL (after refining)	425±10	425±10	425±10
Basis weight, g/m²	60±2	60±2	60±2
Bulk, cc/g	2.09±0.15	2.12±0.05	2.07±0.12
Tensile index, N.m/g	33.3±2	20.2±3	32.6±2
Tear index, mN.m²/g	6.3±0.4	3.2±0.3	3.8±0.6
Double fold, no.	45±2	19±1	25±3

IX. Mechanical properties of unbleached pulp handsheets (mean of four readings is reported, along with the standard deviation).

Parameter	Areca Leaves	Wheat Straw	Hardwood
CSF, mL (before refining)	560±10	600±10	660±10
CSF, mL (after refining)	425±10	425±10	425±10
Basis weight, g/m²	60±2	60±2	60±2
Bulk, cc/g	2.15±0.12	2.1±0.14	2.10±0.10
Tensile index, N.m/g	64.4±3	25.49±3	42.6±2
Tear index, mN.m²/g	10.8±0.5	4.7±0.5	4.9±0.5
Burst index, kpa-m²/gm	4.6±0.02	3.6±0.02	3 .9±0.01
Double fold, no.	151±2	20±1	30±1

X. Mechanical properties of bleached pulp handsheets (mean of four readings is reported, along with the standard deviation).

sheets, it was about 56.5% and 54.6% higher than for wheat straw and hardwood, respectively.

Blending of ANL and hardwood fiber with wheat straw

The strength properties of different blends of hardwood and ANL with wheat straw fiber are given in **Table XI** and **Table XII**. The blending of wheat straw fiber with ANL fibers showed better physical properties than blending with hardwood fiber. As can be seen from Table XI, by adding 25%, 50%, and 75% ANL fiber to the wheat straw fiber, the tensile index showed improvement by approximately 28.6%, 77.6%, and 109.4%; tear index by 21.3%, 59.6%, and 95.7%; and burst index by 5.6%, 13.9%, and 19.4%, for the respective blends. Similarly, in Table XII, when wheat straw pulp was blended with hardwood pulp at 25%, 50%, and 75%, the strength properties of wheat straw pulp also increased; tensile index improved by 12.2%, 20.0%, and 26.3%; tear index by 8.2%, 30.6%, and 51.0%; and burst index by 2.8%, 5.6%, and 5.6% for the respective blends. Thus, more improved physical properties of wheat straw pulp handsheets were observed when blended with ANL fiber as compared to hardwood fiber. The blending of wastepaper with ANL sheath pulp has been done elsewhere to make high-quality paperboard, and improved tear, tensile and burst strength was observed [6].

CONCLUSIONS

The chemical content of Areca nut leaf fiber is comparable to wheat straw and hardwood, which are materials currently being used by the paper industry. The lignin content of the material is lower as compared to hardwood. The bleachability of the material is also good, and more than 80% ISO brightness could be achieved by using a $D_0(EOP)D_1$ bleaching sequence. Better physical properties in terms of tensile, tear, and burst index were observed as compared to wheat straw and hardwood pulp handsheets. The ANL fibers contain cellulose comparable to other materials and required low AA during pulping to achieve the targeted kappa pulp. Good bleachability of the pulp was also noted. The most important finding of our work was the high physical properties of paper from ANL fibers, which were higher than those for

Parameter	Wheat Straw:Areca Nut Leaves				
	100:0	75:25	50:50	75:25	100:0
Grammage, g/m²	60±2	60±2	60±2	60±2	60±2
Bulk, cc/g	2.1±0.22	2.3±0.21	2.9±0.23	2.9±0.24	2.8±0.24
Tensile index, N.m/g	25.5±3	32.8±2	45.3±3	53.4±4	64.6±5
Tear index, mN.m²/g	4.7±0.5	5.7±0.5	7.5±0.7	9.2±1	10.8±1
Burst index, kpa-m²/gm	3.61±0.02	3.8±0.02	4.1±0.02	4.33±0.01	4.58±0.03
Double fold, no.	20±1	35. ±3	60±4	90±3	151±4

XI. Blending with wheat straw pulp (mean of four readings is reported, along with the standard deviation).

Parameter	Wheat Straw:Hardwood				
	100:0	75:25	50:50	75:25	100:0
Grammage, g/m²	60±2	60±2	60±2	60±2	60±2
Bulk, cc/g	2.1±0.02	2.62±0.02	3.0±0.02	3.16±0.03	2.12±0.03
Tensile index, N.m/g	25.5±2	28.6±4	30.62±3	32.19±3	35.8±5
Tear index, mN.m²/g	4.9±0.5	5.3±1	6.4±0.7	7.4±0.8	8.3±1
Burst index, kpa-m²/gm	3.6±	3.7±1.5	3.8±2	3.8±1.5	3.9±2
Double fold, no.	188±5	106±7	32±3	20±2	10±1

XII. Blending of hardwood pulp with a wheat straw pulp (mean of four readings is reported, along with the standard deviation).

hardwood and wheat straw pulp handsheets. Thus, ANL fiber can be used as a substitute for hardwood pulp and where agro-based industries are challenged by the low mechanical properties of paper products. Our next step with Areca nut leaf will be to develop flexible packaging materials that require high strength properties using other agro-residues. **TJ**

ACKNOWLEDGEMENTS

The authors are thankful to the department of paper technology, IIT Roorkee, Saharanpur Campus. The authors also gratefully acknowledge the Ministry of Human Resource & Development for their financial support.

LITERATURE CITED

1. Arifuzzaman Khan, G.M., Shahrear Palash, S.R., Shamsul Alam, M., et al., *Polym. Compos.*, 33(5): 764(2012). https://doi.org/10.1002/pc.22204.
2. Poddar, P., Islam, M.S., Sultana, S., et al., *J. Mater. Sci. Eng.* 5(5): 1(2016). https://doi.org/10.15761/AMS.1000113.
3. Julie Chandra, C.S., George, N., and Narayanankutty, S.K., *Carbohydr. Polym.* 142: 158(2016). https://doi.org/10.1016/j.carbpol.2016.01.015.
4. Jayamani, E., Hamdan, S., Rahman, M.R., et al., *Procedia Eng.* 97: 545(2014). https://doi.org/10.1016/j.proeng.2014.12.282.
5. Padmaraj, N.H., Kini, M.V., Pai, B.R., et al., *Procedia Eng.* 64: 966(2013). https://doi.org/10.1016/j.proeng.2013.09.173.
6. Raghupathy, R., Viswanathan, R., and Devadasi, C.T., *Bioresour. Technol.* 82(1): 99(2002). https://doi.org/10.1016/S0960-8524(01)00141-9.
7. Rajan, A., Kurup, J.G., and Abraham, T.E., *Biochem. Eng. J.* 25(3): 237(2005). https://doi.org/10.1016/j.bej.2005.05.011.
8. Elanthikkal, S., Francis, T., and Akhtar, S., *J. Nat. Fibers* 18(9): 1261(2021). https://doi.org/10.1080/15440478.2019.1689885.
9. Dewi, I.A., Wijana, S., Royyani, D.E., et al., *IOP Conf. Ser.: Earth Environ. Sci.* 475: 012090(2020). https://doi.org/10.1088/1755-1315/475/1/012090.
10. Jong, O.K., Yong, T.M., and Jaafar, M.R., *IOP Conf. Ser.: Mater. Sci. Eng.* 824: 012014(2020). https://doi.org/10.1088/1757-899X/824/1/012014.
11. Wise, E., Murphy, M., and D'Addieco, A.A., *Pap. Trade J.* 112(2): 35(1946).
12. Banagara, A.R., Venkateshappa, S.C., Kamath, S.S., et al., *Mater. Today: Proc.* 5(14): 28080(2018). https://doi.org/10.1016/j.matpr.2018.10.049.
13. Poddar, P., Sultana, S., Akbar, M.A., et al., *MOJ Polym. Sci.* 2(2): 48(2018).
14. Alam, I., Kumar, J., and Sharma, C., *TAPPI J.* 20(7): 469(2021). https://doi.org/10.32964/TJ20.7.439.

15. Tripathi, S., Singh, S., Gangwar, A., et al., *IPPTA* 25(2): 121(2013).
16. Tripathi, S.K., Alam, I., and Bhardwaj, N.K., *Nord. Pulp Pap. Res. J.* 35(3): 325(2020). https://doi.org/10.1515/npprj-2020-0017.

ABOUT THIS PAPER

Cite this article as:
Jaishwal, K., Alam, I., and Sharma, C., *TAPPI J.* 21(9): 469(2022). https://doi.org/10.32964/TJ21.9.469

DOI: https://doi.org/10.32964/TJ21.9.469

ISSN: 0734-1415

Publisher: TAPPI Press

Copyright: ©TAPPI Press 2022

About this journal

ABOUT THE AUTHORS

We chose to research this topic in order to promote use of Areca nut leaf (ANL), which is a huge agro-waste, as a raw material for making paper, as well as to mitigate raw material scarcity facing the paper industry. We found that ANL fiber can be used as a substitute for hardwood pulp and that it also imparts improved mechanical strength compared to hardwood and wheat straw pulp.

Industries are searching for alternates to scarce raw materials, and ANL provides one option. In addition, agro-based industries like paper have faced low mechanical strength in products. By using ANL, issues with mechanical properties may be minimized.

Our next step is to develop flexible packaging materials that require high strength properties using ANL in conjunction with other agro-residues.



Jaishwal



Alam



Sharma

Jaishwal is a Master's student, Alam is research scholar, and Sharma is professor in the Department of Paper Technology at the Indian Institute of Technology Roorkee, Saharanpur campus, in Saharanpur, Uttar Pradesh, India. Email Sharma at chhaya.sharma@pt.iitr.ac.in.

Economic and competitive potential of lignin-based thermoplastics using a multicriteria decision-making method

CÉDRIC DIFFO TÉGUIA, NIMA GHAVIDEL MEHR, WOLFGANG G. GLASSER, AND PAUL R. STUART

ABSTRACT: As a result of new lignin extraction plants hatching and increasing volumes of technical lignin becoming available, a variety of lignin derivatives, including phenolic resins and polyurethane (PU) foams, are reaching the marketplace or being used as intermediate products in many industrial applications. In the spectrum of possible lignin derivatives, thermoplastics appear particularly attractive due to a symbiosis of market, policy, and technology drivers.

To assess the preferredness for lignin-based thermoplastics, this paper adapted a risk-oriented methodology formerly applied to assess lignin usage in various applications (phenol-formaldehyde [PF] resins, PU foams, and carbon fiber applications) to the case of lignin-based thermoplastics using hydroxypropylated lignin (HPL) and miscible blends of lignin and polyethylene oxide (PEO). The HPL is considered for garbage bags and agricultural films applications, while lignin-PEO blends are used as replacement for acrylonitrile butadiene styrene (ABS) in applications such as automotive parts. In the methodology, two phased-implementation strategies were defined for each thermoplastic derivative, considering perspectives for profit maximization (90 metric tons/day integrated units) and revenue growth (350 metric tons/day overall capacity), which were considered for implementation within a softwood kraft pulping mill. A set of six criteria representative of the main economic and market competitiveness issues were employed, and their respective importance weights were obtained in a multicriteria decision-making (MCDM) panel.

Early-stage techno-economic estimates were done as a basis for the calculation of decision criteria. Compared to product derivatives previously assessed, capital investment for thermoplastic strategies appeared marginally higher due to the required lignin modification steps (on average 30% higher at similar capacity, and 6% for higher-scale revenue diversification strategies). Higher operating costs were also observed due to increased chemical expenses for all thermoplastic strategies, which are ultimately balanced by revenues associated with targeted thermoplastic products, leading to greater annual margins and cash flow generation over the project lifetime for thermoplastic strategies compared to other product applications (58% to 66% higher on average, at similar scale). Benefits of improved economics were reflected in economic criteria, internal rate of return (IRR), and cash flow on capital employed (CFCE), as well as in the price competitiveness criterion, CPC. Overall, the combination of relatively high lignin content in the plastic formulation and the less costly modification method contributed to lignin-PEO strategies, gaining the top two rankings. Based on their overall scores, both strategies defined for HPL would also integrate the group of "preferred" strategies, but are outranked by strategies that consider lignin positioning on PU foam applications.

Application: This paper highlights the market and technical drivers for the use of lignin in bio-based thermoplastic products such as garbage bags, agricultural films, and automotive parts. Additionally, the potential preference for such applications is assessed against phenolic resins and polyurethane foams previously studied, using a multicriteria approach.

Mismanaged single-use plastics pose multiple threats to the economy (e.g., tourism, fisheries, agriculture) and human health (e.g., water and food chain contamination), and perhaps most importantly, they pose threats to the environment (e.g., ocean and land pollution, loss of biodiversity) [1]. Regulatory measures such as bans and levies have been applied in more than 60 countries, with scopes varying from one geographical area to another. For instance, various incentive mechanisms exist in many European countries to encourage a broader use of bioplastics; lightweight plastics are increasingly banned at the state or city level in North America; and many African countries enforce a complete ban on the production and use of plastic bags [2]. Apart from regulations, more efficient waste management systems and a full transition to a circular economy can substantially reduce the pollution caused by single-use plastics [3]. Nonetheless, while such efforts can considerably contribute to pollution reduction, the current production of bioplastics remains as low as 1% of total plastic consumption [4].

Bioplastics, in general, include one or a combination of bio-based, biodegradable, or compostable plastic materials.

Bio-based plastics, as opposed to fossil-based plastics, originate from renewable resources such as first or second-generation biomass [5]. Although they generally degrade in nature, not all bio-based plastics are recognized as biodegradable from a regulation standpoint. Indeed, distinctions are made between biodegradable and compostable plastics based on the level of degradation after a given time period when exposed to naturally occurring microorganisms. This situation is highlighted by different standards; for example, in the United States, there are ASTM D6400-12 "Standard specification for labeling of plastics designed to be aerobically composted in municipal or industrial facilities" and ASTM D6868-17 "Standard specification for labeling of end items that incorporate plastics and polymers as coatings or additives with paper and other substrates designed to be aerobically composted in municipal or industrial facilities," and in Europe, there is EN 13432:2000 "Packaging – Requirements for packaging recoverable through composting and biodegradation – Test scheme and evaluation criteria for the final acceptance of packaging."

Even though the concept of biodegradability has received considerable attention in past decades, major concerns remain regarding the environmental impact of bioplastics leakage into natural systems [6]. Furthermore, current technology and end-life infrastructure prohibit plastics from being both recyclable and biodegradable/compostable, and therefore one characteristic has to be favored in the design phase. Since composting and biodegradation generate low-value products such as water and carbon dioxide (CO_2), recyclability is often more desirable, as it retains the plastic material in the economy [7]. Benefits from both properties can be combined in a manner similar to efforts made by Avantium and BASF in developing polyethylene furanoate (PEF), a bio-based recyclable material to substitute for polyethylene terephthalate (PET), which is petroleum based [8,9].

From a market standpoint, the rationale for bioplastics is closely linked to their scale-up potential and to expected environmental benefits. The global production of plastic materials was more than 360 million metric tons in 2020 and remained quite stable despite the COVID-19 pandemic, with most plastics being used in the packaging business (approximately 40%), followed by building and construction [10]. The demand is greatest for polypropylene (PP), polyethylene (PE), and polyvinyl chloride (PVC), of which around 29 million metric tons were consumed in Europe alone [10]. Acrylonitrile butadiene styrene (ABS) is expected to become one of the most attractive markets in the plastics industry, as it is the largest volume engineering thermoplastic resin and a key player in the segments of appliances and electronics, as well as automotive parts [11]. The global ABS market was estimated at around US$25B in 2019, with a compound annual growth rate (CAGR) of about 7% between 2020 and 2027 [12]. Although polyurethane (PU) and PP are the most widely used plastic polymers in the automotive industry, ABS is expected to experience fast growth due to its suitability in the manufacture of parts that need resistance to chemicals, such as shrouds, pipes, and electronic housings [13-15]. Therefore, it represents a promising opportunity to commercialize larger volumes of bio-based materials in coming years. Bio-based plastics could also have an important position in the segment of personal protective equipment, where they are preferred as a means to avoid plastic waste pollution related to single-use applications, such as medical gloves [16]. Furthermore, bio-based plastics address a continued rise in demand for compostable and biodegradable bags used in shopping and waste collection applications [17].

EVOLUTION OF THE LIGNIN FIELD TOWARDS THERMOPLASTICS

One of the main factors that still hinders the use of bioplastics is the production cost, which is primarily dictated by the feedstock expense, e.g., sugars or starches [18]. In this context, fibrous materials and lignin can play a major role in overcoming this challenge while addressing the issue of sustainability [19]. Lignin, in particular, is the second most abundant biopolymer after cellulose and constitutes approximately 30% of non-fossil carbon in the biosphere [20]. In recent years, implementation of new lignin extraction technologies by pulp and paper companies such as Domtar (Plymouth, NC, USA), Stora Enso (Sunila, Finland), and West Fraser (Hinton, AB, Canada) has significantly increased availability of technical lignins. In addition, with the recent lignosulfonates installation by Borregaard, the LignoTech plant in Fernandina Beach, FL, USA, the capacities of new units range from nearly 10,000 to 150,000 metric tons/year [21-24]. Major South American pulp and paper producers such as Klabin and Fibria-Suzano are also embarking upon lignin production at pilot and commercial scale, leveraging different types of biomass and hence different lignin structures [25,26]. From a market perspective, the global size of the lignin market is estimated at approximately US$794M with an annual growth rate of 1.9% from 2019 to 2025 [27], which demonstrates the considerable potential in this area.

In such a dynamic economic environment where there is a competitive race to access markets for lignins, the need for consistently delivering high-quality lignin products is crucial. Providers of lignin extraction technologies endeavor to increase their process efficiency, as well as deliver high-grade products with low impurity levels. For example, the VTT Technical Research Centre of Finland has developed the CatLignin process that is able to produce a highly-reactive catechol-rich lignin that could surpass phenol replacement levels for phenolic resin production above 50% without chemical modification [28]. Furthermore, the biotechnology company MetGen provides a controlled enzymatic process that oxidizes and fractionates lignin and yields a product aiming at high-value applications [29,30].

In this regard, Valmet has tailored and optimized its trademarked LignoBoost process in order to focus research towards different lignin end-markets [31]. Nevertheless, one of the major challenges in the commercial production of lignin is to maintain a consistent quality over time, mainly due to feedstock and process variations [32]. This could be addressed by a better stabilization of process operations once the lignin extraction unit is implemented, as lignin has a quasi-invariable structure in wood [33]. Even though lignin remains primarily used as an energy source in existing mills, several added-value applications have been developed in recent years [34,35] as a result of research and development efforts mainly pursued by pulp and paper companies, but also by biochemical industrial players. For example, Stora Enso and UPM have successfully incorporated lignin in the production of phenolic resins for the wood products industry [36,37], while the USDA's Forest Products Laboratory has played a significant role in the development of lignin-based carbon foams [38]. Also, lignin-based water barrier coatings have already been commercialized [39], along with other efforts to promote lignin use in thermoplastic applications such as compostable bags [40] and engineered parts for musical instruments or design objects [41,42]. In addition to Valmet's and Biochemtex's collaboration in the development of bio-PET incorporating lignin [43,44], the Natural Research Council of Canada (NRC) is actively developing lignin-based composite and plastic products, including PU foams [45,46] and lignin thermoplastic pellets using various resins [47].

PROCESSES FOR THE PRODUCTION OF LIGNIN-BASED THERMOPLASTICS

Due to the presence of various functional precursors in lignin polymer chains, most lignin-based polymeric materials, such as resins and foams, bear a highly cross-linked nanostructure. The large amount of lignin potentially available at commercial scale as a bio-based aromatic precursor, together with its sustainability, cost-effectiveness, and biodegradability, have attracted increasing interest for developing lignin-based thermoplastics as alternatives for petroleum-based products [48]. On the other hand, obtaining high-performance thermoplastics using lignin is challenging due to its relatively low molecular weight, high polydispersity, and rigidity [49].

To alleviate the previously noted obstacles, as well as to improve the thermoplasticity, processability, thermal stability, and mechanical properties of lignin, various methods can be considered. Those include plasticization, blending with polymers with low glass transition temperatures (Tg), and chemical modifications. These methods are known to reduce the natural Tg of lignin, which is in the range of 90°C to 170°C [48]. Plasticization of hardwood and softwood lignin using agents such as water, ethylene glycol, or lactic acid improves the mobility of lignin chains by increasing the free volume in the matrix [50]. Mixing lignin with synthetic polymers in miscible blends using polyethylene oxide (PEO), PET, or poly(N-vinyl pyrrolidone) (PVP), for example, has proven promising for forming a compound with a Tg lower than that of lignin. It has been used, for instance, in the production of lignin-based carbon fibers [51,52]. Chemical modification techniques, including esterification (e.g., acetylation), etherification (e.g., hydroxypropylation), grafting, and copolymerization help to mask the reactive hydroxyl groups on the lignin polymer chain, thus hindering its thermosetting properties [53-56]. Among lignin modification methods, hydroxypropylation as applied by Cao et al. [57] and lignin-polymer blending using PEO as applied by Akato et al. [58] are among the most advanced.

In order to produce a dry hydroxypropylated lignin (HPL) powder, lignin obtained from precipitation in a kraft process is dissolved in a sodium hydroxide (NaOH) solution to neutralize its acidic functional groups, then made to react with propylene oxide (PO) at pH in a range between 10 and 12.5. Thus chemically-modified lignin is further processed with an aliphatic polyester (e.g., polylactic acid, PLA) or an aromatic polyester (e.g., polybutylene adipate/terephthalate, PBAT) to produce film products such as trash bags and agricultural films, or injection molded products such as flower pots or toys [57]. Using that method, Glasser et al. produced HPL-based polymer blends with enhanced biodegradability and mechanical properties satisfying performance standards up to a 25%–30% lignin content [59].

While assessing lignin incorporation into composites for automotive parts, Akato et al. [58] used PEO as an interfacial adhesion promotor, taking advantage of hydrogen bonding between PEO ether linkages and lignin phenolic and aliphatic hydroxyl groups. Using that approach, blends of methanol-fractionated softwood kraft lignin and PEO (10% of lignin content in weight) were added up to 30% weight content in ABS formulation with no deleterious impact on mechanical properties. In contrast with HPL, which is a uniform substance once chemically modified, blends of lignin and PEO would form a solution with limited miscibility. Nonetheless, the method was demonstrated to also work with organosolv lignin, and it is considered promising for producing a performant and cost competitive bio-based ABS replacement.

RISK ASSESSMENT OF LIGNIN BIOREFINERY STRATEGIES

In light of the state-of-the-art regarding possible lignin derivatives, it is critical for potential implementers of lignin extraction technologies to assess the benefits and limitations of different product strategies. For that matter, a multi-perspective risk-oriented approach has been suggested to assess emerging biorefinery product-process options [60], which has been successfully used in the context of a pulp and paper mill considering a lignin-based biorefinery to produce phenolic resins, PU foams, or carbon fibers [61].

Category	Criterion	Interpretation
Economic Risk	Internal rate of return (IRR)	Measure of **project profitability under normal market conditions**, considering all phases of the biorefinery strategy. A hurdle rate can be set at 20%, considering the risk level expected in Year 5 of the project.
	Cash flow on capital employed (CFCE)	Ability to generate cash flows from the capital investment over the life of the project, and thereby to **improve the value of the company by lowering its debt**.
Market Risk and Competitiveness	Revenue diversification (RD)	Potential to meet revenue growth targets from new bioproducts, over the revenue from the mill in its current situation. It indicates an ability to mitigate market risk by being **less dependent on pulp sales, due to a more diversified source of revenues**.
	Competitiveness on production costs (CPC)	Robustness of the biorefinery strategy relative to an **aggressive price-cutting strategy from the competition**, based on assumptions of a low-end production price for the competition.
	Resistance to energy and chemicals market uncertainty (RECMU)	Vulnerability of the strategy to **production cost volatility due to the volatility of feed material costs** (product transportation and logistics not included).
	Robustness to poor market conditions (RPMC)	Ability to **afford process operation under poor market conditions** for a 6-month period, expressed by EBITDA* as a percentage of the capital investment.

* EBITDA = earnings before interest, taxes, depreciation, and amortization.

I. Decision criteria and agreed-on interpretation for evaluation of lignin strategies.

In this approach, a phase-implementation strategy is defined for each product-process combination with the purpose of mitigating specific risks, considering value chain penetration as well as market and technology uncertainties. Residual risks that are not addressed via the phased implementation are therefore highlighted and translated into decision criteria used in a multicriteria decision-making (MCDM) panel to identify preferred strategies. Early-stage techno-economic estimates are obtained using a large-block analysis and further used for the calculation of MCDM criteria. In the study conducted by Diffo Téguia et al. [61], six criteria (**Table I**) representing economic and competitiveness problematics were used to assess the set of strategies defined. Criteria selection followed a two-step approach to achieve a set of important criteria (as evaluated individually) [62], forming a consistent family (as evaluated as a whole) [63]. It then constitutes a pertinent basis to assess other lignin product derivatives, such as thermoplastics, which were not considered in that study.

Given the current context of emerging lignin-based thermoplastics and recent progress of lignin modification technologies, this paper aims to assess the attractiveness of thermoplastic derivatives under economic and market competitiveness perspectives, taking other pertinent lignin derivative products as benchmark.

METHODOLOGY

The methodology developed for this study leverages the assessment performed in [61], in order to provide a comparable basis between lignin-based thermoplastics and other lignin derivatives. It is slightly adapted to consider thermoplastic options, as shown in **Fig. 1**, especially regarding the definition of strategies and the pricing basis for techno-economic estimates.

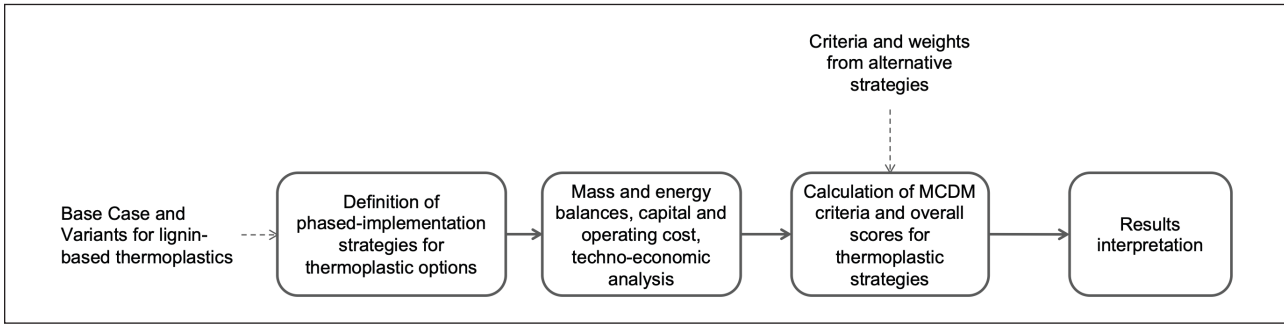

1. Methodology to assess the preference for thermoplastics among lignin derivatives.

DEFINITION OF STRATEGIES FOR THERMOPLASTIC OPTIONS

The context foundation remains the implementation of a lignin biorefinery within a 1500 air dried (a.d.) metric tons/day kraft softwood pulp mill, where a 30 bone-dry (b.d.) metric tons/day lignin precipitation unit is running. Strategies are defined within (1) profit-oriented and (2) revenue-oriented perspectives, following a phased-implementation approach. For this study, the distribution of lignin derivatives in the portfolio is done in a manner that emphasizes the production of thermoplastics, with the objective to fully benefit from higher market demand compared to other lignin derivatives considered. Four new strategies have been defined, the detailed descriptions of which are provided in the next section and summarized in **Table II** for the group of profit-oriented strategies and in **Table III** for the group of strategies seeking revenue growth.

In a way consistent with strategies formerly defined, lignin is sold as an intermediate product; for example, to a plastic compounder or an end-product manufacturer. This study focuses on two thermoplastic alternatives, resulting either from the hydroxypropylation of lignin (referred to as hydroxypropylated lignin, HPL) or from the blending of lignin with PEO (referred as lignin-PEO blends). It is considered that HPL is commercialized for garbage bags and agricultural mulch films applications, while lignin-PEO blends are commercialized as an ABS replacement.

The definition of strategies is agnostic of lignin quality, in terms of the fact that it considers that lignins extracted either from kraft or from solvent pulping (SP) processes would result in satisfying product properties and performances. The integration of an HPL unit into the lignin precipitation process is inspired from Glasser et al. [59] and is illustrated in **Fig. 2**, where the lignin cake after one stage of precipitation and filtration and without acid washing (the lignin cake would be around pH 10) is fed to a

<table>
<tr><th>Lignin Biorefinery Strategies</th><th>Phase 0
Year 0 – Year 4</th><th colspan="2">Phase I
Year 5 – Year 9</th><th>Phase II
Year 10 – Year 30</th></tr>
<tr><td>Base case 30 metric tons/day lignin precipitation</td><td colspan="2">•Year 0: 100% lignin burned
•Year 1: 28 metric tons/day burned, 2 metric tons/day to board mills
•Year 2: 24 metric tons/day burned, 6 metric tons/day to board mills
•Year 3: 18 metric tons/day burned, 6 metric tons/day to board mills, 6 metric tons/day to PF resin market</td><td colspan="2">•Year 4: 12 metric tons/day burned, 6 metric tons/day to board mills, 12 metric tons/day to PF resin market
•Year 5: 6 metric tons/day burned, 6 metric tons/day to board mills, 18 metric tons/day to PF resin market
•Year 6+: 6 metric tons/day to board mills, 24 metric tons/day to PF resin market</td></tr>
<tr><td>Ligno 90•PF</td><td rowspan="6">Same as Base Case</td><td colspan="2">Increase of lignin precipitation capacity to 90 metric tons/day
•Year 5: 6 metric tons/day burned, 6 metric tons/day to board mills, 48 metric tons/day to PF resin market
•Year 6: 6 metric tons/day to board mills, 84 metric tons/day to PF resin market</td></tr>
<tr><td>Ligno 90•PF PU</td><td colspan="2">Same as Ligno 90•PF, except:
•Year 5: 33 metric tons/day to PF resins, 15 metric tons/day to PU foams
•Year 6: 54 metric tons/day to PF resins, 30 metric tons/day to PU foams</td></tr>
<tr><td>Ligno 90•PF CFs</td><td colspan="2">Same as Ligno 90•PF, except:
•Year 5: 33 metric tons/day to PF resins, 15 metric tons/day to CFs
•Year 6: 54 metric tons/day to PF resins, 30 metric tons/day to CFs</td></tr>
<tr><td>Resin 90</td><td>Same as Ligno 90•PF</td><td>Acquisition of a resin producer
•Year 10: 290 metric tons/day of resin produced
•Year 11: 435 metric tons/day of resin produced</td></tr>
<tr><td>Ligno 90•PF HPL</td><td colspan="2">Same as Ligno 90•PF, except:
•Year 5: 24 metric tons/day to PF resins, 24 metric tons/day to HPL
•Year 6: 24 metric tons/day to PF resins, 60 metric tons/day to HPL</td></tr>
<tr><td>Ligno 90•PF Lignin-PEO</td><td colspan="2">Same as Ligno 90•PF, except:
•Year 5: 24 metric tons/day to PF resins, 24 metric tons/day to Lignin-PEO
•Year 6: 24 metric tons/day to PF resins, 60 metric tons/day to Lignin-PEO</td></tr>
<tr><td colspan="5">PF = phenol-formaldehyde; PU = polyurethane; CFs = carbon fibers; HPL = hydroxypropylated lignin; PEO = polyethylene oxide.</td></tr>
</table>

II. Implementation phases of profit-oriented strategies.

Lignin Biorefinery Strategies	Phase 0 Year 0 – Year 4	Phase I Year 5 – Year 9	Phase II Year 10 – Year 30
Base case 30 metric tons/day lignin precipitation	•Year 0: 100% lignin burned •Year 1: 28 metric tons/day burned, 2 metric tons/day to board mills •Year 2: 24 metric tons/day burned, 6 metric tons/day to board mills •Year 3: 18 metric tons/day burned, 6 metric tons/day to board mills, 6 metric tons/day to PF resin market •Year 4: 12 metric tons/day burned, 6 metric tons/day to board mills, 12 metric tons/day to PF resin market •Year 5: 6 metric tons/day burned, 6 metric tons/day to board mills, 18 metric tons/day to PF resin market •Year 6+: 6 metric tons/day to board mills, 24 metric tons/day to PF resin market		
Ligno 90 + SP•PF	Same as Base Case	Increase of lignin precipitation capacity to 90 metric tons/day •Year 5: 6 metric tons/day burned, 6 metric tons/day to board mills, 48 metric tons/day to PF resin market •Year 6: 6 metric tons/day to board mills, 84 metric tons/day to PF resin market Solvent pulping demo plant[1]	Increase of SP to full capacity[2]
Ligno 90 + SP•PF PU		Same as Ligno 90 + SP•PF, except lignin distribution: 6 metric tons/day to board mills, 220 metric tons/day to PF resins, 124 metric tons/day to PU foams	
Ligno 90 + SP•PF CFs		Same as Ligno 90 + SP•PF, except lignin distribution: 6 metric tons/day to board mills, 220 metric tons/day to PF resins, 124 metric tons/day to CFs	
Ligno 90 + SP•PF HPL		Same as Ligno 90 + SP•PF, except lignin distribution: 6 metric tons/day to board mills, 84 metric tons/day to PF resins, 260 metric tons/day to HPL	
Ligno 90 + SP•PF Lignin-PEO		Same as Ligno 90 + SP•PF, except lignin distribution: 6 metric tons/day to board mills, 84 metric tons/day to PF resins, 260 metric tons/day to Lignin-PEO	

PF = phenol-formaldehyde; PU = polyurethane; SP = solvent pulping; CFs = carbon fibers; HPL = hydroxypropylated lignin; PEO = polyethylene oxide.
[1] The demo plant extracts 9 b.d. metric tons/day of lignin from 50 b.d. metric tons/day of hardwood.
[2] There is a capacity ramp-up of the full-scale plant from Year 10-12, resulting in 220, 270, and 350 b.d. metric tons/day of lignin extracted.

III. Implementation phases of revenue-oriented strategies.

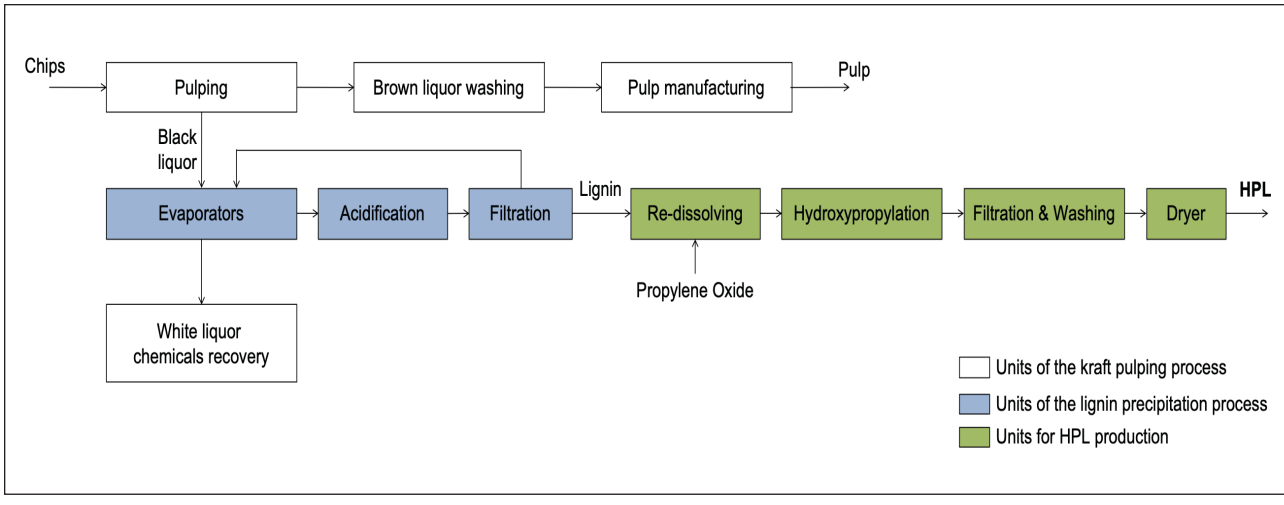

2. Process configuration for the production of hydroxypropylated lignin (HPL) from lignin precipitation.

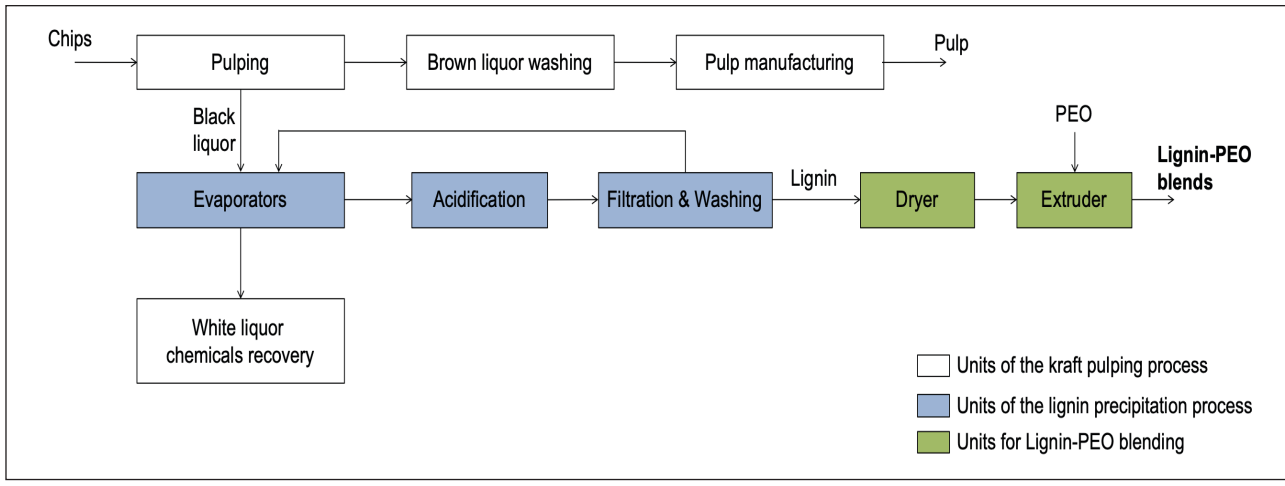

3. Process configuration for the production of lignin- polyethylene oxide (PEO) blends from lignin precipitation.

redissolving tank. The process configuration for lignin-PEO blends is inspired from Akato et al. [58] and illustrated in **Fig. 3**, where lignin exiting from the lignin precipitation or the SP process would be directly fed to the extruder, along with PEO.

TECHNO-ECONOMIC ANALYSIS

Information for mass and energy balances for HPL and lignin-PEO blends was collected from respective reference sources in the literature, and capital and operating cost estimates were achieved using a large-block analysis approach where process units shared with former strategies remained unchanged.

The main assumptions for thermoplastic strategies reside in basis for feed material unit costs and product prices. In this case also, costs for propylene oxide and polypropylene oxide were correlated with crude oil price using historical data, and estimated over the project lifetime considering a long-term average crude oil price of US$80/barrel [64,65]. For decision criteria using high-end feed material unit costs in their calculation, correlations were done with a long-term maximum crude oil price of US$150/barrel.

Since lignin-PEO blends are positioned as ABS replacement, its market price is also correlated with crude oil, with a long-term minimum crude oil price of US$55/barrel used to estimate the low-end market price for ABS. In the case

Feed Material, Product	Unit Cost, Product Market Price Estimates, US$/metric ton			Basis
	Nominal	Minimum	Maximum	
PO	1,365	-	1,540	• Correlation with crude oil price at US$80/barrel for the nominal values. • Low- and high-end values are correlated with crude oil prices of US$55/barrel and US$150/barrel, respectively.
PEO	1,425	-	1,730	
Lignin-PEO blends	2,550	2,180	-	
HPL	2,160	1,915 (mulch films) 1,680 (garbage bags)		• Correlation with corn price at US$3.8/bushel for the nominal value, using PLA as reference product. • Low-end market prices: PLA used as reference product for mulch films; LDPE used as reference for garbage bags, which is correlated with crude oil price at US$55/barrel.

PO = propylene oxide; PEO = polypropylene oxide; HPL = hydroxypropylated lignin; PLA = polylactic acid; LDPE = low-density polyethylene.

IV. Assumptions for feed material costs and product prices.

of HPL, since the main benefit of lignin is improving the plastic biodegradability, PLA is considered as the market reference both for agricultural mulch films and garbage bags. Therefore, the HPL price is correlated with the corn price, considering a projected long-term average corn price of US$3.8/bushel [66]. For criteria using low-end market prices, it is assumed that under poor market conditions, it would be more difficult to take advantage of the biodegradable aspect of garbage bags, for which it is less essential, compared to agricultural mulch films. Thus, low-density polyethylene (LDPE) is considered a more appropriate benchmark in such conditions, and its low-end price is estimated using correlations with crude oil price at US$55/barrel. The values obtained for feed materials costs and product prices are presented in **Table IV**.

DECISION CRITERIA AND SCORES FOR THE STRATEGIES

In addition to the techno-economic figure, the economic and competitiveness potential of thermoplastic strategies is assessed using the set of criteria in Table I. Although the consideration of additional criteria values relative to thermoplastic strategies could lead to a different appreciation of the relative importance of criteria, it is essential for the purpose of the comparison that preferences of project decision-makers, expressed through lower- and upper-bounds for the criteria as well as tradeoff values between them, are adequately represented. Therefore, utility functions and criteria weights from the previous study are reconducted and used to calculate overall scores for the strategies.

Indicator	Ligno 90• PF	Ligno 90• PF PU	Ligno 90• PF CFs	Resin 90	Ligno 90• PF HPL	Ligno 90• PF Lignin-PEO	Note/Comment
Lignin production capacity	90 metric tons/day	90 metric tons/day	90 metric tons/day	90 metric tons/day 435 metric tons/day resin	90 metric tons/day	90 metric tons/day	
Production rate by application	PF resin: 90 metric tons/day	PF resin: 60 metric tons/day PU foams: 30 metric tons/day	PF resin: 60 metric tons/day CFs: 30 metric tons/day	PF resin: 90 metric tons/day	PF resin: 30 metric tons/day Garbage bags: 39 metric tons/day Mulch films: 39 metric tons/day	PF resin: 30 metric tons/day ABS: 67 metric tons/day	Production rates for thermoplastic applications refer to lignin derivatives, i.e., after modification (HPL or blending).
Capital investment	US$ 32M	US$ 33M	US$ 39M	US$ 146M	US$ 46M	US$ 35M	Marginal variations due to equipment addition for lignin modification.
Annual operating costs (Phase II)	US$ 6M/year	US$ 7M/year	US$ 7M/year	US$ 104M/year	US$ 20M/year	US$ 14M/year	Added cost related to chemicals required for lignin modification.
Annual revenues (Phase II)	US$ 21M/year	US$ 41M/year	US$ 36M/year	US$ 287M/year	US$ 67M/year	US$ 67M/year	Product recipes lead to comparable revenues for the thermoplastic strategies.
Annual EBITDA (Phase II)	US$ 15M/year	US$ 34M/year	US$ 29M/year	US$ 183M/year	US$ 47M/year	US$ 53M/year	Despite higher costs, thermoplastic strategies generate greater margins.
NPV (Phases I and II combined)	US$ 17M	US$ 70M	US$ 49M	US$ 164M	US$ 79M	US$ 102M	Over the project lifetime, both thermoplastic strategies generate significant cash flows.

PF = phenol-formaldehyde; PU = polyurethane; CFs = carbon fibers; HPL = hydroxypropylated lignin; PEO = polyethylene oxide; ABS = acrylonitrile butadiene styrene; EBITDA = earnings before interest, taxes, depreciation, and amortization; NPV = net present value.
* Strategies descriptions are provided in Tables II and III.

V. Summary of techno-economic results for profit-oriented strategies.

BASE CASE AND VARIANTS

For each of the thermoplastic products considered, a phased implementation strategy has been defined following profit maximization and revenue growth perspectives. All strategies share a common Phase 0 similar with business-as-usual of the case study mill for the first six years, and a capacity increase of the lignin precipitation unit from 30 metric tons/day to 90 metric tons/day. For strategies *Ligno 90•PF HPL* and *Ligno 90•PF Lignin-PEO*, the amount of lignin dedicated to the PF resin application is capped at 30 metric tons/day, combining amounts used internally and sold over-the-fence, and all additional amounts are sold either as HPL or lignin-PEO blends (Table IV). It is considered that half of HPL is sold in the garbage bags segment, and the other half for agricultural mulch films.

In Group II for strategies involving SP, Phase I is similar for all strategies, and product diversification occurs in Phase II. For new strategies, *Ligno 90 + SP•PF HPL* and *Ligno 90 + SP•PF Lignin-PEO*, the amount of lignin dedicated to the PF resin application is capped at 90 metric tons/day, and all amounts of lignin resulting from solvent pulping are positioned on thermoplastic segments (Table III).

Indicator		Ligno 90 + SP•PF	Ligno 90 + SP•PF PU	Ligno 90 + SP•PF CFs	Ligno 90 + SP•PF HPL	Ligno 90 + SP• PF Lignin-PEO	Note/Comment
Lignin production capacity		350 metric tons/day					
Production rate by application		PF resin: 350 metric tons/day	PF resin: 226 metric tons/day PU foams: 124 metric tons/day	PF resin: 226 metric tons/day Carbon fibers: 124 metric tons/day	PF resin: 90 metric tons/day Garbage bags: 169 metric tons/day Mulch films: 169 metric tons/day	PF resin: 90 metric tons/day ABS: 290 metric tons/day	Production rates for thermoplastic applications refer to lignin derivatives, i.e., after modification (HPL or blending).
Capital investment	Total project cost	US$ 432M	US$ 438M	US$ 436M	US$ 470M	US$ 450M	Lower economies of scale with lignin-PEO due to the limited scalability of extruders.
	Company contribution	US$ 153M	US$ 156M	US$ 154M	US$ 164M	US$ 159M	
Annual operating costs (Phase II)	Total costs	US$ 123M/year	US$ 127M/year	US$ 126M/year	US$ 170M/year	US$ 145M/year	Added cost related to chemicals required for lignin modification.
	Company contribution	US$ 60M/year	US$ 62M/year	US$ 61M/year	US$ 85M/year	US$ 73M/year	
Annual revenues (Phase II)	Total revenues	US$ 222M/year	US$ 305M/year	US$ 284M/year	US$ 386M/year	US$ 388M/year	Higher market prices for thermoplastic derivatives magnify revenue increase at higher scale, compared to other strategies.
	Company share	US$ 120M/year	US$ 162M/year	US$ 151M/year	US$ 207M/year	US$ 208M/year	
Annual EBITDA (Phase II)		US$ 60M/year	US$ 100M/year	US$ 90M/year	US$ 123M/year	US$ 208M/year	Although the impact of single products tends to be diluted in the context of multi-product portfolios, the role of thermoplastic derivatives on margins improvement is significative.
NPV (Phases I and II combined)		US$ 6M	US$ 50M	US$ 37M	US$ 65M	US$ 80M	Since cash flow increase related to thermoplastics implementation occurs further in time (after Year 10), its impact on NPV is mitigated.

PF = phenol-formaldehyde; PU = polyurethane; CFs = carbon fibers; HPL = hydroxypropylated lignin; PEO = polyethylene oxide; ABS = acrylonitrile butadiene styrene; EBITDA = earnings before interest, taxes, depreciation, and amortization; NPV = net present value.
* Descriptions of strategies are provided in Tables II and III.

VI. Summary of techno-economic results for revenue-oriented strategies.

RESULTS AND INTERPRETATIONS

Techno-economic assessment

The result of the techno-economic analysis is summarized in **Table V** for profit-oriented strategies, and in **Table VI** for revenue-oriented ones. In Table VI, the "company contribution" refers to the share of cost or revenues attributed to the forestry company under the joint venture assumptions considered for Group II strategies. In comparison with strategies leading to other lignin derivatives, thermoplastic-oriented strategies require marginally higher investment related to equipment for lignin modification, and higher operating cost due to chemicals consumption; NaOH and PO in the case of HPL, and PEO in the case of lignin-PEO blends. For both applications considered, the margin and NPV increase tend to provide a rationale for the higher cost.

Combined with the process configuration and the market price for targeted applications, the product formulation – 3:10 PO over dry lignin for HPL and 1:10 PEO over dry lignin for lignin-PEO blends on a weight basis – plays a distinguishing role between thermoplastic strategies. Lower lignin content and market price for HPL result in comparable revenues for both strategies; however, strategies leading to lignin-PEO blends benefit from lower chemical consumption and a simpler process, which result in a more significant margin creation.

EVALUATION OF DECISION CRITERIA

Values obtained from the calculation of decision criteria for thermoplastic strategies are presented in **Table VII** and are put in perspective against the best-performing strategy leading to other lignin derivatives. They appear among top-performing strategies for all criteria, in a way that emphasizes respective strengths and differences between profit-oriented and revenue-oriented strategies. Both

Criterion*	Ligno 90• PF HPL	Ligno 90• PF Lignin-PEO	Ligno 90 + SP•PF HPL	Ligno 90 + SP• PF Lignin-PEO	Best-performing Among Other Strategies (Value)	Note/Comment
Internal rate of return (IRR)	48%	62%	29%	31%	Ligno 90•PF PU (57%)	Over time, margin increase satisfyingly balances the investment on lignin modification. HPL strategies are somehow disadvantaged by higher capital costs.
Cash flow on capital employed (CFCE)	3.6	5.1	1.5	1.7	Ligno 90•PF PU (4.5)	Lower investment requirements make the lignin-PEO strategy the most capital-efficient. In comparison, HPL is less efficient than the PU foam strategy.
Revenue diversification (RD)	10%	10%	63%	64%	Ligno 90 + SP•PF PU (51%)	At higher scale, the impact of thermoplastics on revenue increase is more significant.
Competitiveness on production costs (CPC)	64%	75%	45%	54%	Ligno 90•PF PU (65%)	The low-end market price for HPL as garbage bags makes it less robust compared to PU foams and ABS.
Resistance to energy and chemicals market uncertainty (RECMU)	19%	23%	65%	75%	Ligno 90 +SP•PF PU (83%)	Chemicals required to modify lignin make thermoplastic strategies more vulnerable to volatility than PU foams and CFs strategies.
Robustness to poor market conditions (RPMC)	31%	51%	21%	28%	Ligno 90•PF PU (22%)	Under poor market conditions, relatively higher market prices make thermoplastic strategies more robust than other strategies at similar scale.

PF = phenol-formaldehyde; HPL = hydroxypropylated lignin; PEO = polyethylene oxide; PU = polyurethane; ABS = acrylonitrile butadiene styrene; CFs = carbon fibers.
* Criteria definitions are provided in Table I, and descriptions of strategies in Tables II and III.

VII. Summary of criteria evaluation for thermoplastic strategies.

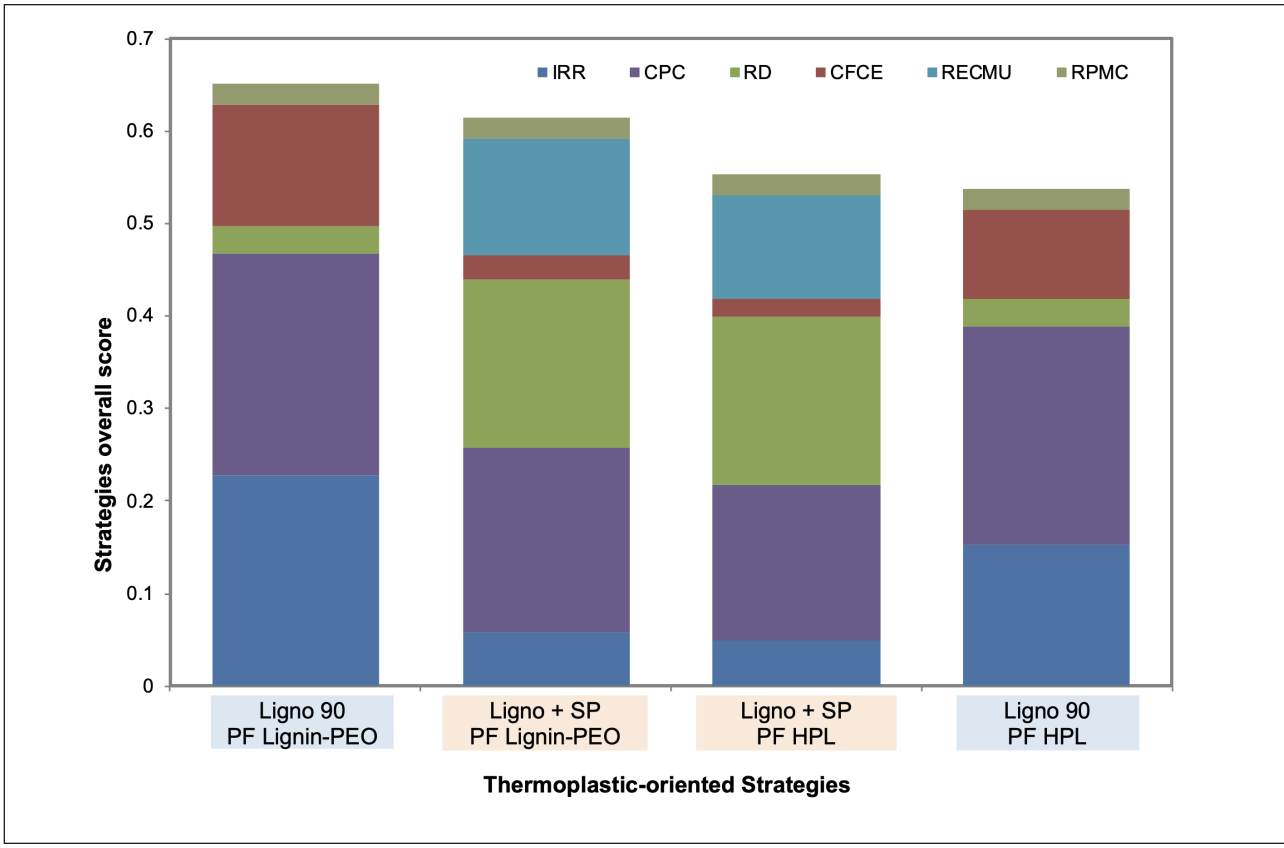

4. Overall scores for thermoplastic strategies. (Criteria definitions are provided in Table I, and descriptions of strategies in Tables II and III.)

profit-oriented strategies, *Ligno 90•PF HPL* and *Ligno 90•PF Lignin-PEO*, present high scores on economic criteria, as well as on price competitiveness. Capital costs related to lignin modification into HPL limit the profitability and capital efficiency of the strategy *Ligno 90•PF HPL*, which remains among the most cost competitive despite the low-end market price considered for garbage bags. Strategies seeking revenue growth, *Ligno 90 + SP•PF HPL* and *Ligno 90 + SP•PF Lignin-PEO*, are the best-performing regarding revenue diversification; however, they are more sensitive to fluctuations on feed materials markets compared to other revenue-oriented strategies that consume less chemicals.

UPDATED RANKING OF STRATEGIES

Overall scores obtained by combining criteria values with their respective weights are presented in **Fig. 4** for thermoplastic strategies, and in **Fig. 5** for the entire set of strategies. Scores for strategies leading to PF resin, PU foams, and carbon fibers are unchanged, and the overall picture is updated by the inclusion of scores for thermoplastic strategies.

Among thermoplastic strategies, those producing lignin-PEO blends appear as top-performing under both profit-oriented and revenue-increasing perspectives, due to a combination of economic and competitiveness advantages. There is a clear distinction between strategies at the 90 metric tons/day scale; however, strategies involving solvent pulping have closer scores (11% difference between revenue-oriented strategies compared to 21% difference between profit-oriented strategies). This is due to a lower influence of benefits associated with thermoplastics compared to higher capital and operating costs at that scale.

Interestingly, the profit-oriented strategy has the greater score among options producing Lignin-PEO blends, while it is the revenue-oriented strategy that performs better among options to HPL. Indeed, the limited scores for internal rate of return (IRR) and cash flow on capital employed (CFCE) disadvantage the *Ligno 90•PF HPL* strategy, while *Ligno 90 + SP•PF HPL* is favored by revenue diversification (RD) and resistance to energy and chemicals market uncertainty (RECMU). Nonetheless, strategies leading to PU foams remain better ranked than those leading to HPL. The overall performance of thermoplastic strategies might lead to questioning the vertical integration approach towards onsite PF resin manufacturing through strategy *Resin 90*, which was formerly identified among Preferred strategies but is out of the Top 6 in the updated ranking.

DISCUSSION

From **Fig. 5**, it can be interpretated that all thermoplastic strategies would integrate the group of Preferred strategies

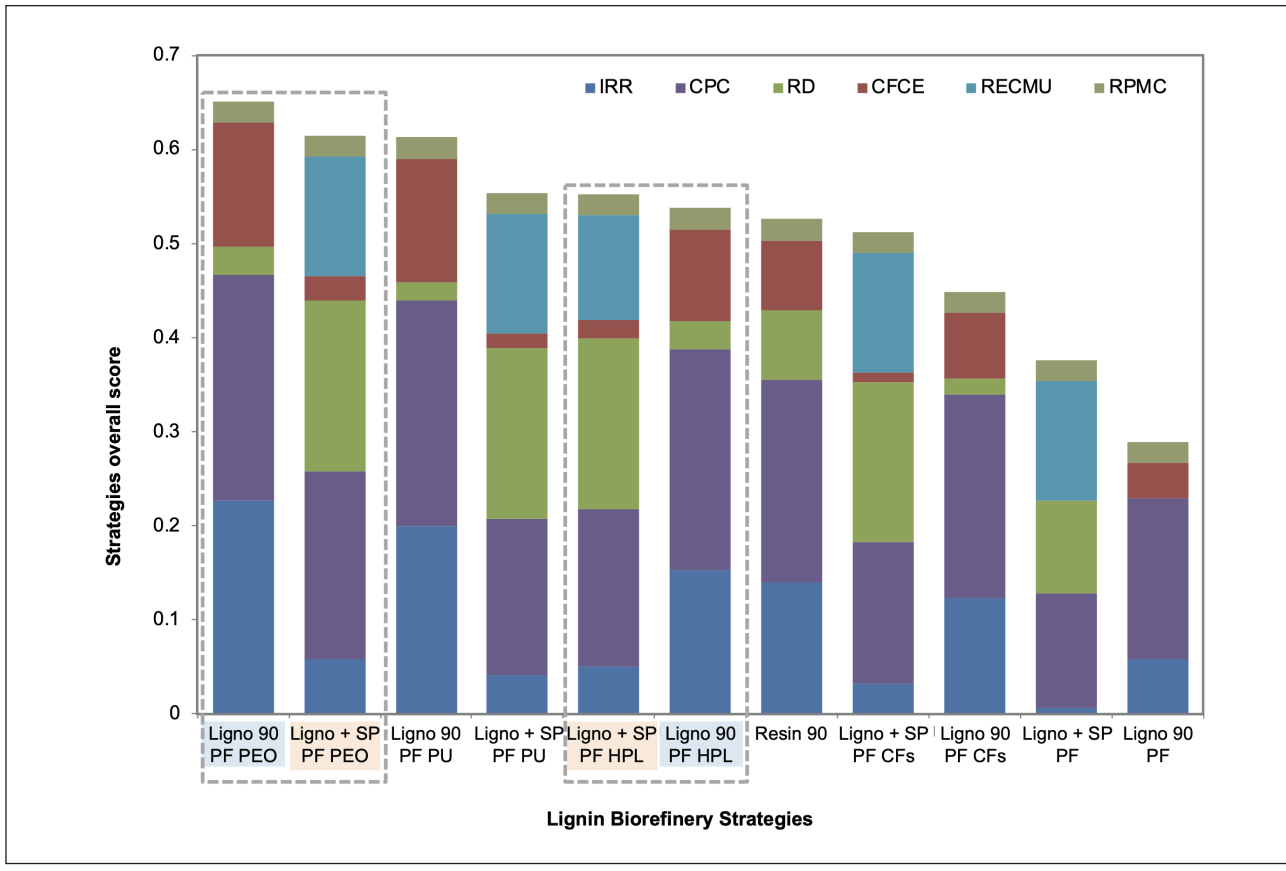

5. Updated scores of strategies and rankings resulting from criteria evaluation. (Criteria definitions are provided in Table I, and descriptions of strategies in Tables II and III.)

formerly identified by project decision-makers. Lignin-based thermoplastics are promising derivatives; however, the ranking of strategies for PU foam production demonstrates that thermoplastics will not be preferred under all circumstances. Winning conditions for lignin-based thermoplastics could be interpretated as: (1) minimal requirements for lignin modification; (2) maximized lignin content in the plastic formulation for performances at least similar to competing products; and (3) a market application ideally not dependent on crude oil fluctuations, where a decent market price can be targeted.

Under assumptions considered in this study, the strategy towards lignin-PEO blends appears superior to others. Given projections for the demand on the ABS market (6% CAGR in 2018-2023), the risk can be considered moderate for the expectable return, especially if uncertainty on technology demonstration is addressed. Recent advancements from major players in the lignin sector tend to confirm ABS replacement as a one of the most promising segments. Nonetheless, HPL might become preferred in scenarios where policies make biodegradability mandatory for plastics usage, thus creating a higher market demand and a potential premium for such products.

Although only biodegradability has been highlighted in the case study, recyclability is another aspect of value proposition associated with bioplastics that is worth emphasizing when applicable. Recyclability is increasingly recognized as essential for the circular economy; therefore, validating that lignin integration into the plastic formulation does not negatively impact this characteristic becomes critical for market adoption.

Also, the preference for lignin-based thermoplastics over other derivatives is dependent on the assumption that kraft and Organosolv lignins are compatible with targeted applications. For example, the presence of unpleasant odors from plastic parts are potential showstoppers for the adoption of lignin derivatives in applications where the end-product contributes to the comfort of the user, such as for interior automotive parts. The ability and easiness to address important end-product characteristics might become distinguishing factors between lignin types. If for a given lignin type, additional efforts are required to make it more suitable, the impact of added capital and operating costs on criteria such as IRR and CFCE needs to be monitored.

From a business flexibility point of view, having access to several lignin types while implementing business phases over time provides the forestry company a stronger business model in which different lignin types can be dedicated to market segments more appropriately. One of the main challenges for a forestry company resides in the mitigation

of the business risks that pursuing thermoplastic derivatives represents. While a vertically-integrated forestry company with an easier access to the PF resin value chain would better benefit from selling lignin as a phenol replacement in the short term to mitigate market risk before integrating the thermoplastics segment, a horizontally-integrated company can consider opportunities more broadly.

CONCLUDING REMARKS AND PATH FORWARD

Environmentally-friendly policies and market dynamics are among the drivers that make bioplastics one of main centers of interest as circular economies are being established. This creates favorable conditions for a larger commercialization of lignin-based thermoplastics in various segments where forest product companies can seize promising opportunities. The present study assessed the potential of lignin-based thermoplastics by adapting an approach used for identifying preferred strategies leading to PF resins, PU foams, and carbon fibers, based on a techno-economic analysis and the evaluation of a multi-disciplinary set of criteria. Thermoplastic applications assessed included HPL for biodegradable garbage bags and agricultural mulch films, and lignin-PEO blends for ABS replacement.

Techno-economic estimates showed that marginal capital investments were required to implement lignin modification techniques leading to desired thermoplastics and resulted in significant margin creation as compared to other lignin derivatives. The simplicity and cost effectiveness of the lignin modification process, the lignin content in the plastic formulation, and the market price for the targeted application appeared to play an important role in the economic return. The strategy for production of lignin-PEO blends at low volume obtained the highest overall score as a result of a combination of these factors.

Based on their scores and ranking, all strategies defined for thermoplastic derivatives would be considered among Preferred strategies, along with the strategies leading to lignin-based PU foams. In addition to the option *Ligno 90•PF Lignin-PEO*, that has the top rank, the two strategies involving thermoplastics at high scale appeared both competitive and robust and can further create business flexibility advantages through the horizontal integration of different lignin types into various market segments.

For lignin-based thermoplastics to be successful, the suitability of the lignin type and expected end-product performance for the targeted application must be validated, along with the definition of a strong value proposition. As regulations and policies evolve to support the establishment of a circular bioeconomy, there is increasing use of recycled plastic materials and a rising demand for biodegradable plastics. Lignin-based thermoplastics represent a unique opportunity for forestry companies to build strong competitive advantages from lignin, which improves the biodegradability of plastic blends where it is integrated. **TJ**

ACKNOWLEDGMENTS

The authors are grateful for the financial support received from the Program on Energy Research and Development (Project OERD-CEV-19-106) and the Forest Innovation Program of the Canadian Forest Service (CFS Biorefinery Flagship Project) at Natural Resources Canada. The authors would also like to thank academic partners in the project, Pauline D'Hollander and Pedro Fardim from KU Leuven (Belgium), and the industrial partner C12XL Technologies, that provided technical information and contributed to the validation of assessment results.

LITERATURE CITED

1. United Nations Environment Programme, "Single-use plastics: A roadmap for sustainability," United Nations Environment Programme, Nairobi, Kenya, 2018.
2. Hasson, N., "From plastic to paper," *Paper Advance*, Fisher International, Charlotte, NC, USA, April 2019. Available [Online] https://www.paperadvance.com/news/market-analysis/from-plastic-to-paper.html <12Sept2022>.
3. Crippa, M., De Wilde, B., Koopmans, R., et al., "Business models, product and service design," in *A Circular Economy for Plastics: Insights from Research and Innovation to Inform Policy and Funding Decisions* (M. De Smet and M. Linder, Eds.), European Commission, Brussels, 2019, pp. 87-110.
4. European Bioplastics, "Bioplastics market data 2018," European Bioplastics, Berlin, December 2018. Available https://www.european-bioplastics.org/wp-content/uploads/2016/02/Report_Bioplastics-Market-Data_2018.pdf <12Sept2022>.
5. European Environment Agency (EEA), "The circular economy and the bioeconomy — Partners in sustainability,'" European Union, Luxembourg, 2018.
6. United Nations Environment Programme, "Biodegradable plastics and marine litter: Misconceptions, concerns and impacts on marine environments," United Nations Environment Programme, Nairobi, Kenya, 2015.
7. World Economic Forum, Ellen MacArthur Foundation, and McKinsey & Company, "The new plastics economy: Rethinking the future of plastics," Ellen MacArthur Foundation, Isle of Wight, UK, 2016.
8. Jong, E.D., "PEF: The next generation polyester based on 100% renewable resources," *IEA Bioenergy Conf.*, International Energy Agency, Paris, 2015.
9. Berkel, J.V., "PEF packaging opportunities: A new value chain from development to commercialization," *World Congr. Ind. Biotechnol.*, Biotechnology Innovation Organization, Washington, DC, 2017.
10. PlasticsEurope and European Association of Plastics Recycling, "Plastics – the Facts 2021," PlasticsEurope/European Association of Plastics Recycling, Brussels/Brussels, 2021. Available [Online] https://plasticseurope.org/wp-content/uploads/2021/12/Plastics-the-Facts-2021-web-final.pdf. <12Sept2022>.
11. IHS Markit, *Chemical Economics Handbook® (CEH) – Acrylonitrile-Butadiene-Styrene Resins (ABS)*, IHS Markit, London, 2020.
12. Fortune Business Insights, "Acrylonitrile butadiene styrene market size, share & COVID-19 impact analysis, by application (appliances, automotive, consumer goods, construction, electronics, and others), and regional forecast, 2020-2027," Fortune Business Insights, Maharashtra, India, 2020.

13. Fortune Business Insights, "Automotive plastics market size, share & COVID-19 impact analysis, by type, by application, and regional forecast, 2020-2027," Fortune Business Insights, Maharashtra, India, 2020.
14. Grand View Research, "Automotive plastics market size, share & trends analysis report by product (PP, ABS, PU, PE, PC, PA, PVC, PMMA), by application (powertrain, interior/exterior furnishings, electrical components), by process, by region, and segment forecasts, 2021-2028," Grand View Research, San Francisco, 2021.
15. Global Market Insights, "Global automotive plastics market size, share and industry analysis report by product and application, regional, growth potential, competitive market share & forecast, 2021-2027," Global Market Insights, Selbyville, DE, USA, 2022.
16. Research Dive, "Biodegradable plastics market by material type, application, and regional analysis: Global opportunity analysis and industry forecast, 2021-2028," Research Dive, Pune, India, 2021.
17. Grand View Research, "Biodegradable plastic market size, share & trends analysis report by type (starch-based, PLA, PHA, PBAT, PBS), by end-use (packaging, consumer goods, agriculture), by region, and segment forecasts, 2020-2027," Grand View Research, San Francisco, 2020.
18. Shen, L., Haufe, J., and Patel, M.K., "Product overview and market projection of emerging bio-based plastics," Utrecht University, Utrecht, Netherlands, 2009.
19. Mohanty, A.K., Misra, M., and Drzal, L.T., *Natural Fibers, Biopolymers, and Biocomposites*, CRC Press, Boca Raton, FL, USA, 2005.
20. Boerjan, W., Ralph, J., and Baucher, M., *Annu. Rev. Plant Biolog*. 54(1): 519(2003). https://doi.org/10.1146/annurev.arplant.54.031902.134938.
21. Domtar, "Domtar inaugurates commercial lignin production," Domtar Corporation, Fort Mill, NC, USA, 12 March 2013. Available [Online] https://www.prnewswire.com/news-releases/domtar-inaugurates-commercial-lignin-production-197328071.html <13Sept2022>.
22. Macdonald, C., "Commercial-scale lignin line starts at Hinton," *Pulpandpapercan.com*, 6 April 2016. Available [Online] https://www.pulpandpapercanada.com/news/commercial-scale-lignin-line-starts-at-hinton-1100000214 <13Sept2022>.
23. Bredal, T.H., "LignoTech Florida plant officially opened," Borregaard, Sarpsburg, Norway, 27 June 2018. Available [Online] https://www.borregaard.com/company/news-archive/lignotech-florida-plant-officially-opened/ <13Sept2022>.
24. Valmet, "Valmet-supplied LignoBoost plant now handed over to Stora Enso's Sunila mill in Finland," Valmet Oyj, Espoo, Finland, 6 October 2015. Available [Online] https://www.valmet.com/media/news/press-releases/2015/valmet-supplied-lignoboost-plant-now-handed-over-to-stora-ensos-sunila-mill-in-finland/ <13Sept2022>.
25. *PetroNotícias*, "Klabin inicia planta piloto para extração de lignina com technologia da Valmet," *PetroNotícias*, Brazil, 12 February 2020. Available [Online] http://petronoticias.com.br/klabin-inicia-planta-piloto-para-extracao-de-lignina-com-tecnologia-da-valmet/ <13Sept2022>.
26. Suzano, "Ecolig," Suzano report 2020," São Paulo, Brazil, 2020.
27. Grand View Research, "Lignin market size, share & trends analysis report by product (ligno-sulphonates, kraft, Organosolv), by application (macromolecule, aromatic), by region (APAC, MEA, North America, Europe), and segment forecasts, 2019-2025," Grand View Research, San Francisco, 2019.
28. Kruus, K. and Hakala, T., "The making of bioeconomy transformation," VTT Technical Research Centre of Finland Ltd., Espoo, Finland, 2017.
29. Sherwood, J., "Sunburst delivers first tons of high-purity lignin and sugar," Sweetwater Energy, Rochester, NY, USA, 16 February 2021. Available [Online] https://www.sweetwater.us/sunburst-delivers-first-tons-of-high-purity-lignin-and-sugar/ <13Sept2022>.
30. Hämäläinen, V., Grönroos, T., Suonpää, A., et al., *Front. Bioeng. Biotechnol*. 6: 20(2018). https://doi.org/10.3389/fbioe.2018.00020.
31. Valmet, "The next generation LignoBoost – tailor-maid lignin production for different lignin bioproduct markets," Valmet Oyj, Espoo, Finland, 26 May 2017. Available [Online] https://www.valmet.com/globalassets/media/downloads/white-papers/power-and-recovery/next_generation_lignoboost_whitepaper.pdf <13Sept2022>.
32. Bjork, M., "Lineo™ by Stora Enso – A step towards the bio-based society," *PAPTAC Int. Lignin Conf.*, PAPTAC, Brossard, QC, Canada, 2018.
33. Glasser, W., "Opportunties and challenges of lignin utilization as biopolymer," *PAPTAC Int. Lignin Conf.*, PAPTAC, Brossard, QC, Canada, 2018.
34. Li, T. and Takkellapati, S., *Biofuels, Bioprod. Biorefin.* 12(5): 756(2018). https://doi.org/10.1002/bbb.1913.
35. O'Dea, R.M., Pranda P.A., Luo, Y., et al., *Sci. Adv.* 8(3): eabj7523(2022). https://doi.org/10.1126/sciadv.abj7523.
36. Stora Enso, "Aiming at future with 100% bio-based resin," Stora Enso Oyj, Helsinki, 15 February 2019. Available [Online]. https://www.storaenso.com/en/newsroom/news/2019/2/aiming-at-future-with-100-bio-based-resin <13Sept2022>.
37. Valkonen, S., "Lignin based binders: An industrial reality, latest developments," *11th Int. Conf. Wood Adhesives*, Forest Products Society, La Grange, GA, USA, 2017.
38. Kelleher, S. and Moreland, T. "Revolutionary carbon foam from wood," U.S. Department of Agriculture, Washington, DC, 30 July 2021. Available [Online] https://www.usda.gov/media/blog/2018/10/18/revolutionary-carbon-foam-wood <13Sept2022>.
39. Edye, L., "Renewable and recyclable lignin-based water barrier coatings for paper and board," *PAPTAC Int. Lignin Conf.*, PAPTAC, Brossard QC, Canada, 2018.
40. Sustainable Biomaterials, "CNRE of VT pioneers biodegradable plastic bags," Virginia Polytechnic Institute and State University, Blacksburg, GA, USA, 3 December 2020. Available [Online] https://sbio.vt.edu/about-us/news-publications/news/xylo-bag.html <13Sept2022>.
41. Tecnaro GmbH, "Thermoplastics made of lignin," BIOPRO Baden-Württemberg GmbH, Stuttgart, Germany, 29 March 2010. Available [Online] https://www.biooekonomie-bw.de/en/articles/pm/tecnaro-gmbh-thermoplastics-made-of-lignin/ <13Sept2022>.
42. Schweizer, M., "Lignin-based biocomposites – Applications and new developments," *Bio-Composites in Construction (BCIC) Int. Conf.*, PAPTAC, Brossard, QC, Canada, 2015.
43. Valmet, "Valmet and Biochemtex to collaborate in developing technology for lignin derived biochemicals," Valmet, Espoo, Finland, 3 May 2016. Available [Online] https://www.valmet.com/media/news/press-releases/2016/valmet-and-biochemtex-to-collaborate-in-developing-technology-for-lignin-derived-biochemicals/ <13Sept2022>.

44. Karlsson, H., "Extracting a low ash lignin from black liquor using the LignoBoost™ technology – A status update and view of next generation lignin extraction," *PAPTAC Int. Lignin Conf.*, PAPTAC, Brossard, QC, Canada, 2018.

45. Maillard, D., Osso, E., Faye, A., *J. Appl. Polym. Sci.* 138(18): e50319(2020). https://doi.org/10.1002/app.50319.

46. Ajao, O., Benali, M., Faye, A., et al., *Ind. Crops Prod.* 167: 113435(2021). https://doi.org/10.1016/j.indcrop.2021.113435.

47. Ton-That, M.T., Li, H., Patenaude, E., et al., WO 2018/035598 A1 (Mar. 1, 2018).

48. Wang, C., Kelley, S., and Venditti, R., *ChemSusChem* 9(8): 770(2016). https://doi.org/10.1002/cssc.201501531.

49. Dias, O., Negrao, D., Gonçalves, D., et al., *Mol. Cryst. Liq. Cryst.* 655(1): 204(2017).

50. Bouajila, J., Dole, P., Joly, C., et al., *J. Appl. Polym. Sci.* 102(2): 1445(2006). https://doi.org/10.1002/app.24299.

51. Kadla, J.F. and Kubo, S., *Macromolecules* 36(20): 7803(2003). https://doi.org/10.1021/ma0348371.

52. Zhang, M. and Ogale, A., *Carbon* 69: 626(2014). https://doi.org/10.1016/j.carbon.2013.12.015.

ABOUT THIS PAPER

Cite this article as:
Diffo Téguia, C., Mehr, N.G., Glasser, W.G., et al., *TAPPI J.* 21(9): 479(2022). https://doi.org/10.32964/TJ21.9.479

DOI: https://doi.org/10.32964/TJ21.9.479

ISSN: 0734-1415

Publisher: TAPPI Press

Copyright: ©TAPPI Press 2022

About this journal

53. Sadeghifar, H., Cui, C., and Argyropoulos, D.S., *Ind. Eng. Chem. Res.* 51(51): 16713(2012). https://doi.org/10.1021/ie301848j.

54. Wang, C. and Venditti, R.A., *ACS Sustainable Chem. Eng.* 3(8): 1839(2015). https://doi.org/10.1021/acssuschemeng.5b00416.

ABOUT THE AUTHORS



Diffo Téguia

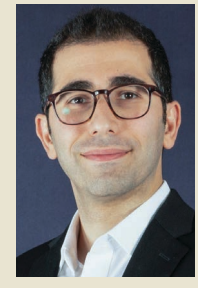

Mehr

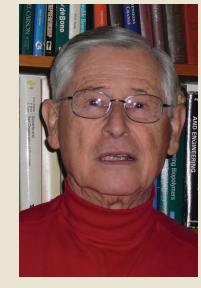

Glasser



Stuart

There is growing interest for the definition of technology and business strategies to facilitate the development of the bioeconomy in general, and particularly in the forest sector. This includes the development of new bio-based products, such as lignin derivatives. The current study complements two papers we published in the March 2017 [59] and April 2017 [61] issues of *TAPPI Journal*.

The most challenging aspect of this research is related to the scarcity of viable market and cost information on bio-based plastics. To address this, the pricing and market penetration strategy has been defined based on products that the lignin-based plastics would substitute.

The significant discovery in this research is related to the extent at which lignin-based thermoplastics could be competitive compared to phenolic resin and polyurethane foam applications that are typically favored. Another interesting aspect of this research is that although lignin is generally appreciated for its thermoset properties (e.g., for adhesive applications), it can play an important role in thermoplastic resins, with the resulting product being competitive in multiple aspects when compared to other lignin derivatives.

The information published in this paper could help mills to: (1) define strategies for the development of lignin-based products to better valorize black liquor; (2) understand how phased implementation helps mitigate risks associated with such strategies; and (3) identify how existing lignin precipitation processes could be modified and/or rendered flexible for the production of multiple derivatives.

Although no continuation has been established for this research at the moment, it could be extended in multiple ways, including the application of the methodology to other lignin derivatives, its application to other bioproducts and bioeconomy development context, or the development of new decision criteria for different implementation cases in the pulp and paper sector.

Diffo Téguia and Mehr are process engineers at Natural Resources Canada, CanmetENERGY, in Varennes, QC, Canada. Glasser is professor emeritus, Sustainable Biomaterials, at Virginia Polytechnic Institute and State University, Blacksburg, VA, USA. Stuart is professor in the Chemical Engineering Department at Polytechnique Montreal in Montreal, QC, Canada. Email Diffo Téguia at cedric.diffo@gmail.com.

55. Gordobil, O., Robles, E., Egüés, I., et al., *RSC Adv.* 6(90): 86909(2016). https://doi.org/10.1039/C6RA20238A.

56. Dehne, L., Vila, C., Saake, B., et al., *J. Appl. Polym. Sci.* 134(11): 44582(2017). https://doi.org/10.1002/app.44582.

57. Cao, N., Oden, K., and Glasser, W., U.S. pat. 9,000,075 B2 (Apr. 7, 2013).

58. Akato, K., Tran, C., Chen, J., et al., *ACS Sustainable Chem. Eng.* 3(12): 3070(2015). https://doi.org/10.1021/acssuschemeng.5b00509.

59. Glasser, W., Loos, R., Cox, B., et al., *TAPPI J.* 16(3): 111(2017). https://doi.org/10.32964/TJ16.3.111.

60. Diffo Téguia, C., Chambost, V., Sanaei, S., et al., "Strategic transformation of the forest industry value chain," in *Forest Value Chain Optimization and Sustainability*, CRC Press/Taylor & Francis Group, Boca Raton, FL, USA, 2016.

61. Diffo Téguia, C., D'Amours, S., Albers, R., et al., *TAPPI J.* 16(4): 229(2017). https://doi.org/10.32964/TJ16.4.229.

62. Bouyssou, D., "Building criteria: A prerequisite for MCDA," in *Readings in Multiple Criteria Decision Aid* (Carlos A. Bana e Costa, Ed.), Springer Verlag, Berlin, 1990. https://doi.org/10.1007/978-3-642-75935-2_4.

63. Roy, B. and Bouyssou, D., *Aide multicritère à la décision: Méthodes et cas*, Economica, Paris, 1993.

64. IEA, "World energy outlook 2015," International Energy Agency, Paris, 2015.

65. EIA, "Annual energy outlook 2015 with projections to 2040," U.S. Energy Information Administration, Washington, DC, 2015.

66. O'Donoghue, E., Hansen, J., and Stallings, D., "USDA agricultural projections to 2027," U.S. Department of Agriculture, Washington, DC, 2018.

Fiber-based characterization of pulp refining

RICHARD J. KEREKES AND J. DAVID MCDONALD

ABSTRACT: Fiber development in pulp refining can be characterized by three parameters: number of impacts on pulp, *N*; energy per impact, *I*, and bar force on fibers, *F*. These parameters enable comparisons of radically different refining conditions; determination of intensity for hardwoods and softwoods; assessment of effect of bar width on fiber shortening; and predictions of tensile strength increases.

Application: Simple equations for *N*, *I*, and *F*, using readily available data, can be used to understand and guide the operation of refiners.

Refining is typically controlled by specific refining energy (*E*) to describe total refining action and specific edge load (*SEL*) to describe the intensity at bar crossings. Although these parameters have proven useful over the years, they have a shortcoming in not accounting for refining action from the perspective of pulp. During refining, fibers experience a number of impacts at bar crossings that impose forces that strain fibers and expend energy. From a fiber perspective, this suggests that refining should be characterized by number, energy, and force of impacts.

Although refining has been previously characterized by number and intensity of impacts as summarized in [1], this approach has not been widely used. Reasons for this may be complexity in calculating the parameters, or more likely, lack of perceived benefit over *E* and *SEL*. The objective of this paper is to address these issues by simplifying the calculations and demonstrating the benefits of what may be called fiber-based characterization of refining. To do so, this paper will focus on work from the University of British Columbia, where this topic has been extensively studied over the years.

ANALYSIS

Fibers passing through refiners are subjected to a number of impacts, *N*, each of intensity *I* (energy per mass per impact). The product of these parameters is specific refining energy, *E*:

$$E = N \cdot I \tag{1}$$

Variables *N* and *I* are entirely independent of one another. In contrast, both *E* and *SEL* depend on power, and consequently cannot be controlled separately by power adjustment, which is the principal means of online control.

Parameter *N* depends on capturing fibers from grooves and imposing force on them in gaps created by a succession of bar crossings. Values of *N* have been calculated over the years in various ways [1]. More recent approaches have been based on fiber trapping [2], and still more recently, floc trapping [3]. The latter approach will be discussed here.

Impacts on pulp, *N*, are imposed by bar crossings. A key factor governing *N* is the total potential number of bar crossings a fiber may experience, N_B, defined by a point moving along a stator bar. This is a key variable in determining *N*. It is governed by the cutting-edge length of the refiner plates, *CEL(m/s)*; volumetric flow rate through the refiner, *Q* (m^3/s); groove depth, *D*; and groove width, *G* [4]:

$$N_B = \frac{2 \cdot D \cdot G \cdot CEL}{Q} \tag{2}$$

To be impacted at a bar crossing, fibers must be captured from grooves and transported into gaps. At typical refining consistencies, fibers are captured as flocs, which are about a fiber length in size and therefore a cubic fiber length in volume. The floc mass per bar length is given by $\rho C_s l^2$, where *l* is fiber length (*m*), C_s is consistency (fraction), and ρ is density of fibers (kg/m^3).

The probability of capture at any bar crossing is the ratio of this mass to the total fiber mass in the groove, $2\rho C_s DG$. This probability multiplied by N_B gives *N*.

$$N = \frac{l^2 \cdot CEL}{Q} \tag{3}$$

Thus, *N* depends on *CEL* (bar edge length X rotational speed), flow rate through the refiner (*Q*), and fiber length (*l*).

Intensity, I

Intensity, *SEL*, was defined empirically as net power *P* divided by the *CEL* [5]. The *SEL* was later shown rigorously to be the energy expended per bar crossing per bar length

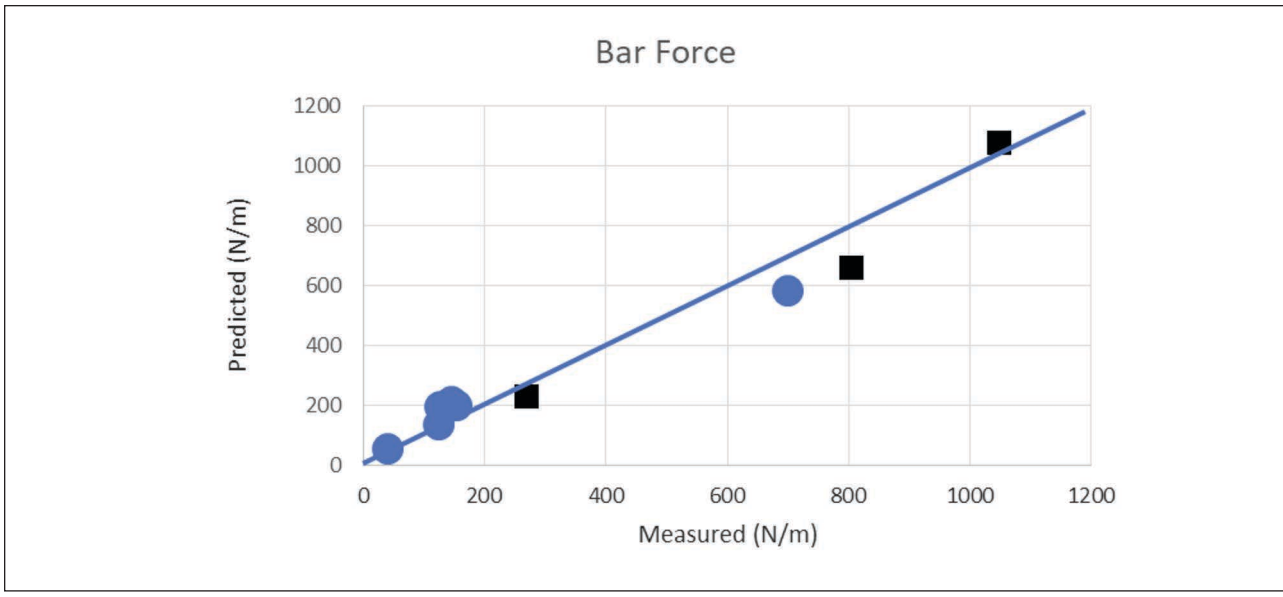

1. Comparison of predicted to measured bar forces: ● are "direct force comparisons" and ■ are from "fiber shortening" [12].

[6]. Bar angle may be accounted for in various ways, for example, by TAPPI TIP [7], the modified edge load [8], and more comprehensive approaches by Roux et al. [9]. Discussion of these angle corrections is beyond the scope of this study, which will focus on action on fibers.

From a fiber perspective, the key intensity is energy expended per mass of fiber during a bar crossing, *I*. Accordingly, *SEL* must be divided by the captured mass $\rho C_s l^2$, to give *I* in *J/kg*:

$$I = \frac{SEL}{\rho C_s l^2} \tag{4}$$

Clearly, small values of fiber length give large values of *I* for a given *SEL*.

Force, F

Forces produce strains in fibers that break bonds in fibers, and when too large, break fibers. During a bar crossing, the largest force occurs over sliding distance *s* from the leading edge of a bar surface [10]. This force is of key interest in refining. It may be represented as force per bar length per bar crossing, obtained simply by factoring *SEL*, the energy expended per bar crossing per bar length into force in the direction of motion, *F (N/m)* and distance *s (m)*. This force, divided by the fraction along bar length covered with fibers, *z*, gives force per bar length on pulp, *F*:

$$F = \frac{SEL}{z.s} \tag{5}$$

The size of *s* depends on fiber length and bar width *W* [10]. When bar widths are larger than a fiber length, *s* extends a distance of about a fiber length, *l*, so *l* determines *s*. [11] On the other hand, when bar width *W* is smaller than a fiber length, bar width determines *s*. In both cases, there is a small overhang length that depends on consistency and fiber length. These considerations are described in [10] and summarized below:

$$s = l + 5C_s l \qquad \text{when} \quad l<W \tag{6}$$

$$s = W + 5C_s l \qquad \text{when} \quad l>W \tag{7}$$

Bar force predicted by Eq. 5 has been shown to represent the average bar force, whether the source is mechanical friction, hydrodynamic drag, or a combination of these [12]. It has been verified by experimental measurements using a sensor embedded on a refiner bar, as shown in **Fig.** 1 for *z*=1.

Force *F* can be further devolved into force on individual fibers [6]. This was found to predict individual fiber shortening [13], but the calculation is too complex for ready use.

In summary, Eq. 4 and Eq. 5 are fiber-based parameters derived from *SEL*, which is the energy expended per bar length per bar crossing. Parameter *I* is the energy expended per mass fiber per impact, i.e., specific energy on pulp per impact. The force per bar length on fibers is *F*. These parameters are not independent, but they measure different aspects of refining action. Together with *N*, they give a fiber-based characterization of the refining process, *NIF*. We now explore uses of this approach.

EXAMPLES OF APPLICATIONS

Three-parameter characterization of refining

Howard et al. [14] showed by principal component analysis that three independent factors were responsible for the majority of the changes in pulp produced by refining. This

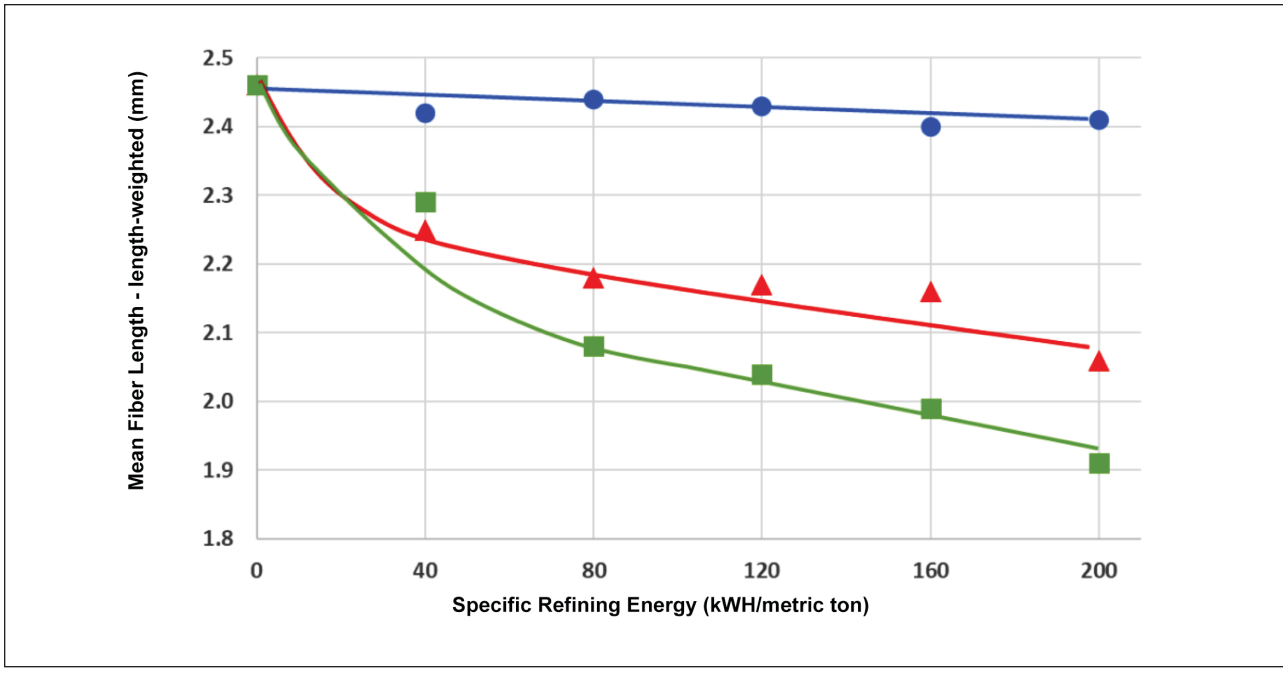

2. For a common SEL of 1.0 J/m, the average fiber length is lower for smaller bar widths, which impose greater bar force, F: ● (4.2 mm, 340 N/m), ▲ (2.0 mm, 400 N/m), and ■ (1.0 mm, 670 N/m) [10].

finding suggests that three parameters may be required to characterize the process of refining as well. We postulate that this is the case, and that *NIF* are the three parameters, each reflecting the following:

N : refiner capacity to inflict impacts on fibers
I : internal and external fibrillation
F : fiber shortening and fines generation

The following examples demonstrate some applications of *NIF*.

Predicting fiber shortening

Fibers are shortened by a single impact of large force. As shown in Eqs. 5-7, short fibers and small bar widths lead to large bar forces for a given *SEL*, and hence, fiber shortening. This is illustrated in **Fig. 2** for bars of different widths at a constant *SEL* [10]. The smallest *F* gives only a slight length reduction. For northern bleached softwood kraft (NBSK) pulp, fiber breakage was entirely avoided when *F*<200 N/m. Most importantly, Fig. 2 shows that *SEL* on its own does not reflect fiber shortening.

This observation raises an interesting theoretical question: how narrow can bars be? In the limit at *W=0*, bars become sharp blades. In this case, *s* is determined solely by captured fibers, i.e., $s = 5C_s l$. As an example, for C_s=0.04, *l*=2.5 mm, *s*=0.5 mm. To avoid cutting, (*F*<200 N/m), *SEL*<0.1 J/m. In short, *SEL* must be very small to avoid fiber shortening.

Predicting tensile strength increase

Increased tensile strength of paper is the most common objective of refining. The effect of successive impacts on pulp can be modeled by a cumulative probability equation employing *N*, *I*, and *P*, where *P* is the probability of tensile increase at an impact [15]. This probability is the product of intensity, *I*, and a parameter α reflecting fiber and fiber network response to an impact.

$$P = \alpha I \tag{8}$$

Increase in tensile strength ΔT is expressed as as a fraction of the maximum potential tensile strength increase, ΔT_{max} and obtained from Eq. 9 below. The ΔT_{max} is estimated from PFI refining at 12,000 revolutions. This is a widely available refiner and operating condition known to give very large tensile increase:

$$\frac{\Delta T}{\Delta T_{MAX}} = 1 - (1 - \alpha I)^N \tag{9}$$

Parameter α has been obtained by a nonlinear fit of refining data for several pulps to Eq. 9. The data were obtained in tests conducted in a batch mode by multiple passes through a 12-in. disc refiner. The N_B was determined for one pass and multiplied by the number of passes to determine the total N_B. The *N* was calculated from this [3]. An example of a fit for for NBSK is shown in **Fig. 3**. Values of for several pulps are listed in **Table I**.

The values of α in Table I, ranging from 1.6X10^{-6} to 3.3X10^{-6} kg/J, are remarkably similar for different pulps. The resulting levels of *P* are small, just a few percent. This suggests that α has deep significance, perhaps linked to

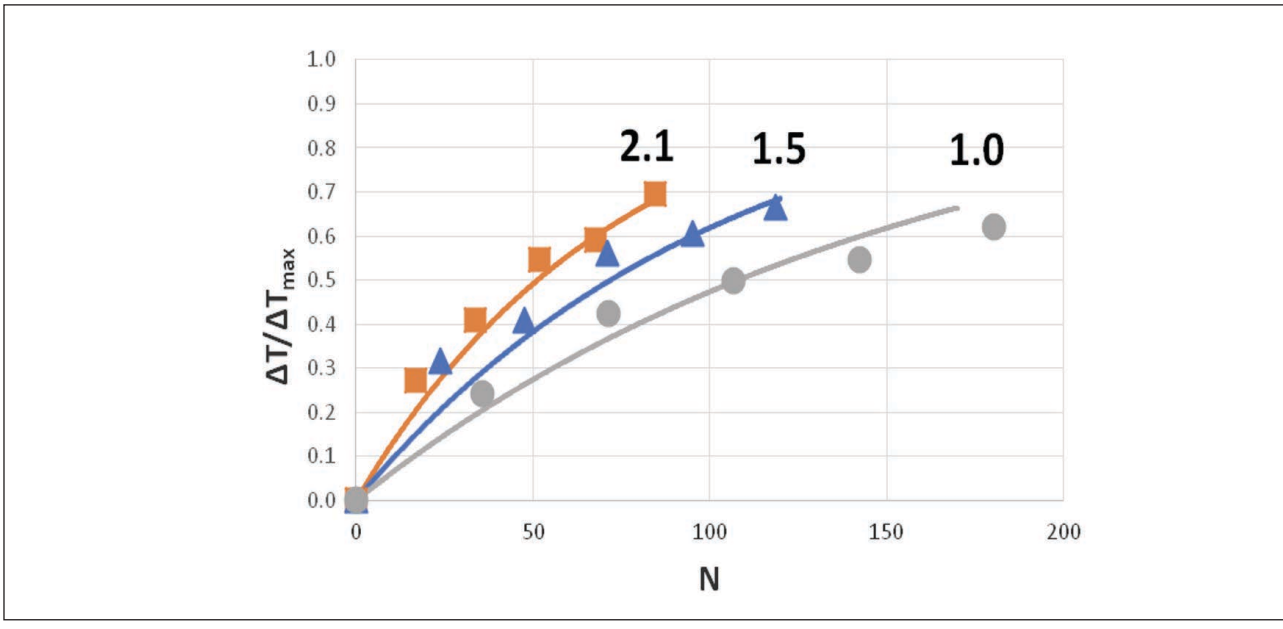

3. The fit of Eq. 9 to western Canadian northern bleached softwood kraft (NBSK) pulp laboratory data using plates with a bar width of 4.2 mm for SEL of 1.0, 1.5, and 2.1 J/m [3].

Pulp	α^* 10^{-6}, kg/J
Western Canada (NBSK)	1.6
Eastern Canada (NBSK)	2.8
Eastern Canada spruce (NBSK)	2.8
Southern pine	3.0
Eucalyptus	2.1–3.3
NBSK = northern bleached softwood kraft (NBSK) pulp.	

I. Values of for several pulps (Eq. 5) from [3].

transmittal of forces primarily at fiber crossings rather than over entire fibers.

In the early stages of refining where $\alpha IN << 1$, Eq. 9 may be simplified into a linear form:

$$\frac{\Delta T}{\Delta T_{Max}} = \alpha E \qquad (10)$$

However, at larger levels of energy, tensile increase becomes nonlinear, as shown in **Fig. 4**.

Comparing hardwoods and softwoods

It is well known that *SEL* for hardwoods must be significantly smaller than *SEL* for softwoods. For example, Baker [16] recommended *SEL*=0.2 J/m for hardwoods and *SEL*= 2.0 J/m for softwoods. These *SEL*s differ by an order of magnitude. However, when expressed as intensity *I*, they have a similar value: 7.8 kJ/kg for 0.8 mm-length hardwood and *I*= 8.0 kJ/kg for 2.5 mm-length NBSK.

The influence of intensity on hardwoods and softwoods at a conventional refining energy of *E*=120 kWh/ton is shown in **Fig. 5**. We note that higher intensities mean fewer impacts at a given energy, but show this comparison on the basis of equal energy, as is common. It is apparent that at the recommended level of *I*=8 kJ/kg, both pulps reached the same high level of tensile increase.

Comparing PFI mill to industrial refiners

Although the PFI mill is a widely used laboratory refiner, its geometry and operation differ substantially from mill refiners. Compared to the Escher-Wyss laboratory refiner, which is representative of mill refiners, the PFI mill produces larger tensile strength at equal freeness, but lower tensile at equal energy [18].

This disparity is partly due to large difference in *N* and *I*. At a typical operating condition of 6000 revolutions, PFI energy is 1000 kWh/metric ton [17], giving *N*=3600 and *I*=1 kJ/kg [18] This intensity is about 1/10 of industrial refiners. It is also about the intensity employed in compression tests to produce tensile increase in the absence of shear [15], which suggests that the action of the PFI is primarily compression.

This was confirmed by lowering intensity in the Escher-Wyss refiner to about *I*=1 kJ/kg [18]. At equal energy, the Escher-Wyss refiner gave a far larger tensile and lower freeness than did the PFI. The likely cause is differing levels of shear. In industrial refiners, shear is imposed by fibers restrained by two bar edges during compression in contrast to only one bar edge in the PFI. The importance of this factor was demonstrated in experiments on the PFI in which bars were placed on the smooth housing [19]. Doing so brought the PFI results closer to industrial refining.

In summary, the PFI mill is a high-energy, low intensity

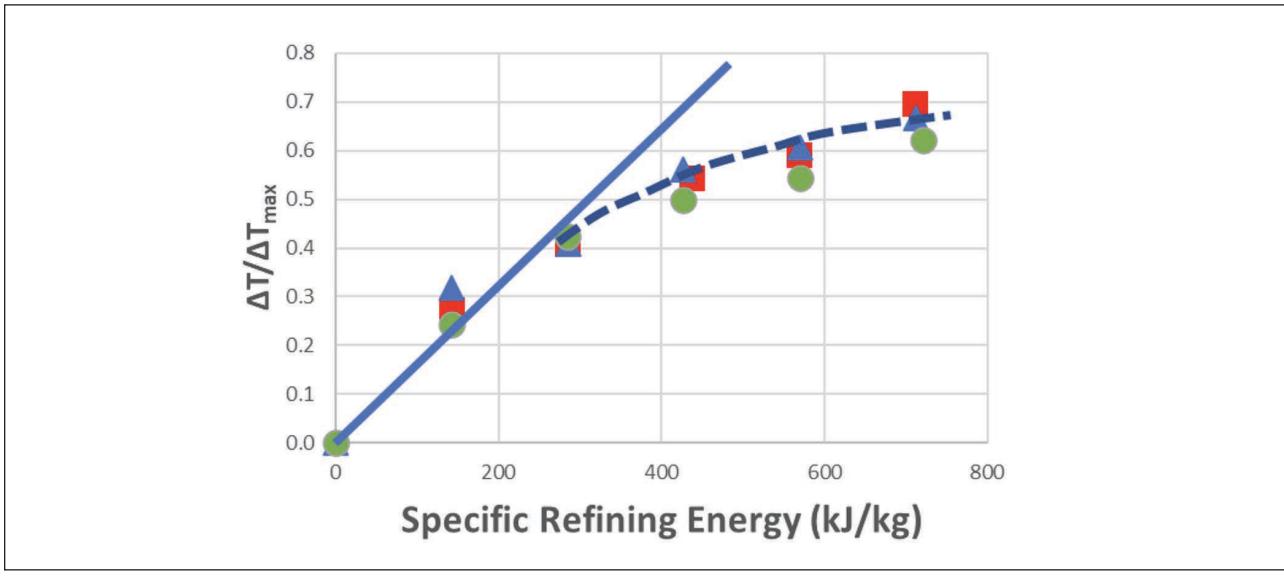

4. The increase in tensile strength is proportional to energy in the early stages of refining with slope of α = 1.6X10^{-6} kg/J. The data is for a western Canadian NBSK pulp at SEL of: ● 1.0, ▲ 1.5, and ■ 2.1 J/m [3].

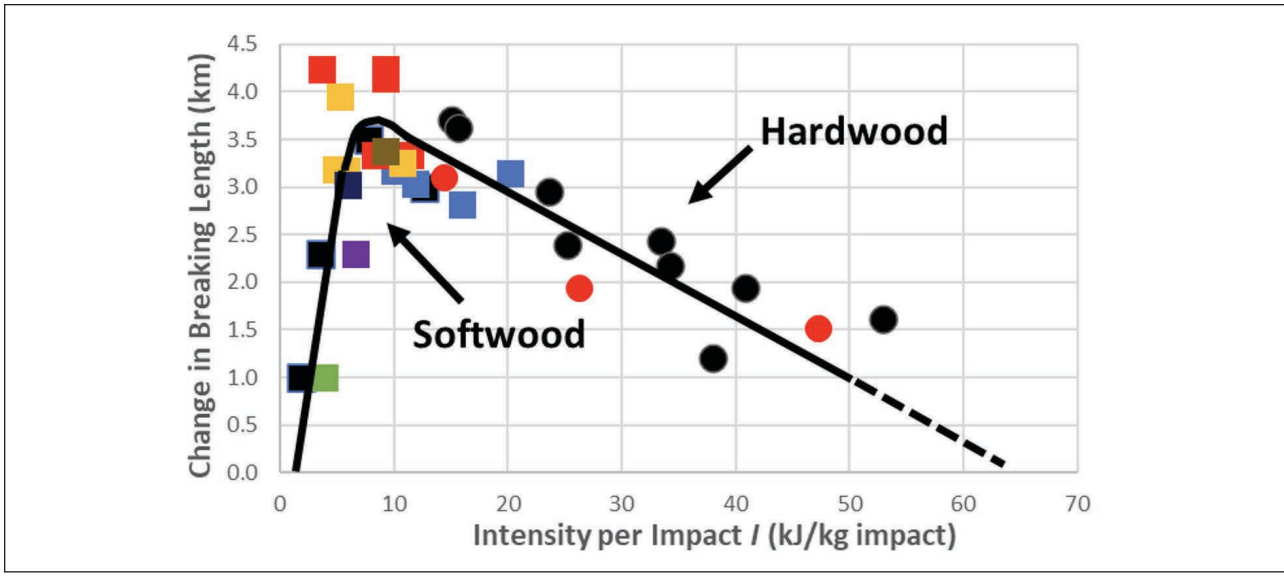

5. Intensity, I, for a range of softwoods ■ and hardwoods ● at a common energy of 120 kWh/metric ton [3].

device that applies a large number of impacts. Due to its geometry, it promotes compression over shear to a greater extent than conventional refiners. Accordingly, although useful for some purposes, care should be exercised in predicting conventional refining from PFI results.

Estimating the effect of flow recirculation

In some refiners, a portion of the discharge flow is recirculated back to the entry flow to maintain flow in the refiner within a design range. This means that some pulp passes through the refiner once and some many times. The result is a mixture of pulps refined at a common *I* but differing *N*. This may affect some pulp properties.

Parameter *N* is proportional to the number of passes, *n*. The fraction of pulp subjected to *n* passes depends on the fraction recirculated, *R*, which is given by Eq. 11 [20]. An example for differing levels of *R* is shown in **Fig. 6**.

$$\frac{F_P(n)}{F_P} = R^{n-1}(1-R) \tag{11}$$

Comparing high consistency and low consistency refining of mechanical pulp

Mechanical pulp has traditionally been produced by high consistency (HC) refining, but there is a growing trend toward low consistency (LC) refining in the second stage. It is therefore useful to compare the LC intensity with HC in-

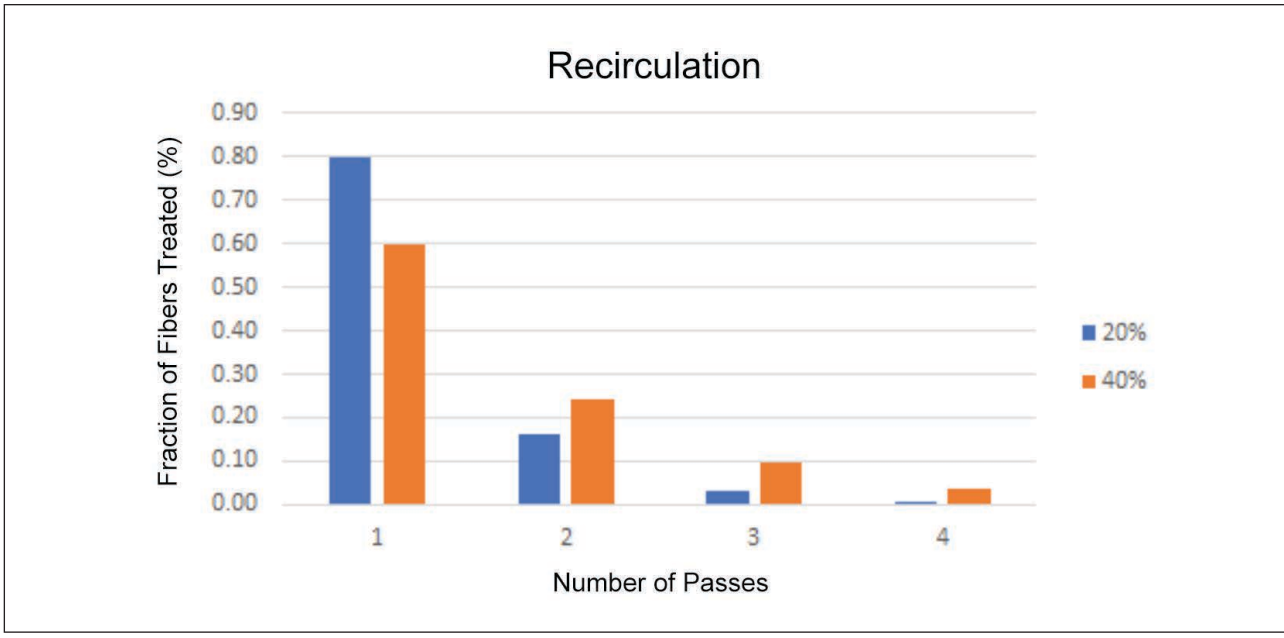

6. Pulp fractions experiencing different numbers of passes at recirculation rates of 20% and 40%.

tensity in this stage [21]. However, the vast difference in LC and HC rheology makes this comparison difficult.

High consistency pulp is a heterogeneous, compressible, three-phase mixture, whereas LC pulp is a liquid suspension, acting as a continuum [21]. The compressibility of HC pulp introduces uncertainty in the residence time and mass of pulp in the refiner. Accordingly, intensity calculated from the *SEL* is not comparable to that for a "full-flow" LC refiner. A fiber-based approach addresses this issue.

Miles and May [22] determined N and I from a force balance on pulp in the radial direction. This gave N, which, with specific energy E, gave intensity I [22]. Miles and May found HC intensity to be about I=2 kJ/kg [21,22]. Assuming fiber length of 1.5 mm and 4% consistency, this would correspond to about SEL=0.2 J/m. This is at the lower end of the range in use [23].

In summary, fiber-based characterization enables comparisons between radically different types of refining.

SUMMARY AND CONCLUSIONS

This paper has summarized key aspects of a fiber-based characterization of pulp refining and shown that three parameters are required to fully characterize the process. These are: number of impacts on pulp, N; energy per mass per impact, I; and bar force, F. Simplified equations are given to calculate these parameters, along with examples of benefits from using them. The benefits include comparisons between radically different types of refiners; commonly recommended intensity levels for hardwoods and softwoods; effect of small bar widths on fiber shortening; and a predictive equation for tensile strength. It is hoped that these examples spark further interest among researchers and practitioners in the employment of fiber-based characterization to derive greater value from the fiber resource by refining. **TJ**

LITERATURE CITED

1. Kerekes, R.J., *Nord. Pulp Pap. Res. J.* 5(1): 3(1990). https://doi.org/10.3183/npprj-1990-05-01-p003-008.
2. Lundin, T., Batchelor, W., and Fardim, P., *TAPPI J.* 7(7): 15(2008).
3. Kerekes, R.J., Heymer, J.O., and McDonald, J.D., *Nord. Pulp Pap. Res. J.* 36(4): 696(2021). https://doi.org/10.1515/npprj-2021-0012.
4. Heymer, J.O., Olson, J.A., and Kerekes, R.J., *Nord. Pulp Pap. Res. J.* 26(3): 283(2011). https://doi.org/10.3183/npprj-2011-26-03-p283-287.
5. Brecht, W. and Siewert, R., *Papier* 29(10): 4(1966).
6. Kerekes, R.J. and Senger, J.J., *J. Pulp Pap. Sci.* 32(1): 1(2006).
7. TAPPI, "Refiner plate intensity," *Technical Information Paper TIP 0508-0*, TAPPI Press, Atlanta, 1994.
8. Meltzer, F.P. and Rautenbach, R., *Das Papier* 48: 578(1994).
9. Roux, J.-C., Bloch, J.-F., Bordin, R., et al., "The net normal force per crossing point: A unified concept for the low consistency refining of pulp suspensions," in *Advances in Pulp and Paper Research, Oxford 2009, Trans. of the XIVth Fund. Res. Symp.* (S.J. l'Anson, Ed.), Oxford, 2009, pp. 51–83, FRC, Manchester, 2018.
10. Kerekes, R.J. and Meltzer, F.P., *Nord. Pulp Pap. Res. J.* 33(2): 220(2018). https://doi.org/10.1515/npprj-2018-3028.
11. Goncharov, V.N., "Force factors in a disk refiner and their effect on the beating process," *Bumazh. Promst.* 12(5): 12(1971) [English Trans.].
12. Kerekes, R.J. and McDonald, J.D., *Nord. Pulp Pap. Res. J.* 36(4): 714(2021). https://doi.org/10.1515/npprj-2021-0044.
13. Berg, J.-E., Sandberg, C., Engberg, B.A., et al., *Nord. Pulp Pap. Res. J.* 30(2): 225(2015). https://doi.org/10.3183/npprj-2015-30-02-p225-229.

14. Howard, R.C., Poole, R., and Page, D.H., *J. Pulp Pap. Sci.* 20(5): J137(1994).
15. Goosen, D.R., Olson, J.A., and Kerekes, R.J., *J. Pulp Pap. Sci.* 33(2): 110(2007).
16. Baker, C.F., *Tappi J.* 78(2): 147(1995).
17. Welch, L.V. and Kerekes, R.J., *Appita* 47(5): 387(1994)
18. Kerekes, R.J., *TAPPI J.* 4(3): 8(2005).
19. Bovin, A., *Sven. Papperstidn.* 81(1): 359(1978).
20. Kerekes, R.J., *TAPPI J.* 13(4): 29(2014).
21. Kerekes, R.J., *BioResources* 10(4): 8795(2015).
22. Miles, K.N. and May, W.D., *J. Pulp Pap. Sci.* 16(2): 430(1990).
23. Luukkonen, A., Olson, J.A., and Martinez, D.M., *J. Pulp Pap. Sci.* 36(1-2): 28(2010).

ABOUT THIS PAPER

Cite this article as:
Kerekes, R. and McDonald, J.D., *TAPPI J.* 21(9): 497(2022). https://doi.org/10.32964/TJ21.9.497

DOI: https://doi.org/10.32964/TJ21.9.497

ISSN: 0734-1415

Publisher: TAPPI Press

Copyright: ©TAPPI Press 2022

About this journal

ABOUT THE AUTHORS

Refining is a key operation in papermaking that can greatly enhance the value of the fiber resource. Improved tools to control the process will assist papermakers in obtaining this value. This paper summarizes and condenses nearly 30 years of research in a simple, usable form for papermakers.

In this study, choosing the topics of highest importance and simplifying them while maintaining scientific rigor was challenging. It was satisfying to find the degree to which fiber-based characterization of refining can unify what appears to be vastly different approaches to fiber modification. Although the concept of fiber-based refining has been around for many years in various forms, it is surprising that it has not been exploited by the industry.

As new engineers are hired into the pulp and paper industry, mills should encourage them to apply concepts in this paper to enhance refining for improved pulp properties. We have few topics related to this study that remain to be studied in detail. The main one is the low probability of producing desired fiber changes during each bar crossing in refiners.

Kerekes is professor emeritus at the University of British Columbia, Pulp and Paper Centre, in Vancouver, BC, Canada. McDonald is president of JDMcD Consulting Inc. in Vaudreuil-Dorion, QC, Canada. Email McDonald at mcdonald.jdavid@gmail.com.



Kerekes



McDonald

The Mechanism of Bonding

W. BOYD CAMPBELL

Three factors are involved in cellulose bonding—available area, contact, and hydrogen bonding. Since the use of the electron microscope and the synthesis of cellulose, it has become clear that the primary form of cellulose is elementary fibrils with about 100 molecules cross-section and about 400 sq. m. area per g. Because of internal bonding only a small part of this area is available. Consideration of various possibilities indicates that exterior surface of fibers, which varies from 1.0 to 2.3 sq. m. per g. depending on the degree of beating, is the main source of usable area. Wet pressing, which is much more intense than average pressure applied, is first factor in securing contact and is much assisted by softening due to internal fibrillation by beating. More intimate contact is brought about by liquid internal tension on drying. Final hydrogen bonding differs from crystallizing force in that there is no need for parallel orientation in the fibers to be bonded but does require close contact. Tension during drying will diminish the bonding between surfaces at right angles to the tension.

WHEN we consider the mechanism of the bonding of cellulose fibers in the making of paper, we find that there are three fundamental factors involved. First we have to think of what surfaces are to be bonded; next, how these surfaces are to be brought together; and, finally, how they are to locked in position.

The matter of surfaces of cellulose is quite complicated because there are so many different surfaces which may be involved. To consider these it is necessary to look at the structure of fibers. As long as the botanists concerned with such structure were restricted to the use of light microscopes, they had to deduce, by a sort of circumstantial evidence, the existence of structural elements which were below the limits of resolution by light, that is, below about 0.5 μ. They had indications by polarized light and from the way fibers broke up by mechanical and chemical action. Out of such indications they deduced that the cell wall was made up of fibrils of somewhat indeterminate size, but which were more or less parallel to each other and arranged at various angles to the fiber axis at different depths in the cell wall. But there was always a feeling that possibly these fibrils were merely due to lines of fracture of the cellulose material.

W. BOYD CAMPBELL, Consultant, Montreal, Que.

Of late years, the electron microscope has greatly extended the lower limits of resolution. It is comparatively easy to see structures having dimensions of 100 A or 0.01 μ. The actual existence of elementary fibrils has been pretty well demonstrated and there is a growing feeling that they have nearly the same dimensions in all cellulose. What these dimensions are is not quite so generally agreed upon. Frey-Wyssling puts them as somewhere between 50 × 60 A. and 30 × 100 A. and having 100 molecules of cellulose in their cross section.

Still later, J. R. Colvin, of the Canadian National Research Laboratory, has been able to grow cellulose fibrils without the presence of any living material. Working on the principle that materials are elaborated in living organisms by enzyme catalysts plus suitable base compounds, he has separated the enzymes from certain bacteria, and, with these as catalyst director, glucose as raw material, and ATP as energy transformer, he has been able to grow cellulose. Not only does the cellulose grow, but it grows in fibrils of about the size found in materials of more conventional growth. Moreover, the fibrils grow, not by cellulose molecules ranging themselves side by side in a crystalline array, but by additions to the tip of the fibril. In view of all this, it seems rather certain now that cellulose, as we know it, is actually made up of such fibrils. By the use of a

The "Campbell effect" and fiber bonding: *TAPPI Journal* revisits relevant research

TAPPI Journal's Editorial Board has noted the importance of certain "classic" papers that are as important and relevant today as ever, but may only be available through libraries and institutions. The above paper by W. Boyd Campbell is one such research paper. It was selected by Gerard "Gerry" J.F. Ring, Ph.D., professor emeritus at the University of Wisconsin-Stevens Point (UWSP) and a member of the *TAPPI Journal* Editorial Board, after discussing it recently with a coating manufacturer.

According to Ring, this well-cited paper is about the famous "Campbell effect," which demonstrates that there is sufficient force generated by evaporation in the dryer section of paper machines to bring fiber surfaces together and enable fiber-to-fiber bonding. He notes that this effect is often discussed in surface chemistry courses, as well as in paper physics courses.

You can find more such historical papers in recent issues of *TAPPI Journal*, along with their associated DOI information.

CITE THIS PAPER: Campbell, W.B., *Tappi* 42(12): 999(1959). https://doi.org/10.32964/TJ42.12.999

little imagination, it is possible to guess that the other carbohydrates—pentosans and hemicellulose—and probably lignin, are formed in similar manner by other enzyme catalysts and other base materials.

In growth of the wood cell, the cellulose is produced in a watery medium. At the same time, lignin and the hemicelluloses are also produced and largely fill in the spaces between the cellulose fibrils. In the wood cell, the secondary wall, which holds the main body of the cellulose, contains about 15%, by weight, of lignin. This is almost completely removed by cooking and bleaching. The noncellulose carbohydrates are removed somewhat less completely. With this removal we are left with a mass of fibrils, more or less regularly arranged, with interstices filled with water until the pulp is dried.

Calculating on the basis of 100 molecules of cellulose cross section and the dimensions by Frey-Wyssling, such fibrils have a surface area of 400 to 450 sq. m. per g. of cellulose. Purves and associates (*J. Amer. Chem. Soc.* 66: 59 (1944) found 300 to 400 sq. m. per g. in cotton cellulose which had been swollen in caustic soda and dried by solvent exchange. But cotton linters, dried directly from water, showed only 8 sq. m. per g., and ramie only 5 sq. m. per g. This was by a chemical method. Apparently, the drying abolishes a great deal of surface by bonding the fibrils together.

But this vast surface is of little direct interest to the papermaker; it is buried within the fiber and not available to make contact with other fibers. Depending somewhat on the severity of the cooking process, this lot of fairly parallel fibrils is enclosed in more or less of the primary layer. This primary layer consists of a somewhat tangled mass of fibrils which do not readily become untangled to show up as the visible fibril bundles of beaten pulp. Instead, it acts somewhat as a sort of cellophane skin enclosing the inner, more orderly, arrangement. Similar to cellophane, this skin has little ability to bond to similar skins. On swelling the inner mass, this skin may bunch up to form constrictions around the fiber. Between these constrictions, the swelling shows up under the microscope as balloon structures. Unless this layer is mostly removed by the cooking process, as it usually is in the sulphites, it must be broken up by beating before any great strength is reached.

By beating, and this includes all mechanical handling of pulp in water, the rather closely packed lot of fibrils inside the fiber are shaken apart so that the fiber swells. Further beating may cause some bundles of fibrils to break out from the mass and become visible as fibrillae. Such a process does not affect the total surface area appreciably. According to the studies of Russell and myself (*Can. J. Research*, B15: 13 (1937)) beaten pulp absorbs only about 4% more water from vapor than does unbeaten. This can be taken to indicate that it has only about 4% more total surface.

Robertson in Montreal and Ingmanson in Appleton, have measured specific surface and specific volume by the permeability method. They show the unbeaten pulp to have an external surface area of about 0.8 sq. m. per g., and a specific volume of about 1.8 cu. cm. per g., for pulp from which fines had been removed by screening. While the value for specific volume would indicate about 1.2 g. water per g. of dry cellulose, the meaning of this is not clear for it includes water in the lumen space. The surface of fibrils and fibril aggregates inside the fiber volume is not included in the 0.8 sq. m. per g.

On beating, these values increase greatly, especially in the early stages. Specific volume increases to as much as 5.5 cu. cm. per g. and specific surface to 4.0 sq. m. per g. or greater. Again the meaning of this is unclear. Specific volume, in this method, means the volume through which liquid does not flow to any appreciable extent. From the concentration of cellulose in a fiber swollen to a specific volume of 5.5, it would appear that a "consistency" of 20% counts as solid. The specific surface means the surface over which water does flow. It is not new surface necessarily, since most of it already existed as internal surface.

It is probably not even correct to think of the whole calculated 400 sq. m. surface of the elementary fibrils as actually existing. Much of this must disappear in the formation of the fibril aggregates such as are visible in beaten pulp. From the measurements of sorption versus relative vapor pressure we can, by making some simple assumptions, calculate a total surface of about 130 sq. m. per g.

Of this, the 4 sq. m. per g. external surface measured by the permeability method is only a small part, so we must infer that most of the surface is still interior. In any case, most of the external fibril aggregates and all of the interior ones will, on drying, contact and bond to their parent fibers. So, for the contact between fiber and fiber required to make paper, we must rely chiefly on the swollen condition of fibers. If the swollen volume of a fiber is x times that of the unswollen, and it crosses a similarly swollen fiber, the projected area of the crossing will be x times the area of the unswollen fiber crossing. We may expect, then, that the area available for bonding will be increased about in the proportion of the swollen volume. Both Robertson and Ingmanson have found support for this.

The next part of the problem is how to bring surfaces into contact close enough to lead to bonding. Wet pressure is the first move in this direction. If we apply a wet pressure of W p.s.i. to the sheet, the load must be carried by the areas where fibers cross each other. As these areas are much less than the total area of the sheet, the pressure per unit area of pressing must be many times W, especially as some crossings will carry no load because neighboring ones are in thicker regions. Obviously, the pressing operation has an importance other than water removal.

Next comes water removal by drying. For the removal of all water except that actually in very close contact with fiber surface, there is little effect on the paper structure. The water simply evaporates. But when this is gone, and water must evaporate from fine crevices in or between fibers or fibril bundles, another pressure effect comes into play. Evaporation of this water is accompanied by shrinkage. Cellulose itself, that is the crystal cellulose which makes up the fiber bundles, does not shrink. It is the water between these which sets up a tension drawing the cellulose surfaces together and so makes the over-all shrinkage.

To explain this, it is necessary to look at the physics of liquids, in general, and water, in particular. Even in the vapor form, where molecules are comparatively

CITE THIS PAPER: Campbell, W.B., *Tappi* 42(12): 999(1959). https://doi.org/10.32964/TJ42.12.999

far apart, there is an attraction of molecule to molecule which must be taken into account in precise measurements. In Van der Waals' equation, this factor takes the form of a value, a/v^2, which must be added to the pressure term, p, of the familiar "pv." When v becomes very small, as it does when the vapor becomes liquid, this term becomes very large. It is usually termed the intrinsic pressure of the liquid. Since it is difficult to conceive of any way of getting a grip on water so as to measure this tensile strength directly, it has never been so measured. But it can be calculated in several independent ways with reasonably good agreement between them. For water it amounts to 11,000 or 12,000 atm.

When water, or any liquid which wets the walls, is in a capillary tube, it is drawn upward; it is under tension. The amount of such tension can be calculated in either of two ways, (1) from surface tension and the capillary diameter, or (2) from the lowering of the vapor pressure at the exposed liquid surface when equilibrium is established. For water, this tension amounts to 142 atm. at 90% relative vapor pressure (RVP), 936 atm. at 50% RVP, and 3110 atm. at 10% RVP.

As soon as the amount of water in a cellulose fiber or a mass of cellulose, such as paper, becomes low enough to be in equilibrium with a relative vapor pressure less than 100%, this tension force comes into play to draw the solid surfaces together. That is, provided the solid surfaces are already close enough to each other so that the space between is filled with water when the humidity goes below the 100%. If the solid surfaces are free to move, or are restrained only by a force less than this tension, they will ultimately come into real contact or contact except for a molecular layer of water between them.

Since our wet pressure acted to press together surfaces lying in the plane of the sheet, the great majority of bonded surfaces in paper will also be in the plane of the sheet. There will, of course, be bonded surfaces in other planes, but these depend for their formation on chance contacts. Those which are at right angles to the sheet and parallel to the machine direction will have most strength because there is little impediment to shrinkage and consequent bonding of these. But those which are at right angles to sheet and to machine direction will be weak since the sheet tension will oppose their shrinkage and bonding. Surfaces at intermediate angles will, of course, have intermediate strength.

At the present time it in usual to refer the strength of the bonding to hydrogen bonds; that is, to regions where the hydrogen atom of a group such as OH finds itself close to an atom of oxygen or some other element with one or more pairs of unshared electrons. In such case, the positive hydrogen finds itself attracted to two different negative centers and holds them together. The energy associated with such bonds can be calculated from the data of infrared spectroscopy. It varies somewhat depending on the structure of the molecules taking part and on the closeness of the oxygen atoms being joined. Calculating from the number of probable bonds per square centimeter of crystal cellulose and an energy of 3.5×10^{-13} ergs per bond, the crystal is held together by an energy of about 500 ergs per sq. cm. Since the bonding of chance contacts must be much less than this because of lack of conformity of structure, the bonding which gives paper its strength must also be much less than this. This is made very evident by the ease with which water penetrates these bonded areas and replaces cellulose-to-cellulose bonds by cellulose-to-water bonds. Water cannot penetrate the crystal bond areas since entrance of one water molecule would require the breaking of many cellulose-to-cellulose bonds.

Probably some experiments quoted by F. P. Bowden, of Cambridge University, in *Endeavour*, January 1957, will help clarify some ideas of such bonding.

Sheets of good mica can be split, with care, so as to leave molecularly smooth surfaces. The energy of the splitting can be measured; it was found to be about 300 ergs per sq. cm. for first splitting and about 250 ergs per sq. cm. if the surfaces were brought together again and split a second time. This is not far from the energy calculated for the bonding in the cellulose crystals. But the energy per unit surface has little to do with the *force* required to separate them. This latter depends on how many bonds must be broken simultaneously. When the two mica surfaces were separated by a shear force in the plane of the surface, the force was found to be 10 kg. per sq. mm. or 1000 kg. per sq. cm. In the splitting, the force was very small because only a comparatively few bonds were being broken at one instant. But the shear action required the breaking of several million times as many at once.

The strength of paper corresponds to the tensile shear in the case of the mica. It is probable that, even where fibers are broken, the rupture is one of shear between bonded fibrils inside the fiber. That fibers are broken is evidence that the bonding of these to neighboring fibers is stronger than whatever bonding exists in the fiber itself and which may be due to primary chemical bonds or to hydrogen bonding or both.

If this view of strength development is correct, we must look at strength in machine direction as due to the bondings in the plane of the sheet plus incidental bondings due to shrinkage which can take place across the sheet. Strength in cross direction does not have such addition since, for the most part, sheet tension does not permit of much bonding in the plane giving such strength.

It should also be pointed out that not all bondings contribute to the final breaking load. A great deal of bonded surface is broken in the earlier stages of loading while distortions take place in the course of setting up of the continuous chains of bonded units which carry the final load. This earlier breaking of bonds does not affect the load which the sheet can carry but it does affect the amount of stretch remaining available. That is, if the loading is released before the final break, the breaking load obtained on a second application will not be affected, though many bonds were broken before it was applied. But a considerable portion of the stretch used up in such early loading is lost and is not available the second time, though the total stretch of the two loadings is not affected.

Received Oct. 15, 1959. Presented at the Symposium on Fundamentals of Fiber Attraction and Bonding Sponsored by the Technical Association of the Pulp and Paper Industry, Appleton, Wis., Sept. 9–11, 1959.

TAPPI JOURNAL
WWW.TAPPI.ORG
THE PAPER AND PACKAGING INDUSTRIES' TECHNICAL RESOURCE
OCTOBER 2022 | VOL. 21 NO.10



NONWOVENS **521**
Effectiveness of masks in the suppression of COVID-19 cases during the ongoing pandemic in India
Shreyas Ganesh, Mirza M.O. Khyum, Kenneth N. Kikanme, and Seshadri Ramkumar

RECYCLING **533**
A new method of studying the fundamental mechanisms involved in pigment liberation from recycle papers
Kaiwu Huang, Kris Strickland, Aaron Noble, Roe-Hoan Yoon, and Cesar Basilio

NONWOOD PULPING **543**
Utilization of palm fiber as papermaking materials: Microscopic structure and chemical pulping
Zhulin Li, Shuai Gao, Lei Tang, Ding Liu, Qun Li, Guoyo Tian, and Zhaojiang Wang

TISSUE **553**
Research on improving the basis weight measurement accuracy of tissue paper based on PSO-BP neural network
Lianhua Hu, Yuxiu Feng, and Jin Ma

NANOCELLULOSE **563**
Nanocellulose–cationic starch–colloidal silica systems for papermaking: Effects on process and paper properties
Larden J. Garland, Brandon D. Leib, Nelson A. Barrios, and Martin A. Hubbe

NANOCELLULOSE **572**
Effects of orders of addition in nanocellulose–cationic starch–colloidal silica systems for papermaking
Brandon D. Leib, Larden J. Garland, Nelson A. Barrios, and Martin A. Hubbe

October 2022

TABLE OF CONTENTS VOL. 21 NO. 10

517 EDITORIAL
Vipin Varma joins *TJ* Editorial Board as expert on environmental and sustainability topics
Monica Shaw

521 NONWOVENS
Effectiveness of masks in the suppression of COVID-19 cases during the ongoing pandemic in India
Shreyas Ganesh, Mirza M.o. Khyum, Kenneth N. Kikanme, and Seshadri Ramkumar

533 RECYCLING
A new method of studying the fundamental mechanisms involved in pigment liberation from recycle papers
Kaiwu Huang, Kris Strickland, Aaron Noble, Roe-Hoan Yoon, and Cesar Basilio

543 NONWOOD PULPING
Utilization of palm fiber as papermaking materials: Microscopic structure and chemical pulping
Zhulin Li, Shuai Gao, Lei Tang, Ding Liu, Qun Li, Guoyo Tian, and Zhaojiang Wang

553 TISSUE
Research on improving the basis weight measurement accuracy of tissue paper based on PSO-BP neural network
Lianhua Hu, Yuxiu Feng, and Jin Ma

563 NANOCELLULOSE
Nanocellulose–cationic starch–colloidal silica systems for papermaking: Effects on process and paper properties
Larden J. Garland, Brandon D. Leib, Nelson A. Barrios, and Martin A. Hubbe

572 NANOCELLULOSE
Effects of orders of addition in nanocellulose–cationic starch–colloidal silica systems for papermaking
Brandon D. Leib, Larden J. Garland, Nelson A. Barrios, and Martin A. Hubbe

»**COVER CREDIT**: Indo-U.S. collaborative research shows that face masks have a role in preventing the spread of airborne microbes (p. 521). The outcome of such research highlights wide-ranging applications for textiles and nonwovens in medical and industrial applications.

TAPPI JOURNAL
WWW.TAPPI.ORG

Editor-in-Chief
Douglas W. Coffin coffindw@miamioh.edu
+1 513 529-0771

Associate Editor
Peter W. Hart peter.hart@westrock.com
+1 409 276-3465

Editorial Director
Monica Shaw mshaw@tappi.org
+1 770 367-9534

PRESS Manager
Jana Jensen jjensen@tappi.org
+1 770 209-7242

***TJ* EDITORIAL BOARD**

Brian N. Brogdon, FutureBridge Consulting & Training LLC
brian.brogdon@gmail.com, +1 678 581-9114

Ravi Challa, Suominen Corporation
Ravi.Challa@suominencorp.com, +1 843 680 2586

Douglas W. Coffin, Miami University
coffindw@miamioh.edu, +1 513 529-0771

Mahendra Doshi, Doshi and Associates
mahen@aol.com, +1 920 832-9101

Marc Foulger, Valmet
marc.foulger@valmet.com +1 315 767-2920

Peter W. Hart, WestRock
peter.hart@westrock.com, +1 409 276-3465

Carl J. Houtman, USDA Forest Products Laboratory
choutman@fs.fed.us, + 1 608 231-9445

Vamsi Jasti, Ahlstrom-Munksjo Nonwovens LLC
jvamsik1@gmail.com, +1 818 585-3524

Lucian Lucia, North Carolina State University
lucian.lucia@gmail.com, +1 919 889-7059

John A. Neun, John A. Neun LLC
john.neun@gmail.com, +1 518 275-8139

Jim Niemiec, Jim Niemiec Consulting LLC
jim.niemiec@outlook.com, +1 715 213-4766

Steven P. Ottone, Omya
steven.ottone@omya.com, +1 919 641-7854

Gaurav Pranami, Imbed Biosciences
gpranami@imbedbio.com, +1 515 230-7005

Arthur Ragauskas, Oak Ridge National Laboratory
aragausk@utk.edu

Seshadri Ramkumar, Texas Tech University
S.Ramkumar@ttu.edu, +1 806 742-4567

Gregg Reed, Imerys
gregg.reed@imerys.com, +1 478 553-5747

Gerard J.F. Ring, University of Wisconsin—Stevens Point
gerrryring@wi-net.com, +1 715 592-3732

Scott Rosencrance, Kemira Chemicals
scott.rosencrance@kemira.com, +1 770 429-2753

Vipin Varma, NCASI
vvarma@ncasi.org, +1 352 244-0965

Junyong Zhu, USDA Forest Products Laboratory
jzhu@fs.fed.us, +1 608 231-9520

Join TAPPI *today!*
TAPPI JOURNAL is a free benefit of TAPPI membership, and is only available to members. To join TAPPI, to renew your TAPPI Membership, or to learn about other valuable benefits, visit www.tappi.org.

TAPPI, 15 Technology Parkway S., Suite 115, Peachtree Corners, GA 30092, publishes *TAPPI JOURNAL* monthly.

ATTENTION PROSPECTIVE AUTHORS: All papers published are subject to *TAPPI JOURNAL's* peer-review process. Not all papers accepted for review will be published. Before submitting, check complete author guidelines at http://www.tappi.org/s_tappi/doc.asp?CID=100&DID=552877.

Statements of fact and opinions expressed are those of individual authors. TAPPI assumes no responsibility for such statements and opinions. TAPPI does not intend such statements and opinions or construe them as a solicitation of or suggestion for any agreed-upon course of conduct or concerted action of any sort.

Copyright 2022 by TAPPI, all rights reserved. For copyright permission to photocopy pages from this publication for internal or personal use, contact Copyright Clearance Center, Inc. (CCC) via their website: www.copyright.com. If you have questions about the copyright permission request process, please contact CCC by phone at +1 978 750-8400. To obtain copyright permission to use excerpts from this publication in another published work, send your specific request in writing to Editor, TAPPI JOURNAL, 15 Technology Parkway S., Suite 115, Peachtree Corners, GA 30092, USA; or by fax to +1 770 446-6947. Send address changes to TAPPI, 15 Technology Parkway S., Suite 115, Peachtree Corners, GA 30092, USA; Telephone +1 770 446-1400, or FAX +1 770 446-6947. www.tappi.org

Editorial



MONICA SHAW | EDITORIAL DIRECTOR
mshaw@tappi.org

Vipin Varma joins *TJ* Editorial Board as expert on environmental and sustainability topics

Editor's Note: *This column is part of a series that profiles the background and expertise of* TJ*'s editorial board members. These volunteer members spend long hours overseeing the peer review process and contributing to* TJ*. TAPPI would like to express its gratitude to the editorial board members for their hard work and willingness to share their expertise with the forest products community.*

— Monica Shaw, Editorial Director

TAPPI and the *TAPPI JOURNAL* (*TJ*) editorial staff would like to welcome a new member to the TJ Editorial Board, Vipin Varma, Ph.D., who is vice president, Manufacturing Programs, at the National Council of Air and Stream Improvement (NCASI), headquartered in Cary, NC, USA. NCASI develops technical information that is critical for forest products companies to meet and surpass their environmental and sustainability goals. Vipin will provide expertise on environmental, sustainability, air emissions, and water topics relevant to the pulp and paper industry. In his position on the *TJ* Editorial Board, he succeeds Paul Wiegand, NCASI's vice president for Water and Chemical Management Programs, who served from 2007 to 2022.

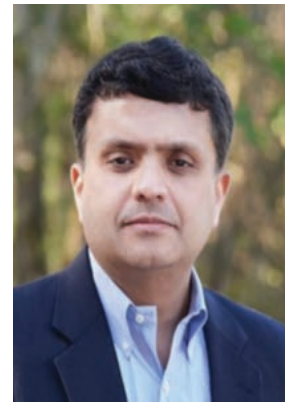

New member of* TAPPI Journal *Editorial Board, Vipin Varma, Ph.D.

Vipin holds a Ph.D. in Chemical Engineering from Auburn University, with a dissertation topic of "Alkali profiling – A tool to enhance (optimize) delignification." He also received an MBA from The Wharton School in the areas of Corporate Strategy and Entrepreneurship, with a focus on Finance.

Vipin joined NCASI as a senior research engineer in 1998 and managed several research projects on quantifying air toxics emissions and assessing Maximum Achievable Control Technology (MACT) compliance options. He led the industry group in developing compliance approaches for Phase II of the MACT rule, specifically the Clean Condensate Alternative (CCA). He liaised with the U.S. Environmental Protection Agency (EPA) on validating CCA compliance approaches and developed technical information that informed the subpart S Residual Risk and Technology (RTR) review.

In 2011, Vipin rejoined NCASI after a stint at Vorbeck, a graphene startup, where he led technology, product, and market development in the United States and the European Union. He has led the Air Quality and Wood Products programs at NCASI since 2011 and was recently promoted to the position of vice president, Manufacturing Programs.

As a member of the *TJ* Editorial Board, Vipin brings a deep understanding of the forest products industry, environmental and sustainability topics, and technology and market forces that drive commercial and business success. Through his participation, he expects to benefit from further exposure to research and technology developments.

"I'm always looking for innovative ways to tap into broad-based expertise in unrelated areas and use it as an enabler," he said.

Industry involvement and perspectives

Vipin originally joined TAPPI in 1994 while at Auburn University, because, in his words, "as a graduate stu-

dent, I recognized fairly quickly that TAPPI is a must-have resource for professionals new to the pulp and paper industry." He has found membership beneficial on multiple levels.

"The breadth and depth of resources available to TAPPI members makes it easy to follow the changes underway in the industry," said Vipin. "This has enabled me to be better-informed and more effective in my technical and leadership roles."

During his tenure in the industry, Vipin finds that the biggest technical and resource changes include the "modification of pulping technologies to meet emerging market needs, energy and chemical recovery improvements, and the development of chemicals and additives for additional functionality, as well as improved processing technologies for making final products." When it comes to the challenges facing the pulp and paper industry, he sees scalability of innovation as a top priority.

"Further commercialization of next-generation manufacturing technologies and future strides in the development of integrated facilities for pulp, paper, byproducts, and advanced biomaterials manufacture are tremendous opportunities for this industry," Vipin said.

"Further commercialization of next-generation manufacturing technologies and future strides in the development of integrated facilities for pulp, paper, byproducts, and advanced biomaterials manufacture are tremendous opportunities for this industry."

— VIPIN VARMA

On a personal note, Vipin enjoys reading, sketching, and hiking. In addition, he is an avid stamp collector. He also participates in multiple Alumni Advisory groups and volunteers in several community activities. **TJ**

Effectiveness of masks in the suppression of COVID-19 cases during the ongoing pandemic in India

SHREYAS GANESH, MIRZA M.O. KHYUM, KENNETH N. KIKANME, AND SESHADRI RAMKUMAR

ABSTRACT: Perhaps the worst predicament faced by humanity in the twenty-first century is the COVID-19 pandemic, which is caused by the SARS-CoV-2 virus. Most parts of the world, including India, went into lockdowns for some period because of the massive increase in cases throughout 2020. Face masks became an important countermeasure for protecting the populace, health professionals, and medics, particularly during the period prior to the mass availability of vaccines.

This study intends to evaluate the effectiveness of face masks in limiting the spread of the virus. The data for the number of COVID-19 cases was analyzed from January 1, 2022 to May 31, 2022, using Python programming. This timeframe involved face mask mandates and no mask requirement, and hence was considered to be ideal for analyzing the usefulness of face masks. A decline in cases during the mandate was observed, while the opposite occurred without the mandate. The outcome of the research showed that face masks are effective additional measures against the spread of SARS-CoV-2. This study elevates the value of personal protective equipment (PPE), such as face masks, made with nonwovens and other fabrics, as lifesavers in the case of airborne diseases such as COVID-19 and other pulmonary disorders.

Application: This study shows that extra precautions like wearing face masks helped stop the spread of SARS-CoV-2 along, with vaccinations.

Face masks are textile materials that have gained prominence during the current COVID-19 pandemic. Earlier during the pandemic, due to the unavailability of nonwoven three-ply surgical masks, many different cloth masks evolved, which are generally referred to as face coverings. A simple categorization of the face masks that evolved includes: 1) filtering facepiece respirators (FFRs), commonly known as N95 masks; 2) surgical masks; 3) face covers; and 4) face covers with enhanced filtration called FISORS [1]. The FFRs and surgical masks have different nonwoven components in them. Surgical masks today have electrically charged meltblown webs and spunbond fabrics. The FISOR mask combines a cloth face covering with a nonwoven (spunbond-meltblown-spunbond) three-ply surgical mask [2]. Prior to the mass availability of vaccines, face masks played an important role in saving lives. Face masks serve as a valuable countermeasure in controlling the spread of virus. This paper endeavors to highlight the usefulness of face masks in reducing the number of daily COVID-19 cases in India from January 2022 to May 2022 [2]. As the purpose of this study was to understand the face mask mandate's effect on reducing the COVID-19 cases in India, the efficacy of the type of face mask on the spread of SARS-CoV-2, the mask's structure, and other factors are beyond scope of this paper.

As of September 21, 2022, the COVID-19 outbreak has spread to 228 countries and territories worldwide, with 610,393,563 confirmed cases and a death toll of 6,508,521 [3]. There were 44,547,599 cases and 528,403 deaths confirmed in India, making it the country with the second-highest number of cases and deaths [4]. The disease is mainly transmitted through ejected respiratory droplets (>5 μm) [5], smaller aerosols (<5 μm) [6], and direct contact with an infected person [7], and it can be spread by asymptomatic, pre-symptomatic, and symptomatic patients [8,9] through coughs or sneezes. Since the SARS-CoV-2 virus spreads through air, the drop in reported cases could be attributable to the reduction in aerosol concentrations in the air during the initial lockdown in India on March 24, 2020 [10]. Physical distancing has also proven to be an effective strategy in the fight against spread of the virus. One can avoid catching and transmitting COVID-19 by having adequate airflow. People should maintain distance between one another to decrease the likelihood of transmitting the virus; therefore, avoiding crowded situations is recommended [11]. Despite social distancing being widely adopted and face masks being used to prevent the spread of the virus, there is still some doubt that lingers in the minds of the populace regarding the usefulness of using face masks. The N95 respirators or similar high-quality masks have



1. Different types of masks worn by the Indian public: (a) surgical mask, (b) N95 mask, and (c) cloth mask.

been recommended for wear by health care professionals caring for patients with suspected or confirmed SARS-CoV-2 [12]. However, masks must be used to provide a proper fit and seal against the face of the person using it [13]. Also, in India, three-ply medical masks and N95 respirator masks are recommended for those working in hospitals, quarantine centers, clinical laboratories, and primary health care/community settings [14], whereas the civilian population commonly uses surgical masks (**Fig. 1a**), N95 or KN95 (Fig. 1b) masks, and cloth masks (Fig. 1c), with the majority using surgical-type masks made with polypropylene nonwoven fabrics.

Face coverings made of different household fabrics provide protection based on the number of layers [15]. Sterilization or washing is recommended based on the microbial load in the case of repetitive use of cloth face coverings [16]. Recent research looked at incorporating functional properties to face mask components to enhance their protection capabilities against microbes [17].

While there have been developments in countermeasures against SARS-CoV-2, relative roles of contact vs. airborne transmission pathways in the COVID-19 pandemic are not fully understood [18,19]. The effectiveness of face coverings in preventing the spread of COVID-19 has been investigated in the United States [20]. Analysis has been carried out using mathematical and/or empirical modeling approaches [21,22], simulation experiments [23], and participatory surveys [24]. In the current study, actual confirmed case data were used in the analysis. We examined the efficacy of face coverings as a preventive measure by evaluating new daily cases and cumulative cases in India from January 2022 to May 2022, and the rate of new cases was compared between the time period of the mask mandate (January 1, 2022 to March 31, 2022, and April 24, 2022 to May 31, 2022) and the time period without the mask mandate (April 1, 2022 to April 23, 2022).

RESULTS AND DISCUSSION

Following the drop in the rate of daily cases, the Indian government called for a removal of the mask mandate, with over 43.03 million people infected in the country and 831.24 million being fully vaccinated as of March 31, 2022, which is one of the prime reasons for the decline in cases. COVID-

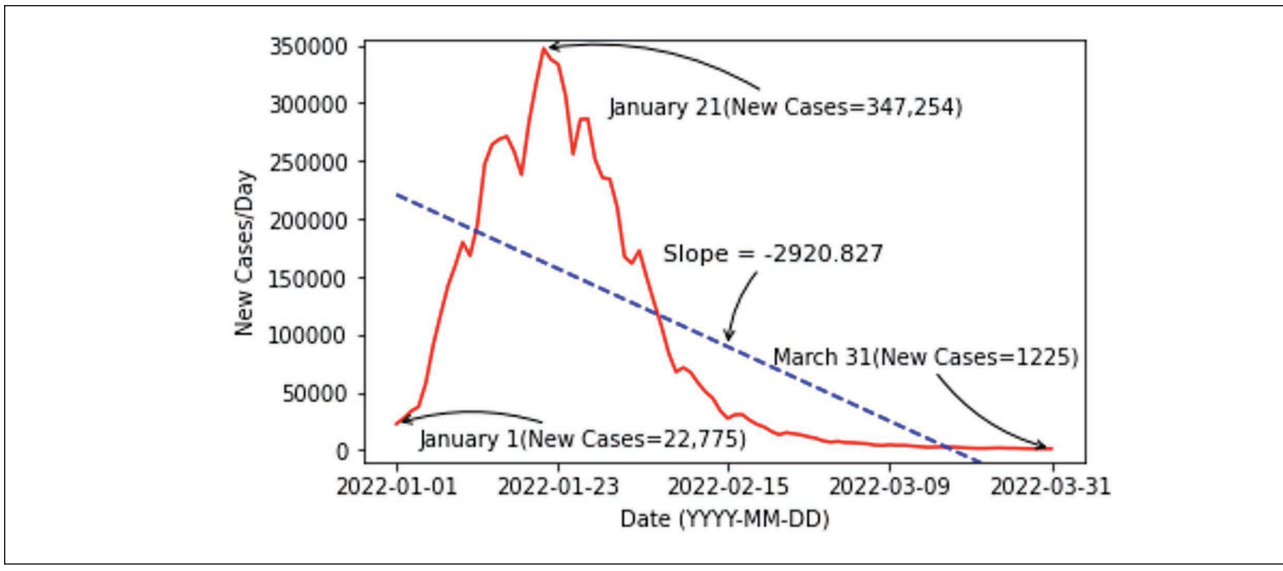

2. Graph showing daily new cases during mask mandate for the period January 1, 2022 to March 31, 2022.

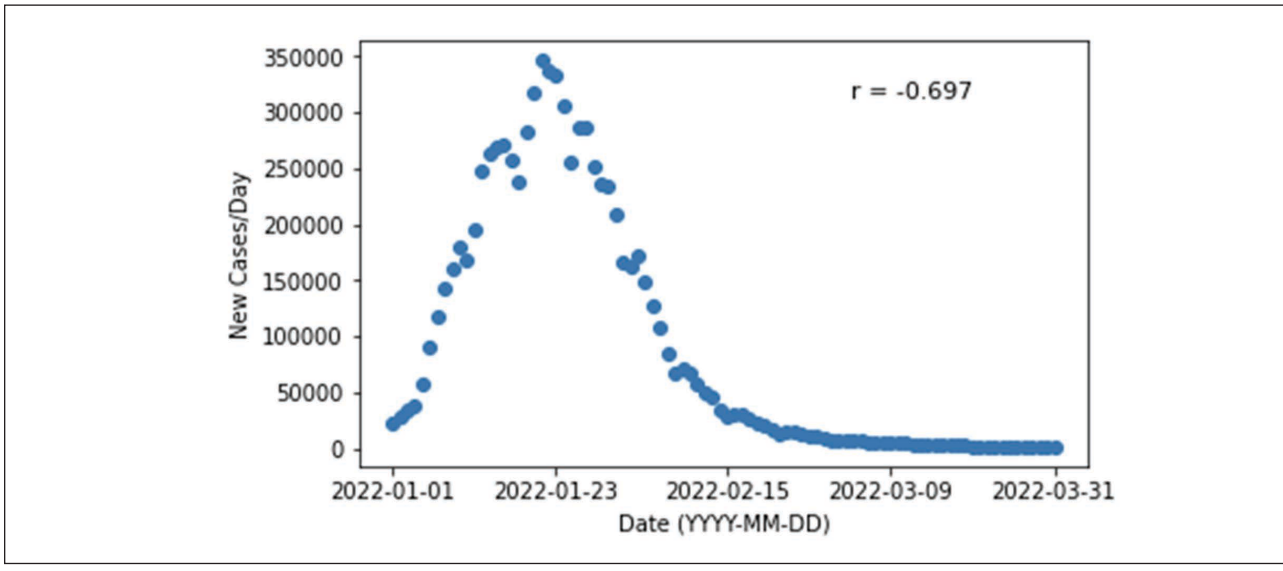

3. Scatter plot showing the correlation between the number of daily new cases vs. time (January 1, 2022 to March 31, 2022). The plot shows a negative Pearson's correlation of -0.697.

19 vaccines that provide immunity were understood to reduce the magnitude of potential infection waves. Significant reduction in mortality occurs when prioritizing individuals over 60 years old, but all vaccination strategies result in appreciable gains compared to no immunization [25]. As a result, states like Delhi, Maharashtra, and Telangana ultimately removed the requirement of masks in public starting April 1, 2022 [26, 27]. However, due to the mutating nature of the SARS-CoV-2 virus, there was an apparent increase in the number of daily new cases and the growth rate of cumulative cases across the nation. While vaccinations prevented severe infections and hospitalizations, other countermeasures such as face masks and enhanced hygiene helped with curtailing spread of the virus.

Mask mandate timeframe (January 1, 2022 to March 31, 2022)

As is evident from **Fig. 2**, after plotting the new daily cases during this time period, the slope came out to be -2920, which is an average decline of about 2920 cases per day for the three-month period (January 1, 2022 to March 31, 2022). Considering this time period, a statistically significant ($p<0.001$) negative Pearson's correlation of -0.697 (**Fig. 3**) was observed between the date and the number of daily new cases. The result indicates that the number of new cases decreased during this timeframe. During the early days in January 2022, even though the face mask mandate was in effect, the rise in cases could have been attributed to the incubation period of up to 14 days for the

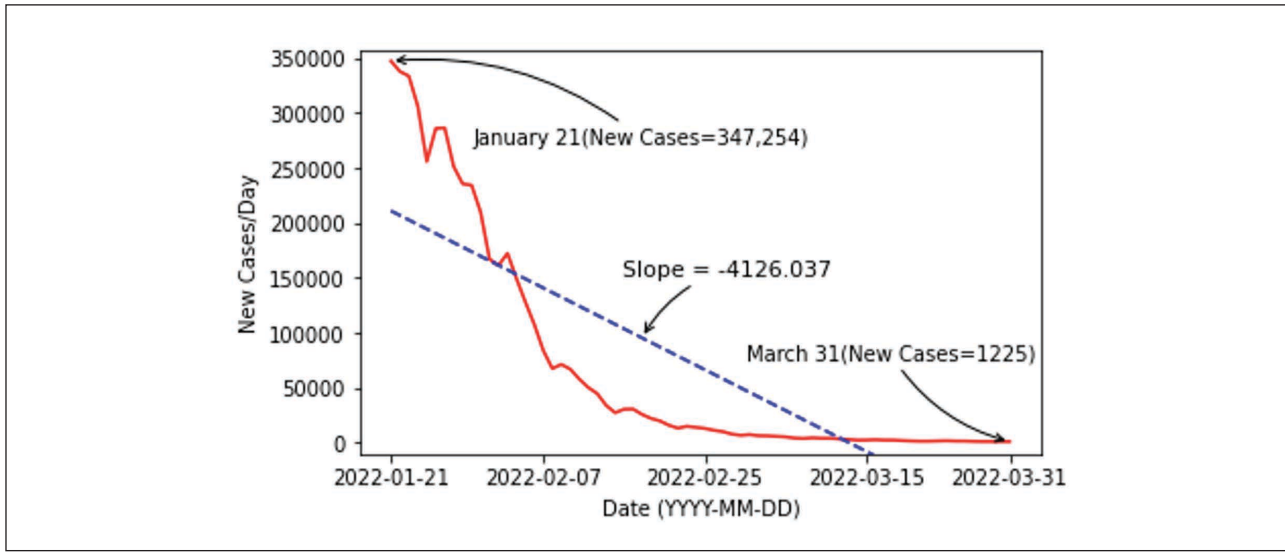

4. Graph showing daily new cases during the mask mandate for the period January 21, 2022 to March 31, 2022.

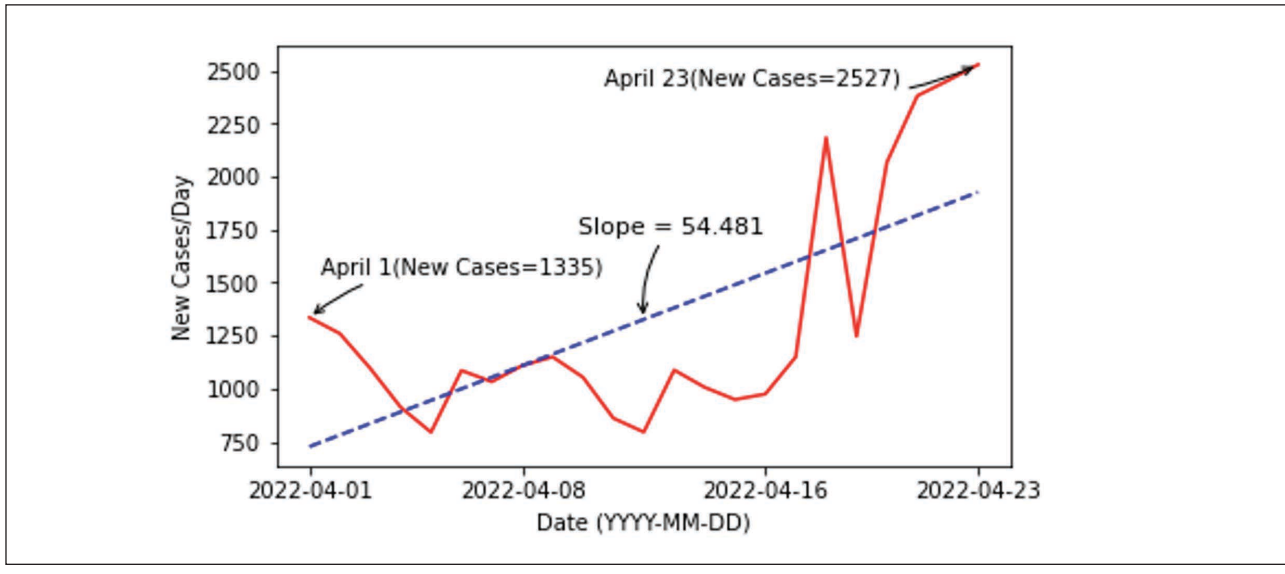

5. Graph showing daily new cases by date after the removal of the mask mandate from April 1, 2022 to April 23, 2022.

mutating virus, which started spreading prior to the beginning of the new year [28]. Following the incubation period, actual cases were reflected as peaking after about two weeks. After peaking, with the face mask mandate in place, cases/day started falling, indicating the usefulness of extra protection measures such as face masks, as social distancing could not be strictly practiced due to no lockdowns.

Figure 4 gives a clear indication of the influence of additional protection measures like face masks in reducing the daily new cases. Once the face mask mandate was in full swing, the effect was visible in about 2 to 3 weeks' time, as is evident from the negative slope of -4126 as compared with the negative slope of -2920 for the period starting from January 1, 2022. Given that there is negative slope in the period when the face mask mandate was in effect, this fact supports the hypothesis that face masks have a positive influence on curbing spread of the virus.

No mask mandate timeframe (April 1, 2022 to April 23, 2022)

As is evident from Fig. 5, during the period from April 1 to April 23, 2022, when the mask mandate was not in effect, the rate of cases saw a spike, with the slope being 54.481 (i.e., a rise of about 54 new cases a day). A scatter plot of the daily number of new cases from April 1, 2022, until April 23, 2022, shows that the removal of the mask mandate on April 1, 2022, could be the reason for the increase in the number of cases. Cases peaked on or about two weeks after the mandate was in effect. In Fig. 6, the dates were placed on the x-axis of the graph and the y-axis indicates the number of new cases per day, and the Pearson's correlation be-

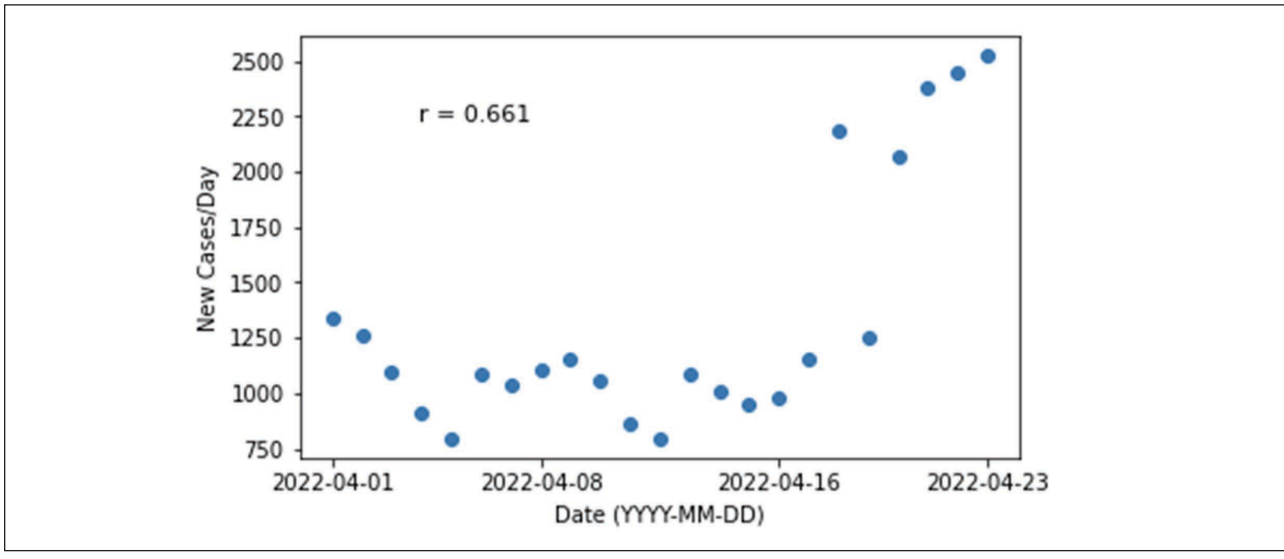

6. Scatter plot showing a correlation between the number of new cases daily vs. time (April 1, 2022 to April 23, 2022). The plot shows a positive Pearson's correlation of 0.66.

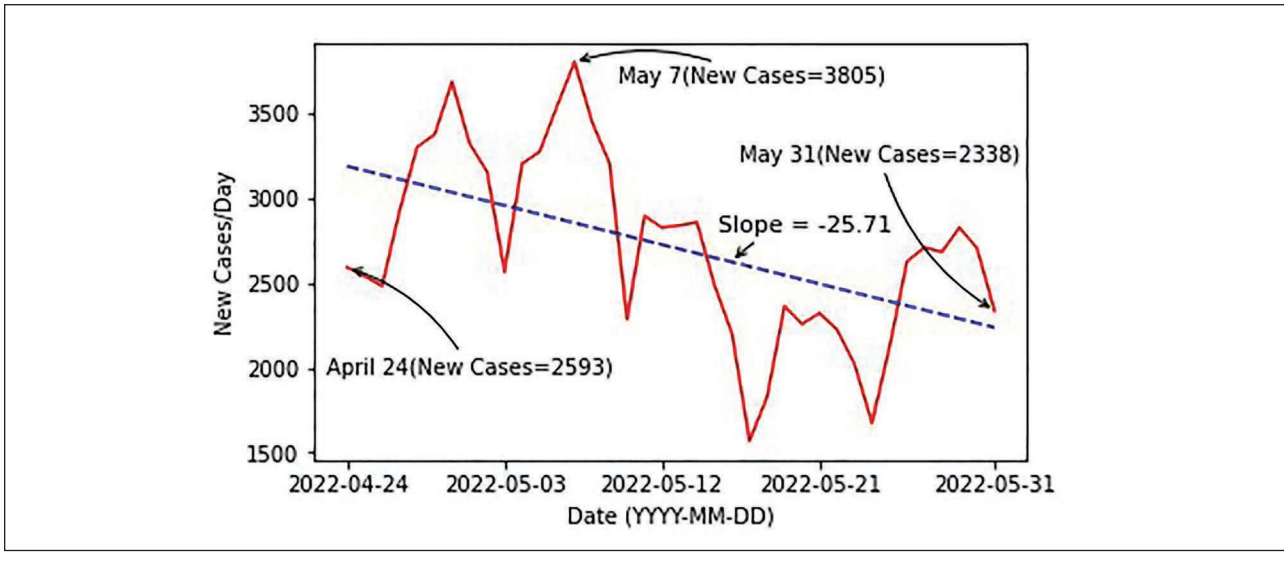

7. Graph showing daily new cases by date after the reinstatement of the mask mandate from April 24, 2022 to May 31, 2022.

tween the two variables was calculated. In examining the data, a positive Pearson's correlation (0.661) was found, suggesting that the days without the mask mandate directly contributed to the daily increase in cases (Fig. 6). Analysis also showed statistical significance ($p<0.001$).

Reinstatement of mask mandate (April 24, 2022 to May 31, 2022)

As is evident from **Fig. 7**, after reinstatement of the mask mandate on April 24, 2022 [29], the number of cases from April 24, 2022 to May 31, 2022, saw a drop, with a negative slope of 25.71, indicating a drop of almost 26 cases each day. However, the initial two weeks still saw spikes in cases due to the transition timeframe [30]. It is evident that the mask mandate contributed to a decrease in cases, leading to its reinstatement on April 24, 2022.

As is evident from **Fig. 8**, the analysis showed a negative Pearson's correlation (-0.52) between the rate of cases with the passage of days, which is statistically significant ($p<0.001$). This demonstrated that the number of daily new cases decreased with days when face masks were used.

Prediction of cases vs. actual cases

The number of cumulative cases for March 2022 was considered to predict the number of cases during April 2022 (**Table I**). The linear regression prediction of the number of cases was much less than the actual number of cases during April. However, the coefficient of determination (0.966) for the date vs. cumulative case count graph (**Fig. 9**) is very high, affirming the accuracy of the prediction. The maximum difference between the predicted value for the cases and the actual values was about 47,599. Furthermore, re-

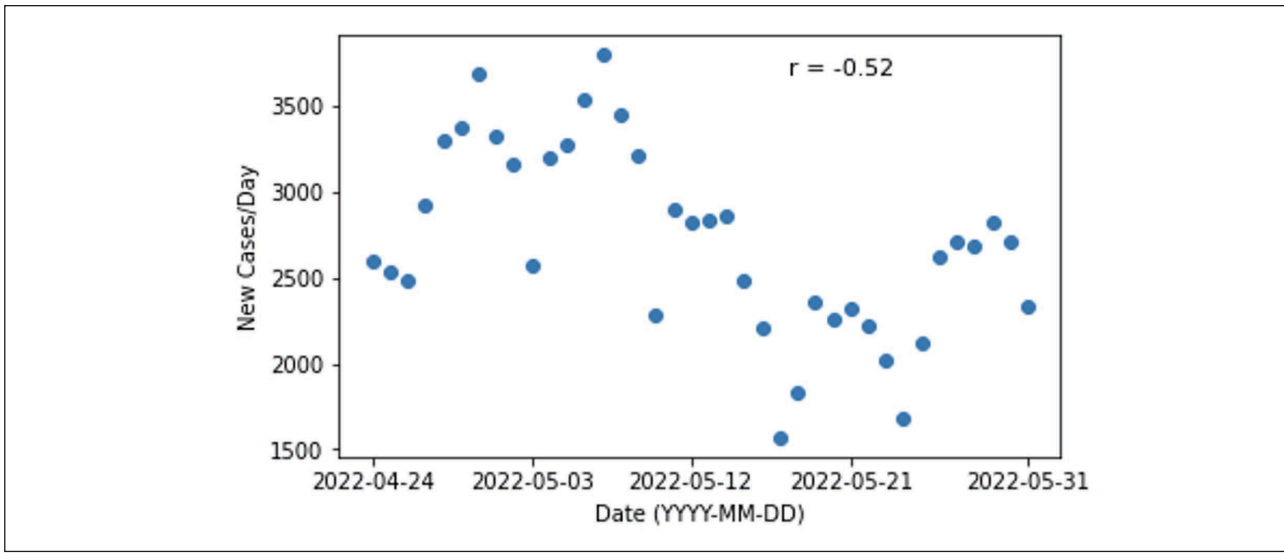

8. Scatter plot showing the correlation between the number of daily new cases vs. time (April 24, 2022 to May 31, 2022) since the reinstatement of the mask mandate. The plot shows a negative Pearson's correlation of -0.52.

Date	Actual Cumulative Cases	Predicted Cumulative Cases
2022-04-01	43,025,775	42,978,175
2022-04-02	43,027,035	42,980,419
2022-04-03	43,028,131	42,982,664
2022-04-04	43,029,044	42,984,908
2022-04-05	43,029,839	42,987,152
2022-04-06	43,030,925	42,989,397
2022-04-07	43,031,958	42,991,641
2022-04-08	43,033,067	42,993,885
2022-04-09	43,034,217	42,996,130
2022-04-10	43,035,271	42,998,374
2022-04-11	43,036,132	43,000,618
2022-04-12	43,036,928	43,002,863
2022-04-13	43,038,016	43,005,107
2022-04-14	43,039,023	43,007,351
2022-04-15	43,039,972	43,009,596
2022-04-16	43,040,947	43,011,840
2022-04-17	43,042,097	43,014,084
2022-04-18	43,044,280	43,016,329
2022-04-19	43,045,527	43,018,573
2022-04-20	43,047,594	43,020,817
2022-04-21	43,049,974	43,023,062
2022-04-22	43,052,425	43,025,306
2022-04-23	43,054,952	43,027,550

I. Table giving daily new cases and rate of increase of cumulative cases in India for the time period from April 1, 2022 to April 23, 2022, when the mask mandate was not in effect.

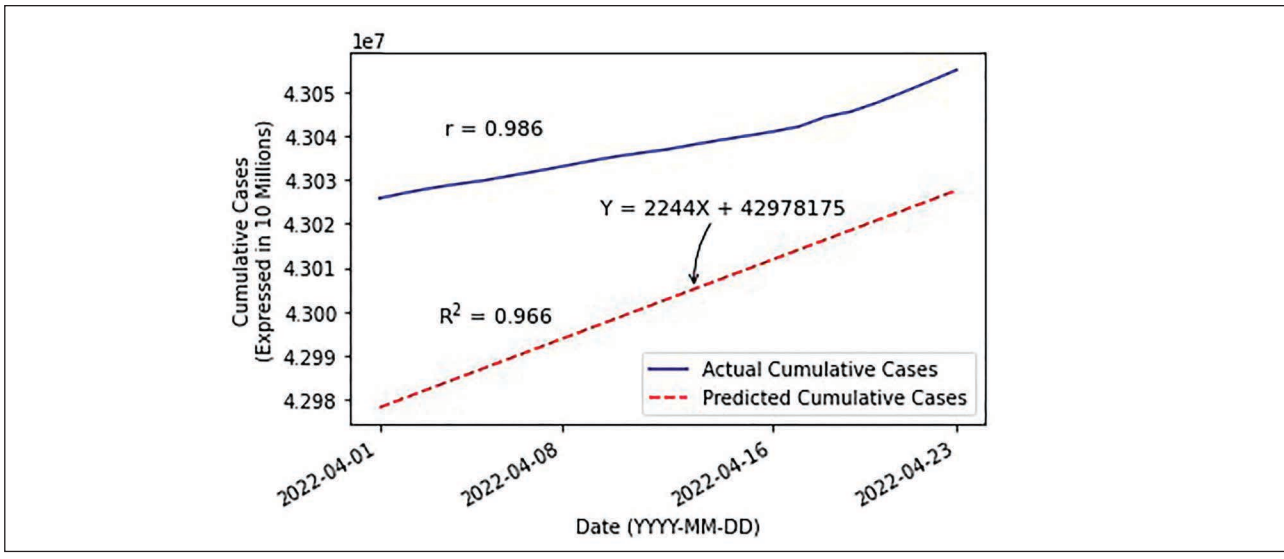

9. Graph showing the cumulative number of cases, broken down by day, for April 1, 2022 to April 23, 2022, when the mask requirement was lifted. The blue line represents the actual monthly cumulative cases, while the red line represents a prediction based on the previous month's data.

moving the mask mandate was associated with an increase in the daily number of cases, as demonstrated by a positive Pearson's correlation (0.986) between the daily cumulative cases and the date for the period April 1, 2022 to April 23, 2022, which was statistically significant ($p<0.001$). There is good correlation between the actual and predicted cumulative cases, as is evident from the positive Pearson's correlation (0.986).

MATERIALS AND METHODS

Data sources

The data for daily new cases and cumulative cases for the entire Indian population was obtained from the WHO data source for all countries [31]. The values for the number of single and fully vaccinated people in the country were given by Our World in Data [32].

Data analysis

Statistical analysis, including Pearson's correlation analysis and regression analysis, were performed using Python (v 3.9.13), an open-source programming language. The data was stored using the Numbers spreadsheet application for the macOS operating system from Apple. Pandas library for Python was used to import and manipulate the data for calculations and plotting. Graphs were plotted using Matplotlib library functions and Scilearn library functions in Python. The p-value for the analysis was determined at <0.001. As a case in point, we used the cumulative case data of March 2022 to predict the values for the period April 1, 2022 to April 23, 2022. We have focused on the data for April 2022 to showcase that with the lack of a supplemental protection requirement such as face masks, the number of cases increased compared to the predicted value. This again proves the hypothesis that even with vaccination, due to the mutating nature of the virus, additional countermeasures play an important role in controlling the spread of the virus.

CONCLUSIONS

Lockdowns, quarantine, physical distancing, isolation, stay-at-home orders, and shelter-in-place have all been used to slow the spread of SARS-CoV-2, with little or no debate about their effectiveness and complete compliance with these rules. However, because the use of face coverings is a contentious issue, its implementation varied greatly from one location to the next. In addition, different states in India implemented the usage of masks to varying extents. Generally, physical distance rules can be met during lockdown, quarantine, shelter-in-place, and isolation. However, since the world cannot remain in lockdown eternally, the usage of protection in the form of face masks and face coverings is essential for reducing or stabilizing infection rates.

The study considered the time period from January 1, 2022 to May 31, 2022 to prove the effectiveness of masks in mitigating the spread of COVID-19 in India. Importantly, in most of the countries, COVID-19 peaked during January 2022, while vaccinations were in full swing. This indicated the emergence of mutations and hence the need for additional safety measures.

The analysis of daily new cases during the time period January 1, 2022 to May 31, 2022 showed that the rate of daily new cases increased when the mask mandate was removed from April 1, 2022 to April 23, 2022 with a positive Pearson's correlation (0.66) and then dropped from April 24, 2022 to May 31,2022 with a negative Pearson's correlation (-0.52) after the mandate was reinstated. Analysis shows that in addition to vaccinations, additional safety measures such as the use of face masks played a role in preventing the spread of SARS-CoV-2. **TJ**

LITERATURE CITED

1. Ramkumar, S., "The basics and the alternatives," *Advanced Textiles Source*, 25 May 2020. Available [Online] https://advancedtextilessource.com/2020/05/25/the-basics-and-the-alternatives/ <4Oct2022>.
2. Ramkumar, S. and, Mirza, K., "Masking strategy to counter infection," Int. Fiber J., 31 January 2022. Available [Online] https://www.fiberjournal.com/masking-strategy-to-counter-infection/ <4Oct2022>.
3. WHO, "WHO coronavirus (COVID-19) dashboard," World Health Organization, Geneva. Available [Online] https://covid19.who.int <4Oct2022>.
4. WHO, "Coronavirus disease (COVID-19) pandemic," World Health Organization, Geneva. Available [Online] https://covid19.who.int/region/searo/country/in <4Oct2022>.
5. Lee, B.U., *Int. J. Environ. Res. Public Health* 17(19): 6960(2002). https://doi.org/10.3390/ijerph17196960.
6. Chia, P.Y., Coleman, K.K., Tan, Y.K., et al., *Nat. Commun.* 11: 2800(2020). https://doi.org/10.1038/s41467-020-16670-2.
7. WHO, "Coronavirus disease (COVID-19): How is it transmitted?," World Health Organization, Geneva, 23 December 2021. https://www.who.int/news-room/questions-and-answers/item/coronavirus-disease-covid-19-how-is-it-transmitted <4Oct2022>.
8. Rab, S., Javaid, M., Haleem, A., et al., *Diabetes Metab. Syndr.* 14(6): 1617(2020). https://doi.org/10.1016/j.dsx.2020.08.021.
9. Rothe, C., Schunk, M., Sothmann, P., et al., *N. Engl. J. Med.* 382(10): 970(2020). https://doi.org/10.1056/nejmc2001468.
10. Kumar, S., *Sci. Total Environ.* 745: 141021(2020). https://doi.org/10.1016/j.scitotenv.2020.141021.
11. CDC, "How to protect yourself and others," Centers for Disease Control and Prevention, Atlanta, 11 August 2022. Available [Online] https://www.cdc.gov/coronavirus/2019-ncov/prevent-getting-sick/prevention.html <11Oct2022>.
12. CDC, "Types of masks and respirators," 8 September 2022. Available [Online] https://www.cdc.gov/coronavirus/2019-ncov/prevent-getting-sick/types-of-masks.html <11Oct2022>.
13. O'Kelly, E., Arora, A., Pirog, S., et al., *PLoS One* 16(1): e0245688(2021). https://doi.org/10.1371/journal.pone.0245688.
14. Mohfw.gov, "Novel coronavirus disease 2019: Guidelines on rational use of Personal Protective Equipment," Indian Ministry of Health and Family Welfare, Directorate General of Health Services, 1 April 2020. Available [Online] https://www.mohfw.gov.in/pdf/GuidelinesonrationaluseofPersonalProtectiveEquipment.pdf <4Oct022>.

ABOUT THIS PAPER

Cite this article as:
Ganesh, S., Khym, M., Kikanme, K., et al., *TAPPI J.* 21(10): 521(2022). https://doi.org/10.32964/TJ21.10.521

DOI: https://doi.org/10.32964/TJ21.10.521

ISSN: 0734-1415

Publisher: TAPPI Press

Copyright: ©TAPPI Press 2022

About this journal

ABOUT THE AUTHORS



Ganesh



Khyum



Kikanme



Ramkumar

This research was carried out to observe and describe the trend of COVID-19 cases in India during and without the face mask mandate. Our previous research was on the effectiveness of face mask mandates for different states in the United States. The current research supports the finding that a face mask mandate helped in curtailing the spread of SARS-CoV-2 in India.

The most difficult aspect of this research was obtaining quality quantitative data. This was addressed using Python programming.

Our analysis shows that in addition to vaccinations, additional safety measures such as the use of face masks played a role in preventing the spread of SARS-CoV-2. It was interesting to find that the number of daily cases increased every time the mask mandate was removed.

For companies that produce PPE, such as those in the nonwovens industry, this research shows the need for increasing the efficacy of individual face coverings in a cost-effective manner. Our next step will be to examine the effectiveness of face mask mandates during the pandemic in other countries.

Ganesh is a Computer Science and Engineering student at PES University, Electronic City Campus, Bengaluru, India. Khyum and Kikanme are graduate research assistants and Ramkumar is professor at Texas Tech University in Lubbock, TX, USA. Email Ramkumar at s.ramkumar@ttu.edu.

15. Ayodeji, O.J., Hilliard, T.A., and Ramkumar, S., *Int. J. Environ. Res.* 16: 11(2022). https://doi.org/10.1007/s41742-021-00390-6.
16. Narasimhan, S., Balakrishnan, M., Ayodeji, O.J., et al., *TAPPI J.* 21(1): 23(2021). https://doi.org/10.32964/TJ21.1.23.
17. Ayodeji, O.J., Mirza MO K., Racheal, T.A., et al., *J. Hazard. Mater. Adv.* 7: 100128(2022). https://doi.org/10.1016/j.hazadv.2022.100128.
18. Zhang, R., Li, Y., Zhang, A.L., et al., *Proc. Natl. Acad. Sci.* 117(26): 14857(2020). https://doi.org/10.1073/pnas.2009637117.
19. Li, Y., Zhang, R., Zhao, J., et al., *Sci. Total Environ.* 748: 141560(2020). https://doi.org/10.1016/j.scitotenv.2020.141560.
20. Ayodeji, O.J. and Ramkumar, S., *Int. J. Environ. Res. Public Health* 18(7): 3666(2021). https://doi.org/10.3390/ijerph18073666.
21. Eikenberry, S.E., Mancuso, M., Iboi, E., et al., *Infect. Dis. Model.* 5: 293(2020). https://doi.org/10.1016/j.idm.2020.04.001.
22. Stutt, R.O.J.H., Retkute, R., Bradley, M., et al., *Proc. R. Soc. A* 476(2238): 20200376(2020). https://doi.org/10.1098/rspa.2020.0376
23. Aydin, O., Emon, B., Cheng, S., et al., *Extreme Mech. Lett.* 40: 100924(2020). https://doi.org/10.1016/j.eml.2020.100924.
24. Sickbert Bennett, E.E., Samet, J.M., Clapp, P.W., et al., *JAMA Intern. Med.* 180(12): 1607(2020). https://doi.org/10.1001/jamainternmed.2020.4221.
25. Foy, B.H., Wahl, B., Mehta, K., et al., *Int. J. Infect. Dis.* 103: 431(2021). https://doi.org/10.1016/j.ijid.2020.12.075.
26. Anon., "List of states where Covid-19 mask not mandatory anymore. Explained," *Hindustan Times*, 1 April 2022. https://www.hindustantimes.com/india-news/list-of-states-where-covid-19-mask-not-mandatory-anymore-explained-101648789690816.html <4Oct2022>.
27. Dirchi, R., "Covid-19 update: States where Covid-19 mask not mandatory anymore. What experts have to say," *Mint*, 1 April 2022. Available [Online] https://www.livemint.com/news/india/covid19-update-states-where-covid-19-mask-not-mandatory-anymore-what-experts-have-to-say-11648797250096.html <4Oct2022>.
28. CDC, "Clinical considerations for care of children and adults with confirmed COVID-19," clinical presentation, Centers for Disease Control and Prevention, 27 May 2022. Available [Online] https://www.cdc.gov/coronavirus/2019-ncov/hcp/clinical-care/clinical-considerations-presentation.html#:~:text=Data%20suggest%20that%20incubation%20periods,from%20exposure%20to%20symptom%20onset <4Oct2022>.
29. Anon., "Mask mandatory rule is back: States, UTs which made it compulsory," *Hindustan Times*, 25 April 2022. Available [Online] https://www.hindustantimes.com/india-news/mask-mandatory-rule-is-back-states-uts-which-made-it-compulsory-101650898622625.html <4Oct2022>.
30. Lauer, S.A., Grantz, K.H., Bi, Q., et al., *Ann. Intern. Med.* 172(9): 577(2020). https://doi.org/10.7326/m20-0504.
31. WHO, "WHO coronavirus (COVID-19) dashboard: Data information," World Health Organization, Geneva. Available [Online] https://covid19.who.int/data <5Oct2022>.
32. Our World in Data, "Coronavirus (COVID-19) vaccinations," University of Oxford/Global Change Data Lab. Available [Online] https://ourworldindata.org/covid-vaccinations?country=IND <5Oct2022>.

A new method of studying the fundamental mechanisms involved in pigment liberation from recycle papers

KAIWU HUANG, KRIS STRICKLAND, AARON NOBLE, ROE-HOAN YOON, AND CESAR BASILIO

ABSTRACT: Deinking flotation is the most efficient and widely used method of removing ink particles from printed papers to improve the recyclability. A prerequisite for successful deinking flotation is detachment of pigments from paper fibers, a subprocess known as liberation. The degree of liberation is usually determined via hyperwashing tests, which are costly and time consuming. Furthermore, they provide no information on the fundamental mechanisms controlling liberation.

In the present work, we developed a new method in which ζ-potentials of the particles in a pulp are measured and analyzed. If pigments are not liberated from paper fibers, a frequency distribution plot gives a single peak, while two peaks appear when they are liberated. One can readily determine the degrees of liberation from the peak positions and peak heights. In addition, the ζ-potential data can be used to construct disjoining pressure isotherms using the DLVO theory that are useful to better understand the fundamental mechanisms involved and the roles of different reagents used to improve pigment liberation.

Application: Flotation deinking is widely used to remove ink from paper fibers. A prerequisite to flotation is the liberation of ink particles from fibers. We have developed a new method of determining the degree of liberation. The new method will also be useful for better understanding the mechanisms involved in liberating ink particles from paper fibers.

Recycling of wastepaper is important for improving environmental sustainability and economic returns. A ton of recycled paper can save 17 trees, 250 lb of carbon dioxide (CO_2) per year, 380 gal of oil, 3 yd^3 of landfill space, 4000 kWh of energy, and 7000 gal of water [1]. A critical factor affecting the overall yield of paper recycling is the efficiency of the deinking process [2]. Generally, a deinking process involves various steps, e.g., screening, pulping, flotation, washing, thickening, and bleaching [3].

Flotation deinking can effectively remove the ink particles to improve the quality of the recycled fibers [4-5]. The effective particle size range for flotation is usually between 10 and 100 μm [6-7]; therefore, the ink particles outside this range are removed by water washing and screening. Flotation efficiencies are typically less than 60%, which makes it necessary to repeat the process 4 to 5 times. One of the reasons for the poor efficiencies is the difficulty in liberating ink particles from spent paper fibers. It is generally recognized that liberation is a prerequisite for flotation deinking. It is, therefore, important to know the degree of liberation prior to flotation deinking. A conventional way to determine the degree of liberation is to perform a hyperwashing test in which a pulp is washed using a screen for several times while monitoring brightness changes. While the hyperwashing tests are relatively easy to perform and useful for feedstock evaluation, they are also time consuming and require lots of water. Moreover, they do not give fundamental information that can be used to improve the liberation process.

In the present work, a new method of determining the degree of pigment liberation from recycle papers printed with oil-based ink has been developed. In this method, ζ-potential measurements are conducted on a pulp sample, and the resultant data are subsequently used to determine the fraction of the pigments liberated from paper fibers on the basis of the frequency distribution curves. The ζ-potential data can also be used to construct disjoining pressure isotherms that can be used to better understand the mechanisms involved in liberation and to identify the reagents that can improve liberation and thereby increase the recyclability of postconsumer paper products.

EXPERIMENTAL

Materials

An artificial pulp and an old newsprint (ONP) pulp were prepared to study the mechanisms of pigment liberation from the papers printed with oil-based ink. The artificial pulp was prepared by mixing carbon black (Orion Engineered Carbon LLC; Senningerberg, Luxembourg) and clean cellulose fibers (Thiele Kaolin Company; Sandersville, GA, USA) in water. The ONP printed with oil-based ink was obtained from *The Roanoke Times* in Roanoke, VA, USA. Hydrochloric acid (HCl, Thermo Fisher Scientific; Hampton, NH, USA) and sodium hydroxide (NaOH, Fisher Scientific) were used for pH

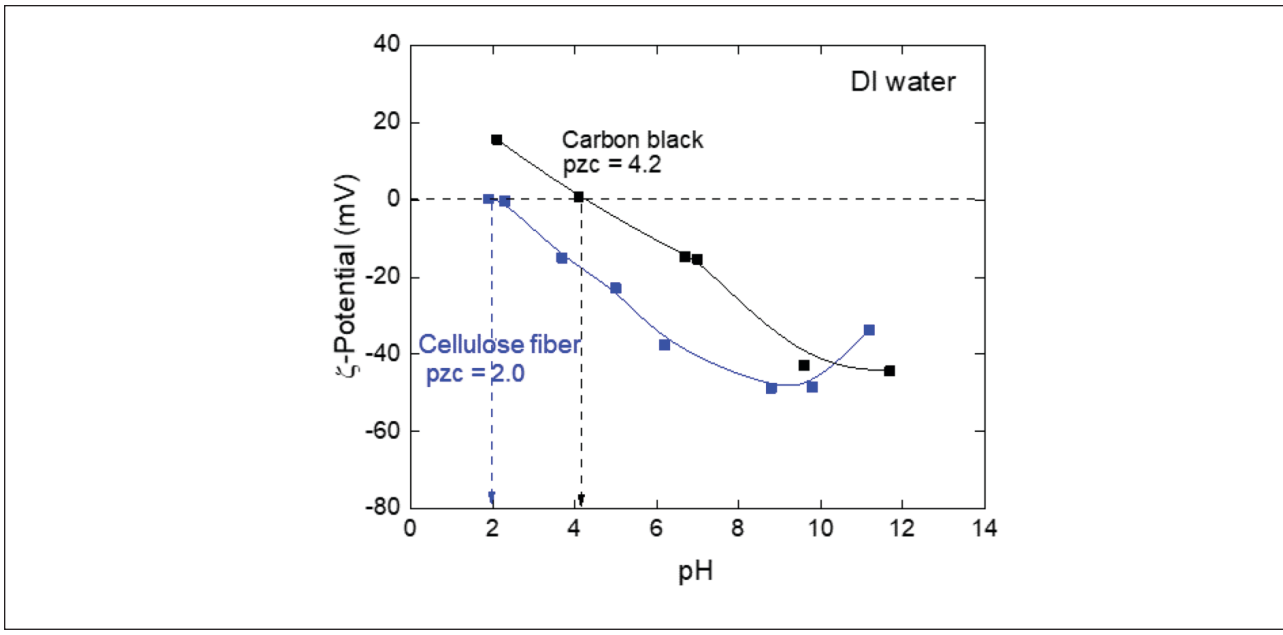

1. The ζ-potentials of carbon black particles and cellulose fiber as a function of pH (DI = deionized; pzc = point of zero charge).

adjustment. In some pulping tests, hydrogen peroxide (H_2O_2, 30% solution, Fisher Scientific) and sodium silicate (Na_2SiO_3, >97%, Fisher Scientific) were used as additives. For ζ-potential measurements, Ultrapure water with a resistivity of >18.2 MΩ•cm was obtained from a Direct-Q 3 UV water purification system (Merck; Kenilworth, NJ, USA).

Methods

The ζ-potentials of the carbon black, cellulose fiber, and ONP pulp were measured using a Malvern Zetasizer ZEN3600 (Malvern Panalytical; Malvern, UK). For the case of single component systems, e.g., carbon black and cellulose, particle suspensions were prepared by mixing 0.05 g sample in 50 ml Ultrapure water. A particle suspension was agitated by means of a vortex mixer for 5 min, followed by 10-min conditioning in an ultrasonic bath. All the ζ-potential measurements were conducted at room temperature. For the case of binary systems, e.g., carbon black and cellulose fiber mixture (artificial pulp) or the ONP pulp, the particle suspensions were diluted to ~0.01% solids by weight.

A series of pulping and hyperwashing tests were conducted on a sample of ONP printed with oil-based ink. The ONP sample was shredded first and mixed with water at 15% solids by means of a Hobart mixer (Hobart; Troy, OH, USA) for 20 min at a medium agitation setting. In a given test, 20 g of pulp (3 g dry equivalent) were diluted to 0.5% solids by adding 580 g of water. The sample was then agitated for 2 min at 250 rpm and subjected to screening at 50 mesh. The screen overflow was collected and then mixed with water again to bring the total weight back to 600 g at ~0.5% solids. The hyperwashing step was repeated once more. After the second washing cycle, the screen overflow was collected and then brought back to 600 g total with water to obtain a final suspension of ~0.5% solids. The sample was then agitated at 250 rpm for 30 s. Finally, the sample was filtered and dried at 60°C.

Washed samples were dried and subjected to ISO brightness measurements using the standard procedure. The brightness measurements were made in four different places on a pad and averaged. The scanning electron microscope (SEM) images of the pad were also taken using a JEOL IT-500 SEM (JEOL Ltd.; Tokyo, Japan).

RESULTS AND DISCUSSION

A series of ζ-potential measurements were conducted as a means to determine the number densities of particles with different surface charge characteristics suspended in water. In the present work, carbon black (CB) was used as a surrogate for the black pigment in oil-based ink, while cellulose fiber (CF) was used as a surrogate paper fiber. **Figure 1** shows the ζ-potentials of CB and CF particles suspended in Nanopure water (Thermo Fisher Scientific) as a function of pH. As shown, the CB samples exhibited positive ζ-potentials at pH < 4.2, while they became negative at pH > 4.2. Thus, the point of zero charge (pzc) of the CB sample was pH 4.2. On the other hand, the pzc of the CF sample was pH 2.0, at which the CF surface was uncharged.

Note here that the ζ-potentials of the CB and CF particles were substantially different from each other, which makes it easy to determine if the two different materials existed as dispersed particles, representing liberated state, or interact with each other to form coagula, representing interlocked state. If the latter is the case, the ζ-potentials of the coagula should assume a value between the two components at a given pH. This method of studying the interactions between CB and CF particles, as applied for studying

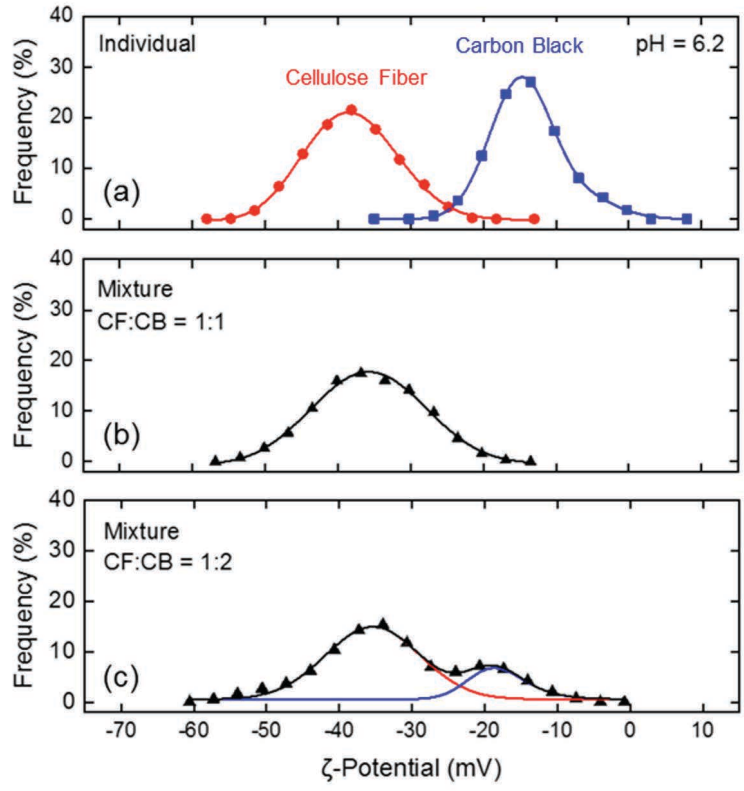

2. a) The ζ-potential distributions of carbon black (CB) and cellulose fiber (CF); b) ζ-potential distribution of a 1:1 mixed CB and CF suspension; and c) ζ-potential distribution of a 1:2 mixture. All measurements were conducted at pH 6.2.

pigment liberation from recycle paper, is similar to the method of studying the interactions between bubbles and particles in flotation, coal and clay particles in coal beneficiation, and bitumen and clay particle interactions in the heavy oil extraction process on the basis of distributed ζ-potentials of the particulate materials involved [8-10].

The data presented in **Fig. 2b** show the results of the ζ-potential measurement conducted with a 1:1 mixture by weight of CB and CF in Nanopure water. The measurements were conducted at 0.5% solids. As shown, the frequency distribution of particles at different ζ-potentials exhibited a single peak at -37.0 mV, indicating that the CB and CF particles interacted with each other to form coagula at pH 6.2, despite the fact that both were negatively charged.

To better understand the mechanisms involved in the coagulation between the CB and CF particles, we carried out DLVO calculations using the ζ-potential data presented in Fig. 2a. Equation 1 represents a form of the DLVO theory [11-12],

$$\Pi = \Pi_d + \Pi_e = -\frac{A_{132}}{6\pi h^3} - \frac{\varepsilon\varepsilon_0\kappa^2}{2\sinh(\kappa h)}\left[\left(\psi_1^2+\psi_2^2\right)\cos ech(\kappa h) - 2\psi_1\psi_2\coth(\kappa h)\right] \quad (1)$$

in which Π is the disjoining pressure in the thin liquid film (TLF) formed between CB and CF in aqueous phase. If Π, which is given in units of mN/m², is negative (Π < 0), the TLF will rupture and the CB and CF will heterocoagulate. If Π > 0, the two particles will stay dispersed in water. The Π term consists of the van der Waals-dispersion force component (Π_d) and the electrical double-layer (EDL) force component (Π_e). The disjoining pressures vary with the separation distance (h) between two interacting surfaces in close proximity, and are functions of the permittivity of vacuum (ε_0), dielectric constant of water (ε), reciprocal Debye length (κ^{-1}), double-layer potential (ψ_1) of cellulose fiber, and the same (ψ_2) of CB. Thus, the first term of Eq. 1 represents the pressure in the film due to the van der Waals force, while the second term represents the same due to the EDL force.

The Π_d can be calculated if the Hamaker constant (A_{132}) for the interaction between CF 1 and CB 2 in water 3 are known. In the present work, A_{132} has been calculated using the combining rule [13],

$$A_{132} = \left(\sqrt{A_{11}} - \sqrt{A_{33}}\right)\left(\sqrt{A_{22}} - \sqrt{A_{33}}\right) \quad (2)$$

in which A_{11} = 5.8x10^{-20} J [14], A_{22} = 1.1x10^{-19} J [15], and A_{33} = 3.7x10^{-20} J [13] represent the Hamaker constants in vacuo. Substituting these values into Eq. 2, one obtains A_{132} of 0.68x10^{-20} J.

Equation 1 has been plotted in **Fig. 3** using the

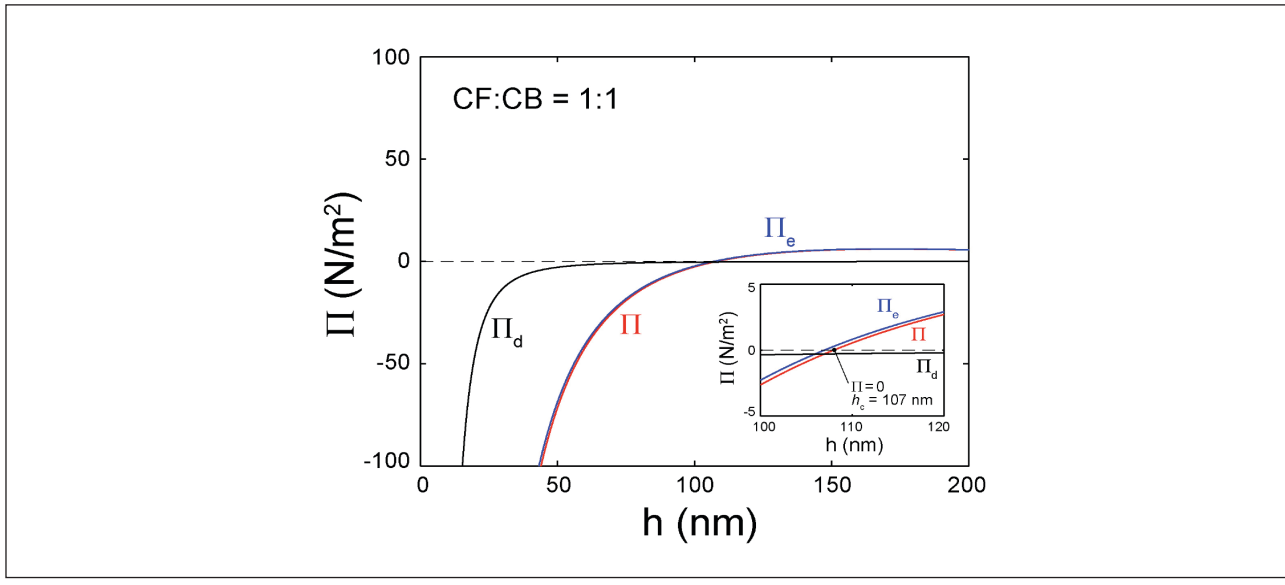

3. Disjoining pressure isotherm (Π(h)) for the interaction between carbon black (CB) and cellulose fiber (CF) in water: Π_d represents the van der Waals component of Π, and Π_e represents the electrical double-layer (EDL) force component of Π; A_{132} = 6.8x10^{-21} J, ψ_1 = -38.7 mV, ψ_2 = -12.7 mV, and k^{-1} = 96 nm.

ζ-potential data presented in Fig. 2a. The results show that the pressure (or force) barrier to film rupture is very small. Therefore, the CF and CB particles should heterocoagulate readily with each other, as was the case when the CF and CB were mixed at a 1:1 weigh ratio. When the two different materials were mixed in Nanopure water at a 1:2 ratio, a second peak appeared at a lower ζ-potential (-20.8 mV), as shown in Fig. 2c. It appears that the CF particles had a limited capacity to accommodate all of the CB particles in view of the large difference in particle sizes involved. Due to the large particle size (d_{50} = 480 μm) of the CF in the mixture relative to the particle size of CB (d_{50} = 2.4 μm), the surface area of the CF substrate, on which CB particles can adsorb, may be limited. Since the heights of the two peaks in Fig. 2c represent the number densities of the CF and CB particles, one can calculate the fraction of the CB particles that are not associated with CF from the peak heights. The peak heights for CF and CB are 14.9% and 6.7%, respectively, which gives 31.0% as the fraction of the free CB particles. This number may be equivalent to the degree of liberation. In this case, the liberation is driven by the limitation in the surface area of the CF substrate.

The inset of Fig. 3 shows changes in Π, Π_d, and Π_e, with film thickness h at separations close to the critical film thickness (h_c = 107 nm), where Π = 0 and hence the TLF should rupture. A consequence of film rupture is, of course, the heterocoagulation between CF and CB particles, which is not a desired situation for pigment liberation and hence for deinking flotation.

Note also at the inset that Π becomes negative at h below the h_c. In this region, both the EDL and van der Waals forces were negative (or attractive); however,

$$\left|\Pi_e\right| > \left|\Pi_d\right| \quad (3)$$

this indicates that the EDL force was more attractive than the van der Waals force, and the driving force for film thinning and rupture was the EDL force. This is contrary to many colloidal systems in which coagulation is induced by the attractive van der Waals force. The unexpected observation can be attributed to the fact that A_{132} was small for the interaction between CF and CB particles in water, which in turn can be attributed to the fact that A_{11} and A_{22} are small, as both are carbon-based materials with small atomic weights.

Figure 4 shows the distributed ζ-potentials measured with an ONP sample (from *The Roanoke Times*) dispersed in the tap water in the absence of any reagent. The paper was printed with an oil-based ink. As shown, the frequency distribution shows a single peak at ζ= -32.6 mV, indicating that the ink particles were heterocoagulated with little or no liberation of CBs from CF substrates.

The same ONP sample was subjected to another set of ζ-potential measurements after conditioning the pulp in the presence of a set of chemicals, which included 1.8% Na_2SiO_3, 0.6% NaOH, and 0.7% H_2O_2 by weight of ONP. These are the standard reagents that are used to determine the recyclability of papers printed with ink. The result in this case shows a bimodal ζ-potential distribution with two peaks, one at -31.5 mV and the other at -14.9 mV, the latter representing the CB pigments liberated from the CF substrates. The percentage distributions represented by the two peak heights are 21.1% and 5.2% for the CF and CB particles, respectively, in the pulp, from which one can estimate the degree of liberation of the CB pigment to be 19.8%. In this case, the liberation is driven by the EDL force,

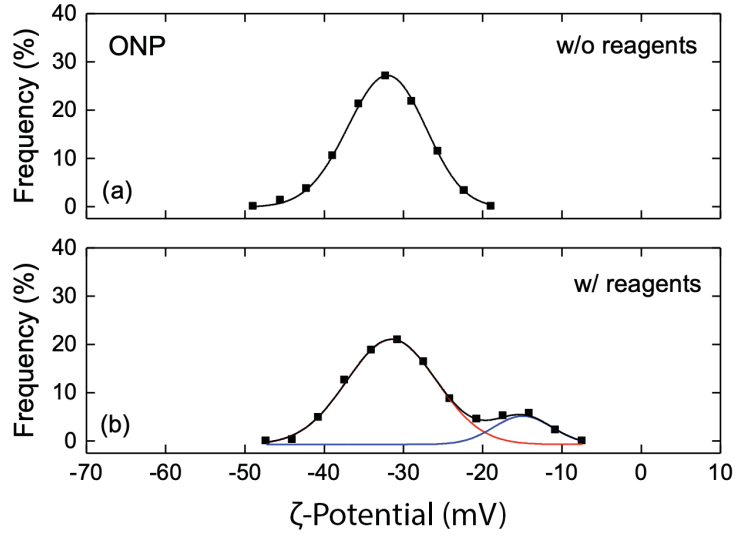

4. a) The ζ-potential distribution of an old newsprint (ONP) printed with oil-based ink; and b) ζ-potential distribution in the presence of chemical additives: 1.8% sodium silicate, 0.6% sodium hydroxide, and 0.7% hydrogen peroxide.

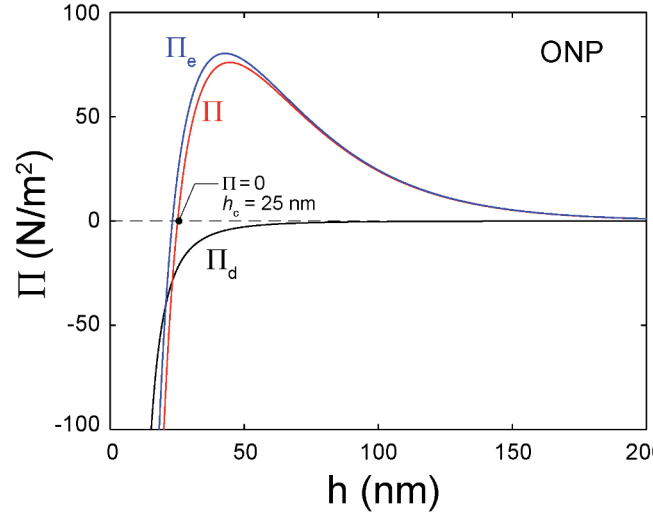

5. Disjoining pressure isotherm (Π(h)) for the interactions between wood fiber and pigment in oil-based ink: Π_d represents the van der Waals component of Π, and Π_e represents the EDL force component of Π_e: $A_{132} = 6.8 \times 10^{-21}$ J, $\psi_1 = -31.5$ mV, $\psi_2 = -14.9$ mV, and $k^{-1} = 31$ nm.

which gave rise to a high force (or disjoining pressure) barrier, as can be seen in **Fig. 5**.

Using the two peak ζ-potentials as the double-layer potentials for CF substrate (ψ_1 = -31.5 mV) and for CB pigments (ψ_2 = -14.9 mV), a DLVO calculation has been carried out using Eq. 1, with the resulting $\Pi(h)$, $\Pi_d(h)$, and $\Pi_e(h)$ isotherms presented in Fig. 5. In this calculation, we used the same Hamaker constant ($A_{132} = 0.68 \times 10^{-20}$ J) as for the isotherms obtained for the artificial mixtures (Fig. 3). A distinct difference between the two different calculations was that the disjoining pressure isotherms for the ONP sample showed orders of magnitude higher force barrier, which may provide a mechanism by which CB pigments stay liberated from the CF substrates. A high force barrier will provide a kinetic stability for the binary mixtures of the CF and CB particles in an aqueous medium and hence keep the CB pigments liberated from the CF substrates.

It may be of interest to discuss the reasons for the difference between the $\Pi(h)$ isotherms observed for the artificial mixtures of CF and CB particles (Fig. 3) and the $\Pi(h)$ isotherms observed for the ONP sample (Fig. 5). According to the Π_e term of Eq. 1, which is known as the Hogg-Healey-Fuerstenau approximation [16], the large difference between ψ_1 = -38.8 mV and ψ_2 = -12.7 mV was responsible for

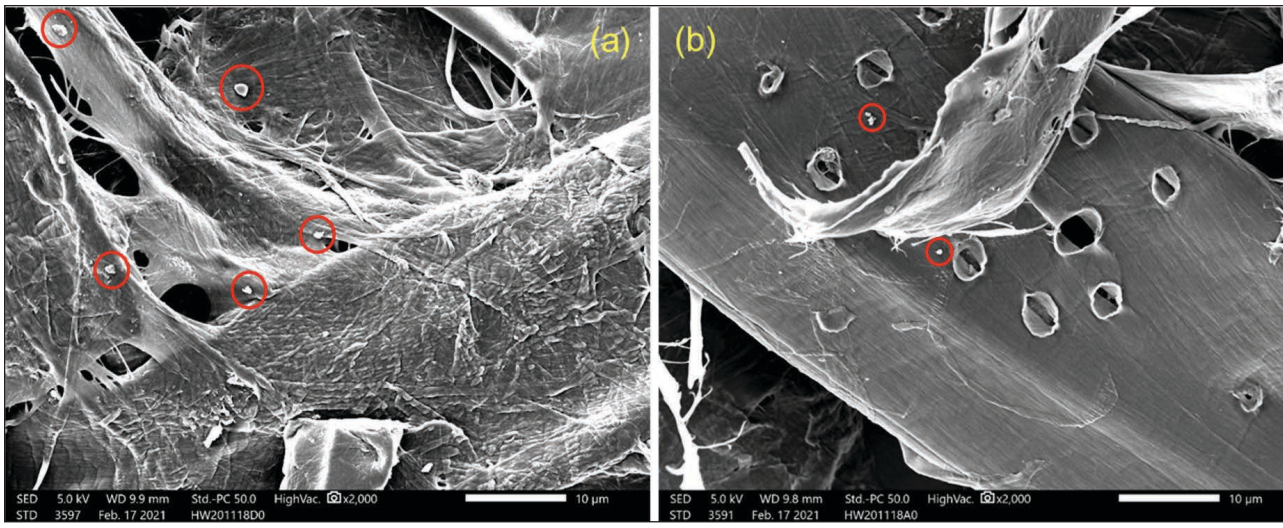

6. a) Scanning electron microscope (SEM) images of paper pads made from an ONP in tap water; b) SEM images of the ONP samples after a sodium silicate treatment. The pigment's oil-based ink are red circles.

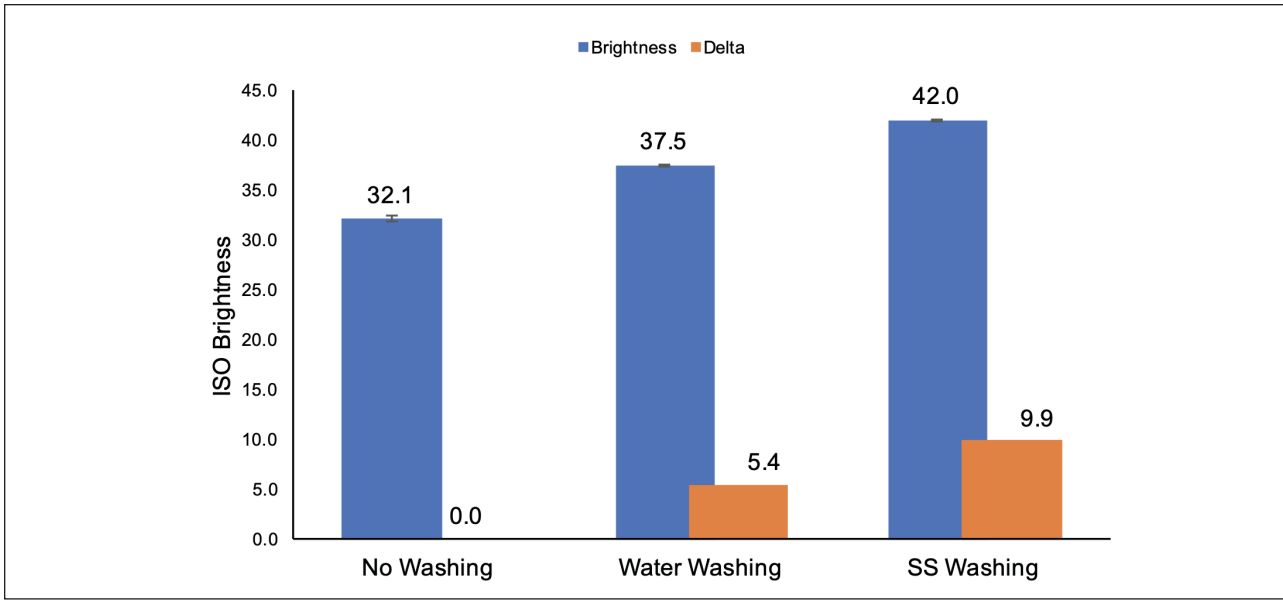

7. Effect of sodium silicate (SS) on the brightness improvement during the pulping and hyperwashing tests.

the attractive force, despite the fact that they were of the same sign, and it was responsible for the heterocoagulation. For the ONP sample, ψ_1 = -31.5 mV and ψ_2 = -14.9 mV, which also created attractive forces but only at very thin films below h < 23 nm. At h values close to that of h_c = 25 nm, the EDL force is repulsive, while the van der Waals force is attractive. Thus, the driving force for the heterocoagulation of the CF and CB particles present in the ONP pulp was the van der Waals force, which was the opposite of the case with the artificial sample and also with the ONP sample in the absence of the chemical additives.

The favorable situation with regard to CB liberation from the ONP slurry was created by the reagents used to promote liberation and hence deinking flotation. Sodium silicate may be responsible for the increase in the negative ζ-potential (or -ψ_2) from -12.7 to -14.9 mV. The use of H_2O_2 may also be responsible for the increase in the negative zeta-potential via oxidation of carbon to carbonyl or carboxylates. The polyelectrolyte may also be responsible for the decrease in ψ_1 of CF from -38.7 to -31.9 mV by way of removing some adherents (e.g., clays, submicronic wood fibers, etc.) from the surface, as shown in the SEM images given in **Fig. 6**. The use of NaOH may also be responsible for the decrease in ψ_1 of fibers in that the ζ-potential of fibers decreased considerably as the pH was increased above 10. In the presence of the reagent additives, the Debye length (κ^{-1}) decreased from 96 nm to 31 nm, which also contributed to the high force barrier observed with the ONP sample.

By virtue of the reagent packages used to improve the recyclability of the ONP sample, liberation of the CB pig-

ments used in the ONP sample was greatly improved, as shown in Fig. 4b and in Fig. 6. The small particle size of the pigments is one of the reasons for the difficulty encountered in deinking flotation.

The results presented in Figs. 4–6 show that Na_2SiO_3 was beneficial for liberating pigments from the ONP sample printed with oil-based ink. As validation of these findings, **Fig. 7** shows the result of the ISO brightness measurements conducted on the same sample after two stages of hyperwashing with and without Na_2SiO_3. Also shown is the result obtained after pulping the sample without hyperwashing. After hyperwashing, the brightness was increased by 5.4 over the result obtained without water washing, while the method of using Na_2SiO_3 increased the ISO brightness by 9.9. These results confirmed that increasing pigment liberation is critically important for improving the brightness of the ONP and hence its recyclability. The brightness improvement would have been more significant, if NaOH and H_2O_2 had also been used in conjunction with Na_2SiO_3.

The brightness increase of 9.9 shown in Fig. 7 is equivalent to a 30.8% increase in ISO brightness over the case of no washing and hence no liberation, which may be related to the 19.8% increase in the degree of liberation of the CB pigment from the CF substrate. This slight deviation is not unexpected, considering that the degree of liberation was a rough estimation based on the peak heights of the CF and CB frequency distribution curves presented in Fig. 4b. It would have been better to use the area under the ζ-potential distribution curves rather than the peak heights. Further work is, therefore, necessary to develop a rigorous mathematic algorithm to determine the degree of liberation more accurately. As has already been noted, pigment liberation is a prerequisite to flotation deinking. In this regard, improving pigment liberation is critically important in increasing the recyclability of printed papers.

Some investigators were skeptical of the role of Na_2SiO_3 in deinking flotation [17-18], while others reported beneficial effects [3,19-21]. The data obtain in the present work support the observation of the latter investigators. The results presented in Fig. 7 actually show that Na_2SiO_3 is an enabling reagent in the sense that, without it, the ζ-potential data show that the degree of CB liberation was practically zero. Also, the disjoining pressure isotherms presented in Fig. 3 and Fig. 5 show the fundamental mechanisms involved in liberation. The new method of determining the degree of pigment liberation from recycle paper is being tested for water-based ink. It can be used to study the liberation of pigments of various colors. The method is also useful for testing different reagents that can improve pigment liberation and thereby increase the recyclability of printed papers. Furthermore, the experimental data obtained in the present work can be used to construct disjoining pressure isotherms that can be useful for better understanding the fundamental mechanisms involved.

CONCLUSION

A new method of studying pigment liberation from recycle papers printed with oil-based ink has been developed. It consists of determining the number densities of pigments and fibers by measuring their characteristic ζ-potentials. Under conditions of favorable liberation, a ζ-potential distribution gives two peaks, with the relative peak heights providing information on pigment liberation. Under conditions of unfavorable liberation, only a single peak appears. Using the characteristic ζ-potentials of the pigments and fibers, one can also construct the disjoining pressure isotherms using the DLVO theory, which can be used to better understand the roles of different reagents that are used to control the surface properties of the materials involved. The results obtained in the present work show that control of EDL forces is critical for controlling pigment liberation and hence improving the recyclability of printed papers. **TJ**

ACKNOWLEDGEMENT

The authors would like to acknowledge the financial support from the REMADE Institute (Project number: 18-02-RR-15).

LITERATURE CITED

1. LeBlanc, R., "Paper recycling facts, figures, and information sources," *liveabout.com*, Dotdash Meredith, New York, 29 July 2018. https://www.liveabout.com/paper-recycling-facts-figures-and-information-sources-2877868.
2. Ng, H.T., Bhattacharyya, M.K., Mittelstadt, L.S., et al., "Deinking of HP digital commercial prints: Effect of chemicals and their loadings on deinkability," *NIP & Digital Fabrication Conf.* (Vol. 2009, No. 1, pp. 173-176), Society for Imaging Science and Technology, Springfield, VA, USA, 2009.
3. Bajpai, P., *Recycling and Deinking of Recovered Paper*, Elsevier, Amsterdam, 2013.
4. Liu, J., Vandenberghe, J., Masliyah, J., et al., *Miner. Eng.* 20(6): 566(2007). https://doi.org/10.1016/j.mineng.2006.11.005.
5. Zhao, Y., Deng, Y., and Zhu, J.Y., *Prog. Pap. Recycl.* 14(1): 41(2004).
6. Marchildon, L., Lapointe, M., and Chabot, B., *Pulp Pap. Can.* 90(4): 90(1989).
7. Julien Saint Amand, F. and Perrin, B., *Pulp Pap. Can.* 94(10): T284(1993).
8. Xu, Z., Liu, J., Choung, J.W., et al., *Int. J. Miner. Process.* 68(1-4): 183(2003). https://doi.org/10.1016/S0301-7516(02)00043-1.
9. Liu, J., Xu, Z., and Masliyah, J., *J. Colloid Interface Sci.* 287(2): 507(2005). *https://doi.org/10.1016/j.jcis.2005.02.037.*
10. Wu, C., Wang, L., Harbottle, D., et al., *J. Colloid Interface Sci.* 449: 399(2015). *https://doi.org/10.1016/j.jcis.2015.01.040.*
11. Derjaguin, B.V. and Landau, L., *Acta Physicochim: URSS* 14: 633(1941).
12. Verwey, E.J.W. and Overbeek, J.Th.G., *Theory of the Stability of Lyophobic Colloids*, Elsevier, Amsterdam, 1948.
13. Israelachvili, J.N., *Intermolecular and Surface Forces*, Academic Press, Cambridge, MA, USA, 2011.

14. Bergström, L., Stemme, S., Dahlfors, T., et al., *Cellulose* 6(1): 1(1999). https://doi.org/10.1023/A:1009250111253.
15. Hartley, P.A., Parfitt, G.D., and Pollack, L.B., *Powder Technol.* 42(1): 35(1985). https://doi.org/10.1016/0032-5910(85)80036-X.
16. Hogg, R., Healy, T., and Fuerstenau, D.W., *Trans. Faraday Soc.* 62: 1638(1966). https://doi.org/10.1039/tf9666201638.
17. Mak, N. and Steven, J., "Characteristics of fatty acids as an effective flotation de-inking collector," *Res. Forum Recycl.*, 2nd, TAPPI Press, Atlanta, 1993, p. 145.
18. Mathur, I., "Preferred method for removal of filler from deinked pulp," *Recycl. Symp.*, TAPPI Press, Atlanta, 1994, p. 53.
19. Mahagaonkar, M., Banham, P., and Stack, K.R., *Prog. Pap. Recycl.* 6(2): 50(1997).
20. Ferguson, L.D., *Tappi J.* 75(7): 75(1992).
21. Ferguson, L.D., *Tappi J.* 75(8): 49(1992).

ABOUT THIS PAPER

Cite this article as:
Huang, K., Strickland, K., Noble, A., et al., *TAPPI J.* 21(10): 533(2022). https://doi.org/10.32964/TJ21.10.533

DOI: https://doi.org/10.32964/TJ21.10.533

ISSN: 0734-1415

Publisher: TAPPI Press

Copyright: ©TAPPI Press 2022

About this journal

ABOUT THE AUTHORS

This work has been funded by REMADE, which in turn has been funded by the U.S. Department of Energy. The objective of the project is to study ways to improve deinking flotation, which will in turn increase the tonnage of recycle papers in the United States.

We have been actively developing more efficient methods of improving the efficiency of separating mineral fines. A key to improving the separation efficiency is to improve mineral liberation. In the present work, we have developed a new method of determining the degree of ink particle liberation from recycle papers. The method consists of measuring the zeta-potentials of both ink particles and paper fibers. We may be able to apply the same methodology to determine the degree of mineral liberation.

We were able to develop this method because we have expertise in advanced colloid chemistry. We used the DLVO theory to determine the disjoining pressure in the wetting films between ink particles and paper fibers. The theoretical analysis made it possible to find that control of electrical double layer force is the key to improve the liberation of ink particles from fibers. We were surprised that the degree of liberation of ink particles is quite low. Control of surface forces is important for achieving a high degree of liberation of ink particles from recycle papers.

There should be many other reagents aside from those we have used in the present work that can increase the double layer force and thereby improve the liberation and hence the efficiency of deinking flotation. As we noted in our conclusion section, we are in the process of studying the liberation of ink particles from water-based papers and developing more powerful reagents than the one we used in the present work to improve the liberation of ink particles.

Huang is research associate, Strickland is graduate research assistant, Noble is associate professor, and Yoon is professor in the Department of Mining and Minerals Engineering at Virginia Tech in Blacksburg, VA, USA. Basilio is group leader at Thiele Kaolin Company in Sandersville, GA, USA. Email Yoon at ryoon@vt.edu.


Huang


Strickland

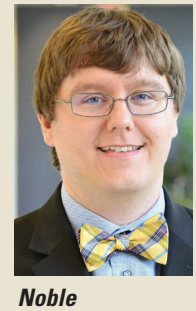
Noble


Yoon


Basilio

Utilization of palm fiber as papermaking materials: Microscopic structure and chemical pulping

ZHULIN LI, SHUAI GAO, LEI TANG, DING LIU, QUN LI, GUOYO TIAN, AND ZHAOJIANG WANG

ABSTRACT: The microscopic structure and pulping properties of palm fiber were explored. Soda cooking and sulfate cooking were conducted and compared in terms of physical strength of the obtained pulps. Sulfate pulp showed better performance than soda pulp, as indicated by the 23% higher tensile index, 49% higher tear index, and 36% higher burst index.

To further elevate physical strength, long fibered pulp (LFP), namely commercial softwood sulfate pulp, was mixed with sulfate pulp of palm fiber at levels from 20% to 50%. At the blend level of 50%, tensile index of 52.13 N•m/g, tear index of 15.63 mN•m²/g, and burst index of 3.42 kPa•m²/g were attained. The lignin in spent liquor from pulping was isolated and characterized. Soda lignin of palm fiber was mainly composed of guaiacyl and syringyl units, and showed weight-average molecular weight of 3616 g/mol.

Application: We explored the properties of soda pulp and sulfate pulp of palm fiber. Comparison was made with hardwood and softwood pulp in terms of fiber length and physical strength. The reported results suggested the feasibility of palm fiber for papermaking.

The palm tree is one of the common tree species in tropical areas and has important economic value. Palm trees are not only ornamental plants, but they are also an important source of wood. The leaf of the palm can be used to make palm-bark rain capes. Palm fiber is used to make household goods. As a high-quality natural fiber, palm fiber is not actually fully exploited. Global fiber production has been 107 million metric tons since 2018 and is expected to grow to 145 million metric tons by 2030. No more than 10% of natural plant fibers such as palm and hemp are used [1]. As a type of natural fiber with excellent properties, palm fiber is not only widely planted, but also an abundant source. However, most palm fiber is burned and represents a waste of fiber resources.

The efficient utilization of biomass resources has been realized with the improvement in the population's environmental awareness. In order to realize efficient utilization of palm fiber, biomass refining [2] was introduced. The surface of palm fiber is sags and crests, and the cross section is honeycomb [3], and it has a low degree of crystallinity, a large specific surface area, and large pore cover [4]. The structure and nature of palm fiber determine its application. Upon further study, palm fiber has been widely used; for example, it can be used for bio-composites, and there have been comprehensive reviews on the bio-composites of palm fibers [5]. Polymer matrix composites were prepared by using palm fiber and S-glass [6]. The test results show that the composite material had good adhesion and was a high strength element for structural applications. With epoxy resin as matrix, palm sheath fiber and bagasse fiber were used to prepare composite materials. The experimental results showed that the composite materials had good flexural properties and hardness, and could be used to develop automobile dashboards [7]. The oil palm empty fruit bunch cellulose was dissolved in a sodium hydroxide (NaOH)/urea solvent and mixed with sodium carboxymethylcellulose (NaCMC) and crosslinker epichlorohydrin (ECH) to make a superabsorbent hydrogel [8]. The results showed that the formed hydrogel attained highest gel fraction, water absorption, degree of swelling, and transparency values at 10% of ECH.

Palm fiber has low density and porous structure. Palm fiber was used to prepare activated carbon with good adsorption performance and had a broad application prospect in the field of sewage treatment and air purification [9]. In addition, palm fiber is sustainable and biodegradable, which can change clay properties and provide reference and application for related engineering [10]. Furthermore, oil, natural gas, and other fossil energy reserves have been gradually depleted, and fuel ethanol, a renewable clean energy, has gradually become an important part of the energy structure [11]. Palm fiber has been converted into bioethanol by enzymatic hydrolysis or fermentation [12]. Palm fiber is also a kind of papermaking material with high yield and good properties. The utilization of palm fiber as a papermaking material can not only solve the pollution prob-

lem from fiber waste, it can also alleviate the shortage of raw materials for papermaking [13]. Pulping and biomass refining are new strategies for efficient utilization of palm fiber [14]. Pretreatment of palm fiber removed most of the lignin and increased glucose yield [15]. Many studies have demonstrated the feasibility of palm fiber for pulping and papermaking [16,17].

Early studies focused on chemical pulping of palm fiber by soda and sulfate processes [18-20]. In the present work, in order to explore the pulping property, the microscopic structure of palm fiber was studied by computerized tomography. Chemical pulping was conducted. Also, long fibered pulp (LFP), namely softwood sulfate pulp, was blended with the pulp of palm fiber to improve the physical strength of the paper sheet. The structure of lignin in spent liquor was also characterized.

MATERIALS AND METOHDS

Raw materials and chemicals

Palm fiber was collected from a farm located in Malaysia. The palm fiber was dedusted with hot water before cooking. After air-drying, the fiber was size-reduced to 3–5 cm in length. Sodium hydroxide, sodium sulfide, and anthraquinone were purchased from Sigma Aldrich (St. Louis, MO, USA). All the chemicals were analytical grade in purity and used without further purification.

Chemical pulping and making of handsheets

Laboratory scale pulping experiments were performed in a 15 L vertical rotary autoclave (Kumagai Riki Co. Ltd.; Tokyo) with four bombs of 1 L capacity each. The pulping conditions are listed in **Table I**. The cooking temperature, anthraquinone dosage, liquid-to-solid ratio, and holding time in each case were fixed at 160°C, 0.05%, 1:5(m/v), and 2 h, respectively. The level of sodium hydroxide for the soda process and the sulfate process was same, from 16% to 25% on the mass basis of palm fiber. Sulfidity of the sulfate process was 20%. The spent liquor was separated from the undispersed fiber through filtration and water washing. The undispersed fiber was then mechanically milled using a high-consistency refiner (BR30-300C; Kumagai Riki Kogyo Co. Ltd.) at a disc gap of 0.15 mm or 0.3 mm. The pulp from the soda process and the sulfate process was observed by optical microscope (Axio Scope A1, Zeiss; Oberkochen, Germany). The obtained pulp from the refiner was then beaten to Canadian Standard Freeness from 300±50 mL prior to papermaking. In order to improve the physical strength of paper, LFP was mixed with palm fiber pulp at levels from 20% to 50% for papermaking. The paper sheets of basis weight of 60 g/m² were fabricated by an RK3AKWT sheet former (Frank-PTI GMBH; Birkenau, Germany) according to TAPPI T 205 sp-12 "Forming handsheets for physical tests of pulp."

Samples	Alkali Charge, %	
	Sodium Hydroxide	Sulfidity
Soda-16	16	-
Soda-20	20	-
Soda-25	25	-
Sufate-16	16	20
Sulfate-20	20	20
Sulfate-25	25	20

I. Palm fiber pulping conditions for the soda process and the sulfate process.

Microstructure detection of palm fiber

Micro computerized tomography (micro-CT) was used to obtain cross-sectional images of untreated palm fiber at a resolution of 300 nm. Scanning electron microscope (SEM) was used to obtain surface topography images of palm fiber with a Hitachi Regulus 8220 SEM (Hitachi; Tokyo, Japan) that operated at an acceleration voltage of 5 kV.

Molecular weight determination of lignin

The purified lignin was obtained from spent liquor. First, the liquors were acidified with 72wt% sulfuric acid (H_2SO_4) until reaching pH 2. The resulting precipitates were centrifuged and washed by 0.01M H_2SO_4 or distilled water. Finally, the precipitates were cryo-dried after dialysis. For lignin acetylation, 10 mg purified lignin was transferred into a 5 mL vial. Then, 2.5 mL pyridine and 2.5 mL acetic anhydride solution were added and mixed with lignin. After 72 h at dark, the acetylated lignin sample was obtained after freeze drying. Next, 6 mg acetylated lignin was dissolved in 3 mL tetrahydrofuran (THF) for molecular weight determination by gel permeation chromatography (Waters e2695, NYSE:WAT technology, Waters Corp; Milford, MA, USA). The injection volume was 25 µL. The flow rate was 1 mL/min, and the column (300 mm length × 8 mm diameter, 15 mL volume) temperature was 40°C.

Structure characterization of lignin

Nuclear magnetic resonance (NMR) analysis of lignin, including two-dimensional-heteronuclear single-quantum correlation (2D-HSQC) and proton nuclear magnetic resonance (^{1}H NMR), were conducted using an NMR spectrometer (AVANCE III 400 MHz, Bruker; Billerica, MA, USA) as previously described. About 60 mg lignin was dissolved in 0.5 mL dimethyl sulfoxide-d_6 (DMSO-d_6) solution and transferred to a 5 mL nuclear test cube for testing. Tetramethylsilane (TMS) was used for internal referencing of chemical shifts. The relaxation delay (D1) was 1 s, and the acquisition time was 4.5 s.

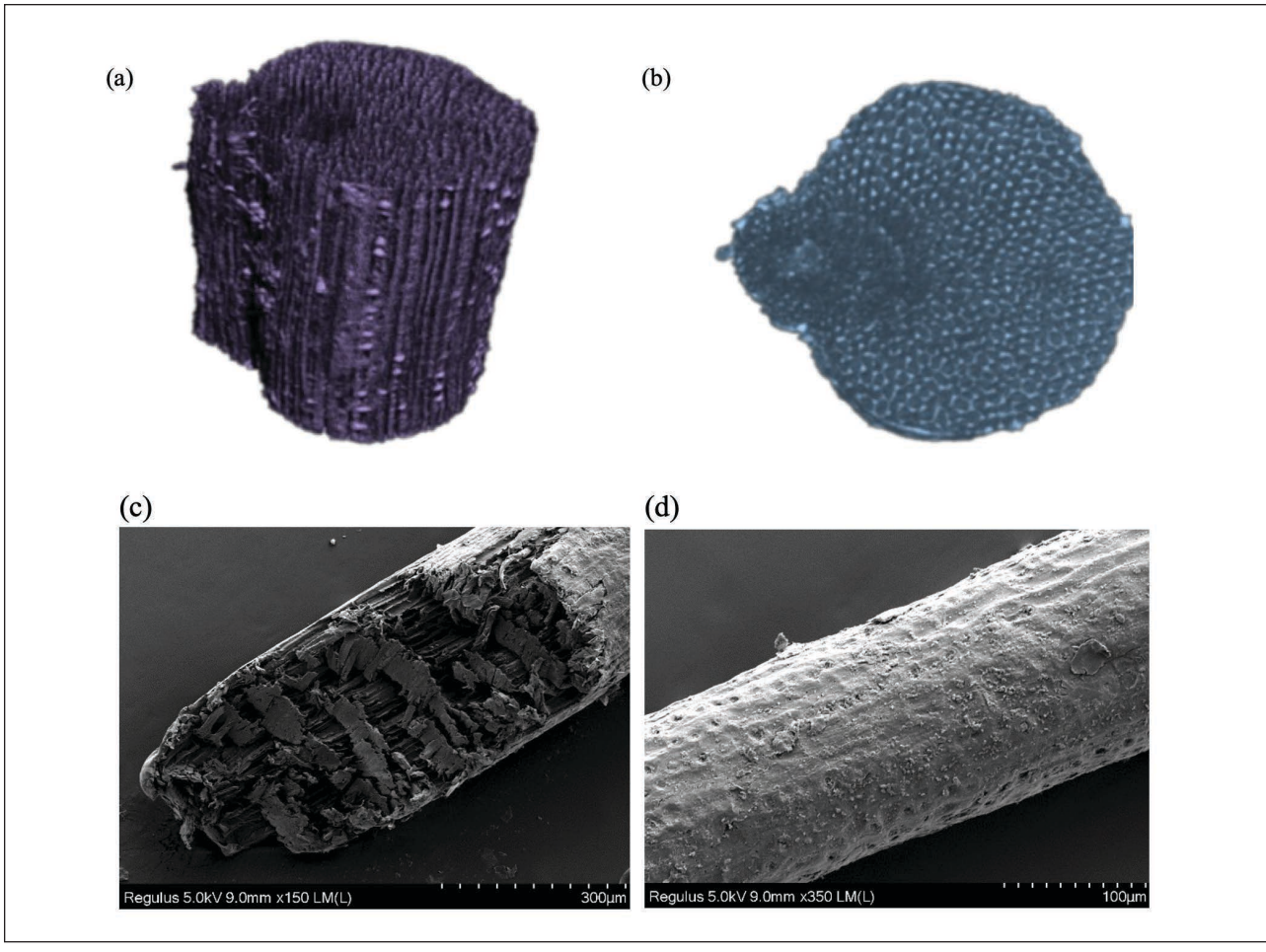

1. The cross-sectional images (a,b) and surface topography images (c,d) of palm fiber obtained by micro computerized tomography (micro-CT) and scanning electron microscope (SEM), respectively.

Determination of physical properties of handsheets

The paper handsheets were prepared using soda and sulfate pulp. For the paper sheets, physical properties were determined, including yield, tensile strength (Chinese National Standard GB/T 12914-2018 "Paper and board – determination of tensile properties – constant rate of elongation method 20 mm/min)," tear strength (GB/T 455-2002 "Paper and board – Determination of tearing resistance"), and burst strength (GB/T 454-2020 "Paper – Determination of bursting strength). All measurements were performed at least three times.

RESULTS AND DISCUSSION

Microscopic structure of palm fiber

The cross-sectional images of untreated palm fiber (**Fig. 1a** and Fig. 1b) were obtained by micro-CT. The surface topography images of palm fiber (Fig. 1c and Fig. 1d) were obtained by SEM. The palm fibers are cylindrical in form with a diameter of about 1.0 mm. Palm fiber is covered with a dense and rough surface. From the cross-sectional image (Fig. 1a), the microfibers are very neatly arranged inside of palm fiber. From the transverse image (Fig. 1b), the xylem cell can be recognized by the gray-colored microfibers and cell corners that are white in color. Zhang et al. [21] also studied the structure and properties of palm leaf sheath fiber. It was reported that the white particles can improve the frictional force and facilitate defibering during the beating process. Christina et al. [22] indicated that the particles were rich in silicon and have a good antibacterial property because of the compact structure of particles.

Yield and physical strength of palm fiber pulp

The pulp yield from the soda process and sulfate process in **Table II** demonstrated that Soda-16 showed the highest pulp yield at 83.4%, which means a mild delignification. Soda-16 actually belonged to chemical mechanical pulp. The micrograph of Soda-16 in **Fig. 2** showed the length of fibers from 0.2–0.4 mm and the width of fibers from 20–30 µm. These dimensional values suggested that the chemical mechanical pulp of palm fiber was very small fines. The yields of Soda-25, Sulfate-16, Sulfate-20, and Sulfate-25 were 45.6%, 49.5%, 45.2%, and 41.8%, respectively, which are

Handsheet Samples	Yield, %	Tensile Index, N•m/g	Tear Index, mN•m²/g	Burst Index, kPa•m²/g	Brightness, %ISO
Soda-16	83.4	22.30	6.48	2.10	19.2
Soda-20	56.3	23.64	6.21	2.03	19.1
Soda-25	45.6	24.90	6.16	1.90	19.1
Sulfate-16	49.5	17.74	4.85	1.89	19.5
Sulfate-20	45.2	25.12	7.09	2.31	19.6
Sulfate-25	41.8	30.61	9.16	2.59	19.2
Sul/LFP-20*	-	28.81	9.82	2.16	22.2
Sul/LFP-40	-	44.91	13.27	2.98	22.8
Sul/LFP-50	-	52.13	15.63	3.42	23.5
LFP		75.80	14.30	5.02	32.3

Sul = Sulfate-16; LFP = long fiber pulp, namely, commercial softwood sulfate pulp; 20 = blend level of 20% LFP, which also follows for 40% and 50% below.

II. Pulp yields from palm fiber for the soda process and the sulfite process, as well as the physical strength of the pulps.

typical values for pulp yield of chemical pulp. The big drop in pulp yield from 83.4% for Soda-16 to 49.5% for Sulfate-16 indicated the positive effects of sulfidity in boosting delignification. The average length of Sulfate-16 fiber was 1.3 mm, which is twice as long as that of Soda-16. Furthermore, the fiber surface of Sulfate-16 became much smoother than Soda-16. From Fig. 2, no significant difference was observed among the microstructures of Sulfate-16, Sulfate-20, and Sulfate-25. It is necessary to make a comparison of fiber length and width between palm fiber pulp and wood pulp. For wood pulp fibers, biometry showed a range in length (0.70–0.84 mm for hardwood, 1.57–1.96 mm for softwood) and in width (18.0–19.1 µm for hardwood, 29.8–37.2 µm for softwood) [23]. For the chemical pulp of palm fiber in Fig. 2, pulp fiber showed an average length of 0.5 mm and an average width of 22 µm. Comparatively, the fiber length of palm fiber pulp was much shorter than wood pulp.

The physical strength of pulps is listed in **Table II**. The tensile index and tear index showed close values for soda pulps, from 22.3 to 24.9 N•m/g. The increase in chemical dosage showed little effect on the tensile strength for soda pulping. On the contrary, the tensile index and tear index depended on chemical dosage for the sulfate pulps. The tensile index increased from 17.74 N•m/g for Sulfate-16 to 30.61 N•m/g for Sulfate-25. The burst index increased from 4.85 mN•m²/g for Sulfate-16 to 9.16 mN•m²/g for Sulfate-25.

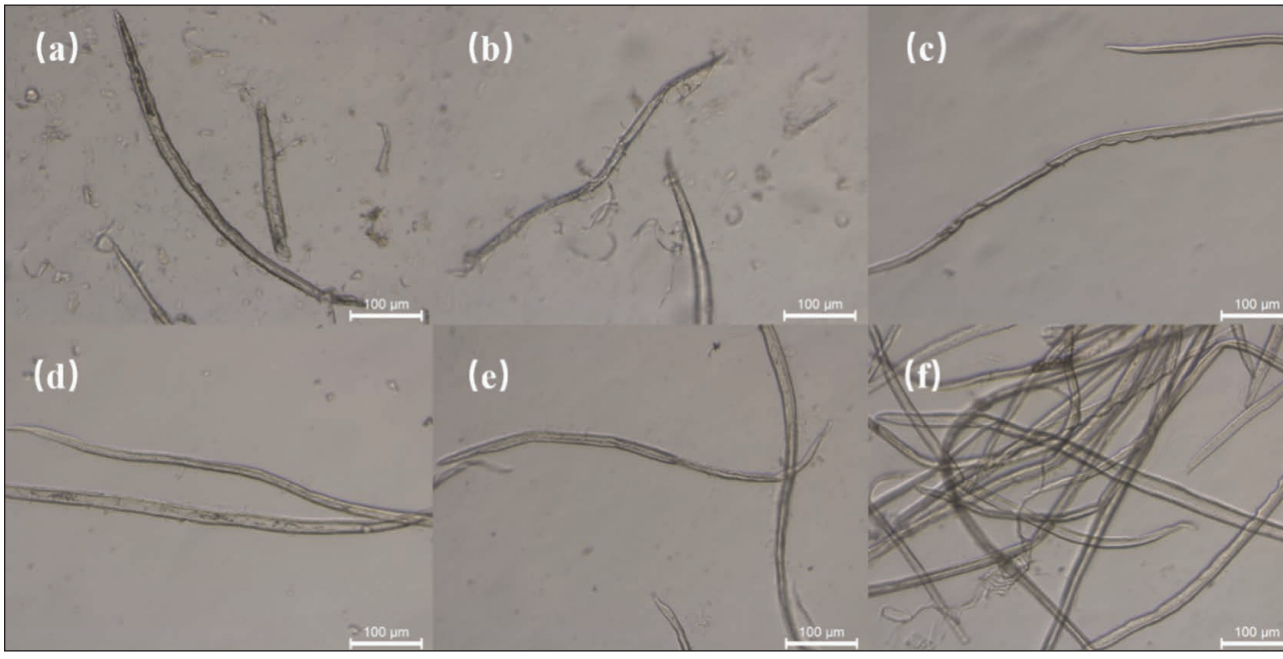

2. Microscope images of pulps from the soda process and the sulfate process: (a) Soda-16, (b) Soda-25, (c)(f) Sulfate-16, (d) Sulfate-20, and (e) Sulfate-25.

Label*	Mw, g/mol	Mn, g/mol	PDI, Mw/Mn	Reference
Soda-palm	3616	1915	1.9	
Indulin kraft	4290	530	8.1	[27]
Soda-P1000	3270	620	5.2	[27]
Alcell	2580	600	4.3	[27]
OS-W	1960	450	4.4	[27]
OS-P	2180	570	3.8	[27]
OS-S	2030	420	4.9	[27]
MAL-Pine	5300	2400	2.2	[28]
MAL-Eucalyptus	5420	2600	2.1	[28]
MAL-Corn stalk	7680	3070	2.5	[28]
MAL-Bamboo	8520	3410	2.5	[28]

* Soda-palm was isolated from spent liquor of Soda-25. Indulin kraft is softwood kraft lignin from Ingevity, North Charleston, SC, USA. Soda-P1000 is soda lignin from mixed wheat straw and Sarkanda grass. Alcell is organosolv lignin from mixed hardwoods of maple, birch, and poplar from Repap Technologies, Vancouver, BC, Canada. OS-W, OS-P, and OS-S are three organosolv lignins extracted from wheat straw, poplar, and spruce, respectively, using the acid-catalyzed ethanol-based organosolv process. MAL-Pine, MAL-Eucalyptus, MAL-Corn stalk, and MAL-Bamboo were obtained by mild acidic dioxane isolation process.

III. Comparison of weight-average molecular weight (Mw), number-average molecular weight (Mn), and polydispersity (PDI) of palm fiber soda lignin with other technical lignins.

Results in Table II also showed that pulp from the sulfate process was superior in physical strength to that from the soda process in physical strength. However, the physical strength of palm fiber pulp was not as good as pulps from other biomass. Wenchao Jia et al. [24] produced kraft pulp from acacia wood with tensile index of 57.63 N•m/g and tear index of 16.93 mN•m²/g. Yuan et al. [25] prepared kraft pulp from bamboo with tensile index of 50.0 N•m/g. Lísias Pereira Novo et al. [26] prepared soda pulp from sugarcane with tensile index of 52.1 N•m/g and burst index of 3.71 kPa•m²/g. In order to improve the physical strength of pulp, LFP was mixed with Sulfate-16 pulp at levels from 20% to 50% for papermaking. The results indicated that the physical properties of the papers were greatly improved. The tear index increased by 102% from 4.85 mN•m²/g for Sulfate-16 to 9.82 mN•m²/g for Sul/LFP-20 with a blend level of 20%. The burst index increased by 57% from 1.89 kPa•m²/g for Sulfate-16 to 2.98 kPa•m²/g for Sul/LFP-40 with a blend level of 40%. In this way, the application of palm fiber in the paper industry is feasible for producing paper products with promising strength.

Molecular weight distribution of soda lignin from palm fiber

The lignin of in spent liquor of Soda-25 was purified and acetylized for molecular weight determination. A wide molecular weight distribution was observed for Soda-25 lignin, ranging from $10^{2.8}$ g/mol to $10^{4.2}$ g/mol (**Fig. 3**). The weight-average molecular weight (Mw), the number-average molecular weights (Mn), and polydispersity (PDI) were 3616 g/mol, 1915 g/mol, and 1.88, respectively. For a better understanding of palm fiber lignin, molecular weight of technical lignins [27] and mild acidolysis lignins [28] (MAL) from softwood, hardwood, and herbaceous biomass are provided in **Table III** for comparison. The Mw of Soda-palm was 3616 g/mol, which is higher than Mw of 3270 g/mol for soda lignin from wheat straw and Sarkanda grass (Soda-P1000), but lower than the Mw of 4290 g/mol for softwood kraft lignin (Indulin kraft, In gevity; North Charleston, SC, USA). It is worth mentioning that the PDI of Soda-palm was closer to

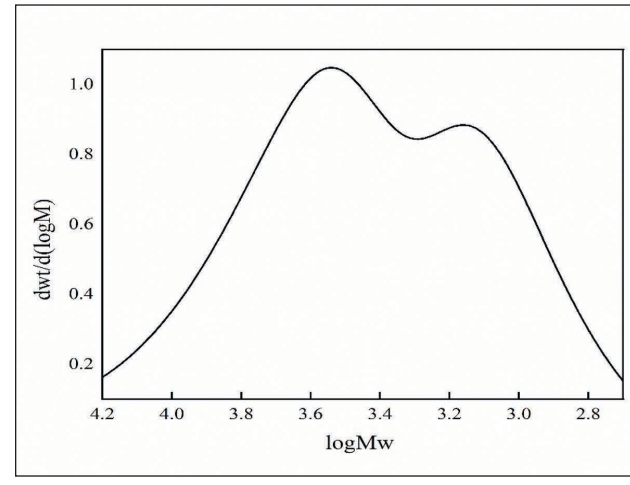

3. Molecular mass distribution of Soda-25 lignin from palm fiber.

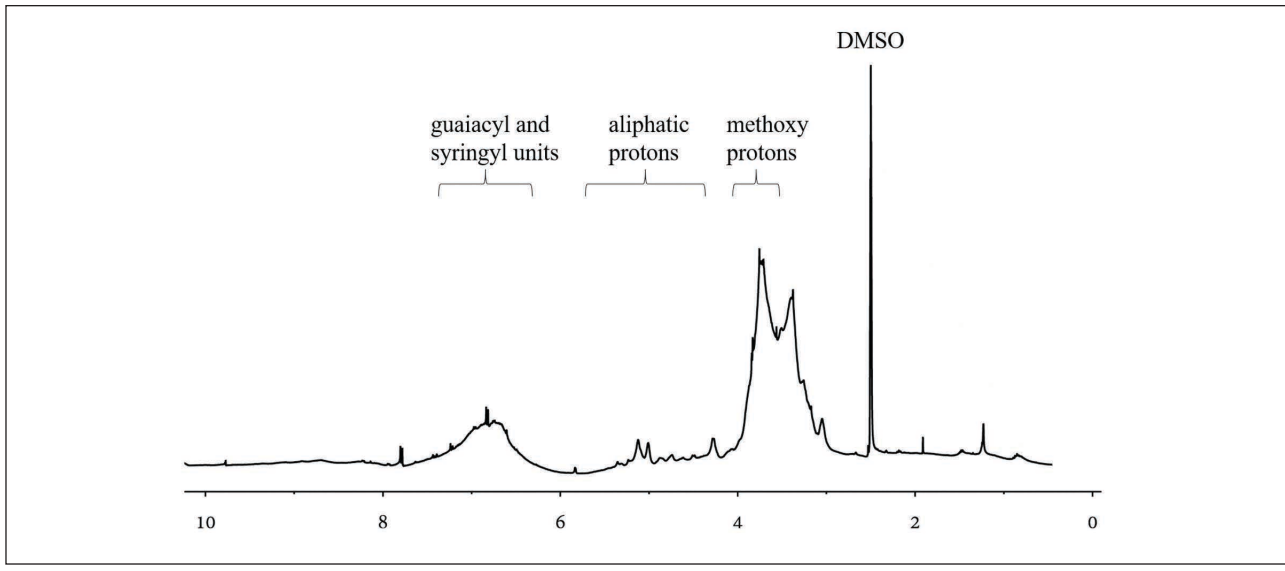

4. Proton nuclear magnetic resonance (1H NMR) spectrum of Soda-25 lignin from palm fiber.

1.0 than any other of the lignins listed in Table III, which indicated better homogeneity or uniformity of lignin molecules. Molecular weight of organosolv lignins (Alcell [Repap Technologies; Vancouver, BC, Canada], OS-W, OS-P, OS-S) were lower than soda and kraft lignin (Soda-palm, Indulin kraft, Soda-P1000). This is possibly attributed to the intense cleavage of lignins during organosolv pulping. Mild acisolysis lignins in Table III were obtained by mild acid dioxane isolation process, and therefore had much higher molecular weight. This was confirmed by comparison of Mw between MAL-Pine and Indulin kraft.

Structural characteristics of lignin

Lignin is a three-dimensional biopolymer built from phenylpropane units, including the guaiacol (G), syringe (S), and *p*-hydroxyphenyl (H) units. The ^{1}H NMR spectrum of palm fiber Soda-25 lignin is shown in **Fig. 4**. According to literature [29], the signal at 6.2–7.5 ppm originates from the aromatic proton. This is mainly the signal of the S unit at 6.2–6.8 ppm and G unit at 6.8–7.3 ppm. The signal of the H unit from 7.3 ppm to 7.5 ppm was comparatively weak, which indicated the low level of H unit in palm fiber Soda-25 lignin. The chemical shift of primarily aliphatic protons

Label	C/H, ppm	Assignment
Methoxyl	53.5/3.04	C_{β}-H_{β} in β-β′resinol substructure (B)
A_{γ}	59.3/3.42 and 3.68	C_{γ}-H_{γ} in γ-hydroxylated β-O-4 substructure (A)
C_{γ}	71.1/3.82 and 4.15	C_{γ}-H_{γ} in β-β′ resinol substructure (C)
C_{α}	87.5/4.5	C_{α}-H_{α} in β-5 resinol substructure (C)
A_{α}(S)	71.7/4.86	C_{α}-H_{α} in β-O-4′substructure(A) linked to an S-unit
A_{β}(G)	83.1/4.28	C_{β}-H_{β} in β-O-4′substructure(A) linked to a G-unit
B_{γ}	65.2/3.64	C_{γ}-H_{γ} in β-5′phenylcoumaran substructures (B)
$S_{2,6}$	103.9/6.69	$C_{2,6}$-$H_{2.6}$ in etherified syringyl unit (S)
$S'_{2.6}$	106.2/7.24	$C_{2,6}$-$H_{2.6}$ in oxidized syringyl unit (S)
G_2	110.9/6.98	C_2-H_2 in guaiacyl unit (G)
G_5	114.9/6.73 and 6.93	C_5-H_5 in guaiacyl unit (G)
$H_{2,6}$	127.8/7.23	$C_{2,6}$-$H_{2,6}$ in the *p*-hydroxycinnamic unit (H)

IV. The ^{13}C-^{1}H NMR spectroscopy corresponding to the main lignin structural units in the heteronuclear single quantum coherence (2D-HSQC) map.

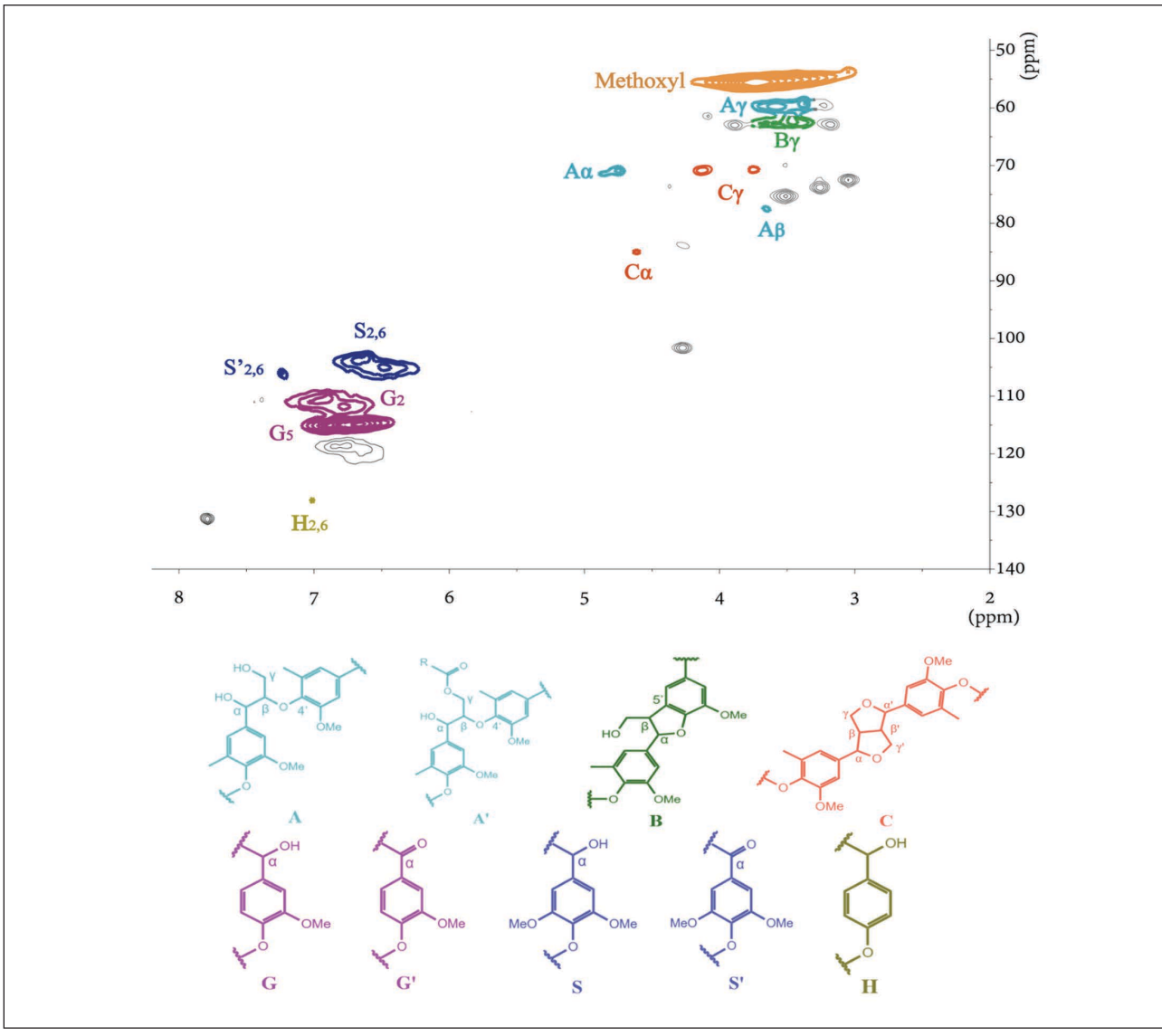

5. The two-dimensional-heteronuclear single-quantum correlation (2D-HSQC) spectra of palm fiber soda lignin: (A) β-O-4′ alkyl-aryl ether; (A′) γ-OH with p-coumaroylated β-O-4′ alkyl-aryl ether; (B) β-5′ phenylcoumaran; (C) β-β′ resinol; (H) p-hydroxyphenyl units; (G) guaiacyl units; and (S) syringyl units.

was located from 4.0 ppm to 6.0 ppm. The proton at 4.3 ppm was attributed to lignin having β-O-4 inter-unit linkages. The strong signal between 3.5 ppm to 4.0 ppm was attributed to protons in methoxy (-OCH_3) of lignin.

To obtain more detailed chemical information on the lignin, quantitative 2D-HSQC NMR of the Soda-25 lignin from palm fiber was conducted. The heteronuclear single quantum coherence (2D-HSQC) spectrum of palm fiber Soda-25 lignin is shown in **Fig. 5**. The structures were assigned to NMR signals [30], according to **Table IV**. In Fig. 5, β-O-4 (A), β-5 (B), and β-β (C) interunit linkages were identified in the palm fiber Soda-25 lignin. Compared with the β-O-4 (A) substructures, notably, phenylcoumaran β-5 (B) was at a higher level. In the aromatic region, the signals of guaiacyl (G) and syringyl (S) units were strong, while the signal of the p-hydroxyphenyl (H) unit was quite weak. The proportion of S:G:H was 1:1:0.09. This indicated that very few p-hydroxyphenyl (H) units were present in palm fiber Soda-25 lignin, which is consistent with the results of ^{1}H NMR analysis.

CONCLUSION

The microscopic structure of palm fiber was studied by micro-CT and SEM. The pulp was obtained by the soda process and the sulfate process. Microscopic analysis demonstrated that the palm pulp fibers were shorter than woody fibers. The physical strength of pulp was greatly improved by adding LPF. Soda lignin from palm fiber had higher molecular weight than hardwood. Structural characterization by NMR revealed the lignin was composed of G and S units. **TJ**

ACKNOWLEDGEMENT

The authors kindly acknowledge funding support (ZR2021MB129) from the Department of Science and Technology of Shandong Province.

LITERATURE CITED

1. Chares, S.M. and Perumalsamy, M., J. *Cleaner Prod.* 05: 100304(2021).
2. Kumar, A.M., Surendra, S., Anil, P., et al., *Renewable Sustainable Energy Rev.* 127(C): 109876(2020).
3. Chen, C.J., Zhang, Y., Wang, G.H., *J. Donghua Univ.* 31(5): 617(2014).
4. Zhang, T.H., Guo, M., Cheng, L., et al., *Cellulose* 22(2): 1039(2015). https://doi.org/10.1007/s10570-015-0570-x.
5. Senthilkumar, K., Saba, N., Rajini, N., et al., *Constr. Build. Mater.* 174(20): 713(2018). https://doi.org/10.1016/j.conbuildmat.2018.04.143.
6. Venkatesan, S.P., Boobalan, L., Bennet, S., et al., *Mater. Today: Proc.* 47(P14): 4373(2021). https://doi.org/10.1016/j.matpr.2021.05.184.
7. Marichelvam, M.K., Manimaran, P., Verma, A., et al., *Polym. Compos.* 42(1): 512(2021). https://doi.org/10.1002/pc.25843.
8. Salleh, K.M., Zakaria, S., Sajab, M.S., et al., *Int. J. Biol. Macromol.* 118(Pt.B): 1422(2018). https://doi.org/10.1016/j.ijbiomac.2018.06.159.
9. Ooi, C.H., Cheah, W.K., Sim, Y.L., et al., *J. Environ. Manage.* 197(15): 199(2017). https://doi.org/10.1016/j.jenvman.2017.03.083.
10. Qu, J. and Zhu, H., *J. Renewable Mater.* 9(4): 767(2021). https://doi.org/10.32604/jrm.2021.013816.
11. Tuandung, H. and Nhuan, N., *Fermentation* 7(4): 314(2021).
12. Ragab Tamer, I.M., Alminderej Fahad, M., ElSayed Wael, A., et al., *Sustainability* 13(24): 13660(2021). https://doi.org/10.3390/su132413660.
13. Saferi, S.K.A. and Yusof, Y., *Appl. Mech. Mater.* 315: 443(2012). https://doi.org/10.4028/www.scientific.net/AMM.315.443.
14. Gomes, F.J.B., Santos, F.A., Colodette, J.L., et al., *Nat. Resour.* 5(9): 419(2014). https://doi.org/10.4236/nr.2014.59039.
15. Palamae, S., Dechatiwongse, P., Choorit, W., et al., *Carbohydr. Polym.* 155(2): 491(2017). https://doi.org/10.1016/j.carbpol.2016.09.004.

ABOUT THE AUTHORS

Palm fiber is abundant in South Africa, and many companies would like to use it as a pulping material. The fiber is very hard and dense in structure, and it is very difficult to dissolve the lignin and isolate the cellulose fibers. For this reason, the microscopic structure of palm fiber was first observed by micro-CT. Most importantly, microscopic images of the pulp fibers were obtained. Comparison was made with other woody fibers. This was very helpful in the explanation of pulp strength.

The cellulose fibers from palm are short compared with woody fibers. The most difficult aspect of this research was determining how to make the paper handsheet strong enough. To address this, we blended in long-fibered softwood kraft pulp at various levels, which was very helpful.

We found that cellulose pulp contains mainly short fibers and fines, which explains the low physical strength of pulp. It was very interesting to see that microfibers in palm fiber are very neatly arranged in the vertical direction.

This study informs mills of the pulping conditions for palm fiber. In addition, it provides a good understanding of this pulp fiber's biometry, including width and length, as well as its difference from woody pulp fibers.

As physical strength is very important, a new pulping process should be developed for palm fiber that can isolate its long fibers and keep the integrity of the fibers.



Li, Z.

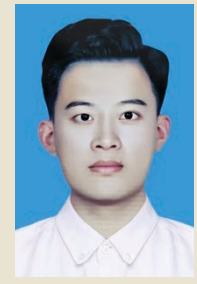

Gao



Tang

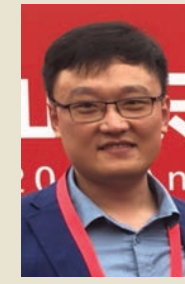

Liu



Li, Q.



Tian



Wang

Z. Li and Gao are master's degree candidates, Tian is assistant professor, and Wang is professor at the State Key Laboratory of Biobased Material and Green Papermaking, Qilu University of Technology (Shandong Academy of Sciences), in Jinan, China. Tang is technical director and Liu is manager of the Technical Department at Shengquan Group Co. Ltd., in Jinan, China. Q. Li is professor at Tianjin University of Science and Technology in Tianjin, China. Email Wang at wzj@qlu.edu.cn.

16. Daud, W.R.W. and Law, K.N., *BioResources* 6(1): 901(2011). https://doi.org/10.15376/biores.6.1.901-917.
17. Jarupan, L., Hunsa Udom, R., and Bumbudsanpharoke, N., *J. Nat. Fibers* 19(7): 2772(2021). https://doi.org/10.1080/15440478.2021.1889433.
18. Jiménez, L., Serrano, L., Rodríguez, A., et al., *Bioresour. Technol.* 100(3): 1262(2008). https://doi.org/10.1016/j.biortech.2008.08.013.
19. Sharma, A.K., Anupam, K., Swaroop, V., et al., *J. Cleaner Prod.* 106: 422(2015). https://doi.org/10.1016/j.jclepro.2014.03.095.
20. Rosli, W.D.W., Law, K.N., Zainuddin, Z., et al., *Bioresour. Technol.* 93(3): 233(2003). https://doi.org/10.1016/j.biortech.2003.11.016.
21. Zhang, T., Guo, M., Cheng, L., et al., *Cellulose* 22(2): 1039(2015). https://doi.org/10.1007/s10570-015-0570-x.
22. Prychid, C.J., Rudall, P.J., and Gregory, M., *Bot. Rev.* 69(4): 377(2003). https://doi.org/10.1663/0006-8101(2004)069[0377:SABOSB]2.0.CO;2.
23. Morais, F.P., Bértolo, R.a.C., Curto, J.M.R., et al., *Mater. Lett.: X* 4: 100028(2019). https://doi.org/10.1016/j.mlblux.2019.100028.
24. Jia, W., Zhou, M., Yang, C., et al., *J. Bioresour. Bioprod.* 7(3): 180(2022). https://doi.org/10.1016/j.jobab.2022.05.002.
25. Yuan, Z., Kapu, N.S., Beatson, R., et al., *Ind. Crops Prod.* 91(30): 66(2016). https://doi.org/10.1016/j.indcrop.2016.06.019.
26. Novo, L.P. and Bras, J., *J. Renewable Mater.* 6(2): 160(2018). https://doi.org/10.7569/JRM.2017.634165.
27. Constant, S., Wienk, H.L.J., Frissen, A.E., et al., *Green Chem.* 18(9): 2651(2016). https://doi.org/10.1039/C5GC03043A.
28. Yuan, J.M., Li, H., Xiao, L.P., et al., *Fuel* 319: 123758(2022). https://doi.org/10.1016/j.fuel.2022.123758.
29. Guan, Y., Shu, T., Gao, H., et al., *Int. J. Biol. Macromol.* 172: 178(2021). https://doi.org/10.1016/j.ijbiomac.2021.01.005.
30. Shakeel, U., Li, X., Wang, B., et al., *Process Biochem.* 117: 198(2022). https://doi.org/10.1016/j.procbio.2022.03.026.

ABOUT THIS PAPER

Cite this article as:
Li, Z., Gao, S., Tang, L., et al., *TAPPI J.* 21(10): 543(2022). https://doi.org/10.32964/TJ21.10.543

DOI: https://doi.org/10.32964/TJ21.10.543

ISSN: 0734-1415

Publisher: TAPPI Press

Copyright: ©TAPPI Press 2022

About this journal

Research on improving the basis weight measurement accuracy of tissue paper based on PSO-BP neural network

LIANHUA HU, YUXIU FENG, AND JIN MA

ABSTRACT: The near-infrared (NIR) sensor can be used for measuring the basis weight and moisture of tissue paper, but the measurement accuracy is not ideal for this paper grade. The weight range of the tissue is 10~30 g/m², indicating that it is a low gram weight paper. The temperature and humidity of the production environment significantly impact an NIR sensor.

This paper focuses on improving the measurement accuracy of tissue paper basis weight. In order to reduce the influences of temperature and humidity, a mathematical model based on a particle swarm optimization back propagation (PSO-BP) neural network is proposed. In comparison with multiple linear regression measurement models, the basis weight measurement error with the PSO-BP model is within ± 0.5 g/m². This model can effectively improve the measurement accuracy and has a good effect on overcoming the basis weight nonlinear effect caused by the changes in ambient temperature and humidity.

Application: The PSO-BP neural network model can eliminate the nonlinear effects of temperature and humidity on basis weight, which provides a new idea for online measurement of paper basis weight for mills in the future.

For tissue paper, basis weight (BW) is an important quality indicator [1]. Higher quality requirements are put forward for the accuracy of online detection [2]. As a green measurement technology, the near-infrared (NIR) sensor has a fast measurement speed, no radiation, no damage, and can analyze and measure multiple components at the same time [3]. Many studies have been focused on NIR for measurement of paper BW and moisture of paper [4-7]. When paper moisture absorbs NIR light, NIR light of different wavelengths will absorb in different components of the paper [8]. In the IR, 1.94 μm is the specific absorption wavelength for water, the signal at 1.83 μm is unaffected by water, the wavelength at 2.10 μm is absorbing fibers, and the wavelength at 2.29 μm is influenced by lignin and latex [9]. According to the above relationship and the reference technology, the paper basis weight can be obtained. However, the temperature and humidity in the environment will have a nonlinear effect on the basis weight of the paper [10,11]. Tissue paper is also more affected by these two factors because of its thinness.

At present, many fields use multi-sensor data fusion to increase information input to predict power generation, rainfall, wind, etc. [12-17]. In order to solve the influences of temperature and humidity on measurement accuracy, this paper uses a particle swarm optimization algorithm (PSO) [18,19] to optimize a back propagation (BP) neural network [20,21] model by combining an IR sensor and temperature and a humidity sensor to reduce measurement error. According to relevant data, the detection accuracy of high basis weight paper-type sensors both in China and overseas is only ±1 g/m² [22]. Multiple linear regression is a commonly used measurement model in engineering. Compared with the model in this paper, the results show that the measurement error of the PSO-BP model is within ±0.5 g/m², which confirms the validity of the model proposed in this paper.

EXPERIMENTAL

The experiment is divided into offline measurement and online measurement. The BW obtained by offline measurement of the sample is used as the output y of model training. The voltage, temperature, and humidity values are measured online when the sample is placed in the sensor. The NIR sensor is used to measure the voltage values of different wavelengths. According to the voltage values and Eq. 1 and Eq. 2 in the "Online data collection and processing" section below, the products x_1, x_2, and x_3 of the mass absorption coefficient and the BW are obtained. The measured temperature and humidity fusion x_1, x_2, and x_3 are used as the input of PSO-BP measurement model, and the actual BW of tissue paper is used as the output to train the neural network. Then, new sample inputs are selected, the paper BW is measured using the trained network, and errors are analyzed in combination with the actual measured values. **Fig. 1** shows the experimental flow.

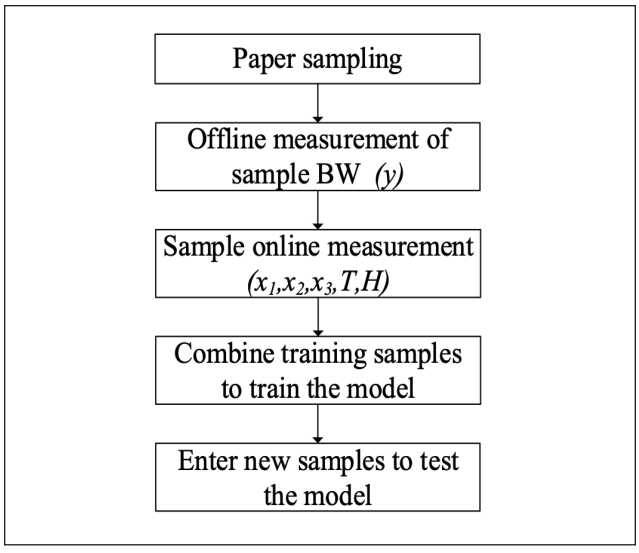

1. Experimental flow chart.

Experimental equipment

The equipment for the experiments included:

1. Paper and paperboard circular BW sampler (TST-A518-1, Dongguan Texter Testing Instrument Co., Ltd.; Guangdong, China).
2. Electronic balance (accuracy of 0.0001 g)
3. Paper sample container (polyvinyl chloride [PVC] plastic releasable bag is generally selected)
4. Oven
5. Dryer
6. The NIR sensor mainly consists of an IR light-transmitting part and a detector (**Fig. 2a**). The main IR light source of the transmitting part is a halogen bulb, and the output signal of the detector receiving part is the voltage signal of four wavelengths, which is the original data from the experiment.
7. The temperature and humidity sensor (Fig. 2b) has a stable signal and measurement accuracy of ± 3% relative humidity (RH) and ± 0.5°C, and can dynamically measure the temperature and humidity of the working environment online.

Offline measurement of experimental samples

As this research primarily studies the BW measurement of tissue paper, the BW of one layer of tissue paper is between 10~20 g/m², so the sample with the BW range of about 16 g/m² was primarily selected as the research object. In order to ensure the measurement accuracy, paper samples of 6 g/m², 10 g/m², 13 g/m², and 18 g/m² were selected for experiments. In the measurement process, the first step was sampling and sample treatment. Sampling and temperature and humidity treatment are carried out according to GBT 24328.5-2009 [23], a National Standard of the People's Republic of China for tissue paper and its products. In order to ensure the uniformity of sampling size, the sampling size of the sampler was 0.01 m² in the experiment [24], and the area deviation was within ±1%. After sampling, electronic balance with an accuracy of 0.0001 g was used to measure each sample, and the value was taken after the balance was stable. During the measurement, the balance was operated according to specifications and to prevent the airflow from affecting the balance. All experimental results were obtained in a laboratory environment with a constant temperature and humidity range. The temperature was 27°C~29°C, and the humidity was 69%~71%. Figure 3 shows samples of the different grams of tissue paper selected for study.

Online data collection and processing

The sample was measured online using an NIR sensor, and according to the characteristics of different wave-

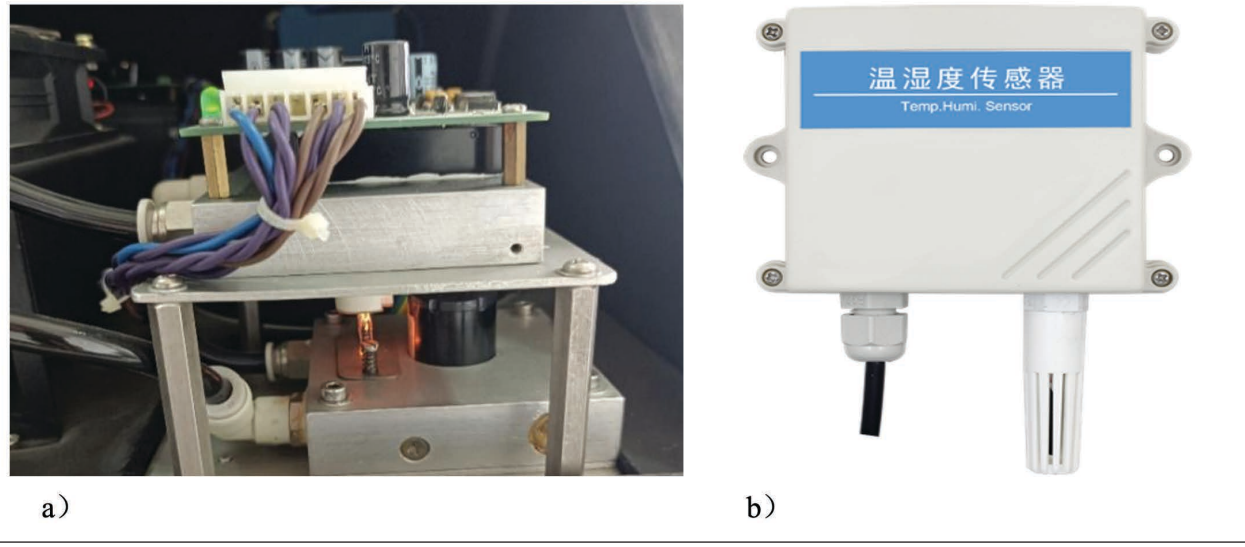

2. Experimental equipment: a) near-infrared sensor and b) temperature and humidity online sensor.



3. Paper samples.

lengths, it was converted into the input x through voltage calculation. When the paper moisture absorbs NIR light, other components in the paper also absorb NIR light to varying degrees. In order to avoid the influence of other components on the measurement results during moisture measurement, the NIR light measurement technology adopts the reference method. Reference technology uses different substances to have different absorption characteristics for NIR light. The 1.83 μm wavelength signal is not affected by moisture in the paper, and can be used as a reference signal for moisture measurement. The measurement of moisture in paper is based on the specific absorption properties of water in the 1.94 μm wavelength NIR light. At this wavelength, the radiation transmission is comparable to the 1.8 wavelength intensity for obtaining moisture content.

Tissue paper mainly includes components such as moisture, fibers, and chemical additives that have one or several characteristic absorption wavelengths in the NIR band. The fiber in the paper has better absorption characteristics at the wavelength of 2.10 μm, and the wavelength of 2.29 μm is mainly affected by the lignin and chemical additives in the paper. The wavelength signals at these two locations can be used to correct moisture measurement errors caused by changes in lignin or chemical additive content. The calibration algorithms all calculate the ratio of the signal at 1.83 μm to each of the other three signals, taking the natural logarithm of these three ratios, temperature, and humidity as inputs to the quantitative model for PSO-BP prediction.

According to the measured voltage signal, it can be concluded that:

$$\begin{aligned} T_R &= V_{183}/V_{183-0} \\ T_W &= V_{194}/V_{194-0} \\ T_F &= V_{210}/V_{210-0} \\ T_C &= V_{229}/V_{229-0} \end{aligned} \tag{1}$$

where T is the standard signal at different wavelengths of NIR light. Subscripts in T_R, T_w, T_F, and T_c represent reference, water, fiber, and chemicals. The V represents the voltage signal, the subscript of the voltage signal represents the wavelength, and the subscript "0" is the voltage in the case of no paper.

According to the Beer-Lambert absorption law:

$$\begin{aligned} x_1 &= \ln\left(T_R/T_W\right) \\ x_2 &= \ln\left(T_R/T_F\right) \\ x_3 &= \ln\left(T_R/T_C\right) \end{aligned} \tag{2}$$

where x_1, x_2, and x_3 are the products of mass absorption coefficient and BW.

Since the main components of tissue paper are fiber and moisture and they contain small amounts of chemical additives, lignin, and other components, the paper BW can be obtained as follows:

$$BW = ax_1 + bx_2 + cx_3 \tag{3}$$

In Eq. 3, a, b, and c are constants that can be obtained by calibration of measured values.

Equation 3 shows that the inputs x_1, x_2, and x_3 have a linear relationship with the paper BW. In practical application, multiple linear regression analysis is usually used in problem analysis with multiple independent variables. The three independent variables in the model are the parameter x. The dependent variable is the actual BW of paper.

Let the multiple linear regression be:

$$y = d_0 + d_1x_1 + d_2x_2 + d_3x_3 \tag{4}$$

In this model, y is BW, x is input, and d is the coefficient of the linear model. The coefficients of the transmission characteristics were determined by linear regression modeling analysis using the experimental data measured by NIR light. Solving the system of equations in MATLAB (MathWorks; Natick, MA, USA), the linear regression equation between input and output is:

$$y = 146.03x_1 - 168.65x_2 - 78.92x_3 + 27.5691 \tag{5}$$

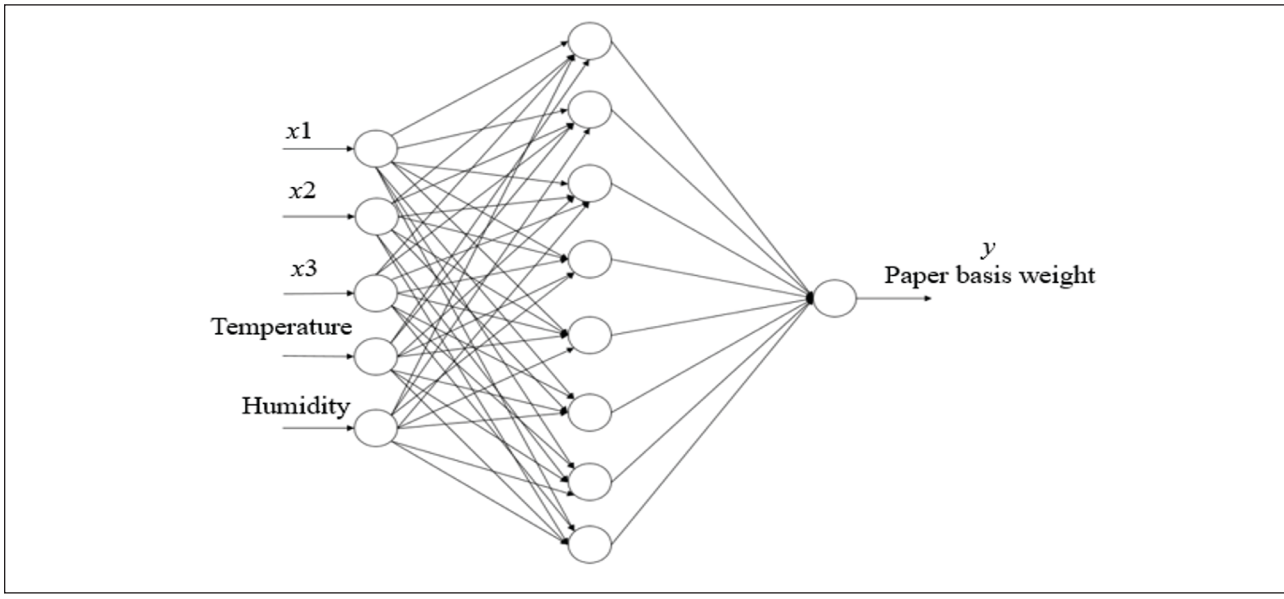

4. Back propagation (BP) neural network structure.

Establishment of PSO-BP prediction model

The structure of the BP neural network includes the input layer, hidden layer, and output layer. The BP neural network is trained according to the method of error back propagation calculation. The principle is to correct the weights of each layer from back to front by collecting the errors generated each time. When the learning error and learning times of the network reach the specified target, the output value can be predicted through the input.

The three important parameters x_1, x_2, and x_3 are measured by the sensor, and the temperature and humidity in the air are used as inputs for the neural network, so the input layer sets five nodes. The actual weighing value of tissue paper is the output value y of the model, and the number of nodes in the output layer is 1. In the selection of the number of hidden layers, one hidden layer is selected to avoid overfitting and computer over operation. In general, the number of nodes in the hidden layer is positively correlated with the nonlinear degree of the network. The more the number of nodes, the higher the nonlinear degree. However, if the number of nodes is too large, the network operation will increase and the network operation efficiency will decrease. If the number of nodes is too small, it is difficult to judge the nonlinear relationship between the input value and the output value, which leads to a larger error. The number of nodes that selects the hidden layer in the neural network is generally less than twice the input. In practical problems, the selection of the number of hidden layer nodes first determines the approximate range and then uses the trial-and-error method to determine the optimal number of nodes. Therefore, the range of hidden layer nodes in this study was less than 10, and eight nodes were selected through comparison.

Figure 4 shows the BP network structure of the algorithm model. When establishing the measurement model, y is the actual BW value.

The basic idea of the BP network is to correct the network weights w_{ij} and T_{li} and the thresholds θ_i and θ_l, to minimize the mean square error.

The input of the hidden layer node is:

$$net_i = \sum_j w_{ij} x_j - \theta_i \tag{6}$$

where x_j denotes the input, w_{ij} denotes the network weight between the input layer and the hidden layer, and θ_i denotes the network threshold between the input layer and the hidden layer.

The input to the output layer node is:

$$net_l = \sum_i T_{li} x_i - \theta_l = a_1 \tag{7}$$

where x_i denotes the hidden layer node, T_{li} denotes the network weight between the hidden layer and the output layer, and θ_l denotes the network threshold between the hidden layer and the output layer.

The network structure of the final prediction model is shown in **Fig. 5**. It can be seen that the structure has five input nodes, eight hidden nodes, and one output node; a_0 is the input, a_1 is the hidden layer output, and a_2 is the output. The W and b denote the weight and bias between different layers, respectively. In this model, the tansig hyperbolic tangent sigmoid transfer function in MATLAB was selected for the hidden layer, and the purelin linear transfer function in MATLAB was selected for the output layer.

However, the initial weights and thresholds of the BP neural network model need to be selected. It is difficult to select the suitable parameters at one time, which can cause poor training results. Debugging training parameters many

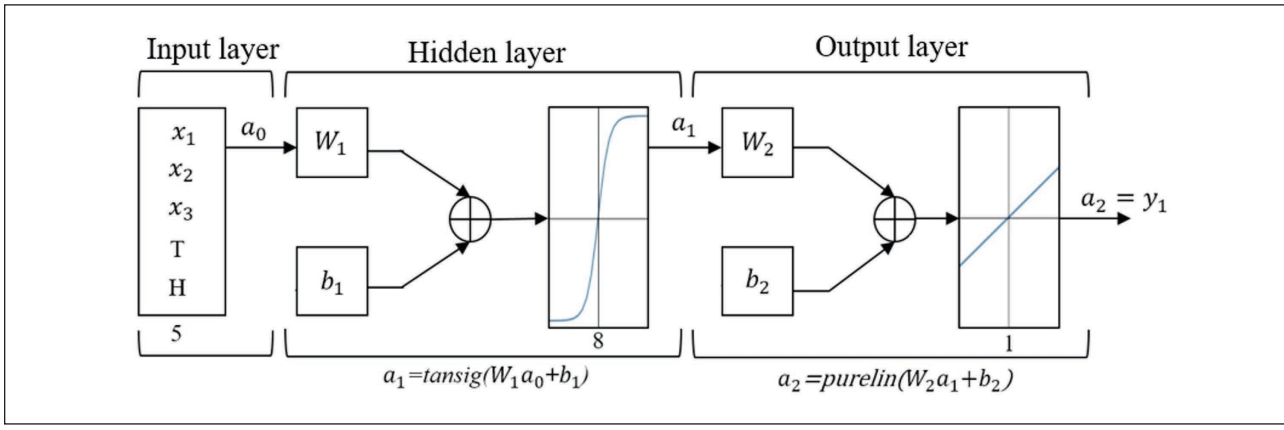

5. Neural network model.

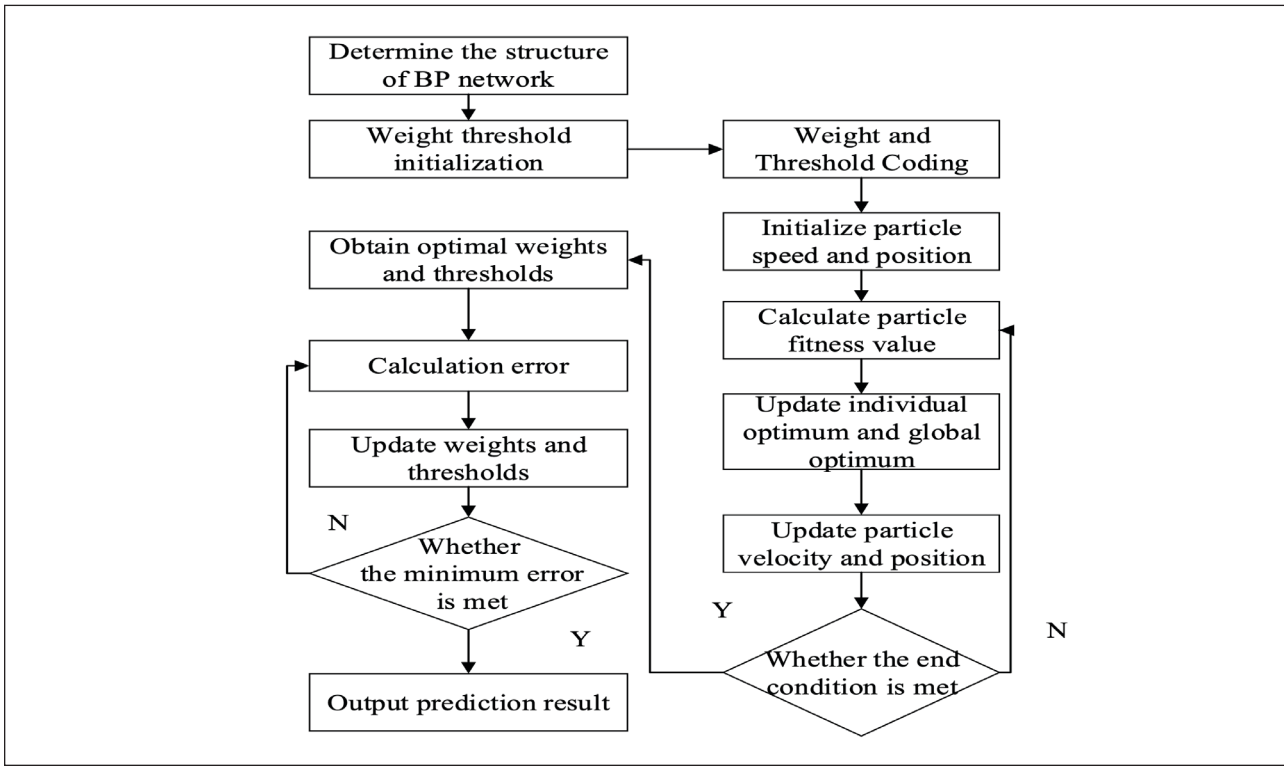

6. Flow chart of particle swarm optimization back propagation (PSO-BP) neural network.

times not only wastes time but also leads to overfitting of training. The PSO algorithm can automatically adjust and match the optimal parameters of the BP neural network through its strong global search ability and can rapidly improve the learning performance and global convergence speed of the network [25].

The essence of particle swarm optimization is a random search algorithm. The trajectory of each particle is mainly determined by the current position of the particle itself, the historical optimal position of the particle itself, and the historical optimal position of the particle swarm. Through these three factors, the particle can adjust the movement speed and position in real time, and can repeatedly iterate to find the optimal solution. The process of the PSO algorithm optimizing BP network is shown in **Fig. 6**.

The adjustment of several parameters in a PSO optimization algorithm has a great impact on the performance of the algorithm, including population size, inertia weight, acceleration coefficient, maximum speed of particles, etc. In the particle swarm optimization model, the particle swarm size is generally set between 20 and 50, and the difficulty gradually increases according to the specific problem. The model training based on different swarm sizes shows that when the swarm size is 20 and 50, the running effect is better than when the swarm size is 30 and 40. When the swarm size is 20, the running time is faster than when the swarm size is 50. Considering the running speed and running effect, the number of particle swarm size is

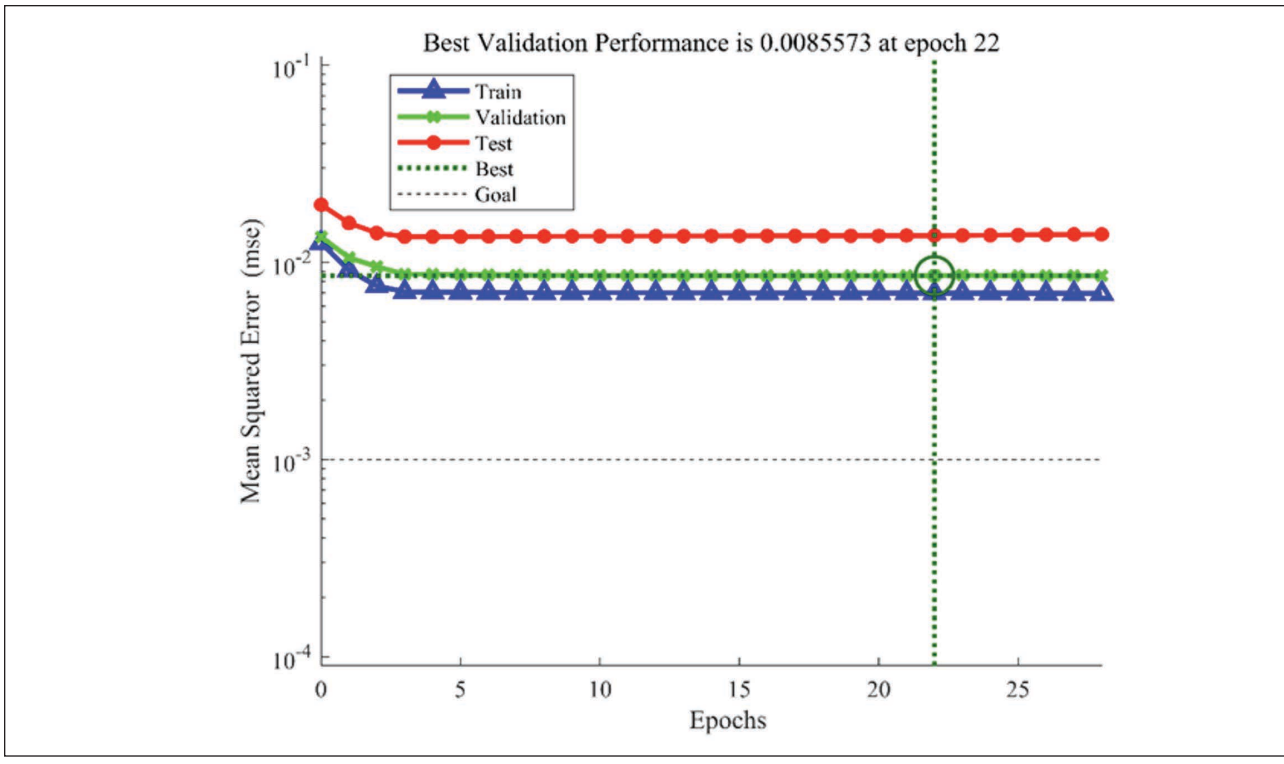

7. The PSO-BP training network paper basis weight measurement error.

selected as 20. The inertia weight controls the ability of global optimization and local optimization, and the value range is between 0.8 and 1.2. The acceleration constant is used to adjust the maximum step size of the search, and 1.5 is usually chosen to make the individual experience as important as the group experience and to avoid falling into a local optimum. The maximum speed range is tuned and between -0.5 and 0.5 to avoid getting stuck in local optima.

During the training process of the PSO-BP neural network in MATLAB, the PSO algorithm stops running when the desired goal is reached. Once the mean square error reaches the desired value, the BP network will stop learning to complete the model training.

RESULTS AND DISCUSSION

When selecting training samples, 1000 groups of raw data of 10 g/m², 13 g/m², 16 g/m², and 18 g/m² were selected for PSO-BP neural network training. The trained model can

Sequence	x_1	x_2	x_3	Temperature, °C	Humidity, %	Actual Basis Weight, g/m²
1	0.1171	0.0481	0.2983	18.2292	35.7083	15.92
2	0.1119	0.0261	0.2700	18.2986	35.6215	15.61
3	0.1121	0.0375	0.3177	18.2292	35.5637	15.91
4	0.1204	0.0612	0.2727	18.2292	35.5637	16.33
5	0.1199	0.0620	0.2766	18.2292	35.4190	15.55
6	0.1222	0.0536	0.3015	18.1944	35.4190	16.24
7	0.1124	0.0489	0.2681	18.1944	35.3322	15.86
8	0.1104	0.0299	0.3104	18.2986	35.1586	15.65
9	0.1189	0.0356	0.2970	18.2292	35.1586	15.53
10	0.1197	0.0369	0.3070	18.2986	35.0139	15.42

I. Data from training samples.

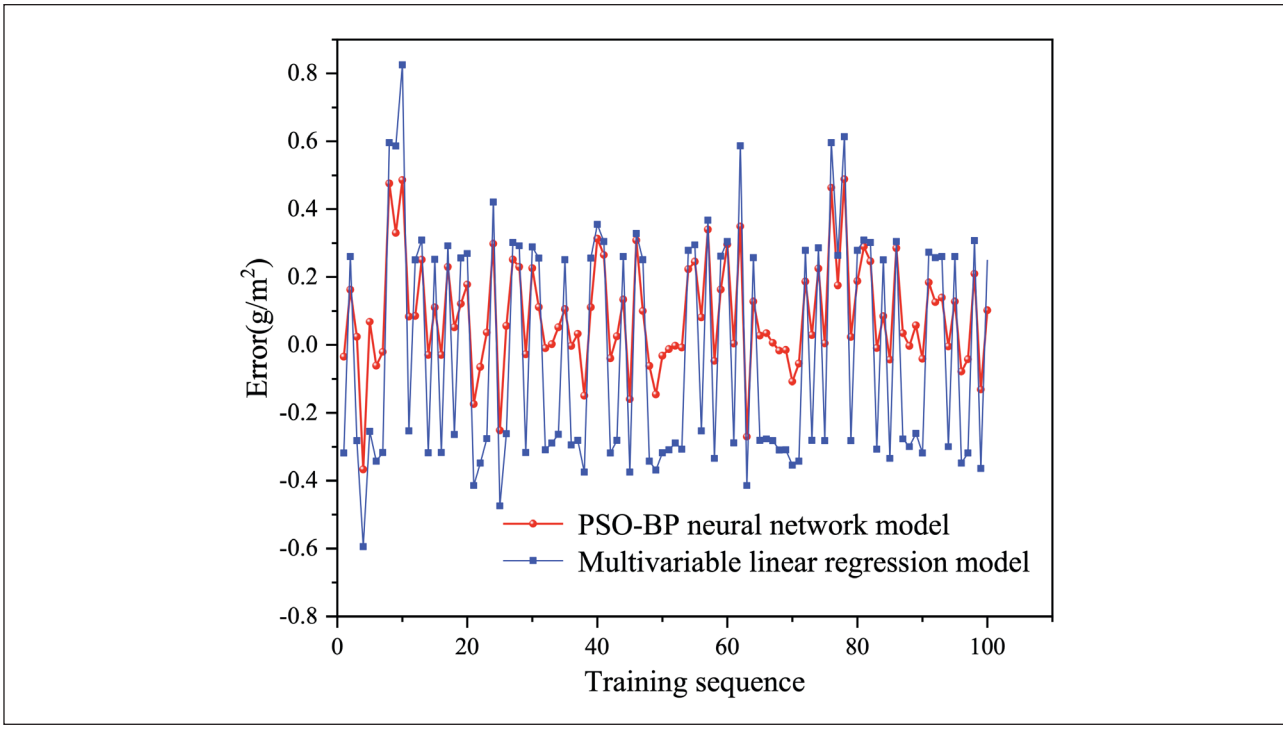

8. Error comparison of two model algorithms.

be applied in the BW range of 10~20 g/m². **Figure 7** shows the process from start of training to model convergence. Epoch is the number of times the neuron weights and thresholds are adjusted based on the output error return during computation. It can be seen that the model training speed is fast and reaches the best state after 22 iterations. The input and output of some training samples are shown in **Table I**.

One-hundred groups of sample data were selected as the PSO-BP neural network test data, and the prediction results of the model were compared with the results of the multiple linear regression model. **Figure 8** indicates that the PSO-BP neural network model can improve the measurement accuracy in the NIR light tissue quantitative measurement system. The BW fluctuation of the product BW measurement standard is ±1 g/m². The measurement deviation of PSO-BP is controlled within ±0.5 g/m². Compared with the measurement deviation of multivariate linearity of ±0.9 g/m², the measurement accuracy is significantly improved.

The 100 sets of test data show that the PSO-BP neural network model can improve the measurement accuracy of the NIR light tissue BW measurement system. Compared with the linear model, the PSO-BP neural network model takes into account the nonlinear effects of ambient temperature and humidity on the measurement results, so the measurement accuracy is higher and the error is lower.

Hence, in the NIR light paper BW measurement system, the intelligent BW measurement model based on adaptive PSO-BP neural network technology can effectively overcome the nonlinear drift in the measurement process and solve the nonlinear problem in the measurement system.

CONCLUSION

This research focused on the problem of measurement error caused by the interference of ambient temperature and humidity in the BW of tissue paper. The offline and online measurement of toilet paper produced by 10 different papermaking enterprises was carried out in the laboratory, and the BW measurement mathematical model was established according to the measurement results. Drawing on the idea of multi-sensor data fusion and adding the input of temperature and humidity, the paper BW measurement model based on the PSO optimized BP algorithm is proposed to further improve the accuracy of the measurement results. As a nonlinear model, the PSO-BP neural network model effectively solves the problem of BW measurement of tissue paper caused by the nonlinear drift of temperature and humidity changes in the air. At the same time, the acquisition speed and processing speed of the PLC control system of the paper mill meets the hardware requirements of the model. Therefore, combined with measurement accuracy and usability, the model represents a positive development trend for paper mills in the future. **TJ**

ACKNOWLEDGMENTS

The authors gratefully acknowledge the fund of Shaanxi University of Science and Technology (BJ15-19), along with the Youth Innovation Team of Shaanxi Universities.

LITERATURE CITED

1. Chen, Y., Du, S., and Yuan, Z., *Chin. J.* 32(10): 112(2013).
2. Adamopoulos, S., Passialis, C., Voulgaridis, E., et al., *Drewno* 57(191) :145(2014).
3. Chu, X., Shi, Y., Chen, B., et, al., *J. Instrum. Anal.* 38(6): 603(2019).
4. Dong, P., "Study of paper moisture and weight testing techniques based on near-infrared radio," Master's thesis, Chang' an University, Xi'an, China, 2009.
5. Kangasraasio, J., *Measurement* 44(10): 1937(2011). https://doi.org/10.1016/j.measurement.2011.08.024.
6. Ye, W. and Sun, Y., *Laser Infrared* 30(4): 230(2000).
7. Yu, D.H., Li, L., Cao, L.H., et al., *Adv. Mater. Res.* 562: 1348(2012). https://doi.org/10.4028/www.scientific.net/AMR.562-564.1348.
8. Tsuchikawa, S., *Appl. Spectrosc. Rev.* 42(1): 43(2007). https://doi.org/10.1080/05704920601036707.
9. Hu, L. and Ma, J., *TAPPI J.* 21(5): 247(2022). https://doi.org/10.32964/TJ21.5.247.
10. De Ruvo, A., Lundberg, R., Martin-Löf, S., et al., *Fundam. Prop. Pap. Relat. Its Uses, Trans. Symp.*, British Paper Board Industry Federation, London, 1976, p. 785.
11. Liu Jianghao, G.S., Wang, Y., Li, X., et al., *J. Beijing Inst. Graphic Commun.* 21(4): 5(2013).
12. Azmi, M., Araghinejad, S., and Kholghi, M., *Iran. J. Sci. Technol., Trans. B: Eng.* 34(B1): 81(2010).
13. Bashari, M., Rahimi-Kian, A., Farhangi, S., et al., *Smart Grid Conf.*, Institute of Electrical and Electronics Engineers (IEEE), Piscataway, NJ, USA, 2014. https://doi.org/10.1109/SGC.2014.7090856.
14. Huang, L., Liu, X., Wei, H., et al., "Urban rainfall forecasting method based on multi-model prediction information fusion," *6th IEEE Int. Conf. Inf. Manage. (ICIM)*, Institute of Electrical and Electronics Engineers (IEEE), Piscataway, NJ, USA, 2020, p. 210.
15. Moran Loza, J.M., Perez Cisneros, M.A., and Garcia Arreola, A., "Artificial neural networks vs regression techniques in the forecasting of contaminants in the Santiago River, based on the sample of a pollutant, through data fusion," *Int. Conf. Smart Technol. Smart Nation (SmartTechCon)*, Institute of Electrical and Electronics Engineers (IEEE), Piscataway, NJ, USA, 2017, p. 183. https://doi.org/10.1109/SmartTechCon.2017.8358366.
16. Shao, H. and Deng, X., *Int. J. Electr. Power Energy Syst.* 83: 79(2016). https://doi.org/10.1016/j.ijepes.2016.03.059.

ABOUT THIS PAPER

Cite this article as:
Hu, L., Feng, Y., and Ma, J., *TAPPI J.* 21(10): 553(2022). https://doi.org/10.32964/TJ21.10.553

DOI: https://doi.org/10.32964/TJ21.10.553

ISSN: 0734-1415

Publisher: TAPPI Press

Copyright: ©TAPPI Press 2022

About this journal

ABOUT THE AUTHORS

As an important indicator of paper quality, paper basis weight is easily affected by the nonlinear effects of temperature and humidity in the environment. A method is needed to overcome nonlinear effects to improve measurement accuracy.

There are currently no studies applying machine learning and smart algorithms to paper measurement. This study draws on the idea of multi-sensor data fusion and solves the nonlinear effect of temperature and humidity through a PSO-BP network to improve the measurement accuracy.

This is the first time that the intelligent algorithm has been applied to the basis weight measurement of paper. The establishment and debugging of the mathematical model were difficult. The offline weighing value and online measurement value were combined as a sample set, and the model was debugged based on experience.

Through this study, we discovered a new method to improve the measurement accuracy of infrared sensors. The proposed model effectively overcomes the nonlinear change of temperature and humidity, and it improves the accuracy of the infrared sensor.

The acquisition speed and processing speed of paper mill PLC control systems meets the hardware requirements of the model. The training speed and measurement accuracy of the model are suitable for online measurement in paper mills. The next step is to improve the applicability of the algorithm and make the model suitable for other types of paper in addition to tissue. The model was successfully tested in the laboratory paper machine scanner, and the next step is to realize online measurement in paper mills.



Hu



Feng



Ma

Hu is associate professor, Feng is a Master's student and Ma is a Master's student in the College of Mechanical and Electrical Engineering, Shaanxi University of Science and Technology, Xi'an, Shaanxi, China. Email Hu at hulianhua@sust.edu.cn

17. Tan, Y., Teng, Z., Zhang, C., et al., *4th IEEE Int. Conf. Power Energy Appl. (ICPEA)*, Institute of Electrical and Electronics Engineers (IEEE), Piscataway, NJ, USA, 2021, p. 104.

18. Liu, Y., Chen, J., and Guo, Q., *J. Beijing Univ. Chem. Technol., Nat. Sci. Ed.* 42(04): 95(2015).

19. Huang, Y., Lu, H., Xu, K., et al., *Comput. Sci.* 46(01): 245(2019).

20. Jin, W., Li, Z.J., Wei, L.S., et al., *5th Int Conf. Signal Processing, 16th World Computer Congr.*, Institute of Electrical and Electronics Engineers (IEEE), Piscataway, NJ, USA, 2000, p. 1647.

21. Li, J., Cheng, J.-H., Shi, J.-Y., et al., "Brief introduction of back propagation (BP) neural network algorithm and its improvement," in *Advances in Computer Science and Information Engineering* (D. Jin and S. Lin, Eds.), Advances in Intelligent and Soft Computing, Vol. 169, Springer, Berlin/Heidelberg. https://doi.org/10.1007/978-3-642-30223-7_87.

22. Hu, L., Li, X., and Tang, W., *China Pulp Pap.* 30(2): 46(2011).

23. National Standard of the People's Republic of China, General Administration of Quality Supervision, GB/T 24328.5-2009[S], "Tissue paper and its products. Part V. Quantitative measurement," 2009.

24. Su, D., Chen, H., Zhao, G., et al., *Agric. Sci. Technol.* 18(10): 1948(2017).

25. Chao Ren, N.A., Wang, J., Li, L., et al., *Knowl. Based Syst.* 56: 226(2014). https://doi.org/10.1016/j.knosys.2013.11.015.

Nanocellulose–cationic starch–colloidal silica systems for papermaking: Effects on process and paper properties

LARDEN J. GARLAND, BRANDON D. LEIB, NELSON A. BARRIOS, AND MARTIN A. HUBBE

ABSTRACT: Laboratory tests were conducted to better understand effects on the papermaking process and handsheets when recycled copy paper furnish was treated with combinations of nanofibrillated cellulose (NFC), cationic starch, colloidal silica, and cationic retention aid (cPAM; cationic polyacrylamide). Dosage-response experiments helped to define conditions leading to favorable processing outcomes, including dewatering rates and the efficiency of fine-particle retention during papermaking. Effects were found to depend on the addition amounts of cationic starch and colloidal silica added to the system. It was shown that the presence of a polymer additive such as cationic starch was essential in order to achieve large strength gains with simultaneous usage of NFC.

Application: Papermakers can regard NFC as an option for increasing the bonding strength of the resulting paper beyond what generally can be achieved with conventional wet-end additives. However, as shown in the present work, other additives, such as cationic starch and colloidal silica, may be required at suitable levels of addition to achieve the potential benefits of nanocellulose.

The dry strength of paper products is critically important in many applications, including printing and packaging. Strength is often the limiting factor that determines whether it is possible to reduce the basis weight or the amount of premium virgin fibers within a paper product. It is well known that paper's strength critically depends on the interfiber bonding [1]. Papermakers employ mechanical refining as a primary tool to increase the bonding between kraft pulp fibers [2]. However, there are practical limits to refining. With increased refining, the material becomes increasingly broken down with the release of cellulosic fines. Especially when they are not attached to the fiber surfaces by the use of retention aids, these fines can adversely affect the rates of dewatering [3]. Excessive refining reduces the inherent strength of a fiber, which eventually damages paper strength [1]. In addition, kraft pulp fibers that have been recovered from used paper tend to have a reduced ability to bond to each other [4].

Very highly fibrillated cellulose material, which in this research paper will be called nanofibrillated cellulose (NFC), offers a means to greatly increase interfiber bonding within paper. This is an attractive option, since NFC can be made from widely available, relatively inexpensive material, i.e., kraft pulp fibers [5,6]. Some recent studies have shown that NFC offers a way to achieve high increases in the bonding strength of paper [5,7]. However, due to its small size, NFC particles can be difficult to retain efficiently during paper's formation [8,9]. In addition, the NFC can choke up drainage channels within the wet web, leading to slow dewatering [7].

Though the overall effects of NFC on paper strength and the dewatering during paper's formation have been well known [5], it has been less common for such studies to also report effects due to other papermaking additives. Three exceptions to that rule are worth noting. Petroudy and coauthors showed large benefits when a cationic acrylamide copolymer (retention aid) was used in combination with microfibrillated cellulose prepared from bagasse pulp [10]. The tensile strength of the resulting paper was increased by 28% with the addition of 1% of the MFC to the fiber suspension. The dewatering rate was maintained when using the retention aid, whereas it became slower when the MFC was used alone. Merayo et al. achieved an 11% increase in paper's tensile strength with just 0.5% of NFC added to the furnish, and again a cationic retention aid was used to maintain high fines retention and to avoid a decrease in drainage [11]. Followup work achieved a higher tensile strength increase at a 1.5% addition level of NFC, with use of a cationic retention aid to maintain retention of the fine materials [12]. Cationic starch had been utilized in a study by Manninen et al. [13], but drainage properties had not been monitored. Thus, there has been a need to consider paper strength, dewatering, and other outcomes in systems that include such additives as NFC, cationic starch, cationic retention aid, and colloidal silica.

Recent work by Rice et al. [14] demonstrated a treatment strategy whereby NFC was pretreated first by cationic starch and then by colloidal silica. Not only did this combination contribute to a large increase in the paper's dry strength, but it also helped to overcome the negative effect

of NFC on the drainage rate. The focus of the cited work was on the preparation of paper products having low apparent density. In particular, the described treatment system made it possible to achieve high gains in paper stiffness with greatly reduced refining of the main kraft pulp component. The objective of the present work is to better understand the results obtained in the earlier study and to widen the focus beyond the high-bulk category of paper products. Thus, the attention here will include relatively dense paper products, such as writing paper, linerboard, and other packaging products. A further goal is to study the factors contributing to dewatering, first-pass retention, the uniformity of formation, and physical properties of the resulting paper.

The present article, which is based on laboratory research carried out by students at North Carolina State University (Raleigh, NC, USA), deals with some issues that have arisen in recent studies of the use of highly fibrillated cellulose products in papermaking. Laboratory tests can provide opportunities for multiple replications, as well as precise definition, of the compositions and procedures. The idea was to establish a baseline for additional needed work. To add to that baseline, results of further laboratory studies are embodied in two companion articles, which are also appearing in this journal. One of those companion articles focuses on previously unknown effects of the orders of addition of the chemical agents. The third article in this set focuses on the likely mechanisms. In addition, there will be an ongoing need for followup work at the pilot-scale and commercial levels of papermaking.

EXPERIMENTAL

Chemicals and materials

The fiber furnish used throughout this work was prepared by the repulping of 100% recycled copy paper (trademarked Boise ASPEN 100 Multi-use Recycled Copy Paper, Packaging Corporation of America, Boise Paper Division).

Nanofibrillated cellulose (NFC), in dry form, was obtained from the University of Maine (Orono, ME, USA). Three versions were employed: spray-dried, freeze-dried, and TEMPO-oxidized. In addition, a microfibrillated cellulose product was obtained in slurry form from Stora Enso Oyj (Helsinki). The default level of addition (except for the blank) was 5% on a furnish dry-mass basis. The way this was chosen is that (a) 5% is enough to have a very large effect in decreasing the rate of dewatering, and (b) the amount is not so high as to be outside the range of interest of papermakers (but on the high side).

The cationic starch was Chargemaster L340 from Grain Processing Corp. (GPC; Muscatine, IA, USA). This is a pregelatinized paste version having a relatively high cationic starch density. The paste was kept in a refrigerator. Batches of starch were prepared at 1% solids, using warm water.

The colloidal silica type used in most of the work was Fennosil 2180, a product of Kemira Oyj (Helsinki). This is a high-structured (gel-type) colloidal silica. Some tests also were carried out with Fennosil 5000 (medium-structure gel-type) and Fennosil 615 PA EN (low structure). Each colloidal silica product was diluted to 1% actives before its use in the experiments.

Accurac 90, a very-high-mass cationic copolymer of acrylamide (American Cyanamid), served as the retention aid for this work. The dry powder was diluted with agitation for an hour to a solids content of 0.1% before its use in the tests.

Deionized water was used for dilution of all chemical additives. Tap water was used for preparation of handsheets. The sodium sulfate was reagent grade. A diagram depicting the options for order of addition of additives in this type of experiment already appeared in the article by Rice et al. in this journal [14].

Pulp preparation

For preparation of batches of 0.5% solids pulp suspension, the paper taken from reams was assumed to have a constant 6% moisture content. The kilograms of dry paper were determined by multiplying the total intended volume of pulp in liters (e.g., 60 L) by 0.005 over 0.94 (where 0.94 is the solids content of the paper). The paper was torn into pieces, each smaller than 1/8 of a sheet. The pieces were soaked overnight. Then, the damp paper pieces were subjected to no-load "brushing" treatment (no weight applied) for 15 min with a laboratory Hollander beater, with a pulp consistency of approximately 2%. The pulp was added to a roll-around plastic barrel and diluted to a consistency greater than 0.5% (slightly below the target volume). With a probe of electrical conductivity inserted into the pulp suspension, and with vigorous agitation, increasing amounts of ca. 5% sodium sulfate were added, aiming for a final conductivity of 1000 μS/cm. This was followed by final adjustment of the consistency to 0.5%. Pulp was kept in a cold room when being stored for up to two weeks, and it was allowed to warm up to room temperature overnight before testing.

Dewatering tests

Two essentially equivalent devices were employed to obtain Schopper-Riegler filtrate mass as a function of drainage time. A majority of tests were carried out using the Mutek DFR-05 device from BTG Inc. (London), using the following settings: spin for 10 x at 700 rpm, then 10 s at 800 rpm, and then release.

Some supplementary tests were carried out with a portable modified Schopper-Riegler tester. The standard device of this type is described in the ISO 5267 Test Method "Pulps — Determination of drainability — Part 1: Schopper-Riegler method." The modified device replaces the capillary opening and side spout with a simple large central opening for the filtrate to pass through. By this means, the filtrate mass can be measured as a function of time using an analytical balance having a measurement precision of 0.1 g.

Retention tests

The efficiency of retaining fine particles, including mineral fillers and cellulosic fines, was evaluated using a Britt dynamic drainage/retention jar [15,16]. A conventional 200-mesh stainless-steel screen was employed. In a typical test, there was a 30 s delay between addition of each successive additive to the mixture under a continuous agitation, usually at 600 rpm. An indication of the unretained fines was obtained by measurement of the turbidity of filtrate [17]. Reported mean values and 95% confidence intervals of the mean were based on ten replicate tests, which involved five samples taken from the device (with pairs of measurements obtained with a gentle overturning of the capped vial and retesting). Because the initial readings routinely exceeded the measurable range, it was standard procedure to dilute each specimen by a factor of ten and then multiply the reading by 10. Based on the Beer-Lambert Law [18], the turbidity in NTU units is expected to be approximately proportional to the contents of insoluble solids in the filtrate.

Flocculation tests

The degree of flocculation among fibers in the suspension, including change in flocculation due to various additives, was evaluated with use of a Photometric Dispersion Analyser (PDA, low-gain version) from Rank Brothers Ltd. (Bottisham, UK). The PDA unit was set up such that 0.5% consistency suspension was drawn into clear flexible tubing having an inner diameter of approximately 6 mm (Tygon S3 E-3603 NSI, OD ca. 8.5 mm). The tubing was passed through the sensing zone of the PDA, in which the change in transmission of white light was measured as a function of time. Both gain constants were set to 1.0, and the "Root-mean-squared" (RMS) and "Filter" buttons were depressed, thus providing the RMS value of deviations from the mean intensity of transmitted light through the tubing. This unitless value provides an indication of the degree of flocculation, though it is not specifically related to floc size or floc density by any known theory.

Streaming potential tests

Zeta potential information for the fiber surfaces was obtained by running streaming potential tests on pads of fibers drawn against a filter screen by a specified vacuum (700 mm Hg). The change in electrical potential was evaluated by placing welding wire probes on the two sides of the screen, with the use of fine Tygon tubing and plumber's adhesive to fully insulate the submerged parts of the wires except for the intended measurement areas. For each individual measurement (with at least four replications), the initial value from a millivolt meter (with accuracy 0.1 mV) was obtained once a stable value had been reached, usually about 30 s after the start of vacuum application. At that point the vacuum was broken, using a quick-release fitting in the tubing, and a zero-vacuum value was obtained after waiting 2 s. The zeta potential was then calculated from Eq. 1:

$$\zeta = 4\pi\ \Delta E\ \eta\ \lambda\ /\ (\Delta P \varepsilon) \quad (1)$$

where ΔE is the change in measured streaming potential (vacuum applied – without vacuum), η is the shear viscosity of the solution (assumed to equal that of pure water), λ is the electrical conductivity, ΔP is the difference between the applied vacuum level and zero, and ε is the dielectric constant. After applying corrections for the effects of temperature on electrical conductivity and viscosity, the following version of the equation was used in the calculations:

$$\zeta(\text{mV}) = 12.27\ \Delta E(\text{mV}) * [\lambda(\mu\text{S/cm})/\Delta P(\text{mm Hg})] * [1+(25-\theta)/44.74]/\ [1+(25-\theta)/223.7] \quad (2)$$

In this equation, θ stands for the temperature in °C.

Charge demand titrations

The cationic demand or the anionic demand values of various aqueous mixtures (usually sampled as 10 mL aliquots) were obtained using a CA Touch streaming current detector from emtec Electronic (Leipzig, Germany). The device features a polytetrafluoroethyene (PTFE) piston (diameter approximately 15 mm) that moves up and down at about 4 Hz within a loosely fitted PFTE boot (gap width less than 1 mm). By means of electrode probes near the base of the boot and above the annular region, the device essentially senses the presence and sign of charge of an electrical double layer at the PTFE surfaces. Because those surfaces will be coated by polyelectrolytes and colloidal material from an aqueous sample, it can be used for detection of the endpoint of a titration with known polyelectrolytes. Poly(diallyldimethylammonium chloride) (polyDADMAC) (0.001 molar solution) was used as the cationic titrant, and the potassium salt of poly(vinyl sulfate) (PVSK) was used as the anionic titrant (0.001 M).

RESULTS

Characteristics of the fiber suspension

As shown in **Table I**, the pH of the fiber suspension remained within the range of 8.3 to 8.9 for all of the experimental conditions considered. This pH range is consistent with the usage of 100% recycled fiber content xerographic copy paper as the fiber furnish for this work. Recycled office paper can be expected to contain about 10% to 25% of calcium carbonate ($CaCO_3$ filler), which will tend to buffer the pH when it is placed into water [19]. None of the listed treatment conditions included enough acid content to dissolve the $CaCO_3$ and overpower its pH-buffering effect.

Results for zeta potential (calculated from the streaming potential test results) showed clear effects related to the additives considered in this work. For example, adding cationic polyacrylamide (cPAM) retention aid at a level of just 0.05% (solids basis) to the suspension decreased the nega-

Specimen	pH	Zeta Potential, mV	Cationic Demand, µeq/L
100% DIP (default)	8.6	-21.4	23.2
DIP + 0.05% cPAM	8.3	-14.9	17.8
DIP + 5% NFC	8.6	-32.4	31.6
DIP + NFC + cPAM	8.7	-25.6	20.2
1% cationic starch + NFC + DIP + cPAM	8.4	-19.5	7.8
2% cationic starch + NFC + DIP + cPAM	8.8	-8.8	-34.4
5% cationic starch + NFC + DIP + cPAM	8.6	14.9	-157
10% cationic starch + NFC + DIP + cPAM	8.7	19.1	-404
1% cationic starch + NFC + DIP	8.9	-15.6	9.6
2% cationic starch + NFC + DIP	8.8	8.0	-32
5% cationic starch + NFC + DIP	8.8	3.8	-161
10% cationic starch + NFC + DIP	8.7	4.2	-401

DIP = deinked pulp; NFC = nanofibrillated cellulose; cPAM = cationic polyacrylamide (retention aid).

I. Properties of fiber suspensions.

tive zeta potential (absolute value) by about 30%. By contrast, the individual effect of adding nanofibrillated cellulose (freeze-dried type) to the deinked pulp (DIP) furnish was to make the zeta potential even more negative. This is consistent with the expected negative charge of freeze-dried NFC. The zeta potential was shown to become less negative or more positive with increasing addition levels of cationic starch. As shown in the table, between a 2% and a 5% level of cationic starch addition (based on solids) was sufficient to overcome the charge demand of the fibers and nanocellulose (whether or not cPAM was present), thereby giving a positive zeta potential.

As described earlier, the cationic demand results shown in Table I were based on filtrates obtained from the corresponding mixtures after stirring. In most cases, the sign of cationic demand was opposite to that of the measured zeta potential. This is because slurry systems having a negative zeta potential are likely to have an excess of negatively charged dissolved and colloidal titratable substances in the aqueous phase. An exception to the rule was found in the system with 2% cationic starch with NFC, DIP furnish, and cPAM. In that case, the zeta potential was still negative, though the charge titration showed an excess of cationic substances in the filtrate. Related observations were reported by Strazdins [20], who attributed such findings to progressive permeation of cationic polymers into the mesopores of kraft fibers.

Effects of nanofibrillated cellulose addition

In principle, nanofribrillated cellulose can improve paper strength due to increased interfiber bonding. The high flexibility of NFC in the wet state allows it to efficiently fill spaces between adjacent rough fiber surfaces. It is assumed that progressively more solid-to-solid hydrogen bonds will be established both within the NFC and also with the fiber surfaces as water becomes evaporated during drying of the paper. The strength testing data (**Fig. 1**) showed that increasing the nanofibrillated cellulose percentage increased the breaking length of the paper. As suggested by the 95% confidence interval bars, a significant increase in strength was already apparent at the 0.5% level of addition (based on solids). Thereafter, the breaking length continued to increase, though less sharply.

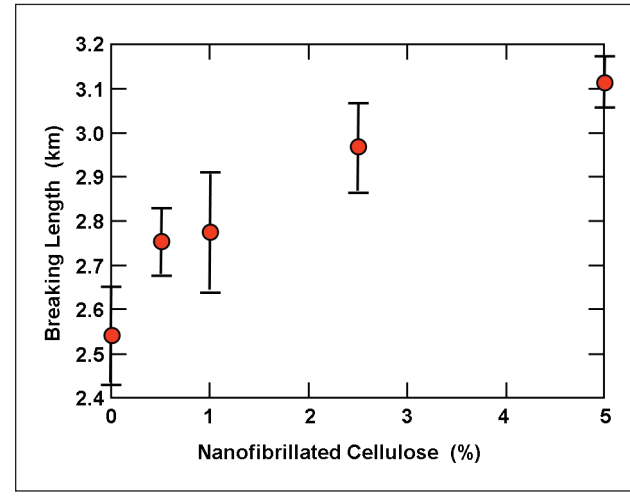

1. Effect of nanofibrillated cellulose addition level on the tensile strength of handsheets.

Beyond the issues related to statistical significance, it is important to also stress that papermakers have a range of

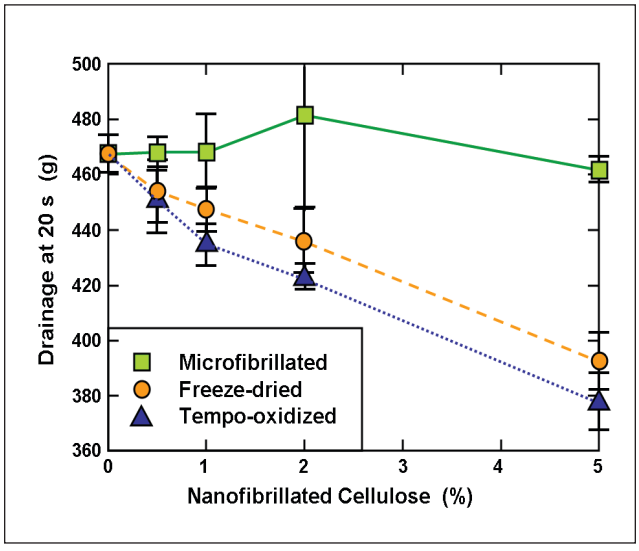

2. Effect of nanofibrillated cellulose addition level on the dewatering rate of 100% recycled copy paper furnish.

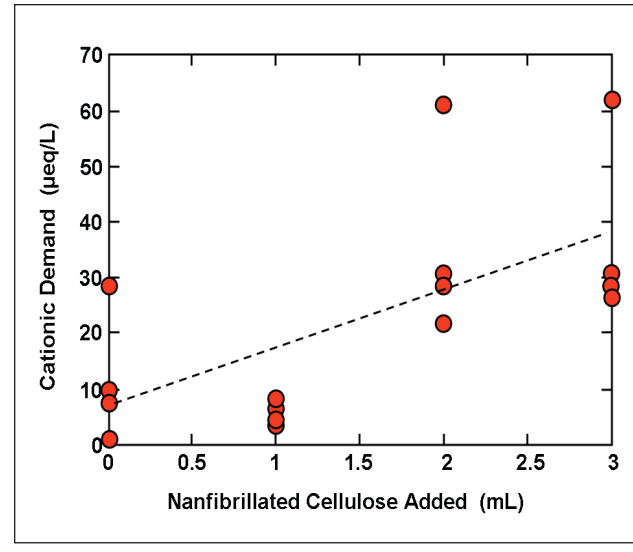

3. Cationic demand as a function of the addition level of nanofibrillated cellulose to default furnish.

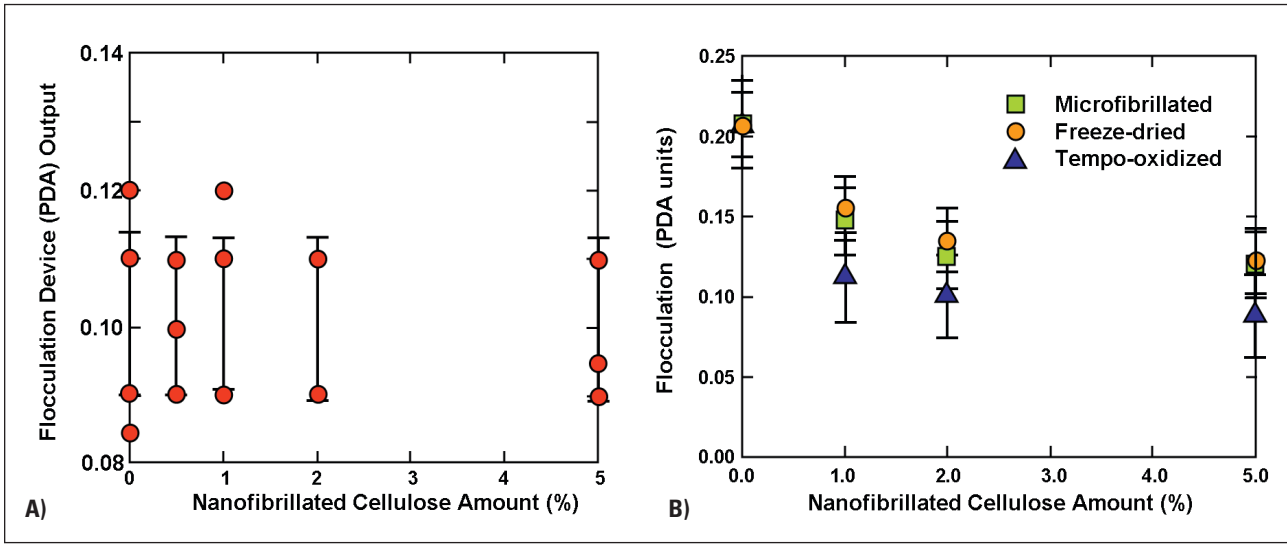

4. Effect of nanofibrillated cellulose addition on the flocculation level of the default furnish: A) with no other additives; and B) with subsequent treatment by cationic polyacrylamide (cPAM) retention aid at the 0.05% level based on solids.

options to increase paper strength, and some of them may be cheaper or easier to implement than the addition of NFC. For example, papermakers usually will have the option of increasing the level of refining of the main fiber furnish. Production teams continually weigh such issues as refining levels of the main furnish, as well as the usage of cationic starch. The addition of NFC may or may not provide an additional approach that can be considered, depending on whether there are constraints on refining levels or the use of strength additives.

However, in addition to increasing bonding strength, the usage of NFC can also decrease drainage rates (**Fig. 2**). For drainage testing, three types of nanofribrillated cellulose were tested. Those types were microfibrillated, freeze-dried, and TEMPO-oxidized. The data showed that drainage measured 20 s after opening of the sealing cone decreased as more nanofibrillated cellulose was added. It can be challenging to retain nanofribillated cellulose particles on the fiber. This can result in flow channels within the wet web of paper being blocked, resulting in a decrease in drainage [21,22,23]. Based on the results shown in Fig. 2, the three types of NFC did not all have the same effects on dewatering. The two NFC products from the University of Maine gave relatively large decreases in drainage rates that were almost linear with respect to added amounts.

The microfibrillated cellulose, by contrast, did not have a significant effect on dewatering (at least not in the absence of other additives). As shown by the top line in Fig. 2, even at an addition level of 5%, the microfibrillated cellulose did not adversely affect dewatering under the condi-

tions of testing. These results help to reinforce the point made earlier that papermakers will have choices. By employing a cellulose product having an intermediate level of fibrillation, there may be opportunities to achieve benefits of enhanced bonding with less or no penalty in terms of decreased rates of water removal.

Cationic demand gives information on how much of a highly charged polymer is needed to neutralize the surface of a sample when added to papermaking furnish. The data in **Fig. 3** show that the cationic demand increased as the amount of nanofribrillated cellulose dosage was increased. This is to be expected, since nanofibrillated cellulose has a negative charge.

Part A of **Fig. 4** shows that addition of NFC (type = freeze-dried) had no significant effect on fiber flocculation in the absence of other additives. By contrast, part B of the figure shows that in cases where the furnish had also been treated with cPAM copolymer retention aid, subsequent addition of any of the three types of NFC decreased the level of flocculation. The latter findings can be attributed to the NFC adsorbing the cPAM from the aqueous phase, thereby leaving less of the cPAM available to participate in bridging flocculation among the fibers [24].

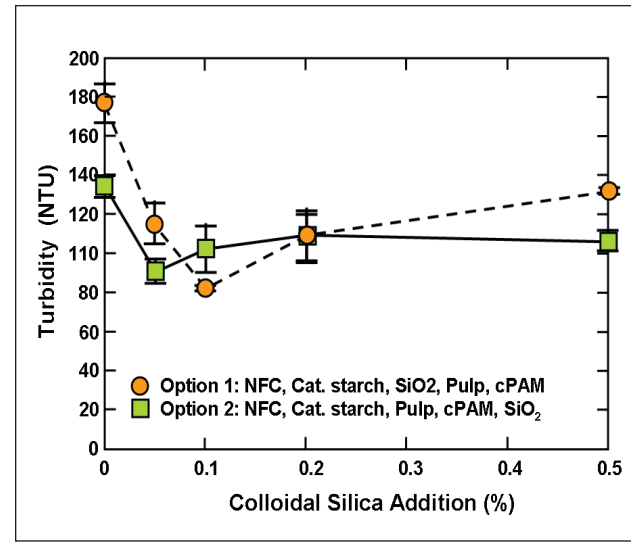

5. Effects of colloidal silica addition level and order of addition on the efficiency of fine particle retention in systems where nanofibrillated cellulose (NFC) at the 5% level had been treated with cationic starch (cat. starch), then added to the pulp, followed by treatment by cationic polyacrylamide (cPAM) retention aid. The addition orders were as shown in the legend (SiO_2 = silicon dioxide).

Effects of cationic starch addition

As was shown earlier in Table I, increasing cationic starch dosage led to an increase in cationic character of the furnish. These effects were shown by the less negative or more positive values of zeta potential of the fiber, based on the streaming potential tests. In addition, the filtrate had a decreased cationic demand with increasing cationic starch addition levels. These results are to be expected due the cationic starch's positively charged nature. Furthermore, as shown in Fig. 1, cationic starch addition led to increased strength in paper.

Effects of nanoparticle addition

Addition of colloidal silica or sodium montmorillonite (bentonite) to untreated papermaking furnish is known to not have significant effects on drainage, flocculation, or other aspects of the papermaking process. This is because, like the fibers and nanocellulose, the colloidal silica or bentonite have a negative charge, and hence they don't interact with each other. By contrast, **Fig. 5** shows clear effects of colloidal silica addition to systems with nanofibrillated cellulose that also involved treatments with cationic starch. The "Option 1" mentioned in the figure involves pretreatment of the NFC with cationic starch, followed by colloidal silica, final addition of the treated NFC to the fiber suspension, and final addition of the retention aid. "Option 2" is similar, except that the addition of colloidal silica is moved to the very end of the preparation, after the addition of cPAM to the combined furnish. As shown, in both cases the addition of even 0.05% SiO_2 (on a solids basis to the combined furnish) yielded a major increase in retention efficiency, as indicated by the turbidity of the filtrate in a Britt jar test. Increased amounts of SiO_2 above 0.1% did not further increase retention efficiency.

DISCUSSION

Results shown in this article have considered mainly individual effects of different components in a system of highly fibrillated cellulose (including different types), cationic starch (including different levels), and colloidal silica (at different levels) on some process-related aspects and product quality aspects of papermaking. The present work is related to earlier reported results that focused on the manufacture of bulky paper products [14]. It was shown in t he cited work that the combination of NFC, cationic starch, and colloidal silica could be optimized, along with major decreases in refining levels, to achieve high increases in strength, while maintaining high bulkiness and satisfactory dewatering rates. The present article supports those results, but it also shows potential for improving the strength of more typical paper grades, such as copy paper.

The final figure shown in this article provides a segue to the main topic of the next article in this series. As shown in Fig. 5, different results were obtained depending on the detailed order of addition of additives. The earlier-reported work by Rice et al. [14] showed promising results when colloidal silica had been added to a suspension of NFC that had been pretreated with cationic starch. It is more conventional in the paper industry to add colloidal silica as the final additive, after a very high-mass cationic retention aid, i.e. cPAM [25,26]. Such issues, and more, will be considered in the next article [27].

CONCLUSIONS

In terms of dewatering, fine-particle retention, and the level of flocculation among fibers, promising results were obtained in a 100% recycled copy paper furnish when adding combinations of nanofibrillated cellulose (NFC), cationic starch, and colloidal silica. Dosage-response curves were developed for individual additives to the furnish. The addition of NFC, at increasing levels with no other additives, decreased dewatering in an approximately linear manner. The cationic demand of the furnish increased with increasing addition of NFC. Adding NFC to the furnish affected the level of fiber flocculation only when the furnish was subsequently treated by cationic polyacrylamide (cPAM) retention aid. This was because the cPAM interacted with colloidal silica rather than just with fibers and fines. Fine-particle retention was optimized at a certain level of colloidal silica, with the results depending on the order of addition of the additives. **TJ**

ACKNOWLEGEMENTS

Larden Garden and Brandon Lieb were supported by Research Experience for Undergraduates funds from the Engineering Enhancement Fee during the summer of 2021. The work of Martin Hubbe is supported by an endowment from the Buckman Foundation. The following undergraduate students from the Paper Science and Engineering program in the Department of Forest Biomaterials at North Carolina State University are gratefully acknowledged for their work in carrying out some of the experimental procedures, processing data, and contributing to the interpretation of data: Morgan Davis, Tressa Glackin, Kaitlyn Pittmann, Caleb Smith, Samuel Webb, Erik Dahlgren, James Lewis, Peter Gough, Josh Carter, Natalie Laux, Caroline Lewis, Victor Yeh, John Bedard, Katie Krull, Allie Temple, Jessica Bey, Michael Hughes, Matthew Hinson, and Jonathan Simis.

LITERATURE CITED

1. Page, D.H., *Tappi* 52(4): 674(1969).
2. Gharehkhani, S., Sadeghinezhad, E., Kazi, S.N., et al., *Carbohydr. Polym.* 115: 785(2015). https://doi.org/10.1016/j.carbpol.2014.08.047.
3. Hubbe, M.A., Sjöstrand, B., Nilsson, L., et al., *BioResources* 15(4): 9672(2020). https://doi.org/10.15376/biores.15.4.Hubbe.
4. Weise, U., "Changes in wood pulp fibers caused by water removal," in *COST Action E1 Paper Recyclability: Improvement of Recyclability and the Recycling Paper Industry of the Future* (A. Blanco, C. Negro, I. Gaspar, et al., Eds.), Office for Official Publications of the European Communities, 1998.
5. Lavoine, N., Desloges, I., Dufresne, A., et al., *Carbohydr. Polym.* 90: 735(2012). https://doi.org/10.1016/j.carbpol.2012.05.026.

ABOUT THE AUTHORS

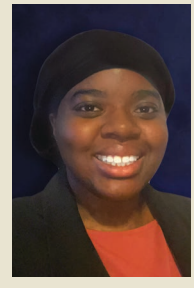

Garland

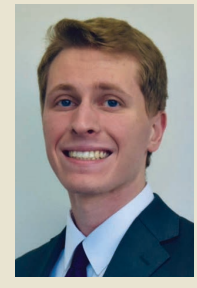

Leib



Barrios



Hubbe

Nanocellulose represents an important opportunity for papermakers to increase the bonding strength of their products, but it tends to interfere with drainage. The authors of this paper are at North Carolina State University in the Department of Forest Biomaterials. The work was supported in part by Research Experience for Undergraduates funds during the summer of 2021.

Important findings were reported in the past by Rice, Pal, Gonzalez, and Hubbe in *TAPPI J.* 17(7): 395(2018). This work, by contrast, deals with dense paper products. The authors were motivated to carry out this work due to a need to follow up on earlier promising research results, with the help of some newly acquired equipment for automated evaluation of dewatering rates.

The challenge in this research was to characterize the effects of different combinations of nanofibrillated cellulose with cationic starch, colloidal silica, and cationic acrylamide. It was discovered that there appear to be optimum treatments levels. The most interesting finding was that the combined system did not have any adverse effect on paper uniformity.

This research shows that mills finding themselves in a situation where they need additional bonding strength have an additional option, for which the factors are now better known.

This is the first in a set of three articles on the topic in *TAPPI Journal*. The second one, which appears in this issue as *TAPPI J.* 21(9): 572(2022), deals with issues of orders of addition. The third one (Nelson et al.) will deal with mechanistic aspects.

Garland and Leib are undergraduate students, Barrios is a graduate student in the Ph.D. program, and Hubbe is a professor in the Department of Forest Biomaterials at North Carolina State University, Raleigh, NC, USA. Email Hubbe at hubbe@ncsu.edu.

6. Yi, T., Zhao, H.Y., Mo, Q., et al., *Materials* 13(22): 5062(2020). https://doi.org/10.3390/ma13225062.
7. Salas, C., Hubbe, M., and Rojas, O.J., "Nanocellulose applications in papermaking," in *Production of Materials from Sustainable Biomass Resources* (Z. Fang, R.L. Smith, Jr., and X.-F. Tian, Eds.), Biofuels and Biorefineries Series 9, Springer, New York, 2019, Chap. 3, pp. 61-96. https://doi.org/10.1007/978-981-13-3768-0_3.
8. Ding, Q.J., Zeng, J.S., Wang, B., et al., *Carbohydr. Polym.* 186: 73(2018). https://doi.org/10.1016/j.carbpol.2018.01.040.
9. Wang, S.D., Gao, W.H., Chen, K.F., et al., *TAPPI J.* 17(3): 157(2018). https://doi.org/10.32964/TJ17.03.157.
10. Petroudy, S.R.D., Syverud, K., Chinga-Carrasco, G., et al., *Carbohydr. Polym.* 99: 311(2014). https://doi.org/10.1016/j.carbpol.2013.07.073.
11. Merayo, N., Balea, A., de la Fuente, E., et al., *Cellulose* 24(7): 2987(2017). https://doi.org/10.1007/s10570-017-1302-1.
12. Campano, C., Merayo, N., Balea, A., et al., *Cellulose* 25(1): 269(2018). https://doi.org/10.1007/s10570-017-1552-y.
13. Manninen, M., Kajanto, I., Happonen, J., et al., *Nord. Pulp Pap. Res. J.* 26(3): 297(2011). https://doi.org/10.3183/npprj-2011-26-03-p297-305.
14. Rice, M.C., Pal, L., Gonzalez, R., et al., *TAPPI J.* 17(7): 395(2018). https://doi.org/10.32964/TJ17.07.395.
15. Britt, K.W., *Tappi* 56(3): 83(1973).
16. Britt, K.W., and Unbehend, J.E., *Tappi* 59(2): 67(1976).
17. Milliken, J.O., "Spectrophotometric determination of fines retention using the dynamic retention/drainage jar," *Seattle Retention and Drainage Short Course*, 1977, p. 55.
18. Ricci, R.W., Ditzler, M.A., and Nestor, L.P., *J. Chem. Educ.* 71(11): 983(1994). https://doi.org/10.1021/ed071p983.
19. Pöykiö, R. and Nurmesniemi, H., *Environ. Chem. Lett.* 6(1): 47(2008). https://doi.org/10.1007/s10311-007-0110-5.
20. Strazdins, E., *Tappi* 60(7): 113(1977).
21. Britt, K.W., Unbehend, J.E., and Shridharan, R., *Tappi J.* 69(7): 76(1986).
22. Kumar, P., Wei, H.L., Ramarao, B.V., et al., *Chem. Eng. Commun.* 152-153: 287(1996). https://doi.org/10.1080/00986449608936569.
23. Hubbe, M.A. and Heitmann, J.A., *BioResources* 2(3): 500(2007). https://doi.org/10.15376/biores.2.1.1-2.
24. La Mer, V.K. and Healy, T.W., *Rev. Pure Appl. Chem.* 13: 112(1963).
25. Andersson, K. and Lindgren, E., *Nord. Pulp Pap. Res. J.* 11(1): 15(1996). https://doi.org/10.3183/npprj-1996-11-01-p015-021.
26. Hubbe, M.A., "Microparticle programs for drainage and retention," in *Micro and Nanoparticles in Papermaking* (J.M. Rodriguez, Ed.), TAPPI Press, Atlanta, 2005, Chap. 1, pp. 1-36.
27. Leib, B., Garland, L.J., Barrios, N.A., and Hubbe, M.A., *TAPPI J.* 21(9): 572(2022).

ABOUT THIS PAPER

Cite this article as:
Garland, L., Leib, B., Barrios, N., et al., *TAPPI J.* 21(10): 563(2022). https://doi.org/10.32964/TJ21.10.563

DOI: https://doi.org/10.32964/TJ21.10.563

ISSN: 0734-1415

Publisher: TAPPI Press

Copyright: ©TAPPI Press 2022

About this journal

Effects of orders of addition in nanocellulose–cationic starch–colloidal silica systems for papermaking

BRANDON D. LEIB, LARDEN J. GARLAND, NELSON A. BARRIOS, AND MARTIN A. HUBBE

ABSTRACT: Two orders of addition were compared when preparing paper handsheets from recycled copy paper furnish in combination with nanofibrillated cellulose (NFC), cationic starch, colloidal silica, and cationic retention aid (cPAM; cationic polyacrylamide). Faster dewatering and higher fine-particle retention were obtained at equal optimized dosages of additives when the colloidal silica was added last, after addition of the cPAM. The same order of addition also provided a higher gain in the paper's tensile strength. However, higher paper stiffness was achieved when the colloidal silica was instead added to the NFC, after its pretreatment with cationic starch. Results were consistent with the principle that papermaking additives added shortly before sheetforming tend to have the largest effects on drainage and retention. The results also demonstrated a sensitivity to the relative dosages of positively and negatively charged additives.

Application: Changing the order of addition of various chemical additives to the papermaking process often can be achieved with near-zero capital investment. The results in this paper provide an example where the order of addition can be expected to have important consequences.

Two articles published in this journal showed that favorable combinations of paper properties and rates of drainage of the wet web of paper can be achieved when using certain combinations of nanofibrillated cellulose (NFC), cationic starch, and colloidal silica [1,2]. It was reported recently that the efficiency of fine-particle retention depended on the order in which the ingredients were mixed together [2]. Accordingly, the present article considers two specific options regarding when to add colloidal silica. In one set of tests ("Option 1"), the colloidal silica was used as part of the pretreatment of NFC, subsequent to the addition of cationic starch. This was the procedure employed in work reported by Rice et al., which focused on the achievement of strong, stiff paper sheets at low values of apparent density [1]. In another set ("Option 2"), the colloidal silica was instead used as the final additive to the system, after a cationic polyacrylamide (cPAM) retention aid. Such conditions are consistent with modern papermaking processes in systems that do not contain NFC. The goal of this work was not only to shed light on potentially favorable papermaking practices, but also to explore a wider picture of effects related to retention, flocculation, and properties of the resulting paper when NFC is used with other papermaking additives.

The topic of order of addition of papermaking additives, though well known to practicing papermakers, has received only minor attention in published articles. For instance, it has been shown that the order of addition can be key to the performance of certain two-component retention aid systems [3]. Such cases are explained by the fact that a high-charge cationic additive needs to be applied first, so that there will be positively charged sites on fiber surfaces upon which the other additive, a negatively charged retention aid, is able to bind.

Some of the earliest published reports describing the usage of combinations of high-mass cationic polymers and either colloidal silica [4] or bentonite [5,6] indicated that the cationic polymer solution would be added first and the tiny mineral products would be added last to the mixture during the papermaking process. In that way, it has been proposed that the nano- or microparticles would be able to complete the system of bridging between solid surfaces. In particular, it was proposed that some idle loops and tails of cationic polymer extending from adjacent solids surfaces might both become bound to the same negatively charge bentonite particle [7].

By selecting the points of addition, papermakers can purposely subject the treated furnish to the relatively high hydrodynamic shear stress of a pressure screen [8]. The tendency of the screen system to disperse fiber flocs after treatment with a retention aid appears to explain why cPAM has been recommended to be added before the screen, whereas the bentonite was recommended to be added post-screen [5,9]. It has been established that the hydrodynamic conditions needed to shear apart fibers from each other are much less severe than the conditions needed to shear small particles, such as mineral fines, from fiber surfaces, if one assumes that the same retention aid systems are binding

all such solids together [10,11]. In the case of colloidal silica, however, sometimes the opposite order of addition has been practiced [12,13]. It has been proposed that the very small size of the colloidal silica particles allows them to pass into the interior of coils of cationic polymers [14]. Then, as the cationic polymer wraps itself onto the negatively charged particles, the bridges are shortened. The resulting contraction of the system is credited with a wringing effect that squeezes water out of the wet web of paper, thus promoting the release of water during the paper forming process.

Potential increases in interfiber bonding can motivate papermakers to consider adding highly fibrillated cellulose products to the papermaking furnish, but there have been concerns about slower rates of dewatering. The present work made use of differently prepared NFC, which was provided in dry form by the University of Maine (Orono, ME, USA). It is well known that NFC can be prepared from, for instance bleached softwood kraft pulp, by providing sufficiently high levels and durations of hydrodynamic shear or micro-grinding. When such materials are dried, for instance in preparation for storage or shipping, it has been shown that a partly irreversible loss of surface area can occur [15]. The loss can be attributed to the action of capillary forces that bring the cellulosic surfaces into molecular contact as the water evaporates [16]. Dense hydrogen bonding that forms between the adjacent cellulosic surfaces may be only partly reversible if and when the material is placed back into water [17]. These problems can be at least partly overcome by subjecting the bleached cellulose pulp to TEMPO-mediated oxidation before preparation of the NFC [18]. Not only does such treatment decrease the amount of energy needed to prepare the NFC, but it also facilitates the full redispersion of the dried NFC when it is mixed with water.

Following up on results shown by Garland et al. [2], the present work focusses on systems in which slurry from a master batch of repulped 100% recycled copy paper was treated with set amounts of NFC that had been pretreated with cationic starch. Colloidal silica was added either to the cationic starch-treated NFC or as the final additive to the process. The slurry of treated NFC was combined with the furnish, then treated with retention aid (cPAM), and finally with optional colloidal silica, if it had not been added earlier. The test runs with earlier addition of colloidal silica correspond to the procedures followed by Rice et al. [1]. In that work, the focus was on how best to prepare the NFC, and the option of adding the colloidal silica later was not tried due to lack of time. The addition of colloidal silica as the final additive corresponds to conventional papermaking practices that do not involve NFC [4,12]. Focusing on the role of the colloidal silica, addition very shortly before the headbox can be justified by anticipated benefits from fresh interactions between the cationic polymer and the colloidal silica. The transient nature of such effects has been demonstrated with respect to retention [19,20]. Thus, late addition of colloidal silica, just after cPAM, might be expected to achieve a boost in retention and dewatering.

EXPERIMENTAL

Chemicals and materials

The chemicals and materials employed in this work were all the same as those specified in a previous article [2]. Briefly stated, the main fiber furnish was prepared by repulping of a 100% recycled copy paper product (trademarked Boise ASPEN 100 Multi-use Recycled Copy Paper, Packaging Corporation of America, Boise Paper Division). The NFC consisted of the spray-dried, freeze-dried, and TEMPO-oxidized products supplied by the University of Maine. The cationic starch was Chargemaster L340 from Grain Processing Corp. (GPC; Muscatine, IA, USA). The colloidal silica used in the reported tests was Fennosil 2180 from Kemira Oyj (Helsinki). The cationic retention aid was Accurac 90, a very-high-mass cationic copolymer of acrylamide (American Cyanamid). Dilution and other preparation steps were the same as reported earlier [2].

As was noted at the beginning of this paper, the TEMPO-oxidized NFC product is of interest because the chemical treatment facilitates the fibrillation process and allows the material to be more fully redispersed after drying. The freeze-drying procedure provides an intermediate option whereby drying can take place with much less development of inter-particle hydrogen bonding and greater ability to be redispersed upon immersion in water.

Procedures

The basic procedures used for the reported work were the same as reported earlier [2].

Because the focus of this part of the work was on the order of addition, some details are shown in **Table I**. A key aspect is that the addition levels of different substances generally referred to the total dry mass of the ingredients used to form a sheet. Such a manner of presentation was intended to allow easier focus on effects of changing the order of addition.

Matched levels of chemical treatments were combined with the same repulped 100% xerographic copy paper furnish in the two patterns shown in Table I. A figure depicting the options for order of addition of the NSF, cationic starch, cellulosic fiber furnish, cationic retention aid, and colloidal silica, relative to a hypothetical paper mill process, was presented in an earlier paper in this journal [1].

RESULTS

Dewatering tests

As was shown in Table I, Option 1 involves optional colloidal silica being added to the suspension of NFC after treatment with cationic starch. The NFC is added to the fiber furnish only after these pretreatments. The cationic retention aid (cPAM) is the final additive to the mixture of

Item (in order of addition)	Level, % of dry mass of sheet	Role in Papermaking
Nanofibrillated cellulose (NFC)	5%	Potential bonding agent
Cationic starch	Various	Retention adjunct for NFC; also as a bonding agent
Colloidal silica (Option 1)	Either 0.5X or 1.0X the dry mass of cationic starch	Dewatering aid when used in sequence with a cationic polymer
100% recycled copy paper	To make 100%	The fiber furnish
Cationic retention aid	0.05%	Fine-particle retention
Colloidal silica (Option 2)	Either 0.5X or 1.0X the dry mass of cationic starch	Dewatering aid when used in sequence with a cationic polymer

I. Orders of addition of the additives in the two main options considered in this study.

pretreated NFC and furnish. By contrast, in the case of Option 2, the NFC is pretreated only with cationic starch. After adding the cationic starch-treated NFC to the furnish, the final additives are cPAM and then the colloidal silica. As shown in the table, the net amounts of additives were the same in Options 1 and 2, but the order of addition was different. Option 1 matches the procedure used in earlier work reported by Rice et al. [1], whereas Option 2 is more typical of current industrial practices.

Figure 1 shows that Option 2 resulted in much faster drainage than Option 1. The mass amounts shown correspond to readings taken 20 s after releasing the sealing cone. Here, the greatest drainage was achieved at the 0.1 silica-to-solids ratio. There did not seem to be much significant difference when the amount of silicon dioxide (SiO_2) was increased above this ratio, with the mass of filtrate remaining at a plateau level. Option 1 resulted in overall slower rates of dewatering, but there was a more prominent peak at the optimum colloidal silica level of 0.05%.

When silica levels were equal to that of starch, higher drainage rates tended to be achieved, as shown in **Fig. 2**. This ratio of colloidal silica to cationic starch was more significant the higher the starch level became. Regardless of the order of addition that was used, less silica used than starch resulted in less drainage than with equal dry masses of silica and starch, and this effect was most notable at higher cationic starch levels.

An unanswered question remaining after the work reported by Rice et al. [1] was whether strength benefits of NFC addition might continue to rise with increasing addition of cationic starch, up to very high levels. Though such a practice would be costly in terms of the required amounts of additives, sometimes papermakers have a need to boost strength gains in order to meet product specifications. Earlier work by Heermann et al. revealed continual strength increases to very high levels when forming in-situ polyelectrolyte complexes [21]. A concern, however, is that the higher chemical addition levels might have potential to hurt paper machine operating variables, such as the dewatering rates. As shown in Fig. 2, at the lower addition ratio of colloidal silica, there appeared to be an optimum level of cationic starch, beyond which further increases produced no further gains in dewatering rates. However, as shown by the positions of the diamond symbols, it was possible to maintain rapid dewatering by employing a sufficient colloidal silica dosage, even at very high cationic starch levels.

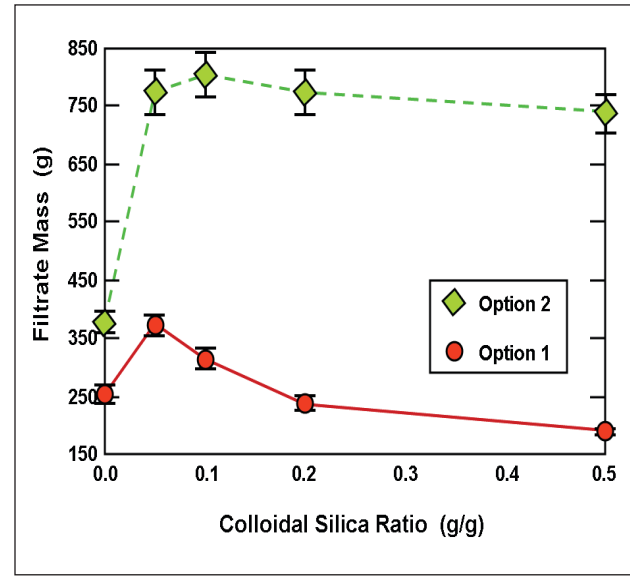

1. Effect of the ratio of colloidal silica to nanofibrillated cellulose (NFC) on the mass of filtrate collected in 20 s after opening the sealing cone, with 0.1 parts of cationic starch added per 1 part of NFC before addition to the furnish.

Figure 3 considers a different set of experiments in which no colloidal silica and no cPAM retention aid were used. Two mixing procedures were compared. In Method 1, the cationic starch was mixed well with the NFC before addition to the fiber suspension. In Method 2, the NFC was added directly to the fiber suspension and then cationic starch was added to the mixture and agitated. As shown, regardless of the order of addition, dewatering became

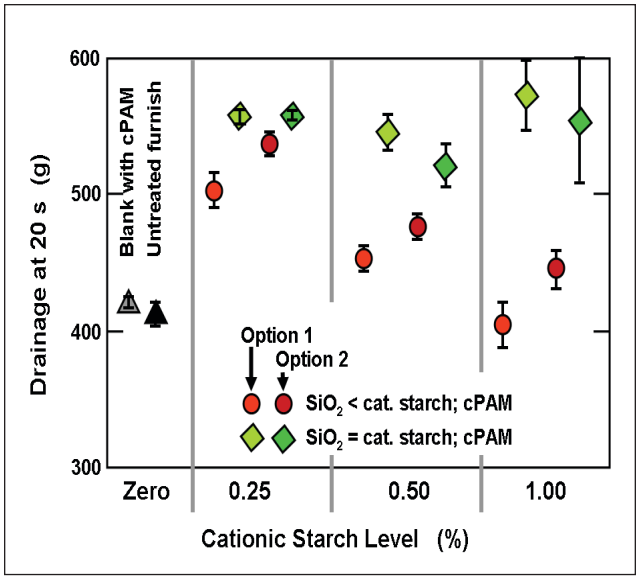

2. Effect of cationic starch variable, orders of addition, and the ratio of colloidal silica (silicon dioxide; SiO_2) to cationic starch on the mass of filtrate collected within 20 s of opening of the sealing can in systems with cationic polyacrylamide (cPAM) retention aid treatment.

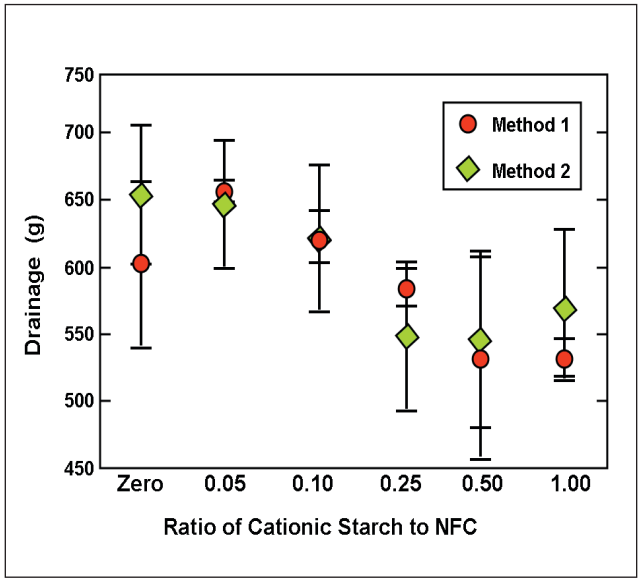

3. Effect of the relative amount of cationic starch, as well as its order of addition, on the amount of filtrate collected 20 s after opening of the sealing cone in systems not including either colloidal silica (SiO_2) or cationic retention aid. (Method 1 = add cationic starch to NFC before its addition to the suspension; Method 2 = add cationic starch last.)

slower when the cationic starch level was above 0.1 (as a ratio relative to NFC). As can be seen from the overlapping of 95% confidence intervals of the mean values, there was no statistically significant difference in the results for the two different orders of addition of the cationic starch.

To understand why the order of addition did not appear as important in the absence of the colloidal silica and

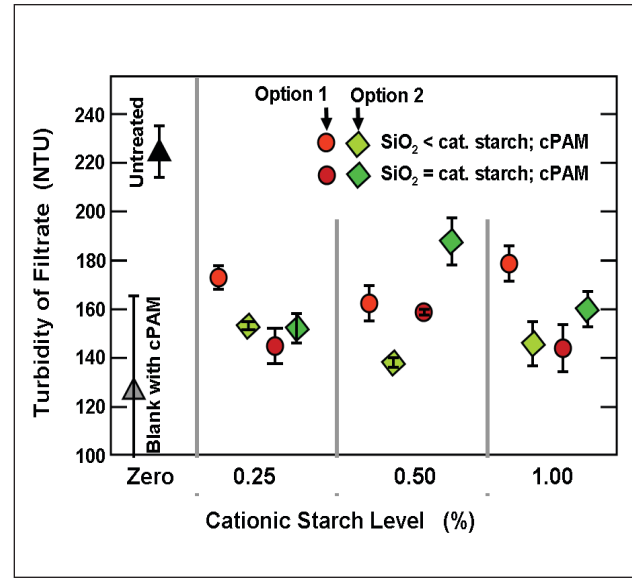

4. Effects of cationic starch level, order of addition of colloidal silica (SiO_2), and ratio of colloidal silica to cationic starch on the turbidity of filtrate in Britt jar tests.

cPAM, it is worth noting that those two additives have potential to contribute to very strong dewatering effects, which has been called the "microparticle effect" [4,12]. Most previously reported work involving those additives in papermaking systems have been limited to orders of addition in which colloidal silica and cPAM were the final additives, most often with the colloidal silica added last.

Retention tests

In this work, the turbidity of filtrate from testing with a Britt drainage/retention jar [22,23,24] was used as an indication of the efficiency of fine-particle retention. As a general finding, both options involving NFC, cationic starch, colloidal silica, and cPAM resulted in effective retention of fine particles, contributing to lower turbidity values in comparison to the blank. As shown in **Fig. 4**, lower turbidity was most often achieved when using Option 2 in cases when the colloidal silica added was less than the starch. When Option 1 was applied for silica levels being less than that of the starch added, higher turbidity resulted. The overall finding was that all of the systems involving cationic starch, colloidal silica, and cPAM retention aid were shown to be effective in retaining fine materials within the ranges of addition considered.

Although changes in turbidity can be effectively used to estimate changes in retention efficiency in general, there will be a need in future work to quantify the retention efficiency of NFC itself. Due to the small diameters of NFC fibrils (e.g., 5 to 20 nm), their contribution to scattering visible light will be low. Thus, they are hard to detect by optical measurements. A practical approach may be to assume that the retention efficiency of NFC itself is likely to follow the same trends as the retention of fillers and cellulosic

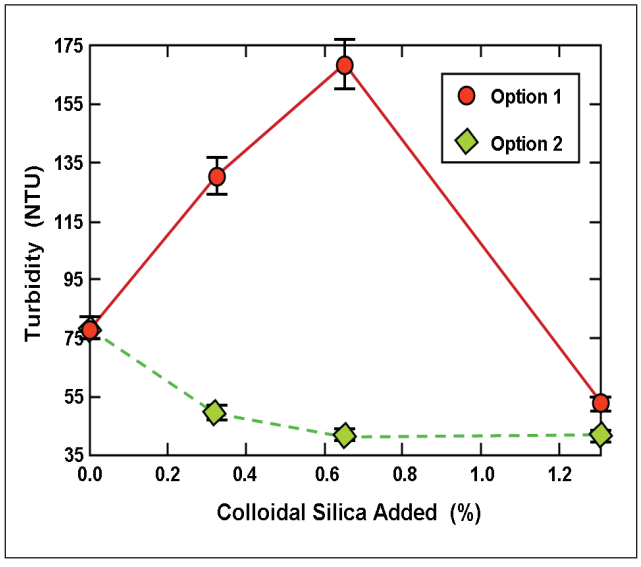

5. Effect of colloidal silica addition level and order of addition on the turbidity of filtrate during Britt jar testing of systems in which NFC, cationic starch, colloidal silica, and cationic retention aid were added to a fiber suspension from 100% recycled copy paper.

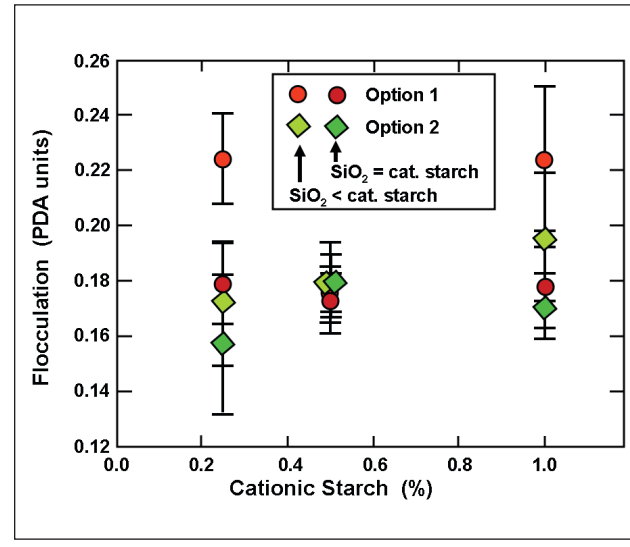

6. Effect of cationic starch level, order of addition of colloidal silica (SiO_2), and ratio of colloidal silica to cationic starch on the flocculation degree of fiber suspensions.

fines, both of which can be estimated by measurements of white water turbidity or filterable solids content. In principle, by maintaining a relatively high level of fines retention in a paper machine system, one might avoid a tendency for NFC to build up in the process water system.

Figure 5 shows results for systems with constant levels of NFC (5%) and cationic starch (0.5%) relative to furnish solids. As indicated, Option 2 yielded far lower turbidity levels than Option 1. Additionally, Option 1 exhibited an increase in turbidity up to 0.65% silica added and then tended to decrease in turbidity to 1.3% silica added. It should be noted that it is unclear whether 0.65% silica addition was the turning point for this sudden decrease in turbidity for Option 1. Option 2 tended to decrease in turbidity but leveled off at around 0.65% silica addition.

The fact that the turbidity rose with increasing colloidal silica when using Option 1 (pretreatment of the NFC with cationic starch and colloidal silica) is consistent with an agglomeration mechanism. One can expect the cationic starch (positively charged) to coat the NFC surfaces. Then, the colloidal silica (negatively charged) will be expected to bridge those positively charged surfaces, resulting in agglomerates that are large enough to scatter light efficiently. But as long as the system has a net positive charge, due to the cationic starch, there will not be an excess of colloidal silica still available to interact with the cationic retention aid, which is added later in the case of Option 1. The strong decrease in turbidity at the highest level of colloidal silica (1.3% addition) is consistent with there being an excess of colloidal silica, after interacting with the cationic starch. That excess of colloidal silica then will be available to interact with the cationic retention aid, giving overall results relatively close to those of Option 2, which represents a more typical order of addition in modern papermaking.

Flocculation tests

At two of the conditions considered, Option 2 resulted in a lower level of flocculation than Option 1. As shown in **Fig. 6**, this was not the case for a starch level of 0.5%. In that case, the flocculation was essentially the same for the two optional orders of addition. When the amount of silica added was equivalent to that of the added starch, as compared to less silica than added starch, flocculation levels were typically less. The least amount of flocculation achieved was associated with 0.25% starch added when silica was equivalent to the amount of starch added for Option 2. This small amount of flocculation was also achieved for the same conditions as just mentioned, when starch addition was at 1%. In general, though some of the experimental conditions showed significant increases in fiber flocculation, most of the results did not show important differences in flocculation, even when the colloidal silica was added last (Option 2). This is notable in light of the earlier statement that agents added very late to a papermaking wet-end system often have the largest effects on retention aid dewatering. The generally low levels of flocculation found in this work suggest that relatively uniform, unflocculated fiber sheets can be prepared using the described program of papermaking additives.

Handsheet properties

During handsheet testing, ratios of colloidal silica to cationic starch were 0%:0%, 0.25%:0.5%, and 0.5%:0.5%, respectively. As shown in **Fig. 7**, Option 2 (adding colloidal silica last) consistently yielded greater breaking length than Option 1 (with the colloidal silica added as part of the pre-

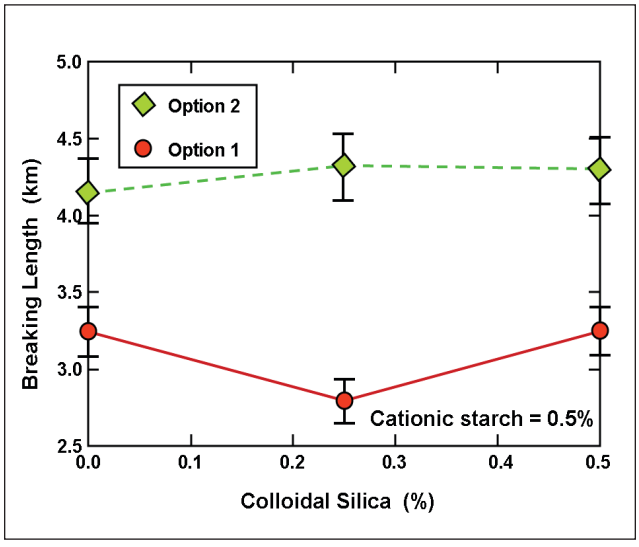

7. Effect of colloidal silica level and order of addition on the tensile strength of handsheets containing NFC, cationic starch, colloidal silica, and cationic retention aid: Option 1 is to add colloidal silica to an NFC-cationic starch mixture before its addition to the fiber suspension. Option 2 is to add the colloidal silica at the very end, after cationic retention aid.

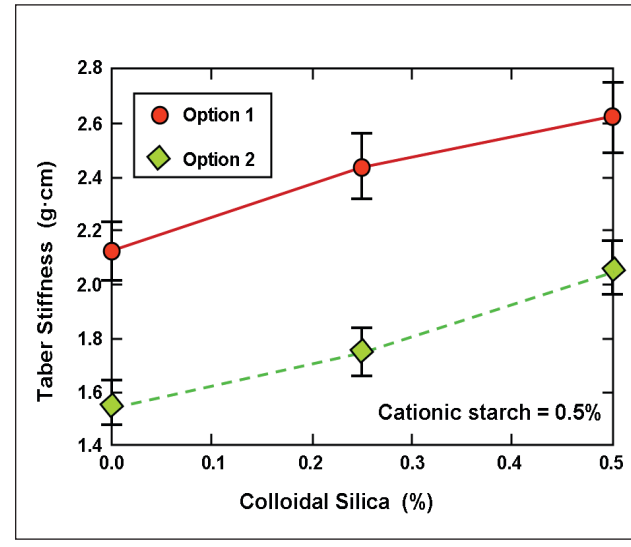

8. Effect of colloidal silica addition level and order of addition on the Taber stiffness of handsheets prepared from 100% recycled copy paper with NFC, colloidal silica, and cationic retention aid.

treatment of NFC, together with cationic starch). Option 1 gave a noticeably lower breaking length. However, the surprise in Fig. 7 is the fact that the level of cationic starch (in the range of zero to 1% of total solids) did not have a statistically significant effect when considering the results as a whole. Note that in the case of Option 2 (upper curve), the 95% confidence bars overlap each other for all of the conditions. In the case of Option 1 (lower curve), there was not a consistent trend. It is worth bearing in mind that handsheet tests often underestimate paper strength due to the low hydrodynamic shear conditions employed, which can lead to higher flocculation of the fibers. When handsheets are being prepared with the addition of dry strength additives and flocculating chemicals, the strength results may be unreliable [25].

From **Fig. 8**, as the silica additive percentage was increased, Taber stiffness increased, regardless of the order of addition that was used. However, Option 2 had noticeably lower Taber stiffness than Option 1 throughout all trials.

It is worth noting that stiffness results tend to be less affected by nonuniformity of the paper, due to the presence of fiber flocs. The fact that the results agree with the earlier findings of Rice et al. [1] support the concept that adding at least a part of the colloidal silica earlier in the process may provide an important option for papermakers.

DISCUSSION

Two principles are known to be important when seeking an optimum order of addition of papermaking additives. First is a general expectation that additives injected into the furnish very shortly before formation of the sheet are most likely to have big effects on retention and drainage attributes. Evidence to support this concept comes from the fact that very high-mass copolymers of acrylamide, i.e., "retention aids," are almost always added to papermaking furnish in commercial papermaking operations [26]. The point of addition for cPAM is usually either after or immediately before a screen system in the approach to a paper machine forming section. This first rule was evidenced most clearly in the present results for Britt jar tests (Fig. 5). It is clear that the combination of cationic starch with subsequent colloidal silica as the final additive was very effective. When the colloidal silica had instead been utilized as part of a pretreatment system for the NFC, it apparently was no longer available to interact with the cPAM retention aid (as the final additive), which explains the much higher filtrate turbidities when employing Option 1 (adding the colloidal silica to the NFC and cationic starch mixture).

The second rule is that any negatively charged additives ought to be injected at a point in the system where the surfaces have already been treated with enough of a positively charged additive to create suitable anchoring points on fiber surfaces.

A third lesson that the present experimental results are providing is that a specific chemical or mechanism treatment (or order of addition) can often have complex effects relative to the goals of papermaking. Thus, an order of addition providing high stiffness of the paper (Option 1) was not conducive to the fastest dewatering or efficient fine-particle retention. Thus, once some interesting findings are obtained in laboratory work, it may be necessary to consider more than one arrangement of addition points on a commercial paper machine when attempting to find the overall most suitable additive program.

As has been shown at various points in the previous dis-

cussion, the ratio of colloidal silica to cationic starch appears to have had significant effects. In principle, that might be due to the interactions among oppositely charged additives to the system. It can be hypothesized that peak performance of some systems might be achieved when there is a balance between positive and negative charge amounts. Such issues will be considered in a future article in this series.

CONCLUSIONS

The order of addition of colloidal silica showed important effects in papermaking wet-end systems including nanofibrillated cellulose (NFC), cationic starch, colloidal silica, and cationic retention aid in the presence of fibers from 100% recycled copy paper. Adding the colloidal silica last, after the cationic retention aid, yielded the highest drainage, first-pass retention, and breaking length of the resulting handsheets. However, the highest stiffness of the paper was achieved when the colloidal silica was added to a mixture of cationic starch and NFC before their addition to the fiber suspension. By increasing the amount of colloidal silica relative to cationic starch in either order of addition, it was possible to maintain a favorable dewatering rate, even at a high addition level of cationic starch. **TJ**

ABOUT THIS PAPER

Cite this article as:
Leib, B., Garland, L., Barrios, N., et al., *TAPPI J.* 21(10): 572(2022). https://doi.org/10.32964/TJ21.10.572

DOI: https://doi.org/10.32964/TJ21.10.572

ISSN: 0734-1415

Publisher: TAPPI Press

Copyright: ©TAPPI Press 2022

About this journal

ACKNOWLEGEMENTS

Larden Garland and Brandon Leib were supported by Research Experience for Undergraduates funds from the Engineering Enhancement Fee during the summer of 2021. The work of Martin Hubbe is supported by an endowment from the Buckman Foundation. The following undergraduate students from the Paper Science and Engineering program in the Department of Forest Biomaterials at North Carolina State University are gratefully acknowledged for

ABOUT THE AUTHORS

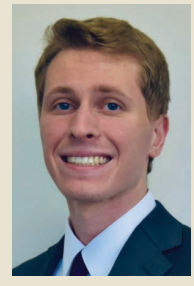

Leib

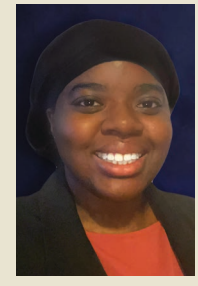

Garland



Barrios



Hubbe

Papermakers can switch addition points for chemical additives at almost zero cost. As shown in this paper, there sometimes can be benefits to the papermaker. This is the second paper in a set. The first, which appears on p. 563 of this issue, describes the experimental approach and gives evidence that the order of addition could be important. This article follows up in detail.

The authors of this paper are at North Carolina State University in the Department of Forest Biomaterials. The work was supported in part by Research Experience for Undergraduates funds from the Engineering Enhancement Fee during the summer of 2021. The authors were motivated to carry out this work due to a need to follow up on earlier promising research results, with the help of some newly acquired equipment for automated evaluation of dewatering rates

During this project, it was a challenge to study a large number of variables. The project required the work of four primary researchers (the authors) and a team of additional helpers described in the Acknowledgements.

The authors found that tests involving retention efficiency, drainage rates, fiber flocculation, and handsheet properties need to be viewed together in order to better understand chemical additives for papermaking. An interesting finding was that while the state-of-the art recommendation for order of addition of some chemical additives often gave the most promising results, this was not so in every case.

Depending on production constraints or product goals, this study shows that mills can choose between two promising orders of addition for chemical additives. The third and final paper in this series by Barrios et al. will consider mechanistic aspects.

Garland and Leib are undergraduate students, Barrios is a graduate student, and Martin A. Hubbe is a professor in the Department of Forest Biomaterials at North Carolina State University, Raleigh, NC, USA. Email Hubbe at: hubbe@ncsu.edu.

their work in carrying out some of the experimental procedures, processing data, and contributing to the interpretation of data: Benen Tarpley, Blaine Mercer, Parker Janson, Wallace Layman, James Lewis, Erik Dahlgren, Peter Gough, Samuel Webb, Sophia Mills, Abby Saul, Jared Brew-Thompson, Autumn Satterfield, John Bedard, Katie Krull, Allie Temple, Jack Powell, Eduardo Sanchez, Austin Schott, and Cade Wanner.

LITERATURE CITED

1. Rice, M.C., Pal, L., Gonzalez, R., et al., *TAPPI J.* 17(7): 395(2018). https://doi.org/10.32964/TJ17.07.395.
2. Garland, L.J., Leib, B.D., Barrios, N.A., et al., *TAPPI J.* 21(10): 563(2022).
3. Mueller, P., Gruber, E., and Schempp, W., *Wochenbl. Papierfabr.* 127(7): 460(1999).
4. Andersson, K. and Sandström, A., *Nord. Pulp Pap. Res. J.* 1(2): 26(1986). https://doi.org/10.3183/npprj-1986-01-02-p026-030.
5. Langley, J.G. and Litchfield, E., *Papermakers Conf.*, TAPPI Press, Atlanta, 1986, p. 89.
6. Langley, J. and Holroyd, D., U.S. pat. 4,753,710 (Jun. 28,1988).
7. Asselman, T. and Garnier, G., *J. Pulp Pap. Sci.* 27(8): 273(2001).
8. Hubbe, M.A. and Wang, F., *TAPPI J.* 1(1): 28(2002).
9. Asselman, T. and Garnier, G., *Colloids Surf., A* 170(2/3): 79(2000). https://doi.org/10.1016/S0927-7757(00)00487-8.
10. McKenzie, A.W., *Appita* 12(4): 104(1968).
11. Hubbe, M.A., *Colloids Surf.* 16: 249(1985). https://doi.org/10.1016/0166-6622(85)80257-2.
12. Hubbe, M.A., "Microparticle programs for drainage and retention," in *Micro and Nanoparticles in Papermaking* (J.M. Rodriguez, Ed.), TAPPI Press, Atlanta, 2005, Chap. 1, pp. 1-36.
13. Hubbe, M.A., *Lignocellulose* 3(1): 69(2014).
14. Andersson, K. and Lindgren, E., *Nordic Pulp Pap. Res. J.* 11(1): 15(1996). https://doi.org/10.3183/npprj-1996-11-01-p015-021.
15. Peng, Y.-C., Gardner, D.J., and Han, Y.-S., *Cellulose* 19: 91(2012). https://doi.org/10.1007/s10570-011-9630-z.
16. Page, D., *J. Pulp Pap. Sci.* 19(4): J175(1993).
17. Pönni, R., Vuorinen, T., and Kontturi, E., *BioResources* 7(4): 6077(2012). https://doi.org/10.15376/biores.7.4.6077-6108.
18. Isogai, A., Saito, T., and Fukuzumi, H., *Nanoscale* 3(1): 71(2011). https://doi.org/10.1039/C0NR00583E.
19. Carlson, U., "Some aspects of microparticle flocculation," *EUCEPA 24: Pap. Technol.: The World Pulp Pap. Week*, EUCEPA, Paris, 1990.
20. Lenze, C.J., Peksa, C.A., Sun, W.M., et al., *Cellulose* 23(6): 3951(2016). https://doi.org/10.1007/s10570-016-1077-9.
21. Heermann, M.L., Welter, S.R., and Hubbe, M.A., *TAPPI J.* 5(6): 9(2006).
22. Britt, K.W., *Tappi* 56(3): 83(1973).
23. Britt, K.W. and Unbehend, J.E., *Tappi* 59(2): 67(1976).
24. Milliken, J.O., "Spectrophotometric fetermination of fines retention using the dynamic retention/drainage jar," *Seattle Retention and Drainage Short Course*, 1977, p. 55.
25. Roberts, J.C., Au, C.O., and Lough, C., *Tappi J.* 69(10): 88(1986).
26. Pelzer, R., "Polyacrylamies (PAM) as retention aids," in *Chemical Additives for the Production of Pulp and Paper* (Zellscheming Technical Committee Chemical Additives [CHAD], Ed.), Deutscher Fachverlag, Frankfurt, Chap. 7.3, pp. 139-151.

TAPPI JOURNAL
WWW.TAPPI.ORG
THE PAPER AND PACKAGING INDUSTRIES' TECHNICAL RESOURCE **NOVEMBER 2022** | VOL. 21 NO.11

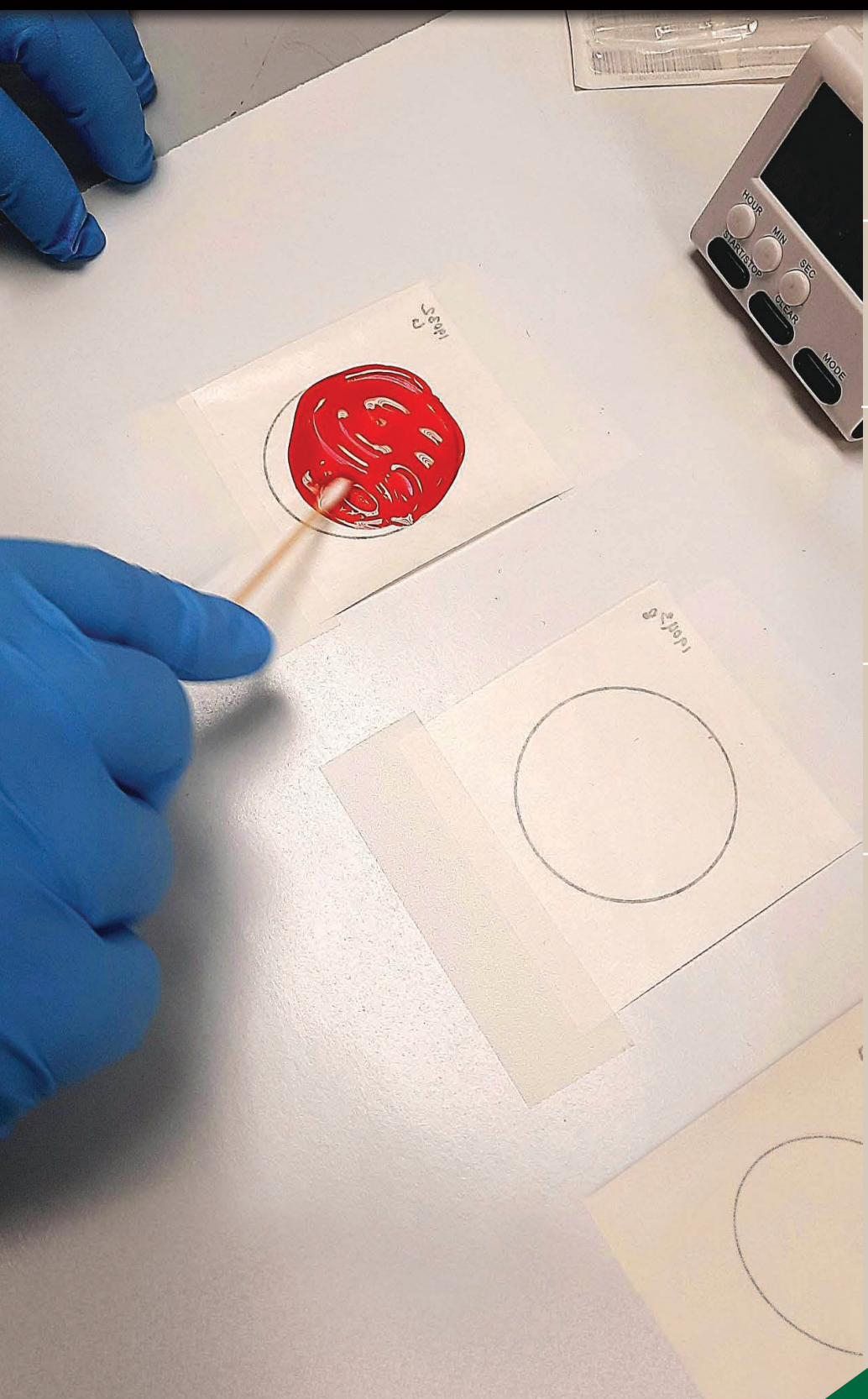

PAPERBOARD COATING **589**
Review of coating cracking and barrier integrity on paperboard substrates
Joel C. Panek and Peter W. Hart

COATING SYSTEMS **605**
Modeling the influence of rheology on smooth rod coating systems
John A. Roper III, Douglas W. Bousfield, and Gregory W. Welsch

BARRIER COATING **617**
Coatings for sustainable paper-based flexible packaging: Barrier properties and processability
Hanze Ying, Luqing Qi, Dave Malotky, Joseph Harris, Bernhard Kainz, Ray Drumright, William Liechty, and Jonathan Mason

BARRIER COATING **625**
Novel test method for measuring defects in barrier coatings
Dustin Burton, Don Ventresca, and Gregory W. Welsch

BARRIER COATING **645**
Improvements in oil and grease resistance (OGR) test methodology for waterborne barrier coatings
Allyson Marianelli, Brian Einsla, Elizabeth Show, Samantha Woodfin, Bo Shuang, Kevin Henderson, Mike Linsen, Jonathan DeRocher, and Shawn Oliver

SPECIAL COATING CONTENT

November 2022

TABLE OF CONTENTS VOL. 21 NO. 11

585 EDITORIAL
The road to sustainable packaging: New research on aqueous barrier coating
Steven P. Ottone

589 PAPERBOARD COATING
Review of coating cracking and barrier integrity on paperboard substrates
Joel C. Panek and Peter W. Hart

605 COATING SYSTEMS
Modeling the influence of rheology on smooth rod coating systems
John A. Roper III, Douglas W. Bousfield, and Gregory W. Welsch

617 BARRIER COATING
Coatings for sustainable paper-based flexible packaging: Barrier properties and processability
Hanze Ying, Luqing Qi, Dave Malotky, Joseph Harris, Bernhard Kainz, Ray Drumright, William Liechty, and Jonathan Mason

625 BARRIER COATING
Novel test method for measuring defects in barrier coatings
Dustin Burton, Don Ventresca, and Gregory W. Welsch

645 BARRIER COATING
Improvements in oil and grease resistance (OGR) test methodology for waterborne barrier coatings
Allyson Marianelli, Brian Einsla, Elizabeth Show, Samantha Woodfin, Bo Shuang, Kevin Henderson, Mike Linsen, Jonathan DeRocher, and Shawn Oliver

»**COVER CREDIT**: Researchers at Trinseo LLC have developed a new Defect Characterization test (p. 625) for characterizing the surface quality of water-based barrier coatings applied on paper and paperboard substrates. This cost-effective method uses dyed oil and a simple image analysis procedure to quickly test representative paper and board samples. The test method was designed to rule out simple coating defects as a cause for barrier coating failures as opposed to assuming the coating materials themselves were not effective. This technique has been developed as a pre-test before extensive barrier testing is completed.

TAPPI JOURNAL
WWW.TAPPI.ORG

Editor-in-Chief
Douglas W. Coffin coffindw@miamioh.edu
+1 513 529-0771

Associate Editor
Peter W. Hart peter.hart@westrock.com
+1 409 276-3465

Editorial Director
Monica Shaw mshaw@tappi.org
+1 770 367-9534

PRESS Manager
Jana Jensen jjensen@tappi.org
+1 770 209-7242

***TJ* EDITORIAL BOARD**

Brian N. Brogdon, FutureBridge Consulting & Training LLC
brian.brogdon@gmail.com, +1 678 581-9114

Ravi Challa, Suominen Corporation
Ravi.Challa@suominencorp.com, +1 843 680 2586

Douglas W. Coffin, Miami University
coffindw@miamioh.edu, +1 513 529-0771

Mahendra Doshi, Doshi and Associates
mahen@aol.com, +1 920 832-9101

Marc Foulger, Valmet
marc.foulger@valmet.com +1 315 767-2920

Peter W. Hart, WestRock
peter.hart@westrock.com, +1 409 276-3465

Carl J. Houtman, USDA Forest Products Laboratory
choutman@fs.fed.us, + 1 608 231-9445

Vamsi Jasti, Ahlstrom-Munksjo Nonwovens LLC
jvamsik1@gmail.com, +1 818 585-3524

Lucian Lucia, North Carolina State University
lucian.lucia@gmail.com, +1 919 889-7059

John A. Neun, John A. Neun LLC
john.neun@gmail.com, +1 518 275-8139

Jim Niemiec, Jim Niemiec Consulting LLC
jim.niemiec@outlook.com, +1 715 213-4766

Steven P. Ottone, Omya
steven.ottone@omya.com, +1 919 641-7854

Gaurav Pranami, Imbed Biosciences
gpranami@imbedbio.com, +1 515 230-7005

Arthur Ragauskas, Oak Ridge National Laboratory
aragausk@utk.edu

Seshadri Ramkumar, Texas Tech University
S.Ramkumar@ttu.edu, +1 806 742-4567

Gregg Reed, Imerys
gregg.reed@imerys.com, +1 478 553-5747

Gerard J.F. Ring, University of Wisconsin—Stevens Point
gerrryring@wi-net.com, +1 715 592-3732

Scott Rosencrance, Kemira Chemicals
scott.rosencrance@kemira.com, +1 770 429-2753

Vipin Varma, NCASI
vvarma@ncasi.org, +1 352 244-0965

Junyong Zhu, USDA Forest Products Laboratory
jzhu@fs.fed.us, +1 608 231-9520

Join TAPPI *today!*
TAPPI JOURNAL is a free benefit of TAPPI membership, and is only available to members. To join TAPPI, to renew your TAPPI Membership, or to learn about other valuable benefits, visit www.tappi.org.

TAPPI, 15 Technology Parkway S., Suite 115, Peachtree Corners, GA 30092, publishes *TAPPI JOURNAL* monthly.

ATTENTION PROSPECTIVE AUTHORS: All papers published are subject to *TAPPI JOURNAL's* peer-review process. Not all papers accepted for review will be published. Before submitting, check complete author guidelines at http://www.tappi.org/s_tappi/doc.asp?CID=100&DID=552877.

Statements of fact and opinions expressed are those of individual authors. TAPPI assumes no responsibility for such statements and opinions. TAPPI does not intend such statements and opinions or construe them as a solicitation of or suggestion for any agreed-upon course of conduct or concerted action of any sort.

Copyright 2022 by TAPPI, all rights reserved. For copyright permission to photocopy pages from this publication for internal or personal use, contact Copyright Clearance Center, Inc. (CCC) via their website: www.copyright.com. If you have questions about the copyright permission request process, please contact CCC by phone at +1 978 750-8400. To obtain copyright permission to use excerpts from this publication in another published work, send your specific request in writing to Editor, TAPPI JOURNAL, 15 Technology Parkway S., Suite 115, Peachtree Corners, GA 30092, USA; or by fax to +1 770 446-6947. Send address changes to TAPPI, 15 Technology Parkway S., Suite 115, Peachtree Corners, GA 30092, USA; Telephone +1 770 446-1400, or FAX +1 770 446-6947. www.tappi.org

Editorial

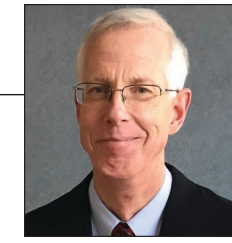

STEVEN P. OTTONE
TAPPI Journal Editorial Board

The road to sustainable packaging: New research on aqueous barrier coating

This *TAPPI Journal* Special Coating Issue looks at hot topic research being done in coatings for paper and paperboard. We can feel the "earth shifting" in paper and paperboard packaging due to the strong call by consumers and brand owners for more sustainable and environmentally friendly options. This is the first *TAPPI Journal* Special Coating Issue to highlight efforts within the paper coating community to produce more sustainable packaging.

In this issue, there are five research papers to explore on the barrier coating topic. Four of these papers were originally presented at TAPPICon 2022 and were well received there. They were chosen for peer review and publication in *TAPPI Journal* by myself, Jim Niemiec, and Gregg Reed, as members of the Editorial Board and TAPPI's Coating and Graphic Arts (CGA) Division.

The last four papers described here were those presented at PaperCon, while the first paper listed below offers a comprehensive review of work done across the industry to study the sources of fold cracking in aqueous barrier coatings.

- From researchers at WestRock, this paper (p. 589) describes how published literature on coating cracking is useful, but is still limited in terms of what is directly beneficial for commercial applications. This review emphasizes the value in taking time to properly understand the relevant literature and distinguish what is valid, where gaps exist, and what effective paths can close these gaps. Its content can be used to guide product development and fundamental research.
- A second paper (p. 605) from researchers at PaperCote, the University of Maine, and Trinseo discusses modeling of application processes used for barrier coatings. It addresses the knowledge gap around rod loading of smooth rods to obtain various coat weights by employing a simplified mode to estimate the influence of process parameters like speed, rod diameter, viscosity, and rod loading on coat weight.
- The third manuscript (p. 617) from researchers at Dow discusses a specific waterborne barrier coating solution that was designed and tailored for sustainable paper-based flexible packaging applications. It performs well in terms of good liquid/gas barrier, high heat-seal/hot-tack, and low coefficient of friction (CoF).
- From researchers at Trinseo (p. 625), the fourth paper describes a complementary test to the 3M Kit, Hot Oil, and other tests for assessing water-based barrier coating defects. Called the Defect Characterization test, it offers additional accuracy in a short amount of time and with a small paper sample.
- The final paper from researchers at Dow (p. 645) reviews new oil and grease resistance (OGR) test methods for waterborne barrier coatings. It describes additional, more aggressive 3M Kit-type solutions that can be utilized immediately in mills with minimal modifications to their current workflow.

It has been our pleasure to be able to guide peer review and publish these fine works for your review. So, read, absorb, question, and use the ideas here to guide your own perspective and efforts within the sustainable packaging space. **TJ**

Steven P. Ottone is a technical service manager, Market Development and Innovation, for Omya, Inc., Cincinnati, OH, USA.

Review of coating cracking and barrier integrity on paperboard substrates

JOEL C. PANEK AND PETER W. HART

ABSTRACT: Barrier packaging formats are major growth areas for the pulp and paper industry. It is technically challenging to maintain barrier properties during converting and end-use applications. Improved manufacturing capabilities and coating formulation knowledge will help maintain barrier integrity and enable growth of barrier products in challenging applications. These improvements will accelerate product development and commercialization, and allow faster response to product performance issues such as cracking.

The literature on coating cracking provides knowledge mostly on the effects of coating formulations and to a lesser extent on substrate effects. Despite a large number of publications dedicated to coating failures, the approach to improve coating cracking remains empirical, and the transferability between studies and to real life applications has not been well established. Model development that successfully predicts commercial performance is in its infancy. However, some of these simplified models do a fairly good job predicting experimental data. The current work reviews the state of understanding as regards coating and barrier cracking and highlights the need for more research on cracking and barrier integrity.

Application: Through this review, readers will learn more about coating cracking and the current state of knowledge on the topic. This can be used to guide product development and fundamental research.

Coating applications used to impart barrier properties to paperboard surfaces are a major growth area for the pulp and paper industry. As the desire to replace plastic with paper-based solutions accelerates, the need for more robust barrier applications will become paramount. Volume demand for functional and barrier coating applications in paper and board packaging reached almost 3 million metric tons globally in 2018, with a value of $7.8 billion. The market is forecast to grow at a rate of 5.0% across the five years to 2024, pushing market value to almost $11.0 billion and worldwide consumption to just under 4 million metric tons [1].

Barrier coatings tend to work extremely well when applied to a flat surface. Unfortunately, these coatings often experience damage and fracture during the bending, scoring, deep drawing, and press forming processes required to successfully convert a flat sheet into a functional package. Improved understanding of the fundamental aspects of barrier integrity will enable growth of barrier products in challenging applications, accelerate product development and launch, and allow faster response to product issues.

The current work on coating cracking attempts to clarify what is known about the mechanisms that cause damage to the barrier, to identify gaps in the existing knowledge, to propose potential driving mechanisms for crack initiation and propagation, and to recommend areas that require additional research.

REVIEW OF THE LITERATURE

The literature on coating cracking primarily provides knowledge on the effects of coating formulations and to a lesser extent on substrate effects. Despite a large number of publications, the approach to improve coating cracking remains mostly empirical, and the transferability between studies to real-life applications has not been successfully established.

Early work — publication coatings

Much of the work in the early literature has been around the cracking of publication grades during folding. These give insight into deformation during the folding event, but these coating layers are quite different than barrier coatings due to the high pigment content. Early pioneering works by Colley [2,3] and by Jopson and Towers [4] on the cracking of lightweight magazine paper provide interesting examples. These studies do not provide significant insights into barrier applications due to the grades studied, the methods employed to quantify strength loss (i.e., damage), and a lack of mechanistic explanations. Guyot, Bacquet, and Schwob [5] describe different types of cracking behavior that depend on the relative properties of the coating and how these are related to the relative tensile properties of the coatings, which is conceptually useful. Detailed examples of these different types of cracking are shown in **Fig. 1**.

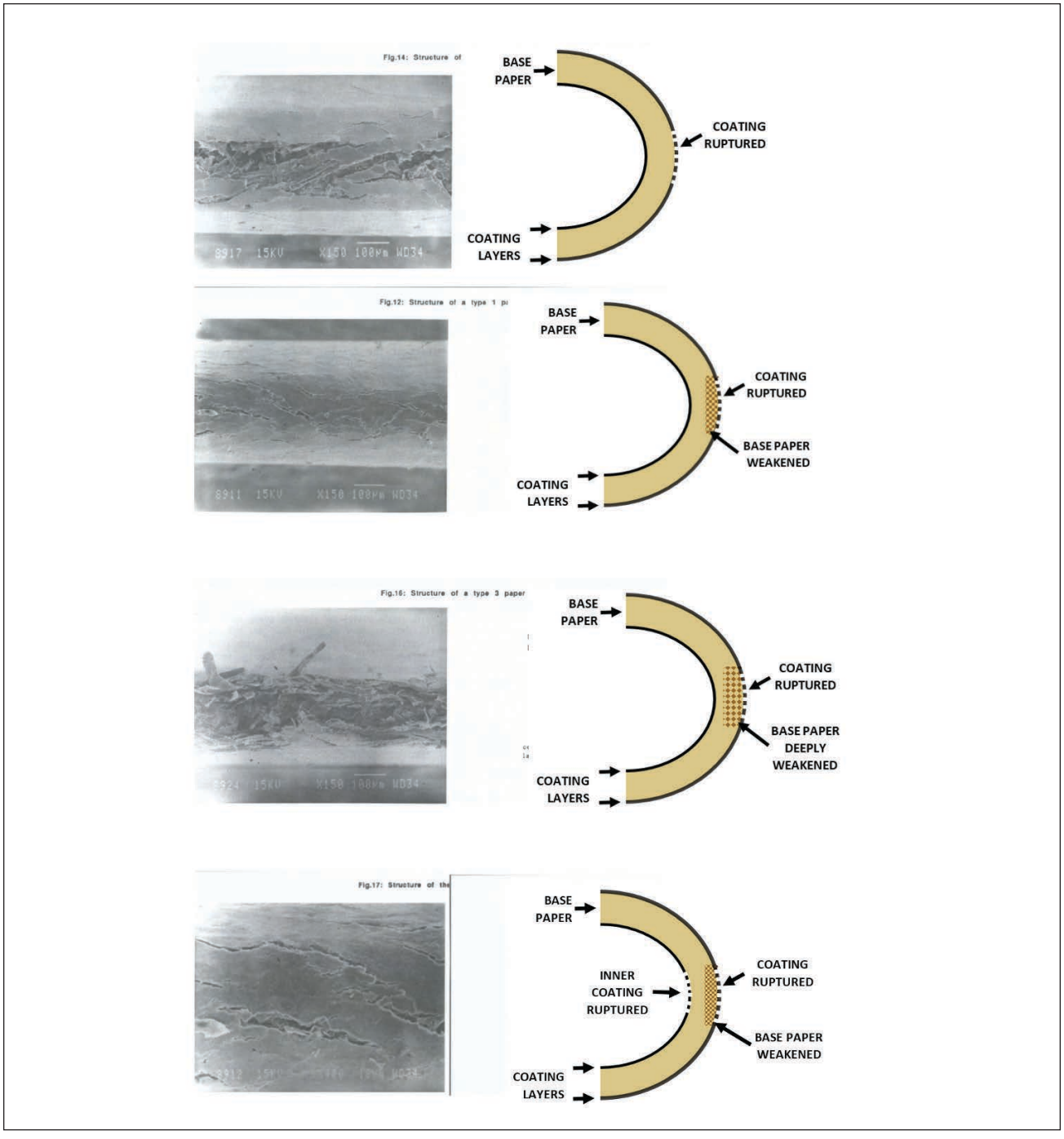

1. Four types of cracking behavior described by Guyot et al. [5]. For clarity, sketches on the right were redrawn based on the originals.

Fundamental studies

Barbier, Larsson, and Ostlund observed the initiation of cracks in the paper surface as paper was folded and compared this with numerical analysis [6-8]. They used an experimental jig to fold paper (**Fig. 2**), which allowed observation of crack initiation and deformation of the cross section. Their model (**Fig. 3** shows example output) had sound governing equations and reasonable outputs for the time (ca. 2005); however, it did not show any correlations with experimental cracking results. Shortcomings in the model, such as out-of-plane deformation, damage mechanics, and plastic deformation, could potentially be overcome with modern commercial numerical codes.

Rätto et al. described an interesting method to evaluate cracking mechanisms employing a double-notched specimen deformed in tension [9]. A double-notched specimen was produced for isolated coating layers and coated paper strips and deformed in tension using a "micro material tes-

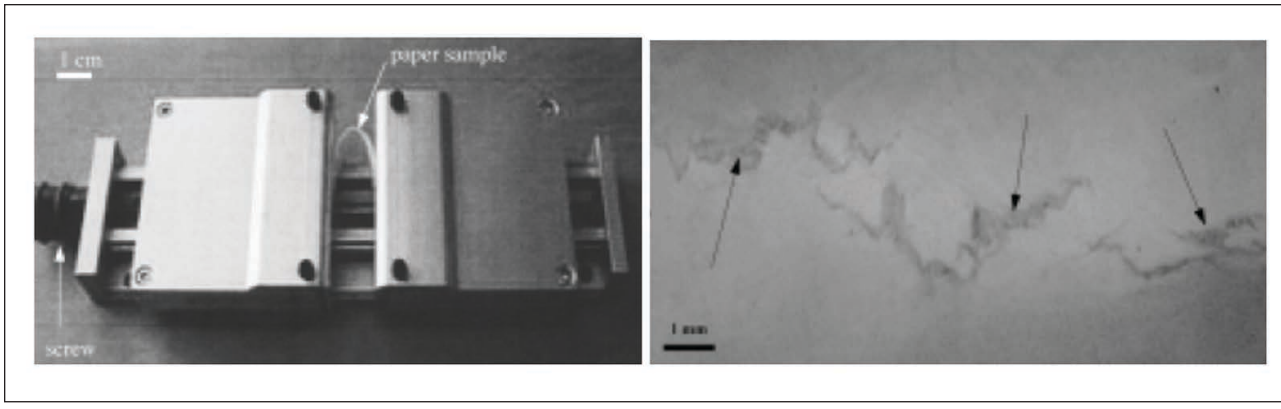

2. Experimental jig used and experimental cracking results from Barbier et al. [6].

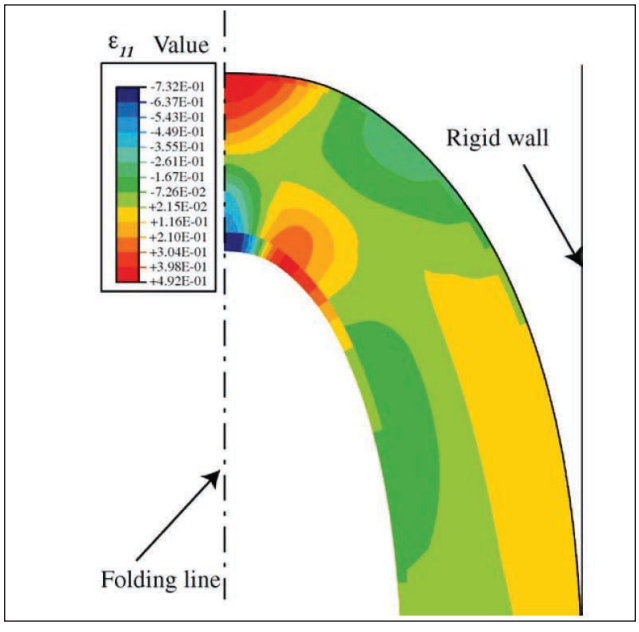

3. Numerical modeling results from Barbier et al. [8].

ter." A thermo camera and a high-speed camera were used to track crack initiation and propagation. The results were presented as crack area vs. time; time to crack initiation; and maximum propagation speed. This novel method has the potential to measure fracture energy and provide further insight into the failure mechanism.

Alam et al. used modeling to provide a calculation of the balance between bending stiffness and cracking of paperboard [10-12]. While the proposed model attempts to incorporate parameters around the coating structure, clear connections with the experiments were lacking. The model is elaborate but not validated, so the accuracy of the strain distribution is unclear. Experimentally, the folding method is complex (first heating to 160°C and then folding in a Prufbau printability tester), which leads to dynamic conditions that are inherently difficult to model. Fold cracking is quantified as a tensile strength ratio of a folded vs. unfolded sample, rather than a direct measure of damage. There is no convincing experimental evidence that the proposed ideal structure (a thin, stiff inner coating layer; a thick, low-stiffness middle coating; and a thin, low-stiffness outer coating) is indeed better.

Zhu et al. [13-15] used a combination of experimental testing and modeling to investigate the effect of pigment type on damage in barrier coatings. The effects of pigment type on water (moisture) vapor transmission rate (WVTR) of folded samples was studied [13]. The WVTR was measured on paperboard with a grid of 6 fold lines. Scanning electron microscope (SEM) images of the folded regions were analyzed to characterize cracking. The crack area calculated from WVTR showed a good correlation with the crack area as measured by SEM, though the numbers were different by two orders of magnitude (**Fig. 4**). The authors point out that this difference is likely caused by limitations in detecting cracks with SEM. The deformation of a coating layer on a paper substrate during a two-point bend was simulated to clarify the effects of pigment shape and modulus on local stress and strain distributions. The coating layer was modeled as a matrix with evenly distributed particles that were either platey or spherical. The material properties were isotropic and linear elastic. The simulated structure was folded 5°, with the coated layer on the convex surface. Contour maps show the progression of stress and strain from the upper (coated) surface in contact with the clamp, to the lower surface away from the clamp (**Fig. 5**). The maximum stress and strain were higher for the higher modulus particles, which simulated kaolin. The measured crack area showed a monotonically increasing correlation with max stress, as determined from the simulation (Fig. 4).

In another work [14], coated samples were wrapped around rods with progressively smaller radii to determine the curvature at which cracking visually appears. This was combined with a theoretical simulation of a column under deflection to describe the strain state on the surface; the material model was similar to that used in [13]. Contour maps from the simulation show the strain in the coating layer at the fold line (**Fig. 6**). The simulation results show that higher strain concentrations are caused by a higher

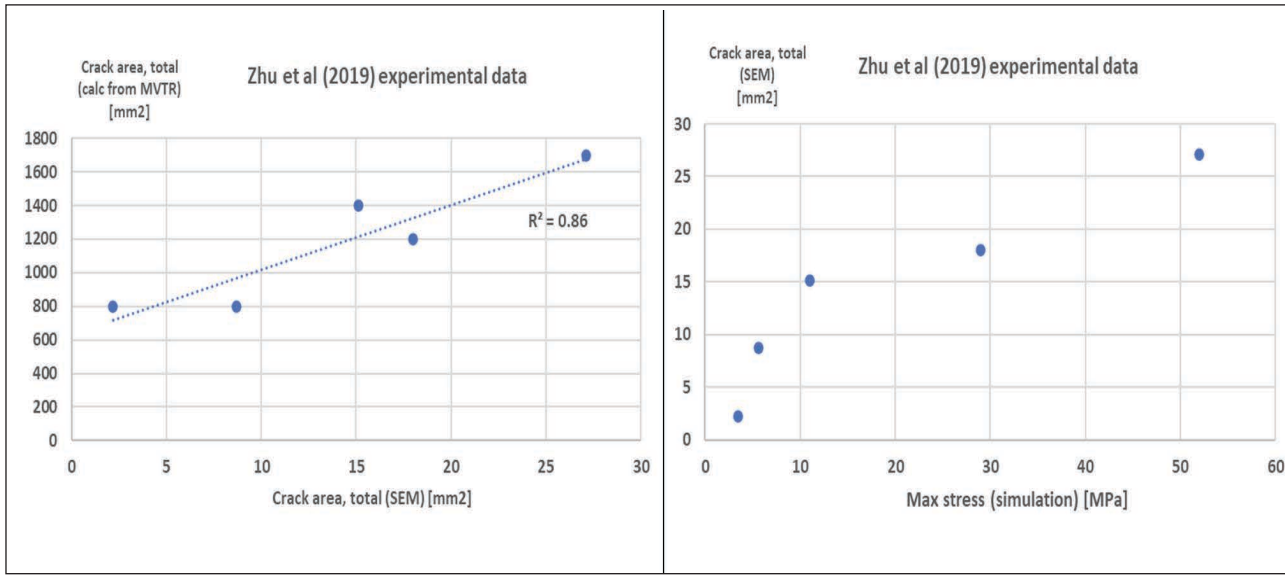

4. Crack area calculated from moisture (water) vapor transmission rate (MVTR) vs. measured crack area (left); and measured crack area vs. maximum stress from the simulation (right). Graphs produced from data in Zhu et al. [13]. (SEM = scanning electron microscopy.)

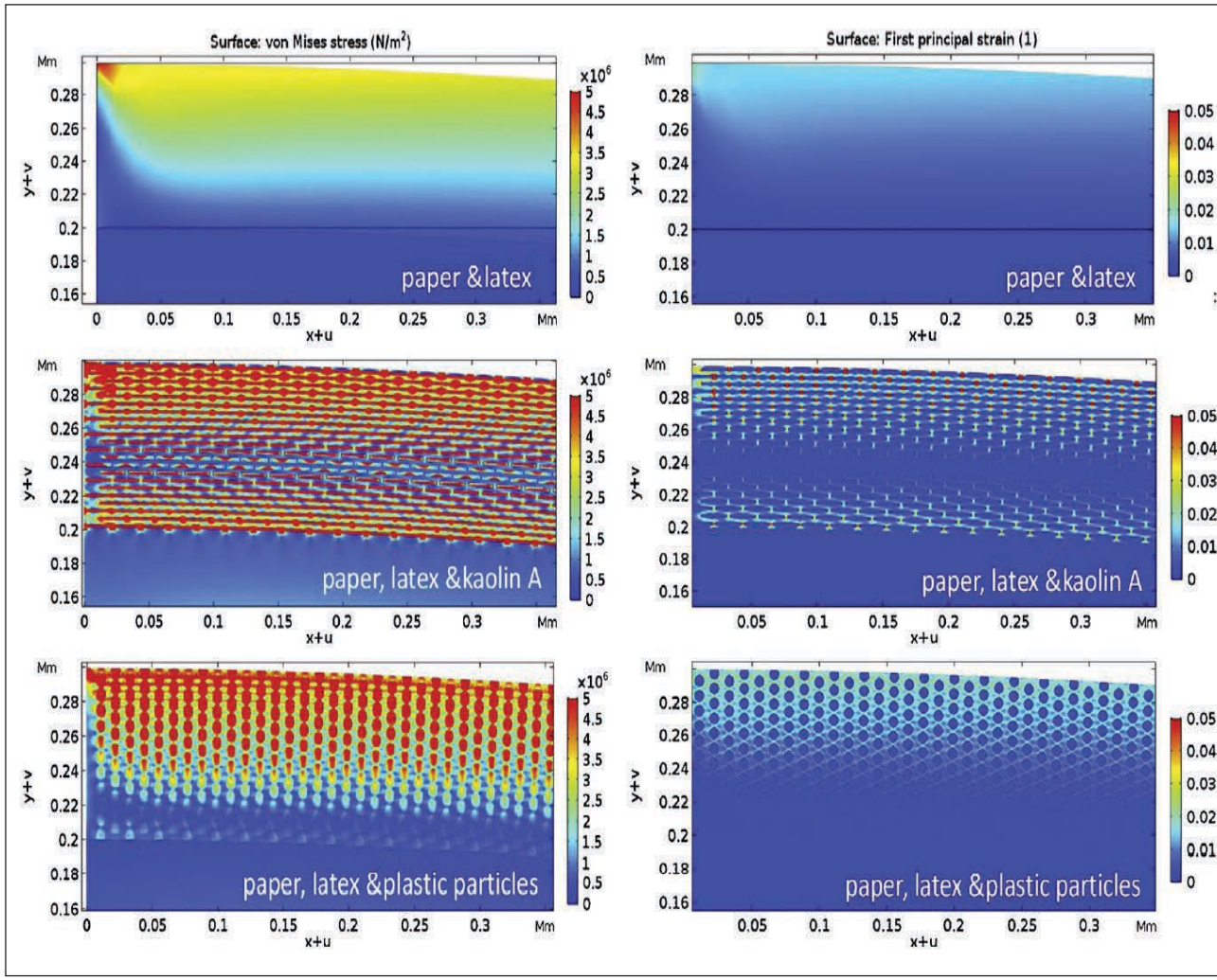

5. Stress and strain contour plots for simulations on the effect of particle size and modulus [13].

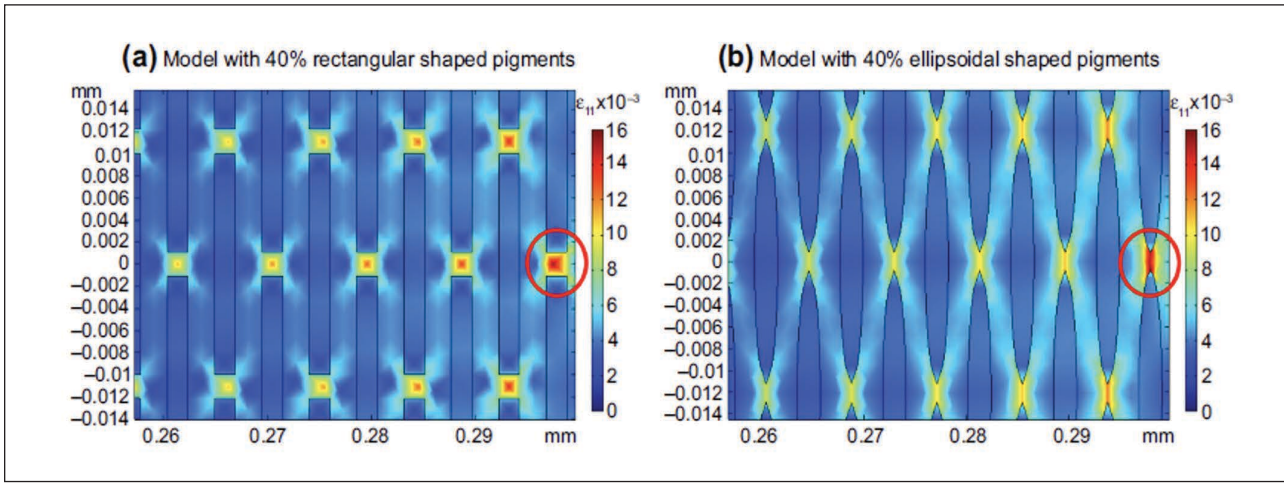

6. Strain contour at the midpoint of the column; the x-axis is the distance from the concave side [14].

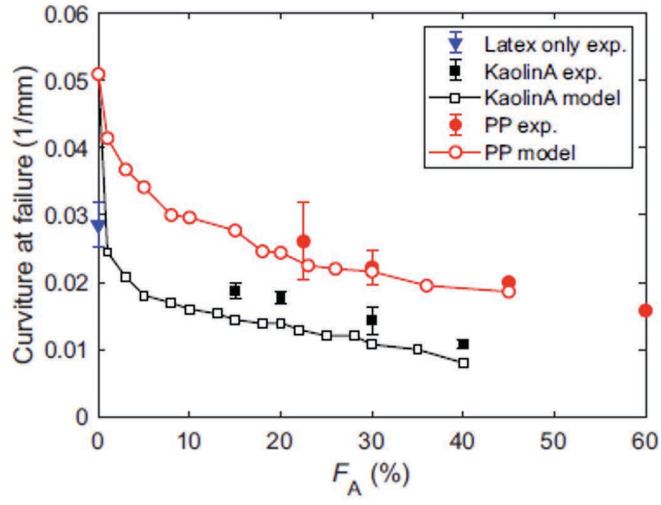

7. Comparison between experimentally determined curvature and theoretically predicted failure curvature (F_A) [14]. (PP = plastic pigments.)

difference between particle modulus and matrix modulus and by high aspect ratio particles. Based on an assumed failure strain of 0.9% (failure strain of the latex), the model correctly predicted the trends due to the pigment type and concentration (**Fig. 7**). The absolute values differed by 15%–25%, which was attributed to the resolution of the experimental measurements and limitations of the model. The results from this body of work are encouraging; in spite of the simplicity of the model, the model correctly predicts that more particles and higher modulus particles will lead to more cracking.

Coating formulation effects

Kim et al. demonstrated that a lower glass transition temperature (Tg) latex produced a lower amount of cracking and that printing can increase the amount and severity of cracking [16]. They suggest that lower Tg latex shows less cracking because it produces good film formability. They also state that ink and varnish make the coating more brittle, which directionally makes sense; however, these statements are not validated. Other researchers such as van Gilder [17] have identified that low Tg binder latex is known to have higher strain at failure than high Tg binder.

Oh et al. showed that either increased starch addition in the base coat or a higher Tg binder in the top coat caused an increase in the number of large cracks [18,19]. This work supports a strain-based failure criteria that suggests the changes that produce a lower strain to break result in increased crack areas. These researchers showed that the number of large cracks increases with a greater amount of starch in the pre (base)-coat, and they suggest that the precoat has a larger influence on cracks than the top coat. It was shown that the biggest driver of cracking was starch content in the base coat, but tensile data for those coatings were not presented. **Figure 8** could potentially be a very good demonstration of these effects, but it can only be as-

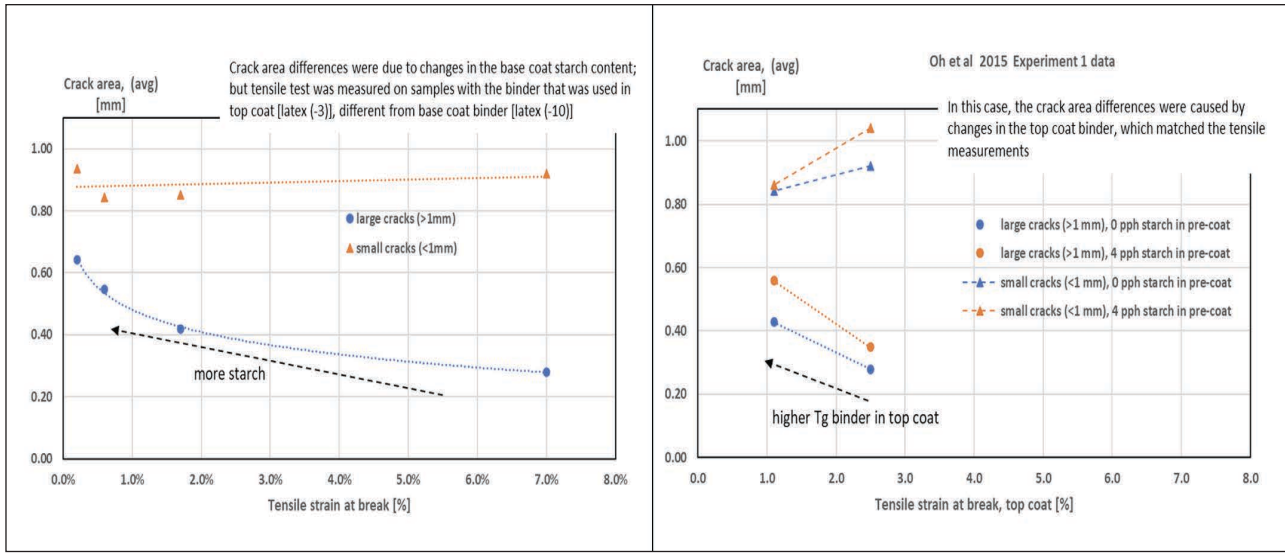

8. Crack area vs. tensile strain at break for starch addition (left) and binder glass transition temperature, Tg (right). Graphs produced from data in Oh et al. [18].

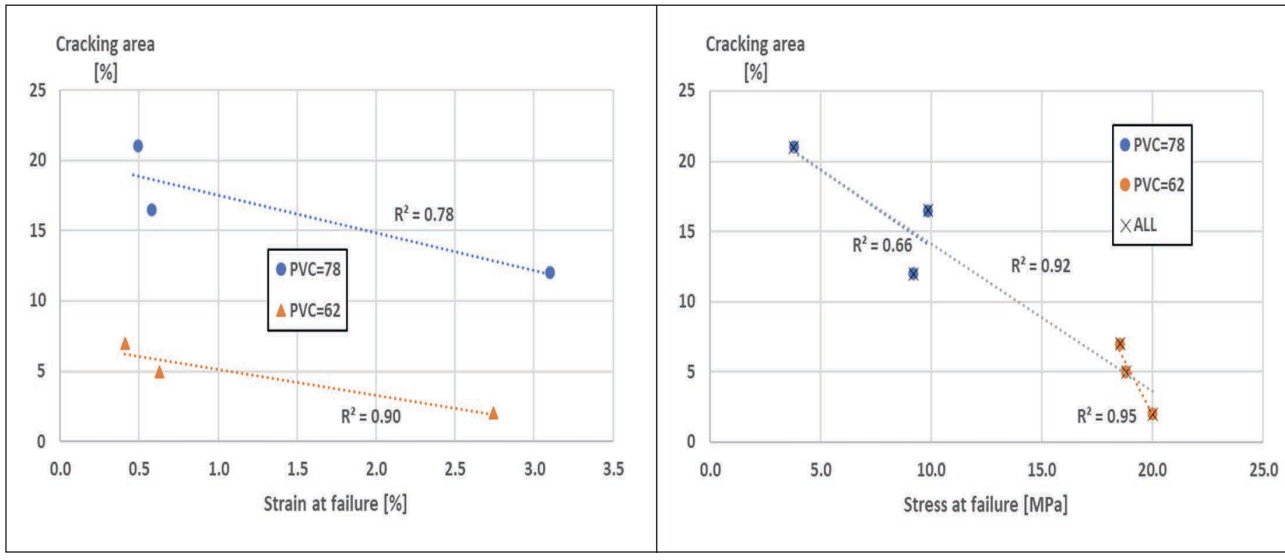

9. Cracking area vs. strain at failure (left) and stress at failure (right). Graphs produced from data reference [21]. (PVC = pigment volume concentration.)

sumed that the trend for more starch would be the same. Their comments on the effect of top coat vs. base coat are inconclusive, since different materials were used in each (base: low Tg coating with starch addition; top: higher Tg coatings with no starch addition).

Following along the same path, Wang and Ding studied the effect of coating parameters on cracking [20]. Their experimental results show that high binder, more clay pigment, and low coating thickness are better for low fold cracking. They give broad directional explanations, but do not quantify the effects.

Najafi et al. showed that a higher amount of pigment volume concentration (PVC) and starch have a detrimental effect on cracking [21]. The research describes measuring the strain at failure of a freestanding coating layer and how the pigment content correlates with crack area when folding. This work focused on high pigment content coatings. As such, the properties of the base sheet were not characterized, except for thickness and permeability. This work mostly agrees with Oh et al. [18] and states that strain at failure explains the effect of starch content, but that it fails to explain the latex effect. It is possible that stress at failure might provide a better explanation for both the effect of starch content and the latex effect (**Fig. 9**). Perhaps a fracture energy-based criterion would be better. Varney and Bousfield developed a model of the coating layer to simulate coating performance based on component properties [22,23]. This is an interesting approach, but so far, the pre-

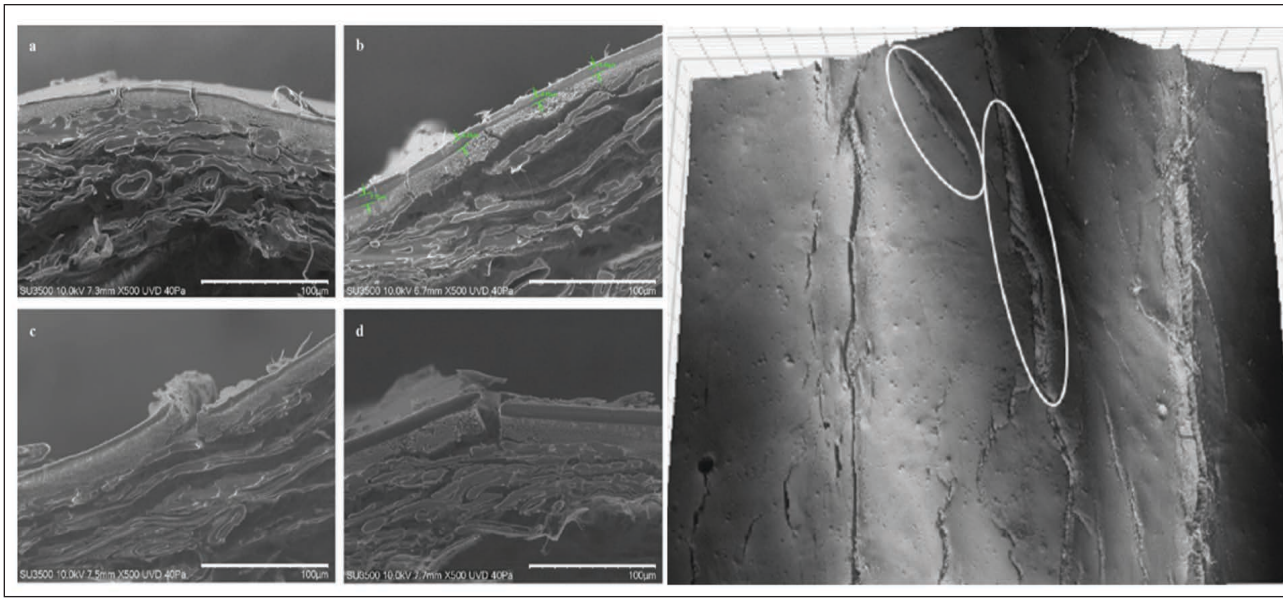

10. Images of coating damage from [24].

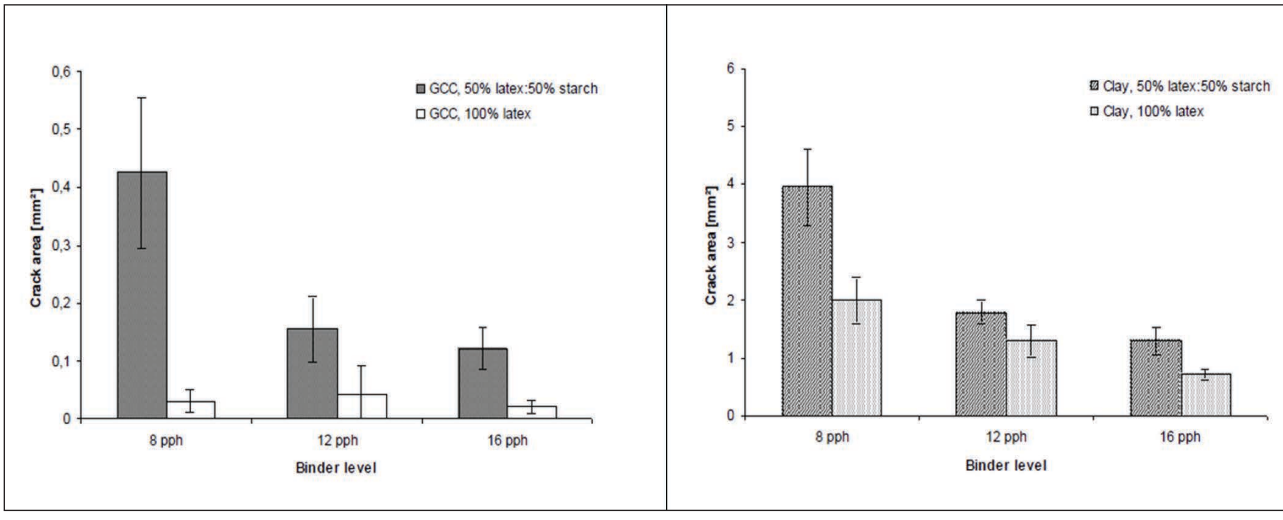

11. Cracking results for ground calcium carbonate (GCC)-based coatings (left) and clay-based coatings (right), including effect of starch [25]. Note difference in the y-axis scale between the graphs.

dicted performance has not correlated well with experimental results.

Javed et al. studied starch-based barrier coatings and the effects of plasticizer on cracking [24]. This work provides interesting images (e.g., **Fig. 10**), observations, and discussion; however, clear explanations of these findings are not established. There are good suggestions on what could be driving cracking, but they are difficult to quantify. The gaps are somewhat obvious: it is difficult to model the stresses and strains that develop in such a complex system; it is difficult to measure the correct properties of the coating layer, particularly out-of-plane properties; and it is difficult to quantify structural variation and defects that may affect fracture.

In a series of papers, Rättö and Hornatowska investigated effects of coating composition on cracking [9,25-27], particularly differences in the amount of cracking and failure morphology between ground calcium carbonate (GCC) and clay pigments. Results are shown in **Fig. 11.** It is important to note that in the first and second articles [25,26], they only creased the samples but did not specify the creasing tooling that was used, whereas in the third article [27], they creased and folded the samples.

Higher binder, less starch, and GCC pigment are best for low cracking. The binder and starch effects corroborate what has been shown by other researchers. GCC-based coatings typically have a perpendicular crack, which is indictive of tensile failure, while cracks in clay-based coatings typically show a diagonal crack, which is indictive of out-of-plane tensile or shear failure (**Fig. 12**). This is con-

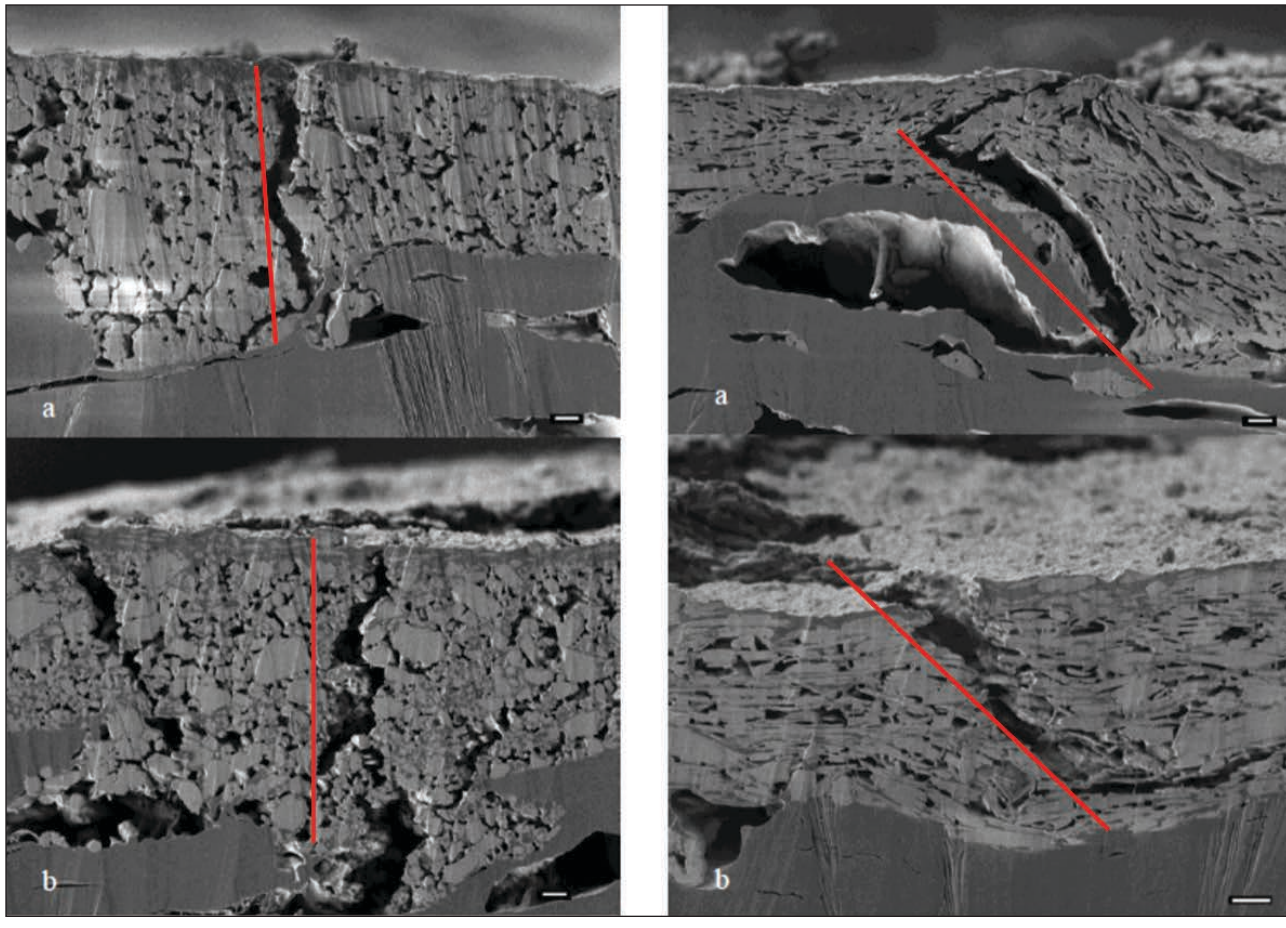

12. Cross-section images of coating after failure for: a) GCC coatings (left) and b) clay coatings (right) from Ratto et al. [26]. Lines highlight fracture direction.

sistent with the assumed properties of the coatings; i.e., this particular clay produces a coating that is stronger in tension and weaker out-of-plane, due to its shape. The implications are that the potential for coating failure cannot be characterized by the in-plane tensile properties only. They suggest that failure occurs when stress exceeds the corresponding strength, which could be in-plane tension or out-of-plane shear, depending on the full structure and properties. They also look at the effect of the substrate on a large scale (board vs. copy paper). A theoretical framework for calculating failure is discussed, but it remained at a qualitative level. Measured properties of the different coatings were not included; rather, only qualitative trends were described.

Zhu et al. [13-15] presented work that showed high aspect ratio pigments are good for barrier properties until they are folded. For performance after folding, they recommend to minimize the amount of pigment. The use of thick base stock or coating layers increased the potential for cracking, as did high pigment loadings and high pigment aspect ratio. Modulus differences between latex and pigment also increased the likelihood of failure. Lower modulus, more deformable pigments tended to exhibit improved failure resistance as compared with higher modulus, more rigid pigments.

Substrate effects

Sim et al. investigated the effect of mechanical properties of base paper on cracking [28]. They showed that the base paper can have an effect on fold cracking, though it remains unclear why it has an effect. The effect due to changing the softwood (SW) content, although significant, was relatively small; the cracking increased from 0.2% to 0.9% as the softwood content was increased from 0 to 100%. The mechanical properties showed substantial increases over that range, so it is hard to conclude that they are related when the cracking change was so small. The change in cracking may be due to physical structure, such as surface roughness, not the mechanical properties. The impact of refining (quantified as freeness) showed a larger effect on cracking. Highly refined (low freeness) hardwood (HW) combined with lightly refined (high freeness) softwood (SW) showed the highest amount of cracking. The SW freeness did not have a significant effect when combined with a mid-level freeness HW. There do not appear to be any clear correlations with the reported mechanical properties.

Conditions	Printing	Creasing	Folding, initial	Finishing	Reference #
Heat to 150°F	No	No	Manual	Cobb roller	2
Heat to 150°F	No	No	Mechanical device	Mechanical device	4
50% RH, room temp.	No	No	Mechanical device		6
50% RH, room temp.	No	Yes	Bending tester	Roller nip	29
Heat to 160°C	No	No	Prufbau tester		11
50% RH, room temp.	No	Die cutter	Calender nip		16
50% RH, room temp.	Laboratory printing	No	Mechanical device		18,19,28
50% RH, room temp.	IGT tester, cyan	Yes	Manual	Roller, 10 kg	9,24-27
50% RH, room temp.	Spray paint, black	No	Laboratory folding machine		21
50% RH, room temp.	IGT tester	No	IGT		20
50% RH, room temp.	None	None	Manual, 2 x 3 grid	4200 Pa pressure for 5 min	13

I. Sample prep for cracking evaluation (RH = relative humidity).

This study did not include bending stiffness or internal strength measures.

Kim et al. [16] and Oh et al. [19] both showed a difference in cracking degree due to the folding orientation (defined as the axis the sample is folded across, **Fig. 13**). A machine direction (MD) fold gives lower cracking than a cross direction (CD) fold and showed a different response to the binder properties. Cracking that occurs due to MD folding appears to be correlated with strain at break of the coating (as in the previous work), while cracking due to CD folding increases as strain at break goes up and appears to show a negative correlation with strength (**Fig. 14**). The authors' explanation for the difference in MD and CD response is interesting, but inconclusive. They claim that the discrepancy between MD and CD fold cracking is due to differences in curvature at the fold tip during folding that affects the point at which the cracks initiate. This suggests that the substrate properties play a significant part in the deformation and that the dynamics of crack growth are important.

The lowest grammage paper they used (110 g/m²) did not show a difference between MD and CD, did not show an effect due to pigment content and showed the lowest amount of cracking. This indicates that the strain on the outer surface is driving the cracking; the thicker the material, the greater the strain.

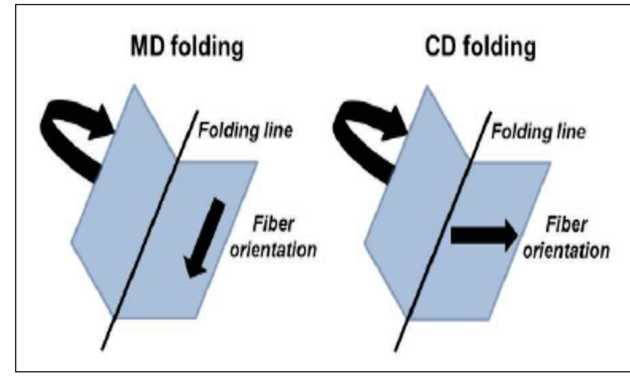

13. Definition of machine-direction (MD) and cross-direction (CD) folding, from Oh et al. [19].

Creasing effects

Articles related to crease cracking include Nagasawa [29], who investigated damage to an aluminum layer; Tanninen [30], who investigated the effect of creasing tooling on a barrier coating during die cutting and tray forming; and the work by Panek [31] and Mirzaei [32], who investigated reverse-side cracking of the fiber surface.

Nagasawa et al. studied cracking of aluminum foil (as opposed to standard coating) on paper [29] and included the effects of creasing depth on the magnitude of failure. Nagasawa's work related creasing tooling and creasing

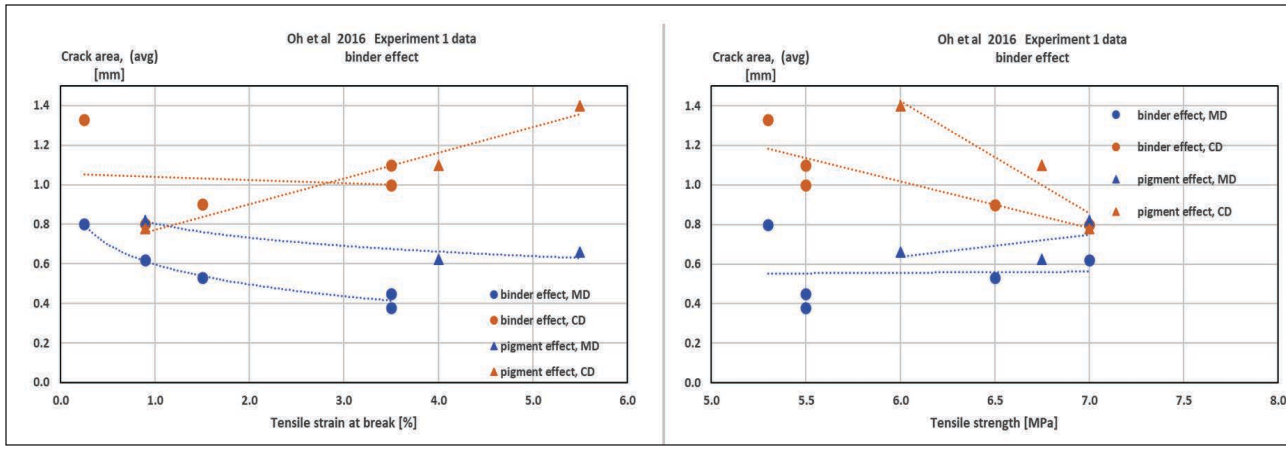

14. Crack area vs. strain at break (left) and crack area vs. strength (right). Graphs produced from [19].

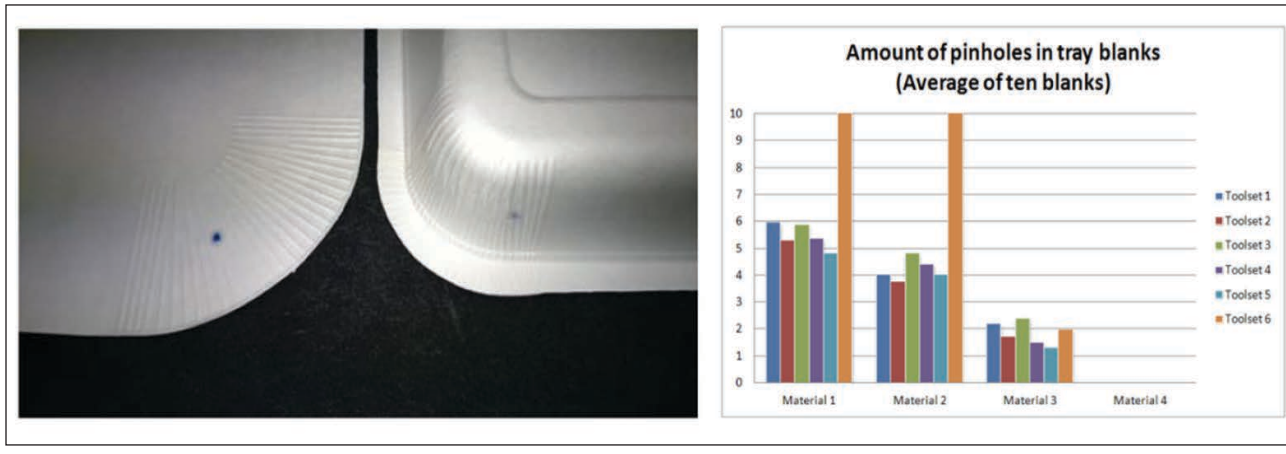

15. Analysis of pinholes in trays [30].

depth to a creasing shear strain and showed that cracking increased above a creasing shear strain (calculated). They suggest that the aluminum foil strain at break was important for failure, but did not conclusively validate this.

Tanninen studied effects of creasing tooling on cracking that occurs during die cutting and tray press forming of biopolymer dispersion-coated paperboards [30]. This work shows that damage is done in the die cutting/creasing process, and a range of tooling did not have a significant effect beyond a "worn toolset." **Figure 15** shows these details. Tanninen's comments suggest that coating cracking is sensitive to the creasing depth, but low enough pressure/creasing depth apparently could not be obtained in their studies to experimentally validate this assumption.

Panek et al. [31] derived a creasing draw (draw is the amount or depth of substrate drawn into the creasing tool) to describe the severity of creasing, and demonstrated that reverse-side (fiber) cracking would increase exponentially beyond a critical creasing draw. They suggest an operating window concept, such that the creasing conditions should remain to the left of the critical draw to minimize cracking. **Figure 16** details this operating window concept.

Mirzaei et al. [32] used the concept that the material properties will affect both the cracking resistance (post-peak energy) and the driving force for cracking (bending force, z-direction [ZD] compressive modulus) to propose a stability index as a ratio of the cracking resistance divided by the driving force. They demonstrated a correlation between cracking degree and the stability index. As an interesting point, they demonstrated that the addition of surface (size press) starch had a larger effect on increasing the driving force, but had no effect on the cracking resistance. **Figure 17** shows the impact of size press-applied surface starch and demonstrates the stability index.

DISCUSSION

The essence of barrier integrity is to control the onset and severity of damage to coatings during converting and end use. The outcome is practical knowledge to expand the range of materials (such as bio-based) and package configurations for paperboard-based packaging in barrier applications. In this case, we are addressing damage to coated paperboard under two-dimensional folding. The failure mechanism that coating will crack when its strength is exceeded by a driving force is likely true. But application of this concept towards coating cracking, and by extension,

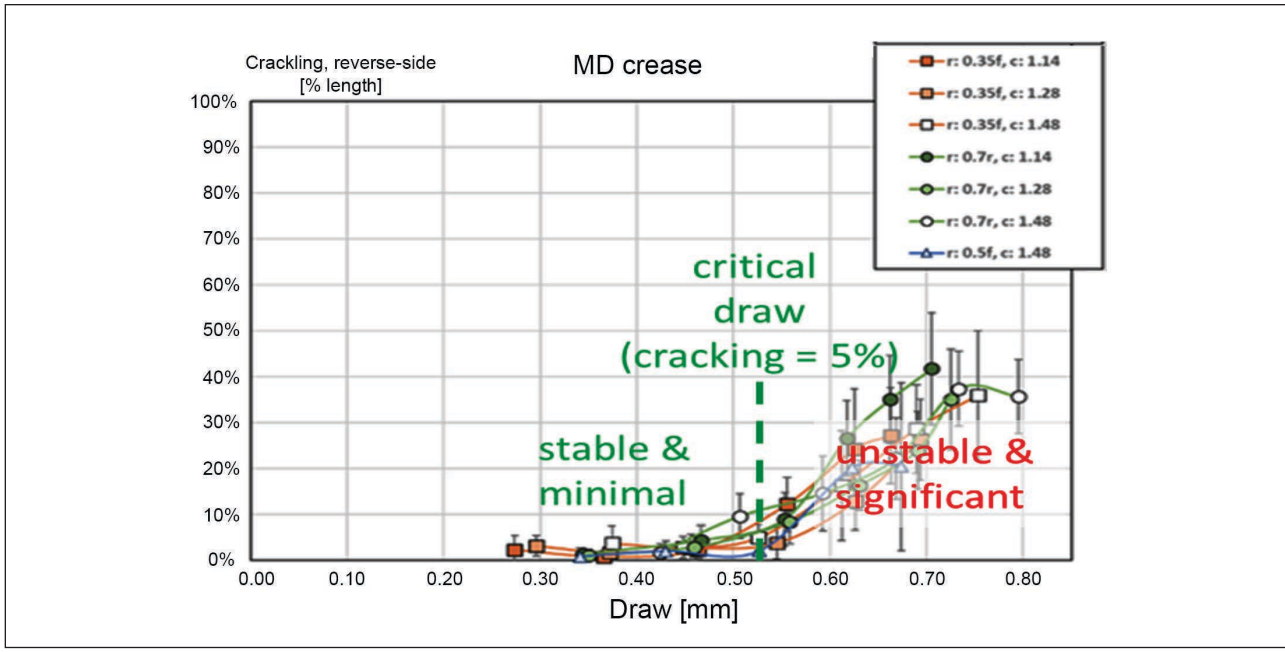

16. Critical draw concept from Panek et al. [31].

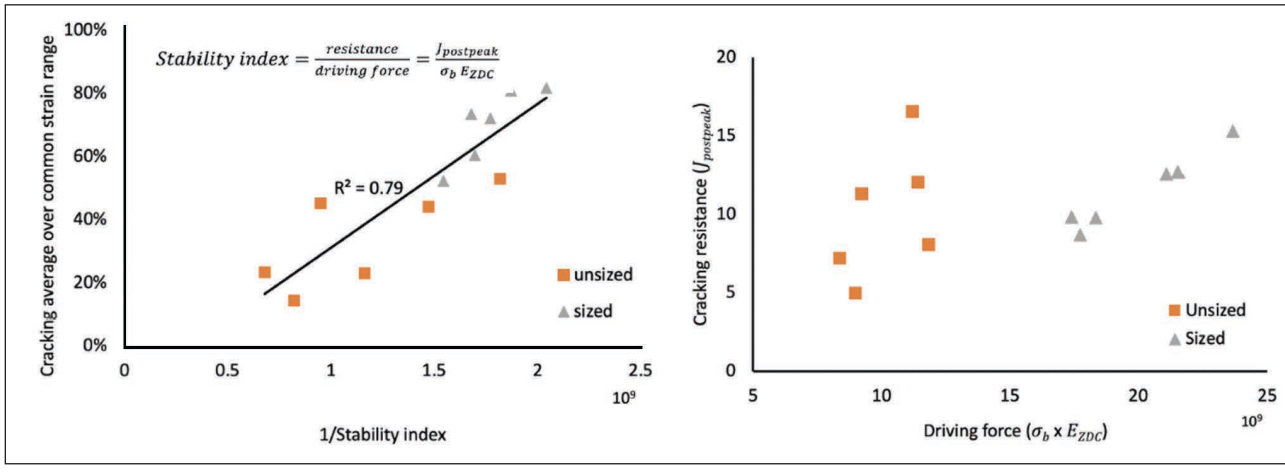

17. Stability index proposed by Mirzaei et al. [32], and the effect of the surface starch (sized vs. unsized) on the cracking resistance and driving force for cracking (bending force, z-direction (ZD) compressive modulus).

to barrier damage remains at a qualitative level. It is uncertain which property best describes the strength and is unclear how to best describe the driving force. Three areas that are integral for advancement in understanding cracking are: a) testing and analysis methods; b) material properties and structure; and c) modeling and simulation.

Testing and analysis

Testing and analysis should be standardized for reliable results and for transferability. Tests should be well-defined, precise, reproducible, and repeatable. Deformation, forces, and damage should be quantified to an extent that is feasible. Analysis should present the results in a format that is understandable, meaningful, and transferable.

Some type of folding has been used for all the coating cracking tests described here, which is summarized in **Table I**. Folding is simple to do and typically causes cracks. However, methods vary and the reproducibility across the methods is unknown. Sample preparation methods, sample orientation, and mechanics of folding should be described well enough for somebody to repeat the work and understand what may cause differences.

Folding can be complete or progressive. Complete folding is deforming the sample across a line to the point of surface-to-surface contact at 180°. This is commonly done with the belief that this represents an extreme condition that produces a maximum level of damage. In practical applications, it is assumed that the actual damage may be less, but it is unlikely to be worse. This type of test should be repeatable and reproducible, provided that the method

Characteristic	Apparatus	Metric	Reference #
Loss in strength	Tensile or burst test	Loss in strength	2,4,11
Cracks	Microscope	Strain (calculated) at which cracks first appear	6
Cracks	Microscope	Width, frequency	29
Cracks	Microscope	Cracked area (no details)	16
Cracks	Scanner, image analysis	Cracked area (includes details)	9,18-21,25-28
Cracks	High speed camera	Cracked area	9
Cracks	Microscope (optical, SEM); surface profiles	Cracked area, frequency	24
Cracks	Visual ranking	Cracking degree	20,24
Cracks	SEM	Area, number, width	13
Barrier	OTR	Difference	23
Barrier	WVTR	Absolute values	13

SEM = scanning electron microscope; OTR = oxygen transmission rate; WVTR = water vapor transmission rate.

II. Quantification of crack at fold.

is described well and accurately followed. Shortcomings are that it is difficult to know exactly what is happening, which hinders analysis and modeling.

Progressive folding involves evaluating samples at intermediate levels of folding or continuously monitoring the material directly during folding. This can be used to evaluate the initiation and progression of damage by monitoring for damage as deformation progresses. The point of damage initiation can be used to describe the amount of deformation that the system can withstand before barrier performance is compromised. Progressive folding is best done using a bend test with defined geometry and constraints so that the deformation is quantifiable and the stress and strain states can be approximated. Folding to intermediate levels can be to prescribed angles (such as 30° or 90°) or by folding around rods of different diameters [14]. While this approach may be tedious and limited in resolution, depending on the number of levels, it still gives a good approximation as to when damage first occurs and insight into how to control it. Continuous monitoring can be done with a proper video camera and experimental setup. Digital image correlation (DIC) is ideal for this approach. However, this requires equipment and method development.

Quantification of the amount of damage is necessary for analysis. Methods used in the literature are summarized in **Table II**. Damage can be quantified as a characteristic of the physical structure, such as crack density and area, or it can be quantified as differences in barrier performance. Accurate measurement of the physical structure can be challenging. The majority of tests evaluate visual damage to the coating by using magnification (microscope, scanner) to amplify the presence of cracks. The use of ink to provide contrast and scanning to provide accurate measures is useful, but it is important to calibrate the measurements, document limitations in precision, and understand effects due to image analysis settings. Scanning electron microscopy is useful, but it requires the correct equipment and can be tedious. Damage generally means cracks in the coating; however, damage can occur and affect barrier performance without being visually obvious, even under magnification. Damage to coatings (particularly barrier coatings) should be evaluated with relevant and sensitive tests for which the coatings were designed. These tests include oxygen transmission rate (OTR), moisture vapor transmission rate (MVTR), porosity, and staining. Characterization of crack morphology is useful to understand effects in more detail and provide insight into the mechanisms that cause damage. More detailed analysis of crack morphology may be needed for accurate correlations with barrier performance.

Material properties and structure

Material properties and structure should be more thoroughly characterized to allow more accurate analysis and identification of secondary effects. This includes identifying all relevant characteristics and determining these at an appropriate level. Even though coating formulations have clear effects on cracking, key properties that affect failure and mechanisms that drive failure have not been clearly established. Relationships between coating cracking and material properties have been shown in certain cases, but

the transferability to other cases is inconclusive. Trends can be different, depending on the size scale of the cracks. The following comments are on characteristics that influence cracking, recognizing that much still needs validation.

Generally, coatings should be tough and uniform. Toughness is likely a better descriptor, as it encompasses both strength and strain and can be quantified with a fracture energy. The coating should be tough in all modes, including out of plane tensile and shear. Uniformity in the structure will help to minimize stress concentrations, which will lead to failure. Non-uniformity can originate from variations in the physical structure and from differences in properties of the coating components. The smoothness of the substrate will affect uniformity of the coating and the presence of stress concentrations. Intrusion of fibers into the coating (e.g., raised fibers) can be detrimental.

The substrate should be relatively weak out-of-plane and locally delaminate during folding, which reduces the surface strain. The best measurements of out-of-plane properties are not established, but documentation of relevant measurements such as ZD tensile (ZDT), Scott bond, and shortspan compression is helpful. The optimum in-plane properties are unclear. There is reason to believe that the substrate should be tougher in-plane than the coating to provide cohesive support and minimize the amount of stress on the coating. At the same time, there is reason to believe that the substrate should have a relatively low modulus to minimize the stress during folding. The balance between maximizing strength while minimizing driving forces is complex and dependent on the system.

Accurate measurement of coated paperboard is challenging and has many limitations. It is relatively non-uniform and has a discrete (non-continuous) structure as compared with the scale of damage. Coating layers are a composite that have a variable interface with a fibrous structure, which makes it difficult to characterize. At high levels of deformation, the material typically shows non-linear and ductile mechanical behavior, and damage is occurring to the substrate during deformation. A coated layer that is deformed within a span of millimeters (as during folding) does not necessarily have the same properties that are measured as an isolated coating with a standard tensile test.

Having described these limitations, it is vital to continue developing characterization methods. It is important to understand shortcomings and validate the transferability of properties across different configurations. At the same time, sound approximations of properties by indirect measurement, calculation, or assumption are useful in advancing knowledge.

Modeling and simulation

Modeling and simulation can be a powerful tool to explain effects, predict results, and guide further work. While the benefits are enticing, there is still a long way to go in modeling coating cracking. Folding to small radii of curvature is an obvious cause of damage, but it is inherently difficult to model. It is a composite system under high deformation, where complex stress states, non-linear effects, and damage become more prevalent. Multiple modes can drive the initiation and propagation of damage. The relative properties of the materials, their physical structure, and the extent of deformation all can play a role. There are many challenges, but advances in knowledge of material behavior and computational methods will bring us closer to solutions, one step at a time. Recent work has shown the usefulness of relatively simple models to correlate pigment characteristics with experimental results [13,14].

Models should be fundamentally sound, validated, and with mechanisms that relate damage with driving factors. It should be on the right level: detailed enough to capture essentials, but not too complex to require excessive parameters and a high computational cost. The ability to accurately describe an entire physical system should not be an initial requirement. At a minimum, a model needs to provide a better description of the region of interest. A model can be effectively employed as a virtual microscope, providing focus on specific aspects of cracking damage.

CONCLUDING REMARKS

Published literature on coating cracking is useful to understand, but it is still limited in terms of what is directly beneficial for commercial applications. There is qualitative knowledge on what affects cracking, but there are still gaps in quantifying effects and unknowns in fundamentally understanding why. Further advances in standardizing testing, measuring key properties, and modeling the mechanisms will be important to develop a more comprehensive set of knowledge and tools available to predict coating and barrier damage. **TJ**

LITERATURE CITED

1. Smithers, "The future of functional & barrier coatings for paper & board to 2024," Smithers, Akron, OH, USA, 30 August 2019.
2. Colley, J., *Appita* 35(4): 299(1982).
3. Colley, J., *Appita* 35(6): 499(1982).
4. Jopson, R.N. and Towers, K., *Coating Conf.*, TAPPI Press, Atlanta, 1995, p. 459.
5. Guyot, C., Bacquet, G., and Schwob, J.M., "Folding resistance of magazine papers," *Coating Conf.*, TAPPI Press, Atlanta, 1992.
6. Barbier, C., Larsson, P.-L., and Östlund, S., *Nord. Pulp Pap. Res. J.* 17(1): 34(2002). https://doi.org/10.3183/npprj-2002-17-01-p034-038.
7. Barbier, C., Larsson, P.-L., and Östlund, S., *Compos. Struct.* 67(4): 395(2005). https://doi.org/10.1016/j.compstruct.2004.01.025.
8. Barbier, C., Larsson, P.-L., and Östlund, S., *Compos. Struct.* 67(4): 383(2005). https://doi.org/10.1016/j.compstruct.2004.01.024.
9. Rättö, P. and Hornatowska, J., "Dynamic aspects of crack development in coating layers," *Adv. Coat. Fundam. Symp.*, TAPPI Press, Atlanta, 2010.

10. Salminen, P., Carlsson, R., Sandas, S., et al., "Combined modeling and experimental studies to optimize the balance between fold crack resistance and stiffness for multilayered paper coatings—Part 1: Introduction and modeling studies," *PaperCon*, TAPPI Press, Atlanta, 2008.

11. Salminen, P., Carlsson, R., Sandas, S., et al., "Combined modeling and experimental studies to optimize the balance between fold crack resistance and stiffness for multilayered paper coatings—Part 2: Pilot coater experimental studies," *PaperCon*, TAPPI Press, Atlanta, 2008.

12. Alam, P., Toivakka, M., Carlsson, R., et al., *J. Composite Mater.* 43(11): 1265(2009). https://doi.org/10.1177/0021998308104227.

13. Zhu, Y., Bousfield, D., and Gamlich, W.M., *Prog. Org. Coat.* 132: 201(2019). https://doi.org/10.1016/j.porgcoat.2019.03.031.

14. Zhu, Y., Bousfield, D., and Gamlich, W., *J. Coat. Technol. Res.* 18: 1117(2021). https://doi.org/10.1007/s11998-021-00465-1.

15. Zhu, Y., Bousfield, D., and Gamlich, W., *Nord. Pulp Pap. Res. J.* 37(1): 97(2021). https://doi.org/10.1515/npprj-2021-0052.

16. Kim, C.-K., Lim, W.-S., and Lee, Y.K., *J. Ind. Eng. Chem.* 16: 842(2010). https://doi.org/10.1016/j.jiec.2010.05.001.

17. Kan, C.S., Kim, L.H., Lee, D.I., et al., *TAPPI J.* 80(5): 191(1997).

18. Oh, K., Sim, K., Jung, Y.B., et al., *Nord. Pulp Pap. Res. J.* 30(2): 361(2015). https://doi.org/10.3183/npprj-2015-30-02-p361-368.

19. Oh, K., Seo, D., Youn, H.J., et al., *Nord. Pulp Pap. Res. J.* 31(2): 347(2016). https://doi.org/10.3183/npprj-2016-31-02-p347-353.

ABOUT THIS PAPER

Cite this article as:
Panek, J.C. and Hart, P.W., *TAPPI J.* 21(11): 589(2022). https://doi.org/10.32964/TJ21.11.589

DOI: https://doi.org/10.32964/TJ21.11.589

ISSN: 0734-1415

Publisher: TAPPI Press

Copyright: ©TAPPI Press 2022

About this journal

20. Wang, Q. and Ding, N., *Nord. Pulp Pap. Res. J.* 35(3): 419(2020). https://doi.org/10.1515/npprj-2019-0051.

21. Najafi, S., Bousfield, D., and Tajvidi, M., *TAPPI J.* 18(2): 93(2019). https://doi.org/10.32964/TJ18.2.93.

22. Varney, D.H. and Bousfield, D.W., *TAPPI J.* 17(1): 21(2018). https://doi.org/10.32964/TJ17.01.21.

23. Varney, D.H. and Bousfield, D.W., *TAPPI J.* 18(2): 101(2019). https://doi.org/10.32964/TJ18.2.101.

24. Javed, A., Rättö, P., Järnström, L., et al., *Nord. Pulp Pap. Res. J.* 33(2): 336(2018). https://doi.org/10.1515/npprj-2018-3039.

ABOUT THE AUTHORS

We studied this topic for the purpose of improving our ability to enhance performance of barrier coated packages in demanding applications. The intent of this review was to clarify what has been done in previous research in order to give guidance on what research should be done in the future.

The most challenging aspect of this review was to distill learnings from the research of others and combine them with our own beliefs and observations to the point we could propose what we believe to be an effective route forward. Coating cracking is an area where it is fairly straightforward to get some sort of results, but difficult to quantify what is occurring on a local level. Due to this, it is important to distinguish what are validated conclusions from what is speculation.

This study emphasizes the value in taking the time to properly read and understand relevant literature. There are conclusions and beliefs that are not truly supported; at the same time, there are observations and results that are overlooked or downplayed. It is important to take a step backward and distinguish what is valid, where there are gaps, and what effective paths can close these gaps.

Much of previous work on this topic has been hindered by lack of knowledge on what is occurring at a local level. The tools and knowledge available to us as a community have developed so that we can measure deformation on a small scale and more accurately model stresses and strains. Coupled with implementing defined and repeatable methods, we are better positioned to advance knowledge in this area.

With further study and advancement of knowledge and evaluation methods in this area, mills can benefit through more effective product development. We hope this study encourages and provides guidance for more fundamental research on this topic. Internally, we are completing research on setting up digital image correlation (DIC) to measure surface deformation during folding and are developing standard methods to fold samples.



Panek



Hart

Panek is senior principal R&D scientist and Hart is director, Fiber Technology and Innovation, at WestRock in Richmond, VA, USA. Email Panek at joel.panek@westrock.com.

25. Rättö, P. and Hornatowska, J., *Nord. Pulp Pap. Res. J.* 25(4): 495(2010). https://doi.org/10.3183/npprj-2010-25-04-p495-501.

26. Rättö, P., Hornatowska, J., Changhong, X., et al., *Nord. Pulp Pap. Res. J.* 26(4): 485(2011). https://doi.org/10.3183/npprj-2011-26-04-p485-492.

27. Rätto, P., Hornatowska, J., and Barbier, C., *Nord. Pulp Pap. Res. J.* 27(4): 714(2012). https://doi.org/10.3183/npprj-2012-27-04-p714-720.

28. Sim, K., Youn, H.J., Oh, K.D., et al., *Nord. Pulp Pap. Res. J.* 27(2): 445(2012). https://doi.org/10.3183/npprj-2012-27-02-p445-450.

29. Nagasawa, S., Endo, R., Fukuzawa, Y., et al., *J. Mater. Process. Technol.* 201: 401(2008). https://doi.org/10.1016/j.jmatprotec.2007.11.253.

30. Tanninen, P., Saukkonen, E., Leminen, V., et al., *Nord. Pulp Pap. Res. J.* 30(2): 336(2015). https://doi.org/10.3183/npprj-2015-30-02-p336-343.

31. Panek, J.C., Smith, S., and Coffin, D.W., *TAPPI J.* 19(4): 219(2020). https://doi.org/10.32964/TJ19.4.219.

32. Mirzaei, B., Harksen, T., Smith, S., et al., *TAPPI J.* 20(2): 81(2021). https://doi.org/10.32964/TJ20.2.81.

Modeling the influence of rheology on smooth rod coating systems

JOHN A. ROPER III, DOUGLAS W. BOUSFIELD, AND GREGORY W. WELSCH

ABSTRACT: Rod coating methods are of interest for the application of barrier coatings, especially at off-line facilities that may run at moderate speeds and narrow web widths. At lower line speeds and lower coating solids, it is difficult to achieve good coat weight control because of poor loading of the rod. While there is extensive literature available about blade and roll coating, there seems to be less reported on the rod loading of smooth rods to obtain various coat weights. Much of the work is around metering rods working on applicator rolls at high speeds that are associated with the metered size press, with a focus on ribbing instabilities. This work employs a simplified model, neglecting some complex features of rubber deformation and film split, to estimate the influence of the process parameters such as speed, rod diameter, viscosity, and rod loading on the coat weight obtained. As found in practice, at low speed and low viscosities, the coat weight-load curve is steep, leading to poor control of the coat weight and coat weight uniformity. If the viscosity is increased, the curve is modified, and control is possible with rod loading in a normal range. For shear thinning fluids described by the Carreau model, the power law index and other parameters need to be in the correct range to obtain the desired effect. Modeling predictions show a steeper dependence of coat weight with rod pressure when compared to pilot coater data. This may be caused by missing details in the mechanical loading of the rod related to tube pressure or from neglecting the impact of filter cake formation of the applied coating in the model.

Application: The model and experimental results should help guide the smooth rod coating of paper grades, especially for barrier coatings applied off line.

Smooth rod coating is a well-established coating process for the paperboard industry and offers advantages over blade coating in providing a more uniform surface coverage. This feature makes rod coating an attractive option for applying barrier coatings, especially on off-line coaters or at packaging converting facilities. Over the years, the industry has developed a working knowledge for using rod coaters to apply highly pigmented coatings at medium-to-high line speeds. It is well known that rod applied coat weights have a lower response to rod pressure than blade coating. This necessitates the switch to different rod diameters and/or changing the coating solids to access a target coat weight range. However, the increasing use of smooth rod applied barrier coatings at relatively low line speeds and possibly lower solids creates the challenge of selecting the right rod diameter and tuning the rheology of the coating to achieve a high enough coat weight for good barrier performance. Because many barrier coatings are low in pigmentation and have Newtonian-like rheology, the coat weight response to rod pressure can deviate from the empirically known behavior of highly pigmented, shear-thinning paper coatings.

Despite the widespread use of rod coaters, there is little published work on the fundamentals of smooth rod coating. A limited amount of literature dates from the 1990s, and much of this work focuses on the use of a smooth rod to apply coatings to the transfer roll on metered size press (MSP) coaters. The MSP coaters can operate at much higher line speeds, so there were several issues, such as rod spitting and ribbing, that needed to be addressed. Some excellent experimental and sophisticated modeling work was done on the topic [1,2]. Another publication highlighted the importance of extensional viscosity for determining coat weights on a rod coater [3].

In contrast, blade coatings and roll coatings have been extensively studied both experimentally and theoretically. The models for these methods of application have grown increasingly complex and now incorporate features such as coating dewatering and deformation of backing rolls, as well as flexing of the blade under an applied load. Such a detailed understanding is lacking for rod coaters; for example, not knowing how a given rod diameter with a given coating rheology will respond to applied pressure, which is the subject of this investigation.

The motivation behind this work is to apply the well-established framework for modeling of roll and blade coatings [4-7] to smooth rod coatings to better understand the fundamentals of smooth rod coating. The strategy will be to start with a simple model to look at the effect of coating viscosity, rod diameter, and coating speed on coat weight for both Newtonian and shear-thinning coating, while ig-

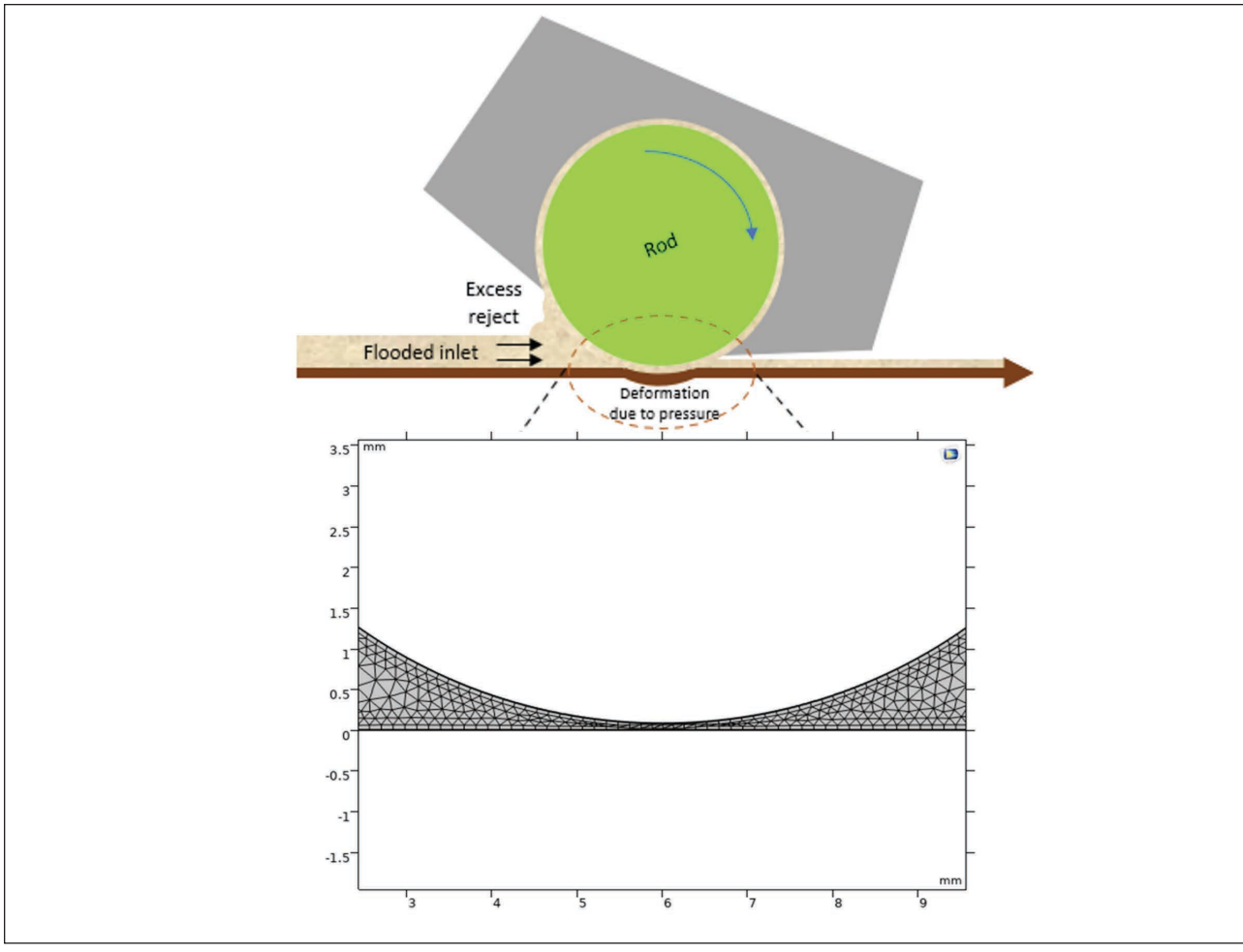

1. Side view of rod coating with excess coating supplied upstream and film split downstream. The rod often rotates slowly. The region of interest is zoomed, and the finite element mesh is shown.

noring features like compressibility, film split, dewatering, and wall slip. These simulations are compared to published experimental results. The work presented here is a first step in developing robust models for rod coatings.

MODEL DEVELOPMENT

The flow between a metering rod and a substrate is known to follow lubrication analysis well. The complexity comes from the exit region of the rod and the film split that occurs there. In that region, some of the coating will stay with the rod and the rest will move with the web. **Figure 1** shows the situation of interest. The amount of fluid that stays with the rod is likely small if the rotational speed of the rod is low. The film split location is controlled by a balance of viscous and surface tension forces.

Because of the interest in studying shear thinning fluids and other complex viscosities, a commercial finite element code is used (COMSOL Multiphysics Version 5.4, COMSOL AB; Stockholm, Sweden). The bottom part of Fig. 1 shows the mesh that is used for physics-controlled meshing. The geometry is generated by subtracting a circle equal to the rod diameter from a rectangle of the region of interest. The circle position is the gap between the rod and the web plus the rod radius. The laminar flow physics is selected and either Newtonian or non-Newtonian rheology is selected. This causes the program to solve the normal conservation of mass and momentum equations. The boundary conditions are the web velocity at the lower boundary, the rod velocity at the top boundary, and a zero-gauge pressure condition for the inlet and outlet regions. The influence of the film split is neglected here because of the focus on rod loading; most of the pressure generation is in the region in the center of the nip. In addition, rubber or web deflection is neglected. A typical pressure distribution is shown in **Fig. 2**. Pressure builds in front of the rod but then rapidly falls to subambient values right after the minimum gap. This agrees with other reported predictions, although a number of factors are neglected here, as shown in **Table I**.

Most experimental measurements of the pressure distribution do not show a pronounced subambient pressure, as in Fig. 2. This may be caused by the short duration of the pulse, cavitation phenomena, film split invading the region, or the relaxation of rubber deformation. In view of the com-

Assumptions	Potential Impact on Modeling Results
Flat nonporous substrate with no filtercake formation	Earlier modeling work with metered size press (MSP) coatings showed that filter cake formation was a key factor in coat weight control.
Rheology unchanged due to dewatering	Past work modelling blade coating suggests filter cake formation is more important than viscosity change.
No extensional viscosity effects	Extensional viscosity will increase the pressure needed to achieve a target coat weight, but overall trends should be similar [3].
No deformation of substrate or backing roll	Past modeling of roll coatings suggests impact on film split and ribbing instabilities, as well as negative pressure pulse at the exit. There is an uncertain impact on coat weight response.
No cavitation or film split at the exit of the rod nip and not including this in the loading calculation	While coating that makes it through the minimum gap will end up on the web, the load predictions may be influenced by this. Experimental pressure measurements show only a small subambient pressure, possibly due to cavitation.
Rod is not rotating and no water lubrication layer on the rod	Rod rotation speed is small compared to web velocity. Rod rotation is known to impact rod spitting and streaking. Lubrication may help coating to slip under rod as plug flow, increasing coat weight and lowering effective shear rate.

I. List of model assumptions.

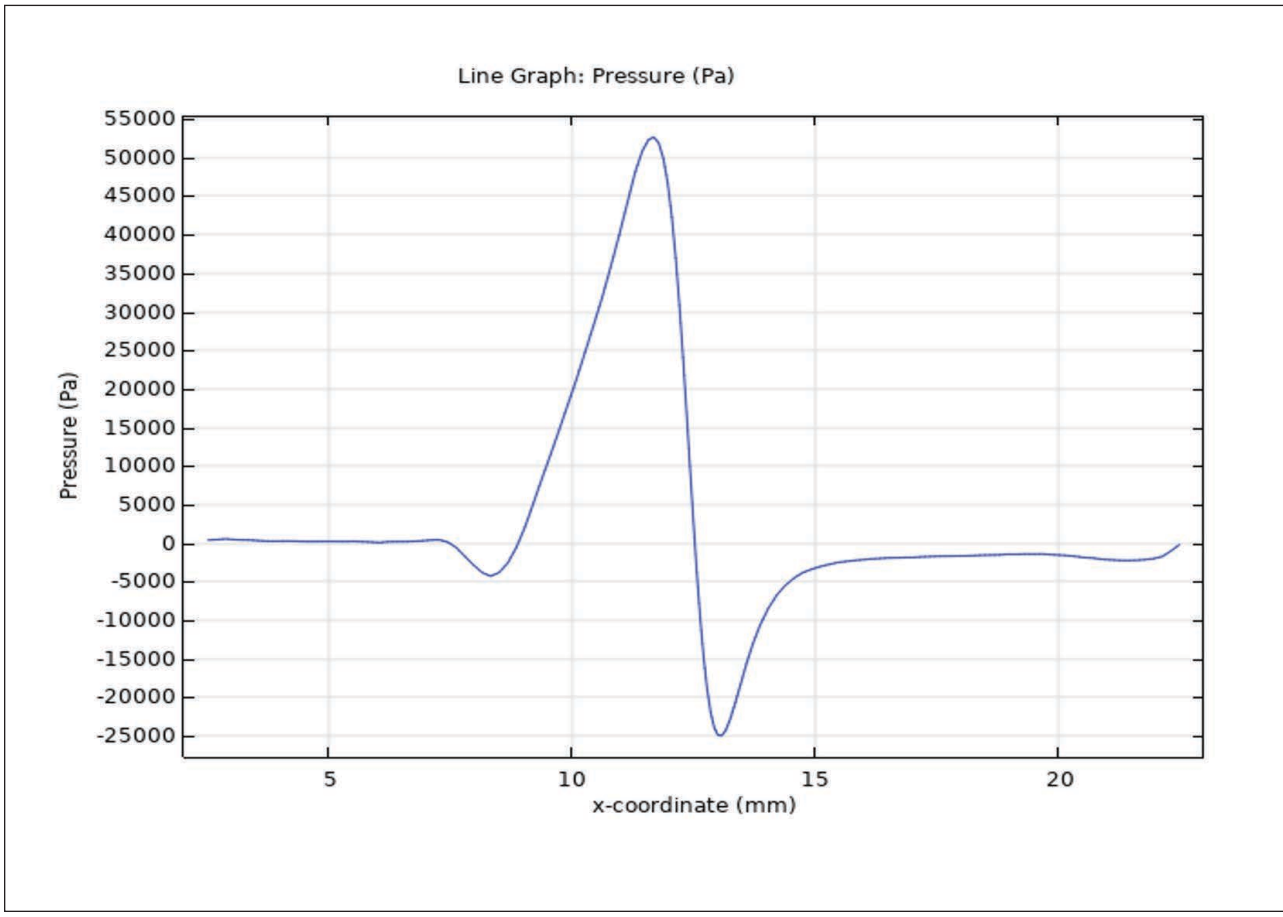

2. Pressure predictions for rod diameter of 25 mm, velocity of 10 m/s, viscosity of 10 mPas, and a rod-web gap of 50 mm.

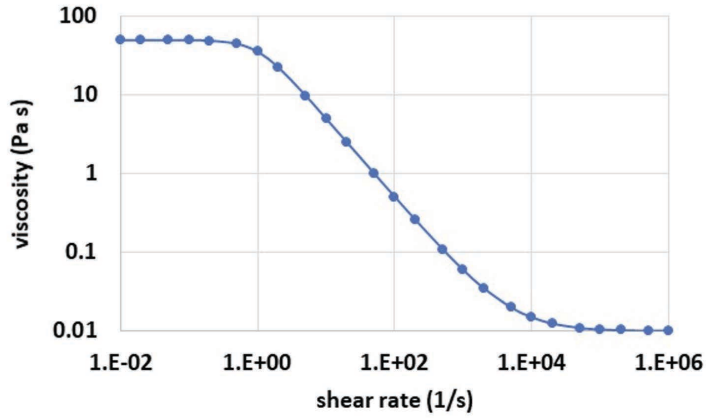

3. Typical shear thinning behavior described by Carreau model.

plexity and uncertainty of this region, the pressure distribution is not certain. Therefore, to determine the rod loading, only the pressure distribution in front of the minimum gap is integrated to obtain the estimated rod loading. The coat weight or coating thickness is determined by integrating the velocity profile at the exit of the region, which should match the net flow anywhere along the region to conserve mass.

To investigate the influence of rubber deformation on the behavior of the rod coater, the lubrication approximation for fluid flow in a thin gap is used. This assumes incompressible Newtonian flow and that the gap between the rod and the paper is small compared to the rod diameter. The lubrication equation is:

$$\frac{dP}{dx} = \frac{12\mu}{h^3}\left(\frac{Uh}{2} - Q\right) \tag{1}$$

where h is the distance from the rod to the paper, U is the web speed, m is viscosity, and Q is the flow rate through the nip per unit width. The pressure P increases as fluid is pulled into the gap and then decreases as it moves out of the rod-paper gap. Taking into account the rubber deformation can be done by allowing the gap to be a linear function of the local pressure [8]. A simple equation is:

$$h = ho + P/K_E \tag{2}$$

where ho is the gap for no rubber deformation, and K_E is some constant that should depend on the hardness of the rubber or the elastic modulus of the rubber backing. This equation changes the geometry of the rod-paper gap as a function of the local pressure.

The lubrication equation is integrated numerically with boundary condition of no pressure at inlet and exit of the region, adjusting Q to obtain the exit pressure condition.

When thickeners are added to coatings, often a shear thinning rheology is obtained. One convenient method to capture a broad range of shear rates typical of these fluids is the Carreau model, given as:

$$\mu = \mu_\infty + (\mu_o - \mu_\infty)(1 + (\lambda\gamma)^2)^{(n-1)/2} \tag{3}$$

where μ_{oo} and μ_o are the high shear rate and low shear rate viscosity limits, λ is a time constant, and n is the power law index. **Figure 3** shows the viscosity function of a Carreau fluid.

In practice, the actual gap between the rod and the web is not known, but what is controlled is the rod loading by a pressure tube. The tube presses a rod support structure against the rod toward the web. When forces are balanced with the hydrodynamic lift, some gap will be obtained. To convert rod loading to the pressure tube applied, details of the support structure and how it interacts with the pressure tube and the rod are needed. Here, just the rod loading in N/m is reported, which represents the force per unit length of the rod, but when comparing with pilot data, the rod diameter is used to convert the force per width to a pressure. A force balance can also be used to link tube pressure to rod loading. The coat weight at that loading is then of interest.

Because of the number of parameters, dimensionless groups can be used to simplify the situation. Natural scaling parameters are the web velocity, rod diameter, and viscosity. A dimensionless rod loading F^* is obtained by dividing load F by viscosity and velocity. Others have suggested this scaling [2]. A Reynolds number is obtained from density, web velocity, rod diameter, and viscosity. A dimensionless coat weight can be obtained by dividing wet thickness by rod diameter. Here, the coat weight is reported for a dimensionless rod loading (F^*) and a Reynolds number (Re)

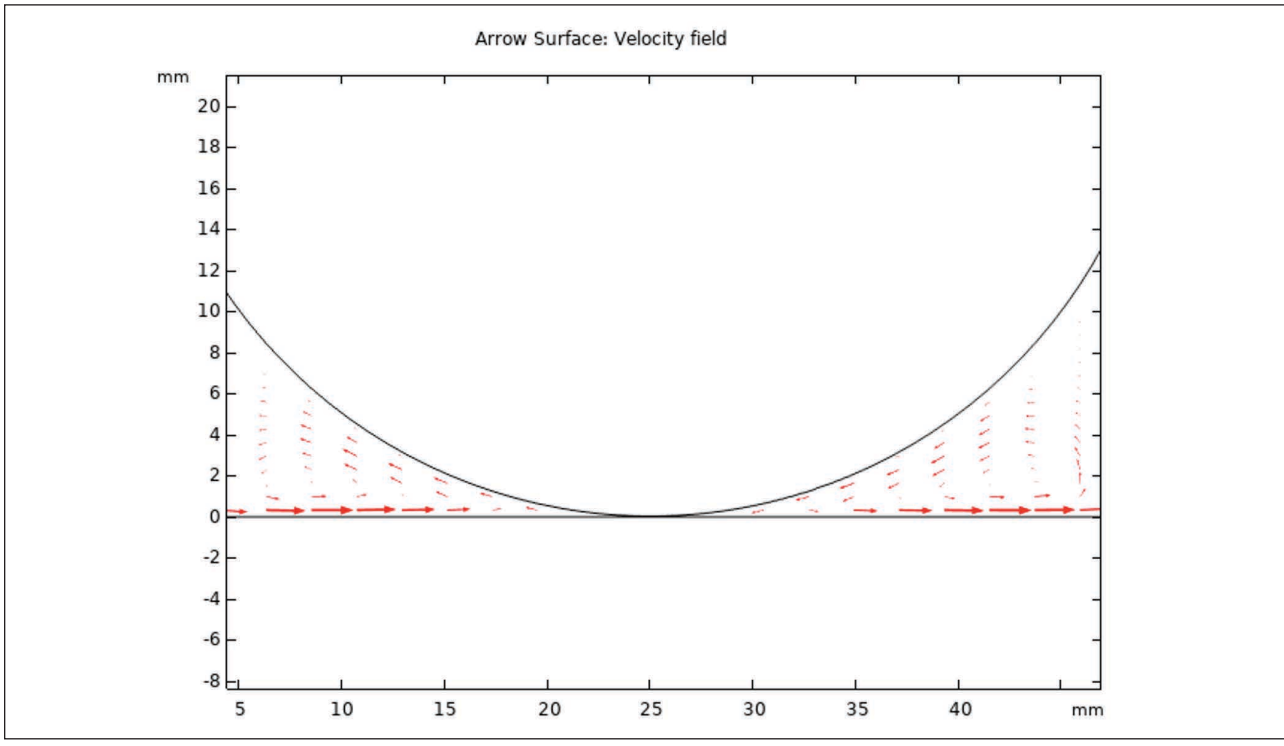

4. Velocity distributions for base case: left is for the inlet region, and right is for the exit region.

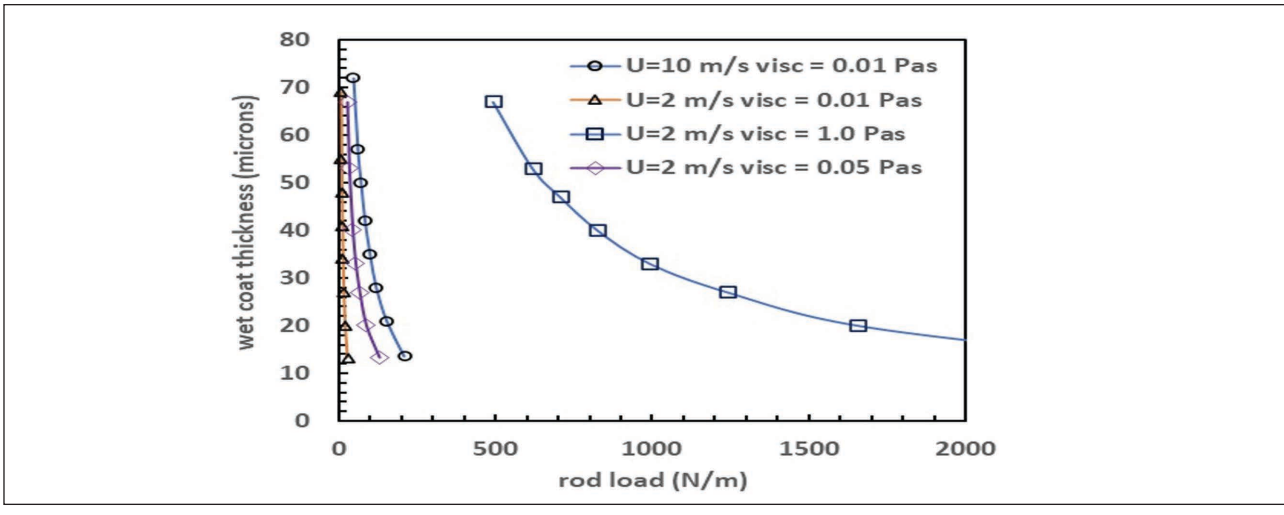

5. Results for a Newtonian fluid with viscosities of 0.01, 0.05, and 1.0 Pas at velocities of 2 and 10 m/s for a 25-mm rod.

defined as:

$$F^* = F/(U\mu) \quad (4)$$

$$Re = \varrho UD/\mu \quad (5)$$

MODEL RESULTS

The velocity field and pressure distribution agree with what others have reported. **Figure 4** shows the velocity vectors in the inlet and outlet region of the rod. As expected, fluid is pulled into the nip by the web, but the small gap causes most of the fluid to be rejected and turned back. Figure 4 shows that most of the fluid that does get through the nip should tend to travel with the web. The circulation region shown on the outlet side likely does not exist because of the film split that would occur.

The influence of rod loading on expected coating wet thickness is shown in **Fig. 5** for a high-velocity case and two low-velocity cases. For velocity of 2 m/s and viscosity of 0.01 Pas, the curve is steep and near the y-axis, which indicates that a small change in the rod load leads to a large change in wet thickness. This condition would lead to difficulties in controlling the coat weight, and even along the rod, fluctuations in coat weight would be expected. The

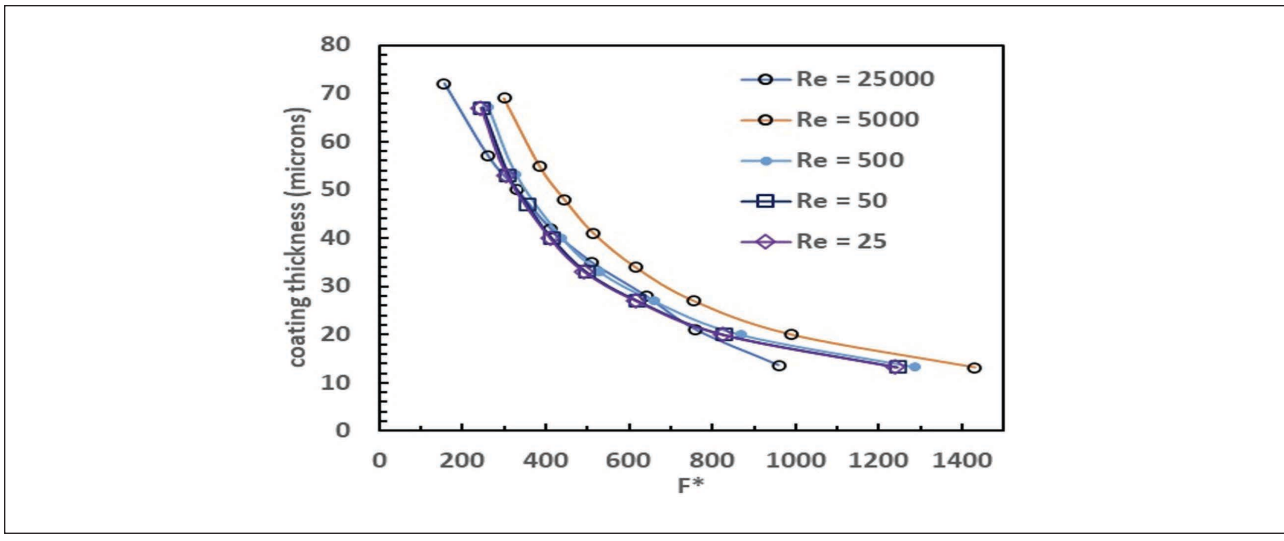

6. Wet coating thickness as a function of the dimensionless rod loading $F^* = F/U\mu$.

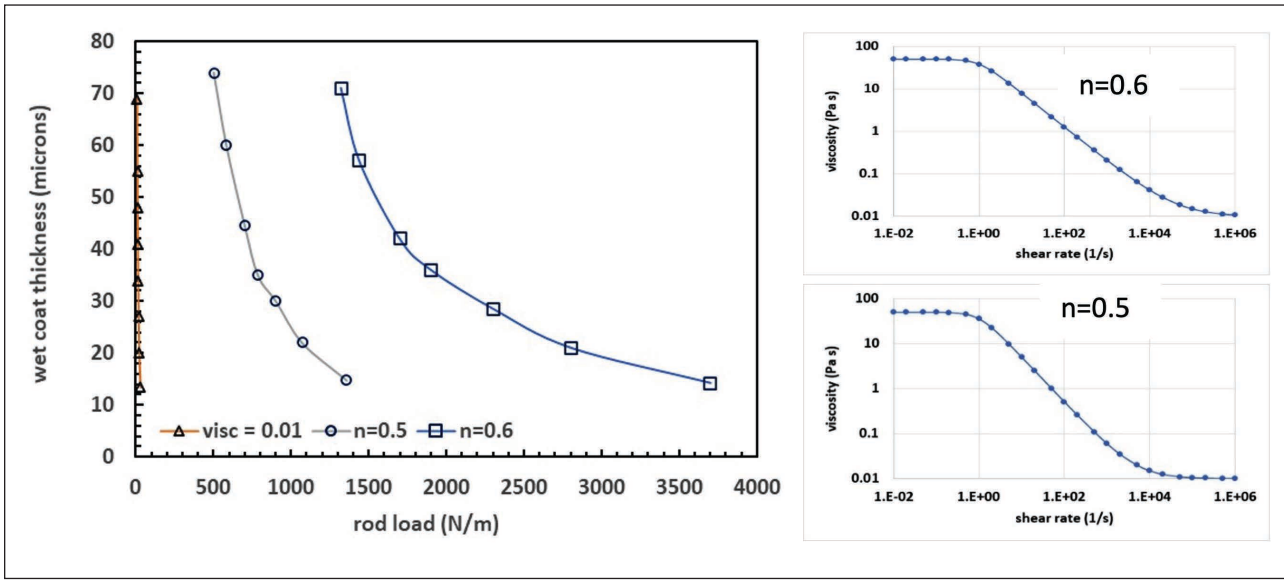

7. Rod loading for Carreau cases with $\lambda = 1$ *s;* $h_{oo} = 0.01$ *Pas;* $h_o = 100$ *Pas, and* $n = 0.5$ *and 0.6.*

conditions just do not generate much hydrodynamic lift on the rod to allow this to operate. For the high-speed low-viscosity case, the situation is better, but it could be a challenge depending on the pressure control and the uniformity of the situation. For the high-viscosity low-speed case, a range of rod loading gives a nice response to coat weight. This steep response is why wire-wound or grooved rods are of high value where the metering does not depend on rod loading via hydrodynamic forces.

Also of note is that the coating thickness is highly dependent upon the gap that is set and that the ratio of wet thickness to gap is in the range of 0.66 to 0.7; this result agrees well with the volume metering reported by Hanumanthu and Scriven [9].

For the Newtonian case, these different curves tend to collapse onto a single trend line when plotted as F^*. **Figure 6** shows the results for the cases in Fig. 5 plus another curve for a web velocity of 1 m/s. The conditions for different Reynolds numbers represent different web velocities. These are all for the same rod diameter of 25 mm.

For the Carreau model, when the high shear viscosity is set to 0.01 Pas, the model then predicts larger viscosities and hydrodynamic lift than the Newtonian case if the shear rates are not large in the nip region. **Figure 7** shows the results for the Newtonian case in Fig. 5, and the Carreau model with $n = 0.5$ and $n = 0.6$ and the zero shear viscosity of 100 Pas and $\lambda = 1.0$ s. The Carreau model cases push the loading results to a higher value of loading with a systematic change in thickness vs. load. This is because $n = 0.5$ and $n = 0.6$ cause the shear thinning to span over a large shear rate range. The shear rate at the minimum gap is ~40,000 1/s for the low wet thickness case. Multiple simu-

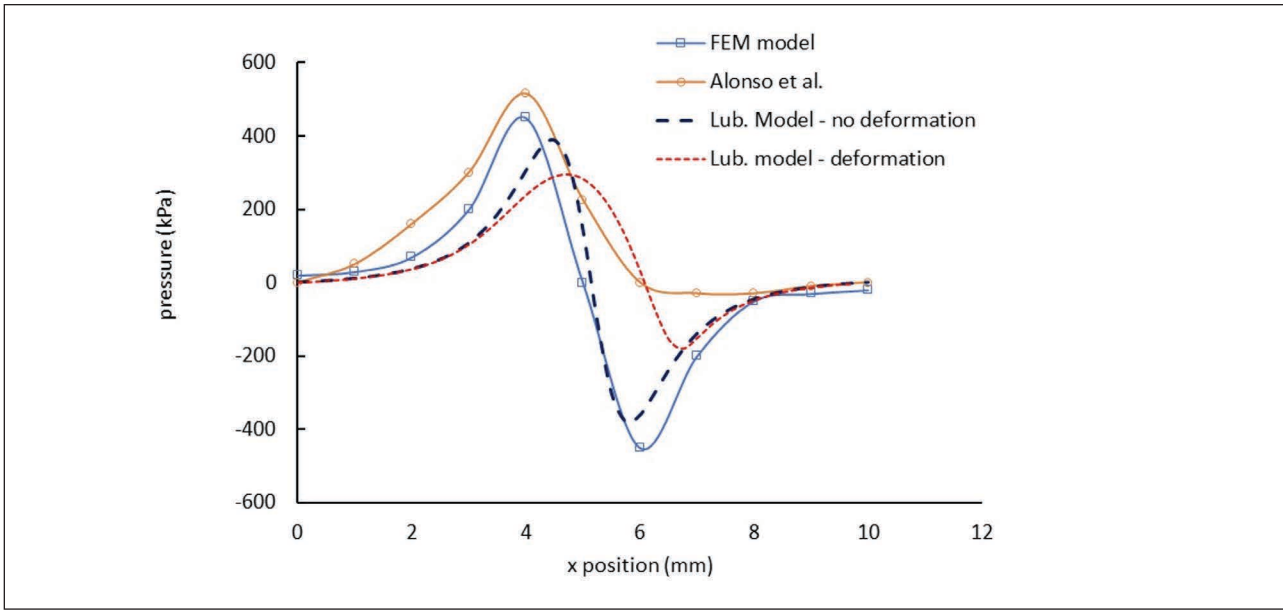

8. Measured pressure distribution by Alonso-Romero [10] compared to the finite element method (FEM) model and the lubrication model without deformation and the lubrication model accounting for deformation.

lations varying the Carreau model parameters suggest that the shear thinning behavior in this shear rate range is more important than the magnitude of the high shear viscosity in determining the coat weight vs. rod load response.

Comparison with pressure profile data

Accounting for deformation in the nip reduces the subambient pressure at the rod exit. The results are shown in **Fig. 8** for the same rod diameter, web speed, and gap using a Newtonian viscosity of 0.03 Pas as reported by Alonso-Romero [10]. While the exact parameters that account for the rubber hardness (deformation) are not known, as the parameter K_E is reduced, the shape of the pressure distribution does move closer to that reported in terms of a smaller subambient pressure. Without deformation, the lubrication model predicts a similar shape as the finite element model in that the positive and negative pressure values are symmetrical. The pressure is underpredicted because the lubrication equation does not take into account the non-Newtonian rheology. High deformation is hard to converge numerically, but the trend is clear in that the subambient pressure decreases as rubber deformation occurs. Therefore, using just the positive part of the pressure distribution to calculate load seems like a good approximation when neglecting the rubber deformation.

Comparison with pilot coater data

The predictions of our simplified model were compared to pilot coater data that was generated on the Trinseo pilot coater in Midland, MI, USA. This pilot coater study used coatings at three different solids levels, applied with rod diameters ranging from 9 mm to 19 mm using three different rod loading pressures [11]. The pilot coater data was analyzed using statistical software to develop predictive models. The analysis showed that solids level was a key parameter, but it appeared as a quadratic factor and as a cross term between solids and rod diameter, meaning there was no simple linear response. For example, when using the largest diameter rod at the highest solids, the coat weight was lower than that of using smaller diameter rods at the same rod pressure. Also, in some cases coat weight increased as rod pressure increased, similar to the response of a bent blade. This suggests that, much like blade coating, the geometry in the nip zone between the rod and substrate (which in turn depends on the degree of deformation of the backing roll) can lead to different classes of flow behavior. Understanding this aspect of rod coating is outside the scope of this modeling effort. Because of these complexities, a subset of the pilot coater data was selected to compare with modeling predictions. This subset of data showed the expected trends of increasing coat weight with rod diameter and decreasing coat weight with increasing pressure for all the rod diameters selected.

One of the challenges in using the pilot coater data is how to convert the measured applied pressure in an inflatable rubber tube located behind the rod bed assembly to the effective load on the rod in terms of force per unit width. As shown in **Fig. 9**, each rod diameter is mounted in its own rod holder that could transmit the tube pressure differently than one might expect from the change in rod diameter alone. In addition, the pressure applied to the rubber tube needs to deform the tube itself, which could change the dimensions in contact with the rod bed. An exact comparison could be done if a calibration is performed by applying pressure in the rubber tube and mea-

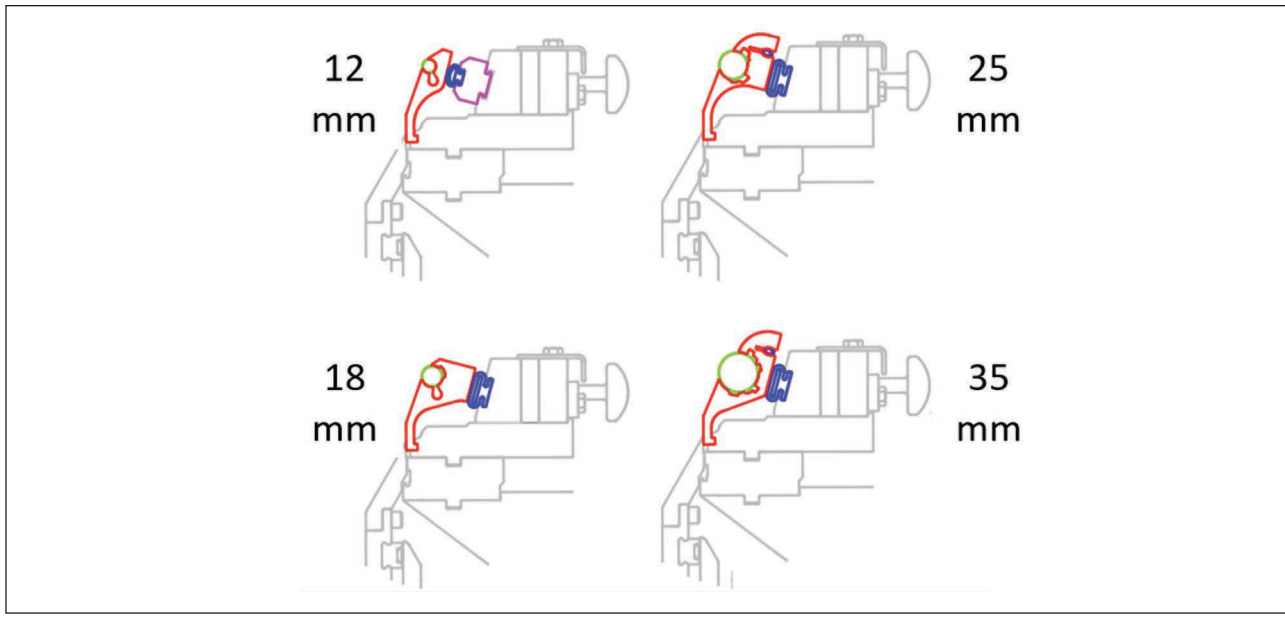

9. Schematic of rod holder geometries showing changes in how tube pressure is transmitted.

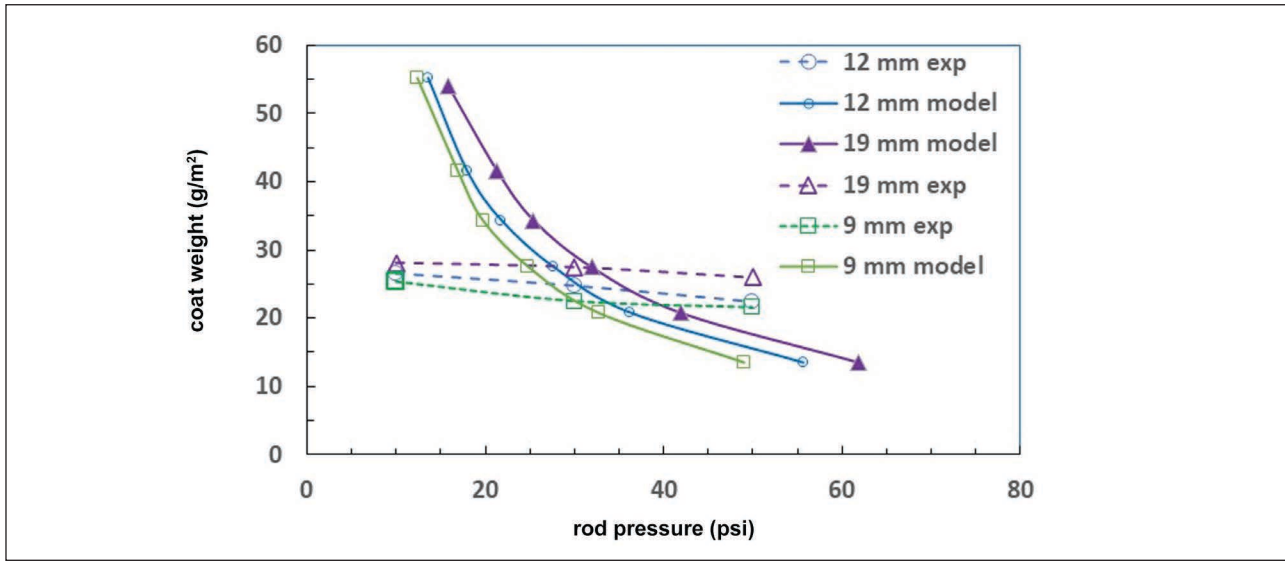

10. Comparison of coat weight response to rod pressure for three rod sizes for web velocity of 2.5 m/s and coating solids of 64.8% with a high shear viscosity of 76 cp.

suring the force that the rod pushes against a force measuring system. For the purposes here, a calibration constant is used to match the coat weight obtained for the 64.8% solids case at 30-psi rod load for the speed of 2.5 m/s for each rod size. The pressure is multiplied by the rod diameter to give a force per unit width. This value is found to be around a factor of 35, 40, and 45 times higher than the model predictions for rod sizes of 9, 12, and 19 mm, respectively. Therefore, these factors are used to adjust the model predictions to compare the trends of the results.

Figure 10 shows the comparison of the model with the pilot trials for the three rod sizes at solids of 64.8% and a velocity of 2.5 m/s. The wet thickness is converted to coat weight knowing the solids and also using the solids to calculate the effective density of the coating. As can be seen, the model predicts a steeper response of coat weight to rod pressure than is seen in the pilot coater data. A number of issues can cause this response, including the rubber tube deformation reducing the transmitted load at high pressures; motion of the rod normal to the web being inhibited from mechanical friction; or assumptions in the model, such as not including the backing roll deformation, filter cake formation, the exit region of the rod, or extensional viscosity effects.

This comparison shows the complexity of the system but gives some hope that a deeper understanding is pos-

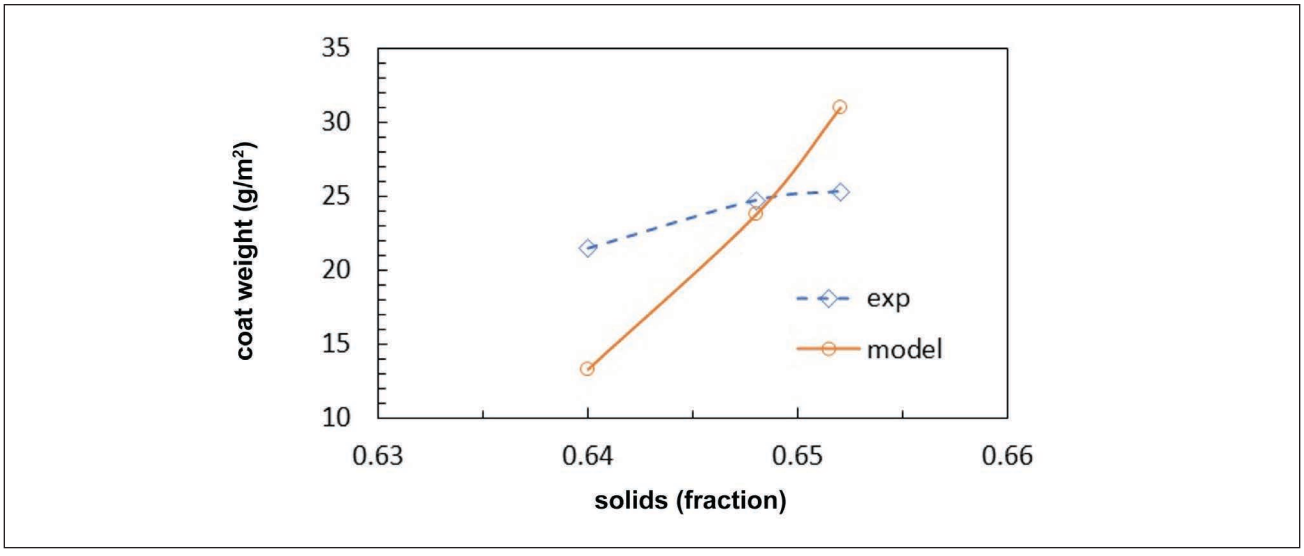

11. Comparison of the pilot trial with the model for rod diameter of 12 mm, speed of 2.5 m/s, and three solids levels at 30-psi rod load. The viscosities for 64, 64.8, and 65.2 solids are 61.4, 76.1, and 97.5 cps, respectively.

sible. As the rod load goes to zero, in theory, the coat weight should go to a high value as the model indicates, but the pilot data shows the coat weight going to some limit. As the tube pressure goes to a high value, the coat weight should decrease a significant amount. If this is not seen, the mechanism for the difference should give insight as to better control of this coating method.

The steepest response of the pilot coater data was the dependence of coat weight on solids. **Figure 11** compares the results for the 12-mm rod at 2.5 m/s at three solids. The model was run for various gaps until the pressure predictions matched the 30-psi load using the calibration factor. The model predicts that the dependence should be even steeper than what was seen in the trial. The high solids load has two effects: 1) the viscosity increases, and 2) the same wet thickness carries more solids. The increase in viscosity the rheology profile of the coating to a desirable range shown in the model results. The next step in this research will be to incorporate additional features like filter cake formation into the model to better match with the experimental results.

ABOUT THE AUTHORS

Smooth rods are often used to apply barrier coatings, which have different rheology and lower solids than traditional paper coatings. This makes it difficult to select the proper combination of rod diameter, rod pressure, and coating rheology to get good control of coat weight. We felt that modeling could be a useful approach to predict these parameters. This research builds on our earlier work using modeling to understand the fundamentals of blade coater runnability.

The most difficult aspect of this research was validating the model predictions against experimental results. This was addressed by getting access to pilot coater run conditions for an earlier published study of smooth rod coatings on paperboard.

Personally, this research led to a deeper appreciation for the differences between blade and rod coating processes. The most surprising finding was the large impact of the shear thinning index on the coat weight vs. rod pressure response compared to the limited impact of high shear viscosity.

Mills might benefit from gaining the ability to get higher coat weights for low solids coatings by tuning



Roper



Bousfield



Welsch

Roper is Fellow/consultant at PaperCote LLC in Midland, MI, USA. Bousfield is Calder professor in the Paper Surface Science program, Department of Chemical and Biomedical Engineering, at the University of Maine in Orono, ME, USA. Welsch is Global Innovation Leader for the Latex Binders Business at Trinseo LLC in Midland, MI, USA. Email Roper at jaroperiii@gmail.com.

causes a thicker wet layer to generate the same rod loading compared to a low viscosity coating.

Again, various assumptions of the model can explain the different trends. For example, if rubber deformation is taken into account, the shape of the nip changes, allowing less coating under the rod at the same rod loading. This would cause the high solids coat weight prediction to decrease and the low solids case to increase. More work is needed to understand why these trends are different.

CONCLUDING REMARKS

The influence of coating rheology on the coat weight control of a smooth rod is predicted using a finite element code neglecting other issues such as rubber deformation, cavitation, and film split phenomena. For the Newtonian cases, at low speeds and moderate viscosities, the coat weight-loading curve is steep, because there is not enough hydrodynamic lift at normal coat weight ranges to support rod loading. The Newtonian cases collapse onto a similar master curve for a wide range of parameters, whereas the Carreau model cases do not. By including shear thinning behavior, likely caused by a thickener addition, the coat weight/load curves are pushed to ranges that allow for good control of the coat weight. The correct values of parameters necessary to obtain this behavior will depend on the rod diameter, speed of operation, and the desired coat weight.

The coat weight vs. pressure response predicted by the model shows a much steeper change in coat weight as pressure is increased compared to pilot coater data. The reasons for this difference are not clear but could come from the differences in tube pressure-rod loading geometry or from neglecting fluid penetration and filter cake formation in the model. **TJ**

LITERATURE CITED

1. Reglat, O. and Tanguy, P., *TAPPI J.* 81(5): 195(1998).
2. Trefz, M. and Seiz, R., *TAPPI Metered Size Press Forum II, Proc.*, TAPPI Press, Atlanta, 1998, p. 85.
3. Kokko, A., Kuni, S., and Grankvist, T., *Adv. Coat. Fundam. Symp., Proc.*, TAPPI Press, Atlanta, 1999, p. 79.
4. Benjamin, D., Carvalho, M., and Anderson T., et al., *TAPPI Coating Conf., Proc.*, TAPPI Press, Atlanta, 1994, p. 109.
5. Carvalho, M. and Scriven, L., *TAPPI J.* 77(5): 201(1994).
6. Roper III, J. and Attal, J., *TAPPI J.* 76(5): 55(1993).
7. Pajari, H., Mansikka-aho, J., Ketoja, J., et al., *Adv. Coat. Fundam. Symp., Proc.*, TAPPI Press, Atlanta, 2003, p. 243.
8. Coyle, D.J., *Chem. Eng. Sci.* 43(10): 2673(1988). https://doi.org/10.1016/0009-2509(88)80011-3.
9. Hanumanthu, R. and Scriven, L., *Adv. Coat. Fundam. Symp., Proc.*, TAPPI Press, Atlanta, 1995, p. 109.
10. Alonso-Romero, S., "Metering film hydrodynamics in film coating," Ph.D. thesis, École Polytechnique Montreal, Montreal, 2000.
11. Cynecki, W., Welsch, G., Obermiller, D., et al., *Coat. Graphic Arts Conf.*, TAPPI Press, Atlanta, 2006, p. 155.

ABOUT THIS PAPER

Cite this article as:
Roper, J.A., III., Bousfield, D.W., and Welsch, G.W., *TAPPI J.* 21(11): 605(2022). https://doi.org/10.32964/TJ21.11.605

DOI: https://doi.org/10.32964/TJ21.11.605

ISSN: 0734-1415

Publisher: TAPPI Press

Copyright: ©TAPPI Press 2022

About this journal

Coatings for sustainable paper-based flexible packaging: Barrier properties and processability

HANZE YING, LUQING QI, DAVE MALOTKY, JOSEPH HARRIS, BERNHARD KAINZ, RAY DRUMRIGHT, WILLIAM LIECHTY, AND JONATHAN MASON

ABSTRACT: In this study, the use of waterborne barrier dispersions from trademarked BLUEWAVE Mechanical Dispersion Technology as thin coatings for paper-based flexible packaging was investigated. Prototypes were designed and examined for their performance in process, rheology, barrier, heat-seal/hot-tack, and coefficient of friction (CoF). Compositional details such as the type and amount of base resins and dispersants were found to significantly impact performances and were key to the development of new prototypes that deliver the performance profiles for implementation in paper-based flexible packaging applications.

Application: This paper describes a waterborne coating solution with good liquid/gas barrier, high heat-seal/hot-tack, and low CoF. It was designed and tailored for paper-based flexible packaging applications

Consumer demand for sustainable packaging is fueling interest and growth in paper packaging [1], but challenges remain for paper to deliver barrier and process performance equivalent to incumbent plastic solutions. Polymeric coatings have been applied to enhance the performance of paper [2], but the industry still lacks well-rounded solutions that allow the broad use of coated paper in flexible packaging.

Due to their porous nature, paper substrates require coatings to provide sufficient liquid/gas barrier and protect the content within from leaking or deteriorating [2,3]. Other than the barrier, there is also a long list of other factors to consider, mostly related to addressing the processability issues in the flexible packaging process, to enable the implementation of new technologies. For example, dispersions need to have high solids content and low viscosity to fit in the existing coating capabilities of both paper mills and converters. They are preferred to be waterborne with a low level of volatile organic compounds (VOC) to minimize environmental, health, and safety risks.

The dry coatings on the paper should have sufficient heat-seal/hot-tack properties to ensure the good integrity and sealing of packages coming from high-speed lines with short sealing and cooling time [4]. The coatings also need to have low enough coefficient of friction (CoF) to avoid overheating caused by friction of coated paper against parts in high-speed packaging lines [5]. Finally, the coatings are expected to deliver a complete performance profile with thickness low enough to maintain the repulpability/recyclability and the sustainability profile of paper packaging [6].

In this study, we investigated coating solutions based on BLUEWAVE Mechanical Dispersion Technology, a trademarked twin screw extruder-based mechanical dispersion process from The Dow Chemical Company. This technology targets all previously mentioned major challenges. Studies were designed and conducted to understand the structure-property relationships of the materials that balance performance requirements for paper-based flexible packaging.

MATERIALS AND METHODS

All dispersions were prepared using the twin screw extruder-based mechanical dispersion process. The solids-viscosity curves were determined by measuring the dispersion solids (Sartorius Moisture Analyzer Model MA35; Sartorius AG, Göttingen, Germany) and viscosity (Brookfield DV III Ultra Viscometer, 50 rpm, spindle #3; Brookfield Engineering Laboratories, Middleboro, MA, USA) at each stage of stepwise dilution.

Coating dispersions were applied to a paper substrate with drawdown bars targeting coat weights of 6–8 g/m^2. This substrate was a commercially available low porosity 62 g/m^2 packaging paper with a Gurley porosity of 23000 s/100 mL (following the method based on TAPPI Standard Test Method T 460 "Air resistance of paper [Gurley method]") and Parker Print Surf (PPS) roughness of 1.6 µm. All coatings were cured at 100°C for 2 min before testing, unless otherwise specified.

The moisture barrier was measured with the "perm cup" technique based on ASTM E96 "Standard test methods for gravimetric determination of water vapor transmission rate

of materials," in which a coated paper sample was attached to a jar containing desiccants. The amount of moisture absorbed by desiccants was determined gravimetrically over time to determine the rate of moisture penetration through the coated paper.

The water barrier was measured with a "Cobb tester" as water uptake per unit area represented by gram per meter squared (g/m²) at 23°C for 30 min based on TAPPI T 441 "Water absorptiveness of sized (non-bibulous) paper, paperboard, and corrugated fiberboard (Cobb tester)."

The oil/grease barrier was measured based on TAPPI T 559 cm-12 "Grease resistance for paper and paperboard" (also named "Kit test"), in which a score rating of 1–12 (12 is the highest performance) was assigned based on the breakthrough of the highest numbered Kit solvent mixture. Folded Kit was not measured but would be good to include for future studies. Typically, our olefinic copolymer (OCP) based barrier coatings are very flexible and have good folding resistance performance.

The static and dynamic CoF were measured by texture analyzer with sliding friction rig following the method based on TAPPI T 549 "Coefficients of static and kinetic friction of uncoated writing and printing paper by use of the horizontal plane method."

Both heat-seal and hot-tack properties were characterized by a heat-seal/hot-tack testing system (Enepay MAGMA 3; Enepay Corp., Raleigh, NC, USA). The heat-seal test followed ASTM F88 "Standard test method for seal strength of flexible barrier materials," with the following conditions: seal jaw pressure: 0.5 N/mm; dwell time: 0.5 s; pull speed: 4 mm/s; and aging between sealing and pulling: 2 weeks. The hot-tack test followed ASTM F1921 "Standard test method for hot seal strength (hot tack) of thermoplastic polymers and blends comprising the sealing surfaces of flexible webs," with the conditions of: seal jaw pressure: 0.5 N/mm; dwell time: 0.5 s; pull speed: 200 mm/s; and pre-test delay between sealing and pulling: 0.2 s.

Morphologies of paper coating were examined using scanning electron microscopy (SEM) using an FEI Nova NanoSEM (Thermo Fisher Scientific; Waltham, MA, USA).

RESULTS AND DISCUSSION

The waterborne dispersions in this study were prepared by a twin screw extruder-based mechanical dispersion process that has previously been used to develop other prototypes in the barrier paper space [7,8]. In the process, resins and dispersants/stabilizers are fed into the twin screw extruder and later emulsified/dispersed with the addition of water and base, resulting in micron-sized polymer particles in waterborne dispersions with high solids content (up to 60%). **Table I** lists all prototypes involved in this study. Two types of high molecular weight OCP, OCP-1 (lower melt flow index [MFI] = 6, 190°C, 2.16 kg) and OCP-2 (higher MFI = 25) resins containing monomers of C2-C8 alkenes, were stabilized by dispersants based on acid copolymers. Hard base was added to deprotonate the acid groups and induce the surface-active properties of dispersants.

The solids-viscosity profile of dispersion products is key

Prototype	Base Resin Type	Dispersant Levels
A	OCP-1	High
B	OCP-1	Very high
C	OCP-1	Medium
D	OCP-2	High
E	OCP-2	Medium
F	OCP-1	Low
G	OCP-1	Very low

I. Compositions of waterborne barrier dispersions involved in this study (OCP = olefinic copolymer). The corresponding weight ratio of surface-active acid groups in each of the dispersant levels: very low: <0.9%; low: 0.9%–1.1%; medium: 1.1%–1.3%, and high: >1.3%–1.5%, and very high: >1.5%

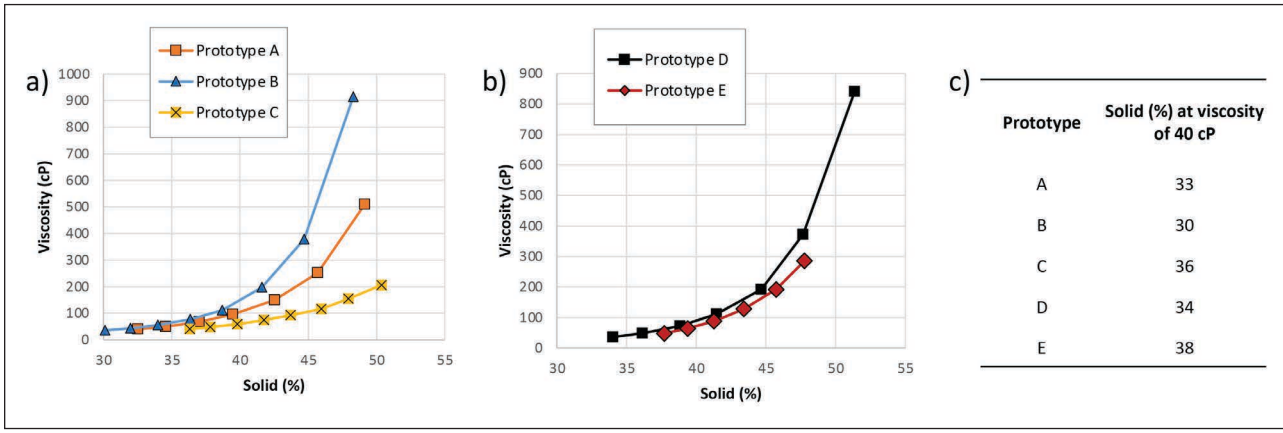

1. Solids-viscosity profiles of various waterborne barrier dispersions: a) solids-viscosity relationship of OCP-1 based prototypes A-C; b) Solids-viscosity relationship of OCP-2 based prototypes D-E; and c) solids levels of prototypes A-E when their viscosities are at the level of 40 cP. Prototypes F and G demonstrated similar rheological behavior.

a)

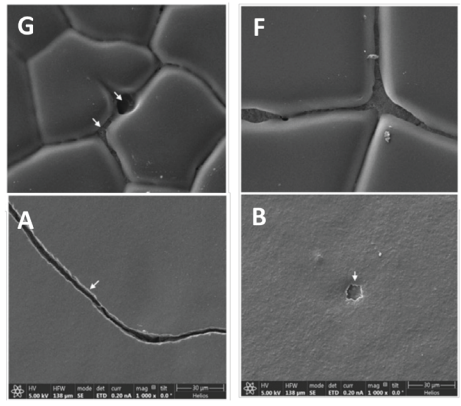

b)

Prototype	MVTR 38 °C/90% RH g/m²*day	Cobb 23 °C/30 min g/m²	Oil and grease barrier KIT
G	582	18.2	6
F	534	8.2	7
A	212	5.2	9
B	86	2.8	12

2. Relationship of coating morphology vs. moisture barrier performance: a) top-down scanning electron microscope (SEM) images of coatings from prototypes A, B, F, and G, showing the reduction of defects or cracks with the increase of dispersant levels; and b) values of moisture transmission rate measured at the tropical condition (38°C, 90% relative humidity [RH]), Cobb water barrier measured at 23°C/30 min, and oil/grease barrier measured with "Kit test" (MVTR = moisture vapor transmission rate).

a)

Prototype	curing temp (C)	seal temperature (C)		
		110	140	170
B	100	P	P	P
	150	P	P	P
D	100	P	P	M
	150	F	F	F

P	Pass, fiber tear
M	Marginal, partial fiber tear
F	Fail, delamination

b)

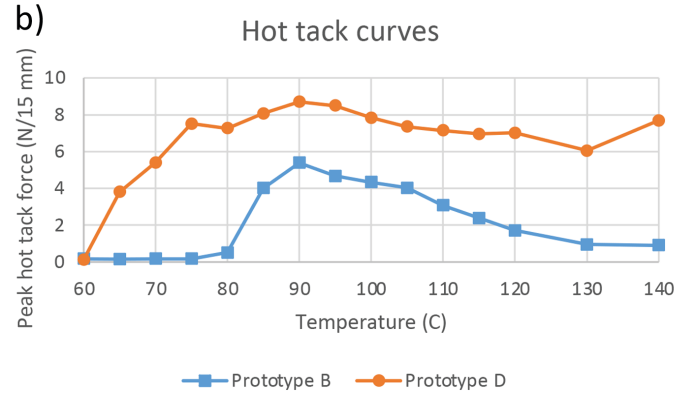

3. Sealing behaviors of waterborne barrier dispersions: a) failure mode of heat-seal testing for prototype B and D when cured and sealed at various temperatures; and b) relationship of hot tack peak force vs. seal temperature for prototypes B and D.

to implementation at paper mills/converters. High solids content facilitates fast speed in the coating lines, especially for customers with limited drying capacities. Low viscosity (<100 cP) is critical for customers adopting specific coating application methods, such as rotogravure printing. **Figure 1** shows the solids-viscosity profiles for part of the prototypes. Figures 1a and 1b show the solids-viscosity curves upon dilution, and Fig. 1c shows the solids levels of dispersions at the viscosity of 40 cP, which is a relevant level for value chain partners. By adjusting process and composition parameters, the viscosity can be tuned at the same solids level. All prototypes in the table have >30% solids content at the viscosity of 40 cP, which works well for most paper mill/converter customers.

Figure 2 reveals the relationship of the moisture barrier levels to the coating morphologies. Prototypes A, B, F, and G have the same base resin but different dispersant levels. As the level of dispersants is increased, coatings with fewer cracks or defects were observed in the top-down morphology, as shown in Fig. 2a; thus, there was better moisture barrier performance (lower moisture transmission rate), as shown in Fig. 2b. These trends were observed for water and oil/grease barrier measurements as well. With the appropriate coating compositions and morphologies, like the prototype B, the dispersions can achieve moisture barrier levels of 50~100 g/m²*day at tropical conditions (38°C/90% relative humidity [RH]) with a thickness of 6–8 g/m². This performance makes them suitable for many food packaging applications [9,10].

Both "heat-seal" and "hot-tack" behaviors were ex-

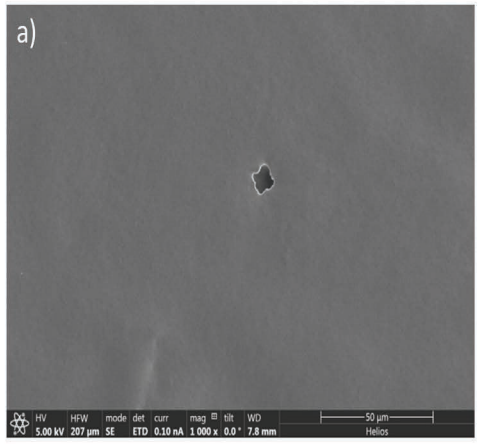

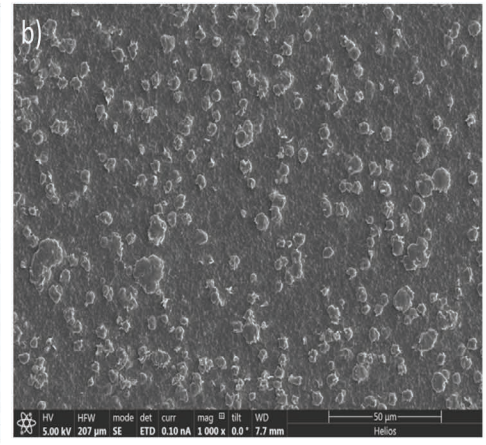

c)

Prototype	CoF static	CoF dynamic
B	1.01	0.68
B+additive	0.10	0.09
D	1.10	0.87
D+additive	0.08	0.07

4. Reduction of coefficient of friction (CoF) from the additive. Top-down SEM images were taken for prototype B, a) without and b) with the presence of the additive. The image clearly shows the distribution of the additive at the coating surface; c) shows static and dynamic CoF (coated paper to coated paper) values for prototypes B and D, with or without the presence of the additive.

amined for various prototypes. These two tests are similar, with the major difference being the intervals between the "hot jaw sealing" and "pulling apart" processes. Heat-seal test has long intervals, which can vary, but were typically set at 2 weeks in our studies. It mimics the sealing strength of packaging in consumers' hands long after production [4]. Hot-tack test has very short intervals, which were typically at 0.2 s in our studies. It mimics the "form-fill-seal" process in the packaging line, in which the content gets filled almost immediately after the bottom seal of the package is made [5]. Higher hot-tack performance allows the packaging line to operate at a faster speed.

Figure 3 shows a tradeoff in the selection of base resin type for the optimized sealing performance. In Fig. 3a, OCP-1 based prototype B passed the failure mode assessment across a wide range of curing and sealing temperatures, while OCP-2 based prototype D shows "delamination" issues (coating delaminates from the paper substrate), especially when coatings were cured at higher temperatures. Interestingly, although OCP-1 based prototype B delivers sufficient hot-tack performance, OCP-2 based prototype D showed even better performance with higher peak strength and wider operation temperature windows. While the heat-seal property is a "must-have" for packaging forming, the coating also needs sufficient blocking resistance to avoid sticking issues with paper during manufacturing, storage, transportation, and use. At most industrial scenarios where temperatures are below the heat-seal onsets (equal or less than 60°C), both B and D have no blocking issues based on the standard method of ASTM D918-99 "Standard test method for blocking resistance of paper and paperboard," as shown in Fig. 3b.

Figure 4 shows our effort to lower the CoF for prototypes to allow the coated paper to run at high speed in a packaging line without overheating issues. A silicone-free low molecular weight wax additive was found to efficiently lower the CoF (coated paper to coated paper, both dynamic and static) of both OCP-1 based and OCP-2 based prototypes down to <0.1 as shown in Fig. 4c. The efficient blooming of the additive to the coating surface was found to be the key to sufficient CoF reduction, as shown in Figs. 3a and 3b as an example of prototype B morphologies before and after the additive spiking.

CONCLUSION

A series of dispersions prepared by a twin screw extruder-based mechanical dispersion process were designed and examined for their performance in process, rheology, barrier, heat-seal/hot-tack, and coefficient of friction (CoF), all of which are closely connected to the successful implementation of coated paper in sustainable flexible packaging applications.

- It was found that adjustments to process and composition parameters have a significant impact on solids-viscosity profile, coating morphologies, and barrier performance.
- The selection of base resin type affects the sealing behaviors, including "heat-seal" and "hot-tack."
- An additive was also identified that segregates to the coating surface and efficiently controls the CoF of coatings.
- In summary, this study identified a few leading prototypes, such as prototypes B and D, that deliver the performance profiles for implementation in paper-based flexible packaging applications. **TJ**

LITERATURE CITED

1. Mordor Intelligence, "Paper packaging market — growth, trend, COVID-19 impact, and forecasts (2021-2026)," Mordor Intelligence, Hyderabad, Telangana, India, 2020. Available [Online] https://www.mordorintelligence.com/industry-reports/paper-packaging-market# <04Nov2022>.
2. Global Market Estimates, "Global barrier coated flexible paper packaging market size — forecasts to 2026," Global Market Estimates, Brooklyn, NY, USA, 2021. Available [Online] https://www.globalmarketestimates.com/market-report/global-barrier-coated-flexible-paper-packaging-market-3164 <04Nov2022>.
3. Auhorn, W.J, "Papers with barrier properties," in *Handbook of Paper and Board* (H. Holik, Ed.), 1st edn., Wiley-VCH, Weinheim, Germany, 2006, Chap. 3.6.8.12.
4. Morris, B.A., *The Science and Technology of Flexible Packaging: Multilayer Films from Resin and Process to End Use*, William Andrew Publishing, Norwich, NY, USA, 2017, pp. 181-257. https://doi.org/10.1016/B978-0-323-24273-8.00007-1.
5. Morris, B.A, *The Science and Technology of Flexible Packaging: Multilayer Films from Resin and Process to End Use*, William Andrew Publishing, Norwich, NY, USA, 2017, pp. 435-462. https://doi.org/10.1016/B978-0-323-24273-8.00012-5.
6. Kimpimäki, T. and Savolainen, A., "Barrier dispersion coating of paper and board," in *Surface Applications of Paper Chemicals*, Chapman & Hall, London, 1997, pp. 208-228. https://doi.org/10.1007/978-94-009-1457-5_12.

ABOUT THIS PAPER

Cite this article as:
Ying, H., Qi, L., Malotky, D., et al., *TAPPI J.* 21(11): 617(2022).
https://doi.org/10.32964/TJ21.11.617

DOI: https://doi.org/10.32964/TJ21.11.617

ISSN: 0734-1415

Publisher: TAPPI Press

Copyright: ©TAPPI Press 2022

About this journal

ABOUT THE AUTHORS

We chose to study this topic because paper packaging is a next-generation sustainable solution. Previous research was on cupstock applications, while this research extends to the flexible packaging space.

The most difficult aspect of this study was finding the right additive for coefficient of friction (CoF) reduction. We screened more than 10 candidates to find the right option.

We found that balancing all metrics is needed to achieve products that work for their application. The most interesting finding was the reversed heat-seal and hot-tack trend.

This research can help enable paper mills to convert paper to something suitable for barrier flexible packaging without sacrificing the recyclability. The next step is to drive for further enhanced barrier properties while maintaining other good properties.

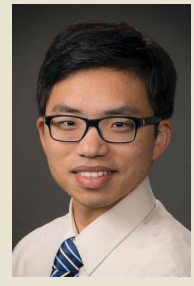

Ying

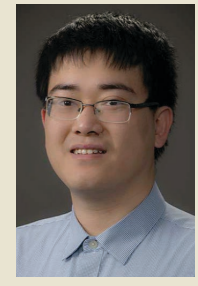

Qi



Malotky



Harris



Kainz



Drumright



Liechty



Mason

Ying is associate research scientist in the Department of Coating Materials at Dow Inc. in Midland, MI, USA. Qi is associate research scientist, Malotky is senior research scientist, and Harris is R&D/TS&D technologist in the Department of Core Research and Development at Dow Inc. in Midland, MI, USA. Kainz is principle TS&D scientist in the Department of Coating Materials at Dow Inc. in Rheinmünster, Germany. Drumright is senior R&D/TS&D Fellow in the Department of Coating Materials at Dow Inc. in Midland, MI, USA. Liechty is senior R&D/TS&D leader in the Department of Coating Materials at Dow Inc. in Collegeville, PA, USA. Mason is associate R&D/TS&D director in the Department of Coating Materials at Dow Inc. in Midland, MI, USA. Email Ying at hying@dow.com.

7. Piwowar, A., Rosen, K., Ellison, C., et al., "Polyolefin based waterborne barrier coatings for paperboard," *PaperCon*, TAPPI Press, Peachtree Corners, GA, USA, 2019.

8. Katzenstein, J., Rosen, K., Ellison, C., et al., "Polyolefin based waterborne barrier coatings for paperboard," *PaperCon*, TAPPI Press, Peachtree Corners, GA, USA, 2017.

9. Wu, F., Misra, M., and Mohanty, A.K., *Prog. Polym. Sci.* 117: 101395(2021). https://doi.org/10.1016/j.progpolymsci.2021.101395.

10. Wang, J., Gardner, D.J., Stark, N.M., et al., *ACS Sustainable Chem. Eng.* 6: 49(2018). https://doi.org/10.1021/acssuschemeng.7b03523.

Novel test method for measuring defects in barrier coatings

DUSTIN BURTON, DON VENTRESCA, AND GREGORY W. WELSCH

ABSTRACT: In the last several years, activity to develop water-based barrier coatings (WBBCs) that meet challenging packaging performance requirements has increased dramatically. Cellulose-based packaging solutions can provide a more sustainable packaging option for replacing single-use plastic-based options like extrusion-based and laminated materials. An advantage of WBBCs is the opportunity to reduce the coating thickness applied, as long as the barrier requirements can be met. A challenge that must be overcome is the ability to maintain a defect and pinhole-free coating layer after coating and drying to retain the barrier performance. Many formulation and coating parameters can affect the barrier coating layer quality; however, methods for detecting more subtle differences in these types of studies are not widely available.

Work was carried out to develop a quantitative technique for detecting and measuring the quantity and size of defects in the barrier coating layer. A test method has been developed using a combination of dyed oil and image analysis to be able to characterize the imperfections in the coating surface. The use of dyed oil serves two purposes. First, it better simulates the types of materials, in this case, oils and grease, for which the barrier coating is expected to hold out. Second, it also provides contrast between the coating and failure points for testing.

An image analysis technique is employed to characterize the number and size of the imperfections. For the former, it reduces the testing time required if a quality control or laboratory technician counts the dots. For the latter, it assists with judgment on the source of the root cause of the imperfection, such as base sheet defects, coating dispersion issues, or perhaps micro-blisters in the coating, as some examples.

To show the benefit of this technique, several pilot coating studies were designed to see if the new technique could be utilized to detect differences in WBBC performance. Both process and chemical variables were evaluated. With refinement, it is believed this technique can be utilized in development work, as well as for a potential quality control technique for manufacturing of coated paper and paperboard products

Application: With the refutation of many current oil and grease resistance (OGR) test methods, it was time to develop a more accurate and easily administered test. The test technique described here is easier to administer, provides the user with better data, and allows the user to better see and identify defects in coated paper that has been exposed to oil and grease.

In the last several years, activity to develop water-based barrier coatings that meet challenging packaging performance requirements has dramatically increased [1]. Cellulose-based packaging solutions can provide a more sustainable packaging option for replacing single-use plastic-based options like extrusion-based and laminated materials. An advantage of water-based barrier coatings (WBBCs) is the opportunity to reduce the coating thickness applied, as long as the barrier requirements can be met. A challenge that must be overcome is the ability to maintain a defect and pinhole-free coating layer after coating and drying to retain the barrier performance. Even a high-quality barrier material will perform poorly if defects exist in the coating layer. Many formulation and coating parameters can affect the barrier coating layer's quality; however, methods for detecting more subtle differences in these types of studies are not widely available.

A test that not only identifies defects in the film, but also measures count, size, and the shape of defects is crucial to further develop WBBC coatings. Although dyed oil applications may have been used by producers in the past, taking this data one step further and making a detailed examination of barrier failures can tell us so much more than a simple qualitative analysis. Using a readily available software product, one can analyze these dots to show that even minor changes in the paper coating process can have an overall change in defect creation, and the frequency, shape, and size of defects created.

Another activity of interest was to determine if we could find a correlation between the size and number of imperfections and their relation to barrier failures. To show the benefit of this technique, several pilot coating studies were designed to see if we could utilize the new technique to detect differences in WBBC performance. Both process and chemical variables were evaluated. With refinement, it is believed this technique can be utilized in development work, as well as for a potential quality control technique for manufacturing of coated paper and paperboard products.

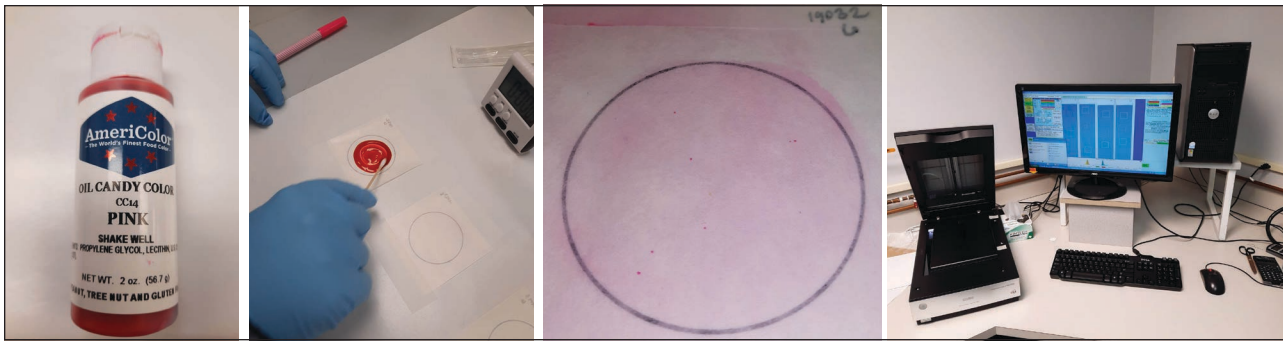

1. Dyed oil, application technique, treated sample after dye application, and test equipment.

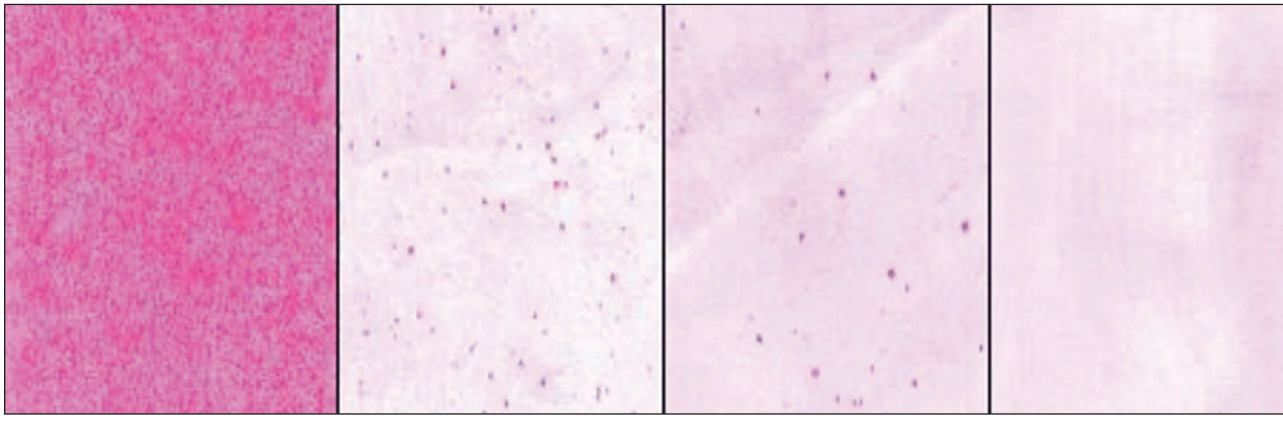

2. Visual representation (after dying) of pinhole improvement with increased coat weight.

BACKGROUND

For years, the 3M Kit test (TAPPI Standard Test Method T 559 "Grease resistance test for paper and paperboard") has been used to test the oil and grease resistance (OGR) performance of uncoated substrates. In those cases, fluorocarbon-based chemicals were used to treat the fiber or used in starch sizing to promote oil and grease resistance. Over time, the method continued to be utilized as a de facto standard for WBBCs applied to paper and paperboard. The industry has reported that, for such WBBCs, Kit test ratings did not always correlate well with package performance in the field, where the barrier is exposed to a variety of oils and/or grease.

If the coated substrate has defects or pinholes, a premature failure may arise. For example, a known WBBC that has passed numerous 3M Kit tests with a value of 12 may give results with a much lower value if pinholes or other defects are present, especially if the defects are not apparent to the human eye. The 3M Kit test fluid drops may simply "settle" into the defect, giving the appearance of a failure. The 3M Kit test is used to test the holdout of the barrier coating or the degree of repellency and/or the anti-wicking characteristics of the coating, not to test if the coated substrate is defect free. So, for the 3M Kit test to give accurate holdout readings, the substrate must first be determined to be defect free. Some procedures require technicians to test around defects, whereas some others may not.

After years of hearing from customers, co-suppliers, and other industry participants that an improvement to the 3M Kit test was needed, we decided to investigate new methods for detecting defects, which are typically the root cause of barrier failures. After a variety of initial experiments, it was discovered that applying dyed oil to the surface of coated substrates helped to identify defects in the coating. After analyzing the samples, it was determined that we could learn more about the defects than simply to read around them; thus, the Defect Characterization test was created.

EXPERIMENTAL

Defect Characterization test – A novel test method for barrier coating quality

A test method has been developed using a combination of a dyed oil and an image analysis technique to be able to count the imperfections quickly and easily in the coating surface. The use of dyed oil serves two purposes. First, it better simulates the types of materials, in this case, oils and grease, for which the barrier coating is expected to hold out. Second, it provides contrast between the coating and failure points for the image analysis after testing. An image analysis technique is then used to characterize the number and size of the imperfections. The technique can reduce the testing time required if a quality control or laboratory technician needs to count the defects. It can also be used to assist with judgment as to the source of the root cause

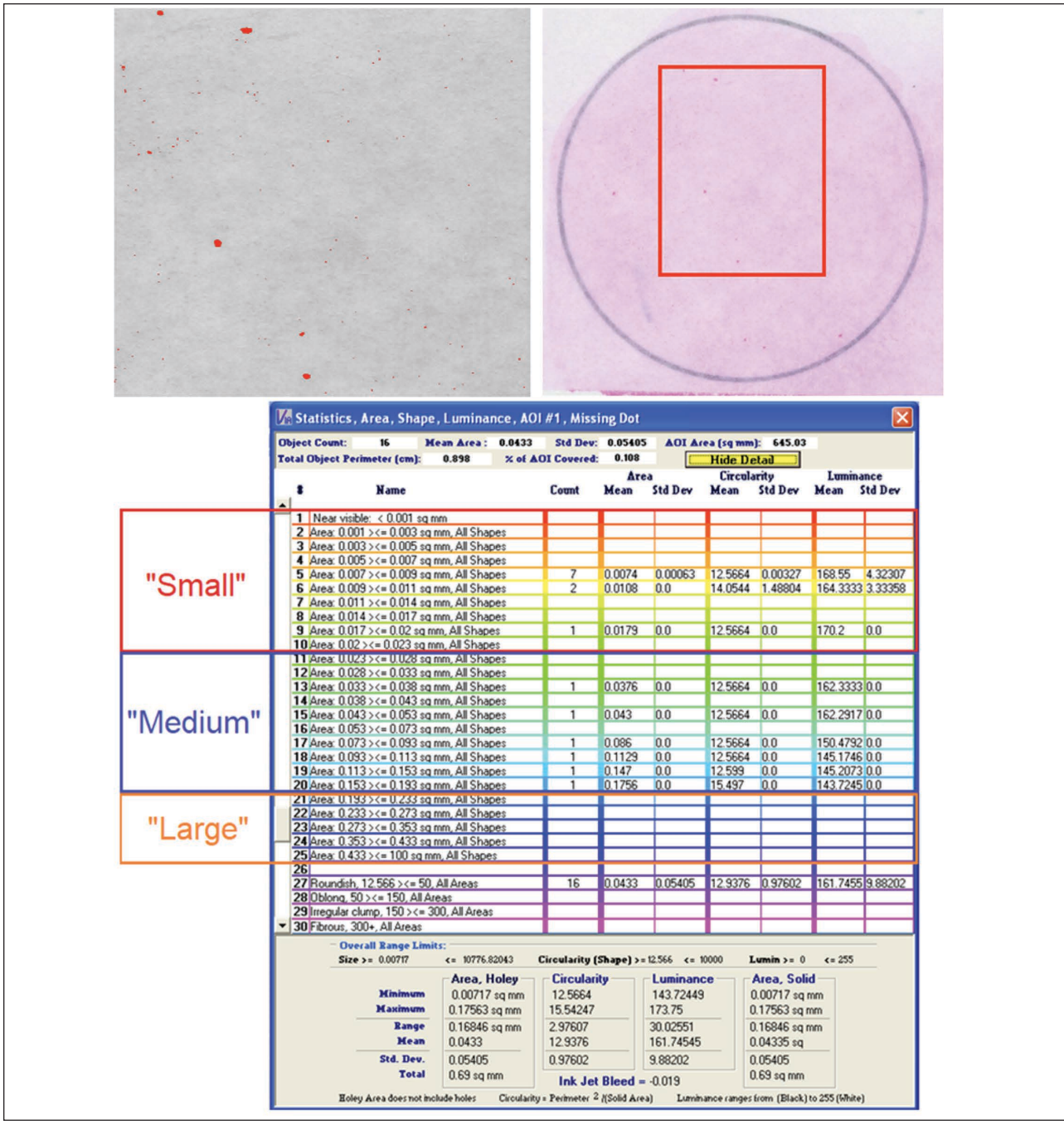

3. Selecting analysis area, exploded image, data, and interpretation.

of the imperfection, such as base sheet defects, coating dispersion issues, or perhaps micro-blisters in the coating, as some examples. Locating these defects can complement other methods used to investigate sources of issues, such as scanning electron microscopy (SEM) techniques.

The Defect Characterization test is conducted by applying a 1-mL quantity of dyed oil to each sample, swirling the dyed oil in a circular pattern covering a 2-in. (5-cm) diameter circle. After the 10 s has expired, the dyed oil that did not penetrate the surface of the sample is removed with an absorbent wipe. The dyed oil chosen for this test is an oil that is typically used in the candy coloring industry. The base ingredient is propylene glycol. The color pink was chosen because it gave the best contrast between defect and white coatings; green- and blue-dyed oils were also evaluated and could also work. We believe other oils could be used, especially if the fluid could be dyed similarly to create the contrast required for good imaging (**Fig. 1**).

After removing the excess dyed oil from the substrate, an image analysis procedure is immediately carried out. The larger defects are readily apparent (**Fig. 2**), but to gain insightful knowledge, such as an accurate count and differ-

Test Element	3M Kit Test	Defect Characterization Test
Area selection	Varies by company; some avoid defects	Any selected area
What is tested?	Spot/drop	Larger sample size
Test area size	~ 0.25 cm^2	6.5 cm^2
Number of fluids applied	1 to 12	1
Fluid selection	See Table VII	Food-grade dyed oil
Estimated test time/sample	5 min	5 min
Equipment cost	Medium*	High**

* Flammable solvents (heptane, toluene) and castor oil mixtures, consumables, fume hood.
** Food-grade oil, consumables, scanner, and image analysis software.

I. Test comparison.

ences in size and shape, we use a combination of an Epson Perfection V750 Pro Scanner (Epson; Suwa, Nagano, Japan) and Verity IA software (Verity IA Software; Milwaukee, WI, USA).

The program and scanner were originally set up for measuring mottle on printed samples by extracting certain color variations. An additional feature in the software included dot count. By using the dyed oil, the defect-free areas remain a light pink color, while the defects absorb more of the dyed oil, giving it a dark pink appearance. By adjusting the sensitivity setting in the image analysis program, we can easily extract the darker-colored dots from the lighter-colored background. The program then counts all the imperfections and categorizes them by size, and if desired, shape as well. This data can be quite relevant in the paper coating industry because one can change the frequency and size of imperfections based on trial conditions (formulation changes, base paper changes, dryer condition changes, etc.), as we will attempt to illustrate in our work.

The most relevant results (**Fig. 3**) derived from the Defect Characterization test are the total count of defects and their sizes or cumulative area. The software can detect dots in the scanned image that are nearly invisible to the human eye. For this work, the dots are categorized into three different sized segments: small, medium, and large. Small dots range in size from < 0.001–0.023 mm^2. Medium dots range in size from 0.023–0.193 mm^2. Large dots are anything greater than 0.193 mm^2. When analyzing samples, the area analyzed is a 6.5 cm^2 sized measurement of the applied oil. This is what has been selected, but it could be modified as needed.

When comparing the new Defect Characterization test method to other barrier testing methods, we believe the key advantage is in assisting with troubleshooting the root cause of failures, i.e., defects. As with most coating applications, even if the paper and coating design are optimized to meet the intended barrier application requirements, the coating process must be executed with minimal-to-zero quality issues. Existing test methods do not adequately help with that analysis. In some cases, procedures state to test around obvious defects. Another benefit of the new test method is in eliminating the need for hazardous chemicals and reducing the time to check the coated sheet. A comparison of the Defect Characterization test against the 3M Kit test can be found in **Table I**.

Dot size and count seems to be sufficient data for most applications, but future work may include a further analysis

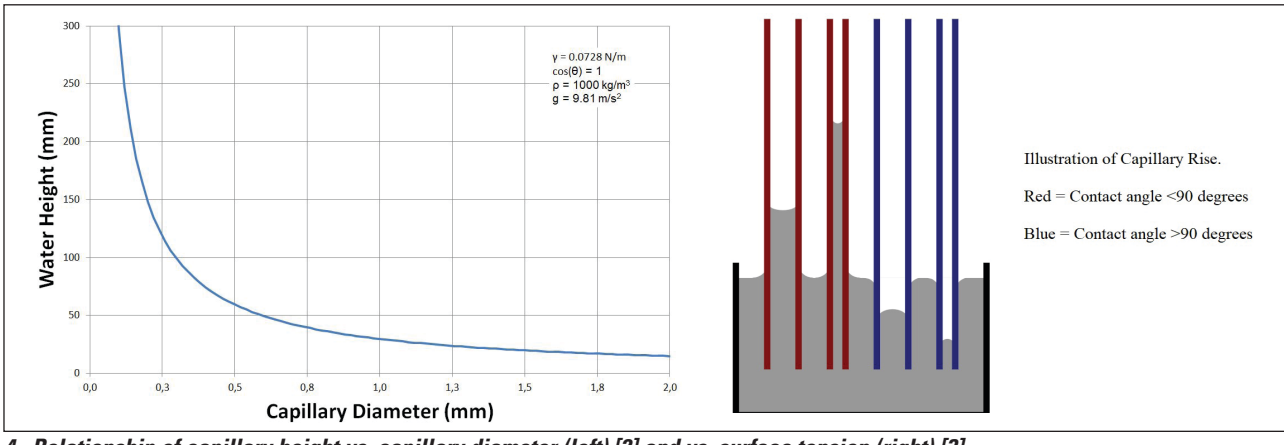

4. Relationship of capillary height vs. capillary diameter (left) [2] and vs. surface tension (right) [3].

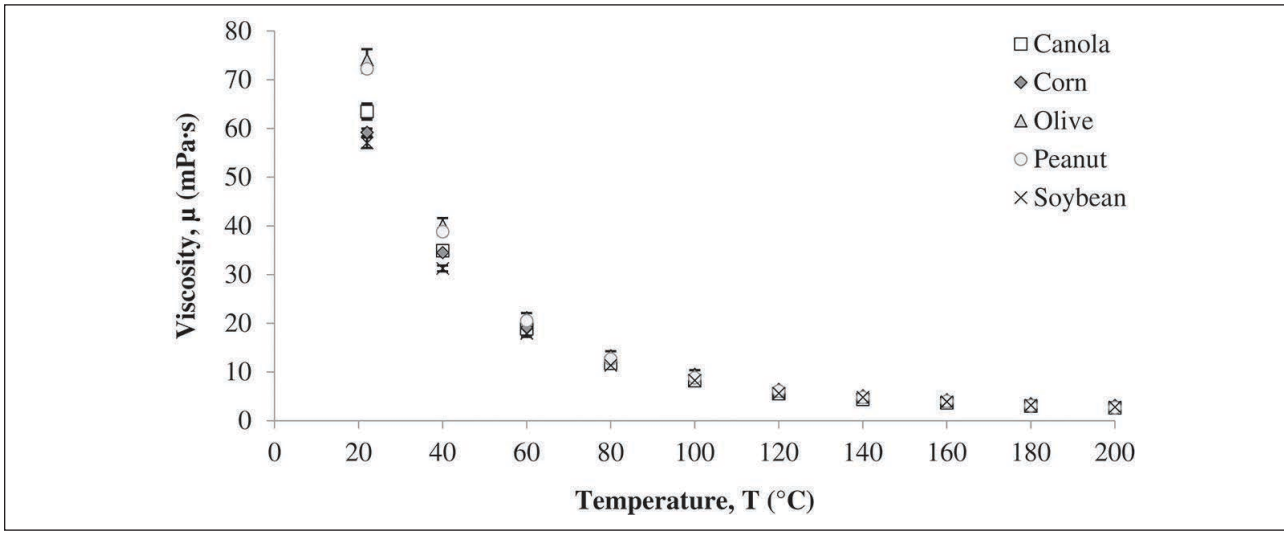

5. Viscosity vs. temperature for five oil types [4].

of data. Data such as dot shape, circularity, blister identification, microscopic evaluation of dyed substrates, and cross-sectional imaging of dyed substrates may be evaluated.

Correlation of Defect Characterization test and barrier testing

Another activity of interest was to determine if we could find correlations between the size, number, and cumulative area of imperfections and their relation to barrier coating failures when tested with two different OGR testing methods (to be described later).

For this evaluation, we consider the defects in coatings to be porous, similar to a capillary. Many references can be found that discuss the role capillary forces can play in fluid transport, and they typically refer to the Young-Laplace equation where a pressure differential can induce fluid transport in capillaries. When the equation (see Appendix for all equation references) is further simplified for capillary flow, it is shown that differential pressure is proportional to the surface tension of the fluid and is inversely related to the radius of the capillary. Higher capillary pressure can give rise to higher fluid transport in smaller diameter capillaries (**Fig. 4**). This suggests smaller capillaries can transport fluid to a greater extent or height in a column than larger capillaries.

If we assume that the defects or pores are capillaries, then many small- or medium-sized capillaries may be as problematic as the large, more obvious defects from the perspective of oil or grease transport. It is also known that for laminar flow in a pipe or tube, Poiseuille's law states the flow rate is inversely proportional to the fluid viscosity. Therefore, more viscous materials will not travel as far in a capillary as those with a lower viscosity. This is important, as testing with materials that do not represent either the viscosity or surface tension of the fluid in question could lead to erroneous results. This again is one aspect of the 3M Kit test we were trying to address by developing a new technique to focus on defect analysis. Also, from Poiseuille's law, we know that as the length of the tube increases, the flow will decrease as well. This suggests, and is also intuitive, that for higher coat weights (i.e., coating thickness), fluid transport is slower, as the capillaries would be longer. This also suggests that in any place where a defect exists, the capillary is shorter and transport times will be faster for the fluid. Again, all equations discussed here can be found in the Appendix.

In many cases, barrier coatings need to perform when in contact with fluids that change viscosity based on conditions of use. One example is in fast food applications where hot food is introduced against the surface of the container. Initially, the oil or grease is quite hot and has significantly lower viscosity than what is experienced at room temperature after cooling (**Fig. 5**) [4]. In these cases, the viscosity of the fluid at 100°C is 5 times lower than at room temperature. As described earlier, differential pressure is proportional to viscosity, so in this case, the ability for hot oil to transport through a capillary would be 5 times greater than oil that has cooled to room temperature. A similar relationship occurs with surface tension, for which for the same oil types are shown in **Fig. 6** [4]. The relation with surface tension suggests that a fluid with lower surface tension could travel faster through a capillary vs. a fluid with high surface tension.

The purpose of this review is to draw attention to the fact that the selection of one material or test condition may not adequately represent the actual conditions of use. Hence, the strategy to make sure the barrier coating is thoroughly tested for defects may provide the best method for ensuring that a quality coated sheet is produced. If one can produce a defect-free coating and the design of the coating is such that it performs when no defects are present, then a quality barrier product would be produced. Although not

T (°C)	γ_{oil} (mN/m) Canola oil	Corn oil	Olive oil	Peanut oil	Soybean oil
Determined using KRÜSS goniometer					
23 ± 0	$31.3 \pm 0.3^{b,c}$	$31.6 \pm 0.1^{a,b}$	31.9 ± 0.0^{a}	$31.3 \pm 0.1^{b,c}$	$31.3 \pm 0.4^{b,c,d}$
40	$30.5 \pm 0.2^{e,f}$	$30.7 \pm 0.1^{d,e}$	$30.9 \pm 0.0^{c,d,e}$	$30.3 \pm 0.2^{e,f}$	30.6 ± 0.3^{e}
60	29.6 ± 0.2^{g}	29.7 ± 0.1^{g}	$30.0 \pm 0.0^{f,g}$	29.7 ± 0.0^{g}	$29.9 \pm 0.0^{f,g}$
80	28.6 ± 0.2^{h}	$28.5 \pm 0.1^{h,i}$	28.8 ± 0.2^{h}	28.8 ± 0.1^{h}	28.7 ± 0.4^{h}
100	27.7 ± 0.1^{j}	27.7 ± 0.1^{j}	27.7 ± 0.0^{j}	27.7 ± 0.1^{j}	$27.9 \pm 0.1^{i,j}$
120	26.5 ± 0.1^{k}	$26.4 \pm 0.2^{k,l}$	26.6 ± 0.1^{k}	26.5 ± 0.0^{k}	27.0 ± 0.0^{k}
140	$25.6 \pm 0.2^{m,n}$	25.3 ± 0.2^{n}	$25.7 \pm 0.5^{m,n}$	$25.5 \pm 0.1^{m,n}$	$25.9 \pm 0.1^{l,m}$
160	24.6 ± 0.1^{o}	$24.1 \pm 0.1^{o,p}$	$24.3 \pm 0.0^{o,p}$	24.5 ± 0.0^{o}	24.5 ± 0.3^{o}
180	$23.5 \pm 0.0^{q,r}$	$23.0 \pm 0.3^{r,s}$	23.1 ± 0.1^{r}	$23.0 \pm 0.1^{r,s}$	$23.8 \pm 0.1^{p,q}$
200	22.4 ± 0.1^{t}	22.0 ± 0.2^{t}	–	21.3 ± 0.4^{u}	$22.5 \pm 0.1^{s,t}$

6. Comparison of surface tension values for five oils at different temperatures [4].

evaluated here, the authors believe the new Defect Characterization test method could be modified to utilize other dyed oils to better simulate the application of interest.

Pilot coater conditions

A series of pilot coater trials (**Table II**) were run at the Trinseo LLC pilot coater located in Midland, MI, USA (**Fig. 7**) to evaluate both process and chemical variables on pinhole/defect formation and corresponding relationship to OGR performance. Barrier coating systems were coated on a flooded nip coater at 1500 ft/min (450 m/min) with a rigid blade using a coat weight ladder approach typically ranging between 5.5 to 11.5 g/m² (3 to 7 lb/3300 ft²). For each coat weight, drying was adjusted in a balanced, stepwise fashion across the air flotation dryers to target 4.3% moisture at the reel. The one exception to this was in Study II, where a coat weight of 6.7 g/m² (4.0 lb/3300 ft²) was targeted and drying was changed as described later. All barrier coated paper was back side-coated to prevent curl with a conventional pigmented paper coating targeting 6.7 g/m² (4 lb/3300 ft²). A coat weight ladder approach was utilized for two reasons. First, this allowed the data to be statistically modelled for drawing firmer conclusions on the new test method. Second, we know fiber coverage is a critical aspect in delivering appropriate barrier performance, so it was important to ensure we had a range in coat weight that would, in the end, produce conditions that were satisfactory in performance to draw sound conclusions. In each case, a single layer of a styrene-acrylate-based starch-containing emulsion system was utilized. In some cases, variations of this system are also described, if applicable in each study.

Study	Pilot Coater Objective Description
I	Base sheet comparison
II	Drying strategy and coalescing aid
III	Barrier system type

II. Pilot coater study description.

Study I – Base sheet comparison

Papermakers have a multitude of variables to consider when it comes to the design of their paper. Improvements are, however, often limited by process constraints or cost drivers in materials. At the same time, they must consider how to balance the design of the base sheet for a barrier grade against the needs for the majority of their production. There are also cost considerations related to transitions to steady-state when moving from grade to grade. Since base sheet design is extremely important for nearly all coated paper performance requirements, the first step was to evaluate how sensitive the new test method could be in detecting a standard from a higher-performing base sheet.

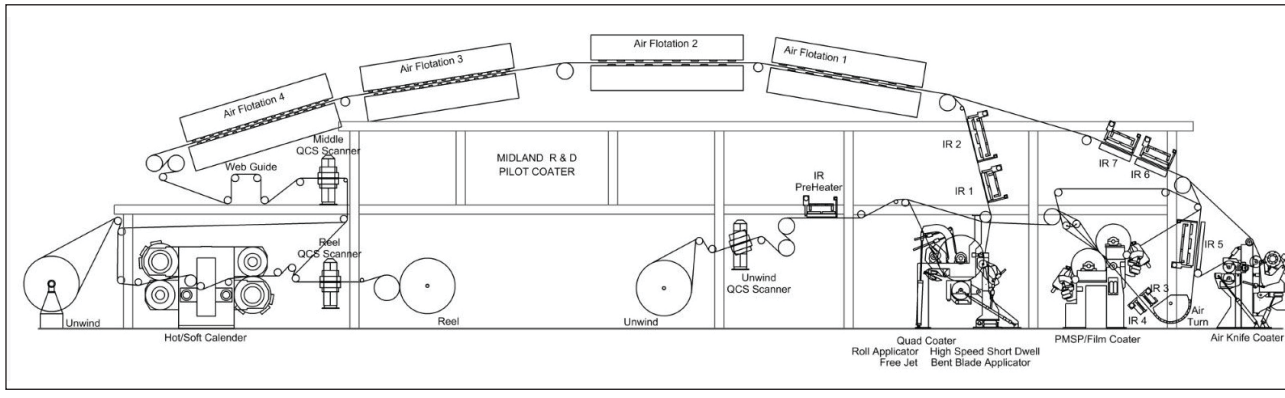

7. Trinseo pilot coater (Midland, MI, USA) layout and dryer configuration.

Base Sheet	Basis Weight — Uncoated	Roughness, um	Porosity, s
H	64 g/m² (38 lb/3300 ft²)	5.2	55
I	80 g/m² (48 lb/3300 ft²)	4.7	154

III. Base sheet description Study I.

Drying Strategy	Drying Strategy Description	Final Moisture
Balanced	Moderate temperatures and nozzle velocities across the 4 AF dryers	4.5%
Early AF	Higher temperatures and nozzle velocities in first 2 of the 4 AF dryers	4.5%
Late AF	Higher temperatures and nozzle velocities in last 2 of the 4 AF dryers	4.5%
IR, Early AF	IR1 used with Early AF strategy	4.5%
IR, Late AF	IR1 used with Late AF strategy	4.5%
IR, Early AF	IR1 used with Early AF strategy	2.0%
IR, Late AF	IR1 used with Late AF strategy	2.0%
AF = forced air flotation; IR1 = 2 rows of gas-fired infrared (IR) drying.		

IV. Drying strategy descriptions Study II.

Two different woodfree base sheets were evaluated to see if the new defect test method was able to detect differences in the two designs. A rougher sheet makes it more challenging to achieve a uniform barrier coating without defects, especially at low coat weights. Rougher sheets can promote more air entrainment during coating as air is trapped between the paper surface and the coating layer during application; during drying these may appear as bubbles or craters if they are trapped during coating coalescence. Sheet porosity also plays a role, as it has a significant effect on coating penetration. In this case, details on furnish type, filler, or other process variables were not provided by the supplier. However, indications were given that Base Sheet I should perform better as a base paper for a single-coated barrier than Base Sheet H. We looked for indications of fewer pinholes at equal coat weight, as well as the potential difference in the distribution of small, medium, and large pinholes. Some basic base sheet tests results are shown in **Table III**.

Study II – Drying strategy and coalescing aid

The influence of the drying strategy has been studied as it relates to end-use performance properties and in water-based barrier coatings on paper [5,6]. Many water-based barrier coatings are typically quite high in binder content and are formulated below the critical pigment volume concentration. To cure these systems, water vapor must transport out of the coating and not contribute to defect formation in the form of micro-blisters or other defects.

In this work, we use the Defect Characterization test method to evaluate if a higher frequency or certain dot size can be detected. Five different drying strategies were evaluated on the pilot coater for a common barrier system and base sheet, as shown in **Table IV**. In the table, AF is used to represent the 4 forced air flotation dryers, and IR1 is used to represent the 2 rows of gas-fired infrared (IR) drying (Fig. 7). Also evaluated were two different final moisture contents for the two IR conditions, including a very low moisture condition to represent harder drying conditions.

Barrier System	Description
B	Proprietary SA-SCE Barrier System
C	Barrier System B with 1.0 parts coalescing aid

V. Barrier system description for Study II.

It is typical in architectural coatings with film-forming binders to use a coalescing aid to soften the polymer by lowering the glass transition temperature to assist in film formation and binder coalescence. In those cases, drying is typically done in ambient conditions with slow water transport. For barrier coatings containing high levels of binder, some have suggested that coalescing aids could improve film formation and reduce defects. In this evaluation, we decided to evaluate the use of a coalescing aid, glycerol, as a system component (**Table V**). For Barrier System C, glycerol was added at a level of 1 part to Barrier System B. This was assessed within the same drying evaluation described previously.

Barrier System	Description	Coating Surface Tension, dynes/cm	Paper Total Surface Energy, mN/m
X	Proprietary SA-SCE Barrier System X	46.5	58
Y	Barrier System X with 0.5 parts higher surfactant	37.4	52
Z	Proprietary SA-SCE Barrier System Z	N/A	54

VI. Barrier system description for Study III.

Rating	Castor Oil, g	Toluene, ml	Heptane, ml
1	969	0	0
2	872	50	50
3	775	100	100
4	678	150	150
5	581	200	200
6	485	250	250
7	388	300	300
8	291	350	350
9	194	400	400
10	97	450	450
11	0	500	500
12	0	550	550

VII. Kit test solutions.

Study III – Barrier system comparison

It has been well documented that the wettability of a substrate can play an important role in the ability of the coating to wet out and stretch to cover the substrate to prevent craters and coating defects [7]. To test that theory, Barrier System Y was evaluated by adding 0.5 parts of a common wetting agent (sodium dioctyl sulfosuccinate) to Barrier System X. Coating surface tension values and their impact on the coated paper surface energy are shown in **Table VI**, as well as the impact on the coated paper surface energy. A third condition was also evaluated, as shown in Table VI, with another proprietary change made to the same SA-SCE barrier system, shown as Barrier System Z. The purpose of this study was to demonstrate whether the new test method was capable of detecting differences between materials and process changes.

Comparative barrier test methods

3M Kit test

The 3M Kit test measures the repellency or anti-wicking behavior of paper and paperboard when subjected to various oils/solvents and was conducted per the TAPPI Standard T

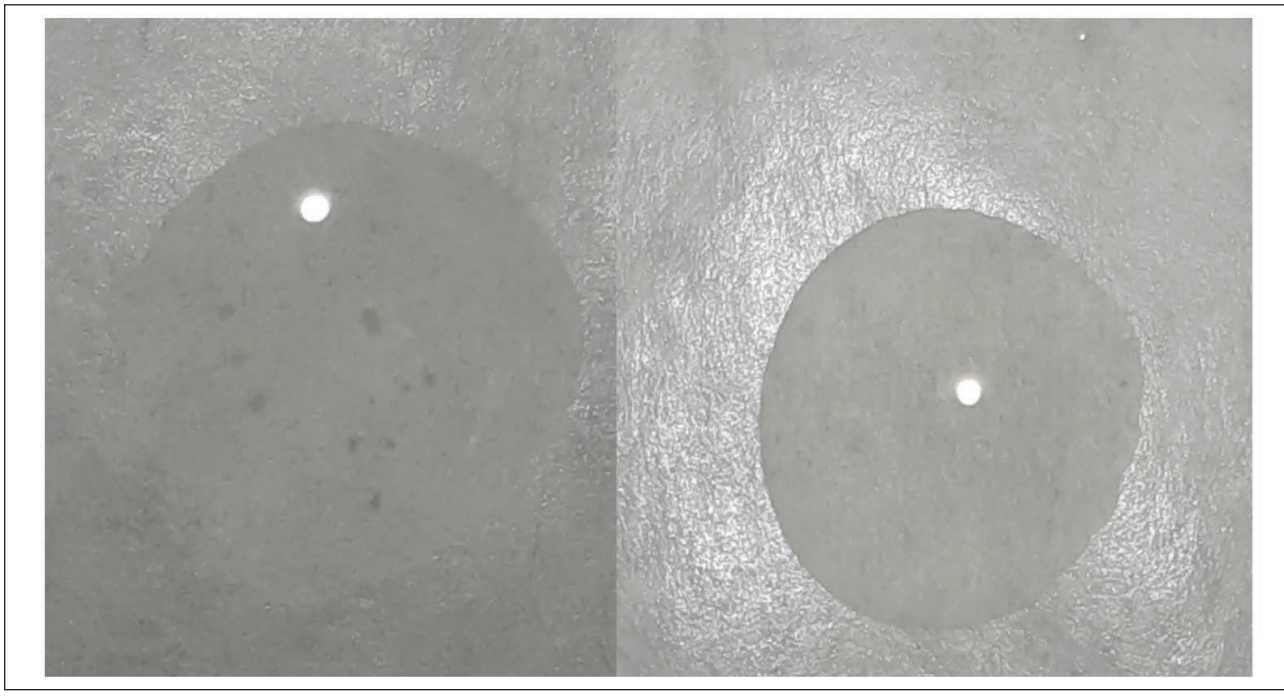

8. Example of a "failed" sample (left) vs. a "passing" sample (right).

Rating	Characterization	Description
0	No penetration	No visible pinholes, spots, or stains.
1	< 10 pinholes	More than 1 pinhole, less than 10 pinholes visible.
2	< 25 pinholes	More than 11 pinholes, less than 25 pinholes visible.
3	< 50 pinholes	More than 26 pinholes, less than 50 pinholes visible.
4	> 50 pinholes	More than 50 pinholes visible.
5	Small spots	Small spots visible.
6	Large spots	Large spots visible.
7	Stain(s)	One or more stains, not able to tell if sample is penetrated.
8	Stain/fail	Stain is kept within barrier ring but has penetrated the sample.
9	Complete fail	Stain goes beyond barrier ring or has caused ring to lift.

VIII. Hot Oil Circle test failure rating system descriptions.

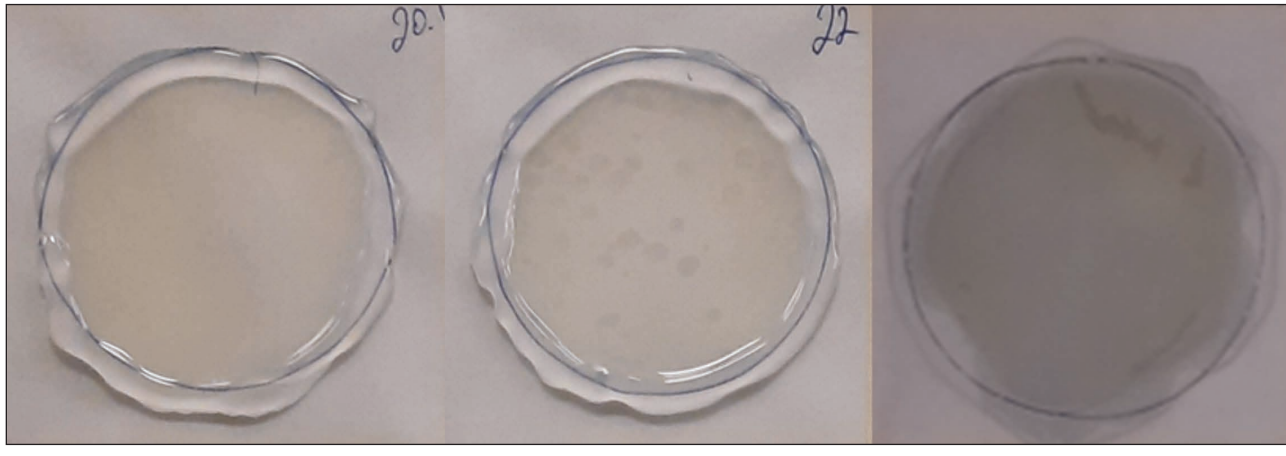

9. Example of a rating of 0 (left; no penetration), a rating of 3 (center; >26 but <50 pinholes), and a rating of 9 (right; complete fail).

559. Kit testing was conducted on flat samples. A series of Kit solutions was prepared using combinations of castor oil, toluene, and heptane, as shown in **Table VII**. A lower Kit value represents a "less harsh" treatment (higher percentages of castor oil), while a high Kit value represents a "harsher" treatment (higher percentages of toluene and heptane).

Higher values, therefore, indicate better barrier performance. The liquid is applied to the substrate using a dropper. A single drop is evaluated for 15 s. After 15 s have expired, the substrate is examined for failures in the coating (typically a stain or pinhole). If considered a failure, a less harsh Kit solution is tested until a sample has passed the examination (drop sits on top of the substrate without penetration or staining). This Kit solution would be recorded as a "pass" for results. **Figure 8** shows testing examples.

Hot Oil Circle test

The Hot Oil Circle test is used to analyze oil barrier properties. Preheated oil (corn oil at 60°C) is applied to the barrier surface. Various time treatments are evaluated from immediate to 24 h. The front (coated) and the back side of the paper samples can be evaluated for oil stain penetration. For this study, testing was carried out at room temperature. Visual observations were made prior to testing and immediately after applying the tempered oil. Observations were also conducted 15 min, 30 min, 45 minutes, 60 min, and 24 h after oil exposure.

Examples may be found in **Figure 9**, and **Table VIII** describes the internally used rating system.

RESULTS AND DISCUSSION

For each of the three pilot coater studies, the new test method was utilized to generate the defect data set for each set of samples. Within the data sets, we looked for any correlations between the types of defects in size, frequency, and area, along with the resulting barrier test results. A summary of the coating run data and formulation tests can be found in the Appendix for the appropriate studies.

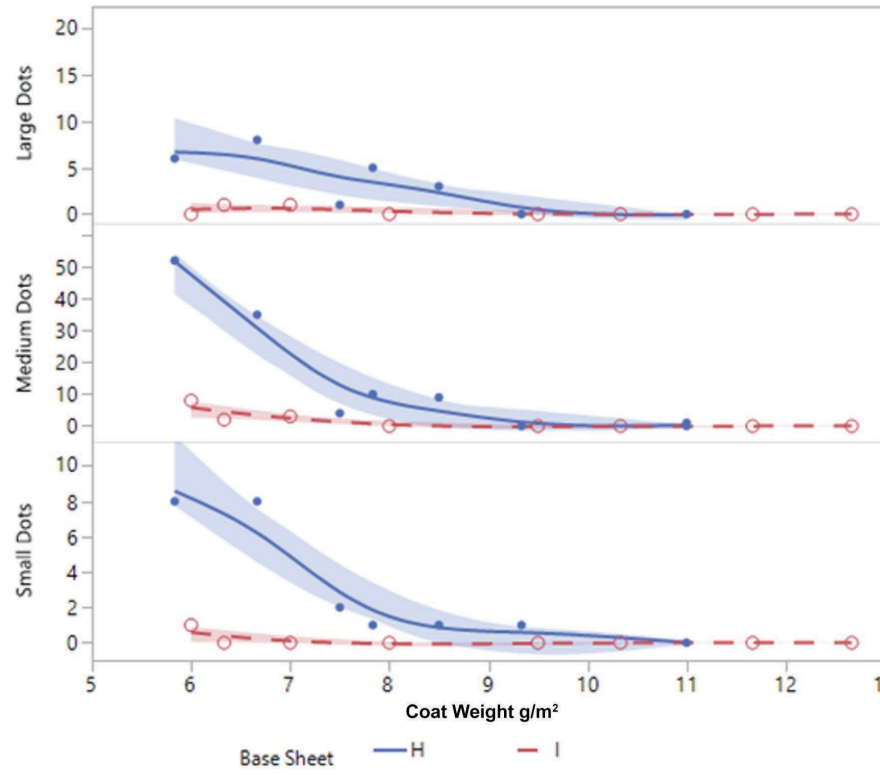

10. Dot size and dot count vs. coat weight for each base paper.

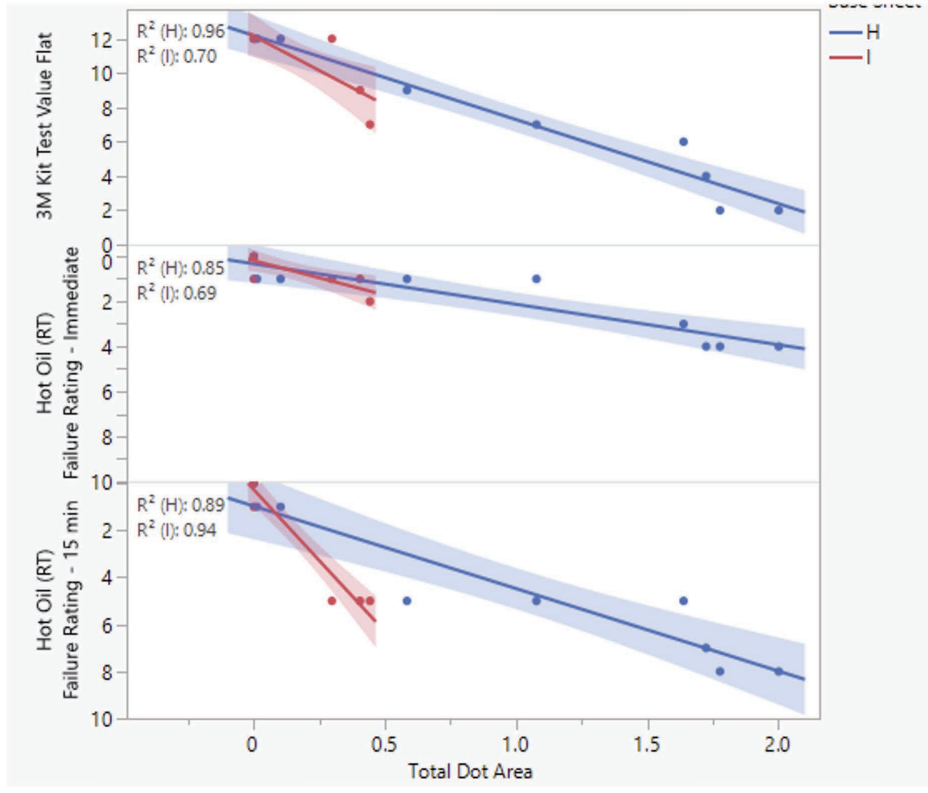

11. Barrier performance vs. total defect area (R^2 = coefficient of determination).

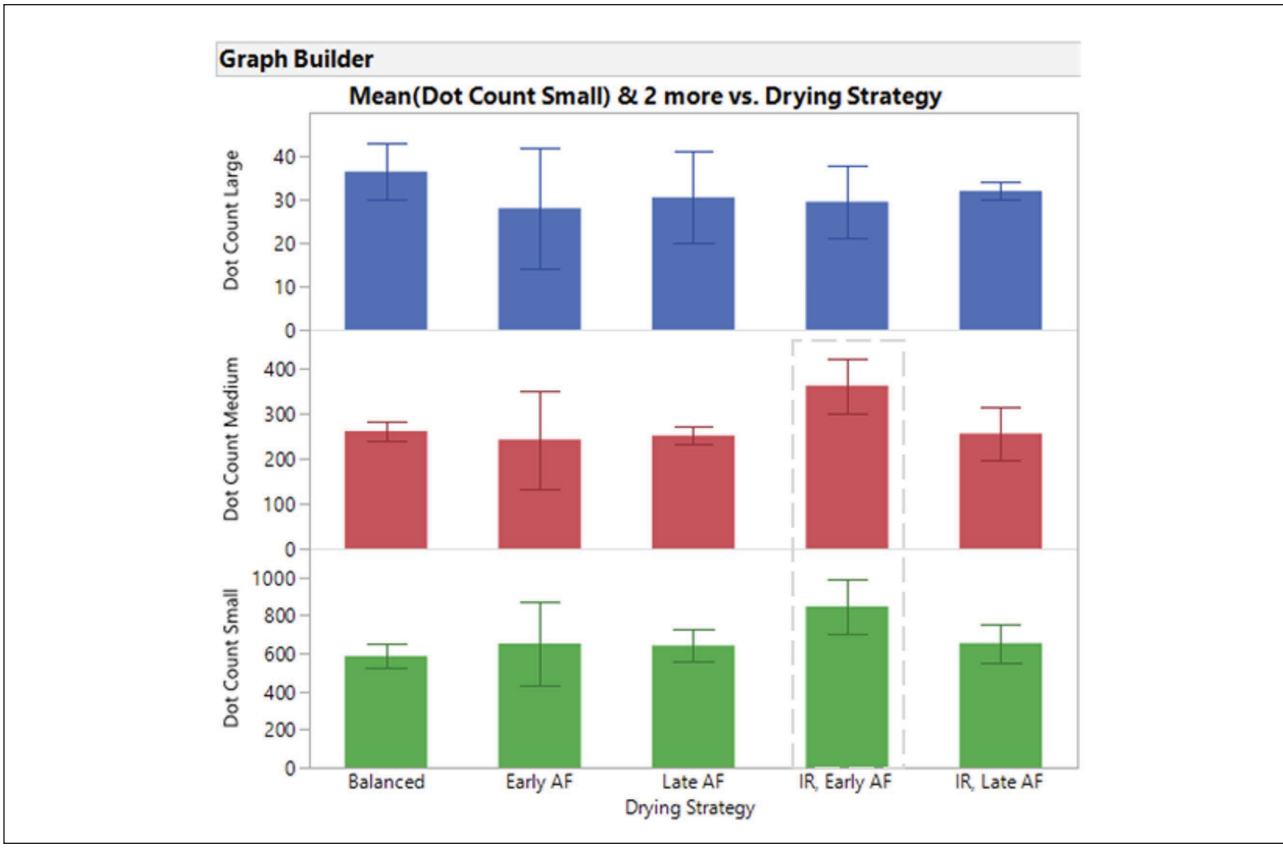

12. Effect of drying strategies in Study II. See Table IV for descriptions of drying strategies.

Study I – Base sheet comparison

For this evaluation, a simple dot plot with a smoothed line fit was constructed comparing, for each dot size (large, medium, small), the dot count vs. applied coat weight for all trial conditions over each base sheet. These results were generated using the Defect Characterization test method. In this case (**Fig. 10**), it was very apparent that Base Sheet I had dramatically fewer dots of all three dot classifications than Base Sheet H. A significant improvement in the small-sized dots ranging from >0.001–0.022 mm2 and the medium-sized dots ranging in size from 0.023–0.193 mm2 was observed.

Data from the Defect Characterization test was evaluated for correlation against two barrier test protocols, the 3M Kit test and a Hot Oil Circle test, both described earlier. For the hot oil test, two time treatments (immediate and 15 min) are compared. For both papers, lower measured defect area (dot size times frequency), as determined from the image analysis of the stained area, correlated well with both test methods (**Fig. 11**).

Study II – Drying strategy and coalescing aid

As described earlier in the Experimental section, Study II was aimed at identifying whether various drying strategies could influence defect formation in WBBC systems. Additional activity was to evaluate the use of a coalescing aid in this type of system to seal off the film through more complete coalescence of the binder materials, as the hypothesis. In this case, a non-optimized base sheet was used, so defect counts are quite high. Defect data was collected utilizing the new test method. **Figure 12** shows the comparative dot counts for all three classifications of dot size and indicates that high energy IR drying combined with harder early air flotation drying promoted the generation of more medium and small defects. Most other drying strategies are comparable and show a lower level of defects.

The comparison considered like conditions where the effect of coalescing aid, described as Barrier System C, was compared to the system without coalescing aid, Barrier System B (**Fig. 13**). In the case of Barrier System C, the effect of the glycerol addition resulted in a statistically significant increase in defects, especially in the medium and small classification. Although glycerol has a very high boiling point (290°C), evaporation can occur above 20°C and in aqueous mixtures. This could explain why the selection of this material and drying at elevated temperature led to more defects, perhaps from microblisters migrating through the coating during consolidation and film coalescence.

For the conditions with an IR drying strategy (many coated paper machines today use some), a lower moisture target (2.7%) was also evaluated. **Figure 14** shows the re-

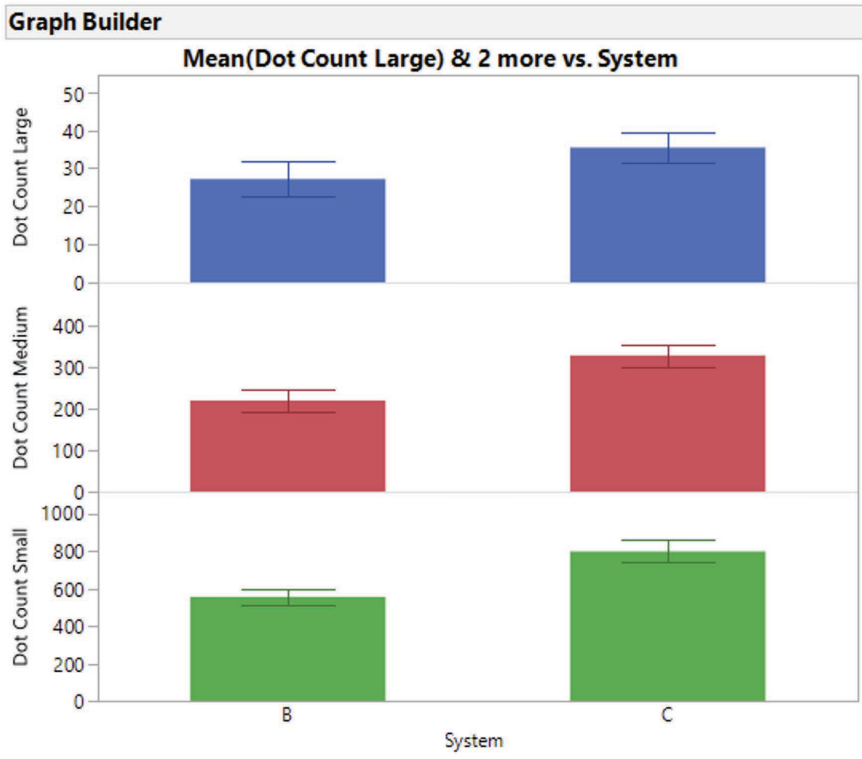

13. Effect of coalescing aid (B = no, C = yes).

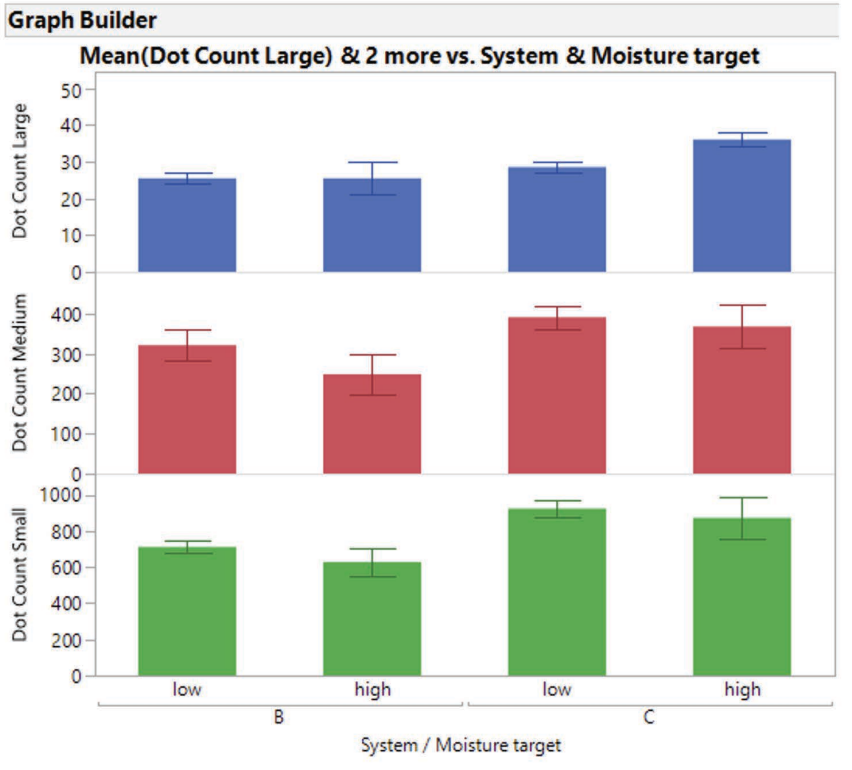

14. Effect of moisture target and coalescing aid (B = no, C = yes).

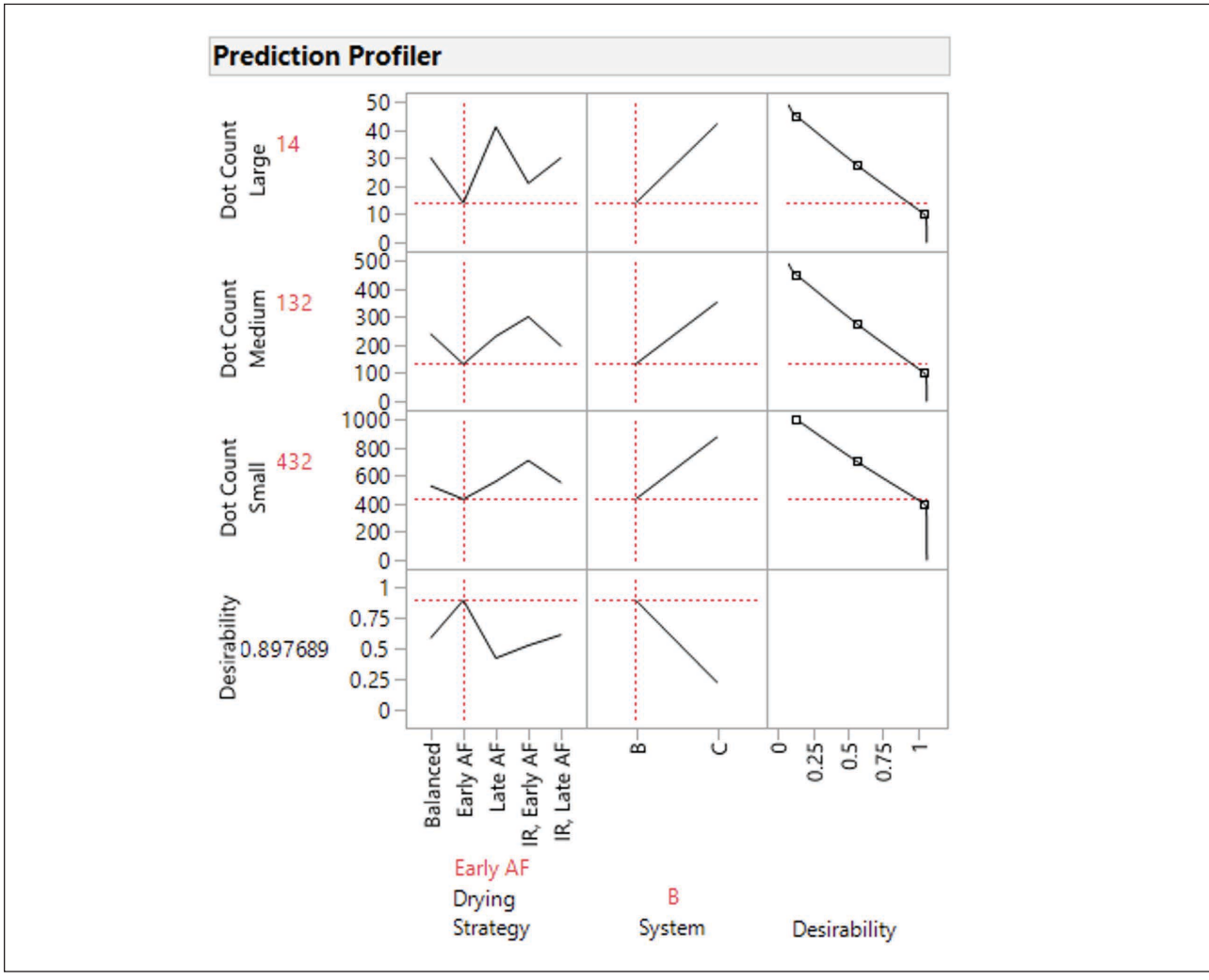

15. Predictive model and drying/chemistry optimization for reduced defects in Study II. See Table IV for descriptions of drying strategies.

lationship between target moisture (when IR drying is used) and the effect of coalescing aid. In all cases, the coalescing aid modification, Barrier System C, resulted in higher dot counts for all three classifications, as presented earlier. It was also observed that the more typical high moisture target (4.3%) led to the fewest defects for the medium and small classifications. This could indicate that the higher drying energy, which produced higher sheet temperatures to drive moisture to the lower target, creates more medium and small defects.

For pilot coater Study II, data could be modeled against the two primary variables of the system (coalescing aid: Barrier System "B" = no; Barrier System "C" = yes"), and **Fig. 15** shows drying strategy at equal final target moisture. In this case, by using a prediction profiling tool, we can determine the optimal set of conditions to minimize the defects (dot count). In this case, not using early IR drying and front-loading the air flotation drying to the earlier dryer sections reduces dot count. As shown earlier, the use of glycerol as a coalescing aid was not effective.

Study III – Barrier system comparison

For this evaluation, a simple dot plot with a smoothed line fit was constructed comparing, for each dot size (large, medium, small), the dot count vs. applied coat weight for the three trial conditions in Study III. The focus of this study is not specifically the chemistry changes, but whether or not the new test method is capable of detecting differences in barrier coating systems. As observed from **Fig. 16**, it is apparent that moving from Barrier System X to Barrier System Y to Barrier System Z shows a marked improvement in reducing the number of defects in all defect classifications. To be stated in another way, for constant coat weight at values below 8 g/m², the "Y" and "Z" systems offer more efficient coverage and fewer defects.

For pilot coater Study III, data could be modeled against the two primary variables of the Barrier System ("X" vs. "Y" vs. "Z") and coat weight (**Fig. 17**). With the prediction profiling tool, using statistically significant models for each output, we can determine the optimal system at constant coat weight (minimize the defects/dot count). In this case,

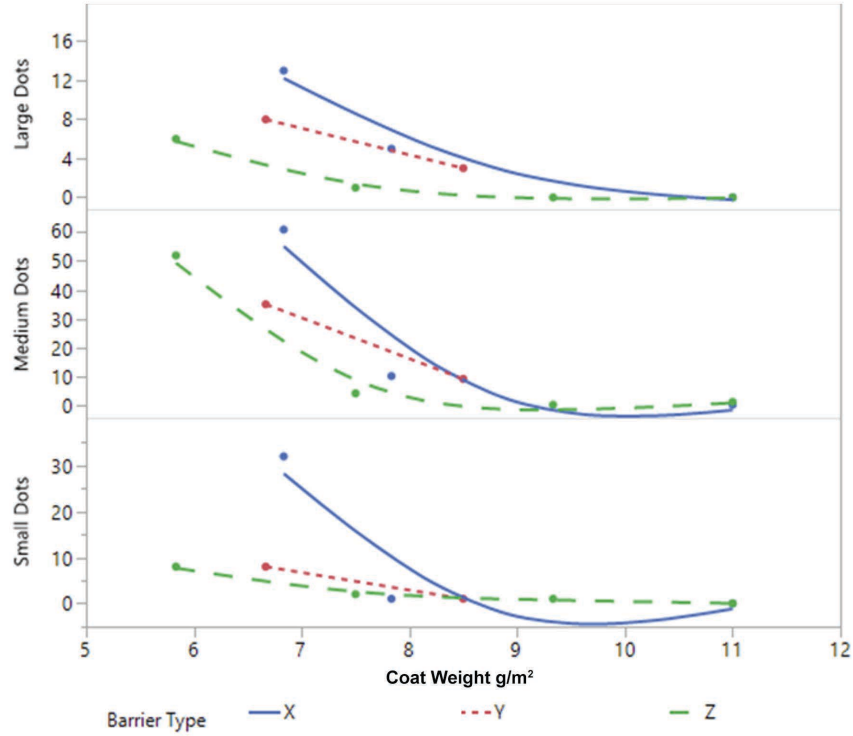

16. Dot size and dot count vs. barrier system type.

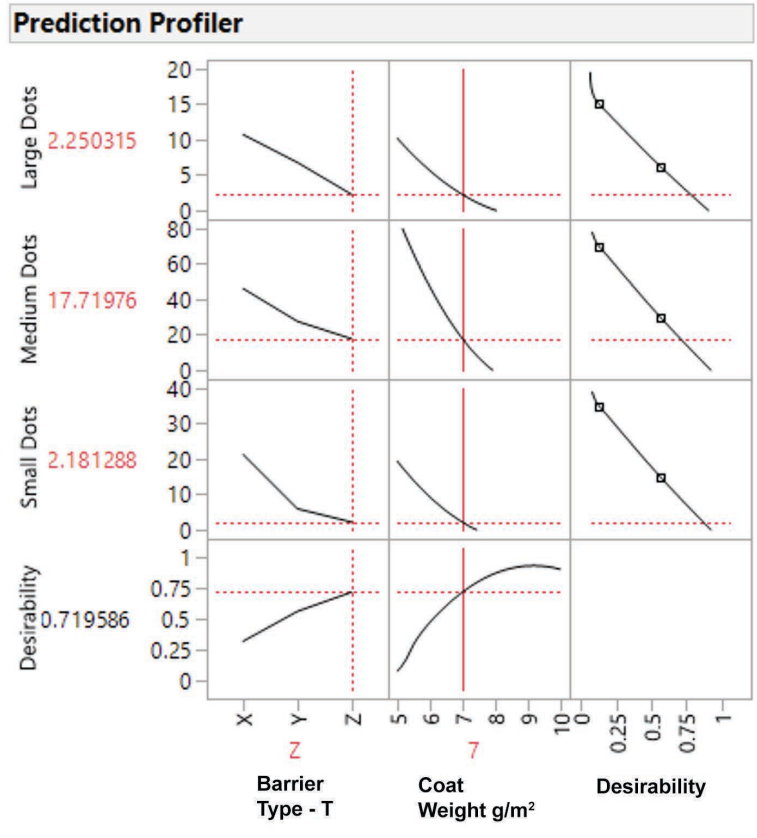

17. Predictive model for barrier type optimization for reduced defects in Study III.

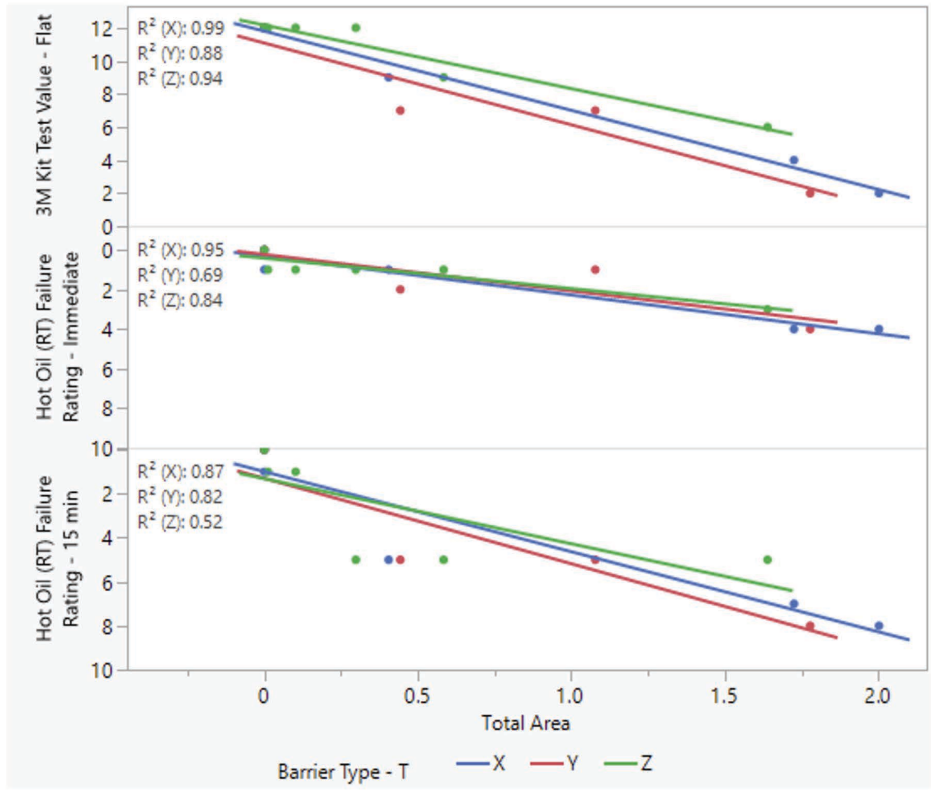

18. Barrier system performance vs. total defect area (R^2 = coefficient of determination).

the data suggest Barrier System Z is the best at 7 g/m² coat weight and lower.

Data from the Defect Characterization test was evaluated for correlation against the two barrier test protocols as presented earlier. For all systems, lower measured defect area correlated well with both barrier test methods, as shown in **Fig. 18**. For each barrier system, a linear fit was performed, and the coefficient of determination (R^2) values are shown. In most cases, the correlation was very good, but it was especially so for the 3M Kit test and the immediate ratings for the Hot Oil test. For the longer time evaluation of the Hot Oil test at 15 min, the R^2 values were not as good, and it appears there could be a step-change in performance that relates to a saturation level reached at total defect area levels above 0.25 mm².

CONCLUSIONS

In conclusion, the Defect Characterization test has been shown to correlate with other barrier test results and has been able to detect defect changes brought about by process and formulation changes. The impact of changes in drying strategy and formulation components were detected and quantitatively measured by the change in size and frequency of film defects. The Defect Characterization test may have a higher upfront cost than the traditional 3M Kit test (if wanting more than pass/fail data), but the accuracy, safety, and ease of conducting the test likely supersede the costs. Although the equipment used for image analysis is extremely helpful to examine the defects in high detail, we do believe a simple application of dyed oil to the substrate can quickly identify basic defects without the use of additional equipment. If only needing pass/fail data, dyed oil is a much cheaper investment than what is required to carry out other barrier testing (various oils, chemicals, fume hoods, ovens, etc.), and there is a substantial cost savings involved. If necessary, the dyed oil can be applied directly to a roll of paper, eliminating the need to slab down rolls to obtain sheet samples, creating significant time savings.

Like the 3M Kit test, other barrier tests require a defect-free surface. Tests such as the Hot Oil Application test, Contact Angle, and even Cobb may give less than desired outcomes if defects are present (premature failures, lower contact angles, complete saturation failures). The Defect Characterization test may not replace these barrier tests but will ensure that additional testing on the substrate will be more accurate. If such coatings have been proven to be effective in the past from a coating design and performance perspective, testing beyond the Defect Characterization test may not even be necessary. **TJ**

ACKNOWLEDGEMENTS

We would like to acknowledge Trinseo LLC for sponsoring this research paper. Additionally, the efforts of the staff members at the pilot coater and testing labs in Midland, MI,

USA, are greatly appreciated. We also wish to thank Dr. Pekka Salminen for his support in providing the references relating to fluid transport theory for barrier coating performance.

LITERATURE CITED

1. Smithers Pira, "The future of functional and barrier coatings for paper and board to 2024," Smithers Pira, Leatherhead, Surrey, UK, 2019.
2. Luyken, H., "Water height in a capillary tube plotted against diameter," personal work, Wikipedia. Available [Online] https://en.wikipedia.org/wiki/Jurins_law <18Nov2021>.
3. Konečný, E., "Illustration of capillary rise," personal work, Wikipedia. Available [Online] https://en.wikipedia.org/wiki/Young%E2%80%93Laplace_equation <18Nov2021>.
4. Sahasrabudhe, S.N., Rodriguez-Martinez, V., O'Meara, M., et al., *Int. J. Food Prop.* 20(sup 2): 1965(2017). https://doi.org/10.1080/10942912.2017.1360905.
5. Emilsson, P., "Multi layers to drying strategy to avoid pinholes by sustainable barrier coating," *PaperCon*, TAPPI Press, Peachtree Corners, GA, USA, 2017.
6. Habermahl, L.K., Pollock, M., Attal, J., et al., *TAPPI Coat. Conf.*, TAPPI Press, Atlanta, 1997, p. 111.
7. Yang, A., Salminen, P., Vervoort, S., et al., *Appl. Rheol.* 21(2): 23607(2011). https://doi.org/10.3933/applrheol-21-23607.

ABOUT THIS PAPER

Cite this article as:
Burton, D., Ventresca, D., and Welsch, G.W., *TAPPI J.* 21(11):625(2022). https://doi.org/10.32964/TJ21.11.625

DOI: https://doi.org/10.32964/TJ21.11.625

ISSN: 0734-1415

Publisher: TAPPI Press

Copyright: ©TAPPI Press 2022

About this journal

ABOUT THE AUTHORS



Burton



Ventresca



Welsch

As the local barrier capabilities expert within Trinseo, I (Burton) spend much of my day working with, testing, and developing barrier coatings. I have noticed that the existing tests associated with barrier coatings are lackluster and need improvements. This research compliments existing barrier-type testing, improving its accuracy by determining whether the face of the sheet is defect free before performing any other forms of barrier-type testing.

The most difficult aspect of this study was determining how to analyze the data. I discovered that if we used a dyed oil rather than a natural-occurring color, the defects become more apparent and the color can then be extracted using existing analytical extraction methods to give accurate counts of dyed defects.

An interesting finding in this work has been how many customers have been waiting for a test like the Defect Characterization test presented here, and how many really dislike existing test methods. It was also surprising to find that a number of commercially available products have defects on the surface.

For mills, the Defect Characterization test can be completed in a short amount of time using a small paper sample. The next step in this work is to determine what the shape of defects is trying to tell us. Can we pinpoint if the defect is a fisheye, undercoated fiber, pinhole, or blister? There is also more work to be done in determining whether the type of defect affects the overall performance of the barrier.

Burton is senior research technologist and Welsch is Global Innovation leader for Trinseo LLC in Midland, MI, USA. Ventresca is technical service and development specialist for Trinseo LLC in Petrolia, ON, Canada. Email Burton at DBurton@trinseo.com.

APPENDIX

Reference equations

Young-Laplace equation

Simplified equation for a capillary tube:

$$\Delta p = \frac{2\gamma}{R}.$$

where:
Δp = differential pressure between the two ends
γ = surface tension
R = radius of the capillary

Hagen-Poiseuill equation

$$\Delta p = \frac{8\mu LQ}{\pi R^4} = \frac{8\pi\mu LQ}{A^2} \quad \textbf{or} \quad Q = \frac{\pi \Delta p\, r^4}{8\,\mu\, L}$$

where:
Δp = differential pressure between the two ends
L = length of the pipe
μ = dynamic viscosity
γ = surface tension
Q = volumetric flow rate
R = pipe radius
A = cross-section of the pipe

Study I data

Study I data was derived from analyzing data from Study III with modeling and data analysis on base sheet changes, as shown in the following table.

RUN NUMBER	11.0	11.1	11.2	12.0	12.1	12.2	19.0	19.1	20.0	20.1	17.0	17.1	17.2	17.3	18.0	18.1	18.2
BASESHEET	H	H	H	I	I	I	H	H	I	I	H	H	H	H	I	I	I
MACHINE SETTINGS																	
Blade (B=Bent)	20-45	20-45	20-45	20-45	20-45	20-45	20-45	20-45	20-45	20-45	20-45	20-45	20-45	20-45	20-45	20-45	20-45
Rod (G=Grooved)																	
Head Angle	49.7	49.7	49.7	49.7	49.7	49.7	49.7	49.7	49.7	49.7	49.7	49.7	49.7	49.7	49.7	49.7	49.7
Head Stops (in.)																	
Applicator Roll Speed (%)	22	22	22	22	22	22	22	22	22	22	22	22	22	22	22	22	22
Applicator Roll Gap (in.)																	
Coater Speed (FPM)	1500	1500	1500	1500	1500	1500	1500	1500	1500	1500	1500	1500	1500	1500	1500	1500	1500
Coated Side	Felt	Felt	Felt	Inside	Inside	Inside	Felt	Felt	Inside	Inside	Felt	Felt	Felt	Felt	Inside	Inside	Inside
RUN VARIABLES																	
Basestock Moisture (%)	3.8	3.8	3.7	3.4	3.2	3.2	3.6	3.6	3.2	3.3	3.9	3.8	3.6	3.5	3.5	3.4	3.2
Coat Weight (lbs./3300 SF)	4.1	4.7	6.6	3.8	4.8	7	4	5.1	3.6	5.7	4.5	5.6	6.6	3.5	4.2	6.2	7.6
Moisture (%)	3.6	4.1	4.1	4.1	4.4	4.3	4	4	4.5	5.6	4.2	4.6	4.5	3.5	4.2	3.8	4.1
Tube Load (PSI)	23.9	13.9	6	16.1	9.5	5	19.4	11.9	15.9	6	23.9	21	12.9	23.8	16.9	10.9	8

Study II data

Formulation	B	C
Parts		
Modified proprietary SA-SCE barrier system	100	100
Coalescing aid	0	1
Associative thickener	0.5	0.5
Defoamer	0.07	0.07
Testing		
% Solids	44.6	44.3
pH NaOH	8.0	8.0
Viscosity @ 20 rpm, w/#4	3550	3180
Viscosity @ 100 rpm, w/#4	1268	1176
Hercules max rpm viscosity	54.9	48.3

NaOH = sodium hydroxide.

RUN NUMBER		3	4	5	6	7	8	9	10	11	12	13	14	15	16
FORMULATION		B	B	B	B	B	C	C	C	C	C	B	B	C	C
MACHINE SETTINGS															
Blade	(B=Bent)	15/40	15/40	15/40	15/40	15/40	15/40	15/40	15/40	15/40	15/40	15/40	15/40	15/40	15/40
Rod	(G=Grooved)														
Head Angle		44.7	44.7	44.7	44.7	44.7	44.7	44.7	44.7	44.7	44.7	44.7	44.7	44.7	44.7
Applicator Roll Speed	(%)	22	22	22	22	22	22	22	22	22	22	22	22	22	22
Coater Speed	(FPM)	1500	1500	1500	1500	1500	1500	1500	1500	1500	1500	1500	1500	1500	1500
RUN VARIABLES															
Basestock Moisture	(%)	6.8	6.5	6.1	6.3	6.0	7.1	7.0	6.8	6.9	6.8	6.4	6.0	7.0	6.7
Coat Weight	(lbs./3300 SF)	3.7	3.9	3.9	3.9	3.9	3.8	4.0	4.0	3.9	4.0	4.1	4.0	4.3	4.1
Moisture	(%)	4.4	4.4	4.1	4.3	4.2	3.6	4.6	4.4	4.3	4.4	2.2	2.8	2.9	2.7
Tube Load	(PSI)	9.8	8.0	7.6	7.9	7.1	8.9	6.3	6.2	5.9	6.2	7.7	7.3	6.0	6.3
DRYER SETTINGS															
IR Preheat	(%)	100	100	100	100	100	100	100	100	100	100	100	100	100	100
IR Zone 1	(%)	100	100	100			100	100	100			100	100	100	100
IR Zone 2	(%)		100	100				100	100			100	100	100	100
TEC 1 Temperature	(°F)	250		400		475	300		400		500		500		500
Pressure	(in. of water)	0.7		1		1.3	1.3		1		1.5		1.5		1.5
TEC 2 Temperature	(°F)	250		400		475	300		400		500		500		500
Pressure	(in. of water)	0.7		1		1.3	1.3		1		1.5		1.5		1.5
TEC 3 Temperature	(°F)	250	250		375		300	250		400		400		400	
Pressure	(in. of water)	0.7	1		1		1.3	1.7		1.3		1		1.3	
TEC 4 Temperature	(°F)	250	250		375		300	250		400		400		400	
Pressure	(in. of water)	0.7	1		1		1.3	1.7		1.3		1		1.3	
SHEET TEMPERATURE															
IR Preheat	(°F)	144	146	149	147	149	145	145	147	146	148	147	149	145	147
Before TEC 1	(°F)	117	153	155	87	90	114	152	153	87	87	154	155	152	154
After TEC 1	(°F)	119	107	140	92	140	116	97	125	85	132	104	165	95	152
After TEC 2	(°F)	130	111	156	92	175	137	103	152	87	184	106	190	99	192
After TEC 3	(°F)	145	144	140	146	134	154	144	138	147	132	165	150	160	149
After TEC 4	(°F)	158	160	146	173	134	173	159	140	177	125	200	149	189	142
Reel	(°F)	86	86	86	86	86	86	86	86	89	87	89	87	89	88

Study III data

Formulation	X	Y	Z
Parts			
Proprietary SA-SCE Barrier System X	100	100	
Proprietary SA-SCE Barrier System Z			100
Na DOSS		0.5	
Alcogum L229	0.5	0.5	0.5
Foamaster	0.05	0.05	0.05
Test Results			
% Solids	47.1	47.1	47.5
pH NaOH	7.9	7.9	7.8
Viscosity @ 100 rpm, w/#	1460	1870	2212
Hercules maximum rpm viscosity	72.0	89.1	89.4

Na DOSS = sodium dioctyl sulfosuccinate wetting agent; Alcogum L229 = rheology modifier and wetting agent from Nouryon (Amsterdam); Foamaster = mineral oil defoamer from BASF (Ludwigshafen; Germany); NaOH = sodium hydroxide.

RUN NUMBER		11.0	11.1	11.2	12.0	12.1	12.2	19.0	19.1	20.0	20.1	17.0	17.1	17.2	17.3	18.0	18.1	18.2
FORMULATION		X	X	X	X	X	X	Y	Y	Y	Y	Z	Z	Z	Z	Z	Z	Z
MACHINE SETTINGS																		
Blade	(B=Bent)	20-45	20-45	20-45	20-45	20-45	20-45	20-45	20-45	20-45	20-45	20-45	20-45	20-45	20-45	20-45	20-45	20-45
Rod	(G=Grooved)																	
Head Angle		49.7	49.7	49.7	49.7	49.7	49.7	49.7	49.7	49.7	49.7	49.7	49.7	49.7	49.7	49.7	49.7	49.7
Head Stops	(in.)																	
Applicator Roll Speed	(%)	22	22	22	22	22	22	22	22	22	22	22	22	22	22	22	22	22
Applicator Roll Gap	(in.)																	
Coater Speed	(FPM)	1500	1500	1500	1500	1500	1500	1500	1500	1500	1500	1500	1500	1500	1500	1500	1500	1500
Coated Side		Felt	Felt	Felt	Inside	Inside	Inside	Felt	Felt	Inside	Inside	Felt	Felt	Felt	Felt	Inside	Inside	Inside
RUN VARIABLES																		
Basestock Moisture	(%)	3.8	3.8	3.7	3.4	3.2	3.2	3.6	3.6	3.2	3.3	3.9	3.8	3.6	3.5	3.5	3.4	3.2
Coat Weight	(lbs./3300 SF)	4.1	4.7	6.6	3.8	4.8	7	4	5.1	3.6	5.7	4.5	5.6	6.6	3.5	4.2	6.2	7.6
Moisture	(%)	3.6	4.1	4.1	4.1	4.4	4.3	4	4	4.5	5.6	4.2	4.6	4.5	3.5	4.2	3.8	4.1
Tube Load	(PSI)	23.9	13.9	6	16.1	9.5	5	19.4	11.9	15.9	6	23.9	21	12.9	23.8	16.9	10.9	8
DRYER SETTINGS																		
IR Preheat	(%)																	
IR Zone 1	(%)																	
IR Zone 2	(%)																	
TEC 1 Temperature	(°F)	275	275	450	350	350	475	300	375	325	350	325	375	500	350	375	500	500
Pressure	(in. of water)	0.5	0.5	1	1.5	1.5	1.5	1	1.5	1	2	0.7	1	1.3	0.5	1	1.5	1.5
TEC 2 Temperature	(°F)	275	275	450	350	350	475	300	375	325	350	325	375	500	350	375	500	500
Pressure	(in. of water)	0.5	0.5	1	1.5	1.5	1.5	1	1.5	1	2	0.7	1	1.3	0.5	1	1.5	1.5
TEC 3 Temperature	(°F)	275	275	450	350	350	475	300	375	325	350	325	375	500	350	375	500	500
Pressure	(in. of water)	0.5	0.5	1	1.5	1.5	1.5	1	1.5	1	2	0.7	1	1.3	0.5	1	1.5	1.5
TEC 4 Temperature	(°F)	175	175	450	350	350	475	300	375	325	250	325	175	175	350	175	300	175
Pressure	(in. of water)	0.5	0.5	1	1.5	1.5	1.5	1	1.5	1	2	0.7	1	1.3	0.5	1	1.3	1.3
SHEET TEMPERATURE																		
IR Preheat	(°F)	72	72	72	74	73	73	69	69	70	70	73	72	68	69	69	69	69
Before TEC 1	(°F)	74	74	72	74	74	74	71	71	71	71	76	76	70	70	69	69	70
After TEC 1	(°F)	119	116	132	126	128	137	116	124	122	126	122	130	136	121	128	139	144
After TEC 2	(°F)	128	124	138	158	144	150	134	146	147	140	128	135	155	146	155	170	177
After TEC 3	(°F)	149	138	170	189	184	199	157	177	178	183	149	167	194	164	193	217	231
After TEC 4	(°F)	139	140	189	206	207	224	178	199	199	194	170	170	168	174	213	218	206
Reel	(°F)	79	79	85	98	105	110	82	84	96	101	89	92	84	82	96	103	104

Improvements in oil and grease resistance (OGR) test methodology for waterborne barrier coatings

ALLYSON MARIANELLI, BRIAN EINSLA, ELIZABETH SHOW, SAMANTHA WOODFIN, BO SHUANG, KEVIN HENDERSON, MIKE LINSEN, JONATHAN DEROCHER, AND SHAWN OLIVER

ABSTRACT: Paper-based food packaging is becoming more popular due to consumer demands for sustainable packaging options. Waterborne paper coatings that provide performance properties (i.e., resistance to oil and grease) not inherent to paper and board substrates offer improved sustainability profiles over earlier paper treatment options, including fluorocarbon treatment and coating with extruded plastics. The continued development of new paper coating technologies requires re-evaluation of current test methods and development of new methods to ensure lab evaluations can serve as accurate predictors of real-world performance.

This paper provides an overview of commonly used oil and grease resistance (OGR) test methods within the paper coatings industry, and then describes improvements and developments made to two key methods: the 3M Kit test and an internally developed oil breakthrough test. The combined use of these adapted methods provides a more efficient testing workflow and a more complete understanding of the OGR performance of barrier coatings.

Application: The development of new barrier coatings for paper packaging requires robust and quantitative methods for performance evaluation. This paper reviews industry standard oil and grease resistance (OGR) test methods and describes improvements to two key methods: the 3M Kit test (TAPPI Standard Test Method T 559) and an internally developed oil breakthrough test.

As the demand for more sustainable food packaging continues to grow, focus has shifted towards paper-based packaging. However, paper by itself has poor barrier performance against many of the substances food packaging is in contact with, including oil/grease, water, moisture vapor, and oxygen. This lack of barrier performance highlights the need for paper coatings that impart resistance to substrates and enables them to be used in applications such as quick service restaurant containers, sandwich and bakery wraps, and cups.

Paper-based oil and grease resistant (OGR) packaging has traditionally been achieved through either wet-end treatment with perfluoroalkyl substances (PFAS) or coating paper with extruded plastics. The PFAS are currently facing regulatory and consumer pressure due to increasing environmental and health concerns [1], while extrusion-coated paper products often require thick coatings that can impact product cost and recyclability. Waterborne paper coatings offer a more environmentally friendly alternative without the use of fluorochemicals or the need for thick films.

Robust, quantitative, and rapid performance testing is critical to ensure that new product candidates meet expectations both in a laboratory setting when compared with competitive offerings, but more importantly in the real-world application where they will be employed.

A traditional method for evaluating the oil and grease resistance (OGR) of paper food wraps is the 3M Kit test (TAPPI Standard Test Method T 559 "Grease resistance test for paper and paperboard"), which was developed to test the degree of repellency and/or the anti-wicking properties of fluorocarbon-treated paper or paperboard. Because it was not designed to evaluate film-based barrier performance, its practicality is decreasing as PFAS-treated materials are being phased out of the market. Additionally, the test method suffers from limitations including short evaluation time (15 s), inherent subjectiveness of the operator, and the use of solutions (blends of castor oil, toluene, and heptane) that the final product will not likely be exposed to (**Table I**). While paper suppliers still request Kit data when evaluating new barrier coatings, many admit the test does not predict real-world performance in their targeted application area.

Another well-known method, the RP2 test developed by Ralston Purina to predict performance of pet food packaging, evaluates performance over longer periods of time at elevated temperatures [2-4], but is much more time consuming from a data collection/analysis standpoint and relies on manual counting of grid squares with oil breakthrough.

The ASTM F119-82 "Standard method for rate of grease penetration of flexible barrier materials" describes a comparable method for evaluating longer-term resistance to oils and similarly requires a significant time commitment for testing and analysis.

3M Kit Test Solution Compositions			
Kit #	% Castor Oil	% Toluene	% Heptane
1	100.0	0.0	0.0
2	91.9	4.6	3.5
3	83.5	9.3	7.2
4	74.6	14.3	11.0
5	65.4	19.5	15.0
6	55.8	25.0	19.2
7	45.7	30.7	23.6
8	35.1	36.7	28.2
9	24.0	43.0	33.1
10	12.3	49.6	38.1
11	0.0	56.5	43.5
12	0.0	51.5	48.5

I. Compositions of Kit solutions (in weight/weight%).

Other relevant OGR standardized test methods include: TAPPI T 454 "Turpentine test for grease resistance of paper," TAPPI T 507 "Grease resistance of flexible packaging materials," and the Solvay fatty acid test. **Table II** describes several OGR test methodologies that could be evaluated and compared in the future to expand on this work.

The oil breakthrough test described in this paper (**Fig. 1**) reflects an internally developed method designed to address key gaps and challenges associated with the previously described tests. The test evaluates resistance to breakthrough of a test oil (typically vegetable oil) onto underlying graph paper over a period of 24 h at elevated temperature (60°C). The test provides additional flexibility of test conditions, with the ability to use customer-specific test liquids in the place of vegetable oil, change the length and temperature of the test, and fold the coated substrate prior to evaluation to probe film flexibility.

Although the PFAS-treated materials that the Kit test was designed to evaluate are being phased out of the market, the short duration of the test could be beneficial for screening studies if a correlation was established between Kit scores and longer-term OGR performance. Some of the work in this paper was completed to determine whether the Kit test can still provide relevant performance information to aid in down-selection of high performing candidates for additional testing.

This paper describes improvements to the internally developed oil breakthrough test and the Kit test. First, more aggressive Kit solutions were added to enhance differentiation between high-performing samples. Second, an image analysis program was developed to reduce human error in measurement and increase experimental efficiency for the oil breakthrough test. The combination of these adapted methods provides a more complete understanding of the OGR performance of barrier coatings.

EXPERIMENTAL METHODS

Coating preparation

Coating formulations were prepared targeting the maximum solids content possible for each coating based on solids content of binders, additives, and thickeners (between 39%–50% solids) and a Brookfield viscosity of 600 cP at 100

Method	Test Liquid	Time	Temperature	Weight	Results
TAPPI T 559 "Grease resistance test for paper and paperboard" (3M Kit)	Solutions containing castor oil, toluene, and heptane	15 s	Room temperature (23°C)	None	Most aggressive solution without breakthrough
RP2	Proprietary synthetic oil	24 h	40°C	5 g sand	Percent of stain on grid paper
ASTM F119-82 "Standard method for rate of grease penetration of flexible barrier materials"	Animal oil, mineral oil, vegetable oil, and other reagents	Until sample failure	40°C or 60°C	50 g weight	Time at which sample failure/penetration occurs
TAPPI T 454 "Turpentine test for grease resistance of paper"	Dyed turpentine	Up to 30 min	Room temperature (23°C)	5 g sand	Time at which sample failure/penetration occurs
TAPPI T 507 "Grease resistance of flexible packaging materials"	Oleic acid, vegetable oil, mineral oil, and other fats/oils	4 h	60°C	408 g block	Number and area of stained spots
Fatty acid test	Solutions containing castor oil, oleic acid, and octanoic acid	5 min	60°C	None	Most aggressive solution without breakthrough/ discoloration

II. Summary of various oil and grease resistance (OGR) test methods.

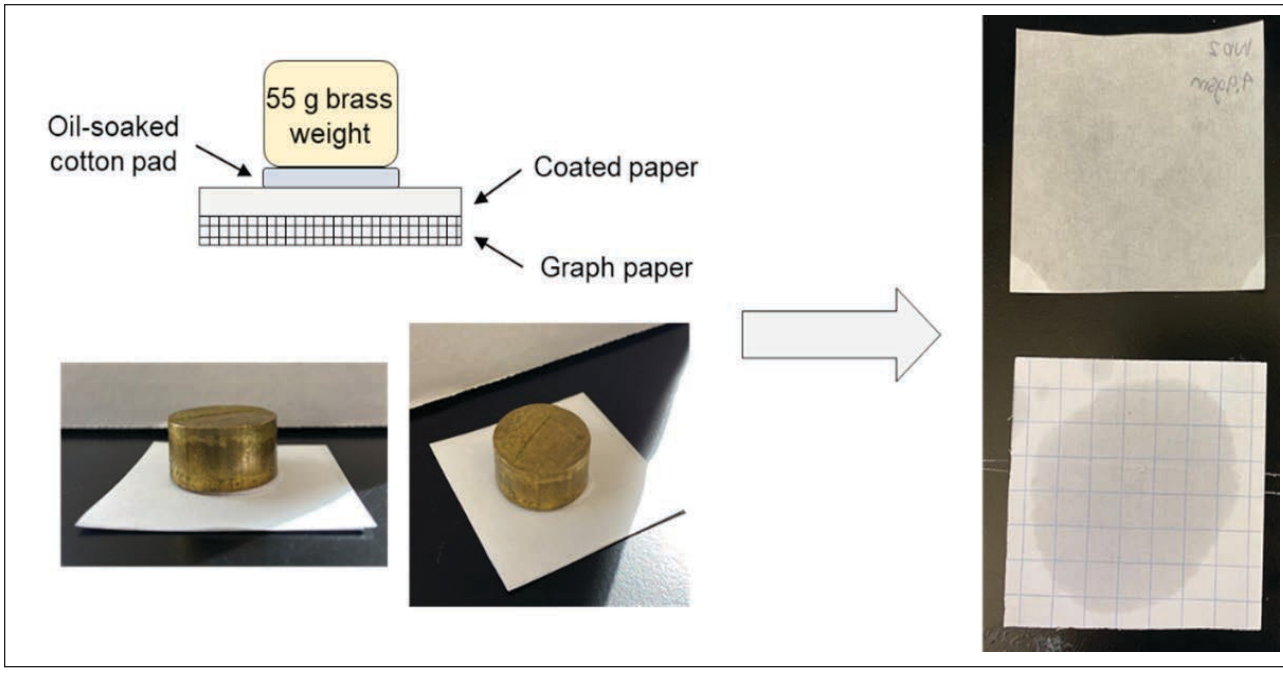

1. Illustration of oil breakthrough test procedure for oil and grease resistance.

rpm. Latex binders were mixed with each other, additives, deionized water, and an alkali-swellable emulsion thickener under constant stirring for approximately 20 min using an overhead benchtop mixer.

Preparation of coated paper samples

Hand drawdowns

Formulated coatings were applied to NewPage (Miamisburg, OH, USA) freesheet paper (basis weight: 58 g/m², roughness: 4.00 µm, Gurley porosity: 24.6 s) in the machine direction using an automated coater (K Control Coater, RK Print Coat Instruments; Royston, UK) equipped with various wire wound rods to achieve coat weights ranging from 4–10 g/m². Samples were dried at 80°C for 2 min. Coat weights were determined by calculating the difference between the basis weight of the substrate and the average weight of at least six 2 in. x 3.5 in. punched out coated samples. Coated paper was conditioned in a temperature-controlled room for at least 1 h in accordance with TAPPI T 402 "Standard conditioning and testing atmospheres for paper, board, pulp handsheets, and related products."

Performance testing

3M Kit testing

Coated paper samples were tested for oil and grease resistance using TAPPI T 559. Kit solutions composed of castor oil, toluene, and heptane in varying ratios were applied dropwise to the coated substrate, allowed to sit for 15 s, and then wiped away. Any occurrence of solvent breakthrough or substrate discoloration was classified as a failure for that Kit solution. The Kit score for a given sample was assigned using the number of the highest (most aggressive) Kit solution that passed on that coated substrate. Higher Kit scores indicate better performance. Kit tests were performed in replicates of six.

Oil breakthrough test

Coated paper samples were also evaluated for oil and grease resistance using an internally developed oil breakthrough test. Coated paper substrates were cut to 2 in. x 2 in. squares and weighed, before being placed coated side facing up atop graph paper squares (also cut to 2 in. x 2 in. and weighed). A 1-in. diameter cotton pad was placed on top of the coated substrate and then saturated with 600 µL of vegetable oil via pipette addition (Crisco pure vegetable oil, B&G Foods; Parsippany-Troy Hills, NJ, USA). Immediately after saturating cotton pad with oil (within 5 min), a 55 g brass weight was placed on the cotton pad, and the samples were placed in the oven at 60°C for 24 h. After cooling samples for 5 min at room temperature (23°C), the weight and cotton pad were removed, and any remaining oil was wiped from the substrate. The coated substrate and graph paper were both weighed to calculate the amount of oil absorbed by each substrate, and the number of squares on the graph paper with visible oil breakthrough was counted. Lower breakthrough percentages indicate better performance. Each sample was tested in replicates of nine. A step-by-step protocol for this test method is included in the Appendix.

RESULTS AND DISCUSSION

Multiple waterborne latex dispersions were applied at varying coat weights and evaluated using both the Kit and oil breakthrough tests (**Fig. 2**). A weak correlation between

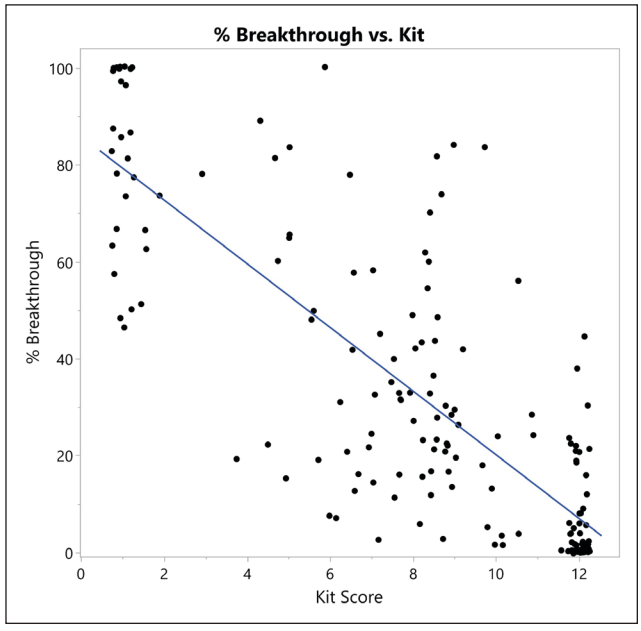

2. Percentage of oil breakthrough from oil breakthrough test as a function of Kit score (1-12) for waterborne latex dispersions at various coat weights. Data points have been jittered to aid visibility of densely populated graph areas. The coefficient of determination (R^2 = 0.65) between Kit and oil breakthrough test performance demonstrates a weak correlation between the two data sets.

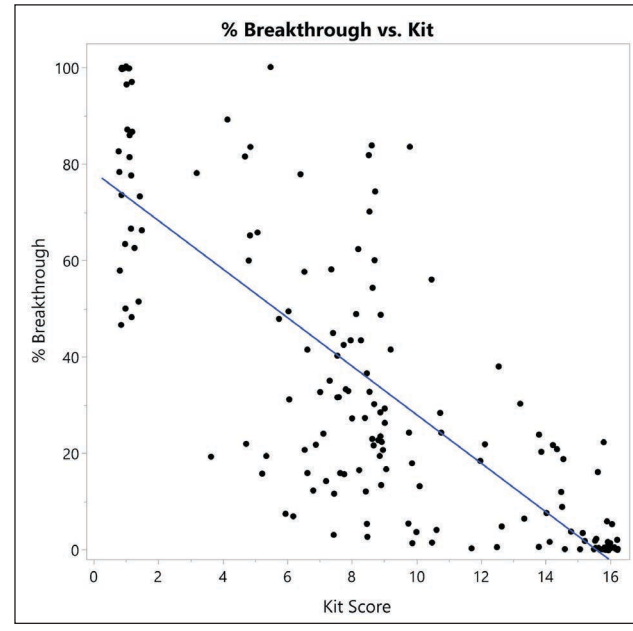

3. Percentage of oil breakthrough from the oil breakthrough test as a function of Kit score (1-16) for waterborne latex dispersions at various coat weights. Data points have been jittered to aid visibility of densely populated graph areas. The coefficient of determination (R^2 = 0.64) between Kit and oil breakthrough resistance demonstrates a weak correlation between the two data sets.

the two types of data was identified, although there is significant spread in the data that makes it challenging to predict performance of one test based on the performance of another. Samples with low Kit scores (<6) consistently resulted in poor oil breakthrough resistance as well, with breakthrough percentages >40%. This finding enabled the use of Kit testing as a screening method to identify and eliminate coatings with poor performance, which improved experimental efficiency, as the oil breakthrough test is much more time-consuming than the Kit test. Unfortunately, coated samples with the maximum Kit score (12) had oil breakthrough ranging from 0–45%, suggesting the Kit scores cannot always be used to predict high performance in the oil breakthrough test.

A recently published patent by Taniguchi [5] describes the use of additional, more aggressive Kit solutions (13-16) to achieve further differentiation between samples with high Kit performance. Following the trends identified in original Kit solution compositions, solutions 13-16 were prepared using increasing proportions of heptane to toluene (**Table III**).

Kit #	Castor Oil, %	Toluene, %	Heptane, %
13	0	46.4	53.6
14	0	41.2	58.8
15	0	35.8	64.2
16	0	30.2	69.8

III. Compositions of additional Kit solutions, Kit 13 – Kit 16 (in weight/weight%).

When Kit testing was conducted using the expanded set of 16 solutions, the correlation between Kit and oil breakthrough resistance remained similar (**Fig. 3**). However, coated samples with the new maximum Kit score (16) now had oil breakthrough ranging from 0–25%, suggesting an increase in the likelihood that a sample that had excellent Kit performance will also have good oil breakthrough resistance. Figures 2 and 3 are comprised of the same data set representing the same samples, with the only difference being the range of Kit solutions used. In Fig. 2, many samples achieved the maximum Kit score of 12, while in Fig. 3, those same samples had a range of Kit scores between 12 and 16, highlighting the improved ability to differentiate between samples with high Kit performance. Internal testing procedures were updated to include the four additional Kit solutions in future testing to aid in the screening and down-selection of large sample sets.

The combination of Kit and oil breakthrough testing provided a broader understanding of the OGR performance of current products and new candidates. However, the oil breakthrough test required a significant time commitment not only for the procedure itself but also for data analysis. The initial method for analysis of oil breakthrough test data included measuring the amount of oil absorbed into the coated substrate and the underlying

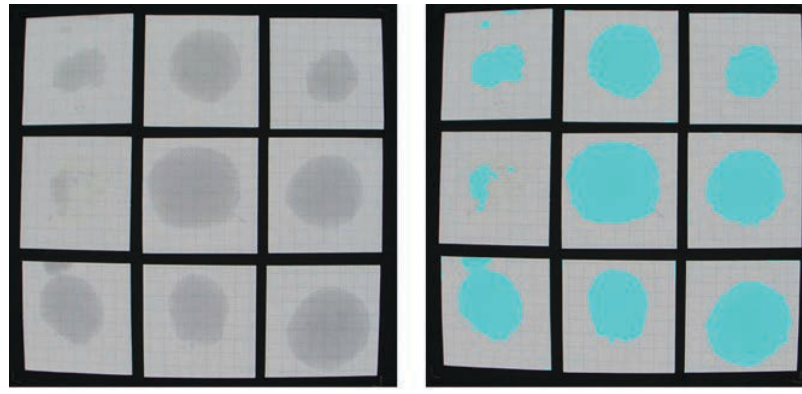

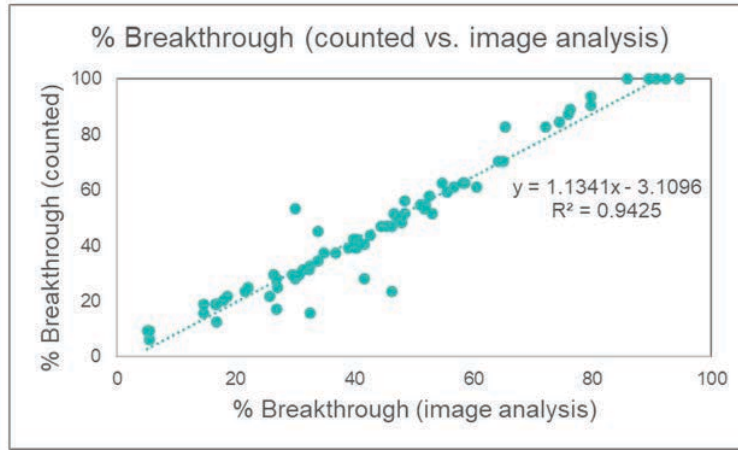

4. Raw (left) and analyzed (right) images of nine replicates of oil breakthrough testing. The analyzed images are highlighted to indicate areas identified as having oil saturation. A plot of the percentage of breakthrough collected via manual counting by the percentage of breakthrough collected via image analysis shows a strong linear correlation, with $R^2 = 0.9425$.

graph paper, along with estimating the amount of oil breakthrough by counting the number of saturated squares within the graph paper. This method proved to be time consuming and thus limited both the number of coatings evaluated and the number of replicates completed per sample, decreasing the usefulness of the test and the statistical strength of the data.

Through collaboration with an internal digitalization team, an image analysis program (and associated image capture station) was developed to measure the amount of oil breakthrough on the underlying graph paper to eliminate the need for manual counting. Up to nine replicates per sample can be imaged and analyzed at once, and the measured area of breakthrough is highlighted in the resultant images, allowing for manual confirmation of results (**Fig. 4**). The correlation between data collected using image analysis and data collected via manual counting was strong, with $R^2 = 0.9452$ (Fig. 4). Adoption of the image analysis program increased the efficiency of oil breakthrough test data analysis by 80% (i.e., from 8 h to 2 h for a set of 12 samples evaluated at 2 coat weights each).

The oil breakthrough test can be modified to evaluate performance over a range of conditions (time, temperature, pressure) against different test liquids to more closely mimic customer testing and real-world use cases. Because the end applications for OGR paper can vary significantly, some packaging may need to withstand heated oil/grease (hamburger wrappers or microwavable containers), while others only need to perform at room temperature (bakery wraps). Similarly, some applications require performance for a longer period of time (snack packaging), while others only require OGR for short windows of time (sandwich wrap).

To better understand how performance varies with test conditions, three coating samples were evaluated using the oil resistance test with vegetable oil as the test solution at three different conditions: 24 h at 60°C, 24 h at room temperature, and 1 week at room temperature (**Fig. 5**). The three samples exhibited different levels of sensitivity to the changing test conditions, with Sample 1 being most impacted and Sample 2 being least impacted. Unsurprisingly, samples generally performed better when evaluated at room temperature for 24 h than at 60°C for 24 h or room temperature for 1 week. In the case of Samples 2 and 3, a student's t-test revealed no statistical difference between the performance at 60°C for 24 h and room temperature for 1 week, suggesting that in some cases the added stress from elevated temperature may be able to mimic the effect of longer test periods.

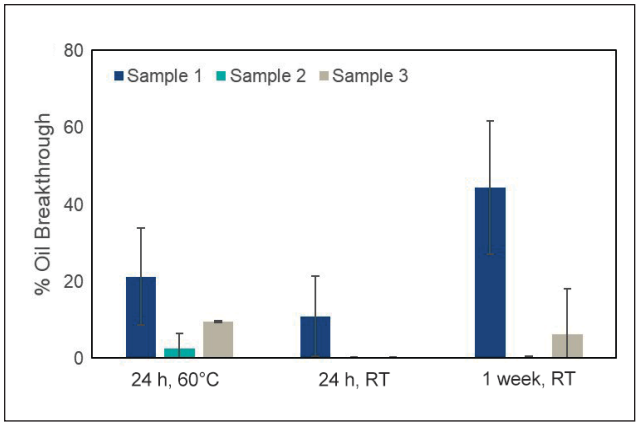

5. Oil breakthrough results for three different coating samples at moderate coat weights (6–8 g/m²) at three different test conditions: 24 h at 60°C, 24 h at room temperature, and 1 week at room temperature (RT). Error bars represent the standard deviation of nine replicates.

While these findings should be further probed with a broader range of coating samples and test periods to better understand the correlation between increased temperature and increased evaluation time, the ability to evaluate the impact of longer exposure times without having to increase testing time would be useful for increasing workflow efficiency.

RECOMMENDATIONS/FUTURE WORK

This research paper investigated the relationship between two OGR test methods. As the market space continues to grow, the number of test methods, both standardized and customer-specific, is also likely to expand.

- A larger comparison study that evaluates the same coatings and substrates across a broader range of test methods would be beneficial to allow researchers to identify correlations between test methods and more easily predict performance for specific customers/application spaces.
- The identification or development of test methods that can differentiate between barrier failure mechanisms would allow a more targeted approach to product development.
  - Low quality of barrier film, including pinholes and inflexibility, could be resolved through addition of film formation aids.
  - Poor oil resistance properties of the barrier material itself would need to be addressed through material composition.
  - Due to the long evaluation time of the oil breakthrough test, poor performance could be caused by film defects, inherent material properties, or a combination of both.

CONCLUSIONS

Modifications were made to both the 3M Kit test and the oil resistance test to improve performance testing capabilities and achieve a broader understanding of oil and grease resistance of waterborne latex paper coatings.

- The inclusion of four additional Kit solutions of increasing severity (13-16) afforded the opportunity to achieve better differentiation among high performing coatings and enhanced our ability to use the Kit test as a screening method when evaluating a large volume of coatings.
- The oil breakthrough test provided coating breakthrough data with a more directly applicable test liquid over longer periods of time, but the original protocol was incredibly time consuming. The use of an internally developed image analysis program reduced data analysis time by 80%.
- These advancements have resulted in a broader and more robust oil and grease resistance testing protocol that can be easily modified to suit customer-specific evaluations. **TJ**

LITERATURE CITED

1. Schaider, L.A., Balan, S.A., Blum, A., et al., *Environ. Sci. Technol. Lett.* 4: 105(2017). https://doi.org/10.1021/acs.estlett.6b00435.
2. Ralston-Purina Company, *Packaging Reference Manual Volume 06 – Test Methods*, Ralston Purina Company, St. Louis, MO, USA.
3. Liu, Y., U.S. pat. 2005/0223789 (Oct. 13, 2005).
4. Jho, C., Borsody, I., and Ghosh, T., U.S. pat. 2006/0122318 (Jun. 8, 2006).
5. Taniguchi, T., Jpn. pat. JP3488675B2 (Jan. 19, 2004).

APPENDIX

Standard operating procedure for oil breakthrough test

1. Heat oven to 60°C (or desired temperature).
2. Cut nine samples of each coated substrate to be evaluated to 2 in. x 2 in. squares.
3. Cut nine 2 in. x 2 in. squares of underlying test paper (grid paper if using grid squares to count approximate breakthrough area or white copy paper if using image analysis software).
4. Place each sample of coated substrate coated side up on top of a square of test paper. It is best practice to prepare the samples on a tray so they can be quickly placed into the oven after preparation.
5. Place a 1-in. diameter round cotton pad on top of each coated substrate.
6. Using a pipette, dispense 600 µL of vegetable oil (or desired test liquid) onto the cotton pad.
7. Place a 55 g circular brass weight (1-in. diameter) on top of the saturated cotton pad.
8. Place the prepared samples in the oven for 24 h (or desired evaluation time).
9. Upon removal of the samples from the oven, allow them to cool at room temperature (23°C) for 5 min.

10. Remove the brass weights, cotton pad, and coated substrate.
11. If using graph paper as the underlying substrate, capture photographs of each square of graph paper, then use the grid squares to measure the percentage of the square with oil breakthrough. If using image analysis software, capture photographs of each square of copy paper to import into analysis software.
12. Results are reported in percentage of the underlying test square with oil breakthrough present. Lower percentages represent better oil resistance of the coated substrate.

ABOUT THIS PAPER

Cite this article as:
Marianelli, A., Einsla, B., Show, E., et al., *TAPPI J.* 21(11): 645(2022). https://doi.org/10.32964/TJ21.11.645

DOI: https://doi.org/10.32964/TJ21.11.645

ISSN: 0734-1415

Publisher: TAPPI Press

Copyright: ©TAPPI Press 2022

About this journal

ABOUT THE AUTHORS

Test method improvement is critical to evaluation of experimental candidates for product development. The improved test methods in this research paper provide a broader understanding of the oil and grease resistance (OGR) of experimental candidates.

The most challenging aspect of this research was the variability in data points, due in part to the roughness/porosity of paper substrates and local variability in coating thickness. This was addressed by conducting statistical analyses on experimental data to ensure an appropriate amount of replicates were evaluated and that observed impacts were supported by data.

We reviewed new oil and grease resistance (OGR) test methods as part of this research. We found that though there is a broad range of oil and grease resistant (OGR) test methods, overall the methods have more similarities than differences.

The additional, more aggressive Kit solutions described here can be utilized immediately in mills with minimal modifications to their current workflow. The correlation between Kit performance and oil breakthrough performance can provide additional confidence that the Kit-screened materials can perform as expected during real-world evaluations.

An ideal next step would be a broader study comparing performance of multiple coatings across a larger number of test methods to identify trends and correlations between methods. An additional follow-up project would be the development of a test method that can distinguish between mechanisms of failure (i.e., poor film formation vs. poor inherent grease resistance of coating).



Marianelli



Einsla



Show



Woodfin

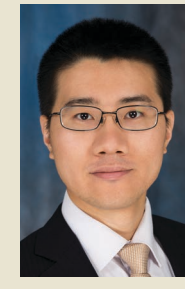

Shuang



Henderson



Linsen



DeRocher

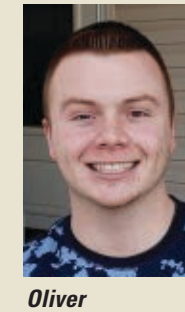

Oliver

Marianelli is associate research scientist, Einsla is senior research scientist, Snow is R&D/TS&D technologist, Woodfin is senior R&D/TS&D technician, Henderson is senior TS&D scientist, Linsen is senior TS&D specialist, DeRocher is senior TS&D scientist, and Oliver was a senior R&D/TS&D technician for Dow Coating Materials in Collegeville, PA, USA. Shuang was a research scientist at Dow Polyurethanes in Freeport, TX, USA. Email Marianelli at amarianelli@dow.com.